Proceedings of the 10th Asian Conference on

SOLID STATE IONICS

ADVANCED MATERIALS FOR EMERGING TECHNOLOGIES

Kandy, Sri Lanka 12 – 16 June 2006

Editors

B. V. R. Chowdari

M. A. Careem

M. A. K. L. Dissanayake

R. M. G. Rajapakse

V. A. Seneviratne

Asian Society for Solid State Ionics

World Scientific

SOLID STATE IONICS

ADVANCED MATERIALS FOR EMERGING TECHNOLOGIES

This page is intentionally left blank

Proceedings of the 10th Asian Conference on

SOLID STATE IONICS

ADVANCED MATERIALS FOR EMERGING TECHNOLOGIES

Kandy, Sri Lanka 12 – 16 June 2006

Editors

B. V. R. Chowdari
National University of Singapore
Singapore

M. A. Careem
M. A. K. L. Dissanayake
R. M. G. Rajapakse
V. A. Seneviratne
University of Peradeniya
Sri Lanka

Asian Society for Solid State Ionics

World Scientific

NEW JERSEY • LONDON • SINGAPORE • BEIJING • SHANGHAI • HONG KONG • TAIPEI • CHENNAI

Published by

World Scientific Publishing Co. Pte. Ltd.

5 Toh Tuck Link, Singapore 596224

USA office: 27 Warren Street, Suite 401-402, Hackensack, NJ 07601

UK office: 57 Shelton Street, Covent Garden, London WC2H 9HE

British Library Cataloguing-in-Publication Data

A catalogue record for this book is available from the British Library.

Proceedings of the Tenth Asian Conference on Solid State Ionics

ISBN 981-256-877-8

Printed in Singapore by World Scientific Printers (S) Pte Ltd

Organization

Organizers

Postgraduate Institute of Science &
Faculty of Science, University of Peradeniya, Sri Lanka

Asian Society for Solid State Ionics

International Advisory Committee

T W Anderson	Sweden	S Greenbaum	USA	J-L Souquet	France
M Armand	France	C Granquist	Sweden	GV Subba Rao	Singapore
A K Arof	Malaysia	A R Kulkarni	India	Dale Teeters	USA
B Rambabu	USA	R G Linford	UK	Wenji Wang	China
S Badwal	Australia	A Manthiram	USA	A R West	UK
D Brinkman	Switzerland	B-E Mellander	Sweden	W Weppner	Germany
P G Bruce	UK	S S Pandian	India	M Yahaya	Malaysia
S Chandra	India	S Prabaharan	Malaysia	O Yamamoto	Japan
BVR Chowdari	Singapore	J-Y Sanchez	France	H-I Yoo	Korea
John Furneaux	USA	S Selladurai	India	M Yoshimura	Japan
Maria Forsyth	Australia	Kamal Singh	India	Roger Frech	USA
		S Skaarup	Denmark		

Local Advisory Committee

Director, Postgraduate Institute of Science
Dean, Faculty of Science, University of Peradeniya
Kirthi Tennekone, Institute of Fundamental Studies
D T B Tennekoon, University of Peradeniya
T Ariyaratne, University of Colombo
W Siripala, University of Kelaniya
G Dharmaratne, University of Ruhuna
R Kumaravadivel, University of Jaffna
S Pathmanathan, Eastern University
S Thantrigoda, Sri Jayawardanepura University

Organizing Committee

M A K L Dissanayake (Co-Chairman)
M A Careem (Co-Chairman)
R M G Rajapakse (Coordinator)
V A Seneviratne (Secretary)

R Ahilan	L R A K Bandara	B A Karunaratne	K Premaratne
N Balasooriya	P W S K Bandaranayake	B S B Karunaratne	G K R Senadeera
N C Bandara	Jagath Gunathilake	D M M Krishantha	H H Sumathiapala
H M N Bandara	O A Ileperuma	Kumudu Perera	Kamal Vidanapathirana

Sponsoring Organizations

Materials Research Society of Singapore (MRS-S)
Asian Society for Solid State Ionics (ASSSIS)
Abdus Salam International Centre for Theoretical Physics (ASICTP), Trieste, Italy
International Programmes in Physical Sciences (IPPS), Uppsala, Sweden
National Science Foundation (NSF), Colombo, Sri Lanka
University Grants Commission (UGC), Colombo, Sri Lanka
Postgraduate Institute of Science (PGIS), University of Peradeniya, Sri Lanka
Faculty of Science, University of Peradeniya, Sri Lanka

Preface

The field of Solid State Ionics deals with ionically conducting materials in the solid state and numerous devices based on such materials. Solid State Ionic Materials cover a wide spectrum, ranging from inorganic crystalline and polycrystalline solids, ceramics, glasses, polymers, composites and also nano-scale materials.

A large number of Scientists in Asia is engaged in research in Solid State Ionic Materials and Devices. The Asian Society for Solid State Ionics has played a key role in organizing a series of bi-ennial conferences on Solid State Ionics in different Asian countries starting from 1988. The last two conferences were held in Langkawi Island, Malaysia (2002) and Jeju Island, Korea (2004). The present conference, organized by the Postgraduate Institute of Science (PGIS) and the Faculty of Science, University of Peradeniya, Sri Lanka, is the tenth in the series and it also coincides with the 10^{th} Anniversary of the Postgraduate Institute of Science (PGIS).

Research papers based on a wide variety of solid state ionic materials and devices are published in the proceedings. The topics cover inorganic crystalline and poly crystalline solids, ceramics, glasses, polymers, composite materials and nano-scale materials as well as devices such as solid state batteries, fuel cells, sensors, electrochromic devices and so on. The aspects covered include, theoretical studies and modeling, experimental techniques, materials synthesis and characterization, device fabrication and characterization and many more.

Our sincere thanks are extended to all the invited speakers and the authors of the contributed papers for their prompt cooperation which enabled the publication of the Proceedings in time.

We express our gratitude to all the sponsors listed in the Proceedings for their sponsorship and interest in this activity. In particular, we are grateful to the Materials Research Society of Singapore for sponsoring the entire cost of publication of the Proceedings. The International Programme in Physical Sciences (IPPS), Uppsala, Sweden has been supporting the Solid State Ionics Research Project at Peradeniya since 1984. The Director of IPPS, Prof. Lennart Hasselgren deserves our fondest gratitude. We mention with pride that the Peradeniya group completes its 20^{th} year of solid state ionics research this year.

We are grateful to the Vice-Chancellor of the University of Peradeniya and the Dean and the Staff of the Faculty of Science at Peradeniya, and the Staff of the Postgraduate Institute of Science for their active cooperation rendered in organizing the Conference.

Last, but not least, we thank the International and Local Advisory Committees for their guidance and the Local Organizing Committee for their untiring efforts which has made this event a success.

20 April 2006

B. V. R. Chowdari
M. A. Careem
M. A. K. L. Dissanayake
R. M. G. Rajapakse
V. A. Seneviratne

Contents

Contributed Papers

Contributed Papers

Contributed Papers

Contributed Papers

CHALLENGES AND OPPORTUNITIES OF SOLID STATE IONIC DEVICES

WERNER WEPPNER

Chair for Sensors and Solid State Ionics
Faculty of Engineering, Chr.-Albrechts University Kiel
Kaiserstr. 2, 24143 Kiel, Germany
ww@tf.uni-kiel.de

High energy density batteries, fuel cells, electrolysis cells, electrochromic devices, chemical sensors, thermoelectric converters or photogalvanic solar cells are solid state ionic devices of large practical interest in view of our energy and environmental problems. The engineering of new or improved devices is commonly based on individual materials considerations and their interaction in galvanic cells. Conflicts exist in view of the formation of chemically stable interfaces of functionally different electrolyte and electrode materials, simultaneous high energy and power densities because of commonly low conductivities of chemically stable materials, fast chemical diffusion in electrodes which should have a wide range of non-stoichiometry, practical problems of using less expensive polycrystalline materials which have high intergranular resistances and finally reaching both ionic and electronic equilibria at the electrolyte-electrode interfaces at low temperatures. Simultaneously high ionic conductivity and chemical stability may be reached by designing structures of large poly-ions of the non-conducting components. Electrodes should not be made of metallic conductors but of electronic semi-conductors with fast enhancement of the diffusion of the electroactive ions by internal electrical fields. Device considerations are based on the development of single element arrangements (SEAs) which incorporate the electrodes into the electrolyte in the case of fuel and electrolysis cells. The same simplification may be applied for electrochromic systems which consist of a single active layer instead of the conventional three materials. A new design of active chemical sensors probing the environment by the magnitude of the applied voltage or current may overcome the limitations of cross-sensitivities and interfacial reactions, which allows simultaneous sensing of several species by a single galvanic cell.

1. Introduction

The science and technology of Ionics is based on the phenomenon of ionic transport in the solid state. Since the very beginning of Nernst's discovery of ionic transport in several refractory oxides in the 1890's [1], there has been interest in the curiosity and application of this phenomenon. Major break-throughs have occurred with the understanding of the role of defects and the observation of ionic transport in solids as a quite general phenomenon [2] which may be also observed at ambient temperature [3]. The conductivities of several silver and alkaline ion conductors are of the same order of magnitude as the electronic conductivity in semi-conductors and ionic transport in common liquid electrolytes [4].

Both the numbers and mobilities of the defects play important roles. Doping with aliovalent ions is a common tool which turned out to be very successful, but structural pecularities are more frequently the cause of high ionic conduction. In the

latter case, many sites are available for the moving ion which are energetically nearly equivalent and serve as fast pathways for the ions.. The transition from doping to structural disorder is continuous and there are examples for both features, e.g., solid solutions of Li_4SiO_4 and Li_3PO_4 [5] which form extraordinarily large numbers of lithium vacancies.

In spite of the fast progress in disclosing many new compounds with fast ionic transport, progress is rather slow in most technologies where ionic and mixed electronic-ionic conductors play an essential role, e.g., fuel cells, batteries, electrochromics, sensors and thermoelectric converters. This is due to the fact that individual materials are rather meaningless for applications and instead the interfaces between ionically and mixed conducting materials are predominantly important [6]. This situation is similar to electronics where junctions between two different materials play the important role and not the electronic conductivity in bulk materials. Ionic devices take - in addition to the electronic junctions - advantage of the energetic equilibration of the mobile ions across the interface and the blocking of the ionic conductor for the electronic charge carriers in the bulk which therefore have to move through the outer circuit and may perform work in this way.

It is apparent that the ionic junctions are more complex because of the equilibration and motion of several charge carriers at interfaces and the alternating motion of different charge carriers in the different materials of the electrical circuit. Accordingly, specific engineering of solid state ionic devices is required which has to take into account the materials requirements of interfaces which appear to be often contradictary. The conflict in developing appropriate materials will be described and solutions of engineering ionic devices will be given for the development of materials and entire devices.

2. Requirements and Conflicts

A substantial number of fast predominantly ionically conducting solid electrolytes and mixed conducting electrodes with high chemical diffusion rates is presently known. In addition to these properties, several other requirements have to be fulfilled, which are often contradictory.

Interfacial Stability. The electrical fields occur at the electrolyte/electrode interfaces over a distance of atomic dimensions. Chemical reactions should therefore not occur within this regime over the lifetime of the device.

In a first approach it seems appropriate to choose materials which exist in thermodynamic equilibrium. As illustrated in Fig. 1 for a (quasi-) ternary lithium system, the electrolyte E should be located in the phase diagram in-between the positions of the anode A and cathode C on the straight line toward the lithium corner. Two-phase regimes have to exist in-between. Such systems may exist, however, the electrolyte and the electrodes have to have quite different functional properties. It is not very likely to find many systems in which this requirement is fulfilled, since the electronic and stoichiometric requirements are too different.

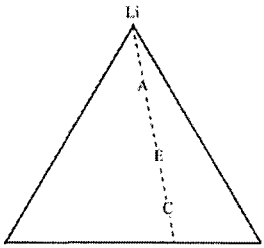

Fig. 1. Ternary or quasi-ternary lithium system with ideal compositions of the electrolyte E in-between the anode A and cathode C on a straight line which passes through the lithium corner. 2-phase regimes exist in-between the three phases. Anode and cathode should have wide ranges of non-stoichiometry in the direction of the lithium corner, while the electrolyte has a rather narrow stoichiometric width. Appropriate electronic and ionic conductivities of the three phases should exist.

Furthermore, a close mechanical contact has to exist at the interface in order to provide sufficiently large areas of ionic and electronic exchange. Since many systems have to undergo thermal cycling during preparation, the expansion coefficients should be as close as possible.

Energy vs. Power Density. For high energy densities electrodes have to be employed with large differences in the activities of the mobile component, i.e., electrolytes have to be employed with high decomposition voltages. In order to achieve also high current densities, it is necessary that the ions show high mobilities. Figure 2 compiles the decomposition voltage as a function of the activation energy of the ionic conductivity in the case of binary lithium ion conductors. In the limiting case of very high temperatures, the conductivities become more and more the same for all ionic conductors and the activation energy is accordingly reflecting the inverse of the conductivity at lower temperature at which the device is being employed. There is accordingly a dilemma in choosing either materials with high ionic conductivity but low stability or materials with low conductivity but high decomposition voltage. This is readily understood from the point of view that high decomposition voltages require strong chemical bonds which is in contrast to weak ones required for low interaction between the ions to allow

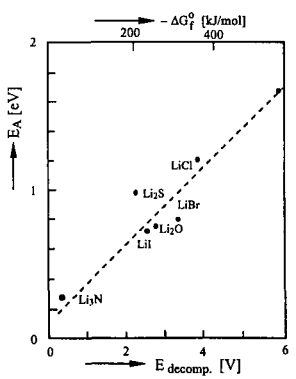

Fig. 2. Activation energy of the ionic conductivity vs. the decomposition voltage of binary lithium ion conductors. For a given temperature, the activation energy is inversely proportional to the conductivity. Therefore, chemically stable compounds show low conductivities while compounds with low chemical stability have high ionic conductivities. Strong chemical bonds prevent the ions from moving.

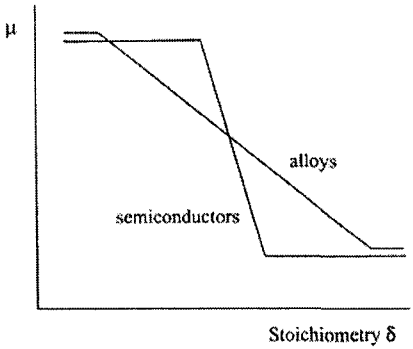

Fig. 3. The range of non-stoichiometry of compounds depends on the concentration of electronic charge carriers. The chemical potentials of the components are constant in 2-phase mixtures according to Gibbs' phase rule (in the case of binary or quasy-binary compounds), while the chemical potential of the neutral component drops over the range of stoichiometry. The chemical potential of the neutral component may be expressed by those of the ions and electrons. Considering that the chemical potential depends logarithmically on the concentration, the chemical potentials of the lithium ions, which are present in large numbers, may be considered to be constant. The electrons then control the drop of the chemical potential of the neutral component which is rapid in the case of small concentrations of electrons.

high mobilities.

Chemical Diffusion in Electrodes. In order to minimize concentration polarization, the ions have to be rapidly transported from the interior of the anode to the interface with the electrolyte and at the opposite interface into the cathode. For this purpose, high mobilities of the electroactive ions are required in both electrodes. In addition, the motion of the ions should be enhanced by the internal electrical fields generated by simultaneously moving electrons. The large enhancement of the motion of ions in chemical diffusion processes requires a small number of electronic charge carriers, which corresponds to a small stoichiometric width (Fig. 3). This is in contrast to the requirement of large reservoirs for the mobile ions in the electrodes.

The requirements of large phase widths and fast chemical diffusion in the electrodes are accordingly commonly not fulfilled simultaneously.

Practical Problems. The preparation of practically useful ionic conductors often involves the application of high temperatures, sputtering or evaporation. It is common that the compounds include some components that have high vapour pressures and other ones that have very low volatility. It is necessary to avoid the formation of compounds, which have eventually different stoichiometries than anticipated.

Further, for practical reasons, polycrystalline materials should be used instead of single crystals. These show commonly large resistances at the grain boundaries which are often larger than the bulk resistance. An example is shown in Fig. 4 which shows the polycrystalline structure of the fast ion conductor $Li_{0.3}Sr_{0.6}Ti_{0.5}Ta_{0.5}O_3$ [7]. The knowledge on this transport of ions across interfaces is presently quite limited.

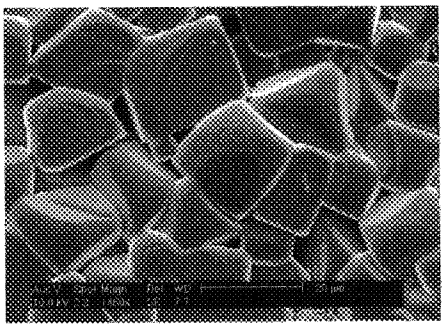

Fig. 4. Polycrystalline structure of the fast ion conductor $Li_{0.3}Sr_{0.6}Ti_{0.5}Ta_{0.5}O_3$. Large resistances are commonly observed at grain boundaries which are often larger than the bulk conductivity. Other materials are known with comparatively small contributions of the grain boundaries to the total conductivities.

Several investigations on the chemical composition of near-surface regimes have shown that major deviations occur compared to the bulk. Commonly, these are segregations of impurities or dopants. A practically important example is yttria stabilized zirconia of the composition 0.9 ZrO_2 - 0.1 Y_2O_3 which has been investigated by LEIS first in the pristine state after room temperature preparation followed by subsequent increase in temperature and analysis of the surface composition [8]. Starting at a temperature of about 900 °C, monolayers of impurity metal (Na, Si, Ca) oxides have been observed. Underneath these layers, yttria has been drastically enriched and the concentration has been increased to 45 %. Similar results have been observed for tetragonal zirconia which has a nominal yttria concentration of 3 mol-% but is enhanced at the surface up to 30 mol-%.

Chemical Non-Equilibria. Nernst's law requires thermodynamic equilibria at the electrolyte-electrode interfaces. The energies of both electrons and ions have to become balanced and thermodynamically most favourable phases should be formed. Very often, slow kinetics and relaxation processes prevents equilibration. An example is the interface between platinum and the oxide ion conductor zirconia,

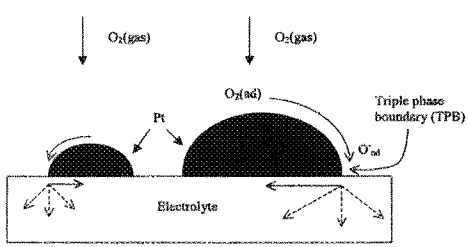

Fig. 5. Contact of the electronic lead with an oxide ion conducting zirconia electrolyte. Oxygen from the gas may be only incorporated into the zirconia lattice at the triple point electrolyte/platinum/gas. The voltages are generated by the electronic junction between the platinum plagues and the electrolyte. The response time is given by the diffusion of oxygen in zirconia along the phase boundary and electrons in the platinum.

which is used in the commercial λ-probe (Fig. 5) [9]. The oxygen molecules from the gas may take up electrons at the surface of platinum and may be only incorporated into the zirconia lattice at the triple point electrolyte/platinum/gas. The voltages are, however, generated along the entire interface Pt/ZrO_2. Only electrons may be exchanged at this interface since the solubility of oxygen in Pt is negligibly small. This junction is fully identical with a common electronic Schottky junction of a metal-semiconductor interface. However, the electronic concentration in zirconia is variable upon the change in the oxygen partial pressure of the gas. In case of an increase in the oxygen partial pressure, oxygen will be incorporated into the lattice, which decreases the number of electrons due to ionisation of the oxygen. The electrostatic potential drop across the interface will increase at the edge near the triple point since a larger concentration difference of the electrons between the two phases is generated. In the center of the platinum contact, the former concentration difference still exists and the voltage drop across the interface is lower in the center of the platinum contact than at the edges.

Other kinetic effects are based on side reactions, especially when a less stable compound is formed then thermodynamically favorable It has to be also taken into consideration that only the redox process which includes the electrons from the electrode and the ions from the electrolyte generate the voltage. E.g., the formation of Na_2CO_3 in electrochemical CO_2 sensors based on fast solid state sodium ion conductors is assumed to take place at the interface between the sodium ion conductor and the electronic lead. This process involves both CO_2 and O_2 from the gas besides e^- from the electronic lead and Na^+ from the electrolyte. If, by kinetic reasons, sodium oxide is being formed initially before this compound reacts subsequently with CO_2 to form Na_2CO_3, only the energy of formation of the oxide is seen by the cell voltage. The energy of the later reaction with CO_2 is converted into heat [10].

The various problems mentioned here require careful design and engineering of appropriate materials and their interplay in devices. In the following, solutions and concepts will be given, which are based on systematic understanding of functional materials properties.

3. Materials Considerations

Most approaches in developing ionic devices are based on trial-and-error. It appears favorable, however, to follow more systematic paths of materials and device development.

Simultaneous High Conductivity and Chemical Stability. As an example, the strong electrostatic interaction between lithium cations and chlorine anions has been overcome by employing another chloride which is capable to screen partially the attractive forces of the anions. $AlCl_3$ has been employed to form the new ternary compound $LiAlCl_4$. The structure consists of large $AlCl_4^-$ tetrahedra with aluminium in the centre and four chlorine ions at the corners. The lithium ions are located in-between with a substantially decreased cationic-anionic interaction. As shown in

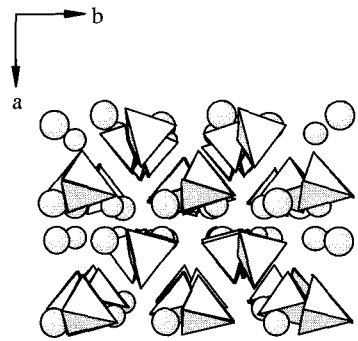

Fig. 6. Structure of the lithium ion conductor $LiAlCl_4$. The $AlCl_4^-$ anions form tetrahedra. The lithium ions are located in-between and have much less chemical interaction with the chlorine ions compared to LiCl.

Fig. 6, the lithium ions are mobile along various pathways. The motion is 3-dimensional, but channels are especially visible in a-direction. The ionic conductivity of $LiAlCl_4$ has been found to be one of the highest among all lithium ion conductors [11].

An example of forming large structural units of the counter ions and ionic defects for fast ionic motion is $Li_4SiO_4 + Li_3PO_4$ which are completely miscible. Si and P form tetrahedra with oxygens at the corners and lithium ions in-between. Replacement of the 4-valent SiO_4^{4-} by the 3-valent PO_4^{3-} substitutes three lithium ions and generates one lithium vacancy. A maximum ion conductivity is found in the case of approximately 50 % replacement [5].

In addition to the improvement of the lithium ion conduction in solids by the addition of different cations, the ionic conduction and stability have been improved by doping the non-conducting partial lattice. Examples are new compounds being formed along the quasy binary sections lithium halides - lithium nitride [12]. The aliovalent anions generate defects in the lithium partial lattice, which results in lithium ion conductivity values in-between those of Li_3N and LiHal.

Kinetic Stability. Conventional organic electrolytes employed in commercialised lithium ion batteries show instabilities with the electrodes which are summarized under the acronym SEI (Solid Electrolyte Interface). The formation of several different layers has been reported. This effect contributes to the limitations in the lifetime of the presently commercially available lithium ion batteries.

Only components with extraordinary low diffusion coefficients should be employed. The interfacial layer growth rate is related to the chemical diffusion in the product phase, but may be also controlled by polarisations such as redox and transfer processes. Assuming the parabolic rate law for bulk controlled growth, the thickness of the grown layer after a period of time τ is given by $L = \left(2\tilde{D}\tau\right)^{1/2}$, where $\tilde{D}$ is the chemical diffusion coefficient.

Assuming that L is only 1 Å, for a lifetime of the device of 10 years, the chemical diffusion coefficient should be smaller than 10^{-25} cm^2/s. Such a value is rather low as compared to gases or liquids but not uncommon at all for many atomic species in the solid state. E.g., it has been estimated that Zr^{4+} diffuses at a rate slower than 10^{-50} cm^2/s in zirconia at room temperature.

In view of the large variation in the concentration of the electrons across the electrolyte it is essential that the mobilities of the electronic charge carriers are very low. Otherwise, small concentrations of impurities would readily result in predominant electronic conductivities. This aspect may be taken into consideration as a criterion in the search for new ionic conductors [13,14]. All suitable solid ionic conductors have small polaron type electronic conduction. The mobility is low because of the relaxation of the surrounding lattice. The activation energies are similar to those for the motion of ions and have been found to be even substantially higher in some cases [13].

Semiconducting Electrodes. Textbooks commonly require metallic conducting electrodes. Practically no voltage drop should occur before the electrons have reached the electrode/electrolyte interface where the redox process takes place. This requirement is in conflict with fast diffusion of the electro-active component. The concentration polarization should be minimized in order to reduce energy losses and to provide high power densities.

The low concentration of electronic charge carriers for high enhancement factors of the chemical diffusion requires high mobilities of the electrons in order to make the material predominantly electronically conducting. This has so far been best fulfilled in the case of intermetallic lithium compounds, especially Li_3Sb which holds the presently highest Wagner factor of $W = 7 \cdot 10^4$ [15]. High values have also been observed for Li_3Bi, LiAl, $Li_{22}Sn_5$, $Li_{22}Si_5$, $Li_{13}Sn_5$, $Li_{13}Si_4$, etc. These intermetallic compounds have higher chemical diffusion than the self-diffusion of lithium in molten lithium or the self-diffusion of copper in molten copper at 1100 °C. Accordingly, the ions are diffusing at liquid like rates in the solid state.

4. Device Considerations

In some applications it is not required to change the compositions of the electrodes in contact with the electrolyte during operation, e.g. in the case of fuel or electrolysis cells. In some other cases, only a minor change in the composition is required, e.g. in the case of electrochromic devices or chemical sensors. In these cases, electrodes may be omitted and the entire galvanic cell may be formed by a single material of the same thermodynamic phase which has a compositional gradient. This approach has been named SEA concept [10] which stands for Single Element Arrangement.

SEA Concept for Fuel and Electrolysis Cells. Solid ionic conductors show commonly ionic conductivities independent of the activity of the electro-active component. The number of ionic defects, which contribute to the ionic conductivity, is very large and does not depend on the variation of the activity of the mobile

component, which is imposed from the outside by the oxidizing and reducing gases

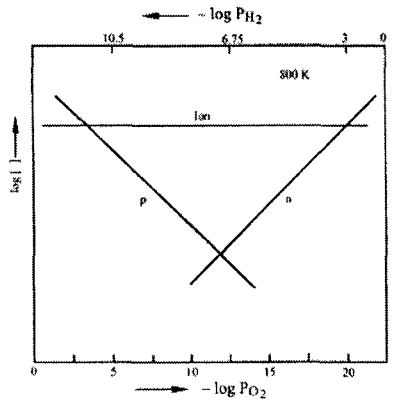

Fig. 7. Dependencies of the concentrations of excess electrons and holes as minority charge carriers in a proton or oxide ion conductor as a function of the partial pressure of hydrogen and oxygen at T = 800 K. An activity of water of 1 is assumed.

at the cathode and anode in fuel cell operation mode and anode and cathode in electrolysis operation mode, respectively. That means, the ionic conductivity of the oxide ion or proton conductor is the same anywhere in the electrolyte. This does not hold, however, for the electronic minority charge carriers. Their conductivities depend strongly on the oxygen and hydrogen activity as described by Brouwer diagrams. The uptake of oxygen into the electrolyte is accompanied by a decrease in the concentration of free electrons or increase in the concentration of holes. Similarily, the uptake of hydrogen is accompanied by a decrease of the concentration of holes or an increase in the concentration of free electrons.

The dependencies of the concentrations of the electronic minority charge carriers on the partial pressure of hydrogen and oxygen are shown in Fig. 7. Depending on the ionic and electronic defect chemistry of the material, predominant hole conduction may be achieved at the air or oxygen electrode while predominant excess electronic conduction may prevail at the hydrogen or fuel electrode side. The electrolyte may serve in this way also as electrodes under the given partial pressures of the gases. No separate electronic leads are necessary, except possibly a grid of good electronic conduction in order to avoid high resistances of the current collection along the surface. In practical cases, those grids are simultaneously the bi-polar plates, which carry the gas along perpendicular channels. No separate electrodes with a chance of chemical reactions, poor contact, high interfacial resistances and different expansion coefficients are needed any longer.

Instead of making an ionic conductor more electronically conducting at the electrodes, the SEA concept has been also approached from the opposite side of employing originally electronic conductors. $SrFeO_3$ and $SrSnO_3$ are commonly known as semi-conductors. Solid solutions of both compounds generate appreciable disorder and ionic conductivity, which results in a predominantly ionically conducting regime in-between the oxygen partial pressures established in a fuel cell. This has been observed by measuring cell voltages in the range of 800 mV at 750 °C. Together with the impedance measurements under high and low oxygen partial

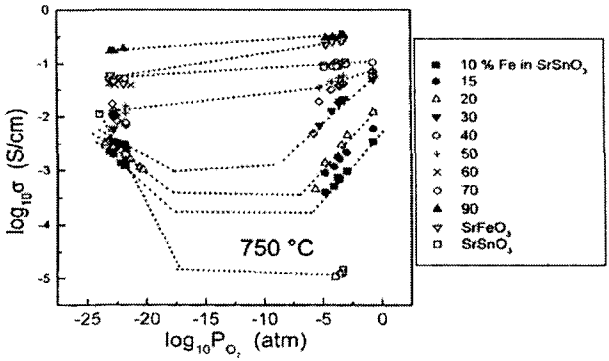

Fig. 8. Conductivities of $SrSnO_3$ with various amounts of Fe replacing Sn in increments of 10 % from 0 - 100 %. Excess electronic conductivity is observed at low oxygen partial pressures while predominant hole conduction is observed at high oxygen partial pressures. In-between, ionic conducting regimes are observed which provide voltages up to 800 mV.

pressures, this results in the Brouwer diagram shown in Fig. 8. It seems, however, that the ionically conducting regime is not yet large enough for practical application and has to be improved in further work.

SEA Concept for Electrochromic Devices. Common electrochromic devices consist of three layers of the electrochromic active material (often WO_3), the liquid or solid electrolyte and a suitable counter electrode plus electronic leads (commonly ITO), i.e., 5 layers have to be prepared which should be all-together thin enough in the case of windows with variable transmission in the visible. The coloration occurs as a result of the change in the chemical composition by a current flux in at least one of the layers.

Alternatively, the chemical composition may be changed in compounds with an originally homogeneous composition by the application of voltages. There is no special restriction whether the materials are predominantly ionically or electronically conducting. It is only required that ions are mobile and may move over the distance of the thickness of the layer within the given period of the switching time of the device.

The compound becomes oxidized at one side and reduced at the opposite side. If a starting composition at or near the ideal stoichiometry is being used, the material shows a higher excess electron concentration at the negative electrode side and a higher hole concentration at the positive electrode side. This is accompanied by color changes in appropriately chosen materials at one or even both sides.

Successfully engineered materials should include chemical elements which may be reduced at the negative electrode side and elements which may be oxidized at the positive electrode side. Examples of such materials are $Li_xLa_{y(2-x)/3}Fe_zTi_{1-y}O_3$ which includes reducible titanium and oxidizable Fe and $Li_{0.3}Sr_{0.6}Ta_{0.5}Ti_{0.5}O_3$ [16]. The electrochromic effect of this material has been successfully demonstrated by employing samples in the shape of bars which became sectioned after the

application of the voltage and separately characterized subsequently. Colored areas have been observed at both electrode sides. The oxidation and reduction occurs via the motion of lithium ions. In view of Duhem-Margules' law, the lithium activity is related to the oxygen activity.

Theta Sensors. Also the engineering of chemical sensors may take advantage of new concepts in order to overcome the limitations of poor reproducibility and cross sensitivity. The arrangements are simplified by considering that the solid electrolytes may play a more active role than previously attributed. So far, electrolytes are employed to generate a voltage according to Nernst's law in potentiometric sensors or to act as a filter and pump for passing the component of interest through the ionic conductor in amperometric sensors. All previous devices may be called "passive" since the action of the gas on the voltage or current is observed.

In the Theta (θ) sensors, the solid ionic conductor plays a more "active" role [17]. The voltage or current are changed with time, i.e., a variable activity of the electro-active component is imposed on the gas. There has to be a chemical reaction occuring at the interface which may be rate-determined by various processes, including concentration polarization, redox and absorption processes. The reactions will change with time with the applied voltage or current and may thus provide a finger print of more than one component. A single galvanic cell may be sufficient to detect simultaneously a large fraction or even the entire gas composition. The gas is forced to respond to a driving force which is generated by the applied voltage. Besides varying the activity of the electro-active component it is also possible to apply activities of other components by employing secondary equilibria, e.g. employing one of the fast sodium ion conductors with Na_2CO_3 at the surface which relates the sodium activity to partial pressures of CO_2 and O_2.

5. Conclusions

New approaches in engineering solid state ionic devices have to overcome many conflicting requirements by developing simpler and more reliable materials design. The advantages of solid ionic and mixed conducting materials have hardly been taken into account. Reliability, safety and energy densities are favourable features which may overcome the present limits of liquid systems.

Various requirements can be met by new approaches to design suitable individual materials. The chemical stability may be improved to accommodate the highest possible voltage drops across the electrolyte and suitable structures may provide high ionic conductivities. Electrodes may be engineered with fast chemical diffusion to reach high power density rates. Compromises have to be made, however, and there is still a major degree of innovation with regard to appropriate materials needed. Most important is the need in bringing the materials together to generate solid state galvanic cells. New concepts may overcome the limitations of generating reaction products at the interfaces and to avoid the interface at all. Controlling and reading both voltage and current offers many new opportunities in the design of gas sensors for the detection of multiple numbers of species in gases or

liquids. Many new technologies will come up in the future following new designs of appropriate devices.

6. References

[1] W. Nernst, Patentschriften Nr. 107533 (Oct. 2, 1897), 109907 (June 19, 1898); Siemens & Halske, Patentschrift Nr. 113775 (March 9, 1899); AEG, Patentschriften Nr. 114241 (April 9, 1899), 115500 (April 9, 1899), 119270 (Aug. 20, 1898), 121207 (Nov 29, 1898), 122078 (March 15, 1899) 122079 (March 15, 1899), Kaiserliches Patentamt, Berlin.

[2] C. Tubandt and E. Lorenz, Nernst Festschrift, W. Knapp, Halle, **446** (1912), Z. Phys. Chem. **87**, 513 (1914).

[3] J.N. Bradley and P.D. Green, Trans. Faraday Soc. **62**, 2069 (1966); B.B. Owens and G.R. Argue, Science **157**, 308 (1967); Y.F. Yao and J.T. Kummer, J. Inorg. Nucl. Chem. **29**, 2453 (1967); R.H. Radzilowski, Y.F. Yao and J.T. Kummer, J. Appl. Phys. **40**, 4716 (1969); N. Weber and J.T. Kummer, Proc. Ann. Power Sources Conf. **21**, 37 (1967).

[4] W. Weppner, Ionics **1**, 1 (1995).

[5] Y.W. Hu, I.D. Raistrick and R.A. Huggins, J. Electrochem. Soc. **124**, 1240 (1977).

[6] W. Weppner, Ionics **7**, 404 (2001).

[7] V. Thangadurai and W. Weppner, J. Electrochem. Soc., in print.

[8] M. de Ridder, R.G. van Welzenis, H.H. Brongersma, S. Wulff, W.F. Chu and W. Weppner, Nucl. Instr. and Meth. in Phys. Res. B **190**, 732 (2002).

[9] E.D. Tsagarakis and W. Weppner, in: Solid State Ionic Devices: Ceramic Sensors (E.D. Wachsman, W. Weppner, E. Traversa, M. Liu, P. Vanysek and N. Yamazoe, Eds.), Proc. Vol. 2000-32, The Electrochem. Soc., Pennington, NJ, 2001, p. 285.

[10] W. Weppner, in: Solid State Ionics: Trends in the New Millenium (B.V.R. Chowdari et al., Eds.), World Scientific Publ. Co., Singapore, 2000, p. 409; to be presented at the Intl. Conf. on Ionic Devices, Nov. 28-30, 2003, Chennai, India.

[11] W. Weppner and R.A. Huggins, Phys. Lett. **58A**, 245 (1976); J. Electrochem. Soc. **124**, 35 (1977).

[12] P. Hartwig, W. Weppner and W. Wichelhaus, Mat. Res. Bull. **14**, 493 (1979); P. Hartwig, W. Weppner, W. Wichelhaus and A. Rabenau, Solid State Communications **30**, 601 (1979); Angew. Chem. **92**, 72 (1980); Angew. Chem. Int. Ed. Engl. **19**, 74 (1980).

[13] W. Weppner, Electrochim. Acta **22**, 721 (1977).

[14] W. Weppner and R.A. Huggins, J. Electrochem. Soc. 124, 1569 (1977); J. Solid State Chem. **22**, 297 (1977).

[15] W. Weppner, in: Materials for Lithium-Ion Batteries (C. Julien and Z. Stoynov,Eds.), Kluwer Acad. Publ., Dordrecht, NL, 2000, p. 431.

[16] M. Klingler, W.F. Chu and W. Weppner, Ionics **3**, 289 (1997); V. Thangadurai and W. Weppner, to be published.

[17] J. Liu and W. Weppner, Applied Physics A **55**, 250 (1992).

This page is intentionally left blank

Part I
Ionically Conducting Inorganic Solids

This page is intentionally left blank

Invited Papers

This page is intentionally left blank

Multinuclear NMR studies of mass transport of phosphoric acid in water.

J. R. P. Jayakody[1], E. S. Mananga[2], A. Khalfan[2], S. H. Chung[3], R. Lopato[3], and S. G. Greenbaum[2]

[1] Department of Physics, University of Kelaniya, Kelaniya, Sri Lanka

[2] Department of Physics & Astronomy, Hunter College of CUNY, New York, NY 10021 USA

[3] Department of Chemistry and Physics, William Paterson University of New Jersey, Wayne, NJ 07470 USA

ABSTRACT

Mass transport phenomena in phosphoric acid, an important fuel cell compound, of varying concentration were studied by multinuclear NMR measurements including pulsed gradient spin-echo (PGSE) and static field gradient techniques. The latter method was developed in order to be able to measure self-diffusion as a function of applied hydrostatic pressure. The high pressure measurements were carried out at 288 K, and variable pressure up to 2.5 kbar. The high pressure data were obtained for four different concentrations of phosphoric acid in water in the range of 6% - 100% by weight. The calculated activation volume for ^{1}H nuclei, increasingly dominated by the water protons, decreased as the acid concentrations decreased, exhibiting behavior approaching that of liquid bulk water. In addition ^{31}P data show higher activation volumes than the corresponding ^{1}H data, mainly due to the larger molecular size of the phosphate groups compared to water molecules. This difference is a factor of two for 100% acid, suggesting a proton transport mechanism for high concentration acid which involves the hopping transfer of protons between the larger phosphate groups. Using ^{1}H and ^{31}P pulsed gradient spin-echo techniques, self-diffusion coefficients have been measured for a range of phosphoric acid concentrations (6~100 wt %) over the temperature region from 293 to 363 K. The data show again that protons diffuse faster than the phosphorus carrying species. Different activation energies are obtained above and below 12 wt % acid concentration, suggesting the presence of ion association effects at this concentration.

Introduction

Phosphoric acids have many important industrial applications such as in the food and detergent industries[1]. In addition, their use as proton conductors in electrochemical devices such as fuel cells and solid state batteries[2] is another area

which has recently attracted considerably interest. For this reason it is essential to know the ion transport mechanism in these materials in order to optimize the proton conductivity of polymeric membranes containing phosphoric acid for efficient fuel-cell performance. In this regard the important experimental parameters are viscosity, ionic conductivity, and self-diffusion coefficients, which characterize the translational mobility of a molecular or ionic species in homogeneous media. In particular, temperature-dependent measurements of these variables provide valuable information on molecular organization and interactions with the environment. A number of conductivity[3,4,5,6,7] and diffusion measurement[8,9,10,11] have been reported for various concentrations of phosphoric acids. Previous NMR investigations of mass transport in phosphoric acid systems have demonstrated that phosphate transport is vehicular, while proton transport occurs via a Grotthus hopping mechanism[8,12,13] which is not associated with movement of the whole ion or molecular species through the viscous medium (as in the vehicular mechanism). In this mechanism the electric conduction is believed to occur by the disassociation of hydrogen-bonded protons and their transfer from one solvated acid molecule to a neighboring one in the solution. From the same investigations they have demonstrated that phosphate ion transport mechanism is vehicular.

In this investigation, self-diffusion coefficients are measured and then used to evaluate mass transport in phosphoric acid, a useful material for fuel cell applications. In general, the study of ion transport in polymers can be greatly assisted by employing pressure and temperature as independent thermodynamic variables. Molecular motions and ionic diffusion are associated with volume fluctuations that can be probed directly by performing measurements as a function of pressure. The activation volume associated with ionic and molecular motion, which is a measure of the volume change of the material as the ions or molecules pass from an equilibrium position to a saddle point, can be derived directly from the variable pressure data. Activation volumes for four different phosphoric acids concentrations are reported in the present work. Self-diffusion measurements are customarily made by the pulsed gradient spin-echo (PGSE) method[14,15], but in first part of this work the static gradient associated with the fringe field of the NMR magnet was used. Two advantages of the static gradient are its typically much larger magnitude than obtainable with NMR probe gradient coils, and the relative ease of incorporating a pressure cell into the experiment.

For the second part of this work, complementary ^{31}P self-diffusion coefficients have been measured using the PGSE diffusion measurements as a function of temperature to probe the motion of the ions for different concentrations of phosphoric acid in aqueous solutions (6~wt 100%). While there are published

reports[8,11] of temperature-dependent ^{31}P and ^{1}H self-diffusion NMR measurements on phosphoric acid, we are not aware of any self-diffusion NMR investigations for concentrations less than 85% H_3PO_4.

Experimental Details

Analysis grade phosphoric acid (85%) from Sigma Chemicals was used without further purification. Stock solutions of 85% phosphoric acid in water were prepared. Solutions of desired concentrations were then prepared by dilution of the stock solution.

High pressure measurements were carried out for four different concentrations of phosphoric acid in the range of 6% - 100% for ^{1}H species and 100% and 85% acids used for ^{31}P species. For NMR measurements the solutions were placed in to 0.6 cm x 0.5 cm x 0.18 mm hermetically sealed thin polyethylene bags, which were shown to produce a negligible proton NMR background signal compared to the signal from the solution. This was necessary in order to isolate the sample from the pressure transmitting fluid. The naturally existing field gradient of a conventional 7.3 T superconducting magnet was used for the measurements. The central field and gradient strength were varied continuously, within the limits of the magnet, by moving the NMR probe head within the bore of the magnet. The position of the NMR coil (which contains the sample) determines both the resonant frequency and the magnetic field gradient. A home-built counter controlled motorized stage, capable of moving the probe in precise steps of 0.25 mm, was used to center the coil at a field gradient strength ($G = dB_z/dz$) of 0.28 T/cm for ^{1}H nuclei and for ^{31}P nuclei. These values were determined experimentally using the standard self-diffusion coefficient of water.[16] Accurate variation of the pressure (0 to 2.5 kbar) was carried out using an ENERPAC 11-400 hydraulic system fitted to a sealed Cu-Be alloy high-pressure chamber (bomb) inside of which resides the NMR excitation coil and sample. Electronic connection between the coil inside the pressure bomb and external matching and tuning capacitors was facilitated by a high pressure hermetic feed through.

A homebuilt broadband NMR spectrometer operating at 74 MHz (the central field value corresponding to the position of the sample in the fringe-field) and utilizing a phase cycled spin-echo pulse sequence ($\pi/2$ - τ - π - τ - *acquire*) was used to detect the proton and phosphorus echo signal from the sample. Pulse widths ($\pi/2$) were typically of 2.6 μs duration.

For PGSE NMR measurements, the solutions were placed in a 5 (OD) x 20 mm NMR tubes and sealed with the sample cap and parafilm. The temperatures was varied from 293 to 363 K with equilibration times of 20 - 25 minutes between

each temperature change. The PGSE NMR measurements were performed on a Chemagnetics CMX-300 spectrometer with a ^{1}H and ^{31}P Larmor frequencies of 301.0 and 121.8 MHz respectively. The NMR experiments were carried out using a 5mm dual broad band gradient PGSE probe provided by Nalorac. Self-diffusion coefficients were obtained using the Hahn spin-echo pulse sequence ($\pi/2$ - τ - π). For a diffusing system in the presence of a magnetic field the application of square-shaped magnetic gradients of magnitude g and duration δ results in attenuation of the echo amplitude A. This attenuation may be represented by $A(g) = \exp[-\gamma^2 g^2 D \delta^2(\Delta-(\delta/3))]$, where γ, D and Δ represents the nuclei's gyromagnetic constant, self-diffusion coefficient, and gradient delay. Applied gradient strengths ranged from 0.2 - 1.2 T/m, δ and Δ ranged from 1 - 10 and 10 - 40 ms respectively. The resulting echo profile vs. gradient strengths is fitted to the above equation and D is extracted. Uncertainties in self-diffusion coefficient measurements are ~5%.

Results

Proton spin echo intensities $M(\tau)$ were measured as a function of the pulse separation, τ, and self-diffusion coefficients D were extracted from the data using equation (1), below.[17]

$$M(\tau) = M_0 \exp\{-2/3\,[3\tau/T_2 + (\gamma G)^2 D\tau^3]\} \qquad (1)$$

In this expression M_0 is the maximum magnetization (at $\tau = 0$) and γ is the proton gyromagnetic ratio. To assist in the analysis, proton transverse relaxation times T_2 were measured independently and the data were fit to a linearized version of equation (1) with slope = $2(\gamma G)^2 D/3$ and intercept = $2/T_2$. In this way the diffusion coefficients were gathered with respect to applied pressure. The self-diffusion coefficients for ^{1}H species and ^{31}P as a function of pressure for different concentrations of phosphoric acids are plotted in Fig.1.

The data in Fig. 1 can be further analyzed to yield the activation volume Δv associated with the diffusing water molecules according to equation (2).

$$\Delta v = -kT\left(\frac{\partial \ln D}{\partial P}\right)_T \qquad (2)$$

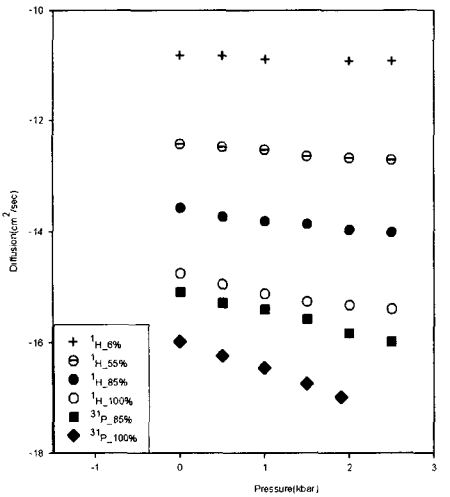

Figure 1. Semi log plot of the self-diffusion coefficient, as the function of pressure for different acid concentrations at temperature 288K

The activation volumes for four different concentrations of phosphoric acids are given in table I.

Table 1: Activation volumes for different concentrations of phosphoric acids.

Acid Concentration %	Activation volume of ^{1}H (cm^3/mol)
6	0.97 ± 0.08
55	3.15 ± 0.25
85	4.20 ± 0.34
100	6.13 ± 0.49
Acid Concentration %	Activation volume of ^{31}P (cm^3/mol)
85	8.70± 0.70
100	12.60± 1.00

Figure 2 shows plots of ^{31}P diffusion coefficients as a function of inverse temperature for the range of phosphoric acid concentrations investigated.

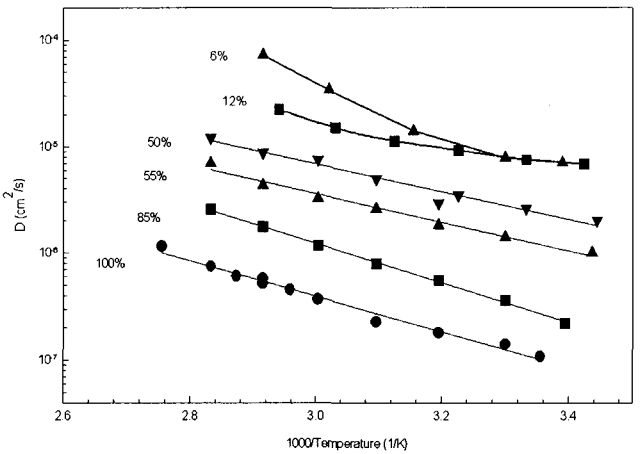

Figure 2. ^{31}P self-diffusion coefficients for various concentrations of H_3PO_4 as a function of inverse temperature. Solid lines are guides for the eye.

The slopes of the lines for concentrations 50~100% in Fig. 2 are approximately constant indicating that the activation energies in these materials are similar to the reported value[8] of 0.38eV for 85% solution. Below 50%, a distinct curvature in the data is noted.

Figure 3 shows the ^{1}H and ^{31}P diffusion coefficients for the 100% H_3PO_4 solution, reproduced from reference 8.

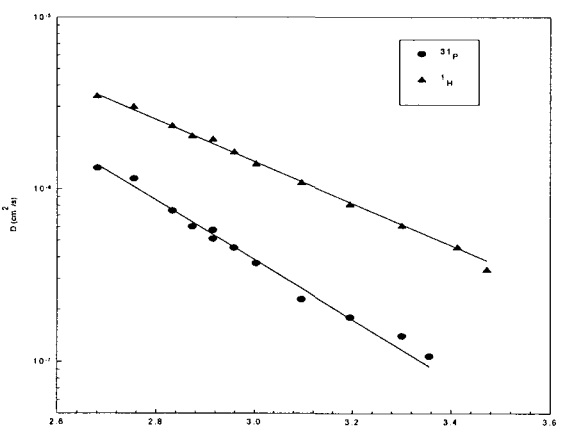

Fig. 3. ^{31}P and ^{1}H self-diffusion coefficients for 100% H_3PO_4 as a function of inverse temperature. The solid lines are non-linear least squares fits to the Arrhenius relation (from reference 8).

The effect of temperature upon diffusion coefficients at constant pressure can usually be represented satisfactorily by a simple Arrhenius-type equation of the form $D=D_0\exp(-E_a/k_BT)$ where T is the temperature in Kelvins, k_B is the Boltzmann constant, E_a is the average activation energy for diffusion and D_0 is the diffusion prefactor. From Figs. 2 and 3, it can be seen that the diffusion coefficients closely follow an Arrhenius relationship over the temperature range investigated. The calculated activation energy values from a non-linear least squares fit to the Arrhenius relation is shown in Table 2.

Table 2. 100% H_3PO_4 (aq) solution. Arrhenius diffusion equation fitting parameters.

Nucleus	D_0 (10^{-3} cm^2 /s)	E_a (eV)
^{31}P	0.61	0.34
^{1}H	6.61	0.24

The activation energy values obtained for the 100% solution are similar to those found for the 85% solution[8].

Discussion

Pressure dependence

The self-diffusion coefficients of proton and phosphorous species decrease with increasing acid concentration and also with increasing pressure as both factors cause restrictions for proton and phosphorous motions. The first factor is due to the increase of viscosity of the solution with increasing acid concentration. In addition, the activation volume of proton Δv increases with increasing acid concentration, altogether by a factor of six as the acid concentration increases from 6% to 100%. This result provides evidence of the Grotthuss hopping mechanism in which the proton hops from H_3PO_4 to $H_2PO_4^-$, and between nearby water molecules through the formation of intermediate H_3O^+ ions in all but the 100% acid sample. The calculated activation volume for ^1H for low acid concentration 6% is relatively small and approaches the value of liquid bulk water, an expected result because the ^1H NMR signal is dominated by water. This behavior has been previously observed by others[8,17,19] in conductivity and diffusion results.

Another observation is that the activation volume Δv of ^{31}P increases with increasing acid concentration from 85% to 100%. In addition ^{31}P data show higher activation volumes than the corresponding ^{1}H data, as expected mainly due to the larger molecular size of the phosphate groups compared to water molecule. The likely mechanism for anion transport in this system is the vehicular-type in which $H_2PO_4^-$ is the main negative charge carrier.

Temperature dependence

In agreement with the pressure-dependent data Fig. 3 shows that the protons diffuse faster than the phosphorus carrying species in the 100% phosphoric acid sample indicating that there are two separate transport mechanisms for the phosphorus and proton species. The higher activation energy of 0.34 eV obtained for the slower phosphorus diffusion is consistent with ion transport associated with a vehicular type mechanism whereas the lower activation energy value of 0.24 eV obtained for proton diffusion is consistent with that of proton hopping transport. The latter value is related to the dissociation of an H-bonded proton in the phosphoric acid solution and is within the range of values for H-bond strengths in aqueous solutions[20].

The curvature noted in the ^{31}P data of Fig. 2 for the 12% and 6% concentration suggests a complex diffusion mechanism not expected for simple isotropic fluids. This behavior occurs in a concentration regime where anomalous ion transport is reported to take place[9]. In an attempt to delineate these anomalies in the ion transport of H_3PO_4, we have made detailed ^{31}P T_1 and self-diffusion coefficients over the concentration range c=0.01 to 14.6 M. The isotherm of ^{31}P self-diffusion at 303 K shows a monotonic 30-fold increase with decreasing concentration. However in the vicinity of 12% phosphoric acid, a pronounced dip in both the T_1 and D data as a function of concentration is observed. These results, which will be reported elsewhere, suggest that phosphoric acid is especially prone to ion association in the vicinity of 12% H_3PO_4.

Summary

Proton and ^{31}P NMR self-diffusion measurements of aqueous phosphoric acid solutions ranging from 6 to 100 wt% acid were carried out, under both variable temperature and variable pressure conditions, the former yielding activation energies and the latter providing activation volumes. Both kinds of measurements demonstrate more facile mobility of protons, whether as a hopping species or within intact water molecules, than phosphate ions. Proton transport in high acid content solutions proceeds via a Grotthus hopping mechanism, whereas phosphate

ion transport occurs through a vehicular mechanism, with a nearly constant activation energy from 100% down to 50% acid. Non-Arrhenius behavior is noted for the 12% solution and attributed to ion significant pairing effects.

Acknowledgements

The authors wish to acknowledge the assistance of Dr. S. Bajue (Medgar Evers College) in the preparation of the phosphoric acid solutions. The reseach at Hunter College was supported by grants from the Office of Naval Research and the Air Force Office of Scientific Research. SHC is grateful for grant support from the Research Corporation, WPU Center for Research and A.R.T.

References

1. A. D. E. Toy and E. N. Walsh, Phosphorous Chemistry in Everyday Living, *American chemical Society*, Washington, DC, 1987.
2. S. Chandra, in Proceeding of the *II International Symposium on Solid state Devices*, edited by B. V. Chowdari and S. Radakrishna, *World Scientific Publication, Singappore* (1988), P. 265.
3. N. N. Greenwood and A. Thompson, *J. Chem. Soc.* 1959, 3485.
4. D. T. Chin and H. H. Chang, *J. Appl. Electrochem.* **19**, 95 (1989).
5. E. N. Tsurko, R. Neueder, J. Barthel and A. Apelblat, J. Solution Chem. **28**, 973 (1999)
6. D. I. MacDonald and J. R. Boyack, *J. Chem. Eng. Data* **14**, 380 (1969).
7. J. J. Fontanalla, M. C. Wintersgill, J. S. Wainright, R. F. savinell and M. Litt, *Electrochem. Acta*, **43**, 289 (1998).
8. S. H. Chung, S. Bajue and S. G. Greenbaum, *J. Chem. Phys.* **112**, 8515 (2000).
9. H. Chakrabati, *J. Phys. Condense Matter* **8**, 7019 (1996)
10. A. Das and S. N. Changdar, Radiat. *Phys. Chem.* **45**, 773, (1995)
11. T. Dipple, K. D. Kreuer, J. C. Lassegues and D. Rodriguez, *Solid State Ionics* **61**, 42 (1993).
12. C. D. J. Van Grotthuss, *Ann. Chem. (Paris)* **58**, 54 (1806)
13. R. A. Robinson and R. H. Stokes, *Electrolitic Solution (Butterworth, London*, 1955).
14. E. O. Stejskal and J. E. Tanner, *J. Chem. Phys.* **42**, 288 (1965).
15. P. T. Callaghan, Aust. *J. Phys.* **37**, 359 (1984).
16. M. Holz, *Phys. Chem. Chem. Phys.* **2**, (2000).
17. C. P. Slichter Principles of magnetic resonance.
18. J. R. P. Jayakody, P. E. Stallworth, E. S. Mananga, J. Farrington-Zapata and S. G. Greenbaum, *J. Phys. Chem.* **B 108,** 4260 (2004)

19. J. J. Fontanella, M. C. Wintersgill, R. S. Chen, Y. Wu, and S. G. Greenbaum, *Electrochem. Acta*, **40,** 2321(1995).
20 J.N. Murrell and E.A. Boucher, *Properties of Liquids and Solutions* (Wiley, New York, 1982).

Crystalline, Glassy and Polymeric Electrolytes: Similarities and Differences in Ionic Transport Mechanisms

Jean Louis Souquet
Laboratoire d'Electrochimie et de Physicochimie des Matériaux et des Interfaces (UMR CNRS, INPG, Université Joseph Fourier Grenoble, N° 5631), ENSEEG BP 75 - 38402 Saint Martin d'Hères - France

Abstract

Ionocovalent crystals or glasses as well as molten salts or salt polymer complexes are currently studied as electrolytes for high energy density batteries. Their large Red/Ox stability range results from their thermodynamic or kinetic characteristics.

For all these electrolytes, charge carriers are the consequence of local deviations from electroneutrality, identified as point defects for ionic crystals or partial dissociation in disordered structures. The charge carriers formation derives from a similar activated process.

The main difference comes from the migration process, which depends on the dynamic properties of the surrounding medium. When the structural relaxation time is large, an activated process, mainly enthalpic, prevails for charge carriers migration. It is the usual case for ionic crystals or glasses. In the liquid or overcooled liquid states, the structural relaxation time of the medium is shorter that the time required for the activated migration process to occur and a local reorganization of the medium vanishes the energy barrier and provides the free volume necessary to ionic migration. In that case, the migration is mainly an entropic process.

The configurational entropy necessary to this process decreases with temperature and vanishes at the so called ideal glass transition temperature which can be estimated by extrapolation of the transport properties or of the thermodynamic characteristics of the medium. However, at the experiment time scale, this configurational entropy disappears at a somewhat higher temperature, the glass transition temperature at which the structural relaxation time corresponds to the measurement time.

Some glass forming ionic melts studied in a large temperature scale, over and below the glass transition temperature, evidence the two, enthalpic and entropic, migration mechanisms, allowing the determination of the thermodynamic characteristics of the charge carriers formation and migration.

Some recent results indicate that entropic process, associated to long scale deformations, may also exist in crystalline structures.

30 YEARS OF NMR/NQR EXPERIMENTS IN SOLID ELECTROLYTES

DETLEF BRINKMANN
Physik-Institut, University of Zürich
Winterthurerstrasse 190, CH-8057 Zürich, Switzerland
E-mail: Detlef.Brinkmann@physik.unizh.ch

Nuclear Magnetic Resonance (NMR) and Nuclear Quadrupole Resonance (NQR) experiments in solid electrolytes started around 1975 when a new interest arose in solids with high ionic conductivity. The emphasis of this revue is on experiments rather than theoretical issues. We will present typical NMR/NQR studies which demonstrate the power of these techniques to elucidate dynamic and static behavior of these solids at a microscopic level. Because of the overwhelming wealth of results accumulated in the last 30 years, we will be limited to some characteristic examples.

1. Introduction

Since Solid State Ionics is an interdisciplinary subject involving chemistry, physics, and material sciences, the research comprises many methods, among these Nuclear Magnetic Resonance (NMR) and Nuclear Quadrupole Resonance (NQR). Indeed, NMR and NQR are spectroscopic methods with the ability to probe static and dynamic properties of a solid at the microscopic level. This paper passes revue of some typical NMR/NQR experiments performed in solid electrolytes starting around 1975 when a new interest arose in solids with high ionic conductivity. The emphasis of this revue is on experiments rather than theoretical issues.

The experiments range from relatively simple ones like the well-known line narrowing and magic-angle spinning measurements to quite sophisticated techniques. These comprise: (i) measurements of the diffusion coefficient employing the pulsed-field gradient and the static fringe-field method; (ii) the experimentally related NMR imaging; (iii) measurements of various NMR/NQR parameters at high pressure. (iv) various types of nuclear relaxation, in particular spin-lattice relaxation. A special class are NMR double resonance experiments like spin-echo double resonance (SEDOR), rotational-echo double resonance (REDOR), and two-dimensional Fourier transform NMR (2D-FT NMR).

A wealth of information about these materials can be acquired, for instance: (1) the kind and number of diffusing ions and their diffusion pathways (one- or two-dimensional character of the motion); (2) details of the ion hopping frequencies like prefactor, activation energy, and activation volume (via pressure studies); (3) correlation effects and cooperative phenomena of these motions; (4) local symmetry, nature of bonding, and imperfections; (5) order-disorder phenomena and phase transitions.

The progress made in these NMR studies has been reviewed in several papers [1-3]. General NMR background knowledge is provided by, for instance, Ref. [4]; Ref. [5] lists some books with special emphasis on chemistry.

2. Chemical Shift and Magic Angle Spinning

In principle, the NMR experiment is the observation of the nuclear Zeeman effect, that is the splitting of the magnetic energy levels of magnetic nuclei in a static magnetic field. A radio-frequency field applied at the proper frequency, induces transitions between these levels and gives rise to an NMR signal at a certain frequency ν. From these signals one deduces information on static and dynamic properties of the solid electrolyte at its molecular level. We will start with the discussion of some structural information.

For nuclei with a nuclear spin 1/2 (*e.g* ^{1}H, ^{19}F, ^{31}P, ^{107,109}Ag), the NMR frequency, ν, measured in an *external* static magnetic field, B_0, is given by $2\pi\nu = \omega = \gamma(B_0 + \Delta B)$. Here, γ is the gyromagnetic ratio, which has a unique value for each magnetic isotope, and ΔB is an additional *local* field. Nowadays, external fields of the order 7 to 10 Tesla or even more are employed; the corresponding frequencies are in the range of 50 to 100 MHz. Since nearly all stable chemical elements (with the exception of argon and technetium) possess at least one isotope with a nuclear magnetic dipole moment, an NMR experiment can be performed in nearly each solid. Of course, a low natural abundance of the magnetic isotope (for instance 0.037 % for ^{17}O in the case of oxygen) and other inherent properties of the sample may cause problems.

ΔB arises from electric currents induced by B_0 in the electron cloud of the molecule under investigation. Since $\Delta B \sim B_0$, the resonance equation may be rewritten as $\omega = \gamma B_0(1 - \sigma)$, where $\sigma = -\Delta B / B_0$ is the shielding or screening constant of the order 10^{-6} to 10^{-5}. Since σ depends on the chemical environment, the frequencies of NMR signals of the same isotope in *different* compounds or in *inequivalent* sites of the same compound are shifted against each other. This effect is called chemical shift which is of fundamental importance for the chemical structure analysis by NMR.

In order to acquire the information about local environments, the NMR lines with different chemical shifts must be distinguished, hence they should not overlap. If the lines cannot be resolved, they must be narrowed artificially; this can, for instance, be accomplished by *magic-angle spinning* (MAS). Let us assume the magnetic moments are coupled by magnetic fields arising from their dipole moments; this coupling contributes to the finite linewidth. In this case, the angular dependent factor of the coupling is $A = 1 - 3\cos^2\Theta_{jk}$ where Θ_{jk} is the angle between B_0 and the vector r_{jk} joining two magnetic moments j and k. If such a pair rotates rapidly enough about a certain axis, the factor A is replaced by its time average: $< A > = (1 - 3\cos^2\Theta')(1/2)(3\cos^2\alpha_{jk} - 1)$. Here, Θ' and α_{jk} are the angles the molecular rotation axis makes with B_0 and r_{jk}, respectively. If the whole sample is rotated *artificially*, Θ' is the same for all pairs of nuclei. By choosing Θ' = 54° 44' (the *magic angle*), the factor $1 - 3\cos^2\Theta'$ will

be zero, hence A will vanish, and the line is narrowed. The MAS method is not restricted to dipolar couplings. It can also be used to eliminate other interactions provided the angular factor of the interaction is made up of $l = 2$ spherical harmonics. This is the case for chemical shift anisotropy and first order quadrupole splittings to be discussed later.

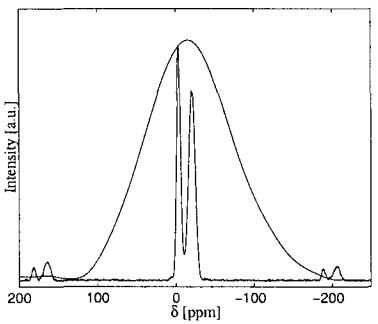

Fig. 1. Broadline and MAS ^{31}P spectra (not to scale) in 0.35 LiF × 0.65 $LiPO_3$ at 81.0 MHz with 15 kHz spinning speed. "Spinning sidebands" around ± 200 ppm are due to the MAS technique. From [6].

Figure 1 shows the static and the MAS spectrum of ^{31}P in 0.35 LiF × 0.65 $LiPO_3$ as a function of the relative chemical shift, δ. This glass is an important electrolyte because of its wide range of anion substitution and the large variety in composition. The compound consists of PO_4 tetrahedra, with P in the center, which are interconnected via bridging O ions, thus forming a glassy network. The number of these bridges per tetrahedron varies from 0 to 3, depending on the degree of polymerization. F atoms are embedded in the glassy structure preferentially by substituting bridging O ions. Thus, LiF is not only a dopant, it also modifies the network via further depolymerization, thus increasing the number of end groups. Obviously, MAS is essential to separate the lines. A detailed analysis revealed that fluorinated end groups show up in the *end*-group peak (at δ = -4 ppm) and not in the -6 ppm peak which arises from *middle* units. The intensity of the signals is a measure for the number of nuclei contributing to the signal. Therefore, the increase of the end-group peak intensity with x indicates progressive depolymerization of the glass structure due to doping.

In some materials, the *artificial* line narrowing accomplished by MAS is not necessary: nature does the narrowing for us. At sufficient high temperatures, the fast ion movements average out, to a certain extent, the fluctuating local magnetic fields and reduce the linewidth; this effect is known as *motional narrowing*. There are two limiting cases: the ion under consideration is mobile in a more or less stationary surrounding or the ion is stationary and its neighborhood is mobile, for instance because of diffusing ions or rotating molecules.

In the absence of any motion, that is at sufficiently low temperatures, one observes the rigid-lattice linewidth, $\Delta\nu_{RL}$. If the temperature is gradually increased, the linewidth, $\Delta\nu$, decreases in a smooth step and reaches, at sufficiently high temperature, a limiting value, the residual linewidth, $\Delta\nu_r$, which is due to interactions not affected by the atomic movements. Quite often, the ion dynamics and hence the fluctuating fields can be described by a thermally activated correlation

$$\tau = \tau_0 \exp(E/kT), \qquad (1)$$

where E is the activation energy and τ_0 is the prefactor. A phenomenological rela-

tion between the correlation time and the various linewidths is as follows: $(\Delta\nu)^2 = (\Delta\nu)_r^2 + \frac{2}{\pi}(\Delta\nu)_{RL}^2 \tan^{-1}(2\pi\alpha\tau \cdot \Delta\nu)$, with the factor $\alpha \approx 1$.

3. Quadrupole Interactions

When we are dealing with nuclei with a spin larger than ½ we may take advantage of the fact that these nuclei posses an electric quadrupole moment, eQ, which interacts with electric field gradients (EFG) present at the nuclear site (if its symmetry is non-cubic) and arising from all the surrounding charges. This quadrupole interaction causes the NMR signal to split (in an ordered structure) or to broaden (in "powder" samples). For instance, nuclei like ^{7}Li, ^{11}B, ^{23}Na, and ^{63,65}Cu with spin 3/2 yield a spectrum of 3 components. The separation of these lines depends on the strength of eQ and the EFG and on the orientation of the EFG tensor with respect to the magnetic field. Since the NMR frequencies are very sensitive to even minor changes of the EFG, nuclei of the same isotope but located at inequivalent sites are easily distinguished: they yield different triplets.

These quadrupole effects may be a gold mine for structural and dynamical studies of solid electrolytes. The EFG reflects any slight rearrangement of charges in the neighborhood of the nucleus under investigation. Thus, quadrupole effects are the ideal tool to investigate, among others, structural phase transitions, the changes of the atomic disorder or order (for instance at the transition from a high- to a low-conducting phase), the presence of imperfections (which alter the EFG), and the nature of bonding which is associated with different charge arrangements. Since the EFG is a tensor, its symmetry reflects the local symmetry of the nuclear site.

As an example, let's look at Li_3N, which belongs to those solid electrolytes most exhaustively studied by NMR [7]. Li_3N is a layer-structure with different NMR spectra for the inter-layer Li(1) and the intra-layer Li(2) nuclei. Increasing the temperature enhances the ion exchange between the two inequivalent sites; finally, at about 600 K, this process is so rapid that one observes only an "averaged" triplet. The exchange process has been monitored by the temperature dependence of several NMR parameters: the quadrupole shift (with respect to the NMR frequency in the case of zero EFG), the spin-lattice relaxation (see next section), and the diffusion coefficient (see further below). They all yield the same temperature dependent Li hopping frequencies thus supporting the ion exchange model. This is an instructive example for the necessity to perform comprehensive NMR experiments in order to establish the validity of a microscopic model.

4. Spin-lattice relaxation

There is no doubt that one of the unique powers of NMR is the ability to study the dynamics in a solid at the molecular level by performing relaxation experiments. Here, we will restrict ourselves to nuclear spin-lattice relaxation which is the process how a nuclear spin system approaches thermodynamic equilibrium with the lattice, by which we mean all the other degrees of freedom in the sample, beside the nuclear spins. The time constant of this process is called spin-lattice relaxation

time, T_1. In simple cases, the relaxation is brought about by local magnetic fields fluctuating at the Larmor frequency and inducing transitions in the spin system. If the correlation function, G(t), of these fluctuations is known, one can extract, from the data analysis, motional correlation times, τ, which are related to microscopic processes such as diffusion of ions and vacancies, moving defects, molecular rotations etc.

In the early days of NMR, relaxation data were analyzed by making the simple assumption of an exponential correlation function: $G(t) = G(0) \cdot \exp(-t/\tau)$. A Fourier transform of *G(t)* leads to the spectral density function and then to the well-known Bloembergen-Purcell-Pound (BPP) formula for the spin-lattice relaxation rate:

$$\frac{1}{T_1} = C^2 \left[\frac{\tau}{1+(\omega_0\tau)^2} + \frac{4\tau}{1+(2\omega_0\tau)^2} \right],$$

where C is a measure of the strength of the fluctuating local field. Similar to Eq. (1), one often assumes, for τ, an Arrhenius behavior and identifies τ with the thermally activated mean residence time of jumping ions. The data then yield the activation energy, E, and the attempt frequency, $1/\tau_0$, of the atomic process. Fig. 2 sketches the BPP formula in a *ln-ln* plot.

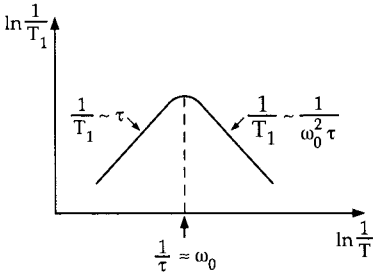

Fig. 2. Schematic plot of the BPP formula for the spin-lattice relaxation rate.

The BPP formalism works quite well for gases, liquids, and several solids and it has been applied in several areas of solid state physics. In many solid electrolytes, however, it is only qualitatively correct. The failure of the BPP model has the same origin as the inadequacy of the independent-particle model: solid electrolytes are many-particle systems with correlated particle movements and interactions between the ions. These facts are not properly accounted for by an exponential correlation function.

There are some straightforward improvements or extensions of the BPP formula [3]. For instance, one may take into account the discrete character of the crystal lattice and specific models of atomic motion or one may pay attention to the reduced dimensionality of the compounds. Here, we will mention two simple extensions of the formula.

The first example is the consideration of a *temperature* dependent concentration of vacant sites in solid electrolytes. In Li_3N, vacancy-induced diffusion allowed us to interpret the temperature and orientation dependent T_1 values of both ^7Li and ^6Li. The ansatz for the concentration of vacant Li sites is as follows:

$$c(T) = c_0 + c_0' \exp(-E_{fv}/kT) \qquad (2)$$

c_0 is the temperature independent concentration, c_0' is an appropriate prefactor, and E_{fv} is the formation enthalpy for vacancies. The analysis of the data yields $c \approx 2$ %; this result was confirmed much later by x-ray studies.

In our second example, we consider again the phosphate glass x LiF ×(1-x) $LiPO_3$. We are now interested in the relaxation of the stationary P ions [8] and we will pay attention to the inherent disorder of the glass. The disordered structure results in a distribution of bond lengths and angles which can be taken into account by assuming a Gaussian distribution of activation energies with a center E_0 and half width ΔE:.

$$\Gamma(E) = \frac{1}{\Delta E (2\pi)^{1/2}} \exp\left[-\frac{(E - E_0)^2}{2(\Delta E)^2}\right]$$

We modify Eq. (1) by substituting τ_0/Z for the factor τ_0 where Z is the partition function being related to the entropy of migration, S, via $S=-k\ lnZ$. Z can be identified with the number of vacant neighboring sites which can be reached by a hopping ion; we assume Z to be 6 as in a simple-cubic surrounding. Physically reasonable $1/\tau_0(E)$ values can be estimated for sinusoidal potentials.

Above about 250 K, the Li diffusion in x LiF × (1-x) $LiPO_3$ is thermally activated. For this region, we consider the P dipole-dipole interaction to be dominated by the heteronuclear P-Li coupling and, hence, the homonuclear P-P coupling to be negligible. We have calculated the ^{31}P T_1 in two frames of reference, the laboratory (as in all previous discussions) and the rotating frame. The latter is a coordinate system rotating around the direction of B_0 with angular velocity ω_0. Relaxation in this frame is caused by low frequency fluctuations with $T_{1\rho}$ as the characteristic decay time of the nuclear magnetization. The formulae for T_1 and $T_{1\rho}$ were fitted to the corresponding experimental data *simultaneously* over the whole frequency range from several kHz to 81.0 MHz. The result for 0.35 LiF ×65$LiPO_3$ is: E_0 = 0.72 eV, ΔE = 0.143 eV, $\tau_0 = 0.94\ 10^{-13}$ s. For $LiPO_3$, we obtain E_0 = 0.817 eV. For both samples, our E_0 values surprisingly well compare with activation energies obtained by DC conductivity measurements. This agreement is not obvious, since DC conductivity cannot reflect details of an activation energy distribution as the microscopic NMR method does. The increase of ΔE with doping might be explained with the larger variety of Li sites due to the incorporation of F ions in the phosphate network.

We note that the success of this analysis is based on a large amount of experimental data. To avoid heating of the sample beyond the glass transition temperature, we only measured on the low-temperature side of the relaxation rate maximum. However, in view of the fact that the fit of the relaxation data covers a wide range of frequencies, the highest frequency being 1000 times larger than the lowest, we regard the result as convincing evidence for the validity of our model.

Further improvements of models which interpret spin-lattice relaxation in solid electrolytes must relate the experimental data to *details* of the microscopic movements of the ions. By taking into account the many-body character of the

substance, one must calculate a specific correlation function which is appropriate for the microscopic motion under investigation, whether it is a crystalline or a disordered compound. Several concepts have been proposed along these lines, for instance the the *Coupling Model* developed by Ngai [9] and various microscopic models proposed by Funke and coworkers [10]; however, their discussion is beyond the scope of this review.

5. High-pressure Experiments

Only a few NMR studies in solid electrolytes are performed at elevated pressure because experiments and especially NMR measurements are more easily performed at ambient pressure. Since both temperature and pressure are the thermodynamic variables which determine the state of a solid, NMR experiments at high pressure can provide additional information. In some cases pressure is found to be a complementary variable to temperature, in other cases pressure is the essential variable. Pressure affects NMR parameters like relaxation time, linewidth, line splitting, and resonance frequency. To illustrate the situation, we will discuss a few examples from the Zürich laboratory. In all experiments, hydrostatic pressure is transmitted by helium gas to the probe head allowing experiments up to 0.7 GPa; temperature is varied between 77 and 300 K, and the field strength is 5.1 Tesla. A detailed review of these studies has been published earlier [11].

An example concerns again Li_3N [11], which, at ambient pressure and 300 K, exists in the α phase. Applying a pressure of 0.42 GPa at 300 K transforms this phase into a β phase. Domains rather than a single phase are formed at the phase transition, these domains being arranged in a hexagonal symmetry pattern around the "old" *c* axis of the α phase. The new phase can be recovered at normal pressure. The larger spin-lattice relaxation rate of the β phase indicates an increase of the ionic conductivity.

For pressure studies beyond 1 GPa, a new device is necessary: the diamond-anvil cell. The disadvantage of the method is that only extremely small samples can be used. Nevertheless, we succeeded to measure the pressure dependence of the Knight shift and the self-diffusion of ^{7}Li and ^{23}Na in Li and Na metal, respectively, up to about 8 GPa [12]. As much as we know, no solid electrolytes have been studied so far by the NMR diamond-anvil cell method.

6. Measurement of the Diffusion Coefficient

Up to now, we have met NMR experiments which usually allow us to determine *several* relevant parameters of the solid. Can NMR measure the unique and most important parameter of a solid electrolyte, namely the diffusion coefficient? The temperature and concentration dependence of the diffusion coefficient, *D*, delivers information essential for the understanding of the conduction mechanism. Using Einstein's equation, $D = f < r^2 > / 6\tau$, D can be related to the mean square jump distance, $< r^2 >$, and the jump rate, $1/\tau$, of the diffusing ion; f is the spatial correlation factor. In principle, τ can be obtained from relaxation time and

linewidth data, and with $< r^2 >$ known from the structure, one could determine D. Since the relaxation or linewidth data must be interpreted by a suitable model, the whole procedure of determining D would be model dependent - and this is a disadvantage.

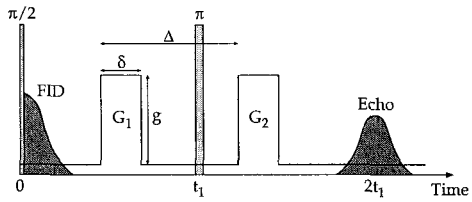

Fig. 3. Arrangement of radio-frequency ($\pi/2,\pi$) and field-gradient (G_1, G_2) pulses in the pulsed-field gradient (PFG) experiment to measure the diffusion coefficient. One observes the spin-echo signal (after Fourier transformation). FID is the free-induction decay signal induced by the $\pi/2$ pulse.

Skejskal and Tanner [13] invented an elegant alternative , the *pulsed-field gradient* (PFG) technique which is a model independent method to measure D by NMR. In its simplest version (see Fig. 3), the method employs the Hahn $\pi/2-\pi$ spin-echo experiment used in many of the experiments described so far. In addition, a magnetic field gradient pulse is applied after each radio-frequency (*rf*) pulse. These gradients "label" the diffusing ions by their respective Larmor frequency. In the absence of diffusion, the effects of G_1 and G_2 cancel. However, if spins change their spatial position between the application of the gradient pulses, the spin-echo signal will be attenuated. If one measures the echo amplitudes A_G and A with and without gradient pulses, respectively, the diffusion coefficient D_{NMR} follows from the relation [13]

$$\ln\frac{A_G}{A}=\gamma^2 D_{NMR}\delta^2(\Delta-\frac{1}{3})g^2.$$

The meaning of δ, Δ, and g is given in Fig. 3. The steady background gradient is assumed to be very small with respect to g.

The PFG method differs from the well-known tracer technique, which measures the diffusion coefficient, D_T, in several important and advantageous points: (i) the nuclear magnetic moment labels the diffusing ion; (ii) the labeled atoms are natural constituents of the material rather than "impurities"; (iii) the time elapsing between the gradient pulses defines precisely the time over which diffusion is observed, (usually in the millisecond range); (iv) the experiment itself is non-destructive, parameters like temperature can be changed for the very same sample and samples may be reused for other experiments.

The magnitude of the diffusion coefficient is a valuable information by itself. The NMR methods allow, however, to gain additional knowledge by measuring, for instance, the anisotropy of D_{NMR}, as in Li_3N and β-$LiAlSiO_4$, or the pressure dependence of D_{NMR}. Further, one may combine D_{NMR} with the diffusion coefficient, D_σ, derived from conductivity measurements via the Nernst-Einstein equation. This results is the Haven ratio, $H_R = D_{NMR}/D_\sigma$, which reveals correlation effects in the ion dynamics. For instance, in the crystalline Ag conducting

KAg_4I_5 and $RbAg_4I_5$ compounds, which undergo a phase transition in the superionic phase, we detected an unusually low value of H_R of about 0.5. Such values may be the result of a "caterpillar" effect; that is a cooperative motion of two or more ions in such a way that a jumping ion causes other ions to jump in the same direction. At the transition form the high- to the low-temperature phase, H_R decreases implying an increase of the number of ions involved in the caterpillar movement. In the low-temperature phase of $RbAg_4I_5$, D_{NMR} of ^{109}Ag is about 3 $\times 10^{-13}$ m^2/s. For comparison: the diffusion coefficient of water at 300 K is about 10^{-9} m^2/s.

While in many crystalline solid electrolytes the diffusion coefficient displays an Arrhenius temperature dependence (and thus directly yields the activation energy), the diffusion coefficient in superionic polymers quite often follows the Vogel-Tammann-Fulcher equation

$$D \cdot T^{-1/2} = A \cdot \exp[-E/k(T - T_0)].$$

In the framework of the "free-volume model", E is an apparent activation energy and T_0 is the ideal glass transition temperature at which the free volume, which is available for segmental motion, tends to zero and thus translational motion ceases.

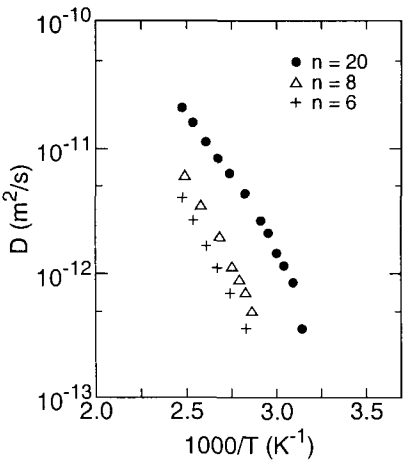

Fig. 4. ^7Li diffusion coefficient in $(PEO)_n$ - $(LiClO_4)$ for various values of n. From [14].

As an example, Fig. 4 displays the temperature dependence of the ^7Li diffusion coefficient in a polyethylene oxid (PEO) based polymer, $(PEO)_n$ - $(LiClO_4)$ taken from Ref. 14 where also other examples are given.

If smaller values of D_{NMR} are to be measured (and to overcome technical problems of the PFG method), one may employ the static fringe-field (SFF) method employ the static fringe-field (SFF) method which uses the constant gradient of the fringe or stray field of a superconducting magnet where gradients up to the order of 100 T/m are available [15,16]. In a simple version, the SFF method uses three $\pi/2$ *rf* pulses, the normal echo appears after the first two pulses and a "stimulated" echo is produced by the third *rf* pulse. The field gradient affects the strength of the stimulated echo during the two t_1 time intervals (compare Fig. 3). From the ratio of the two echoes, D_{NMR} is evaluated. Among several applications of the SFF method we mention, as an example, the study of segment diffusion in entangled PEO melts [17].

7. NMR Imaging

The production of anatomical images from humans and animals by NMR Imaging is well established in medicine and non-medical applications become increasingly important. As we have seen in the previous Section, the position of a magnetic nucleus in a magnetic field gradient is labeled by the NMR frequency, in other words: the atomic position is encoded onto the frequency. Therefore, once a PFG apparatus has been developed, it seems straightforward to construct an NMR imaging device.

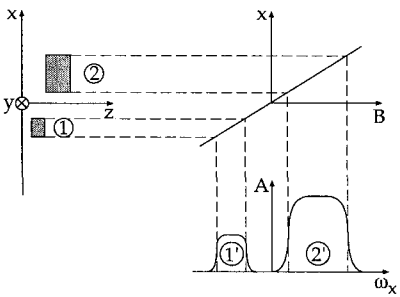

Fig. 5. Principle of frequency encoding in NMR imaging of a two-dimensional object.

Fig. 5 sketches the principle for imaging a two-dimensional object. Two rectangular samples 1 and 2 are placed in the xz plane. The magnetic field (oriented along the z axis) varies with x as shown. Thus the spins of the samples "see" different magnetic fields according to their position. The pulse experiment then produces the images 1' and 2'. By scanning the various frequencies of a sample, a one-, two- or three-dimensional (1D, 2D, 3D) NMR image is constructed. For instance, for a 2D image, a gradient along the x direction encodes the x coordinate onto the frequency and a second gradient perpendicular to the first one encodes the y coordinate into the phase of the NMR signal. Then, 2D Fourier transform of the data points delivers the image.

For an acceptable NMR image, one requires the linear resolution of the image, Δx, to be as small as possible. Δx must comply with the relation $\Delta x = 2\pi\Delta\nu/\gamma G$, where $\Delta\nu$ is the natural width of the NMR line and G is the applied field gradient which encodes the spatial information. For instance, if proton signals with $\Delta\nu$ = 1 kHz should yield an image with a spatial resolution of 60 mm, a gradient of 0.4 T/m is required. However, for many nuclei such as Li, Na, Al, and Ag, which are important in solid electrolyte studies, much larger gradients are necessary since γ is smaller and the linewidth is much larger. Another serious limitation arises from an inherent property of the sample: the very short nuclear spin-spin relaxation time, T_2, which is a measure for the time length of the NMR signal (for instance of the FID in Fig. 3) and hence defines the time over which the encoding takes place. In solids, T_2 can be up to 10^6 times shorter than in liquids or in "soft" materials like rubber.

The first NMR image of a solid electrolyte has been produced by Suits and White [18]: the 2D ^{23}Na image of a Na-β-alumina crystal. In our laboratory, we employed the 2D technique for imaging mobile Li ions in a $(PEO)_8$ - $(LiClO_4)$

polymer electrolyte film [19]. The resolution was about 0.2 mm in each direction; that is quite promising in view of the low Li content of only 1.6 mole%.

NMR Imaging offers the possibility to monitor the behavior of electrolytes in charging and re-charging cycles of batteries, to observe phase transitions and dynamical processes on a microscopic level, and to investigate interfaces. We hope, for the future, to find more NMR imaging examples for solid electrolytes; elastomers are already frequently studied.

References

1. J.L. Bjorkstam and M. Villa, *Magnetic Reson. Rev.* **6** , 1 (1980).
2. D. Brinkmann, *Magnetic Reson. Rev.* **14**, 101 (1989).
3. D. Brinkmann, *Progress in NMR Spectroscopy* **24**, 527 (1992).
4. C.P. Slichter, *Principles of Magnetic Resonance*, Springer (Berlin, Heidelberg, New York, 1990).
5 (i) Atta-u-Rahman, *Nuclear Magnetic Resonance – Basic Principles*, Springer (New York, Berlin, Heidelberg, Tokyo, 1986). (ii) J.W. Akitt, *NMR and Chemistry*, Chapman & Hall (London, New York, Tokyo, 1992). (iii) A.I. Popov K.H. Hallenga (editors), *Modern NMR Techniques and Their Application in Chemistry*, Marcell Dekker (New York, Basel, Hong Kong, 1991).
6. D. Brinkmann, S. Berger, and J. Roos, in: *Solid State Ionics - Materials and Devices*, eds. B.V.R. Chowdari and Wenji Wang, World Scientific, p. 167 (Singapore, 2000).
7. D. Brinkmann, M. Mali, J. Roos, R. Messer, and H. Birli, *Phys. Rev. B* **26**, 4810 (1982).
8. D. Brinkmann , in: *Solid State Ionics - Science & Technology ,* eds. B.V.R. Chowdari, K. Lal, S.A. Agnihotry, N. Khare, S.S. Sekhon, P.C. Srivastava, and S. Chandra, World Scientific, p. 93 (Singapore, 1998).
9. K.L. Ngai, *Solid State Ionics* **105**, 225 (1998) and references therin.
10. K. Funke, in: *Solid State Ionics – The Science and Technology of Ions in Motion*, eds. B.V.R. Chowdari, H.-L. Yoo, G.M. Choi, and J.-H. Lee, World Scientific, p. 19 (Singapore, 2004) and ref erences therein.
11. D. Brinkmann , in: *NMR Basic Principles and Progress*, eds. P. Diehl, E. Fluck, H. Günther, R. Kosfeld, and J. Seelig, Vol. **24**, p. 1 Springer (Berlin-Heidelberg, 1990).
12. R. Bertani, M. Mali, J. Roos, and D. Brinkmann, *J. Phys.: Con dens. Matter* **2,** 7911 (1990).
13. E.O. Stejskal and J.E. Tanner, *J. Chem. Physics* **42**, 288 (1965).

14. D. Brinkmann, in: *Solid State Ionics - Material and Applications*, eds. B.V.R. Chowdari, S. Chandra, Shri Singh, and P.C. Srivastava, p. 179; World Scientific, p. 179 (Singapore, 1992).
15. (i) R. Kimmich, W. Unrath, G. Schnur, and E. Rommel, *J. Magn. Reson.* **91**, 136 (1991). (ii) R. Kimmich and E.J. Fischer, *J. Magn. Reson.* **106**, 229 (1994).
16. P.J. McDonald, *Progress in NMR Spectroscopy* **30**, 69 (1997).
17. E.J. Fischer, R. Kimmich, N. Fatkullin, and G. Yatsenko, *Phys. Rev. E* **62**, 775 (2000).
18. B.H. Suits and D. White, *Solid State Comm.* **50**, 291 (1984).
19. M. Sonderegger, J. Roos, C. Kugler, M. Mali and D. Brinkmann, *Solid State Ionics* **53-56**, 849 (1992).

ANALYSIS OF CONDUCTIVITY AND NMR MEASUREMENTS IN $Li_{3x}La_{2/3-x}TiO_3$ FAST Li^+ IONIC CONDUCTOR: EVIDENCE FOR CORRELATED Li^+ MOTION

O. BOHNKE [1] AND J. EMERY [2]

[1] *Laboratoire des Oxydes et Fluorures, UMR 6010 CNRS*

[2] *Laboratoire de Physique de l'Etat Condensé, UMR 6087 CNRS*

Institut de Recherche en Ingénierie Moléculaire et Matériaux Fonctionnels, FR CNRS 2575

Université du Maine, Av. O. Messiaen, 72085 LE MANS Cedex 9, France

E-mail: odile.bohnke@univ-lemans.fr

A. ORLIUKAS AND T. SALKUS

Department of Physics, Vilnius University Sauletekio al. 9, LT-2040 VILNIUS Lithuania

J.C. BADOT

Laboratoire de Chimie Appliquée de l'Etat Solide (UMR7574 CNRS) ENSCP 11 rue P et M Curie 75231 PARIS France

The dynamics of lithium ions in the polycrystalline fast ionic conductor $Li_{3x}La_{2/3-x}TiO_3$ has been investigated by conductivity spectroscopy in the wide frequency range from 1Hz to 1GHz and by ^7Li NMR spin-lattice relaxation measurements (T_1 and $T_{1\rho}$) in the temperature range from 150K to 600K. The results of T_1 and $T_{1\rho}$ clearly reveal the presence of two thermally activated Li^+ motions: a slow one, attributed to the long-range Li^+ translation which gives rise to the dc conductivity and a fast one, attributed to a localised motion of Li^+ in the A-cage of the perovskite. At high frequency, a dispersive behaviour of the conductivity with frequency is observed. The analysis of this dispersive behaviour along with the analysis of the activation energy of the ionic motion at fixed frequencies clearly reveal the existence of the correlated motion of the moving ions. The real microscopic energy barrier of the long-range ionic motion is obtained at high frequency and agrees with the values of ^7Li NMR relaxation times measurements ($T_{1\rho}$) obtained at 62.5 kHz. These complementary techniques allowed us to describe the different motions of the moving ions in this oxide and to attain the real value of the microscopic energy barrier.

1. Introduction

The development of high lithium ion conductors is attracting much attention because of their potential applications in electrochemical devices such as high-energy lithium

ion batteries, electrochromic systems, supercapacitors and electrochemical sensors. Apart from the application point of view, the understanding of the microscopic diffusive ionic motion in a host matrix is another important problem both for fundamental reasons and to learn to optimise the ionic conductivity in electrolytes. This last point is a very difficult one since the *a priori* prediction of structure and properties of inorganic solid materials seems at present totally impossible. Indeed, high mobility of charge carriers in a given host matrix is difficult to predict. If every one agrees with the fact that an open framework structure with vacancies is favourable for mobility, the charge carrier mobility is greatly influenced by the interactions the mobile species experiences during its hopping through the conductive pathways. Therefore, different techniques, able to probe the motion of charge carriers, can be used to shed any light on ionic hopping dynamics. Techniques such as impedance, dielectric and Nuclear Magnetic Resonance (NMR) spectroscopies are helpful for this purpose. They have to be associated with X-Ray or Neutron Diffraction techniques since the perfect knowledge of the crystallographic structure is also an important point. The study of diffusive ionic motion is then an exciting topic since it covers fields like physics, chemistry and materials science.

The perovskite-type Li ion conductors $Li_{3x}La_{2/3-x}TiO_3$ have attracted much attention because of their high conductivity, i.e., $\sigma = 10^{-3}$ S cm^{-1} for $x = 0.11$ at room temperature, first reported by Belous et al.[1] and afterwards by Inaguma et al.[2]. These compounds (named hereafter LLTO) belong to a solid solution. The composition range of this solid solution is $0.06 < x < 0.14$ for compounds prepared below 1200 °C[3,4]. They are purely lithium ion conductors, they have a high electrochemical stability window (greater than 4V), they are stable in dry and hydrated atmospheres and the phase is stable in a wide temperature range from 4K to 1600K. Despite these unique features, the presence of the easily reducible Ti^{4+} precludes their use as electrolyte materials in batteries with lithium metal anode. However, this solid solution deserves further attention towards studying diffusive lithium motion.

The aim of this paper is to present experimental results obtained by conductivity spectroscopy in a wide frequency range from 1Hz to 1 GHz as well as ^{7}Li NMR spin-lattice relaxation measurements in the temperature range from 150 to 600 K. We will show how these techniques are complementary and we will present the particular contribution of each of them to describe the microscopic motion of the charge carriers and its behaviour with temperature. Our attention will be focused on the ion correlation phenomenon and on the determination of the true activation energy of the charge carrier transport process.

2. Experimental

The solid solution compound, with composition $x = 0.11$, is prepared by conventional solid-state reaction from Stoechiometric amounts of TiO_2 (99.5 %)

from Riedel Haen, Li_2CO_3 (99.997 %) from Aldrich and freshly dehydrated La_2O_3 (99.999 %) from Rhone-Poulenc. The starting materials are mixed and pressed into pellets (diameter: 13 mm, thickness ≈ 2 mm, P = 250 MPa). They are first heated at 850 °C for 4 hours in a Pt crucible and then heated up to 1050 °C for 12 hours. After grinding and pressing, the pellets are heated twice for 12 hours at 1100 °C and 1150 °C respectively. After a new grinding, a last heating treatment is performed on small pellets (diameter: 3 mm, thickness slightly smaller than 1 mm, P = 4 GPa) at 1250°C for 12 hours. The heating sweep rate is 5 °C.mn^{-1}. A natural cooling in the furnace to room temperature (RT) follows all the heating treatments.

The samples were characterized by powder X-ray diffraction The patterns were recorded at room temperature on a D500 Siemens diffractometer (radiation CuKα, 2θ range = 9° - 129°, step 2Δθ = 0.04°, time by step = 18 s) and analysed through the Rietveld method with the Fullprof software.

Total conductivity measurements were performed by complex impedance spectroscopy in the 10 MHz – 1 Hz frequency range. A sine wave potential of 400 mV (r.m.s.) was used as the electrical input signal applied to a pellet onto which ion blocking Pt electrodes have been sputtered. The measurements were carried out in dry N_2. The electrical response of the sample was determined with a Solartron 1260 Impedance Gain-Phase Analyzer. The impedance measurements in the 1 MHz – 1 GHz frequency range were carried out in air in the temperature range from 300 to 600 K, with a coaxial impedance spectrometer set-up. The data analysis has been performed as described in a previous paper[5].

T_1, and $T_{1\rho}$ relaxation times were carried out in the 150 K – 900 K temperature range. The Larmor frequencies for ^7Li was ν_0 = 116 MHz. The amplitude of the radio-frequency field was ν_1 = 62.5 kHz. The experimental set-ups and the procedure used to determine the spin-lattice relaxation times, T_1, and the spin-lattice relaxation times in the rotating frame, $T_{1\rho}$, were described in[6-8].

3. Results

3.1. Crystallographic structure

LLTO is structurally well described either in the P4/mmm[4] or Cmmm [9] space groups. The structural model, based on the P4/mmm space group obtained from the refinement of powder X-Ray diffraction (XRD) patterns (Fig. 1), consists of a tetragonal distortion of the cubic ABO_3 perovskite unit cell with a = b ≈ 3.87 Å and c ≈ 2a. Fig.2 shows a schematic view of the unit cell with the TiO_6 octahedra and the A-cages formed by 12 oxygen ions belonging to 8 different octahedra. The model based on the Cmmm space group involves a slight tilting of the octahedra. However, in these two structural models, the La^{3+} ions are unequally distributed in the two sites 1a and 1b, quoted La1 and La2 respectively, centres of two adjacent cages of the perovskite network along the c-direction. This unequal distribution of La^{3+} ions is responsible for the doubling of the c axis parameter and for the presence of the

superstructure lines (hkl with l = 2n+1). The broadening of the superstructure diffraction lines is related to the presence of antiphase domains, this phenomenon creates here a disordered situation in the regular succession ...La1-La2-La1...along the c axis. This implies the existence of La^{3+}-rich layers and La^{3+}-poor layers in the (a,b) planes of the perovskite structure. The La^{3+} preferential occupancy of the La1 site probably causes the slight tilting of the octahedra.

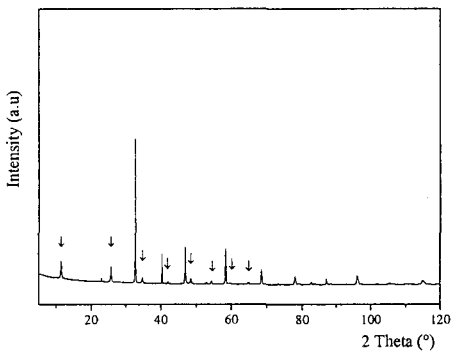

Figure 1. Powder XRD pattern of $Li_{3x}La_{2/3-x}TiO_3$ (x=0.11) obtained by solid state reaction (↓ superstructure lines).

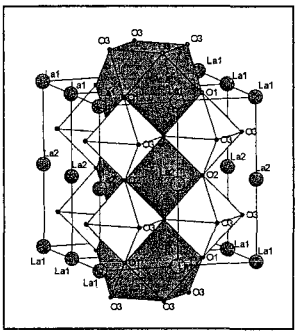

Figure 2. Crystal structure of LLTO. La1 = La^{3+}, Li^+ or vacancies in position (0,0,0), La2 = La^{3+}, Li^+ or vacancies in position (0,0,1/2).

3.2. ^{7}Li NMR relaxation times

The general behaviour of the spin-lattice relaxation times T_1 for ^{7}Li nucleus as a function of temperature is shown in Fig. 3. The following general features of the T_1 spin-lattice relaxation are: (i) only one T_1 is observed whatever the method used (inversion-recovery or saturation), (ii) the presence of a minimum around 350 K, (iii) a particular behaviour around 200 K and (iv) a strong asymmetry around the minimum. These two last features have been particularly discussed by Emery et al.[6-8]. A unique T_1 does not agree neither with the observation of two kinds of Li^+ ions in the structure nor with the fact that ^{7}Li has a I = 3/2 spin value. However this experimental result suggests that the spin-spin relaxation time is fast enough to allow a unique spin temperature[10].

T_1 experiments indicate that a motion with characteristic correlation time τ_c, $\approx 10^{-9}$ s at 350 K, is probed by the nuclei. τ_c verifies the relationship $\omega_0\tau_C \approx 1$ at the minimum of the T_1 *vs* 1000/T plot. We recall that $\omega_0 = 2\pi\nu_0$. The correlation time of the Li motion is thermally activated and follows the relationship:

$$\tau_c = \tau_0 \exp\left(\frac{E_a}{kT}\right) \qquad (1)$$

where E_a is the activation energy of the correlation time and k the Boltzman constant. This leads to an attempt frequency of 10^{11} Hz. This value is quite small if compared to the typical phonon frequency, namely $10^{12} - 10^{13}$ Hz.

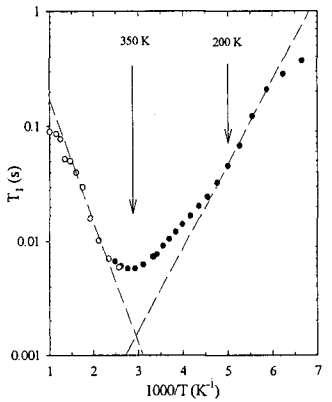

Figure 3. Logarithmic plot of the spin-lattice relaxation time T_1 for ^{7}Li (ν_0 = 116 MHz) as a function of inverse of temperature for LLTO (x = 0.11). The dashed lines represent the linear regressions of the data at low (E_a = 0.14 eV) and high temperatures (E_a = 0.20 eV).

Fig. 4 shows the spin-lattice relaxation time in the rotating frame, $T_{1\rho}$, for the ^{7}Li nucleus. The main features appearing in this figure are: i) two values of $T_{1\rho}$ at low temperature and only one value above 300 K, ii) the presence of minima around 270 K, iii) a particular behaviour around 200 K, as for T_1 curve. Each curve $T_{1\rho}$ *vs* 1000/T exhibits a minimum. The presence of these two relaxation times suggests that two different Li^+ ions can be differentiated in this oxide. According to the relationship $\omega_1\tau_C \approx 1$ at the minimum, the correlation time of the motion probed by $T_{1\rho}$ is close to 10^{-6} s. It appears at 280 K for the slowest one ($T_{1\rho}^S \approx 0.3$ ms) and around 250 K for the fastest one ($T_{1\rho}^F \approx 70$ μs).

The minimum of the relaxation time T_1, measured at ω_0 = 116 MHz and those of the relaxation times $T_{1\rho}$, measured at ω_1 = 62.5 kHz for ^{7}Li nucleus, occur in the same temperature range: at 350 K for T_1 and at 280 K and 250 K for the two $T_{1\rho}$. The three decades between the Larmor angular frequency ω_0 and the angular frequency of the radio-frequency field ω_1 cannot be compensated by the observed temperature difference at the minima of T_1 and $T_{1\rho}$. This result means that T_1 and $T_{1\rho}$ probe two different Li^+ motions: a fast one probed by T_1 at 116 MHz with a correlation time $\tau_c \approx 10^{-9}$ s at 350 K and a slow one probed by $T_{1\rho}$ at 62.5 kHz with a correlation time $\tau_c \approx 10^{-6}$ s at 280 K.

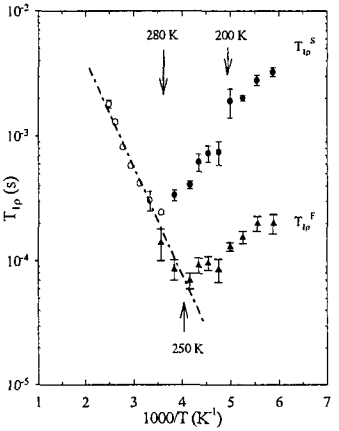

Figure 4. Logarithmic plot of the spin-lattice relaxation times in the rotating frame $T_{1\rho}$ for ^{7}Li (ν_1 = 62.5 kHz) as a function of inverse of temperature for LLTO (x = 0.11). The dashed line represents the linear regression of the data at high temperatures (E_a = 0.20 eV).

3.3. Conductivity spectroscopy

One of the main advantages of frequency dependent measurements is that the contributions of the bulk material and the interfaces (i.e. grain boundary and electrode/electrolyte interfaces) can easily be separated if the time constants of each relaxation process are sufficiently different This is clearly shown in Fig. 5 which is a typical plot of the real part of the conductivity of LLTO as a function of frequency, recorded at 340 K, in the frequency range from 1 Hz to 1 GHz. Three contributions : the contribution of the bulk conductivity, of the grain boundary conductivity and of the electrode effects to the real part of the conductivity are clearly observed, as frequency decreases. The long-range conductivity process (or translation motion of the mobile ions) is indicated by the presence of a plateau in the real part of σ'. The plateau at high frequency ($\approx 10^7$ Hz at 340 K) corresponds to the dc-conductivity (σ_{dc}) and to the Li^+ translation motion into the bulk of the material. The sudden decrease of conductivity is related to blocking of the moving ions at the grain boundaries. The second plateau at intermediate frequency ($\approx 10^3$ Hz at 340 K) corresponds to the Li^+ translation motion into the grain boundary of the ceramic. The second decrease of conductivity at low frequency is due to the blocking effect of the Pt electrodes.

In an ionic conductor, σ_{dc} probes the long-range ionic dynamics. Fig. 6 shows a typical plot of the variation of σ_{dc} as a function of temperature, plotted in an Arrhenius fashion, in the 200 – 600 K temperature range. The dc-conductivity is obtained from the high frequency plateau shown in Fig.5.

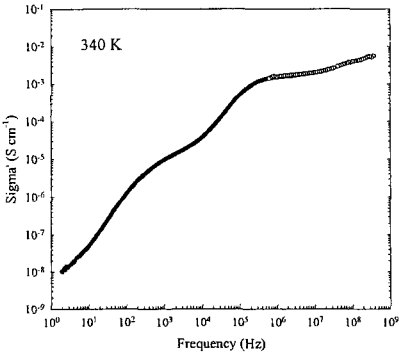

Figure 5. Real part (σ') of complex conductivity, σ*, as a function of frequency for $(La_{2/3-x}Li_{3x}\square_{1/3-2x})TiO_3$, x = 0.11 at 340 K.

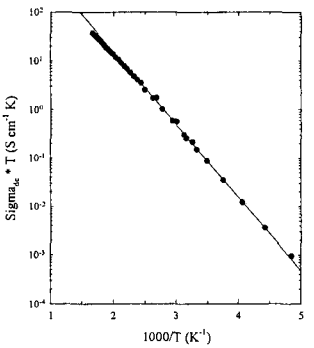

Figure 6. Arrhenius plot of the dc-conductivity of $(La_{2/3-x}Li_{3x}\square_{1/3-2x})TiO_3$, x = 0.11. The full line represents the Arrhenius law.

Below 400 K, σ_{dc} follows a classical Arrhenius law :

$$\sigma_{dc} = \frac{\sigma_0}{T} \exp\left(-\frac{E_a}{kT}\right) \qquad (2)$$

The mechanism of conduction is thermally activated with an activation energy E_a = 0.30 eV and a pre-exponential factor of 2 10^4 S cm^{-1} K. Above 400 K, the plot displays a curvature, as previously reported by several authors, either on polycrystalline or single crystal LLTO[2,6,11-18]. Some authors suggested to describe this behaviour with a Vogel-Tamman-Fulcher (VTF)-type relationship, generally

used in glasses and polymers[12,15,16]. In such a behaviour, the mechanism of conduction is thermally assisted and is characterised by a very small activation energy. The ionic diffusion would be no more thermally activated but would occur as a result of the redistribution of free volume in the matrix. In these ceramic oxides, we could postulate that this redistribution would become possible at high temperature because of the thermal vibration of the ions of the matrix through which the mobile ions move. This point is not yet clearly established and is always matter of discussion.

Fig. 7 presents some plots of the real part of the conductivity as a function of frequency, in the frequency range from 1 MHz to 1 GHz, at different temperatures. As temperature increases, the conductivity increases and the spectrum shifts to high frequencies. Therefore, for a given frequency, the relaxation probed at low temperature can be different from the relaxation probed at high temperature. For example, we can probe a relaxation in the bulk of the ceramic at low temperature and we can probe another relaxation, in the grain boundary, at high temperature. This is observed in Fig. 7 if we follow the conductivity at 1 MHz, for example.

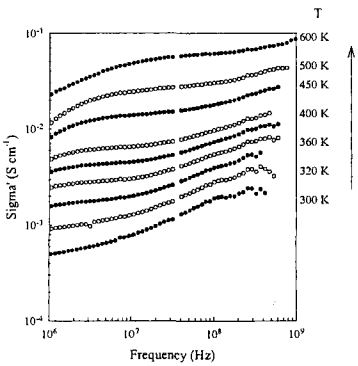

Figure 7. Real part (σ') of complex conductivity, σ^*, as a function of frequency (in the radio frequency range) for $(La_{2/3-x}Li_{3x}\square_{1/3-2x})TiO_3$, $x = 0.11$ at different temperatures.

The impedance data have been recorded every 10 K. It is then possible, by plotting the conductivity as a function of temperature for a given frequency, to clearly observe this phenomenon. This is shown in Fig. 8 where conductivity is plotted as a function of temperature at 1 MHz, 10 MHz and 100 MHz. It can be observed that the conductivity increases as frequency increases.

From Figs. 7 and 8 it can be observed that at 1 MHz the conductivity is due to the hopping of Li^+ ions into the bulk of the ceramic at low temperature. At 300 K, the dc-conductivity is measured. As temperature increases, the impedance spectrum

shifts to high frequency and around 400 K a decrease of conductivity, due to the blocking effect of the grain boundaries, is recorded. This is shown in Fig. 8. An activation energy of 0.27 eV, associated to the hopping process of Li^+ ions into the bulk, is determined at 1 MHz and below 400 K. The same phenomenon is observed in Fig. 8 at 10 MHz. However the decrease of conductivity due to the grain boundaries blocking effect occurs at higher temperatures, as expected by the shift of the impedance spectra with temperature. Furthermore, the activation energy of the Li^+ hopping process decreases to 0.25 eV at 10 MHz. Finally, at 100 MHz, the blocking effect of the grain boundaries is no more observed in the temperature range investigated. The hopping process of the moving ions in the grains is recorded at high temperature and an activation energy of 0.23 is measured. The S-shape of the curve at 100 MHz reveals the presence of another motion of the mobile species. This motion is a very fast one and its activation energy is around 0.20 eV.

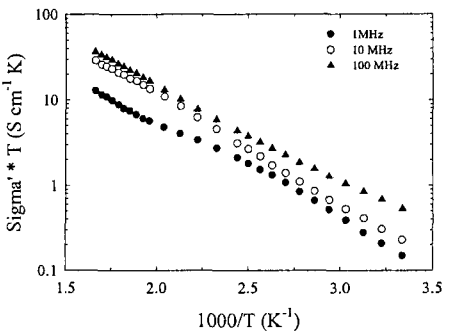

Figure 8. Arrhenius plot of the real part (σ') of complex conductivity, σ*, as a function of inverse of temperature for $(La_{2/3-x}Li_{3x}\square_{1/3-2x})TiO_3$, x = 0.11 at different frequencies.

4. Discussion

^7Li NMR relaxation times measurements clearly evidenced that Li^+ ions undergo two different motions in the bulk of the oxide. This result has been already discussed in our previous papers[7,8,19]. The main conclusion drawn in these papers is that the fast motion of Li^+, probed by the spin-lattice relaxation time, T_1, at 116 MHz, can be attributed to the localised motion of Li^+ ions inside the A-cage of the perovskite structure. Its correlation time is thermally activated (E_a = 0.20 eV), $\tau_c \approx 10^{-9}$ s at 350 K. The slow motion, probed by the spin-lattice relaxation time in the rotating frame, $T_{1\rho}$, at 62.5 kHz, can be attributed to the translational motion of the Li^+ ions from one A-cage to a next vacant one. Its correlation time is also thermally activated (E_a = 0.20 eV), $\tau_c \approx 10^{-6}$ s at 280 K. This ionic long-range motion gives rise to the dc-conductivity of the oxide. The determination of the dc-conductivity, measured by

impedance spectroscopy, showed that the long-range motion of Li^+ is thermally activated with an activation energy of 0.30 eV below 400 K. A large discrepancy can be observed between these two results although these two measurements are related to the same ionic motion in the material. Such a discrepancy between these two techniques, E_a (dc-conductivity) > E_a (NMR) is generally encountered in studying solid electrolytes. This is generally explained by the correlation motion of the ionic species and by the difference in both techniques, NMR being a technique that probes microscopic motion and impedance spectroscopy at low frequency being a technique that probes macroscopic motion. These above results give experimental evidence for such correlated motion.

In structurally disordered solid electrolytes it is well known that the mobile species do not perform random hopping. The concept of random hopping implies a dipersionless conductivity. This is not experimentally observed and the existence of a frequency dependent conductivity, as shown in Fig. 7, rules out the possibility of a random hopping. As described by Funke[20], dispersive hopping conductivity can be interpreted in terms of "unsuccessful" forward-backward hopping sequence. At low frequency, when the time window is long, the probability to observe forward-backward hopping sequence is relatively high. Such hopping sequence does not contribute to the dc-conductivity since it leads to ineffective hops for conductivity. As frequency increases, or when the time window decreases, this sequence becomes less and less observed. Therefore, the conductivity increases. Finally, when the time window is sufficiently short every observed hop is seen as individual hop. This final step corresponds to observation of random hopping.

The activation energy of the hopping process determined at low frequency is then an apparent one because during this time interval of duration $1/\omega$ the ion will undergo several hops either in the forward direction or in the backward direction. The observed motion is then correlated. When frequency is sufficiently high and the time of observation is sufficiently short to see individual hops then the motion is observed without any correlation effect. This change from correlated motion to random motion can be detected by the analysis of the conductivity curves plotted at a given frequency in an Arrhenius fashion, as shown in Fig. 8. Such a plot can also help to determine any change of conduction mechanism of the mobile species as temperature increases. The slope of the curve gives the activation energy of the migration process observed.

It is known that when an ac signal is applied to a material, only the species with motions that will be able to follow this alternative signal will be observed. The slowest ones, which have much inertia, will not be observed. As temperature increases, the motion rate will increases and then some new motions may appear. This is what is observed in Fig. 8. The curve relative to the conductivity at 1 MHz shows that at low temperature the observed motion is the translation of the ions from

A-cage to A-cage corresponding to dc-conductivity. This is the motion probed by the spin-lattice relaxation time in the rotating frame $T_{1\rho}$, shown in Fig. 4 Around 350 K, the conductivity decreases because of the blocking effect of the grain boundaries. Above this temperature the translation of the Li^+ ions into the grain boundaries is observed and will limit the conductivity. At 10 MHz, the translation of the ions from A-cage to A-cage is observed at intermediate temperature, between 350 and 500 K. Above 500 K the grain boundaries blocking effect is observed and below 350 K a new motion appears. At 100 MHz, the translation from A-cage to A-cage appears above 500 K. At low temperature a new and fast motion is clearly observed. This is the fast motion probed by the spin-lattice relaxation time T_1, as shown in Fig. 3. This motion has been attributed to the localised motion of Li^+ inside the A-cage. In Fig. 3 the contribution of the A-cage to A-cage motion of Li^+ is observed around 600 K.

As soon as the different motions of Li^+ have been characterised their activation energy can be determined. For the long-range motion of Li^+ from A-cage to A-cage the activation decreases from 0.30 eV for the dc-conductivity, to 0.27 eV at 1 MHz, 0.25 eV at 10 MHz and 0.23 eV at 100 MHz. The decrease of the activation energy as frequency increases indicates that a highly correlated hopping process is observed at low frequency. As frequency increases and consequently as the time window decreases a less and less correlated hopping process can be observed leading to the decrease of the activation energy that becomes very close to the uncorrelated motion observed by NMR (E_a = 0.20 eV). For the localised motion of Li^+ inside the A-cage an activation energy of 0.20 eV has been determined at 100 MHz, the same value as the one determined by the spin-lattice relaxation time T_1.

5. Conclusion

These two techniques, that probed the Li^+ motions in LLTO, are proved to be complementary. ^7Li NMR measurements revealed the presence of two motions of the moving ions and the presence of two kinds of Li^+ ions in the perovskite structure. The conductivity spectroscopy also revealed the presence of different motions of the Li^+ ions into the bulk of the oxide. However it has been shown that the Li^+ motion from A-cage to A-cage, that leads to the dc-conductivity and that is probed by $T_{1\rho}$, is seen as highly correlated. This leads to an activation energy which is higher than the true energy barrier that encounter the mobile ion during his hop from one A-cage to the next vacant one. To obtain the true energy barrier it is necessary to observe the individual hops. This is possible at high frequency when the time domain of the observation is short. In these conditions, the activation energy obtained by both techniques are reconciled. Furthermore, the fast motion of Li^+ probed by the spin-lattice relaxation time of ^7Li nuclei, T_1, is also evidenced by conductivity spectroscopy at high frequency, in the radio frequency regime.

References

1. A.G. Belous, G.N. Novitskaya, S.V. Polyanetskaya, Y.I. Gornikov, *Russian J. Inorg. Chem.* 32, 156 (1987).
2. Y. Inaguma, C. Liquan, M. Itoh, T. Nakamura, T. Uchida, H. Ikuta, M. Wakihara, *Solid State Comm.* 86, 689 (1993).
3. A.D. Robertson, S. Garcia-Martin, A. Coats, A.R. West, *J. Mater. Chem.* 5, 1405 (1995).
4. J-L. Fourquet, H. Duroy, M-P. Crosnier-Lopez, *J. Solid State Chem.* 127, 283 (1996).
5. R. Sobiestianskas, A. Dindune, Z. Kanepe, J. Ronis, A. Kezionis, E. Kazakevicius, A. Orliukas, *Mater. Sci. Eng. B* 76, 184 (2000).
6. O. Bohnke, J. Emery, A. Veron, J-L. Fourquet, J-Y. Buzaré, P. Florian, D. Massiot, *Solid State Ionics* 109, 25 (1998).
7. J. Emery, O. Bohnke, J-L. Fourquet, J-Y. Buzaré, P. Florian, D. Massiot, *Comptes Rendus de l'Académie des Sciences* 4, 845 (2001).
8. J. Emery, O. Bohnke, J-L. Fourquet, J-Y. Buzaré, P. Florian, D. Massiot, *J. Phys: Condens. Matter* 14, 523 (2002).
9. Y. Inaguma, T. Katsumata, M. Itoh, Y. Morii, *J. Solid State Chem., 166*, 67 (2002).
10. E.R.Andrew, D.P.Tunstall, *Proc. Phys. Soc.* 78, 1 (1961).
11. M. Itoh, Y. Inaguma, W.H. Jung, L. Chen, T. Nakamura, *Solid State Ionics,* 70/71, 203 (1994).
12. O.Bohnke, C.Bohnke, J.-L.Fourquet, *Solid State Ionics,* 91, 21 (1996).
13. Y. Inaguma, J. Yu, T. Katsumata, M. Itoh, *J. Ceram. Soc. Japon,* 105, 6, 548 (1997).
14. Y. Inaguma, Y. Matsui, J. Yu, Y.J. Shan, T. Nakamura, M. Itoh, *J.Phys.Chem.Solids,* 58, 6, 843 (1997).
15. J. Emery, J-Y. Buzaré, O. Bohnke, J-L. Fourquet, *Solid State Ionics,* 99, 41 (1997).
16. C. Leon, J. Santamaria, M.A. Paris, J. Sanz, J. Ibarra, L.M. Torres, *Phys.Rev. B,* 56, 9, 5302 (1997).
17. A.K. Ivanov-Schitz, V.V. Kireev, N.G. Chaban, *Solid State Ionics,* 136-137, 501 (2000).
18. .A. Paris, J. Sanz, C. Leon, J. Santamaria, J. Ibarra, A. Varez, *Chem.Mater.,* 12, 1694 (2000).
19. O. Bohnke, J. Emery, J-L. Fourquet, *Solid State Ionics,* 158, 119 (2003).
20. K. Funke, *Prog. Solid State Chem.,* 22, 111 (1993).

TRANSPORT PATHWAYS FOR IONS IN DISORDERED SOLIDS FROM BOND VALENCE MISMATCH LANDSCAPES

S. ADAMS
Department of Materials Science and Engineering,
National University of Singapore, Singapore 117576
E-mail: mseasn@nus.edu.sg

Starting from the simple bond valence (BV) concept commonly used to judge the plausibility of atomic positions in inorganic crystal structures, a method to analyze energy landscapes and to identify transport pathways for mobile ions in solid electrolytes has been developed. The approach is particularly valuable for analysing transport mechanisms and structure conductivity relationships in disordered solids, where the averaged information directly available from crystallographic methods cannot provide a sufficiently detailed picture. For systems where ion transport occurs in a nearly rigid matrix, e.g. ion conducting glasses, the BV analysis may be based on static structure models from reverse Monte Carlo fits to experimental diffraction data. The assumption that conduction pathways correspond to structure regions where the BV mismatch for the mobile ion remains below a threshold value then enables us to predict activation energy and ionic conductivity of ion conducting glasses from the relative volume of the percolating pathways in the structure model. Moreover BV mismatch landscapes provide further insight into transport mechanisms as they allow enumerating the number of accessible sites for mobile ions (irrespective of their occupancy), as well as quantifying the reduced local dimensionality or the medium-range ordering of transport pathways. The BV analysis of molecular dynamics simulation trajectories extends the application range to systems involving complex reorientation processes (provided that suitable empirical force-fields are available for a system) and permits to extract information on time and temperature dependencies.

1. Introduction

A proper understanding of the relationship between ion transport and structural peculiarities is essential to gain a deeper insight in ionic conduction in disordered electrolytes. Structural information can be obtained experimentally by a wide range of techniques; mainly neutron and x-ray diffraction for general information as well as NMR, EXAFS and vibrational spectroscopy for local information on specific parts of the structure. Presently the only viable method to generate structure models of glassy materials from experimental data is by reverse Monte Carlo (RMC) fitting. RMC produces static models that quantitatively agree with diffraction, EXAFS and NMR data, as well as additional bonding constraints based on further experimental or chemical knowledge.[1-4] In this way experimental data can be translated into a consistent model of the distribution and local environment of the potentially mobile

ions, an essential step towards an understanding of the conduction process. Still it has to be emphasized that RMC models are no unique structure solutions and their interpretation is thus limited to a statistical extraction of characteristic features.

In previous work we discussed how the bond valence method can be utilized to perform such a statistical analysis of ion transport pathways within the RMC models yielding predictions of ionic conductivity.[5-9] Here, the investigation of ion transport mechanisms is extended by discussing the number, distribution and connectivity of "equilibrium sites" (relaxed sites) for the mobile type of ions in various metaphosphate and diborate glasses.

Alternatively the relation between structure and conductivity can be investigated using molecular dynamics (MD) simulations, which should in principle permit to derive all the required structural and dynamical information (within the limitations imposed by the system size and the simulated period). Effectively the MD approach has shown to be a useful tool in obtaining insight into the conduction mechanism and its correlation to the atomic structure (see e.g. Balasubramanian & Rao,[10] Habasaki & Hiwatari,[11] Jund et al.,[12] Yuan & Cormack,[13]). Besides the computational effort required to reach simulation time scales exceeding the nanoseconds regime for the inevitably complex structure models, the most serious limitation is the problem to obtain realistic interatomic potentials between the particles in chemically complicated glasses that quantitatively reproduce experimentally known structural or dynamical properties of the glasses. Here we discuss a comparison of RMC models for glassy $LiPO_3$ with a MD simulation of the same material to elucidate the possibility of using MD simulations or a combination of RMC and MD as the basis for a bond valence analysis of the time evolution of ion transport pathways.

2. Techniques

Details of the slightly modified reverse Monte Carlo method used to build static structure models have recently been described elsewhere.[9] For comparison a dynamic structure model of $LiPO_3$ of the same size (4000 atoms, NVT, T=300K) has been generated by MD simulations using an established 3-body force field[14] starting from the RMC configuration and keeping the experimentally known density fixed. The analyses of ion transport pathways in the RMC model as well as in a set of 100 snapshots from the MD trajectory have been performed using a bond valence approach.

Empirical relationships between bond length and the bond valence (BV) are widely used to identify plausible equilibrium sites for an atom in a crystal structure as sites where the BV sum of the atom matches its oxidation state (*cf.*, e.g. Brown[15]). A modification of the BV approach that improves the assessment of non-

equilibrium site energies by a systematic adjustment of BV parameters to the bond softness[8,16-18] extends the application range of this simple tool to structure - property relationship studies in solid electrolytes. For that purpose "accessible" sites for a mobile ion *A* in a local structure model are identified using empirical relationships between the bond length R and a so-called bond valence $s_{A\text{-}X}$

$$s_{A\text{-}X} = exp[(R_0\text{-}R)/b] \tag{1}$$

as sites where the mismatch of the bond valence sum *V(A)*

$$|\Delta V(A)| = \left| \sum_X s_{A-X} - V_{id}(A) \right| + \sum_X p_{A-X} \tag{2}$$

over the $s_{A\text{-}X}$ from all adjacent counterions X approaches the ideal valence $V_{id}(A)$ (which equals its oxidation state). To enhance the chemical plausibility of BV mismatch "energy landscapes", $|\Delta V(A)|$ contains a penalty function $p_{A\text{-}X}$ that discriminates against sites where a matching *V(A)* is achieved by unfavourable strongly asymmetric coordinations (for details see Adams, 2006) and is complemented by hard minimum distance and soft coordination number constraints. In contrast to most conventional BV parameter sets our *softBV* parameters are based on the assumption that not only the counterions of the first coordination shell but all counterions up to a cut-off radius of 4-8Å (depending on sizes and polarisabilities of the ions involved) contribute to *V(A)*. This is indispensable for modelling ion transport pathways as it avoids artefacts in the BV sum variation, when an ion moves across the border of its coordination shell.

BV ion transport pathway models are based on the supposition that paths between accessible sites, along which $|\Delta V(A)|$ remains sufficiently low represent probable ion transport paths. Isosurfaces of fixed maximum BV sum mismatch $|\Delta V(A)|$ for a certain ion type *A* will thus enclose regions that an *A* ion in the pathway may reach with a certain activation energy E_A. Low BV mismatch regions that include both occupied and vacant sites therefore enable local jumps of *A*. A long-range transport requires pathways that extend through the whole structure. For periodic models this is equivalent to spanning the model box.

Determining the "pathway volume" for a given maximum value of $|\Delta V|$ yields a simple and reliable way of characterising ion transport pathways in local structure models of disordered systems.[6,8] A pathway model for glassy $LiPO_3$ is shown as an example in Fig. 1. To evaluate the pathway volume *V(A)* has to be calculated for a hypothetical A^+ ion at each point in the structure. In practice, the structure model (containing typically 4000 atoms) is divided into a primitive grid containing ca. 4 million cubic volume elements (0.2-0.3 $Å)^3$. A volume element is considered to

belong to the conduction pathway if $|V - V_{ideal}|$ for a hypothetical A at this site is below a fixed threshold value or if the sign of $(V - V_{ideal})$ alters within the volume element. The second condition cushions effects of the limited grid resolution. Accessible volume elements that share common faces or edges belong to the same "pathway cluster". It is assumed that these pathway clusters contribute to *dc* conductivity only if they percolate through the structure model. The remaining restricted pathway clusters are considered to contribute only to *ac* conductivity.

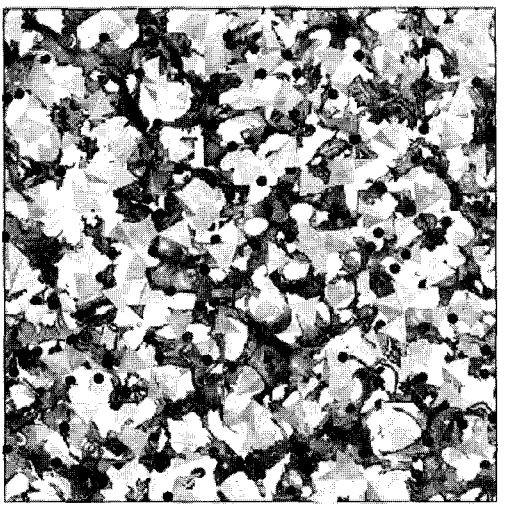

Fig. 1: Bond valence model of Li^+ transport pathway (visualized as dark grey isosurface of constant Li BV mismatch) through a structure model of $LiPO_3$ arising from a RMC fit to neutron and X-ray data. (Li: black spheres; PO_4 groups: light grey tetrahedra. The graph shows a projection of ¼ of the 47000 Å^3 model only to limit the overlap of the pathways).

3. Results and Discussion

3.1 *Revision of the correlation between pathway volume and the conductivity*

In a previous study we could show that the volume fraction F of the percolating pathways can be used to predict the activation energy E_A for *dc* conduction and thereby (in the case of glasses) also of the room temperature conductivity.[5] As mentioned above, the threshold value for $|\Delta V|$ can be chosen to some extent arbitrarily. When comparing pathways for different types of mobile ions, we find that the most suitable value will, as discussed further below, depend on the mass m_A of the mobile ion.[6] A comparison of pathways in different materials became possible by compensating for the mass dependence through a scaling of the pathway volume fraction F for the same BV mismatch threshold. Although this works well, it bears the disadvantage that further characteristics of the pathways for different types of mobiles cannot be compared easily. Therefore we suggest an alternative type of scaling, namely to compensate for the mass dependence when choosing the bond valence mismatch threshold. It turns out that again a fairly general correlation for a wide range of glass systems is found when the threshold value $|\Delta V|_{max}$ of the BV mismatch is chosen to vary with the square root of the cation mass (cf. Fig. 2):

$$|\Delta V(A)|_{max} = |\Delta V_{th,0}|_{max} \cdot \sqrt{m_A} \qquad (3)$$

In this work we employ a BV mismatch threshold of 0.026 v.u. / $amu^{1/2} \cdot m_A^{1/2}$ (v.u. = valence units; *amu* = atomic mass unit), which leads to valence mismatch thresholds ranging from 0.068 v.u. for Li to 0.27 v. u. for Ag. Due to the limited grid resolution using much smaller valence mismatch thresholds would bear the danger of missing some of the local bond valence sum minima.

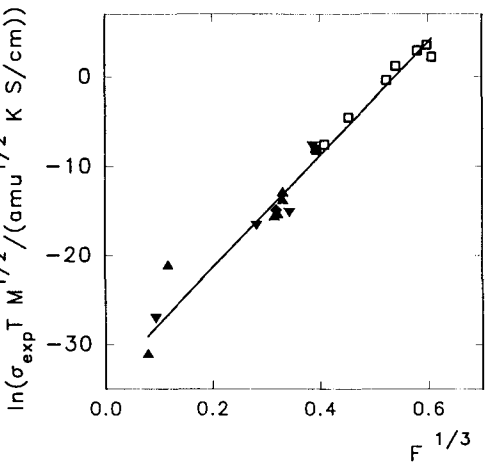

Fig. 2: Correlation between volume F of percolating pathways F and room temperature conductivity of various glass systems (mobile ion: Ag:□, Li:▲ , Na: ▼, Rb: ◆) for a mass-dependent BV mismatch threshold as specified in Eq. 3.

3.2 *Enumeration of sites for mobile ions in the metaphosphate glasses*

In contrast to ion transport in crystalline solid electrolytes that is well understood in terms of interstitial, interstitialcy or vacancy mechanisms, there is a continuing debate whether comparable conduction mechanisms prevail in glasses. As a first step towards a deeper insight, it appears indispensable to count (and classify) all sites that a mobile ion can visit in a given glass structure. Such attempts have been undertaken previously on the basis of molecular dynamics trajectories for a number of glass systems using different routines to identify suitable sites (see eg. Lammert *et al.*[19]). Identifying those sites that have actually been occupied by the mobile ions for a certain while however results in the fundamental uncertainty that the resulting number will depend on the simulated period. This becomes a serious drawback for systems with low cation mobilities such as mixed alkali glasses. The detection of "equilibrium sites" for RMC models of various metaphosphate glasses APO_3 (where $A^+ = Li^+, Na^+, Rb^+, Ag^+$), AgI-doped $AgPO_3$ and halide doped alkali diborate glasses using the bond valence method may however be (approximately) identified with an analysis of the complete energy landscape for the modelled local structure snapshot at a certain instant. As glasses are always metastable states, the term "equilibrium sites" only refers to the fact that these sites are energy minima for the A^+ for the frozen anion arrangement. The method therefore yields a complete inventory of all available sites for A^+ at a given instant irrespective of their occupancy, but of course lacks the information on time evolution.

For each of the systems the starting point is the identification of "accessible" sites within the RMC structure model. To account for the above-mentioned mass

dependence of the conversion between activation energy and bond valence mismatch we employed the cation mass dependent valence mismatch threshold of 0.026 v.u. / $amu^{1/2} \cdot m_A^{1/2}$ (cf. Tab. 1). For the investigated glasses the condition of a sufficiently low BV mismatch alone will not produce individual sites but a continuous network of sites with only marginal differences in their bond valence mismatch. The BV approach suggests that if a cation can reach the appropriate bond valence sum in various ways it will prefer the coordination that leads to the most uniform distribution of individual bond valences (*equal valence rule*[15]). Together with the knowledge that the coordination number (CN) for equilibrium sites of a certain cation in oxide salts will vary only over a limited range this can be used to resolve the pathways into equilibrium sites and jump paths between these sites.

Tab. 1: Enumeration of "equilibrium" site clusters (relaxed sites) for the mobile ions in various metaphosphate or diborate glasses.

	Criteria		*"equilibrium site clusters"*			
	$\|\Delta V\|$ / *v.u.*	CN range	*sites / ions*	*av. site radius / Å*	*simultaneously accessible*	*simultaneously accessible eq. sites / ion*
$LiPO_3$	0.068	4-6	**2954 / 800**	**0.32**	**1339**	**1.67**
$NaPO_3$	0.125	4-6	**2084 / 800**	**0.41**	**872**	**1.09**
$RbPO_3$	0.240	4-8	**1693 / 800**	**0.42**	**556**	**0.70**
$Li_{0.5}Na_{0.5}PO_3$ (Li^+)	0.068	4-6	**1396 / 400**	**0.28**	**631**	**1.58**
$Li_{0.5}Na_{0.5}PO_3$ (Na^+)	0.125	4-6	**819 / 400**	**0.34**	**383**	**0.96**
$AgPO_3$	0.270	2-6	**(154 / 768)**	**1.75**	**1018**	**1.33**
10AgI-90$AgPO_3$	0.270	2-6	**(214 / 853)**	**1.60**	**1193**	**1.40**
30AgI-70$AgPO_3$	0.270	2-6	**(314 / 1000)**	**1.44**	**1533**	**1.53**
50AgI-50$AgPO_3$	0.270	2-6	**(178 / 1200)**	**2.23**	**1902**	**1.59**
Li_2O-$2B_2O_3$	0.068	4-6	**2201 / 600**	**0.36**	**1023**	**1.71**
LiCl-Li_2O-$2B_2O_3$	0.068	4-6	**2508 / 720**	**0.38**	**1286**	**1.79**
Na_2O-$2B_2O_3$	0.125	4-6	**1045 / 600**	**0.46**	**570**	**0.95**

In accordance to a suggestion by Brown[15] anions X are classified as coordinating a monovalent cation A^+ if the A-X distance corresponds to an individual bond valence $s_{A\text{-}X} \geq 0.04$ v.u. A survey of cation coordinations in sets of well-determined, fully ordered inorganic crystal structures extracted from the Inorganic Crystal Structure database[20] using this CN definition demonstrates that the ranges of preferred CN for Li^+, Na^+, Rb^+ and Ag^+ in oxides and oxyhalides are 4-6, 4-6, 4-8 and 2-6, respectively. Only sites that lead to a CN within this range qualify as equilibrium sites. As none of the investigated cations tends to form multiple bonds, sites leading to individual bond valences significantly > 1/4 for the

alkali glasses or > 1/2 for the Ag glasses are also eliminated. For alkali glasses these criteria locate clusters of equilibrium sites that are sufficiently small (about 10 grid sites or corresponding to an equivalent radius of the site of 0.4 Å, cf. Tab. 1) and thus can only be occupied by a single cation. (This size should not be mistaken with the ion radius, which is already accounted for implicitly when calculation the BV sum. It rather describes the variability of the position for the centre of the ion and thus resembles an atomic displacement parameter.)

Due to the tendency of silver ions to occur in low CN configurations (which imposes the less strict coordination number constraint $2 \leq CN \leq 6$) the same formalism leads to considerably larger "equilibrium site clusters" in silver ion conducting glasses that may be occupied by several Ag^+ at the same time. Thereby the values found for the Ag^+ conducting glasses are not directly comparable. On the other hand this also suggests a higher degree of correlation between the elementary hop processes in Ag^+ ion conducting glasses.

The formalism described so far does not take into account, whether all "equilibrium site clusters" can be occupied simultaneously. Effectively the criteria (applied to a grid with limited resolution) will produce a considerable number of closely neighbouring clusters and thereby overestimate the number of relevant sites. A more relevant quantity is the number n_{site} of "equilibrium sites" that have a suitable minimum distance from each other to be occupied independently. n_{site} is assessed by running systematically through all sites. Wherever an accessible site within an equilibrium site cluster is identified, all surrounding sites up to a distance of $2r_A$ are eliminated before continuing the loop. Appropriate A-A exclusion distances $2r_A$ are again derived from sets of reliable reference crystal structures that contain short A-A distances (for details see Adams *et al.*[9]) The resulting exclusion radii $r_{Li} = 1.17$ Å, $r_{Na} = r_{Ag} = 1.38$ Å for Na and Ag and $r_{Rb} = 1.85$ Å are slightly smaller than the respective metallic radii and consistent with the minimum distance criteria employed in the RMC modelling of the investigated systems.

Although the choice of threshold values $|\Delta V|$ is guided by the considerations discussed above (e.g. regarding the systematic mass dependence, limitations by grid resolution, etc.) it remains to some extent arbitrary. Therefore it needs to be tested to which extent results depend on a specific choice of $|\Delta V|$. Results for the alkali metaphosphate glasses are summarised in Fig.3, where characteristic properties of the pathways and "eq. sites" are shown as a function of the chosen value of $|\Delta V|$. In each graph the (ion mass dependent) value selected for the analysis in Tab.1 is marked by a broken vertical line. When ΔV is raised the pathway volume fraction increases nearly linearly (after an initial plateau region, where the pathway volume is mainly determined by the sign change criterion; Fig. 3i). The number of clusters forming the pathways goes through a maximum for ΔV values that for all investigated systems are smaller than the chosen threshold value (Fig. 3ii). The ratio

between the number of simultaneously accessible "equilibrium sites" for A^+ and the number of A^+ in the structure model varies only slowly with the choice of ΔV (Fig. 3 iii). Thereby the conclusion that the mechanism for ion transports will depend on the type of mobile ion, is hardly affected by the choice of a particular threshold value for ΔV. Li^+ ion transport in $LiPO_3$ occurs via a significant fraction of unoccupied sites, while unoccupied Rb^+ sites are rare in $RbPO_3$ so that ion transport resembles more a "vacancy"-type mechanism.

To control the relevance of the pathway clusters, Fig. 3iv indicates the correlation between pathway sites (that as shown in Fig. 3i contain only ca. 1% of the total volume of the structure model) and the cation sites of the RMC model. Again grid resolution limits the precision of this analysis. Therefore three variants of the correlation are plotted: Curves (a) in Fig. 3iv display the percentage of modelled A^+ sites that are located within one of the "accessible" volume elements; while versions (b) and (c) additionally include the face-sharing or face- and edge-sharing neighbours of accessible sites. Even for curve (c) this means that the BV pathway is within the region that the A^+ probes by its thermal vibrations and such a A^+ should therefore be considered as mobile. For $LiPO_3$ and $NaPO_3$ this includes ca. 80% of the alkali ions, while the number is reduced to ca. 60% for the $RbPO_3$ glass.

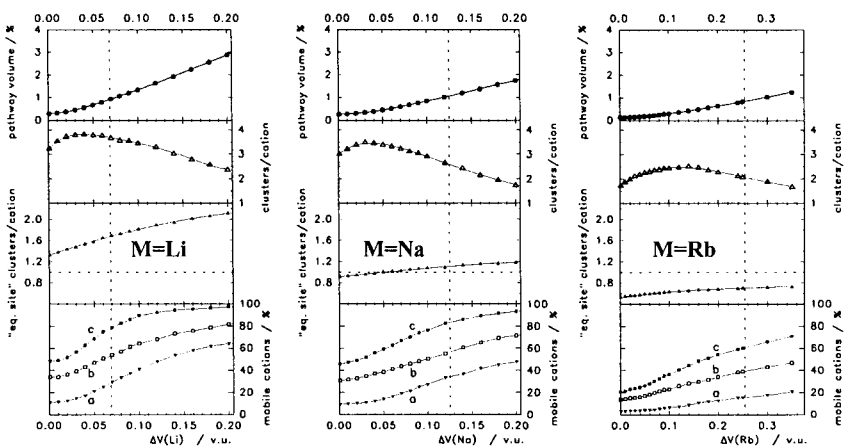

Fig. 3: Variation of quantities characterizing the bond valence pathways in reverse Monte Carlo models of MPO_3 glasses (M = Li, Na or Rb from left to right) as a function of the chosen bond valence mismatch threshold: (i) pathway volume fraction; (ii) number of clusters per cation; (iii) number of "equilibrium site clusters" per cation; (iv) percentage of M^+ ions that are located (a) within volume elements belonging to the pathway; (b) in volume elements that belong to the pathway or their face sharing neighbours; (c) in volume elements that belong to the pathway or their face or edge-sharing neighbours. The dashed vertical line indicates the mass-dependent threshold value for $|\Delta V|$ chosen in this work.

3.3. Comparison of pathways in RMC and MD-generated structure models of $LiPO_3$

To elucidate the possibilities of applying our bond valence analysis formalism to structure models from MD simulations the characteristics of Li^+ pathways in RMC- and MD-generated structure models of glassy $LiPO_3$ are compared. In the case of the MD model results are averaged over 100 snapshots from a short trajectory (30 ps) after a relaxed state has been reached in a previous simulation run. The analysis of coordination number distributions for the Li^+ in both models seems to emphasizes the similarity of both structure models (CN(Li) = 4.49 ±0.85 from MD simulations, 4.57±1.07), but the broader distribution already hints at the slightly more disordered nature of RMC models. Fig. 4 however reveals potential problems for a straightforward application of the BV analysis to the MD model: the average BV sum V(Li) for the Li atoms in the MD model V(Li) = 0.826 ± 0.121 v.u. is significantly lower than V(Li) = 0.927 ± 0.154 v.u. for the RMC model. Average BV sums slightly below V_{id} = 1 v.u. for monovalent cations are to be expected and generally observed in RMC structure models due to the snapshot type nature of the models (BV parameters are determined from stable, well-ordered reference structures, where the time-averaged cation positions represents local energy minima). Still the displayed example indicates that the suitability of a MD simulation force field for this kind of analysis has to be verified in every case.

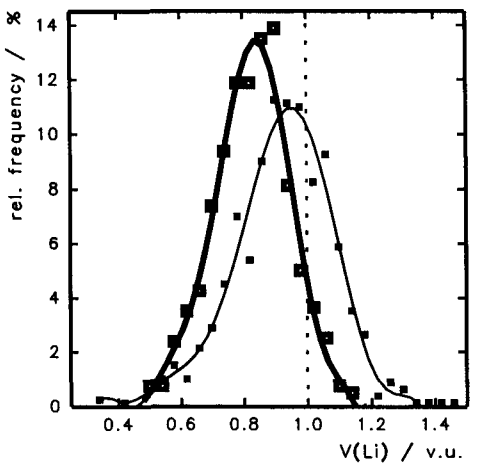

Fig. 4: Bond valence sum distribution of Li atoms in a RMC model of glassy $LiPO_3$ (filled symbols) as well as in a series of snapshots from a molecular dynamics simulation of $LiPO_3$ at T=300K (open symbols). Solid lines as a guide to the eye.

For minor BV sum deviations adapting the reference value V_{id}. may be a practical workaround. The influence of such adaptations on the characteristic quantities for the Li pathways in both types of structure models is shown as a function of $|\Delta V| = |V-V_{id}|$ in Fig. 5 for three choices of V_{id}: 0.825, 0.9 and 1.0 valence units (v.u.), and two values, 0.925 and 1.0 v.u., for the RMC model. As to be expected the pathway volume fraction is highest if V_{id} is chosen in accordance to the maximum of the respective BV sum distribution. V_{id}=1v.u. is not a suitable choice for the MD case, but the similarity in the $|\Delta V|$ dependence for the remaining

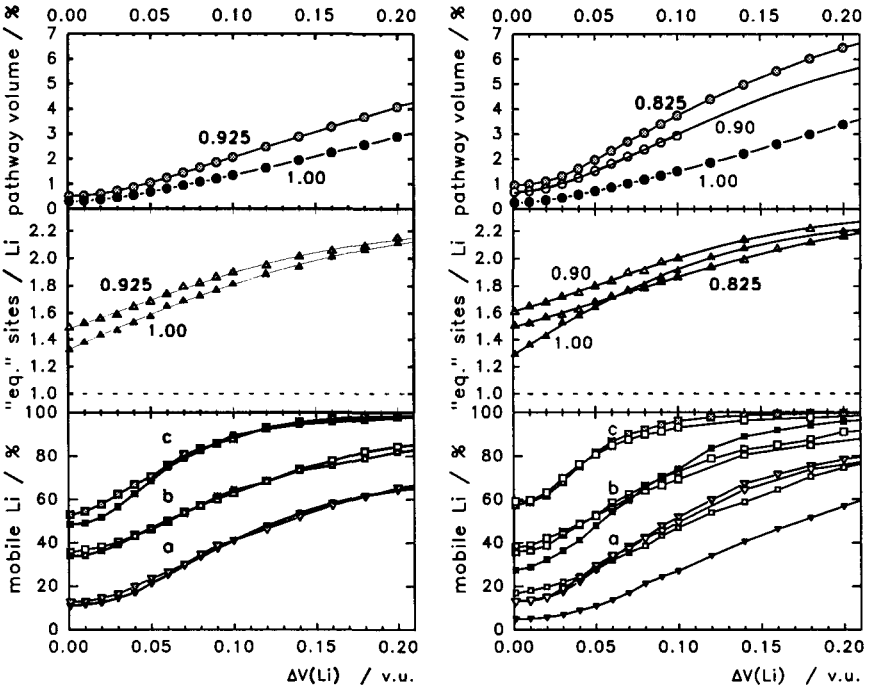

Fig. 5: Comparison of bond valence pathway models for $LiPO_3$ based on RMC models (l.h.s.) or MD simulations (r.h.s.) for different choices of the ideal bond valence sum V_{id} with respect to (i) percentage of "accessible" volume elements; (ii) number of sites with matching BV sum and CN, divided by number of Li in model; (iii) percentage of Li in model, for which (a) the respective volume element itself, (b) the volume element or its face-sharing neighbour, (c) the respective volume element or its face- or edge-sharing neighbour is "accessible".

four curves implies that an approximate conversion between the most suitable V_{id} for RMC and MD can be found for a given force field. For any of the choices of structure model, V_{id} , and $|\Delta V|$ the number of "equilibrium sites" for Li^+ significantly exceeds the number of Li^+ ions in the structure, so that there are always free target sites for hopping processes. The percentage of mobile Li, which measures the degree of congruency between the Li positions of the structure model and the BV pathways leads to unsatisfactory results for the MD structure model and V_{id} = 1v.u.. The slight overestimation of Li-O bond lengths by the MD force field can be compensated by assuming a slightly smaller V_{id} in the analysis.

4 Conclusions

The application of the bond valence analysis to static structure models from reverse Monte Carlo fits (based on experimental diffraction data) has been demonstrated to

provide predictions of ion transport properties. Although an exact localisation of the most suitable sites for the mobile ions in local structure models may require a higher resolution than could be applied in the present study, the study still provides semiquantitative results regarding differences in the number of available sites for the mobile ions and thereby in the transport mechanisms for glassy solid electrolytes.

The application to Molecular Dynamics simulation trajectories adds the possibility to systematically analyze time, temperature or pressure dependencies of energy landscapes for the mobile ions, but characteristics of the respective structure models have to be kept in mind: Cations in MD snapshots have a narrower distribution of BV sums and coordination numbers than RMC models, but (depending on the force field) the average BVS of the mobile ions may differ from the oxidation state. For minor deviations an adaptation of the expected bond valence sum to the specific MD force-field will allow an application of the BV analysis formalism.

Acknowledgements

Financial support by NUS Academic Research Fund is gratefully acknowledged.

References

1. D.A. Keen, R.L. McGreevy, *Nature* **344**, 423 (1990).
2. R.L. McGreevy, *Nucl. Inst. Meth. In Phys. Res.* A **354**, 1 (1995).
3. R.L. McGreevy, 2001 *J. Phys.: Condens. Matter* **13**, R877 (2001)
4. J. Swenson, L. Börjesson, R.L. McGreevy, W.S. Howells, *Phys. Rev.* B **55**, 11236 (1997).
5. S. Adams, J. Swenson, *Phys. Rev. Lett.* **84**, 4144; *Phys. Rev.* **B 63**, 054201 (2000).
6. S. Adams, J. Swenson, *Phys. Chem. Chem. Phys.* **4**, 3179 (2002).
7. J. Swenson, S. Adams, *Phys. Rev. Lett.* **90**, 155507 (2003).
8. S. Adams, J. Swenson, *Solid State Ionics* 175, 665 (2004).
9. S. Adams, J. Swenson, *J. Phys.: Condens. Matter* **17**, S87 (2005).
10. S. Balasubramanian, K.J. Rao; *J. Non-Cryst. Solids* **181**, 157 (1995).
11. J. Habasaki, Y. Hiwatari, *Phys. Rev.* B **59**, 6962 (1999).
12. P. Jund, W. Kob, R. Jullien, *Phys. Rev.* B **64**, 134303 (2001).
13. X. Yuan, A.N. Cormack, *J. Non-Cryst. Solids* **319**, 31 (2003).
14. T,M. Alam, J.J. Liang, R.T. Cygan, *Phys. Chem. Chem. Phys.* **2** 4427 (2000)
15. I.D. Brown, *The Chemical bond in Inorganic Chemistry – The Bond valence Model*, Oxford University Press, New York (2002).
16. S. Adams, *Acta Crystallogr. B , Structural Science* **57**, 278 (2001).
17. S. Adams, *softBV web pages: http://kristall.uni-mki.gwdg.de/softBV/* (2003).

18. S. Adams, to appear in *Solid State Ionics*.

19. H. Lammert, M. Kunow, A. Heuer, *Phys. Rev. Lett.* **90**, 215901 (2003).

20. Inorganic Crystal Structure Database, Fachinformationszentrum Karlsruhe, Germany, (1997).

The Proton Conductivity of Condensed Phases of Water: Implications on Linear and Ball Lightning

Kirthi Tennakone
Institute of Fundamental Studies,Sri Lanka

Abstract

Ice is a proton conductor, with conductivities ranging from 10^{-6} to 10^{-9} S m^{-1} depending on the purity of the sample. Electronically ice is highly insulating with conductivity of the order 10^{-12} S m^{-1} or below. Mobile protons in ice originate from disruption of hydrogen bonds and strong electric fields enhance bond breakage. Ice particle acquires electrification during formation of thunder clouds and ice play a crucial in role charge separation leading to lightning. It is suggested that charges of ice particles in clouds originates from inductive charge separation and transfer of the mobile positive charge to the streaming air. Thus ice particles gain a negative charge and moist air drifting upwards becomes more positive. Consequently, most thunder clouds have a negative charge in the region closer to the ground.

Although many explanations are proposed, the elusive phenomenon of ball lightning continues to resist theoretical understanding and laboratory reproduction. Ball lightning originates in the electrical active atmosphere as a luminous sphere drifting in air with the capability of bouncing from walls and penetrating openings smaller than the ball. It is suggested that ball lightning is a negatively charged sphere constituted of an outer shell of ice. Water dipoles are oriented radially by the electric field and protons acquire a high mobility in the tangential direction. As the electron conductivity of the shell in radial direction is very small, the charge slowly leaks to the atmosphere as a corona discharge. Model naturally explains how the ball could penetrate a hole or bounce from a surface as a differential electrostatic stress could develop in the ball as result of the proton conductivity. Details of the models and suggestions for experimental verification of the proposed concepts will be presented.

Contributed Papers

This page is intentionally left blank

PROTON TRANSPORT IN NANOCRYSTTALINE BIOCERAMIC MATERALS: AN INVESTIGATIVE STUDY OF SYNTHETIC BONE WITH THAT OF NATURAL BONE

HRUDANANDA JENA and B. RAMBABU

Solid State Ionics Laboratory, Department of Physics,
Southern University A & M College, Baton Rouge, Louisiana –70813, USA

RAMSEY SAUNDERS

Health Physics Section, Department of Physics
University of West Indies –St. Augustine Campus, Trinidad

Abstract

Hydroxy apatite ($Ca_{10}(PO_4)_6(OH)_{2)}$ is a ceramic material. This has been used for biological applications such as bone and teeth enamel. In this paper various preparation methods including sonochemical followed by microwave sintering technique has been used to prepare the material. The material was characterized by XRD, TEM, SEM and its electrical transport (proton) is measured by impedance spectroscopy. The conductivity measured is $0.091x10^{-6}$ to $19.20x10^{-6}$ Scm^{-1} at 25 - 850^0C range of temperature at 100 kHz applied frequency. Conductivity found to increase with increasing applied frequency at a given temperature of measurement. The prevalence of protons in the lattice has been confirmed by proton NMR studies. The results of the experimental observations on proton migration in the apatite lattice for electrical conduction are discussed.

1.Introduction

Hydroxy apatite, $Ca_{10}(PO_4)_6(OH)_2$ (Ca-HAp) is a bio-ceramic and is an alternative candidate for hard tissue replacements such as stainless steel and titanium based solids [1-4]. The existing materials such as stainless steel etc. are prone to corrosion, wear, fibrous tissue encapsulation, inflamation, implant loosening due to poor adhesion, and stress shielding which leads to bone resorption. Ceramic based hydroxyapatite (HAp) are better suited as these are bioactive providing an interfacial bond between the implant and the surrounding tissue forms, leading to good fixation, and generally no fibrous tissue encapsulation. The

major drawbacks however are their low strength, low toughness and brittleness, which limit their use for non-load applications, such as coatings and implants in non-stressed areas of the body. A possible solution is to obtain nanocomposites based on hydroxyapatites that show superior mechanical properties. A prerequisite for the formation of HAp based nanocomposites is to obtain uniform nano size particles of HAp through innovative chemical methods. A number of chemical routes have been reported in literature for the synthesis of submicron particles of HAp with narrow size distribution. In our investigation we will emphasize on achieving nano-hydroxyapatite by hydrothermal or sonochemical reaction methods. These methods will be extended to synthesize other alkaline earth substitutions in the hydroxyapatite. The alkaline earth substitutions are strontium (Sr), barium (Ba) and magnesium (Mg). The alkaline earth analogues of Ca-HAp find use as bone replacement, bone fillings, bone adhesives and for the treatment of osteoporosis. Attempts will also be spared to substitute HAp with other elements (compatible to body tissues) to enhance mechanical strength so that these HAp can be used in load bearing areas of the body. Since these materials are going to be used in human body and need to be thoroughly characterized by various sophisticated techniques and various tests should be conducted in vivo.

In this study an attempt has been made to synthesize nano-composites of Ca-HAp with varying Ca^{2+} to $(PO_4)^{3-}$ ratio and alkaline earth (Ba, Sr and Mg) doping at Ca-site of the HAp by using sonochemical, hydrothermal followed by microwave sintering. The structural and transport properites will be correlated with the natural human bone powder measured under identical experimental conditions. The ordering mechanism of hydroxy groups in hydroxy-apatite $Ca_{10}(PO_4)_6(OH)_2$, which is the major constituent of mammalian bones and tooth enamel has been discussed. Apart from its use as biomaterials, Ca-HAp may be a candidate for future proton conductors for proton conducting ceramic fuel cell application as well

as the composite electrolyte in the direct methanol fuel cells and also for sensor applications.

2. Experimental

2.1 Hydrothermal method

In hydrothermal method stoichiometric concentrations of $NH_4H_2PO_4$ and $Sr(OH)_2.8H_2O$ were taken and added to the teflon bowl. The bowl was sonicated along with the contents of the bowl in an ultra sonic sonicator (40W) for 30 minutes. Then the bowl was kept in a stainless steel autoclave. The autoclave was heated at 150°C for 5 h. The contents of the bowl were filtered and dried at 95°C in an oven. The powders were examined by X-ray Diffractometry (XRD), Transmission electron microscopy (TEM) and FTIR (Fourier Transform infra-red spectroscopy). Electrical conductivity measurements were carried out on these pellets by EIS (Electrochemical Impedance Spectroscopy). Similar procedures were followed to prepare the Sr, Ba and Mg substituted compositions.

2.2 Urea combustion method

In this method stoichiometric concentrations of $CaCO_3$ and $NH_4H_2PO_4$ (ADP) were taken. $CaCO_3$ was converted to $Ca(NO_3)_2$ by dissolving in 1:1 HNO_3 and ADP was added to the solution. Then Urea (H_2N-CO-NH_2) was added to the reactant mixture (3 times the molar concentrations of reactants). The entire mixture was heated on a hot plat at 100 ^{0}C. The solution frothed and formed a fluffy mass (precursor). The precursor was brown in color. The brown color precursor on calcinations turned white by burning out all the excess carbon present in the precursor.

2.3 Sonochemical reaction

The sonochemical technique needs to be started with the hydroxide gels of the constituent elements of the HAp. The reactants were mixed in a stoichiometric proportion and were irradiated in a sonochemical reactor with 300-750 watt of power. Then the product formed was filtered and sintered by microwave heating. Various other techniques will also be attempted to improve the properties and bio-compatibility of the material.

2.4 Characterization of the materials

The powders were characterized by XRD, TEM (Transmission Electron Microscopy), FTIR and NMR. The electrical transport studies were carried out at 25-800^{0}C in air.

3.Results and discussions

$Ca_{10}(PO_4)_6(OH)_2$ (Ca-HAp) was prepared by various methods. The urea burning method did not yield HAp at room temperature. The precursor formed was calcined at 600-800^{0}C /4h. The solution mixture of Ca-nitrate and di-ammonium phosphate solution formed slurry like precursor. The precursor on calcination yielded the product. The presence of urea and nitrate groups in the precursor enhanced the growth of the Ca-HAp crystals on calcinations by providing *in situ* heating. The crystalline pattern obtained in the XRD is shown in Fig.1. The crystalline pattern (urea combustion) obtained in urea method is attributed to the provision of *in situ* heating by

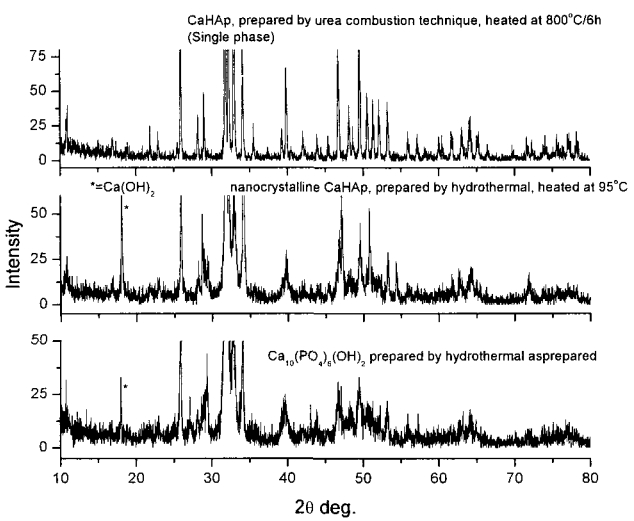

Figure 1. XRD pattern of Ca-HAp prepared by various methods

exothermic decomposition of the complex gel in addition to external heat-treatment given at 800°C/4h. However, in hydrothermal process, the crystallites grow and are nano-crystalline in nature as evident from the XRD pattern (Fig.1).In case of hydrothermal method the crystallites grow under pressure (2 atmosphere pressure) and 150°C. This condition increases the solubility of the ions in the solvent medium and makes them to react faster and form the product. The powders obtained in all these routes were characterized by X-ray diffraction (XRD), Transmission electron microscopy (TEM) (Fig. 2a) .The formation of single phase of HAp was confirmed by XRD analysis. XRD peak broadening and TEM examination of the powders confirmed the nano-crystalline nature of the powders. The TEM micrograph also showed the needle like structures of the crystallites (Fig. 2b).The urea combustion method needed heat-treatment of the pre-cursor at 400-800°C to burn out the carbon present in the precursor, on the other hand hydrothermal method yielded nano-crystalline product without further heat – treatrment.

The sonochemically treated starting materials before proceeding to hydrthermal treatment yielded needle shaped HAp. The needle shaped nano-rods may be of great importance to fabricate high strength bone material. Electrical transport properties of these compositions were carried out by ac impedance technique.

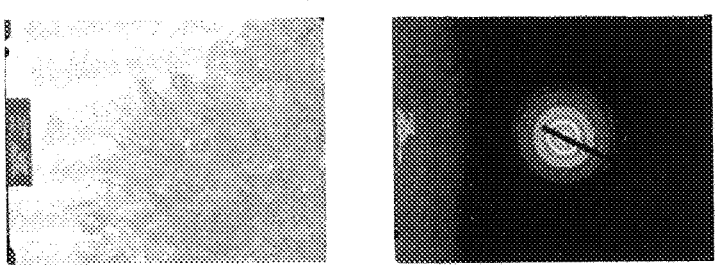

(a) (b)

Figure 2 (a) TEM micrograph of Ca-HAp , showing ascicular structure (b) Selected Area Electron Diffraction pattern of Ca-HAp ,.

The broadness of the XRD pattern is also an evidence of the nano-crystallinity. The nanocrystalllinity was also confirmed from TEM studies. The TEM micrographs are given in the Fig. 2 (a). The ring pattern in selected area electron diffraction (SAED) pattern (Fig.2b) of the powders gives further evidence on the nano-crystalline nature of the particles.

The presence of hydroxyl groups were also confirmed from the FTIR experiments (Fig.3).The powders of HAp were initially analyzed by IR (Fig.3). The characteristic bands of the $v2(PO_4^{3-})$ is observed at 566 and 601 cm^{-1}, $v1(PO_4^{3-})$ at 954 cm^{-1}, and the $v3(PO_4^{3-})$ to the 1087 and 1022 cm^{-1}. These reflections indicate the classification of the polyhedrons of PO_4^{3-} in Ca-HAp. Besides, at 3566 cm^{-1} a main vibration vOH^-) is observed, joined to bands at 3400 and 1629 cm^{-1} (H-O-H) from water absorption of synthesis process. The band at 628 cm^{-1} is attributed to the OH^- groups.

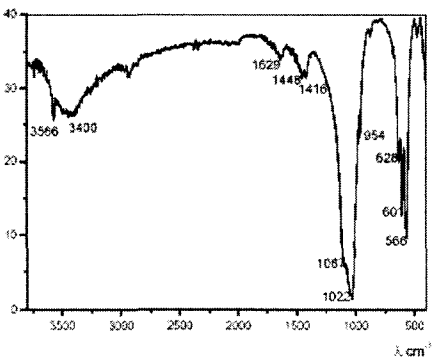

Figure 3 IR spectra of Ca-HAp

The conductivity of CHAp is observed to be 0.05mS/cm at 500^{0}C. The measurement of various properties of $Ca_5Sr_5(PO_4)_6(OH)_2$, $Ca_5Mg_5(PO_4)_6(OH)_2$ $CaBa_5(PO_4)_6(OH)_2$ compositions is to be carried out to find its suitability to justify its use as biomaterials for vertebrates. The presence of protons in the lattice has been investigated by proton NMR and FT-IR spectroscopy measurements. The details of NMR and FT-IR are

beyond the scope of this paper. The conductivity of Ca-HAp at 25^0C in case of as -prepared sample indicates that the adsorbed H_2O takes part in the electrical conduction at room temperature measurements. On heating the pellet to 100^0C a decrease in conductivity is observed which is attributed to the loss of adsorbed water. However, on heating the pellet above 100^0C an increase in conductivity is observed. The conductivity was observed to increase with increasing temperature. The trend in conductivity, temperature and frequency are given in the Fig. 4. Conductivity of the pellet increases with increasing frequency. The typical value of conductivity measured is $0.091x10^{-6}$ Scm^{-1} at 25^0C and $19.26x10^{-6}$ at 850^0C with an applied frequency of 100 kHz. Further conductivity of the pellet increases with increasing frequency at a particular temperature.

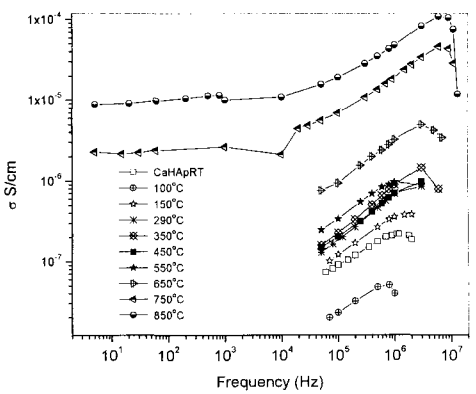

Figure 4 Electrical conductivity of Ca-HAp

The increase in conductivity is attributed to the participation of hydroxyl proton in the Ca-HAp lattice. This observed phenomenon may be attributed as the ion (proton) conducting ceramic. Apart from its use as a bioceramics, it appears that CaHAP will turn out to be a progressive system to be used

as an electrolyte in developing new breed of low temperature solid oxide fuel cells (LT-SOFCs) and high temperature polymer electrolyte fuel cells (PEMFCs).

4. Conclusions

The preparation of Ca-HAp by sonochemical and hydrothermal method is an economical process and yields nano-crustalline powders free from contaminants and contains hydroxyl groups. The hydroxyl groups are helpful for biological tissue compatibility. The work on comparison of natural bone with the synthetic ones are in progress. Urea combustion method produces micro-crustalline particles and contains carbon as impurity phases if calcined at low temperatures. The proton conductivity is reported for the first time in off stoichiometric Ca-HAp prepared by sonochemical and hydrothermal techniques.

Acknowledgement:

BRB acknowledge the support of U.S-DOE-NREL and U.S-DOE-NETL through grants # ACQ-4-33623-01, #DE-FG26-03NT4195. H. Jena thank the IGCAR for granting extraordinary leave for availing exchange visitor assignment in Southern University, USA.

References

1.An Introduction to bioceramics, Ed. L.L.Hench and J. Wilson, Advanced series in Ceramics, vol.-1, World Scientific, New Jersey, (1993)

2.H.K.Varma, and R. Sivakumar, Materials Letter **29**(1996) 57-61

3.H.G. Zhang, Q. Zhu, and Z.H.Xie, Mater. Res. Bull., **40** (2005) 1326-1334

4.T.Sampath Kumar, I. Manjubala, J. Gunasekaran, Biomaterials **21** (2000) 1623

SYNTHESIS AND PROPERTIES OF THE NANOSTRUCTURED FAST IONIC CONDUCTOR $Li_{0.3}La_{0.56}TiO_3$

Q.N. PHAM[1], O. BOHNKE1, A. BOULANT[2] AND J. EMERY[2]

[1] *Laboratoire des Oxydes et Fluorures, UMR 6010 CNRS*

[2] *Laboratoire de Physique de l'Etat Condensé, UMR 6087 CNRS*

Institut de Recherche en Ingénierie Moléculaire et Matériaux Fonctionnels, FR CNRS 2575

Université du Maine, Av. O. Messiaen, 72085 LE MANS Cedex 9, France

E-mail: odile.bohnke@univ-lemans.fr

M. VIJAYAKUMAR

Department of Physics, College of William and Mary, Williamsburg 23187, Virginia, USA

The preparation of a pure and nanostructured phase of the fast lithium conductor $Li_{0.30}La_{0.56}TiO_3$ at low temperature (350 °C for 2 h) is reported for the first time. The synthesis has been carried out by the Pechini-type in-situ polymerizable method. It has been shown that the molar ratios ethylene glycol / citric acid and citric acid / metals, as well as the temperature, are crucial parameters during this synthesis. A careful control of the temperature during polyesterification allowed us to prepare nano-sized phase of oxide and to avoid the formation of thermally stable impurities. The crystallite size (20 –30 nm) of the oxide has been determined by the analysis of the broadening of the powder X-Ray diffraction lines. The particles size has been confirmed by Transmission Electron Microscopy and the macroporous character of the powder has been evidenced by Scanning Electron Microscopy.

1. Introduction

Nano-sized materials may offer anomalous and interesting properties. This has already been observed in nano-electronics. The size effect, which is based on the quantum-mechanical confinement effect, leads to the increase of the energy of delocalized electrons with decreasing size. Such phenomenon has been proved to be valuable in varistors, PCT ceramics or gas sensors applications. More recently, it has been pointed out that ionic transport properties may also be changed by size effect. In a series of recent papers, Maier[1] shows that "regardless of fashion and prejudice" the field of nano-ionics can lead to "substantially new insights regarding fundamental issues, but also to novel technological perspectives". The importance of nano-ionics to electrochemistry comes from the fact that the density of interfaces becomes very high when particle size decreases. This increase of interface density can then lead to a drastic change of both the local and the overall ionic transport properties of solids but also to storage or sensor properties of these materials.

Therefore the properties of nano-structured ionic conductors deserve to be explored extensively. In such a context, the attempt to synthesise nano-structured $Li_{0.30}La_{0.56}TiO_3$ appeared to be of great interest.

The perovskite-type lithium lanthanum titanate, $Li_{3x}La_{2/3-x}TiO_3$, is well known to be a high lithium ionic conductor having bulk conductivity of 10^{-3} S cm^{-1} at room temperature for x=0.10 [2]. Due to this high ionic conductivity, these compounds (hereafter called LLTO) have been studied for long time to explore the conduction mechanism and their potential use in various applications[3]. So far, most of the LLTO compounds have been prepared from the powder mixtures of oxides and carbonates by conventional solid-state reaction method. This method of preparation requires an extensive heat-treatment (1150 °C) for long time (24 hours) with intermediate grinding to achieve complete chemical reaction. Such a high temperature procedure leads to grain growth and to lithium loss (up to 20 mole %)[4]. In order to overcome these disadvantages, low temperature procedures were then considered. In this context, the span of preparation procedures is enormous. The synthesis of fine grain complex multicomponent oxide ceramics with good compositional homogeneity and high purity requires the use of a good mixing of the components at the molecular level. In an account that focuses on the synthesis and characteristics of ceramics, Kakihana *et al.* illustrated the advantages of the Pechini-type in-situ polymerizable method over other solution techniques to prepare pure and homogeneous oxides[5]. This procedure is based on the formation of polyesters obtained from metal chelated citric acid and polyhydroxyl alcohol[6]. The chelation process is based on the mixture of cation (M) precursors solution in an aqueous citric acid (CA) solution. These chelates undergo polyesterification when heated with ethylene glycol (EG). The reaction which is carried out in ambient atmosphere leads to metallic-citrate polyester. Heating of the polymer causes its decomposition and the formation of a powder precursor by pyrolysis. Further appropriate heat-treatments yield fine oxide powder.

In the present study, we will describe the polymerizable precursor method we used. We will particularly emphasise the role of the two EG/CA and CA/M molar ratios as well as the pyrolysis temperature as crucial parameters during the synthesis to prepare nano-sized phase of LLTO and to avoid the formation of impurities. Herein, we demonstrate, for the first time, that the synthesis of pure LLTO is possible at low temperature. The study of the crystallite size of LLTO was carried out by the analysis of the broadening of the X-ray diffraction (XRD) lines. The size of the crystallites thus obtained was confirmed by Transmission Electron Microscopy (TEM). Furthermore, the macroporous character of the powder has been evidenced by Scanning Electron Microscopy (SEM).

2. Experimental

For the synthesis of $Li_{0.30}La_{0.56}TiO_3$, Ti fine powder (99 %, 325 mesh) from Alfa Aesar, Li_2CO_3 (99.997 %) from Aldrich and La_2O_3 (99.999 %) from Rhone-Poulenc were used as starting materials. The titanium solution was prepared by dissolution of Ti powder with hydrogen peroxide (30 %) from Carlo Erba and ammonia (35 %) from Fischer Scientific. Lithium carbonate and lanthanum oxide were dissolved in nitric acid from extra pure HNO_3 (65 %) from Riedel de Haën. The polymer precursor was prepared from the above solutions with CA (99.5 %) and EG (99 %) from Aldrich. The detailed procedure of the synthesis is given in the next part of the paper.

Powder XRD patterns (slow scans) have been recorded at room temperature with a Philips X'Pert PRO diffractometer (CuK_α radiation), equipped with a linear X'Cellerator detector, in the 2θ range from 8 to 120° with an increment step of 0.0167° and a total collecting time of 7 h 33 min. The fluoride $Na_2Ca_3Al_2F_{14}$ (NAC)[7] was used as an instrument standard (*std*) for determining the instrumental broadening. The mean coherence length (L) was calculated using the Scherrer formula[8]:

$$L = \frac{K\lambda}{\beta\cos(\theta)} \tag{1}$$

where β is interpreted as a volume averaged crystallite dimension perpendicular to the reflecting planes (intrinsic peak width in radian), θ is the diffraction angle, λ is the X-ray wavelength and K is the Scherrer constant that depends on the crystallite shape (K = 0.94 for spherical crystallites[9]). It was the first model, and the simplest approach, established on size broadening and later on generalized to estimate grain size by XRD. The β value is obtained by fitting some Bragg peaks using the WinFit software.

Besides, the Rietveld method[10] using the X'Pert HighScore Plus program (PANalytical, Almelo, The Netherlands) was used for the microstructural refinement with a peak shape described by a pseudo-Voigt function. The width and shape of a diffraction peak are a convolution of both the instrumental broadening and the broadening arising from the sample. The crystallite size (L) and micro strain (e) were described by the following relationships:

$$L = \left(\frac{180}{\pi}\right)\frac{\lambda}{(W - W_{std})^{0.5}} \tag{2}$$

$$e = \frac{[(U - U_{std} - (W - W_{std}))]^{0.5}}{\frac{1}{100}\left(\frac{180}{\pi}\right)4(2\mathrm{Ln}2)^{0.5}} \tag{3}$$

The U parameter contains the information about the strain broadening while the W parameter is related to the size broadening.

Microstructure observations were performed using a Hitachi 2300 SEM. Thin specimens for TEM study were obtained by ultrasonically dispersing particles in ethanol and depositing one drop of the resulting suspension on a Cu grid covered with a holey carbon film. After drying, the grid was fixed in a side-entry ± 30° double-tilt specimen holder and introduced in a JEOL-2010 electron microscope operating at 200kV.

3. Results and Discussion

3.1 Synthesis of pure phase $Li_{0.30}La_{0.56}TiO_3$

One of the crucial steps in the herein used modified Pechini-type method was to prepare a highly water soluble precursor to avoid the use of alkoxides, which are not stable in open air, as previously reported11. The formation of water-resistant peroxo-citrato-metal complex during the synthesis of LLTO, instead of alkoxides that are extremely sensitive to moisture, is of great importance for inexpensive and convenient aqueous synthesis of these ceramics for commercial applicability of these oxides. The main goal of this Pechini-type synthesis method is to obtain a polymeric network made of randomly and homogeneously distributed cations able to lead to a powder precursor by decomposition of the organic matrix. The crucial parameters of this synthesis are the amounts of CA and EG and the polymerisation temperature. The amounts of CA and EG govern the distance between the cations in the polymeric network. Small amounts of both CA and EG help the cations to be close one to the other. The heat flow generated from the organic matrix decomposition is enough to locally synthesise the oxide. Therfore, polymerisation, decomposition of the organic matrix and chemical reaction occur almost simultaneously at low temperature and in a short time. The polymerisation temperature is also an important parameter because it controls the kinetics of the polymerisation reaction and then the viscosity of the solution. A low viscosity will help to obtain an homogeneous distribution of the cations and to avoid the formation of impurities. We showed that these impurities (mainly $Li_2Ti_3O_7$ and $La_2Ti_2O_7$) are thermally stable and can not be decomposed by heat treatment. We have clearly demonstrated that a careful control of the polymerisation temperature, after esterification, can minimise the formation of these impurities.

In this work, we studied the particular compound $Li_{0.30}La_{0.56}TiO_3$ which is the best conductor of the solid solution $Li_{3x}La_{2/3-x}TiO_3$. Fig.1 shows the flow chart of the synthesis procedure used to prepare this compound. We used small amounts of CA and EG, i.e. CA/M = 1 and EG/CA = 1. After esterification at 60 °C for 1 h and 90 °C for 30 min, a heating at 120 °C for 20 min on a hot plate is performed. A grey powder is obtained indicating that polymerisation and partial decomposition of the organic compounds occurred. At this temperature, LLTO is not yet formed. Afterwards the powder is heated at 350 °C for 2h in an oven. A white powder is then obtained. Slow scan powder X-ray diffraction patterns have been recorded at room

temperature for LLTO obtained by either the herein used low temperature synthesis procedure route (Fig. 1) or the classical high temperature solid state chemical reaction route. Fig. 2 shows the two spectra indicating the formation of a pure phase of LLTO at temperature as low as 350 °C. Very small amount of $La_2Ti_2O_7$ can be detected in both compounds. The main difference in these diffraction diagrams is the broadness of all the diffraction lines of LLTO obtained by the polymerizable method. It can be observed that the superstructure lines (hkl with l = 2n+1) are broader than the other diffraction lines (hkl with l = 2n) suggesting a disorder of the oxide.

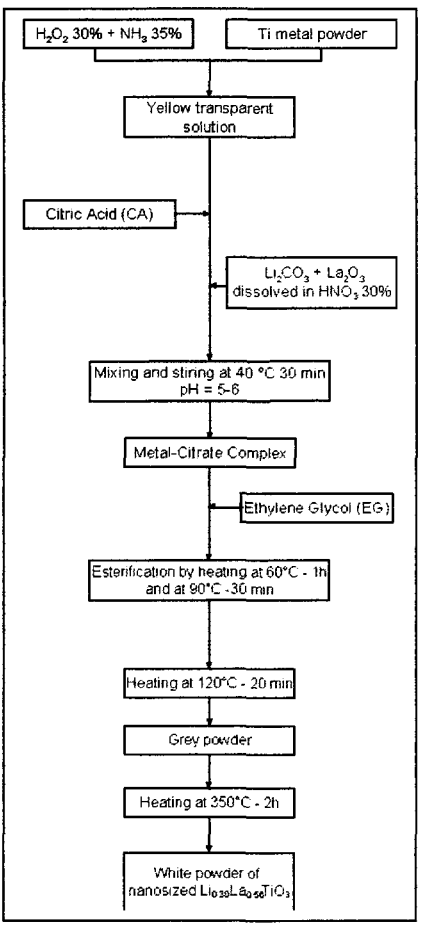

Figure 1. Flowchart for the preparation of nanosized LLTO.

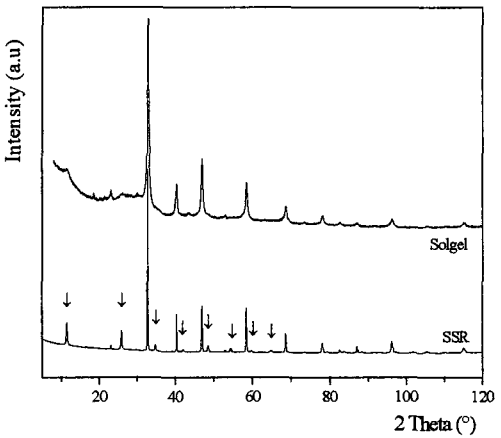

Figure 2. Powder XRD patterns of $Li_{0.30}La_{0.56}TiO_3$ obtained by solid state reaction (SSR) or Pechini-type in-situ polymerizable method at 350 °C for 2 h. (↓ superstructure lines)

3.2 Nanostructure of $Li_{0.30}La_{0.56}TiO_3$

The determination of the grain size has been carried out by the analysis of the slow scan XRD pattern of the powder. Generally, this method provides a powerful and non-destructive way for the analysis of microstructure of materials, via the analysis of diffraction-line broadening. However, this method of determining crystallite size is not trivial and different and sometimes conflicting procedures appeared in the literature. In a first approximation, we used the Scherrer relationship (1) to estimate the grain size. An average crystallite size of 32 nm has then been determined. However, it is worth noting that the choice of the Bragg peaks, the mathematic function used to extract the Full Width at Half Maximum (FWHM) values can affect the correctness of the result (error as high as 70 % can be attained). Furthermore, the strain broadening effect is neglected in this procedure. This may lead to an underestimation of the grain size.

To go further in this study, we used the Rietveld method to estimate the size and the strain parameters. By this way, a pseudo-Voigt function is used and both Lorentzian and Gaussian contributions were refined to obtain L and e values, as described in the experimental section. Owing to the unequal distribution of La^{3+} ions into the two A-sites of the perovskite structure LLTO is not cubic. In a first approximation, we assumed that this compound adopts an ideal cubic symmetry. A Rietveld refinement was then performed on the space group $Pm\bar{3}m$ (ICSD: 92238): a = 3.8819 (2) Å, R_p = 5.86, R_{wp} = 7.75. The average crystallite size (coherence

length) is 23 nm with a micro strain parameter of 0.16 %. When using the superstructure lines as a "second phase", as suggested by Fourquet *et al.* [15], the Rietveld refinement, with a P 4/mmm space group (ICSD: 82671) leads to a = 3.8817(9) Å, c = 7.7700(4) Å, R_p = 7.39 and R_{wp} = 10.31. The reliability factors are slightly higher than in the cubic assumption. An average crystallite size of 26 nm with a micro strain parameter of 0.10 %, close to the previous one, are found. However, the U, V, W values for the superstructure lines are not determined with good accuracy. These values of 23 nm and 26 nm are in very good agreement with the previous one determined with the Scherrer equation (32 nm). Furthermore, the small values of strain parameter of 0.16 % and 0.10 % obtained in both assumptions allowed us to validate the use of the Scherrer relationship. To confirm these we used electron microscopic techniques to characterise the microstructure of LLTO and confirm these previous results.

SEM micrograph of LLTO obtained at 350 °C is presented in Fig. 3. It reveals the macroporous character of the powder with a pore size around 1μm. At the present time, macroporous materials also deserve much attention because of their possible use in various electrochemical applications, such as sensors or batteries. The low temperature synthesis used in our study may also offer some interesting way to prepare such macroporous membrane.

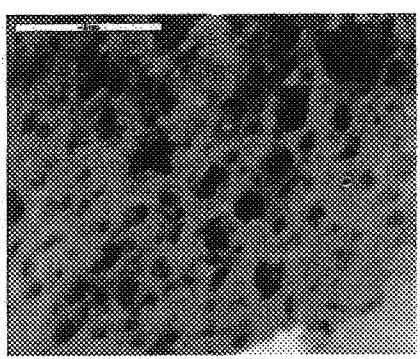

Figure 3. SEM micrograph of $Li_{0.30}La_{0.56}TiO_3$ prepared by the Pechini-type in-situ polymerizable method at 350 °C for 2 h.

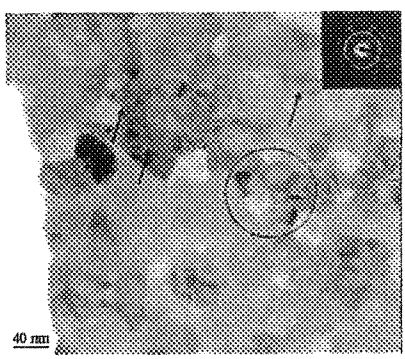

Figure 4. TEM image of $Li_{0.30}La_{0.56}TiO_3$ prepared by the Pechini-type in-situ polymerizable method at 350 °C for 2h.

Fig. 4 shows a low resolution TEM image revealing small grains of 20-30 nm size and presenting faceted borders, as shown in the black circle. The crystallinity of the sample is evidenced by the rings with sharp spots of the corresponding selected area diffraction pattern (at the right top) as well as by the presence of fringes (black arrows). It is worth noting that the powder is not perfectly crystallised owing to the

low temperature process used. However, these observations confirm the nanostructure of LLTO powder. The presence of these nano particles are then able to explain the broadness of the diffraction lines observed in the XRD pattern of Fig. 2. Some recent results obtained by NMR will be discussed during this presentation.

4. Conclusion

We have reported the detailed procedure used to prepare nanosized fast ionic lithium conductor $Li_{0.30}La_{0.56}TiO_3$. By adjusting both the CA/M and EG/CA molar ratios and the pyrolysis temperature, it has been possible to obtain a pure phase of LLTO. This phase is made of crystallites of 20 – 30 nm size as determined by the analysis of the width of the XRD lines and by TEM. This phase shows a macroporous character that can offer some advantages for particular electrochemical applications.

References

1. (a) J. Maier, *Solid State Ionics, 154-155*, 291 (2002). (b) J. Maier, *Solid State Ionics, 157*, 327 (2003). (c) J. Maier, *Solid State Ionics, 148*, 367 (2002). (d) J. Maier, *Nature Materials, 4*, 805 (2005).
2. (a) A.G. Belous, V.I. Butko, G.N. Novitskaya, S.V. Polianetskaya, B.S. Khomenko, Yu M. Poplavko, *Ukr. Fiz. Zh., 31*, 4, 576 (1986). (b) Y. Inaguma, C. Liquan, M. Itoh, T. Nakamura, T. Uchida, H. Ikuta, M. Wakihara, *Solid State Comm.* 86, 689 (1993).
3. (a) S. Stramare, V. Thangadurai, W. Weppner, *Chem. Mater., 15,* 3974 (2003) [and ref herein]. (b) O. Bohnke, J. Emery, J-L. Fourquet, J-C. Badot, *Recent Research Developments in Solid State Ionics*, Vol.1 (2003) Edt S.G. Pandalai [and ref herein].
4. (a) Y. Inaguma, L. Chen, M. Itoh, T. Nakamura, *Solid State Ionics, 70/71,* 196 (1994). (b) J. Emery, J-Y. Buzaré, O. Bohnke, J-L. Fourquet, *Solid State Ionics,* 99, 41 (1997).
5. M. Kakihana, M. Yoshimura, *Bull. Chem. Soc. Jpn, 72*, 1427 (1999).
6. U.S. Patent 3,330,697 (1967).
7. G. Courbion, G. Ferey, *J. Solid State Chem., 76*, 426 (1988).
8. P. Scherrer, *Nachr. Göttingen, 2*, 98 (1918).
9. H.P. Klug, L.E. Alexander, *X-ray Diffraction Procedures for Polycrystalline and Amorphous Materials,* 2nd ed.; Wiley-Interscience: New York, 618-687 (1974).
10. H.M. Rietveld, *J. Appl. Crystallogr. 2*, 65 (1969).
11. (a) M. Kakihana, J. Szanics, M. Tada, *Bull. Korean Chem. Soc.* 20, 8, 893 (1999). (b) M. Kakihana, M. Tada, M. Shiro, V. Petrykin, M. Osada, Y. Nakamura. *Inorg. Chem.*, 40, 891 (2001). (c) M. Vijayakumar, Y. Inaguma, W. Mashiko, M-P. Crosnier-Lopez, C. Bohnke, *Chem. Mater.*, 16, 2719 (2004).

HYDROGEN PRODUCTION : CERAMIC MATERIALS FOR HIGH TEMPERATURE WATER ELECTROLYSIS

A. HAMMOU

Laboratoire d'Electrochimie et de Physicochimie des Matériaux et des Interfaces (LEPMI) (UMR CNRS-INPG-UJF Grenoble, N°5631) ENSEEG BP 75 38402 Saint Martin d'Hères – France
E-mail : Abdelkader.Hammou@lepmi.inpg.fr

Hydogen, H_2 is regarded as the main energy vector for the future. Today, the world production of hydrogen rises to 550 billion Nm^3 (44 Mt) corresponding to 1,5% of the primary energy production. Contrary to fossil fuels, H_2 does not exist in a native form and its use obviously requires its fabrication and storage. The future status of H_2 as a fuel for electricity production (fuel cells) and for automobile transportation makes necessary a considerable increase of its production. Some H_2 manufactoring processes are briefly described in the first part of this article : (i) steam methane reforming, (ii) water decomposition by thermochemical cycles, (iii) water decomposition by photoelectrochemistry, (iv) water or organic compounds decomposition in using bacteria or alguae. The second part concerns the H_2 production by water electrolysis. This manufactoring process does not exceed 1% of the total production of hydrogen. It is expected that the electrolysers working at high temperature (700-900°C) using ceramic oxides based electrolytes are the more promising. Two groups are considered : electrolysers with proton conductors or oxide ion conductors as electrolytes. Proton conductors belong to the perovskite oxides family $MCe_{1-x}Ln_xO_3$ with M = Ba, Sr and Ln = Lanthanide. For these conductors, few results on water electrolysis at high temperature are available in the litterature and will be shown here. Electrolysers using oxide ion conductors are more promising. The selected materials are those developped for SOFCs : YSZ for the electrolyte, Ni based cermets for the cathode materials and $La_{1-x}Sr_xMO_{3\pm\delta}$ with M = Mn, Co, Ni, Fe ... The electrochemical characteristics of the anodic and cathodic interfaces as well as the perfomances of electrolysers working at high temperature are presented.

1. Introduction

Hydrogen is regarded today as the principal energy vector of the future. Its principal assets reside in its abundance, mainly in water, the high value of the energy released (120 MJ/kg) and the absence of greenhouse gas emissions after combustion. Hydrogen is nowadays especially used as a chemical component for ammonia fabrication, gasoline and gas oil desulfurization in refineries and methanol manufactoring. Its use as a fuel is restricted to very specific sectors like the propulsion of spacecrafts. Contrary to fossil fuels, hydrogen does not exist in a native state and so its use requires its production. There should be added to this the constraints related to its transport and storage. The annual world production of hydogen rises today to 550 billion Nm^3 (44 Mt) corresponding to 1.5% of the primary energy production. The new status of hydrogen as a fuel for electricity production (fuel cells) and automobile traction, obliges for a significant increase of this product in the future. In the following, some of the most hydrogen production modes are described, the last one being dedicated to water electrolysis at high temperature in using ceramic oxides.

2. Chemical processes of hydrogen production

Hydrogen may be produced through the conversion of natural resources like crude oil, natural gas (CH_4), coal and biomass products[1,3]. Other production ways involve chemical cycles including successive reactions at high temperature[4].

2.1a. Steam methane reforming

The chemical reactions involved here are :

(1) Reforming (catalyst : Ni, Al_2O_3, $CaAl_2O_4$) :

$CH_4 + H_2O \Leftrightarrow CO + 3H_2 \qquad \Delta_r H_1^\circ = 206 \text{ kJ/mol}$

Efficiency : 89%

(2) Water shift conversion (catalyst : $Fe_2O_3 + Cr_2O_3$) :

$CO + H_2O \Leftrightarrow CO_2 + H_2 \qquad \Delta_r H_2^\circ = -41 \text{ kJ/mol}$

Efficiency : $CO \approx 0.25\%$

(3) Results : $CH_4 + 2H_2O \Leftrightarrow CO_2 + 4H_2 \qquad \Delta_r H_3^\circ = 165 \text{ kJ/mol}$

2.1b. The partial oxidation of methane

(1) Oxidation (catalyst : Fe) :

$CH_4 + 1/2\ O_2 \Leftrightarrow CO + 2H_2 \qquad \Delta_r H_1^\circ = -36 \text{ kJ/mol}$

(2) Water shift conversion (catalyst : $Fe_2O_3 + Cr_2O_3$) :

$CO + H_2O \Leftrightarrow CO_2 + H_2 \qquad \Delta_r H_2^\circ = -41 \text{ kJ/mol}$

(3) Results : $CH_4 + H_2O + 1/2\ O_2 \Leftrightarrow CO_2 + 3H_2 \qquad \Delta_r H_3^\circ = -77 \text{ kJ/mol}$

The obtained hydrogen is purified on molecular sieves by decarbonation and methanation to eliminate CO and CO_2 traces.

2.2. *Water decomposition by thermochemical cycles (TCC)*

The TCC principle is based on the water dissociation through several chemical reactions at high temperature. The chemical reactions of three TCC are shown in the following :

- ***The Iodine-Sulphur cycle***

(1) $H_2SO_4 \rightarrow H_2O + SO_3 \qquad (400 - 600°C)$

(2) $SO_3 \rightarrow SO_2 + 1/2\ O_2 \qquad (800 - 900°C)$

(3) $2HI \rightarrow H_2 + I_2 \qquad (200 - 400°C)$

(4) $SO_2 + 2H_2O + I_2 \rightarrow H_2SO_4 + 2HI \qquad (25 - 120°C)$

H_2SO_4 and HI are recycled.

In the hybrid Westinghouse cycle, the reactions (3) and (4) are replaced by the electrolysis of SO_2 in aqueous medium :

$SO_2 + 2H_2O \rightarrow H_2SO_4 + H_2$

$(T = 20 - 110°C \qquad P = 2 - 10 \text{ bar}) \qquad E_{rev} = 0.17 \text{ V}$

- ***The UT-3 cycle***

$$CaO + Br_2 \rightarrow CaBr_2 + 1/2\ O_2 \quad (550°C)$$

$$CaBr_2 + H_2O \rightarrow CaO + 2HBr \quad (725°C)$$

$$Fe_3O_4 + 8HBr \rightarrow 3FeBr_2 + 4H_2O + Br_2 \quad (250°C)$$

$$3FeBr_2 + 4H_2O \rightarrow Fe_3O_4 + 6HBr + H_2 \quad (575°C)$$

- ***The Sulfates cycle***

$$xH_2O + xSO_2 + MO_x \rightarrow M(SO_4)_x + xH_2$$

$$M(SO_4)_x \rightarrow xSO_2 + MO_x + \frac{x}{2}O_2 \qquad M = Fe, Ni, Zn, Mn \ ...$$

As all of these thermochemical cycles operate at high temperature, manufactoring units must be localised close to power stations. In addition, the used chemical compounds should be abundant and regenerated completely. A particular difficulty is related to the reactants recycling.

2.3. Other H_2 production modes

These modes are still requiring a significant fundamental reseach mainly in terms of material stability and efficiency improvment. Number of them more or less involve the solar energy as

- the water decomposition by photoelectrochemistry : in this technique, performances of the photoanodes (TiO_2, WO_3, Fe_2O_3, AsGa ...) must be enhanced in order to reduce charge carriers recombination especially,
- the high temperature water decomposition using the energy provided by solar furnaces,
- the use of microorganisms like bacteria and alguae[5].
- ...

3. Electrolytic production of hydrogen

Hydrogen produced by water electrolysis represents less than 1% of the total production. This process is applied when the electricity cost is low and/or to obtain hydrogen of high purity. The involved reaction is simply

$$H_2O \rightarrow H_2 + \frac{1}{2}O_2 \qquad \Delta_r H° = 285\ kJ/mol$$

with a standard potential equal to 1.481 V at 298 K [6].

For the industial electrolysers using aqueous electrolytes, the operating potential lies between 1.7 and 2.1 V which corresponds to an efficiency of 70-85%. Supplying water should be pure enough to avoid mud formation, chloride free to reduce the electrodes corrosion and having a conductivity of some $\mu S.cm^{-1}$. Generally, the electrolyte is a KOH solution whose concentration changes with temperature, typically from 25 w% at 85°C to 40 w% at 140°C. Nickel-based alloys are frequently used as cathode and anode materials. The major drawback of this electrolytic production of hydrogen is its high cost in comparison with the steam methane reforming process.

An alternative to liquid water electrolysers can be found with electrolysers using the "all solid state" technology which is developped for fuels cells using solid

electrolytes. Let us recall that in fuel cells, the reaction is exactly the reverse of the water electrolysis one. The idea is to use in some extent the same materials (electrolytes, electrodes, interconnects) for the electrolysers. Properties of these materials were extensively studied these last decades and their performances and durability are reasonnably known today.

3.1. Electrolysers with polymeric membrane

To be used as an electrolyte, a polymeric membrane should be a pure ionic (H^+ or OH^-) conductor in both oxidizing and reducing conditions. In addition, platinum based catalysts are used to improve the electrode kinetics. The most promising membranes belong to the perfluorosulfonic ionomers family, among them Nafion. Nowadays, Nafion shows the best characteristics in proton conductivity, chemical and electrochemical stability and mechanical resistance. Unfortunately, the prohibitive cost of this membrane and catalysts constitutes serious technological and financial limitations. On the other hand, one expects that the same factors responsible for power losses in fuel cells will be encountered in electrolysers, namely (i) the electrolyte degradation by the OH radicals produced at the electrodes, (ii) the existence of mixed potentials, (iii) the overvoltages related to the water oxidation and to mass transport in the diffusion layers. For the membranes, an alternative can be found with ionomers slightly or no fluorinated within the families of alkyl- or aryl-acids grafted on various polymeric chains like polyoxanes, polyphosphazenes, polyvinylidene fluoride, polytrifluorostyrene, polybenzoxazole, polysulfones, polyimides, poly-ether-ketones, polyparaphenylene ... For catalysts, it is worthy to try less noble materials like transition metal alloys and solid solution oxides with perovskite structure. For the mechanical resistance, a partial answer could be brought by the use of a multilayer membrane configuration and/or a composite membrane with low cost products [7].

3.2. Electrolysers with ceramic membranes

The operating temperature of such electrolysers lies between 700 and 900°C where water is in gaseous state. At these temperatures, one observes (i) a significant improvment of the ionic conductivity of the electrolytes and the electodes overvoltages, (ii) a lower value of the thermodynamic potential of water decomposition and (iii) the elimination of the difficulties due to the gas bubbling. Moreover, the solid state makes possible the deposition of the active components in thick layers (few ten microns) which allows to obtain high power and energy densities. Nevertheless, several problems are still to be solved : the electrical and electrochemical stability of materials (electrolytes and interconnects) in both oxidizing and reducing atmospheres, the compatibility of the expansion cœfficients between the device components, the structural stability in regards to thermal cycling. Taking into account these conditions, the selected electrolyte materials belong to the two following groups : protonic (H^+) conductors and oxide (O^{2-}) conductors. Electrical conductivity of some ceramic proton conductors is shown in Fig. 1 [8].

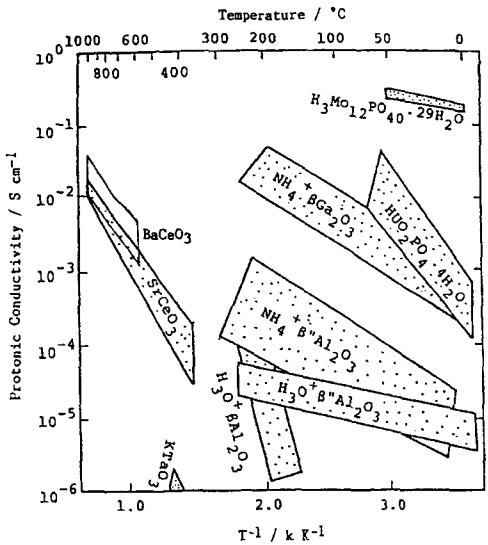

Figure 1. Electrical conductivity of ceramic proton conductors [8].

The rare earth (Ln) doped cerates family was the most investigated because of their thermal and chemical stability. The general formula of these compounds is $MCe_{1-x}Ln_xO_{3-\delta}$ with M = Ba, Sr and $x \leq 0.1$. In water free atmosphere, the ionic species responsible of charge transport is O^{2-} with a vacancy mechanism. Protons are introduced by the following reactions

$$H_2O + V_O^{\bullet\bullet} \longrightarrow O_O^x + 2H_i^{\bullet}$$

$$H_2O + V_O^{\bullet\bullet} + O_O^x \longrightarrow 2OH_O^{\bullet}$$

or

$$H_2 + 2O_O^x + 2h^{\bullet} \longrightarrow 2OH_O^{\bullet}$$

Proton migration is very likely due to H^+ jumping between two occupied adjacent oxygen sites [9] :

$$OH_{O1}^{\bullet} + O_{O2}^x \longrightarrow O_{O1}^x + OH_{O2}^{\bullet}$$

Iwahara et al. has shown that, depending on the hydration kinetics and the nature of the Ln dopant, these materials exhibit a mixed ionic conductivity (H^+ + O^{2-}) as shown in Fig. 2 , the protonic one being predominant at low temperature [10].

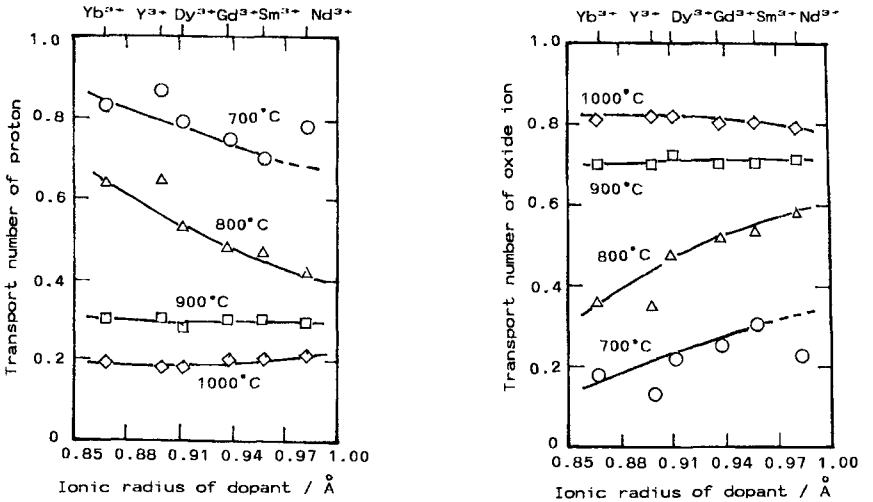

Figure 2 : Variation of H^+ and O^{2-} transport numbers versus Ln ionic radius at different temperatures in air[10].

Fig. 3 shows the current-voltage characteristics of an electrolyser using the protonic electrolyte $SrCe_{0,9}Yb_{0,1}O_{3-\alpha}$ and porous platinum electrodes between 800 and 900°C [11]. A faradaic efficiency of 90% is obtained under these conditions because of the onset of electronic conductivity within the electrolyte.

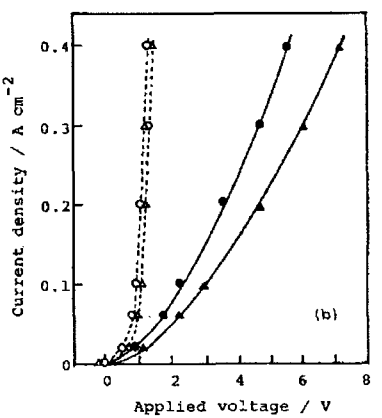

Figure 3 : Current-Voltage characterisics of the H_2O, Pt/ $SrCe_{0,9}Yb_{0,1}O_{3-\alpha}$ /Pt, O_2 electrolyser at 800°C (○, ●) and 900°C (Δ, ▲) [11], dotted lines show the voltage excluding ohmic loss.

Taking into account the above results, there is a risk in using this family as electrolytes in water electrolysis at high temperature. Further studies are to be carried out to improve their electrochemical stability.

To perform water electrolysis at high temperature, O^{2-} electrolyte conductors seem to be the more promising materials. The most investigated belong to the zirconia, ceria and gallia-based solid solutions as $Zr_{0.85}Y_{0.15}O_{0.1.925}$, $Ce_{0.9}Gd_{0.1}O_{1.195}$ and $La_{0.9}Sr_{0.1}Ga_{0.8}Sr_{0.2}O_{2..85}$. Taking into account the severe operating conditions of water electrolysis at high temperature, only Yttria Stabilized Zirconia (YSZ) fulfills the required criteria. Ohmic losses resulting from its relative low conductivity may be lowered by reducing the electrolyte thickness [12]. Materials to be considered for these electrolysers are those used for SOFC, that is

- electrolyte : YSZ,
- anode material : LSM ($La_{1-x}Sr_xMnO_3$)
- cathode material : Ni/YSZ cermet
- interconnect : MO-doped lanthanum chromite with M = Mg, Sr or metallic alloys.

Anode and cathode materials should be tailored with an accurate control of porosity and compostion gradient. In the following, some particular features concerning the electrodes reactions are mentionned. Fig. 4 shows the current-voltage curve as well as impedance spectra of the Ni/YSZ interface for water reduction [13].

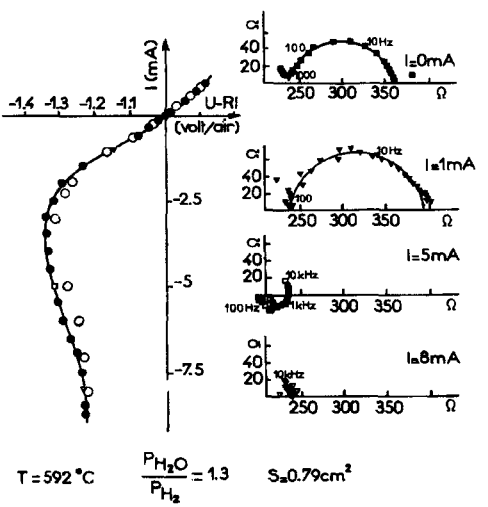

Figure 4 : Current-potential curve and impedance diagrams of the H_2/H_2O, Ni/YSZ interface at 592°C [13].

For polarisations lower than –1360 mV/air at 592°C, a catalytic effect is observed with a significant increase of current. This behavior is explained by the extension of the reactive zone due to a superficial reduction of the electrolyte. The cathodic reaction takes place not only on the triple point contact zones but also on the free

surface of the electrolyte, a zone where the later becomes a mixed conductor. The influence of the water composition is shown in Fig. 5 [14]. The catalytic effect of water is clearly expressed. Such a behavior can help to think about the cathodic gas composition for water reduction.

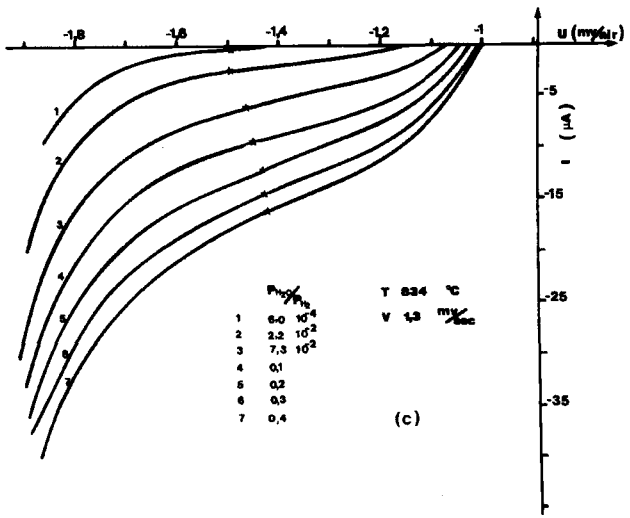

Figure 5 : Influence of the $P(H_2O)/P(H_2)$ ratio on the current-potential characteristics of the Ni/YSZ interface at 834°C [14].

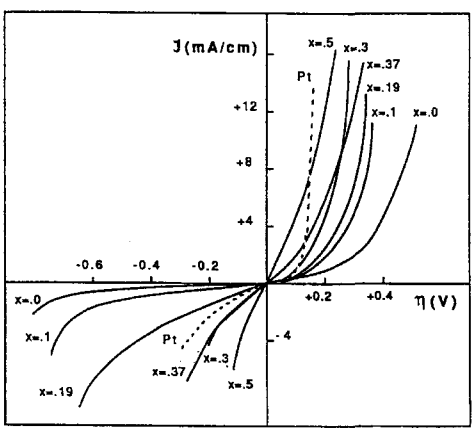

Figure 6 : Current density vs overvoltage of the O_2, $La_{1-x}Sr_xMnO_3$/ YSZ interface at 960°C in air [15].

The O_2, LSM/YSZ interface has been extensively studied by Hammouche et al. [15-18]. Fig. 6 shows the current-voltage curves for this interface in relation to the anode material composition. The Pt electrode response is represented for comparison. For a

given composition, this figure shows that the anodic overpotential (O^{2-} oxidation) is systematically lower than the cathodic one (O_2 reduction) for high electrode polarizations. On the other hand, the anodic overvoltage is an increasing function of dopant content. Finally, Pt electrode exhibits the highest current density for anodic overvoltages lower than 0.12 V approximately. The results corresponding to the $La_{0.5}Sr_{0.5}MnO_3$ composition are shown in Fig. 7.

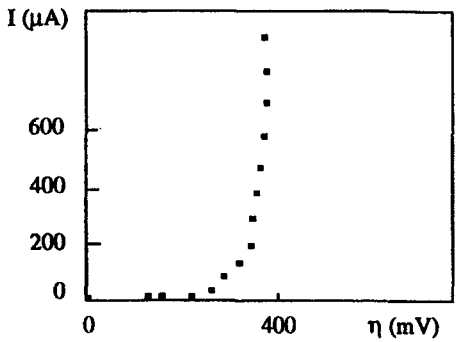

Figure 7 : Anodic current-overpotential curve for the O_2, $La_{0.5}Sr_{0.5}MnO_3$/YSZ interface at 960°C in air [16].

In the 200-380 mV range, the current I-overpotential η variation obeys the following exponential law :

$$I = I_o \exp\frac{2F}{RT}\eta$$

with I_o = 2μA. For higher anodic overpotentials, the representative curve becomes quasi vertical.

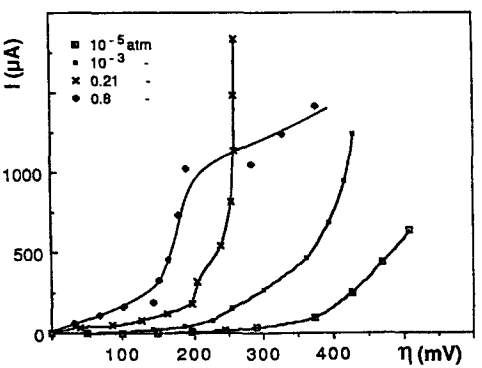

Figure 8 : Influence the oxygen partial pressure on the anodic polarisation of the O_2, $(La_{0.9}Sr_{0.1})_{0.85}MnO_3$ /YSZ electrode at 960°C [18].

The influence of the oxygen partial pressure on the anodic polarisation of the

O_2, $(La_{0.9}Sr_{0.1})_{0.85}MnO_3$ /YSZ electrode is shown in Fig. 8. The overpotential is a decreasing function of P_{O2} indicating that a high oxygen partial pressure improves the anode response.

A large programme (HOT HELLY-Dornier Systems, Friedrichshafen, Lurgi) for steam electrolysis at high temperature has been developped in the eighties using these materials [19-22]. A current density of about 0.5 Acm^{-2} was achieved at 1.33 V corresponding to an electrical energy consumption of 3.2 kWh Nm^{-3} H_2 (see Fig. 9).

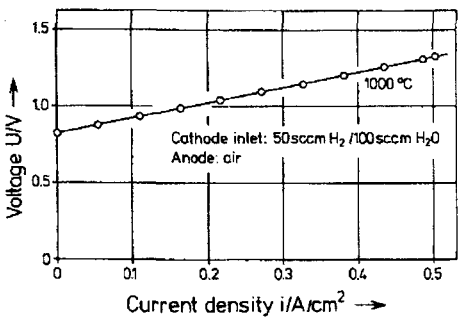

Figure 9 : Current –voltage characteristic of a single electrolysis cell [21].

Performances of a stack of seven cells are shown in Fig. 10 indicating the important role of steam in the gas mixture to be electrolysed.

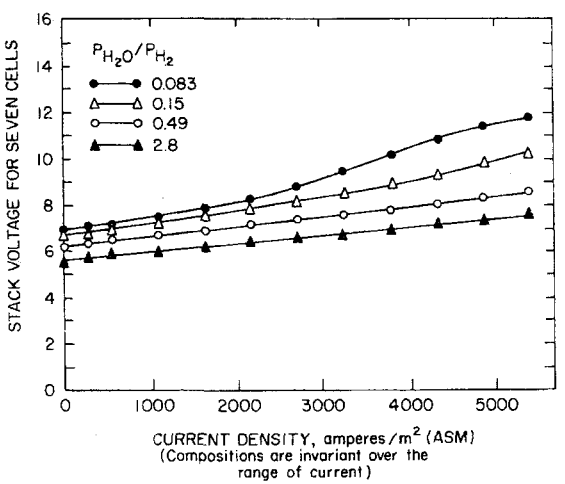

Figure 10 : Cell performance of a high temperature solid oxide cell stack of seven cells produced by Westinghouse corporation[20].

A long term test (1000 h) at a current density of 0.3 Acm^{-2} has demonstrated a remarkable stability of both the voltage (1.07 V) and the faradaic efficiency (100%) for the whole period [21]. However, more studies are to be carried out including (i) the new cathode materials like $Ln_2NiO_{4+\delta}$ (Ln = La, Nd, Pr) and $La_{1-x}Sr_xMn_{1-y}Fe_yO_{3\pm\delta}$, (ii) the microstructure (porosity and composition gradients) of the cermet anodes and the composite cathodes and (iii) the recent techniques of cells and stacks fabrication [23,24]. Finally, the performances of an electrolyser using the SOFC components and the novel fabrication techniques should be established to serve as a reference in the future.

References

1. J. A. Turner, M. C. Williams and K. Rajeshwar, *Interface* **13**, 24 (2004).
2. E. D. Wachsman and M. C. Williams, *Interface* **13**, 24 (2004).
3. J. P. Jonchère and C. Baudoin, *L'actualité chimique* **12** , 20 (2001).
4. T. Alleau, *L'actualité chimique* **12** , 26 (2001).
5. Y. Nicolet and J. C. Fontecilla-Camps, *L'actualité chimique* **12** , 34 (2001).
6. P. Schultz, *L'actualité chimique* **1** , 3 (2002).
7. C. Iojoiu, M. Maréchal, F. Chabert and J.Y. Sanchez, *Fuel Cells* **3**, 344 (2005).
8. H. Iwahara in Proton Conductors, P.Colomban Ed , Cambridge University Press 122 (1992).
9. K. D. Kreuer, E. Schonherr and J. Maier, *Solid State Ionics* **70-71**, 278 (1994).
10. H. Iwahara, T. Yajima and H. Ushida, *Solid State Ionics* **70-71**, 267 (1994).
11. H. Iwahara in Proton Conductors, P. Colomban Ed., Cambridge University Press 511 (1992).
12. B.C.H. Steele, *C.R. Acad. Sci. Paris* **1**, Serie IIc, 533 (1998).
13. E.J.L. Schouler, M.Forest, E. Fernandez and P. Fabry, *Solid State Ionics* **5**, 559 (1981).
14. E. Fernandez, PhD Grenoble University (1980).
15. A. Hammouche, E. Siebert and A. Hammou, *Mat. Res. Bull.* **24**, 367 (1989).
16. E. Siebert, A. Hammouche and M. Kleitz, *Electrochimica Acta* **40**, 1741 (1995).
17. A. Hammouche, E. Siebert, A. Hammou and M. Kleitz, *J. Electrochem. Soc.* **138**, 1212 (1991).
18. A. Hammouche, PhD National Polytechnic Institute of Grenoble (1989).
19. W. Dônitz, R. Schmidberger and E. Steinheil, *J. Hydrogen Energy* **5**, 55 (1980).
20. F.J. Salzano, G. Skapardas and A. Mezzina, *J. Hydrogen Energy* **10** (12), 801 (1985).
21. W. Dônitz and E. Erdle, *J. Hydrogen Energy* **10** (5) 291 (1985).
22. K. H. Quandt and R. Streicher, *J. Hydrogen Energy* **11**, 309 (1986).
23. F. Mauvy, C. Lalanne, J.M. Bassat, J.C. Grenier, H. Zhao, P. Dordor and Ph. Stevens, *J. Eur. Ceram. Soc.* **25**, 2669 (2005).
24. G. Caboche, L.C. Dufour and F.Morin, *Solid State Ionics* **144**, 211 (2001).

INFLUENCE OF THE SINTERING TEMPERATURE ON pH SENSOR ABILITY OF $Li_{3x}La_{2/3-x}TiO_3$. RELATIONSHIP BETWEEN POTENTIOMETRIC AND IMPEDANCE SPECTROSCOPY MEASUREMENTS

Q.N. PHAM, C. GALVEN, O. BOHNKE, C. BOHNKE

Laboratoire des Oxydes et Fluorures, UMR 6010 CNRS
Institut de Recherche en Ingénierie Moléculaire et Matériaux Fonctionnels, FR CNRS 2575
Université du Maine, Av. O. Messiaen, 72085 LE MANS Cedex 9, France
E-mail: odile.bohnke@univ-lemans.fr

The ability of $Li_{0.30}La_{0.56}TiO_3$ ceramic surface to respond to pH variation has been investigated. The influence of the heat-treatment (or sintering temperature) of the membrane after synthesis on its surface sensitivity has been studied by potentiometric measurements and Electrochemical Impedance Spectroscopy (EIS) with a four-electrodes symmetric cell in different pH buffered solutions. These techniques allowed us to determine the thermodynamic and the kinetics parameters of the oxide surface. The sub-Nernstian response can be explained by means of the site-binding model that describes the charging mechanism of oxides by surface reactions. The intrinsic buffer capacity, β_{int}, of the oxide surface is a key parameter that defines the response of the pH sensor. We will discuss how this parameter influences the properties of the surface oxide and therefore the sensitivity of the membrane to pH variations.

1. Introduction

The lithium lanthanum titanate $Li_{3x}La_{2/3-x}TiO_3$, with $0.06 < x < 0.14$, (hereafter named LLTO) is one of the fastest crystalline lithium ionic conductors owing to its crystallographic structure. A maximum conductivity of 10^{-3} S cm^{-1} at room temperature was first reported by Belous et al.[1] and afterwards by Inaguma et al.[2] for the $x = 0.11$ compound of the solid solution. Generally, pure ionic conducting ceramics are good candidates for sensitive element in potentiometric sensors because of the fast ion exchange that can occur between the ions of the analysed solution and the ions of the ceramic membrane[3]. Therefore, these titanates, which are not hygroscopic, have been tested for Li^+ ion-selective electrodes (ISE). We have shown in a previous paper[4] that the LLTO membrane can be used to detect the Li^+ activity in anhydrous solutions through a Li^+ ion exchange mechanism. The potentiometric response shows a Nernstian behaviour with a Li^+ sensitivity of 72 mV/decade at 25°C. This high sensitivity can be correlated to a localised hydroxylation of the oxide surface with the residual water present in the solution in combination to the Li^+ exchange reaction. Unfortunately, the attempts to use LLTO

as a membrane for Li^+ ion-selective electrode in aqueous solutions failed. On the other hand, we have clearly demonstrated the ability of this membrane to be used as pH sensor[5,6]. It is worth noting that this material is not chemically sensitive to humidity and CO_2.

The aim of this paper is to put some light on the response mechanism of H^+ ion-selective electrode in buffered solutions of different pH and to determine both thermodynamic and kinetic parameters involved in this mechanism. Therefore, potentiometric experiments have been carried out with LLTO as a membrane in an ion-selective electrode as a function of the pH of the solution. Furthermore, Electrochemical Impedance Spectroscopy (EIS) has been investigated with a four-electrode configuration cell to investigate the interfacial phenomenon. This technique has been extensively used to study membrane and membrane/solution interface[6,7]. It is well known that these two techniques are complementary and allow to elucidate different aspects of the response mechanism. Potentiometric experiments, which allow to determine the thermodynamic parameters, involve the determination of the open-circuit potential (E_{oc}) of the whole potentiometric cell whereas EIS, which allows the determination of the kinetic parameters, may lead to separate the different interfaces, such as the bulk/grain boundary interface of the ceramic membrane, the membrane/solution interface present in the studied cell and allows to follow interfacial phenomenon evolution when pH varies. We will also show how the heat-treatment performed on the membrane influences the pH sensor sensitivity.

2. Experimental

LLTO powder of the nominal composition x = 0.10 was prepared by a modified Pechini-type chemical route, as described previously[8]. This technique of synthesis of oxides affords many advantages compared to the classical solid state reaction one (low temperature, short time of synthesis and formation of very small grains of oxide). Pellets of ~10 mm of diameter, obtained by isostatic pressing (500 MPa) of the synthesised powder, were heated at different temperatures from 1000 °C to 1200 °C for sintering.

For potentiometric (E_{oc}) measurements, the pellet was fixed with a two-components Araldite™ glue on the end side of a glass tube. To avoid the presence of a solid-solid interface jonction, a liquid internal reference Ag/AgCl/KCl was used. The external reference was also Ag/AgCl/KCl electrode. The open-circuit potential was recorded with a high input impedance Keithley 6517 Electrometer.

A four-electrode symmetric cell was used for impedance spectroscopy in buffered solutions (Fig.1). Two Pt plates were used as counter and working electrodes. Two Saturated Calomel Electrodes (SCE) were used as reference electrodes. The active membrane area of LLTO was about 0.4 cm^2. The impedance measurements were carried out at room temperature, typically over the frequency

range from 500 kHz to 0.01Hz with 30 points per decade, in buffered solutions with pH varying from 1.3 to 12. A Solartron 1260 Frequency Gain-Phase Analyser coupled to a Solartron 1287 Electrochemical Interface were used. The electrochemical system behaves linearly in the voltage rangevarying from 10 to 100 mV (r;m.s), so an ac applied voltage of 20 mV was chosen. The impedance data were analysed by using the Zview 2.7 software.

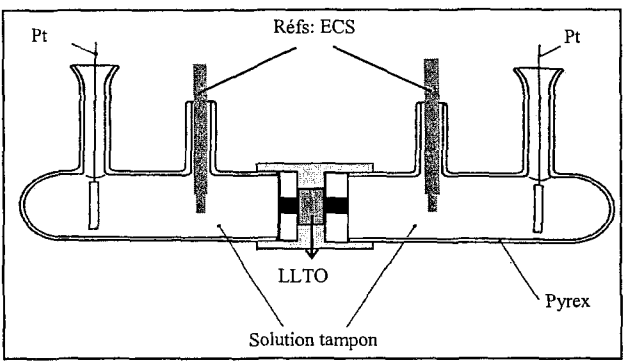

Figure 1. The four electrode configuration cell used for impedance spectroscopy

3. Results

3.1 Potentiometric measurements

The influence of the sintering temperature on the sensitivity of the pH sensor has been investigated. Sintering has been carried out at 1000 °C, 1025 °C, 1050 °C, 1100 °C, 1150 °C and 1200 °C for 2 h. The increase of the sintering temperature leads to an increase of the grain size of the ceramic, as shown in Fig. 2.

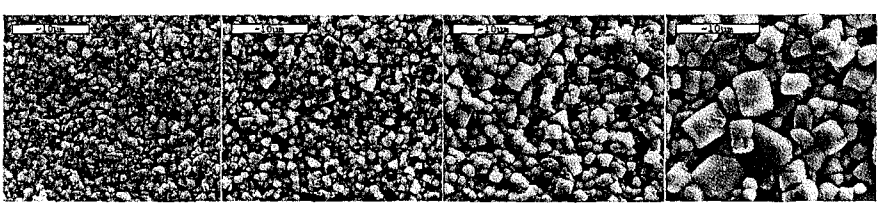

A - 1000°C – 2h **B** - 1100°C – 2h **C** - 1150°C – 2h **D** - 1200°C – 2h

Figure 2. Scanning Electron Microscopy of the ceramic after sintering.

The compactness of the membrane increases as sintering temperature increases. At 1000°C the compactness is only 78 %. It increases drastically above this temperature to reach 92 % at 1025°C and 96 % at 1050°C. From 1100 to 1200°C the compactness remains equal to 97 %. Fig. 3 shows that the sensitivity of the

membrane to the pH depends strongly on the sintering temperature. The highest sensitivity (50 mV/unit pH) has been obtained for the membrane sintered at 1150 °C for 2h with a linear response from pH = 1.3 to pH = 11.5. However this sensitivity is slightly smaller than the theoretical one, i.e. 58.2 mV per decade at 20 °C.

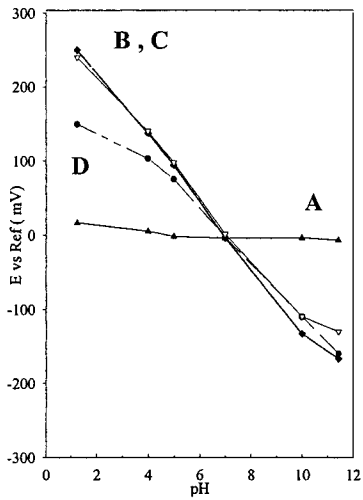

Figure 3. Potentiometric response of the LLTO membrane as a function of pH at room temperature. Sintering temperature : A - 1000°C, B - 1100°C, C - 1150°C, D - 1200°C. Sintering time : 2 hrs. The reference electrode is a RedRod™ electrode from Radiometer.

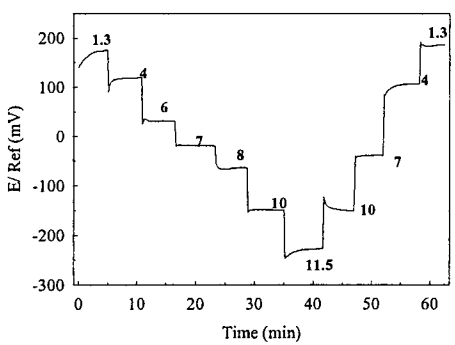

Figure 4. Room temperature response of the LLTO membrane as a function of time when pH is varied from 1.3 to 11.5 and back to 1.3.

Fig. 4 shows that the response of the membrane to a pH variation is fast (in the order of 10 s for a variation of one unit of pH) and that it is reproducible. The fast

response is directly linked to the fast ionic conductivity of the ceramics that allows the charge carriers to be very mobile.

3.2 Impedance spectroscopy

Fig. 5 shows typical impedance diagrams of a LLTO membrane (heat-treated at 1150 °C for 2h) in solution of different pH, plotted in the Nyquist plane. Two semicircles are evidenced: one in the 500 kHz – 100 Hz frequency range and another one in the low frequency part of the diagram, 100 Hz-0.01 Hz. The high frequency semicircle does not change with the pH of the solution and is then attributed to the Li^+ motion in the grain boundary of the LLTO ceramic. The low frequency semicircle varies with the pH of the solution and is then attributed without doubt to the LLTO/solution interface.

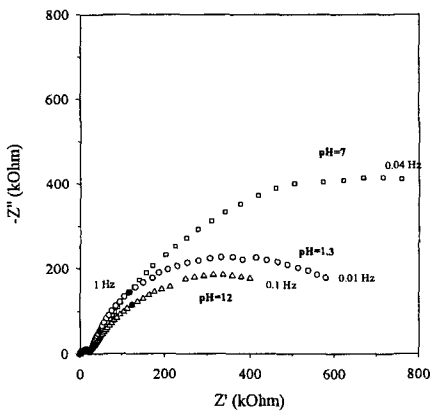

Figure 5. Impedance diagrams in the Nyquist plane of the LLTO membrane (1150 °C – 2h) in buffered solutions of different pH: O = 1.3, □ = 7, Δ = 12.

All the other membranes give the same impedance diagram as shown in Fig.5 with two relaxations except the membrane heat-treated at 1000 °C. This will be discussed during the presentation. The data have been further analysed to extract the electrochemical parameters, i.e. resistance and capacitance of the LLTO/solution interface, by using an electrical equivalent circuit. Among the equivalent circuits proposed for an ion-selective membrane in contact with an electrolyte[7,9], the electrical circuit presented in Fig. 6 is able to fit all our experimental diagrams with good agreement. The circuit (a) is a schematic representation of the impedance measured between the two reference electrodes of the four-electrode cell shown in Fig. 1. In this circuit, three relaxations are shown; two identical relaxations (R_{ct}, CPE_{ct}) for the impedances of the ceramic interface at the two membrane/electrolyte interfaces and (R_{gb}, CPE_{gb}) for the impedance of the grain boundary of the ceramic

membrane. Since the same solution is used in both sides of the cell, the symmetry of the cell allows us to reduce the circuit (a) to the circuit (b) with only two relaxations, as observed experimentally. The relationships between the resistances and the CPEs are as follow: Rct = $R_1/2$ and $CPE_{ct} = 2CPE_1$.

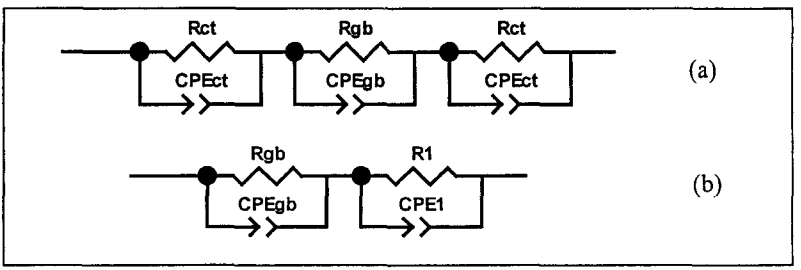

Figure 6. Electrical equivalent circuits used to analyse the impedance data. (a) circuit assumed for membrane between two solutions; (b) reduced circuit for symmetric cell.

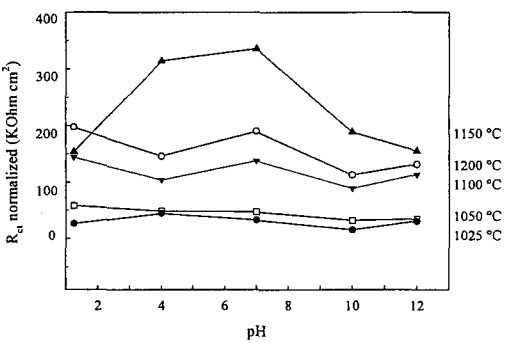

Figure 7. Resistance of the ceramic interface as a function of solution pH for ceramics sintered at different temperatures from 1025 °C to 1200 °C.

4. Discussion

The potentiometric response of the membrane (also named Galvani potential) is due to the charging of the oxide surface that depends on the pH solution. The mechanism involved in the charging of the oxide surface can be described by the site-binding model introduced by Yates et al.[10]. In this model, the oxide surface is assumed to be amphoteric, meaning that the surface hydroxyl groups can be neutral, protonized (thus positively charged) or deprotonized (thus negatively charged) depending on the pH of the solution. The charging of the surface oxide is then the result of an

equilibrium between the Ti-OH surface sites and the H^+ ions in the bulk of the solution according to the two reactions:

$$\text{Ti-OH} \leftrightarrow \text{Ti-O}^- + \text{H}^+ \quad (1)$$

$$\text{Ti-OH} + \text{H}^+ \leftrightarrow \text{Ti-OH}_2^+ \quad (2)$$

Both reactions are characterised by intrinsic dissociation constants K_a and K_b.

$$K_a = \frac{\upsilon_{TiO^-} a_{H_S^+}}{\upsilon_{TiOH}} \quad (3) \qquad K_b = \frac{\upsilon_{TiOH} a_{H_S^+}}{\upsilon_{TiOH_2^+}} \quad (4)$$

where υ_i is the surface activity of the species i and $a_{H_S^+}$ is the surface activity of H^+. The occurrence of these equilibrium will built up a charge at the oxide surface. Because of charge neutrality, an equal but opposite charge is built up in the electrolyte solution. This charge separation leads to the so-called double-layer capacitance. The potential difference that appears between the electrolyte solution and the oxide surface will vary with the pH of the solution. According to the theory developped by Bousse and later on by van Hal[11], the resulting equation for the sensitivity of the potential to changes in the bulk pH is given by:

$$\Delta\psi = -2.3\frac{RT}{F}\alpha\,\Delta pH_{bulk} \quad (5)$$

with

$$\alpha = \frac{1}{\frac{2.3kTC_{dif}}{q^2\beta_{int}} + 1} \quad (6)$$

The value of α varies between 0 and 1. The factor β_{int} is the intrinsic buffer capacity which is a measure of how the surface is able to store charge and therefore measures the sensitivity of the surface. C_{dif} is the differential capacity. β_{int} can be expressed in terms of acidic and basic equilibrium constants, K_a and K_b, and of the density of available sites on the surface. K_a and K_b as well as the density of the available sites are oxide dependent. From relationship (5) it can be seen that the sub-Nernstian response can now easily be explained by means of a value of α different of 1. α approaches 1 for a high value of β_{int} and a small value of C_{dif}. It is then easily understood that any oxide heat-treatment can influence the intrinsic buffer capacity and then the slope of the potentiometric response of the oxide, as experimentally observed in Fig. 3. Fig. 7 shows that an increase of the interfacial resistance is associated to an increase of the buffer capacity.

5. Conclusion

This study clearly showed that the LLTO membrane can be used as pH sensor. It is shown that the sensitivity of the oxide surface depends strongly on the heat-treatment of the ceramic after synthesis. The response of the ceramic to any pH variation is fast (owing to the high ionic conductivity of the titanate material), and highly reproducible. The sintering temperature influences the sensitivity of the membrane through the intrinsic buffer capacity parameter, β_{int}. The highest sensitivity has been found when the ceramic is sintered at 1150 °C. The mechanism involved in the charging of the oxide surface, which is at the origin of the experimental potential measured, can be described by the site-binding model that assumes that the oxide surface is made of amphoteric groups, Ti-OH, that can be a source or a sink of protons. Equilibrium between these neutral groups and the protonized and deprotonized groups occurs when the ceramic is in contact with a solution of given pH. These equilibrium govern the response of the oxide surface and the sensitivity of the pH sensor.

References

1. A.G. Belous, G.N. Novitskaya, S.V. Polyanetskaya, Y.I. Gornikov, *Russian J. Inorg. Chem.* 32, 156 (1987).
2. Y. Inaguma, C. Liquan, M. Itoh, T. Nakamura, T. Uchida, H. Ikuta, M. Wakihara, *Solid State Comm.* 86, 689 (1993).
3. N. Imanaka, G. Adachi, *J. Alloy. Comp.* 250, 492 (1997).
4. Q.N. Pham, O. Bohnke, C. Bohnke, *Electrochim. Acta* (in press).
5. C. Bohnke, H. Duroy, J-L. Fourquet, *Sens. Actuators B*, 89, 240 (2003).
6. C. Bohnke, J-L. Fourquet, *Electrochim. Acta*, 48, 1869 (2003).
7. (a) J. R. Sandifer, R. P. Buck, *Electroanalytical Chemistry and Interfacial Electrochemistry* 56, 385 (1974); (b) J. Mertens, P. V. D. Winkel, J. Vereecken, *Bioelectrochem. Bioenerg.* 5, 699 (1978); (c) F. Mauvy, Ch. Gondran, E. Siebert, *Electrochim. Acta* 44, 2219 (1999); (d) W. Zhang, U. E. Spichiger, *Electrochim. Acta* 45, 2259 (2000); (e) B. Pejcic, R. De Marco, *Electrochim. Acta* 49, 3525 (2004).
8. M. Vijayakumar, Y. Inaguma, W. Mashiko, M-P. Crosnier-Lopez, C. Bohnke, *Chem. Mater.* 16, 2719, (2004).
9. K. N. Mikhelson, J. Bobacka, A. Ivaska, A. Lewenstam, M. Bochenska, *Anal. Chem.* 74, 518 (2002).
10. D.E. Yates, S. Levine, T.W. Healy, *J. Chem. Soc. Faraday Trans.* 1, 70, 1807 (1974).
11. R.E.G. van Hal, J.C.T. Eijkel, P. Bergveld, *Adv. Coll. Interf. Sci.* 69, 31 (1996).
12. P. Bergveld, *Sensors and Actuators B*, 88, 1 (2003).

MICROSTRUCTURE CHRACTERIZATION AND IONIC CONDUCTIVITY OF NANO-SIZED CeO_2-Sm_2O_3 (x = 0.05 - 0.2) SYSTEM PREPARED BY COMBUSTION ROUTE

K. SINGH

Sant Gadgebaba Amaravati University, Amaravati – 444602, India.

S. A. ACHARYA

Department of Physics, J.D.I.E.T., Yavatmal, India.

S. S. BHOGA

Department of Physics, RTM Nagpur University, Nagpur-440033, India.
e-mail: msrl1@hotmail.com

Nano-sized $Ce_{(1-x)}Sm_xO_{2-\delta}$ (x = 0.05 - 0.2) were synthesized through combustion synthesis route. The thermo-chemical properties of the precursor were studied by TGA/DTA. Crystal structure and microstructure were characterized by means of X-ray powder diffraction (XRD) and scanning electron microscopy (SEM). The complex impedance spectroscopy used to evaluate contribution from grain, grainboundary and electrode-electrolyte interface in the temperature range 200 - 700^{0}C reveals that the dopant concentration not only influences the conductivity of grain, but also that of grainboundary. Concurrently, total conductivity exhibits maximum for x = 0.15

1. Introduction

Solid electrolytes exhibiting high oxygen ion conductivity have been of special interest for their technological application in high temperature systems such as solid oxide fuel cells (SOFCs), oxygen sensors, electrochemical oxygen pumps, etc. The solid oxide fuel cells (SOFCs) have been promising energy conversion system with a great potential for high efficiency and low pollution [1, 2]. The state of the art electrolyte material yttria-stabilized zirconia (YSZ) based SOFC have been expected to operate in the temperature range 800-1000^{0}C. Reducing the operating temperature allows the use of cheaper construction materials and more reliable seals. New materials have, thus, been investigated to reduce the operating temperature to 500-700^{0}C [3]. Now they have been christened as intermediate temperature solid-oxide fuel cells (IT-SOFCs).

Gadolinium (GDC) and samarium (SDC) doped ceria have been attractive materials as electrolytes for IT-SOFCs [4, 5]. Amongst these, the samarium doped ceria, has been found to exhibit high ionic conductivity, as well as high stability [6]. However, there have been some contradictions in the literature concerning the exact composition having maximum conductivity [7]. For example, according to Huang et al [8] and Yahiro et al [9], $Ce_{0.80}Sm_{0.20}O_{1.9}$ compositions show maximum

conductivity, while Steele [10] and Zha et al [11] observed a maximum for $Ce_{0.85}Sm_{0.15}O_{1.95}$. Interestingly, the existing literature reveal that the attention have been mainly focused on total conductivity of ceria solid solutions; but very less attention has been focused on the effect of Sm content on the grain, grain boundary and total conductivities.

For the practical SOFC applications, due to gas-tight or leak-proof requirement, solid electrolytes should be highly dense. The high density achieving at low sintering temperature is of great importance, because it provides better mechanical properties to the electrolytes, saves energy and most importantly the possible co-firing of SDC electrolytes with other SOFC elements. Materials fabricated by soft chemical routes, have, generally, resulted in nanoscale range and exhibit rapid densification at relatively lower sintering temperature.

In the present work, cerium and samarium nitrates salts were used to form ceria solid solutions [$Ce_{(1-x)}Sm_xO_{2-\delta}$ (x = 0.05 - 0.2)] through the glycine-nitrate combustion synthesis route and characterized. The chief emphasis is on reducing the sintering temperature and high oxy-ion conductivity at moderate temperatures.

2. Experimental

Hexahydrates of cerium nitrates ($Ce(NO_3)_3.6H_2O$) and samarium nitrate ($Sm(NO_3)_3.6H_2O$), Aldrich Chemicals (99.9 % purity), were used as an initial ingredients. Various compositions of samarium doped ceria (SDC) with formula $Ce_{1-x}Sm_xO_{2-x/2}$, where x = 0, 0.1, 0.15 and 0.2, were prepared by combustion route [12, 13]. Requisite amount of cerium nitrate and samarium nitrate were weighed using Mettler 163 AE electronic balance. Later, they were mixed thoroughly and dissolved in distilled water. Appropriate amount of glycine fuel was added to the above solution with continuous stirring so as to achieve complete homogenization. The aqueous redox solution, containing metal nitrates and glycine, when introduced into a vertical muffle furnace, which was preheated to 550^{0}C boils, froths, ignites and catches fire. At high temperature, the metal nitrates decompose to metal oxides and oxides of nitrogen, which leads to a voluminous foamy combustion residue in less than 10 minutes. The flame persisted for about 2 minutes. The foam (pale yellow in color) was then lightly ground in a silica basin with porcelain pestle to obtain fine powders. The powders were then transferred carefully into a silica crucible and calcined at 800^{0}C for 3hrs in air so as to obtain well-crystallized powder.

The thermo-chemical properties, temperature range 30-1000^{0}C, were investigated by means of simultaneous DTA and TGA using TA instrument (TA -

4000). The X-ray powder diffraction scans were recorded using a Rigaku X-ray diffractometer with CuK_α radiation. The microstructures of the sintered specimens were observed by scanning electron microscope (SEM). Grain size was determined following the linear intercept method.

The discs, dimension 13 mm diameter and 1-2 mm thickness, of calcined powders were obtain by pressing uniaxially at pressure 7 tons/cm^2 for electrical characterization. Platinum was sputtered onto both parallel opposite sides of the sintered SDC pellet so as to achieve good ohmic contact. The real and imaginary parts of complex impedance was measured by two-probe method, using HP 4192A lf impedance analyzer, in the frequency and temperature range 5 Hz - 13 MHz and 200 – 700^{0}C, respectively.

The relative density was obtained using the formula

$$\text{Re}\,lative\ Density = \frac{X - ray\ density - Experimental\ density}{X - ray\ density} \qquad (1)$$

The experimental density of the sintered specimens was determined following Archimedes principle. The X-ray density was obtained from the experimental lattice parameters and unit formula.

2. Results and Discussion

3.1 Thermal and Structural Characterization

The as-synthesis, prior to sintering, powders of all compositions are found in amorphous form with some carbon and nitrogen residue. The DTA/TGA patterns for all compositions shown figure 1 (a-d) exhibit almost similar trend i.e. gradual weight loss of 6-9 %. The endothermic peak at 50^{0}C corresponds to loss of water or water of crystallization. The SDC(x=0.1) and SDC(x=0.15) compositions show two sharp endothermic peaks in the temperature range 250 to 400^{0}C, without accompanying any sudden change in mass. Furthermore, curves show no change above 800^{0}C indicating proper combustion and crystallization.

It is worth mentioning here that all the experimental characteristic lines found coincided with the JCPDS data corresponding to cubic CeO_2. No line(s), in XRD pattern, corresponding to Sm_2O_3 confirmed the formation of solid solution. The variation of lattice constant, a, (obtained from the XRD data) with dopant content is shown in figure 2. Evidently, lattice constant increases with increase in dopant concentration. A linear relation between a and x, for present study, represented by Eq. (2) is in good agreement with Vegard's rule

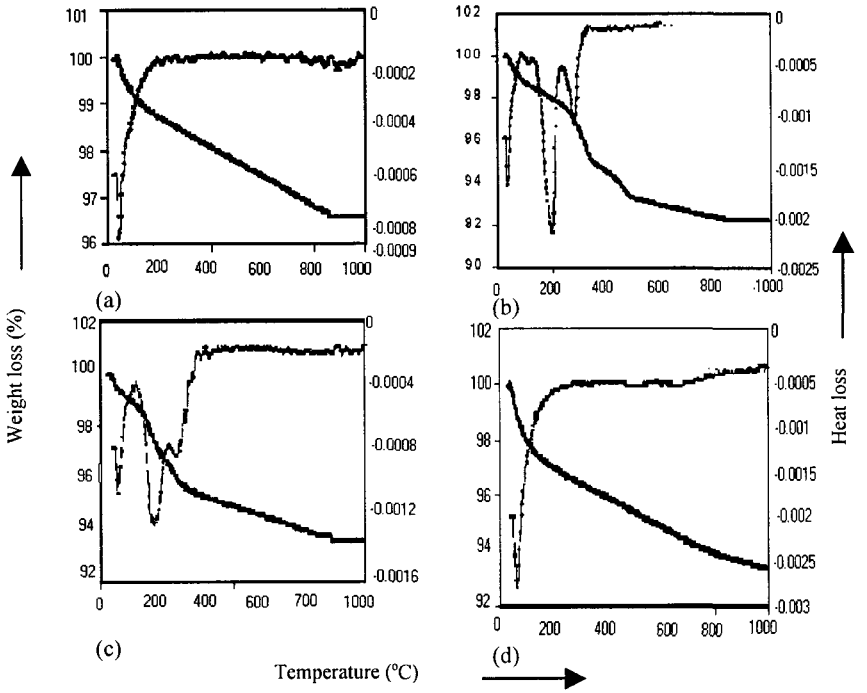

Figure 1: TGA / DTA curves of SDC powder at different dopant concentration (a) $x = 0.05$, (b) $x = 0.1$, (c) $x = 0.15$, and (d) $x = 0.20$.

$$a(x) = 5.372 + 0.0022x \qquad (2)$$

The effect of sintering temperature on grain size is shown in figure 3. It is, in general for all samples, to seen hat the grain size increases with sintering temperature; and packing rate is found to slow down at about sintering temperature

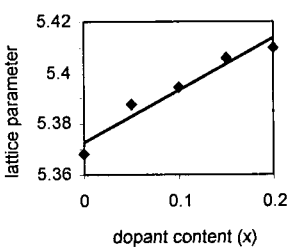

Figure 2: Variation of lattice constant with dopant content.

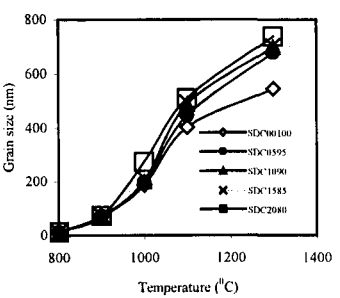

Figure 3: Variation of grain size with sintering temperature for SDC system.

1100^{0}C. The variation of grain growth with the dopant concentration, shown in figure 4, reveals that the grain size remains almost same for all dopant level for low

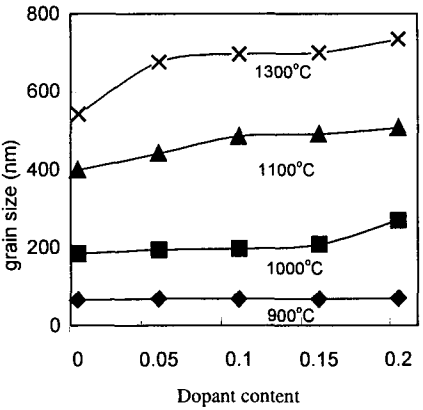

Figure 4 : *Variation of grain size with Sm content(sintered at different temp).*

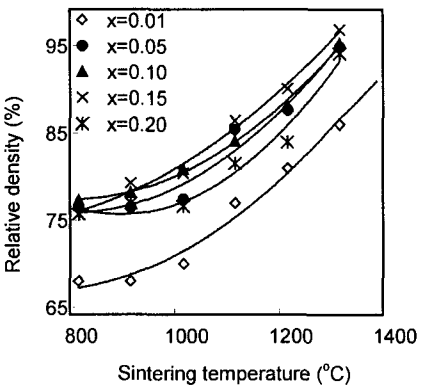

Figure 5 : *Variation of relative density for the samples of SDC system.*

sintering temperature. At higher temperature, however, the grain growth is accelerated with dopant content. Furthermore, the densification rate increases with dopant content, however, it retards at x = 0.20 (figure 5). The packing density, all the samples under study, seen almost close to X-ray density after sintering at 1300^{0}C for 3 hours. The pure CeO_2 exhibits smaller grain size as well as density as compared to Sm-doped ceria. The rate of grain growth (figure 3) exhibits sudden change at about 1100^{0}C, thus, the sintering effect was studied in detail by varying the time at this temperature. It is found that maximum relative density is achieved for the sintering duration of 8 hours at 1100^{0}C, which is much lower than that has been achieved at 1300^{0}C for 3 hours duration.

Microstructures of samples due to different sintering conditions are shown in figures 6(a-f). The surface view of SDC(x=0.15) pellet, calcined at 800^{0}C, reveals high porosity and no proper formation of crystallites. Grain size, however, is found of the order of nanometer range. Sintering at 1000^{0}C for 3 hours (figure 6b) gives rise to almost three times grain growth, but still with high porosity. The microstructure of sample sintered at 1100^{0}C for 3 hours (figure 6c) suggests commencement of densification. Furthermore, the grain size is doubled. The sample sintered at 1300^{0}C for 3 hours (figure 6d) reveals highly dense structure with the formation of a well-defined grain separated by grainboundary. A close look at the figure also indicates that the grains growth is almost doubled compared to

specimens sintered at 1100^{0}C. A comparative study of figures 6a-e along with figure 4, suggests that the densification proceeds with grain growth.

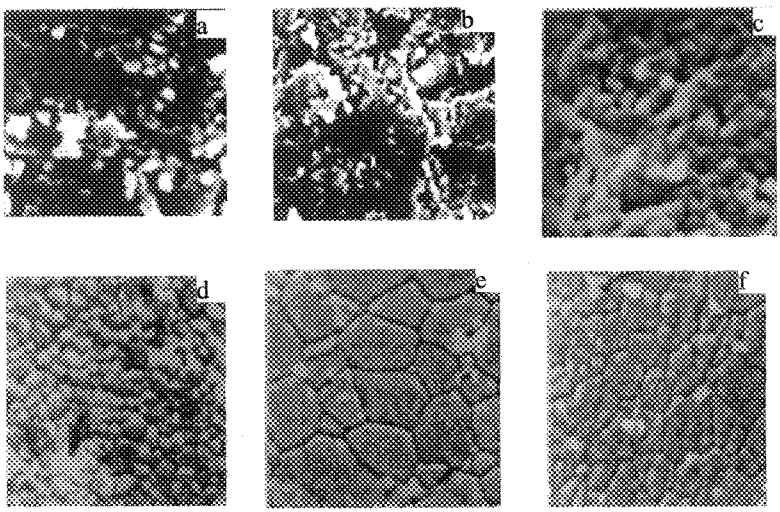

Figure 6: Microphotograph of (a) SDC(x=0.15) as calcined at 800°C (b) SDC sintered at 1000°C (c) SDC sintered at 1100°C (d) SDC sintered at 1000°C (e) SDC sintered at 1100°C for 5 hrs and (f) SDC sintered at 1000°C.

Figure 6e, sample sintered at 1100^{0}C for 5 hours, reveals increased densification accompanied by grains growth with increase in sintering duration. Additionally, grains are seen uniform in size and shape, and there is no evidence of exaggerated grain growth or segregation or agglomeration of grains. Sintering at the same temperature for the duration of 8 hours (figure 6f), gives maximum densification; well grain growth separated by sharp grain boundary. The packing density is found to be above 94% and, hence, impermeability to gases.

3.2 Electrical Conductivity

Arrhenius plots of $Ce_{1-x}Sm_xO_{2-\delta}$ (x = 0.05 – 0.2) are depicted in figure 7. The variation of conductivity as a function of dopant concentration, temperature ranges from 230 to 700^{0}C, is shown in figure 8. From the figures, it can be seen that, during the entire temperature range, SDC(x=0.15) exhibits the highest conductivity followed by the composition x = 0.2, 0.1, 0.05 in the descending order.

Chief advantages of combustion synthesis over other typical wet-chemical synthetic routes, sol-gel hydrothermal treatment, oxalate co-precipitation and

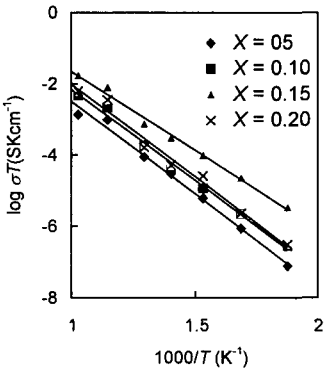

Figure 7: Arrhenius plot for $Ce_{1-x}Sm_xO_{2-\delta}$ *(x = 0.05 – 0.2)*

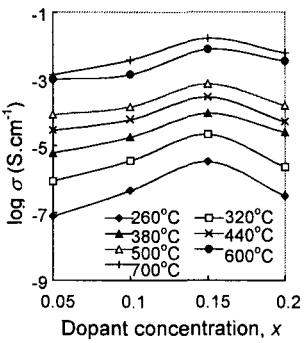

Figure 8: Variation of s_T with dopant content *for* $Ce_{1-x}Sm_xO_{2-\delta}$ *system*

carbonate co-precipitated, lies in the following aspects: (a) Rare-earth nitrates with fuel (glycine-nitrates or urea) form the solid solution easily at very low temperature. (b) Homogenous powders with high surface areas. (c) A simple preparation process (dry forming and pressure less sintering). (d) The low densification temperature (1100^0C). Hence, the combustion route facilitates the fabrication of dense SDC electrolytes with ease.

Samarium doping accelerates grain growth and densification, however, densification retards at x = 0.20. The inhibition effect of dopants on grain growth have previously also been observed in many other materials, such as MgO-doped Al_2O_3 [14], yttrium-doped CeO_2 and ZrO_2 [15, 16]. Such a behavior has been explained using the core space charge model [17]. Guo et al attributed inhibition phenomenon to the decrease in space charge potential with increasing dopant content [18]. In nanoscale range, since a comparatively larger grain diffuses much faster, the densification is accelerated by dopant content. Sudden fall in densification, for x = 0.20, in spite of grain growth, is attributed to retarding defect interaction. The low fabrication temperature achieved in this work is manifestly due to nanoscale particle size, which facilitates good compaction with uniformity in the green bodies. This is in accordance with Herring's scaling law [19]. Samarium doping introduces oxygen vacancies into the host CeO_2 lattice so as to achieve the charge neutrality. The Sm'_{Ce} and $V_0^{\cdot\cdot}$ point defects tend to cluster due to Coulombian attraction, and the tendency further increases with increasing dopant concentration. Subsequently, it leads to the formation of large number of (Sm'_{Ce} - $V_0^{\cdot\cdot}$) pair defect aggregation cluster. It, eventually, slows down the mobility of cations thereby decrease in densification.

4. Conclusion

Powders prepared following combustion synthesis route, with glycine-nitrates as fuel, gives ultra fine particles of uniform crystallite dimension 6-15 nm. The DTA / TG, XRD, and SEM studies, useful in assessing the sinterability, suggest that the fine particles facilitates the fabrication of dense ceramics at relatively lower temperature, 1100^0C. The densification and the grain growth of CeO_2 are further accelerated due to samarium doping. The 0.15 fraction of Sm in CeO_2 offers maximum conductivity.

Acknowledgements

The authors are thankful to UGC for providing financial assistance under DRS (SAP) to undertake this work.

References

1. N. Q. Minh and T. Takahashi, Science and Technology of Ceramic Fuel Cells, Elsevier, Amsterdam, (1995).
2. P.J.Gellings and H.J.M. Bouwmeester, The CRC Handbook of Solid State Ionics Electrochemistry, CRC Press, Boca Raton, FL, (1997).
3. H.L.Tuller, Solid State Ionics, **131**143 (2000).
4. B. C. H. Steele, Solid State Ionics, **129** 95 (2000).
5. M. Mogensen, N.M. Summes, G.A. Tompsetrt, Solid State Ionics, **129** 63 (2000).
6. K. Egushi, T. Setogushi, T. Inoue, and H. Arai, Solid State Ionics, **52** 165 (1992).
7. D. Y. Chung and E. H. Lee, Journal of Alloys and Compounds, **374** 69 (2004).
8. W. Huang, P. Shuk and M. Greenbelt, Solid State Ionics, **100** 23 (1997).
9. H. Yahiro, Y. Eguchi, K. Eguchi, and H. Arai, J. Appl. Electrochem., **18** 527 (1988).
10. B. C. H. Steele, Solid State Ionics, **129** 95 (2000).
11. S. Zha, C. Xia, and G. Meng, Journal of powder Sources, **115** 44 (2003).
12. K.C. Patil, S.T. Aruna and T. Mimani, Curr. Opin. Solid State Mater. Sci., **6** 507 (2002).
13. S.T. Aruna, M. Mathuraman, and K.C. Patil, J. Mater. Chem., **7** 2499 (1997).
14. W.D.Kingery, H. K. Bowen, and D.R. Uhlmann, Introduction to ceramics, New York: Wiley; (1976) p. 456.
15. D.D. Upadhyaya, R. Bhat, S. Ramamathan, S.K. Roy, H. Schubert, G. Petzow, J. Eur. Ceram. Soc., **14** (1994).
16. S.L.Hwang and I.W. Ch337en, J. Am. Ceram. Soc., **73** 3269 (1990).
17. J. Jamnik, J. Maier and S. Pejovnik., Interfaces in solid ionic conductors: equilibrium and small signal picture, Solid State Ionics, **75** 51 (1995).
18. X. Guo, Solid State Ionics, **96** 247 (1997).
19. C. Herring, J. Appl. Phys. **21** 301 (1950).

RED SOIL IN NORTHERN SRI LANKA IS A NATURAL MAGNETIC CERAMIC

K. AHILAN* and S. KETHEESWARAN

Department of Physics,
University of Jaffna,
Sri Lanka

M. BENNETT and M. C. ARONSON

2477 Randall Laboratory,
Department of Physics,
University of Michigan,
Ann Arbor 48109-1120, USA

The scope of the studies is to explore electric and magnetic properties of Fe^{3+} ion rich red soils in Northern Sri Lanka. Six samples were collected at different locations in Northern Jaffna peninsula, Sri Lanka for this investigation. Reported studies involve current-voltage (IV) measurements at room temperature of fresh, moisture-freed (115°C at 48 hrs), and annealed (1000°C at half an hour) conditions. At the fresh condition moisture dominates and is responsible for much of its transport properties. However, we are reporting that Fe^{3+} ions influence its transport properties in the moisture-freed and annealed conditions. Even though moisture-freed and annealed samples follow sub-linear IV behaviour the quantitative values suggest that the samples are very close to insulators (or semiconductor-insulator boundary). High field magnetization measurements up to 7 T at 1.8 K show all the samples reach the saturation moments around at 2.5 T, where the behaviour is very much similar to ferromagnetic materials. The highest saturated moment reported is $\sim 10^{-3}$ μ_B/Fe^{3+} and the lowest is 6.5×10^{-4} μ_B/Fe^{3+}. Also, we are presenting the inverse magnetic susceptibility-temperature ($1/\chi(T)$) measurements from room temperature (300 K) down to 1.8 K, which suggest that critical temperature T_c is around 30 K. Perhaps, the red-soil be a natural magnetic ceramic.

1. Introduction

Natural ceramic materials have been attracted lots of interest in recent time due to its unique applications. Minerals, soils etc are also considered as natural ceramic materials, which have been drawn attention of researchers all around the world for a long time. Soil is one of the important national resources of any country. Physical studies reported related to soils in Sri Lanka are relatively poor and almost nothing in Jaffna, Northern Sri Lanka. Some of the important properties such as colour, texture, structure, density, porosity etc are used for the

*Email: kahilan@jfn.ac.lk

classification of soils. Soils in Valikamam North (15–20 km north to Jaffna peninsula) and some other isolated pockets in Jaffna area have very rich content of red soils. This particular soil is one of the favourites and suitable places for farming in Northern Sri Lanka. However, its chemical and some physical properties suggest that its wealth is not only limited to agriculture or plant science but also be a potential candidate or a replacement as a raw material for mineral based small or large scale industries.

It is well documented that the *hematite* (α-Fe_2O_3) is responsible for its red colour in these soils. Some literature further says that the hematite is antiferromagnetically ordered and highly resistive and interestingly intrinsic semiconduction may be attained at higher temperatures in pure specimens.[1]

Soil is the most complex scientific entity in the earth. In general it is made up of range particles that are largely inorganic oxides of silicon, aluminum, iron, carbon, calcium, and magnesium, with a fragment of many other chemicals, including organic components and compounds. Some soils are almost completely organic in nature, but form a distinct minority in the whole. The weathering of rock minerals into smaller and chemically transformed components forms most soils.[2]

Investigations of electrical and magnetic properties, and preliminary understanding of transport properties are initial objectives of this study. Therefore the work presented here mainly involves preliminary studies of electrical and low magneticfield transport properties and high magneticfield magnetization measurements in the samples collected from various locations in Northern Sri Lanka.

2. Materials and Methods

Samples were collected nearly a foot or two below the earth's surface (to avoid additional contamination) at six different locations such as **A**-Punnalikadduvan, **B**-Chunnakam, **C**-Achchuveli, **D**-Innuvil, **E**-Kopay, and **F**-Nilavarai. After filtering (remove unwanted contamination, nomenclature used "fresh sample") a part of these samples were moisture-freed at 115°C (laboratory oven) for 48 hrs and annealed at 1000°C for half an hour (Carbolite furnace used, maximum operating temperature 1200°C).

Highly electrical resistive Pyrex material was used for the sample containers for both electeical and low magneticfield transport measurements. The sample containers were prepared with the dimension 15 mm × 10 mm × 5 mm. A small

hole of 1 mm diameter was drilled at the centre of two sides and the contact wires were inserted through the holes.

Computer controlled Keithley- 2400 digital source meter is employed for all current-voltage (IV) DC-measurements. I-V measurements performed also at 500, 1000, 1500 and 4000 Gauss low magnetic fields (electromagnet) at room temperature. The fields were applied perpendicular to the direction of current.

Quantum Designs SQUID based magnetometer (Magnetic Phenomena Measurement System MPMS), was employed for dc magnetization measurements for temperatures from 1.8 K–300 K, and in fields up to 7 Tesla. The work has been carried out at Michigan, USA.

3. Results and Findings

Chemical characterization (Table 1) clearly indicates that the significant Fe^{3+} ion variation among the samples collected at different locations. In more Fe^{3+} ions are the dominant contributor in this soil than other ions presented. Therefore we believe that these ions may play a significant role in the transport process in these red soils.

The current-voltage measurements were performed at room temperature for fresh (Fig. 1), moisture-freed (Fig. 2) and annealed (Fig. 3) samples. Comparing the Figs. 1 and 2 it is clear that the electrical transport of fresh soils is dominated by the moisture, since a significant drop in the current was observed in all moisture-freed samples. However, it is interesting to note that, in the Fig. 1, a few samples show linear behaviour (follow Ohmic character) above 1 V and the sample B almost saturates above 3 V, but the reason for this discrepancy yet to be known. The current through the rest two samples is low (nA order) this is probably due to less moisture in these areas.

Table 1 Chemical characterization all six fresh samples are tabulated above.[3]

Samples	Fe^{3+} (ppm)	Fe^{2+} (ppm)	Ca^{2+} (ppm)	Mg^{2+} (ppm)	Al^{3+} (ppm)
A	42617	1943	11102	1528	1339
B	37524	1563	7826	1201	2045
C	31627	1206	11648	1528	2926
D	27071	1463	9828	764	1963
E	26267	704	6188	2293	4738
F	22783	670	10556	437	1609

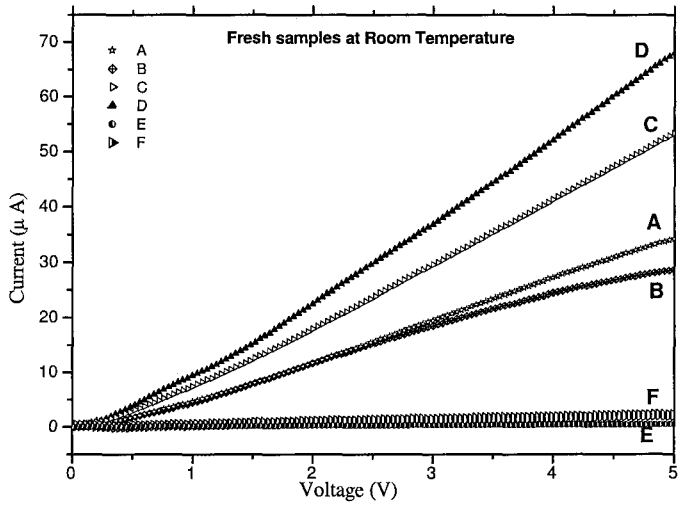

Fig. 1. Current-Voltage plot of six fresh samples at room temperature. A few samples follow nearly a linear behaviour above 1 V and a couple samples show saturation at above 3 V.

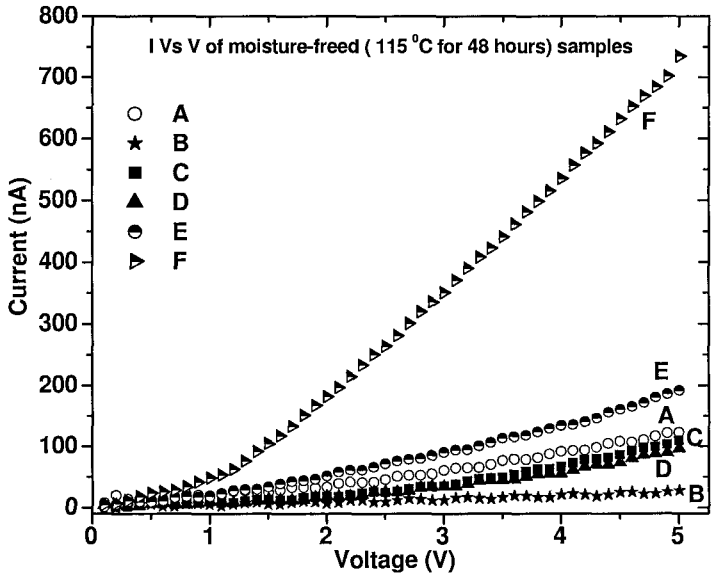

Fig. 2. Current-Voltage plot of six moisture-free samples at room temperature. A few samples follow clear linear behaviour and some samples show high reduction of current than its fresh samples.

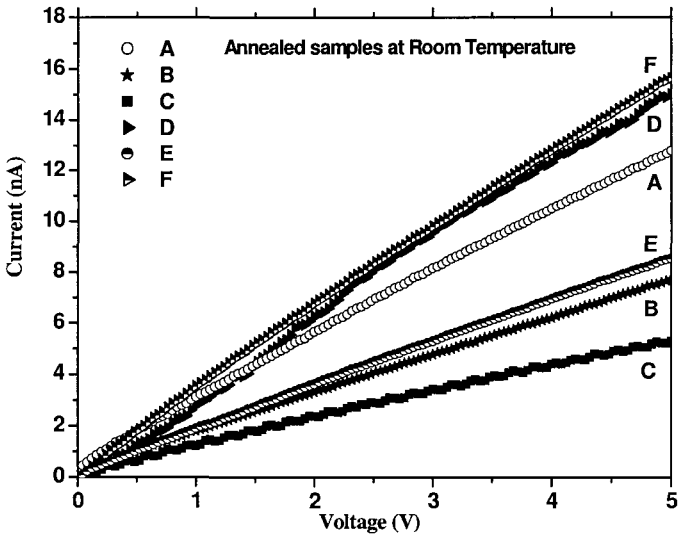

Fig. 3. Current-Voltage plot of six annealed samples at room temperature. All samples nearly follow linear or sub-linear behaviour. But current values suggest samples are become insulators after annealing.

After moisture-freed and annealed two or three orders of magnitude drop in the current is seen in all the samples (Figs. 2 and 3), i.e, the behaviour nearly same as insulating materials (or at the semiconductor-insulator boundary), however all samples follow nearly linear/sub-linear I-V behaviour. Except the sample F all other samples are reporting less than 200nA at 5 V in moisture-freed condition (Fig. 2). It is reasonable to say that higher Fe^{3+} ion concentration (> 30,000 ppm) samples show more decrease in the current than the lower ion concentration samples. Perhaps due to increase of ionic scattering that lowers the current.[3] However, for better understanding we require more extended studies in verity of samples.

I-V measurements at low magneticfields, up to 1500 G, were performed in the fresh sample E at room temperature is shown in the Fig. 4. This reveals that the order of magnitude suppression in the current, i.e increase in the resistivity, at small field of 500 G, however, no further noticeable change is reported at 1000 G or 1500 G (Fig. 4). The inset is the same measurement for the sample A (high Fe^{3+} ion content), the behaviour still persists as the sample E at low fields. The possible reason for this behaviour is due to Fe^{3+} ion-alignment at low magnetic fields and enhancing field induced scattering with the water molecules. Similar behaviour was noticed in all samples but in slightly varying magnitudes.

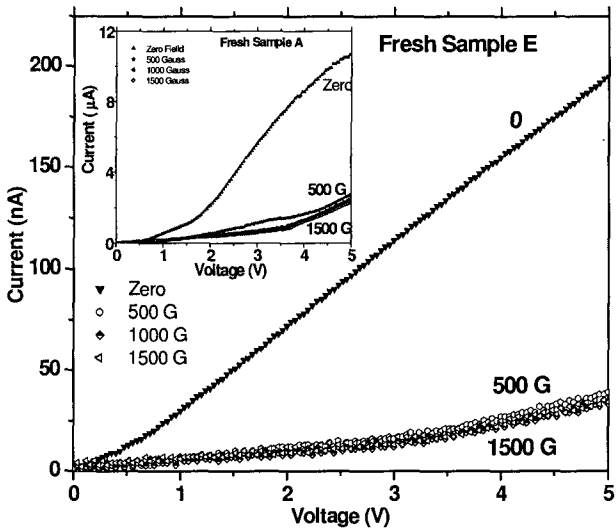

Fig. 4. Current-Voltage plot of a fresh sample E at room temperature at low magnetic fields applied perpendicular to the current direction. Field suppresses the current nearly by 5 times at 5 V. Inset shows the same measurement for the fresh sample A.

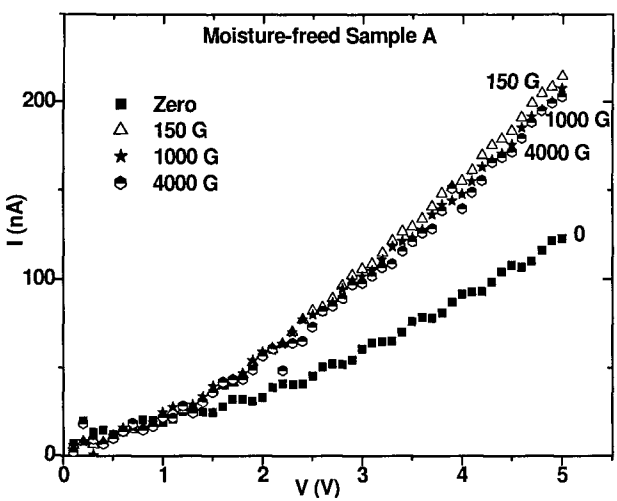

Fig. 5. Current-Voltage plot of a moisture-freed sample A at room temperature at low magnetic fields applied perpendicular to the current direction. The behaviour differs from the fresh sample, where reasonable increase of current is observed for the fields above 150 G. But further increase in the field up to 4000 G does not make much difference in the current. The behaviour persists in number of samples.

Similar type of measurement was carried out for the moisture-freed samples (Fig. 5) and annealed samples. However, the behaviour reported here shows exactly opposite to the fresh samples. In other words, perpendicular magnetic field enhances the conduction for both moisture-freed and annealed samples (not given due to slightly high signal to noise ratio). This behaviour has been recorded in number of samples. Probably due to field-induced alignment of Fe^{3+} reduces the scattering in the absence of water molecules. However, one requires high field studies at varying temperatures, probably at low temperatures, for further clarifications.

High magneticfield magnetization measurements were carried out up to 7 T at 1.8 K is plotted for six samples are given the Fig. 6. Moments are started to align slowly with the field and saturates around at 2.5 T. The quantitative values suggest that the saturated moments are small compared to normal ferromagnets, but the behaviour follows similar trend as ferromagnetic materials, probably the weak-ferromagnet. Highest moment reported is ~ 10^{-3} μ_B/Fe^{3+} for the sample E and the lowest is 6.5×10^{-4} μ_B/Fe^{3+} for the sample A. It seems little interesting, since the sample A shows the least moment per Fe^{3+} although it has highest number of Fe^{3+} (Table 1), in contrast to the sample E which contains relatively low ions.

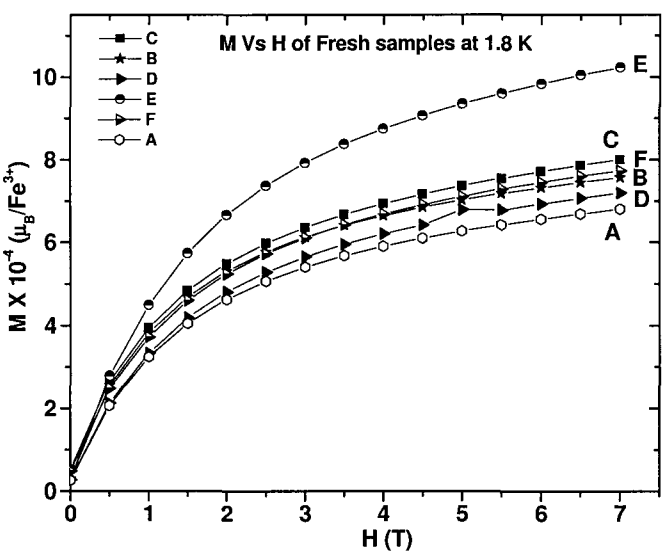

Fig. 6. M-H curves to the fresh samples up to 7 T at 1.8 K. It shows that the moments saturate at 2.5 T. Among the samples, sample E reports the highest moment and the sample A is the lowest. Even though the saturated moments report small value the behaviour is similar to ferromagnets.

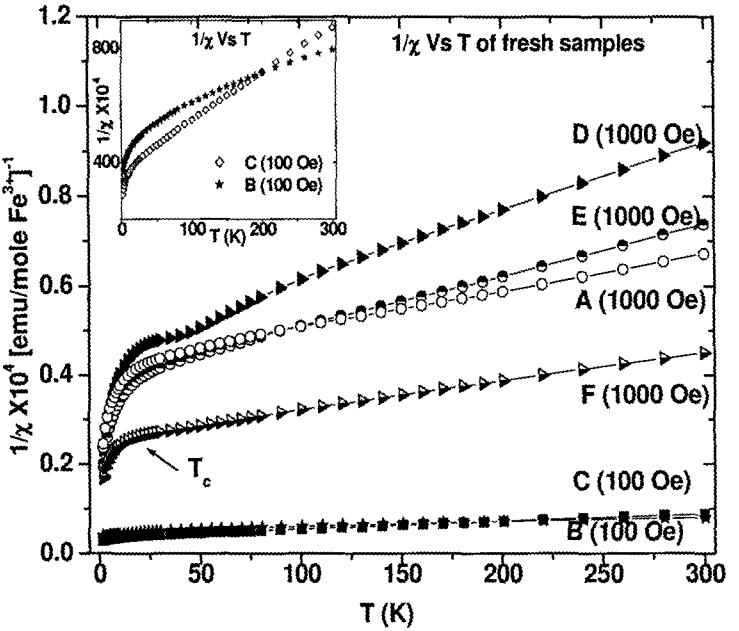

Fig. 7. Temperature dependence of inverse magnetic susceptibility is plotted in the main figure. Samples show T_C ~ 30 K. The inset is plotted to show the same for the samples B and C again, since T_C is not clear in the main figure.

Temperature dependence of inverse magnetic susceptibility is plotted in the Fig. 7. Field cooling has been done for samples B and C is at 100 Oe and for others at 1000 Oe. All samples report that the paramagnetic state become ferromagnetic at 30 K, i.e, T_C ~ 30 K. The inset is plotted to show the same for the samples B and C, since it is not very clear in the main figure.

4. Conclusion

Fe^{3+} ions in red-soils are certainly playing a crucial role in its electric and magnetic transport properties. However, at the fresh condition as we expected moisture dominates and responsible for much of its transport properties. Also we reported a few situations that Fe^{3+} ions determine the electric and magnetic transport properties in the moisture-freed and annealed red-soils. High field magnetization measurements suggest that this soil could be a weak ferromagnet with the critical temperature around 30 K. We are stepping closer in identifying a natural magnetic ceramic in the northern Sri Lankan soils.

However, the investigation is still at its early stage, therefore the studies require more evidences and extended and closer examinations at various conditions and external parameters to confirm the claim concretively.

References

1. R. T. Shuey, *Semiconducting ore minerals*, Elsevier Scientific Publishing Company (1975).
2. H. Bohn, B. McNeal and G. O'Connor, *Soil Chemistry*, John Wiley & Sons, 2nd Edition (1985).
3. S. Ketheeswaran, K. Rajendram, R. Srikaran and K. Ahilan, *JSA, 14th Annual Session*, April (2006) (submitted).
4. H. D. Scott, *Soil Physics*, Iowa State University Press (2000).
5. N. J. Hartsock, T. G. Mueller, G. W. Thomas, R. I. Barnhisel, K. L. Wells, and S. A. Shearer, *Soil Electrical Conductivity Variability*.

NEUTRON SCATTERING STUDY OF $LiNiO_2$

K. BASAR*, XIANGLIAN, H. HONDA AND T. SAKUMA
Institute of Applied Beam Science, Ibaraki University, Mito 310-8512, Japan
**E-mail: nd4612a@mcs.ibaraki.ac.jp*

H. TAKAHASHI
Institute of Applied Beam Science, Ibaraki University, Hitachi 316-8511, Japan

O. ABE
Faculty of Engineering, Ibaraki University, Hitachi 316-8511, Japan

N. IGAWA AND Y. ISHII
Japan Atomic Energy Agency, Tokai 319-1195, Japan

Neutron scattering experiments have been performed on $LiNiO_2$ composites at room temperature. Rietveld refinement analysis on the neutron scattering results of $LiNiO_2$ was performed by assuming hexagonal type structure with space group R-3m. The analysis of crystallite size of $LiNiO_2$ is performed from the FWHM of the Bragg lines using Scherrer equation. It is found that the crystallite size of $LiNiO_2$ increases with the increase of annealing temperature. The intensity of the Bragg lines and the background scattering of $LiNiO_2$ composites have been used to estimate the percentage of $LiNiO_2$ formed in the annealing process.

1. Introduction

$LiNiO_2$ and $LiCoO_2$ are important materials that can be applied as cathode materials for lithium-ion batteries because of its high energy density.[1,2] $LiCoO_2$ is structurally more stable than $LiNiO_2$ but more expensive and environmentally toxic. Presently, based on its advantages $LiNiO_2$ becomes particularly attractive as cathode material in lithium-ion batteries. Unfortunately due to the complexity of the structure, $LiNiO_2$ is more difficult to prepare compared to $LiCoO_2$. $LiNiO_2$ exists in two crystal structures: cubic and layered hexagonal. Only the latter can be applied as cathode material. Different methods and starting materials to produce this sample

have been reported in literature.[3]

Studies on the structure of $LiNiO_2$ which is obtained from many different methods and starting materials have been widely discussed. $LiNiO_2$ has a structure of hexagonal with space group R-3m.[3-5] The electrical conductivity at low temperature is explained by the variable range hopping mechanism due to mixing of cations.[6]

In this paper we report the neutron scattering study of $LiNiO_2$. The average crystallite size of $LiNiO_2$ is discussed and the amount of crystalline $LiNiO_2$ produced in the annealing process is estimated.

2. Experimental

The sample was prepared by dry mixing of starting materials LiOH and NiO then milled by high-energy planetary milling for 3 hours at frequency 3 Hz to perform a ground product. After that, the mixture was heated at temperature 400°C for 5 hours. We divided the whole sample into three parts: sample A which had no further heating process, sample B annealed at 500°C for 5 hours and sample C annealed at 650°C for 5 hours.

Thermal analysis of ground product of LiOH and NiO has been performed using TG (Thermal Gravimetry) measurements in the condition of dry N_2. The measurements were taken in the temperature range from room temperature to 750°C.

Neutron scattering measurements at room temperature have been performed for $LiNiO_2$ composites (sample A, B and C) by HRPD (High Resolution Powder

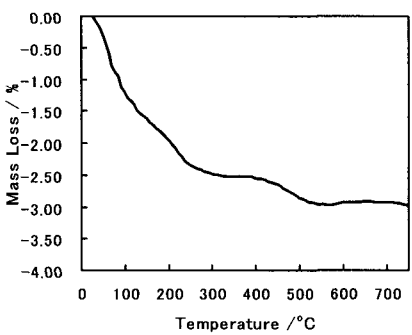

Fig. 1. TG curve of ground product of LiOH and NiO.

Diffractometer) installed at JRR-3 in Japan Atomic Energy Agency (JAEA). Powder samples were set in a vanadium container of 8 mm in diameter. Incident neutron wavelength of 1.823 Å which is monochromatized by Ge (331) was used and the data were collected in the 2θ range from 10° to 150° with step angle 0.05°. The neutron scattering experiments were done for 63.9, 46.6 and 50.4 hours for sample A, B and C, respectively.

3. Results and Analysis

TG curve of ground product is shown in Fig. 1. TG curve shows large mass loss about 2.5% if the ground product was heated up to 300° C. Up to 100° C the large mass loss in the sample is mainly caused by vaporization of water molecule that might be contained in the sample. We assume that the reaction to perform $LiNiO_2$ from the ground product of LiOH and NiO is shown as follows

$$2LiOH + 2NiO \rightarrow 2LiNiO_2 + H_2 . \quad (1)$$

This reaction occurs at high temperature when the ground product was heated by annealing process. As the hydrogen gas H_2 is resulted in the reaction, the mass loss of the ground product in the TG measurement is due to the H_2 formation. The mass of H_2 is about 1% of total mass of starting materials. Complete reaction of $LiNiO_2$ is shown by the minimum of mass loss curve around $600^{\circ}C$ or more. From TG curve, it is suggested that the reaction to perform crystalline $LiNiO_2$ starts at temperature around 200° C. Relatively, the H_2 mass losses at 400 and $500^{\circ}C$ are about 60 and 90% comparing to H_2 mass loss at $600^{\circ}C$.

Figure 2 shows the neutron scattering intensity from powder $LiNiO_2$ composites for sample A, B and C after experimental time correction. This correction is needed because of the difference in the measuring time for sample A, B and C. Strong Bragg lines of $LiNiO_2$ from sample A are observed at 2θ around 52 and 77°. The Bragg lines of $LiNiO_2$ become clearer and sharper in the sample B. Other $LiNiO_2$ peaks in sample B appear at 2θ around 22, 40, 58, 70, 82, 101, 106, 117 and 126°. The clearest and sharpest Bragg lines of $LiNiO_2$ appear in the scattering intensities of sample C.

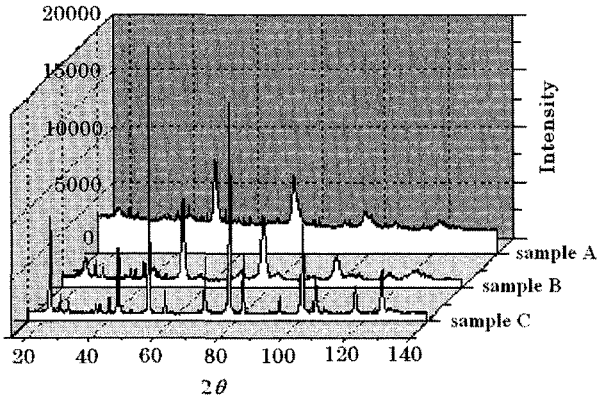

Fig. 2. Neutron scattering intensities of $LiNiO_2$ composites at room temperature.

High intensity of background scattering from sample A was also found in Fig. 2. The intensity of background scattering of sample A is almost 50% of the highest intensity of Bragg line. The background scattering intensities that include the contribution from vanadium sample cell and the incoherent scattering of atoms become smaller in the sample B and C as shown in the neutron scattering results in Fig. 2. We assume that the formation of $LiNiO_2$ crystalline is not complete in the sample A and B, and the change of background intensities are mainly from incoherent scattering of atoms. Based on these assumptions, it is obtained that the differences of the background intensities are proportional to the number of hydrogen atoms (Δn_H) that have large incoherent scattering cross section, namely:

$$\Delta I_{\text{background}} \propto \Delta n_H \,. \tag{2}$$

The large background intensity is caused by the existence of atom H in the sample A where atom H has a large incoherent scattering cross section by neutron beam. Although the crystalline $LiNiO_2$ has been formed, a large amount of starting material LiOH could still exist in the sample A. The existence of atom H from LiOH in the sample A makes the background scattering large. The amount of atom H in the ground product decreases by annealing process. Crystalline $LiNiO_2$ was formed by annealing the ground product at high temperature.

Table 1. Atomic sites, occupancy g and positions in $LiNiO_2$ used in the refinement analysis.

Atom	Site	g	x	y	z
Li	3(a)	1.0	0	0	0
Ni	3(b)	1.0	0	0	0.5
O	6(c)	2.0	0	0	z

Table 2. R factors, lattice parameters a and c, position of oxygen atoms z and temperature parameters B obtained from the refinement analysis.

sample	R_{wp} (%)	R_I (%)	R_F (%)	a (Å)	c (Å)	z	B_{Li} (Å^2)	B_{Ni} (Å^2)	B_O (Å^2)
A	5.68	3.42	1.73	2.899	14.206	0.249	5.69	1.37	0.43
B	9.04	1.00	0.50	2.899	14.206	0.247	3.19	0.69	0.81
C	8.67	7.60	4.09	2.892	14.222	0.245	0.71	0.25	1.44

Rietveld analysis has been performed on the neutron scattering intensities of sample A, B and C using RIETAN-2000.[7] It is assumed that the crystal $LiNiO_2$ belongs to hexagonal symmetry with space group R-3m. Lithium, nickel and oxygen atoms occupy 3(a), 3(b) and 6(c) sites, respectively. Atomic positions in $LiNiO_2$ unit cell used in Rietveld refinement are shown in Table.1. Split pseudo-Voigt function has been used as profile function in the refinement.[8] In the refinement calculation, we excluded several small peaks that do not coincide with the Bragg line of $LiNiO_2$. The occupation factor g of atom Li, Ni and O are 1.0, 1.0 and 2.0, respectively as shown in Table 1. R factors, the oxygen position z and temperature parameters B from the refinement results are shown in Table 2.

The width of Bragg lines of $LiNiO_2$ in the sample A, B and C shows a tendency to decrease by increasing the annealing temperature. The average crystallite size of $LiNiO_2$ formed in the annealing process from ground product has been analyzed from peak width of Bragg line using Scherrer equation:

$$t = \frac{K\lambda}{D\cos\theta}, \tag{3}$$

where t is the average crystallite size in angstrom, K is a constant and equal to 0.9, λ the wavelength of incident beam, D the FWHM (full width at half maximum) of Bragg line and 2θ the scattering angle of Bragg line. The full width at half maximum of Bragg line D_{meas} which is obtained from measurements should be corrected with the instrumental resolution D_{inst} using the relation

$$D^2 = D^2_{\text{meas}} - D^2_{\text{inst}} . \tag{4}$$

The resolution curve D_{inst} of HRPD for 12' collimator used in the experiments is shown in Fig. 3. The value of D_{meas} was obtained from Rietveld refinement by following equation

$$D^2_{\text{meas}} = 8\ln 2\left[U\tan^2\theta + V\tan\theta + W\right], \tag{5}$$

where U, V and W are three parameters of Gaussian function obtained in the refinement calculation.

The average crystallite sizes of $LiNiO_2$ which were calculated using eq. (3) for three different samples A, B and C are shown in Fig. 4. Two main peaks (104) and (018) of $LiNiO_2$ are used in the calculation. These two peaks are selected because they appear clearly in the three samples A, B and C. The average sizes of $LiNiO_2$ are about 30, 40 and 120 Å for sample A, B and C, respectively. These sizes are in the range of nanostructure materials. It is shown in Fig. 4 that annealing temperature has a strong influence to the average crystallite size of $LiNiO_2$. The average crystallite size of $LiNiO_2$ increases with the increasing of annealing temperature.

If we assume that almost all starting materials change to $LiNiO_2$ in the sample C, the relative amount of $LiNiO_2$ which was formed in the sample A and B can be estimated by comparing the area of the Bragg line of $LiNiO_2$. The estimated relative amount of crystalline $LiNiO_2$ is shown in Fig. 5. Assuming that 100% of starting materials change to crystalline $LiNiO_2$ in the sample C, the percentage of crystalline

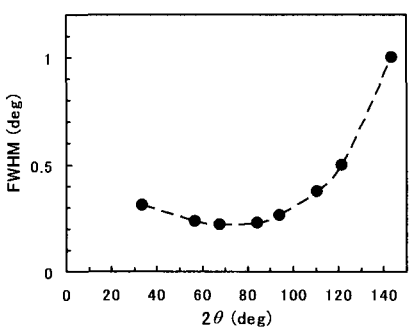

Fig. 3. Instrumental resolution D_{inst} for 12' collimator of HRPD used in the experiments.

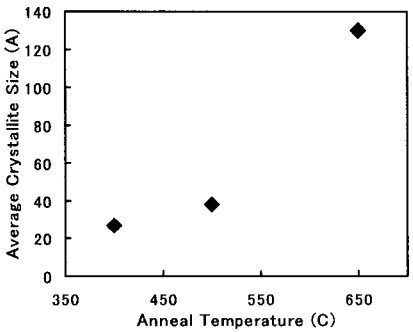

Fig. 4. Average crystallite size of $LiNiO_2$.

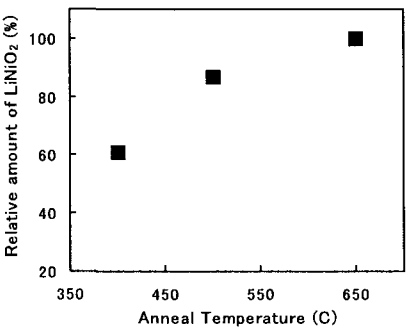

Fig. 5. Relative amount of $LiNiO_2$ obtained by annealing process.

$LiNiO_2$ formation in sample A and B are about 61 and 87%, respectively. This estimation is almost same with the analysis of mass loss from the TG data. The background intensities of sample A, B and C are explained by the percentage of crystalline $LiNiO_2$. The amount of crystalline $LiNiO_2$ formed by annealing process increases with the annealing temperature.

4. Conclusions

Crystalline $LiNiO_2$ has been prepared by annealing the ground product of LiOH and NiO. Neutron scattering experiments and Rietveld analysis have been performed on the $LiNiO_2$ composites. The large background scattering intensities of $LiNiO_2$ composites show that some parts of starting materials are still exist in the composites. The average crystallite size of $LiNiO_2$ increases with the increase of annealing temperature. The amount of $LiNiO_2$ formed in the annealing process increases by the annealing temperature.

5. References

1. J. R. Dahn, U. von Sacken and C. A. Michal, *Solid State Ionics* **44**, 87 (1990).
2. R. Kanno, H. Kubo, Y. Kawamoto, T. Kamiyama, F. Izumi, Y. Takeda and M. Takano, *J. Solid State Chem.* **110**, 216 (1994).
3. V. Bianchi, D. Caurant, N. Baffier, C. Belhomme, E. Chappel, G. Chouteau, S.

Bach, J. P. Pareira-Ramos, A. Sulpice and P. Wilmann, *Solid State Ionics* **140**, 1 (2001).

4. H. Arai, S. Okada, H. Ohtsuka, M. Ichimura and J. Yamaki, *Solid State Ionics* **80**, 261 (1995).
5. W. Li, J. N. Reimers and J. R. Dahn, *Phys. Rev.* **B 46**, 3236 (1992).
6. J. Molenda, P. Wilk and J. Marzec, *Solid State Ionics* **146**, 73 (2002).
7. F. Izumi and T. Ikeda, *Mater. Sci. Forum* **321-324**, 198 (2000).
8. H. Toraya, *J. Appl. Crystallogr.* **23**, 485 (1990).

PREPARATION AND PROPERTIES OF LIFEPO$_4$ NANORODS

L. Q. MAI, L. XU, W. CHEN†, Q. XU, H. X. LIU, X. J. ZHAO, CH. V. SUBBA REDDY

Institute of Material Science and Engineering, Wuhan University of Technology, Wuhan 430070, P.R. China

LiFePO$_4$ nanorods have been synthesized using a rheological reaction followed by a self-assembling process, and characterized by XRD, TEM, FTIR, cyclic voltammogram, model battery, etc. The results show that the LiFePO$_4$ nanorods with length of 50~100 nm and nanorod diameter of 20~50 nm are grown orderly with certain direction, resulting in better conductivity and insertion/extraction reversibility of Li^+ ions.

1. Introduction

LiFePO$_4$ is an attractive candidate for use as a cathode material in lithium ion batteries based on environmental and safety considerations [1, 2]. The main problem of the LiFePO$_4$ is that synthesis is not easy because of the iron oxidation state. The oxidation state control has been usually done by the furnace heating with the reductive or inert gas flow for several hours as shown in the previous reports [3-7]. In addition, alternative synthetic processes have developed continually, Yang et al. [8] used pure hydrothermal synthesis and Franger et al. [9] tried mechanochemical activation and rapid heat treatment. Recently, Higuchi et al [10]. showed the possibility of the microwave processing to make the LiFePO$_4$. They prepared precursors by solid state mixing and calcined it with the microwave under the inert atmosphere. However, iron precursors act as microwave absorbers and therefore selection of the iron precursors is restricted in that case. Although the attempts have been made to find the proper fabrication procedures, it is important to prepare rod-like LiFePO$_4$ nanomaterials for improving structure and electrochemical performance of LiFePO$_4$ because the nanorod materials haveunique properties originated from their high surface area and low dimensionality. To the best of our knowledge, the synthesis of LiFePO$_4$ nanorods has not been reported. In the present work, LiFePO$_4$ nanorods have been synthesized using a rheological reaction followed by a self-assembling

† Corresponding author. Tel.: +86 27 87651107; fax: +86 27 87864580.
E-mail address:chenw@mail.whut.edu.cn (W. CHEN)

process, and characterized by XRD, TEM, FTIR, cyclic voltammogram, model battery, etc.

2. Experimental

$LiFePO_4$ nanorods were prepared in a rheological phase reaction method followed by a self-assembling process. $LiOH{\cdot}H_2O$, $FeC_2O_4{\cdot}2H_2O$ and $NH_4H_2PO_4$ with molar ratio of 1.5:1:1 were dissolved in distilled water and stirred for 10 min, the resulting rheological phase slurry was put into the Teflon-lined autoclave with a stainless steel shell. The autoclave was kept at 180 ℃ and autogenerated pressure (about 2.5 MPa) for 24 h, then allowed to cool to room temperature naturally. The final gray product was washed with distilled water and dried at 80 ℃ for 8 h.

XRD experiments were performed using a D/MAX-III X-ray diffractrometer with Cu Kα radiation and graphite monochrometer. TEM images were taken in a JEM-100cx II microscope operating at 80 kV. Fourier transform infrared (FTIR) absorption spectra were recorded using a 60-SXB IR Spectrometer with a resolution of 4 cm^{-1}. The test cells containing 1 M $LiPF_6$-EC-DEC 1:1 volume ratio were charged and discharged at a 0.1 C rate. Cyclic voltammogram (CV) test was performed on an Auto Lab instrument with a scanning rate of 0.1 mV/s between 1.7 and 4.5 V. All potentials are cited in this paper with respect to the reference Li^+/Li. HP-4294A apparatus was used to investigate the electrical properties of the samples.

3. Results and discussion

3.1. *XRD Analysis*

Figure 1 shows the XRD pattern of synthesized $LiFePO_4$. All peaks can be indexed as pure and well-crystallized $LiFePO_4$ phase with an ordered olivine structure and a space group of Pnma. The lattice parameters calculated by the XRD data (Figure 1) of the material are a=1.0342 nm, b=0.6005 nm, and c=0.4693 nm, which are very close to the standard data given by JCPDS 83-2092. The XRD result demonstrates that the a rheological self-assembling route developed in the present work could synthesize single-phased product $LiFePO_4$ with no unwanted impurity phases, such as Li_3PO_4- and Fe^{3+}-related compounds[4]. Conventional solid state methods, although carried out under carefully controlled conditions, have shown the unwanted presence of the impurity phases Fe_2O_3 and $Li_3Fe_2(PO_4)_3$ [1]. Another advantage is that the sample can be prepared by this process without sintering. This makes it simple to

prepare $LiFePO_4$ olivine materials. In comparison with the previous solid state processes, the rheological self-assembling process reduces the synthesis temperature of $LiFePO_4$. It is evident that the soft solution environment remarkably accelerates the reaction kinetics of the formation of $LiFePO_4$.

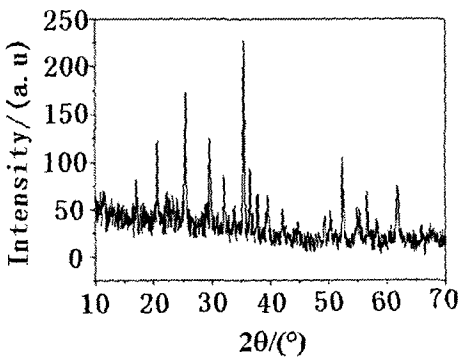

Figure 1. XRD pattern of the $LiFePO_4$ nanorods.

3.2. *TEM Analysis*

TEM analysis was carried out on the sample, as shown in Figure 2. The micrograph reveals the formation of rod-like nanostructure, whose length range is from 50 nm to 100 nm and diameter range is from 20 to 50 nm. Almost all nanorods are grown directionally and are well connected with linear grain boundaries. As far as the TEM results are concerned, no such information is available in the literature to compare with our results. However, one can not

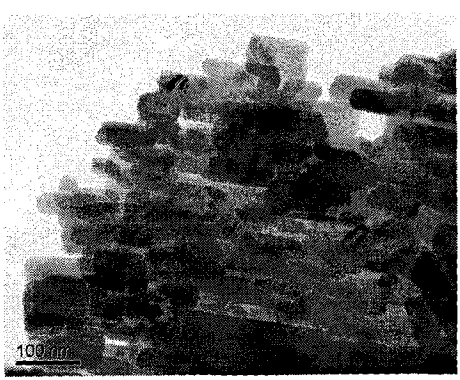

Figure 2. TEM images of the $LiFePO_4$ nanorods.

expect the above features, such as nanorod morphology and directional growth, in a similar compound prepared via solid-state reaction at high temperature. The aforementioned features are very desirable for a material to be employed as an active electrode material in a modern rechargeable Li ion battery.

3.3. *FTIR Analysis*

The FTIR spectrum of synthesized $LiFePO_4$ is shown in Figure 3. The characteristic absorption band of $LiFePO_4$ at 1445 cm^{-1} is associated with the vibrations of P-O-Fe bond in $LiFePO_4$ whereas the band situated at 1077 and 972 cm^{-1} corresponds to the characteristic absorption of the $[PO_4]^{3-}$. The absorption band of $LiFePO_4$ between 635 and 470 cm^{-1} is associated with the vibrations of P-O bond in $LiFePO_4$. Notably, the characteristic absorption band of Li-O bond at 405 cm^{-1} is weak, indicating the weak interaction between Li and O atoms, which enables Li^+ ions to insert/extract easily in the ordered olivine structure of $LiFePO_4$ [11].

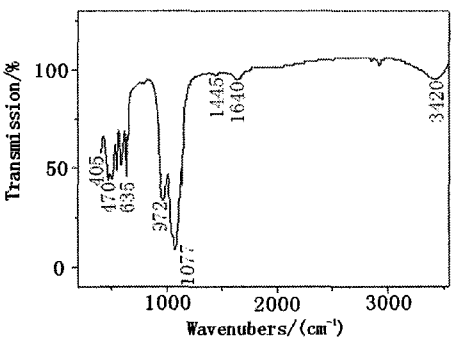

Figure 3. FTIR spectrum of the $LiFePO_4$ nanorods.

3.4. *Electrochemical Analysis*

The first charge-discharge curve shown in Figure 4 displays a voltage plateau around 3.3~3.5 V which corresponds to Li insertion/extraction. The initial charge/discharge capacity is 109 and 105 mAh/g, respectively. The discharge capacity of the cell with prepared $LiFePO_4$ nanorods decreases from 105 mAh / g in the first cycle to 75.0 mAh / g in the twentieth cycle, as shown in Figure 5. The electrochemical performance of the $LiFePO_4$ nanorods is better than the values of pure $LiFePO_4$ reported by others [12].

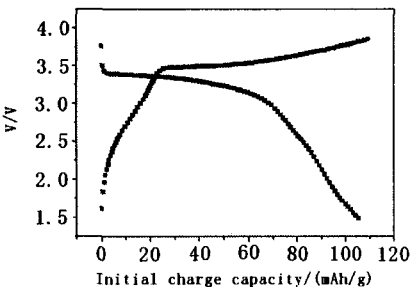

Figure 4. Initial charge/discharge curve of the $LiFePO_4$ nanorods.

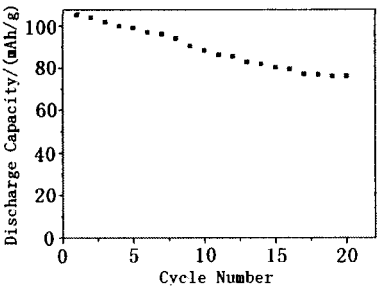

Figure 5. Cycling property curve of the $LiFePO_4$ nanorods

In order to further understand the electrochemical performance of $LiFePO_4$ nanorods, cyclic voltammetry was carried out. The CV curve of $LiFePO_4$ in the first cycle is shown in Figure 6. It exhibits a pair of redox peaks around 3.4 V vs. Li^+/Li, but the peak profiles of the as-prepared $LiFePO_4$ were more symmetric and spiculate than that attained by others, indicating little conductivity restriction comparing to the latter. As for cyclic voltammogram, the potential interval between anodic peak and cathodic peak is an important parameter to value the electrochemical reaction reversibility. As shown in Figure 6, $LiFePO_4$

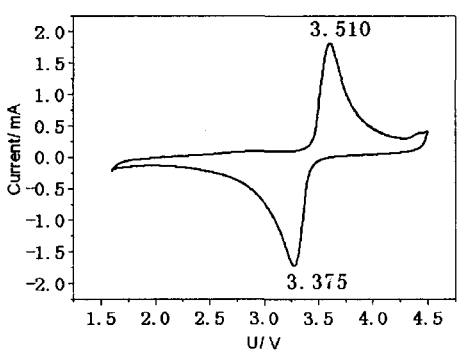

Figure 6. Cyclic voltammogram curves of the $LiFePO_4$ nanorods

nanorods exhibits an anodic peak at 3.510 V and a corresponding cathodic response at 3.375 V. The potential interval of $LiFePO_4$ nanorods was 0.135 V, much less than the value 0.151 V reported by Mi *et al* [13]. The well-defined peaks and smaller value of potential interval shows the enhancement of electrode reaction reversibility. Notably, the electrical conductivity of $LiFePO_4$ nanorods

is 10^{-5} S/cm, which is five orders of magnitude higher than those of bulk materials (10^{-10} S/cm) [14]. The good performance of the as-synthesized $LiFePO_4$ sample most likely result from the favorable nanorod structure, uniform size distribution as well as phase purity, all of which result in turn from our novel synthesis method. Besides its simplicity, the method is also versatile in that other lithium transition metal phosphates such as $LiNiPO_4$, $LiCoPO_4$ and solid solutions of different lithium transition metal phosphates with favorable physical characteristics can be easily synthesized by this method as well.

4. Conclusions

In summary, the rheological self-assembling method has been developed to directly synthesize $LiFePO_4$ nanorod materials. The $LiFePO_4$ nanorods with length of 50~100 nm and nanorod diameter of 20~50 nm are grown orderly with certain direction, resulting in better conductivity and insertion/extraction reversibility of Li^+ ions. The high-yielding cost-saving synthetic procedure is expected to be applied in large-scale fabrication of $LiFePO_4$ nanorods and appears attractive for its uses in lithium intercalation devices.

Acknowledgments

This work was supported by the National Natural Science Foundation of China (Grant No. 50372046), the Key Project of Chinese Ministry of Education (Grant No. 104207), the Foundation for Innovation Research Team of Hubei Province (No. 2005ABC004), Nippon Sheet Glass Foundation for Materials Science and Engineering (2005), the Teaching and Research Award Program for Outstanding Young Professors in Higher Education Institute, MOE, P. R. China and the Wuhan Youth Chenguang Project (2006).

References

1. K. Padhi, K. S. Nanjundaswamy and J. B. Goodenough, *J. Electrochem. Soc.* **144,** 1189 (1997).
2. S. Andersson, B. Kalska, L. Haggstrom and J. O. Thomas, *Solid State Ionics* **130**, 41 (2000).
3. A. S. Andersson and J. O. Thomas, *J. Power Sources* **97**, 498 (2001).
4. Yamada, S. C. Chung and K. Hinokuma, *J. Electrochem. Soc.* **148**, A224 (2001).
5. S.Y. Chung, J. T. Bloking and Y. M. Chiang, *Nat. Mater.* **1**, 123 (2002).
6. H. Huang, S.C. Yin and L.F. Nazar, Electrochem. *Solid State Lett.* **4**, A170 (2001).

7. F. Croce, A.D. Epifanio, J. Hassoun, A. Deptula, T. Olezac and B. Scrosati, Electrochem. *Solid State Lett.* **5,** A47 (2002).
8. S. Yang, P. Y. Zavalij and M. S. Whittingham, *Electrochem. Commun.* **3,** 505(2001).
9. S. Franger, F.L. Cras, C. Bourbon and H. Rouault, *J. Power Sources* **119,** 252 (2003).
10. M. Higuchi, K. Katayama, Y. Azuma, M. Yukawa and M. Suhara, *J. Power Sources* **119**, 258 (2003).
11. W. Chen, L. Q. Mai, Q. Xu, Q. Y. Zhu and H. P. Yang. *Mater. Sci. Eng. B*, **100**, 221 (2003).
12. M. S. Whittingham, *Chem. Rev.* **104**, 4271 (2004)
13. H. Mi, G. S. Cao and X. B. Zhao. *Mater. Lett.*, **59**, 127 (2005).
14. S. Y. Chung, J. T. Bloking and Y. M. Chiang. *Nature Mater.* **2**, 123 (2002).

STRUCTURAL AND ELECTROCHEMICAL PROPERTIES OF MONOCLINIC AND ORTHORHOMBIC MoO_3 PHASES

O. M. HUSSAIN
Thin Film Laboratory, Department of Physics, Sri Venkateswara University, Tirupati-517 502, India

C. V. RAMANA
Nanoscience and Surface Chemistry Research Group, Dept of Geological Sciences University of Michigan, Ann Arbor, MI 48109, USA

K. ZAGHIB
Institut de Recherche d'Hydro-Québec, Varennes, QC, Canada J3X 1S1

C. M. JULIEN
Institut des Nanosciences de Paris (INSP), Université Pierre et Marie Curie CNRS-UMR 7588, 140 rue de Lourmel 75015 PARIS, France
E-mail: Christian.Julien@insp.jussieu.fr

This work reports new trends on the structural and electrochemical properties of two polymorphs of the well-known Mo-O system. Two crystalline phases have been obtained: the monoclinic β-MoO_3 and the orthorhombic α-MoO_3. The structure and morphology of these oxides were studied as a function of the temperature and the ambient of heat treatment to determine the optimum conditions for single phase synthesis. Results from XRD, SEM and Raman measurements are presented. The electrochemical lithium intercalation into the prepared trioxides was attempted as the intercalation host for secondary lithium batteries Cycling performance showed a high ability of both polymorphs to form lithium intercalation compounds. For the β-MoO_3 phase, the maximum lithium uptake 1.9 Li^+/Mo leads to the gravimetric capacity 353 mAh/g, while the α-MoO_3 phase develops a specific capacity 298 mAh/g for 1.6 Li^+/Mo inserted.

1. Introduction

Layered intercalation compounds have been known for a long time, and a considerable variety of host frameworks that can incorporate atomic guest species have been investigated.[1] Few binary oxides exist with layered structures (e.g. MoO_3, V_2O_5) which are able to form A_xMoO_3, $A_xV_2O_5$. These are phases inserted by alkali ions called "bronzes" that exhibit new interesting features. Within this group of oxides studied, specially the molybdenum oxides have received special attention due to their physico-chemical and electrochemical properties.[2-4]

Molybdenum is known to exist in a number of oxidation states and a variety of oxides, sub-oxides, hydroxides, and hydrated complexes.[5] The oxides and oxide-hydrates of molybdenum in its highest oxidation state display a

variety of structural types involving linked MoO_6 octahedra. Hitherto, two polymorphs of molybdenum trioxides are known to exist: the monoclinic β-MoO_3 and the orthorhombic α-MoO_3. The metastable phase β-MoO_3 has a structure similar to that of ReO_3, while the α-MoO_3 structure can be described in terms of layered lattice in which distorted MoO_6 octahedra share edges and vertices to form corrugated two-dimensional sheets separated by a van der Waals gap.

The electrochemical properties of the lithium insertion into some anhydrous and hydrated molybdenum oxides have been reported previously.[3-10] The amount of Li^+ ions inserted into hydrated compounds is higher than the lithium uptake 1.5 and 2 Li/Mo obtained for anhydrous α-MoO_3 and β-MoO_3, respectively. Kumagai *et al.*[7-8] reported that crystalline $MoO_3 \cdot 2H_2O$ phase can accommodate reversibly more than 2.5 Li/Mo. The suitability of $MoO_3 \cdot \frac{1}{3}H_2O$ as positive electrode in Li batteries has been reported by Guzman *et al.*[9] Several characteristics of the lithium intercalation in molybdenum trioxide hydrate, $MoO_3 \cdot 2/3H_2O$, and the anhydrous Mo_5O_{14} phase have been studied by Nazri and Julien.[10] The lithium uptake into anhydrous Mo_5O_{14} was found 1.45 Li/Mo at the first cycle. The Li//Mo_5O_{14} cell delivered capacity as high as 280 mAh/g.

On the basis of our previous studies, the anhydrous α-MoO_3 and β-MoO_3 phases have been synthesized by a sol-gel method. The products have been tested as active material in electrochemical Li cells. The in-situ structural evolution of the layered Li_xMoO_3 phase is also reported.

2. Experimental

Crystalline α-MoO_3 was synthesized by thermal decomposition of acid molybdic $MoO_3 \cdot 1H_2O$ (purum from Aldrich-Chimie). The samples were obtained by thermal annealing in a two-zone tube furnace with a 50 cm^3/minute argon flow. After 2 h purge, the furnace temperature was ramped from room temperature to the desired heat treatment over 1 h period. Samples were heat treated at 750 °C for 48 h. Crystalline β-MoO_3 was prepared by the cation exchange method reported by McCarron[11] using sodium molybdate $Na_2MoO_4 \cdot 2H_2O$ dissolved in distilled water. The aqueous solution was passed through an acid resin (Dowex 50WX8-300). A green dried powder was obtained after water evaporation. The final product β-MoO_3 was prepared by heating the pale-greenish precursor at 270 °C for 4 h in a flowing oxygen ambient.

Powder XRD data were obtained using CuK_α radiation (λ=1.5406 Å) with a Philips X'Pert diffractometer. Raman spectra were recorded on a Jobin-Yvon U1000 double monochromator using the 514.5 nm line from a Spectra-Physics 2020 argon-ion laser. Standard photon-counting techniques were used for detection. In a typical spectral acquisition, six RS spectra each recorded with a resolution of 2 cm^{-1} were averaged. Care was taken against sample photo-decomposition using low excitation power of 10 mW.

The non-aqueous cell assembly had the configuration Li/1M $LiPF_6$ solution of EC-DEC (1:1)/MoO_3. A cell was constituted by a pellet cathode

pressed at 0.5×10^5 Pa with an area of 0.8 cm^2 cathode, a glass-fiber separator (Whatman GF/C), and a lithium-metal foil anode. This assembly were sandwiched between nickel foils as current collectors. Electrochemical titration measurements were carried out using a Mac-Pile system at current densities in the range 0.1-0.2 mA/cm^2. Kinetics parameters have been determined by the GITT method from the variation of the cell voltage vs. time during the relaxation period following a long discharge or charge.[12]

3. Results and discussion

The thermal decomposition of the MoO_3-$1H_2O$ raw powders occurred continuously in the range 100-450 °C. TG/DTA curves showed successively the water removal, the formation of the monoclinic phase, the exothermic reaction corresponding to the β-MoO_3 → α-MoO_3 transition and finally the growth of the α-MoO_3 crystalline phase.[4] XPS data confirmed the binding energy for Mo $2p_{3/2}$ core level corresponding to the Mo(VI) atoms in the MoO_6 octahedra.

3.1. Structure and morphology

Structural properties of molybdenum trioxides were studied using X-ray diffraction (XRD) and Raman scattering (RS) experiments. Fig. 1 shows the XRD patterns of β-MoO_3 and α-MoO_3 crystalline samples. The main features of the XRD patterns can be indexed in the monoclinic (*$P2_1/n$* S.G.) and orthorhombic (*Pbnm* S.G.) system, respectively. Single crystals of α-MoO_3 have the shape of elongated platelets with the (010) axis perpendicular to the basal plane and the (001) axis along the longest edge. The orthorhombic structure was formed above 500 °C. The layered arrangement causes van der Waals interactions between parallel layers formed by MoO_6 octahedra that share edges in the (001) direction and are connected by corners in the (100) direction. The (0*k*0) intense Bragg lines suggest that this compound is a layered structure packed in the direction of the *b*-axis.

The X-ray pattern of β-MoO_3 coincides with that reported by Parise et al.[13] This phase adopts an ReO_3-related structure. The common structural arrangement of this material is the MoO_6 octahedral unit, which is repeated along three directions through shared corners. Lattice parameters of mobybdenum trioxide are listed in Table 1.

Table 1. Lattice parameters of the MoO_3 phases.

Phase	Space group	Lattice parameters (Å)
α-MoO_3	*Pbnm*	a=3.9621 Å, b=13.858 Å, c=3.972 Å
β-MoO_3	*$P2_1/n$*	a=7.118 Å, b=5.379 Å, c=5.566 Å, β=91.87°

Fig. 2 shows the typical SEM pictures of molybdenum trioxide samples. The elongated morphology of the α-MoO_3 samples is clearly observed, while

the β-MoO_3 displays smaller particles. The α-MoO_3 single crystal might be easily cleaved to form very thin slabs. Thus, the crystal forms of the final products MoO_3 are different from each other.

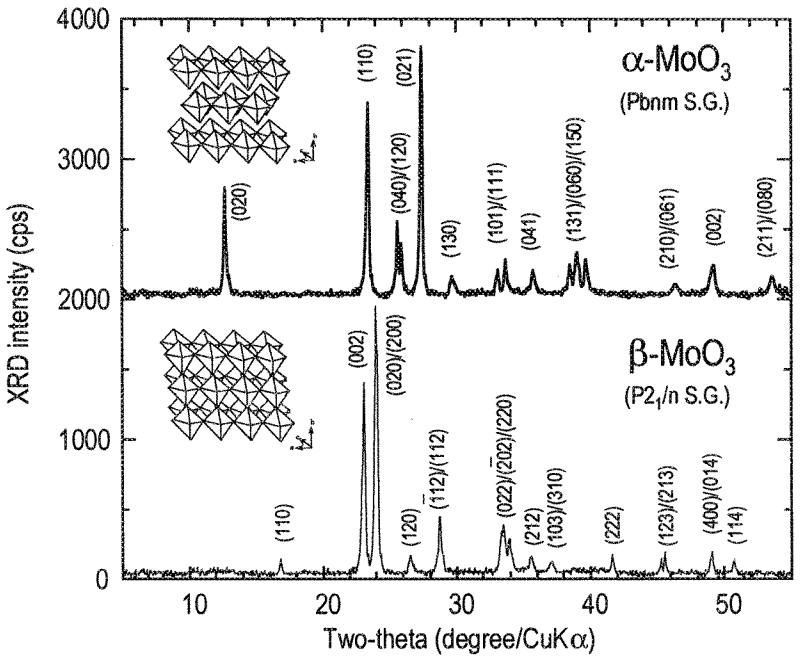

Figure 1. XRD patterns of α-MoO_3 and β-MoO_3 crystals.

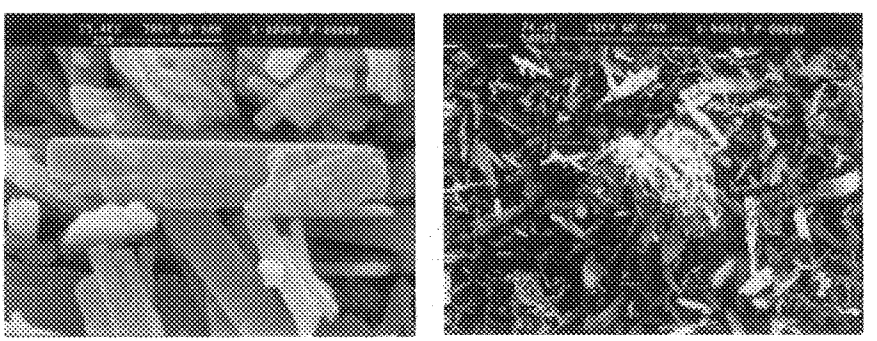

(a) (b)

Figure 2. SEM images of α-MoO_3 (a) and β-MoO_3 (b) crystalline powders.

Fig. 3 shows the RS spectra of β-MoO_3 and α-MoO_3 crystalline samples. The spectral fingerprints of the two phases are clearly seen in their Raman features. The RS spectrum of α-MoO_3 can be analyzed using the orthorhombic D_{2h}^{16} symmetry. The spectrum is dominated by the internal modes involving

stretching and bending modes of Mo-O bonds in MoO_6 distorted octahedra. The multiplicity corresponds to the various Mo-O lengths varying from 0.167 to 0.233 nm for the α-MoO_3 structure. The highest Raman band at 994 cm^{-1} is due to the vibration of the shortest Mo=O bonds, the so-called *molybdyl* mode. The RS spectrum of β-MoO_3 suggests a close similarity with pattern observed for WO_3. With the absence of the molybdyl mode and the shift of the O-Mo_3 stretching vibration, the Mo-O stretching region of β-MoO_3 is dissimilar to that of α-MoO_3.

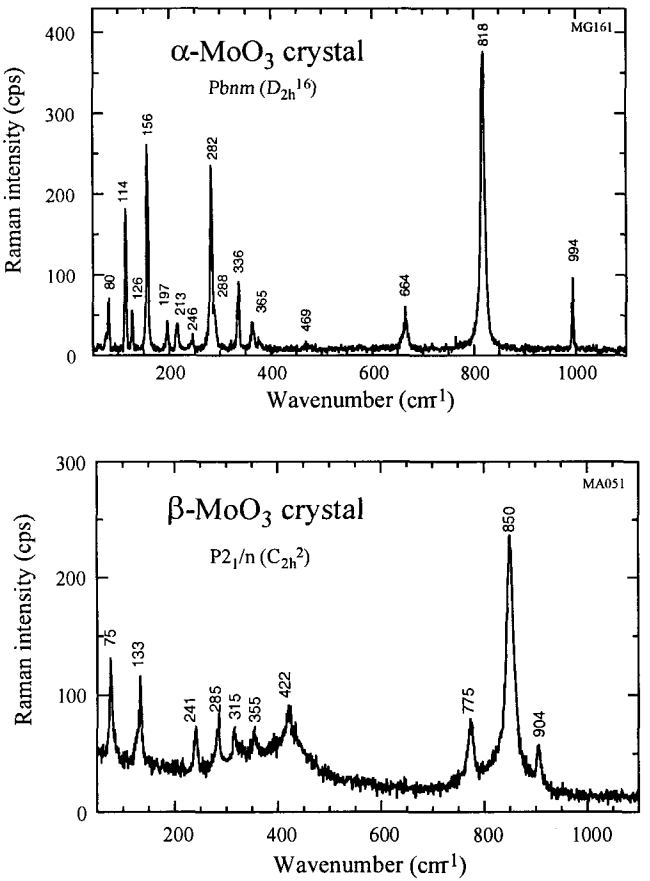

Figure 3. Raman scattering features of α-MoO_3 and β-MoO_3 crystals. Spectra were recorded at room temperature with the 514.5 nm laser line at excitation power density 10 kW/cm^2.

3.2. Electrochemical features

Fig. 4 shows the first discharge-charge curves of the Li//MoO_3 cells using the synthesized α-MoO_3 and β-MoO_3 materials as positive electrodes and non-

aqueous 1M $LiPF_6$ solution of EC-DEC (1:1) electrolyte. The cells were cycled at 0.1 mA/cm^2 that corresponds to a C/8 rate. An initial voltage of ca. 3.25 V was measured for both Li//MoO_3 cells. Anhydrous α-MoO_3 give a discharge capacity of 298 mAh/g corresponding to the faradaic yield 1.6 e$^-$/Mo in the potential range 3.5-1.0 V. This value is in fair agreement with previous data of 1.3-1.6 e$^-$/Mo.[4-7] The discharge-charge curve for the Li//β-MoO_3 cell displays electrochemical features different than the Li//α-MoO_3 cell. The first discharge reaction occurs at a lithium uptake x=1.9 leading to a specific capacity of 353 mAh/g. Comparing the discharge-charge profiles (Fig. 4), we remark different stepwise-discharge behaviours as follows.

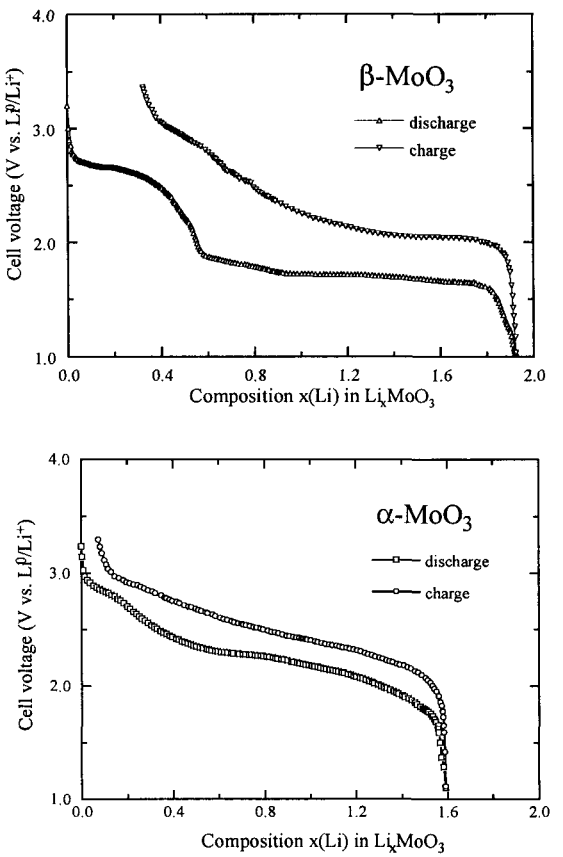

Figure 4. First discharge-charge curve of the Li//MoO_3 cells cycled at 0.1 mA/cm^2 including α- and β-phase electrode.

The cell potential for the Li//β-MoO_3 cell displays three distinct regions. A first plateau at 2.65 V is followed by a rapid decrease around x(Li)=0.4, i.e. a capacity of 75 mAh/g, to reach a large voltage plateau at 1.7 V. In the same

range of potential, the charge process occurs differently with the disappearance of the initial voltage plateau. The cell exhibits a capacity loss of 24% probably due to structural modification upon the lithium insertion-deinsertion process. The polarization during charge is observed to increase with an increasing cell number for β-MoO_3 materials.

The α-MoO_3 phase gives a discharge capacity slightly smaller (1.6 e^-/Mo) than that of β-MoO_3 but a much higher capacity retention (ca. 95%). The discharge curve exhibits a voltage plateau at 2.27 V centred at x=0.75, while the charge curve displays a monotonous increasing profile. Molybdenum trioxide was found to react readily with lithium forming two well-defined discharge products, according to the X-ray data, which are similar to the known high temperature Li_2MoO_3 phase.[14] The electrochemical lithium insertion into the MoO_3 framework can be described according the following reaction

$$xLi^+ + xe^- + [Mo^{VI}]O_3 \leftrightarrow Li_x[Mo^{(6-x)}]O_3, \qquad (1)$$

assuming the reduction from Mo(VI) to Mo(V) and Mo(IV) oxidation states.

Satisfactory charge-discharge efficiency and storage capability are other favourable features of the Li//α-MoO_3 cells. Upon lithiation of Li_xMoO_3, the electronic conductivity increases from 10^{-4} S/cm for x=0 to ca. 10^{-1} S/cm for $0.3 \leq x \leq 0.9$ to form a molybdenum bronze.[2] The chemical diffusion coefficients of Li^+ ions in Li_xMoO_3 obey an quadratic law against x(Li).[2] A maximum value of ca. 10^{-9} cm^2/s has been reported for $x \approx 0.6$. Li mobility was shown to slightly decrease upon subsequent discharge-charge cycles due to irreversible structural and morphological changes of the host matrix. However, when the cell was charged, the oxidation of Mo produces a resistive compound which induces a large polarization of the cell at the end of the charge process. This effect is highly beneficial for battery operation because the MoO_3 electrode works as a self-limiting current material.

To confirm the above suggestion, the structural changes occurring in the Li_xMoO_3 electrode materials during Li intercalation were followed by *in-situ* X-ray diffraction measurements using a specially designed electrochemical cell.[5] Fig. 5 shows the XRD patterns of the α-MoO_3 electrode during discharge. This result shows that, upon lithium insertion in the layered host matrix, the structural properties are preserved. From the shape and positions of the Bragg lines shown in Fig. 5, there is an indication that the framework structure of MoO_3 is almost unchanged during discharge reaction up to 1.5 Li/Mo. However, one can observe the formation of a ternary phase, i.e. appearance of Bragg peaks at ca. 2θ=47° for x>0.5 Li/Mo. The new Bragg peaks disappear upon delithiation, that indicates continuous structure reorganization and complete reversibility of the insertion-deinsertion process for anhydrous material in the potential range 3.5-1.2 V. The crystalline structure appears with well-developed MoO_6 octahedra. This configuration prevents repulsive forces between inserted ions which could be the origin of the strong stepped voltage in β-MoO_3. After an intercalation/deintercalation cycle the original host lattice may be retained

practically unchanged because the structure of the host matrix is determined by strong covalent Mo-O bonds.

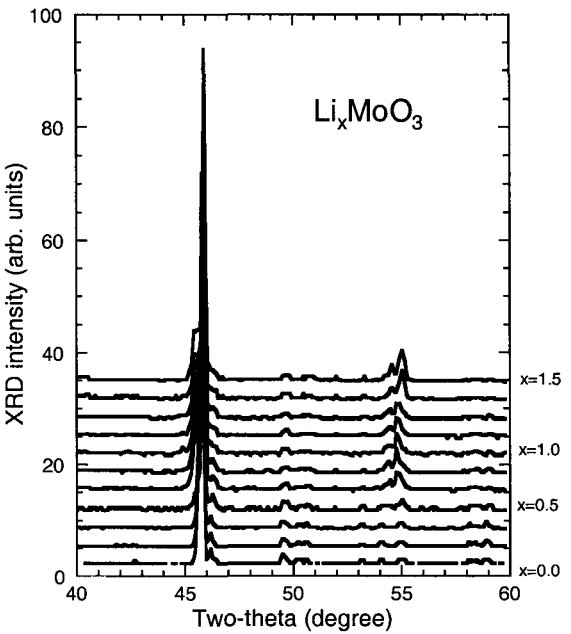

Figure 5. In-situ x-ray patterns of anhydrous Li_xMoO_3 as a function of the degree of lithium insertion during the first discharge.

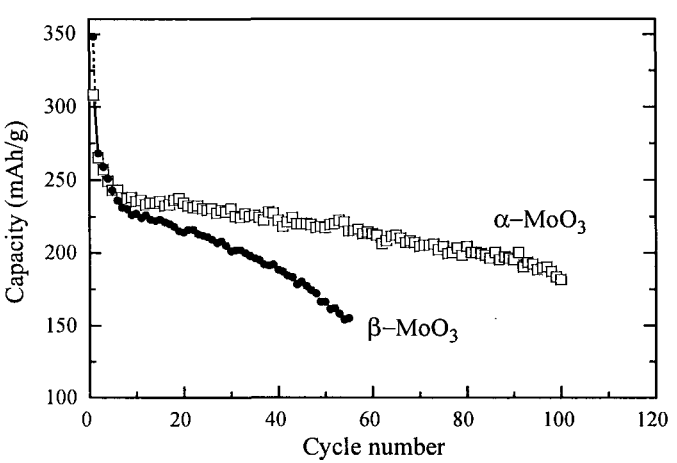

Figure 6. The long-term cycling behavior of the Li//MoO_3 cells.

Fig. 6 shows the long-term cycling behavior of the Li//MoO_3 cells. The variation in the storage-charge capacity of Li//MoO_3 cell as a function of cycle number of such cells when cycled between 3.2 and 1.2 V under a current density of 0.1 mA/cm^2. The Li//α-MoO_3-type cell was charged and discharged more than 100 times and up to the 100th cycle the decrease of the specific capacity is 180 mAh/g. The Li//α-MoO_3 cell exhibits a larger decrease in capacity retention. After 55 cycles, this cell delivered only 148 mAh/g. The cycling behavior can be modeled using the relation giving the capacity as a function of the cycle number

$$C = C_0(1-\delta)^n \qquad (2)$$

where C_0 is the initial capacity, n the cycle number and δ the fraction loss per cycle. For the Li//α-MoO_3 cell, we obtain δ=0.1%.

3.3. Kinetics of Li ions

Kinetics of Li^+-ions insertion in Li_xMoO_3 have been studied in the composition $0<x<1.6$. Fig. 7 displays the chemical diffusion coefficients of Li^+ ions in the Li_xMoO_3 host materials. The compositional dependence of D^* in MoO_3 is rather a quadratic function which is due to the nature of the empty sites in the host structure. The behavior of the curves can be modeled using the relation

$$D^* = W D_0 = x\beta(1-x), \qquad (3)$$

where D_0 is the component diffusion, W is the thermodynamic factor and β is an interaction parameter related to the repulsive interaction energy between alkali ions.[15]

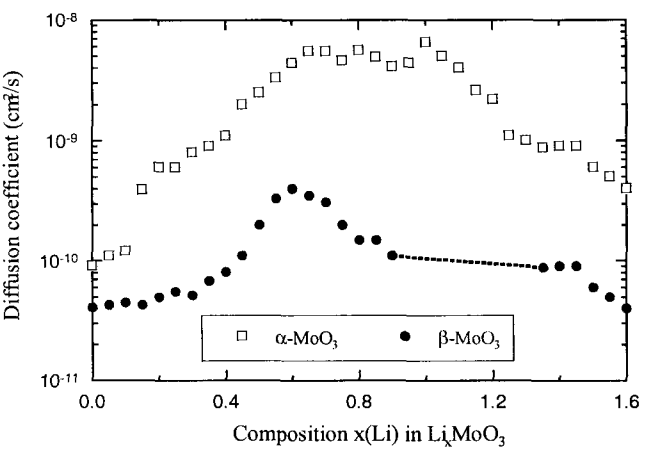

Figure 7. The chemical diffusion coefficients of Li^+ ions in the Li_xMoO_3 host materials.

The maximum of D^* ($D^*=4\times10^{-9}$ cm^2/s in the anhydrous α-MoO_3 phase corresponds with the half-filling site number. The chemical diffusion coefficients of Li^+ in the β-MoO_3 powders exhibit different features: (i) values are smaller by one order of magnitude than for α-MoO_3, and (ii) D^* remains almost constant in the range $0.9<x<1.6$. This behavior may be attributed to a blocking effect for the Li^+ diffusion. Thus, the ideal lattice gas model can be applied in which the ion-ion interaction energy is negligible. The compositional dependence of the thermodynamic factor in molybdenum oxides shows a variation from 3 to 300 in the range $0<x<1.5$, indicating a strong electronic contribution on the insertion reaction in MoO_3 at high values of x.

4. Conclusion

This work has shown a comparison between the structural and electrochemical properties of two molybdenum trioxides, the anhydrous α- and β-phases. The electrochemical properties of these molybdenum oxides are strongly related with their structural characteristics. Thermodynamics and kinetics of lithium-ion insertion appears to be a function of the structural arrangement of MoO_6 octahedra in the host lattice. Diffusion coefficient can be modelled using either a simple model for site occupancy or an ideal lattice gas model.

References

1. P. G. Dickens and M. F. Pye, in *Intercalation Chemistry*, ed. by M. S. Whittingham and A. J. Jacobson, Academic Press, Inc, New York, 1982, p. 539.
2. C. Julien and G. A. Nazri, *Solid State Ionics* **68**, 111 (1994).
3. C. Julien, A. Kelfa, J.-P. Guesdon, A. Gorenstein, *Appl. Phys. A* **59**, 173 (1994).
4. B. Yebka, C. Julien, G. A. Nazri, *Mater. Res. Soc. Symp. Proc.* **548**, 229 (1999).
5. C. Julien and B. Yebka, *NATO ASI Series* **3-85**, 263 (2000).
6. N. Kumagai and K. Tanno, *Electrochim. Acta* **32**, 1521 (1987).
7. N. Kumagai and K. Tanno, *J. Appl. Electrochem.* **18**, 857 (1988).
8. A. Martinez-de-la Cruz and I. Juarez-Ramirez, *J. Power Sources* **133**, 268 (2004).
9. C. Guzman, B. Yebka, J. Livage, and C. Julien, *Solid State Ionics* **86-88**, 407 (1996).
10. G.-A. Nazri and C. Julien, *Ionics* **2**, 1 (1996).
11. E.M. McCarron III, J. Chem. Soc. Commun. 336 (1986).
12. W. Weppner and R.A. Huggins, *J. Electrochem. Soc.* **124**, 1569 (1977).
13. J.B. Parise, E.M. McCarron III, W. Sleight, *Mater. Res. Bull.* **22**, 803 (1987).
14. J.M. Reau, C. Fouassier, C. Gleitzer, *Bull. Soc. Chim. Fr.* 4294 (1967).
15. B. Yebka, C. Julien, *Solid State Ionics* **90**, 141 (1996).

PREPARATION OF ZIRCON ($ZrSiO_4$) CERAMICS VIA SOLID STATE SINTERING OF ZrO_2 AND SiO_2 AND THE EFFECT OF DOPANTS ON THE ZIRCON YIELD

U. DAHANAYAKE AND B.S.B. KARUNARATNE
Department of Physics, University of Peradeniya, Peradeniya, Sri Lanka.
Email: udahanayake@yahoo.com, bsbk@pdn.ac.lk

The feasibility of the preparation of doped zircon ($ZrSiO_4$ or $ZrO_2.SiO_2$) via solid state sintering of precursor oxides (ZrO_2 and SiO_2) and the dopants has been investigated. In this study, Y_2O_3, Yb_2O_3, Fe_2O_3, CaO, MgO, Li_2CO_3 and Na_2CO_3 were used as dopants with a concentration level of 10 mol %. The sintered pellets were subjected to X-Ray Diffraction (XRD) analysis and the zircon yield was calculated using the XRD data. It was revealed that the zircon yield in the dopant oxide added samples was very high (57-100% depending on the dopant) and the ionic radius difference between the host Zr^{4+} and the dopant cation has a direct implication with the zircon yield. Although it could be observed that the addition of trivalent or divalent cations enhanced the zircon yield, addition of monovalent cations completely hindered the zircon formation.

1. Introduction

Zircon ($ZrSiO_4$) is well known for its low thermal expansion coefficient and low thermal conductivity.[1] Important commercial deposits of mineral zircon are mined in Australia, South Africa, USA, India and Sri Lanka, the greatest portion of which is used directly in the manufacture of refractories. Minerals always contain impurities in different concentration levels and hence the properties of mineral zircon may be quite different from those of pure zircon. Since our main research interest is the electrical characterization of doped zircon ceramics prepared using mineral zircon as the starting material, it was intended to prepare high-purity zircon in the laboratory for a comparative study. The preparation of high-purity zircon powders is generally accomplished via sol-gel and hydrothermal methods using suitable precursors. However, the preparation of zircon via solid state sintering of precursor oxides (ZrO_2 and SiO_2) is not commonly reported in literature. The results of a preliminary study on preparation of doped zircon via solid state sintering of precursor oxides and the dopants (Y_2O_3, Yb_2O_3, Fe_2O_3, CaO, MgO, Li_2CO_3 and Na_2CO_3 with a concentration level of 10 mol %) are reported in this paper, along with the probable crystallographic explanation for the formation of zircon.

2. Experimental

ZrO_2, SiO_2 (Johnson Matthey / Purity 99.9 % / 325 mesh), Y_2O_3, Yb_2O_3, Fe_2O_3 (Aldrich / purity 99.99), CaO, MgO (Johnson Matthey / Purity Grade 1) and Li_2CO_3, Na_2CO_3 (BDH AnalaR) were used as starting materials. The required amount of dopant was weighed and added to the equimolar mixture of ZrO_2 and SiO_2, such that it would give the composition of 10 mol% doped zircon upon addition. An equimolar mixture of ZrO_2 and SiO_2 (without any dopants) was also prepared for comparison. Each powder batch was wet ball milled for 72 hours using water as the milling fluid and Al_2O_3 pebbles as the milling media. The ball milled powders were calcined for 3 hours at different temperatures depending on the dopant used in order to promote the decomposition of carbonates (deliberately added or present as impurities) to oxides and to accomplish the removal of residual water (if present) from the powders. The powders devoid of deliberately added carbonates were calcined at 700 °C. Since the dissociation temperature of Na_2CO_3 is 850 °C, the powders with deliberately added Na_2CO_3 were calcined at 900 °C whereas those with Li_2CO_3 were calcined at 1350 °C in view of the fact that the dissociation temperature of Li_2CO_3 is as high as1310 °C. Then the powders were uniaxially pressed in a stainless steel die under a pressure of 225 MPa. The green pellets prepared from the equimolar mixture of ZrO_2 and SiO_2 (without any dopants) were sintered at three different temperatures (1500, 1600 and 1676 °C) for 5 hours using a Carbolite (HTF 18/3) high temperature furnace in order to see the optimum sintering temperature at which it would give the maximum zircon yield. The optimum temperature was found to be 1600 °C and hence the doped samples were sintered at that temperature for 5 hours. The sintered samples were then subjected to XRD analysis using a Philips X-Ray spectrometer with Cu K_α radiation.

3. Results and Discussion

Zircon synthesis, via sintering of precursor oxides ZrO_2 and SiO_2, is difficult in the absence of a reaction promoter such as an alkali halide or a transition metal.[2] The difficulty of sintering can easily be explained by the crystallographic consideration, as illustrated in figure 1. For the combination reaction between ZrO_2 and SiO_2 to take place, i.e. for the complete formation of $ZrSiO_4$, both the movement of Zr^{4+} in the direction of big arrows ($\Rightarrow$) and the formation of the island-like lattice of SiO_4 tetrahedra by the insertion of SiO_2 component, straining the anions in the ZrO_2 structure in the direction of the little arrows ($\rightharpoonup$), should be permitted (figure 1). This crystallographic consideration supports the fact that the activation energy for the combination reaction between ZrO_2 and SiO_2 is kinetically very high, so the

combination reaction is permitted only at higher temperatures. However, the temperature should be essentially below 1676 °C, which is the dissociation temperature of $ZrSiO_4$.

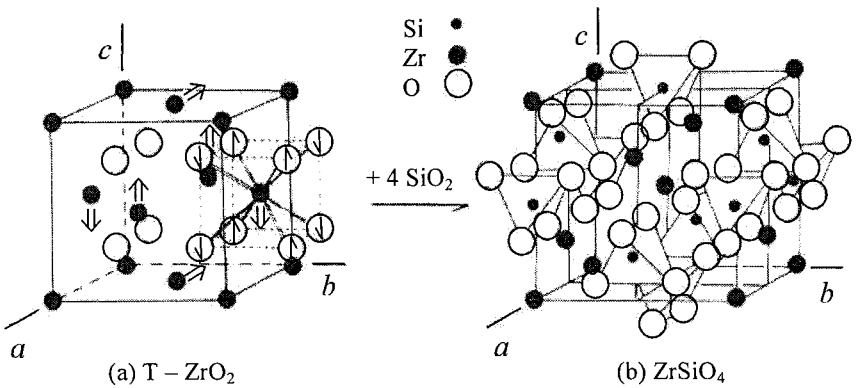

Figure 1. The crystallographic representation of the combination reaction between ZrO_2 and SiO_2 (a) Tetragonal - ZrO_2 (b) $ZrSiO_4$. [2]

The recombination of dissociated ZrO_2 and SiO_2 has been investigated by some researchers [3, 4] and reported that the surface structure of dissociated ZrO_2 and SiO_2 is slightly distorted and the recombination is rapidly accelerated above 1450 °C. This rapid recombination of dissociated ZrO_2 and SiO_2 indicates that the zircon synthesis may be readily performed, if the surface structure of these two precursor oxides is slightly distorted.[4] Also the formation of $ZrSiO_4$ via sintering of ball milled ZrO_2 and SiO_2 powders has been studied by few researchers and the effects of slurry verses dry milling, sintering time and particle size on zircon yield have been examined.[5] There it has been found that a very high zircon yield could be obtained via slurry milling, cold pressing and sintering of the precursor oxides. Also it has been reported that a kind of disturbed lattice structure may be obtained through prolonged slurry milling by mechanochemical activation of the surface layer of these precursor oxides.[5] In conformity with those findings, the oxide powders were subjected to wet ball milling in the present work (as described in the experimental section) prior to the compaction. Figure 2 shows the XRD spectra of the samples sintered for 5 hours at three different temperatures (1500, 1600 and 1676 °C). The zircon yield, α_{Zr}, in the resulting samples was calculated using the following equation.[6, 7]

$$\alpha_{Zr} = \frac{I_{Zr(200)}}{I_{Zr(200)} + I_{m(11\bar{1})} + I_{m(11\bar{1})} + I_{t(11\bar{1})}} \quad (1)$$

Here, I is the peak intensity of XRD and the numbers in parentheses are the plane indices. Subscripts Zr, m and t stand for $ZrSiO_4$, monoclinic-ZrO_2 and tetragonal-ZrO_2, respectively.

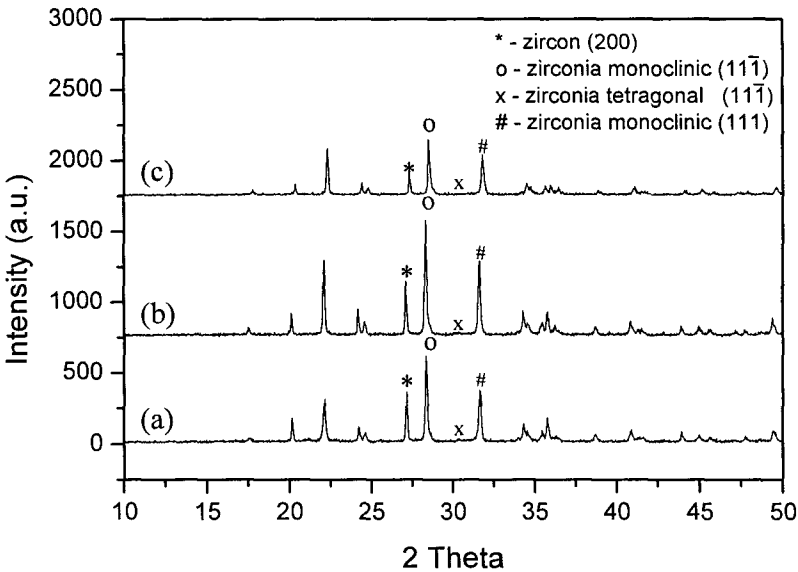

Figure 2. The XRD spectra of the samples (ZrO_2+SiO_2) without any dopants sintered at (a) 1500 °C (b) 1600 °C and (c) 1676 °C for 5 hours.

The zircon yield for different sintering temperatures, calculated using eq. (1), is given in the table 1. Although the zircon yield was quite low even at the highest sintering temperature tested, the formation of zircon was evident in all the three samples. It could be observed that the zircon yield in the sample sintered at 1600 °C (25 %) was higher that that in the sample sintered at 1500 °C (23 %) most probably due to the increase in the sintering temperature. However, the zircon yield in the sample sintered at 1676 °C (17 %) was lower than those in the 1500 and 1600 °C sintered samples since partial dissociation of zircon may take place at 1676 °C (which is the dissociation temperature of zircon).

Table 1. The zircon yield in the samples (ZrO_2+ SiO_2) sintered at different temperatures for 5 hours.

Sintering temperature (°C)	Zircon yield (%)
1500	~23
1600	~25
1676	~17

It has been found that the particle size of ZrO_2 and SiO_2 powders should be very fine, typically in the range of 0.5-1 μm, in order to get a higher zircon yield in the sintering process of these precursor oxides.[5] Therefore the most likely reason for the observed low zircon yield in the present work may be the coarser particle size of the starting powders (325 mesh –45 μm). Prolonged ball milling would be necessary in order to reduce the particle size down to 0.5-1 μm, which is time consuming and disadvantageous in a practical point of view.

Figure 3 shows the XRD spectra of zircon samples with dopant oxides sintered at 1600 °C for 5 hours. It is readily noticeable that the zircon yield in all these five samples is higher than that in the sample without any dopants sintered at 1600 °C for 5 hours. Table 2 gives a comparison between the zircon yield in the dopant oxides added samples and that in the sample without any dopants, calculated using the eq. (1).

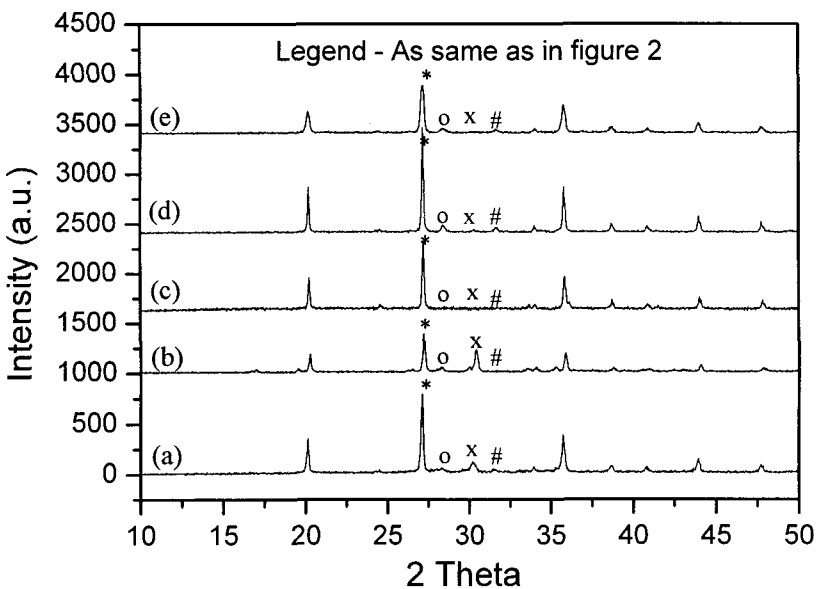

Figure 3. The XRD spectra of the samples (ZrO_2+SiO_2+ 10 mol % dopant oxide) sintered at 1600 °C for 5 hours (a) Y_2O_3 (b) Yb_2O_3 (c) Fe_2O_3 (d) CaO and (e) MgO.

Table 2. The comparison between the zircon yield in the dopant oxides added samples and that in the samples without any dopants sintered at 1600 °C for 5 hours.

Sample	Zircon yield (%)
10 mol% Y_2O_3 doped zircon	~76
10 mol% Yb_2O_3 doped zircon	~57
10 mol% Fe_2O_3 doped zircon	~100
10 mol% CaO doped zircon	~85
10 mol% MgO doped zircon	~79
Without any dopants	~25

A new processing technique to synthesize zircon, which has a higher yield at a relatively low temperature, using $ZrOCl_2$ as the ZrO_2 source and $Si(OC_2H_5)_4$ as the SiO_2 source, together with some amount of Y_2O_3, has been reported elsewhere[8] and found that at a given temperature, the formation rate of zircon in Y_2O_3 added system was very high (more than 70%), whereas that in system without Y_2O_3 was very low (less than 7%). It has been speculated there that the incorporation of Y^{3+} into ZrO_2 resulting in a disturbed ZrO_2 lattice structure was accounted for the high formation rate of zircon in the Y_2O_3 added system. In particular, a disturbed lattice structure of ZrO_2 is more desirable in the reaction between ZrO_2 and SiO_2, because it is known that SiO_2 migrates in to ZrO_2, not vice versa.[9] Hence, in the present work, the most likely reason for the higher zircon yield in dopant oxide added samples is the formation of a kind of distorted lattice structure of ZrO_2 upon the incorporation of these dopant cations in the ZrO_2 host structure. As far as the trivalent dopant oxides are concerned, the zircon yield in 10 mol% Y_2O_3 doped zircon and that in 10 mol% Fe_2O_3 doped zircon were found to be higher than the zircon yield in 10 mol% Yb_2O_3 doped zircon (table 2) indicating that the level of distortion in the ZrO_2 structure when Yb^{3+} is incorporated might be less than those when Y^{3+} or Fe^{3+} is incorporated. In the case of divalent dopant oxides, the zircon yield in 10 mol % CaO doped zircon was superior to that in 10 mol % MgO doped zircon.

One should pay attention on the difference between the ionic radius of the host ion and that of the substituting ion, as far as the degree of distortion of a lattice structure obtained by substitution of foreign atoms is concerned. A significant difference between the ionic radii of these two ions would give rise to a higher level of distortion in the lattice structure, whereas almost equal ionic radii of these ions would give rise to a lower level of distortion. Therefore, the level of distortion in the ZrO_2 structure when Yb^{3+} is incorporated should clearly be lower than those when Y^{3+} or Fe^{3+} is incorporated because the ionic radius of Zr^{4+} (0.980 Å) is closer to that of Yb^{3+} (1.120 Å) than those of Y^{3+} (1.155 Å) and Fe^{3+} (0.640 Å). Similarly, in

the case of Ca^{2+} (1.260 Å), having an outlying ionic radius may give rise to a higher distortion level in the ZrO_2 structure than Mg^{2+} (1.030 Å) upon doping. Please note that all the ionic radii considered herein are eight-coordinated since Zr^{4+} is known to be eight-coordinated in the ZrO_2 structure.

Although it could be observed that the addition of trivalent or divalent cations enhanced the zircon yield, addition of monovalent cations completely hindered the zircon formation. The XRD spectra of 10 mol% Li_2CO_3 doped zircon and 10 mol% Na_2CO_3 doped zircon are shown in figure 4 and it can be observed that the peak corresponding to zircon (200) is absent in both the spectra resulting in zero zircon yield according to the eq. (1).

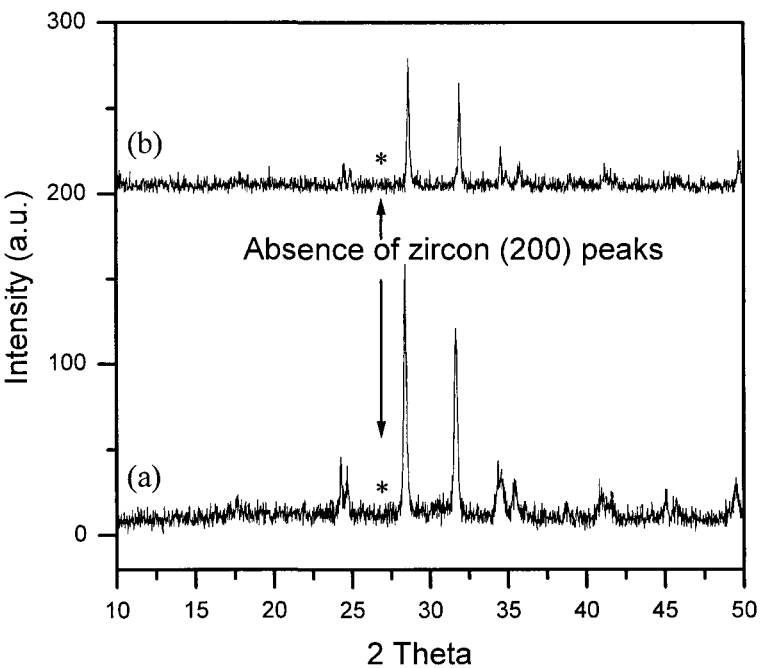

Figure 4. The XRD spectra of the samples (ZrO_2+SiO_2+ 10 mol % dopant carbonate) sintered at 1600 °C for 5 hours (a) Li_2CO_3 and (b) Na_2CO_3

4. Conclusions

In the samples prepared from the equimolar mixture of ZrO_2 and SiO_2 (without any dopants) the zircon yield was quite low with the highest being 25% when the samples were sintered at 1600 °C for 5 hours. The zircon yield in the sample sintered at 1500 °C for 5 hours and that in the sample sintered at 1676 °C for 5 hours were 23% and 17% respectively. The observed low zircon yield in these samples indicates that the wet ball milling (with the ball milling parameters used in the present work) has not mechanochemically activated the surface layer of these precursor oxide powders. It was also speculated that the coarser particle size of the starting precursor oxide powders would result in low zircon yield in the samples. However, it was revealed that the zircon yield in the dopant oxides added samples was very high (57-100% depending on the dopant) most probably due to the distortion of the surface layer of ZrO_2 powders upon the substitution of doping cations in the place of Zr^{4+} in the ZrO_2 structure. It was also revealed that the ionic radius difference between the host Zr^{4+} and the dopant ion has a direct implication with the zircon yield. Although it could be observed that the addition of trivalent or divalent cations enhanced the zircon yield, addition of monovalent cations completely hindered the zircon formation.

Acknowledgments

The financial assistance by the University of Peradeniya (grant numbers: PGIS/RG/2000/01 and PGIS/RG/2001/07) is greatly acknowledged.

References

1. E. C. Subbarao, D. K. Agrawal, H. A. McKinstry, C. W. Sallese and R. Roy, *J. Amer. Ceram. Soc.***73 (5)**, 1246 (1990).
2. Y. Kanno, *J. mater. Sc.* **24**, 2415 (1989).
3. H. B.Barlett, *J. Amer. Ceram. Soc.* **14**, 837 (1931).
4. V. H. Stott and A. Hilliard, *Trans. Brit. Ceram. Soc.* **48**, 133 (1949).
5. D. R. Spearing and J. Y. Huang, *J. Amer. Ceram. Soc.* **81(7)**, 1964 (1998).
6. T. Mori and H. Yamamura, *J. Amer. Ceram. Soc.* **75**, 2420 (1992).
7. Y. Shi, X. X. Huang and D. S. Yan, *J. Eur. Ceram. Soc.* **13**, 1113 (1994).
8. C. Du, Q. Yuan and Z. Yang, *J. Mat. Sci. letters.* **18**, 965 (1999).
9. R. A. Eppler, *J. Amer. Ceram. Soc. Bull.* **56**, 213 (1977).

PREPARATION AND PROPERTIES OF VANADIUM DOPED ZnTe CERMET THIN FILMS

M. S. HOSSAIN, R. ISLAM AND K. A. KHAN*

Department of Applied Physics and Electronics, University of Rajshahi, Rajshahi-6205, Bangladesh. Tel: +880 721 750254, Fax: +880 721 740064
**Email: kakhan_ru@yahoo.ca*

The planar specimen of ZnTe:V cermet films as well as ZnTe films were prepared onto glass substrate by e-beam evaporation of the element in vacuum at ~10^{-6} torr. The effects of various deposition conditions on the electrical properties of the cermet devices have been studied in detail. It is found that ambient pressure, source to substrate distance and beam current play important role in obtaining films. The deposition rate of the films was maintained at about 2.05 nms^{-1}. The current-voltage characteristics of vacuum deposited ZnTe:V cermet thin films were studied under the high electric field (>10^6 Vm^{-1}) as a function of film thickness ranging 100 to 200 nm and containing 0 to 10% V in ZnTe matrix at temperature ranging 300 to 413 K. The composition and thickness dependence of the activation energy as well as thermoelectric power measurements were done in the 300 to 413 K temperature ranges. The results of dc conductivity and thermoelectric power obey an activated conduction mechanism. Thermo power result also suggests that the simultaneous bipolar conduction of both carriers take place.

1. Introduction

In recent years, the II-VI family of compound semiconductors, in particular Zinc Telluride (ZnTe) has been the focus of great interest due its low cost and high absorption co-efficient for application to photovoltaic and photo electrochemical cells[1,2,3,4]. ZnTe has a direct band gap of 2.2 to 2.3 eV at room temperature and usually a p-type semiconductor. Literature[5] reports indicate that ZnTe exhibits improved photorefractive response when it is doped with vanadium. Vanadium is believed to be a deep donor in ZnTe and it has attractive use in a variety of applications, including optical power limiting, optical computing and optical communication[6]. Moreover, ZnTe:V offers superior photorefractive performances for the application of optical data processing and power combining in operation of 800-900 nm band region compared with the large band gap semiconductor (such as GaAs as CdTe) where their energy band gap limit their use below ~900 nm.

Although there have been a number of investigations on the electrical[7,8], optical[9,10] and electro optical properties of ZnTe[7,9,11] and ZnTe:V[5,6] films by a number of researchers, no systematic study appears to have been done on the electrical and optical properties, in particular on vanadium doped ZnTe films at varying deposition conditions. Hence, there is a need to study how varying deposition conditions affect the physical properties of doped ZnTe film to assesses its usefulness in a variety of photosensitive operation in optoelectronic devices including optical data processing and computing. In this paper, we present and

discussed the preparation of ZnTe as well as vanadium doped ZnTe films and the effects of different variables on the physical properties of the films.

2. Experimental

2.1. *Cermet Thin Film Preparation*

Cermet sandwich structures containing a mixture of ZnTe powder (99.999% pure) and vanadium powder (99.999% pure), obtained from Aldrich Chemical Company, USA, were deposited by electron bombardment heating technique in vacuum (Coating Unit; Edwards, Model: E306) at a pressure of 6×10^{-6} torr. The ZnTe:V cermet films were deposited at a rate of 2.05 nms^{-1} to a thickness of 100 to 250 nm, respectively containing 0 to 10 wt% V. Each material was weighted by an electrical balance (Mettler TOLEDO, AB 204) having a resolution of $\pm$ 0.0001 gm, according to percentage composition to be used. The percentage composition of starting materials in the evaporant mixture, was determined as[12]

$$\text{Weight\%V} = \frac{W_V}{W_V + W_{ZnTe}} \times 100\% \quad (1)$$

where, W_V and W_{ZnTe} are the weights V and ZnTe, respectively. Then the materials were grinded together using a pestle and mortar and thoroughly mixed. The lower Al (Aluminium) electrode and upper Al or Cu (Copper) electrodes were evaporated during the same pump down cycle. The films were deposited onto glass substrate at room temperature. The three masks (one for ZnTe:V films and others two for electrode) were used for the deposition of sandwich devices. The substrate holder was about 0.09 m above the source. A mechanical shutter was operated from outside, isolated the substrates from the evaporants.

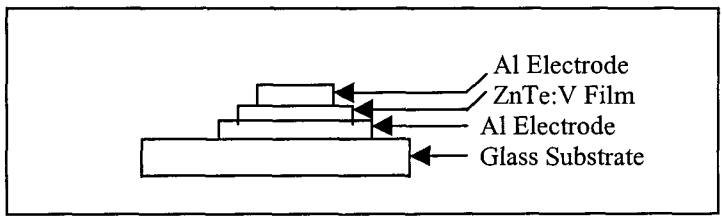

Figure 1. Schematic diagram of sandwich unformed film structure of Al/ZnTe:V/Al cermet device.

The deposition chamber was thoroughly cleaned with emery paper and cotton-wool by wetting acetone and was then dried with a dryer. A small quantity of source materials was loaded into clean cermet-hearth based on the source turret. Cleaned substrates were placed on the substrate-holder and the chamber bell jar was placed on the base plate. When the chamber pressure reduced ~10^{-6} torr, deposition was

then started with beam current of 40-50 mA by turning on the low tension control switch. The preparation of Al/ZnTe:V/Al sandwich cermet thin films, which were deposited onto the glass substrate at room temperature for measuring I-V characteristics of various conditions and its schematic diagram is shown in Figure 1.

2.2. *Measurement Technique*

I-V characteristics of sandwich structure Al/ZnTe:V/Al cermet thin films were measured as a function of temperature in the 300-413 ranges. The glass substrate was heated by a specially designed heater and the temperature was measured by a chromel-alumel thermocouple placed on the middle of the substrate. A d.c. power supply (Heathkit, Model: IP-2717A) was used to pass a constant d.c. current through the test sample. An electrometer (Keithley, Model: 614) monitored the current through the sample and a digital multimeter (Model: DM-206) was used to measure the potential differences across each sample. Digital multimeter (Model: DL-711) was also used to measure the current. The thickness was measured by the Tolansky[13] interference method with an accuracy of $\pm$ 5 nm.

3. Results and Discussion

It is well known that Metal/Insulator/Metal (MIM) sandwich structure can under go a forming process under certain conditions, during which the electrical conductivity of the sample increases, by several orders of magnitude[14]. The forming process depends on the ambient pressure, temperature, electric field, cermet thickness and electrode materials. Since the deposition variables as well as the effects of temperature play important role on conductivity, authors studied their effects in detail.

3.1. *Effects of Ambient Pressure*

The effect of ambient pressure on I-V characteristics of sandwich device Al/ZnTe:V/Al at composition 2.5wt% V, of cermet film thickness 150 nm is shown in Figure 2. It is evident from the graphs that with the decrease of ambient pressure, the device conductivity is found to increase in all investigated cermet devices. The main feature of the conduction mechanisms is that it exhibits non-ohmic behaviour in the high field region ($5x10^6$ to 10^8 Vm^{-1}).

3.2. *Effect of Source to Substrate Distance*

Three sets of each 150 nm thick Al/ZnTe:V/Al cermet structure with composition of 2.5wt% V, were deposited at a variable source to substrate distance of 0.08, 0.09 and 0.10 m, respectively. The d.c. I-V characteristics of their study indicates that

structure grown at source to substrate distance of 0.09 m, offers the highest conduction.

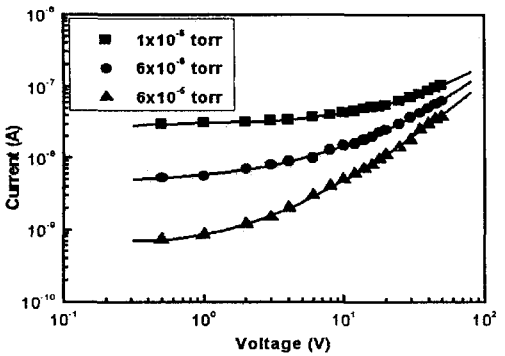

Figure 2. I-V curves of a 150 nm Al/ZnTe:V/Al cermet film deposited at 2.5wt% V.

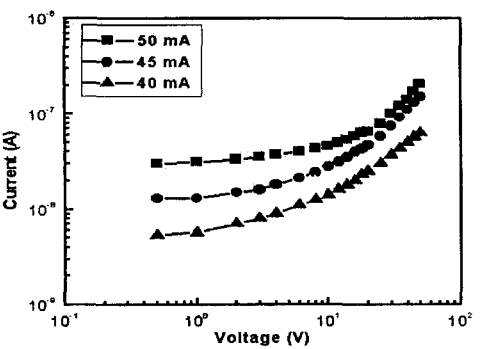

Figure 3. I-V curves of different beam current for a 150 nm sandwich devices grown at 2.5wt% V.

3.3. *Effect of Beam Current*

The role of beam current in cermet devices has been studied in details. The dependency of beam current on the I-V characteristics of a 150 nm thick Al/ZnTe:V/Al cermet structure, grown at a composition of 2.5wt% V, at a pressure of 6×10^{-6} torr, were studied at beam current of 40, 45 and 50 mA, respectively and their results are shown in Figure 3. It indicates from the graphs that the conduction

mechanism increases with the increasing of beam current. The cause of the increase is due to the increasing of particle compactness and of the increase of the metal islands of the deposited structure.

3.4. *Effect of Composition*

Cermet sandwich structure contain a mixture of vanadium powder in Zinc Telluride matrix is very important. To study the effect of composition four samples each of 200 nm thick Al/ZnTe:V/Al cermet films were deposited at a composition of 0 to 10wt% V, respectively at a pressure of 6×10^{-6} torr and their I-V characteristics are shown in Figure 4. The curves show that as the metal concentration increases, the higher the current flowing through the devices. The effects may be due to the case with which metallic filaments are formed in samples of higher vanadium content.

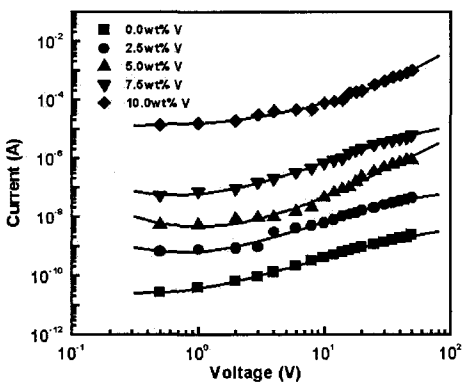

Figure 4. I-V curves for a 200 nm thick Al/ZnTe:V/Al devices deposited at variable compositions.

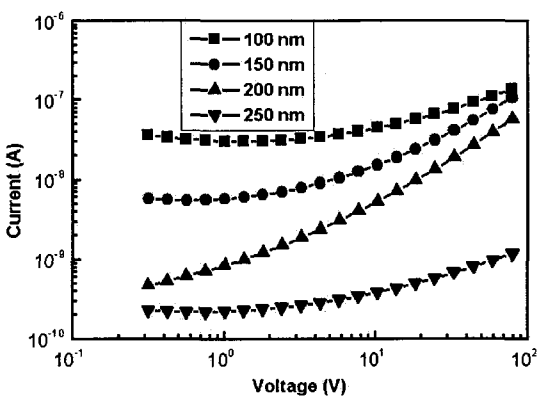

Figure 5. I-V curves of ZnTe:V films deposited at 2.5wt% V at variable thickness.

3.5. *Effect of Thickness*

To study the thickness effect of I-V characteristics of a Al/ZnTe:V/Al sandwich devices of thickness of 100, 150, 200 and 250 nm, respectively deposited at a fixed composition 2.5wt% V are shown in Figure 5. It is evident from the graphs that as the thickness decreases the conduction mechanism increases in all the devices. This is due to the effects of increasing metallic filamentary path as its thickness decreases.

3.6. *D.C. Conductivity Activation Energy*

The composition and thickness dependence of the activation energy could be investigated over the range of temperature studied. The conductivity, which is related to the electron transport process in the material, can be expressed by Criado et. al.[15] the following relation of Eq. (2),

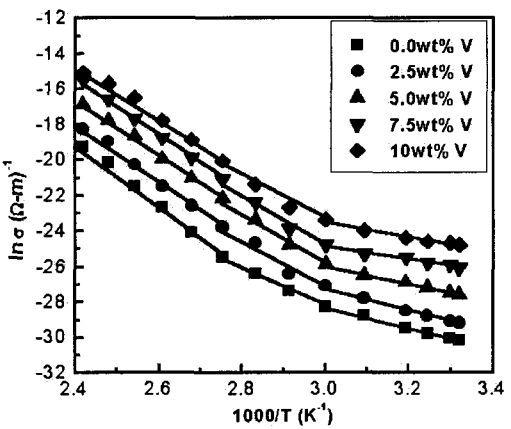

Figure 6. Variation of lnσ vs. T^{-1} for five compositions of ZnTe: V of 200 nm thick at fixed bias 15 V.

$$\sigma_{dc} = \sigma_0 \exp\left(\frac{-\Delta E_\sigma}{k_B T}\right) \tag{2}$$

where, σ_{dc} is electrical d.c. conductivity, σ_0 is constant, ΔE_σ is activation energy, k_B is Boltzman constant and T is the absolute temperature. Figure 6. shows the variation of conductivity with inverse temperature at fixed bias of 15 V d.c. for 200 nm thick ZnTe devices prepared at variable compositions. From the graphs, the activation energy for five compositions was calculated from the slope of the curves and their values were tabulated in Table 1. Similar calculation of activation energy with thickness of 100 and 150 nm, respectively were also done.

It may be seen from the Table 1 that there is no discrete value of E_σ which covers the whole temperature range but rather a spectrum of activation energies. It is seen from Table 1 that the value of activation energy depends on thickness, composition and temperature as well. It is also seen that at a particular thickness, the activation energy is decreased as the vanadium concentration increases in ZnTe matrix and at a fixed composition, activation energy increases with increasing of temperature in all spectrum of temperature range.

Table 1. Activation energies for D.C. conductivity of ZnTe:V cermet sandwich devices.

Thickness	Cremate Compositions	Activation energies, E_σ in (eV)		
		Temperature ranges in (K)		
nm	wt%	301-333	333-363	363-413
200	0.0	0.51432	0.96532847	1.03562471
	2.5	0.49539	0.87433364	1.00618704
	5.0	0.47069	0.85198858	0.99442047
	7.5	0.44451	0.74941631	0.85869414
	10.0	0.42176	0.62209124	0.74829619

3.7. *Thermoelectric Effect*

The thermoelectric power measurements were carried out on the planar thin films samples of various compositions 2.5 to 10 wt% V in the temperature range 303 to 403 K by using integral method. Seebeck voltage was measured with respect to a copper contact film by connecting the positive terminal of the electrometer to the cold opened end. From the study, the thermoelectric power varies with temperature for various compositions. All investigated samples show the mixed-carrier behaviour and bipolar in nature. This behaviour means the Fermi level may be formed midway between the conduction and valance band, as discussed by Mott[16].

4. Conclusions

Vanadium doped ZnTe cermet films of composition 0 to 10wt% V, were prepared onto glass substrate by e-beam evaporation technique. The effects of various deposition parameter such as ambient pressure, source to substrate distance, dopant composition and beam current have been studied in details and their effects play an important role in the conduction mechanism of the devices. The deposition rate of the cermet film was maintained at about 2.05 nms^{-1}. The composition and thickness dependence of the activation energy as well as thermoelectric power measurements was done in the 300 to 413 K temperature ranges.

The results of d.c. conductivity and thermoelectric power obey an activated conduction mechanism. Thermo power result also suggests that the simultaneous bipolar conduction of both carriers take place.

Acknowledgements

One of the author's M. S. Hossain is indebted to Rajshahi University of Engineering & Technology, Bangladesh for providing the grants & study leave during this work.

References

1. A. Z. Nozik and R. Memming, *J. Phys. Chem.* ***100****, 13061 (1996).*
2. J. O. M. Bockris and K. Uosaki, *J. Electrochem. Soc.* ***124,*** *1348 (1997).*
3. K K. Mishra and K. Rajeshwar, *J. Electrochem. Soc.* ***273****, 169 (1978).*
4. D. Ham, K. K. Mishra and K. Rajeshwar, *J. Electrochem.Soc.* ***138****, 100 (1991).*
5. M. Ziari, W. H. Steier and P. M. Ranon, *Appl. Phys. Lett.* ***60****(9), 1052 (1992).*
6. J. Kreissl and K. Irmscher, *Phys. Rev.* ***B53****(4), 1917 (1996).*
7. H. Dong-Hun, C. Shin-Jung and P. Su-Moon, *J. Electrochem. Soc.* ***150****(5), C342 (2003).*
8. A. K. S. Aquili, Z. Ali and A. Maqsood, *Appl. Surf. Sci.* ***167****, 1 (2000).*
9. A. Mondal, S. Chaudhuri and A. K Pal, *Appl. Phys. A* ***43****, 81 (1987).*
10. H. Bellakhder, A. Outzourhit and E. L. Ameziane, *Thin Solid Films,* ***382****, 30 (2001).*
11. R. L. Gunshor, L. A. Koladziejski, N. Otsuka and S. Datta, *Surf. Sci.* ***174****, 522 (1986).*
12. A. S. Khan, *PhD Thesis, Rajshahi University, (1999).*
13. S. Tolansky, *Multiple Beam Interferometry of Surfaces and Films, Oxford University Press, (1948).*
14. R. R. Verderber, J. G. Simmons and B. Eales, *Phil. Mag.* ***16****, 1049 (1967).*
15. J. Criado, A. I. Gomez, E. Calleja and E. Munoz, *Appl. Phys. Lett.* ***52****, 660 (1988).*
16. N. F. Mott and E. A. Davis, *Electronic Processes in Non-Crystalline Materials, 2nd Edn. Clarendon Press, Oxford, UK, 47, 48, 235, 271 & 273 (1979).*

Dynamical Properties and Electronic Structure of Lithium-ion Conductor

M. Kobayashi[a1], Y. Maruyama[a], H. Ogawa[a], M. Kamimura[a],
S. Ono[b], Y. Seki[c], S. Kashida[c]
[a]Department of Physics, Niigata University, Niigata 950-2181, Japan
[b]Faculty of Engineering, Doshisha University, Kyoto 610-0321, Japan
[c]Department of Environmental Science, Niigata University,
Niigata 950-2181, Japan

Abstract A computer simulation by a molecular dynamics method is performed to study the properties of structure and Li ion diffusion in $La_{4/3-x}Li_{3x}\square_{2/3-2x}Ti_2O_6$ ($\square$=vacancy), which is the perovskite-type Li ion conductor. In the low Li concentration, Li ions conduct a two-dimensional motion, while Li ions diffuse a three-dimensional motion in the high Li ion concentration. The partial distribution function for Li-Ti and the diffusion paths of Li ions suggest that Li ions stay for a long time at off-site positions which are 2.7Å away from a body-centered Ti ion. The Li ion concentration dependence of σ is in approximate agreement with experiments. The energy band dispersion and the density of states are calculated using the linear-muffin-tin-orbital (LMTO) method. The energy contour map shows the stable position of Li ions is off centers of the vacant La sites.

1 Introduction

The superionic material $(LaLi)TiO_3$ has the highest lithium ionic conductivity up to now. Studies on solid state Li ion conductors are performed actively at this moment because of their useful application in solid state high energy rechargeable batteries, electrochromic devices and sensors. Solid state electrolytes have many advantages compared to liquid or polymer based electrolytes such as high electrochemical stability with favorable anodes and cathodes, no leakage, flexibility in cell design and possible high operational temperature [1, 2].

Recently, Zou and Inoue have measured the microstructure and Li ion conductivity of $La_{4/3-x}Li_{3x}Ti_2O_6$. They have referred recent researches of Li ion conductor
$La_{4/3-x}Li_{3x}\square_{2/3-2x}Ti_2O_6$ ($\square$=vacancy), which has Li ion conductivity as high as $10^{-3}(\Omega cm)^{-1}$ at room temperature [3, 4, 5].

[1]Corresponding author: michi@phys.sc.niigata-u.ac.jp

It was found that a solid Li ion conductor $Li_{0.34}La_{0.51(1)}TiO_{2.94(2)}$ shows high ionic conductivity more than $2 \times 10^{-5}(\Omega cm)^{-1}$ at room temperature [6]. The compound had a cubic perovskite structure with a lattice constant 3.871Å. Inaguma *et al.* anticipated that Li ions perform a two-dimensional conduction in the low concentration region of $x < 0.21$ and a three-dimensional conduction in the high concentration region [6]. Katsumata *et al.*[7] also tried MD simulations to the Li ion conductor $La_{0.6}Li_{0.2}TiO_3$. The first peak of the pair distribution function $g_{\text{Li-Ti}}(r)$ for Li-Ti was observed at $r = 2.7$Å, which is the distance between Ti ion and bottleneck. Their model potentials and results have been refered to organize our computer simulations. In 2005, Yashima *et al.* [8] have experimented a neutron powder diffraction study of $La_{0.62}Li_{0.16}TiO_3$. They have found that at 77K Li ions are located at 2c site on (002) La deficient layer, while at room temperature they are spread over a wide area and diffuse along the path of 2c-4f-2c or 2c-2d-2c on the (002) layer.

Ruiz *et al.* [9] measured the ionic conductivity of $La_{1.33-x}Li_{3x}Ti_2O_6$ for three kinds of concentration $x = 0.29, 0.21$ and 0.09. From Arrhenius plot, they got the activation energy $E_a = 0.48$eV for $x = 0.29$ and 0.09 and $E_a = 0.44$eV for $x = 0.21$. So they got a reverse V type concentration dependence in conductivity.

Recently we have investigated the structural and dynamical properties of the Li ion conductor $La_{4/3-x}Li_{3x}\square_{2/3-2x}Ti_2O_6$ using MD simulations [10]. The MD method provides us a microscopic picture of the diffusion process of Li ions in a system. The MD calculations are based on the assumption that Newton's equation of motion with a two-body central-force interaction can give a reasonable description of the motion of ions in the system. We now address the investigation of the electronic structure of Li ion conductors [11].

2 Crystal Structure of (LaLi)TiO_3

The schematic structure of $La_{4/3-x}Li_{3x}\square_{2/3-2x}Ti_2O_6$ is shown in Fig.1. The structure is constituted by A1-site, B-site and A2-site in repetition [12, 13]. A1-site is occupied by La ions and Li ions, while A2-site is occupied by La ions, Li ions and vacancies as shown in Fig.1. B-site is dominated by Ti ions and O ions.

It is known that the occupation ratio of each ion in each site is different by Li ion concentration. In A1-sites, La ion concentration decreases and Li ion concentration increases with increasing x. Almost all vacancies are present on A2-sites, not on A1-sites. In A2-sites, Li ion concentration increases and vacancies decrease with increasing x. La ion concentration on A1-site predominates that on A2-site. This disordered structure is closely connected with the

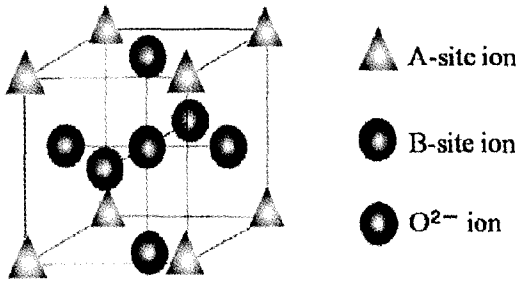

Figure 1: The upper A-site and the lower A-site are called A1-site and A2-site, respectively.

Li ion conductivity and the conduction path.

3 MD Calculations

Effective interionic potentials used here are composed of three interactions, Coulomb interaction, Born-Mayer repulsion and Van der Waals interaction. The values of parameters are prepared in order that the partial pair distribution functions and ionic conductivities may satisfy the calculated results by Katsumata *et al.* [7] and the experimental results by Inoue *et al.* [3, 4, 5]. Ref.[14] is also used to get ready for the model potential.

3.1 Pair Distribution Functions

In order to investigate the structure of (LaLi)TiO_3, we have calculated the partial pair distribution functions $g_{ij}(r)$ for all pairs of ions. From $g_{ij}(r)$ for La-La, Li-Li, Ti-Ti, and O-O in $x = 0.09$, we see that La ions and O ions form a nearly well defined fcc lattice. When Li ions are placed at proper corner sites of cube, namely on A1-site or A2-site, the ionic distance length of Li-Ti is about 3.35Å. However, after the simulation, the nearest neighbor distance of the first peak of $g(r)$ for Li-Ti is 2.7Å as shown in Fig.2. This means that Li ions are not at corner sites of each cube. This result has been already found by also Katsumata *et al.* [7]. At first, Li ions are set at the equivalent sites with those of La ions. When the system comes to a state of thermal equilibrium, Li ions situate at off-site positions as figured in Fig.3, not at cubic corners. Taking the off-site position of Li ions is congruent with a recent neutron diffraction study by Yashima *et al.* [8].

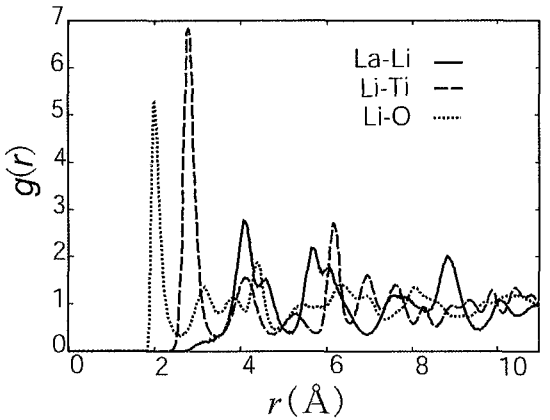

Figure 2: Partial pair distribution functions for Li-La, Li-Ti and Li-O in $x = 0.21$

3.2 Mean Square Displacement

The mean square displacements (MSDs) $< |\mathbf{r}(t)-\mathbf{r}(0)|^2 >$ for Li ions are shown in Fig.4 for the cases of $x = 0.29$. We see that the MSDs of all components increase with time and then Li ions in the case of $x = 0.29$ perform a three-dimensional diffusion. But for the case of $x = 0.09$, the MSDs of x- and y- components increase with time, while z- component shows to be constant approximately. This means that Li ions for the case of $x = 0.09$ conduct a two-dimensional diffusion.

The linear region in the functions $< |\mathbf{r}(t) - \mathbf{r}(0)|^2 >$ may be related to the diffusion coefficient D by the well-known equation

$$< |\mathbf{r}(t) - \mathbf{r}(0)|^2 >= nDt + C, \tag{1}$$

where C is a constant term. $n = 2, 4, 6$ are taken for the cases of one-, two- and three-dimensional diffusion, respectively. The calculated diffusion coefficient D and ionic conductivity σ of Li ions are shown in Table 1. From experimental results by Inoue and Zou [3, 4, 5], we can estimate as $\log \sigma \simeq -1.7 \sim -1.0(\Omega \cdot \mathrm{cm})^{-1}$. Experiments by Katsumata *et al.* [7] showed that $D \sim 1.3 \times 10^{-6}\mathrm{cm}^2/\mathrm{s}$ at $x = 0.067$ and $T = 500\mathrm{K}$. As shown in Table 1, we get $D = 1.5 \sim 2.5 \times 10^{-6}\mathrm{cm}^2/\mathrm{s}$, $\log \sigma = -2.5 \sim -2.0(\Omega \cdot \mathrm{cm})^{-1}$. These calculated results agree with experimental results substantially. We get that the ionic conductivity of Li ions in the high concentration region has a saturating or decreasing tendency. The saturation-typed concentration dependence in the conductivity also coincides with experiments [3, 4, 5].

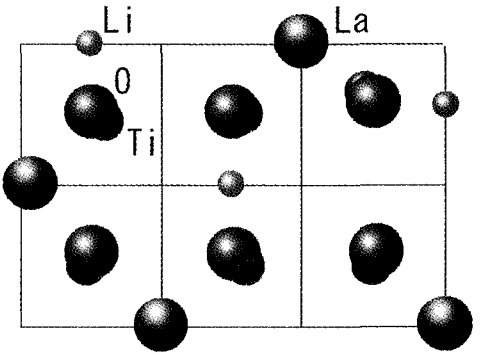

Figure 3: Schematic position of each ion after simulations

Table 1: Concentration dependence of D and σ. σ has the minimum value at $x = 0.09$ and takes the maximum value at $x = 0.21$.

concentration x	$D(\mathrm{cm}^2/\mathrm{s})$	$\sigma(\Omega \cdot \mathrm{cm})^{-1}$	$\log \sigma$
0.09	2.27×10^{-6}	3.20×10^{-3}	-2.50
0.21	2.52×10^{-6}	8.17×10^{-3}	-2.09
0.29	1.48×10^{-6}	6.64×10^{-3}	-2.19

The experimental results of σ by Ruiz *et al.* [9] and Inaguma *et al.* [16] support approximately our calculated concentration dependence of σ shown in Table 1.

3.3 Trajectory of Li Ions

It is one of useful points of the MD method to observe directly the motion of Li ions by investigating trajectories of Li ions.

In the case of $x = 0.09$, the motion of Li ions seem to be inactive, as compared with the case of $x = 0.29$. A few Li ions for $x = 0.09$ might migrate on the same A2-site layer. There is a few jump diffusion along the c-axis, but we can not observe the continuous jump along the c-axis. Then we may understand that Li ions for $x = 0.09$ conduct the two dimensional motion approximately.

In the case of $x = 0.29$, Li ions are very active on each A2-site layer and also jump frequently between A1-site and A2-site and migrate continuously like A2-site $\rightarrow$ A1-site $\rightarrow$ A2-site. We see that the three dimensional conduction of Li ions strengthen for the case of $x = 0.29$.

Fig.5 shows the trajectories of ions on a some A2-site for the case of $x = 0.29$. Diffusing particles and large vibrating particles represent Li ions. Small

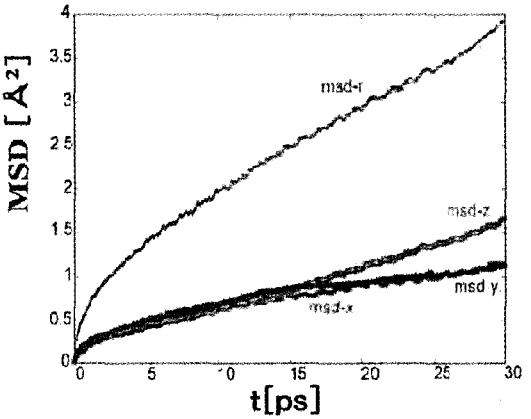

Figure 4: Mean square displacements of Li ions for $x = 0.29$

vibrating particles show La ions. When Li ions on the A2-site jump to the neighboring A1-sites, the diffusion paths of those ions are projected on the same A2-site. We see that Li ions stay at off-site positions and migrate on the diffusion path along the lattice axis approximately.

4 Electronic Total Energy Calculation

Electronic band calculations have been done using the full-potential linear-muffin-tin-orbital (FP-LMTO) program LMTART [18, 19], where the local density approximation (LDA) has been used. Our result of occupying of off-center position by Li ions satisfies with the result of neutron diffraction experiment [8].

5 Discussions and Conclusion

Hole burning spectroscopy is known as one of the optical method to study the conduction mechanism in superionic conductors. Hattori presented the studies on elementary migration of Li ions in $La_{0.5}Li_{0.5}TiO_3$ doped with Pr^{3+} ions in the Asian Conference on Solid State Ionics [17]. It was reported that Li ion is located at an off-center position, and the resonance frequency is lower as about $17.9cm^{-1}$ for Li^6 and $16.3cm^{-1}$ for Li^7. He pointed out that this low resonance frequency corresponds to the low potential energy of Li^+ motion between off-center positions.

Electronic band calculations have been done using the full-potential linear-

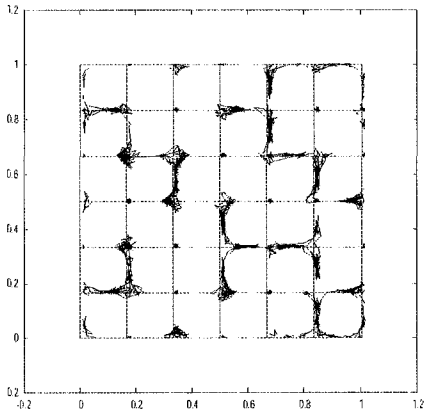

Figure 5: Trajectories of Li ions in some A2-site for $x = 0.29$. Small tracks on the cross points show the lattice vibration of La ions.

muffin-tin-orbital (FP-LMTO) program LMTART [18, 19], where the local density approximation (LDA) has been used. Recently Kashida *et al.* [20, 21] have conducted the LMTO band structure calculation for a mixed perovskite type Li ion conductor $LaLiTiO_3$. They have calculated the total electron energy as a function of Li ion pathway parallel to the [110] direction. They have got that the starting point of off-center position has a minimum energy.

In this paper, we have done the MD simulation for the Li ion conductor $La_{4/3-x}Li_{3x}\square_{2/3-2x}Ti_2O_6$. We have calculated the partial distribution functions $g_{ij}(r)$ for all pairs of ions. From $g_{\text{Li-Ti}}(r)$ the nearest neighbor distance of Li-Ti has been 2.7Å, which suggests that Li ions stay at off-site positions, not at the bcc lattice points. It has been also shown that Li ions change their motion from two-dimensional conduction to three-dimensional conduction with increasing of concentration for Li ions. The concentration dependence of the ionic conductivity σ has been in approximate agreement with experiments. Our result of occupying of off-center position by Li ions satisfies with both results of the neutron diffraction experiment [8] and also the electronic band calculations by Kashida *et al.* [20, 21].

Taking into consideration on the configuration of vacancies, it might be possible to study these materials from the viewpoint of the percolation method.

Acknowledgements

M.K. would like to express his sincere thanks to Professor N. Inoue for his useful discussions. Authors wish to express their thanks to Associated Professor F. Shimojo for his useful instruction regarding the MD simulation. M.K. is supported in part by the Uchida Energy Science Promotion Foundation.

References

[1] T. Kudo, O. Yamamoto and H. Iwahara, "Fuel Cells" (Uchida Rohkakuho, 2005)(in Japanese).

[2] V. Thangadurai and W. Weppner, Ionics **6** (2000) 70.

[3] Y. Zou and N. Inoue, "The First International Discussion Meeting on Superionic Conductor Physics" (Kyoto, Sep., 2003).

[4] Y. Zou, N. Inoue, K. Ohara, V. Thangaduri and W. Weppner, Ionics **10** (2004) 463.

[5] N. Inoue and Y. Zou, Solid State Ionics **176** (2005) 2341.

[6] Y. Inaguma, L. Chen, M. Itoh, T. Nakamura, T. Uchida, M. Ikuta and M. Wakihara, Solid State Commun. **86** (1993) 689.

[7] T. Katsumata, Y. Inaguma, M. Itoh and K. Kawamura, J. of Ceramic Society of Japan **107** (1999) 615.

[8] M. Yashima, M. Itoh, Y. Inaguma, Y. Morii, J. of the American Chemical Society **127** (2005) 3491.

[9] A.I. Ruiz, M.L. Lopez, M.L. Veiga and C.Pico, Solid State Ionics **112** (1980) 291.

[10] Y. Maruyama, H. Ogawa, M. Kamimura and M. Kobayashi, submitted.

[11] S. Ono, S. Kashida, and M. Kobayashi, Meeting Abstracts of the Phys. Soc. Jpn. Vol.60,No.2,Part4 (2005) p.568.

[12] O. Bohnke, H. Duroy, J.L. Fourquet, S. Ronchetti and D. Mazza, Solid State Ionics **149** (2002) 217.

[13] D. Mazza, S. Ronchetti, O. Bohnke, H. Duroy and J.L. Fourquet, Solid State Ionics **149** (2002) 81.

[14] H. Tanaka, H. Tabata, K. Ota and T. Kawai, Phys. Rev. B **53** (1996) 21.

[15] D. Beeman, J. Comp. Phys. **20** (1976) 130.

[16] Y. Inaguma, L. Chen, M. Itoh and T. Nakamura, Solid State Ionics **70/71** (1994) 196.

[17] T. Hattori, "Solid State Ionics: Trends in the New Millennium, pp.751-761" edited by B.V.R. Chowdari (World Scientific, 2002).

[18] S. Y. Savrasov, Phys. Rev. B **54** (1996) 16470.

[19] W. Shimosaka, S. Kashida and M. Kobayashi, Solid State Ionics **176** (2005) 349.

[20] S. Kashida, S. Ono and M. Kobayashi, Extended Abstracts of the 31th Symposium on Solid State Ionics in Jpn. (2005) p.34.

[21] S. Ono, Y. Seki, S. Kashida, and M. Kobayashi, to be submitted.

Cuprous Ion Conducting Montmorillonite- Polypyrrole Nanocomposites

D. M. M. KRISHANTHA, R. M. G. RAJAPAKSE*, D. T. B. TENNAKOON, W. M. A. T. BANDARA and P. N. L THILAKARATHNA

Department of Chemistry, University of Peradeniya, Peradeniya, Sri Lanka
Email: rmgr@pdn.ac.lk

Solid state polymer–Silicate nanocomposite based on Polypyrrole-Cu^{+}-montmorilonite were prepared and electrical properties were investigated. In this preparation, Na-montmorillonite (Na^{+}-MMT) was purified by repeated washing with distilled water and the intergallery cations were exchanged for Cu(II). The cupric ions exchanged–MMT($Cu(II)^{-}$- MMT) was again exposed to pyrrole in aqueous acidic solution to yield polypyrrole-Cu^{+}-MMT nanocomposite. DC polarization test and AC impedance measurement reveal that the materials are mixed conductors. The ionic conductivity is due to the motion of cuprous ions which is facilitated by microstructure of polypyrrrole present in the intergalleries. An electrochemical cell was fabricated using the materials which can be represented by $Cu_{(s)}$/ Cu^{+}-PPY-MMT/$Cu_2SO_{4\ (s)}$/$Na_2SO_{4(S)}$-$Na_2S_2O_{8(s)}$/ and gave a 1.00 V. The cell is rechargeable.

Key words: Montmorillonite, Polypyrrole, Mixed conductors, Single ion conductor

1. Introduction

Electroactive polymers continue to receive considerable attention not only due to their interesting electronic and optical properties but also because of their intriguing solid state characteristics [1, 2]. Research on electroactive polymers has recently been focused on developing materials with well defined microstructure controllable at the nanometer scale. Layered materials such as smectite clays (e.g., montmorillonite, MMT) evoked a great amount of attention for the preparation of such materials with microstructure [3]. The lamellar structure, high in-plane strength and stiffness as well as high aspect ratio [4] are favorable factors to choose MMT as host materials.

Generally, polymer-clay nanocomposite (PCN) are prepared by exchanging the intergallary cations for monomer cations followed by polymerization with the aid of the external oxidant such as ammonium peroxydisulphate or ferric chloride. This would lead to the formation of the polymer both *in situ* and *ex situ* of the MMT clay [5, 6, 7]. Although these PCN materials have been extensively studied over past decades, interest in alternative approaches to synthesize microstructure materials in which the polymer is present only within the intergallary of MMT is still growing. As such we have developed a method called spontaneous polymerization technique for synthesized such PCN materials. [8]. In order to effect this we use Cu(II) ions present within the intergalleries of MMT

to spontaneously polymerize pyrrole inserted into the same intergalleries. The Cupric ions are then converted into cuprous ions and are stabilized within the control environment by coordination through O^- groups in the tetrahedral layers of MMT and N-functionality of polypyrrole.

In this publication, we prove that the materials are mixed conductors. The ionic conductors are due to the migration of Cu^+ ions facilitated by microstructure within the intergalleries.

2. Methods and materials

A dry mass of 2 g purified MMT was treated with 100 cm^3 of 0.5 mol dm^{-3} $CuSO_4$ (aq) solution for 24 h to exchange cations present in the clay for Cu(II). The amount of Cu(II) ions present in the sample is well above that required for cation exchanged capacity of the clay portion. The resultant colloidal solution was centrifuged, and the supernatant discarded. The slurry obtained was then stirred with distilled water for 24 h, the suspension is subsequently centrifuged and the supernatant discarded. This procedure was repeated until the supernatant was free of SO_4^{2-} ions [tested using $BaCl_2$ (aq)].

The slurry thus obtained is the MMT containing hydrated cupric ions present within interlayer spaces of MMT [Cu(II)-MMT]. 0.5 g of dry Cu(II)-MMT was stirred with 100 cm^3 of 0.05 mol dm^{-3} pyrrole in 0.1 mol dm^{-3} HCl(aq) solution for 24 hours. This has resulted in a black suspension, which was purified by the repeated washing procedure and described above and characterized by XRD and conductivity measurements. The supernatant of pyrrole treated Cu(II)-MMT was tested for Cu(II) using aqueous ammonia and for pyrrolium ions with acidified ferric chloride solution.

AC impedance technique was employed to obtain electrical resistance of the materials. The acquisition of the AC electrical data in the frequency range 5 Hz to 13 MHz was accomplished by 4192A LF- impedance analyzer. The temperature dependence of the electrical conductivity was studied in the temperature range 25 ^0C and 120 ^0C in dry air. XRD experiments were done on a Seimens D-5000 diffractometer with Cu K_α (λ = 0.1540562) radiation. For these analysis a thin layer of Cu(I)-PPY-MMT was deposited on a clean glass plate by allowing a few drops of respective colloidal solution to dry it.

3. Results and Discussion

In previous publications [3, 9, 10], we made use the intercalation of monomer cation in clay through ion exchange followed by polymerization using an external oxidant such as $S_2O_8^{2-}{}_{(aq)}$ or $Fe^{3+}{}_{(aq)}$. We then developed a spontaneous

poimerization by monomers within the intergalleries of MMT [8]. Ironically, the oxidant use Cu (II) in capable of oxidative polymerization of pyrrole only when it

is present within the confined environment where it is coordinated by O^- groups in the tetrahedral layers and N-functionalities. When $Cu^{2+}_{(aq)}$ is stirred with pyrrole in acidic medium no signs of polymerization is observed. This is because the potential required for the one electron oxidation of pyrrole to pyrrolium cation(Py^+) is higher than that of is achieved through the reduction of $Cu^{2+}_{(aq)}$ .As we know $Cu^{2+}_{(aq)}/Cu^{+}_{(aq)}$ and $Cu^{2+}_{(aq)}/Cu$ have standard potentials 0. 5 V and 0. 337 V respectively. Though Cu(I) is highly unstable as it is in aqueous medium. Thus in the aqueous medium formation of $Cu^{+}_{(aq)}$ is not possible and it can be exist as a complex ion or insoluble salt. This explains the inability of $Cu^{2+}_{(aq))}$ to oxidatively polymerize pyrrrole in aqueous medium. When Cu^{2+} is co-ordinated by ligands there will be a overpotential its reduction. The Cu^{+} ion which is formed by one electron reduction is also co-ordinated by ligands. Therefore it can exist undergoing disproportionation.

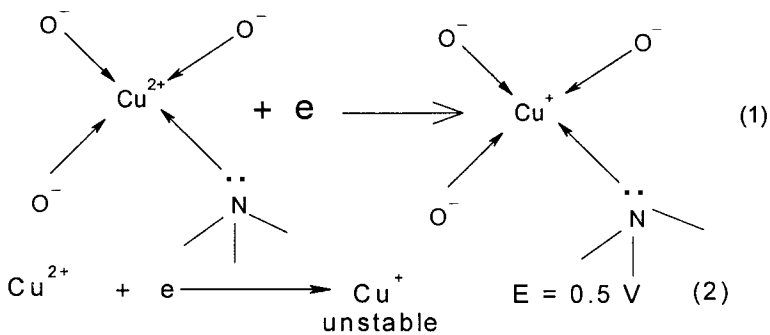

The standard potential for the reaction (1) is expected to be somewhat higher than that of reaction (2). The potential of the reaction (1) is sufficient to enough the one electron oxidation of pyrrole leading to the formation of Py^+ which will subsequently undergo polymerization to the resulting the formation of polypyrrole.

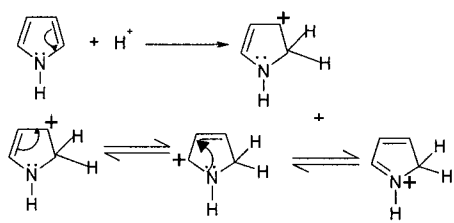

Figure 1. Resonance structure of pyrrolium ion

The product pyrrolium ion is stabilized through resonance (Fig 1).

It is very interesting to note the mechanism of spontaneous polymerization of pyrrole when Cu(II)-MMT is exposed to an aqueous solution of pyrrrole in the acidic medium. When the pyrrole is inserted into the intergalleries, for each two pyrrole units intercalated one Cu^{2+} ion is expelled from Cu(II)-MMT. This is found by analyzing the supernatant solution which is found to have $Cu^{2+}_{(aq)}$ leach from Cu(II)-MMT due to uptake of pyrrole. It is therefore possible that pyrrole is inserted to cation exchanged to pyrolium ions. The acidic medium employed would ensure the presence of Py^{+} ions in the solution for the respective ion-exchange.

The pyrrolium ions then oxidatively polymerize by co-ordinated Cu(II) present in Cu(II)-MMT. This explained he formation of shiny dark black slurry when Cu(II)-MMT treated with pyrrole in aqueous acidic solution. Since the polymerization can be effected only within the confined environment, the polymer form should reside only in the interlayer spaces. Thus, this route of spontaneous polymerization produces only *in situ* polymer and there are no segments attached to the external surfaces of the clay *(ex situ)*

The d-spacings measured by XRD at a few selected temperatures of Cu(I)-MMT-PPY are shown in table 1. Also shown in table 1 is the d spacing of Cu(I)-MMT-PPY heat treated at 200 °C when exposed to H_2O.

Table 1. The d-spacing measured by X-ray diffraction studies montmorillonite containing Cu(I) and polypyrrole (PPY) [Cu(I)-PPY-MMT] at different temperatures.

MATERIAL	d-spacing (Å)			
	25 °C	150 °C	200 °C	After wetting with H_2O
Cu(I)-PPY-MMT	16.10	16.20	16.30	16.30

It is interesting that there is no significant changes in d spacing when Cu(I)-MMT-PPY sample is heat treated at temperature well above 100 °C to remove water if present. Apart from a very slight enhancement due to expansion, there is no detectable reduction of d spacing due to the removal of hydrated water layers upon heat treatment. It is therefore likely that 16.10 Å is the inherent d spacing of bare Cu(I)- PPY- MMT which does not contain any hydrated water layers. This fact further supported by reluctance of Cu(I)- PPY- MMT to uptake water when wetted with water. As opposed to this simple inorganic cation exchange MMT readily taken up water by expanding d spacing by 3 Å units per each water layer

[11]. Thus, it can be concluded that PPY in Cu(I)- PPY- MMT made the clay hydrophobic.

The presence of polypyrrole coordinated to O^- groups in the tetrahedral layers is evidenced from the FTIR analysis. This study has already been reported [8].

3. 1 AC Impedance studies of Cu(I)-PPY-MMT

The four probe technique used to measure DC conductivity of Cu(I)-PPY-MMT given a value of 0.42 S cm^{-1} at 25 °C. Since the DC conductivity is due to electronic motion these values may be assigned to be due to electronic conductivity.

AC impedance analysis of Cu(I)-PPY-MMT give added evidence to mix electrical conductivity. When these studies carried out using stainless steel blocking electrodes, semicircle and the low-frequency straight line with 60° inclination (Fig 2.) are observed. The diameter of the semicircle given the electronic resistance and the warberg impedance region of straight line is due to ionic diffusion.

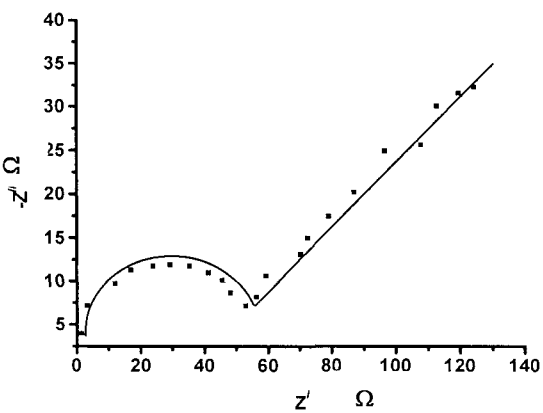

Figure 2. The AC Impedance spectra of montmorillonite containing Cu(I) and polypyrrole [Cu(I)-PPY-MMT] blocking stainless steel electrodes.

The temperature dependence of the conductivity follows the Arrhenius behaviour with two different activation regions(Fig . 3). The activation energy at the lower temperature region is 0.09 eV while that at the higher temperature region is 0.23 eV . These values are lower than those of Cu(II)-MMT [8]. A significant enhancement of ionic conductivity due to the introduction of

polypyrrole within the intergalleries suggests that the polypyrrole matrix is facilitating the motion of cuprous ions in the solid nanocomposite. The ionic conductivities of the composite range from 0.66 x 10^{-3} S cm^{-1} to 1.50 x 10^{-3} S cm^{-1} in the temperature range from 25 °C to 120 °C clearly show that this composite material has ionic conductivity comparable to that of fast ion conductor glasses of cuprous salts [12].

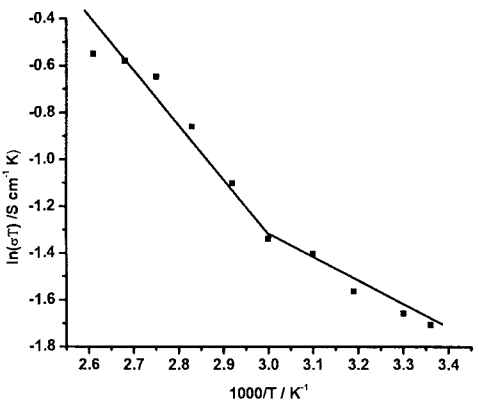

Figure 3. Arrhenius plot for the temperature dependence of electrical conductivity for montmorillonitecontaining Cu(I) and polypyrrole [Cu(I)-PPY-MMT].

3. 2 Fabrication of electrochemical cell

Just like their wide spreading applications in electric/optic/magnetic fields, polymers due to their flexibility and easiness in fabrication, have attracted extensive attention for their inherent advantages and potential applications in ion-conducting batteries. Ion-conducting polymer, an alternative name for polymer electrolyte, is an electrically conducting polymer in which chare transport by ions. The classical example is poly(ethylene oxide) (PEO) containing salts. PEO was the first polymer reported to exhibit high ionic conductivity at elevated temperature when complex with alkali metal salts [13]. However, electronically conducting polymers such as polyaniline, polypyrrole etc have low ionic conductivities at those conditions [14]. When hybrid materials were prepared with the electronically conducting polymer and MMT, we have found that rather than pristine polymer, it posses high ionic conductivity (Cu(I)-PPY-MMT). It is

therefore we thought that the fabrication of a cell with this hybrid material should have several advantages. They are (1) easy to prepare (2) this material (Cu(I)-PPY-MMT) is hydrophobic, it is easy to use in ALC (3) and it can be used in wide range of temperature (25 ^{0}C to 100 ^{0}C).

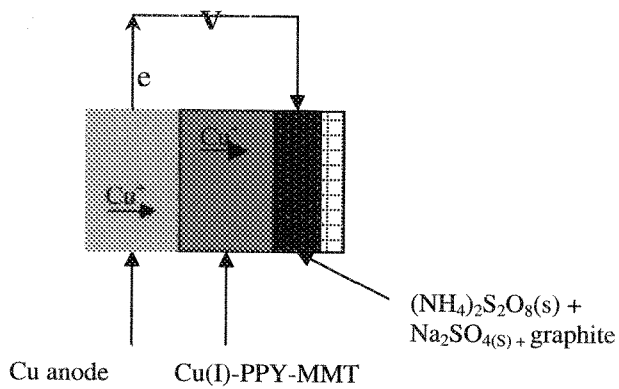

Figure 4. Diagram of the designed electrochemical dell

In order to verify the moving ions in Cu(I)- PPY-MMT nanocomposite an electrochemical cell was prepared in which the nanocomposite used as solid electrolytes. The cell has the following composition.

Cu/MMT-Cu^+-polypyrrole/$(NH_4)_2S_2O_8(s)$ + $Na_2SO_{4(S)}$-graphite

The electrode reaction expected are at the anode $Cu_{(s)}$ oxidized forming Cu(I).

$$Cu_{(S)} \longrightarrow Cu^+ + e$$

Cu(I) ion thus formed is moved along the solid electrolyte Cu(I)-MMT-PPY which is fast ion conductor for Cu(I) ions.

At the cathode

$$S_2O_8^{2-}(s) + 2e^- \longrightarrow SO_4^{2-}(s)$$

And the Cu(I) ions migrated towards the cathode reacts with sulphate ions forming $Cu_2SO_{4(s)}$. The Cu_2SO_4 layer form between the cathode and the anode

prevent the short-circuiting of the two electrodes due to the electronic conductivity of PPY present in the nanocomposite. The cell has a voltage of 1 V at 25 °C and is stable for several days. It gradually decreases upon discharging. Cell reaction can be reverse by applying appropriate voltage showing that the above cell is rechargeable.

The formation of Cu_2SO_4 is proved by XRD studies of the cathodic graphite pellet. The surface of the graphite pellet in contact with the solid electrolyte was observed to gradually because white when the cell is discharging. The XRD analysis of the surface gives characteristic peaks to identical to Cu_2SO_4 (Fig. 5). It is therefore a direct evidence to prove that the moving ions in Cu(I)-MMT-PPY is indeed Cu(I) and that it is single ion (Cu(I)) conductor as a giant anions of clay sheets are fixed in position.

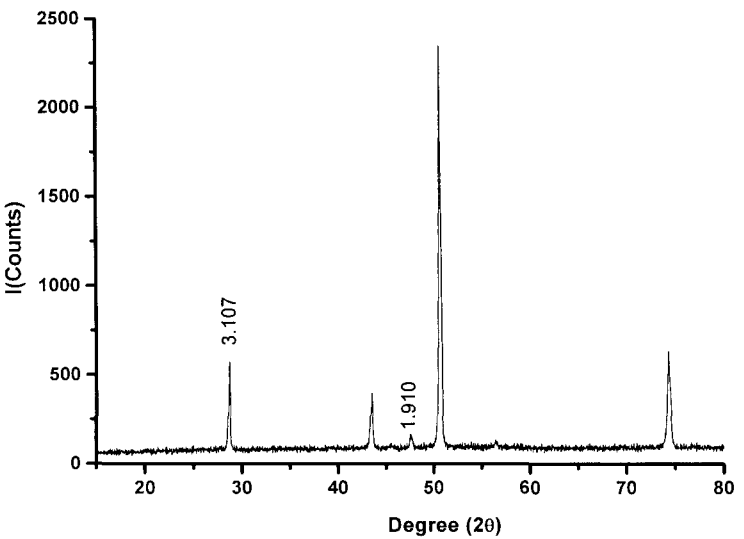

Figure 5. XRD pattern of the deposited sample on cathodic plate

4. Conclusion

The spontaneous polymerization technique can be used to prepare single ion conducting polypyrrole-MMT nanocomposites. The Cu(II)-exchanged MMT is found to spontaneously polymerize PPY giving Cu(I)-PPY-MMT which is found to have ionic conductivities. XRD analysis of the cathodic Cu plate showed the presence of cuprous sulphate on its surface. It confirms that these materials posses ionic conductivity due to mortion of the cuprous ions. The intercalated polymer layer of such materials facilitate for ionic conduction. So, these cupros

ion conducting polypyrrole /montmorillonite nanocomposites are found to be useful solid electrolytes/electrode for several other all-solid-state batteries including a solid-state lead accumulator. All these batteries are found to be rechargeable.

Acknowledgement: *We acknowledge the financial support from the Sri Lankan National Science Foundation (Grant No. RG/2001/C/04 to RMGR).*

References

1. T. A. Skotheim, *Hand book of conducting Polymers* (1986)
2. H. Kuzmany, M. Mehring and. S. Roth, eds(spriner, Berlin,Heidelberg,) (1989)
3. W. M. A. T. Bandara, D. M. M. Krishantha, , J. S.H. Q. Perera, R. M. G. Rrajapakse and D. T. B. Tennakoon *J. Composite.Material* **39** (2005).
4. Pinnavaia,T.J.Science 1983,365
5. W. Chen, T. Wen, A. Gopalan, *Synth. Met.* **128**,179, (2002)
6. Q. Wu, Z. Xue, Z. Qi., F . Wang,. *Polymer.* **41,2029** (2000)
7. B. H. Kim, J. H. Jung,, J. W. Kim, H. J. Choi, Joo. *Synth Met.* **121,**1311, (2001)
8. D.M.M. Krishantha, R.M.G. Rajapakse, D.T.B. Tennakoon and H.V.R. Dias, *Journal of Composite Materials*, American Society for Composites, (JCM)-manuscript no:-JCM0501015, In Press
9. R.M.G. Rajapakse, D.T.B. Tennakoon, J.S.H.Q. Perera, W.M.A.T. Bandara, D.M.M. Krishantha *Journal of Composite Materials* **39,** 1985 (2005),
10. D.M.M. Krishantha, R.M.G. Rajapakse, D.T.B. Tennakoon and H.V.R. Dias, *Electrochemica Acta,* In Press.
11. R. E. Grim, *Clay Mineralogy* 2,261 McGraw-Hill International Series, Sydney, Australia (1968).
12. B. BychkoV, A. Bolotov, Y. Grushko, Vlasov, G. Wortmann, *Solid States Ionics.* **90,289** (1996)
13. P. G., Burce, C. A. Vincent, *J. Chem. Soc. Faraday. Trans.*, **89,** 3187(**1993)**
14. J. E. Mark, *Physical Properties of polymer hand Book.* American Institute of Physics, Woodbury, New York, **(1996).**

FREQUENCY DEPENDENCE OF CONDUCTIVITY STUDIES ON A NEWLY SYNTHESIZED SUPERIONIC SOLID SOLUTION/MIXED SYSTEM: [0.75AgI: 0.25AgCl]

R. K. NAGARCH AND R. KUMAR*

Solid State Ionics Research Laboratory, Department of Physics & Electronics,

Dr. H.S. Gour University Sagar (M.P.) – 470003, India

Email: ranveerssi@yahoo.com

ABSTRACT

The ionic conductivity as a function of frequency has been studied on a newly synthesized fast Ag^+ ion conducting mixed system/solid solution: [0.75AgI:0.25AgCl]. In the present paper dc conductivity as a function of frequency and temperature has been studied, activation energy (Ea) values were calculated from Arrhenius plots and compared with the ac conductivity. Ionic transport parameters of the present superionic system have already been reported earlier. Log σ vs. log f variation shows dispersion at higher frequency region and obeys Jonscher's power law.

Key words: superionic solid, conductivity, activation energy etc.

(1). INTRODUCTION:

There is a large class of materials which conduct predominately by motion of ions, the extreme examples being the so-called *fast ion conductor* or *superionic conductors*. Ordinary ionic conduction relies on the formation of lattice defects under the action of thermal excitation, thus creating vacancies through which ion motion may proceed under the action of external electric field [1-2]. This leads to Arrhenius temperature dependence with an activation energy given by the energy of formation of a defect. Silver ion conducting superionic solids are well known due to their high ionic conductivity at ambient temperature. In majority of these Ag^+ ion conducting superionic solids, a large number of systems have been developed and reported in glassy/amorphous and composite phases, in which AgI has been used as a host or salt [1-8]. The Ag^+ ion conducting superionic systems in these phase, have attracted wide spread attention in recent year due to their possible technological application in solid state batteries, fuel cell, sensor etc. [2-3]. Hence amongst the various solid-state ionic conducting materials a silver ion conducting superionic solid electrolyte have attracted considerable interest in the recent year. Already in 1994, Agrawal and co-workers have developed & reported a new alternative host salt [0.75AgI:0.25AgCl] [9]. This new alternative host salt was prepared by *"twin roller quenching method"* and by annealing the material. Structural characterizations as well as transport properties have also been investigated and reported [9-10]. This new alternative host salt has been used in place of conventional host salt AgI. Using this newly synthesized alternative host salt in place of conventional host salt AgI, several glassy and composite electrolyte systems have been investigated. It has been reported that this new solid solution: [0.75AgI:0.25AgCl] yield better composite electrolyte as well as glassy/amorphous electrolyte systems [11-18].

In the present studies, we report here the preparation, frequency dependence of conductivity on the newly synthesized fast silver ion conducting solid solution:

[0.75AgI:0.25AgCl]. This system was prepared by melt quenching method (quenched in liquid nitrogen). The ionic conductivity has been evaluated using Z'-Z'' (Cole-Cole) complex impedance plots. Ionic conductivity was studied as a function of frequency and temperature. The dc conductivity has been evaluated from logσ vs. log f plots. Activation energy E_a was calculated from temperature dependence of ionic conductivity studies.

(2). EXPERIMENTAL DETAILS:

2.1 sample preparation:

Commercially available reagent grade chemical compounds; AgI and AgCl (purity >98%) [Supplied by Reidel Pvt. Ltd. India] were used, as supplied. These compounds were mixed homogeneously heated at ~ 700^0C in electric furnace. The heated precursor melt was cooled rapidly (i.e. quenched in liquid nitrogen) to form the new host salt [0.75AgI:0. 25AgCl]. Finally the finished product was thoroughly ground and pressed at 2-3 ton/cm^2 to form pellets of dimension of area 1.3 cm^2 and thickness 0.1 to 0.25cm. The surfaces of pallets were coated with silver paint and pellets were sandwiched between the sample holder for transport measurements.

2.2 Conductivity studies:

The frequency and temperature dependence conductivity measurements in terms of Z and θ have been made on new superionic system: [0.75AgI:0. 25AgCl] in the frequency range of 42Hz to 5MHz and in temperature range of 30-200°C. A HIOKI LCR bridge (model 3532-50 Japan) was used for the conductivity measurements. The activation energy (E_a) evaluated from Arrhenius type plots and the dc electrical conductivity was obtained from log σ vs. log f plots at different temperatures.

3. RESULTS AND DISCUSSION:

3.1 Frequency and temperature dependence of conductivity studies by impedance spectroscopy (IS):

The true bulk ac conductivity has been obtained using true bulk resistance (R_b) of sample at various fixed temperature. The real and imaginary parts of impedance of the system have been measured using Z and θ data in the frequency range of 42Hz to 5MHz. Figure 1 shows the complex impedance Z'-Z'' (Cole-Cole) plot for quenched host salt at room temperature. The point of intersection of this impedance plot at the real axis indicates the bulk resistance of the sample. A semicircle or a capacitive arc at high frequencies is observed in this plot, which is associated with the kinetics of the charge transport in the bulk of the sample [19]. A linear region is observed adjacent to this arc at low frequencies that is attributed to the charge transfer at the electrode/sample interface [19]. The arc of the plot could be fitted to a semicircle indicating that the electrical bulk response of the system can be represented by a parallel circuit of a resistance 'R' and a capacitance 'C'. Here 'R' represents the bulk resistance of the sample and 'C' the geometric capacitance of the parallel-plate capacitor formed by the electrodes and the separating sample. The true bulk ac conductivity (σ_{ac}) has been calculated from the impedance plots as usual the bulk resistance R_b is obtained from the intercept of the semicircles with the real axis and using the formula:

$$\sigma = l/R_b A \quad (1)$$

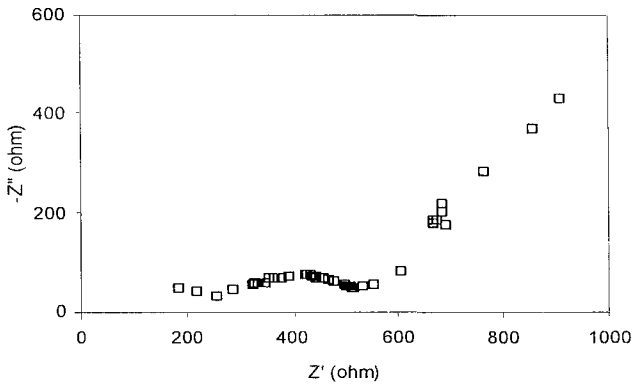

Fig 1. Complex impedance (Z'-Z") Cole-Cole plot at room temperature for host salt: [0.75AgI:0. 25AgCl]

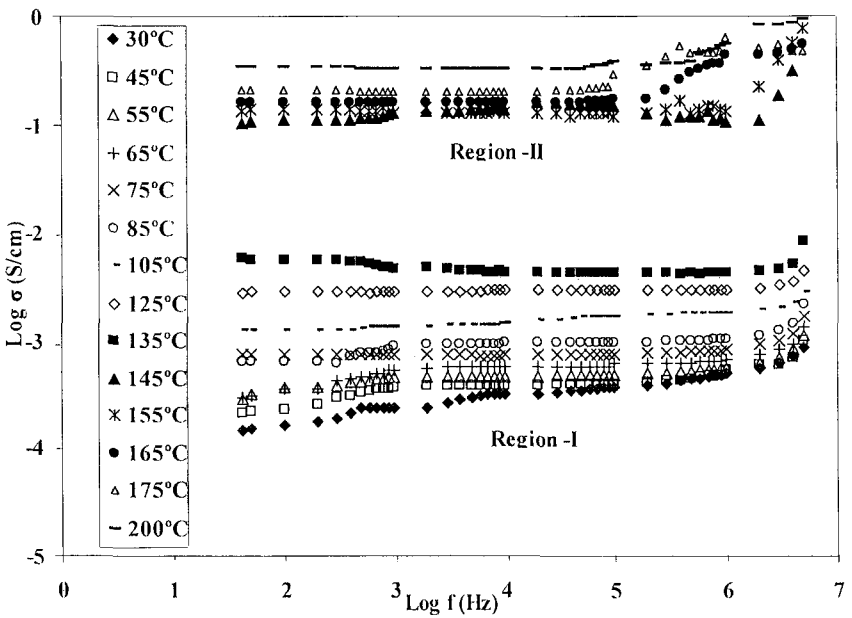

Fig 2. Log σ vs. log f plot for host salt: [0.75AgI:0. 25AgCl] at various temperatures

where 'l' is the thickness and A is the contact area of the sample. AC conductivity ($\sigma_{ac} \sim 6.0x10^{-4}$ S/cm) was achieved at room temperature for the new host salt (quenched in liquid nitrogen). The variation of conductivity with frequency at various fixed temperature has been studied for the new host salt. Figure 2 shows

the frequency dependence of conductivity at various temperatures. It is obvious from figure that the conductivity is almost independent with frequency for all temperatures in the low frequency region. Hence a frequency-independent plateau region observed in all plots for different temperatures, which corresponds to the dc conductivity of the system. In the higher frequency region the frequency dispersion is also predominant in all plots in this figure. Hence it is noted from this figure that the conductivity is depend on frequency at higher frequency region and obey Jonscher's power law [20-21].

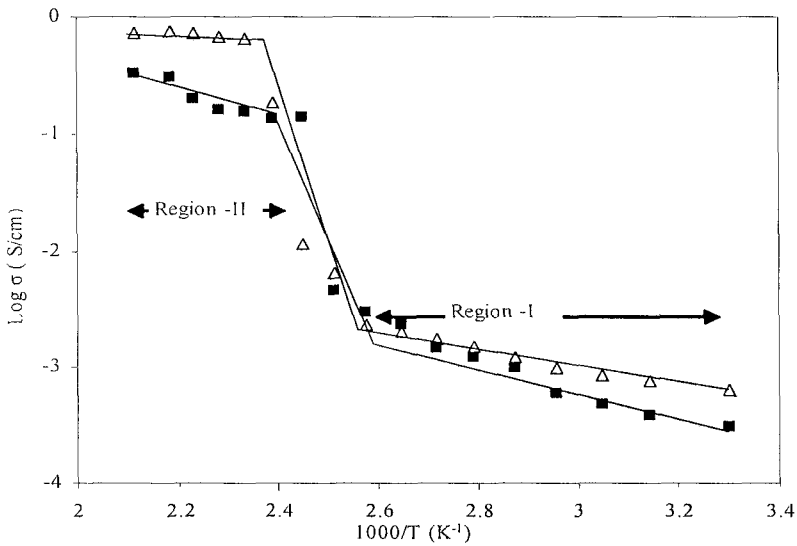

Fig 3. Log σ vs. 1000/T plots for host salt: [0.75AgI:0. 25AgCl] (■) for dc conductivity and (Δ) for ac conductivity

frequency independent plateau region of these plots. The dc conductivity (σ_{dc} ~ $3x10^{-4}$ S/cm) at room temperature was obtained for the present system. The temperature dependence of conductivity was found to obey the Arrhenius relation and can be written as follow:

$$\sigma (T) = \sigma_0 \exp (-E_a/kT) \qquad (2)$$

where σ_0 is pre- exponential factor and E_a is activation energy. The variation of both the ac and dc conductivities of the host salt with temperature were studied and plotted in Figure 3. It is clear from the figure 3 that conductivity increases with increasing temperature up to about 135°C, an abrupt change occurs after this temperature, then conductivity almost independent with temperature. One can obviously note from this Figure that, both plots exhibit identical nature of the log σ versus 1/T variation as observed in pure AgI [22]. The present system shows β → α -like phase transition at ~ 135°C for both the ac and dc conductivity variations, which is similar to the behavior as observed in AgI conductivity variation [9-10, 22]. It can also be clearly noted that the present system have Arrhenius type behavior in both the temperature region –I & -II. Region –I and

region –II indicated in figure 3 corresponds to β and α -like phase transition respectively. The temperature variation of ac & dc conductivity exhibits identical behavior in both the temperature regions. The Arrhenius type equations can be expressed as follows for both the ac and dc conductivity in both the temperature region.

$\sigma_{ac}(T) = 2.59 \times 10^{-1}\ (0.161/kT)$ (region –I)
$\sigma_{ac}(T) = 2.00 \times 10^{0}\ (0.05/kT)$ (region –II)
$\sigma_{dc}(T) = 4.26 \times 10^{-2}\ (0.172/kT)$ (region –I)
$\sigma_{dc}(T) = 1.9 \times 10^{-1}\ (0.061/kT)$ (region –II)

The activation energy values were obtained (~0.161 & 0.172 eV) for the system for both the ac & dc conductivity variation respectively in region –I (30^0-135^0C). Smaller the activation energy value indicates that the Ag^+ ion transport easy in this system. On comparing both the energies it can be concluded that the activation energy values are almost same for both the ac & dc conductivity. Hence both the conductivity variations are in close agreement to each other.

(4). CONCLUSION:

A new Ag^+ ion conducting solid solution [0.75AgI:0.25AgCl] has been synthesized by quenching method (quenched in liquid nitrogen). This new host salt yield better two-phase composite electrolyte system as well as glassy systems to those of convential host salt AgI. The temperature and frequency dependence conductivity has been studied. The conductivity is dependant on frequency at higher frequency region and obeys Jonscher's power law. The frequency-independent plateau region observed in the log σ vs. log f variation in the system, which corresponds to dc conductivity. The dc conductivity has been evaluated from log σ vs. log f variations for the system and compare with ac conductivity, which are in the good agreement with each other in temperature dependence studies.

ACKNOWLEDGEMENT:

The financial support by Third World Academy of Science (ICTP); Italy by Project No. 00-0046, RG/PHYS/AS is gratefully acknowledged.

REFERENCES:

[1] A.K. Jonscher, J. Phys. D Appl. Phys. **R57,** 32 (1999)
[2] S. Chandra, "Superionic Solids – Principles and Application" (North Holland, Amsterdam). (1981)
[3] A.L. Lasker and S. Chandra, (eds) "Superionic Solids and Solid Electrolytes-Recent Trends" (Academic Press, New York). (1989)
[4] K. Shahi and J.B. Wagner Jr, J. Electrochem. Soc. **128,** 6 (1982)
[5] M.C.R. Shastry and K.J. Rao, Solid State ionics, **51,** 331 (1992)
[6] K. Shahi and J.B. Wagner Jr, Solid State Chem. **42,** 107 (1982)
[7] A. Chiodelli and A. Magistris, Solid State Ionics, **18-19,** 356 (1986)
[8]] R.C. Agrawal and R. K.Gupta J. of Mater Sci. **34,** 1131 (1999)
[9] R.C. Agrawal, R.K. Gupta, R. Kumar and A. Kumar, J. Mater Sci. **2,** 3673 (1994)

[10] R.C. Agrawal, R. Kumar, R.K. Gupta, M. Saleem, J. Non-Crystalline Solids, **181,** 110 (1995)
[11] R.C. Agrawal and R. K.Gupta, J. Mater. Sci., **32,** 3327 (1997)
[12] R.C.Agrawal, R. K. Gupta, C.K. Sinha, R. Kumar and G. P. Pandey, Ionics **10,** 113 (2004).
[13] R. C. Agrawal, Mohan L. Verma, R. K. Gupta and, S. Thaker Solid State Ionics **473,** 136 (2000)
[15] R.C. Agarwal and R.Kumar, J. Phys. D Appl. Phys **27,** 2431 (1994)
[16] R. K, Nagarch R, Kumar and R. C. Agrawal, J. Non – Cryst. Solids (In Press 2006)
[17] R Kumar, R. K. Nagarch, R.S Sharma and R. C Agrawal, Indian J., Phys **79 (7),** 687 (2005).
[18] Ranveer Kumar, Nidhi B Jain., R. K. Nagarch and R. C. Agrawal **79 (7),** 745 (2005).
[19] J.R. Macdonald, (eds.), Impedance Spectroscopy, Wiley New York, (1987)
[20] A.K. Jonscher, Nature **267,** 673 (1977)
[21] A. K. Jonscher, in: M. H. Francombe (eds.), Physics of Thin Films, Academic Press, London and New York. **11,** (1980)
[22] R.C. Agarwal, K. Kathal, R. Chandola and R.K. Gupta in; "Solid State Ionics: Materials and Applications" (eds.) B.V.R. Chowdari, S. Singh and P. C. Srivastava (World Scientific, Singapore) 363, (1992).

DIFFUSE X-RAY AND NEUTRON SCATTERING FROM POWDER PbS

XIANGLIAN, K. BASAR, H. HONDA, T. HOJO AND T. SAKUMA*

Institute of Applied Beam Science, Ibaraki University, Mito 310-8512, Japan

**E-mail: sakuma@mx.ibaraki.ac.jp*

H. TAKAHASHI

Institute of Applied Beam Science, Ibaraki University, Hitachi 316-8511, Japan

N. IGAWA AND Y. ISHII

Japan Atomic Energy Agency, Tokai 319-1195, Japan

Diffuse X-ray and neutron scattering from powder PbS were measured at 15 and 294 K. Oscillatory diffuse scattering was clearly obtained at 294 K. The values of correlation effects decrease with the increase of inter-atomic distance. As the scattering amplitude (f_{Pb}) in X-ray scattering and scattering length (b_{Pb}) in neutron scattering of Pb are much greater than those of S (f_S, b_S), the contributions to the oscillatory diffuse scattering from the thermal correlation between second nearest neighboring atoms (Pb-Pb) were observed by X-ray and neutron scattering. The clear contribution to the diffuse scattering from second nearest neighboring atoms was first obtained.

1. Introduction

Diffuse scatterings contain information about a short-range-order in a disordered arrangement (static disorder) and thermal vibration of atoms (thermal disorder) in crystals.[1,2] Anomalously strong and oscillatory diffuse scattering from α-AgI type solid electrolyte has been studied in X-ray and neutron scattering experiments. For the superionic conductors that have disordered structure, the diffuse scattering has been reported on α-AgI and α-CuAgSe.[3,4] The first peak of the oscillatory diffuse scattering was due to static and thermal disorder. The oscillatory forms were also observed even from ordered crystals at room temperature due to the correlation effects between thermal displacements of atoms.[5-8] The intensities of the diffuse scattering showed clear temperature dependence. The correlation effects between

first nearest neighboring atoms were taken in and the profile of the diffuse scattering had been analyzed.[9] Recently, the relation between inter-atomic distance and the values of thermal correlation has been investigated by the computer simulation.[10]

In this paper, the diffuse scatterings from X-ray and neutron diffraction measurements have been carried out for powder PbS at 15 and 294 K. The fine form of diffuse scattering was discussed with the correlation effects between thermal displacements of second nearest neighboring atoms (Pb-Pb).

2. Experimental

X-ray diffraction measurements were carried out for a powder PbS by using CuKα radiation at 15 and 294 K. X-ray diffraction data were collected for 4 sec per step at 0.05° intervals over the 2θ range from 10° to 90° by a step-scan mode. The reflection from the (002) plane of a pyrolytic graphite crystal monochrometer was used.

Neutron scattering measurements at temperature 15 and 294 K have been performed on powder PbS by HRPD (High Resolution Powder Diffractometer) installed at JRR-3 in Japan Atomic Energy Agency (JAEA) for 1 day. Powder samples were set in a vanadium container of 10 mm in diameter. Incident neutron wavelength of 1.823 Å which is monochromatized by Ge (331) was used and the data were collected in the 2θ range from 2.5° to 162.45° with step angle 0.05°.

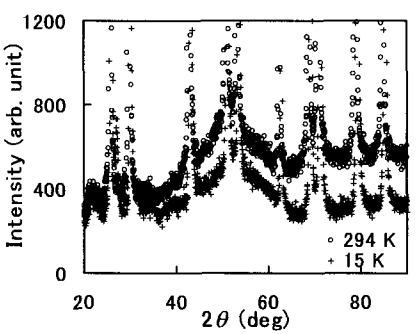

Figure 1. Diffuse X-ray scattering intensities of PbS at 15 K (plus mark) and 294 K (circle mark).

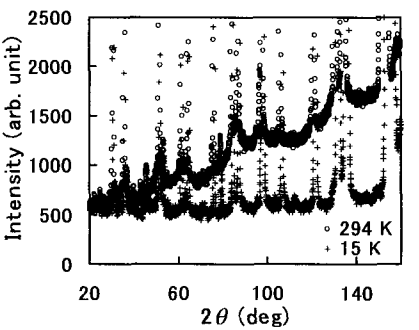

Figure 2. Diffuse neutron scattering intensities of PbS at 15 K (plus mark) and 294 K (circle mark).

3. Results and Analysis

The observed diffuse X-ray and neutron scattering intensities of PbS were shown in Figs. 1 and 2, respectively. Some peaks of diffuse scattering that performs an oscillating profile could be observed at 2θ around 30, 50 and 70° for X-ray and 30, 60, 90 and 140° for neutron data. The intensity of diffuse scattering at 15 K is smaller than that of 294 K.

In the analysis of diffuse X-ray scattering, the intensity of diffuse scattering including the correlation effects between thermal displacements of atoms is expressed as follows;

$$I_{\mathrm{B}} = I_{\mathrm{o}} K N_{\mathrm{o}} \sum_{s} n_i f_{s(i)} f^{*}_{s(i)} \left[1 - \exp\left(-2M_{s(i)}\right)\right]$$

$$+ I_{\mathrm{o}} K N_{\mathrm{o}} \sum_{s} \sum_{s'} n_i f_{s(i)} f^{*}_{s'(j)} \left[\exp\left\{-\left(M_{s(i)} + M_{s'(j)}\right)\left(1 - \mu_{rs(i)s'(j)}\right)\right\}\right.$$

$$\left. - \exp\left\{-\left(M_{s(i)} + M_{s'(j)}\right)\right\}\right] Z_{s(i)s'(j)} \frac{\sin(Qr)}{Qr} + I_{\mathrm{o}} K N_{\mathrm{o}} \sum_{s} \sigma_{\mathrm{inc}} + C\,, \qquad (1)$$

where $f_{s(i)}$ is atomic scattering factor for atom in site $s(i)$, K a function depending on the polarization factor, N_{o} the number of the unit cell in unit volume, and Z the number of sites belonging to the s' th j-type neighbor around an s th i-type site. n_i corresponds to the number of i atoms per unit cell. Two sites $s(i)$ and $s'(j)$ are apart by the distance r. $\exp(-M_i)$ (=$\exp\{-B_i(\sin\theta/\lambda)^2\}$) is Debye-Waller factor of the i atom. σ_{inc} is incoherent scattering cross-section of atoms. The constant C is added for the corrections of background noise. The oscillatory form is expressed as $\sin(Qr)/Qr$, where Q is equal to $4\pi\sin\theta/\lambda$. The correlation effects among the thermal displacements of atoms μ are written as follows;

$$\mu_{r_{s(i)s'(j)}} = \frac{2\left\langle \Delta\mathbf{r}_{s(i)} \cdot \Delta\mathbf{r}_{s'(j)} \right\rangle}{\left\langle \Delta r^2_{s(i)} \right\rangle + \left\langle \Delta r^2_{s'(j)} \right\rangle}\,. \qquad (2)$$

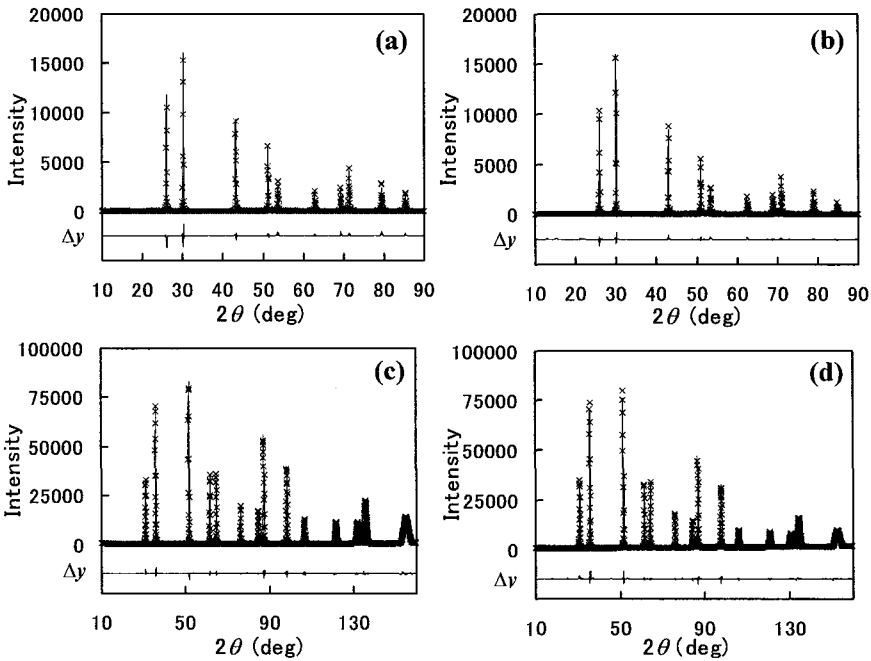

Figure 3. Rietveld refinements patterns for PbS: (a) X-ray, 15 K; (b) X-ray, 294 K; (c) neutron, 15 K; (d) neutron, 294 K. The solid lines are calculated intensities, the crosses (×) are observed intesities. The solid lines at the bottom part of each curve (indicated by Δy) show the difference between calculated and observed intensities.

The values of the correlation among the thermal displacements of $s(i)$ and $s'(j)$ atoms is 0 in the case of no correlation among atomic displacements, and in the case of perfect correlation μ is $2\sqrt{B_{s(i)}B_{s'(j)}}/\left(B_{s(i)}+B_{s'(j)}\right)$. In the case of diffuse neutron scattering analysis, we replace the atomic scattering factor f with neutron scattering length b of atom and K=1 in the eq. (1).

Rietveld analysis has been performed on the X-ray and neutron scattering intensities of PbS using RIETAN-2000.[11] The crystals of PbS are assumed to belong to NaCl type structure with the space group Fm3m where Pb and S atoms occupy 4(a) and 4(b) sites, respectively. The Debye-Waller temperature parameters were obtained from the analysis of Bragg lines intensities of PbS. The obtained final results of the structural parameters (a: lattice constant, B: Debye-Waller temperature parameter) and the reliability factors R at 15 K and 294 K by Rietveld refinement

Table 1. Structure parameters (a: lattice constant, B: Debye-Waller temperature parameter) and R factors obtained by Rietveld refinement analysis.

	X-ray		Neutron	
	15 K	294 K	15 K	294 K
a (Å)	5.919(6)	5.931(2)	5.914(2)	5.930(5)
B_{Pb} (Å^2)	0.041	0.223	0.038	0.621
B_S (Å^2)	0.097	0.720	0.092	0.769
R_{wp} (%)	15.520	10.10	6.590	5.090
R_I (%)	6.340	4.510	0.980	1.810
R_F (%)	4.320	3.00	0.590	1.030
S	2.144	2.009	3.014	2.708

analysis are shown in Table 1. The Rietveld refinements patterns for PbS at 15 and 294 K by X-ray and neutron measurements are shown in Fig. 3. The number of neighboring atoms Z and interatomic distances used in the calculation are shown in Table 2.

In Fig. 1 a large diffuse scattering peak was observed at 2θ around 50° at 15 K. The similar diffuse scattering peak existed also at 294 K in Fig.1. This peak would be related to a static disorder that would be occurred because of the grinding process in the X-ray sample preparation. In the case of neutron measurement where no grinding in the sample preparation was performed, such a peak did not occur at 15 and 294 K in Fig. 2. In order to analyze the temperature influence of the diffuse scattering intensities, the differences between the intensities at 294 and 15 K have been investigated. Figures 4 and 5 show the difference between intensity at 294 and 15 K for X-ray and neutron scattering, respectively.

The diffuse scattering intensities of PbS consist of three components:

$$I = I_{Pb-S} + I_{Pb-Pb} + I_{S-S}, \tag{3}$$

where $I_{Pb\text{-}S}$, $I_{Pb\text{-}Pb}$ and $I_{S\text{-}S}$ are contribution from first nearest Pb-S, second nearest Pb-Pb and S-S pairs, respectively. The values of correlation effects between the first

Table 2. Number of neighboring atoms Z and inter-atomic distances r in the crystal PbS.

	Z	X-ray		Neutron	
		$r_{15\,K}$ (Å)	$r_{294\,K}$ (Å)	$r_{15\,K}$ (Å)	$r_{294\,K}$ (Å)
Pb-S	6	2.959(5)	2.965(6)	2.957(1)	2.965(3)
-Pb	12	4.185(2)	4.193(4)	4.181(3)	4.192(9)
-S	8	5.126(4)	5.136(4)	5.121(7)	5.135(8)
-Pb	6	5.919(6)	5.931(2)	5.914(2)	5.930(5)
S-Pb	6	2.959(5)	2.965(6)	2.957(1)	2.965(3)
-S	12	4.185(2)	4.193(4)	4.181(3)	4.192(9)
-Pb	8	5.126(4)	5.136(4)	5.121(7)	5.135(8)
-S	6	5.919(6)	5.931(2)	5.914(2)	5.930(5)

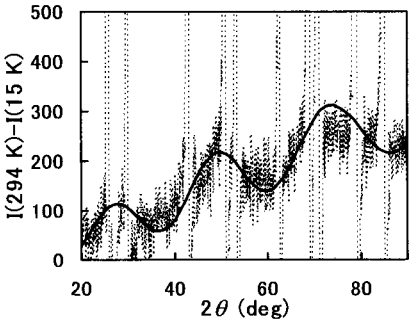

Figure 4. The difference between intensities at 294 K and 15 K for X-ray scattering. The dotted and solid line show the observed and calculated intensities, respectively.

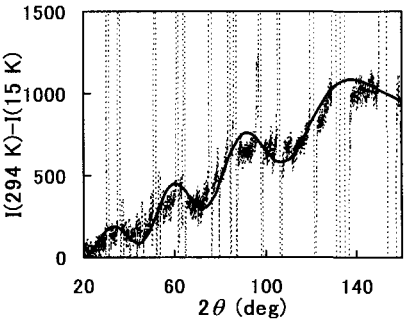

Figure 5. The difference between intensities at 294 K and 15 K for neutron scattering. The dotted and solid line show the observed and calculated intensities, respectively.

and the second nearest neighboring atoms are 0.6 and 0.45, respectively. The other values of correlation effects are assumed to be 0. The values of correlation effect decrease with the inter-atomic distances. The contribution from each component at 294 K is shown in Figs. 6 and 7 for X-ray and neutron case, respectively. It is obtained from the calculation that the oscillating scheme in the diffuse scattering profile of PbS is mainly from the contribution of Pb-Pb pair as shown in Figs. 6 and 7. The peak positions coincide with those of $\sin(Qr_{\text{Pb-Pb}})/Qr_{\text{Pb-Pb}}$, where $r_{\text{Pb-Pb}}$ is the atomic distance between second nearest Pb-Pb atoms. The nearest atomic distance between Pb-Pb pair in the crystal of PbS is about 4.19 Å. The strong contribution from Pb-Pb pair (second nearest neighboring atoms in the crystal of PbS) was caused by the large atomic scattering factor or neutron scattering length of Pb. Atomic scattering factor f and neutron scattering length b of atom Pb are greater than those of S. The contributions of S-S pair are relatively small in the whole scattering angle in Figs. 6 and 7.

In the former reports,[4,12] there are two peaks of diffuse scattering in the 2θ region from 20 to 90° by CuKα radiation. The positions of peaks correspond to those of $\sin(Qr)/Qr$, where r is the atomic distance between first nearest neighboring atoms. The three peaks of diffuse scattering of PbS were observed in the same 2θ range by CuKα radiation as shown in Fig. 1. The contribution to the diffuse scattering from second nearest neighboring atoms was first confirmed.

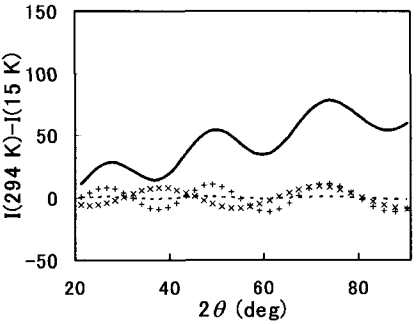

Figure 6. The difference between calculated X-ray diffuse scattering intensity at 294 and 15 K: total intensity I (solid line); contribution from Pb-Pb pair $I_{Pb\text{-}Pb}$ (plus mark), Pb-S pair $I_{Pb\text{-}S}$ (cross mark) and S-S pair $I_{S\text{-}S}$ (broken line) in crystal PbS.

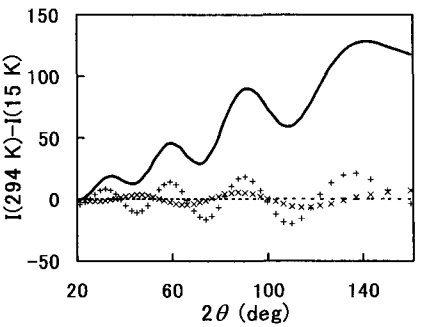

Figure 7. The difference between calculated neutron diffuse scattering intensity at 294 and 15 K: total intensity I (solid line); contribution from Pb-Pb pair $I_{Pb\text{-}Pb}$ (plus mark), Pb-S pair $I_{Pb\text{-}S}$ (cross mark) and S-S pair $I_{S\text{-}S}$ (broken line) in crystal PbS.

4. Conclusions

The correlation effects between thermal displacements of first and second nearest neighboring atoms were used to explain the profile of the oscillatory diffuse X-ray and neutron scattering of PbS. The main contribution to oscillatory diffuse scattering of PbS is from the contribution from second nearest neighboring atoms (Pb-Pb pair). The clear contribution from second nearest neighboring atoms was first obtained.

5. References

1. T. Sakuma, *Bull. Electrochem.* **11**, 57 (1995).
2. T. Sakuma and J. O. Thomas, *J. Phys. Soc. Jpn.* **62**, 3127 (1993).
3. T. Sakuma, *J. Phys. Soc. Jpn.* **62**, 4150 (1993).
4. K. Basar, T. Shimoyama, D. Hosaka, Xianglian, T. Sakuma and M. Arai, *J. Therm. Anal. Cal.* **81**, 507 (2005).
5. A. Thazin, M. Arai and T. Sakuma, in: B.V.R. Chowdari (Ed.), Solid State Ionics, World Scientific Pub., Singapore, 2002, pp. 777.
6. T. Sakuma, Y. Nakamura, M. Hirota, A. Murakami and Y. Ishii, *Solid State Ionics* **127**, 295 (2000).

7. M. Arai, K. Ohki, M. Mutou, T. Sakuma H. Takahashi and Y. Ishii, *J. Phys. Soc. Jpn. Suppl.* **A. 70**, 250 (2001).
8. T. Sakuma, T. Shimoyama, K. Basar, Xianglian, H. Takahashi, M. Arai and Y. Ishii, *Solid State Ionics* **176**, 2689 (2005).
9. T. Sakuma, Y. Nakamura, M. Hirota, M. Arai and Y. Ishii, *J. Phys. Chem. Solids* **60**, 1503 (1999).
10. K. Nakamura, K. Ihata, Y. Yokoyama, K. Nomura and M. Kobayashi, *Ionics* 7, 178 (2001).
11. F. Izumi and T. Ikeda, *Mater. Sci. Forum* **321-324**, 198 (2000).
12. T. Sakuma, *J. Phys. Soc. Jpn.* **61**, 4041 (1992).

ELECTRON AFFINITY AND WORK FUNCTION OF PYROLYTIC MnO_2 THIN FILMS PREPARED FROM $Mn(C_2H_3O_2)_2.4H_2O$

A. K. M. FARID UL ISLAM, R. ISLAM AND K. A. KHAN*

Department of Applied Physics and Electronics, University of Rajshahi, Rajshahi-6205, Bangladesh. Tel: +880 721 750254, Fax: +880 721 740064
**Email: kakhan_ru@yahoo.ca*

Undoped MnO_2 thin films have been prepared by a modified spray pyrolysis technique onto glass substrate in the thickness range 85-380 nm at a deposition rate of 6.7 nm/min and the effects of different variables on electrical and optical properties has been studied in detail. X-ray diffraction and Transmission Electron Microscopy studies show that MnO_2 films are homogenous and polycrystalline in structure. The Hall effect and thermoelectric studies indicate that the deposited samples are n-type semiconductor. Optical study in the entire wavelength range 0.3-2.5 μm range exhibits a high transmittance in the visible as well as in the infrared. The position of Fermi-level (E_F) is obtained from thermoelectric measurement and optical data exhibits a value of band gap. The calculation of electron affinity and work function are done in the polycrystalline MnO_2 samples. Their values are 2.94 to 297 eV and 2.83 to 287 eV, respectively. The calculation reveals that the bond between manganese and oxygen are considered as the principal bond and within the limits of native and foreign impurity contents, MnO_2 is more co-valent than ionic which supports the results of earlier works.

1. Introduction

Oxides of Manganese are of considerable interest because of their phase transformations as well as their uses in energy related device applications[1-4]. Manganese dioxide thin films are technology very important because of their potential use in electrochemical[1, 5], electrochromic[1] and fuel cell[6, 7] devices. In spite of much work on this material[1-7], conclusive evidence that would resolve differences of opinion concerning some of the properties of these oxides is lacking. This is attributable mainly variations in the film deposition techniques and also to some basic differences in the apparatus used by the different workers.

Very recently the authors designed an apparatus for the deposition of MnO_2 thin films by Spray Pyrolysis process. Undoped MnO_2 thin film prepared by this apparatus are of highly transparent (>90%) in the visible as well as in the entire infrared regions[8, 9, 10]. Before using this films as an electrode in cell fabrications, extensive studies of their different properties like the electron affinity and work function, with which we are concerned in this presentation, are important. To obtain the highest output from a n-oxide semiconductor/ p-base semiconductor cells, the conduction band discontinuity ($\Delta E_c = \chi_c - \chi_{oc}$) should be zero[9], χ_c and χ_{oc} are the electron affinity of the base semiconductor and the oxide semiconductor, respectively. An analysis shows that to get optimum performance, the work function of the oxide semiconductor should be less than or equal to the electron affinity of

the p-type base semiconductor. Thus, information about the work function and the electron affinity is required. From this point of view, the results of present investigation may be useful in making the electrodes in fuel cells operation considering MnO_2 thin films as one of the components.

2. Experimental

Undoped MnO_2 thin films prepared from a solution of Mn $(C_2H_3O_2)_2.4H_2O$ onto glass substrate by a suitable spray pyrolysis technique. It is a very simple, indigenous, low cost technique, which has not been used before for the deposition of MnO_2 films. The basic reaction involved in this process is

$$Mn(C_2H_3O_2)_2.4H_2O + H_2O \quad MnO_2 + 2CH_3COOH + 3H_2O + H_2 \qquad (1)$$

The detailed MnO_2 film preparation technique and its optimised parameters were described already in author's other work[8].

2.1. *Measurement Technique*

Electrical conductivity σ was measured as a function of temperature in the 303-413K ranges. The glass substrates were heated by a specially designed heater and the temperature was measured by a chromel-alumel thermo-couple placed on the middle of the substrate. The conductivity was obtained by applying a d.c. 1.5 V bias across the film with lead contact and recording the current and voltage simultaneously by using a four-probe Van-der-Pauw technique[10]. The thickness was measured by the Tolansky[11] interference method with an accuracy ± 5 nm. Optical studies were carried out with Perkin-Elmer Lamda-19 double beam spectrophotometer.

3. Results and Discussion

3.1. *Structural Study*

X-ray diffraction of MnO_2 films were done using a diffractrogram, Model MAC Science M18 X HF-SRA, Japan, using monochromatic Cu-K_α radiation. Peak intensities were recorded corresponding to 2θ values. Figure 1. shows an X-ray diffractogram of MnO_2 film of thickness 200nm deposited at a substrate temperature of 593K. The spectrum has remarkable peaks and indicates the films are polycrystalline in structure. Transmission Electron Microscopy was used to characterize microstructure of MnO_2 thin films. From the analysis of electron diffraction pattern the studied sample shows a homogeneous and polycrystalline in structure.

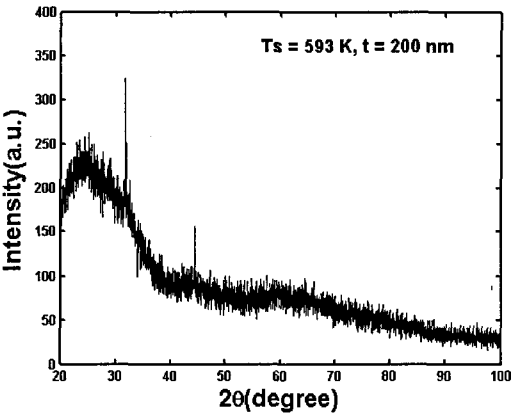

Figure 1. XRD pattern of MnO_2 film of thickness 200 nm deposited at substrate temperature 593 K.

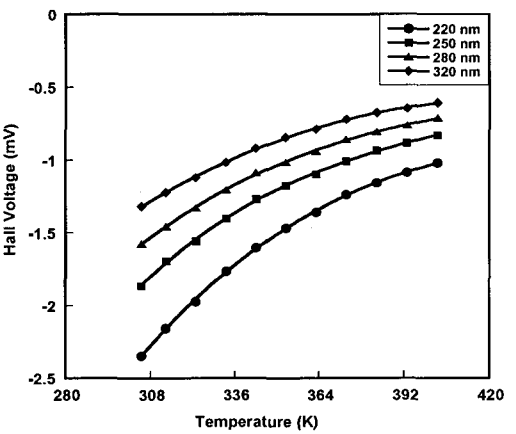

Figure 2. Variation of Hall voltage with temperature of annealed MnO_2 films.

3.2. *Hall Effect Measurements*

Hall effect studies were carried out by Van-der Pauws[10] technique in the temperature 300-410K ranges. The variation of Hall voltage with temperature of the annealed films of thickness 220, 250, 280 and 320 nm, respectively are shown in Figure 2. From this study, the negative sign of Hall voltage indicates that the MnO_2 samples are n-type semiconductor. In as-deposited films, however, it was very difficult to observe any appreciable Hall voltage.

3.3. *Thermoelectric Power*

The thermoelectric power measurement of MnO_2 films are carried out by the integral method[12] in the temperature range 300-410 K by taking pure metallic lead as reference metal. Figure 3. shows the value of thermo e.m.f. at different temperature for four samples of thickness 160, 200, 220 and 250 nm, respectively. It is observed that the thermo e.m.f. is negative with respect to lead (Pb). The negative sign of the thermo e.m.f indicates that the current carriers of the MnO_2 films are electron. Therefore, MnO_2 films are n-type semiconductor, which is well agreed with the Hall effect measurement.

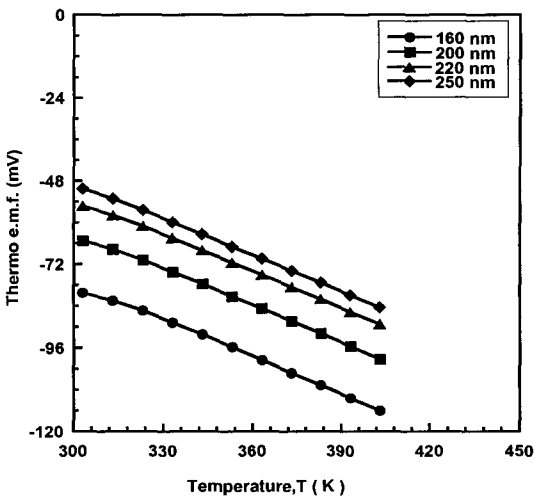

Figure 3. Variation of thermo e.m.f. with temperature of different thicknesses MnO_2 thin films.

3.4. *Optical Measurement*

The spectral normal transmittance $T(\lambda)$ and near normal reflectance $R(\lambda)$ were measured in the $0.3<\lambda<2.5\mu m$ wavelength range by a computerized double beam Perkin-Elmer Lambda-19 spectrophotometer. Figure 4. shows the spectral transmittance /reflectance vs. wavelength spectra for a 200, 280 and 380 nm annealed MnO_2 films, respectively. It is seen that the transmittance $R(\lambda)$ exhibits a significant transmittance in the visible as well as in the infrared region.

From the transmittance data, the optical band gap E_g has graphically been determined from the $(khv)^n$ vs. hv plots where $(khv)^n$ indicates optical absorption, n represents the nature of transition. The plot indicates the transition an allowed

indirect type with a band gap at $E_g = 0.26$ eV which is shown for a thick film of 200 nm in Figure 5.

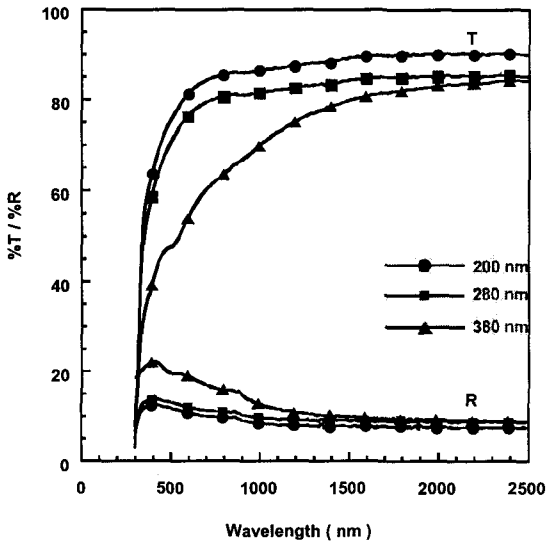

Figure 4. Optical spectra of different thickness of MnO_2 thin films deposited at 593 K.

3.5. *Electron Affinity and Work Function Calculation*

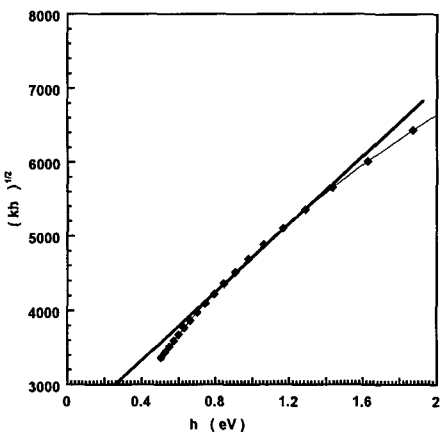

Figure 5. $(khv)^{1/2}$ vs. (hv) plot for a MnO_2 film of thickness 200 nm deposited at 593K.

To obtain the highest performance from an electrode in electrochromic and photoelectrochromic cells, the conduction band discontinuity ($\Delta E_c = \chi_s - \chi_{os}$) should

be zero where, χ_s and χ_{os} are the electron affinities of the base semiconductor and the oxide semiconductor, respectively.

According to Sanderson electronegativity principle[13], when two or more atoms initially different in electronegativity combine chemically, they adjust to have the same intermediate electronegativity within the compound. This intermediate electronegativity is given by the geometric mean of the individual electronegavity of the component atoms. The electronegativity of MnO_2 can be written as

$$E_n(MnO_2) = [E_{Mn} \times (E_O)^2]^{1/3} = [2.20 \times (3.65)^2]^{1/3} = 3.08 \text{ eV} \quad (2)$$

where $E_{Mn} = 2.20$ and $E_O = 3.65$ eV are the electronegativities on Mn and O_2 atoms, respectively and E_n is the electronegativity of MnO_2.

Semiconductors are generally co-valent in nature, but it is an established fact that no bond is purely co-valent or purely ionic in character but always a mixture. Using Sanderson's concept, percentage of ionic character, (y), of the bond between manganese and oxygen can be determined by using Pauling's electronagitivity values[13] in an empirical relation[14]

$$\% \text{ ionic character(y)} = [1 - \exp(-0.25\{E_{Mn} - E_O\}^2)] \times 100\% \quad (3)$$

$$\text{or, \% ionic character(y)} = 40.88\%$$

It may be explained from the calculation that the bonds between manganese and oxygen are considered as the principal bond and within the limits of nature and foreign impurity content, MnO_2 is more co-valent than ionic.

Electron affinity and work function are defined, respectively as the energy required to remove an electron from the bottom of the conduction band E_c, and from the Fermi level, E_F, to a position just outside the surface of the material (vacuum level). Here, in the absence of any straightforward method of determining the electron affinity of the bulk semiconductor, an indirect and empirical method[15] based on the electronegativities of the atoms has been used. In the case of semiconductors, the bulk electronegativity E_n correspond to the intrinsic Fermi-level E_F with respect to vacuum level is

$$E_F \quad E_n = \chi + E_g/2 \quad (4)$$

where χ is the electron affinity and E_g is the optical band gap between the conduction and valence bands. The position of E_F in a bulk semiconductor is determined by the regular crystallographic structure of the intrinsic material. The electronegativity can therefore be assumed here to be a constant parameter and the effect of change in impurity contents possible in the bulk material can be accounted for by a net change in the electron affinity of the sample.

From the optical data of MnO_2 thin films, the band gap E_g is obtained from the plot of $(khv)^{1/2}$ vs. hυ. The position of the Fermi-level E_F obtained from the thermoelectric data for MnO_2 film and the carrier concentration n is determined

from the Hall effect experiment. Figure 6. shows the variation of E_g and E_F, respectively, with carrier concentration n. From the curve (a) and taking E_n = 3.08 eV, the value of electron affinity χ of different MnO_2 samples is determined using Eq. (4).

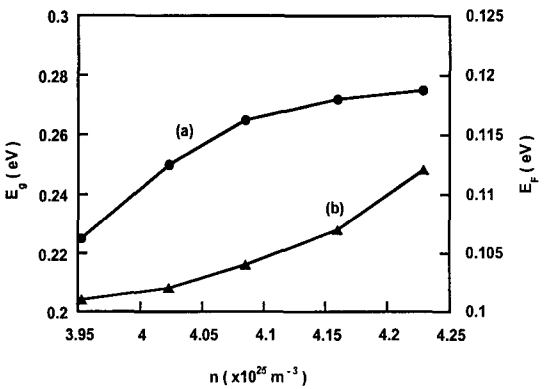

Figure 6. Variation of (a) band gap Eg and (b) Fermi energy E_F vs. carrier concentration n.

Using the values of χ and taking the values of E_F from curve (b), different values of work function (W) are obtained using the following equation[16]

$$W = \chi - E_F \tag{5}$$

The calculated values of electron affinity and work function of MnO_2 films are tabulated in the Table 1. It is found that the work function (W) of the samples varies from 2.83 to 2.87 eV. The values of χ are found to vary from 2.94 to 2.97 eV in the carrier concentration range 4.2×10^{25} to 3.9×10^{25} m^{-3}, respectively. The author's calculated value of electron affinity is well agreed with the reported value of electron affinity by other workers[17,18,19].

Table 1. Calculated values χ (eV) and W (eV) for MnO2 films.

n ($x10^{25}$ m-3)	E_F (eV)	E_g (eV)	χ (eV)	W (eV)
3.952	0.101	0.225	2.968	2.867
4.023	0.102	0.250	2.955	2.853
4.085	0.104	0.265	2.948	2.844
4.160	0.107	0.272	2.944	2.837
4.229	0.112	0.275	2.943	2.830

4. Conclusions

MnO_2 thin film has been prepared by spray pyrolysis technique. The deposition rate was of 6.7 nm/min. X-ray diffraction and Transmission Electron Microscopy studies show that the films are homogenous and polycrystalline in structure.

The calculation electron affinity and work function, are done in the polycrystalline MnO_2 samples. Their values are 2.94 to 297 eV and 2.83 to 287 eV, respectively. The calculation reveals that the bond between manganese and oxygen are considered as the principal bond and within the limits of native and foreign impurity contents, MnO_2 is more co-valent than ionic which supports the results of earlier works.

References

1. V. G. Bhide, Damle R. V and R. H. Dani, *Physica* ***25*** *, 579 (1959).*
2. V.G. Bhide and R. V. Damle, *Physica* ***26*** *, 33 (1960).*
3. R. M. Valletta and W. A. Pliskin, *J. Electrochem. Soc.: Solid State Science.* ***114****, No. 9, 944 (1967).*
4. T. Cordoba de, T. Susan and A. Gorenstein, *Electrochemic Properties of MnO_2 Thin Films*, G. A. Ertors Hugot, C. G. Granqvist and C. M. Lampert, *Proc. SPIE, Optical Material Technology for Energy efficiency and Solar energy Conversion XI, Chromogenics for Smart Windows,* ***1728,*** *92 (1992).*
5. S. Komaba, N. Kumagai, M. Baba, F. Miura, N. Fujita and H. Groult et al, *J. Appl. Electrochem.* ***30****(10), 1179 (2000).*
6. A. Kozawa, *J. Electrochem. Soc.* ***134****(4), 780 (1987).*
7. I. A. Raj and K. I. Vane, *Int. J. Hydro Energy* ***15****(10), 751 (1990).*
8. A. K. M. Faridul Islam, R. Islam and K. A. Khan, *J. Renewable Energy,* ***30,*** *2289 (2005).*
9. H. J. Hovel, *Vol. 2, edited by R. K. Willardson and A. C Beer (Academic Press N. Y. 1975).*
10. K. L. Chopra, *Thin Film Phenomena, New York, McGraw Hill;* ***85*** *(1969).*
11. S. Tolansky, *Multiple Beam Interferometry of Surface & Films, London, Oxford University Press (1948).*
12. V. D. Das and J. C. Mohanty, *J. Appl. Phys.* ***54****(2), 97 (1983).*
13. R. T. Sanderson, *Chemical Periodicity, Reinhold, New York, (1960).*
14. S. H. Maron, and J. B. Lando, *Fundamentals of Physical Chemistry, MacMillan, New York, (1974).*
15. M. A. Butler and D. S. Ginley, *J. Electrochem. Soc.* ***125****, 228 (1978).*
16. M. N. Islam and M. O. Hakim, *J. Material Sci. letters,* ***5****, 63 (1986).*
17. E. B. Rudnyi, E. A. Kaibicheva and L. N. Sidorov, *Rapid Commun. Mass Spectrom. 7, 800 (1993).*
18. G. L. Gutsev, B. K. Rao, P. Li. X. Jena and L. S. Wang, *J. Chem. Phys.* ***113,*** *1473 (2000).*
19. A. Pramann and K. Rademann, *Int. J. Mass, Spectrom.* ***187****, 673 (1999).*

CRYSTAL STRUCTURE AND HEAT CAPACITY OF $Ba_3Ca_{1.18}Nb_{1.82}O_{8.73}$

TOMOTAKA SHIMOYAMA,[A] JUN SAGIYA,[A] TAKEO TOJO,[A]
HITOSHI KAWAJI,[A] TOORU ATAKE,[A] NAOKI IGAWA,[B] YOSHINOBU ISHII[B]

[A]Materials and Structures Laboratory, Tokyo Institute of Technology, Yokohama 226-8503

[B]Japan Atomic Energy Agency, Tokai, Ibaraki 319-1195

The proton conductor $Ba_3Ca_{1.18}Nb_{1.82}O_{8.73}$ (BCN18) was synthesized by a method of solid state reaction. The structural and thermodynamic properties were studied for dry BCN18, water-solved sample (BCN18-H) and deuterated water-solved sample (BCN18-D), by dielectric permittivity and heat capacity measurements, and by powder X-ray and neutron diffraction experiments carried out at SPring-8 and at JAEA, respectively. The existence of OH(OD) group in the water-solved samples was confirmed, and the motion of the group above 230 K was discussed.

1. Introduction

Since the discovery of proton conductors of perovskite-type oxide by Iwahara and Takahashi in 1978 [1], a variety of proton conductors have been found. The proton conductivity of $10^{-2}\sim10^{-3}$ Scm^{-1} has been attained in some perovskite-type oxide compounds at about 600 °C in the atmosphere including hydrogen source such as the hydrogen gas and steam, etc. It is well known that the tetravalent cations at B-site of perovskite oxides, $A^{2+}B^{4+}O_3$, can be substituted with lower valence cations (such as Gd^{3+} or Y^{3+}, etc.), and the substituted compounds exhibit high proton conductivity in hydrogen atmospheres [2]. These materials are of particular interest because of their potential applications as electrolytes in solid state fuel cells, steam electrolyzers and hydrogen sensors, etc. Recently, a new series of complex perovskite oxide, $A_3(B^{2+}B^{5+}_2)O_9$, has been found; the non-stoichiometric compounds (shifted slightly from the ratio of $B^{2+}/B^{5+} = 1 : 2$) show very high proton conductivity [3]. The nonstoichiometry leads to formation of some defects, such as oxygen vacancies in the crystal, and the defects should cause high proton conductivity. Among them, $Ba_3Ca_{1+x}Nb_{2-x}O_{9-3x/2}$ is an excellent candidate as a high temperature proton-conducting electrolyte, since a large amount of water/hydrogen can be solved in the crystal, and the electrical conductivity would be comparable to that of the best oxygen-ion conductors like Y-stabilized zirconia [3-5]. Especially, $Ba_3Ca_{1.18}Nb_{1.82}O_{8.73}$ (BCN18) has been known as the highest proton conductor, and the mechanism of the proton solubility and the conductivity has been studied extensively. However, the structural and thermodynamic properties have not been clarified yet. In the present study, the effects of the water/hydrogen dissolution on the lattice vibrations and crystal structure have been studied by heat capacity, electrical permittivity, X-ray powder diffraction and neutron diffraction measurements.

2. Experimental

Polycrystalline sample of $Ba_3Ca_{1.18}Nb_{1.82}O_{8.73}$ (BCN18) was synthesized by a method of solid state reaction [6,7]. $BaCO_3$ (RARE METALLIC Co., Ltd., 99.99 %), Nb_5O_2 (MITSUI MINING & SMELTING Co., Ltd., 99.99 %) and $CaCO_3$ (RARE METALLIC Co., Ltd., 99.99 %) were weighed and mixed in an alumina motor with small amount of ethanol. The mixture was dried in the air, and the powder was calcined in an alumina crucible at 1000 ℃ for 20 h. The product was ground, pressed into pellets, and then sintered at 1500 °C for 24 h in the air. The dry sample (no water/hydrogen; denoted as dry BCN18) was prepared by heating the specimen at 900 ℃ for 20 h in vacuum. The water-solved sample (BCN18-H) was prepared by holding the dry sample in water vapor of about 3 kPa (saturated vapor pressure of water at room temperature) at 350 ℃ for 60 h. The deuterated water-solved sample (BCN18-D) was also prepared in D_2O vapor by the same procedure.

The dielectric permittivity was measured in the frequency region from 1 kHz to 1 MHz using a LCR meter (Model 4284A, Yokogawa Hewlett Packard, Ltd.) from 20 K to 300 K in helium gas atmosphere. An impedance analyzer (Model 4192A LF Impedance Analyzer, Yokogawa Hewlett Packard, Ltd.) was used for higher temperature measurements up to 420 K from 80 K in the air. For further high temperature region from 300 K to 520 K, the measurement was made in vacuum for the dry BCN18 sample, and in helium gas atmosphere for BCN18-H and BCN18-D samples.

The powder X-ray diffraction measurements with synchrotron radiation were carried out at the BL02B2 beam line of SPring-8 of Japan Synchrotron Radiation Research Institute (JASRI) with a wavelength of 0.41509 Å. The powder neutron diffraction measurements were carried out using the high resolution powder diffractometer (HRPD) installed at the Japan Research Reactor 3 at the Japan Atomic Energy Agency (JAEA) with a wavelength of 1.8233 Å. The neutron diffractionn data were collected with constant monitor counts and a step angle of 0.05° over the 2θ range of 2.5°- 160°. The diffraction patterns were analyzed by the Rietveld method using RIETAN-2000 [8].

The heat capacity was measured from 2 K to 300 K by using a relaxation calorimeter (PPMS, Quantum Design Inc.). For the use of the calorimetry, the sintered sample was shaped into a disk of about 3 mm diameter and 1 mm thickness. The sample mass was about 10 mg.

3. Results and Discussion

From the dielectric measurements of the samples of $Ba_3Ca_{1.18}Nb_{1.82}O_{8.73}$ (dry BCN18 and BCN18-H), the dielectric loss angle, $\tan\delta$, was obtained; the results are shown in Figs.1 and 2. No dielectric dispersion nor relaxation phenomenon is observed in dry BCN18, while a dielectric dispersion is seen in the water-solved samples (BCN18-H (10.4, 6.7 and 15.0 mol%)) above 230 K. In the dispersion region, the value of $\tan\delta$ increases with increasing the water

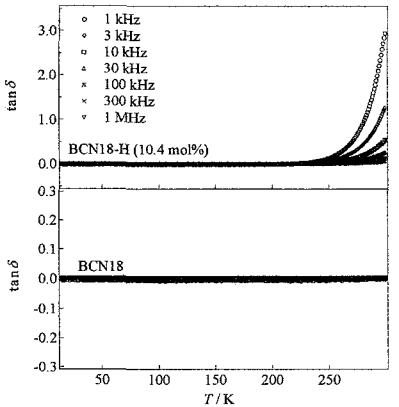

Fig.1. Dielectric loss, tanδ, of dryBCN18 and BCN18-H for various frequencies from 1 kHz to 1 MHz.

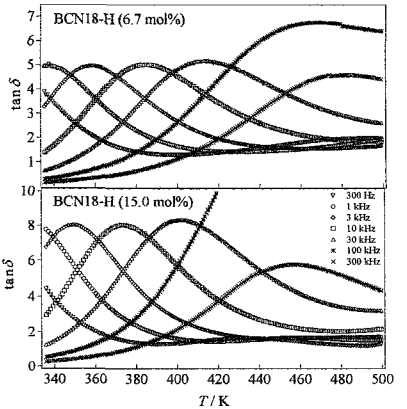

Fig. 2. Dielectric loss, tanδ, of dry BCN18 and BCN18-H for various frequencies from 300 Hz to 300 kHz.

content. The activation energy calculated from Arrhenius plot of the frequency and the peak temperature of tanδ is 0.55 eV, which is reasonable for electric dipole of OH group in the crystal. The proton conduction should be greater than that of oxide ion in this temperature region, where the number of corresponding oxide ion vacancies is negligibly small [9]. Thus, the dipole relaxation should be caused not by hopping of oxide ions, but by orientation of OH group. The present value of the activation energy is close to the value of 0.53 eV obtained from the proton mobility [10].

The powder X-ray diffraction patterns of dry BCN18 and BCN18-H (15.0 mol%) measured with synchrotron radiation at room temperature are shown in Fig. 3. Both patterns are very similar, but the peaks of BCN18-H shift to lower angles compared to dry BCN18. This shows that the crystal lattice expands due to solving of water. A Rietveld refinement has been carried out to clarify the crystal structure of dry BCN18 and BCN18-H. The lattice constant and the atomic displacement factors B of BCN18-H are larger than those of dry BCN18. Especially, the large B value of oxide ions at 24*e*-site indicates that the position of the oxide ion is affected by the proton which exists around the oxide ion.

The neutron diffraction experiments were done at room temperature for dry BCN18 and deuterated water-solved sample (BCN18-D (26.0 mol%)). The results of diffraction patterns are shown in Fig. 4. The peaks of BCN18-D are shifted to lower angles compared to those of dry BCN18 as well as the powder X-ray diffraction. The difference in the relative intensity is clearly observed between dry BCN18 and BCN18-D, which should be caused by the introduction of oxide ions at the oxygen vacancy sites and the deuterons at in the interstitial sites of BCN18-D.

The lattice constant and the large B value of oxide ions at 24*e*-site agree with the results of powder X-ray diffraction experiments. The values of S and R factors are improved by arranging deuterium on 96*j*-site.

The heat capacity of dry BCN18, BCN18-H and BCN18-D has been measured between 2 K and 300 K. The results show no anomaly in the heat capacity curves, which indicates no phase transition in the samples in the covered temperature region. The heat capacity of dry BCN18 was smaller than those of water-solved samples, and the heat capacity increased with increasing the water content.

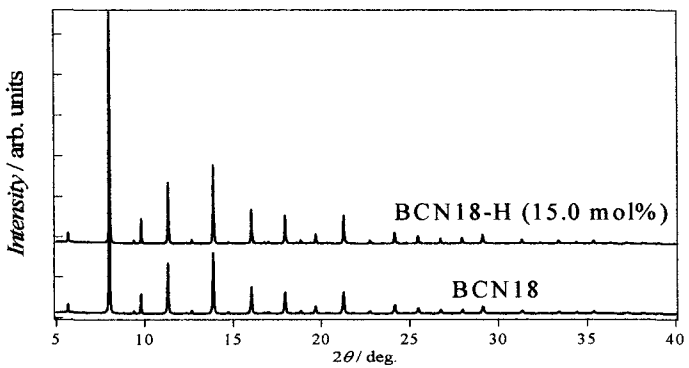

Fig. 3. Powder X-ray diffraction patterns obtained with the synchrotron radiation for dry BCN18 and BCN18-H (15.0 mol%).

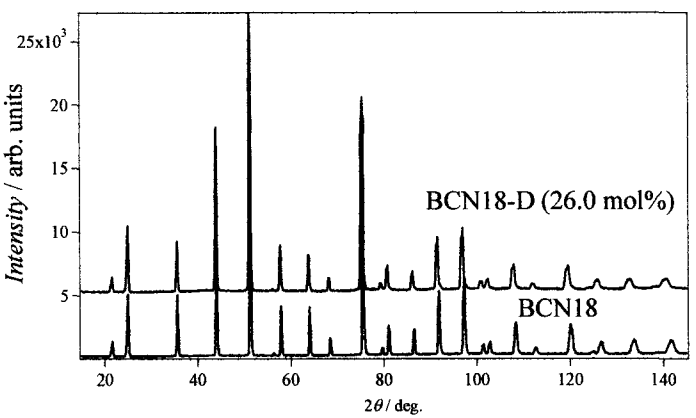

Fig. 4. Neutron diffraction patterns of dry BCN18 and BCN18-D (26.0 mol%).

4. Summary

The samples of proton conducting compound $Ba_3Ca_{1.18}Nb_{1.82}O_{8.73}$ (BCN18) were synthesized by a method of solid state reaction. The structure and the properties of dry BCN18, water-solved sample (BCN18-H) and deuterated water-solved sample (BCN18-D) were studied by dielectric permittivity and heat capacity measurements, and X-ray diffraction and neutron diffraction. The effects of solving of water were clearly detected in the results. The results of dielectric loss, $\tan\delta$, shows relaxation phenomena in the water-solved samples due to the motion of OH group above 230 K. The peak height of $\tan\delta$ increases with increasing of water content in the crystal. From Arrhenius plot of the frequency and the peak temperature, the activation energy was estimated as 0.55 eV, which was comparable to the value of 0.53 eV obtained from the proton mobility [10]. The results of the powder X-ray diffraction and the powder neutron diffraction gave detailed structural information about OH(OD) in the crystal. Further detailed analysis is under way.

References

[1] H. Iwahara, T. Esaka, H. Uchida and N. Maeda, *Solid State Ionics*, **3-4** (1981) 359.

[2] H. Iwahara, *Solid State Ionics*, **52** (1992) 99.

[3] K.C. Liang and S. Nowick, *Solid State Ionics*, **61** (1993) 77.

[4] M. Weller, H. Schubert, *J. Am. Ceram. Soc.*, **69** (1986) 573.

[5] A.S.Nowick, Y.Du, *Solid State Ionics*, **77** (1995) 137.

[6] H.G. Bohn, T. Schober, T. Mono, *Solid State Ionics*, **177** (1995) 219.

[7] B. Groβ, St. Marion, *Solid State Ionics*, **109** (1998) 13.

[8] F. Izumi and T. Ikeda, *Mater. Sci. Forum.*, **198** (2000) 321.

[9] O. Kamishima, Y. Abe, T. Ishii, J. Kawamura and T. Hattori, *J.Phys.-Condens. Mat.* **16** (2004) 4971

[10] H.G. Bohn, T. Schober, T. Mono, W. Schilling, *Solid State Ionics*, **117** (1999) 219.

XPS AND IMPEDANCE INVESTIGATIONS ON AMORPHOUS VANADIUM OXIDE THIN FILMS

M. KAMALANATHAN[1*], R.T. RAJENDRA KUMAR[2], M.VIJAYAKUMAR[3], N.PASUPATHI[1] and S. SELVASEKARAPANDIAN[4]

[1] *Department of Electronics, Erode Arts College, Erode -638009, Tamil Nadu, INDIA*

[2] *School of Physical Sciences, National Center for Plasma Science and Technology (NCPST), Dublin City University, Glasnevin, Dublin, IRELAND*

[3] *Department of Physics, College of William and Mary, Williamsburg, VA-23187, USA*

[4] *Department of Physics, Bharathiar University, Coimbatore-641046, INDIA*

**Email: smvkumar@gmail.com*

The vanadium oxide thin films have been prepared by thermal evaporation method. The films coated on glass and silicon substrate are subjected to vacuum annealing at 573K. The X-ray diffraction analysis shows both as deposited and annealed films are amorphous in nature. Scanning Electron Microscope (SEM) analysis shows vacuum annealed films has smooth surface topography, which is suitable for device applications. X-ray photoelectron spectroscopy (XPS) study shows that the as-deposited vanadium oxide films and vacuum annealed films are sub-stoichiometric nature. Further, the presence of vanadium in lower oxidation states i.e.V^{4+} suggests that the chemical composition of the film is partially vanadium pentoxide (i.e, $V_{2-x}O_{5-y}$). Electrical characterization shows that the resistance of the vanadium oxide film is ~10^6 Ohms. Frequency dependent conduction and impedance studies shows the high resistive electronic conduction process.

1. Introduction

In recent years, the development of thin film rechargeable batteries has attracted a great deal of interest due to their reduced resistance with respect to bulk materials, and due to the technological perspectives of integration with other thin film devices. Especially the miniaturized devices, such as implantable medical devices, CMOS-based integrated circuits, as well as smart IC packages or chips needs rechargeable power supplies [1]. The thin film lithium batteries considered to be best suited for such technological applications, and various researches are in progress towards this goal. The extensive characterizations of electrode materials are essential for construction of better thin film lithium batteries. The transition metal oxides, especially vanadium pentoxide (V_2O_5) are excellent candidate for the electrode materials [2]. V_2O_5 was first suggested as a cathode material for intercalation batteries by Day in the 1970s [3] because of their layered structure and the rechargeable high energy densities and capacities [4]. The properties of the V_2O_5 films strongly depend on the synthesis procedure. The different deposition methods and film characteristics have been reviewed recently [5]. Despite the various studies, however, further improvements in the functional behavior of the films are required and a clear correlation of the structural changes and the electrical properties is necessary. The main purpose of the present work is to study the structure,

composition and electrical properties of V_2O_5 thin films prepared by physical vapor deposition (PVD) and especially the vacuum annealed samples.

2. Experimental

V_2O_5 powder (99.999%, Alfa Aeasar, UK) was used for deposition. Vanadium oxide thin films were deposited on highly cleaned glass and (111) oriented silicon substrates under a vacuum of 10^{-5} mbar by using thermal evaporation technique (HINDHIVAC 12A4). The films were deposited at ambient substrate temperatures followed by vaccum (>10^{-5} mbar) annealing at 573K. The thickness of the films was measured by using multiple beam interferometry method and found to be 180-210 nm. The X-ray diffraction (XRD) patterns of the deposited films were recorded with the help of Rigaku) using Cu Kα radiation (40 kV; 150 mA) in the range from 10° to 70° (2θ) with the scanning speed of 0.02°(2θ)/sec. The SEM and EDAX measurements are carried out on vanadium oxide thin films coated on silicon substrate using JEOL SEM/EDAX system. The dielectric, impedance and ac conduction measurements were carried by using HIOKI 3532 LCR meter in the frequency range 50 Hz to 4 MHz in the temperature range of 300 to 420 K.

3. Results and Discussion

3.1 XRD analysis

The X-ray diffraction (XRD) studies are carried over both as deposited and vacuum annealed samples and shown in Figure 1. The absence of any specific x-ray diffraction lines clearly shows the amorphous nature of thin films. These results i.e, amorphous nature of as deposited and vacuum annealed (at 573K) are in good agreement with recent report by R.T.Rajendrakumar [6]. From featureless XRD spectrum it is quite classical to conclude that both films are amorphous in nature.

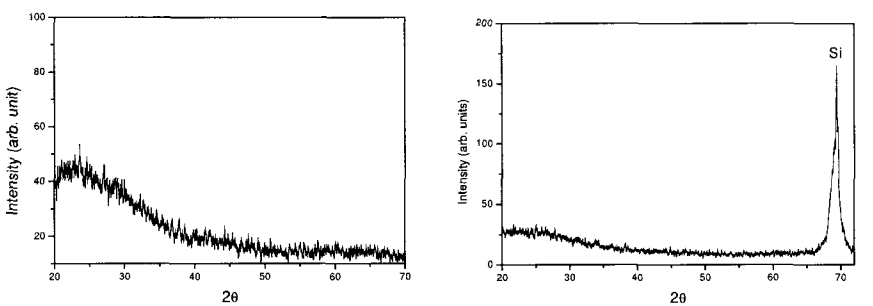

Fig.1 XRD pattern of as deposited (left) and vacuum annealed (right) vanadium oxide thin films. (The peak around 70° in vacuum annealed films is due to silicon substrate)

3.2 Surface morphology

Figure 2 show the micrograph of vanadium oxide film deposited on silicon substrates and vacuum annealed at 573 K. From the figure it is evident that the films are having slight rough surface topography. The as deposited V_2O_5 films (before annealing) show no specific feature (not shown here). But in the case of the films annealed at higher temperature rectangular like grains and also good grain to grain connectivity was observed which ensures the influence of the annealing on the surface morphology of the films.

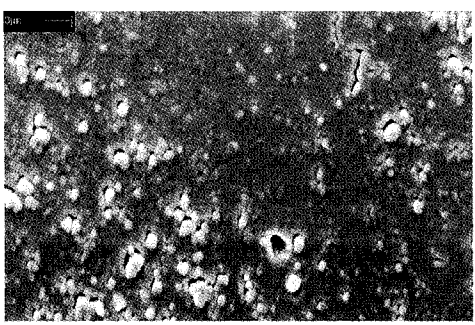

Fig 2. SEM of vacuum annealed vanadium oxide thin films on silicon substrate

It is worth to be mention that rod/plate like surface morphology was reported by Umadevi et al [7] for the screen printed V_2O_5 films. Moshfegh and Ignatiev [8] have observed nearly rectangular shape like microstructure for the V_2O_5 films annealed at oxidizing atmosphere. The role of vacuum annealing at 573K on the film microstructure can be understood by comparing these results with the previous XRD results. The absence of any XRD lines, of these films shows that the small grains, seen in SEM are completely amorphous in nature.

3.3 X-ray Photoelectron spectroscopy

The x-ray photoelectron spectroscopy (XPS) gives qualitative information about the chemical composition of the materials. Figure 3 shows the XPS spectra of vanadium oxide films on silicon substrates in the vanadium to oxygen region (500 - 540 eV). The observed peaks and respective energy position are labeled based on the 284.5 eV C 1s as reference. The peak at ~517.5 ev can be labeled as the photo emission from $V_{2p3/2}$ and is in a good agreement with the previously reported values [7]. It is well known that t the $V_{2p3/2}$ peak with binding energies of 517.5–518.2 eV represents vanadium oxidation state V^{+4} and the V^{+5} oxidation state is known to have peak between 516.5 and 517.2 eV [8]. Since the energy splitting between the V^{+5} and V^{+4} oxidation states is less than 1 eV, it is hard to label the peak by arbitrary

method. However it is possible to distinguish between the two peaks by using the peak deconvolution of the V $2p_{3/2}$ peak. The Gaussian type peak fitting has been carried out and two Gaussian components are found with binding energies of 517.5 eV for V^{+5} and 516.9 eV for the V^{+4} species, respectively. The integral area of the Gaussian component respective to the V^{+4} and V^{+5} peak are found to be 75% and 25% respectively. The presence of V2p3/2 peaks represents V^{5+} species, hence by confirming the formation of V_2O_5 component in the present study.

Other peaks in the spectra can be labelled as V $2p_{1/2}$ (~524 ev) and O1s (533 eV). Since the interference of the oxygen satellite peaks resulting from the Mg $K\alpha_3$ and $K\alpha_4$ radiation (detector material of XPS instrument) with the V $2p_{1/2}$ feature makes its quantitative analysis difficult. As suggested by Coulston et al.[9], the energy difference between the O 1s and V $2p_{3/2}$ lines can be used as a measure for an (effective) "average oxidation state" V^{ox}_{eff} . For well-defined vanadium oxide samples, a linear relation has been reported as [10],

$$V_{eff}^{ox} = 13.82 - 0.68[E_b(O_{1s}) - E_b(V_{2p3/2})] \qquad (1)$$

which yield a value of $V^{ox}_{eff} = 4.4$. However, it has to be taken into account that the above linear relation somewhat dependent on the photoelectron spectrometer.

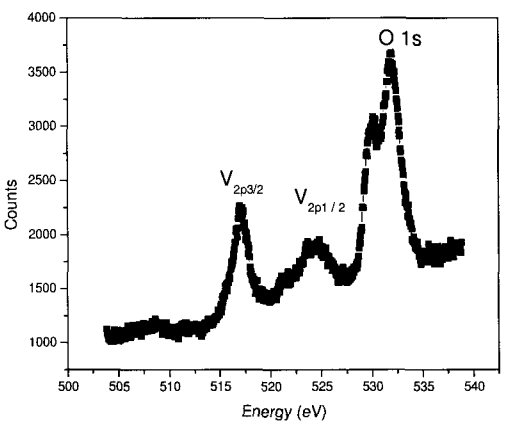

Fig.3. O_{1s} $V_{2p1/2}$ and $V_{2p3/2}$ photoelectron peaks of a vanadium oxide thin films

3.4 Conductance spectra analysis

The AC conductivity $\sigma(\omega)$ of any electrical conductors usually can be described using the Jonscher's universal power law [11].

$$\sigma(\omega) = \sigma_{dc} + A\omega^n \qquad (2)$$

Where n is the frequency exponent in the range 0<n<1. Both σ_{dc} and A are thermally activated quantities.The ac conductivity spectra of vacuum annealed vanadium oxide thin films are shown in Fig. 4. The conductance spectra consist of three different regions. At low frequencies (approx. 10^3Hz), frequency plateau region can be associated with the d.c. conductivity of vanadaium oxides. The high frequency dispersion is associated with the bulk relaxation phenomena in the vanadium oxide. The conductivity spectra curves at various temperatures are fitted to Eq.2 and "n" values are found to be 0.54 over the temperature range studied, which matches with reported values for other disordered materials. This value agrees with amorphous nature of vanadium oxide films.

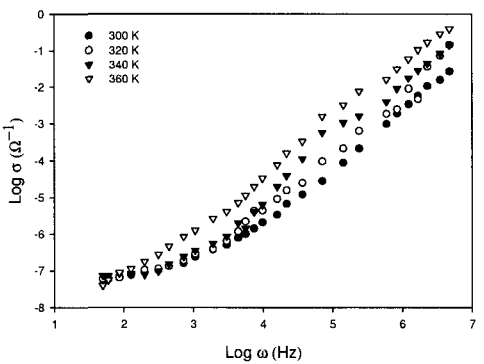

Fig. 4. Conductance spectra of vacuum annealed vanadium oxide thin films

3.5 Impedance Spectra Analysis

Figure 5, show the complex impedance plots also known as Cole-Cole plot, drawn at two different temperatures. The data fall on an asymmetric arc by comparison with a perfect semicircle. It is grossly distorted. These high frequency region semicircles are due to parallel combination of bulk resistance (R_b) and bulk capacitance (C_b) of the vanadium oxide materials. The depression of the semicircle below the real axis shows the non-Debye nature of the material, which is quite common property of disordered and amorphous conductors. The bulk resistance of the sample at various temperatures has been calculated from the low frequency interception of real axis using the programme EQ [12]. The bulk resistance (R_b) extracted from Cole-Cole plot is found to be in the order of 10^6 ohm. The bulk resistance found to be decreasing with increase in temperature, which causes decrease in radius of the semicircle. The associated capacitance was calculated from the relation $\omega RC = 1$ at the arc maximum (Fig.5) and it corresponds to a value of 2 pF, that is attributed to a conduction process through the bulk of the material [13]. The absence of more than one semicircle certainly signifies the dominance of the bulk without the effect of any other capacitive components. It suggests that the

response to originate from single parallel RC combination [14] which is shown in figure 6. The low frequency spike is due to electrode-material interfacial phenomena. The possible charge carrier transformation between electrode and vanadium oxide thin films gives this high dispersion result as a spike. The contribution of this part of the spectrum increases with an increase in temperature due to the increase of conductivity.

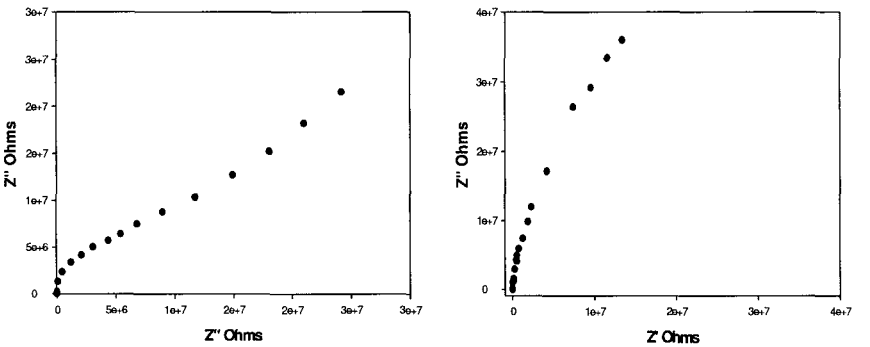

Fig.5. Impedance plot of vacuum annealed vanadium oxide film at 300K (left) and 340K (right)

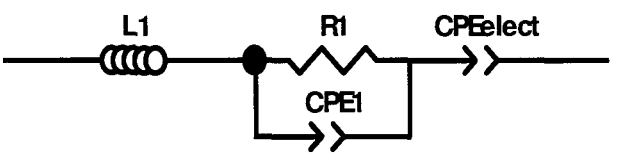

Wires / Bulk Property (low frequency semicircle) / electrode effect

Fig.6 Equivalent circuit analysis of vacuum annealed vanadium oxide film

4. Conclusion

Vanadium oxide thin films are deposited by using vacuum thermal evaporation method and vacuum annealed at 573 K in a vacuum better than 10^{-5} torr. The XRD & SEM analysis shows that the as deposited and vacuum annealed (573K) vanadium oxide films are amorphous with smooth surface. XPS study shows that the as-deposited vanadium oxide films and vacuum annealed films are found to be sub-stoichiometric with more oxygen vacancies.Electrical conductivity of the V_2O_5 films found to be 10^6 ohms and this high resistance may be attributed to the formation of the oxygen vacancies, which has been revealed from XPS.

ACKNOWLEDGMENTS

The author M. Kamalanathan thanks, the Research Scholars of Solid State and Radiation Physics Laboratory, Bharathiar University, India for their fruitful discussions and kind support in film coatings.

References

1. (a) J.B. Bates, N.J. Dudney, B. Neudecker, A. Ueda and C.D. Evans. *Solid State Ionics* **135** (2000) 33. (b) J.-G. Zhang, P. Liu, J.A. Turner, C.E. Tray and D.K. Benson. *J. Electrochem. Soc.* **145** (1998), 1889.
2. (a) A. Talledo and C.G. Granqvist. *J. Appl. Phys.* **77** (1995), p. 4655. (b) D.W. Murphy, P.A. Christian, F.J. Disalvo and J.N. Carides. *J. Electrochem. Soc.* **126** (1979) 497.
3. A.N. Day, B.P. Sullivan, U.S. Pat. 3,655,585 (1972).
4. J.S. Braithwaite, C.R.A. Catlow, J.D. Gale and J.H. Harding. *Chem. Mater.* **11** (1999), p. 1990
5. C.G. Granquist, Handbook of Inorganic Electrochromic Materials. , Elsevier, Amsterdam (1995)
6. R.T. Rajendra Kumar, Ph.D thesis (2002), Bharathiar University, India.
7. G P. Umadevi, C.L. Nagendra, G.K.M. Thutupalli, *Sens. Actuators* A, 39 (1993) 59.
8. A.Z. Moshfegh and A. Ignatiev, *Thin Solid Films*, 198 (1991) 2.
9. M. Abon, K.E.Bere, A.Tuel, P.Delkhere, *J. Catal.* 156 (1995) 28.
10. G.W.Coulston, E.A.Thompson, N.Herron, *J.Catal.* 163 (1996) 122.
11. A.K. Jonscher, Dielectric Relaxation in Solids, Chelsea, London, (1983).
12. B.A. Boukamp. *Solid State Ionics* 18–19 (1986)136.
13. D.C. Sinclair and A.R. West, J. Appl. Phys., 66 (1989) 3850.
14. L.M. Hodge, M.D. Ingram and A.R. West, J. Electroanal. Chem., 74 (1976) 125

SINTERING AND MIXED ELECTRONIC-IONIC CONDUCTING PROPERTIES OF $LA_{1.9}SR_{0.1}NIO_{4+\delta}$ DERIVED FROM A POLYAMINOCARBOXYLATE COMPLEX PRECURSOR

DUAN-PING HUANG, QING XU†, FENG ZHANG, WEN CHEN, HAN-XING LIU, JIAN ZHOU

School of Materials Science and Engineering, Wuhan University of Technology, Wuhan 430070, People's Republic of China

$La_{1.9}Sr_{0.1}NiO_{4+\delta}$ with a pure K_2NiF_4 phase was synthesized from a polyaminocarboxylate complex precursor with diethylenetriaminepentaacetic acid (H_5DTPA) as ligand, and the effect of sintering temperature on the microstructure and mixed electronic-ionic conducting properties of $La_{1.9}Sr_{0.1}NiO_{4+\delta}$ ceramic was investigated in the range of 1400-1600 ℃. Homogeneous and fine powder (100-200 nm) with a pure K_2NiF_4 phase was produced by calcining the complex precursor at 900 ℃ for 2 h in air. The increase of sintering temperature promoted the microstructural densification. Compared with a gradual increase of grain size with sintering temperature in the range of 1400-1500 ℃, there is an exaggerated grain growth in the specimens sintered at 1550 ℃ and 1600 ℃, respectively. Increasing sintering temperature from 1400 ℃ to 1500 ℃ resulted in an enhancement of electrical and ionic conducting properties. Further increase of the sintering temperature above 1500 ℃ declined the electrical and ionic conducting properties. The variation of the mixed conducting properties with sintering temperature was interpreted for the viewpoint of microstructural evolution. With respect to the mixed conducting properties, the preferred sintering temperature was ascertained to be 1500 ℃ for $La_{1.9}Sr_{0.1}NiO_{4+\delta}$. The specimen sintered at 1500 ℃ exhibits an electrical conductivity of 86 S/cm and an oxygen ionic conductivity of 3.8×10^{-2} S/cm at 800 ℃.

1. Introduction

Mixed electronic-ionic conductors have drawn considerable research interest because of their potential in various technological applications, such as cathodes for intermediate temperature (600-800 ℃) solid oxide fuel cells (SOFCs), oxygen separation membranes, membrane reactors for syngas production and catalysts for oxidation of hydrocarbons [1-4]. It has been well established that using the mixed conductors as cathodes for intermediate temperature SOFCs results in a decrease of cathode polarization at the triple phase boundary (TPB) [5, 6]. In the past decade, much work on the cathode materials for intermediate

† Corresponding author. Tel.: +86 27 87863277; fax: +86 27 87864580.
E-mail address: xuqing@mail.whut.edu.cn (Q. Xu).

temperature SOFCs focused on oxygen-deficient perovskite-type oxides such as $La_{1-x}Sr_xFe_{1-y}Co_yO_{3-\delta}$ (LSFC). However, the LSFC materials suffer from excessively high thermal expansion coefficients, making it difficult in matching with other components of intermediate temperature SOFCs. Recently, oxygen hyperstoichiometric $La_2NiO_{4+\delta}$ based compounds with a K_2NiF_4 structure have attracted growing attention as a novel mixed conductor [7-10]. These materials exhibit high oxygen diffusion and surface exchange coefficients at intermediate temperatures together with moderate thermal expansion coefficients around 13.0×10^{-6} K^{-1} [11, 12]. These desired properties make them promising candidate materials as cathodes for intermediate temperature SOFCs.

Microstructure is an important contributing factor to the transport properties of mixed conducting materials [13].Thus, the influence of sintering temperature on the microstructure and mixed conducting properties of $La_2NiO_{4+\delta}$ based compounds is an intriguing subject of significant important. Up to date, the research on this topic is still limited. It has been suggested that partial substitution of lanthanum with lower valence cations, such as Sr, improves the electrical conductivity of $La_2NiO_{4+\delta}$ [14]. In this work, $La_{1.9}Sr_{0.1}NiO_{4+\delta}$ was synthesized from a polyaminocarboxylate complex precursor with diethylenetriaminepentaacetic acid (H_5DTPA) as ligand. The microstructure and mixed conducting properties of $La_{1.9}Sr_{0.1}NiO_{4+\delta}$ ceramics were investigated in the sintering temperature interval 1400-1600 ℃.

2. Experimental

Reagent grade lanthanum hydroxide ($La(OH)_3$), nickel carbonate ($NiCO_3{\cdot}2Ni(OH)_2{\cdot}4H_2O$), strontium carbonate ($SrCO_3$) and diethylenetriaminepentaacetic acid (H_5DTPA) were used as starting materials. The lanthanum hydroxide, strontium carbonate and nickel carbonate were weighed, respectively, according to the nominal composition of $La_{1.9}Sr_{0.1}NiO_{4+\delta}$ and dissolved into deionized water in a beaker. A designed amount of H_5DTPA was then added. The mole ratio of H_5DTPA to total metal cation content was 1.7:3.0. The mixture was stirred at 90 ℃ to form a blue and transparent aqueous solution. The aqueous solution was heated in an oven at 100 ℃ to yield a solid polyaminocarboxylate complex. The solid complex precursor was pulverized and calcined at 800-950 ℃ for 2 h in air. The calcined powders were uniaxially pressed into rectangular bars ($30\times4\times4$ mm^3) and disks (13 mm in diameter and 2 mm in thickness), respectively, followed by sintering at 1400-1600 ℃ for 4 h in air.

The phase development of the calcined powders was examined by a Rigaku D/MAX-RB X-ray diffractometer using Cu Kα radiation. The morphology of the calcined powder and the ceramic specimens was investigated by a Jeol JSM-5610LV scanning electron microscope (SEM). For ceramic specimens, thermally etched surface was used for SEM observation. The density of the ceramic specimens was measured by the Archimedes method using pure ethanol. The rectangular specimens were polished to ensure surface flatness and painted with platinum paste for measuring electrical conductivity. The electrical conductivity was then measured at 50-900 ℃ by a dc four-terminal method in air. Adopting the two-terminal blocking electrode method described by Chen et al. [15], the oxygen ionic conductivity was measured using disk specimen by a TH2818 automatic component analyzer (0.02-300 kHz) at 400-800 ℃ in air.

3. Results and discussion

Fig. 1 shows the X-ray diffraction (XRD) patterns of $La_{1.9}Sr_{0.1}NiO_{4+\delta}$ powders calcined at different temperatures. Calcining the complex precursor at 850 ℃ produced a $K_2NiF_{4+\delta}$ phase (JCPDS card No. 80-1346) together with small amounts of intermediate phases ($LaNiO_3$ and La_2O_3). Raising calcining temperature promoted the development of $La_{1.9}Sr_{0.1}NiO_{4+\delta}$ phase. A pure $La_{1.9}Sr_{0.1}NiO_{4+\delta}$ phase was identified for the powders calcined at 900-950 ℃. Fig. 2 shows the SEM micrograph of $La_{1.9}Sr_{0.1}NiO_{4+\delta}$ powder calcined at 900 ℃, demonstrating uniform and fine particles of 100-200 nm in size. The powder calcined at this temperature was used for investigating the sintering and mixed conducting properties of $La_{1.9}Sr_{0.1}NiO_{4+\delta}$.

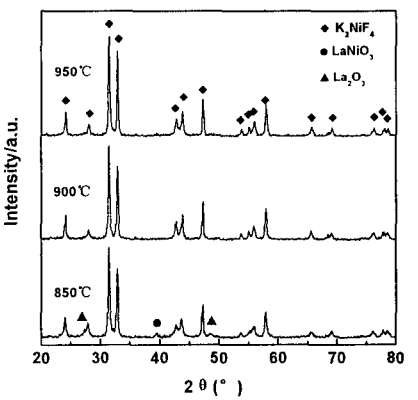

Fig. 1 XRD patterns of $La_{1.9}Sr_{0.1}NiO_{4+\delta}$ powders calcined at different temperatures.

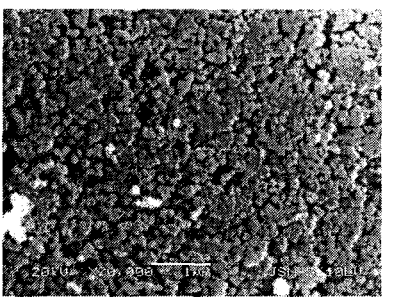

Fig. 2 SEM micrograph of $La_{1.9}Sr_{0.1}NiO_{4+\delta}$ powder calcined at 900 ℃ for 2h.

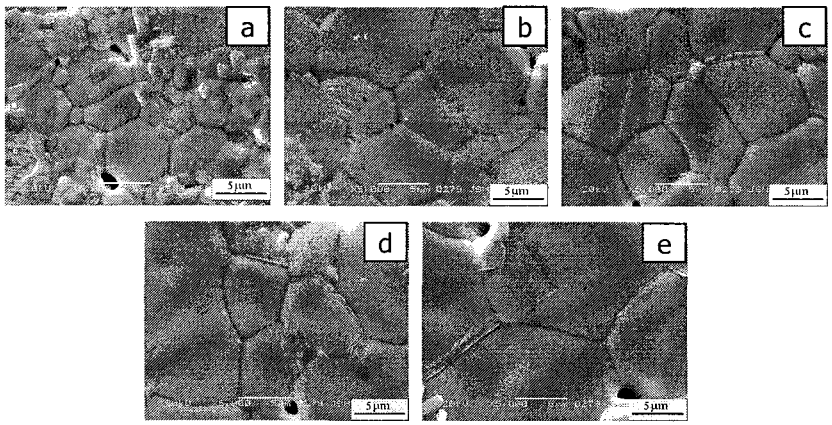

Fig. 3 SEM micrographs of $La_{1.9}Sr_{0.1}NiO_{4+\delta}$ ceramics sintered at different temperature. (a) 1400 ℃; (b) 1450 ℃; (c) 1500 ℃; (d) 1550 ℃; (e) 1600 ℃

Fig. 3 shows the SEM micrographs of $La_{1.9}Sr_{0.1}NiO_{4+\delta}$ ceramics sintered at different temperatures. The increase of sintering temperature promoted grain growth and microstructural densification. Compared with the gradual increase of grain size with sintering temperature in the range of 1400-1500 ℃, there is a facilitated grain growth in the specimens sintered at higher temperatures, implying a considerable increase in the amount of liquid above 1500 ℃.

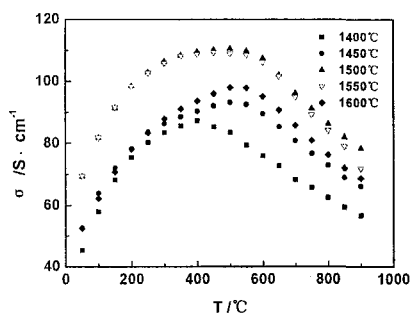

Fig. 4 Temperature dependence of electrical conductivity (σ) for$La_{1.9}Sr_{0.1}NiO_{4+\delta}$ ceramics sintered at different temperatures

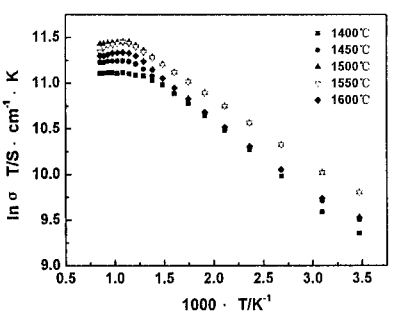

Fig. 5 lnσT versus 1000/T of $La_{1.9}Sr_{0.1}NiO_{4+\delta}$ ceramics sintered at different temperatures

Fig. 4 shows the electrical conductivity (denoted as σ) of $La_{1.9}Sr_{0.1}NiO_{4+\delta}$ ceramics as a function of measuring temperature. Due to the low oxygen ionic transport number of $La_2NiO_{4+\delta}$ based compounds (generally 10^{-4}-10^{-2}), the electrical conductivity measured by the dc four-terminal method can be regarded as the representative of electronic conductivity [8]. The electrical conductivities

of the specimens sintered at different temperatures display an identical variation with measuring temperature, increasing with measuring temperature through a maximum value near 450 ℃ and then decreasing. In the case of a same measuring temperature, the electrical conductivity increases with sintering temperature and attains the largest value at 1500 ℃, followed by a decrease of electrical conductivity with further elevated sintering temperature. Fig. 5 shows the plots of lnσT versus 1000/T for $La_{1.9}Sr_{0.1}NiO_{4+\delta}$ ceramics sintered at different temperatures. The plots are nearly linear at low temperatures, suggesting that small polaron hopping is the predominant mechanism for the electrical conduction [6]. At higher temperatures, the plots present a negative deviation from linearity. It is attributed to an extensive loss of hyperstoichiometric oxygen, decreasing the concentration of electronic carrier [6, 12].

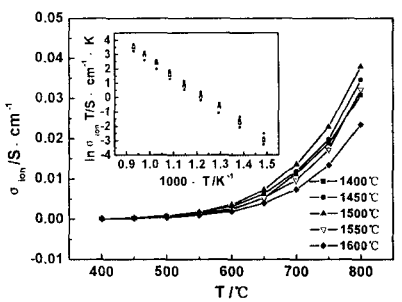

Fig. 6 Temperature dependence of oxygen ionic conductivity (σ_{ion}) for $La_{1.9}Sr_{0.1}NiO_{4+\delta}$ ceramics sintered at different temperature.

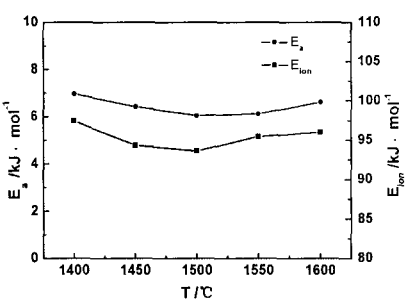

Fig. 7 Activation energy for small polaron hopping (E_a) and oxygen ionic conduction (E_{ion}) of $La_{1.9}Sr_{0.1}NiO_{4+\delta}$ ceramics as a function of sintering temperature.

Fig. 6 shows the temperature dependence of oxygen ionic conductivity (denoted as σ_{ion}) for $La_{1.9}Sr_{0.1}NiO_{4+\delta}$ ceramics sintered at different temperatures. The Arrhenius plots over the whole measuring temperature range yielded straight lines, as showed in the insert. At an identical measuring temperature, the ionic conductivity shows a rather similar variation with sintering temperature to that of the electrical conductivity, with the specimen sintered at 1500 ℃ approaching the highest ionic conductivity as well. The specimen gives an oxygen ionic conductivity of 3.8×10^{-2} S/cm at 800 ℃.

The activation energy for small polaron hopping (E_a) was derived from the linear fit of the plots in Fig. 5 over the low temperature range, while the activation energy for oxygen ionic conduction (denoted as E_{ion}) was calculated from the slopes of the straight lines in Fig. 6. Fig. 7 shows the E_a and E_{ion} of $La_{1.9}Sr_{0.1}NiO_{4+\delta}$ ceramics as a function of sintering temperature. The E_a and E_{ion}

show an analogous change with sintering temperature, slightly varying in the sintering temperature range of 1400-1600 ℃ and attaining the lowest values at 1500 ℃.

It can be noticed that the variation of the mixed conducting properties of $La_{1.9}Sr_{0.1}NiO_{4+\delta}$ ceramics with sintering temperatures is closely associated with the microstructural evolution. With the increase of sintering temperature from 1400 to 1500 ℃, the grain growth and development of microstructural densification enhanced the conduction of electrical carriers. The facilitated grain growth above 1500 ℃ reveals the appearance of excessive liquid. The presence of liquid can improve the mass transport and microstructural densification during sintering. Nevertheless, the amorphous phase formed by the liquid is a kind of heterogeneous component in ceramic bulk, blocking the transport of electrical carriers. The results demonstrate the crucial role of sintering temperature on the microstructure and mixed conducting properties. In terms of the mixed conducting properties, it was ascertained that the preferred sintering temperature of $La_{1.9}Sr_{0.1}NiO_{4+\delta}$ ceramic is 1500 ℃. The specimen sintered at 1500 ℃ exhibits electrical conductivities of 86-107 S/cm at 600-800 ℃, roughly meeting the least requirement (≥100 S/cm) for a cathode material of intermediate temperature SOFCs [5].

4. Conclusions

Homogeneous and fine powder (100-200 nm) with a pure K_2NiF_4 phase was produced by calcining the polyaminocarboxylate complex precursor at 900 ℃ for 2 h in air. The microstructure and mixed conducting properties of $La_{1.9}Sr_{0.1}NiO_{4+\delta}$ ceramics have been investigated in the sintering temperature range of 1400-1600 ℃. The results demonstrate that it is important to adequately control the sintering temperature to obtain desired microstructure and mixed conducting properties. The preferred sintering temperature of $La_{1.9}Sr_{0.1}NiO_{4+\delta}$ was ascertained to be 1500 ℃ with regard to the mixed conducting properties. $La_{1.9}Sr_{0.1}NiO_{4+\delta}$ ceramic sintered at 1500 ℃ exhibits an electrical conductivity of 86 S/cm and an oxygen ionic conductivity of 3.8×10^{-2} S/cm at 800 ℃.

Acknowledgments

This work was financially supported by Natural Science Foundation of China (Grant No. 50572079), the Program for New Century Excellent Talents in University (Grant No. NCET-04-0724) and the Foundation for Innovative Research Team of Hubei Province (Grant No. 2005ABC004).

References

1. R.A. Desouza, J.A. Kilner, *Solid State Ionics* **106**, 175(1998).
2. F.T. Akin, Jerry Y.S. Lin, *J. Membrane Sci.* **231**, 133(2004).
3. P.N. Dyer, R.E. Richards, S.L. Russek, et al., *Solid State Ionics* **134**, 21(2000).
4. V.V. Kharton, A.A. Yaremchenko, E.V. Tsipis, et al., *Applied Catalysis A: General* **261**, 25 (2004).
5. E. Boehm, J.-M. Bassat, M.C. Stil, et al., *Solid State Sciences* **5**, 973(2003).
6. F. Mauvy, J.-M. Bassat, E. Boehm, et al., *Solid State Ionics* **158**, 17(2003).
7. M. Al Daroukh, V.V. Vashook, H. Ullmann, et al., *Solid State Ionics* **158**, 141(2003).
8. V.V. Kharton, A.A. Yaremchenko, A.L. Shaula, et al., *J. Solid State Chem.* **177**, 26(2004).
9. J.A. Kilner and C.K.M. Shaw, *Solid State Ionics* **154-155**, 523(2002).
10. V.V. Kharton, E.V. Tsipis, A.A. Yaremchenko, et al., *Solid State Ionics* **166**, 327(2004).
11. D.M. Bochkov, V.V. Kharton, A.V. Kovalevsky, et al., *Solid State Ionics* **135**, 709(2000).
12. V.V. Kharton, A.P. Viskup, E.N. Naumovich, et al., *J. Mater. Chem.* **9**, 2623(1999).
13. V.V. Kharton and F.M.B. Marques, *Current Opinion in Solid State and Materials Science* **6**, 261(2002).
14. V.V. Vashook, S.P. Tolochko, I.I. Yushkevich, et al., *Solid State Ionics* **110**, 245(1998).
15. C.C. Chen, M.M. Nasrallah, H.U. Anderson, *J. Electrochem. Soc.* **142**, 491(1995).

PREPARATION AND CHARACTERISTICS OF BALL MILLED MgH_2 +M (M= Fe, FeF_3 AND VF_3) NANOCOMPOSITES FOR HYDROGEN STORAGE

N.W.B. BALASOORIYA
Faculty of Applied Sciences, South Eastern University, Sammanthurai (E.P), Sri Lanka.
Email: balasooriya@seu.ac.lk

Ch. POINSIGNON
Laboratoire d'Electrochimie et de Physico-chimie des Matériaux et Interfaces (LEPMI), ENSEEG, INPG, B.P.75, 38402 St. Martin d'Hères, France.
Email: Christianne.Poinsignon@lepmi.inpg.fr

High energy vibrational ball milling device was used under argon atmosphere to prepare two series of nanocomposite of MgH_2 with 5%wt. M (M= Fe, FeF_3 and VF_3) in order to improve the hydrogen storage sorption of the magnesium hydride. Morphology, structural and thermal characterization of the MgH_2 composites was performed by using XRD, SEM and simultaneous TG and DSC techniques. Electrochemical study of hydrogen charge-discharge process in MgH_2 provides distinct information on thermodynamic and kinetics of the Mg-H_2-catalyst system. Electrode potential provides information on the variation of the free Gibbs energy carried out by surface energy modification generated by nanometric grain size and catalyst. Current density of voltammograms reveals improvements carried out by different catalysts on hydrogen sorption-desorption kinetics.

1. Introduction

Magnesium hydride is considered to be one of the most attractive materials for hydrogen storage, because it is abundant, inexpensive, and easy to handle and environmentally friendly. It has attractive property of reversibly absorbs hydrogen with a 7.6 wt.% capacity leading to a high thermodynamic stable hydride (ΔH= -75 kj mol^{-1}). Unfortunately, this adsorption process occurs at 450°C under pressure.[1] High energy ball milling leads to nanometric particles for which Hydrogen desorption occurs at 300°C, addition of transition elements metals or oxides decreases too, this desorption temperature and simultaneously improves its kinetics.[2-4] The role of catalysts is not yet clear that they act on thermodynamic or on kinetics of the H_2-Mg system.

Mg is well known to react quickly with water due to its very low oxidation potential: Mg is oxidized in Mg^{2+} at –2.375 V vs. Standard Hydrogen Electrode (SHE). Fortunately magnesium hydride is more stable in ambient conditions than pure Mg: MgH_2 electrode can disinsert reversibly hydrogen providing the active material be efficiently protected against corrosion in KOH electrolyte. It is clear that Mg/MgH_2 is not a realistic electrode material despite its very large electrochemical capacity (2400 $mAh.g^{-1}$): its potential at 25°C is too high for a negative electrode in a

Ni-MH battery, its kinetics too slow and its sensitivity to corrosion too large. Nevertheless electrochemical methods are useful to study the role of catalysts in the hydrogen storage process at ambient conditions: they provide distinct information on thermodynamic and kinetics of the Mg-H_2-catalyst system and its life time. Electrode potential value is related to the Gibbs free energy variation of nanocrystalline Mg/MgH_2 by relationship in Eq. (1), where the contribution of the nanometric dimension is expressed in $\gamma\Delta A$ the surface energy variation, no more negligible.

$$\Delta G = \Delta H - T\Delta S + \gamma\Delta A = -nFE \quad (1)$$

$$MgH_2 \leftrightarrow Mg + H_2 \quad \text{in gas phase,} \quad (2)$$

Where, A- surface area, γ - surface strain, ΔH-enthalpy and ΔS-entropy variations, F-Faraday constant and n - the number of exchanged electrons in the redox reaction are as in Eq. (2). The kinetics informations are separately obtained from the current density delivered during potentiostatic charge / discharge process and from the recovered capacity during galvanostatic process.

2. Experimental

Two types of MgH_2 powders, named as MgH_2.DF and MgH_2.AB were used as the starting material for the experiments. Fe, FeF_3 and VF_3 catalysts were purchased from Johnson Matthey and Aldrich with 99.8% purity.

Processing of MgH_2 nanocomposites by high-energy ball milling techniques was carried out into two steps: MgH_2 grains and catalysts grains are separately milled to nanometer scale for 48hrs., afterwards the mixture is milled to give the composite using two Fritsch P0 pulverisette for MgH_2-AB and P7 pulverisette for MgH_2-DF, under Argon atmosphere for 24, 48 and 72 hrs., with stainless steel balls, the ball- to-sample-weight ratio being 10:1. All milling experiments, preparation and transfer for characterization have been done under Argon atmosphere to exclude any contact with ambient air.

Structural characterization was performed by X-Ray Diffraction (XRD) analysis using a Siemens D500 equipped with Cu K_α radiation in a θ–2θ configuration. The SEM studies were performed on a Gemini Zeiss ULTRA^{TM} 55 scanning electron microscope using the secondary and back scattered electron mode. EDX analysis was performed on a JEOL JSM 6400 scanning electron microscope equipped with an Energy Microanalyser to identify the materials in the samples. Differential Thermo Analysis (DTA) was carried isochronally (10 K/min) under a constant flow of Helium in a Netzsch Symultaneous Thermal Analyzer STA 409 equipped with a TASC 414/2 controller and Differential Scanning Calorimetry (DSC) in a Netzsch DSC 404 C calorimeter.

Electrochemical experiments were performed on the thin film composite electrodes (φ=13mm),obtained by mixing 60%wt. of Magnesium hydride composites with 10% carbon black and 30% Teflon. Hydrogen electrochemical charge-discharge was driven by a McPile multi channels microprocessor potentiostat-galvanostat controller (Biologic-Claix-France) under slow regimes (10mA.g^{-1}under galvanostatic control or using a 10mV/2 hours potential scan rate) in –1.0 V to 0.2 V potential range (vs. Hg-HgO reference electrode).[5] The electrolytic solution was 6M KOH.

3. Results and Discussion

3.1. Structural characterization of the MgH_2composites

The X-ray diffraction spectra of the MgH_2 mechanically milled for various times shows the crystallite size of the pre-milled MgH_2 was decreased from 52 nm to 32 nm after 72 hours of milling time. The diffraction peaks are very board after milling, indicating the crystallite size was diminished to the nanometer scale.

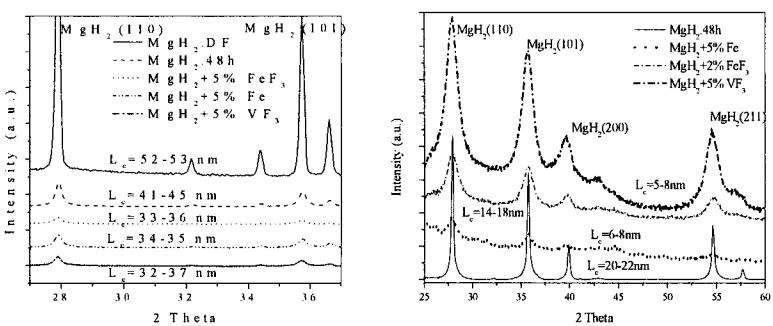

(a) (b)

Figure 1. X-Ray spectra of MgH_2 and its composites after 48hrs., (a) MgH_2 DF (b) MgH_2 AB.

Fig. 1 shows the X – ray diffraction patterns of 48 hours milled β-MgH_2. They reveal the presence of mainly tetragonal β-MgH_2 and VF_3, Fe and FeF_3 and some peaks of meta-stable γ-MgH_2. With increasing milling time, the peaks intensity of the γ-MgH_2 phase increases and the one's of V, Fe and FeF_3 decreased. This indicates physical and chemical transformations of MgH_2 and VF_3, Fe and FeF_3 during the milling process. During further milling the tetragonal β-MgH_2 can not be completely transformed to the orthorhombic γ-MgH_2 under the previous milling conditions.[6] However, Gennari et al.[7] showed that during ball milling of the MgH_2 + M mixtures, a certain amount of the low temperature β-MgH_2 phase transforms into a high pressure metastable γ-MgH_2 phase.

The XRD pattern shows the presence of Mg and MgO (?) that could result of the impurities from milling debris. Due to the low content of transition element, the diffraction peaks from this element are difficult to detect for all pattern, the peaks are broad, indicating the nano-crystalline structure of the composites.

One of the great difficulties in managing nanometric powder is to study of the grain size distribution. High energy ball milling generates a large grain size distribution. An average value can be obtained from the measurements of X-ray diffraction line width in using the Scherrer method, but line broadening in that case is not only due to nanometric size but also to stress and defects generated by ball milling in the material. Complementary TEM investigations are necessary to estimate the average size but the very small quantity of powder does not show really account on the width of grain size distribution.[8]

3.2. Thermal behaviour of the MgH_2 composites

Fig. 2 shows the magnesium hydride milled with different additions release hydrogen in two stages, which occurs in different temperatures, depending on type of the catalyst. It was found by DSC and TG that thermal decomposition of the β-MgH_2 occurs at lower temperatures compared to conventional polycrystalline MgH_2 (which decomposes at temperature above 400°C) as well as planetary milled nanocrystalline MgH_2 (about 400°C).

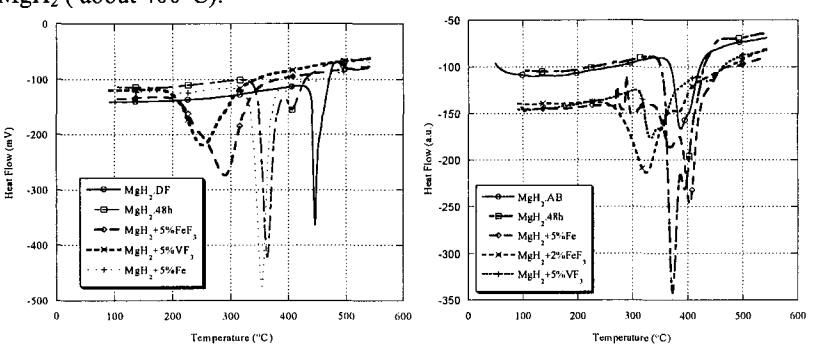

Figure 2. DSC traces for the MgH_2 during milled 48hrs. and it's composites.

3.3. Morphology and microstructural characterization of the MgH_2 composites

Particulate structure of pre-milled and 48 hours milled, is shown in fig. 3. The greater portion of particles is of micron or sub-micron size, through few particles of relatively coarse size. ex. 3-4 microns sizes are also present.

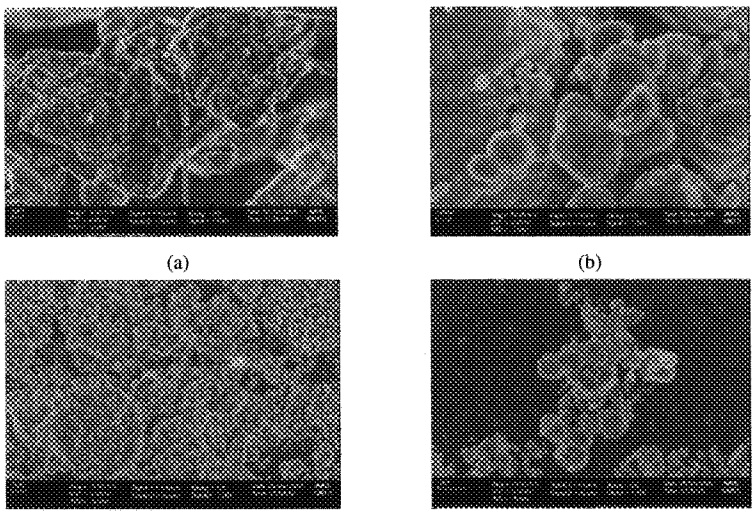

Figure 3. SEM secondary electron image of pre-milled MgH_2.DF (a) and MgH_2.AB (c), 48hrs. milled MgH_2 .DF (b) & MgH_2 .AB (d), and I, 2, 3, & 4 indicate similar EDX spectrum of the MgH_2

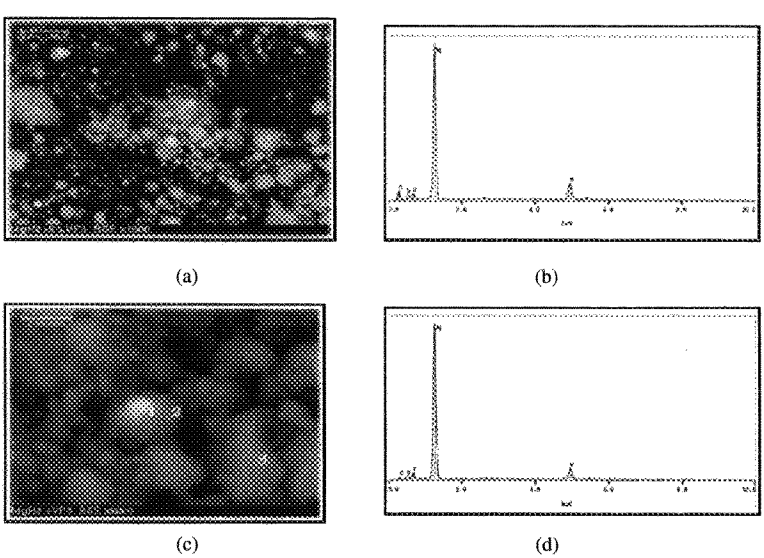

Figure 4: SEM backscattered electron image of 48hrs. milled MgH_2+5%VF_3 composite (a-DF & c-AB). The EDX spectrum indicates mixture of V & Fe as the very bright dots (b & d).

MgH_2 when milled with catalyst develop similar structures. The distribution is

however more uniform. i.e. coarse particles appear less in fraction. In high energy ball milling, a charge of balls and MgH_2 powder is vigorously agitated in a vial. The trapped powder particles between the colliding balls undergo fracturing and re-welding processes which define the ultimate microstructure of the powder. In Figures 3 and 4 of SEM micrograph of ball milled MgH_2, the bright dots in the middle was identified as the catalysts. The surrounding conglomerates of dark grey particles were identified as MgH_2. Therefore, after ball milling the microstructure consist of additive particles coated by a film of MgH_2 .[9]

Fig. 4 shows SEM images of milled MgH_2+VF_3 composite. The powders are porous and made agglomerates of smaller particles. The V powders are broken up to the fine particles during the milling process and are well distributed over the MgH_2 matrix. The catalysts particles are coating the MgH_2 grains or it may not be facilitated H_2 sorption thanks to the creation of VH_2 or intermediates. Vanadium has strong affinity to oxygen; some surface oxidation of vanadium is inevitable during process of MgH_2+V composites. The VO can not be reduced by hydrogen under normal conditions, once the vanadium particles are oxidized; the catalytic effect of chemisorption is lost.[10]

3.4. Electrochemical study

The nanometric MgH_2 composites shaped into plasticized electrodes allow to study of hydrogen charge-discharge process in 6M KOH with electrochemical methods under slow regimes (10 $mA.g^{-1}$ under galvanostatic control or using a 10mV/2 hours potential scan rate) in –1.0 V to 0.2 V potential ranges (vs. Hg-HgO reference electrode). The potential range was selected to avoid hydrogen evolution during charging and oxygen evolution during discharge at the counter electrode.

The potentials of the adsorption and desorption were showed a good reversibility at each cycle of charge and discharge (Fig.5). Discharging and electrochemical desorption of the first phase starts at -0,30V (vs. Hg/HgO) and –0,08V for the second one. Respectively charging and formation of the reduction products is observed at -0,59V and -0,29V. The shifting of these values of the equilibrium potential starts to occur into the last cycle. It proves that adding of the catalyst to MgH_2 does not change strongly the mechanism of reduction or oxidation products and does not lead to formation of different stages at electrochemical discharging and charging of MgH_2. Similar sorption isotherms were obtained for MgH_2 (AB)+5%VF_3 .[11]

The galvanostatic results in the case of MgH_2 milled with FeF_3, shows the electrochemical absorption and intercalation undergoes transformation into two phases at the values about – 0.3V and –0.6V for the process of charging and –0.10 V

and –0.40 V for the electrochemical discharge. The fast regime of electrochemical reaction doesn't influence appearance and exact position of these plateaus in galvanostatic curves. They correspond to the same one, which are already measured after applying a slow potentiostatic regime above MgH_2 milled nanocomposites.[12]

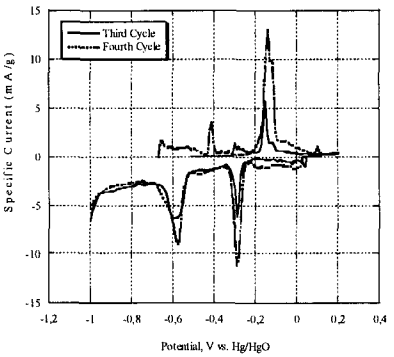

Figure 5. Voltammograme for MgH_2 (AB) +VF_3 between–1.0 V to 0.20 V in 6M KOH under slow current rate (10mV/2h).

4. Conclusions

If Magnesium is definitively too reactant with water to allow electrochemical insertion of hydrogen, the more stable MgH_2 shaped into thin film plasticized electrodes is suitable to study at ambient temperature and atmospheric pressure the Mg-H_2-catalyst system in concentrated KOH. Electrochemical response of the pure hydride electrodes illustrates the importance of the nanometric grain size on discharge potential, kinetics and delivered capacity. Discharge capacity of the smaller nanometric grain size powder is much larger than the one's of larger grain size. Life time of both electrodes is very short: it is significantly improved by the presence of Catalysts, especially fluorinated catalysts in the nanocomposites electrodes.

How the use of additives in milling improves the sorption characteristics of Mg can now be explained. Additives such as V, Nb may be a chemical basis for this, Yavari et. al.,[11] and Schulz et. al.,[10] attribute this is to the catalytic effect of Vanadium and Niobium. V/ Nb acts as hydrogen pump by early dissociating the hydrogen gas in to its atomic form and feeding the atoms to the hot Mg. But the fact that similar or sometimes better improvements and obtained with oxide addition implies that the effect may not always have a chemical basis. The role of additives is also of physical basis: they modify the surface strain and avoid re-agglomeration of the small crystallites during cycling: the free surface easily accessible for hydrogen

is then larger and remains open during cycling. Potential values of the different nanocomposites electrodes is influenced by the chemical composition of electrode because the presence of catalysts modifies significantly their thermodynamics properties in decreasing hysteresis of isotherms and improving their stability; the role of catalysts is evident on life time and discharge/ charge kinetics. For nanocomposites electrodes catalysts modify the surface energy, therefore grain size seems to act in the opposite way than for pure MgH_2: potential of β/γ phases charge plateaus increases with smaller grain size and hysteresis of isotherms decreases.

Acknowledgements

The fellowship given to NWBB by the Ministry of Foreign Affairs (MAE), France through French Embassy of Sri Lanka to carry out research work at LEPMI, INPG is greatly acknowledged.

References

1. J.J. Reilly and R.H. Wiswall, *Inorg.Chem.* **6 (12)**, 2220 (1967).
2. G. Barkhordarian, T. Klassen and R. Bormann, *Scripta Materialia* **49**, 213, (2003).
3. A.R. Yavari, J. F. R .de Castro, G. Heunen and G. Vaughan, *J. Alloys Compounds* **353**, 246 (2003).
4. J.-.L. Bobet, F.J. Castro and B. Chevalier, *J. Alloys Compounds* **376**, 203 (2004).
5. A.H. Thomson, *J. Electrochem. Soc.***126**, 608 (1979).
6. H. Niu and D.O. Northwood, *Int. J. Hydrogen Energy* **27**, (2002).
7. F.C. Gennari, F.J. Castro and G. Urretavizcaya, *J. Alloys Compounds* **321**, 46 (2001).
8. W.J. Botta, J.F.R. de Castro, G. Vaughan and A.R. Yavari, *J. Metastable Amorp. alloys Nanocrys. Mat.* **24-25**, 299 (2005).
9. H. Reule, M. Hirscher, A. Weißhardt and K.Kronmüller, *J. Alloys Compounds,* **305**, 246 (2000).
10. G. Liang, J. Hout, S. Boily, A.Van Neste and R. Schulz, *J Alloys Compounds* **292**, 247 (1999).
11. S. Deledda, A. Borissova, C. Poinsignon, W.J. Botta, A. R. Yavari, M. Dornheim and T. Klassen, *Proceedings of the MH2004,* Cracovie, (2004).
12. C. Poinsignon, A. Borissova and A.R. Yavari, *Proceedings of the ISMANAM,* Paris, (2005).

STRUCTURAL STUDIES OF OXYSULFIDE GLASSES BY X-RAY DIFFRACTION AND MOLECULAR DYNAMICS SIMULATION

R. PRASADA RAO[1]*, M. SESHASAYEE[2] and J. DHEEPA[1]

[1]Department of Physics, Vellore Institute of Technology, Vellore-632 014. India.
E-mail address: rayavarapu2000@yahoo.com

[2]Department of Physics, Indian Institute of Technology Madras, Chennai 600036, India.

Abstract

Amorphous solid electrolytes in the system xLi_2S-$(1-x)P_2O_5$ (with x = 0.5, 0.6, 0.7) has been prepared from a mixture of Li_2S and P_4O_{10} using a mechanical milling technique at room temperature and in inert atmosphere. The oxysulfide powder mechanically milled for 80h with x=0.6 shows ionic conductivity (σ) of 7.89 x 10^{-6} S/cm at room temperature which is the highest in this series. The glass transition temperature (T_g) increases with the increase of Li_2S. X-ray RDF analysis and constant volume molecular dynamics was done for all x. Both Phosphorous and Lithium were found to coordinate with both oxygen and sulfur in various proportions. Various units present around phosphorous and lithium are PO_3S, PO_4, PO_3, PO_4S, LiO_3S, LiO_3, LiO_2S, LiO_4. Changes in structure with x and their influence on σ and T_g are discussed.

Introduction

Kondo et al. [1] reported that the oxysulfide glass $0.01Li_3PO_4$-$0.63SiS_2$-$0.36SiS_2$ showed a high conductivity of 1.4 x 10^{-3} S/cm at ambient temperature and a wide electrochemical window and is chemically stable against lithium metal [2]. Minami's group has reported that mechanical milling is one of the most effective ways of preparing amorphous materials from crystalline powders. The ionic conductivity (σ) of mechanically milled $60Li_2S$-$40P_2S_5$ glass after milling for 20h was reported to be 1.5 x 10^{-4} S/ cm at room temperature [3]. Very few structural reports based on mechanically milled oxysulfide glasses exist. ^{29}Si MAS-NMR and XPS studies for melt quenched glass system $(100-x)(0.6Li_2S$-$0.4SiS_2)$-xLi_xMO_y (Li_xMO_y = Li_4SiO_4, Li_3PO_4, Li_4GeO_4, Li_3BO_3, Li_3AlO_3, Li_3GaO_3 and Li_3InO_3) was reported by Minami et al.[4]. These studies reveal that in the systems with small amounts of Li_xMO_y, the silicon atoms coordinated with both bridging oxygen atoms (BO) and non-bridging sulfur atoms (NBS). The presence of large amounts of these unique silicon structural units brought about high conductivities and high thermal stability of these glasses. On the other hand, presence of non-bridging oxygen (NBO) atoms and S^{2-} units created

by large amounts of Li_xMO_y, lowered these excellent properties. Solid state MAS-NMR measurement revealed that silicon and phosphorus atoms coordinating with both sulfur and oxygen atoms present in oxysulfide glasses were not detected after crystallization.

In order to understand the short range order around P and Li atoms and the emerging structural changes with increasing Li_2O content, X-ray RDF and molecular dynamics study of xLi_2S-$(1-x)P_2O_5$ with x = 0.5, 0.6 and 0.7 was taken up and reported here. To analyze the MD generated configuration of atoms, graph theory techniques [5] were used to completely elucidate the connectivities of the various units present and their ratios. Statistics of chains and rings present were also calculated using this technique.

Glass preparation and characterization

The starting materials, Li_2S and P_4O_{10} were placed in an agate pot of volume 50 ml with ten agate balls of 10 mm diameter and two agate balls of 8 mm diameter. The mechanical milling was conducted using a high-energy ball mill at room temperature in a glove box that was filled with dry nitrogen gas. The diffractogram taken at the start of the milling process for the glass with x = 0.5 showed peaks due to Li_2S and P_4O_{10} (Figure 1). At the end of 80h of milling all the peaks disappeared leaving a halo pattern. The density of these powders were measured using Archimedes principle taking toluene (density 0.863 gm/c.c.) as the immersing medium (Table 1). Ionic conductivity measurement was done at room temperature by Keithley 3330 impedance analyzer in the frequency range 40 Hz-100 kHz.

RDF analysis of xLi_2S-$(1-x)P_2O_5$ glasses.

The system xLi_2S-$(1-x)P_2O_5$ with x=0.5, 0.6 and 0.7 were taken for RDF analysis. X-ray data collection was done under a vacuum of 7 $x10^{-3}$ m. bar using a Philips diffractometer with MoKα radiation. The reduced D(r) contains peaks at 1.8, 2.2, 3.4 and 4 Å and shoulders at 2.7 and 3.1 Å. The peak at 1.8 was assigned to P=S interaction and the peak close to 2 was a mixture of P-S and Li-O. The shoulders at 2.7 and 3.1 were taken to represent Li-S and S-S interactions respectively. P-P interaction was put at 4 Å. Initial intensity values were calculated with these interactions and least squares fit between calculated and observed intensities was carried out. The parameters in a least squares fit were r_{i-j}, the distance between atoms i and j, n_{i-j}, the average coordination number of j around the central i atom and b_{i-j} which equals the mean square variation of r_{i-j}. Least squares refinement of the bonding parameters led to intensity fits shown in figure 2 and table 2 contains the refined parameters. The standard deviations in r_{ij} and n_{ij} are 0.001Å and 0.01 respectively.

Molecular dynamics

Constant volume MD was performed on cubic cells calculated with measured densities [table 1]. Starting at a temperature of 3000 K, the system was cooled by scaling velocities to 2000 K, 1500 K, 1000 K, 750 K, 600 K, 350 K and finally to 300 K with time step size of 10^{-15} s . At each temperature, the system was equilibrated for 20 ps and various parameters such as pair correlation function (PCF) and running coordination number (RCN) for various atomic pairs were averaged for another 80 ps. At 600K, 350 K and 300 K, the equilibration and averaging times were increased to 100 ps each. The interatomic potential used was of the form

$$\phi_{ij} = \frac{Z_i Z_j e^2}{r_{ij}} + A_{ij} \exp(\frac{-r_{ij}}{\rho_{ijo}}) + \frac{k_{ij}}{8(\theta_{jki} - \pi)^2} \left\{ \left[(\theta_0 - \pi)^2 - (\theta_{jki} - \pi)^2 \right]^2 \right\} \exp\left[-\frac{(r_{ik} + r_{jk})}{\rho_{ij}} \right]$$

where Z_i is the atomic number of atom i and θ_0 is the equilibrium angle subtended by $\overrightarrow{r_{ik}}$ and $\overrightarrow{r_{jk}}$. A_{ij}, ρ_{ijo}, k_{ij} and ρ_{ij} are constants of simulation. Z_i for Li, P,S and O are 0.4e, 2e, -0.8e and -0.8e respectively. Initial values for constants of simulation and atomic number Z_i were obtained from MD studies reported for the binary systems xLi_2S-(1-x)P_2S_5 [5]. They were subjected to further adjustments till equilibrium was attained at all simulated temperatures with chemically acceptable bond lengths. Conductivity of the glasses were calculated as reported [5].

Discussion

As reported in earlier studies, Li and P coordinate with both S and O. The overall coordination including O and S around P decreases from 5.4 to 4.3 and around Li increases from 4.1 to 4.4 with increase in x. As x increases, O content decreases and this is reflected in the lower value of $n_{P\text{-}O}$ and $n_{Li\text{-}O}$. S content also increases with x which increases the $n_{Li\text{-}S}$, but $n_{P\text{-}S}$ decreases instead. Bridging sulfur (BS) and Non-bridging sulfur (NBS) denote sulfurs taking part in P-S-P and P-S-Li interactions. Since we cannot distinguish between BS and NBS here, the decrease in $n_{P\text{-}S}$ is assumed to be caused by the decrease in both BS and NBS. Taken together, the above results indicate that as the Li_2S content increases, more sulfurs in state S^{2-} are found near Li^+. The P-P interaction occurring above 4 Å is caused by the P-S-P bridges. The decrease in $n_{P\text{-}P}$ is due to Li, which in its role as a modifier breaks up these bridges. The observed interatomic distances are as found in similar glasses with the exception of the short $r_{P=S}$ for x = 0.5. σ shows an initial increase followed by a decrease for x = 0.7. The glass with minimum σ also has the lowest $n_{P\text{-}O}$ and $n_{P\text{-}S}$ and the highest $n_{Li\text{-}S}$ which indicates low bidging oxygens (BO) and high S^{2-}. This result agrees with the XPS study of (100-x)(0.6Li_2S-SiS_2)-xLi_4SiO_4 [12] wherein the high conductivity in

this system is attributed to the presence of non-bridging sulfurs and bridging oxygens and presence of S^{2-} around Li^{+} diminishes σ.

PCF and RCN plots are shown in figure 3. Parameters obtained from graph theory analysis are given in table 3. P assumes a total coordination of 4 consisting of S and O. Li too bonds with S and O and its coordination varies between 3.5 and 4.1. In P-P PCF, a sharp peak at r = 3.67Å and a weak and broad peak at r = 4.3 Å are present. The large peak at short r due to P-O-P interaction indicates its strong presence and in comparison, the weak peak shows a much smaller number of P-S-P linkages.

Comparing short range parameters between RDF and MD, certain differences are found. Though the MD configuration has a higher proportion of oxygens around P and Li in their coordination spheres for all compositions, the total coordination around P and Li assumes higher values in laboratory prepared glasses. Double bonded sulfurs to P (P=S) are absent in MD glasses. However, the conductivity change with composition remains unchanged between laboratory prepared and MD glasses.

The BO population remains constant between x = 0.5 and 0.6 and decreases for 0.7. Fraction of NBS increases from 0.54 to 0.77 steadily with concomitant decrease in BS population. The sulfur atoms interacting only with Li (S^{2-}) form a very small fraction of the total and it increases with x from 0.04 to 0.08. Since both P and Li coordinate with S and O, various units are found around them. Around P, the units found are PO_3S, PO_4, PO_2S_2 and PO_3S_2 in decreasing numbers. ^{31}P MAS-NMR results of $0.95(0.6Li_2S\text{-}0.4SiS_2)\text{-}0.5Li_3PO_4$ [4] describes the various units around P as POS_3, PS_4, PO_2S_2, PO_4 with POS_3 having the maximum presence which differs from our results due to the very small oxygen content in their glass. Around Li, the units LiO_3S, LiO_3, LiO_2S and LiO_4 are found in decreasing fractions. The angles O-P-O (subtended at P by the coordinating oxygens) and P-O-P (the bridging angle between neighbouring P atoms) lie close to 95^0 and 165^0. The bridging angle is close to reported values in phosphate glasses. But the angle O-P-O is far from the tetrahedral angle of 109^0 found in alkali phosphate glasses. This is to be expected as here the phosphorus is also coordinated to sulfur. The NBOs interact with Li forming Li-O-P linkages which increase with x. So too are the NBS atoms forming Li-S-P contacts which increase at a higher rate with x. The neighbour list around Li formed by Li-S-Li contacts shows a high value for x = 0.7. The average P-O-P chain length remains between 11 and 12 for all the three compositions, though the M_6 parameter sharply decreases for x = 0.7 indicating the rapid decrease of branches in P-O-P chain.

The increase in experimentally measured T_g between x = 0.5 and x = 0.7 is small and the simulated T_g follows the same order. This is perhaps due to a large increase in Li-S-P linkages from 4.3 to 12.7 caused by the decrease in BS populations. σ obtained

from MD and measured values at 300 K are shown in table 1. Though the σ from MD has much higher values, both change with x in the same fashion. Various factors contribute to σ. The increasing Li^+ population as x increases provides more cations. However, structural modifications with compositional changes play a decisive role in determining σ. As Li content increases with x, it also diminishes the BO and BS populations. This in turn creates NBS and S^{2-}. If the ratio NBS/S^{2-} is high, then the conductivity is enhanced. This
is observed in an earlier report, where higher σ is caused by higher populations of NBS and BOs and lower population of S^{2-}. In addition σ is also enhanced by structural features which cause the presence of Li near BO and BS. Larger population of Li found near BO and BS creates better path ways for Li movement, since BO and BS act as weak traps for Li^+, which also contribute to higher σ. In this system, BO varies little between 0.5 and 0.6 and then decreases for x = 0.7. NBS population shows a steady increase and the very small proportion of S^{2-} ions also registers an increase between 0.5 and 0.7. The average number of Li^+ found near BO (LBO) is small and changes little from 0.10(1) for all three glasses and the corresponding number for BS(LBS) takes on values 0.48(6), 0.72(5) and 0.77(7) as x increases. The initial large increase in σ between 0.5 and 0.6 is caused by the unchanging BO and increasing NBS population along with the increase in LBS. The decrease in σ between 0.6 and 0.7, which is not as large as the initial increase is probably due to the decrease in BO and increase in S^{2-} fraction. The increase in NBS in this region seems unable to keep up the increase in σ due to the decreasing BO populations.

Conclusions

Both P and Li coordinate with S as well as O atoms in various proportions. The BS, NBS and S^{2-} populations control the conductivity. The increases in experimentally measured T_g is due to the increase in Li-S-P linkages created by increase in NBS population.

References

[1] S. Kondo, K. Takada and Y. Yamamura, Solid State Ionics, 53-56 (1992), 1183-1186.

[2] K. Takada, N. Aotani, K. Iwamoto and S. Kondo, Solid State Ionics, 86-88 (1996), 877-882.

[3] H. Morimoto, H. Yamashita, M. Tatsumisago and T. Minami, J. Am. Ceram. Soc., 82(5)(1999), 1352-1354.

[4] M. Tatsumisago, H. Yamashita, A. Hayashi, H. Morimoto and T. Minami, J. Non-Cryst. Solids, 274 (2000), 30-38.

[5] R. K. Sistla and M. Seshasayee J. Non-Cryst. Solids, 349 (2004) 22-29.

Parameter	x = 0.5	x = 0.6	x = 0.7
Density (gm/c.c)	2.08	2.12	2.17
σ (S/cm) (exp.) x 10^{-6}	6.68	7.89	1.77
Tg (K) (exp.)	382	385	393
σ (S/cm) (MD) x 10^{-4}	15.39	35.11	27.72
Tg (K) (MD)	449	456	465

Table 1. Physical parameters for system xLi_2S-$(1-x)P_2O_5$ system.

Parameter	x = 0.5	x = 0.6	x = 0.7
r_{P-O} (Å)	1.551	1.553	1.523
n_{P-O}	3.4	3.0	2.8
$r_{P=S}$ (Å)	1.835	1.895	1.944
$n_{P=S}$	0.3	0.5	0.6
r_{P-S} (Å)	2.060	2.090	2.122
n_{P-S}	1.5	1.3	0.9
r_{Li-O} (Å)	2.192	2.195	2.179
n_{Li-O}	1.0	0.9	0.5
r_{Li-S} (Å)	2.604	2.658	2.637
n_{Li-S}	3.1	3.5	3.9
r_{S-S} (Å)	3.111	3.167	3.175
n_{S-S}	1.5	1.8	2.1
r_{S-S} (Å)	3.439	3.447	3.603
n_{S-S}	0.9	1.5	1.6
R_w	5%	6.7%	2.8%

Table 2. Structural parameters obtained from RDF for xLi_2S-$(1-x)P_2O_5$ system.

Parameter	x = 0.5	x = 0.6	x = 0.7
r_{P-O} (Å)	1.62	1.62	1.62
r_{P-S} (Å)	2.12	2.13	2.14
r_{Li-O} (Å)	1.99	1.99	1.99
r_{Li-S} (Å)	2.66	2.65	2.63
n_{P-O}	3.20(2)	2.93(2)	2.67(3)
n_{P-S}	0.65(1)	0.95(1)	1.33(3)
n_{Li-O}	2.67(4)	2.47(2)	2.31(3)
n_{Li-S}	0.83(2)	1.22(2)	1.76(3)
BO	0.36(2)	0.34(2)	0.24(2)
NBS	054(1)	0.66(1)	0.77(1)
#(Li-O-P)/#O	4.81(8)	5.6(1)	6.3(1)
#(Li-S-P)/#S	4.3(2)	7.5(2)	12.7(3)
Avg.(P-O-P) chain length	11(1)	12(1)	11(4)
M_6 (P-O-P)	32(9)	19(8)	3(1)

Table 3. Structural parameters obtained from MD for xLi_2S-(1-x)P_2O_5 system.

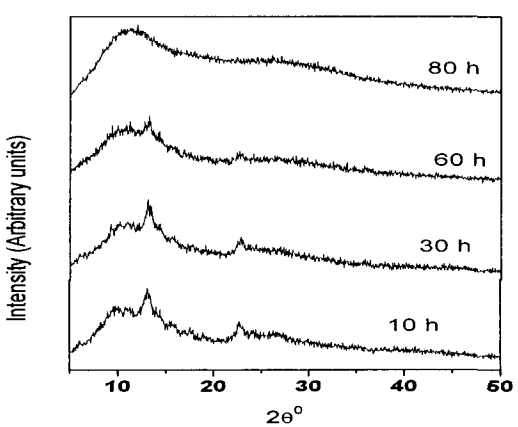

Figure 1. XRD of $0.5Li_2S$-$0.5P_2O_5$ with different periods of milling.

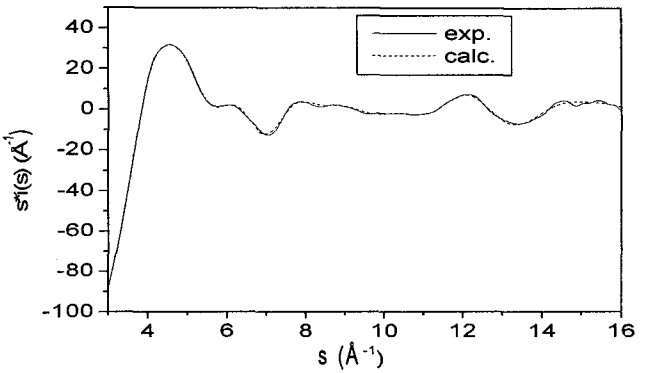

Figure 2. s.i(s) Vs s plot for xLi_2S-(1-x)P_2O_5 glass with x =0.6

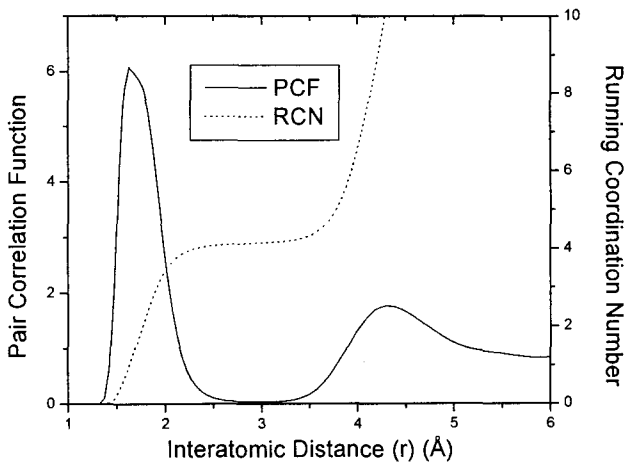

Figure 3. PCF and RCN of P-O in 0.6Li_2S-0.4P_2O_5 glass.

SYNTHESIS, SINTERING AND OXYGEN IONIC CONDUCTING PROPERTIES OF $Bi_2V_{0.9}CU_{0.1}O_{5.5-\delta}$

FENG ZHANG, KAI-QUN XU, QING XU†, WEN CHEN, HAN-XING LIU, DUAN-PING HUANG, JIAN ZHOU

School of Materials Science and Engineering, Wuhan University of Technology, Wuhan 430070, People's Republic of China

$Bi_2V_{0.9}Cu_{0.1}O_{5.5-\delta}$ powder was synthesized by a sol-gel method using EDTA and citric acid as mixed complexing agents. The formation process as well as the phase development and morphology of the synthesized powders were characterized by TG-DSC, XRD and SEM. The results indicate that fine and homogeneous powder (100-200 nm) with a pure Aurivillius phase can be produced by calcining at 450 ℃ for 1h. Compared with the conventional solid state method, the synthesizing method used in this work demonstrates remarkable advantages in producing $Bi_2V_{0.9}Cu_{0.1}O_{5.5-\delta}$ powder, such as simplicity and lowing calcining temperature. The oxygen ionic conducting properties of the ceramic specimen were investigated using AC impedance spectroscopy. The influence of sintering temperature on the microstructure and oxygen ionic conducting properties of $Bi_2V_{0.9}Cu_{0.1}O_{5.5-\delta}$ ceramic was investigated in the range of 560-680 ℃. The ceramic specimen sintered at 640 ℃ for 2h shows a dense microstructure with an average grain size of about 3 μm and a relative density of 93.6 %. The specimen provides an oxygen ionic conductivity of 1.4×10^{-1} S·cm^{-1} at 600 ℃. The difference between the activation energies for the oxygen ionic conducting in low and high temperature ranges is tentatively interpreted in terms of an order-disorder transformation.

1. Introduction

In the past years, there is a continuous research interest on new family of oxygen ionic conductors based on bismuth vanadate, $Bi_2VO_{5.5-\delta}$. $Bi_2VO_{5.5-\delta}$ has an Aurivillius structure, composed of alternating layers of fluoritelike $(Bi_2O_2)^{2+}$ and perovskite-like $(VO_{3.5})^{2-}$. The oxygen ionic transport of $Bi_2VO_{5.5-\delta}$ originates from oxygen-anion hopping between oxygen vacancies located in the perovskite layers. Below the melting point of 820 ℃, $Bi_2VO_{5.5-\delta}$ undergoes two phase transitions in the sequence of $\alpha \xrightleftharpoons{450^\circ C} \beta \xrightleftharpoons{570^\circ C} \gamma$. The tetragonal γ-phase, high temperate phase stable above 570 ℃, has the most disordered structure, leading to the highest oxygen ionic conductivity ($\sigma > 10^{-1}$ S·cm^{-1} at 600 ℃) among the three phases [1,2]. The γ-phase can be stabilized down to room

† Corresponding author. Tel.: +86 27 87863277; fax: +86 27 87864580.
E-mail address: xuqing@mail.whut.edu.cn (Q. Xu).

temperature by partially substituting vanadium with foreign metals such as Co, Cu, Ni, Zn, etc. The resulting family of $Bi_2Me_xV_{1-x}O_{5.5-\delta}$ (abbreviated as BIMEVOX) compounds shows remarkable potential of being used in moderate temperature electrochemical devices, including oxygen pumps, electrochemical sensors, electrodes and oxygen separation membranes [3-5].

The BIMEVOX materials are commonly synthesized by the conventional solid state method. When using the conventional method, a relatively high synthesis temperature and a rather long reaction time are always needed in order to yield a product with a pure Aurivillius phase [6-8]. Investigating alternative synthesis routes to the conventional method is an intriguing subject of significant importance. Research efforts have been directed to the synthesis of the BIMEVOX materials using various chemical methods, such as sol-gel method [9,10], co-precipitation technique [11] and mechanochemical route [12-14]. It has been demonstrated that synthesizing the BIMEVOX materials by a chemical method has advantages of simplifying preparing process, producing powders with desired morphology and enhancing the ionic conducting properties [9]. Therefore, further research on this topic is necessary.

$Bi_2V_{0.9}Cu_{0.1}O_{5.5-\delta}$ is a representative member in the BIMEVOX family. In this work, we report the synthesis of $Bi_2V_{0.9}Cu_{0.1}O_{5.5-\delta}$ by a sol-gel method using EDTA and citric acid as mixed complexing agents. The sintering and oxygen ionic conducting properties of the resulting $Bi_2V_{0.9}Cu_{0.1}O_{5.5-\delta}$ were examined.

2. Experiments

Reagent grade $Bi(NO_3)_3 \cdot 5H_2O$, NH_4VO_3, $Cu(NO_3)_2 \cdot 3H_2O$, $C_{10}H_{16}N_2O_8$ (EDTA) and citric acid were used as starting materials. The nitrates and ammonium metavanadate were weighed, respectively, according to the nominal composition of $Bi_2V_{0.9}Cu_{0.1}O_{5.5-\delta}$. The bismuth nitrate and equimolar amount of EDTA were first dissolved into deionized water in a beaker. Then, citric acid, NH_4VO_3 and copper nitrate were added. The mole ratio of citric acid to EDTA was 3: 1. Small amounts of ammonia solution were dripped to adjust the pH value of the precursor solution. The precursor solution was heated at 110 ℃ in an oven to form a sol and subsequently a gel. The gel was further heated at 160 ℃ to produce a charred foam-like gel. The charred gel was pulverized and calcined at 400-450 ℃ for 1 h. The resultant powders were uniaxially pressed into disks (13mm diameter and 2 mm thickness), and sintered at 560-680 ℃ for 2 h in air.

Thermogravimetric (TG) analysis and differential scanning calorimetry (DSC) analysis of the charred gel were performed using a Netzsch STA449C simultaneous thermal analyzer at a heating rate of 10 ℃·min^{-1} in air. The phase

development of the calcined powders was examined by a Rigaku D/MAX-RB X-ray diffractometer using Cu Kα radiation. The morphology of the calcined powders and microstructure of the ceramic specimens were investigated by a Jeol JSM-5610LV scanning electron microscope (SEM). For ceramic specimens, thermally etched surfaces were used for SEM observation. The non-isothermal sintering behavior was investigated by a NETZSCH DIL 402C dilatometer using uniaxially pressed rectangular bars (5 mm×5 mm×20 mm). The variation in disordering degree of oxygen vacancies was investigated by means of DSC analysis using the Netzsch STA449C simultaneous thermal analyzer at a heating rate of 5 ℃·min^{-1} between 150-650 ℃. The disk specimens were polished to ensure surface flatness and painted with platinum paste on the both surfaces for measuring the oxygen ionic conductivity.

The AC impedance spectroscopy of the specimens was measured using a TH2818 automatic component analyzer (0.02-300 kHz) at 200-600 ℃ in air. Considering the geometric of the disk specimens, the ionic conductivities were determined by fitting measured impedance plots.

3. Results and discussion

Fig. 1 shows the TG-DSC curves of charred $Bi_2V_{0.9}Cu_{0.1}O_{5.5-\delta}$ gel. The faint endothermic peak at 74.8 ℃ was caused by the evaporation of residual NH_3 and adsorbed water, corresponding to a small weight loss of 9.1 %. The two successive exothermic peaks at 312.8 ℃ and 446.4 ℃ are assigned to the thermal decomposition of the charred gel and combustion of remaining organic components, respectively, totally generating a weight loss of 44.9 %. No further DSC peak or weigh loss can be seen thereafter, indicating the completion of the thermal decomposition of the charred gel below 500 ℃.

It was found that calcining temperature has a determinant role on the phase purity and morphology of the calcined powders. Fig. 2 shows the X-ray diffraction (XRD) patterns of the $Bi_2V_{0.9}Cu_{0.1}O_{5.5-\delta}$ powders calcined at different temperatures. After calcining at 400 ℃, most XRD peaks belonging to an Aurivillius phase can be detected. Raising calcining temperature promoted the development of the Aurivillius phase. A pure Aurivillius phase was identified for the powders calcined at 450-550 ℃. Fig. 3 shows the SEM micrographs of the powers calcined at different temperatures. The powder calcined at 400 ℃ consists of relatively large particles. This can be attributed to the existence of residual organic components. Homogeneous and fine particles in the size range of 100-200 nm were observed in the powder calcined at 450 ℃. Further increasing the calcining temperature resulted in an obvious increase of particle

size and a slight sintering of the particles. Hence, it was ascertained that the preferred calcining temperature of $Bi_2V_{0.9}Cu_{0.1}O_{5.5-\delta}$ powder is 450 ℃. Compared with the conventional solid state reaction method [6-8], the EDTA-citrate method used in the present work enables the production of $Bi_2V_{0.9}Cu_{0.1}O_{5.5-\delta}$ powder with a desired morphology through a simple synthesis process and at a relatively lower calcining temperature.

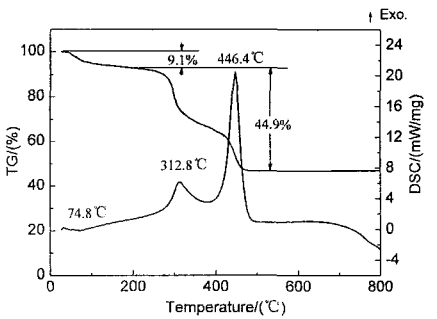

Fig. 1 TG-DSC curves of charred $Bi_2V_{0.9}Cu_{0.1}O_{5.5-\delta}$ gel.

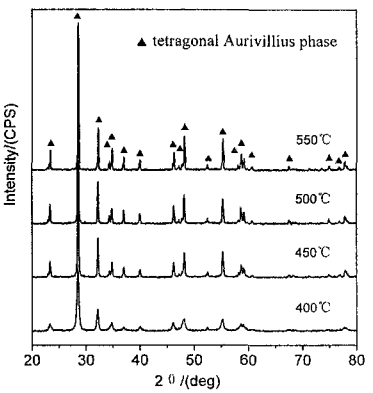

Fig. 2 XRD patterns of $Bi_2V_{0.9}Cu_{0.1}O_{5.5-\delta}$ powders calcined at different temperatures.

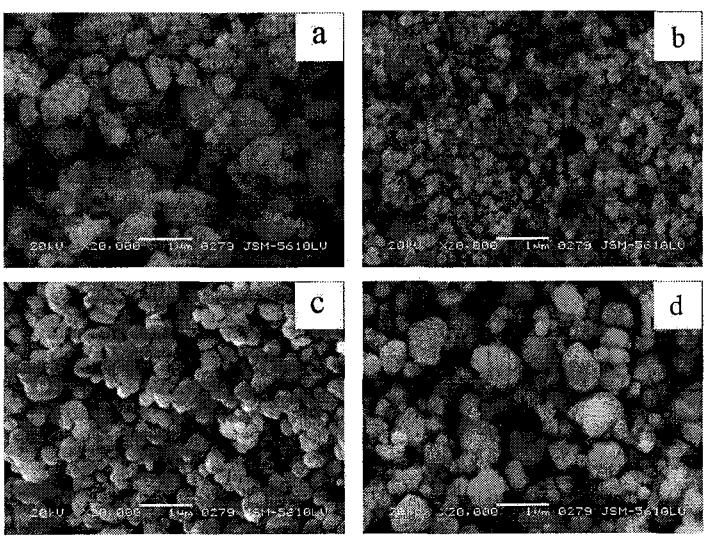

Fig. 3 SEM micrographs of $Bi_2V_{0.9}Cu_{0.1}O_{5.5-\delta}$ powders calcined at (a) 400 ℃, (b) 450 ℃, (c) 500 ℃ and (d) 550 ℃.

The powder calcined at 450 ℃ was used for investigating the sintering and ionic conducting properties. Fig. 4 shows the dilatometric curves of green $Bi_2V_{0.9}Cu_{0.1}O_{5.5-\delta}$ bar. Three characteristic temperatures can be noticed: T_s represents the onset temperature of the shrinkage, T_m corresponds to the temperature of maximum shrinkage rate and T_c indicates the critical temperature above which a creep may occur. It was found that, for $Bi_2V_{0.9}Cu_{0.1}O_{5.5-\delta}$, the shrinkage initiates at approximately 466 ℃ (T_s) and the maximum shrinkage rate appears at 573 ℃ (T_m). In addition, it can be observed that the sintering process tends to end at 700 ℃, with the shrinkage rate becoming nearly negligible at higher temperatures.

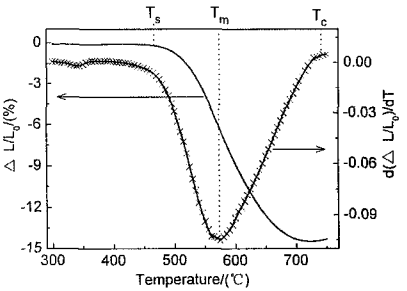

Fig. 4 Dilatometric curves of green $Bi_2V_{0.9}Cu_{0.1}O_{5.5-\delta}$ bar.

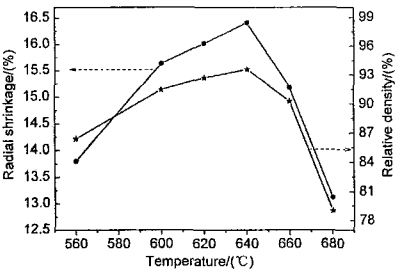

Fig. 5 Radial shrinkage and relative density of $Bi_2V_{0.9}Cu_{0.1}O_{5.5-\delta}$ ceramics as a function of sintering temperature.

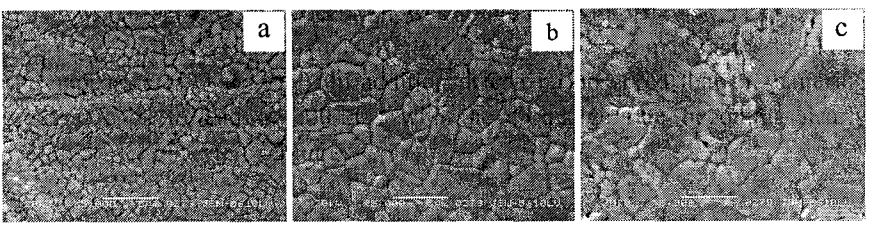

Fig. 6 SEM micrographs of $Bi_2V_{0.9}Cu_{0.1}O_{5.5-\delta}$ ceramics sintered at (a) 600 ℃, (b) 640 ℃ and (c) 680 ℃.

In order to determine the optimum sintering temperature, $Bi_2V_{0.9}Cu_{0.1}O_{5.5-\delta}$ specimens were sintered for 2 h at temperatures between T_m and T_c. Fig. 5 shows the relatively density and radial shrinkage of $Bi_2V_{0.9}Cu_{0.1}O_{5.5-\delta}$ ceramics as a function of sintering temperature. The values of relative densities were calculated with reference to the theoretical density of 7.77 $g \cdot cm^{-1}$, derived from the unit cell parameters based on XRD refinement [8]. The radial shrinkage and relatively density display an identical variation with sintering temperature,

increasing with sintering temperature up to a maximum value at 640 ℃ and then declining. Fig. 6 shows the SEM micrographs of $Bi_2V_{0.9}Cu_{0.1}O_{5.5-\delta}$ ceramics sintered at different temperatures. Rather small grains together with obvious pores can be seen in the specimen sintered at 600 ℃. A dense microstructure with uniform and well grown grains of 3-5 μm was observed for the specimen sintered at 640 ℃. By comparison, the specimen sintered at 680 ℃ presents an abnormal grain growth and distinct pores, which is in agreement with its low relatively density of 79.0 %. Thus, sintering at 640 ℃ was ascertained to be preferred for $Bi_2V_{0.9}Cu_{0.1}O_{5.5-\delta}$ ceramic. Compared with the conventional solid state method [6-8], sintering temperature can be lowered by about 100 ℃ by using the EDTA-citrate method described in the present work.

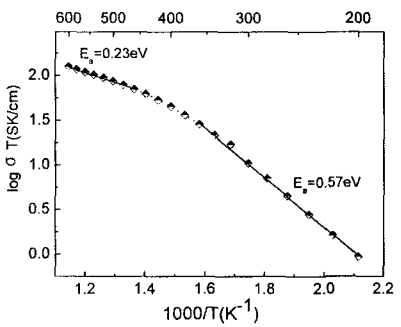

Fig. 7 Arrhenius plot of electrical conductivity for $Bi_2V_{0.9}Cu_{0.1}O_{5.5-\delta}$ ceramic sintered at 640 ℃.

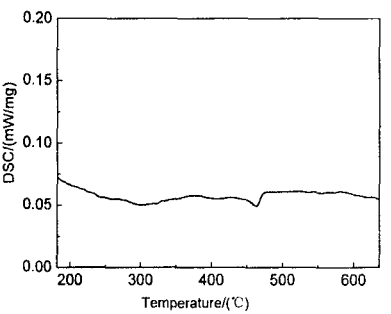

Fig. 8 DSC curve for $Bi_2V_{0.9}Cu_{0.1}O_{5.5-\delta}$ ceramic sintered at 640 ℃.

Fig. 7 shows the Arrhenius plot of oxygen ionic conductivity for $Bi_2V_{0.9}Cu_{0.1}O_{5.5-\delta}$ ceramic sintered at 640 ℃. The plot can be approximately divided into two regions, with a slop change occurring between 360-440 ℃. This is presumably attributed to a γ'-γ transformation during heating [15]. With a tetragonal symmetry, the difference between the γ and γ' phases lies in the disordering degree of oxygen vacancies. The high temperature region of the Arrhenius plot, corresponding to the γ phase, is characterized by highly disordering oxygen vacancies and a low activation energy of 0.23 eV. The low temperature region, corresponding to the γ' phase, gives a higher activation energy of 0.57 eV, which can be explained by a partial ordering of oxygen vacancies [16]. Fig. 8 shows the DSC curve of $Bi_2V_{0.9}Cu_{0.1}O_{5.5-\delta}$ ceramic sintered at 640 ℃. The endothermic peak near 450 ℃ was assumedly caused by the γ'-γ transformation [17,18]. There is, however, a discrepancy between the transformation temperatures measured by the two techniques. This is probably due to the different timescales of the two techniques, with the heating rate of

DSC analysis being comparatively faster than that of ionic conductivity measurement. The specimen sintered at 640 ℃ exhibits a high oxygen ionic conductivity of 1.4×10^{-1} S·cm^{-1} at 600 ℃.

4. Conclusions

$Bi_2V_{0.9}Cu_{0.1}O_{5.5-\delta}$ powder was synthesized by a sol-gel method using EDTA and citric acid as mixed complexing agents. The EDTA-citrate method has been confirmed to be an advantageous process in synthesizing $Bi_2V_{0.9}Cu_{0.1}O_{5.5-\delta}$. $Bi_2V_{0.9}Cu_{0.1}O_{5.5-\delta}$ powder with a pure Aurivillius phase can be produced by calcining at 450 ℃ for 1h in air. The resulting powder consists of superfine and uniform particles of 100-200 nm. $Bi_2V_{0.9}Cu_{0.1}O_{5.5-\delta}$ ceramic sintered at 640 ℃ shows a dense microstructure with uniform grains of 3-5 μm and a relative density of 93.6 %. The specimen provides an oxygen ionic conductivity of 1.4×10^{-1} S·cm^{-1} at 600 ℃. Moreover, experimental evidences have been achieved for the γ'-γ transformation in tetragonal ceramic during heating through ionic conductivity measurement and DSC analysis.

Acknowledgments

This work was financially supported by the Program for New Century Excellent Talents in University (Grant No. NCET-04-0724), Scientific Research Foundation for the Returned Overseas Chinese Scholars (Grant No. 2004-527) and Foundation for Innovative Research Team of Hubei Province (Grant No. 2005ABC004).

References

1. S.N. Achary, M.D. Mathews, S.J. Patwe, et al., *J. Materials Science Letters*, **18**, 355(1999).
2. A.V. Chadwick, C.C. Maltese, G. Morrison, et al., *Solid State Ionics*, **119**, 79(1999).
3. A.A. Yaremchenko, V.V. Kharton, E.N. Naumovich, et al., *Solid State Ionics*, **111**, 227(1998).
4. I. Abrahams, F. Krok, J.A. Nelstrop, *Solid State Ionics*, **90**, 57(1996).
5. J.C. Bovin. *International Journal of Inorganic Materials*, **3**, 1261(2001).
6. J.R. Dygas, M.Malys, F.Kork, et al. *Solid State Ionics*, **176**, 2085(2005).
7. F. Kork, I. Abrahams, W. Wrobel, et al. *Solid State Ionics*, **154-155**, 511(2002).
8. M.C. Steil, J. Fouletier, M. Kleitz, et al. *J. European Ceramic Society*, **19**, 815(1999).
9. C.H. Hervoches, M.C. Steil, R. Muccillo. *Solid State Sciences*, **6**, 173(2004).
10. M.J. Godinho, P.R. Bueno, M.O. Orlandi, et al. *Materials Letters*, **57**, 2540(2003).
11. A.K. Bhattacharya, K.K. Mallick, *Solid State Communication*, **91**, 357(1994).
12. F.C. Fonseca, M.C. Steil, R.N. Vannier, et al. *Solid State Ionics*, **140**, 161(2001).
13. V.V. Zyryanov, *Inorganic Materials*, **41**, 156(2005).

14. V.V. Zyryanov, N.F. Uvarov. *Inorganic Materials*, **41**, 281(2005).
15. I. Abrahams, F. Krok, D. Bangobango et al., *Solid State Ionics*, **86-88**, 261(1996).
16. F. Krok, I. Abrahams, D. Bangobango et al., *Solid State Ionics*, **111**, 37(1998).
17. W. Wrobel, I. Abrahams, F. Krok, et al. *Solid State Ionics*, **176**, 1731(2005).
18. M. Alga, A. Ammar, B. Tanouti, et al. *J. Solid State Chemistry*, **178**, 2873(2005).

SYNTHESIS AND TRANSPORT CHARACTERISTICS OF $PbI_2 - Ag_2O - Cr_2O_3$ SUPERIONIC SYSTEM

S. AUSTIN SUTHANTHIRARAJ* AND VINOD MATHEW
Department of Energy, University of Madras,
Guindy Campus, Chennai-600 025, India
*Email:suthan98@yahoo.com

The present work involves the preparation and characterization of a new superionic system namely, $(PbI_2)_x$ -$(Ag_2O–Cr_2O_3)_{100-x}$ where x = 5, 10, 15, 20, and 25 mol% respectively. The varieties of samples were synthesized by the rapid melt quenching technique. Complex impedance analysis of all these samples was carried out over the frequency range 1 MHz – 20 Hz in the temperature window 300 – 463 K. The Fourier transform infrared (FTIR) spectra were recorded over the wave number region 4000 – 500 cm^{-1} by the KBr pellet method at room temperature. Furthermore, the ionic transport number (t_i) values were obtained for all these specimens by Wagner's polarization technique. Impedance spectral analyses have indicated their room-temperature electrical conductivities to be of the order of 10^{-4} Scm^{-1}.The detailed FTIR results obtained for most of the samples in this system have revealed the absorption bands around 850 cm^{-1} corresponding to CrO_4^{2-} molecular species. The ion transport number values as determined by the Wagner's polarization method were found to be greater than 0.95 thus indicating the ionic nature of this system for device applications.

1. Introduction

The superionic properties of silver ion conducting materials have been extensively studied in view of their important applications in gas sensors. Recent literature show that researchers are still showing wide interest in studying several aspects of systems involving various combinations of glass formers, glass modifiers and dopant salts. [1-5] Among these materials, a major part of work carried out recently in our laboratory has identified and analyzed several new silver based solid electrolytes. [6-9] Initially, Minami studied the effect of chromium oxide as glass former in a silveroxysalt with AgI as the dopant salt. [10] The aim of the present investigation involves the preparation and characterization of a new series of silver ion conducting systems with PbI_2 as the dopant salt viz., PbI_2-Ag_2O-Cr_2O_3 through Fourier transform infrared

(FTIR) studies, impedance spectroscopy and ion transport number measurements by the Wagner's polarization technique.

2. Experimental Procedure

2.1. Material Preparation

Analar grade chemicals of PbI_2 (Aldrich- Purity 99%), Ag_2O (SRL- Purity 99%) and Cr_2O_3 (Aldrich- Purity 98%) were used as starting materials. The appropriate amounts of these starting materials were weighed out according to the stoichometric composition $(PbI_2)_x - (Ag_2O - WO_3)_{100-x}$, $(5 \leq x \leq 25)$, where x = 5, 10, 15, 20, and 25 mol% PbI_2. Subsequently, the mixture was loaded into quartz ampoules and vacuum-sealed. These specimens were then annealed to 823 K for nearly an hour and rapidly quenched to liquid nitrogen temperature followed by storage in darkened desiccators to prevent light-induced reactions.

2.2. Characterization Studies

The electrical conductivity measurements were made using the complex impedance analysis carried out on powdered samples, that were made into pellets of 8 mm diameter and approximately 3 mm thickness under a pelletizing pressure of 5 ton/cm^2, using an HP 4284A Precision LCR meter in the frequency window 20 Hz - 1 MHz and over the temperature range 301 - 463 K.

FTIR spectra were recorded for all the five different samples of the mixed system $(PbI_2)_x - (Ag_2O - Cr_2O_3)_{100-x}$, $(5 \leq x \leq 25)$ in the wave number region 4000 – 500 cm^{-1} at room temperature by the KBr pellet method using a Perkin Elmer RX1 Spectrophotometer with a resolution of 4 cm^{-1}.

Wagner's polarization technique was employed to determine the total ion transport number. In this method, the powdered sample forming the electrolytic phase is pressed between silver (non- blocking) and graphite (blocking) electrodes and made into a pellet using the method described above. Subsequently, a small dc potential (~200 mV) is applied across the cell thus formed and the current and potential difference is noted simultaneously as a function of time. [11] The value for output current at time t = 0 sec

corresponds to total electrical conductivity due to ions and electrons. After 6-7 h, a steady state output corresponding to just the electronic conduction was noted. From the above measured values, the total ion transport number was evaluated.

3. Results and Discussion

3.1. Electrical Conductivity Studies

The room temperature electrical conductivity, σ_{301K} values for the five different compositions in the present system are given in Table1. It can be seen from Table 1 that

Table1. Electrical conductivity and ion transport number data for different compositions of the system $(PbI_2)_x$- $(Ag_2O\text{-}Cr_2O_3)_{100-x}$

Composition,x (mol%)	Room temperature electrical conductivity σ_{RT}, (Scm^{-1})	Total ionic transport number (t_i)
5	1.01×10^{-4}	0.951
10	2.22×10^{-4}	0.970
15	6.50×10^{-4}	0.981
20	1.97×10^{-4}	0.966
25	1.37×10^{-4}	0.958

these samples exhibited electrical conductivities of the order of 10^{-4} Scm^{-1}. The best conducting sample in the present series viz., 15 (PbI_2) – 75 (Ag_2O – Cr_2O_3) possessed conductivity as high as 6.5×10^{-4} Scm^{-1}. The conductivity values thus obtained are comparable to that in the case of the superionic systems AgI – Ag_2CrO_4 and $Cu_xAg_{1-x}I$ – Ag_2O – CrO_3. [12] The observed impedance plots for the typical composition 15(PbI_2) – 75(Ag_2O – Cr_2O_3) obtained at various temperatures (301 – 463 K) are shown in Figure 1. It is well evident from Figure 1 that the bulk resistance of the sample, as evaluated from the latter half of the semicircle corresponding to the high frequency region, decreases as the temperature increases. The bulk and electrode-electrolyte effect can be studied from the depressed semicircle corresponding to the

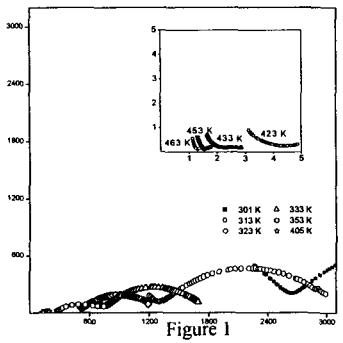

Figure 1

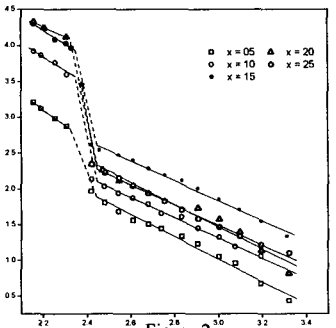

Figure 2

Figure 1. Complex impedance plots (Zcosθ versus Zsinθ) obtained at various temperatures for the mixed system $(PbI_2)_x$ - $(Ag_2O - Cr_2O_3)_{100-x}$, where x = 15 mol%.

Figure 2. Variation of electrical conductivity with temperature for five different compositions in the mixed system $(PbI_2)_x$ - $(Ag_2O - Cr_2O_3)_{100-x}$, $(5 \leq x \leq 25)$

lower frequency region. The bulk resistance was evaluated using the standard equivalent Boukamp circuit program. [13] It may also be noticed that on increasing temperatures the values of the bulk resistance decrease, thus implying an increase in the electrical conductivity. The inset in Figure 1 shows that the value of the bulk resistance goes down by an order at 423 K and above. This feature clearly signifies a corresponding rise in the conductivity by an order indicating the formation of the high conducting α-AgI phase. The variation of electrical conductivity with temperature for all the five different compositions in the present system is shown in Figure 2. The plot is seen to obey the Arrhenius behavior of the form

$$\sigma(0) = (\sigma_0 / T) \exp(-E_a / kT) \qquad (1)$$

where the symbols have their usual meaning. The activation energies for ion migration (Ea) was calculated from the slope of the plot and it was found to range between 0.27 and 0.31 eV, the minimum value associated with the best conducting composition containing x = 15 mol% PbI_2. This trend of the electrical conduction in the present system at different temperatures is found to be in good accordance with the characteristic property of superionic solids [14,15]. This clearly confirms the Hard and Soft Acids and Bases (HSAB) principle of ion exchange reactions between Ag^+ and Pb^{2+} resulting in the formation of AgI. [16,17]

3.2. FTIR Spectroscopic Data

The FTIR patterns recorded for five different compositions of the mixed system $(PbI_2)_x$ -$(Ag_2O–Cr_2O_3)_{100-x}$, $(5 \leq x \leq 25)$ corresponding to x = 5, 10, 15, 20 and 25 mol% PbI_2 in the range 500 – 1200 cm^{-1} are depicted in Figure 3. No characteristic absorption bands were observed beyond 1200 cm^{-1}. The presences of a band around 565 cm^{-1} in the case of all five compositions suggests the symmetric stretching (γ_s) mode of $Cr_2O_7^{2-}$. [18] The absorption band at 878 cm^{-1} for the composition containing x = 5 mol% PbI_2 corresponds to the asymmetric stretching (γ_{as}) mode of tetrahedral CrO_4^{2-} species. The absorption band noticed around 850 cm^{-1} for compositions with

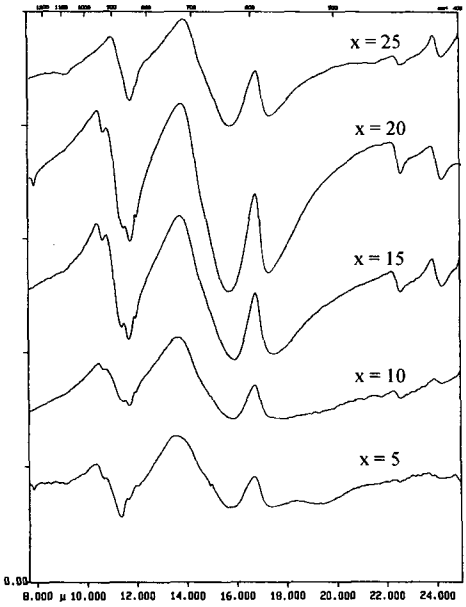

Figure 3. FTIR patterns observed for five different samples of the mixed system $(PbI_2)_x$ - $(Ag_2O - Cr_2O_3)_{100-x}$, $(5 \leq x \leq 25)$

x = 10, 15, 20 and 25mol% PbI_2 may be ascribed to the vibrational mode of CrO_4^{2-} ions. Researchers working on similar systems also reported similar absorption peaks. [19,20] For higher concentrations of the dopant salt, starting from x = 15 mol% PbI_2, new bands appearing within 400 – 450 cm^{-1} may be attributed to the vibrational mode of Pb-O bonds [21]. The absorption peak around 630 cm^{-1} for all the composition in the present system may be assigned to the formation of KIO_4 due to ion exchange reaction between K^+ and Ag^+ during the recording of FTIR spectra. [22] Thus, the FTIR results tend to reveal the presence of anionic species as CrO_4^{2-}, $Cr_2O_7^{2-}$ in the glassy network.

3.3. Ion Transport Number Measurements

The ion transport number data evaluated for all the five different compositions using the Wagner's polarization method are tabulated in Table 1. From Table 1, it is seen that the mobile ion transport number is found to be in the range 0.95 – 0.98. This confirms the fact that the present material under study is mainly a silver ion conductor. It is possible that, in addition to the contribution of silver ions for conduction, there is a strong possibility of the divalent Pb^{2+} ion also contributing to the conduction. Other workers too reported this trend known as the "mixed cation effect". [15,23] From earlier investigations, on the AgI-Ag_2O-Cr_2O_3 system, it was confirmed that the best conducting glass was found in the higher concentration side of silver iodide i.e., above 60mol% AgI. [10] On the other hand, the present system involving the dopant salt PbI_2, has revealed that high ionic conductivities are achieved for comparatively lower concentrations of PbI_2, i.e., about 15mol% PbI_2. There may be two main reasons behind these differences presented above. Firstly, the concentration of the iodine content originating from PbI_2 is double than in the case of AgI. Two I^- ions are provided by one mole of PbI_2 to the silver-chromium-oxide network whereas AgI introduces only one I- ion into the same network. Hence a rapid increase in the number of I^- ions leads to structural deformation of the network and expands the network significantly thus creating pathways for conduction or increasing the mobility of the conducting ions. The above activity of the I^- ion is considered as the "open network model" [24] and that explains a significant rise in conductivity for lower concentrations of PbI_2 content. Secondly, it is highly probable that monovalent Ag^+ ion and divalent Pb^{2+} ion are involved together in the conduction process and as a result exchange interactions between Pb^{2+} and Ag^+ cations may take place. [25] Hence Pb^{2+} ions prefer a link with the chromium oxide network and Ag^+ ions move towards the I^- ions to form micro clusters of AgI. The presence of such micro clusters has been well reported in several

glasses. [15, 26] In addition, the presence of AgI has already been confirmed by the impedance results discussed earlier. Therefore, the higher the concentration of PbI_2 content, the more the Pb^{2+} ions become available to penetrate into the silver-chromium-oxide network.

4. Conclusion

The ion transport and structural investigations on the mixed system $(PbI_2)_x$ - $(Ag_2O–Cr_2O_3)_{100-x}$, $(5 \leq x \leq 25)$ has revealed a glassy network structure involving tetrahedral $Cr_2O_7^{2-}$, CrO_4^{2-} ions and confirmed the presence of α-AgI. The ion transport number measurements identified the present system as a silver ion conducting superionic conductor. The role of PbI_2 as a dopant salt compared to AgI in the same chromium network has also been examined and the reason for the observed high conductivity values at lower concentrations of PbI_2 carefully probed into. The conduction behavior in the present system appears to support the open network model and the cluster pathway model.

Acknowledgement

The authors wish to thank the University Grants Commission, New Delhi for the financial assistance received in the form of a research project [No. F.10-22/2003(SR)].

References

[1] M Foltyn, J E Garbaczuyk, M Wasiucionek and J L Nowinski , *Solid State Ionics* **176**, 2137 (2005).
[2] K P Padmasree, D K Kanchan, H R Panchal, A M Aswathi and S B Bhardwaj, *Solid Stat. Comm.* **136**, 102 (2005)
[3] S Hamakawa, M Aniya,and F Shimojo, *Solid State Ionics* **176**, 2471 (2005)
[4] S Jayaseelan, P Muralidharan, M Venkateswarlu and N Satyanarayana, *Mat. Sci. Engg. B* **119**, 136 (2005).
[5] H Takahashi, N Rikitake, T Sakuma and Y Ishmi, *Solid State Ionics* **175**,

671 (2004).
[6] S. A. Suthanthiraraj and Vinod Mathew, *Indian J. Physics* **79**, 753 (2005).
[7] S. A. Suthanthiraraj and R. Mala, *J. Solid State Electrochem.* **7**, 232 (2003).
[8] S A Suthanthiraraj, S Murugesan and P Maruthamuthu, *J. Mater. Sci. Lett.* **21**, 387 (2002).
[9] S. A. Suthanthiraraj, S. Murugesan and P. Maruthamuthu, *Mater. Res. Bull.* **37**, 2145 (2002).
[10] T Minami, *J. Non-Cryst. Solids* **56**, 15 (1983).
[11] C Wagner, J B Wagner, *J.Phys. Chem.Solids* **33**, 205 (1964).
[12] A Viswanathan and S A Suthanthiraraj, *Mater. Res. Bull.* **28**, 821(1993).
[13] B A Boukamp, *Solid State Ionics* **20**, 31(1986).
[14] R Suresh Kumar and K Hariharan, *Solid State Ionics* **104**, 227 (1997).
[15] G El Damrawi, A K Hassan and H Doweidar, *Physica B* **291**, 34 (2000).
[16] M K P Seydei and S A Suthanthiraraj *J. Mater. Sci.* **28**, 3519 (1993).
[17] V G Chandrasekhar and S A Suthanthiraraj *Solid State Ionics* **62**, 61 (1993).
[18] K Nakamoto, in "Infrared and Raman Spectra of Inorganic and Co-ordination Compounds"5th ed., Part A (John Wiley, New York,1977).
[19] Markus M Hoffmaqnn, J G Darab and J L Fulton, *J. Phys. Chem. A* **105**, 1772 (2001).
[20] A N D Rani and K Hariharan, *Mater. Chem. Phys.* **43**, 243 (1996).
[21] P Tarte, A Rulmont, M Liegeois-Duyckaerts, R Cahay and J M Winand, *Solid State Ionics* **42**, 177(1990)
[22] F A Miller, G L Carlson, F F Bentley and W H Jones, *Spectrochim. Acta* **16**, 135 (1960)
[23] J P Malugani, R Mercier, M Tachez, *Solid State Ionics*, **21**, 131 (1986)
[24] H L Tellur, D P Button, D r Uhlmann, **40**, 93 (1980)
[25] S Hull, D A Keen and P Berastegui, *Solid State Ionics* **147**, 97 (2002)
[26] S H Chang, K K Jeffrey, J R Stevens, *Phys. Rev. B*, **41**, 1654 (1990)

ELECTRONIC CONDUCTIVITY OF $La_{0.8}Sr_{0.2}Ga_{0.8}Mg_{0.2-x}Co_xO_{3-\delta}$ ELECTROLYTES (II)

KATSUHIKO YAMAJI, YUEPING XIONG, HARUO KISHIMOTO, TERUHISA HORITA, NATSUKO SAKAI, MANUEL E. BRITO, HARUMI YOKOKAWA

National Institute of Advanced Industrial Science and Technology (AIST), Energy Technology Research Institute, Central 5, 1-1-1 Higashi, Tsukuba, 305-8565, Japan

Electronic conductivity of cobalt doped LSGM electrolytes ($La_{0.8}Sr_{0.2}Ga_{0.8}Mg_{0.2-x}Co_xO_{3-\delta}$, LSGMC) was directly measured with using a Hebb-Wagner's ion blocking cell. Electronic conductivity of LSGMC electrolytes was measured as a function of oxygen partial pressures. The electronic conductivity of LSGM8282(LSGMC(x = 0) electrolyte shows a linear dependence on $p(O_2)^{1/4}$ in the higher $p(O_2)$ region, which is attributed to the electronic hole conduction. The electronic conductivity of LSGMC was drastically changed with the concentration of cobalt. The electronic conductivity of LSGMC(x = 0.01) also shows a linear dependence on $p(O_2)^{1/4}$ in the higher $p(O_2)$ region, and the conductivity was about the same with that of the LSGM8282. On the other hand, the electronic conductivity of LSGMC(x = 0.05) did not show a linear dependency on $p(O_2)^{1/4}$ but on about $p(O_2)^{1/6}$ in the higher $p(O_2)$ region. The electronic conductivity of both electrolytes in lower $p(O_2)$ region did not show any dependence on $p(O_2)$.

1. Introduction

Doped- lanthanum gallate electrolytes with appropriate double dopant of strontium and magnesium (denoted to LSGM) possess higher oxide ion conductivity than that of YSZ electrolytes[1]. Consequently, LSGM electrolytes are being studied as potential electrolytes for intermediate temperature (IT) SOFCs operated below 800 °C. SOFC Electrolytes should have not only high oxide ion conductivity but also low electronic conductivity. High electronic conductivity enlarges the oxygen permeation through the electrolyte without power generation, which decreases the energy conversion efficiency of the SOFC. Hence, electronic conductivity of various SOFC electrolytes was intensively investigated in some groups. In order to evaluate the minor electronic conductivity in oxide ion conductors, a DC-polarization method with a Hebb-Wagner's ion blocking cell is the most suitable technique[2,3]. In this measurement, the minor electronic conduction can be observed by blocking the major ionic conduction. For oxide ion conductors, this technique was applied to YSZ at first, and some valuable data was obtained[4-6]. For LSGM electrolytes,

electronic conductivity of $La_{0.9}Sr_{0.1}Ga_{0.8}Mg_{0.2}O_{2.85}$ (LSGM9182) was measured by using a Hebb-Wagner's ion blocking cell in our group[7]. The electronic conductivity due to the electronic holes was observed in the higher $p(O_2)$ region over 10^{-5} atm. The transference numbers of oxide ion were 0.988 and 0.994 at 1273 and 873 K, respectively, which indicates that LSGM9182 is an appropriate oxygen ionic conductor as SOFC electrolytes, especially at lower temperatures. The electronic conductivity of LSGM9182 was recently reconfirmed by some researchers with good reproducibility[8,9].

However, the ionic conductivity of LSGM9182 is not sufficient to be utilized for IT-SOFCs with electrolyte supported structures. In order to increase the ionic conductivity, the amount of Sr dopant increased and some transition metals were additionally doped to Ga-site with Mg. As a result, $La_{0.8}Sr_{0.2}Ga_{0.8}Mg_{0.2-x}Co_xO_{3-\delta}$ (LSGMC) was found to be the state of the art in a series of doped- lanthanum gallate electrolytes[10], and the electrolyte has already utilized for a few kW SOFC demo stack[11]. On the other hand, a negligible new problems appeared by doping cobalt. Although the ionic conductivity of LSGMC increases with the amount of cobalt, the transference number of oxide ion, $t(O^{2-})$, of LSGMC decreases with the amount of cobalt in the higher $P(O_2)$ region. This reduction of $t(O^{2-})$ was considered due to the relatively high electronic hole conductivity. In our previous report[12], the electronic conductivity of $La_{0.8}Sr_{0.2}Ga_{0.8}Mg_{0.2-x}Co_xO_{3-\delta}$,($x$ = 0.05 and 0) was measured with a modified Hebb-Wagner's cell. The electrolyte without cobalt dopant showed typical electronic hole conductivity which was proportional to $p(O_2)^{1/4}$ in the higher $p(O_2)$ region. The electronic conductivity was enlarged by doping cobalt and the electronic conductivity was almost proportional to $p(O_2)^{1/6}$.

In this paper, electronic conductivity of LSGMC electrolytes was investigated as a function of the amount of cobalt dopant with a modified Hebb-Wagner's ion blocking cell.

2. Experimental

2.1. *Samples*

LSGMC electrolytes were prepared by a conventional solid-state reaction method as shown in a previous report. The electrolytes were sintered at 1723 K for 5h in air, and the obtained pellets were fully dense after sintering. In XRD measurements, LSGMC showed some small peaks related to a secondary phase with main peaks of a cubic LSGMC phase. We also used some LSGMC powders which were purchased from Seimi Chemical Co., Ltd.. The powders

were also sintered at 1723 K for 5h in air, and the obtained pellets were fully dense after sintering. In XRD measurements, LSGMC also shows some small peaks related to a secondary phase with main peaks of a cubic LSGMC phase.

2.2. *Measurements*

The electronic conductivity was measured with a modified Hebb-Wagner's ion blocking cell. Both surfaces of LSGMC pellets were polished with diamond slurry containing 3 μm diamond powders. Platinum paste (Tanaka Kikinzoku Kogyo K. K., TR-7905) was painted on both surfaces of the pellet as reversible and blocking electrodes, respectively, with diameters of 10 mm. Platinum meshes having platinum leads were attached on the electrodes as a current collector and the sample was fired at T = 1273 K. The blocking electrode was closed into a small chamber with an aluminum spacer and a glass sealant, and therefore, the oxygen was indirectly blocked at the blocking electrode with the closed small chamber during DC-polarization measurement.

The blocking cell was put between aluminum tubes with some elaborate parts to achieve good sealing by fixing the blocking cell and uniformly weighting between the alumina tubes. The outer of the fixed blocking cell was covered with a second aluminum tube to control the atmosphere around the blocking cell. The atmosphere around the reversible electrode was fixed by flowing 1%O_2 gas balanced with Ar. The temperature around the blocking cell was kept to be constant. The schematic views of the ion blocking cell and the cell setting are shown in Fig. 1.

DC-polarization measurements were worked out as follows. DC voltage was applied with using a potentio/galvano-stat. First, a constant voltage was applied between the reversible and the blocking electrode as oxygen was transferred from the blocking to the reversible electrodes. This is important to avoid a gas leakage from the glass sealant due to an increase of pressure in the closed space. When the voltage was applied to the sample, the current changed until an ionic current was fully blocked. In the steady state, the measured current is electronic current governed by electrons and electronic holes in the sample. When the electronic current was observed as a function of applied voltage, the electronic conductivity (σ_e) was determined by the equation as follows.

$$\sigma_e = \frac{L}{A}\left(\frac{dI}{dE_{app}}\right) \tag{1}$$

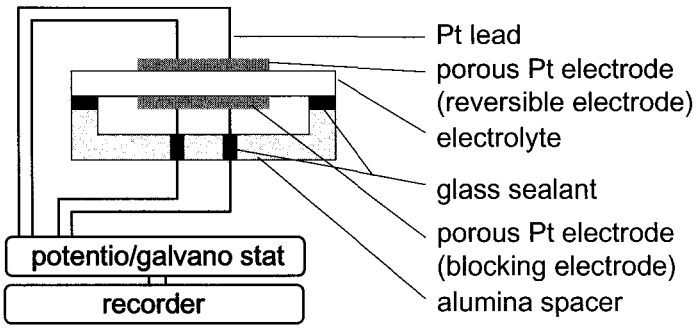

(a) ion blocking cell

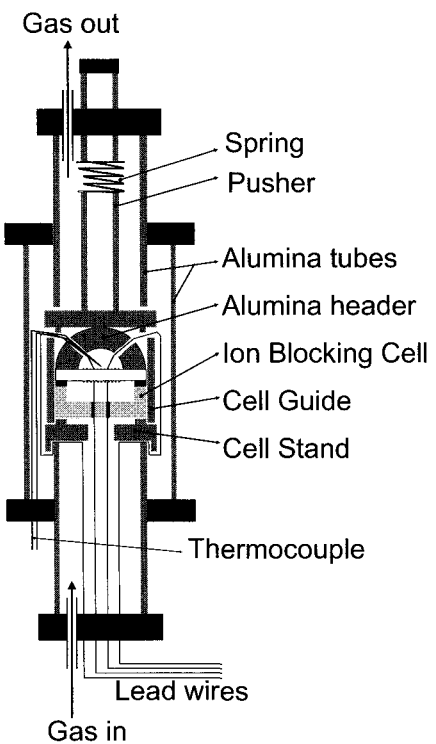

(b) cell setting

Figure 1. Schematic views of the ion blocking cell and the cell setting.

where A and L are the electrode area and the thickness of the sample pellet, respectively. The electronic conductivity are relevant to the oxygen partial pressure at the blocking electrode, $p_{block}(O_2)$, and calculated by using the following equation.

$$E_{app} = \frac{RT}{4F} \ln \frac{p_{rev}(O_2)}{p_{block}(O_2)} \tag{2}$$

where R, T, F and $p_{rev}(O_2)$ are the gas constant, temperature, the Faraday's constant and the oxygen partial pressure around the reversible electrode. The electronic conductivity was evaluated as a function of oxygen partial pressure using the equations 1 and 2.endent and additive.

3. Results

Figure 2 shows the electronic conductivity of LSGMC(x = 0.01) as a function of $p(O_2)$ at T = 1073, 973 and 873 K. The electronic conductivity at

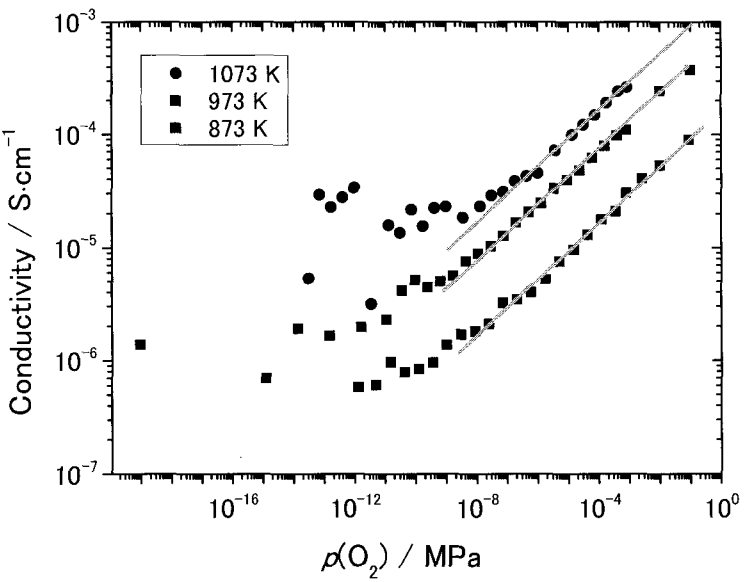

Figure 2. Electronic conductivity of LSGMC(x = 0.01) at T = 1073, 973, 873 K. The solid lines shows a linear dependency of conductivity on $p(O_2)^{1/4}$.

higher $p(O_2)$ region was proportional to 1/4 powers of $p(O_2)$ between T = 1073 and 873 K. When the main carrier of the electronic conduction is electronic holes produced in the electrolyte related to the equilibrium with oxygen, the conduction mechanism is explained with following equations,

$$V_O^{\bullet\bullet} + \frac{1}{2}O_2 = O_O^{\times} + 2h^{\bullet}, \quad [h^{\bullet}] \propto p(O_2)^{\frac{1}{4}} \tag{3}$$

where $V_O^{\bullet\bullet}$, $O_O^{\times}$, $h^{\bullet}$ in eq. 3 are an oxygen vacancy, normal oxide ion on the oxygen site, and electronic hole, respectively.

On the other hand, the electronic conductivity at the lower $p(O_2)$ region did not show any dependency on $p(O_2)$, and the conductivity vs. $p(O_2)$ plot was significantly scattered at the $p(O_2)$ region. In our previous reports, credible electronic conductivity was not obtained at lower $p(O_2)$ region, either. The difficulty of the electronic conductivity measurement in the lower $p(O_2)$ region should be attributed to some lack of reliability in lower $p(O_2)$ region. With lowering $p(O_2)$ especially at higher temperatures, Ga ions in LSGM were reduced at the surface and subsequently vaporized from the surface as Ga_2O etc[13]. In addition, the existence of platinum enhances the gallium depletion from LSGM electrolyte by forming Pt-Ga alloys.

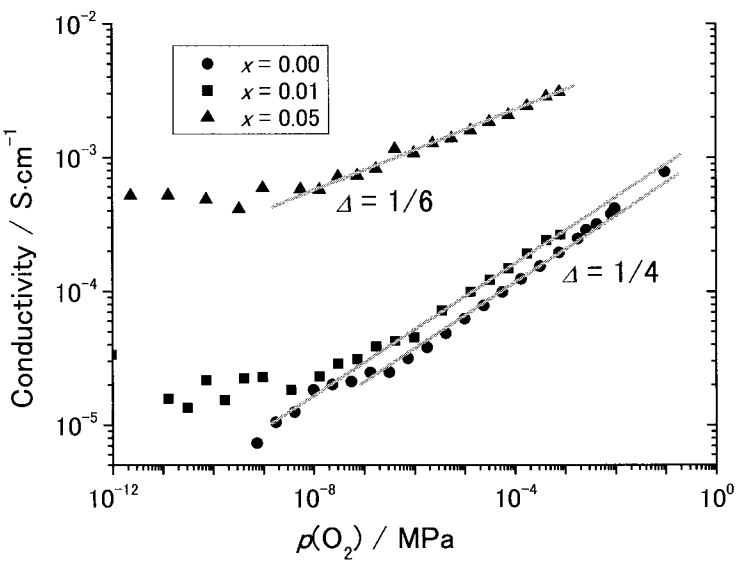

Figure 3. Electronic conductivity of various LSGMC(x = 0.00, 0.01, 0.05) electrolytes at T = 1073 K.

In our previous study, the electronic conductivity of LSGMC(x = 0.00, 0.05) had already been obtained[12]. Figure 3 shows the electronic conductivity of various LSGMC(x = 0.00, 0.01, 0.05) electrolytes at T = 1073 K. The conductivity of LSGMC(x = 0.00 and 0.05) were referred from our previous report. The electronic conductivity of LSGM8282 (LSGMC(x = 0)) showed a linear dependence on $p(O_2)^{1/4}$ in the higher $p(O_2)$ region. The electronic conductivity of LSGMC(x = 0.05) showed a linear dependence on $p(O_2)^{1/6}$ in the higher $p(O_2)$ region. The electronic conductivity of LSGMC(x = 0.01) shows a linear dependency on $p(O_2)^{1/4}$ in the higher $p(O_2)$ region, and was slightly higher than that of LSGM8282 and was significantly lower than that of LSGMC(x = 0.05). From these results, it is determined that the mechanism of electronic holes in LSGMC(x = 0.01) is the same with that of LSGM8282; the hole conduction is due to electronic holes produced in the electrolyte related to the equilibrium with oxygen as shown in eq. 3. The electronic holes did not increase by doping cobalt for LSGMC(x = 0.01) in a wide $p(O_2)$ region, which means that the valence of cobalt ions in LSGMC(x = 0.01) was constant in the higher $p(O_2)$ region. And the electronic conductivity of LSGMC was drastically changed with increasing the cobalt concentration from x = 0.01 to 0.05.

In order to clarify the turning point of the electronic conduction of LSGMC, the electronic conductivity of LSGMC(x = 0.03) is now investigating. The result will be shown in the conference.

4. Conclusion

Electronic conductivity of cobalt doped LSGMC electrolytes ($La_{0.8}Sr_{0.2}Ga_{0.8}Mg_{0.19}Co_{0.01}O_{3-\delta}$, LSGMC($x$ = 0.01) were directly measured with using a Hebb-Wagner's ion blocking cell. The mechanism of electronic holes in LSGMC(x = 0.01) was the same with that of LSGM8282; the hole conduction is due to electronic holes produced in the electrolyte related to the equilibrium with oxygen. The electronic holes did not increase by doping cobalt for LSGMC(x = 0.01) in a wide $p(O_2)$ region, which means that the valence of cobalt ions in LSGMC(x = 0.01) was constant in the higher $p(O_2)$ region.

References

1. T. Ishihara, H. Matsuda and Y. Takita, J. Am. Chem. Soc., **116** 3801 (1994)
2. M. Hebb, *J. Chem, Phys.*, **20** 185 (1952)
3. C. Wagner, *Proc. Int. Comm. Electrochem. Thermodyn. and Kinetics*, 7th Meeting, Lindau 1952, Butterworth, London, 361 (1957)

4. J. W. Paterson, E. C. Bogren and R. A. Rapp, J Electrochem. Soc., **19** 229 (1971)
5. W. Wepner, J. Solid State Chemistry, **20** 305 (1977)
6. T. Kawada, T. Horita, N. Sakai, B. A. van Hassel, H. Yokokawa and M. Dokiya, ISSI Lett. 4 No. 2 6 (1993)
7. K. Yamaji, T. Horita, M. Ishikawa, N. Sakai, H. Yokokawa and M. Dokiya, Proc. of 5th Int. Symp. on SOFC (SOFC-V), The Electrochem. Soc. Proc. Vol., **PV97-40** 1041 (1997)
8. J.-H. Kim and H.-I. Yoo, Solid State Ionics, **140** 105 (2001)
9. J. Weitkamp and H.-D. Wiemhöfer, Solid State Ionics, **154-155** 597 (2002)
10. T. Ishihara, T. Akbey, H. Furutani and Y. Takita, Solid State Ionics, **113-115** 585 (1998)
11. T. Kotani, K. Hosoi, N. Komada, F. Nishiwaki, T. Inagaki, S. Yamasaki, Extended Abstract of 2005 Fuel Cell Seminar, 81(2005)
12. K. Yamaji, Y. Xiong, H. Kishimoto, T. Horita, N. Sakai, M. E. Brito and H. Yokokawa, Proc. of 9th ACSSI, The science and technology of ions in motion, 253 (2004)
13. K. Yamaji, T. Horita, M. Ishikawa, N. Sakai and H. Yokokawa, Solid State Ionics, **135** 389 (2000)

This page is intentionally left blank

Part II
Electrode Materials

This page is intentionally left blank

Invited Papers

This page is intentionally left blank

CATHODIC PROPERTIES OF Al-DOPED $LiCoO_2$ PREPARED BY MOLTEN SALT METHOD FOR LI-ION BATTERIES

M.V. REDDY, G.V. SUBBA RAO AND B.V.R. CHOWDARI *

Department of Physics, National University of Singapore, Singapore 117542

*Corresponding Author. e-mail: phychowd@nus.edu.sg

Abstract

Layered $Li(Co_{1-x}Al_x)O_2$, x=0.05-0.25 phases have been prepared by using the one-pot molten salt method at 850 °C in air and characterized by X-ray diffraction, Rietveld refinement, SEM-EDAX, chemical analysis, BET surface area and density methods. Cathodic properties were studied at ambient temperature in cells with Li-metal as the counter electrode by cyclic voltammetry (CV), galvanostatic charge-discharge cycling (up to 130 cycles) and Impedance spectroscopy. Single-phase compounds with hexagonal layer structure formed for all x. Results showed that for $x \geq 0.05$, the Li-de-intercalation potential during the first charge-cycle occurs at a value slightly higher than that shown by pure $LiCoO_2$ and the structural transitions that occur at ~4.1 V and ~ 4.2 V are suppressed. However, the transition at ~4.5 V is not suppressed. As a consequence, the long-term cyclability of $Li(Co_{1-x}Al_x)O_2$ is greatly improved, when cycled in the potential ranges 2.5-4.3 V and 2.5-4.4 V at the current rate of 30 mA/g. Higher 10^{th} cycle capacities were noted for $x \geq 0.1$-0.2 in the 2.5-4.5 V range but capacity-fading was noted, by 5-7 % at the end of 55 cycles. The observed CV and impedance data have been analyzed and interpreted.

Key words: $Li(Co_{1-x}Al_x)O_2$; Molten salt synthesis; cathodes; Li-ion batteries

1. Introduction

Layered $LiCoO_2$ is commonly used as the cathode material for lithium ion batteries (LIB) due to its high volumetric energy density, excellent cyclability and high operating cell voltage. However, $LiCoO_2$ is usually cycled to an upper cut-off voltage of 4.2 V vs. Li, which gives a specific capacity of ~ 135 $mAhg^{-1}$. In order to obtain a higher capacity, $LiCoO_2$ must be charged to > 4.2 V, but this will cause capacity fading during charge-discharge cycling due to crystal structure transitions that occur with increasing y in $Li_{1-y}CoO_2$. These transitions are reversible: Hexagonal (H1) →monoclinic (M) and M →H1 occur at 4.06 and 4.18 V vs. Li respectively. The H1 → Hexagonal (H1-3) occurs at ~4.55 V and the (H1-3) →

Hexagonal (O1) transition takes place at ~4.63 V [1]. The phase transitions, H1 ↔ M↔H1 in $LiCoO_2$ which are order-disorder type and involve minor unit cell volume changes, can be suppressed by doping at the Co-site with ions like Ni [2], Mg [3], Cr [4], Rh [5] or by incorporating excess Li to form $Li_{1+x}CoO_2$, $x \leq 0.15$ [6-8], Al [9-20] or Ga [21]. The Li-recyclability has been studied in these doped systems.

Doping of aluminum (Al) at the Co-site in $LiCoO_2$ is of particular interest due to the following reasons:1. Low cost, low toxicity and low density in comparison to cobalt. 2. The ionic radius of Al^{3+} ion (0.535 Å) is only slightly smaller than that of Co^{3+} ion (0.545 Å in low-spin configuration) in an octahedral O-coordination, and hence a wide range of solid solution formation can be expected [11,17]. In fact, Takahashi et al. [22] have been able to grow single crystals of $Li(Co_{0.29}Al_{0.71})O_2$ which is iso-structural to $LiCoO_2$. 3. The Al-O bond is stronger than the Co-O bond in $Li(Co_{1-x}Al_x)O_2$ and as a consequence, the Li-O bond is weaker (more ionic) in comparison to $LiCoO_2$. This leads to increased Li-ion mobility in $Li(Co_{1-x}Al_x)O_2$ as has been found by Myung et al. [13] for the composition, x=0.1. Myung et al. [13] and Venkatraman and Manthiram [20] also found a significant decrease in the Co-dissolution, in the charged-state, of the compounds with x=0.1-0.3 in comparison to un-doped $LiCoO_2$. On the other hand, Al-doping in to $LiCoO_2$ leads to higher Li de-intercalation voltage, as predicted and verified experimentally by Ceder et al. [9] and also observed by many groups [10-18]. Also, studies have shown that at least up to 20 charge-discharge cycles, capacity degradation occurs in $Li(Co_{1-x}Al_x)O_2$ for $x \leq 0.25$ [10,11,12,15,18]. Local structural changes at the Co-site during cycling was found to be one of the reasons for the observed behavior [12]. However, Julien et al. [16] found that for x=0.05-0.25 in $Li(Co_{1-x}Al_x)O_2$, the discharge capacity stabilizes in the range 5-16 cycles, even though rapid degradation of capacity occurred during the first 5 cycles with a cut-off potential of 4.4 V vs. Li. Thus, there is a need to examine the long-term cycling behavior of the system, $Li(Co_{1-x}Al_x)O_2$ with various upper cut-off potentials.

The compounds $Li(Co_{1-x}Al_x)O_2$ are usually prepared by the high-temperature (>750°C) reaction in air, using raw materials of mixed hydroxides or nitrates, or through chemical precursors via sol-gel, freeze-drying or microwave method [9-21]. Molten-salt synthesis (MSS) is one of the novel preparation methods to obtain

highly crystalline cathodes materials like, $LiMn_2O_4$ [23], $Li[Ni_{1/2}Mn_{3/2}]O_4$ [24] and $LiCoO_2$ [8,25]. Han et al. [18] employed this method to prepare $Li(Co_{0.8}Al_{0.2})O_2$ at relatively low temperature of 580 °C using the eutectic salt mixture, $LiNO_3$-LiOH. We used the MSS method to prepare $LiCoO_2$ [8], $Li(Ni_{1/2}Co_{1/2})O_2$ [26] and $Li(Ni_{1/3}Co_{1/3}Mn_{1/3})O_2$ [27] and studied their cycling behavior. Presently we report on the preparation of $Li(Co_{1-x}Al_x)O_2$ phases by the MSS using eutectic $LiNO_3$:LiCl and their cycling behavior up to 130 cycles with various upper cut-off potentials.

2. Experimental

The compounds $Li(Co_{1-x}Al_x)O_2$, x = 0.05-0.25 were prepared by using LiCl (Merck) and $LiNO_3$ (Alfar Aesar) salts in the mole ratio 0.12:0.88 (eutectic composition with melting point, 280°C) as the salt flux. The metal nitrates $Co(NO_3)_2.6H_2O$ (Aldrich) and $Al(NO_3)_3.9H_2O$ (Fluka) were the raw materials. The mole ratio of (Co, Al): eutectic was kept at 1: 4. After proper mixing, the mixture was put in an re-crystallized alumina crucible and heated in air, in a box furnace at a heating rate of 3 °C min^{-1} to 850°C for 8 h. The contents were slowly cooled to room temperature by furnace shut-off. The product was thoroughly washed with deionized water several times to remove the excess lithium salts. The residue was dried in an air oven at 150 °C for 24 h, ground to powder and stored in a desiccator.

Powder X-ray diffraction (XRD) patterns were taken using Bruker AXS D8 unit, with Cu K_α radiation. Rietveld refinement of the XRD data was carried out with TOPAS software. The morphology and elemental analysis of powders was determined by scanning electron microscope (SEM) (JEOL JSM-6700F) attached with the EDX analyzer. The Li, Co and Al contents were also determined on selected compositions using inductively coupled plasma (ICP) spectrometer (Thermo Jarrell Ash, IRIS/AP Duo). The Brunauer, Emmett and Teller (BET) surface area of the powders was measured by Micromeritics Tristar 3000 (USA) and density determination was carried out using AccuPyc 1330 pycnometer, Micromeritics (USA).

The electrodes for electrochemical measurements were fabricated with the active material, super P carbon black and binder (Kynar 2801) in the weight ratio 80:10:10 using N-methyl pyrrolidone (NMP) as solvent by the doctor blade technique. Etched Al-foil was the current collector. Lithium metal foil (Kyokuto metal Co., Japan) was the negative electrode (anode) and 1M $LiPF_6$ in ethylene carbonate (EC) + diethyl carbonate (DEC) (1:1 V/V) (Merck) was used as the

electrolyte with Celgard 2502 membrane as the separator. Coin-type test cells were fabricated in an Ar-gas filled glove box as described previously [8,26,27]. Cyclic voltammetry and charge-discharge cycling at a constant current were carried out at ambient temperature (RT=25°C) using the Mac-pile II system (Bio-logic, France) and Bitrode multiple battery tester (Model SCN, Bitrode, USA). The cells were aged for 24 h before measurements. Computer controlled Solartron Impedance/gain-phase analyzer (model SI 1255) coupled with a battery test unit (model 1470) was used for impedance measurements on cells at RT. The frequency range was from 0.35 MHz to 3 mHz with an ac signal amplitude of 5 mV. Data were analyzed by using Z plot and Z view software (Version 2.2, Scribner associates Inc., USA) to obtain the Nyquist plots.

3. Results and Discussion

3.1. Structure and morphology. In the MSS method, the metal nitrates decompose to form the corresponding oxides above 500-600 °C which then will react with the Li-ions from the molten salt-flux to form the desired compounds, $Li(Co_{1-x}Al_x)O_2$. The method also ensures random occupancy of the Al- and Co-ions in the transition metal-layer of the layer structure. In the present study we have not varied the synthesis conditions of temperature (850 °C), time of soaking (8 h) nor the metal-to-salt flux ratio (1:4). The phases with x=0.05, 0.1, 0.15, 0.2 and 0.25 have been prepared which are well-crystalline black powders. The SEM photographs showed sub-micron size platelets characteristic of layer structure (Fig. 1).

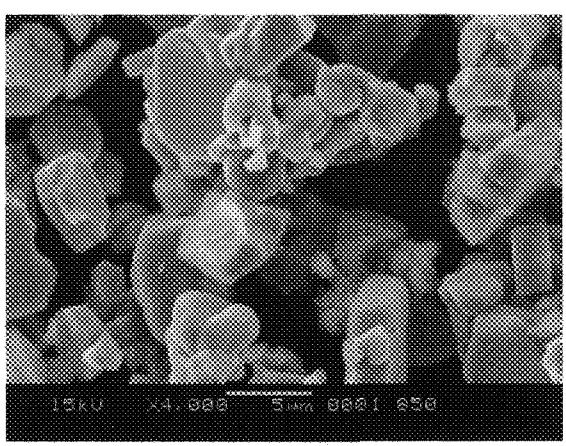

Fig. 1. SEM photograph of $Li(Co_{0.9}Al_{0.1})O_2$. Bar scale, 5 μm.

Chemical analysis showed that the nominal compositions agree with the expected atomic compositions (±0.005): x=0.1: $Li_{1.03}(Co_{0.9}Al_{0.08})O_2$; x=0.15: $Li_{1.03}(Co_{0.85}Al_{0.11})O_2$; x=0.2: $Li_{0.98}(Co_{0.8}Al_{0.2})O_2$. EDAX analysis on the nominal x=0.15 agreed well with the expected atomic composition to within ±0.01. The measured BET surface areas of the powders, shown in Table 1, increase with increasing Al-content, x from 5 to 32 m^2g^{-1}. Apparently, Al-doping prevents the growth of large-size grains of $LiCoO_2$ and help in increasing the surface area. The measured densities of the powders compare well with those calculated from the X-ray data (Table 1). We tested the x=0.1 phase for Li-leachability from the lattice by suspending 0.5 g of the powder in 100 ml of de-ionized water and monitored the pH of the solution for one week. The solution remained neutral indicating that no lithium was leached out.

The XRD patterns of the compounds, $Li(Co_{1-x}Al_x)O_2$ showed characteristic peaks which were indexed on the basis of the $LiCoO_2$ structure, space group, R $\bar{3}$m. Rietveld refinement of the XRD data was carried out with Li ions at the 3b site, Co- and Al- ions randomly distributed at the 3a site and O ions at the 6c site. The fitted pattern for x=0.1 is shown in Fig. 2. The hexagonal *a* and *c* lattice parameters and the *c/a* ratio for various x values, calculated from the Rietveld refined data are given in Table 1. For comparison, the data on pure $LiCoO_2$, synthesized earlier by us employing the MSS method [8] are also given. For all values of x (0.05-0.25), the Rietveld refined parameters R-Bragg, Rwp and GOF were found to be in the range, 0.3-0.7, 2.5-3.0 % and 1.2-1.5, respectively. The oxygen occupancy was 0.253±0.002 for all x, in comparison to the expected ideal value of 0.250. The well-resolved splitting of the XRD peaks assigned to the Miller indices (006,102) and (108,110) for all values of x in $Li(Co_{1-x}Al_x)O_2$, an intensity ratio of more than unity of the (003) and (104) XRD peaks and a large *c/a* ratio of 5.00 are good indications of a well-defined layer structure of the compounds.

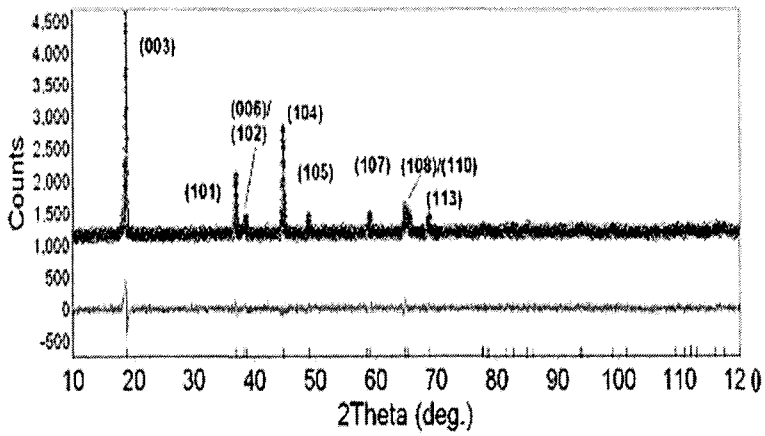

Fig. 2. Rietveld refined X-ray diffraction patterns of $Li(Co_{0.9}Al_{0.1})O_2$. The experimental pattern and calculated patterns are represented as symbols and continuous line, respectively. The difference pattern is also shown. The vertical bars represent the positions of allowed (hkl) reflections (Cu K_α radiation).

The present values of *a* and *c* parameters for various x agree fairly well with those from the literature: Myung et al. [13] for x=0.2 by the MSS method (*a* = 2.81 Å; *c* = 14.090 Å) and Julien et al. [16] for x in the range, 0.05-0.25 by solid state method (e.g., x=0.2: *a* = 2.8104 Å; *c* = 14.085 Å). Contrary to expectations, the *c* parameter increases with increasing value of x even though the ionic radius of Al^{3+} -ion is smaller than that of Co^{3+} ion (Table 1). This has been observed consistently by all the groups in the literature [10-17]. Castro-Garcia et al. [17] explained the increase in *c* axis as due to two competing and opposite effects, viz., polarizing effect of Al^{3+}-ion which tends to distort the structure and increase the *c*-axis, and the ionic size effect which tends to produce a decrease. Indeed, single crystal structure analysis of $Li(Co_{1-x}Al_x)O_2$ with x =0.32 and 0.71 by Takahashi et al. [22] found distortion of LiO_6 octahedra in the structure as a result of Al-doping. As mentioned earlier, the increased c-axis helps in enhancing the Li-ion mobility during de-intercalation- intercalation process.

Table. 1

Hexagonal lattice parameters and physical data of $Li(Co_{1-x}Al_x)O_2$

$Li(Co_{1-x}Al_x)O_2$	*a*, Å (±0.003)	*c*, Å (±0.02)	*c/a*	Expt. density (±0.003) (g/cc)	Calc. density (g/cc)	BET surface area (±0.1) (m^2/g)
x=0.0 (650°C)	2.819	14.069	4.99	---	---	1.1
x=0.05	2.816	14.081	5.00	4.979	4.961	5.6
x=0.10	2.816	14.093	5.00	4.692	4.874	10.3
x=0.15	2.815	14.094	5.00	4.496	4.793	12.9
x=0.20	2.815	14.096	5.00	4.270	4.710	21.8
x=0.25	2.816	14.090	5.00	4.241	4.628	34.0

3.2. Electrochemical studies

Galvanostatic Cycling

Charge-discharge cycling of the cells with $Li(Co_{1-x}Al_x)O_2$, x=0.1, 0.15, 0.2 as cathodes (Li-metal as anode) were carried out up to 130 cycles at ambient temperature at a current density of 30 mAg^{-1}. Cycling was done in the voltage ranges 2.5-4.3 V, 2.5-4.4 V and 2.5-4.5 V. The voltage vs. capacity profiles of the $Li(Co_{1-x}Al_x)O_2$, x= 0.1 and 0.2 are shown in Fig. 3a, b. For clarity, only select cycles are shown. During the first-charge process, the voltage suddenly increased to ~3.9 V from the open circuit voltage (~3.0 V), followed by a plateau till about 40-50 $mAhg^{-1}$ are reached and then gradually increased to the upper cut-off voltage. The voltage plateau is analogous to that encountered in un-doped $LiCoO_2$ which is ascribed to the co-existence of two hexagonal phases, Li_yCoO_2, $y \geq 0.94$ and $y \leq 0.75$ as a result of Li-de-intercalation [1-3]. Possibly, a similar mechanism may be operating in the present case. In order to more clearly delineate the two-phase co-existence, differential capacity vs. voltage plots were extracted from the galvanostatic curves, and are shown in Fig. 4. In these plots, sharp peaks or discontinuities represent two-phase co-existence, whereas smoothly varying curve indicates single-phase de-intercalation/ intercalation reaction. As can be seen, for x=0.1 in $Li(Co_{1-x}Al_x)O_2$ with 4.5 V-cut-off, a sharp peak occurs at ~3.9-3.95 V during charge –discharge reaction both in the first as well as at the 40^{th} cycle (Fig. 4a,b). Similarly, for x=0.2 with 4.4 V-cut-off, the corresponding peaks occur

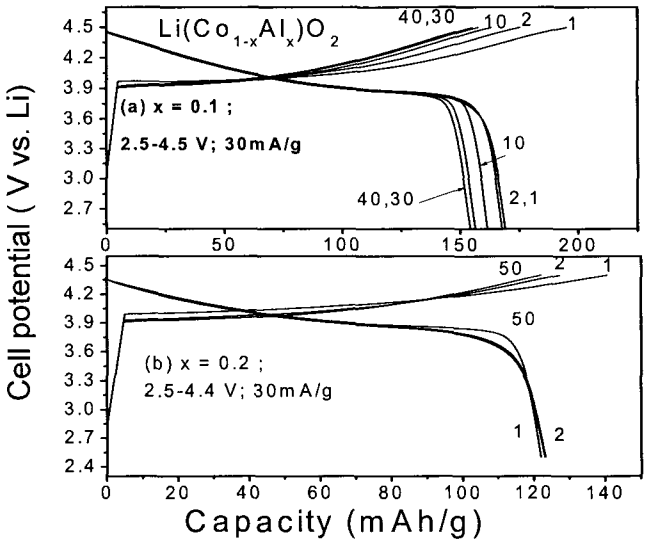

Fig. 3. Voltage vs. capacity profiles of $Li(Co_{1-x}Al_x)O_2$. (a) x= 0.1 ; 2.5-4.5 V, (b) x= 0.2; 2.5-4.4 V, at a current rate 30 mAg^{-1}. The numbers refer to cycle numbers.

at ~3.95-4.0 V during first and 50th cycle (Fig. 4c,d). Julien et al. [16] and Myung et al. [13] also noticed similar peaks at about the same potentials in their differential capacity vs. potential plots for x=0.2. However, Julien et al. [16] mentioned that the seemingly broad band in their plot is indicative of a single-phase topotactic Li-reaction. We note that our differential capacity curves do not show any peaks in the voltage range, 4.1 and 4.2 V, indicating that the crystallographic H1↔M and M↔H1 are suppressed in the Al-doped compounds. On the other hand, there is an indication of a peak during discharge at ~4.4 V for both x=0.1 and 0.2 phases, possibly due to the un-suppressed H1↔(H1-3) transition exhibited by pure $LiCoO_2$ [1,8]. As discussed below, the cyclic voltammograms indeed corroborate the above arguments.

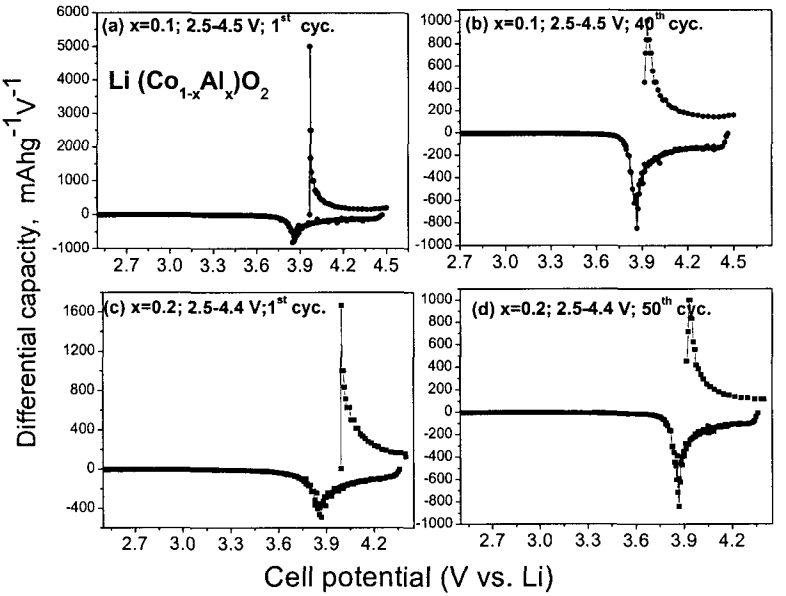

Fig. 4. Differential capacity vs. cell voltage curves extracted from the galvanostatic data of Fig. 3.

Irreversible capacity loss (ICL) between the first-charge and first-discharge capacity was observed for all values of x in $Li(Co_{1-x}Al_x)O_2$, (x=0.1, 0.15, 0.20). The ICL values range from 13-16, 18-20 and 19-25 $mAhg^{-1}$ with the 4.3, 4.4 and 4.5 V cut-off potential respectively. The ICL arises because of the 'formation' or 'conditioning' of the electrode whereby the crystal structure of the active material in the electrode stabilizes with respect Li de-intercalation/ intercalation and makes good contact with the electrolyte and the current collector. The capacity vs. cycle number plots of $Li(Co_{1-x}Al_x)O_2$, x= 0.1, 0.15, 0.2 are shown in Fig. 5. For comparison, the data on pure $LiCoO_2$ from our previous study [8] is included in Fig. 5a. The coulombic efficiency (η), represented by the difference between the charge and discharge capacity for a given cycle, was ~93-95 % during 1-8 cycles but improved to ~98% during subsequent cycles for all x in the potential range 2.5-4.3 V at a current of 30 mAg^{-1}, the 10^{th} cycle reversible capacities for various x are as follows: x=0:157; x=0.1:135; x=0.15:126; x=0.2:103 (±3) $mAhg^{-1}$.

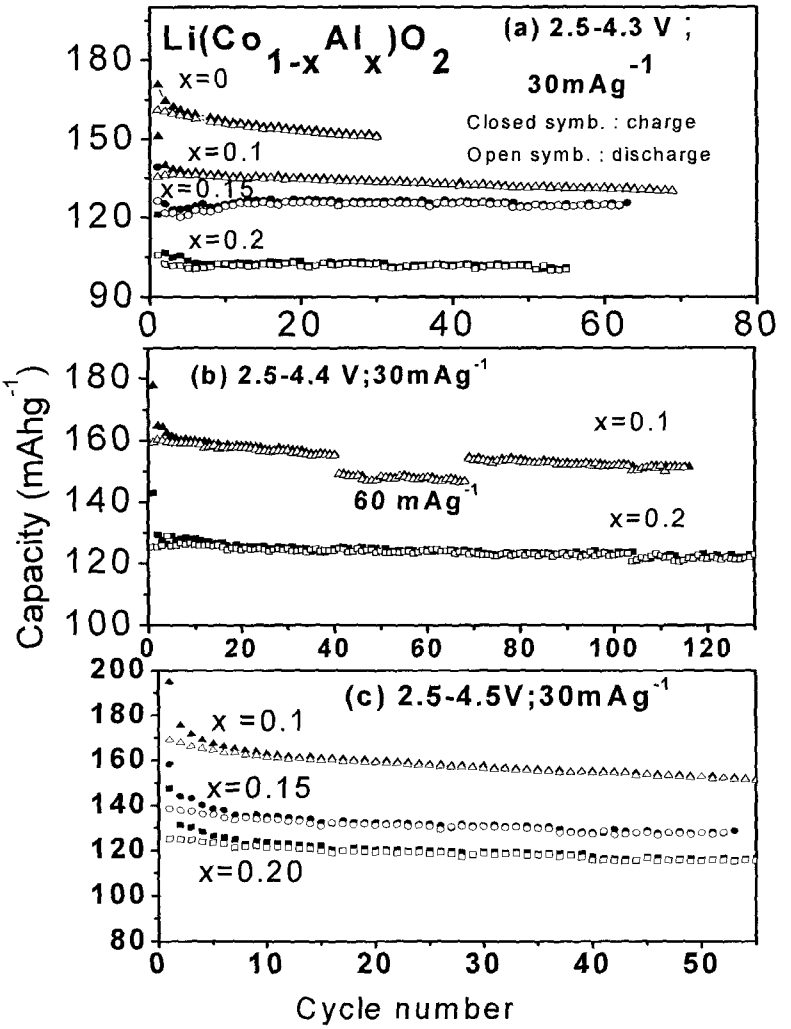

Fig. 5. Capacity vs. cycle number of $Li(Co_{1-x}Al_x)O_2$ in the potential range (a) 2.5-4.3 V, (b) 2.5-4.4 V and (c) 2.5-4.5 V at a current rate of 30 mAg^{-1}. Filled symbols represent the charge and open symbols, the discharge capacity.

It is clear that the capacity decreases with an increase in x because Al is an electro-inactive ion and Al-doping slightly increases the de-intercalation voltage. Significantly, no noticeable capacity-fading is observed for x=0.15 and 0.2 up to 60

cycles, whereas 98% of the capacity is retained at the end of 70 cycles for the x=0.1 compound. This may be compared with the 5% capacity-loss shown by pure $LiCoO_2$ by the 30th cycle (Fig. 5a). Hence, the stable cycling performance of $Li(Co_{1-x}Al_x)O_2$ for x>0.1 can be ascribed to the suppression of the phase transitions occurring in the 4.1-4.3 V region. Our 10th cycle capacity value for x= 0.2 agrees well with the 10th cycle value of 107 $mAhg^{-1}$ reported by Myung et al. [13] in the potential range 2.8-4.3 V. However, they noticed continuous capacity-fading in the range 2-20 cycles.

When cycled in the potential range 2.5-4.4 V at a current of 30 mAg^{-1}, we found that for x=0.1 in $Li(Co_{1-x}Al_x)O_2$, the 10th cycle capacity of 160 (±3) $mAhg^{-1}$ degraded only to 152 (±3) $mAhg^{-1}$ at the end of 115 cycles, which corresponds to 97% capacity-retention (Fig. 5b). To test the rate capability, the current was switched to 60 mAg^{-1} (0.4 C rate, assuming that 1C-rate =150 mAg^{-1}) during 40 to 68 cycles. There was a decrease in the reversible capacity as expected, and the original value was recovered when the current was changed to 30 mAg^{-1}. This shows that the compound has good rate-capability. Ex-situ XRD of the compound, in the discharged state after 65 cycles showed that the crystal structure is stable and the lattice parameters remain almost unchanged. The composition with x=0.2 also shows good cyclability: A stable capacity of 128(±3) $mAhg^{-1}$ is shown in the range, 10-130 cycles. The observed capacities agree well with those reported by Julien et al. [16] (10th cycle capacity of 124 and 120 $mAhg^{-1}$, respectively for x=0.1 and 0.2, in the range 3.6-4.4 V) who also found good cyclability up to 16 cycles. As Julien et al. [16] pointed out, the suppression of phase transitions in $LiCoO_2$ due to Al-doping results in a stable capacity and good cyclability when cycled in the potential range, 3.6-4.4 V. On the other hand, when the upper cut-off potential is increased to 4.5 V, noticeable capacity-fading was found for all values of x. The 10th cycle capacities of 162, 135 and 122 (±3) $mAhg^{-1}$ for x=0.1, 0.15 and 0.2, respectively in $Li(Co_{1-x}Al_x)O_2$ decreased by 5-7% at the end of 55 cycles (Fig. 5c). The coulombic efficiency (η) was 95-96%. The observed capacity-fading can possibly be attributed to the non-suppression of the reversible phase transition (H1↔(H1-3)) occurring at ~4.5 V in $LiCoO_2$. It is well-known that the unit It is well-known that the unit cell volume changes due to the reversible phase transitions, especially the ones at ~4.4 and ~4.6 V will produce an 'electrochemical grinding' effect which will deteriorate

the electrical contact between the particles and with the current collector and lead to capacity-fading [1,8].

Cyclic Voltammetry

The cyclic voltammograms (CV) of $Li(Co_{1-x}Al_x)O_2$ were recorded at a scan rate 58 μVs^{-1} up to 25 cycles with Li metal as the counter and reference electrode in the potential range 2.5-4.4 V and 2.5-4.7 V at ambient temperature. The CV of compounds with the 4.4 V cut-off for x=0.05, 0.1, 0.15 and 0.2 are shown in Fig. 6a-d, respectively. Fig. 6e is the 26^{th} cycle CV for x=0.1 composition and is an extension of the CV of Fig. 6b except that the upper cut-off potential has been increased to 4.7 V. Fig. 6f is the CV of pure $LiCoO_2$ reproduced from our earlier study [8]. The compound was prepared by the MSS method at 650°C using the salt flux, $LiNO_3$+LiCl+KOH. The first cycle CV showed an anodic (Li-de-intercalation) peak at ~4.1-4.2 V for x>0, in comparison to ~4.0 V shown by $LiCoO_2$ (Fig. 6). However, the first cycle cathodic (Li-intercalation) peak is shown at ~3.75-3.85 V which is some what broad for x=0.15 and 0.2. In the second cycle, the anodic peak shifted to a lower potential, clearly seen in Fig. 6a for x=0.05, but the corresponding cathodic peak shifts only slightly, by ~0.05 V, to a higher potential. The shift in the anodic peak potential is an indication of the 'formation' or 'conditioning' of the electrode in the first-cycle and the effect was also seen in the galvanostatic charge-discharge curves. The shifts in the anodic potential are complete by 7 cycles stabilizing at ~ 4.05, 4.02, 4.08V and 4.15 V for x=0.05, 0.10, 0.15 and x=0.2, respectively. The hysteresis (ΔV= the difference between the 5^{th} or 7^{th} anodic and cathodic peak potentials is 0.2 V, 0.18 V, 0.26 V and 0.38 V for x=0.05, 0.10, 0.15 and 0.2 respectively. This shows a decreasing trend of coulombic efficency with an increase in x.

The main anodic/cathodic peaks at ~4.0/3.85 V, seen in Fig. 6 for $LiCoO_2$ and $Li(Co_{1-x}Al_x)O_2$ correspond to the reversible Li de-intercalation/intercalation involving the $Co^{3+/4+}$ couple, in addition to the co-existing phases $Li_{1-y}CoO_2$ with two different values of y, as mentioned earlier. Clearly defined peaks in the differential capacity vs. potential curves also indicate the two-phase co-existence (Fig. 4).

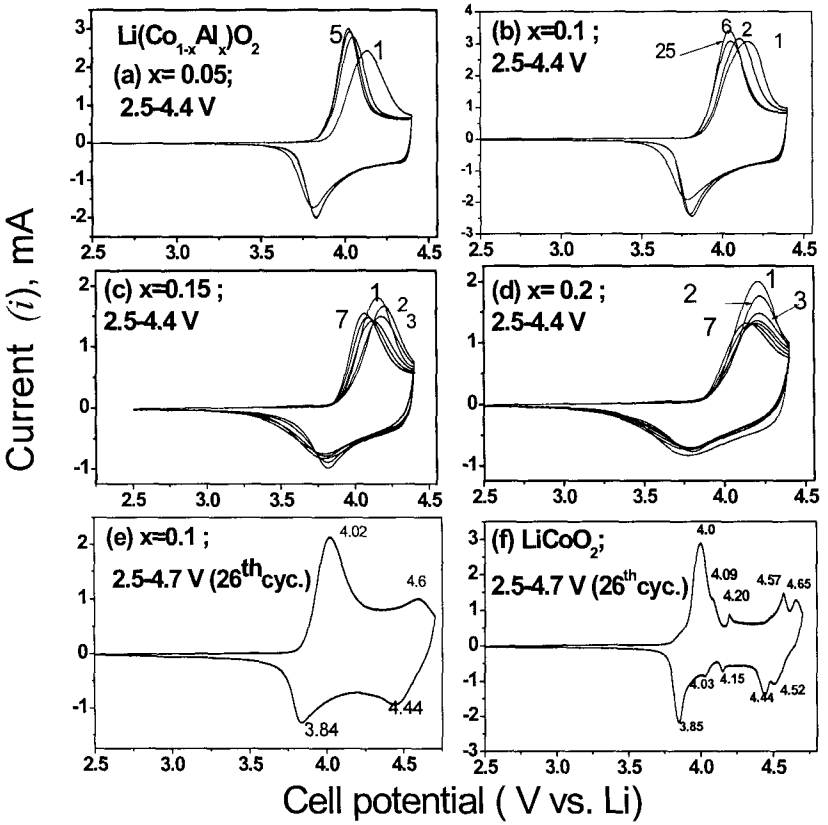

Fig. 6. Cyclic voltammograms of $Li(Co_{1-x}Al_x)O_2$. (a) x=0.05, (b) x = 0.1, (c) x = 0.15 and (d) x =0.20 in the potential range 2.5-4.4 V. The numbers refer to the cycle numbers. (e) Same as (b) for the 26th cycle in the potential range 2.5-4.7 V. Numbers refer to potentials. (f) $LiCoO_2$ (x=0) prepared at 650°C by molten salt synthesis. The 26th cycle curves in the potential range 2.5-4.7 V are shown. The first 25 cycles were in the range 2.5-4.3 V. Numbers refer to potentials. Data reproduced from our previous study [8]. Scan rate is 58 μVs^{-1} vs. Li at ambient temperature.

However, in situ XRD studies are needed to confirm the above. A comparison of the CV for x=0 and for x>0 in Figs. 6a-f reveal that the anodic peaks occurring at 4.09 V and at 4.20 V, and the corresponding cathodic peaks at slightly lower potentials in $LiCoO_2$, are absent in the Al-doped phases, indicating that the so-

called H1↔M and M↔H1 structural transitions are suppressed. This is also shown in the differential capacity vs. potential curves of Fig. 4. However, the 26th cycle CV of the x=0.1 composition in the potential range, 2.5-4.7 V shows an un-resolved anodic/cathodic peak at 4.6/4.4 V analogous to the two doublet peaks in these potential ranges in the CV of $LiCoO_2$ (Fig. 6e and f). This shows that the H1↔(H1-3) and (H1-3)↔O1 structural transitions in $LiCoO_2$ are not suppressed by Al-doping. We verified it for x=0.2 composition as well (Fig. not shown). Hence, the CV data show that cyclability of $Li(Co_{1-x}Al_x)O_2$, x=0.05-0.2 must be good when the upper cut-off potential is restricted to 4.4 V and capacity-fading may occur when cycled to ≥4.5 V, as is indeed shown by the charge-discharge cycling behaviour (Figs. 3 and 5).

Electrochemical impedance Spectroscopy (EIS)

EIS studies on the compound $Li(Co_{0.9}Al_{0.1})O_2$ were carried out at select potentials during the first charge cycle and as a function of cycle number up to 31 cycles in the charged-state. The cell with Li-anode was cycled in the range of 2.5-4.5 V. The spectra as the Nyquist plots (Z' vs. $-Z''$) are shown in Fig. 7 a, b. They were analyzed by fitting to an equivalent electrical circuit shown in Fig. 7c, consisting of resistance (R_i), $R_i||CPE_i$, Warburg element and intercalation capacitance (C_{int}) where CPE_i is the constant phase element [26]. The continuous lines in Fig. 7a,b represent the fitted curve whereas the symbols are the experimental data. The R_e is the combined impedance (resistance) of the electrolyte and cell components. The depressed semicircle in the high-frequency range, 0.3 MHz- 10 kHz is attributed to the surface-film (R_{sf}) resistance, which arises due to the solid electrolyte interphase (SEI) formation on the cathode, whereas that seen in the high-to-medium frequency range, 7 – 0.1 kHz is assigned to the charge-transfer (R_{ct}) resistance due to interphase between electrode and electrolyte. The semicircle in the low-frequency range, 10 -0.1 Hz is attributed to the bulk (R_b) resistance, which comes mainly from electronic conductivity of the active material and ionic conductivity in the pores filled by the composite electrode and also due to inhomogeneous coating of the active material on to the current collector [26,28,29]. The semicircle(s) is usually followed by the appearance of a straight line Warburg-type region. The respective constant phase elements are CPE_{sf}, CPE_{dl} (dl= double layer, in μF) and CPE_b (bulk capacitance, in mF).

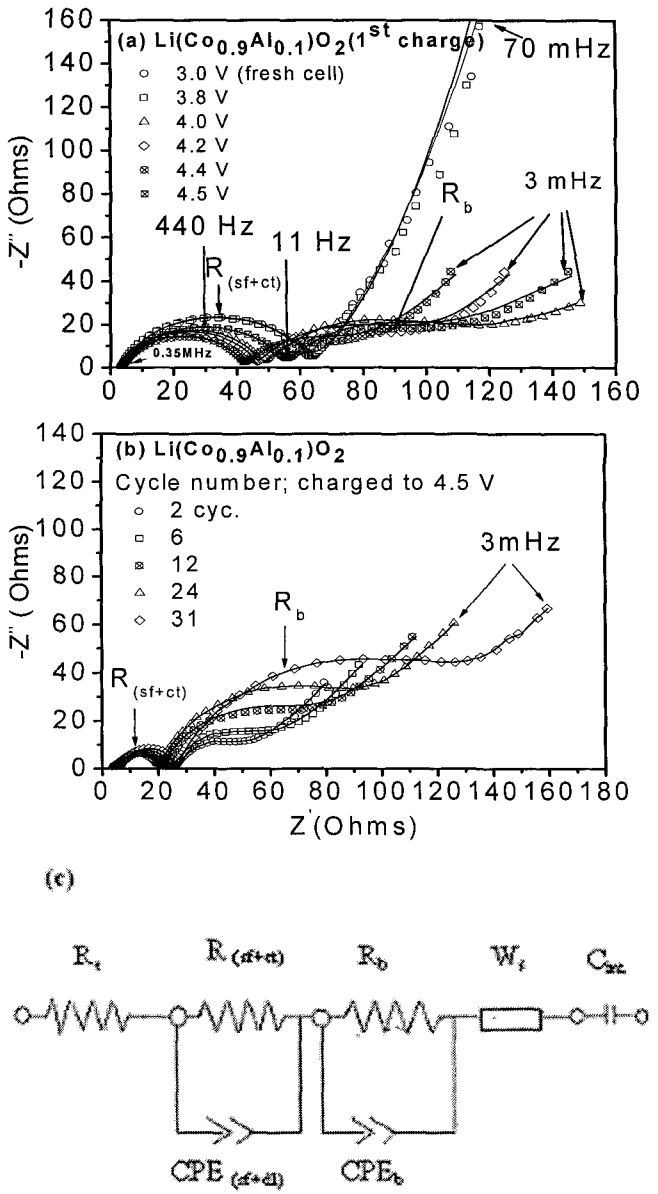

Fig. 7. Nyquist plots (Z' vs. -Z'') of the cell with $Li(Co_{0.9}Al_{0.1})O_2$ as the cathode. (a) During first-charge cycle at various potentials. (b) In the charged-state (4.5 V) at various cycle numbers. Symbols are experimental data whereas continuous lines represent fitting the data to the equivalent circuit shown in (c). Select frequencies are indicated.

The fresh cell (~3.0V) and after charging to 3.8 V show a single semicircle in the high frequency region followed by a Warburg region in the low-frequency range indicating the existence of only surface film resistance, R_{sf}. The fitted value is 57(±3) Ω. The spectrum at 4.0 V clearly shows the development of a second semicircle below 10 Hz, but the Warburg region is not shown (Fig. 7a). With an increase in potential, the effective diameters of both the semicircles decrease. In analogy with the similar spectra observed in other oxide cathodes $Li(Ni_{0.5}Co_{0.5})O_2$ [26] and Mg-doped $LiCoO_2$ [29], the first semicircle in the high-frequency region can be assigned to the sum of $R_{(sf+ct)}$.The second semicircle corresponds to bulk resistance, R_b. With an increase in the potential from 4.0 to 4.4 V, the fitted values of both $R_{(sf+ct)}$ and R_b show a continuous decrease, 42 to 38 (±3) Ω and 57 to 32 (±3) Ω, respectively. The corresponding CPE_{dl} values change from 18 to 27 (± 5) μF. The CPE_b change from 24 to 22 (±5) mF. However, the $R_{(sf+ct)}$ and R_b values at 4.5 V, at the end of first-charge, show a slight increase, to 50 and 31 (±3) Ω, respectively. The impedance spectra as a function of cycle number shown in Fig. 7b are qualitatively different from those in Fig. 7a in that the $R_{(sf+ct)}$ assume low and relatively constant (fitted) value of 17 (±3) Ω irrespective of the cycle number. On the other hand, R_b shows a systematic increase, from 20→31→48→68→98 (±3) Ω as the cycle number increases from 2→6→12→24→31. This trend is a clear indication of the reason for the observed capacity-fading on cycling to an upper cut-off potential, 4.5 V (Fig. 5c). The un-suppressed phase transition at ~4.5 V in the x=0.1 compound, as shown in Figs. 4b and 6e, is most likely responsible for the increase in the R_b on cycling. The $CPE_{(sf+dl)}$ and CPE_b values are in the range 80-100 (±5) μF and 32-22 (±5) mF, respectively. The extracted R_e values are 4 (±2) Ω in all cases.

4. Conclusions

The layered compounds, $Li(Co_{1-x}Al_x)O_2$, x=0.05, 0.1, 0.15, 0.2 and 0.25 have been prepared by the molten salt synthesis method at 850 °C in air using the low-melting salt flux, $0.88LiNO_3 + 0.12LiCl$. They were characterized by X-ray diffraction, Rietveld refinement, SEM, density and surface area measurements. Electrochemical behavior was studied at ambient temperature in cells with Li-metal

as the counter electrode by galvanostatic charge-discharge cycling, cyclic voltammetry (CV) and Impedance spectroscopy. Single-phase compounds formed for all x which showed an increase in *c* lattice parameter as compared to x=0. Results showed that for x≥0.05, the Li de-intercalation potential during the first-charge cycle is slightly higher than that exhibited by pure $LiCoO_2$ and the structural transitions that occur at ~4.1 and ~4.2 V are suppressed. As a consequence, the long-term cyclability of $Li(Co_{1-x}Al_x)O_2$ is improved in the potential range, 2.5-4.3 V and 2.5-4.4 V in comparison to x=0. Thus, for x=0.1, 0.15 and 0.20, stable capacities of 135, 126 and 103 (±3) $mAhg^{-1}$, respectively were obtained up to 60 cycles in the range 2.5-4.3 V at the current rate of 30 mAg^{-1}. For x=0.1 in the potential range 2.5-4.4 V at 30 mAg^{-1}, 97% of the 10^{th} cycle capacity of 160 (±3) $mAhg^{-1}$ is retained at the end of 115 cycles, whereas for x=0.2 a stable capacity of 128 (±3) $mAhg^{-1}$ is exhibited in the range 10-130 cycles. The coulombic efficiency was ~98 %. Higher 10^{th} cycle capacities were observed for x=0.1, 0.15 and 0.2 when cycled in the potential range 2.5-4.5 V, but capacity-fading occurred by 5-7 % at the end of 55 cycles. The non-suppression of the reversible phase transition at ~4.5 V in the compounds for all x might be the reason for capacity-fading and this is corroborated by the CV and impedance data.

Acknowledgement

Thanks are due to Mr. P. Chee Kok for help with XRD measurements.

References

1. Z. Chen and J. R. Dahn, Electrochim. Acta, **49**, 1079 (2004).

2. S. Levasseur, M. Ménétrier and C. Delmas, J. Electrochem. Soc., **149,** A1533 (2002).

3. S. Levasseur, M. Ménétrier and C. Delmas, J. Power Sources, **112**, 419 (2002).

4. S. Madhavi, G.V. Subba Rao, B.V.R. Chowdari and S.F.Y. Li, Electrochim. Acta, **48,** 219 (2002).

5. S. Madhavi, G.V. Subba Rao, B.V.R. Chowdari and S.F.Y. Li, J. Electrochem. Soc., **148,** A1279 (2001).

6. N. Imanishi, M. Fujii, A. Hirano, Y. Takeda, M. Inaba and Z. Ogumi, Solid State Ionics, **140**, 45 (2001).

7. S. Levasseur, M. Ménétrier, E. Suard and C. Delmas, Solid State Ionics, **128**, 11 (2000).

8. K. S. Tan, M. V. Reddy, G. V. Subba Rao and B. V. R. Chowdari, J. Power Sources, **147**, 241 (2005).

9. G. Ceder, Y. –M. Chiang, D. R. Sadoway, M. K. Aydinol, Y. -I. Jang and B. Huang, Nature, **392**, 694 (1998).

10. H. Huang, G.V. Subba Rao and B.V.R. Chowdari, J. Power Sources, **81-82**, 690 (1999).

11. Y. -I. Jang, B. Huang, H. Wang, D.R. Sadoway, G. Ceder, Y. -M. Chiang, H. Liu and H. Tamura J. Electrochem. Soc., **146,** 862 (1999).

12. W.-S. Yoon, K.-K. Lee and K.-B. Kim, J. Electrochem. Soc., **147**, 2023 (2000).

13. S.-T. Myung, N. Kumagai, S. Komaba and H.-T. Chung, Solid State Ionics, **139**, 47 (2001).

14. C. Julien, G.A. Nazri and A. Rougier, Solid State Ionics, **135**, 121 (2000).

15. W.-S. Yoon, K.-K. Lee and K.-B. Kim, Electrochem. Solid State Lett., **4**, A35 (2001).

16. C. Julien, M.A. Camacho-Lopez, M. Lemal and S. Ziolkiewicz, Mater. Sci. & Eng., **B95**, 6 (2002).

17. S. Castro-García, A. Castro-Couceiro, M.A. Señarís-Rodríguez, F. Soulette and C. Julien, Solid State Ionics, **156**, 15 (2003).

18. C. –H. Han, Y. –S. Hong and K. Kim, Solid State Ionics, **159,** 241(2003).

19. P. Elumalai, H. N. Vasan and N. Munichandraiah, J. Power Sources, **125,** 77 (2004).

20. S. Venkatraman and A. Manthiram, Solid State Ionics, **176**, 291 (2005).

21. S. M. Lala, L. A. Montoro, V. Lemos, M. Abbate and J. M. Rosolen, Electrochim. Acta, **51**, 7 (2005).

22. Y. Takahashi, N. Kijima and J. Akimoto, J. Solid State Chem., **178**, 3598 (2005).

23. X. Yang, W. Tang, H. Kanoh and K. Ooi, J. Mater. Chem., **9**, 2683 (1999).

24. J. –H. Kim, S. –T. Myung and Y. –K. Sun, Electrochim. Acta, **49**, 219 (2004).

25. H. Liang, X. Qiu, H. Chen, Z. He, W. Zhu and L. Chen, Electrochem. Commun., **6,** 789 (2004).

26. M. V. Reddy, G. V. Subba Rao and B.V. R. Chowdari, (submitted).

27. M.V. Reddy, G. V. Subba Rao and B.V.R. Chowdari, J. Power Sources (in press).

28. M. D. Levi and D. Aurbach, J. Phys. Chem. B, **108**, 11693 (2004).

29. F. Nobili, S. Dsoke, F. Croce and R. Marassi, Electrochim. Acta, **50**,2307 (2005).

LAYERED ION-ELECTRON CONDUCTING MATERIALS

M.A. SANTA ANA, E. BENAVENTE, G. GONZÁLEZ*
Department of Chemistry, Faculty of Sciences, Universidad de Chile, Las Palmeras 3425, Santiago, Chile
Department of Chemistry, Universidad Tecnológica Metropolitana, Avenida Joé Pedro Alessandri 1242, Santiago, Chile.

Introduction

The characteristics of a given electrochemical device are essentially determined by the properties of the electrochemical cells defining its functionality. Any attempt directed to modify or regulate the characteristics of the device require an adequate selection of the materials used as electrodes and/or electrolytes.

The performance of an electrochemical cell is essentially determined by both, the activity of the electroactive species and its diffusion rate between the electrodes and, in the case of the electrodes, also by its electrical conductivity. The improvement of electrode materials implies therefore to optimize or regulate these variables according to the projected cell or device requirements.

In this work we describe selected features from the intercalation chemistry of the molybdenum disulfide analyzing the synthesis, characterization and properties of a series of organic-inorganic nanocomposites arising from the co-intercalation of organic donors and lithium into the sulfide. The conversion of some of these nanocomposites into functionalized nanotubes is also commented.

Layered Materials

There are a variety of chemical species which present stable laminar structures under normal conditions. This layered compounds are solids formed by pilling up planar or near planar layers. The stacking of the layers, extended along distances farther away than the typical bond distances, leads to characteristic highly anisotropic nanostructured arrangements. While the layers in these solids are constituted by relatively strong ionic-covalent interatomic interactions (150-300 kj/mol), showing electronic structures which may be described by typical electronic bands schemes, interactions between the layers are much weaker, frequently in the range 40-150 kj/mol[1]. Typical examples of these solids are those listed in Table 1.

Table1. Typical Layered Solids

Examples of Layered Solids	**Layer Electronic Structure Nature**	**Electronic Conductivity (Scm^{-1})**
Graphite	Metallic conductor	10^{-4} - 10^{3}
MoS_2, V_2O_5	Semiconductors	10^{-4}-10^{-6}
Synthetic and Natural Clays	Isolators	$< 10^{-12}$

One important and rather general feature in the chemistry of layered compounds is the insertion of chemical species in their interlamellar spaces leading to host-guest

compounds in which the inorganic matrix results functionalized by the inserted species[1,2,3].

Lithium intercalation compounds

A typical and widely known example of such functionalization processes is the intercalation of electron donors like alkali metals. Layered compounds are in general good candidates as materials for electrodes because of its capacity of hosting in the interlamellar spaces appreciable amounts of electroactive species with relatively large diffusion rates. Cobalt and nickel oxides as well as graphite, used respectively as negative and positive electrodes in rechargeable lithium batteries, are relevant examples of these materials[4]. The intercalation of lithium into MoS_2 may be performed chemically by reaction with butyl-lithium as well as by electrochemical reactions using appropriated cells like, for instance, $Au/Li/Li^+(solv)/MoS_2/Au$[5].

Although intercalation processes are generally considered to be topotactic, in the case of the MoS_2 important structural changes are apparent. The coordination of molybdenum by sulfur atom changes from trigonal prismatic in the pristine MoS_2 to an octahedral modification when it is intercalated, thus altering its band structure, changing its electronic conductivity, and promoting further intercalation processes [6,7].

Organic-Inorganic Nanocomposites

Lamellar inorganic matrices may be also intercalated by a variety of organic species leading to host-guest nanocomposites. The intercalation reaction is often an spontaneous process performed under rather mild conditions which may be seen as resulting from the molecular recognition between the organic and the inorganic components. Thus, these lamellar nanoheterogeneous species appear to be the transition between a composite and a conventional compound. Because of the number of possible combinations leading to products with slightly different properties, this approach may be useful for the design of tailor-made materials.

Co-Intercalation of Lithium and Organic Donors into Molybdenum Disulfide

The intercalation of organic species into MoS_2 requires an activation step, which frequently consists in the intercalation of lithium (*ca.* one mole per mol MoS_2) followed of a rapid hydrolysis of the product. There, factors like a light increase in electron charge in the host, the conversion of the trigonal prismatic 2D MoS_2 into the octahedral 1T modification, and the exfoliation of the lamellar solid promote the intercalation of donors in this host[8].

	H_2O		Organic	
Li_xMoS_2 (s)	→	**$Li_x(H_2O)_nMoS_2$ (susp.)**	→	**$Li_xMoS_2(D)_y$**
$x \approx 1$		$x \approx 0.1$	Donor	$x \approx 0.01\text{-}0.3$, $y=0.1\text{-}2.5$
$\Delta c = 6.14$ Å		$\Delta c = 11.4$ Å		$\Delta c = 8\text{-}50$ Å

The intercalation of organic species causes important changes of the interlamellar spaces. As illustrated in Fig.1, these changes may be easily followed by powder X-ray diffraction analysis of the products. Since in lamellar compounds the intensity of the *00l* reflections are abnormally enhanced, the purity of the products as well as the interlamellar distances may be straightforward determined.

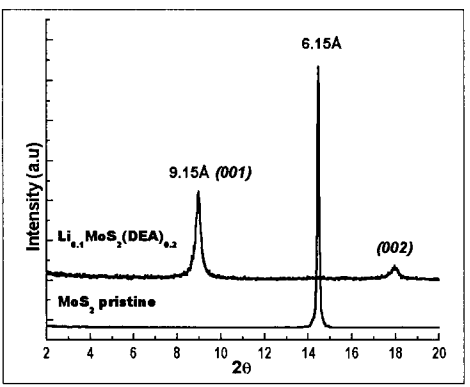

Figure 1. X-ray diffraction pattern of the MoS_2 and $Li_{0.1}MoS_2(DEA)_{0.2}$

In Table 2 are reported selected examples of MoS_2-based nanocomposites obtained by chemical methods. All of them corresponds to pure phases with characteristic stoichiometries and interlamellar distances showing well defined lamellar microstructures . Using simple molecular models for the guest species, it is always possible to corroborate, using geometric criteria, that the structural and analytical characteristic of the compounds agree with the volume in the interlamellar space and the surface on the host molecular sheets respectively[9].

Tables 2. Interlamellar distances of MoS_2-based nanocomposites

Compound*	**Interlamellar distances Å**
$Li_{0.1}MoS_2(DEA)_{0.4}$	9.8
$Li_{0.1}MoS_2(DBA)_{0.2}$	10.5
$Li_{0.1}MoS_2(PEO)_{0.5}$	11.0
$Li_{0.1}MoS_2(PEO)_{1.0}$	16.0
$Li_{0.1}MoS_2(PAN)_{1.1}$	11.5
$Li_{0.32}MoS_2(12\text{-Crown-}4)_{0.2}$	14.0

* DEA: diethyamine; DBA: dibuthylamine ; PEO: polyethylene oxide; PAN: polyacrylonitrile

Changes are however not only limited to the interlamellar distances and stoichiometries. Electrical and electrochemical properties of the products differ

from those of the components. In some cases the structure of the intercalated donor from different from that in the free state

Electrical and ionic conductivity

The electrical conductivity of the intercalation products results in most cases to be considerably higher than that of the pristine MoS_2. As observe in Table 3, it strongly depends on the nature of the intercalated donor. The dependence of the conductivity on the temperature generally shows linear Arrhenius plots in the near room temperature range, increasing steady with the temperature.

Tabla 3 Electrical conductivity of MoS_2 and MoS_2 - donor nanocomposites

Compound	Electrical conductivity σ (298 K) (S cm^{-1})
$Li_{0.1}MoS_2(PEO)_{0.5}$	4.80×10^{-4}
$Li_{0.1}MoS_2(PEO)_{1.0}$	6.60×10^{-3}
$Li_{0.1}MoS_2(PEO)1.4$	1.04×10^{-2}
$Li_{0.2}MoS_2(DEA)_{0.42}$	2.51×10^{-1}
$Li_{0.1}MoS_2(DBA)_{0.19}$	1.97×10^{-1}
$Li_{0.1}MoS_2(Diciclohexylamine)_{0.07}$	3.80×10^{-2}
$Li_{0.32}MoS_2(12\text{-Crown-}4)_{0.2}$	8.50×10^{-2}
$Li_{0.6}MoS_2$ $(PAN)_{1.2}$	3.30×10^{-4}
MoS_2	2.09×10^{-6}

In the intercalation of organic electron-pair donors it is always observed that the products contain lithium in an amount in the range 0.1-0.6 mol per mol MoS_2 depending on the nature of the organic donor. Thus, for instance, values around 0.1, 0.2 and 0.6 in the intercalation of linear polyethers, secondary amines and polyacrylonitrile are respectively observed. That not withstanding, all the compounds behave as mixed ionic-electronic conductors[10].

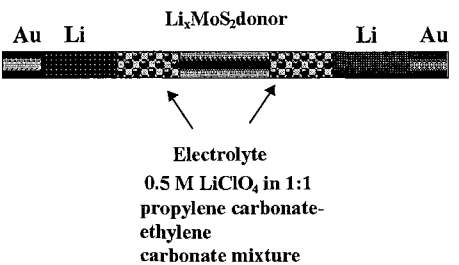

Figure 2. Scheme of the galvanostatic polarization cell.

Although in these compounds the electron conductivity contribution is expected to be many orders of magnitude higher than that of the ionic conductivity, the separation of both contributions may be afforded by galvanostatic polarization-measurements using the cell schematized in Fig 2. Results of a polarization experiment for the compound $Li_{0.1}MoS_2(DBA)_{0.19}$ are shown In Fig.3. As expected the ratio between both contributions is about 10^5 [11].

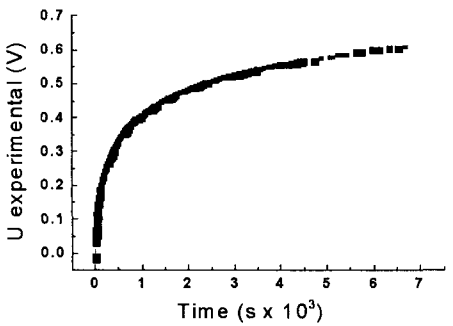

Figure 3.Galvanostatic polarization for the compound $Li_{0.1}MoS_2(DBA)_{0.19}$. Constant current density j = 8μA ·cm^{-1}.

Lithium diffusion coefficients

The ionic conductivity observed in these compounds is associated to the lithium located in the interlamellar phase, so they are a measure of the mobility of the lithium species in this phase. However, in order to asses the quality of the products as eventual electrode materials for electrochemical devices, the lithium diffusion coefficients appears to be more realistic than the ionic conductivity for analyzing the transport of lithium across a given phase.

Lithium diffusion coefficients may be obtained by following the rate at which lithium, deposited on the tested electrode by a short current pulse left the surface for diffusing in the bulk of the material. If the measurements are carried out at different lithium contents and different temperatures, a picture of the macroscopic movement of lithium across the solid may be obtained.

In Table 4 are reported the diffusion coefficients determined for a selected series of nanocomposites intercalated with different organic donors measured under comparable temperature and lithium content conditions. This variable clearly depends on the nature of the interlamellar phase, not only on the organic functional group of the guest but also on the stoichiometry of the phase. There is not any clear relationship between the interlamellar distances in the nanocomposite, the donor ability of the guest or any other characteristic of the products. This property appears to be determined by the particular molecular structure of the interlamellar phase each intercalate (vide infra) [10,12].

Table 4. Diffusion coeficients of Li in MoS_2 and in MoS_2-donor nanocomposites at 298 K.

COMPOUND	X = 0.2 D $cm^2 s^{-1}$	X = 0.4 D $cm^2 s^{-1}$	X = 0.5 D $cm^2 s^{-1}$
$Li_x MoS_2$ Pristine	$1.4\ 10^{-13}$	$4.2\ 10^{-14}$	$1.4\ 10^{-14}$
$Li_x MoS_2$ Restacked	$3.1\ 10^{-13}$	$4.64\ 10^{-14}$	$1.54\ 10^{-14}$
$Li_x MoS_2 (PEO)_1$	$1.0\ 10^{-12}$	$4.5\ 10^{-13}$	$2.6\ 10^{-13}$
$Li_x MoS_2 (PEO)_{0.5}$	$3.0\ 10^{-11}$	$1.0\ 10^{-12}$	$8.5\ 10^{-14}$
$Li_x MoS2 (PAN)_1$	$4.3\ 10^{-11}$	$5.8\ 10^{-12}$	$2.3\ 10^{-13}$ (x =0.6)
$Li_x MoS2 (NMCHA)_{0.4}$	$2.0\ 10^{-12}$	$1.42\ 10^{-12}$	$5.6\ 10^{-13}$ (x =0.6)
$Li_x MoS2 (DEA)_{0.3}$	$1.48\ 10^{-11}$	$1.7\ 10^{-12}$	-----

For the pristine MoS_2 as well as for all of its intercalation products tested in our laboratory, a near linear Arrhenius behavior is observed. In pure MoS_2 a lithium-ion hopping mechanism is apparent, what, as deduced from the constancy of the observed lithium diffusion activation enthalpy, is independent of the amount of intercalated lithium. In the case of lithium co-intercalated with organic donors, where the lithium species are expected to be surrounded not only by the matrix sulfur atoms but by the guest donor atoms (*vide infra*), the process is more complex. The slopes in the Arrhenius plots change with the lithium content. Specially interesting is the co-intercalation of lithium and poly(ethylene oxide), PEO, in which case two pure phases with different stoichiometry may be chemically afforded, $Li_{0.1}MoS_2(PEO)_{0.5}$ and $Li_{0.1}MoS_2(PEO)_{1.0}$.

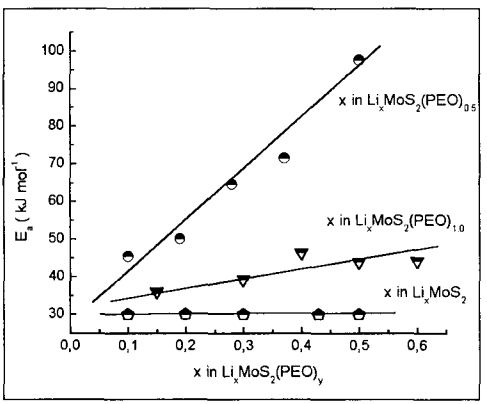

Figure 4. Diffusion activation enthalpy for MoS_2 and PEO-nanocomposites.

As observed in Fig. 4, slightly changes in the diffusion activation enthalpy occurs for the nanocomposites intercalated with one mol PEO per mol MoS_2 while for those containing 0.5 mol a much higher dependence is observed. A plausible

explanation of these observations may be found, as discussed below, in the different structures of the interlamellar phase existing in these two products.

Electrochemical Lithium/Intercalated-Lithium Potentials

Using electrochemical cells similar to those described above, the electrochemical potential of the couple Li-metal/intercalated-Li in the products as prepared chemically as well as in those with different lithium intercalation degrees may be determined. Since electrochemical potentials correspond to the activity of the electroactive species, these measurements permit to investigate the effect of the different co-intercalated donors on the stabilization of the lithium ion in the interlamellar phase as well as on the capacity of the electrode and the variation of the potential in charge-discharge processes.

In Table 5 the average potentials observed for a selected series of intercalated products. It may be there observed, that the presence of the donor in the interlamellar phase clearly increases the lithium ion activity. The magnitude of this effect depends on the nature of the co-intercalated species. That is certainly not an unexpected result, since the Lewis-base nature of the organic guests should increase the stability of the lithium ion by coordinative interactions[13].

Tabla 5. Average quasi-equilibrium potentials for the intercalation of lithium in MoS_2 and MoS_2 – donor nanocomposites. Lithium concentration range: 0.2- 0.6 mol per mol compound.

Compound	Average Potential V (Li/Li^+)
Pristine MoS_2	1.60
Exfoliated MoS_2	1.64
$Li_x MoS_2 (PEO)_1$	2.61
$Li_x MoS_2 (PEO)_{0.5}$	2.78
$Li_x MoS_2 (PAN)_1$	2.84
$Li_x MoS_2 (DEA)_{0.2}$	2.80
$Li_x MoS_2$ (n-MCHA)$_{0.4}$	2.60

More instructive information than the average values in is obtained by analyzing the quasi-equilibrium lithium intercalation curves Some examples are displayed in Fig. 5. As observed, the variation of the potential with the lithium content also depends on the co-intercalated organic guest. Pure MoS_2 displays an extreme case of dependence. Lithium-ion activity strongly decreases with the amount of intercalated lithium. In other words, the metallic character of lithium in the intercalated phase increases significantly along the discharge. These results agree with some XPS experiments performed with the compound $Li_{0.8}MoS_2$ which, as deduced from results observed in Table.6 show that lithium in these compounds displays a behavior more like the metallic lithium than other lithium compounds [14].Clearly in these intercalates host-guest charge transfer is rather incomplete

affecting the electrode capacity. This partial charge transfer has been also deduced from theoretical calculation made for this and other similar compounds[15].

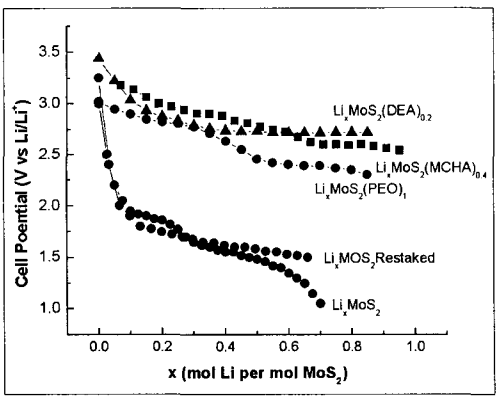

Figure 5. Variation of the quasi-equilibrium potential with the lithium content along the intercalation of lithium into MoS_2 pure and modified by the co-intercalation of donors.

Tabla 6. Binding energies of Li(1s)

Compound	**E_b eV**
$LiBF_4$	59.9
LiCl	58.1
LiBr	56.8
$LiNH_2$	55.8
Li MoS_2	55.6
Li(metal)	55.5

Contrasting with the experiments already discussed, the presence of some intercalate does not only enhance the lithium-ion activity but also permits the incorporation of a higher amount of lithium without major detriment to the cell potential, thus increasing its capacity. However, such an effect is different for each nanocomposite. The explanation may be not always found in an increment of the lithium-host charge transfer since the later has certainly a limit which should be not much higher than that observed for the MoS_2 alone. Probably, that is also related to the state of lithium in the interlamellar phase, which in some cases like in the intercalation of amines, are able to form aggregates (*vide infra*) [16].

Interlamellar Phase Structure

Lamellar structures like those analyzed in this work are intrinsically complicated to be studied by precise crystallographic methods. Due to the high anisotropy of the interactions involved in their constitution, they often shows a low structural tridimensional coherence. That is specially valid for the organic-inorganic nanocomposites in which the organic phase presents a high mobility resembling more a liquid than a solid phase. The structure of the interlamellar phase has to be studied by indirect methods like wide-line nuclear magnetic resonance spectroscopy at variable temperature. In the case of the nanocomposites formed by the co-intercalation of lithium and donor species discussed here, ^{7}Li-NMR studies provide interesting information about the relative position of the lithium atoms in the interlamellar phase. The ^{7}Li-^{7}Li and ^{7}Li-^{1}H second magnetic moments, calculated from the resonance line half high width in the ^{1}H-coupled and decoupled ^{7}Li-spectra at low temperatures (rigid state) permit to determinate by comparison with suitable molecular models both the relative positions of the lithium atoms and the distances between them and the neighboring hydrogen atoms. These studies, limited at the moment to the nanocomposites with poly(ethylene oxide) and secondary amines, show that in the confined state not only the inorganic matrix undergoes changes but also both, lithium and the donors may present conformations different from those in the free state [17].

As shown schematically in Fig. 6 in the PEO derivatives $Li_{0.1}MoS_2(PEO)_{0.5}$ and $Li_{0.1}MoS_2(PEO)_{1.0}$ with second magnetic moments $M_2(^{7}Li\text{-}^{7}Li)$ of 0.014 and 0.050 G^2 respectively, lithium is found coordinated by the polymer oxygen atoms and distributed in a form practically homogenous in the phase. There are however important differences between these nanocompostes. In $Li_{0.1}MoS_2(PEO)_{0.5}$ the interlamellar phase is formed by one polymer layer where lithium is simultaneously coordinated by the polymer and the host sulfur atoms. Meanwhile in $Li_{0.1}MoS_2(PEO)_{1.0}$ where a polymer bilayer is apparent, the lithium atoms are totally surrounded by the polyether oxygen atoms. Moreover, the conformation of the polymer in both cases, a zig-zag conformation in the former and TGG arrangement in the latter differs from the helical conformation, characteristic of the free polymer.

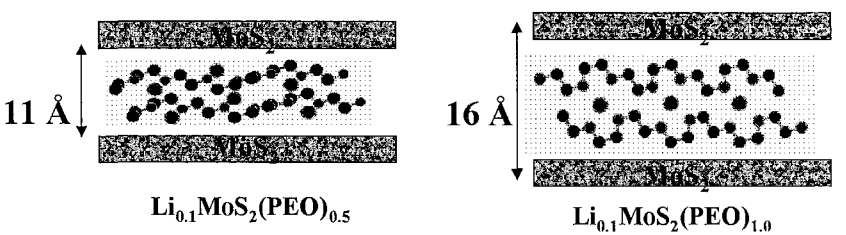

Figure 6. .Schematic representation of the conformation of POE in the MoS_2 interlaminas spaces $Li_{0.1}MoS_2(PEO)_{0.5}$ and $Li_{0.1}MoS_2(PEO)_{1.0}$

These results agree well with the lithium diffusion coefficient studies commented above. In the case of $Li_{0.1}MoS_2(PEO)_{1.0}$ with the lithium in an homogeneous oxygen coordination cage, the diffusion activation enthalpies show

only an small dependence on the lithium intercalation degree. Contrastingly in the compound $Li_{0.1}MoS_2(PEO)_{0.5}$ where there is a mixed coordination around lithium, the changes produced by lithium intercalation are notoriously more drastic (Fig. 4) [18].

Since the MoS_2/amine intercalates show in general relatively high Li/Li^+ potentials, electrical conductivities and lithium diffusion coefficients, it was specially interesting to analyze the state of lithium in the interlamellar phase of these nanocomposites. The ^7Li-^7Li second magnetic moments obtained from the ^7Li-NMR spectra result to be surprisingly high, in a range 1.3-1.6 G^2 [17]. This data reveals that in this compounds there is an agglomeration of lithium atoms. Using simple molecular models it is possible to deduce that observed Li-Li interactions corresponds to the formation of lithium metal clusters. In diethylamine a trinuclear species is stabilized, while for the di-butyl and di-pentyl derivatives the formation of tetranuclear aggregates is observed. The tendency of lithium to form aggregates is well known in lithium, however the three-nuclear as well as the stabilization of Li cluster by secondary amines is somewhat surprisingly. The role of the amine in these intercalates appears to be the formation of a coordination cage around the cluster, showing a pseudo-micellar behavior. Although the latter is common for long chain derivatives, it has been not observed before for small amines. Thus, the behavior of both lithium and amine in these nanocomposites appears to be induced by confinement effects.

The peculiar arrangement of the components of the interlamellar phase should have a marked influence on both the thermodynamics and kinetics of lithium in these compounds, thus bearing to special electrical and electrochemical properties.

Conversion of Lamellar Nancomposites into Tubular Structures

Finally it is interesting to comment the possibility of obtaining one dimensional objects, specifically nanotubes, starting from lamellar organic-inorganic nanocomposites similar to those commented above.

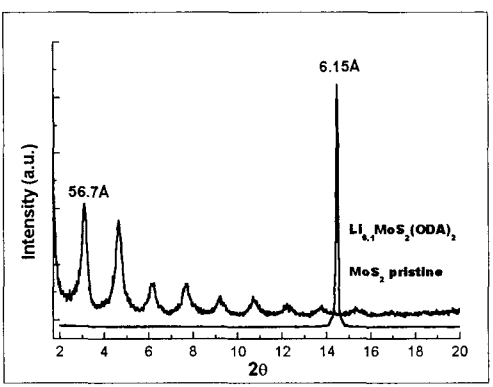

Figure 7. X-ray diffraction pattern of the MoS_2 and $Li_{0.1}MoS_2$(octadecylamine)$_2$

The intercalation of long chain amines into MoS_2 leads to high ordered laminar structures (Fig 7). Such a regular arrangements in the perpendicular direction to the molecular MoS_2 planes is possibly due to cooperative effects caused by the self-assembling of the amphiphilic organic donors, which indeed, are found forming organic bilayers in the host interlamellar spaces.

The treatment of these products under hydrothermal conditions *i.e.* temperature in the range 100-150 °C and auto-generated pressures, leads to multiwall MoS_2 nanotubes, which retain in the interlamellar spaces the organic donor. Selected images of these products are shown in Fig.8 [19].

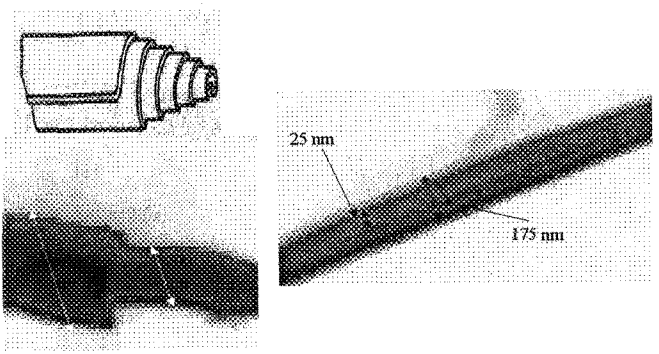

Figure 8. TEM image of MoS_2 nantotubes.

As observed in the figures, these nanotubes displaying a multilayer constitution appear to be generated from the lamellar intercalated precursors by a rolling up process. Such a mechanism, rather plausible given the reaction conditions much softer than those normally used for generating carbon nanotubes and inorganic fullerenes, appears to be also valid for other nanocomposites. Indeed, many V_2O_5-based functionalized tubular structures have been prepared using this method. Although experiments performed until now are limited to lamellar matrices intercalated with long chain amines, we think that other structurally similar organic-inorganic nanocomposites may be also prepared either directly by rolling up bi-dimensional precursors or by exchanging the donors from the interlamellar spaces. The benefits associated to the high anisotropic electrical and electrochemical behavior expected for one dimensional structures encourage further research in this field.

Conclusions

The lamellar MoS_2-based organic-inorganic nanocomposites described in this work show electrical and electrochemical properties which, from the point of view of its use as electrode in electrochemical devices, are better than the pristine inorganic sulfide. The relative easy methods used for the preparation of these nanocomposites and, specially, the dependence of their properties on the nature of

the organic donor co-intercalated with lithium make these products interesting in the design of electrode materials with predetermined electrochemical properties. Moreover, the intrinsic anisotropy of the products open the possibility of their utilization in intelligent devices. The chance of converting these bidimensional laminar products in functionalized one dimensional tubular nanostructures enhances the interest in the chemistry of this kind of intercalation compounds.

Acknowledgements. Research partially founded by FONDECYT (Grant 1050344, 7050085, 1030102, 7050081), DI Universidad de Chile and Universidad Tecnológica Metropolitana.

References

1. D. O'Hare, D. W. Bruce, D. S. O'Hare (Eds), Inorganic Materials, Wiley, Chichester, 1992
2. E. P. Gianellis, Adv. Mater. 8 (1996) 1
3. R. Schöllhorn in: J. L. Atwood, J. E. D. Davies, D. D. MacNicol (Eds), Inclusion Compounds, vol 1, Academic Press, London, 1984 (chap. 7).
4. M. Winter, J. O. Besenhard, M. E. Spahr, P. Novák, Adv. Mater, 10 (1998) 725.
5. G. González, M. A. Santa Ana, E. Benavente, Electrochim. Acta, 43 (1998) 1327.
6. M. A. Py, R. R. Haering, Can, J. Phys. 61 (1983) 76.
7. E. Benavente, M. A. Santa Ana F. Mendizábal, G. González, Coord Chem Rew 224 (2002) 87 -109.
8. W. M. R. Divigalpitiya, R. F. Frindt, S. R. Morrison, J. Mater. Res., 6, (1991) 1103.
9. M. B. Dines, Science, 188 (1975) 1210.
10. M. A. Santa Ana, E. Benavente, G. González, J. Coord. Chem. 54 (2001) 481.
11. V. Sánchez, E. Benavente, M. A. Santa Ana, G. González, Chem. Mater. 11 (1999) 2296.
12. G. González, M. A. Santa Ana, E. Benavente, J. Phys. Chem. Solids, 58 (1997) 1457.
13. G. González, M. A. Santa Ana, V. Sánchez, E. Benavente, Mol. Cryst and Liq. Cryst. 353 (2000) 301.
14. G. González, H. Binder, Bol. Soc. Chil Quim. 41 (1996) 121
15. F. Mendizábal, M. A. Santa Ana, E. Benavente, G. González, J. Chil. Chem. Soc., 48 (2003) 69.
16. A. C. Bloise, J. P. Donoso, C. J. Magon, J. Schneider, H. Panepucci, E. Benavente, V. Sánchez, M. A. Santa Ana, G. González, J. Phys. Chem., B 106 (2002) 11698.
17. E. Benavente, M. A. Santa Ana, G. González, F. Becker-Guedes, N. C. Mello, H. C. Panepucci, T. J. Bonogamba, J. P. Donoso, Electrochim. Acta 48 (2003) 1997.
18. G. González, M. A. Santa Ana, E. Benavente, V. Sánchez, N. Mirabal, Mol. Cryst. and Liq. Cryst. 374 (2002) 229.
19. V. Lavayen, N. Mirabal, E. Benavente, J. Seekamp, C. M. Sotomayor Torres, G. González, in H. Kuzmany, J. Fink, M. Mehring, S. Roth (Eds). CP685, Molecular Nanostructures: XVII Int' l. Winterschool/Euroconference on Electronic Properties of Novel Materials, 2003, 473.

$LINI_{0.80}Co_{0.20}O_2$ CATHODE THIN-FILM PREPARED BY RF SPUTTERING FOR ALL-SOLID-STATE RECHARGEABLE MICROBATTERIES

X. J. ZHU, C. HU, W. ZHANG, X. Y. GAN, M. H. CAO, D. B. LUO, W. CHEN, Q. XU, J. ZHOU AND H. X. LIU*

State Key Laboratory of Advanced Technology for Materials Synthesis and Processing, Wuhan University of Technology, Wuhan 430070, Hubei, PR China
**Email: lhxhp@mail.whut.edu.cn*

$LiNi_{0.80}Co_{0.20}O_2$ thin-films have been prepared by RF magnetron sputtering on Pt substrate. The films before and after annealing were identified by XRD, SEM and electrochemical measurements. The as-deposited film was amorphous phase. After annealing at 600~800 ℃, well-crystallized $LiNi_{0.80}Co_{0.20}O_2$ films were obtained. The degree of crystallization of the as-deposited films is strongly affected by the annealing temperature. As a result, the 700℃-annealed film has relatively complete layered structure, high specific capacity and good cycleability. The first discharge capacity of the $LiNi_{0.80}Co_{0.20}O_2$ film annealed at 600, 700 and 800℃ is about 44.5, 55.3 and 46.2 μAh/cm^2·μm, respectively. The corresponding 50th discharge capacities are 40.2, 49.4 and 42.4% of the first discharge capacity.

1. Introduction

With the development of the micro-scale processing techniques and materials, electronic and communication devices become smaller and more precise. In particular, the demands for on-chip power alignment of functional parts and peripheral circuits for controlling these parts are increased. The reduction in size and power requirement of electronic devices is the major driving force behind the development of all-solid-state thin-film microbatteries. Applications focus on the improvement of existing consumer and medical products, such as smart cards, sensors, implantable defibrillators, and neural stimulators, as well as on the integration with electronic chips and microelectromechanical systems [1-7].

Recently, RF magnetron sputtered metal oxide thin films, particularly, those composed of $LiCoO_2$, have emerged as a leading candidate for use as cathode layers in all-solid-state thin-film microbatteries, due to the advantage of high specific capacity, high operating voltage, ease of preparation and long cycle-life [8-10]. However, the limited capacity of the $LiCoO_2$, high cost and toxicity of cobalt have been regarded as drawbacks. To improve the performance of all-solid-state thin-film microbatteries, $LiNi_{1-x}Co_xO_2$ type of compounds ($0<x<1$), in the form of α-$NaFeO_2$

layered structures, have attracted great interest as cathode film materials for microbatteries [11-13].

In this work, $LiNi_{0.80}Co_{0.20}O_2$ has been prepared by RF magnetron sputtered method. We report the properties of the $LiNi_{0.80}Co_{0.20}O_2$ thin films and the characteristics and performance of lithium cells with the films, and the effect of annealing temperature on the crystalline and capacity of the films has also been discussed.

2. Experimental

The $LiNi_{0.80}Co_{0.20}O_2$ thin films were deposited on Pt substrate by radio frequency (RF) magnetron sputtering from a $LiNi_{0.80}Co_{0.20}O_2$ target with a 2 in. diameter. The $LiNi_{0.80}Co_{0.20}O_2$ target was sintered at 750 ℃ for 2h by cold-pressing the $LiNi_{0.80}Co_{0.20}O_2$ powder, which was synthesized from $LiOH{\cdot}H_2O$, $Ni(CH_3COO)_2{\cdot}4H_2O$ and $Co(CH_3COO)_2{\cdot}4H_2O$ in reagent grade by particulate sol-gel method [14]. The target was 80～85% of theoretical density, and it was 4 mm in thick. After presputtered for 30 min to provide a clean target surface, it was sputtered at an rf power of 100W in an $Ar+O_2$ mixture typically in a ratio of 3:1 at a total flow of about 20 standard cubic centimeter per minute (sccm) and a pressure of 2.7 Pa (20mTorr). The target-to-substrate distance was 5 cm. After the films deposition, they were annealed at the temperature of 600～700℃ for 30 min in flow oxygen.

The structure characterization of the as-deposited films was performed by X-ray diffraction (XRD) and scanning electron microscopy (SEM). The electrochemical characteristics of the films by assembled the 2016-type coin cell were carried out using galvanostatic charge-discharge experiments to characterize the surface layer on as-deposited films, as well as to examine the annealing effect on the films. The coin cells consisted of Li-metal sheet as negative electrode, the as-prepared thin-films as working electrode, and 1 M $LiClO_4$ in EC/DMC (1/1 vol.%) as the electrolyte, which were cycled at a current density of 10 $\mu A/cm^2$ and cut-off voltage in the range of 3.0～4.2V.

3. Results and discussion

Fig.1 shows the XRD patterns for the $LiNi_{0.80}Co_{0.20}O_2$ films before and after annealing at 600, 700 and 800 ℃. It is known that $LiNi_{0.80}Co_{0.20}O_2$ exhibits hexagonal with $R\bar{3}m$ symmetry, which is usually employed as the cathode material in Li-ion batteries due to its good electrochemical properties. The characteristic peak of $LiNi_{0.80}Co_{0.20}O_2$ was identified by index, and the asterisk indicated the peaks originating from Pt substrate. In spite of the fact that the most intensive peak arised from Pt, the as-prepared film can be identified as the $LiNi_{0.80}Co_{0.20}O_2$ phase. The

XRD pattern for the as-deposited film is shown in Fig.1 (a). This pattern exhibited a weak and broad (104) reflection, showing that the film was amorphous phase. This result suggested that the lithium, nickel, cobalt, and oxygen ions might not orderly occupy their idea lattice positions in the layered structure. In other words, it appeared that the as-deposited films did not have a well-crystallized structure. It is believed that the post-annealing of the as-deposited films provides energy for the rearrangement of lithium, cobalt, nickel and oxygen atoms to form layered crystalline $LiNi_{0.80}Co_{0.20}O_2$ films. Therefore, heat treatment plays an important role in obtaining well-crystallized $LiNi_{0.80}Co_{0.20}O_2$. In order to increase the degree of crystallization of the $LiNi_{0.80}Co_{0.20}O_2$ films, the as-deposited films need to undergo a post-annealing at 600～800℃ for 30min. After annealing at 600℃, the (104) reflection of the film was observed, as shown in Fig.1 (b). On increasing the annealing temperature to 700℃, the (104) reflection was developed, as shown in Fig.1(c). Further increasing the annealing temperature to 800℃, the intensity of (104) reflection decreased. It is because high temperature is favor to the crystallization of $LiNi_{0.80}Co_{0.20}O_2$ layered structure, but if the annealing temperature is more than 700℃, lithium evaporation is occurred, resulting in lithium-defected crystalline of $Li_{1-x}Ni_{0.80}Co_{0.20}O_2$ ($0<x<1$). This can also be indicated by later electrochemical measurements.

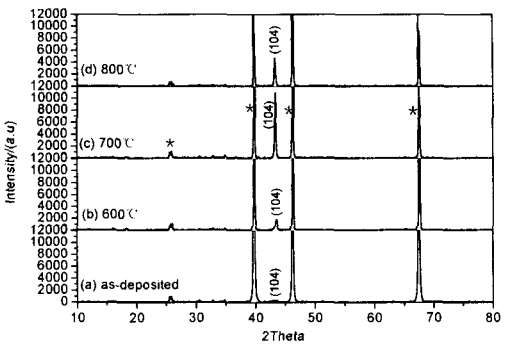

Figure 1 XRD patterns of (a) as-deposited, (b) 600℃-annealed, (C) 700℃-annealed, and (d) 800℃-annealed $LiNi_{0.80}Co_{0.20}O_2$ films.

Fig.2 shows the surface SEM images of the $LiNi_{0.80}Co_{0.20}O_2$ films before and after annealing at 600, 700 and 800℃ for 30min. The surface of the as-deposited film had a ploy-edged morphology. After annealed at 600 and 700℃, the morphology of the grains became smooth due to the shrinkage of the film. Further increasing the temperature to 800℃, the film was cracked, resulting from a combination of intrisinic and thermal stress.

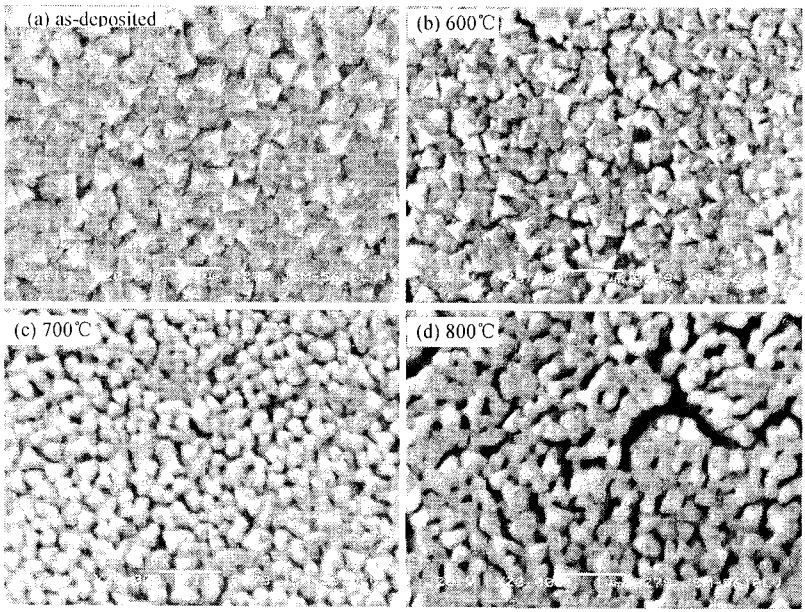

Figure 2 SEM morphologies of (a) as-deposited, (b) 600℃-annealed, (c) 700℃-annealed, and (d) 800℃-annealed $LiNi_{0.80}Co_{0.20}O_2$ films.

From the XRD results and SEM analysis, heat treatment at various temperatures enhanced the crystallization of the as-deposited films. The increasing crystallization suggested that lithium, nickel, cobalt and oxygen atoms rearrange to their ideal crystal position after annealing. Moreover, shrinkage of the film indicated that all the ions were packed into a more close-packing arrangement after annealing.

Fig.3 shows the specific discharge capacity of the as-deposited and the annealed $LiNi_{0.80}Co_{0.20}O_2$ films as a function of cycle number, charge-discharge measurements were carried out at a current density of 10μA/cm^2 in the voltage range of 3.0～4.2V. It is noteworthy that the as-deposited film showed the capacity of about 5μAh/cm^2.μm due to its poor layered structure, and for the films annealed at 600, 700 and 800℃ for 30min, the initial discharge capacities were 44.5, 55.3, 46.2 μAh/cm^2.μm, respectively. During discharging process, the voltage of the 700℃-annealed film droped gradually, compared with those of the 600 and 800℃-annealed films. These results showed that the annealing process was crucial for obtaining electrochemically active $LiNi_{0.80}Co_{0.20}O_2$ films with a well-crystallized layered structure. When the film was annealed at 700℃, the temperature enhanced the mobility of ions and resulted in a greater extent of electrochemically active $LiNi_{0.80}Co_{0.20}O_2$ film. When the film was annealed at 600℃, the temperature was not

enough to form well-crystallized film. But, when the annealing temperature was 800 ℃, the high temperature led to lithium evaporation to form lithium-defected crystalline.

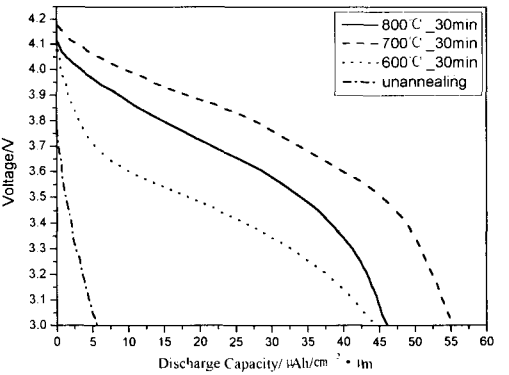

Figure 3 Discharge curves for the unannealed-film and the films annealed at 600, 700 and 800℃ for 30 min in O_2 atmosphere.

The discharge capacity with respect to cycle number is shown in Fig.4. Because the post-annealing can enhance the extent of crystallization of $LiNi_{0.80}Co_{0.20}O_2$ films, the discharge capacity increased with increase in the annealing temperature from 600 to 700℃. After cycling, the capacity of 700℃-annealed film decreased slowly. Compared with the initial discharge capacity, the capacity retention was 40.2, 49.4 and 42.4% for the 600, 700 and 800℃-annealed films after 50 cycles, respectively. The capacity fading of 600 and 800℃-annealed films became worse, resulting from the incomplete crystalline in the layered structure.

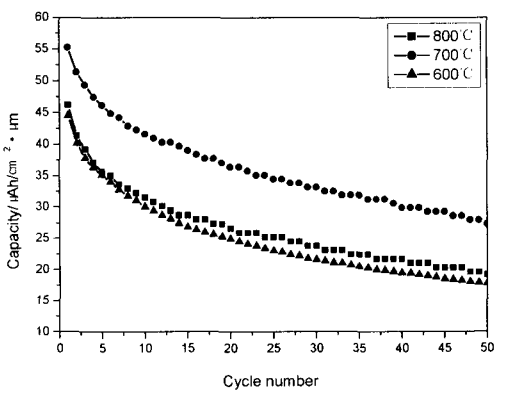

Figure 4 Discharge capacity vs cycle number of 600, 700 and 800℃-annealed films.

Based on the results above, the amount of electrochemically active lithium ions gradually decreased on cycling, and in a well-crystallized structure of $LiNi_{0.80}Co_{0.20}O_2$ film, most lithium ions can intercalate/deintercate repeatedly into the lithium layer of the rhombohedra lattice. Therefore, capacity retention was better on the 700℃-annealed $LiNi_{0.80}Co_{0.20}O_2$ film.

4. Conclusions

$LiNi_{0.80}Co_{0.20}O_2$ thin-films were deposited by RF magnetron sputtering. The as-deposited film was amorphous phase, and the annealed films exhibit (104) preferred orientation. The degree of crystallization and electrochemical properties of the as-deposited films were enhanced by increasing the annealing temperature from 600 to 700℃. Further increasing the annealing temperature to 800℃, the layered structure of the film was incomplete due to lithium evaporation at high temperature. Meanwhile, the surface morphology of 800℃-annealed film became cracked. The initial discharge capacities were about 44.5, 55.3 and 46.2 for 600, 700 800℃-annealed films, respectively, and the corresponding 50^{th} discharge capacities were 40.2, 49.4 and 42.4% of the first discharge capacity.

Acknowledgments

This work was supported by the National Natural Science Foundation of China (No. 20371038) and the Foundation for Innovative Research Team of Hubei Province (No. 2005ABC004)

References

1. K. Shokoohi, J.M. Tarascon, B.J. Wilkens, *Appl. Phys. Lett.* **59**, 1260 (1991).
2. H.K. Kim, O. W. Ok, T.Y. Seong, E.J. Jeon, W.I. Cho, Y.S. Yoon, *J. Vac. Sci. Technol.* **Part A 19 (5)**, 2549 (2001).
3. B.J. Neudecker, N.J. Dudney, J.B. Bates, *J. Electrochem. Soc.* **147**, 517 (2001).
4. H.K. Kim, Y.W. Ok, T.Y. Seong, J.H. Lim, Y.W. Shin, Y.S. Yoon, *J. Vac. Sci. Technol.* **B 20**, 1827 (2002).
5. J.H. Lim, D.J. Choi, H.-K. Kim, W.I. Cho, Y.S. Yoon, *J. Electrochem. Soc.* **148**, A278 (2001).
6. H.K. Kim, T.Y. Seong, J.H. Lim, W.I. Cho, Y.S. Yoon, *J. Power Sources* **102**, 167 (2001).
7. H.K. Kim, T.Y. Seong, Y.S. Yoon, *J. Power Sources* **112**, 67 (2002).
8. J. Pracharová, J. Pridal, J. Bludská, I. Jakubec, V. Vorlíček, Z. Málková, T. D. Makris, R. Giorgi, L. Jastrabík, *J. Power Sources* **108**, 204 (2002).

9. B.J. Neudecker, R.A. Zuhr, J.D. Robertson, J.B. Bates, *J. Electrochem. Soc.* **145**, 4160 (1998).
10. C.L. Liao, K.Z. Fung, *J. Power Sources* **128**, 262 (2004).
11. H.K. Kim, T.Y. Seong, Y.S. Yoon, *Thin Solid Films* **447-448**, 619 (2004).
12. B. Wang, J.B. Bates, F.X. Hart, B.C. Sales, R.A. Zuhr, J.D.Robertson, *J. Electrochem. Soc.* **143 (10)**, 3203 (1996).
13. F.X. Hart, J.B. Bates, *J. Appl. Phys.* **81 (12)**, 7560 (1998).
14. X.J. Zhu, H.H. Chen, H. Zhan, H.X. Liu, D.L. Yang, Y.H. Zhou, *Chinese Journal of Chemistry* **23**, 491 (2005).

This page is intentionally left blank

Contributed Papers

This page is intentionally left blank

NANOCOMPOSITE CATHODE FOR SOFCs PREPARED BY ELECTROSTATIC SPRAY DEPOSITION

A. PRINCIVALLE, E. DJURADO
Laboratoire d'Electrochimie et de Physico-chimie des Matériaux et des Interfaces, ENSEEG-INP Grenoble/UJF/CNRS, BP 75, 1130 rue de la Piscine, 38402 St Martin d'Hères Cedex, France
E-mail : Elisabeth.Djurado@enseeg.inpg.fr

Electrostatic spray deposition (ESD) technique was applied to deposit composite electrodes, which consisted of a mixture of a solid electrolyte (YSZ) and an electrocatalytic material (LSM) with a controlled microstructure on YSZ dense substrates. The influence on film morphology of the process parameters such as nature of precursor solution, deposition temperature, nozzle to substrate distance and precursor solution flow rate was investigated. The results demonstrated a significant role of the salt nature in the precursor solutions in the film morphology. In this work, powder X-ray diffraction analysis showed that no traces of any secondary phases were detected in between LSM hexagonal and cubic YSZ phases after thermal treatment at 800°C, this latter preserving the microstructural properties.

1. Introduction

Main issues in solid oxide fuel cells (SOFCs) development are recently focused on cost reduction and improvement of durability in long-term operation. In this context, SOFCs will be operated at reduced temperature from the traditional 1000°C to 800°C. Consequently, detrimental chemical reactions between the electrode materials and electrolyte will be avoided. A decrease in the operating temperature can be achieved by improving the electrode performance, i.e. reducing the electrode overpotentials especially at the cathode. In general, two research directions are suggested in literature: (i) optimizing the microstructure of the electrochemically active layers[1], (ii) a replacement of pure electronic conductor cathode by mixed ionic electronic conductor (MIEC)[2,3].
Electrostatic spray deposition (ESD) is a processing technique to prepare dense or porous ceramic films. In ESD, a precursor solution is atomized by electric field to an aerosol, which is then directed to a heated substrate where a thin film is deposited. This thin film deposition method is rather simple, cost-effective, and a wide choice of precursors can be used. The composition of the film can be easily controlled by the precursor solution.
The ESD technique is a powerful tool for deposition of porous electrodes[4,5,6] and dense electrolytes[7,8,9]. In order to advance this technology further, a better understanding of the deposition parameters is desirable.
Fuel cells with YSZ electrolyte films prepared by ESD attained a power density of 450 mW/cm^2 and an open circuit voltage (OCV) of about 0.9 V at 770°C[9]. The difference to the theoretical value of 1.1V was attributed to gas leakage through the YSZ film and unsealed experimental setup.
The present study is focused on the preparation of LSM/YSZ composites with different morphologies using ESD technique. The control of the film morphology requires a good understanding of the ESD process, starting with precursor solution atomization and ending with droplet spreading on a substrate. Little work has been previously reported on the

influence of the nature of precursor solution and process parameters (substrate temperature, nozzle to substrate distance and flow rate) on the LSM/YSZ film porosity. One approach to enhance the cathodic performances of an intermediate temperature solid oxide fuel cell (IT-SOFC) is to elaborate a two phase composite electrode, consisted in a mixture of a solid electrolyte (YSZ) and an electronic conducting electrocatalytic material (LSM) which composition and porosity gradually vary. The optimisation of a composite cathode requires improvements of ionic and electronic conductivities to support ion and electron flows as well as porosity for gas supply. Electrostatic spray deposition (ESD) is a powerful tool for deposition of porous electrodes. The present work reports the influence of the nature of precursors solution and the parameters of ESD process on the microstructure of the films based on LSM and YSZ.

2. Experimental Section

The LSM/YSZ films were prepared using a vertical ESD setup similar to that described in the literature[10,11](Figure 1).

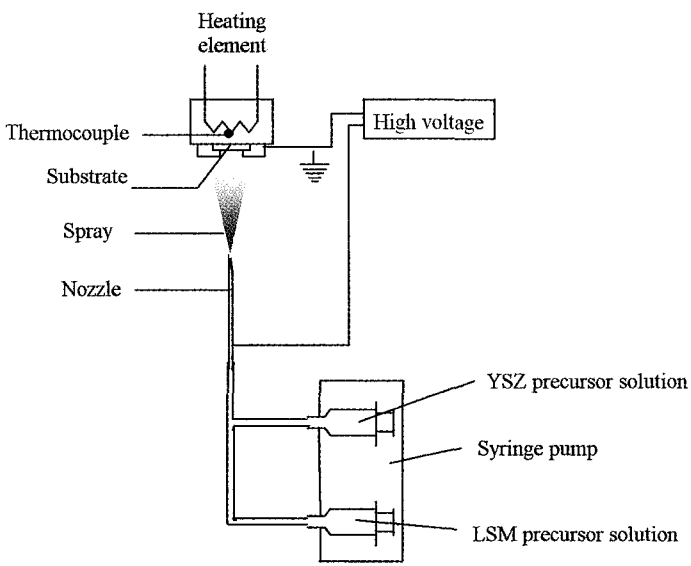

Figure 1. Experimental ESD set-up.

The ESD technique involves atomization of a precursor solution to an aerosol, which is then directed to a heated substrate using an electrical field, where a film is formed. In order to feed two separate precursor solutions simultaneously, the configuration with two separated feed-pipes and syringes was used. The two feed-pipes were connected at the nozzle.

LSM/YSZ composite films were deposited on a hot-pressed polycrystalline YSZ substrate. Disks of homemade YSZ were 20 mm in diameter and 1mm in thickness.

The precursor solution for LSM consisted of lanthanum nitrate, $La(NO_3)_3 \cdot 6H_2O$, 99% (Fluka), strontium chloride, $SrCl_2 \cdot 6H_2O$, 99% (Aldrich) and manganese nitrate, $Mn(NO_3)_2 \cdot 4H_2O$, 98% (Aldrich) dissolved in the 33 vol. % of ethanol, C_2H_5OH, 99.9% (Prolabo) and 67 vol. % of diethylene glycol monobutyl ether (butyl carbitol), $CH_3(CH_2)_3OCH_2CH_2OCH_2CH_2OH$, 99+% (Acros Organics). The precursor solution was prepared according to the stoichiometry of the required film $La_{0.8075}Sr_{0.1425}MnO_{3-\delta}$. The total concentration of the salts in the solution was 0.024 mol/L.

The YSZ precursor solutions were prepared according to the stoichiometry of the required film $(ZrO_2)_{0.92}(Y_2O_3)_{0.08}$. Yttrium chloride $YCl_3 \cdot 6H_2O$ (Alfa Aesar) and either Zr acetylacetonate $Zr(C_5H_7O_2)_4$ (Fluka Chemie) or zirconyl nitrate hydrate $ZrO(NO_3)_2 \cdot aq$ (Fluka Chemie) were dissolved in two different solvent mixtures. A solvent mixture contained 67 vol. % of butyl carbitol and 33 vol. % of either ethanol or water. The total concentration of the salts in this solution was 0.016 mol/L.

Two different precursor solutions were prepared. One was based on Zr acetylacetonate dissolved in ethanol, denoted as YSZacac. A second one was zirconyl nitrate dissolved in water, denoted as YSZnitr. Each solution was containing yttrium chloride and 67 vol. % of butyl carbitol.

Deposition time was 1 h. Flow rate of precursor solution was varied from 0.50 to 1.17 mL/h using a Sage™ M361 syringe pump. The precursor solution was atomized using a positive high voltage from 6 to 10 kV. The deposition temperature was ranging from 260°C to 324°C. The nozzle-to-substrate distance varied from 27 to 47 mm.

Surface morphologies were analyzed using Scanning Electron Microscopy (SEM) (LEO 400).

Samples were post-annealed at a heating rate of 2°C/min in air for 1 h at 800°C in order to investigate the influence of thermal treatment on the morphology and on the reactivity products.

X-ray powder diffraction was carried out using a Siemens D500 $\theta/2\theta$ diffractometer in the Bragg Brentano geometry from 25° to 95° in 2θ (0.04° in 2θ step, 8s as a counting time) with Fe K_α radiation (λ = 0.1936 nm). Phases were identified using DIFFRAC-AT software systems (Socabim, Paris).

3. Results and discussion

Influence of the salt in the precursor solution.

YSZ coatings were deposited by ESD process starting from two different precursor solutions as described previously in the experimental section such as YSZacac and YSZnitr. Figure 2 shows the effect of the precursor salt nature on the morphology of YSZ and LSM films. Dense and cracked YSZ films are obtained when Zracac was used (Figure 2a) while porous and crack-free YSZ films are resulted from the using of zirconyl nitrate as precursor (Figure 2b). LSM films (Figure 2c) are found porous and present a different reticulated porosity compared to YSZ (Figure 2b) in the same ESD conditions but starting from different salts. This behavior can be explained by the size of droplets which results from the dependence on electrical conductivity of the precursor solution[12].

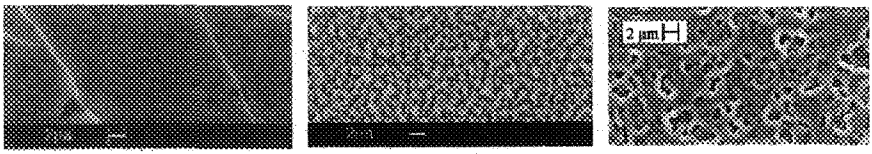

a) b) c)

Figure 2. Influence of the salt nature on the morphology of a) YSZ coating: Zracac, b) YSZ coating : zirconyl nitrate c) LSM coating . Solvent: 33 vol. % ethanol + 67 vol. % butyl carbitol. Precursor solution flow rate: 0.5 mL/h. Deposition temperature: 260°C. Deposition time: 1 h. Nozzle to substrate distance: 27 mm.

Indeed, from the droplet size, d is reciprocally proportional to electric conductivity of liquid σ (S/m) with an exponent of 1/6 for the cone-jet mode as the following:

$$d \propto \left(\frac{1}{\sigma}\right)^{\frac{1}{6}}$$

We have measured the conductivity of our different precursors solutions (Table 1).

	Solution precursor		
	LSM	YSZacac	YSZnitr
conductivity (mS/m)	0.064	0.020	0.86

Table 1: Conductivity of precursor solution

Consequently, the largest droplets were found by spraying YSZacac precursor solutions. These largest droplets spread and formed a humid film when impacted the substrate. In this case, during the drying step, the volume change is very large due to the presence of a larger amount of solution on the substrate surface. A lot of stresses appear and are at the origin of the formation of cracks in YSZ coatings (Figure 2a). The YSZ and LSM coatings obtained by pulverisation of YSZ and LSM nitrate precursors solutions are formed by aerosol containing smaller droplets, especially for YSZnitr. Therefore, these smaller droplets dried faster and did not contain enough solvent for the formation of liquid film when they arrived on the substrate. The droplets did not spread and were just deposited as dried particles onto the substrate surface (Figure 2b). In the case of LSM coating, the droplets size is quite large in order to spread but a simultaneous boiling and drying was occurred at the substrate surface leading to a reticular porous microstructure. Indeed, the boiling point of the LSM solution was found equal to 240°C by thermal analyses and is closed to the deposition temperature (260°C), this latter being certainly slightly cooled when the aerosol is impacting the substrate.

We have demonstrated that the nature of salts is a primordial parameter on the film morphology. We have selected the precursors based on nitrates in the following because of their ability to form porous microstructures. Furthermore, the process parameters such as the deposition temperature, the nozzle to substrate distance and the flow rate of precursor solution can influence the film morphology. These different parameters can influence the porosity of a film, because they control the amount of solution deposited on the substrate.

Influence of deposition temperature

Figure 3 shows different surface morphologies of composite 50 vol. % LSM/ 50 vol. % YSZ films deposited starting from nitrate precursors at two different temperatures 260°C and 324°C for a solution flow rate of 0.50 mL/h. All films were found porous in this temperature domain. The microstructure obtained at 260°C (Figure 3a) can be the consequence of simultaneous boiling and drying of precursor solution. At 324°C (Figure 3b) a different type of porous microstructure was obtained. The agglomeration of interconnected particles was formed instead of the net-like microstructure. At 324°C the arriving droplets do not contain enough solvent for the formation of a liquid film. The droplets do not spread rapidly, they just stick to the previously arrived particles or to the substrate surface.

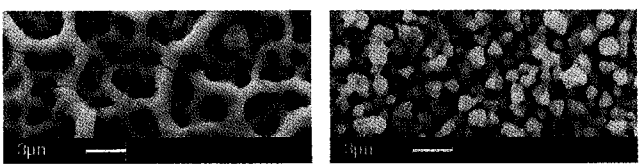

a) b)

Figure 3. Influence of deposition temperature on the morphology of LSM/YSZ coatings: a) 260°C, b) 324°C. Precursor solutions: LSM and YSZnitr. Solution flow rate: 0.50 mL/h. Deposition time: 1 h. Nozzle to substrate distance: 27 mm.

Influence of nozzle to substrate distance

The influence of the nozzle to substrate distance from 37 mm to 47 mm on surface morphology of composite 50 vol. % LSM/ 50 vol. % YSZ films is shown in Figure 4. When the nozzle to substrate distance is increased from 37 mm to 47 mm, we observe a progressive formation of a granular net (Figure 4c). When the distance is increased, the quantity of liquid is decreased in the droplet along the transport due to partial evaporation. These smaller droplets when impacting the substrate bridge together (Figure 4c).

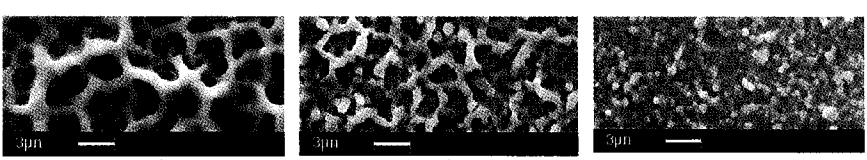

a) b) c)

Figure 4. Influence of nozzle to substrate distance on the morphology of LSM/YSZ coatings: a) 37 mm b) 42 mm c) 47 mm. Precursor solutions: LSM and YSZnitr. Deposition temperature: 260°C. Solution flow rate: 0.5 mL/h. Deposition time: 1 h.

Influence of precursor solution flow rate

Figure 5 shows the surface morphologies of composite 50 vol. % LSM/ 50 vol. % YSZ films deposited at two different precursor solution flow rates, 0.67 mL/h and 1.17 mL/h. Both deposited films were found porous. At the lowest flow rate (Figure 5a) the surface morphology seems to be slightly denser compared to that of films deposited at higher flow rates. The most "three dimensional" network (Figure 5b) was obtained at the highest flow rate with the appearance of some cracks. The increase of the solution flow rate generates an accumulation of liquid on the substrate surface which undergoes a too fast drying process.

a) b)

Figure 5. Influence of precursor solution flow rate on the morphology of LSM/YSZ coatings: a) 0.67 mL/h, and b) 1.17 mL/h. Precursor solutions: LSM and YSZnitr. Deposition temperature: 260°C. Deposition time: 1 h. Nozzle to substrate distance: 37 mm.

To conclude, the main ESD parameters, such as substrate temperature, nozzle to substrate distance and solution flow rate, control the equilibrium between the flux of incoming solution and the solvent evaporation at the substrate surface as shown by Neagu[13] for YSZ coatings.

Influence of thermal treatment on composite coatings.

It is important to control the effect of a thermal treatment on the morphology of LSM/YSZ coatings in order to apply this material as a possible candidate to be used as an electrode for SOFC. Figure 6 shows a quite similar porous and reticulated morphology of the films before and after thermal treatment at 800°C for 1h.

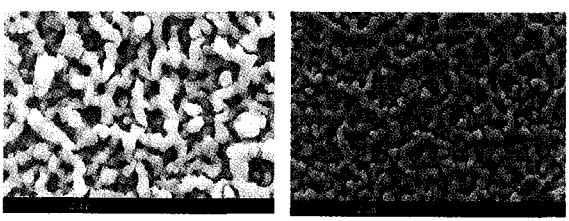

(a) (b)

Figure 6. SEM images of LSM/YSZ films deposited on YSZ (a) as-prepared, (b) after thermal treatment at 800°C for 1 h.

Figure 7 shows XRD patterns of LSM/YSZ films thermally treated for 1 h in air at 800°C. The XRD patterns of the films consisted only of YSZ and LSM phases. The presence of any other phases was not detected. It is necessary to obtain a crystalline mixture of LSM and YSZ phases without any secondary phases in order to be applied as reduced temperature SOFC cathode.

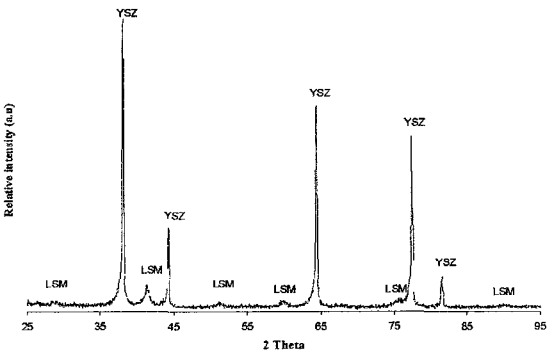

Figure 7. XRD patterns of LSM/YSZ films heat treated for 1 h in air at 800°C

4. Conclusion

In this study, we have investigated the influence of the nature of the precursor solution and of ESD deposition parameters such as the deposition temperature, the flow rate of a precursor solution and the nozzle to substrate distance on the morphology of LSM/YSZ films. This work has allowed to extract the main ESD parameters which have an impact on the porosity control of LSM/YSZ composite. The preparation of these composite cathodes using ESD with simultaneous graded porosity and graded composition is in progress.

References

1. P. Holtappels and C. Bagger, *J. Eur. Ceram. Soc.* **22**, 41 (2002).
2. M. J. L. Østergård, C. Clausen, C. Bagger and M. Mogensen, *Electrochimica Act.* **40**, 1971 (1995).
3. S. Wang , Y. Jiang, Y. Zhang, J. Yan and W. Li, *Solid State Ionics.* **113-115**, 291 (1998).
4. I. Taniguchi, R. C. van Landschoot and J. Schoonman, *Solid State Ionics.* **156**, 1 (2003).
5. K. L. Choy, W. Bai, S. Charojrochkul and B. C. H. Steele, *J. Power Sources.* **71**, 361 (1998).
6. A. Princivalle, D. Perednis, R. Neagu and E. Djurado, *Chem. Mater.* **16**, 3733 (2004).
7. N. H. J. Stelzer and J. Schoonman, *J. Mater. Synthesis and Processing.* **4**, 429 (1996).
8. T. Nguyen and E. Djurado, *Solid State Ionics.* **138**, 191 (2001).
9. D. Perednis and L. J. Gauckler, *Solid State Ionics.* **166**, 229 (2004).
10. C. H. Chen, E. M. Kelder, M. J. G. Jak and J. Schoonman, *Solid State Ionics.* **86-88**, 1301 (1996).
11. C. H. Chen, E. M. Kelder and J. Schoonman, *J. Mater. Sci.* **31**, 5437 (1996).
12 A. M. Ganan-Calvo, *Physical Review Letters.* **79**, 217-220 (1997).
13. R. Neagu, D. Perednis, A. Princivalle and E. Djurado, *Surface and Coatings Technology.* in press (2006).

EFFECT OF THE ADDITION OF NANOPOROUS CARBON BLACK ON THE CYCLING CHARACTERISTICS OF $Li_2Co_2(MoO_4)_3$ FOR LITHIUM BATTERIES

K.M. BEGAM[1], S.R.S. PRABAHARAN[2#]

[1]Department of Electrical and Electronics Engineering,
Universiti Teknologi PETRONAS, Bandar Seri Iskandar,
31750 Tronoh, Perak, Malaysia.
E-mail: mumtajbegam@petronas.com.my

[2]Faculty of Engineering and Computer Science,
The University of Nottingham, Malaysia campus,
Jalan Broga, Semenyih, Selangor, Malaysia.
[#]E-mail: prabaharan.sahaya@nottingham.edu.my

Abstract

We studied the effect of nanoporous carbon black (non-graphitized carbon) on the electronic conductivity of recently identified $Li_2Co_2(MoO_4)$ polyanion material, for which the lattice level conductivity is low similar to the other polyanion materials reported so far irrespective of their structure. $Li_2Co_2(MoO_4)_3$ was found to possess improved conductivity due to the addition of a highly conducting nanoporous carbon black (NCB) as conductive additive besides acetylene black. Inclusion of non-graphitized carbon black facilitated the effective grain-grain contact leading to increased surface particle conductivity between the active grains and thus resulted in enhanced overall conductivity of the electrode in a composite manner. The nano-composite test electrode fabricated with NCB rendered improved charge/discharge properties in the voltage window 4.9 – 2.0 V, when compared to the conventional composite electrode. Accordingly, the nanocomposite electrode delivered the first discharge capacity of 55 mAh/g, about 2.5 times higher than the capacity offered by the conventional composite electrode (23 mAh/g). It was also demonstrated that the presence of NCB enhanced the extended cycling performance in terms of Li^+ insertion and retention of the host structure of the electrode material.

Key words: NASICON-type polyanion materials; Lithium cobalt molybdate, Nanoporous carbon black

Introduction

The search for new cathode materials continues ever since Sony introduced the commercial Li-Ion rechargeable batteries in 1991 based on $LiCoO_2$ as positive electrode material. Amongst Li^+ storage materials, the positive electrode materials having polyanion framework have gained greater attention due to their interesting structural characteristics. Both NASICON-type [1-6] and Olivine-type [7-10] materials occupy a subject of extensive research for many years due to their beneficial electrochemical characteristics. However, polyanion materials generally possess very low lattice electronic conductivity due to their inherent structural

limitations [10-13]. This drawback affects the rate performance of the polyanion materials and poses constraints in using such materials in batteries.

To circumvent the electronic conductivity problem associated with the polyanion materials, quite a few techniques have been proposed over the years. Recently, all these techniques were focused on increasing the electronic conductivity of the composite electrodes through carbon coating on the active material particles or by adding dispersed metal powders. These attempts provided noticeable improvement in the electronic conductivity of the polyanion materials.

Zaghib et al. [14] reported that the presence of carbon as a conductive additive in Olivine-$LiFePO_4$ increases the discharge capacity and utilization of the active material. Sol-gel synthesized $LiFePO_4$ coated with carbon confirmed a highly conducting phase alleviating limitation due to slow electronic transport and small particle size ensured short diffusion length, both contributing to enhanced rate capability. At C/5 discharge rate an initial capacity of 150 mAh/g, and 140 mAh/g after 100 cycles was obtained by Yang and Xu [15].

Scrosati et al. [16] introduced electronically conducting carbon matrix during template prepared nanofibers of $LiFePO_4$ electrode, which could deliver almost 100% of theoretical capacity at a high discharge rate of 3C and 36% of the initial capacity at the enormous discharge rate of 65C providing an excellent rate capability. Recently, our group succeeded in enhancing the electrochemical performance of soft-combustion derived NASICON- $Li_2Ni_2(MoO_4)_3$ polyanion material by incorporating small amounts of mesoporous carbon black [17]. Formation of nano-composites using high surface area carbon is one of the promising techniques by way of increasing the intactness between active grains, offering enhanced electrochemical characteristics. A four fold increase in discharge capacity of nano-composite $Li_2Ni_2(MoO_4)_3$ has been found when compared to conventional composite electrode ($Li_2Ni_2(MoO_4)_3$ + AB+ PTFE) [17].

Ball milling technique was employed to prepare $LiFePO_4$/C composite using sucrose as a conductive additive precursor and a high capacity of 137 mAh/g was achieved at 1C rate without any obvious capacity fade after 60 cycles [18]. Wang et al. [8] synthesized a series of $LiM_xFe_{1-x}PO_4$ (M = Mg, Zr, Ti) phosphates with a layer of amorphous carbon on the surface of $LiM_xFe_{1-x}PO_4$ particles. Amorphous carbon substantially increased the electronic conductivity of the nano-sized $LiM_xFe_{1-x}PO_4$ crystals. Eftekhari [19] used Au to form a mixed $LiFePO_4$/Au film and obtained better battery performance such as higher specific capacity, less capacity fading and faster diffusion process by modifying the low conductivity of $LiFePO_4$.

Following our previous work on $Li_2Ni_2(MoO_4)_3$ nano-composite electrode, in the present work, we describe the improved electrochemical properties of an analogous polyanion material, $Li_2Co_2(MoO_4)_3$ upon adding a nanoporous matrix (NCB) having the mesoporosity [3, 13], thus proving the effectiveness of this method as a simple but an effective way to improve the electrode conductivity.

Experimental

A simple solution based soft-combustion synthesis protocol was adapted to synthesize fine powders of lithium-rich phase of cobalt molybdate, $Li_2Co_2(MoO_4)_3$ at low temperature. A detailed synthesis procedure was described in our earlier work [3, 13]. The material thus synthesized was characterized by various physical characterization techniques as explained earlier [13]. For electrochemical tests, an Arbin battery tester (BT 2000 series - 8 channel unit) was used. Test cells were composed of a composite cathode (working electrode) and thin lithium foil as both reference and counter electrode.

The conductivity of $Li_2Co_2(MoO_4)_3$ was enhanced by using a highly conducting mesoporous nano-sized carbon black (NCB) [Monarch 1400, Cabot Inc, USA, BET surface area: 469 m^2 g^{-1}; Grain size: 13 nm; σ_e; 19.7 S cm^{-1}] besides using acetylene black (AB), [BET surface area: 394 m^2/g; Grain size: 0.1 μm -10 μm; σ_e: 10.2 S cm^{-1}]. Nano-composite positive electrode (cathode) consisted of 65% active material, 5% binder (PTFE) and 30% conductive additive. The conductive additive was composed of equal proportion of AB and NCB (nano-sized particles exhibiting mesoporosity of 3-10 nm). The contents for the electrode were thoroughly mixed using Agate pestle and mortar. Nano-composite positive electrodes were fabricated following the procedure given previously [2, 11].

Results and Discussion

The results for the phase formation temperature (DSC-TG), phase purity and structure of the synthesized powders (XRD), calculation of unit cell parameters (ICSD using POWD 12++), electronic state of different elements present (XPS) and metal content of the synthesized product (ICP) were already presented in our earlier study [13]. Slow scan cyclic voltammetry (SSCV) and constant current galvanostatic charge/discharge test was employed to demonstrate the redox properties (Li^+ extraction/insertion) of $Li_2Co_2(MoO_4)_3$. The facile reversible electrochemical characteristics of $Li_2Co_2(MoO_4)_3$ were confirmed through SSCV. The first 20 galvanostatic charge/discharge cycles, discharge capacity of the material and a preliminary note on nano-composites was also published in our earlier papers [3, 13].

To examine the role of nanoporous carbon black on the electrochemical properties of $Li_2Co_2(MoO_4)_3$, $Li_2Co_2(MoO_4)_3$ [nano-composite cathode]/Li half-cells were tested under galvanostatic conditions between 4.9 and 2.0 V at low current densities: 2.5 mA/g (charge) and 1.25 mA/g (discharge). Our earlier report on the conventional electrode is also taken for comparison.

The first charge/discharge curves obtained using the nano-composite positive electrode (with NCB) are compared to the first charge/discharge curves of the conventional electrode (without NCB) as shown in Fig. 1. Figure 1 shows the clear evidence for the difference between the two cases in terms of IR drop, the amount of lithium removal/insertion and shape of the discharge profiles. The reduced IR (*ohmic*) drop (4.9 – 4.6 V) at the beginning of the discharge process after charge in the case of the nano-composite electrode is well seen in Fig 1

(inset). But, in the conventional case, a large IR (*ohmic*) drop was observed (4.9 – 4.3 V). As for the quantitative amount of Li^+ extraction, 1.25 per formula unit was extracted when charged to 4.9 V (charge cut off) vs. Li^+/Li during the first charge, which was 0.8 in the conventional case. Additionally, there is a significant improvement in the discharge process (lithium insertion reaction). In the former case (nano-composite), 1.25 Li^+ was inserted when discharged down to 2.0 V (discharge cut off) corresponding to a discharge capacity of 55 mAh/g which is 2.5 times higher when compared to our earlier studies on conventional type $Li_2Co_2(MoO_4)_3$ (23 mAh/g for 0.53 Li^+ down to 2.0 V).

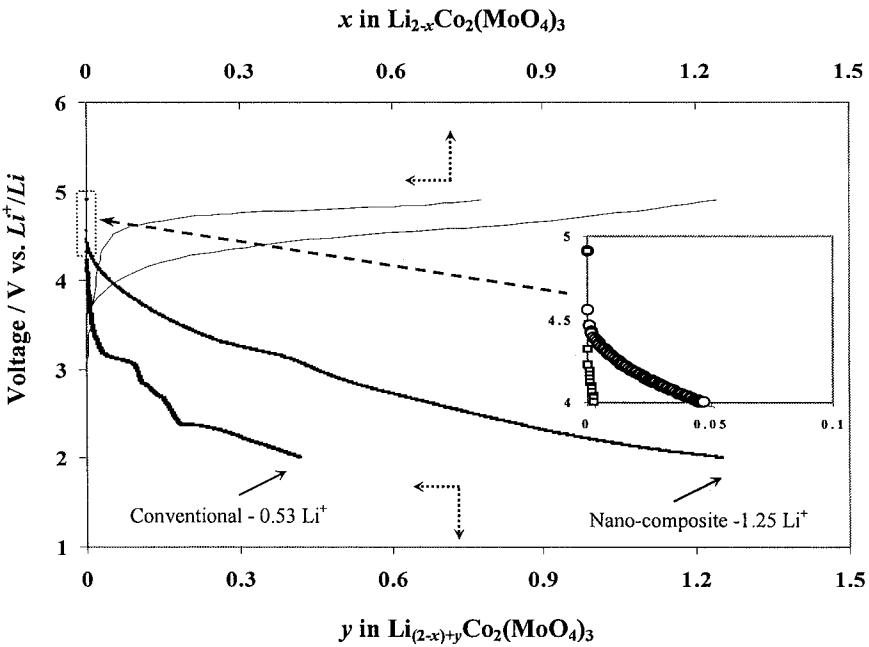

Fig. 1. Comparison of first charge/discharge curves of nano-composite $Li_2Co_2(MoO_4)_3$ and conventional $Li_2Co_2(MoO_4)_3$ vs. Li^+/Li between 4.9 and 2.0 V. Electrolyte: 1 M $LiPF_6$ (EC/DMC)

Interestingly, the nano-composite electrode exhibited a smooth discharge profile from the beginning down to 2.0 V unlike the conventional one, in which a distinct appearance of two-slope features is clearly visible. The role of nanoporous carbon on the electrochemical properties of the host cathode is well understood through these remarkable changes observed in the discharge profile.

The multiple charge/discharge curves of $Li_2Co_2(MoO_4)_3$ [conventional cathode]/Li cell are shown in Fig. 2 cycled under the same experimental conditions. It is visualized that after the first cycle, there was a change in the shape

of the charge and discharge profiles. The distinct potential profile disappeared after the first cycle, and the curves were identical in shape throughout the rest of the cycles studied. It seems that the material had undergone a structural phase transition after the first cycle, which needs further confirmation. Such a shape change in the discharge profile of the nano-composite electrode was not noticed as explained later with reference to Fig. 3.

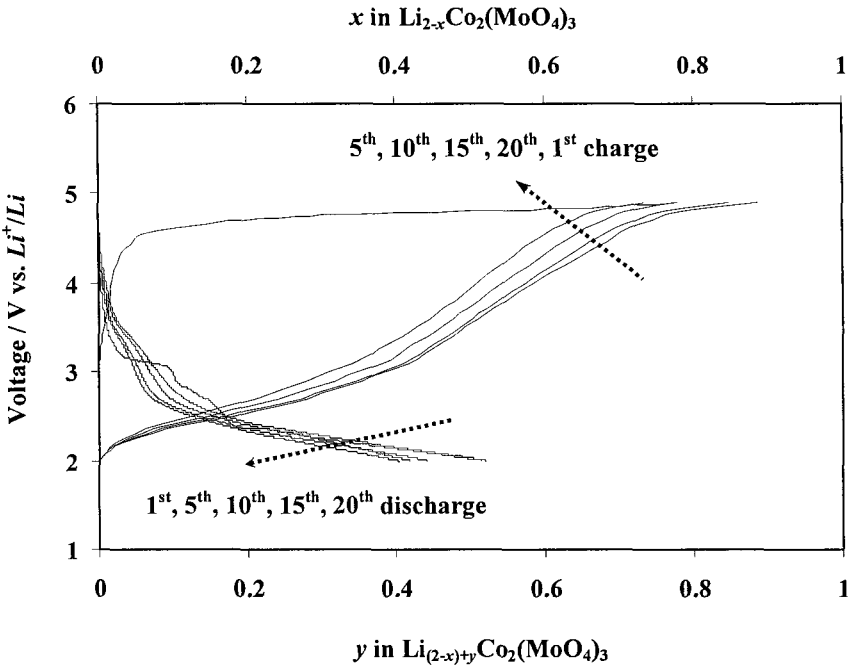

Fig. 2. Electrochemical characteristics of conventional $Li_2Co_2(MoO_4)_3$//Li cell under galvanostatic conditions: Experimental conditions are same as in Fig. 1

Figure 3 presents the multiple charge/discharge curves (first 20 cycles) corresponding to the nano-composite cathode material. It is readily seen that there was a difference between the curves in Figs. 3 and 2. As far as the nano-composite electrode is concerned, no difference in shape was found between the first discharge curve and the rest of the discharge curves, whereas the distinct shape of the curves was evident in the conventional one (fig.2). The amount of Li^+ inserted in the nano-composite cathode during discharge was larger than that in the conventional cathode. All such improved electrochemical properties of the nano-composite electrode originated from the highly conducting nano-sized carbon which ensured better connectivity between the grains. The active participation of nano-sized carbon black is noteworthy in effectively improvising the particle-particle contact leading to overall increase in the conductivity of the cathode material. It is likely that the high porosity of the material helped to retain more electrolytes between the electronic pathways and thus improved the conductivity.

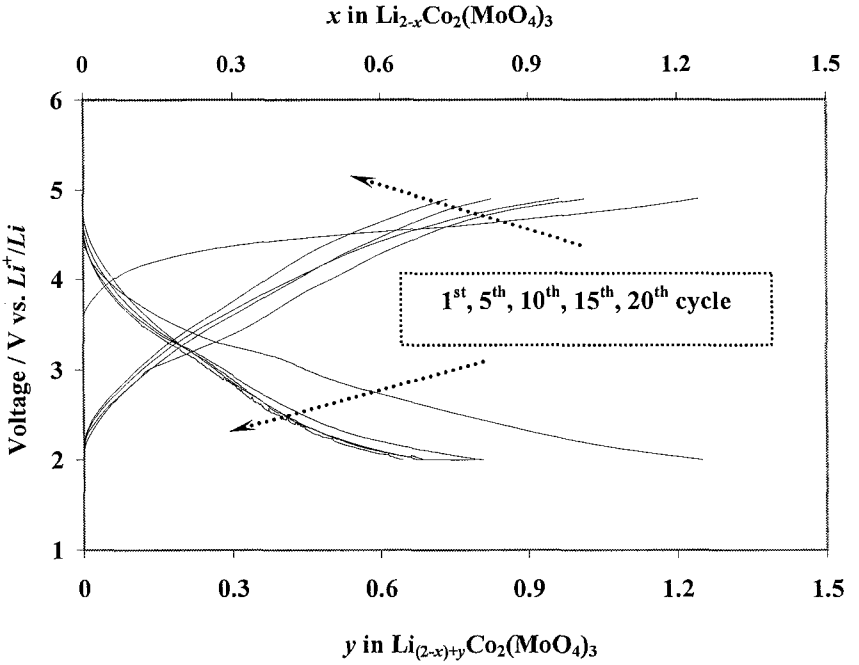

Fig. 3. Electrochemical characteristics of a nano-composite $Li_2Co_2(MoO_4)_3$//Li cell under galvanostatic conditions: Experimental conditions are same as in Fig. 1

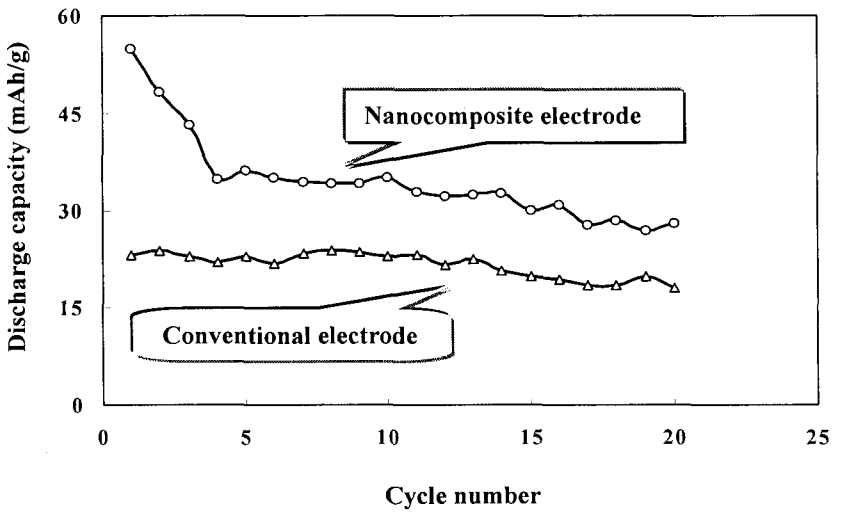

Fig. 4. Discharge capacity of nano-composite and conventional composite $Li_2Co_2(MoO_4)_3$ vs. cycle number

Figure 4 shows the variation of discharge capacity with cycle number corresponding to the conventional and nano-composite $Li_2Co_2(MoO_4)_3$ electrodes for the first 20 cycles. The discharge capacity delivered by the conventional composite $Li_2Co_2(MoO_4)_3$ cathode decreases from 23 mAh/g (1^{st} discharge) down to 17.8 mAh/g at the end of 20^{th} cycle. Whereas, for the NCB added $Li_2Co_2(MoO_4)_3$ cathode, although there is a fall in discharge capacity during the first 4 cycles, the material still delivered 28 mAh/g at the end of 20^{th} cycle. Table 1 provides the electrochemical properties to summarize the improvements made on the NCB added cathode over the conventional electrode. It is clearly seen that the presence of NCB is remarkable in improving the extended cycling characteristics of $Li_2Co_2(MoO_4)_3$. The structural integrity of the nano-composite electrode material upon repeated cycling might also contribute to the enhanced electrochemical behaviour.

Table 1. Improved electrochemical properties (Li^+ insertion and discharge capacity) of nano-composite $Li_2Co_2(MoO_4)_3$ compared to conventional composite $Li_2Co_2(MoO_4)_3$ electrode

Electrochemical properties of $Li_2Co_2(MoO_4)_3$ positive electrode				
Conventional composite electrode*			Nano-composite electrode**	
Cycle number	Amount of Li^+ inserted down to 2.0 V	Discharge capacity (mAh/g)	Amount of Li^+ inserted down to 2.0 V	Discharge capacity (mAh/g)
1	0.53	23	1.25	55
5	0.522	22.9	0.8	36
10	0.52	22.8	0.79	35
15	0.45	19.7	0.69	30
20	0.4	17.8	0.64	28

* AB added $Li_2Co_2(MoO_4)_3$ (conventional)
** AB and NCB added $Li_2Co_2(MoO_4)_3$ (nano-composite)

Conclusion

The effect of adding the nanoporous carbon black as a conductive additive in enhancing the conductivity of $Li_2Co_2(MoO_4)_3$ was demonstrated in this work. The role of nanoporous carbon as additional conductive additive was determined by comparing the electrochemical properties of both the conventional composite

cathode and nano-composite cathode. The test electrode fabricated with NCB as conductive additive has a significant effect on the discharge properties by establishing effective grain-grain contacts, leading to increasing the overall electronic conductivity of the composite electrode. As a beneficial consequence of NCB addition, the discharge was found to enhance a 2.5 times which indeed is a significant measure.

References

[1] A.K. Padhi, K.S. Nanjundasamy, C. Masquelier, S. Okada and J.B. Goodenough, J. Electrochem. Soc. 144 (1997) 1609.

[2] K.M. Begam, Y.H. Taufiq-Yap, M.S. Michael and S.R.S. Prabaharan, Solid State Ionics, 172 (2004) 47.

[3] S.R.S. Prabaharan, S. Ramesh, M.S. Michael and K.M. Begam, Mater. Chem. and Phy. 87 (2004) 318.

[4] K.M. Begam, S. Selladurai, M.S. Michael and S.R.S. Prabaharan, Ionics, 10 (2004) 77.

[5] M.Y. Saidi, J. Barker, H. Huang, J.L. Swoyer and G. Adamson, J. Power Sources, 119-121 (2003) 266.

[6] S.R.S. Prabaharan, M.S. Michael, S. Ramesh and K.M. Begam, J. Electroanal. Chem. 570 (2004) 107.

[7] M.E. Arroyo-de Dompablo, U. Amador and F. Garcia-Alvarado, J. Electrochem. Soc. 153 (2006) A673.

[8] G.X. Wang, S. Bewlay, J. Yao, J.H. Ahn, S.X. Dou and H.K. Liu, Electrochem. Solid-State Lett. 7 (2004) A503.

[9] C. Delacour, L. Laffont, C. Wurm, J.-M. Tarascon and C. Masquelier, J. Electrochem. Soc. 152 (2005) A913.

[10] P. Subramanya Herle, B. Ellis, N. Coombs and L.F. Nazar, Nature Materials, 3 (2004) 147.

[11] K.M. Begam, M.S. Michael, Y.H. Taufiq-Yap and S.R.S. Prabaharan, Electrochem. Solid-State Lett. 7 (2004) A242.

[12] S.R.S. Prabaharan, A. Fauzi, M.S. Michael and K.M. Begam, Solid State Ionics, 171 (2004) 157.

[13] S.R.S. Prabaharan, M.S. Michael and K.M. Begam, Electrochem. Solid-State Lett. 7 (2004) A416.

[14] K. Zaghib, J. Shim, A. Guerfi, P. Charest and K.A. Striebel, Electrochem. Solid-State Lett. 8 (2005) A207.

[15] J. Yang and J.J. Xu, Electrochem. Solid-State Lett. 7 (2004) A515.

[16] C. R. Sides, F. Croce, V.Y. Young, C.R. Martin and B. Scrosati, Electrochem. Solid-State Lett. 8 (2005) A487.

[17] K.M. Begam and S.R.S. Prabaharan, J. Power Sources (in press).

[18] X.Z. Liao, Z.F. Ma, L. Wang, X.M. Zhang, Y. Jiang and Y.S. He, Electrochem. Solid-State Lett. 7 (2004) A515.

[19] A. Eftekhari, J. Electrochem. Soc. 151 (2004) A1816.

PROTONIC CONDUCTION IN TiP_2O_7

V. NALINI *AND T. NORBY

Department of Chemistry, University of Oslo,
Centre for Materials Science and Nanotechnology,
Gaustadalleen 21, NO-0349 Oslo, Norway
E-mail: nalini.vajeeston@kjemi.uio.no

A. M. ANURADHA

Department of Physics, University of Oslo,
Gaustadalleen 21, NO-0349 Oslo, Norway

TiP_2O_7 was synthesized by reacting TiO_2 and 85 % H_3PO_4 and characterized by XRD, TEM and SEM. The electrical conductivity of the sample was examined at 500-1000 °C under various $p(O_2)$, $p(H_2O)$, and $p(D_2O)$ conditions. The conductivity of the material in wet atmospheres was higher than that under D_2O-containing and dry atmospheres, indicating that protonic conduction was dominant in this material in wet atmospheres. The conductivity was mainly independent of $p(O_2)$ at 500-900 °C under oxidizing conditions, confirming predominant ionic (protonic) conduction.

1. Introduction

Although high proton conductivity has been reported for a large number of solid compounds and materials[1] and many of them have been suggested for applications as electrolytes in electrochemical cells, their use in technological devices is still quite limited. Apart from the fact that proton conductivity in the solid state remains significantly below the upper limit for proton conductivity in liquids, major problems arise from the numerous additional material requirements[2]. In the past few decades several perovskite-type oxides have been reported to show protonic-conduction at high temperatures[3-5]. Nevertheless, due to modest proton conductivity, their applications have been limited, except for hydrogen sensors. Rare earth orthophosphates have been demonstrated as high-temperature proton conductors with high chemical stability, but again the conductivities are modest.[6]

Research goes on world-wide to identify new suitable proton conducting materials. Up to date only a limited number of compounds have been identified, and numerous classes of materials are unexplored. We are investigating proton conduction in a variety of materials. Recently, proton conductivity was reported at intermediate temperature ranges in tetravalent metal pyrophosphate mixed electrolytes[7-8]. Moreover Kwon *et al.* discovered proton conductivity in SnP_2O_7 at low temperature[9]. These reports have motivated us to investigate the proton conductivity in TiP_2O_7.

In this article we describe the synthesis and characterization of TiP_2O_7. In order to understand the nature of the conduction we have studied the electrical conductivity in H_2O- and D_2O-containing as well as dry atmospheres.

2. Experimental

2.1. Synthesis

TiP_2O_7 was prepared as described in the literature[10]. TiO_2 and H_3PO_4 (85%) were mixed in stoichiometric amounts at room temperature until a homogeneous slurry was formed. This was heated at 200 °C for 3 h. The obtained powder was ground and dried at 100 °C for 24 h, followed by calcination at 700 °C for 3 h. The formation of single phase crystalline TiP_2O_7 was verified by XRD (Siemens D5000 diffractometer, CuKα radiation). The calcined powder was uniaxially pressed into pellets (10 mm diameter and 2 mm thickness).

Bamberger *et al.*[11] reported that titanium pyrophosphate decomposed at about 1150 °C into titanyl phosphate, and the latter further into TiO_2 (rutile):

$$2TiP_2O_7 \rightarrow (TiO)_2P_2O_7 + P_2O_5$$
$$(TiO)_2P_2O_7 \rightarrow 2TiO_2 + P_2O_5$$

To avoid this thermal decomposition, we sintered our sample at 1050 °C for 3h. The relative density of the sample was obtained from the unit cell dimensions and the mass and dimensions of the sintered pellet.

2.2. Characterization

The sintered sample was crushed for investigation by powder XRD, and unit cell parameters were obtained from least-squares fitting of all peak positions. The structure was furthermore studied by selected area diffraction (SAD) in a TEM (transmission electron microscope; JOEL 2000FX). The crystal morphology at high temperature was also studied using a high temperature stage in the TEM. The microstructure of the sample was analyzed by SEM (scanning electron microscope; FEI Quanta 200F).

Electrical characterization was performed in a ProboStat™ (NorECs AS[12]) measurement cell with two-point electrode setup, using a Hewlett Packard 4192A impedance analyzer at a frequency of 10 kHz and an oscillation voltage of 1.1 V(rms). The electrodes were painted, porous Pt electrodes with diameters around 1 cm. The electrical conductivity was measured at 500-1000 °C under various oxygen and water vapor partial pressures. Oxygen partial pressure, $p(O_2)$, was varied from 1 to 10^{-5} atm by using pure O_2 or Ar/O_2 gas mixtures. Water vapor partial pressure, $p(H_2O)$, was varied from 0.027 to 0.00003 atm by mixing dry gas with gas bubbled through a saturated solution of KBr(aq) at room temperature. The conductivity of the material in a similarly obtained D_2O-containing atmosphere was also measured. The conductivities reported here are not corrected for sample porosity.

3. Result and discussion

3.1. Structural characterization

The material may be suspected to thermally decompose at 1100 °C, and continued heating at 1100 °C for 24 h did in fact change the colour of the samples to yellow

and led to the presence of small amounts of rutile TiO_2 as seen by XRD. The samples for conductivity studies were thus sintered at only 1050 °C, for 3h. The XRD pattern obtained for TiP_2O_7 after sintering is given in figure 1 and matches well those of Norberg *et al.*[13]. This confirms that pure single phase material was obtained after sintering at 1050 °C. The compound exhibited a cubic superstructure (space group: Pa $\bar{3}$; space group no. 205). The lattice parameter was calculated by the least-squares method to be a = 23.5336 Å, in good agreement with the literature value a = 23.5340[13]. Malshikov and Bondar[14] found two polymorphic forms; a high temperature form (above 458 °C) with cubic symmetry (space group: Pa3), and a low temperature form with hexagonal symmetry. On the other hand, Chernorukov *et al.*[15] reported that below 730 °C TiP_2O_7 exist in a cubic α modification (a = 23.52 Å) while above 730 °C it transforms into another cubic (β) modification (a = 7.80 Å). (We observed the phase transition at about 695 °C by conductivity measurements as will be shown below).

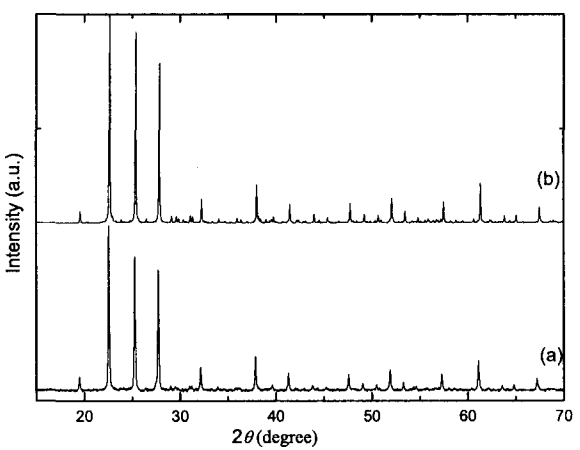

Figure 1. (a) Observed XRD pattern of TiP_2O_7 after sintering at 1050 °C for 3 h. (b) XRD pattern of TiP_2O_7 from Ref. 13.

Selected area diffraction (SAD) patterns seen along the [010] and [$\bar{1}$40] zone axes are shown in figure 2. They are indexed according to the crystal structure with space group Pa$\bar{3}$ (no. 205). Although the crystal structure is primitive cubic, all the reflections are not present in the SAD pattern. The reflection conditions for this space group are given by: General: 0kl: k = 2n and h00: h = 2n, Special: h+k, h+l, k+l =2n for atom positions 4a and 4b. Closely spaced reflections and the presence of the First Order Laue Zone (FOLZ) seen in the middle image in figure 2 confirm the large unit cell dimension of the cubic superstructure. A bright field image is also shown in figure 2. It does not show any difference in contrast due to the presence of domains or precipitations. (The fringe like appearance is due to the

variation in crystal thickness. The thickness decreases from the dark region at the bottom right hand side corner towards brighter top left hand side corner). A study of the phase transition and possible changes in crystal morphology was attempted by *in situ* heating of the specimen inside the TEM. However, the specimen disintegrated into nanosized particles, probably as a result of the vacuum conditions and possibly accelerated by the electron beam.

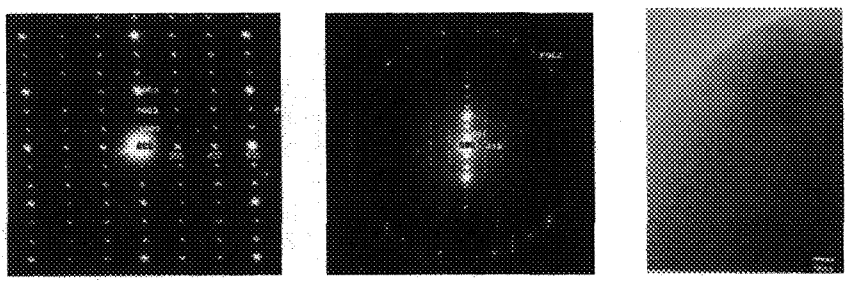

Figure 2. Left and middle: Selected area diffraction (SAD) patterns of TiP_2O_7 after sintering seen along the [010] (left) and [$\bar{1}$ 40] zone axes. Right: Bright field image of the area analysed in the leftmost SAD pattern.

Figure 3 shows the SEM image of the material after sintering. No secondary phase was observed. The relative density was approximately 75%. It should be noted that in order to reduce the thermal decomposition of LaP_3O_9[16] the spark plasma sintering technique was successfully used to reach densities of 92 %, and this may be one way to prepare denser samples also of our phosphate materials in the future.

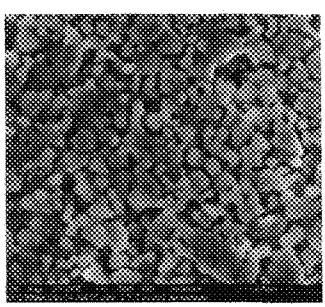

Figure 3. SEM image of TiP_2O_7 after sintering.

3.2. Electrical characterization

Figure 4 shows the temperature dependence of the conductivity for the material under wet, D_2O-containing, and dry atmospheres. Each curve is obtained after

equilibration at 1000 °C, and was recorded during ramps of decreasing temperature of 20 °C/h. The conductivity of the material under wet atmosphere was considerably higher than those under dry atmosphere and D_2O-containing atmosphere. The above results confirm that the material dominantly conducts protons in wet atmosphere.

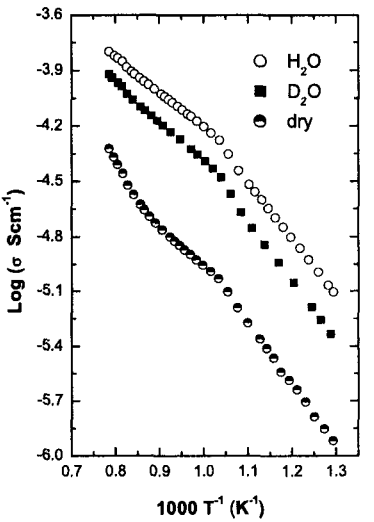

Figure 4. Temperature dependence of the conductivity for TiP_2O_7 in a) wet O_2 ($p(H_2O)$ = 0.027 atm), b) D_2O-containing O_2 ($p(D_2O)$ = 0.027 atm), and c) dry O_2 ($p(O_2)$ = 1 atm in all cases).

The conductivity of TiP_2O_7 under wet oxidizing conditions was $8x10^{-6}$ - $2x10^{-4}$ Scm^{-1} at the measured temperature range, which is higher than that of undoped rare earth phosphates[16-18]. The Arrhenius plots show sharp bends at about 695°C. The activation energy for protonic conduction in the TiP_2O_7 was evaluated as 0.70 eV at 500-674 °C and 0.47 eV at 692-1000 °C. The activation energy for deuteron conduction in the TiP_2O_7 was somewhat higher; 0.74 eV at 500-674 °C. This result suggests semi-classical behavior in the proton hopping process in the material, as observed in proton conducting oxides and phosphates[18-19]. The H/D isotope effect had ratios of 1.3 - 1.7 at 500-1000 °C. All in all these results imply that mainly protons contribute to the conduction, by the Grotthuss hopping mechanism.

The conductivity vs 1/T is shown at two different $p(O_2)$ at constant $p(H_2O)$ in figure 5. The conductivities were near to independent of $p(O_2)$ at 500-900 °C, indicating that the contribution of electronic conduction to the total conductivity in the material was negligible (and protonic conduction predominant) at these temperature ranges. On the other hand, at 1000 °C the conductivities in wet argon were higher than in wet oxygen, suggesting that the material begins to conduct electrons.

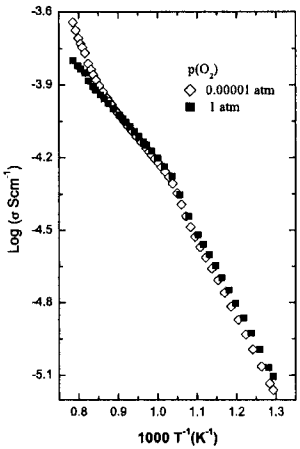

Figure 5. Total conductivity of TiP_2O_7 as a function of 1/T in wet argon and in wet O_2 at $p(H_2O)$ = 0.027atm.

The $p(H_2O)$ dependencies at constant $p(O_2)$ at selected temperatures are shown in figure 6. The conductivity of the material increased by increasing $p(H_2O)$, which suggests protonic conduction. The conductivities were approximately proportional to $p(H_2O)^{1/4}$ at 500-900 °C. The defect structure (including protonic defects) that leads to these dependencies is a matter of interest in our ongoing work.

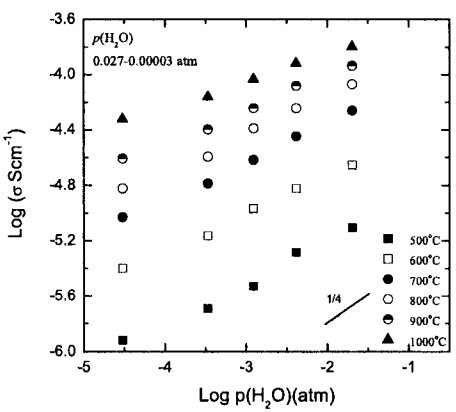

Figure 6. Total conductivity of TiP_2O_7 as a function of $p(H_2O)$ at $p(O_2)$ = 1atm.

4. Conclusion

The electrical conduction in TiP_2O_7 was investigated. The material exists in two different phases at low and high temperature. The conductivity of the material is shown, by the dependence on humidity and the effect of H/D isotopic exchange, to be mainly protonic. The $p(O_2)$ dependencies of the conductivities indicated that below 900 °C the material is mainly a proton conductor, while n-type conductivity contributes significantly to the total conductivity at 1000 °C. The finding of proton conductivity in this material, although at moderate levels, encourages further studies of proton conductivity in tetravalent pyrophosphates at elevated temperatures.

Acknowledgements

This work has been granted by the University of Oslo, FUNMAT@Uio program. The assistance of dr. Reidar Haugsrud is acknowledged.

References

1. K. D. Kreuer, *Chem. Mat.* **8**, 610 (1996).
2. K. D. Kreuer, *Solid State Ionics* **97**, 1 (1997).
3. H. Iwahara, T. Esaka, H. Uchida and N. Maeda, *Solid State Ionics* **3/4**, 359 (1981).
4. T. Norby and P. Kofstad, *J. Am. Ceram. Soc.* **67**, 786 (1984).
5. K. D. Kreuer, *Solid State Ionics* **125**, 285 (1999).
6. T. Norby and N.Christiansen, *Solid State Ionics* **77**, 240 (1995).
7. T. Matsui, S. Takeshita, Y. Iriyama, T. Abe and Z.Ogumi, *J. Electrochem. Soc.* **152(1)**, A167 (2005).
8. T. Matsui, T. Kukino, R. Kikuchi and K. Eguchi, *Electrochem. Solid-State Lett.* **8(5)**, A256 (2005).
9. K. Kwon, M. Yano, H. Sun and J. Park, (S. Korea). *U.S. Pat. Appl.* Publ. US 2005221143 A1 20051006 (2005).
10. J. Sanz, J. E. Iglesias, J. Soria, E. R. Losilla, M. A. G. Aranda and S. Braque, *Chem. Matter.* **9**, 996 (1997).
11. C. E. Bamberger and G. M. Begun, *J. Less-Comman Metals* **134**, 201 (1987).
12. NorECs AS, http://www.norecs.com.
13. S. T. Norberg, G. Svensson, and J. Albertsson, *Acta Cryst.* **C57**, 225 (2001).
14. A. E. Mal'shikov and I. A. Bondar, *Neorg. Mater.* **25(6)**, 984 (1989).
15. N. G. Chernorukov, M. I. Zhuk and E. P. Moskvichev, *Tr. Khim. Tekh.* **3**, 9 (1974).
16. K. Amezawa, Y. Kitajima, Y. Tomii and N. Yamamoto, *Electrochem. Solid-State Lett.* **7**, A511 (2004).
17. K. Amezawa, H. Maekawa, Y. Tomii and N. Yamamoto, *Solid State Ionics* **145**, 233 (2001).

18. N. Kitamura, K. Amezawa, Y. Tomii, T. Hanada, N. Yamamoto, T. Omata and S. Otsuka-Yao-Matsuo, *J. Electrochem. Soc.* **152(4)**, A658 (2005).
19. J. F. Liu and A. S. Nowick, *Solid State Ionics* **50**, 131 (1992).

PREPARATION AND ELECTROCHEMICAL CHARACTERISTICS OF $LiMn_2O_4$ THIN FILM BY A SOLUTION DEPOSOTION METHOD

X.Y. GAN, C. HU, X. J. ZHU, W. ZHANG, M. H. CAO, D. B. LUO, J. ZHOU, W. CHEN, Q. XU AND H. X. LIU*

State Key Laboratory of Advanced Technology for Materials Synthesis and Processing, Wuhan University of Technology, Wuhan430070, Hubei, PR China

* *Email: lhxhp@mail.whut.edu.cn*

Thin film electrode of spinel $LiMn_2O_4$ for rechargeable lithium micro-batteries was prepared by a solution deposition route. The Li-Mn-O solution was deposited on electronically conductive Au substrate by a spin coater. By controlling the fabrication condition, the excellent rechargeability was observed in a test cell which contained the $LiMn_2O_4$ film. XRD and SEM were used to characterize the structures, phase composition, morphology of the thin films. The thermal decomposition behavior of the precursor powder was examined by TG/DSC to determine the temperature of heat-treatment. The electrochemical properties of the thin films were also investigated using cyclic voltammeter (CV) and charge/discharge cycling. The thin films obtained from the optimal processing condition (Li/Mn=1.05:2, dried at 280°C, annealed at 800°C for 30min) were homogeneous, crack-free, and showed good cycling behavior. The capacity loss is about 1.54% after 100 cycles at current density of $50\mu A/cm^2$.

1. Introduction

Rechargeable lithium micro-batteries and their various applications have attracted much attention recently. All-solid-state lithium rechargeable micro-batteries can overcome many problems of secondary batteries while keeping most of the favorable features[1]. Thin film electrodes have simple geometric form without addictives such as polymer binder and conductive materials and therefore make analysis of their electrochemical performances more convenient. During these years, new materials and fabrication techniques of cathode thin films for lithium micro-batteries have been explored[2, 3]. Among these materials, $LiMn_2O_4$ thin film is particularly interesting because of its relatively higher energy density, environmentally benign and

inexpensive[4]. Fabrication of $LiMn_2O_4$ thin films have been reported using various techniques, such as RF magnetron sputtering[5], pulsed laser deposition[6,7], electrostatic spray deposition[8,9], electron beam evaporation[10]. However, these techniques unfortunately require high energy consumption as well as sophisticated instruments. Evidently, the solution deposition method supplies a promising alternative to solve these problems, since it has many advantages due to its excellent control of the stoichimetry of the thin films, lower cost and easy doping[11]. $LiMn_2O_4$ thin films prepared by this method have exhibited good properties[12-16].

In the present work, we have synthesized $LiMn_2O_4$ thin films by an effective chemical solution deposition technique, using a spin coater. By controlling the deposition parameters and heat treatment schedules, we obtained homogeneous, crack-free $LiMn_2O_4$ thin films. The effects of annealing temperature on the structure, morphology and electrochemical properties were studied in detail.

2. Experimental Detail

As for the solution deposition method, the preparation of the precursor solution with good wetting properties and proper viscosity is of great importance. In order to prepare the precursor solution for thin film deposition, lithium acetylacetonate and manganese acetylacetonate (in the molar ratio of 1.05:2) were co-dissolved in 1-butonol and acetic acid through continuous stirring. Precursors of various Li/Mn ratios (1:2; 1.05:2; 1.1:2) employed and it was found that addition of excess lithium was necessary to obtain pure $LiMn_2O_4$ thin films considering the over-evaporation during the annealing schedule. The molar concentration of the precursor solution was maintained $0.4ML^{-1}$. The resulting solution was deposited on electron conductive and polished Au substrate, using a spin-coater (CHEMAT Spin-Coater KW-4A), with a rotation speed of 3000rpm for 30s. The films were then pre-heated on a hot plate (MODELKW-4AH) at 280°C for 10 min to remove the associated organics. The thermal decomposition behavior of the precursor powder which was made from heating the precursor solution at 120°C for 2h was estimated by TG/DSC (NETZSCH STA 499C)at a heating rate of 5°C /min. The pre-heating temperature was decided on the basis of the TG/DSC analysis. The above coating and heating procedures were repeated to get a 0.5μm thick film. Finally, the as-deposited films were converted to a horizontal tube furnace and annealed at different temperature from 700°C ~850°C for 30min in a flow of O_2.

The crystal structure of the fabricated films were measured by a Philips vertical

X-ray diffractometer(PN 3050/60, MPSS) using $K\alpha$ (λ=1.54056 Å) radiation operated at 40KV, 40mA, and analyzed with X'Pert High Score Plus diffraction software. A scanning electron microscope (SEM, Akashi, Seisakusho, JSM-5610V) was used for examining the surface morphology. The electrochemical properties of the prepared $LiMn_2O_4$ thin films were investigated in test cells assembled in a argon filled glove box (MBRAUN), using lithium metal foil as anode and 1M $LiPF_6$/EC/DMC/EMC(1:1:1) solution as electrolyte. The cyclic voltammogram of the films was recorded in the voltage range of 3.5~4.5V. Charge –discharge cycling tests were carried out at a current density of 50μA/cm^2 with a cycle tester (LAND CT2001A).

3. Results and discussion

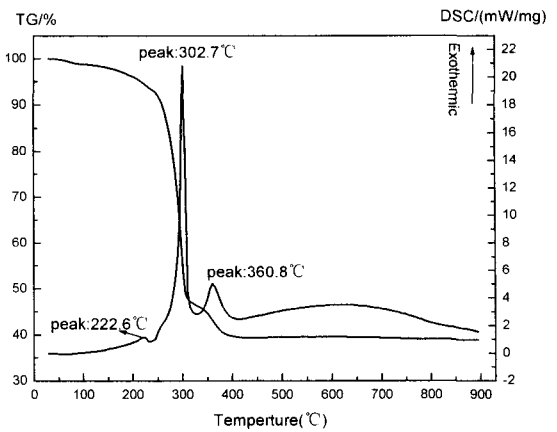

Fig.1. TG/DSC traces of the $LiMn_2O_4$ precursor powder obtained by heating the precursor solution at 120°C for 2h.

The TG-DSC curves of the precursor powder are displayed in Fig.1. It can be seen from the TG trace that there is a 1.24% weight loss below 120°C which is most likely to be the evaporation of the absorbed water. Over the temperature range from 150°C to 400°C, two weigh-loss steps can be detected, which stands for 52.45% and 7.12%, respectively. Two exothermic peaks (at 302.7°C and 360.8°C) were observed in accordance with the two weight-loss steps. According to J.Y. Park' s work [12], the two exothermic peaks are caused by the decomposition and combustion of the organic constituents in the powder. The weight loss terminated at 400°C. Here, we could conclude that the decomposition of the precursor powder occurs at 150~400°C. In this

paper, 280°C was chosen as the pre-heating temperature since too much residual organic materials would be left in the as-deposited films for too low pre-heating temperature. By the same token, a relative high pre-heating temperature does not suit to form a dense, homogeneous, and creek-free film.

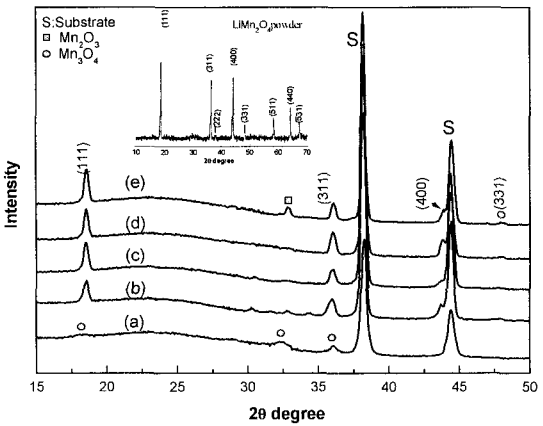

Fig.2. The XRD patterns of (a) as-deposited film; and $LiMn_2O_4$ films annealed at (b) 700°C; (c) 750°C; (d) 800°C; (e) 850°C for 30min.

Fig.2 shows the XRD patterns of the as-deposited $LiMn_2O_4$ films and the $LiMn_2O_4$ thin films annealed at different temperatures. In our experiments, parallel beam optics is employed for thin film analysis. Incident angles are very low (glancing), so radiation does not penetrate far into the substrate. As a result, the interference from the substrate is minimized and the layer peaks exhibit higher intensity. The as-deposited film shows no spinel $LiMn_2O_4$ structure but broadened tetragonal(ICDD code:00-001-1127) Mn_3O_4 peaks. The films crystallized when annealed at 700~850°C. The (111), (311), (400) and (331) peaks of spinel structure (space group Fd3m) were observed. The reflection peak of (111) became stronger and narrower with the increase of annealing temperature, which indicates the improvement of the crystallinity of the films. However, when the temperature was increased to 850°C, the impurity was detected obviously. The peak (2θ=32.9095°) can be attributed to lithium deficient phase Mn_2O_3 which may come from the over-evaporation of lithium at higher temperature. The X-ray diagram of the $LiMn_2O_4$ powder obtained by calcinning the precursor powder at 800°C for 2h is presented as a reference (inserted in Fig.2).

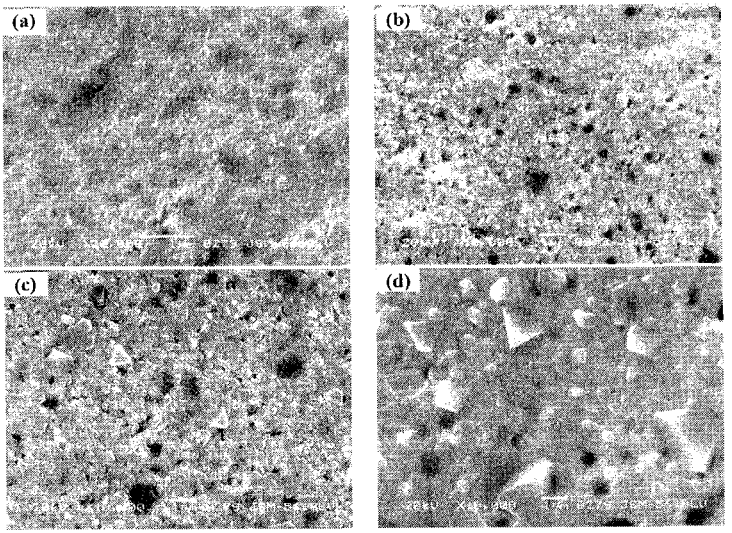

Fig.3. SEM images of the surface of the $LiMn_2O_4$ thin films annealed at (a) 700 °C; (b) 750°C; (c) 800 °C; (d) 850 °C for 30min.

The SEM images of the $LiMn_2O_4$ thin films annealed at different temperatures are given in Fig.3. On increasing the annealing temperature from 700°C to 850°C, the grain size increases. The grain size at 700°C is less than 0.1μm and about 0.1~0.3μm at 750°C. The growth of $LiMn_2O_4$ particles at 700°C and 750 °C seems to be insufficient. When annealing temperature was 800°C, the annealed film was consisted by particles of similar size of about 0.3μm. Few micro-pores probably due to gas evolution during the decomposition and crystallization of the precursor are observed in Fig.2 (b) and Fig.2(c). The porous structure has an advantage when using a liquid electrolyte since it has large area with electrolyte. On the other hand, the structure may cause short-circuits in all-solid state thin-film batteries using solid electrolyte. For the film annealed at 850°C, the particles grow abnormally, and some were larger than 1.5μm.

To investigate the electrochemical properties of the $LiMn_2O_4$ thin films, cycling tests were performed in Li/1M $LiPF_6$+EC+DMC+EMC/$LiMn_2O_4$ cells at a current density of 50μA/cm^2 between 3.0~4.3V at room temperature. Fig.4 compares the voltage profiles of the first cycle for these films. Two typical plateaux around 4.0V and 4.1V were observed under all conditions. Table 1 also listed the discharge capacities of the 1st and 50th cycle, as well as the capacity loss per cycle. In general, as the temperature increases from 700°C to 800°C, the initial discharge capacity increases and the capacity

degradation is improved due to the slight improvement of crystallinity, which has already been indicated in the XRD pattern analysis. The improvement of discharge capacity due to improvement of crystallinity, is generally accepted by many researchers [12,16]. Nevertheless, the discharge capacity decreases significantly when the annealing temperature is increased to 850°C. This may be due to presence of lithium deficient phase Mn_2O_3 and the abnormal-grown particles shown in the XRD pattern and SEM microgram. It is reported that when the particle size is too large, lithium ions do not intercalate into the particles completely, so the discharge capacity will be reduced [17].Therefore, it is found that the film annealed at 800°C possessed best cycle performance and relatively higher discharge capacity. This could be explained by its well crystallized spinel structure, uniform grain and few micro-pores which may help to relax the strain generated from the expansion/contraction during cycling[12, 13].

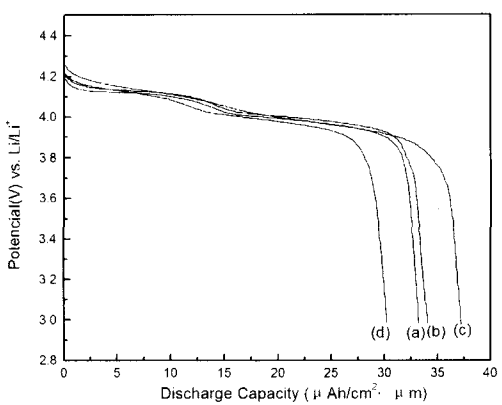

Fig.4. Comparison of the initial discharge curves for the cells Li/1M $LiPF_6$+EC/DMC/EMC/ $LiMn_2O_4$ thin films annealed at various temperatures.

Fig.5 presents the typical cyclic voltammetry curve measured on the $LiMn_2O_4$ thin films annealed at 800 °C between 3.5 and 4.5V at a scan rate of 0.5 mVs^{-1}. Two couples of well-defined current peaks at around 4.0 and 4.1V were observed in the voltammogram and were related to the cubic and tetragonal phases of manganese oxide and to the reversible deintercalation/intercalation of Li^+ ion. It should be noted that the cyclic voltammogram of Fig.5 and the charge-discharge curves in Fig.4 coincide quite well in shape and value.

Table 1 The electrochemical properties of cell Li/1M $LiPF_6$+EC/DMC/EMC/ $LiMn_2O_4$ thin films annealed at 700°C, 750°C, 800°C and 850°C.

	700°C	750°C	800°C	850°C
Initial discharge capacity($\mu Ah/cm^2 \cdot \mu m$)	33.3	34.1	37.3	30.2
Discharge capacity of 50th cycle($\mu Ah/cm^2 \cdot \mu m$)	31.0	32.7	36.1	29.2
The capacity loss per cycle(%)	6.91	4.11	3.21	3.31

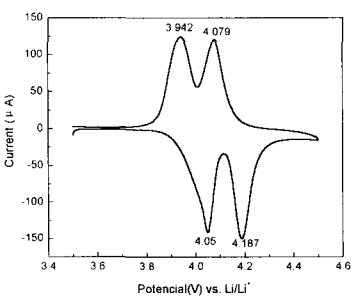

Fig.5. Cyclic voltammogram of the$LiMn_2O_4$ thin film annealed at 800°C for 30min operated in the voltage range 3.5~4.5 V (scan rate: 0.5mV/s).

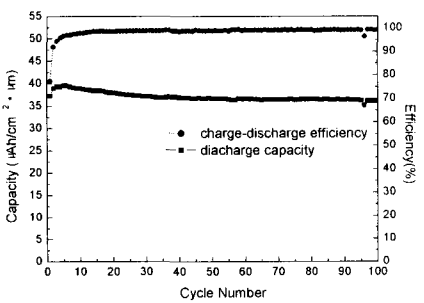

Fig.6.Coulombic efficiency and discharge capacity of the $LiMn_2O_4$ thin films annealed at 800°C during cycling.

Fig.6 shows the cycling performance of the $LiMn_2O_4$ thin films annealed at 800 °C. The discharge capacity and the columbic efficiency were plotted as a function of cycle number. Good columbic efficiencies of near 100% were realized during 100 cycles. Only a small degradation is observed after 100 cycles at room temperature. The capacity loss per cycle after being cycled 100 times is about 1.54%. This result shows that the $LiMn_2O_4$ thin films prepared by the solution deposition route have a stable Mn_2O_4 framework to remain intact over repeated lithium extraction and insertion.

4. Conclusions

$LiMn_2O_4$ spinel structured thin films could be fabricated by solution deposition method, using a spin-coater. By controlling the annealing temperature, $LiMn_2O_4$ spinel

films with stable structure and fine grains could be obtained at 800°C and this resulted in an enhanced capacity and cyclic performance. No appreciable degradation could be observed after 100 cycles at a current density of $50\mu A/cm^2$ at room temperature. It is considered that the solution deposition method can be adopted for the preparation of rechargeable thin-film lithium microbatteries with promising electrochemical properties.

Acknowledgments

This work was supported by the National Natural Science Foundation of China (No. 20371038), and the Foundation for Innovative Research Team of Hubei Province(No. 2005ABC004)

References

1. P. Birke, W.F. Chu and W. Weppner, *Solid State Ionics*, **1-15**, 93(1997).
2. B. Wang, J.B. Bates, F.X. Hart, B.C. Sales, R.A. Zuhr and J.D. Robertson, *J. Electrochem. Soc*, **143**, 3203(1996)
3. S.D. Jones and J.R. Akridge, *Solid State Ionics*, **69**, 357(1994).
4. J.M. Jarascon and D.Guyomard, *Electrochim. Acta*, **38**, 1221(1993).
5. J.B. Bates, N.J. Dudney and D.C.Lubben, *J Power Sources*, **54**, 58-62(1995).
6. M. Rubin, S.J. Wen and T.Richardson , *J Power Sources*, **54**,59-66(1998).
7. J.M. McGraw, C.S. Bahn, P.A. Parillia, J.D. Perkins and D.W. Readey, *Electrochim. Acta*, **45**, 187(1997).
8. I. Uchida, M. Mohamedi and K.Dokko, *J Power Sources*, **97-98**, 518-524(2001).
9. D. Shu, G. Kumar and K.B. Kim, *Solid State Ionics*, **160**,227–233(2003).
10. F.K. Shokoohi, J.M. Tarascon and B.J. Wilkens, *J. Appl Phys Lett*, **59**, 260-262(1991).
11. Y.H. Rho, K. Kanamura, M. Fujisaki, J. Hamagami and S. Suda, T. Umegader, *Solid State Ionics*, **151**,151(2002).
12. Y.J. Park, J.G. Kim, and M.K. Kim, *J. Power Sources*, **76**, 41-47 (1998).
13. Y.J. Park, J.G. Kim, and M.K. Kim, *Solid State Ionics*, **130**, 203-214(2000).
14. S.R. Das, S.B. Majumder and R.S. Katiya, *J. Power Sources*, **139**, 261-268(2005).
15. X.M. Wu, X.H. Li and Z. Wang, *Materials Chemistry and Physics*, **83**, 78-81(2004).
16. K.H. Hwang, S.H. Lee and S.K. Joo, *J. Electrochem Soc*, **141**,3296 (1994).
17. A.D. Roberson and S.H. Lu,*J. Electrochem Soc*, **144**, 3500 (1994).

SYNTHESIS AND CHARACTERISATION OF $LiMPO_4$ (M = Ni, Co)

T.SAVITHA, S.SELVASEKARAPANDIAN, C.S.RAMYA

Solid State and Radiation Physics Laboratory, Bharathiar University,Coimbatore-46, INDIA

E-mail: sekarapandian@yahoo.com

Abstract

$LiNiPO_4$ and $LiCoPO_4$ cathode materials based on Phospho-Olivine structure have been prepared by Pechini – type Polymerizable Technique. Structural and thermal analyses have been done using XRD and TGA/DTA respectively. Formation of nano sized particles has been confirmed from the XRD analysis for both the samples. Conductivity analysis shows the conductivity in the order of ~ 10^{-5} Scm^{-1} for both $LiNiPO_4$ and $LiCoPO_4$ at 303K. Transport parameter such as hopping frequency has been calculated from the conductance spectra.

Keywords: Phospho – Olivine, XRD, TGA/DTA, Pechini – type Polymerizable Technique.

1. Introduction

During the last decade, lithium batteries have been widely used as power sources for portable electronic devices such as cellular phones and laptops because of some valuable advantages of lithium batteries over other types of rechargeable batteries [1]. One of these advantages is the high-voltage performance in voltage range of 3-4 V. More recently, some cathode materials with high redox potential have been proposed, which can be used for the fabrication of 5 V lithium batteries. Two main examples of this class of cathode materials are $LiM_xMn_{2-x}O_2$ (M = Cr, Fe, Co, Ni and Cu) [2] and $LiMPO_4$ (M = Mn, Ni, Fe and Co) [3,4]. The ordered olivine represented by a similar general formula $LiMPO_4$ exhibits hexagonal closed-packed (hcp) oxygen array and tetrahedral sites are occupied by P^{5+} and form PO_4 tetrahedral oxo-anions. Olivine has orthorhombic symmetry with alternate a-c planes of Li and M occupying the octahedral sites, which makes it possible for there to be the two dimensional Li diffusion paths between the hcp oxygen layers [5]. Cathode properties of these olivine type materials has been reported by Shigeto Okada et.al.,[5] and they reported that $LiCoPO_4$ exhibits the highest 4.8 V discharge plateau of 100mAh/g versus Li/Li^+ after initial charging to 5.1 V. They display high redox potentials, fast Li^+ion transport, excellent thermal stability, and energy density comparable to that of conventional lithium metal oxides. In the present investigation one of the sol-gel method, Pechini – type Polymerizable Technique has been used to prepare $LiMPO_4$ (M=Ni , Co) which has several advantages such as, easier to

control stoichiometry, Nano-size particles and good homogeneity. In this paper structural, thermal and electrical properties of the samples has been discussed using XRD, TGA/DTA and ac impedance spectroscopy.

2. Experimental details

Generally, alkoxide precursors are used in solgel method but they are extremely sensitive to moisture and has to be processed under a strictly dry atmosphere. To avoid the use of alkoxide compounds as starting reagents, we have used a Pechini-type Polymerized-Complex (PC) route. This kind of chemical synthesis, based on high viscosity polyesters obtained from citric acid—metal chelates and polyhydroxyl alcohols, was first developed by Pechini. The raw materials $LiNO_3$, $CoNO_3.6H_2O$, $NiNO_3$. $6H_2O$ and $NH_4H_2PO_4$ are dissolved in double distilled deionized water separately to prepare $LiCoPO_4$ and $LiNiPO_4$ respectively. After that citric acid as a chelating agent has been added to the mixture and magnetically stirred well to form transparent metal chelates. Ethylene glycol is then added to the mixture for gelation which results in the formation of low molecular weight oligomers. The temperature is then increased to 150^0 C to promote esterification between hydroxyl group of ethylene glycol and carboxylic acid of citric acid and polymerization. A black polymer precursor which is stable in air is then formed. It can be assumed that the polymer precursor contains lithium, metal ion (nickel & cobalt) and phosphate cations, trapped homogeneously throughout the polymer matrix. Therefore, pyrolysis of the polymer is performed at 350^0C for 2 h in a furnace that yields a black powder precursor, called hereafter ''powder precursor''. The black colour indicates that the powder contains carbon. In order to determine the firing temperature, TGA/DTA analysis has been performed on powder precursor using Perkin-Elmer Thermal Analyser in oxygen atmosphere. The final products are obtained after the calcination of powder precursor at 600^0C and at 800^0C for both the samples. XRD pattern has been taken to confirm the formation of samples with desired phase, using Cu K_α radiation having a wavelength of 1.5417 Å. The resultant samples are spread in a die and a pressure 4000 Kg cm^{-2} is applied to form pellet with 1 mm thickness and 1.0 cm diameter. The pellets are sintered at 600° C for 2 hrs. The impedance measurements are taken by placing the pellet in between two

aluminium blocking electrodes within the frequency range 42Hz to 5MHZ using computer controlled HIOKI 3532 LCZ meter.

3. Results and discussions

3.1 Thermogravemetric (TG) and Differential Thermal (DT) analysis

Fig (1a,b) shows the TG and DTA curves of $LiNiPO_4$ and $LiCoPO_4$ in the temperature range 28^0C to1000^0C at 15^0C/min. Thermogravemetric analysis of both the samples consists of three regions upto 150^0C, 300-600^0C and 600 – 1000^0C. For both the samples, upto 150^0C the first weight loss (~4%) observed in TGA associated with an endothermic peak in Differential Thermal Analysis corresponds to the solvent evaporation[6]. The second weight loss (~3%) can be attributed to the combustion reaction of the raw materials with the evolution of brown gases (CO_2 & NO_2) . The citric acid added provides the local heat for the formation of compound during the decomposition process because of the self-igniting property of its carboxylic acid [7]. The exothermic peak in Differential Thermal Analysis in the range 300-600^0C corresponds to the degradation of polymer and due to the conversion of organic compounds into CO_2 & NO_2.

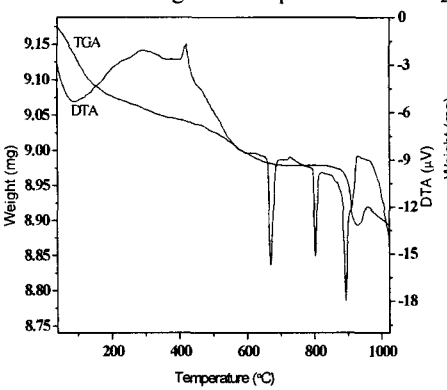

Fig. 1a TG and DTA curve of $LiNiPO_4$

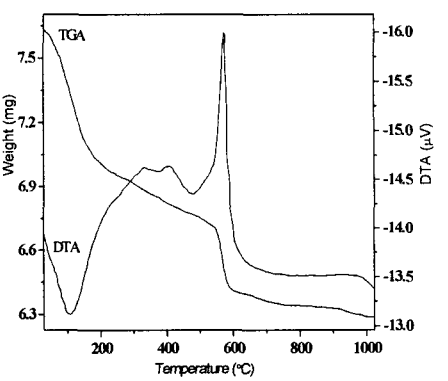

Fig. 1b TG and DTA curve of $LiCoPO_4$

At higher temperatures chemical reactions occur with the exothermic heat energy supplied by the combustion of citric acid which facilitates the process of crystallization of the compound.

3.2 XRD Analysis:

Fig(2a,b) shows the XRD pattern of $LiNiPO_4$ and $LiCoPO_4$. The 2θ values obtained are in good agreement with [PCPDF 32-0578] and [PCPDF 32-0552] for $LiNiPO_4$ and $LiCoPO_4$ respectively. Table 1a,b shows the comparison of 2θ values for maximum intensity peaks obtained in present systems with that of previous reports.

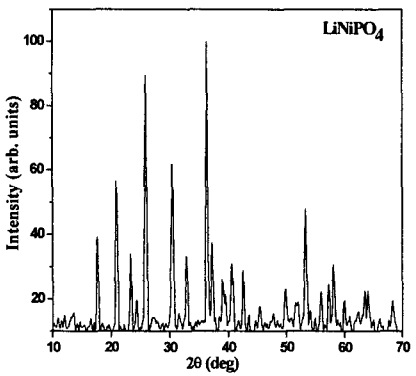

Fig. 2a XRD pattern of $LiNiPO_4$

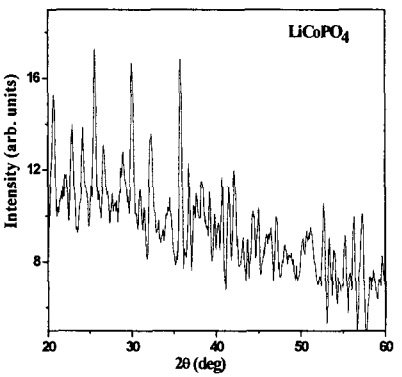

Fig. 2b XRD pattern of $LiCoPO_4$

Table 1a: Comparison of 2θ values of observed and PCPDF file for $LiNiPO_4$

S.No	2θ values (degrees)		Intensity
	Experimental	PCPDF	
1.	17.626	17.632	60
2.	20.895	20.901	60
3.	23.303	23.316	30
4.	25.888	25.922	100
5.	30.439	30.540	65
6.	32.848	32.841	25
7.	36.336	36.326	100
8.	37.233	37.294	35

Table 1b: Comparison of 2θ values of observed and PCPDF file for $LiCoPO_4$

S.No	2θ values (degrees)		Intensity
	Experimental	PCPDF	
1.	20.656	20.802	80
2.	25.641	25.709	95
3.	30.068	30.161	85
4.	32.29	32.486	40
5.	35.824	35.920	100

Average particle size has been calculated using Debye-Scherrer method,

$$D = \frac{0.94\ \lambda}{\beta_{2\theta} \cos \theta} \quad (1)$$

The average particle sizes calculated for $LiNiPO_4$ and $LiCoPO_4$ are ~24 nm. Thus the phosphates prepared by Pechini – type Polymerizable Technique seems to have fewer impurities and also the presence of nanocrystalline phases when compared to phosphates prepared by other conventional solid state reaction methods [8,9].

3.3 Impedance Analysis

Figure 3 shows the Cole – Cole plot for $LiNiPO_4$ and $LiCoPO_4$ at ambient temperature. Cole-Cole plot of $LiNiPO_4$ shows a depressed semicircle at high frequency region and a inclined spike at low frequency. Cole-Cole plot of $LiCoPO_4$ shows two semicircles at high and intermediate frequency region and a inclined spike at lower frequencies. The semicircle corresponds to a parallel combination of resistance and capacitance. The capacitance value has been calculated from the centre of the semicircle at which $\omega RC = 1$ relation obeys and from the slope of the inclined spike. For both the samples the capacitance values calculated from the high frequency semicircle and low frequency spike are in pico and micro farad range, corresponding to the bulk effect and electrode polraisation effect respectively. The capacitance value of intermediate frequency semicircle observed in $LiCoPO_4$ has been found to be in the order of nanofarad, may be attributed to grain boundary effect [10]. Grain boundary resistance has been found to be greater than grain resistance due to the blocking of charges on either side of the grain boundary forming the potential barrier and hence blocking the passage of charge carriers. DC conductivity value has been calculated using

$$\sigma = (1/R_b) * (l/A) \quad (2)$$

and are found to be 1.8×10^{-5} Scm^{-1} and 1.3×10^{-5} Scm^{-1} for $LiNiPO_4$ and $LiCoPO_4$ respectively.

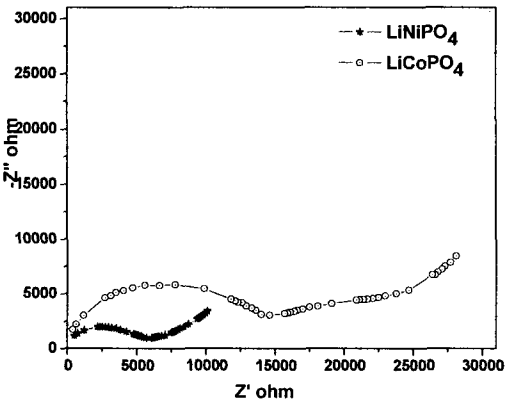

Fig. 3 Cole – Cole plot for $LiNiPO_4$ and $LiCoPO_4$ at 303K

3.4 Conductance spectra

Figure 4 shows the conductance spectra for $LiNiPO_4$ and $LiCoPO_4$ at 303K. The spectra consist of almost a plateau and a high frequency dispersion region. The plateau characterizes the conduction which is mainly by the hopping motion of the mobile ions and determines the dc value of conductivity. As the frequency increases, the conductivity gradually increases and it is well approximated by the Jonscher' Power formula [11],

$$\sigma'(\omega) = \sigma_0 + A\,\omega^{s} \qquad (3)$$

where s is the dimensionless frequency exponent and σ_0 corresponds to dc conductivity.

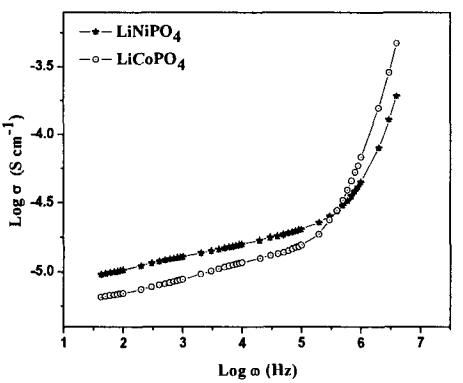

Fig. 4 Conductance spectra for $LiNiPO_4$ and $LiCoPO_4$ at 303K

Hopping rate (ω_H) has been calculated using the relation $\omega_H = 2\sigma_0$. Concentration of charge carriers has been calculated using

$$c' = \sigma_0 kT/(\omega_H e^2 a^2 \gamma) \quad (4)$$

where k is the Boltzmann constant, e is the elementary charge of the ion, a is the hopping distance of the ion (3 Å) and γ is the correlation factor (1/6) and are tabulated in table 2.

Table: 2 Transport parameters calculated from conductance spectra for $LiNiPO_4$ and $LiCoPO_4$

S.No	Transport Paramters	$LiNiPO_4$	$LiCoPO_4$
1.	dc conductivity	$1.8 X10^{-5}$	$1.3X 10^{-5}$
2.	ω_H	$3.6 X 10^5$	$6.5 X 10^5$
3.	c'	$1.5 X 10^{25}$	$6.2 X 10^{24}$
4.	s	1.2	1.4

3.5 Dielectric spectra analysis

Figure 5a shows the variation of log dielectric constant with frequency for $LiNiPO_4$ and $LiCoPO_4$ at 303K. For both the samples at low frequencies the gradual increase in the dielectric constant may be attributed to the space charge accumulation at electrode-electrolyte interface. At higher frequencies due to the periodic reversal of the field dielectric constant decreases. According to dielectric physics, the dielectric loss tan δ mainly consists of two contributions, one from the dielectric polarization relaxation process tan δ_{relax} and another from dc conduction $\tan\delta_{dc}$. So tan δ_{dc} can be expressed as

$$\tan \delta_{dc} = \sigma_{dc}/\omega\varepsilon \quad (5)$$

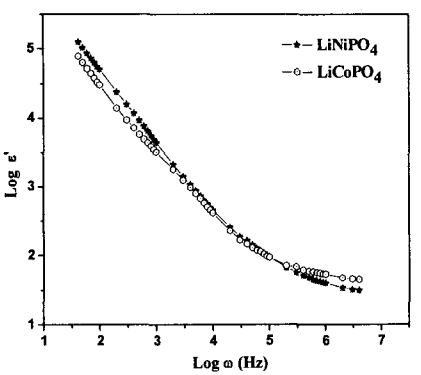

Fig. 5a Log ω Vs Logε' for $LiMPO_4$ (M=Ni,Co)

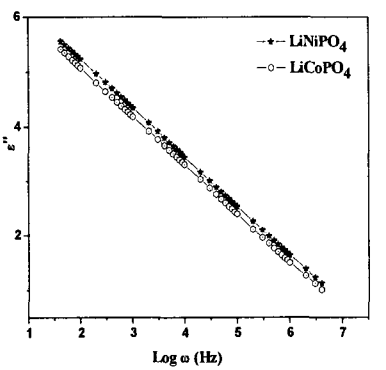

Fig. 5b Log ω Vs Logε'' for $LiMPO_4$ at 303K.

So ε_{dc}'' = σ_{dc}/ω. The slope of log ε_{dc}'' Vs logω is -1. Figure 5b shows the variation of logε_{dc}'' with frequency having a slope value near to unity (-1) at lower frequencies indicates that the dc conduction contribution is predominant in both the samples [12]. This can be explained as at low frequencies the random diffusion of the cations results in a dc conductivity and at higher frequencies a power law dispersion is observed (ε'' α ω) . Thus the presence of mobile ions results in dielectric loss which varies monotonically with frequency and exhibits no peak corresponding to one seen in dipolar relaxation.

4. Conclusion

$LiNiPO_4$ and $LiCoPO_4$ cathode materials based on Phospho-Olivine structure has been prepared by Pechini – type Polymerizable Technique. Formation of the sample has been confirmed by thermal analyses using TGA/DTA. Nano sized particles (~24nm) has been confirmed from the XRD analysis for both the samples. Conductivity analysis shows the conductivity in the order of 10^{-5} Scm^{-1} for both $LiNiPO_4$ and $LiCoPO_4$ at ambient temperature. Dielectric spectra reveals the predominant dc conductivity contribution to the relaxation in both the samples.

References

1. Ali Eftekhari, *J.Electrochem. Soc.*, **151(9)**,A1456-A1460 (2004)
2. M. Stanley Whittingham *Chem. Rev.*, **104,** 4271-4301 (2004)
3. Aniruddha Deb, *J. Phys. Chem. B.*, **108**, 7046 (2004)
4. D. Morgan, A. Van der Ven, *Electrochem. and Solid State Lett.* 7 **(2),** A30-A32 (2004)
5. Shigeto Okada et.al, *J. Power Source* **97-98,** 430-432 (2001).
6. Gianni Antonioli, PierPaoloLottici,*J. Non-Cryst.Solids.*,**177**179-186 (1994).
7. Wu Yang, Youli Qi, *Mat. Chem. and Phys.*, **84**, 52-57 (2004)
8. PCPDF 32-0578, Krabbenhoft, Grant-in-Aid (1980)
9. PCPDF 32-0552, Krabbenhoft, Grant-in-Aid (1980)
10. J. Ross Macdonald in ; (Eds) Impedance Spectroscopy Emphasizing Solid Materials and Systems (1987) Jon Wiley & Sons pubs, Newyork.
11. A.K. Jonsher, *Nature* **267**, 673 (1977)
12. Chen Ang, Zhi Yu, *Appl. Phys. Lett.*, **79(6),** 818-820. (2001)

SYNTHESIS AND ELECTRICAL CHARACTERIZATION OF $LiFeO_2$, $LiCoO_2$ AND NiO COMPOSITIONS

ATHULA WIJAYASINGHE[1,2] AND BILL BERGMAN[2]

[1]*Institute of Fundamental Studies, Kandy, Sri Lanka*

[2]*Department of Materials Science and Engineering, KTH, Stockholm, Sweden*

Binary and ternary compositions of $LiFeO_2$, $LiCoO_2$ and NiO were synthesized and electrically characterized, aiming the application in electrodes of fuel cells and batteries. Materials synthesis were carried out through wet-chemical routes, such as Pechini and glycine-nitrate techniques. Calcination and sintering studies were performed in order to find the optimum conditions for these new materials. The sintered materials were subjected to phase analysis by X-ray diffraction and the electrical conductivity measurements were performed by the d.c. 4-probe method up to 750°C.

The powders prepared by Pechini method result in rather spherical and softly agglomerated particles. The phase analysis reveals the existence of $LiFeO_2$-$LiCoO_2$-NiO solid solution phases of *Fm3m* cubic rock-salt structure in $LiFeO_2$-NiO rich compositions. Increase of the $LiCoO_2$ content of the composition results in the formation of *R3m* layered phase. Electrical conductivity of $LiCoO_2$-NiO binary compositions increases drastically with the $LiCoO_2$ content. While the conductivity is considerably low and decreases with the $LiFeO_2$ content in NiO-$LiFeO_2$ and $LiFeO_2$-$LiCoO_2$ binary systems. In the ternary system, the electrical conductivity increases to a maximum with increasing $LiCoO_2$ content. Altogether, this study shows the behaviour

1. Introduction

From the viewpoint of cost and efficiency, semi-conductive ceramic oxides are the best practical electrode materials for number of electrochemical energy conversion devices such as fuel cells, batteries, photoelectrolysis, chloroalkali cells and electrochlorination[1]. These electrodes must possess adequate conductivity to transfer electrical charge, but be corrosion resistant in the chemical and thermal environment of the cell and often must have catalytic capabilities. In the development of electrode materials, the stability of the material is examined first, followed by evaluation and development of the electronic conductivity. Basically, the compounds that contain multivalent ions have the potential for electronic conductivity due to intrinsic nonstoichiometry or by further enhancement of conductivity through doping, specially in oxide ceramics[2].

This work is based on synthesizing and electrically characterizing binary and ternary compositions of $LiFeO_2$, $LiCoO_2$ and NiO. NiO is used as the cathode material of the Molten Carbonate Fuel Cell (MCFC). However, the dissolution of this state-of-the-art cathode material has been a main obstacle for the commercialization of the MCFC[3]. Apart from NiO, $LiFeO_2$ and $LiCoO_2$ have also been extensively investigated for the MCFC cathode. However, none of these single-phase candidate materials could alone be used in the MCFC, because of their low electronic conductivity or poor oxygen reduction kinetics[4]. The approach of

developing alternative cathodes for MCFC has since been diverted to improving these single candidates by doping or forming into mixed oxides.

$LiCoO_2$ is used also as the cathode material of Li batteries and the $LiCoO_2$ cathode now dominates in the rechargeable lithium battery market. However, the high price of cobalt limits it usages and a cheaper alternative is in a great need for large scale applications[5]. Lithium nickel oxide is also regarded as a candidate for the cathode of Li batteries, and a number of research work is going on to improve its stability by replacing a part of nickel by other materials such as cobalt.

In this study, a number of new compositions under NiO-$LiFeO_2$, $LiFeO_2$-$LiCoO_2$ and $LiCoO_2$-NiO binary systems and, $LiFeO_2$-$LiCoO_2$-NiO ternary system, have been synthesized and electrically characterized. This paper mainly presents the synthesis work and electrical conductivity of these new materials. A brief summary of a cell study using cathodes fabricated form some of the prepared materials, is also presented. A detailed description of the cathode fabrication and in-cell testing is found elsewhere [6-8].

2. Experimental

The feasibility of two wet-chemical techniques, the glycine-nitrate method and the Pechini method, was investigated in order to obtain powder with characteristics appropriate for electrode preparation. For both methods, $LiNO_3$, $Fe(NO_3)_3 \cdot 9H_2O$, $Ni(NO_3)_2 \cdot 6H_2O$ and $Co(NO_3)_2 \cdot 6H_2O$ (Merck, Germany) of analysis grade were used as the starting materials with appropriate organic precursor solutions. Both poweder synthesis processes were completed by calcining ash product at 650 °C for 2h in air. A detailed description of the materials synthesis can be found in the references[6-8]. The synthesized powders were uni-axially pressed at 100 MPa and green pellets of 12 mm in diameter were prepared. The green pellets were subsequently sintered at 1000 °C for two hours in static air.

Scanning Electron Microscopy (SEM, JEOL JSM-840) was employed to investigate the particle morphology. The phase analysis on the sintered materials was carried out with X-ray diffraction (XRD, Philips diffractometer using monochromatic Cu K_a radiation). The electrical conductivity of these materials was determined by performing d.c. conductivity measurements on sintered pellets by the four-probe method up to 750°C.

3. Results and Discussion

3.1. Powder characteristics

The SEM micrographs obtained on 40 mole% $LiFeO_2$-20 mole% $LiCoO_2$-40 mole% NiO ternary powders of System T1, synthesized by the glycine-nitrate method and

the Pechini method are shown in Figure 1(a) and 1(b), respectively. Figure 1(a) shows of having flaky particles of sponge or porous structure for the powders prepared by glycine-nitrate method. These powders, which contain highly irregular shaped and considerable porous particles, may inhibit packing, compaction and attainment of high final properties. Such powder structure indicates subsequent processing problems since internal pores are difficult to eliminate.

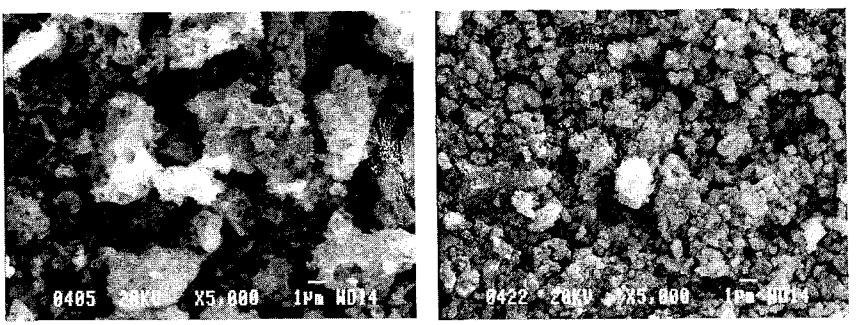

(a) (b)

Figure 1. Scanning electron micrographs of 40 mole% $LiFeO_2$-20 mole% $LiCoO_2$-40 mole% NiO ternary powders. (a). Synthesized by the glycine-nitrate method. (b). Synthesized by the Pechini method.

In comparison, as shown in Figure 1(b), the powder prepared by the Pechini method show of having agglomerated sub-micron size particles. These sub-micron size powder particles are rather spherical shaped, less porous and less irregular when compared to powder prepared by the glycine-nitrate method. Therefore all the remaining powder compositions for this study were synthesized by the Pechini method.

3.2. The phase analysis

The compositional and the phase details of the prepared materials are shown in Figure 2. The compositions, given in the figure, are in mole percentages and the phase details are based on the XRD analysis performed on pellets sintered at 1000 °C for two hours in static air. Materials compositions in the NiO-$LiFeO_2$ (system B1), $LiFeO_2$-$LiCoO_2$ (system B2) and $LiCoO_2$-NiO (system B3) binary systems together with $LiFeO_2$-$LiCoO_2$-NiO ternary compositions in five sub-systems have been investigated. Each of these T1 to T5 ternary sub-systems consists of the $LiFeO_2$-$LiCoO_2$-NiO ternary materials with a constant molar ratio of $LiFeO_2$:NiO and varying $LiCoO_2$ contents. The corresponding $LiFeO_2$:NiO molar ratios for the systems T1, T2, T3, T4 and T5 are 1:1, 3:1, 1:3, 2:1 and 1:2, respectively.

The materials prepared in T1, T2 and T3 systems are based on the ternary compositions starting from the $LiFeO_2$-NiO binary system and extending towards the $LiCoO_2$ end of the ternary system. Ternary compositions of up to 30 mole% of

$LiCoO_2$ were studied under each of these T1, T2 and T3 systems. Ternary compositions starting from the $LiCoO_2$ end and extending down to 40 mole% of $LiCoO_2$ were studied under systems T4 and T5.

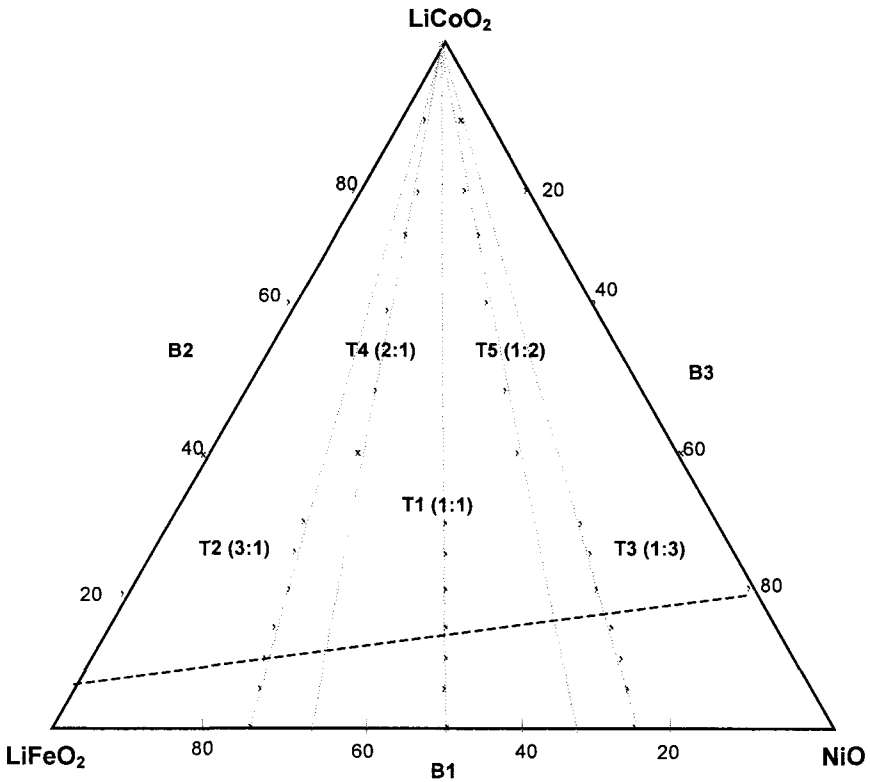

Figure 2. *The compositional and phase details of prepared materials. The compositions are given in mole percentages. B1, B2 and B3 are the binary systems of NiO-$LiFeO_2$, $LiFeO_2$-$LiCoO_2$ and $LiCoO_2$-NiO, respectively. The corresponding $LiFeO_2$:NiO molar ratios for the ternary sub-systems T1, T2, T3, T4 and T5 are 1:1, 3:1, 1:3, 2:1 and 1:2, respectively. The doted (----) line represents the boundary of the $LiFeO_2$ and NiO rich $LiFeO_2$-$LiCoO_2$-NiO solid solution.*

The phase analysis by XRD, indicated the existence of a NiO-$LiFeO_2$ solid solution of the *Fm3m* cubic rock-salt structure, in the NiO-$LiFeO_2$ binary materials prepared under System B1. The material compositions so far investigated under binary systems B2($LiFeO_2$-$LiCoO_2$) and B3($LiCoO_2$-NiO) show the existence of two phases. In both B2 and B3 systems, the *Fm3m* cubic rock-salt structure of NiO and $LiFeO_2$ dominates in the compositions close to NiO and $LiFeO_2$ ends. While the binary compositions close to the $LiCoO_2$ end is dominated by the *R3m* layered phase of $LiCoO_2$. As seen in Figure 2, the ternary materials of systems T1, T2 and T3, containing low $LiCoO_2$ contents, form solid solutions of the *Fm3m* cubic rock-salt

structure rich in $LiFeO_2$ and NiO. Increase of the $LiCoO_2$ content of the composition results in the formation of secondary phase of *R3m* layered structure. The boundary between the $LiFeO_2$-NiO rich solid solution and the multiphase zone is slightly varying among the T1, T2 and T3 ternary sub-systems. The apparent solid solution boundary is in between 10 and 15 mole% of $LiCoO_2$ for System T1 and T2 while it is slightly high, in between 15 and 20 mole% of $LiCoO_2$, for System T3. In $LiCoO_2$ rich materials prepared under the systems T4 and T5, the content of the $LiFeO_2$-NiO rich solid solution phase of *Fm3m* structure, decreases with the increase of $LiCoO_2$ content in the composition. Instead, the content of $LiCoO_2$-rich phase of *R3m* structure increases at the expense of the $LiFeO_2$-NiO rich solid solution phase.

3.3. Electrical conductivity

The d.c. electrical conductivity measurements were performed by the four probe method upto 750 °C. Throughout the measured temperature range, the electrical conductivity of these materials increases in an exponential manner with temperature, as could be expected for semiconductors. However, the trend of increasing conductivity with temperature is different among the materials.

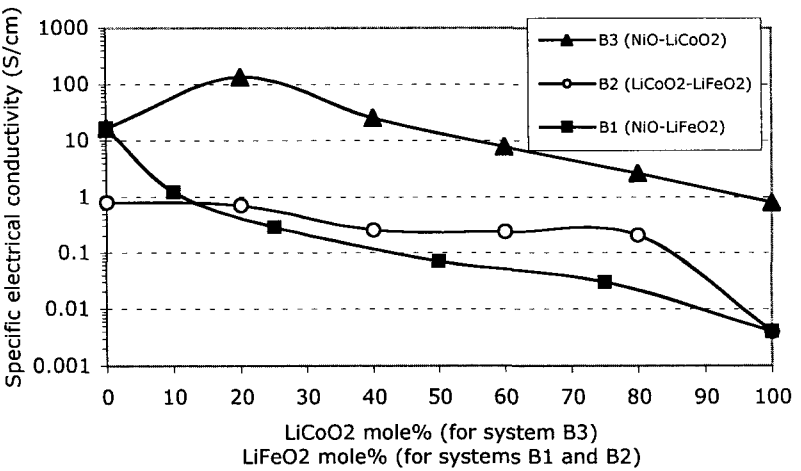

Figure 3. Variation of the specific electrical conductivity in air at 650 °C, with respect to $LiFeO_2$ content in the systems B1(NiO-$LiFeO_2$) and B2($LiCoO_2$-$LiFeO_2$), and with respect to $LiCoO_2$ content in system B3 (NiO-$LiCoO_2$).

The electrical conductivity behaviour of the binary compositions at 650 °C in air, is shown in Figure 3. As expected, the electrical conductivity of the binary compositions of systems B1(NiO-$LiFeO_2$) and B2($LiCoO_2$-$LiFeO_2$) decreases with the increase of $LiFeO_2$ content and it can be ascribed to the very low electrical

conductivity of $LiFeO_2$ with compared to NiO and $LiCoO_2$[4]. Also the electrical conductivity values of these prepared compositions in systems B1 and B2 lay between the electrical conductivity values of the end materials.

However, a completely different behaviour can be seen in System B3(NiO-$LiCoO_2$), where the conductivity increases drastically to a maximum with the increase of $LiCoO_2$ content. Further increase of the $LiCoO_2$ content, significantly decreases the conductivity. In this preliminary study the 20mole% $LiCoO_2$-80 mole% NiO composition of system B3, showed a specific electrical conductivity of about 135 S/cm at 650 °C in air and about 0.01 S/cm at 25 °C in air. This significant room temperature electrical conductivity indicates the possibility of developing these binary materials for cathode of Li batteries, by improving the conductivity while preserving the desired crystal and micro structure.

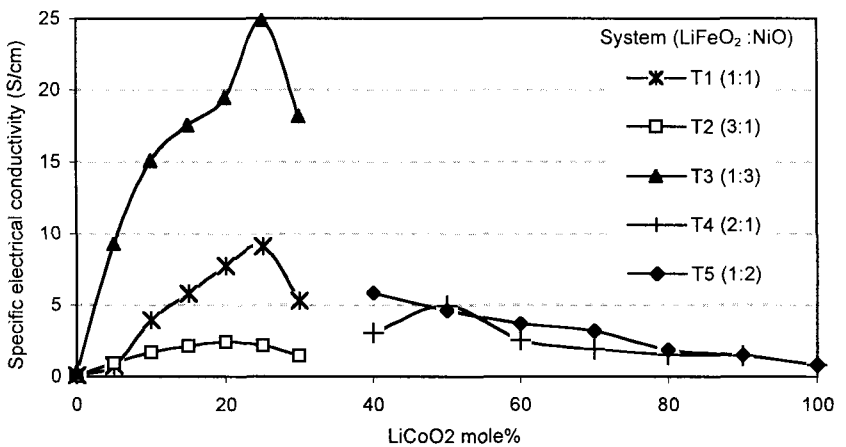

Figure 4. Variation of the specific electrical conductivity of ternary compositions with respect to $LiCoO_2$ content, at 650 °C in air

A quite similar electrical conductivity behaviour was noticed in the ternary materials and the variation of the specific electrical conductivity of them with $LiCoO_2$ content, at 650 °C in air, is shown in Figure 4. A similar trend of increasing conductivity with the content of $LiCoO_2$, can be noticed in the $LiFeO_2$-NiO rich ternary compositions prepared under systems T1, T2 and T3. In each of systems T1, T2 and T3, the increase of $LiCoO_2$ content of the material increases the conductivity to a maximum. This conductivity maximum is slightly shifting towards the materials with higher $LiCoO_2$ content, with decreasing the $LiFeO_2$: NiO ratio in the system. The maximum is shifting from about 20 to 25 mole% of $LiCoO_2$ content, when the $LiFeO_2$: NiO ratio is changing from 3:1 (System T2) to 1:3 (System T3).

As shown in Figure 4, when comparing the electrical conductivity among systems T1, T2 and T3 having the same $LiCoO_2$ content, the materials in System T3 (with the lowest $LiFeO_2$:NiO molar ratio, 1:3) show the highest conductivity. The

materials in System T2 (with the highest $LiFeO_2$:NiO molar ratio, 3:1) show the lowest conductivity, while the conductivity of materials in System T1 lies in between. This behavior is identical to that of the $LiFeO_2$-NiO binary system (B1); the electrical conductivity decreases with increasing $LiFeO_2$ content in the material, due to very low electrical conductivity of $LiFeO_2$.

The electrical conductivity behaviour of the $LiCoO_2$-rich ternary materials prepared under systems T4 and T5 is also presented in Figure 4. A slightly different behaviour, in the variation of conductivity with $LiCoO_2$ content, can be seen in these two systems. In System T4, the conductivity increases to a maximum at around 50 mole% with decreasing $LiCoO_2$ content, followed by a decrease in conductivity with further decreasing of $LiCoO_2$ content down to 40 mole%. In System F, the conductivity increases continuously with decreasing $LiCoO_2$ content of the composition down to 40 mole%.

Altogether, the electrical conductivity study shows the ability of improving the conductivity of $LiFeO_2$, $LiCoO_2$ and NiO by forming them into binary and ternary compositions. The ternary materials, specially the 20-30 mole% $LiCoO_2$ compositions in systems T1 and T3, show promising characteristics for the MCFC cathode application, having adequate electrical conductivity (well above 1 S/cm at the operating temperature of 650 °C). A brief description of a study performed with these materials for the MCFC cathode application is given in the following section..

3.4. Application of $LiCoO_2$-$LiFeO_2$-NiO ternary materials to the MCFC cathode

Table 1. Details of the cell tested cathodes and their electrochemical performance

System		T1		T3	
Composition In mole%	$LiFeO_2$	45	37.5	20	18.75
	NiO	45	37.5	60	56.25
	$LiCoO_2$	10	25	20	25
Electrical conductivity at 650 °C (S/cm)	In bulk material	2.36	8.42	18.5	20.1
	In porous electrode	0.10	1.32	3.09	3.12
Cathode performance at the optimum condition	IR-corrected polarization (mV)	216	90	62	81
	Cathodic IR-drop (mV)	367	159	46	99

The $LiFeO_2$-$LiCoO_2$-NiO materials, which show adiquate electrical conductivity were subjected to cathode fabrication and the cathodes with promissing characteristics were then cell tested. Table I, presents the performance of some of the cell tested cathodes. Among them, both 25 mole% $LiCoO_2$ cathodes of systems T1 and T2, showed performance comparable to that of $LiCoO_2$ cathodes[6,7]. Interestingly, performance comparable to that of state-of-the-art NiO cathode

projected for a commercial MCFC, could be achieved with the 20 mole% $LiCoO_2$ cathode of System T3. Hence the cell performance of these cathodes reveal the possibility of using $LiFeO_2$-$LiCoO_2$-NiO cathodes for the MCFC.

Accordingly, the outcome of the study shows promising characteristics of the $LiFeO_2$-$LiCoO_2$-NiO ternary materials for the applications as cathode materials of the MCFC. It also suggests to investigate the possibility of using $LiCoO_2$-NiO binary compositions as cathode materials for Li-ion batteries.

Conclusion

This study suggests the existence of $LiFeO_2$-$LiCoO_2$-NiO solid solution phases of *Fm3m* structure in $LiFeO_2$-NiO rich compositions. Increase of the $LiCoO_2$ content in the composition results in the formation of *R3m* layered phase. Electrical conductivity of $LiCoO_2$-NiO binary compositions can significantly be increased by controlling the $LiCoO_2$ content. The conductivity is considerably low and decreases with the $LiFeO_2$ content in both NiO-$LiFeO_2$ and $LiFeO_2$-$LiCoO_2$ binary systems. In the ternary compositions, the electrical conductivity increases to a maximum with increasing $LiCoO_2$ content.

References

1. D. W. Richerson, Modern Ceramic Engineering. Marcel Dekker Inc., (1992).
2. J. L. Smith, G. H. Kucera and A. Brown, J. R. Selman, D. A. Shores, H. C. Maru and I. Uchida, Editors, The Electrochemical Society Proceeding Series, Pennington, NJ, **90-16**, 216 (1990).
3. J. R. Selman, in Fuel Cell Systems, L. J. M. J. Blomen and M. N. Mugerwa, Editors, Chap.9, Plenum Press, New York 345 (1993).
4. L. Giorgi, M. Carewska, M. Patriarca, S. Scaccia, E. Simonetti and A. Di Bartolomeo, J. Power Sources, **49**, 227 (1994).
5. M. S. Whittingham, Chem. Rev, **104**, 4271 (2004).
6. A. Wijayasinghe, B. Bergman and C. Lagergren, *J. Electrochem. Soc.* **150(5),** A558 (2003).
7. A. Wijayasinghe, C. Lagergren and B. Bergman, *Fuel Cells,* **2(3),** 1 (2002).
8. A. Wijayasinghe, B. Bergman and C. Lagergren, *Electrochemica Acta,* **49**, 4709 (2004).

NATURAL SRI LANKA GRAPHITE AS CONDUCTING ENHANCER IN MANGANESE DIOXIDE (EMD TYPE) CATHODE OF ALKALINE BATTERIES

N.W.B. BALASOORIYA AND P.W.S.K. BANDARANAYAKE
Department of Physics, University of Peradeniya, Peradeniya, Sri Lanka
Email: balasooriya@seu.ac.lk, kumarab@pdn.ac.lk

Ph. TOUZAIN AND Ch. POINSIGNON
Laboratoire d'Electrochimie et de Physico-chimie des Matériaux et Interfaces (LEPMI), ENSEEG, INPG, B.P.75, 38402 St. Martin d'Hères, France.
Email: Philippe.Touzain@lepmi.inpg.fr, Christianne.Poinsignon@lepmi.inpg.fr

The performances of γ-MnO_2 cathode in alkaline battery depend on the crystallochemical properties of MnO_2 as well as of graphite used to improve electronic conductivity of the cathode mixture. In the present work we have studied the performances of Sri Lanka natural graphite in the reduction process of γ-MnO_2 and compare it with the other synthetic and natural graphites. We also show how crystallochemical and electrochemical properties of the synthetic manganese dioxide depend on defects which are related to the structural parameters P_r and T_w. Where P_r is the rate of ramsdellite-pyrolusite intergrowth and T_w microtwinning which represents the creation of nanostructure aggregates during electrodeposition.

1. Introduction

Manganese oxides including γ-MnO_2 have widely been used as electrodes material in both aqueous and non aqueous batteries[1,2] due to their economical and environmental advantages and safety. The cathodic reduction of manganese dioxide in alkaline electrolytes has been studied by several authors[3-5]. The manganese dioxide electrode of rechargeable batteries has received wider attention during the last three decades.

MnO_2 exists in numerous allotropic forms as natural MD ramsdellite, pyrolusite, synthetic form β-MnO_2 (stoichiometric and ordered), the synthetic and disordered γ-MnO_2 (CMD type) and ε-MnO_2 (EMD type) and all of them have been used in alkaline batteries. In general, the reduction of γ-MnO_2 can be divided into two steps.[4] The first step covers the composition region from MnO_2 to MnOOH and called the "electron-proton insertion process". The insertion of protons from the electrolyte into the γ-MnO_2 structure and the reduction reaction is given by

$$MnO_2 + H_2O + e^- \rightarrow MnOOH + OH^- \qquad (1)$$

Simultaneously, electrons are inserted into the γ-MnO_2 structure, causing the reduction of Mn^{4+} to Mn^{3+} ions. During the reduction process, the potential decreases continuously indicating a single-phase reaction mechanism. Therefore, the first electron reduction is also called homogenous reduction process.[6]

During the first reduction process in concentrated KOH electrolyte, the Mn^{3+} ions in the cathode are dissolved into electrolyte. During the second electron reduction, the Mn^{3+} ions are reduced to Mn^{2+} ions by charge transfer on the surface of the conducting graphite in the cathode mixture. Since the solubility of Mn^{2+} ions in alkaline medium is relatively low compared to that of Mn^{3+} ions, the Mn^{2+} ions precipitate as $Mn(OH)_2$ on the surface of the graphite particles. Therefore, the second electron reduction step is called "dissolution and precipitation" process and consequently, the potential during this process remains constant and it is also called a heterogeneous reduction process.[4]

Alkaline manganese dioxide batteries consist of manganese dioxide, an aqueous electrolyte and powdered zinc. The electrolyte is a concentrated caustic, usually KOH which offers higher conductivity and reduced gassing compared to the acidic electrolyte of the Leclanché cell. On discharge, the manganese dioxide positive plate is reduced to manganese oxyhydroxide and provides the OH^- ions.

The purpose of this study is to investigate the effects of different types of natural and synthetic graphite on reduction of MnO_2 (EMD type; grade of TA and TC) and also the suitability of natural Sri Lanka graphite as a conducting enhancer in alkaline batteries.

2. Experimental

The selected Sri Lankan vein graphite samples (BSSI and KSSI) were crushed using an agate mortar and separated to powder of particle size less than 40 μm using a mechanical sieve-shaker. The natural Madagascar (E1099) graphite, Krömful graphite (UF4) and synthetic TIMREX graphite (KS25) were used as received. X-Ray diffraction (XRD) studies were carried out with a Philips X-Ray generator (using Cu K_α radiation with wavelength λ=1.5406 Å).

The manganese dioxide composite electrode was prepared by mixing 50 mg of EMD (TA grade) powder with 150 mg of particular type of Sri Lanka vein graphite (KSSI) thoroughly in an agate mortar. Pellets of diameter 13 mm were prepared by applying 30 kN hydraulic pressure.

An electrochemical cell was assembled using a composite MnO_2 pellet as the working electrode, Hg/HgO as the reference electrode and a nickel wire as a counter electrode. Electrochemical reduction was performed in 9M KOH aqueous solution using a MacPile potentiostat-galvanostat at room temperature at voltage scan rates of

10 mV in 2 h, 10 mV in 1 h and 25 mV in 1 h in the potential range between the equilibrium potential (U_{eq}) which is around 0.15 V and -0.8 V. The graphs of current (I) versus the rate of intercalation (x) were recorded during the reduction of MnO_2 electrodes.

The anode material was prepared with 90 wt.% of zinc powder (DORAL Zn 101), 5 wt.% of acetylene black (AB: Y20) and 5 wt.% of Algoflon® PTFE (Polytetrafluoroethylene). DME (1,2-Dimethoxyethane) (Aldrich) was added to the mixture and stir well to prepare a composite gel. The gel was sandwiched between two Ni meshes and pressed by applying about 30 kN pressure. A stainless steel disc as a current collector and a non-woven separator were also used. The electrochemical cell was kept under vacuum for about 48 hours after assembling.

3. Results and Discussion

3.1. Characteristics of different grades of EMD

Electrochemically prepared manganese dioxides (EMD) of TA and TC grades were used. They consist of 87.9% and 94% of particles respectively having sizes less than 75 μm, and TC has a narrower particle size distribution than TA. The TA and TC grades have the same advantages of low impurity levels. The major metallic impurities in TA and TC grades are very low levels of As, Co, Cr, Cu, Fe, K, Mo, Ni, Pb and Sb.

The structure of the γ-MnO_2 is disordered and can be described by different distribution of manganese in a hexagonal close packing oxygen network. Electrochemical activity of the γ-MnO_2 is controlled by disorder. The X-ray diffraction pattern of MnO_2 samples could be explained by random intergrowth of pyrolusite layers in a ramsdellite matrix[7] and the major diffraction peaks are (110), (021) and (221). The angular positions of the major peaks are used to quantify the structural disorder of De Wolff disorder (Pr)[7] and microtwining (Tw)[8] as shown in Fig. 1.

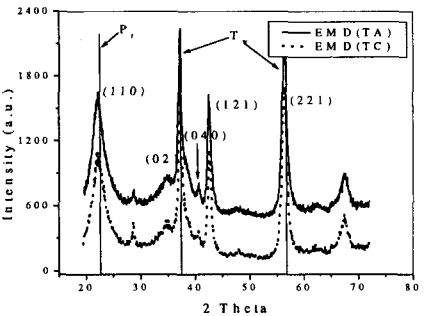

Figure 1. Comparison between the x-ray diffraction pattern (CuK_α) of EMD(TA) and EMD(TC).

3.2. Electrochemical characterization: Potentiostatic reduction of MnO_2

Fig. 2 clearly shows the four potentiostatic reduction peaks of MnO_2 (EMD type; TA) appearing during reduction of all types of natural and synthetic graphites, at scanning rate of 10 mV h^{-1}. The first peak (*S*) is attributed to the reduction of manganese at surface sites. Reduction to Mn^{4+} is associated with the manganese atoms located at the surface sites of manganese dioxide and its incomplete oxygen polyhedron is completed by surface hydroxyl groups or water molecules.[8,9] The second reduction stage found (the broad peak, *A*) in the potential range between -0.06 V and -0.09 V vs. Hg/HgO indicates the reduction of Mn^{4+} ions within the MnO_2 (EMD) structure. But Swinkels *et. al.*[10] proposed that the main peak (*A*) splits into three components is attributed to Mn located at the ramsdellite or in pyrolusite domains or at their frontiers. Chabre *et. al.*[8] have shown that the peak *A* is made of two components and the two possible locations of protons in the tunnel of the ramsdellite structure. The third peak, *B*, at -0.30 V vs. Hg/HgO indicates the reduction of Mn^{4+} ions located in pyrolusite domains within the γ-MnO_2 structure.[11] The homogeneous reduction involves reducing Mn^{4+} to Mn^{3+} and inserting a proton onto an adjacent oxygen ion for charge neutrality. When reducing ramsdellite domains within the MnO_2 structures, there are two different proton locations, each with different energy.[11] However, Poinsignon *et. al.*[12] studied the reduction of MnO_2 allotropic forms (EMD, CMD, ramsdellite and pyrolusite) in 1M KOH and showed that the electron-proton insertion potential of EMD and CMD types were higher than that of the ordered and stoichiometric forms; ramsdellite and pyrolusite, due to structural disorder of intergrowth of pyrolusite and ramsdellite structural blocks and micro-twinning.

During the next electron reduction, the Mn^{3+} ions are reduced to Mn^{2+} ions and indicates in the intense and sharp peak, *C*, at potential -0.44 V vs. Hg/HgO. The peak potential value of the heterogeneous process also depends on the KOH concentration

and on the potential sweep rate.[11] At the end of reduction, the Mn^{2+} ions precipitate as $Mn(OH)_2$ phase on the surface of the graphite particles and indicates in the peak, *D*, at potential -0.55 V vs. Hg/HgO. Mn_3O_4 is formed in the heterogeneous reduction process when the experiments is carried out over an extended period, during which the partially reduced MnO_2 undergoes a chemical transformation resulting in the heterogeneous formation of Mn_3O_4.[13]

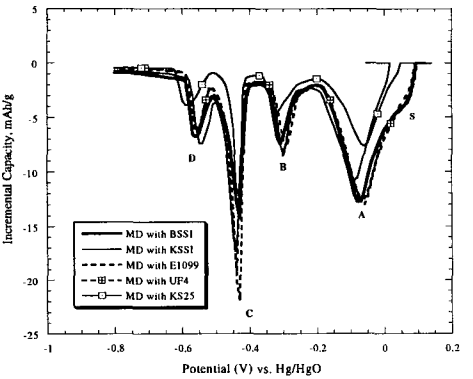

Figure 2. Reduction voltammograms of MnO_2 (EMD type: TA) with natural and synthetic graphite in 9M KOH, scanning rate of 10 mV h^{-1}.

The main effect of the mix valence state influenced by the presence of Mn^{3+} into generate electronic exchange interactions which do not allow to deintercalate Mn^{3+} and Mn^{4+} ions in the starting material. This mix valence state exits until $MnO_{1.75}$. It is due to variation of *a*, *b*, and *c* parameters during topotactic reduction in KOH $\leq$ 1M, vary slowly and this range corresponds to reversible reduction. Rechargeable Zn/MnO_2 alkaline batteries use this property, for that reason this reduction potential is limited.

3.3. The fraction of one electron capacity or reduction yield

The fraction of one electron capacity can be defined as the reduction yield or the rate of reduction. Fig. 3 shows that the fraction of one electron capacity vs. potential of the EMD with different types of natural and synthetic graphite. The four plateaus at *A*, *B*, *C* and *D* indicate the reduction of TA grade at different domains but three plateaus at *A*, *B* and *C* are only observed for TC grade. The reduction yield (about 50%) confirms the good reduction of the electron-proton insertion process. The reduction yield, about 100% is observed during the heterogeneous reduction of Mn^{3+} to Mn^{2+} ions. The highest reduction yield (more than 100%) is observed for EMD with TA and TC grades with the natural graphite from Sri Lanka, Madagascar and Krömful.

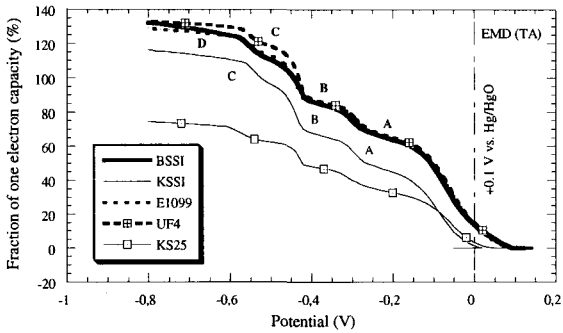

Figure 3. Graphs between the fraction of one electron capacity (%) vs. potential for reduction of MnO_2 (TA) with natural and synthetic graphite in 9M KOH at a scanning rate of 10 mV h^{-1}.

3.4. Effect of natural and synthetic graphite on manganese dioxide electrode behavior

During the homogenous and heterogeneous reduction reactions, the current response of graphite (BSSI, KSSI and KS25) were decreased dramatically and showed a high degree of reduction. At a high content of graphite (75%), the electronic path to MnO_2 particles directly contacted by graphite was quite rich. Fig. 3 clearly shows that the reduction of MnO_2 mainly depend on the type of graphite (natural and synthetic) and the crystallography characteristics. However, that Sri Lanka vein graphite shows good reduction ability.

The particle size of the graphite is an important parameter to determine the overall performance of the MnO_2 reduction. Generally, electronic path among the EMD grains is controlled by the grain size and shape of the graphite powder. The reduction voltammogram figures show that the particle size of graphite, which is related to the geometric surface area, having significant effect on both homogenous and heterogeneous reduction processes. During the both reduction process, the sharp peak indicating high reduction was observed only for large particle size of graphite (more than 24 μm). The particle size of the KS25 graphite consists of 94% of particles less than 24 μm. This is mainly due to increase the geometric interface with the electrolyte and MnO_2 (EMD) particles. The geometric interface between the MnO_2 and electrolyte can be used to interpret the changes in heterogeneous reduction. Small MnO_2 particles have a relatively large surface area available for Mn^{2+} dissolution to occur.[13] However, KS44 graphite is the best graphite, consists of 94% of particles less than 44 μm, which is used for the alkaline battery industry.

3.5. Electrochemical characterization: Galvanostatic reduction of MnO_2

Fig. 4 shows that the galvanostatic reduction of MnO_2 (EMD type: TA) with natural, KSSI at current rate of 0.75 mA g^{-1}. As expressed above, reversibility occurs if reduction potential can be controlled. In Fig. 5, reduction must concern only the part of Ueq to *A* reduction curve. After that, three plateaus are observed at -0.27 V (P-Q), -0.42 V (R-S) and -0.52 V (T-U) vs. Hg/HgO, which indicate the irreversible phase transition in heterogeneous reduction process.

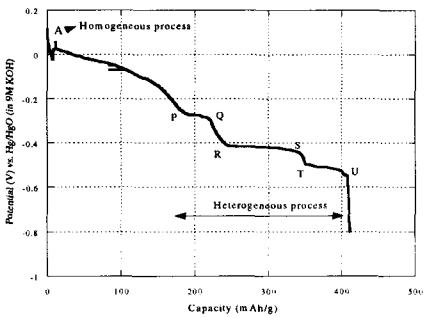

Figure 4. Galvanostatic reduction of MnO_2 (EMD type: TA) with natural (KSSI) graphite in 9M KOH, at specific current of 0.75 mA g^{-1} (current regime of C/250).

The potentiostatic reduction peaks of *C* and *D* in heterogeneous process are confirmed by the galvanostatic results.

The rechargeable zinc/alkaline-EMD with KSSI graphite cell, at current rate 15 mA g^{-1}, indicate that the cell has highest capacity on the first cycle, and that charge and discharge capacities values are about 47 and 32 mAh g^{-1} respectively. However, the theoretical capacity of MnO_2 is about 310 mAh g^{-1}.

The performances of Zn-MnO_2/ graphite batteries are not satisfactory. This may be due to the fact that the current regime used for the experiments is relatively fast for MnO_2. And also the potential range did not limit only to the homogeneous reduction process.

4. Conclusions

The reductions of composite electrodes of manganese dioxide (EMD type) with different types of natural or synthetic graphite in 9M KOH aqueous solution under potentiostatic control show reduction peaks at low scanning rates indicate homogenous reduction process of electron-proton insertion into EMD structure, and heterogeneous process of dissolution and precipitation.

The reduction of MnO_2 mainly depends on current rate, graphite particle size and purity, De Wolff disorder (Pr) and microtwining (Tw) values of the γ-MnO_2. Graphite is a good additive for the reduction of MnO_2 but a trace amount of Fe_2O_3 or Cu in natural graphite adversely affect the suitability of graphite as electrode materials in batteries. Therefore, the morphology and purity of Sri Lanka natural graphite has to be selected very carefully for such applications. Generally the rhombohedral phase content of natural Sri Lanka graphite is about 20% and which is higher than that of Madagascar and Krömful graphite. However, the rhombohedral defects, crystallographic characteristics and other structural defects of the graphite do not show appreciable effect on MnO_2 reduction and its electronic conductivity.

Acknowledgements

The fellowship given to NWBB by the Ministry of Foreign Affairs (MAE), France through French Embassy of Sri Lanka to carry out research work at LEPMI, INPG is greatly acknowledged.

References

1. G. Pistoria, A. and Antonini, *J. Electrochem. Soc.***144**,1553 (1997).
2. C.S. Johnson, M.F. Mansuetto, M.M.Thackeray, Y. Shao-Horn and S.A., Hackney, *J. Electrochem. Soc.*, **144**, 2279, (1997).
3. N.C.Cahoon, and P.Korver, *J. Electrochem. Soc.* **106**, 745 (1959).
4. A. Kozawa and R.A.Powers, *J. Electrochem.Soc.* **113**,870 (1966).
5. C.Julien, C.Letranchant, S.Rangan, M.Lemal, S.Ziolkiewicz, S.Castro-Gracia,L.El-Farh and M.Benkaddour, *Mater. Sci. Eng.* **B76**,145 (2000).
6. A.M.Kannan, S.Bhavaraju, F.Prado, M.Manivel Raja and A.Manthiram, *J. Electrochem. Soc.* **149 (4)**, A483 (2002).
7. P.M.De Wolff, *Acta Crystallogr.* **12**, 341 (1959).
8. Y. Chabre, and J. Pannetier, *Prog. Solid State Chem.* **23**, 1 (1995).
9. A.J. Brown, F.L. Tye and L.L., Wood, *J. Electroanal. Chem.* 122, 337 (1981).
10. D.A.J. Swinkels, K.E. Anthony, P.M. Fredericks and P.R. Osborn, *J.Electroanal.Chem.* **168**, 433 (1984).
11. S.W. Donne, G.A. Lawrance and Dom A.J. Swinkels, *J. Electrochem. Soc.* **144 (9)**,2954 (1997).
12. C. Poinsignon, J.M. Amarilla and F. Tedjar, *Solid State Ionics* 70/71, 649 (1994).
13. D.M., Holton, W.C., Maskel and F.L. Tye, *Power Sources*, L. Pearce (ed), The Paul Press, Ltd., London **10**, 247 (1985).

ELECROCHEMICAL PROPERTIES OF $LiNi_{1-(x+y)}Al_xZn_yO_2$ CATHODE MATERIALS SYNTHESIZED BY EMULSION METHOD

BOK-HEE KIM, SANG-JAE HAN, MIN-JEONG JANG, BYUNG-GUK AHN, MYONG-YOUP SOMG

Division of Advanced Materials Engineering, Research Institute of Advanced Materials Development

Chonbuk National University, 1-664-14, Duckjin-dong, Duckjin-ku, Chonju-city, Chonbuk, 561-756 South Korea

E-mail : kimbh@chonbuk.ac.kr

$LiNi_{1-(x+y)}Al_xZn_yO_2$ composition (x = 0.0-0.10, y = 0.0-0.005) substituted with Al^{3+} and Zn^{2+} was synthesized by an emulsion method and electrochemical properties were investigated. Emulsion-derived powder has porous spherical shape agglomerated with fine particles. The calcined powder was agglomerated shape with nanosized particle under 50nm. The intercalation of Li^+ is higher in $LiNi_{1-(x+y)}Al_xZn_yO_2$ than pure $LiNiO_2$. The 1st discharge capacity and fade rate for 20 cycles were 161 mAh/g, 8.5% in $LiNiO_2$, 168 mAh/g, 7.1% in $LiNi_{0.99}Al_{0.01}O_2$, 163 mAh/g, 5.5% in $LiNi_{0.995}Zn_{0.005}O_2$ and 164 mAh/g, 7.4% in $LiNi_{0.992}Al_{0.006}Zn_{0.002}O_2$ respectively.

1. Introduction

$LiMO_2$ (M=Ni, Co) type compounds have been studied intensively as cathode materials for rechargeable lithium batteries over the past two decades [1-4]. Of these, $LiNiO_2$ is one of the most promising cathode materials due to its high energy density, low cost and environmental pollution compared to $LiCoO_2$ cathode material [5,6]. However, there are some problems to apply $LiNiO_2$ as the cathode electrode because of difficulty to synthesize $LiNiO_2$ single phase due to the high vapor pressure of lithium oxide, cation mixing leading to nonstoichiometric composition $Li_{1-x}Ni_{1+x}O_2$ and unstable structure during charge-discharge process. To improve the electrochemical properties of $LiNiO_2$, several cations have been added into $LiNiO_2$ to substitute Ni. Among them, Al^{3+} is known to prevent the formation of NiO_2, enhance the stability of structure and increase the cell voltage [7,8]. In this experiment, we chose the Zn^{2+} and Al^{3+} as the substituents to become $LiNi_{1-(x+y)}Al_xZn_yO_2$ composition(x = 0.0-0.10, y = 0.0-0.005) because these atoms have one kind of stable valence and investigated the properties of this composition.

Emulsion method is well known to be very effective on the synthesis of multi-component system materials homogeneously because organic phase divides precursor solution into colloids of water-in oil type by high speed rotation. All of these colloids, that is, emulsion have sphere in shape and uniformed composition [9,10]. It suggests that crystalline solid of the multi-component system could be synthesized easily at the proper calcination temperature by the easy decomposition and reaction of the emulsion-derived powder. This emulsion method will be more preferable for the synthesis of $LiNi_{1-(x+y)}Al_xZn_yO_2$ powders than any other process. In this work, we investigated the effects of Al^{3+} and Zn^{2+} substituents on the properties of $LiNi_{1-(x+y)}Al_xZn_yO_2$ synthesized by emulsion method.

2. Experimental Procedure

The starting materials used for the synthesis of $LiNi_{1-(x+y)}Al_xZn_yO_2$ were $LiOH \cdot H_2O$ (99.95%, Aldrich Chemical Company, Inc. U.S.A), $Ni(NO_3)_2 \cdot 6H_2O$, $Al(NO_3)_3 \cdot 9H_2O$ and $Zn(NO_3)_2 \cdot 6H_2O$(99.9%, High Purity Chemicals, Japan). These materials were dissolved into distilled water and mixed on the magnetic stirrer for 24 h to prepare homogeneous precursor solution with the concentration of 0.5 mol/L for $LiNi_{1-(x+y)}Al_xZn_yO_2$ composition. Organic phase for emulsifying was prepared with same composition and same process already reported [9,10]. The precursor solution and organic phase were mixed in the ratio of 2:1 and emulsified to water-in-oil type emulsion at the rotation speed of 4000 rpm for 5 min. The emulsion was sprayed into the petroleum heated at 170℃ to evaporate water included in the emulsion rapidly, filtered and dried at 120℃ in the oven.

The emulsion-derived powder was calcined under oxygen stream at 750℃ for various times with 100℃/h heating and cooling rate. The crystal phase of the calcined powder was examined using X-ray diffractometer (XRD: Rigaku, D/MAX-111A) with CuK_α radiation operated at 40 kV, 40 mA and scanning speed of 4°/min. The shape of the particle and microstructure were observed with a scanning electron microscope (SEM: JEOL JSM-6400). The electrochemical properties of samples were tested at room temperature for 20 cycles with half cell fabricated as Li metal/electrolyte 1M $LiPF_6$-ethylene carbonate (EC) and dimethyl carbonate (DMC) (1:1 in volume)/ positive material. The positive electrode was consisted of $LiNi_{1-(x+y)}Al_xZn_yO_2$ powder as cathode material, acetylene black as conductor and PTFE as binder at the ratio of 88:10:2 by weight. Lithium foil and glass micro-fiber filter (GF/A, Whatman) were used for anode and separator, respectively. The cells were automatically charged and discharged between 2.7 and 4.2 V at 9.5 mA/g.

3. Results and Discussions

3.1. The characteristics of powder

Fig. 1 shows that SEM photographs of the as-dried and calcined powder at 400℃ of $LiNiO_2$ composition selected as one sample because other materials are also almost same shape due to adopting same process to prepare powder. The as-dried powder has the porous spherical shape agglomerated with small particles because this powder was dried by spraying the emulsion into the petroleum heated at 170℃. But the calcined powder has a shape agglomerated with nanosized particles under 50nm. This powder could be reacted easily each other to form $LiNiO_2$ at lower temperature comparatively because each particle has same composition and nanometer size. These are the characteristics of emulsion method which is used to prepare the powder by dividing homogeneous precursor solution into colloid using organic phase [9,10].

$LiNiO_2$ (x = y =0 in $LiNi_{1-(x+y)}Al_xZn_yO_2$) was synthesized at 750℃ for 24h [11], but others were at 750℃ for 36h [12], because the highest discharge capacity of each composition was obtained at each condition respectively. XRD patterns of $LiNi_{1-(x+y)}Al_xZn_yO_2$ synthesized at these conditions are shown in

Fig. 1. All these patterns were identified as single phase of $LiNO_3$ type crystal structure without any other unreacted crystal phase.

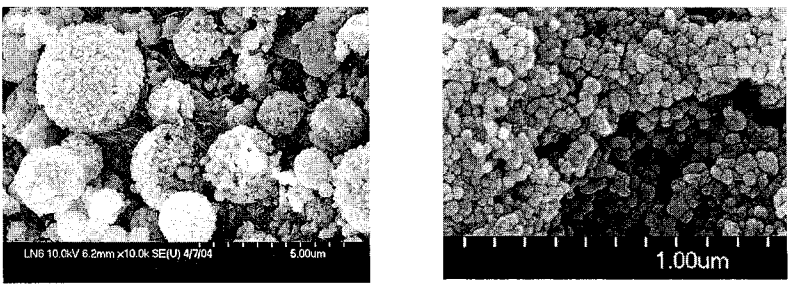

(a) As-dried powder (b) Calcined powder

Fig. 1. SEM photographs of powders of as-dried and calcined at 400℃.

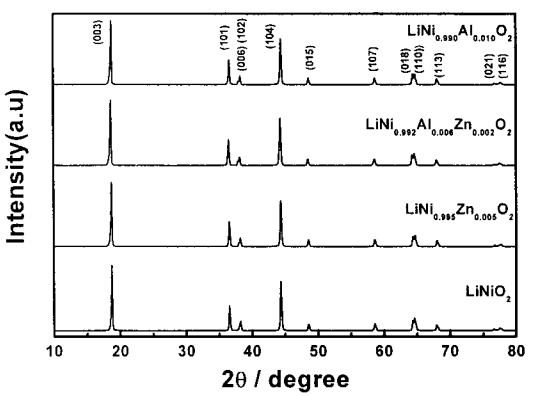

Fig. 2. XRD patterns of $LiNi_{1-(x+y)}Al_xZn_yO_2$ powder synthesized at 750℃.

3.2. Electrochemical properties

The charge-discharge profiles of $LiNi_{1-(x+y)}Al_xZn_yO_2$ were investigated with Al and Zn substitution. Fig. 2 shows the first charge-discharge curves $Li//LiNi_{1-(x+y)}Al_xZn_yO_2$ cells operated between 2.7-4.2V. The deintercalation and intercalation of Li^+ are around 0.74, 0.59 in $LiNiO_2$, 0.70, 0.61 in $LiNi_{0.99}Al_{0.01}O_2$, 0.75, 0.60 in $LiNi_{0.995}Zn_{0.005}O_2$ and 0.73, 0.60 in $LiNi_{0.992}Al_{0.006}Zn_{0.002}O_2$ respectively. The deintercalation

amount of Li^+ in $LiNiO_2$ is high as 0.74 but the lowest value, 0.59 in intercalation than any other compositions. It is considered that excess deintercalation of Li^+ affected the crystal structure stability. Unstabilized crystal structure due to excess deintercalation make Li^+ difficult to intercalate into $LiNiO_2$ crystal. However the deintercalation, 0.70 of Li^+ in $LiNi_{0.99}Al_{0.01}O_2$ is not high but intercaltion is higher than any other materials. It could be considered that crystal structure of $LiNi_{0.99}Al_{0.01}O_2$, is more stable than $LiNiO_2$ due to the fixed atomic valance of Al^{3+}. This stable structure makes Li^+ intercalate into crystal structure easily and good cycle life of charge-discharge property could be expected from deintercalation and intercalation reaction. The deintercalation of Li^+ in $LiNi_{0.995}Zn_{0.005}O_2$ and $LiNi_{0.992}Al_{0.006}Zn_{0.002}O_2$ is similar to $LiNiO_2$ but higher than $LiNi_{0.99}Al_{0.01}O_2$. However intercalation is higher than $LiNiO_2$ but lower than $LiNi_{0.99}Al_{0.01}O_2$. These results could be considered that the substitution

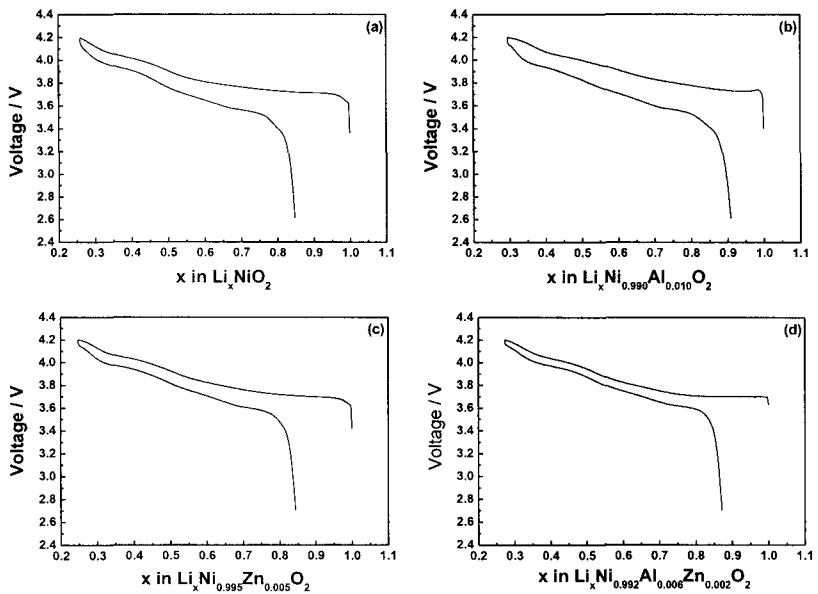

Fig. 3. First charge-discharge profiles of $LiNi_{1-(x+y)}Al_xZn_yO_2$.

of Ni with Zn^{2+} in $LiNiO_2$ also makes the crystal stable as Al^{3+} substitution but Zn^{2+} produces more Ni^{4+} in the structure. This Ni^{4+} would generate Li^+ deintercalation more in this composition.

The 1st discharge capacities were measured and are shown in Fig. 4. The 1st discharge capacities are 161 mhA/g in $LiNiO_2$, 168 mhA/g in $LiNi_{0.99}Al_{0.01}O_2$, 163 mhA/g in $LiNi_{0.995}Zn_{0.005}O_2$ and 164 mhA/g in $LiNi_{0.992}Al_{0.006}Zn_{0.002}O_2$ respectively. The discharge capacity has relation with crystal structure stability of

cathode material as discussed above because discharge capacity is the amount of intercalation of Li^+. The substitution of Al^{3+} and Zn^{2+} in $LiNiO_2$ make this crystal structure more stable due to the fixed atomic valence of these atoms. On the other hand, Ni has various atomic valences such as 3+ and 4+. Various valences of Ni give $LiNiO_2$ ionic conductivity but also make its structure unstable. However the substitution of Al^{3+} and Zn^{2+} in $LiNiO_2$ lower conductivity of this material because this substitution make insulator. These substitutions could make the charge-discharge cycle life stable compared to pure $LiNiO_2$ by substituting optimum amount of Al and Zn which make crystal structure stable.

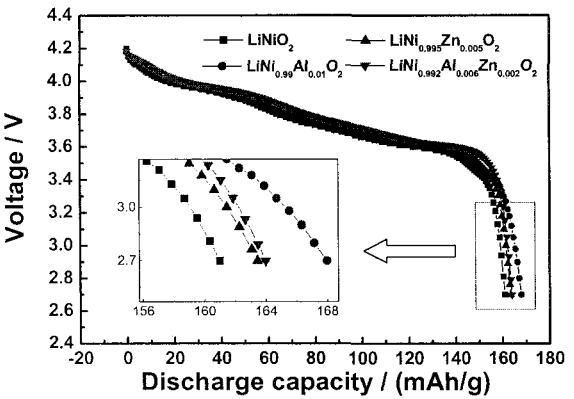

Fig. 4. The 1st discharge capacities of $LiNi_{1-(x+y)}Al_xZn_yO_2$.

Fig. 5 shows the 1st and 2nd derivative capacities of Li//$LiNi_{1-(x+y)}Al_xZn_yO_2$ cell between 2.7 and 4.2V. Pure $LiNiO_2$ and other materials which substituted Ni with Al^{3+} and Zn^{2+} in $LiNiO_2$ have phase transition at the almost same voltage region during charge-discharge. It is considered that substitution amount of Al^{3+} and Zn^{2+} in $LiNiO_2$ is too small to change transition voltage. However phase transition in the 2nd charge was occurred at the lower voltage, 3.67~3.68 V compared to 3.72~3.70 V in the 1st charge. It is well known that the multi-phase transitions and voltage change in $LiNiO_2$ lead to structural change, resulting eventual degradation of electrode performance [13,14].

The discharge capacity cyclabilities of the Li// $LiNi_{1-(x+y)}Al_xZn_yO_2$ cells up to 20 cycles are shown in Fig. 6 and discharge capacity fade rate after 20 cycles is in Table 1. The 1st and 20th discharge capacities are 161, 147 mAh/g in $LiNiO_2$, 168, 156 mAh/g in $LiNi_{0.99}Al_{0.01}O_2$, 163, 154 mAh/g in $LiNi_{0.995}Zn_{0.005}O_2$ and 164, 151 mAh/g in $LiNi_{0.992}Al_{0.006}Zn_{0.002}O$ respectively. From these capacity changes for 20 cycle, fade rate is obtained as 8.5% in $LiNiO_2$, 7.1% in $LiNi_{0.99}Al_{0.01}O_2$, 5.5% in $LiNi_{0.995}Zn_{0.005}O_2$ and 7.4% in $LiNi_{0.992}Al_{0.006}Zn_{0.002}O_2$ respectively. The discharge capacity cyclability of the composition substituted by

Al^{3+} and Zn^{2+} is more stable than pure $LiNiO_2$. The fade of discharge capacity is considered to be related with crystal structure stability closely as expected by the 1st charge-discharge profile.

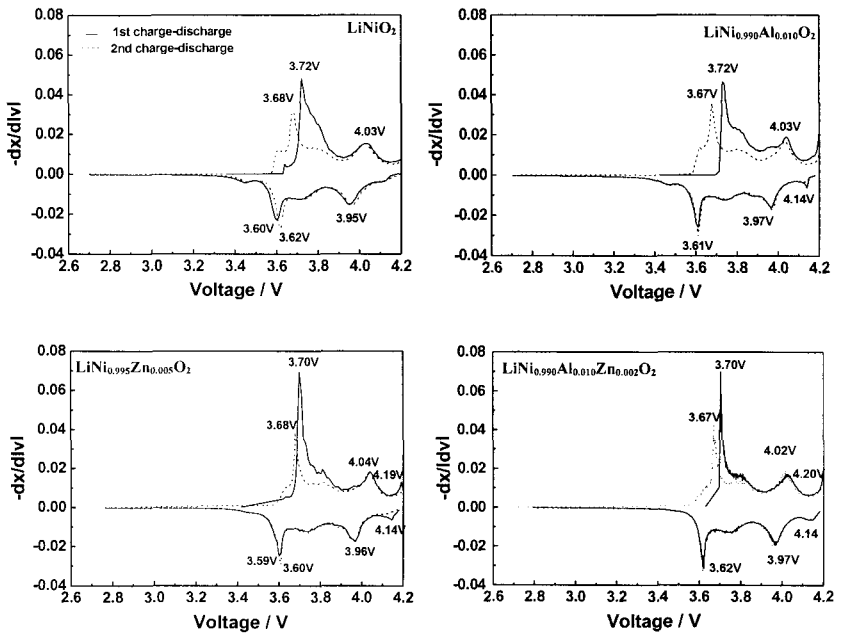

Fig. 5. Plot of the 1st and 2nd derivative capacities of Li//$LiNi_{1-(x+y)}Al_xZn_yO_2$ cells between 2.6 and 4.2V.

Table 1. Fading rate of cathode materials after 20 charge-discharge cycles.

Cathode material	$LiNiO_2$	$LiNi_{0.99}Al_{0.01}O_2$	$LiNi_{0.995}Zn_{0.005}O_2$	$LiNi_{0.992}Al_{0.006}Zn_{0.002}O_2$
Fading rate(%)	8.5	7.1	5.5	7.4

The intercalations of Li^+ are around 0.59 in $LiNiO_2$, 0.61 in $LiNi_{0.99}Al_{0.01}O_2$, 0.60 in $LiNi_{0.995}Zn_{0.005}O_2$ and 0.60 in $LiNi_{0.992}Al_{0.006}Zn_{0.002}O_2$. The 1st, 20th discharge capacity and fade rate are 161, 147 mAh/g, 8.5% in $LiNiO_2$, 168, 156 mAh/g, 7.1% in $LiNi_{0.99}Al_{0.01}O_2$, 163, 154 mAh/g, 5.5% in $LiNi_{0.995}Zn_{0.005}O_2$ and 164, 151mhA/g, 7.4% in $LiNi_{0.992}Al_{0.006}Zn_{0.002}O_2$ respectively. The composition of $LiNi_{1-(x+y)}Al_xZn_yO_2$ substituted by Al^{3+} and Zn^{2+} has the higher intercalation of Li^+, higher discharge capacity and lower fade rate than pure $LiNiO_2$. These results suggest that substituting Ni with optimum amount of Al^{3+} and Zn^{2+} in $LiNiO_2$ make the crystal structure stable, higher the discharge capacity and lower the fade

rate of discharge capacity due to the fixed atomic valence.

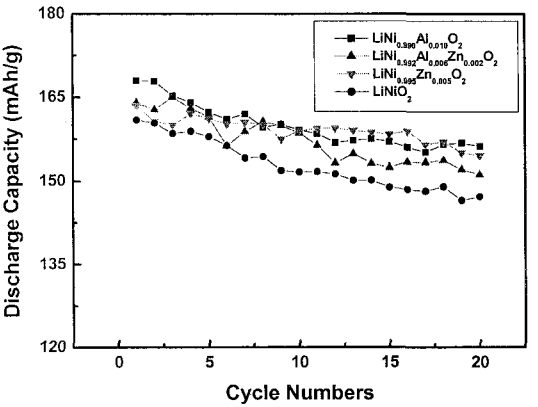

Fig. 6. The discharge capacity cyclability of the Li// $LiNi_{1-(x+y)}Al_xZn_yO_2$ cells.

4. Conclusion

$LiNi_{1-(x+y)}Al_xZn_yO_2$ composition (x = 0.0-0.10, y = 0.0-0.005) substituted with Al^{3+} and Zn^{2+} was synthesized by an emulsion method and electrochemical properties were investigated.

Emulsion-derived powder has porous spherical shape agglomerated with fine particles. The calcined powder was agglomerated shape with nanosized particle under 50nm. The intercalation of Li^+ is higher in $LiNi_{1-(x+y)}Al_xZn_yO_2$ than pure $LiNiO_2$. The 1st discharge capacity and fade rate for 20 cycles 161 mAh/g, 8.5% in $LiNiO_2$, 168 mAh/g, 7.1% in $LiNi_{0.99}Al_{0.01}O_2$, 163 mAh/g, 5.5% in $LiNi_{0.995}Zn_{0.005}O_2$ and 164 mAh/g, 7.4% in $LiNi_{0.992}Al_{0.006}Zn_{0.002}O_2$ respectively.

Acknowledgement

This work was supported by grant No. R01-2003-000-10325-0 from the Basic Research Program of the Korea Science & Engineering Foundation.

References

[1] D. Guyomard, J. M. Tarascon, Solid State Ionics 69, 222 (1994)

[2] R. J. Gummow, A. de Kock, M. M. Thackeray, Solid State Ionics 69, 59 (1994)

[3] Liquan Chen, Xuejie Huang, Erix Kelder, Joop Schoonman, Solid State Ionics 76, 91 (1995)

[4) D. Guyomard and J. M. Tarascon, J. Electrochem. Soc. 139(4), 937 (1992)

[5] T. Ohzuku, A. Ueda, Solid State Ionics 69, 201 (1994)

[6] M. Broussely, F. Perton, P. Biensan, J.M. Bodet, J. Labat, A. Lecerf, C. Delmas, A.Rougier, J.P. Peres, J. Power Sources 54, 109 (1995)

[7] T. Ohuzuku, A. Ueda, M. Kouguchi, J. Electrochem. Soc. 142(12), 4033 (1995)

[8] O. Zhong, U. von Sacken, J. Powder Sources 54, 221 (1995)

[9] Y.-K. Choi and B.-H. Kim, J. Ceram. Soc. of Japan 1255, 261 (2000)

[10] B.-H. Kim, J.-W. Moon, J.-Y. Lee, Y.-K. Choi, J. Ceram. Soc. of Japan 1242, 115 (1999)

[11] Bok-Hee Kim, Jong-Hwan Kim, Ik-Hyun Kwon, Myoung-Youp Song, Ceramics International 2006 (in press) Elsevier

[12] Jong-Whan Kim, Thesis of M.S. in Chonbuk National University (2005)

[13]. A.J. Berlinsky, W.G. Unruh, W.R. Mckinnon and R.R. Haering, Solid State Commun. 31, 135 (1979)

[14]. J.R. Dahn, E.W. Fuller, M. Obrovac, U. von Sacken, Solid State Ionics 69, 265 (1994)

$LINI_{0.80}Co_{0.20}O_2$ CATHODE MATERIALS SYNTHESIZED BY PARTICULATE SOL-GEL METHOD FOR LITHIUM ION BATTERIES

X. J. ZHU, W. ZHANG, X. Y. GAN, C. HU, M. H. CAO, D. B. LUO, Q.XU, W. CHEN, J. ZHOU AND H. X. LIU*

State Key Laboratory of Advanced Technology for Materials Synthesis and Processing, Wuhan University of Technology, Wuhan, Hubei 430070, China

* ***Email:*** *lhxhp@mail.whut.edu.cn*

A particulate sol-gel (PSG) method has been successfully developed to prepare $LiNi_{0.80}Co_{0.20}O_2$ cathode materials, utilizing the reaction of $LiOH \cdot H_2O$ with $Ni(CH_3COO)_2 \cdot 4H_2O$ and $Co(CH_3COO)_2 \cdot 4H_2O$ in water-ethanol system. The thermal history of the as-prepared xerogel was established by thermogravimetric analysis (TGA) and differential thermal analysis (DTA). Powder X-ray diffraction (XRD) confirmed the formation of well-layered α-$NaFeO_2$ structure at temperature of 700 ℃ under flowing oxygen. Scanning electron microscope (SEM) exhibited that the crystalline powder prepared by PSG method had relatively smaller particle size with narrow distribution than the one prepared by solid-state reaction. The first discharge capacity of the material prepared by PSG method was 193.5 mAh/g, and the 15th discharge capacity was 185.1 mAh/g at the current density of 18 mA/g between 3.0 and 4.3 V. Its cycling reversibility was observed to be much better than that of the one by solid-state reaction, which had 182.9 mAh/g of the first discharge capacity and 162.0 mAh/g of the 15th discharge capacity

1. Introduction

Lithium transition metal oxides have attracted much interest due to their possible use as cathode materials for lithium ion batteries [1-5]. $LiCoO_2$ and $LiNiO_2$ are isostructural, having layered structure of α-$NaFeO_2$ type [6]. $LiCoO_2$ has been commercialized, whereas $LiNiO_2$ has not, mostly because preparation of $LiCoO_2$ is easier, and its reliability (safety) is better than $LiNiO_2$'s [7]. Even though its preparation is more difficult, $LiNiO_2$ has several advantages over $LiCoO_2$: higher specific capacity, cheaper price and less environmental pollution [8]. However, solid solutions involving both $LiCoO_2$ and $LiNiO_2$, layered cathode materials of the general formula $LiNi_{1-x}Co_xO_2$ ($0<x<1$) have been scrutinized for possible commercial applications [9-11]. These solid solutions enjoy the advantages of both the end members with better cyclability and safety aspects.

The synthesis route adopted to prepare cathode materials has a direct impact on their electrochemical performance for lithium ion batteries. Traditionally, $LiNi_{1-x}Co_xO_2$ solid solutions were synthesized using the conventional solid-state reaction, which involves very high temperatures for a prolonged period of time with

intermediate grinding. It led to problems with poor stoichiometry control, non-homogeneity. In recent years, low temperature wet chemistry methods of synthesizing cathode active materials gained importance [12], because they can produce small particles with homogeneous distribution and high surface area, which deliver better cell performance. Many cathode materials have been synthesized using the low temperature methods for lithium ion battery applications [13].

In this paper, a modified route called particulate sol-gel (PSG) method has been developed for synthesizing $LiNi_{0.80}Co_{0.20}O_2$. The PSG method is based on using metal carbolysis in a mixture of aqueous or non-aqueous solvents. Due to the formation of single or connected oligomers, the PSG method offers all the advantages and characteristics of the sol-gel process. The structural and electrochemical properties of the synthesized materials were investigated. Furthermore, the microstructure and electrochemical performance of the material synthesized by PSG method were compared with those synthesized by the conventional solid-state reaction.

2. Experimental

$LiNi_{0.80}Co_{0.20}O_2$ were synthesized according to the route shown in Fig.1. $LiOH \cdot H_2O$, $Ni(CH_3COO)_2 \cdot 4H_2O$ and $Co(CH_3COO)_2 \cdot 4H_2O$ in reagent grade, corresponding to a molar ratio of Li:Ni:Co=1.03:0.80:0.20 were first dissolved in deionized water separately to obtain clear solutions. The LiOH solution was added drop by drop into a continuously agitated aqueous solution of $Ni(CH_3COO)_2$ and $Co(CH_3COO)_2$, resulting in pale green colored suspensions. Ethyl alcohol was then added to the solution to facilitate removal of the liquid products. The resulting solution was agitated using a magnetic stirrer and heated at 80 ℃ until it turned out to be a gel. The gel was dried at 120 ℃ for 12 h to become xerogel. Thermal decomposition behavior of the xerogel was examined by thermogravimetric analysis (TG) and differential thermal analysis (DTA, NETZSCH STA 449C, Germany) under flowing oxygen (20 ml/min) at a heating rate of 10 ℃/min. Based on the results of TG/DTA results, the heat treatment temperatures were chosen. Powder X-ray diffraction (XRD, D/MAX-RB, RIGAKU, Japan) measurement using CuK α radiation was employed to characterize the structures of the synthesized powders. Particle morphology of the powders after calcinations was observed using scanning electron microscope (SEM, JSM-5610LV). Rietveld refinement was performed with the XRD data to obtain lattice parameters of the synthesized powders.

The electrochemical performance was studied by assembling 2016 coin-type cells. The cathodes were fabricated by slurring the mixture of 80wt% synthesized material, 15wt% acetylene black and 5wt% PTFE binder using *n*-propanol as a solvent. After rolling the mixture to be a membrane, a circular disc of 1.6 cm in diameter from the membrane was cut out and pressed onto stainless steel mesh as a

current collector, and then dried at 80 ℃ for 12 h in vacuum. The cells were assembled using lithium metal as an anode and 1M $LiClO_4$ in EC-DMC (1:1 by volume) as an electrolyte in an argon-filled glove box. The charge-discharge cycles were carried out at room temperature at a current density of 18 mA/g with cut-off voltage of 3.0 to 4.3 V (vs. Li/Li^+).

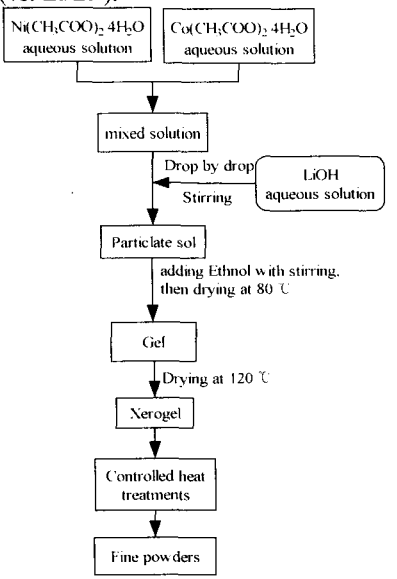

Figure 1. Synthetic procedure of $LiNi_{0.80}Co_{0.20}O_2$ powders by PSG method.

3. Results and discussion

3.1. *Synthesis and characterization*

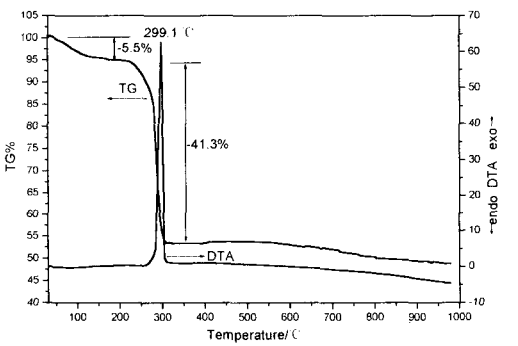

Figure 2. TG/DTA curves for the xerogel precursor at the heating rate of 10 ℃/min in flowing oxygen (20 ml/min)

Fig.2 shows the TG/DTA patterns of the as-prepared xerogel. A 5.5% weight loss prior to 220 ℃ was attributed to the evaporation of either residual water contained in the xerogel or the absorption of moisture by the xerogel powder prior to its analysis. At 220 ℃, the xerogel which were composed of metal acetates, hydroxides and hydroxyl-acetates began to decompose, resulting in a significant weight loss of about 41.3% until the temperature reached 300 ℃. There was a minor weight increasing between 300 and 600 ℃, corresponding to the oxidation of NiO and CoO as well as Li_2CO_3 decomposition. Between 600 and 700 ℃, TG curve was almost flat, corresponding to the formation of crystalline powder. After 700 ℃, the minor weight loss was due to the decomposition of as-formed product or the formation of other crystallinity. DTA analysis revealed the evolution of a sharp exothermic peak at about 299.1 ℃, corresponding to the rapid decomposition of the xerogel. No other sharp endothermic peak was observed except the one at 299.1 ℃, indicating that the xerogel was chemical homogenous during mixing [14]. Considering that insignificant weight loss was observed from 600 ℃ to 750 ℃, we select the range of temperature for the crystallization of the amorphous xerogel.

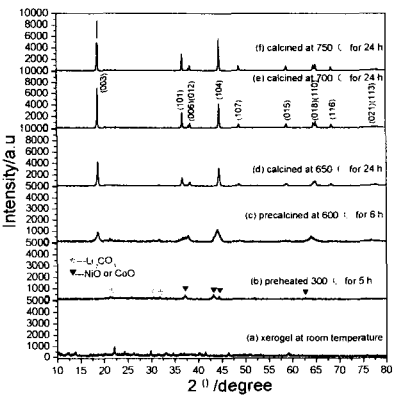

Figure 3. XRD patterns of the xerogel during heat treatment.

Fig.3 shows XRD patterns for the xerogel preheated, precalcined and calcined at various temperatures under flowing oxygen. Fig.3a shows that the xerogel powder at room temperature was mostly consisted of metal acetates, hydroxides and hydroxyl-acetates in that there were no great diffraction peaks. The xerogel preheated at 300 ℃ for 5 h was poor crystalline. Meanwhile, crystalline phase of Li_2CO_3, NiO and CoO were observed in Fig.3b. When the mixture was precalcined at 600 ℃ for 6 h after preheated at 300 ℃, Fig.3c revealed the initiation of layered $LiNi_{0.80}Co_{0.20}O_2$ structure. Fig.3d ~ f show the XRD patterns of the products prepared under different calcination temperatures. It was clear that XRD patterns conformed to the α-$NaFeO_2$ layered structure. For the material calcined at 650 ℃ after precalcined at 600 ℃, the diffraction peaks were broad, indicating low

crystalline of the material. Also, the hexagonal lattice ordering was incomplete at this temperature as further confirmed by the intensity ratio 100/75 of the (003)-(104) peak pair and the splitting degree of (018)-(110) peak pair. It has been reported [15] that the intensity ratio I_{003}/I_{104} of (003)-(104) peak pair should be more than 1.2, and the extent of (018)-(110) peak splitting is a reliable quantitative criterion for the determination of electrochemical activity of nickel-rich $LiNi_{1-x}Co_xO_2$. Hence, it was clear that the calcination temperature of 650 ℃ was not sufficient to impart the hexagonal ordering required for better electrochemical performance. As the calcination temperature was increased to 700 ℃, there was a remarkable improvement in crystallinity of the material as indicated by the sharp peak profile in Fig.3e. The I_{003}/I_{104} ratio increased to 100/56, and (018)-(110) and (006)-(012) were obvious resolution. Further increasing the calcination temperature to 750 ℃, the I_{003}/I_{104} became 100/60 and it was lower than that of the one at 700 ℃.

Table 1 Crystal parameters for $LiNi_{0.80}Co_{0.20}O_2$ synthesized at various temperatures

Temperature/(℃)	a/(Å)	c/(Å)	c/a	Unit cell volume/(Å^3)	I_{003}/I_{104}
650	2.879	14.217	4.939	102.01	100/75
700	2.866	14.174	4.945	100.85	100/56
750	2.868	14.181	4.944	100.98	100/60

Table 1 is the crystal parameters for $LiNi_{0.80}Co_{0.20}O_2$ synthesized at various temperatures. According to Dahn et al. [16], the hexagonal unit cell volume indicates the ordering of the layered structure. If it is lower, the structure is more layered. For the material calcined at 700 ℃ for 24 h, the unit cell volume was 100.85 Å^3, whereas it was 102.01 or 100.98 Å^3 for the material calcined at 650 or 750 ℃, respectively. Based on the results, it can be concluded that the optimal temperature required for complete hexagonal ordering was 700 ℃.

The microstructure of $LiNi_{0.80}Co_{0.20}O_2$ powders is shown in Fig.4. The particle powder obtained by PSG method exhibited an edge-smooth morphology within less-agglomerated grain and small size (Fig.4a and b). In comparison with the $LiNi_{0.80}Co_{0.20}O_2$ powder synthesized by the solid-state reaction, which showed a faceted shape with a wide particle size distribution (Fig.4c and d), it was obvious that the PSG method significantly reduced the particle size of $LiNi_{0.80}Co_{0.20}O_2$ powder, and resulted in a uniform morphology and a narrow distribution. The coarsening of the powder in the solid-state reaction was mainly caused by the higher temperature and larger grain of starting mixture used. As a consequence, the PSG method was confirmed to be an effective method to synthesize powder with a smaller particle size and narrow size distribution.

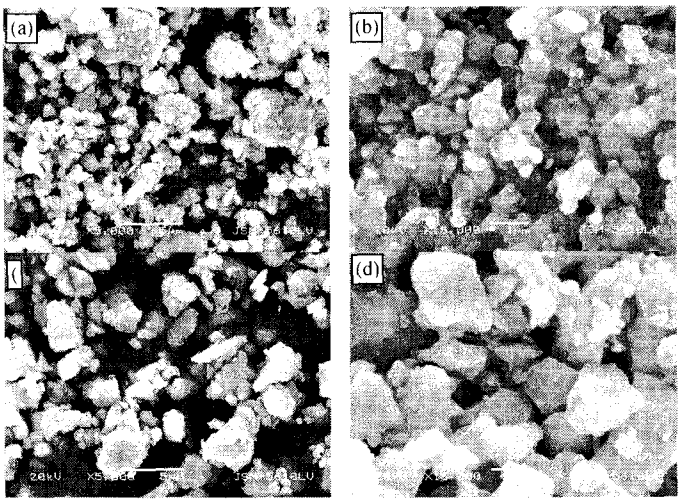

Figure 4. SEM micrograph of $LiNi_{0.80}Co_{0.20}O_2$ prepared by (a) (b) PSG method and (c) (d) solid-state reaction at a magnification of 5,000 and 15,000, respectively.

3.2. *Electrochemical properties*

The cycling performance of the synthesized materials at 650, 700 and 750 ℃ were shown in Fig.5.

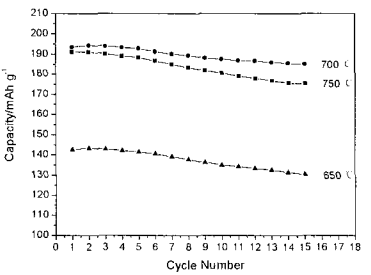

Figure 5. Variation of discharge capacity with respect to cycle number for $LiNi_{0.80}Co_{0.20}O_2$ synthesized by PSG method at different temperatures.

Charge-discharge studies were performed galvanostatically at the current density of 18 mA/g between 3.0 and 4.3 V. The cycling property of the material calcined at 650 ℃ for 24 h showed inferior capacity because of its lower crystalline and lack of hexagonal ordering, as supported by X-ray diffraction results. Its first discharge capacity was 142.5 mAh/g and the 15th discharge capacity was 130.4 mAh/g. When the calcination temperature was increased to 700 ℃, the discharge capacity increased to 193.5 mAh/g for the first cycle and 185.1 mAh/g after 15 cycles. As indicated by X-ray diffraction results, the system became more layered at

700 ℃, and the *3b* lithium and *3a* transition metal ion sites in the layered α-$NaFeO_2$ structure became ordered, facilitating the intercalation-deintercalation process.

Further increasing the calcination temperature to 750 ℃ led to a decrease in capacity with the first and the 15th discharge capacities of 191.1 and 175.2 mAh/g, respectively. The decrease in electrochemical performance of the material calcined at 750 ℃ was mainly attributed to the loss of lithium volatilization due to the higher temperature. The structural studies indicated a decrease in hexagonal ordering when the calcination temperature was increased to 750 ℃. Hence, based on the structural and electrochemical studies, it was clear that the optimal calcination temperature for better performance was 700 ℃.

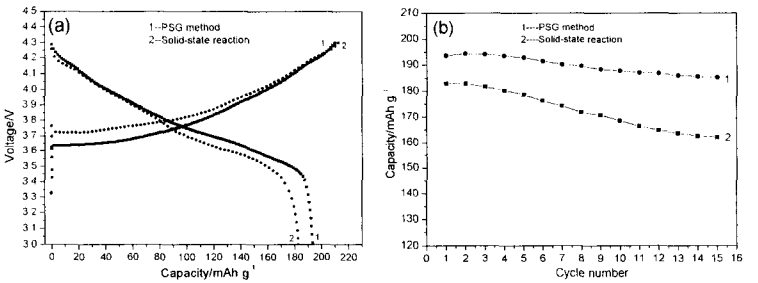

Figure 6. (a) First charge-discharge profiles and (b) discharge capacity vs. cycle number for $LiNi_{0.80}Co_{0.20}O_2$ synthesized by PSG method (1) and by solid-state reaction (2).

Fig. 6a shows the initial charge-discharge curves for $LiNi_{0.80}Co_{0.20}O_2$ synthesized by PSG method at 700 ℃ and by solid-state reaction at a constant current density of 18 mA/g in the voltage range of 3.0~4.3 V. In the case of the sample synthesized by PSG method, the average voltages for the first charge and discharge cycle were obtained 3.84 V and 3.76 V, respectively, compared to 3.89 V, 3.71 V for the sample by solid-state reaction. From the calculation of the average voltage, it was clearly seen that the average charge voltage of the sample by PSG method was somewhat lower and the average discharge voltage was somewhat higher than those of the one by solid-state reaction, respectively. Although their initial charge capacities were almost the same, the initial discharge capacity of the sample (193.5 mAh/g) by PSG method was higher than that of the one (182.9 mAh/g) by solid-state reaction. That was to say, the charge-discharge efficiency of the sample by PSG method was higher than that of the one by solid-state reaction. The cyclability (up to 15 cycles) of $LiNi_{0.80}Co_{0.20}O_2$ by PSG method and by solid-state reaction is shown in Fig. 6b. The $LiNi_{0.80}Co_{0.20}O_2$ by PSG method showed a first discharge capacity of 193.5mAh/g and a 15th discharge capacity of 185.1 mAh/g, compared to 182.9 mAh/g and 162.0 mAh/g for the one by solid-state reaction, respectively. It was observed that the property of $LiNi_{0.80}Co_{0.20}O_2$ synthesized by solid-state reaction deteriorated fast during cycling. Its discharge capacity decreased nearly 20 mAh/g after 15 cycles. On the contrary, the $LiNi_{0.80}Co_{0.20}O_2$ prepared by PSG method exhibited very good cycle reversibility. The decrease of discharge

capacity from 193.5 to 185.1 mAh/g during consecutive 15 cycles was 8.4 mAh/g. This may be explained on the initial formation of xerogel complex, which decided the homogeneity and smaller particle size of the $LiNi_{0.80}Co_{0.20}O_2$ by PSG method, compared to that by solid-state reaction.

4. Conclusions

The particulate sol-gel (PSG) method was developed for synthesizing $LiNi_{0.80}Co_{0.20}O_2$. The PSG precursor was well mixed at the molecular level. X-ray diffraction analysis confirmed the formation of the good layered α-$NaFeO_2$ structure for $LiNi_{0.80}Co_{0.20}O_2$ at the temperature of 700 ℃ for 24 h under flowing oxygen. It delivered a 193.5 mAh/g of initial discharge capacity and 185.1 mAh/g of the 15^{th} discharge capacity between 3.0 and 4.3 V at a current density of 18 mA/g.

Acknowledgments

This work was supported by the National Natural Science Foundation of China (No. 20371038), and the Foundation for Innovative Research Team of Hubei Province(No. 2005ABC004)

References

1. Z.S. Zheng, Z.L. Tang, Z.T. Zhang, J.B. Lu and W.C. Shen, *J. Mater. Sci. Technol.* **4**, 359 (2003).
2. T. Ohzuku and A. Ueda, *Solid State Ionics* **69**, 201 (1994).
3. C.H. Lu and W.C. Lee, *Materials Letters* **40**, 103 (1999).
4. S. Gopukumar, K.Y. Chung and K.B. Kim, *Electrochimica Acta* **49**, 803 (2004).
5. S. Kobayashi, T. Usui, H. Ikuta, Y. Uchimoto and M. Wakihara, *J. Mater. Res.* **19**, 2421 (2004).
6. T.A. Hewston and B.L. Chamberland, *J. Phys. Chem. Solids* **48**, 97 (1987).
7. H. Arai, S. Okada and Y. Sakurai, *Solid State Ionics* **109**, 295 (1998).
8. M. Broussely, F. Perton, P. Biensan, J.M. Bodet, J. Labat, A. Lecerf, C. Delmas, A. Rougier and J.P. Peres, *J. Power Sources* **54**, 109 (1995).
9. X.J. Zhu, H. Zhan and Y.H. Zhou, *Acta Chim. Sinica* **60**, 1742 (2002).
10. K.I. Gnanasekar, H.A. Cathrino, J.C. Jiang, A.A. Mrse, G. Nagasubrahmanian, D.H. Doughty and B. Rambabu, *Solid State Ionics* **148**, 299 (2002).
11. B.J. Hwang, R. Santhanam and C.H. Chen, *J. Power Sources* **114**, 244 (2003).
12. G.T.K. Fey, R.F. Shiu, T.P. Kumar and C.L. Chen, *Materials Science and Engineering: B* **100**, 234 (2003).
13. H.J. Kweon, G.B. Kim, H.S. Lim, S.S. Nam and D.G. Park, *J. Power Sources* **83**, 84 (1999).
14. C.C. Chang, N. Scarr and P.N. Kumta, *Solid State Ionics* **112**, 29 (1998).
15. Y.K. Sun and I.H. Oh, *J. Mater. Sci. Lett.* **16**, 30 (1997).
16. J.R. Dahn, U.V. Sacken and C.A. Michael, *Solid State Ionics* **44**, 87(1990).

PULSED LASER DEPOSITION OF HIGHLY ORIENTED $LiCoO_2$ AND $LiMn_2O_4$ THIN FILMS FOR MICROBATTERY APPLICATIONS

O. M. HUSSAIN*, K. HARI KRISHNA and V. KALAI VANI
Thin Film Laboratory, Department of Physics, Sri Venkateswara University
Tirupati-517 502, India
e-mail: hussainom48@yahoo.co.in

C. M. JULIEN
Institut des NanoSciences de Paris (INSP), Université Pierre et Marie Curie,
CNRS-UMR 7588, Campus Boucicaut, 140 rue de Lourmel, 75015 Paris, France

Thin films of $LiCoO_2$ and $LiMn_2O_4$ were prepared by pulsed laser deposition technique. The influence of deposition parameters on the structure and surface morphology of the films were studied. The $LiCoO_2$ films deposited in oxygen partial pressure of 100 mTorr and at substrate temperature of 300 °C exhibited predominantly (003) orientation of the hexagonal *R-3m* phase indicating that the growth occurs perpendicularly to the substrate surface with an average grain size of 80 nm. Whereas the films grown at higher substrate temperature were polycrystalline with the growth parallel to the substrate surface. The $LiMn_2O_4$ thin films prepared at 300 °C exhibited predominantly (111) orientation indicating cubic spinel structure with *Fd3m* space group.

1. Introduction

Reduction in size and power requirements of microelectronic devices has prompted the scientific research in the development of all solid state thin film microbatteries as light weight, noise free, compact and integrable power source. Investigations are aimed to integrate such microbatteries to complementary metal oxide semiconductor (CMOS) memory chips as a standby power source. These microbatteries must provide high potentials, high energy densities, long shelf life and high recycling capacity.[1-2] The realization of such microbatteries originates from the identification of novel thin film cathode materials with high energy density, high specific capacity and structural stability towards lithium insertion. The most recent candidates belong to the family of lithiated transition-metal oxides with general formula $Li_xM_yO_z$ (where *M*=Co, Mn, Ni, etc.).[3] Among these, $LiCoO_2$ and $LiMn_2O_4$ were found to be more prominent candidates, since they exhibit high potential towards lithium, high energy density, structurally stable in fully lithiated state and can show very good reversibility.[4-5] The synthesis of these compounds in thin film form is of great interest as a result of their possible use as a binder free positive electrode in the fabrication of all solid-state rechargeable microbatteries to power microelectronic devices. Thin films of these compounds have been synthesized by a variety of physical and chemical vapour deposition techniques.[6-8] In the fabrication of cathode

thin films, the formation of open structure with highly oriented grains is found to be more crucial for obtaining a good reversibility.

Recently, pulsed laser deposition technique (PLD) has been widely recognized as promising, versatile and efficient method for the growth of high quality thin films of a variety materials even containing volatile compounds with complex stoichiometry.[9] For this reason, it is well suited for the growth of lithiated transition-metal oxides, where one can overcome the lithium loss due to high volatilization in thin films.[10] When PLD is carried out in the atmosphere of a chemically reactive gas, the flux of laser ablated material interacts with the gas molecules all along the transit from target to the collector surface. The resulting deposited layers were found to have a chemical composition substantially the same as the base or starting material. Hence in the present investigation, thin films of $LiCoO_2$ and $LiMn_2O_4$ are prepared by PLD technique at various deposition conditions. The influence of deposition parameters on the microstructure and surface morphology of these films are investigated.

2. Experimental

Pulsed laser deposition technique was employed for the preparation $LiCoO_2$ and $LiMn_2O_4$ thin films on silicon (100) substrates. The targets were prepared from high purity powders pressed at 5 tons/cm^2 to make pellets of 3 mm thickness and 13 mm diameter and sintered at 800 °C for 10 hrs. The target was rotated at 10 rotations per minute to avoid depletion of material at the same spot. A KrF excimer laser (Luminics PM 882) with a wavelength of 248 nm was used to ablate the target with a pulse repetition rate of 10 Hz. The rectangular spot size of laser pulse was 1 mm × 3 mm with the energy density 300 mJ. The distance between the target and the substrate was typically 4.0 cm. The films were deposited at various substrate temperatures (100 – 700 °C) and oxygen partial pressures (50 – 200 m Torr).

The structure of the films was studied by a Seifert X–ray diffractometer with a nickel filtered CuK_α radiation (λ = 1.5406 Å). The surface morphology of the films was studied by atomic force microscopy (AFM) using a microscope Digital Instruments (3100 series) and scanning electron microscopy (SEM).

3. Results and Discussion

PLD $LiCoO_2$ and $LiMn_2O_4$ films were deposited with a minimum of 100 mTorr of oxygen partial pressure during the film growth. This ambient is required to avoid oxygen deficiency in the films.[11] The thickness of the films was kept at 250 nm for both materials. The films are found to be pinhole free as observed by optical microscopy and well adherent to the substrate surface. The influence of substrate

temperature during the growth on the microstructural properties of thin films was investigated as follows

3.1. $LiCoO_2$ films

The X-ray diffraction patterns of $LiCoO_2$ thin films grown on silicon substrates maintained at 300 °C from a pure $LiCoO_2$ target displayed the presence of two additional small peaks at about 2θ = 45 and 59°, which are attributed to the presence of cobalt oxide impurity (namely the Co_3O_4 phase) due to lithium deficiency.[4] As the amount of Li_2O increased in the target, the XRD patterns develop features expected for the hexagonal $LiCoO_2$ phase. An optimum of 10% excess Li_2O added to the $LiCoO_2$ powder forming the target is necessary to overcome lithium deficiency in the films. Hence, the Li-rich target with a mixture of $LiCoO_2$ and 10% Li_2O was employed for the preparation of $LiCoO_2$ thin films.

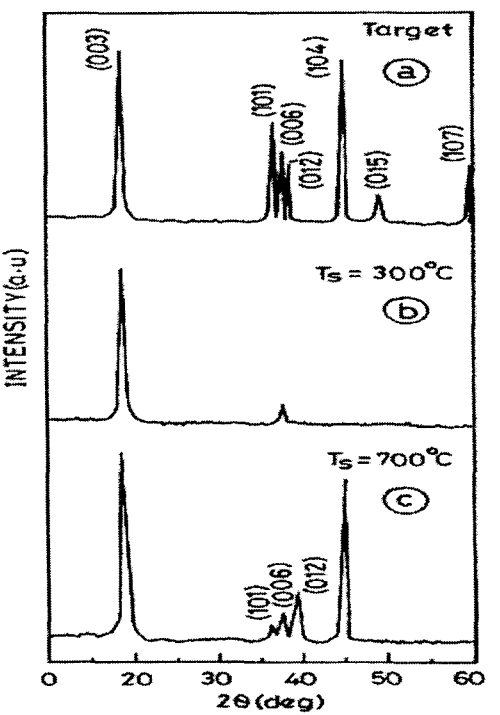

Figure 1. X–ray diffraction patterns of $LiCoO_2$ thin films and target

Figure 1 shows the X-ray diffraction patterns of $LiCoO_2$ thin films grown at different substrate temperatures using the Li-rich target. The X-ray diffraction pattern of $LiCoO_2$ thin films deposited at 300 °C displayed only two peaks at 2θ = 18.97 and 38.48°, which are indexed as the (003) and (006) reflections, respectively, of the hexagonal $LiCoO_2$ O3-phase with *R-3m* space group. The other reflections such as (101), (012) and (104) lines, which are usually observed for crystalline $LiCoO_2$ powder are not observed in the XRD patterns of thin films. The absence of reflection lines other than (00ℓ) lines indicate that the film grows with a preferred *c*-axis (003) orientation perpendicular to the substrate surface. The observed *c*-axis orientation can be explained by the lowest surface energy of (003) plane because it is the most closely packed plane according to Bravais empirical law. Hart et al.[12] reported that very thin $LiCoO_2$ films (t < 100 nm) prepared by rf-sputtering tend to have *c*-axis orientation. The thickness of *c*-axis oriented films obtained in the present study is thicker (t = 250 nm) than the criterion, but the tendency was in agreement with their results. A slight shift in the position of (003) orientation to a higher value with an evaluated lower lattice parameter, c = 14.056 Å, indicates the presence of compressive stresses (bent in concave) in the films due to smaller grain size.[13]

The XRD patterns of $LiCoO_2$ films deposited at higher substrate temperatures (T_s>300 °C) displayed peaks at 2θ = 37.4, 39.09 and 45.29° in addition to (00ℓ) reflections, which are indexed as (101), (012) and (104) reflections. Also it has been observed that the degree of *c*-axis orientation decreased with the increase of substrate temperature. At higher substrate temperature, the intensity of (003) orientation decreased with the increase of (104) orientation indicating the consequence of the film growth parallel to the substrate surface. The films deposited at 700 °C had close reflection patterns to that of pure $LiCoO_2$ powder. Higher deposition temperature provides sufficient thermal energy for the rearrangement of lithium, cobalt and oxygen atoms to grow polycrystalline films with higher grain size. The evaluated lattice parameters a = 2.816 Å, c = 14.062 Å, are in good agreement with powder file data.[14] During the film deposition process at lower substrate temperatures, the film may grow with preferred orientation in order to minimize the surface energy in which the compressive stresses are predominant. Whereas at higher substrate temperatures, the particle size increases due to high kinetic energy and favors the growth parallel to substrate surface.

The atomic force microscopy data demonstrated that the PLD $LiCoO_2$ thin films are homogeneous and uniform with regard to the surface topography. Figure 2 shows the surface morphological images of $LiCoO_2$ films deposited at various substrate temperatures. The AFM picture of $LiCoO_2$ thin films deposited at 300 °C reveals that the film is composed of roughly spherical grains of varying sizes with an average grain size of 80 nm. The root mean square surface roughness of the films derived from AFM data is 8 nm. The films exhibit typical open and porous structure

with small grains. As observed from AFM images, the grain size increases with substrate temperature and it is found to be around 210 nm for the films deposited at 700 °C. The estimated root mean square surface roughness is 12 nm. The dependence of growth and morphology of laser ablated $LiCoO_2$ thin films can be explained on the basis of the difference in mobility of the ablated species on the substrate surface as follows. When the laser beam hits the target, the ions or molecules or atoms of the target material are liberated and impinge on the substrate surface. When the substrate is at high temperatures, the ablated species acquire a large thermal energy and hence a large mobility. This enhances the diffusion density of the ablated species. As a result, the collision process initiates the nucleation and enhances the island formation in order to grow a continuous film with large grains.[15]

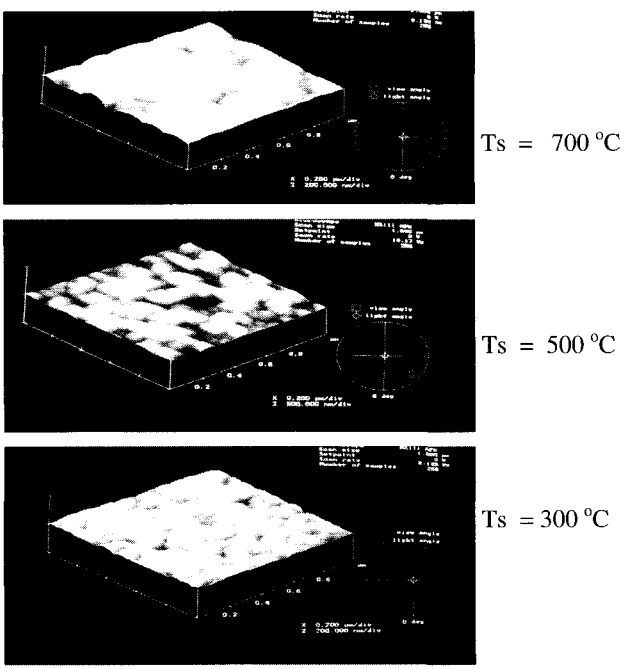

Figure 2. The surface morphology $LiCoO_2$ thin films deposited at various substrate temperatures (T_s).

3.2. $LiMn_2O_4$ thin films

Thin films of $LiMn_2O_4$ were prepared by pulsed laser deposition technique from $LiMn_2O_4$ + 10% Li_2O target. The films were grown on silicon substrates maintained in the temperature range 300 - 600 °C. The X-ray diffraction patterns of $LiMn_2O_4$

films prepared at various substrate temperatures are shown in Fig. 3. The films formed at a substrate temperature less than 200 °C are found to have amorphous structure as revealed from the broad and diffused X-ray diffraction patterns. The films prepared at higher substrate temperatures display XRD peaks at 2θ = 18.6, 38.9 and 44.2° that correspond to (111), (222) and (400) line, respectively, in which the (111) orientation is predominant. All the (hkℓ) values are indexed into the spinel cubic structure of $LiMn_2O_4$ represented by the *Fd3m* space group. The full width at half maximum value of (111) diffraction peaks is used to estimate the grain size. The intensity of diffraction peaks significantly increases and the FWHM decreases with the increase of substrate temperature.

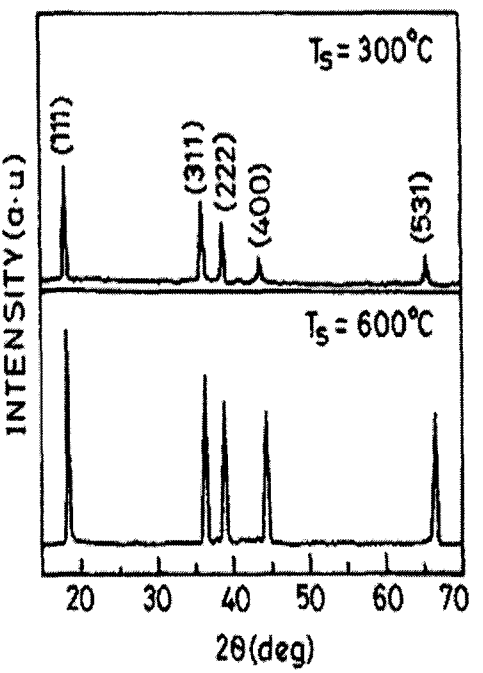

Figure 3. X-ray diffraction patterns of $LiMn_2O_4$ thin films.

The average grain size for the films grown at 300 °C is 60 nm and increases to 190 nm for the films formed at 600 °C. The lattice parameter is estimated from the position of (111) and (400) diffraction peaks. The background silicon substrate peak position was used as standard for calibration. The evaluated cubic lattice parameter of the films formed at 300 °C is a = 8.16 Å, which is slightly less than for the bulk $LiMn_2O_4$ spinel structure (a = 8.24 Å). This lattice parameter deviation may

be attributed to the intrinsic stresses due to small grain size. According to Moon et al.[16] the lower lattice parameter may be due to the formation of a defective spinel structure, such as $Li_{1-x}Mn_{2-2x}O_4$. The grain size and lattice parameter increase with the increase of substrate temperature. The lattice parameter of the films grown at 600 °C was a = 8.23 Å, which is an indication that the film has nearly stoichiometric phase of $LiMn_2O_4$ powder (JCPDS No.35 – 0782). However, further investigations are in progress to identify the chemical composition of the films. Figure 4 shows the surface morphological pictures of $LiMn_2O_4$ thin films recorded with scanning electron microscopy.

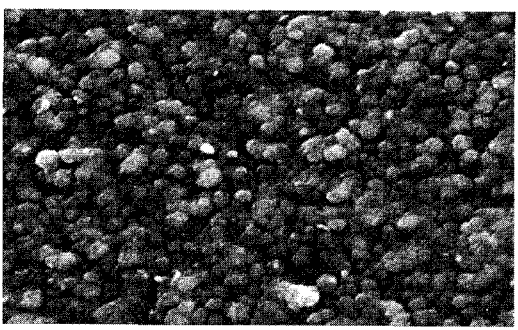

Figure 4. SEM photograph of $LiMn_2O_4$ thin film at T_s = 300 °C.

The scanning electron micrograph of film formed at 300 °C demonstrates that the film surface is comprised of homogeneous distribution of fine roughly spherical grains with an average grain size of 64 nm. It is worth noted that the grain size of our $LiMn_2O_4$ films increases with the increase of substrate temperature.

4. Conclusion

Thin films of $LiCoO_2$ and $LiMn_2O_4$ were prepared by pulsed laser deposition technique The microstructural properties of the grown films were found to be strongly dependent on the substrate temperature. The $LiCoO_2$ thin films deposited from a mixed target with 10% excess of Li_2O at 300 °C in an oxygen partial pressure of 100 mTorr were found to have preferred (003) orientation of hexagonal structure indicating that the film growth is perpendicular to the substrate surface. The surface topography of the films is composed of roughly spherical grains with an average grain size of 80 nm. The grain size of the films increased with the increase of substrate temperature and the film growth was observed to be parallel to the

substrate surface. The $LiMn_2O_4$ films grown at 300 °C exhibited predominantly (111) orientation indicating the cubic spinel structure with an average grain size of 64 nm. Highly oriented $LiCoO_2$ and $LiMn_2O_4$ thin films deposited at lower substrate temperature of 300 °C exhibited the typical open and porous structure with small grain sizes. These results suggest that these films are highly applicable as cathode materials in the fabrication of solid-state microbatteries.

Acknowledgments

The authors wish to acknowledge the University Grants Commission, New Delhi, India, for the providing financial support to carry out this work.

References

1. M. Balkanski, *Solid State Integrable Microbatteries*, North Holland, 1990.
2. N.J. Dudney and B.J. Neudecker, *Current Opinion in Solid State and Materials Science*, **4**, 479 (1999).
3. J. Cho and G. Kim, *Electrochem. and Solid-State Lett.*, **2**, 253 (1999).
4. C. Julien, E. Haro-Poniatowski, O.M. Hussain and C.V. Ramana, *Ionics*, **7**, 165 (2001).
5. B.J. Neudecker, N.J. Dudney and J.B. Bates, *J. Electrochem. Soc.*, **147**, 517 (2000).
6. W.C. West, J.F. Whitacre, V. White and B.V. Ratnakumar, *J. Micro Mechanics and Micro Engineering*, **12**, 58 (2002).
7. V.Kuwate, J. Kuwamura, K. Tonibami, T. Hattori and N. Sata, *Electrochem. Commun.* **6**, 417 (2004).
8. M. Mohamedi, N. Anzue, T. Itoh, I. Uchida, *J. Electrochem. Soc.*, **149**, A19 (2002).
9. C. Julien, E. Haro-Poniatowski, M.A. Camacho-Lopez, L. Escobar-Alarcon and J. Jimenez-Jacquin, *Mater. Sci. Eng. B.*,**72**, 36 (2000).
10. Y. Iriama, M. Inaba, T. Abe and Z. Ogumi, *J. Power Sources*, **81-82**, 1821 (1999).
11. O.M. Hussain, M.C. Rao and C. Julien, *Proc. of International Conference on Instrumentation*, Ed. by Sudhir Agashe, Priti Rege, Neelima Iyer, Thomson, Singapore (2004) p. 115.
12. F.X. Hart and J.B. Bates, *J. Appl. Phys.*, **83**, 7560 (1998).
13. J.B. Bates, N.J. Neudecker, F.X. Hart, H.P. Jun and S.A. Hackney, *J. Electrochem. Soc.*, **147**, 59-70 (2000).
14. T. Ohzuku and A. Ueda, *J. Electrochem. Soc.*, **141**, 2972 (1994).
15. O.M. Hussain, A.S. Swapnasmitha, J. John and R. Pinto, *Appl. Physics – A: Mater. Sci. and Proc.*, **81**, 1291 (2005).
16. H.-S. Moon, W. Lee, Philip J. Reucroft and J.-W. Park, *J. Power Sources*, **199-121**, 710 (2003).

PREPARATION OF $LINI_{0.80}Co_{0.20}O_2$ THIN-FILMS BY SOL-GEL METHOD

X. J. ZHU, C. HU, W. ZHANG, X. Y. GAN, M. H. CAO, D. B. LUO, W. CHEN, Q. XU, J. ZHOU AND H. X. LIU*

State Key Laboratory of Advanced Technology for Materials Synthesis and Processing, Wuhan University of Technology, Wuhan430070, Hubei, PR China

* *Email: lhxhp@mail.whut.edu.cn*

$LiNi_{0.80}Co_{0.20}O_2$ thin films were prepared by spin-coating method using sol-gel, and annealing process. The thermal decomposition behavior of the precursor was investigated by thermogravimetry/differential thermal analysis (TG/DTA). The crystallinity and microstructure were studied by X-ray differaction (XRD), scanning electron microscopy (SEM). Films annealed at 700 ℃ for 60 min exhibit 58.4 μ Ah/cm^2· μ m of the initial capacity and better capacity retention and are therefore considered to be candidates as cathodes for all solid-state thin-film microbatteries. The film electrochemical properties depended on the annealing temperature and time.

1. Introduction

All solid-state thin-film microbatteries are of considerable current research interest [1-3]. Because there is a strong demand for micro power sources which can be completely integrated into electronic circuits, microbatteries can be utilized in various application fields related to microsystems, such as monolithic hybridization with complementary metal oxide semiconductor random access memory (CMOS RAM), backup power for computer memory chips, small sensors, smart cards, etc. Transition metal oxides such as $LiCoO_2$, $LiMn_2O_4$, $LiNiO_2$ and $LiNi_{1-x}Co_xO_2$ are being developed for use as cathodes in rechargeable lithium batteries. The fabrication of $LiCoO_2$ and $LiMn_2O_4$ as cathodes for application in all solid-state thin-film microbatteries has been a particularly active field of research due to the excellent electrochemical properties and ease of manufacture of these materials.

Until now, cathode thin films for microbatteries can be deposited by various techniques such as sputtering [4-6], pulse-laser deposition [7], CVD [8, 9], LSMCD [10], ESD [11], etc. When using these methods, there is difficulty in controlling the stoichiometry of the thin films.

The sol-gel method is well known as a promising thin-film preparation method, which has good advantages in relatively easy stoichiometric control and a high deposition rate [12-14]. Furthermore, it is especially suitable for large-scale industrial utilization.

In this study, $LiNi_{0.80}Co_{0.20}O_2$ thin-films were obtained by means of annealing condition after depositing them by spin-coater method using the sol-gel. The effect of the annealing temperature and time on the crystallinity, and the microstructure and the electrochemical properties of the thin films have been investigated.

2. Experimental Detail

The reagent grade chemicals of $LiCH_3COCH_2COCH_3$, $Ni(CH_3COCH_2COCH_3)_2 \cdot 4H_2O$ and $Co(CH_3COO)_2 \cdot 4H_2O$ were chosen for lithium, nickel and cobalt sources, respectively. $(CH_3)_3COH$ and CH_3COOH were used as solvents. Sols were prepared according to a scheme illustrated in Fig. 1. Chemical compositions of the Li-Ni-Co-O sol were optimized to stabilize sols. The viscosity of the sol influences the nature of the prepared thin films. Molar compositions of starting solutions were $LiCH_3COCH_2COCH_3$/ $Ni(CH_3COCH_2COCH_3)_2 \cdot 4H_2O$/ $Co(CH_3COO)_2 \cdot 4H_2O$/$CH_3COOH$/$(CH_3)_3COH$ =1.0:0.8:0.2:10:20. The sols were coated on the Pt substrate with a spin coater at 3000 rpm for 30 second. The prepared sol films were converted to gel films in the course of the spin-coating process. Nine sol-layers were spin coated, and each layer was dried with a hot plate at constant temperature for 5 min in order to evaporate the solvent and remove organic materials from the acetylacetonate sources. After drying, the films were annealed at 650~750℃ under flowing O_2 in order to obtain good crystallinity. The analysis of the phases on the films was carried out by X-ray diffraction with CuK α radiation (XRD, D/MAX-RB, RIGAKU, Japan). The film morphology and structure were observed by scanning electron microscopy (SEM, JSM-5610LV).

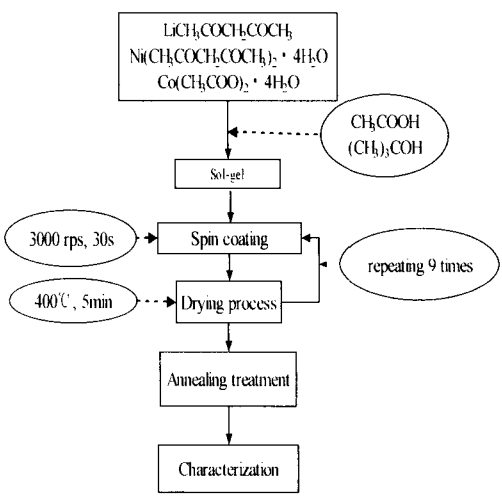

Figure 1 Scheme for preparation of $LiNi_{0.80}Co_{0.20}O_2$ thin films by the sol-gel method.

The electrochemical properties of $LiNi_{0.80}Co_{0.20}O_2$ thin-films were investigated by using 2016- type coin cells, which consist of the thin film cathode, an anode of Li foil and an electrolyte of 1 M $LiClO_4$ in a mixture of ethylene carbonate (EC) and dimethyl carbonate (DMC) (1:1 by volume). The manipulators of assembling cells were conducted in an argon-filled glove box (Merbaun, Germany). Charge-discharge cycling tests were performed galvanostatically at a constant current density of 30 μ A/cm^2 between the voltage range of 3.0~4.2 V using a multichannel battery cycling unit.

3. Results and discussion

The properties of thin-films fabricated by the sol-gel method were very sensitive to the drying temperature. Fig.2 is the curve of the thermogravimetric analysis (TG) and differential thermal analysis (DTA) for the $LiNi_{0.80}Co_{0.20}O_2$ precursor power. The TG curve indicated the initial weight loss associated with the removal of absorbed water and solvents from the start point to 105 ℃, corresponding to the endothermic peak at 101.7 ℃ in DTA curve. There were two large weight loss between 250 and 400 ℃ due to the decomposition of the organic constituents of the precursor power. The two exothermic peaks at 294.7 and 399.5 ℃ were related to the decomposition of acetate and acetylacetonate. Thus, in this study, two drying temperatures were employed. One was 105 ℃ located in the state of the removal of water and solvents in the precursor. Another was 400 ℃ located in the end of the two large weight loss step associated with the decomposition of the acetate and acetylacetonate.

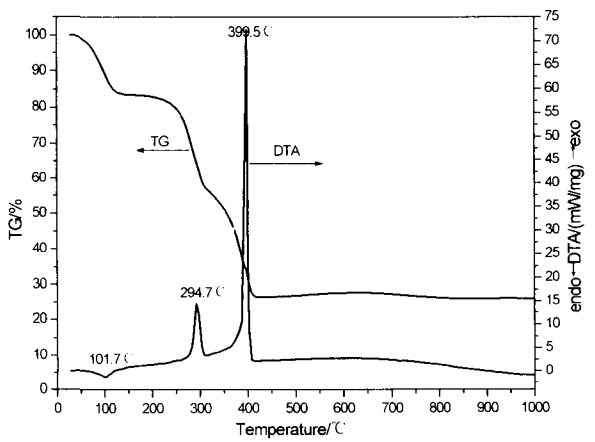

Figure 2 TG-DTA curve for $LiNi_{0.80}Co_{0.20}O_2$ precursor powder

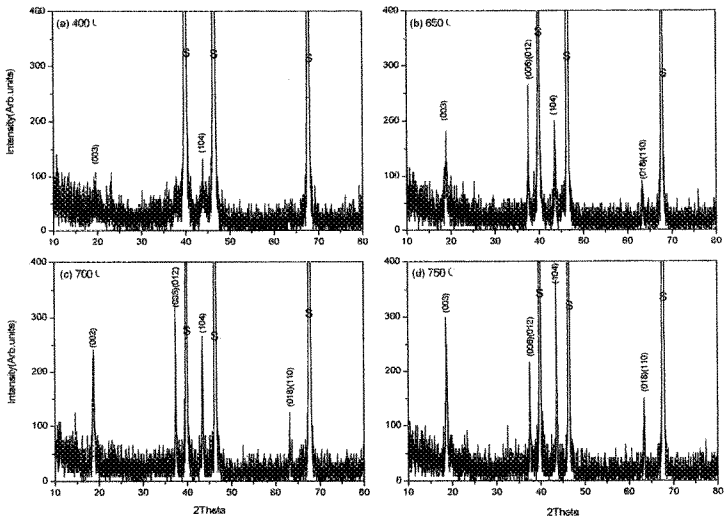

Figure 3 XRD patterns of (a) as-deposited film and the films annealed at (b) 650℃, (c) 700℃ and (d) 750℃.

The X-ray diffraction patterns for the thin-films after drying at 400 ℃ and annealed at 650 ℃, 700 ℃ and 750 ℃ are shown in Fig.3. (003) and (104) reflections of the annealed films were observed, which meant that all films had α - $NaFeO_2$ layered crystalline phase. Peaks marked with S corresponded to the Platinum substrate. The crystallinity increased as the annealing temperature increased. The as-deposited film had poor crystallinity compared with the annealed thin-films. So the as-deposited film was considered to have an unstable layered framework.

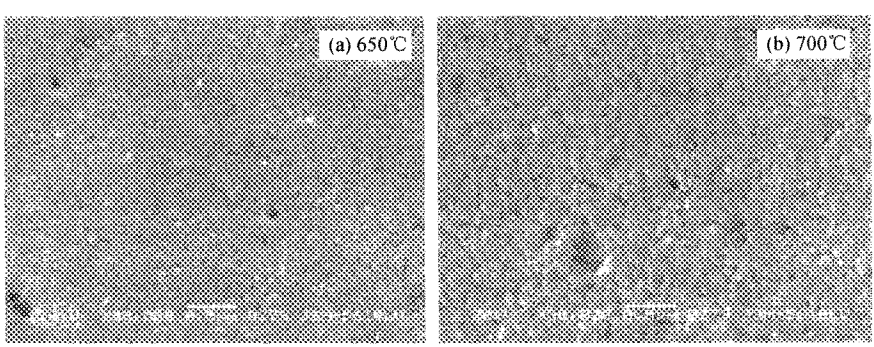

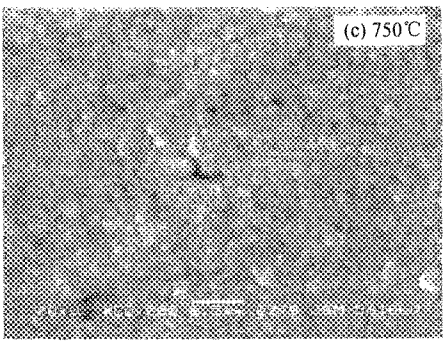

Figure 4 SEM photograph of the thin-films annealed at (a) 650 ℃, (b)700 ℃ and (c) 750 ℃

The surface morphology of the films annealed at different temperatures is shown in Fig.4. On increasing the annealing temperature, the grain size of the film increased. The films had relatively smooth and dense surface and small grains with fairly homogeneous size.

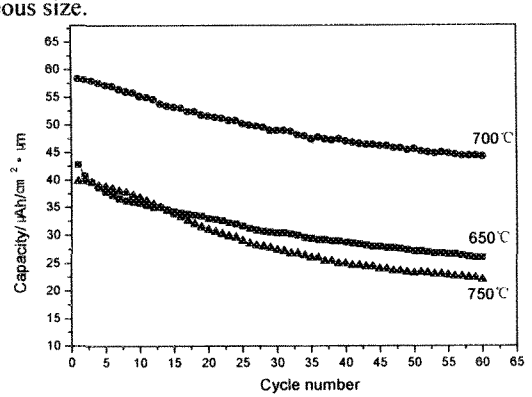

Figure 5 Discharge capacity vs. cycle number, for the thin films annealed at 650, 700 and 750℃, respectively.

The electrochemical properties of the thin-films annealed at various temperatures were characterized by constant current charge/discharge. The discharge capacities of the thin-film/EC and DMC solution/Li cell cycled between 3.0 and 4.2V at 30 μ Ah/cm^2 are given in Fig.5. The film annealed at 650, 700 and 750 ℃ had an initial capacity of 42.8, 58.4 and 40.0 μ Ah/cm^2, respectively. After 60 cycles, the corresponding discharge capacity was 26.0, 44.2 or 22.0 μ Ah/cm^2. Its capacity retention had 60.7%, 75.7% and 55.0%, respectively. The discharge capacity increased as the annealing temperature increased from 650 to 700 ℃, and then decreased from 700 to 750 ℃. So did their capacity retention. This may be due

to an increase in layered $LiNi_{0.80}Co_{0.20}O_2$ crystallinity as the annealing temperature increased. However, at high temperature the layered crystallinity decreased due to lithium evaporation to form lithium structural defects.

Table 1 Electrochemical properties of the thin-films annealed at 700℃ for 10, 30, 60 and 120 min

	10/(min)	30/(min)	60/(min)	120/(min)
Discharge capacity of the initial cycle/(μ Ah/cm^2)	48.7	55.4	58.4	41.4
Discharge capacity of the 20th cycle /(μ Ah/cm^2)	37.4	43.0	51.6	38.2
Capacity retention/ (%)	76.8	77.6	88.4	92.3

The discharge capacity of the thin-films, which varied markedly as the annealing time changed, was also characterized by cycling tests (20 cycles). The initial discharge capacity, the discharge capacity on the 20th cycle and the amount of capacity retention are listed in Table 1.

The discharge capacity increased as the annealing time increased from 10 to 60 min. This may be due to an increase in the layered crystallinity of the thin film. As the annealing time further increased to 120 min, the initial discharge capacity of the thin film decreased. It is considered to be due to the insufficient crystallinity of the thin film resulting from lithium evaporation during longer annealing time. Interestingly, the capacity retention increased as the annealing time increased from 10 min to 120 min. Based on the results above, it was found that the film annealed at 700 ℃ for 60 min had good properties such as a larger discharge capacity (58.4 μ Ah/cm^2) and a moderate rechargeability.

4. Conclusions

$LiNi_{0.80}Co_{0.20}O_2$ thin-films were deposited on Pt substrate by a sol-gel method using a spin-coater. The annealing process was investigated about the effect of annealing temperature and time on the discharge capacity and capacity retention. The crystallinity of the thin-film changed as the annealing temperature and time changed. The best electrochemical behavior was obtained from the film annealed at 700 ℃ for 60 min, which had 58.4 μ Ah/cm^2 of the initial discharge capacity and better rechargeability. From these results, $LiNi_{0.80}Co_{0.20}O_2$ thin films prepared by the sol-gel method may be candidates to serve as the cathode in all solid-state thin-film microbatteries.

Acknowledgments

This work was supported by the National Natural Science Foundation of China (No. 20371038), and the Foundation for Innovative Research Team of Hubei Province(No. 2005ABC004)

References

1. B. J. Neudecker, N. J. Dudney and J. B. Bates, *J. Electrochem. Soc.* **147**, 517 (2000).
2. J. K. Lee, S. J. Lee, H. K. Baik, H. Y. Lee, S. W. Jang and S. M. Lee, *Electrochem. Solid-State Lett.* **2**, 512 (1999).
3. K. Onishi, M. Matsumoto and K. Shigehara, *J. Power Sources* **92**, 120 (2001).
4. B. J. Neudecker, R. A. Zuhr and J. B. Bates, *J. Power Sources* **81-82**, 27 (1999).
5. S. J. Lee, H. K. Buik and S. M. Lee, *Electrochemistry Communications* **5**, 32 (2003).
6. C. L. Liao and K. Z. Fung, *J. Power Sources* **128**, 263 (2004).
7. C. Julien, E. Haro-Poniatowski, M. A. Camacho-Lopez, L. Escobar-Alarcon and J. Jimenez-Jarquin, *Materials Science and Engineering* **B72**, 36 (2000).
8. H. S. Moon, S. W. Lee, Y. K. Lee and J. W. Park, *J. Power Sources* **119-121**, 713 (2003).
9. W. G. Chio and S. G. Yoon, *J. Power Sources* **125**, 236 (2004).
10. K. W. Kim, S. I. Woo, K. H. Choi, K. S. Han, Y. J. Park *Solid State Ionics* **159**, 25 (2003).
11. K. Dokko, N. Anzue, M. Mohamedi, T. Itoh and I. Uchida, *Electrochemistry Communication* **6**, 384 (2004).
12. Y. J. Park, J. G. Kim, M. K. Kim, H. T. Chung and H. G. Kim, *Solid State Ionics* **130**, 203 (2000).
13. Y. H. Rho, K. Kanamura and T. Umegaki, *Chem. Lett.* **13**, 22 (2001).
14. Y. H. Rho, K. Kanamura, M. Fujisaki, J. Hamagami, S. Suda and T. Umegaki, *Solid State Ionics* **151**, 151 (2002).

ELECTROCHEMICAL LITHIUM INSERTION INTO A MANGANESE DIOXIDE ELECTRODE IN AQUEOUS SOLUTIONS

MANICKAM MINAKSHI*, PRITAM SINGH, TOUMA B. ISSA, STEPHEN THURGATE,

Division of Science and Engineering, Murdoch University, Murdoch 6150, Western Australia.

KATHRYN PRINCE AND DAVID MITCHELL

Materials and Engineering Science, ANSTO, PMB 1, Menai, NSW 2234, Australia.

Intercalation of lithium into the vacant sites of a host compound can be achieved electrochemically using non-aqueous electrolytes. The use of aqueous electrolyte is less common because of the reactivity of many lithium intercalation compounds with water. Here we propose that lithium could be intercalated using aqueous solutions, lithium hydroxide as the electrolyte. The X-ray photoelectron spectroscopy (XPS), Scanning electron microscopy (SEM) and Secondary ion mass spectrometry (SIMS) data on the discharged material indicate that lithium is intercalated into the host structure of EMD without the destruction of its core structure. A significant improvement in cell performance was obtained by adding small amounts (< 3 wt %) of titanium disulphide (TiS_2) to the cathode.

Introduction

Lithium-ion batteries now represent the state-of-the art in small-size rechargeable batteries for consumer electronic devices. Commercial lithium-ion batteries rely on the application of one of the well-known lithium intercalation hosts i.e., $LiCoO_2$, $LiNiO_2$, $LiMn_2O_4$ or γ-MnO_2 [1-4]. Recently, novel materials based on transition metal polyanions have also been proposed, and phosphate compounds crystallizing as Nasicon structures appear to hold particular promise [5-6]. For instance, it has been suggested that lithium iron phosphate, $LiFePO_4$, may offer the optimal combination of low cost, favorable electrochemical activity, and low environmental impact [7]. Lithium has been intercalated into these materials using non-aqueous electrolytes. The use of aqueous methods is less common because of the reactivity of many lithium intercalation compounds with water. In one of our previous papers [8] we reported that lithium could be intercalated into γ-MnO_2 from LiOH solution in an aqueous cell.

Giovanali et al. [9] described γ-MnO_2 as an intergrowth structure between ramsdellite and pyrolusite, which are both members of the nsutite group. The basic unit cells are $[MnO_6]$-octahedra joined to form alternating single-and double chains. Ruetschi et al. [10] have summarized the types of MnO_2 materials to be considered important for batteries, among these electrolytically produced manganese dioxide (EMD) is widely used commercially.

In traditional alkaline batteries using KOH as the electrolyte MnO_2 is not suitable for its reversibility, because during discharge the electrode reaction involves the insertion of protons into the ionic lattice of the manganese dioxide according to the equation:

$$MnO_2 + H^+ + e^- \rightarrow MnOOH \qquad \text{Eq. [1]}$$

Whereas, the use of aqueous LiOH as an electrolyte results in the incorporation of lithium ions into the MnO_2 structure during the discharge.

$$Li^+ + e^- + MnO_2 \rightarrow LiMnO_2 \qquad \text{Eq. [2]}$$

The overall reaction of the alkaline Zn/MnO_2 battery using LiOH electrolyte is

$$Li^+ + e^- + MnO_2 \rightarrow LiMnO_2 \qquad \text{Eq. [3]}$$

This reaction in Eq. 3 is similar to that for Li/MnO_2 non-aqueous batteries except that it exhibits slow reversibility. During cell discharge, Li^+ ions are inserted into the γ-MnO_2 structure, causing the reduction of Mn^{4+} ions to Mn^{3+} ions. During oxidation, the γ-MnO_2 reverts to its original phase upon the extraction of Li^+ ions from the structure. However the rate of reversibility is slow due to the formation of Mn_2O_3. The main objective of this paper is to report our findings on

1. Electrolytically produced manganese dioxide (EMD) and to compare with chemically prepared battery grade manganese dioxide (BGM) in aqueous solutions. The purpose is to determine whether the BGM behaved in a manner similar to EMD.
2. Improvement in cell performance by adding small amounts (< 3 wt %) of titanium disulphide (TiS_2) to the cathode.

Experimental

The γ-MnO_2 of EMD type and BGM used in this work were purchased from the Foote mineral company and Sigma Aldrich, respectively. The cell design and experimental details were similar to those reported earlier [8-11]. The cells were discharged/charged galvanostatically at 0.5 mA/cm^2 by using an EG&G Princeton Applied Research Potentiostat/Galvanostat model 273 A, operated by model 270 software (EG&G). The cutoff discharge and charge voltages were 1.0 and 1.9 V, respectively. All electrochemical measurements were carried out at ambient atmosphere. The products formed during charge and discharge cycles were characterized by a Siemens X-ray diffractometer using Philips Co-Kα radiation. X-ray photoelectron spectroscopy (Kratos Ultra Axis Spectrometer) using monochromatic Al Kα (1486.6 eV) radiation was used to analyze the chemical binding energy of the samples. X-ray photoelectron spectroscopy (XPS) analysis was started when the pressure in the analysis chamber fell below 1 x 10^{-9} hPa. Carbon, C (1s), was used as a reference for all the samples. The Surface analysis of the materials was conducted by using a scanning electron microscope (Philips Analytical XL series 20). Secondary Ion Mass Spectrometry (SIMS) spectra were collected on a Cameca ims 5f instrument at the Australian Nuclear Science and Technology Organization (ANSTO), Lucas Heights, Sydney. An O_2^+ primary ion source (12.5 KV) was used to generate secondary ions. A primary beam of 50 nA rastered over an area of 250 x 250μm was used in all experiments. The SIMS positive ion signals corresponding to ^7Li was recorded.

Results and Discussion

Performance characteristics of Zn- γ-MnO_2 of EMD type aqueous LiOH cell: The performance characteristics of MnO_2 in alkaline aqueous Zn-MnO_2 cells containing potassium hydroxide (KOH) as the electrolyte have been reported extensively in the literature [12-14]. Kordesch [14] has reported that the discharge behavior of the cathode material, MnO_2, in the alkaline KOH electrolyte occurs in a heterogeneous phase reaction, i.e. MnO_2 being converted to Mn_2O_3. Hence, the MnO_2 lattice expands and, at a certain point of discharge, the mechanism changes to an irreversible portion of the MnO_2 reduction process. We have investigated the use of LiOH in place of KOH in alkaline Zn - MnO_2 cells. Zn/ MnO_2 / LiOH (aq.) cells were discharged at constant current density (0.5 mA/cm^2) to 1 V cut-off. For comparison, cells containing KOH in place of LiOH were also discharged under identical conditions. Each of the electrolytes contained 1 M $ZnSO_4$ in addition to the saturated solutions of LiOH or KOH. The results for the first discharge cycle for both the cells are shown in Fig. 1. The cell containing LiOH discharged at a higher voltage and had a higher material utilization compared to the cell with KOH electrolyte. The cathode utilization for the LiOH cell was found to be 56 % (162 mAh/g) as compared to 41 % (120 mAh/g), for the KOH cell.

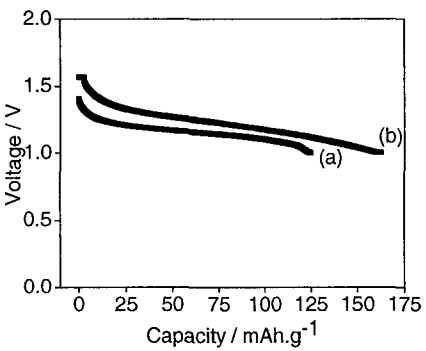

Fig. 1 First discharge curve of Zn-MnO_2 (EMD type) cells using saturated aqueous of (a) KOH and (b) LiOH containing 1 mol. L-1 of ZnSO4 under identical conditions.

The reversibility of the cell Zn-MnO_2 using sat. LiOH as the electrolyte was investigated and their results are shown in fig. 2. The cell could be reversibly discharged and charged. The cathode material utilization was calculated from the initial weight of the active MnO_2 in the cathode and the voltaic efficiency from the observed average charge/discharge voltages. The material utilization of 56% (162 mAh/g) for discharge and 54% (156 mAh/g) for charge and the voltaic efficiency of 83% were obtained. Figure 3 shows the variation of open-circuit voltage versus number of cycles. For the first cycle the open-circuit voltage was 1.8 V and then for the 10^{th} cycle the OCV falls to 1.785 V and for subsequent cycles it decreases to 1.713 V.

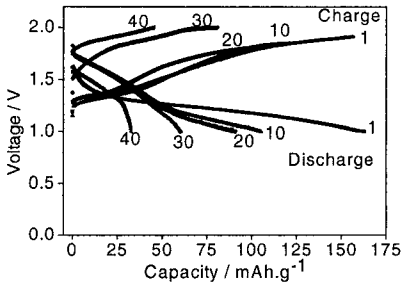

Fig. 2 Cycling behavior of the Zn-MnO_2 (EMD type) battery over subsequent cycles.

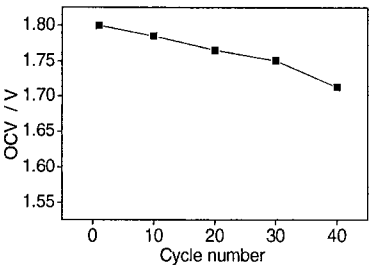

Fig. 3 Variation of the open-circuit voltage vs. cycle number for the Zn - MnO_2 (EMD type) battery.

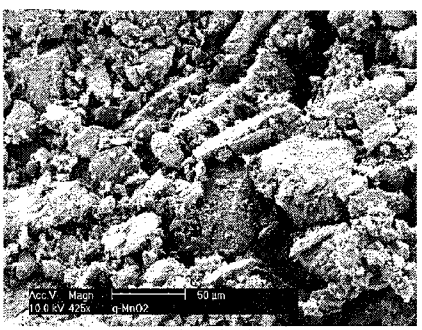

(a) before discharge

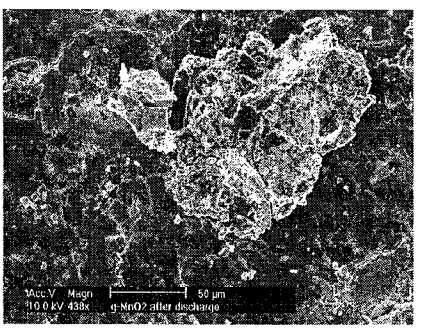

(b) after discharge

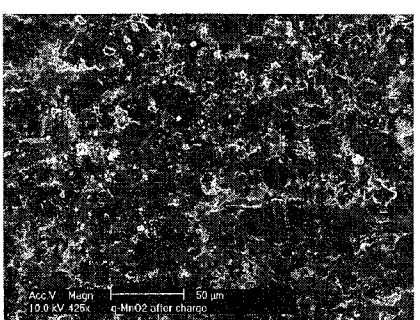

(c) after charge (30^{th} cycle)

Fig. 4 Scanning electron micrographs of the MnO_2 (EMD type) cathode material.

The investigation on the surface morphology that occurs on the cathode material during the process of discharge and recharge has substantially confirmed the presence of a new material as seen in fig. 4. The morphology of as-prepared MnO_2, fig. 4 a, revealed that the particle size of the order of 20-25 µm. The material formed after the discharge had a very different morphology (fig. 4 b). The particle size was of the order 40-50 µm. It appears that during discharge the

original γ-MnO_2 particles agglomerate into larger particles perhaps containing lithium ions intercalated into the material. The micrograph fig. 4 c for recharged sample shows the absence of this agglomeration. However the structural irreversibility of the starting MnO_2 is observed in the morphology, and is most likely the reason for the loss in battery capacity after few cycles, as shown in the cycling behavior, fig. 2. In order to confirm the existence of lithium ions in the solid matrix of the discharged cathode material it was subjected to XPS and SIMS studies. As reported earlier [8], before the XPS and SIMS analysis, the surface of the cathode material was ion bombarded to remove the thick layer of materials (like LiOH, Li_2CO_3 and H_2O) on the surface of the discharged products. LiOH is present because the material is discharged in LiOH, which remains adsorbed at the surface. The lithium carbonate is the result of LiOH reacting with atmospheric carbon dioxide. After ion bombardment, the spectrum shown in Fig. 5 was recorded. The peak at 54.7 eV could be assigned to intercalated lithium [15] into the MnO_2 host structure. To investigate the lithium distribution in the bulk sample MnO_2 the depth profile was carried out. Figure 6 represents the depth profile results for a discharged cathode. It can be seen that while going from surface to bulk, Mn species decreased while Li species slightly increasing in lithium counts. This result agrees with the XPS studies that lithium is present in the structure.

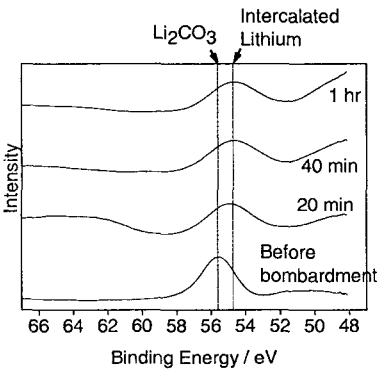

Fig. 5 XPS spectra of Li (1s) for the cathode MnO_2 (EMD type). Time in figure indicates the etching duration.

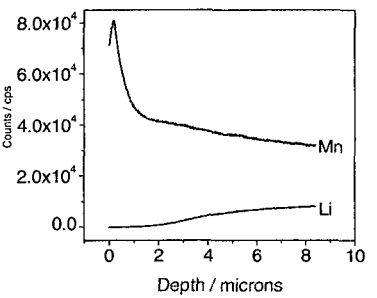

Fig. 6 SIMS depth profile of discharged MnO_2 (EMD type)

Performance characteristics of Zn- BGM- aqueous LiOH cell: Figure 7 shows the difference in the discharge characteristics of the cells containing EMD and the BGM as cathode materials. The open circuit voltage of BGM is higher and the discharge voltage profile is flatter than that for the EMD material under identical conditions. The rate of voltage drop during discharge is almost identical. The delivered discharge capacity for these two materials is almost identical at a 1V

cut-off voltage (ca. 165 mAh/g). In contrast to EMD the BGM shows a sharp drop in voltage, whereas the EMD does not show such drop upto that point. This is probably related to the difference in the composition of the two MnO_2 materials with respect to ramsdellite and pyrolusite, water content and surface area. The BGM exhibit quite different rechargeability when subjected to continuous discharge/charge cycles. As seen in Fig. 8, a 35% drop in the active material utilization occurred at cycle number 2 for this cell. For EMD, the same drop occurred at the 20^{th} cycle (Fig. 2). Thus the EMD is more stable to discharge/charge cycling.

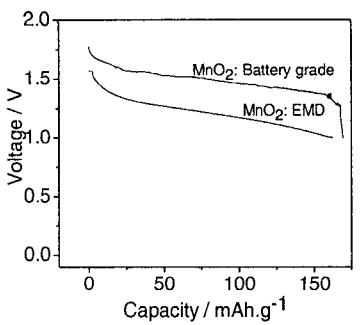

Fig. 7 Comparison of the two different MnO_2 on their first discharge voltage profiles

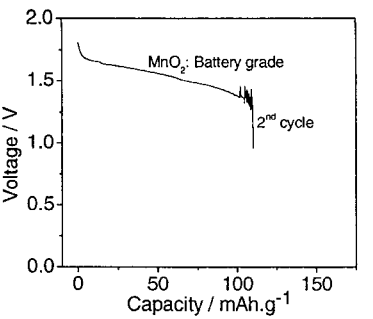

Fig. 8 Voltage vs. discharge capacity of Zn|MnO_2-BGM|LiOH cells on the second cycle

Additive of TiS_2 in the EMD cathode Following the incorporation of the Bi^{3+} additive, several other additives have been explored [12,16]. A potential candidate in this regard has been Ti^{4+} ion [16]. This is usually done by anodic deposition of EMD from an acidic solution of manganese sulphate containing some Ti^{4+} ions. In this work, small amounts of TiS_2 as additives have been employed by physical mixing into EMD and investigated their electrochemical behavior. The SEM micrograph (fig. 9) with the additive of 5 wt% shows a change in morphology i.e. rounded particles around 10μm in diameter. Figure 10 shows the cell performance of the MnO_2 cell by adding various amounts of TiS_2. A significant improvement in discharge capacity was obtained by adding amounts (< 3 wt %) of titanium disulphide (TiS_2) to the cathode. This could be explained in terms of the doping ions known to stabilize the MnO_2 structure towards dimensional changes that occur during the discharge process. However, increasing the doping content from 3 to 5 wt % causes a decrease in the cell capacity. Although not fully understood, increasing the doping content could modify the "open structure" configuration of MnO_2 for intercalation. This probably could be related to the change in surface morphology as reflecting via the SEM micrograph in Fig. 9.

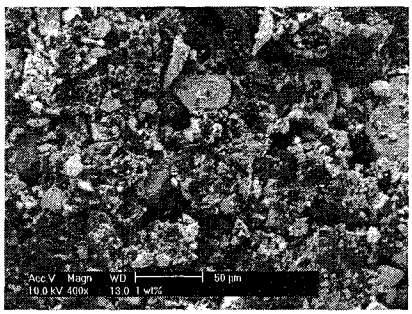

MnO_2 with 1 wt % of TiS_2

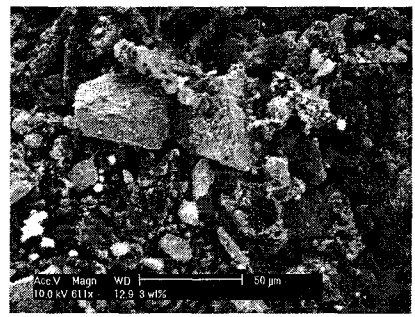

MnO_2 with 3 wt % of TiS_2

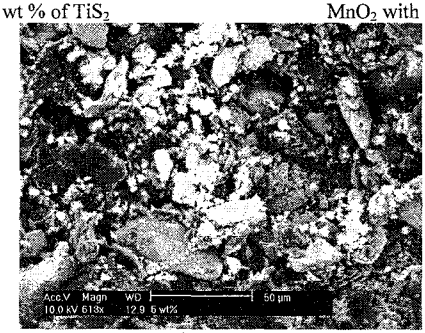

MnO_2 with 5 wt % of TiS_2

Fig 9 Scanning electron micrographs of the cathode MnO_2 in the presence of various amounts of TiS_2 additives

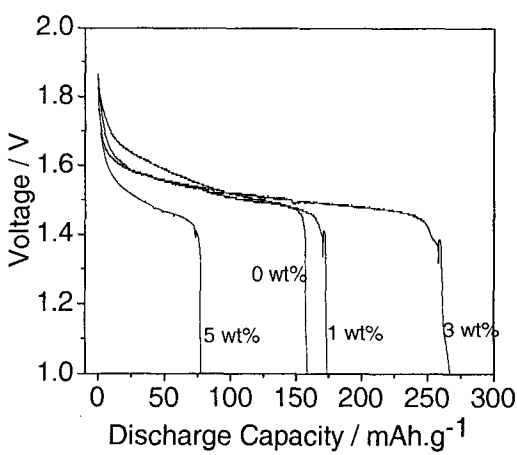

Fig. 10 Comparison of the first discharge behavior of MnO_2 in the presence of various amounts of TiS_2 additives.

Conclusions

The characterization of the products formed when MnO_2 is discharged in a $Zn|MnO_2|LiOH$ cell, indicates that the cell discharge mechanism involves Li^+ intercalation into the host structure. As compared to battery grade material (BGM), electrolytic manganese dioxide (EMD) is found to be more stable to discharge/charge cycling. The incorporation of small amounts of TiS_2 additives into MnO_2 is found to improve the discharge capacity. However, increasing the doping content from 3 to 5 wt % causes a decrease in the cell capacity.

Acknowledgements

The author M. Manickam is grateful to Murdoch University for a research scholarship. The financial support of Australian Nuclear Science and Engineering (AINSE) for carrying out a part of the work at Australian Nuclear Science and Technology (ANSTO) is also acknowledged. The author would like to thank Peter Fallon of Murdoch University for his technical support.

References

[1] C. Delmas and I. Saadoune, Solid State Ionics 53-56 (1992) 370.

[2] J. N. Reimers and J. R. Dahn, J. Electrochem. Soc. 139 (1992) 2091

[3] E. Rossen, J. N. Reimers, and J. R. Dahn, Solid State Ionics 62 (1993) 53.

[4] Tsutomu Ohzuku, Masaki Kitagawa, Taketsugu Hirai, J. Electrochem. Soc.136 (1989) 3169.

[5] M. Manickam, K. Minato, M. Takata, J. Electrochem. Soc.,150 (2003) 1085.

[6] M. Manickam , J. Power Sources 113 (2003) 179.

[7] A. K. Padhi, K. S. Nanjundaswamy and J. B. Goodenough, J. Electrochem. Soc., 144 (1997) 1188

[8] Manickam Minakshi, Pritam Singh, Touma B. Issa, Stephen Thurgate and Roland DeMarco, J. Power Sources, 130 (254) 2004.

[9] R. Giovanoli, in " Proceedings of the Manganese Dioxide Symposium," Vol.2, Tokyo 1980, B. Schumm, H.M. Joseph and A. Kozawa, Editors, paper 7, p. 113, I.C. Sample office, Cleveland, OH.

[10] P. Ruetschi and R. Giovanoli, J. Electrochem. Soc. 135 (1988) 2663.

[11] Manickam Minakshi, Pritam Singh, Touma B. Issa, Stephen Thurgate and Roland DeMarco, J. Power Sources, 153 (2006) 165.

[12] S.W. Donne, G.A. Lawrence and D.A.J. Swinkels, J. Electrochem. Soc., 144 (1997) 2954.

[13] J. Mc. Breen, Electrochimica Acta, 20 (1975) 221.

[14] K. Kordesch, J. Gsellmann, M. Peri, K. Tomantschger and R. Chemelli, Electrochim. Acta, 26 (1981) 1495.

[15] Handbook of X-ray Photoelectron Spectroscopy, Physical Electronics Division, Perkin Elmer Corporation, USA, October 1992.

[16] V.K. Nartey, L. Binder and A. Huber, J. Power Sources 87 (2000) 205.

AC IMPEDANCE SPECTROSCOPIC ANALYSIS OF THIN FILM $LiNiVO_4$ PREPARED BY PULSED LASER DEPOSITION TECHNIQUE

S.SELVASEKARAPANDIAN*, M.S.BHUVANESWARI

a) Solid State and Radiation Physics Laboratory, Department of Physics, Bharathiar University, Coimbatore – 641 046. INDIA.

Email: sekarapandian@yahoo.com

T.GNANASEKARAN K.I.GANASEKAR and E.PRABHU

Materials Chemistry Division, IGCAR, Kalpakkam – 603 102, INDIA.

Rechargeable thin-film batteries have become the topic of widespread research for use in low power applications in the field of Microelectronics and in Microsystems. The fabrication of lithiated vanadium oxides such as $LiNiVO_4$ and $LiCoVO_4$ in thin-film form is of great interest as a result of their possible use as electrode materials in all-solid-state lithium rechargeable microbatteries to power microelectronics. In the present study the preparation of lithium nickel vanadate thin films using Pulsed Laser Deposition technique and their electrical characteristics have been reported. The XRD analysis confirms the formation of thin film $LiNiVO_4$. The impedance analysis gives the grain interior and grain boundary resistance as $3X10^{-4}$ ohms and $8X10^{-3}$ ohms at 623 K respectively. The conductance spectra indicated the electrode polarization effect of the thin film sample. The modulus analysis indicated the non-Debye nature of the sample. The dielectric spectrum shows a low-frequency dispersion of the dielectric constant, which reveals the space charge effects arising from the electrode.

Key words: Thin film; $LiNiVO_4$; PLD; AC conductivity; Modulus spectra; Dielectric analysis.

1. Introduction

$LiNiVO_4$ is one of the promising electrode materials for Li ion rechargeable batteries. $LiNiVO_4$ exhibits an unusual inverse spinel structure in which the Li and Ni atoms equally occupy the octahedrally coordinated interstices and the V atoms occupy the tetrahedrally coordinated interstices [1]. This structure is different from the crystal structures of other lithium incorporated electrode materials, which paved the way for its high electrochemical behaviour [2, 3]. However its interest as bulk electrode materials is limited by its poor capacity retention and a large loss in initial capacity [4]. In order to overcome these problems, thin film $LiNiVO_4$ has been fabricated by rf magnetron sputtering and their electrochemical properties have been reported by Reddy et.al and Lee et.al [5, 6]. Literature survey reveals that there is no

report on the fabrication of $LiNiVO_4$ thin films by pulsed laser deposition (PLD). This method has been successfully used for preparing thin film electrodes, such as $LiCoO_2$, $LiMn_2O_4$ and V_2O_5 [7, 8]. PLD is a simple method to prepare thin film of materials which contain volatile components (such Li based electrode materials) having complex stoichiometries. The main advantage of PLD is their ability to transfer the original stoichiometry of the bulk target to the deposited films [9]. In the present study the preparation of lithium nickel vanadate thin films using Pulsed Laser Deposition technique and their electrical characteristics have been reported.

2. Experimental

$LiNiVO_4$ has been prepared by a solid state reaction method. Stoichiometric amounts of the raw materials Li_2CO_3, NiO and V_2O_5 according to the composition of $LiNiVO_4$ were ground into fine powder using mortar and pestle. The resultant powder has been heated at a temperature of 1023 K in a porcelain crucible. The resultant sample has been cooled slowly, crushed into fine powder and then sprayed in a die. A pressure of around 4000 Kg cm^{-3} has been applied to form a pellet with 0.1 cm thickness and 1.0 cm diameter. The pellet has been sintered at 623 K in air for 3 h.

Thin film of $LiNiVO_4$ has been prepared by pulsed laser ablation technique. A KrF excimer laser operating at 248 nm has been used to deposit thin films on Si (100) substrate. $LiNiVO_4$ prepared by solid state reaction method has been used as the target material. The deposition has been carried out for 20 min. Thin film growth parameters were: fluence, 3 J cm^{-2}, repetition rate, 10 Hz; in situ oxygen partial pressure, 1 X 10^{-1} m bar; substrate temperature, 450 °C; preablation, 2 min; target to substrate distance 4 cm.

Crystalline phases were identified using X-ray diffractometry (XRD) with a thin-film attachment and CuK_α radiation (Rigaku Co., Tokyo, Japan). Microstructure observations were performed using a Hitachi 2300 scanning electron microscope (SEM).

Impedance measurements were made in the temperature range of 583– 623 K. Gold has been coated as electrodes for impedance measurements. The impedance

analyzer HIOKI 3532 controlled by a computer has been used to obtain the electrical measurements in the frequency range of 42 Hz – 5 MHz.

3. Results and discussion

3.1 XRD and SEM analysis

Fig.1 shows the XRD pattern of thin film $LiNiVO_4$. The XRD pattern of thin film $LiNiVO_4$ is dominated by (311) and a (220) peak at 2θ = 36° and 30° respectively. The peaks observed in Fig.1 are confirmed by the JCPDS file No. 01-073-1638.

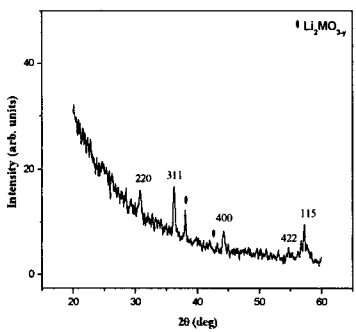

Fig.1. XRD patterns of thin film $LiNiVO_4$

The absence of (111) line in thin film $LiNiVO_4$ may be due to the presence of more vanadium ions on the tetrahedrally coordinated 8a sites [10]. The XRD peaks located around 2θ = 55°, 58° for the thin film sample with medium intensity correspond to (422) and (115) Bragg lines respectively [11]. A low intensity peak has been observed around 38° and 43° for the thin film sample. At first, it has been considered that the 38° and 43° peaks are due to unreacted NiO. But similar peaks has been observed and reported by Orsini et al for the discharge cycle of $LiNiVO_4$ [12]. It has been discussed by them that these new peaks were not due to NiO, but due to the formation of a new phase with formula Li_2MO_{3-y} with y=1 (with M=Ni, V or Ni/V). In the present study the presence of the peak around 38° and 43° indicates the presence of this phase for the thin film $LiNiVO_4$. However the peaks due to inverse spinel have not been altered for the thin film $LiNiVO_4$ which has been inferred from the presence of characteristic peaks of $LiNiVO_4$ for the thin film sample.

The SEM analysis has been carried out mainly to study the morphology of the synthesized compound. Fig. 2 shows the SEM images of the thin film $LiNiVO_4$. The SEM analysis of the thin film LiNiVO4 indicates the uniform particle size of about 50 nm.

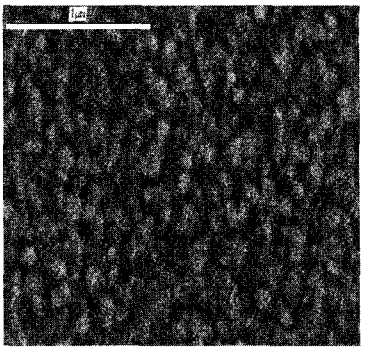

Fig.2. SEM image of thin film $LiNiVO_4$

3.2 Conductivity Analysis

Fig.3 shows the logω vs log σ plot of thin film $LiNiVO_4$ at various temperatures. The ac conductivity σ(ω), usually reaches to a frequency independent plateau at low frequencies and dispersive phenomena at high frequencies, in a variety of crystalline ionic materials. In the present study low frequency dispersion is observed due to electrode polarization effects [13].

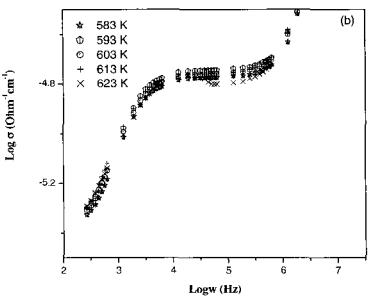

Fig.3. Conductance spectra for thin film $LiNiVO_4$ at various temperatures

In the temperature range studied, the ionic conductivity is high enough to produce a significant build up of charges at the electrodes, which reduces the effective applied field across the sample and hence the apparent conductivity. At mid frequencies the period of the applied field is too short for the charging to occur

and the ac conductivity is generally taken to assume the frequency independent value, which is equal to the true dc conductivity. At very high frequencies the conductivity dispersion follows the power law dependence [14]. he Jonscher's power law equation may be written as,

$$\sigma(\omega) = \sigma_{dc} + A\omega^n \qquad (1)$$

where n is the frequency exponent in the range $0<n<1$. Both σ_{dc} and A are thermally activated quantities. The frequency-independent conductivity is observed in the low frequency region, which indicates the dc conductivity of the material. In the high frequency region, the power law feature $\sigma(\omega) \propto \omega^n$ has been observed. It had been observed from the figure that there is no significant variation in the conductivity with temperature in the temperature range studied.

3.3 Impedance analysis

Fig.5 shows Cole-Cole plot of impedance for $LiNiVO_4$ thin film at different temperatures.

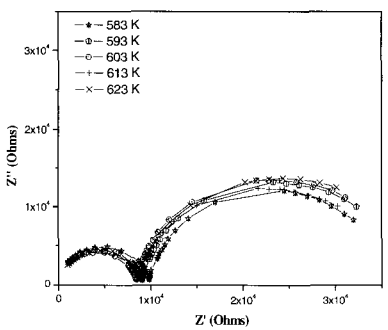

Fig.4. Impedance complex plane plot for thin film $LiNiVO_4$ at various temperatures

There are two components to the impedance, grain interior resistance (R_{gi}), and grain boundary resistance (R_{gb}). The high frequency semicircle has been attributed to the grain interior resistance and the low frequency semicircle is due to grain boundary resistance. The associated capacitance values are calculated using the relation $2\pi f_{max}RC = 1$ and they are found to be in the order of pF and nF, which indicates the nature of the semicircles as grain interior and grain boundary [15]. The large difference in time constants allows the grain interior resistance semicircle to be clearly separated from that of the grain boundary curve. The circular fitting of the complex impedance plot by using the programme EQ developed by Boukamp [16,

17] yields the grain interior resistance (R_{gi}) as 3 $X10^{-4}$ohms and grain boundary resistance (R_{gb}) as 8.$X10^{-3}$ohms at 623 K.The grain interior resistance and grain boundary resistance are contributed by the motion of Li^+ ions along the grains and across the grains respectively.

3.4 Modulus Spectra Analysis

The dielectric response caused by ion relaxation has been studied using the reciprocal quantity $M^* = 1/\varepsilon^* = M' + jM''$, known as the electric modulus [18, 19] in which the electrode polarization artifacts are suppressed. Typical features of modulus spectrum include a broad, asymmetric peak in the imaginary part and a sigmoidal step in the real part. This feature is due to the storage of mechanical stress associated with relaxation processes of the conducting species. Fig.5 shows the frequency dependence of M'' at various temperatures for $LiNiVO_4$ thin film. The broad nature of the peaks can be interpreted as being the consequence of distributions of relaxation time.

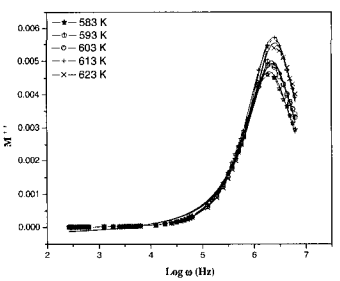

Fig.5. Modulus spectra for thin film $LiNiVO_4$ at various temperatures

The non-exponential conductivity relaxation can be described by a Kohlrausch Williams Watt (KWW) function $\phi(t)$, which represents the distribution of relaxation time in ion conducting materials [20]. The electric modulus can be represented as,

$$M^* = M_\infty \left[1 - \int_0^\infty dt \exp(-i\varpi t) d\phi / dt\right] \qquad (2)$$

and $$\phi = \phi_0 \exp\left[-(t/\tau_0)^\beta\right] \qquad (3)$$

where, τ_0 is conductivity relaxation time and β is Kohlrausch exponent. The smaller the value of β, the greater the deviation with respect to Debye-type relaxation. The

β parameter is most often interpreted as a result of correlated motions between ions. This means that the jump of a mobile ion in a material cannot be treated as an isolated event. Using the modulus formalism, i.e. M″ spectrum, the corresponding full width half height (FWHH) is wider than the breadth of the Debye peak (1.14 decades) and thus results in a value of β = 1.14/FWHH. The modulus peaks are fitted by using the software PEAKFIT and the full width half height (FWHH) values are extracted and the corresponding β values has been calculated using the relation β = 1.14/FWHH. The β parameter is found to be 0.89 and it does not depend on the temperature in the temperature range studied.

3.5. Dielectric analysis

The dielectric properties of any system may be characterized by frequency dependant parameters, which may define the complex permittivity. ε′ and ε″ has been calculated using the impedance data by the following equation

$$\varepsilon^* = 1/(j\omega C Z^*) \qquad (4)$$

where Z^* is complex impedance, $C = (\varepsilon_0 A)/t$, t is thickness of the sample A is effective area of the electrodes, ε_0 is the vacuum permittivity ($8.854X10^{-12}$ F/m), $\omega = 2\pi\nu$ and $j = \sqrt{-1}$. A plot of log ω and ε′ for thin film $LiNiVO_4$ at different temperatures has been presented in Fig.7.

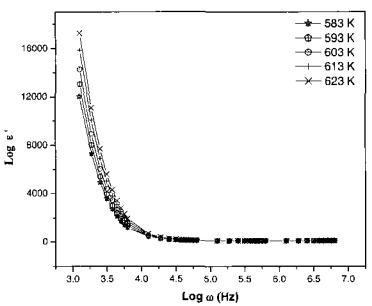

Fig.6. Dielectric spectra for thin film $LiNiVO_4$ at various temperatures

The dispersion of dielectric constant is high at low frequencies at all temperatures. This behavior is attributed to the formation of space charge region at the electrode/electrolyte interface which is familiarly known as $\omega^{(n-1)}$ variation or the

non-Debye type of behaviour, where the space charge regions with respect to the frequency is explained in terms of ion diffusion [21]. At high frequencies due to high periodic reversal of the field at the interface, the contribution of charge carriers especially ions towards the dielectric constant decreases with increasing frequency.

4. Conclusion

Thin film $LiNiVO_4$ has been prepared by Pulsed Laser Deposition technique. The XRD analysis confirms the formation of the inverse spinel thin film $LiNiVO_4$. The impedance analysis indicated the grain interior and the grain boundary response of the thin film $LiNiVO_4$. The conductance spectra indicated the electrode polarization effect of the thin film sample. The modulus analysis indicated the non-Debye nature of the sample. The dielectric spectrum shows a low-frequency dispersion of the dielectric constant, which reveals the space charge effects arising from the electrode. The results indicate that thin film $LiNiVO_4$ is found to have good electrical properties compared to the bulk $LiNiVO_4$ reported elsewhere [22].

Reference:

1. J.B. Bates, N.J. Dudney, B.J. Neudecker, *J.Electrochem. Soc.*, **147,** 59 (2000).
2. S.D. Jonesand, J. R. Akridge, *Solid State Ionics*, **53-56,** 628 (1992).
3. B.J. Neudecker, R.A. Zuhr, & J.B. Bates, *J. Power. Sources*, **81** 27 (1999).
4. B.J. Neudecker, N.J. Dudney, *J.Electrochem.Soc.*,**147,** 517 (2000).
5. S.J. Lee, H.Y. Lee, T.S. Ha, *Elect. & Solid State Letters*, **5 (6),** A138 (2002).
6. M.V. Reddy, C. Wannek, *J. Power Sources* **119-121,** 101 (2003).
7. Y. Iriyama, M. Inaba, T. Abe, Z. Ogumi, *J.Power Sources*, **94,** 175 (2001).
8. D. Singh, W.S. Kim, *Elec.& Solid state Letters* **5 (9),** A 198 (2002).
9. C.V. Ramana, B.S. Naidu, *J.Phys.D:Appl.Phys.* **34,** L35 (2001).
10. G.T.K. Fey, D.L. Huang, *Electrochim. Acta* **45,** 295 (1999).
11. C. Julien, M. Massot, C.P.Vicente, *Mat. Sci and Engg.B.* **75,** 6 (2000).
12. F. Orisini, E. Baudrin, S. Denis, *Solid State Ionics* **107** (1998) 123.
13. M. Sugantha, U.V. Varadaraju, *Solid State Ionics* **95,** 201 (1997).
14. A.K. Jonscher, *Nature* **267,** 673 (1977).
15. J.T.C. Irvine, D.C.Sinclair, A.R.West, *Adv.Mater.* **2,** 138 (1990).
16. B.A.Boukamp, *Solid State Ionics* **20,** 301 (1986).
17. B.A.Boukamp, *Solid State Ionics* **18 & 19,** 136 (1986).
18. Y. Brada, *Phys. Rev. B* **39,** 7645 (1989).
19. D.C. Singclair, A.R. West, *J. Appl. Phys.* **66 (8),** 3850 (1989).
20. G.Williams and D.C.Watts, *Trans.Faraday Soc.* **66,** 80 (1970).
21. F.S. Howell, R.A. Bose, *J. Phys. Chem.* **78,** 639 (1974).
22. S. Selvasekarapandian, M.S. Bhuvaneswari, S. Fujihara, S. Koji, *Acta Materialia* (In press).

Synthesis and Characterization of $LiFePO_4$ Cathode Materials by Microwave Processing

Jian Zhou*, Wenhui Yang, Lin Wang, Guizhen Liu, Hanxing Liu, Shixi Ouyang, Wen Chen
State Key Laboratory of Advanced Technology for Materials Synthesis and Processing, Wuhan University of Technology, Wuhan 430070, P R China

Abstract We report on a novel synthetic method of microwave processing with a domestic 2450MHz microwave synthesis system to prepare $LiFePO_4$ cathode materials. We also studied and report on structure and morphology of the resultant products via three raw materials by XRD and SEM. XRD revealed that a single phase $LiFePO_4$ powder can be synthesized quickly and easily by microwave processing. The results indicate that microwave processing is a promising method of processing $LiFePO_4$ cathode materials.

Key words $LiFePO_4$, cathode material, microwave processing

1. Introduction

An ever growing demand for high density rechargeable batteries for portable electronic devices, electric vehicle systems, and dispersed type energy storage systems is exerting pressure for the development of advanced lithium-ion batteries. Among the known Li-insertion compounds, the layered rock salt systems $LiCoO_2$, $LiNiO_2$, and the manganese-spinel framework system $LiMn_2O_4$ have been used commercially as 4.0 V cathode materials in rechargeable lithium-ion batteries [1-3]. However, because of the toxicity and high-cost of $LiCoO_2$, difficulty in synthesizing phase pure $LiNiO_2$, low energy density and poor cycling properties of $LiMn_2O_4$, considerable effort has been devoted to develop new lithium-insertion compounds to be used as the cathode materials for next generation lithium-ion batteries. Olivine-type lithium iron phosphate ($LiFePO_4$) as a new cathode material, first reported by Paghi et al in 1997[4], attracted worldwide attention and since then has been investigated intensively during last few years [5,6].

Among many advantages of $LiFePO_4$ over other candidates, some are that it has a high theoretical specific capacity (170 mAh/g), an intermediate voltage value (3.45 V versus Li/Li^+), excellent cycling behavior, and low cost and non-toxicity [4,5]. However, the main problem with $LiFePO_4$ is that its synthesis is not an easy task because of the iron oxidation state. Several methods have been explored for its synthesis including solid-state reaction, hydrothermal synthesis, and sol-gel processing [5,6]. However, all of these methods need heat-treatments at high temperatures (500-900°C) for a long time (up to 24 hours), which increases the fabrication cost and difficultly get pure phase and limits the yields.

Microwave synthesis is a novel technique featuring high efficiency and capability to synthesize some compounds that are very difficult or impossible to be fabricated by conventional methods [7,8]. The microwave synthesis is based on a novel heating process whose heating mechanism is fundamentally different from conventional heating methods. In a conventional heating method, the heat generated by external source is transferred to the material via radiation, conduction, or convection. Considerable energy losses and inhomogeneous heating are always serious concerns in the conventional heating processes. The microwave process provides a revolutionary heating method for materials processing and synthesis, in which the energy absorbed by the materials located in microwave field is converted in to heat internally instead of originated from external heating sources. This provides a highly efficient, homogeneous, and uniform heating of the entire work-piece

* Corresponding Author:: Zhoujian@mail.whut.edu.cn

simultaneously. Many different physical phenomena are involved in the microwave-matter interaction during the microwave processing, such as highly enhanced reaction/synthesis kinetics [9].

Microwave synthesis is a novel technique featuring high efficiency and capability to synthesize $LiFePO_4$ at lower temperatures in much shorter time. In 2003, two other research groups reported microwave synthesis of $LiFePO_4$ in a very short time (5-10 minutes) [10,11]. However, their experiments were conducted in a microwave home oven without any atmosphere control, and therefore they could not produce high quality and phase pure $LiFePO_4$.

In this paper we research the microwave synthesis of $LiFeOP_4$ materials in single mode cavity and characterization in microstructure and morphology of $LiFeOP_4$.

2. Experiments

Some $LiFeOP_4$ compounds was synthesized in microwave via solid state reaction using $LiOH{\cdot}H_2O$, ammonium dihydrogen phosphate ($NH_4H_2PO_4$) and iron oxalate ($FeC_2O_4{\cdot}2H_2O$) in 1:1:1 mole rate as the raw materials. Mixture of the precursor powders was pressure to ϕ12×5.6mm disc form samples at 10MPa and heated in the single mode (TE_{10n}) microwave chamber at different temperatures and hold at that temperature for different times, e.g. 2 minute, 2.5 minutes, 10 minutes at atmosphere.

Each sample then will be characterized to determine the phase composition and crystal structure, and enable us to optimize the microwave synthesis parameter to obtain high quality $LiFePO_4$ compounds. Several analytical tools was used for the characterization of microwave synthesized $LiFePO_4$ materials. The X-ray diffraction (XRD) was used to determine the phase composition and crystal structure; the scanning electronic microscope (SEM) was used to examine the grain morphology and particle size of the $LiFePO_4$ compounds. BET analysis of particle surface area was used in micromeritics Gemini 2360 instrument.

3. Results and analyses

XRD patterns of $LiFePO_4$ Compounds synthesized by microwave process are shown in Figure 1.

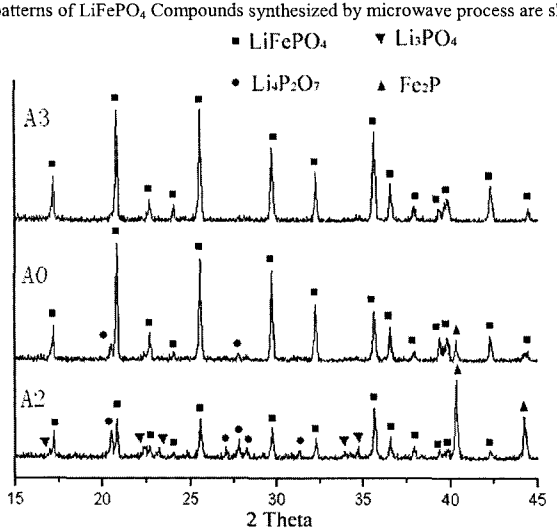

Figure 1. XRD patterns of $LiFePO_4$ Compounds synthesized by microwave process.

A3: 650□×2min, A0: 750□×2.5min, A2: 1000□×10min

As shown in Figure 1, the X-ray diffraction patterns exhibited that the phase pure $LiFePO_4$ was obtained by microwave heating at 650°C in only 2 minutes. The $LiFePO_4$ will decompound with the temperature increasing and longer synthesis time, and become multiphase materials, so conventional methods difficultly get pure phase for the long synthesis time.

The morphology of the microwave synthesized $LiFePO_4$ powder is shown in Figure 2. Since the microwave synthesis was completed in very short time, the obtained $LiFeOP_4$ are in micron size and in good crystal structure, and conventional methods difficultly get good crystal structure in only 2 minutes.

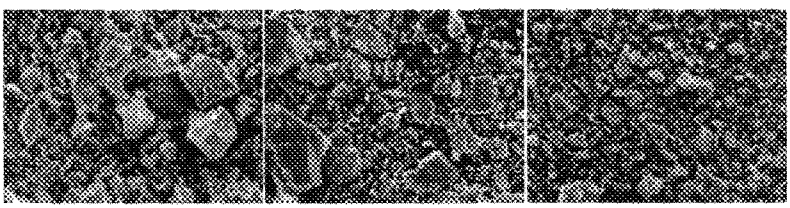

(a) 650□×2min (b) 750□×2.5min (c) 1000□×10min

Figure 2. SEM images of $LiFePO_4$ Compounds synthesized by microwave heating process.

BET analysis of particle surface area show that surface area are 0.2623 sq.m/g in 650□×2min, 4.6102 sq.m/g in 750□×2.5min, 0.1226 sq.m/g in 1000□×10min respectively. For high-density lithium-ion battery applications, it is desired that the synthesized $LiFePO_4$ powder should have very fine particle size, large specific surface area, and high chemical activity. In a conventional heating process, the solid-state reaction takes place at elevated temperatures higher than 600°C, and also requires very long time to obtain phase pure $LiFePO_4$ powder. As we demonstrated in our preliminary study, it is expected that microwave synthesis can lower the synthesis temperature and shorten the processing time substantially. This will enable to obtain very fine powders and good crystal structure.

Classically there are various mechanisms identified in the microwave-materials interaction. Some of them are due to dipole reorientation, space and ionic charge, which are primarily found in insulators or dielectric materials. Other losses, depending upon the material under interaction, include through electric conduction and/or magnetic induction in conductive materials.

4. Conclusion

We conducted a systematic study to determine the optimum processing parameters such as 650□ synthesis temperature, hold at that temperature for 2min, etc.

Microwave heating is a novel approach to synthesize $LiFePO_4$ compound with several advantages over conventional synthesis methods, e.g.:

- Lower synthesis temperatures and shorter synthesis time can minimize the grain growth to facilitate the synthesis of fine particle size $LiFePO_4$ products.
- External field activated synthesis can enhance the diffusion and reaction kinetics to produce highly reactive and phase pure $LiFePO_4$.
- High efficiency processing will achieve considerable energy and cost savings.
- The method is simple and easy to scale-up for commercialization.

Since the microwave synthesis is a relatively new technology, there are still a lot of unknowns. The proposed research work will systematically investigate some unique features of microwave

synthesis processing, external field activated reaction mechanism and kinetics. It is intellectually challenging as the execution entails well-integrated knowledge in physics, chemistry, materials science and microwave engineering.

Acknowlegements

This research was supported by Chinese Nature Science Foundation Committee (50472043) and the Excellent Young Teachers Program of MOE, P R China (EYTP 2003-355).

References

1. K. Mizushima, P.C. Jones, P.J. Wiseman, and J.B. Goodenough, "Li_xCoO_2 ($0<x<1$): A new cathode material for batteries of high energy density", Mater. Res. Bull. **15**, 783-789 (1980)
2. M.G.S.R. Thomas, W.I.F. David, and J.B. Goodenough, "Synthesisi and structural characterization of the normal spinel $Li[Ni_2]O_4$", Mater. Res. Bull. **20**, 1137-1146 (1985)
3. T. Ohzuku, M. Kitagawa, and T. Hirai, "Electrochemistry of manganese dioxide lithium nonaqueous cell (III) x-ray diffractional study on the reduction of spinel-related manganese dioxide", J. Electrochem. Sco. **137**, 769-774 (1990)
4. A.K. Padhi, K.S . Nanjundaswamy,and J.B. Goodenough, "Phospho-olivines as positive-electrode materials for rechargeable lithium batteries", J. Electrochem. Sco. **144**, 1188-1194 (1997)
5. S. Yang, Y. Song, P.Y. Zavalij, and M.S. Whittingham, "Reactivity, stability and electrochemical behavior of lithium iron phosphates", Electrochem. Commun. **4**, 239-244 (2002)
6. J. Lu, Z. Zhang, Z. Tang, and W. Shen, "Characterization of $LiFePO_4$ synthesized by sol-gel processing", Key Eng. Mater. **280-283**, 453-456 (2005)
7. J. Cheng, R. Guo, and Q-M. Wang, "Zinc oxide single-crystal microtubes", Appl. Phys. Lett. **85** (22), 5140-5142 (2004)
8. J. Cheng, D. Agrawal, Y. Zhang, B. Drawl, and R. Roy, "Fabricating transparent ceramics by microwave sintering", American Ceramic Society Bulletin, **79** (9): 71-74, (2000)
9. J. Cheng, D. Agrawal, Y. Zhang, and R. Roy, "Microwave reactive sintering to fully transparent aluminum oxynitride (ALON) ceramics", J. Mater. Sci. Lett., **20**: 77-79 (2001)
10. M. Higuchi, K. Katayama, Y. Azuma, M. Yukawa, and M. Subara, "Synthesis of $LiFePO_4$ cathode materials by microwave processing", J. Power Sources **119-121**, 258 (2003)
11. K.S. Park, J.T. Son, H.T. Chung, S.J. Kim, C.H. Lee, and H.G. Kim, "Synthesis of $LiFePO_4$ cathode materials by co-precipitation and microwave processing", Electrochem. Commun. **5**, 839 (2003)

CHARACTERIZATION OF $Nd_{0.8}Sr_{0.2}CoO_{3-\delta}$ INCLUDING Pt SECOND PHASES AS THE CATHODE MATERIAL FOR LOW-TEMPERATURE FOR SOFCs

JUNG WOON CHOI, HAN JI KIM, HAN BYEL SHIM AND KWANG SOO YOO[a]
Department of Materials Science and Engineering, University of Seoul, Seoul 130-743, KOREA

The perovskites with nominal compositions $Nd_{0.8}Sr_{0.2}CoO_{3-\delta}$ were fabricated as cathode materials of low-temperature operating solid oxide fuel cells (SOFCs) using a solid-state reaction method. The Pt solution to improve electrical properties at low temperature was dispersed into cathode material. X-ray diffraction analysis and microstructure observation for the sintered samples were performed. The ac complex impedance was measured in the temperature range of 600-900°C in air and fitted with a Solatron ZView program. The crystal structure, microstructure, impedance spectra, and polarization resistance of $Nd_{0.8}Sr_{0.2}CoO_{3-\delta}$ were characterized systematically.

1. Introduction

A fuel cell is a device for direct conversion of chemical energy into electrical energy. The solid oxide fuel cell (SOFC) continues to attract interest as a potential reliable, durable, and inexpensive technology for generating electricity from as a bydrocarbon fuels [1]. In the case of cathode materials, they should have high electrical conductivity, adequate porosity for oxygen gas transportation, good compatibility with the electrolyte, and long-term stability. Recently, the porous ceramic structures synthesized from perovskite oxides were used as cathodes of the low operating temperature for SOFCs [2].

In these perovskites, substitution of a divalent cation for a trivalent cation results mostly in inducing electron holes in air. At lower oxygen pressure, however, charge compensation is likely to be achieved through the formation of oxygen-ion vacancies. These oxygen vacancies provide the pathway for the oxide ions through the electrode material. Therefore, the flux through the bulk electrode material is likely to increase. High oxygen flux at modest overpotentials is expected to be an advantage of these materials as SOFC cathodes [3]. Recently there has been a great deal of interest in rare earth cobaltite phases with perovskite structures ($Ln_{1-x}SrCoO_{3-\delta}$) (Ln = lanthanide ion), due to their applications in solid oxide fuel cells [4-7] and as ceramic membranes for high temperature oxygen separation [8,9].

Pt is another probable candidate for cathode because of its high catalytic activity for reduction/oxidation of oxygen. Pt can be recycled even though it is expensive.

[a] Corresponding author: ksyoo@uos.ac.kr

However, the application of Pt to cathodes has not yet been investigated well because we have cheaper lanthanum manganite for high temperature SOFCs so far [10].

The objective of this study was to investigate the electrical properties of the Pt-dispersed $Nd_{0.8}Sr_{0.2}CoO_{3-\delta}$ composition at low temperature. The polarization resistance of the cathode was evaluated by using an impedance analyzer. The interfacial reaction and morphology between the cathode and the electrolyte were observed through a field emission scanning electron microscopy (FESEM). Then the relationship between polarization resistance and porosity was examined.

2. Experimental

An 8-mol% YSZ disk (diameter: 11.5 mm, thickness: 1.6 mm) was used as the solid electrolyte. As starting materials, Nd_2O_3 (Cerac), $SrCO_3$ (Cerac), Co_2O_3 (Tasco), $PtCl_4 \cdot 5H_2O$ (High Purity Chemicals) and 8-mol% YSZ (Tohso) were used in this experiment. The powders were mixed in ethanol and milled for 72 hours, after which the powders were pressed into pellets and calcined at 1000°C for 4 hours. The cathode powders and vehicle (α-terpineol, 2-butoxyethoxy, polyvinyl butyral-co-vinyl alcohol-co-vinyl acetate, polyethylene) were mixed at a 71:29 weight ratio and ground to form the paste.

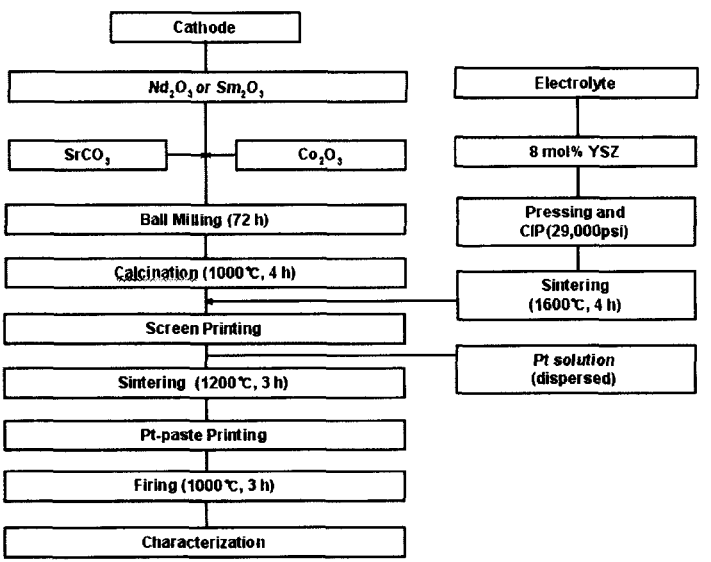

Fig. 1. Flow chart of experimental procedure.

The YSZ disk was prepared by screen-printing a mixed paste (powder : vehicle=71:29). The screen-printed samples were sintered at 1200°C for 3 hours as shown in Fig. 1. Platinum chloride ($PtCl_4 \cdot 5H_2O$) was dissolved in distilled water including hydrochloric acid of 4 vol.% and stirred for 4 hours at a temperature of 60 °C. This Pt solution was impregnated into the screen-printed cathode thick film. After this experimental step, the Pt-paste was formed on the rear side of the YSZ electrolyte as the reference electrode and the counter electrode. The half-cells were all formed, as shown in Fig. 2. The cathode film was observed using an FESEM (Hitachi 4300, Hitachi) and X-ray diffractometer (Rigaku Mini Flex). Porosity was calculated using an Image Analyzer. Electrical properties were measured using an Impedance Analyzer (SI 1260, Solatron) and an Electrochemical Interface (SI 1287, Solatron). Measurements were taken without a DC bias and spectra were obtained within a frequency range of 3 x 10^7-0.01 Hz with applied AC voltage amplitude of 10 mV. All the samples were measured at a temperature range of 600-900°C.

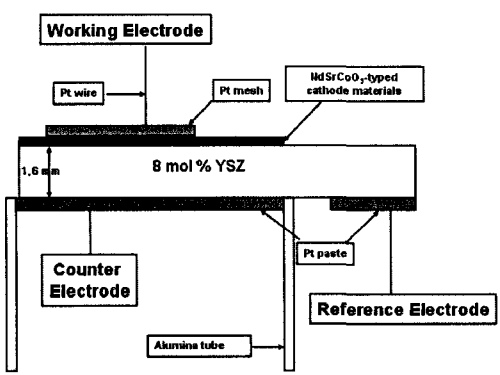

Fig. 2. Schematic diagram of the half-cell.

3. Results and Discussion

3.1 Physical Properties

Figure 3 shows the XRD pattern of the lanthanide cobaltite cathode materials after calcining at 1000 °C for 4 hours. The cathode powders were all determined to have been single-phase. Figure 4 show the microstructure and interface between the cathode and the electrolyte. As seen from the FESEM in these figures, the cathode films on the YSZ electrolyte were very porous and the thickness of the cathode material was about 15 ㎛. We found that cathode particles were well interconnected. The electrode microstructure appeared uniform and showed good and continuous bonding with the dense YSZ electrolyte pellet. In addition, Pt particles were observed from Fig. 4 (b) and (d).

The porosity was calculated by using the Image Analyzer, ranged from 30% to 34%.

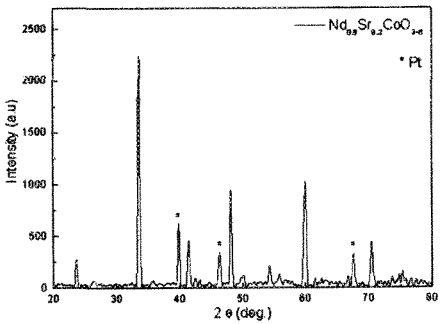

Fig. 3. X-ray diffraction data of the Pt-dispersed $Nd_{0.8}Sr_{0.2}CoO_3$ cathode material.

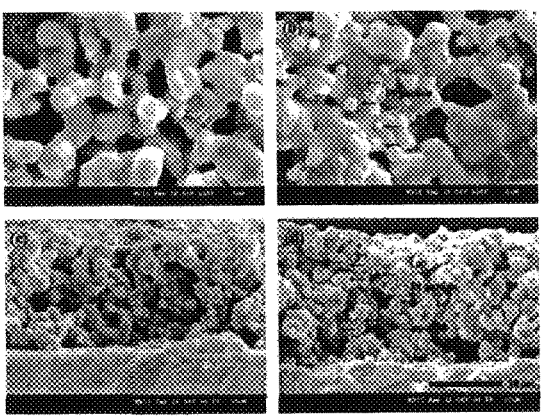

Fig. 4. Surface micrographs of the cathode materials sintered at 1,200℃ for 3 h; (a) $Nd_{0.8}Sr_{0.2}CoO_3$ (b) Pt-dispersed $Nd_{0.8}Sr_{0.2}CoO_3$, (c) $Nd_{0.8}Sr_{0.2}CoO_3$ (cross-sectional), (d) Pt-dispersed $Nd_{0.8}Sr_{0.2}CoO_3$ (cross-sectional).

3.2 Electrical Properties

The impedance measurements were carried out at 600°C, 700°C, 800°C, and 900°C, respectively. As shown in Fig. 5, with increasing operating temperature, both the polarization resistance values (R_2-R_1) and the interfacial resistance values (R_3-R_2) decreased, because the activation energy decreases in high temperature ranges [1]. The polarization resistance of all samples was smaller than the interfacial resistance. The polarization resistance of the $Nd_{0.8}Sr_{0.2}CoO_3$ was 8.53 Ωcm^2 and 2.81 Ωcm^2 at 600℃ and 700℃, respectively. Figure 6 shows the impedance spectra of the Pt-dispersed $Nd_{0.8}Sr_{0.2}CoO_3$. In this figure, the polarization resistances of the sample were 0.018 Ωcm^2 at 600℃, and 0.001 Ωcm^2 at 700℃. Accordingly, Pt-

dispersed $Nd_{0.8}Sr_{0.2}CoO_3$ material was better than $Nd_{0.8}Sr_{0.2}CoO_3$ for the SOFC cathode.

Figures 7 and 8 showed the polarization resistances of the $Nd_{0.8}Sr_{0.2}CoO_3$ and Pt-dispersed $Nd_{0.8}Sr_{0.2}CoO_3$ cathode materials, respectively.

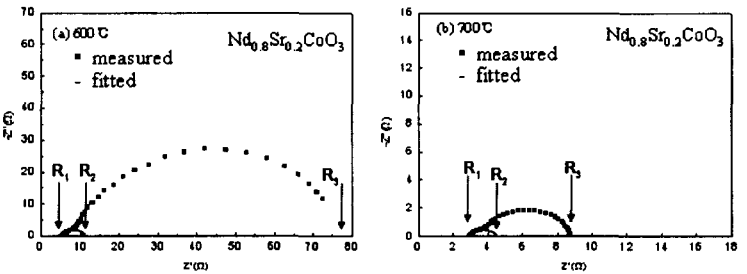

Fig. 5. Impedance spectra of the $Nd_{0.8}Sr_{0.2}CoO_3$ cathode materials sintered at 1200°C for 3 h.

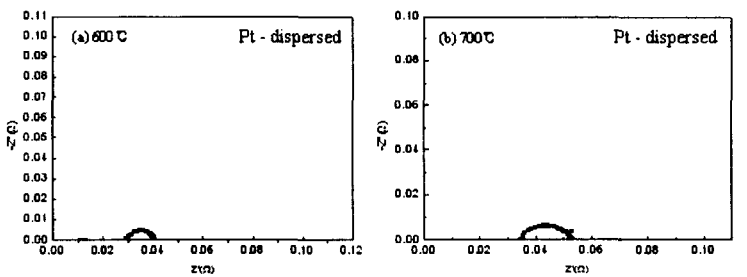

Fig. 6. Impedance spectra of the Pt-dispersed $Nd_{0.8}Sr_{0.2}CoO_3$ cathode materials sintered at 1200°C for 3 h.

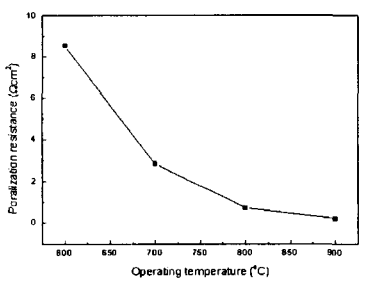

Fig. 7. Polarization resistance of the $Nd_{0.8}Sr_{0.2}CoO_3$ cathode materials.

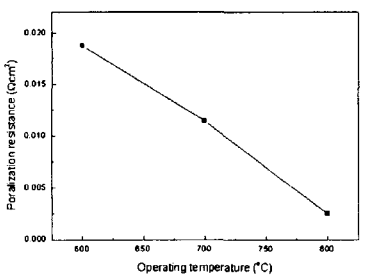

Fig. 8. Polarization resistance of the Pt-dispersed $Nd_{0.8}Sr_{0.2}CoO_3$ cathode materials.

4. Conclusions

The half-cells fabricated with Pt-dispersed $Nd_{0.8}Sr_{0.2}CoO_3$ on the YSZ electrolyte

had good polarization resistance of 0.001 Ωcm^2 at operating temperature of 700°C and even 0.018 Ωcm^2 at 600 °C. And the samples sintered at 1200 °C for 3 hours were observed to have the ideal porosity for cathode materials for low-temperature SOFC.

Acknowledgement

This work was supported by the Core Technology Development Program for Fuel Cells of Ministry of Commerce, Industry and Energy, Korea.

References

1. M. Hrovat, N. Katsarakis, K. Reichmann, S. Bernik, D. Kuscer and J. Holc, *Solid State Ionics*, **83**, 99 (1996).
2. M. T. Colmer, B. C. H. Steels and J. A. Kilner, *Solid State Ionics*, **147**, 41-48, (2002).
3. E. Maguire, B. Gharbage, F. A. B. Marques and J. A. Labrincha, *Solid State Ionics*, **127** 329-335, (2000).
4. S. J. Skinner, *Int. J. Inorg. Mater.*, **3**, 113 (2001).
5. H. Y. Tu, Y. Takeda, N. Imanishi and O. Yamamoto, *Solid State Ionics*, **100**, 283 (1997).
6. R. H. E. van Doorn and A. J. Burggraaf, *Solid State Ionics*, **128**, 65 (2000).
7. S. B. Adler, *Solid State Ionics*, **111**, 111 (1998).
8. A. V. Kovalevsky, V. V. Kharton, V. N. Tikhonovich, E. N. Naumovich, A. A. Tonoyan, O. P. Reut and L. S. Boginsky, *Mater. Sci. Eng.*, **B 52**, 105 (1998).
9. V. V. Kharton, A. A. Yaremchenko, A. V. Kovalevsky, A. P. Viskup, E. N. Naumovich and P. F. Kerko, *J. Membrane Sci.*, **163**, 307 (1999).
10. K. Sasaki, J. Tamura and M. Dokiya, *Solid State Ionics*, **144**, 223 (2001).

THERMODYNAMIC BEHAVIOR OF LITHIUM INTERCALATION INTO NATURAL VEIN AND SYNTHETIC GRAPHITE

N.W.B. BALASOORIYA AND P.W.S.K. BANDARANAYAKE
Department of Physics, University of Peradeniya, Peradeniya, Sri Lanka
Email: balasooriya@seu.ac.lk, kumarab@pdn.ac.lk

Ph. TOUZAIN
Laboratoire d'Electrochimie et de Physico-chimie des Matériaux et Interfaces (LEPMI), ENSEEG, INPG, B.P.75, 38402 St. Martin d'Hères, France.
Email: Philippe.Touzain@lepmi.inpg.fr

Sri Lanka natural vein graphite has various morphologies with different structural and physical characteristics. The identified most abundant morphology, the shiny-slippery-fibrous (SSI) graphite found in two mines, Bogala and Kahatagaha-Kolongaha, has a very high purity over 98% and high crystallinity. The characterization of Li-graphite intercalation process was mainly performed with the initial discharge-charge profiles at the current rate of C/20 and C/40, and cycled between the initial open circuit voltage and 0.005 V vs. Li/Li^+ in lithium cells in 1M $LiPF_6$ (EC/DMC; 1:1). The synthetic KS25 graphite showed much better rechargeability and higher intercalation rate of lithium ions than natural BSSI and KSSI graphite. The irreversible capacity loss of natural vein graphite was partly due to passivation and exfoliation. But the major irreversible capacity loss of the graphite (natural or synthetic) was mainly due to lithium trapping in the internal pore spaces of graphite material or electrode structure. Measurements of the open circuit voltage in lithium cells with graphite as working electrode were used to obtain the thermodynamic factors such as entropy, ΔS, and enthalpy, ΔH, of lithium intercalation into natural and synthetic graphite. These thermodynamic values were determined in discharging process of the lithium cells from 0.005 V to 1.50 V vs Li/Li^+ at C/5 rate. For all the types of graphite, initially large ΔS decreases with lithium concentration and then becomes negative and shows three entropy plateaus indicating the transition of stages in graphite-lithium intercalation compounds. For natural and synthetic graphite ΔH is negative and increases with lithium concentration and follows the staging process of lithium intercalation.

1. Introduction

Highly crystalline graphite is capable to intercalate lithium up to one lithium atom for every six carbon atoms which is denoted by LiC_6. The LiC_6 can be obtained via a direct chemical reaction of metallic lithium with graphite[1] or by electrochemical intercalation with a theoretical specific capacity of 372 mAh/g.[2, 3]

The open circuit voltage (OCV) of a lithium cell of graphitic Li_xC_6 vs. Li metal is a direct measure of the difference of chemical potential for a lithium atom in the Li metal and in the graphite.[4] The entropy and enthalpy changes in the electrochemical reaction of the lithium ion cells are important thermodynamic factors to characterize the electrode materials, to design the thermal capability and heat management.

The entropy change in the cell reaction can be obtained by using of the open circuit voltage (OCV).[5] The cell reaction of the lithium cell is as in Eq. (1`).

$$6C + x\,Li^+ + x\,e^- \Leftrightarrow Li_xC_6 \qquad (1)$$

In the case of a reversible cell reaction under the conditions of constant temperature and constant pressure, the enthalpy change, ΔH, and the entropy change, ΔS, in the cell reaction has the following equation with Gibbs free energy change, ΔG.

$$\Delta G = \Delta H - T\Delta S \qquad (2)$$

The Gibbs free energy change, ΔG, is related to the electromotive force of the cell, E_{emf}. The E_0, OCV, can approximate to the E_{emf}.

$$\Delta G = -F\,E_0 \qquad (3)$$

Where F is the Faraday constant and T is the absolute temperature.
The entropy of formation is:

$$\Delta S = F\left(\partial E0/\partial T\right) \qquad (4)$$

and the enthalpy of formation is;

$$\Delta H = -FE_0 + TF\left(\partial E0/\partial T\right) \qquad (5)$$

The variation of any state function, ΔG, ΔH and ΔS, is related to the addition of incremental amount of lithium into the host material having lithium concentration, *x*, taking metallic *bcc* lithium and graphite.[6]

Natural vein graphite has various morphologies, with different structural and physical characteristics.[7] The purpose of this study is to evaluate the thermodynamic factors during process of lithium electrochemical insertion into a particular type of Sri Lanka natural vein graphite, called shiny-slippery- fibrous graphite from Bogala (BSSI) or Kahatagaha-Kolongaha (KSSI) and to compare its thermodynamic characteristics with synthetic graphite (KS25).

2. Experimental

Natural Sri Lanka vein graphite was collected from graphite mines of Bogala and Kahatagaha-Kolongaha. Synthetic graphite (KS25) was used as received from Timcal Ltd. The selected graphite samples (BSSI and KSSI) were crushed by using an agate mortar and separated for few minutes to the particle size less than 63μm by using a mechanical sieve-shaker.

Content of carbon and sulphur in the natural graphite was estimated using ELTRA CS800 Carbon and Sulphur determinator. X-Ray diffraction (XRD) studies

were carried out with a Philips X-Ray generator (using Cu K_α radiation with wavelength λ=1.5406 Å). XRD was used to verify the structure characteristics of graphite powder. The amount of rhombohedral phase was evaluated from X-ray diffractograms by comparing the integrated intensities of (101) hexagonal and (101) rhombohedral reflections.

Lithium half cells were prepared at fixed temperature (25°C), using natural BSSI, KSSI and synthetic KS25 graphite, as a composite electrode containing with 10% of acetylene black (AB: Y20) as the electrode conducting additive enhancer and 15% of PVDF (Kynar) as a binder, dissolved in DBP (Dibutyl Phthalate) (Sigma). About 10mg of natural graphite was used to each cell. The dried electrode was mounted in a coin type (CR2430) cell, with Li as the counter electrode and reference electrode, and micro-porous propylene sheet (Celgard 2400) as the separator. The electrolyte of 1M $LiPF_6$ in equi-volume mixture of ethylene carbonate (EC) and dimethyl carbonate (DMC) (Aldrich), were prepared in an argon-filled glove box. Electrochemical experiments were performed with a MacPile potentiostat-galvanostat. The coin cells were cycled from 0.005 V to 1.50 V at different current rates of C/20 and C/40 and also five times at a C/5 for thermodynamic studies.

After completed the five cycles, coin cells were placed in a thermostat chamber (Bioblock Scientific) which was connected to the temperature cooler (Bioblock Scientific; Huber). The temperature was decreased from 25°C (room temperature) to 0°C in approximately 5°C intervals and six OCV measurements were made with a 30 minutes gap to relax of the lithium distribution in the active materials. The cell voltage was measured by digital multimeter (Keithley). The cell was discharged at a particular potential and it was placed in the thermostat chamber again to carryout a similar sequence of measurements.

3. Results and Discussion

3.1. Chemical and Crystallography characteristics of natural graphite

The BSSI & KSSI graphites have a high purity over 98%, which indicates good quality graphite. Carbon can be characterized by its interplanar distance (d_{002}) and by its coherence length (L_c) which can be estimated quantitatively by x-ray diffraction (XRD). The L_c values of the natural graphite were calculated with the d_{002} diffraction line using the Sherrer's formula. The average L_c values of natural and synthetic graphite are about 85 nm. Fig.1 shows that the rhombohedral phase content of the synthetic graphite (35%) is higher than the natural graphite one (14-24%). When increasing the rhombohedral phase, it seems that lots of defects were also created, which could affect its electrochemical behavior.[8]

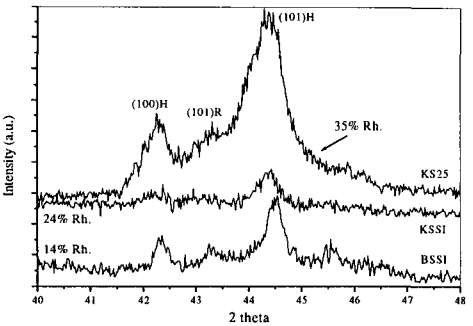

Figure 1. Variation of the rhombohedral phase contents in natural and synthetic graphite

3.2. Rhombohedral phase content and irreversible capacity during the first cycle

The reversible and irreversible capacities of natural vein graphite and synthetic graphite, and current rates are compiled in table 1. From these results, it is obvious that the synthetic KS25 graphite shows much better rechargeability and higher intercalation rate of lithium ions than natural BSSI and KSSI graphite.

Table 1. First reversible and irreversible capacities of the Li/Natural and synthetic graphite cells in 1M $LiPF_6$ (EC/DMC).

Types of graphite	Current rate						$(101)_R/(101)_H$ intensity ratio, %
	C/5		C/20		C/40		
	C_{rev} mAh /g	C_{irr} %	C_{rev} mA h/g	C_{irr} %	C_{rev} mA h/g	C_{irr} %	
BSSI	263	32	301	46	341	23	14
KSSI	244	41	307	31	354	28	24
KS25	298	27	341	29	349	23	35

The irreversible capacity of lithium intercalation into the graphite electrode during the first cycle of Li ion cells is associated with passivation and exfoliation. Passivation corresponds to reductive decomposition of solvents and simultaneous formation of a SEI film.[9] Exfoliation results decomposition of solvent molecules co-intercalated with lithium ions between graphene sheets.[10] Fig.2 shows the irreversible capacity of natural vein graphite is partly due to passivation (*C* plateau at 0.85 V vs. Li/Li^+) and exfoliation (*D* plateau at 0.50 V vs. Li/Li^+). Lithium intercalation in synthetic graphite, high content of the rhombohedral phase shows that there is no great difference between the lithium intercalation capacities in both hexagonal and rhombohedral graphite phases;[11] The best part of the high irreversible capacity loss for natural or synthetic graphite is due to lithium atoms trapping in the internal pore

spaces of graphite material or in the electrode structure.

The reversible and irreversible capacities of Li/natural and synthetic graphite cells were used to calculate the entropy and enthalpy of lithium intercalation.

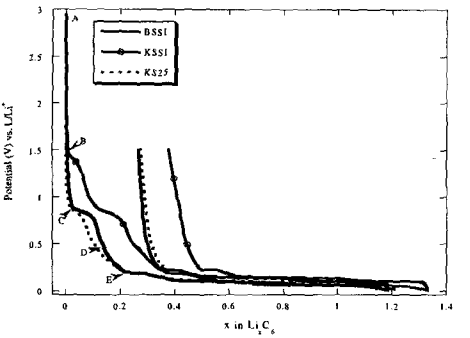

Figure 2. Li/ natural vein and synthetic graphite cells in 1M $LiPF_6$ (EC/DMC), at current rate C/40.

3.3. Variations of entropy and lithium concentration

The entropy of insertion of lithium into BSSI, KSSI and KS25 graphite is large and positive at low lithium concentration. The $\Delta S >> 0$ can be explained as originating by the change in configurational entropy.[12] This higher value of entropy indicates that the heat effect is very exothermic during the first lithium intercalation before it becomes negative around x=0.1.[13] This domain of high positive entropy can be attributed to the order-disorder transformations, and to the transition of layer stacking from AB to AA during intercalation. The shift of graphene layers contributes much less to entropy change compared to order-disorder transformations because low energy is required for the layer shifting.[14] The configurational entropy is zero for the initial materials, lithium, crystalline graphite, and ordered GIC's because the orientation of one unit cell dictates the position of the all atoms in the crystals.

The entropy versus lithium composition curves (Fig.3a) for natural and synthetic graphite show that almost three plateaus correspond to the stage transitions of lithium intercalation. In BSSI graphite, the first plateau was observed when entropy, ΔS, rapidly reaches zero and may be indicate the formation of mixture of the third and lower stages of intercalation compounds. The next plateau which appear at about ΔS = -13 J mol^{-1} K^{-1} indicates the third to second stage transition of intercalation compounds, then ΔS increases shapely up to -4 $Jmol^{-1}k^{-1}$ and makes a third plateau of entropy indicating the second to first stage transition. The entropy of intercalation is unchanged as the stage one compound forms. In KSSI case, the entropy curve is roughly similar to the BSSI case with a weak shift toward positive entropy and high x values. The variation of entropy in KS25 graphite, the first flat curve was observed when entropy, ΔS, reaches -5.28 J mol^{-1} K^{-1} and indicated the formation of a mixture

of the second and lower stages of intercalation compounds. A curve different of the natural graphite ones appeared; ΔS rapidly reaches -1.28 J mol^{-1} K^{-1} and indicated the second to first stage transition of intercalation compounds.

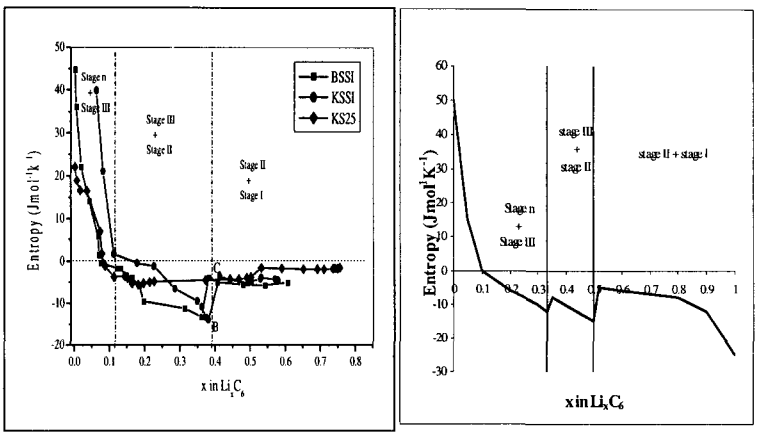

(a) (b)

Figure 3. (a) Variation of the entropy with lithium concentration for natural and synthetic graphite, (b) Theoretical curve

Fig. 3(b) shows that the theoretical curve or expected theoretical curve, indicates the second to first stage transition of intercalation compounds (*B* to *C*) is close to x=0.5 but in Fig. 3(a) corresponds to 0.4. This may be due to loss of some lithium during the lithium intercalation. This figure also shows that the entropy of intercalation process becomes negative at higher lithium concentrations for $x > 0.2$. This behavior is not configuration entropy. This may be vibrational in origin.[13] When lithium intercalated into graphite, the lithium atoms are restricted in their movements normal to the graphene planes, and explore a smaller range of displacements than in lithium metal; the change in vibrational entropy with intercalation is therefore negative.[12]

Al Hallaj et. al.[13]showed when the OCV is below 0.1 V, the intercalated graphite is in ordered first stage and a perfect hexagonal structure is expected that may be due to electrostatic repulsion between the lithium ions, and then ΔS becomes positive. But there is a possibility that the first, second or third stage compounds are not fully ordered, so slight increase of configurational entropy may be expected at the theoretical values of x = 0.33 (transition III/II) and x = 0.50 (transition II/I). It was perfectly observed for experimental x=0.4 (for KSSI and BSSI but 0.5 for KS25) corresponding to the transition between stage II to a mixture of stage II and stage I. It is possible the configurational entropy in the initial first stage or second stage compounds is positive.

3.4. Variations of enthalpy and lithium concentration

The enthalpy of intercalation is negative for all lithium concentrations. The plateaus correspond to the stage transitions of the intercalation compounds. The ΔH is less negative when forming the stage I compound from the stage II compounds for all types of graphite. This indicates of a repulsive lithium-lithium interaction at high lithium concentrations.[12] That also confirms that all the principal bounds between lithium atom and carbon atom are made at the beginning of the intercalation for $0<x<0.1$ (very exothermic bounding).

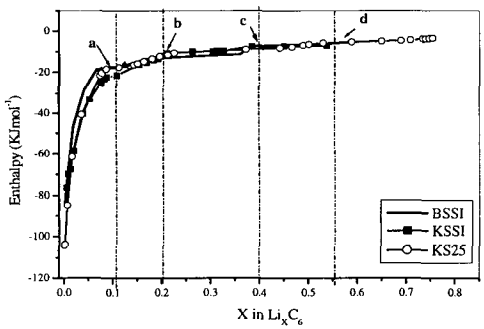

Figure 4. Variation of the enthalpy with lithium concentration for natural and synthetic graphite.

Fig. 4 shows that the three enthalpy changes can be seen in both graphite at about x=0.1, 0.2 and 0.4, which are indicated *a*, *b* and *c* for BSSI and KSSI graphite but only two enthalpy changes can be observed for KS25 graphite at x=0.2 and 0.55, which was labeled '*b*' and '*d*'. These changes correspond to the stage transitions of the intercalation compounds. The point '*a*' of the BSSI and KSSI graphite corresponds to the lower stages-third stage transition, the point *b* corresponds to the third-second stage transition and the point '*c*' correspond to the second-first stage transition. The points '*b*' and '*d*' of the KS25 graphite correspond perhaps to the lower stages-second stage transition and the second-first stage transition respectively.

4. Conclusions

The thermodynamic factors such as entropy and enthalpy of lithium intercalation into natural Sri Lanka vein graphite were obtained by measuring of open circuit voltage (OCV) in lithium cells in 1M $LiPF_6$ (EC/DMC; 1:1). The difference between cutoff potential and OCV measurements are mainly due to the different measuring

conditions such as discharge rate, temperature etc... and to be self-discharge because for the long term OCV measurements at varies temperatures. Our results for the synthetic graphite agreed well with measurements of entropy and enthalpy during discharge processes with Reynier et.al.[6] The entropy of lithium insertion showed shaper features in stage transitions and the enthalpy follows the staging process.

Acknowledgements

The fellowship given by the Ministry of Foreign Affairs (MAE), France through French Embassy of Sri Lanka to NWBB to carry out research work at LEPMI, INPG is greatly acknowledged.

References

1. A. Hérold, *Bull. Soc.Chim.* **187**, 999 (1955).
2. J.O. Besenhard, *Carbon* **14**, 93 (1976).
3. R. Yazami and Ph. Touzain, *J. Power Sources* **9**, 365 (1983).
4. R. Yazami, in: G. Pistoia (Ed.), *Lithium Batteries-New Materials, Development and Perspectives*, Elsevier, Amsterdam, 49 (1994).
5. A.J. Bard, and L.R. Faulkner, *Electrochemical, Methods, Fundamentals and Applications*, J. Wiley & Sons, 48-49 (1980).
6. Y. Reynier, R. Yazami and B. Fultz, *J. Power Sources* **119-121**, 850 (2003).
7. N.W.B. Balasooriya, K. Dahanayake, Ph. Touzain and P.W.S.K. Bandaranayake, *Cey. J. Sci. (Phys.Sc.)* **9**, 41 (2002).
8. K. Guerin, A. Fevrier-Bouvier, S. Flandrois, M. Couzi, B., Simon and P., Biensan, *J. Electrochem. Soc.* **146**, 3660 (1999).
9. S., Zhang. M.S. Ding, K. Xu, J. Allen and T.R. Jow., *Electrochemical and Solid-State letters* **4** , A206 (2001).
10. M.E. Spahr, H. Wilhelm, F. Joho, J.C. Panitz, J. Wambach, P. Novak and N.D., Pavlovsky, *J. Electrochem.Soc.* **149**, A960 (2002).
11. H. Shi, J. Barker, M.Y. Saidi and R. Koksbang, *J. Electrochem. Soc.* **143**, 3466 (1996).
12. Y. Reynier, R. Yazami and B. Fultz, *J. Electrochem. Soc.* **151**, A422 (2004).
13. S. Al Hallaj, R. Venkatachalapathy, J. Prakash and J.R. Selman, *J. Electrochem. Soc.* **147**, 2432 (2000).
14. M.K. Song, S.D. Hong and K.T. NO, *J. Electrochem. Soc.* **148**, A1159 (2001).

This page is intentionally left blank

Part III
Electroactive Polymers

This page is intentionally left blank

Invited Papers

This page is intentionally left blank

ORGANISED OR DISORGANISED? LOOKING AT POLYMER ELECTROLYTES FROM BOTH POINTS OF VIEW

Y-P LIAO, J LIU, Y ZHENG AND P.V.WRIGHT*
Dept of Engineering Materials, University of Sheffield, Mappin St Sheffield S1 3JD UK
D.C. APPERLEY,
EPSRC Solid state NMR Service University of Durham, South Road Durham DH1 3LE UK
A. PRYKE,
Dept. of Chemistry, University of Sheffield, Brook Hill S3 7HF UK

Ionic states in amorphous polymer electrolytes are discussed suggesting that uncoupled neutral and charged aggregates are the more mobile. Low-dimensional systems designed so as to suppress interactions with the polymer and to promote uncoupled aggregates within 2-dimensional cavities are described. The mixed polymer–Li salt systems include block copolymers C18O1O5 (**I**) having an ionophobic mesogenic block (CmO1) and an ion-separating block (CmO5) together with an intercrystalline ion-bridge tetrahydrofuran copolymer **III** to sustain conductivity of the liquid crystal (*lc)* phase into the crystal (*c)* phase. New results describe the replacement of the ionophobic mesogenic block CmO1 by the more mechanically flexible C18O2. ^{7}LiNMR indicates high Li mobility in C18O2 :$LiBF_4$ but lower levels of conductivity (3×10^{-4} S cm^{-1} at 20°C) than in CmO1 copolymers were observed on slow cooling from the isotropic through *lc* and c states.

1. **Introduction**

1.1 ***Amorphous polymer electrolytes***

'Conventional' solvent–free polymer electrolytes are generally amorphous rubbery solids and typically based upon poly(ethylene oxide) -(CH_2-CH_2-O-)- (PEO) modified so as to suppress the tendency for either the polymer or its complex with a lithium salt to crystallise[1]. Such modification may commonly involve skeletal branching[2,3] or the synthesis of a 'comb' structure whereby oligoethoxy chains are affixed to a high molar mass, flexible backbone of a linear polymer such as polyphosphazene[4]. In either case, the interaction of several sequential ether oxygens with the cation of a salt such as $LiBF_4$, $LiPF_6$ or $Li(CF_3SO_2)N$ effects dissolution of the salt. Such systems are readily cast into flexible films 50-100μm in thickness that may be laminated with thin lithium films and a composite cathodic substrate (*e.g.* $LiCoO_2$, graphite and binder) to compile a lithium battery.

However, by the late 1980s it had become apparent that although the required level of conductivity (*ca.* 10^{-3} S cm^{-1}) for lithium batteries of adequate power were achievable at temperatures above *ca.* 60°C ambient conductivities of these solvent-free systems (*ca.* 10^{-5} S cm^{-1}) were inadequate. Constraints on ion mobility arise from the interactions of cations with the polyether matrix and the requirement for the thermal generation of free volume and of microbrownian motion of the polymer chains. This enables the disintegration of the multiple oxygen Li^+ coordinating sites and the creation of new ones. Furthermore, being an organic medium of comparatively low dielectric constant ($\varepsilon \cong 5$) there is a pronounced tendency for

ions to aggregate and these have been studied in some detail in polymer electrolytes[5]. Figure 1 schematically illustrates some ionic states in PEO-based systems. Alongside the single ion sites stabilised by interactions with three or four oxygens, ion aggregates are coupled to sections of chain conforming (often helical) to segments of the well-known crystalline stoichiometric PEO : Li salt structures[6] (see Fig.1(a)). However, aggregates uncoupled to the chains are also present and these include neutral quadrupoles (b) and ion pairs (c) as well as charged species such as the triple ion $(Li_2A)^+$.

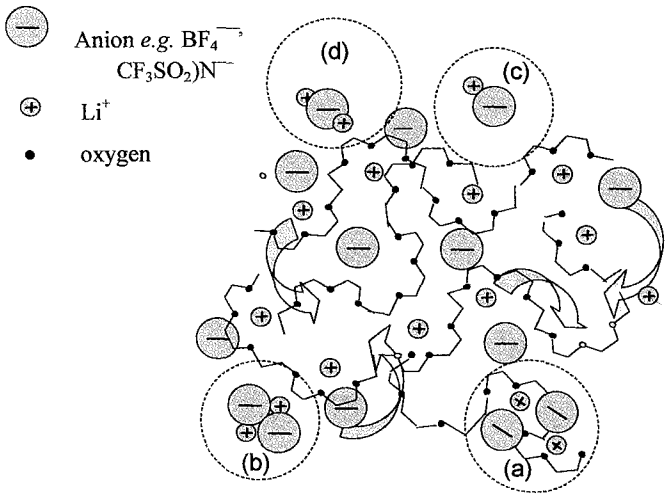

Figure 1. Schematic representation of ion coordination within an amorphous PEO-based electrolyte. (a) an organised microcrystalline group coordinated to the polyether; (b) an uncoupled quadrupole ion aggregate; (c) a dipole ; (d) a charged triple ion. Arrows indicate plausible ion manoeuvres.

These small aggregates, incorporating no more than two large anions, should possess a retarding influence on further crystalline growth arising from extra coulombic stability conferred by the close contacting cation and anion. Such close contact is prohibited in the extended crystallite owing to the large radius ratio. The closer approach, measured by Honig and coworkers[7] using microwave spectroscopy in the vapour phase, amounts to *ca.* 20% reduction in internuclear distance in LiI, for example, and will bring about a proportionate increase in inter-nuclear coulombic attraction with respect to the local interactions in the crystal.

In the dynamic equilibrium between these various states, chain-coupled associates and aggregates are plausibly the strongest constraints on ion mobilities. However, the uncoupled aggregates both neutral and charged may possess the greatest freedom to migrate having a much reduced polarizability relative to the small single Li^+. As a way forward it therefore seemed appropriate to devise a system in which coupled interactions between salt and polymer are inhibited and

interactions involving uncoupled aggregates are promoted. If, at the same time, the uncoupled aggregates were sited within extensive channels the requirement for conformational change in the creation and disintegration of sites is removed.

1.2 *Low-dimensional polymer electrolytes*

With the above qualifications in mind we have in recent years[8-10] been investigating the copolymer systems **I,** which are essentially 'blocky' in structure, of general formula

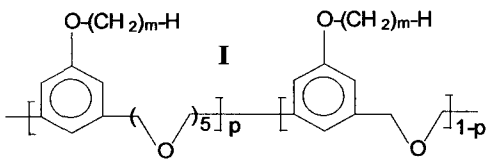

The number of carbons in the n-alkyl side chains, m, may be 16, 18 or mixtures of 18 and 12. The segments are abbreviated CmOn, where n is the number of skeletal oxygens within each segment. In our investigations thus far the copolymers usually comprise CmO1 and CmO5 blocks and are denoted CmO1O5(p%) where the molar proportion of CmO5 units is p%.

Coalescence of the sidechains in an hexagonal crystalline (*c*) phase or a liquid crystal (*lc*) phase above side chain melting (30 - 50°C) brings about self-organisation into channels as shown schematically in Figure 2. These structures are

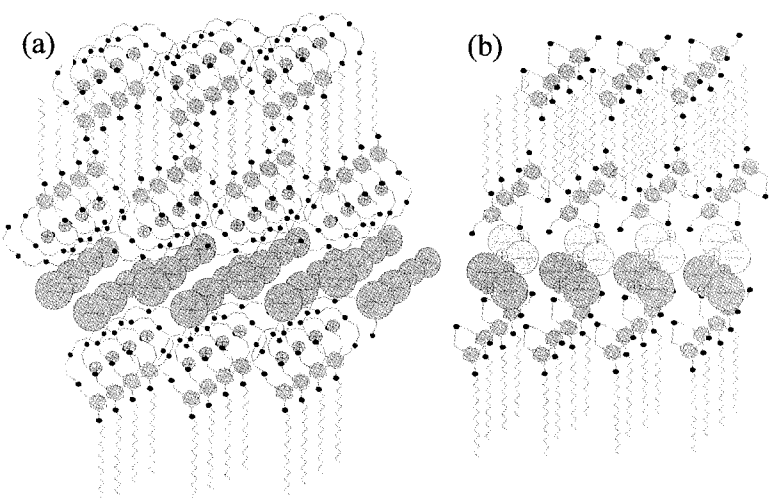

Figure 2. Schematic representations of lithium salt complexes with (a) CmO5 and (b) CmO1 based upon SAXS and WAXS experimental data and molecular dynamics modelling. Small black-filled circles are oxygens.

generally well-defined *c* → *lc (smectic)* transitions, the morphology being evident from striking 'broken fan' textures. The schematic representations are also based upon SAXS data which show well-defined long spacings between 33 Å and 45 Å (the shorter spacings for CmO1 and its salt mixtures), a single WAXS peak below the side chain melting temperature corresponding to an hexagonal side chain lattice (4.1Å), and molecular dynamics modelling of C16O1: salt and C16O5: salt systems. These confirm the side chain coalescence and the distinctly different roles played by the two kinds of block. The tetraethoxy loops of CmO5 encapsulate cations bringing about ion separation. whereas the single skeletal oxygen of CmO1 promotes ion aggregation. However, it will be apparent that the complete separation of like-charged ions in the CmO5 schematic Figure 2(a) must engender unrealistically high coulombic repulsions and is almost certainly an inadequate representation. The high coulombic energies would be alleviated by a degree of exchange between the cationic and anionic channels. This is currently being explored using solid-state NMR and will be discussed in a future publication.

1.3. *Self-organisation from 3-component blends.*

The formation of extensive channels or laminar cavities depends upon the successful self-organisation of a stable liquid crystal (*lc*) phase at temperatures above the side chain melting temperatures in lithium salt complexes of **I**. Thus, optimum conductivities are observed from impedance measurements between conductive glass (ITO) electrodes after slow cooling from the isotropic (*iso*)→*lc* transition observed at ~110°C in the hot-stage polarising microscope. However, cooling into the *c* state causes shrinkage and in 2-component systems gives rise to inter-crystalline gaps which prohibit ion transport causing the conductivity to fall at ambient temperatures. The introduction of a second linear polymer **II** - [- $(CH_2)_4$ - O - $]_{\sim 23}$ - $(CH_2)_{12}$ - and/or **III** $C_{18}H_{37}$-[-$(CH_2)_4$-O-$]_{\sim 50}$-$C_{18}H_{37}$ to serve as an ion-conducting bridge or 'glue' within the intercrystalline spaces formed as **I** cools

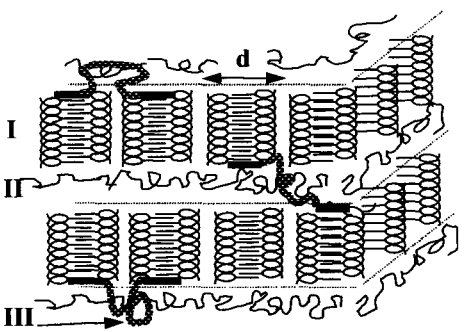

Figure 3. Microphase structure of polymers **I** : **II** : **III** after heat treatment (deblending) Li salt not shown.

apparently sustains the high level conductivity of the *lc* phase ($10^{-4} - 10^{-3}$ S cm^{-1}) down to ambient temperatures[8-10]. Thus self-organisation in 3- or 4-component systems also involves microphase separation of the channel-forming polymer **I** from a blend with **II** and/or **III** (see Fig. 3).

The block copolymers CmO1O5(p%) consist of a major proportion of the rigid skeletal segments CmO1 (70 – 85mol %) and a minor proportion of the cation-encapsulating helical sequences of CmO5. The tendency to blocky sequencing results from the heterophase polymerisation and differences in reactivity of the glycols. Tetraethylene glycol diffuses more slowly into the phase-separated polymeric reaction product. However, blocks are also promoted by sequential addition of the glycols during a 'single pot' reaction.

The rigid (mesogenic) CmO1 sequences supposedly promote the formation of extensive channels or 2-dimensional laminar cavities in the *lc* phase along which the ions and aggregates are mobile. The low dielectric constant and oxygen-deficient CmO1 environment should promote neutral aggregation confirmed[9] by the very low conductivity of the homopolymer complex CmO1 : $LiBF_4$ (1 : 0.1) where the numbers in parenthesis are approximate weight proportions giving saturated salt content (1 : 0.5 molar ratio for CmO1). Neutral aggregates may perhaps be limited in size to LiA and Li_2A_2 by the lateral dimensions of *ca.* 10Å of the channels or cavities as suggested by small-angle x-ray scattering[9,10] as well as by the extra stability of 'contacting ions' described above.

A principal role of the CmO5 segments is to engender ion separation so that neutral aggregates may be 'doped' by Li^+ to Li_2A^+ and $Li_3A_2^+$. Lithium conduction may then proceed by 'hopping' along the rows as discussed below. The lifetime of 'free' Li^+ within this environment is as yet unclear as is the state and mobility of the counter-anions. (The latter may undergo local manoeuvres to attend the cation hopping) A solid-state ^{19}F NMR study of Li^+ and BF_4^- is in progress and will be published presently.

A second role of the CmO5 blocks may also be to function as 'pillars' defining the separation of the CmO1 material. The tetraethoxy loop encapsulating the cation with its counteranion alongside should amount to approximately 10Å across (Figure 2). This is evident[9,10] from SAXS as the increase in long spacing as C16O5 is introduced in copolymerisation with C16O1. Thus, in C16O1: $LiBF_4$ (1 : 0.1) the long spacing increased from *ca.*33Å to 45Å following the introduction of 40mol % of CmO5 segments. Furthermore, although salt-free CmO5 is a flexible polymer, complex formation increases the rigidity of the polymer, as shown by the increase in side-chain melting temperatures, and so contributing to the stability of the *lc* phase.

However, although CmO1O5 polymers are effective mesogens they form hard, mechanically rigid materials at ambient. In contrast with conventional amorphous polymer electrolytes these low – dimensional systems require structural

modifications to 'soften' them for film formation and to conform to electrode interfaces. Furthermore, the rapid polymerisation of ethylene glycol with the 1,3-bis(bromomethyl)-5-alkoxybenzene monomers readily yield high molar mass CmO2 materials which could form the basis of larger scale preparations. In this paper we therefore present new observations on the conductivities and properties of C18O2O5 copolymers in which we examine the possibility that C18O2 sequences can adopt the role of CmO1 blocks, functioning as the mesogenic component in the block copolymers **I.**

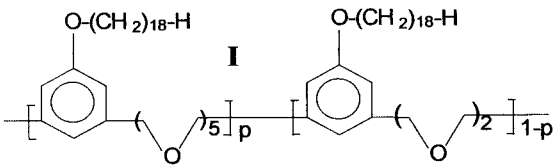

2. Experimental

1, 3-bis (bromomethyl) -5- octadecyl –oxybenzene (**i**) was prepared as described elsewhere[9]. C18O2O5(p%) copolymers were prepared by stirring equimolar quantities of (**i**), tetraethyleneglycol and finely-divided KOH in dimethylsuphoxide /tetrahydrofuran (50/50) at 60°C under argon for 48 hours. Equimolar quantities of (**i**) and ethylene glycol were then added to the mixture and stirring continued for a further 48 hours. The precise composition of the copolymer was difficult to predict but the molar ratios of tetraethylene glycol / ethylene glycol were chosen so as to be *ca.* 10% in excess of the desired copolymer composition, p. The copolymers were purified by quenching the reaction mixture in water, further washing in dilute acetic acid and finally in methanol. The copolymers were finally dissolved in $CHCl_3$, filtered and the solvent removed under vacuum. The copolymer compositions were verified using ^1H NMR as described previously[9] and the molar masses (<M_w> between 15k and 70k) were determined by gel permeation chromatography. The block copolymer **III** $C_{18}H_{37}$-O-[-$(CH_2)_4$-O-]$_{\sim 50}$-$C_{18}H_{37}$ (<Mw> $\cong$ 4000) was prepared by stirring polytetrahydrofuran (<Mn>=1688) with excess (2.5 mol) of octadecyl bromide at 75°C. The sample was fractionated from methanol/water.

Preparation of mixtures: The components were dissolved in CH_2Cl_2 / acetone (50/50) (~10% solution) and the solvents removed by freeze drying from liquid N_2 to yield fine powders. The powders were then fused under vacuum at 50°C.

General procedures: Dimethyl sulphoxide (DMSO) was dried and distilled before use. Other reagents were used without further purification. ^1H NMR was performed using a Bruker AC250 and GPC was carried out using a Hewlett-Packard 1090 liquid chromatograph. DSC was performed on a Perkin Elmer Pyris 1. Conductivity measurements were carried out using a Solartron 1287A EI / 1250 FRA (1Hz-1MHz, 100mV amplitude) using indium-tin oxide (ITO) coated glass electrodes (resistance 40Ω, subtracted from impedance minima) with a cellulose acetate or polyethylene spacer in an evacuated chamber. Optical microscopy was performed using an Olympus BX50 microscope fitted with a 'Coolsnap' digital

camera. ^{7}Li NMR linewidth measurements were performed at the EPSRC NMR Facility at the University of Durham, UK.

3. Results and Discussion

3.1. *Thermal analysis*

Table 1 shows thermal data for the salt-free copolymer series C18O5····C18O2O5····C18O2. The salt-free side chain melting temperatures range between 41.8°C and 49.4°C. Although the extreme polymers in the series are not fully homopolymeric and include 9.3 mol% and 12.5 mol% of C18O1 segments respectively (C18O1 melts at 52.6°C) the 10 degree range in melting temperatures demonstrates the influence of 'free' tetraoxyethylene segments on polymer flexibility when uncoordinated by Li^{+}.

Table 1. Thermal (DSC) data for C18O2O5(p%) copolymers and 3-component complexes with polymer **III** and $LiBF_4$

p (mol% of C18O5)	Salt free polymers **I** C18O2O5(p%)		**I** within complexes **I**:**III**:$LiBF_4$ (1 : 0.6 : ~0.2)	
	T /°C	ΔH /(kJ/mol)	T /°C	ΔH /(kJ/mol)
0*	49.4	36.0	(49.1)	(32.0)
7.5	47.1	35.0	48.9	18.5
13.6	46.6	36.2	52.4	18.4
24.8	45.6	36.2	53.0	20.9
39.6	44.0	36.9	54.0	20.9
70.5	41.0	36.3	50.9	15.3
100‡	41.8	35.1	(52.8)	(25.6)

*contains 12.5 mol% of C18O1; () two-component **I** : $LiBF_4$ (1 : 0.12) complex
‡ contains 9.3 mol% of C18O1; () two-component **I** : $LiBF_4$ (1 : 0.2) complex

Also given in Table 1 are data for **I** within the 2- and 3-component systems of the above copolymers **I** with an ABA copolymer of poly(oxytetramethylene) end-blocked with $-C_{18}H_{37}$ (**III**) and $LiBF_4$ in the weight ratios 1 : 0.5 : *ca.*0.2. The $LiBF_4$ salt content was chosen so as to be equimolar with the repeat unit of copolymer **I**. These data are the second thermal cycles after heating to 100°C in the first. Each system shows two endotherms. The higher temperature endotherm may be readily assigned to side chain melting in the copolymers **I** and the lower to copolymer **III**.

The effect of complex formation with the Li salt is to raise the side chain melting temperatures of **I**, except for the C18O5-free sample and only 1-2 degrees for 7.5% C18O5 system. The salt clearly has a more profound effect on C18O5 melting. The 2-component C18O5 : $LiBF_4$ system melts at 52.8°C so that the temperatures of the copolymer **I** : $LiBF_4$ endotherms are close to each other. The enthalpies of the salt-free copolymers **I** are very similar over the copolymer series amounting to 35-37 kJ mol^{-1} of repeat unit. The two component complex with the C1805-free polymer also has a melting enthalpy close to the salt-free copolymer in accord with the structure Fig. 2(b). However, enthalpies of the copolymers

incorporating C18O5 within their complexes are significantly lower. Thus the thermal data suggests a weaker influence of salt with C18O2 segments than with the C18O5 segments as previously reported for CmO1 systems. Although the overall distribution of salt between copolymers **I** and **III** is not yet clear, the salt in **I** may be preferentially associated with the C18O5 segments.

Although not shown in Table 1, polymer **III** had a second cycle peak melting temperature of 38°C which is *ca.* 3 degrees below its first cycle endotherm peak temperatures. This may suggest, that in the first cycle blend of the two polymers, **III** is stabilised by involvement of its $-C_{18}H_{37}$ termini with the side chains of **I**. After heating to 100°C this stabilisation is lost following microphase separation.

3.2. *Conductivities of 2-component systems*

Figure 4 shows log σ *versus* 1/T for the 2-component system C18O5 : $LiBF_4$ (1 : 0.2). The plot shows a small degree of irreversibility but the conductivity falls as the temperature falls below the sidechain melting temperature (~50°C). The conductivity of the corresponding stoichiometric C18O2 : $LiBF_4$ (1 : 0.12) complex was found to be too low to measure by impedance spectroscopy over the full range of temperature up to 110°C. These observations reflect the conductivities of the 2-component C16On (n = 1 to 5) : $LiBF_4$ series reported previously[9] for which the conductivities generally decreased in the order C16O5 ≅ C16O4 > C16O3 > C16O2 > C16O1 and the conductivity of the C16O1-Li salt system was also too low to measure by impedance spectroscopy. These trends are readily accounted for in terms of the extent of ionisation of the lithium salt induced by the skeletal ether segments in the polymers. The larger tetraethoxy and triethoxy segments in C18O5 and C18O4, respectively, create oxygen-rich environments within the helical loops which readily coordinate Li^+ when the alkyl side chains coalesce. The cation-anion separation permits electrical current. On the other hand, weak ion interactions with the single oxygens of C18O1 and C18O2 promote cation-anion association into *neutral* aggregates $LiBF_4$, $Li_2(BF_4)_2$.

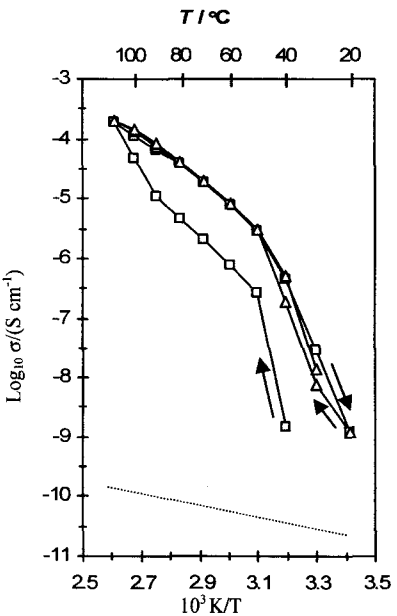

Figure 4. Log σ *versus* 1/T for C18O5 : $LiBF_4$ (1 : 0.2). □, first cycle; △, second cycle; dashed line, approximate result for C18O2 : $LiBF_4$ (1 : 0.12).

3.3. *Solid –state ^{7}Li NMR*

A solid-state NMR study of these systems is in progress. However, we meanwhile note an important result on the poorly ionising C18O2:$LiBF_4$ (1:0.12) complex. Whilst conductivity measurements suggest little independent mobility of ionic states in this system, solid–state ^{7}Li NMR reveals considerable lithium mobility down to sub-ambient temperatures. Figure 5(a) shows the ^{7}Li NMR band shapes for second cycle cooling down to sub-ambient temperatures. The band shapes are complex but may be resolved into Gaussian and Lorentzian components. The half-height line widths for second and subsequent thermal cycles are plotted *versus* temperature in Figure 5(b). Like the conductivity data (see below) the first heating cycle produced broad, scattered ^{7}Li NMR signals consistent with changing

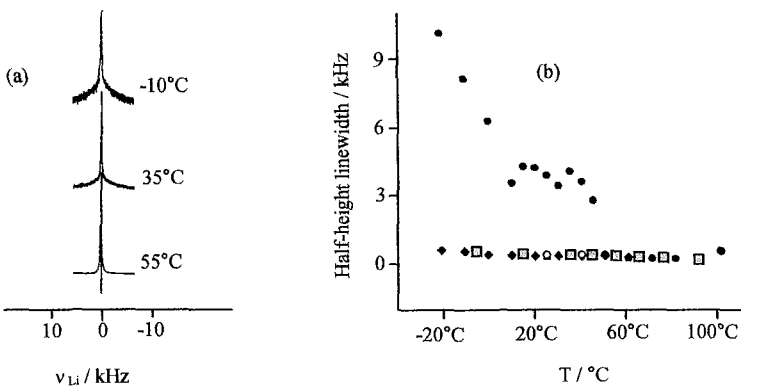

Figure 5. ^{7}Li NMR data for C18O2 : $LiBF_4$ (1 :0.12)
(a) Experimental signals for second cooling at -10°C, 35°C and 55°C;
(b) Line-widths at half-height; •, second heating; □ , second cooling; ◆, third heating; O, third cooling.

morphology and salt-redistribution during the first heating (deblending). However, the narrow linewidths of the second cooling and subsequent cycles show high lithium mobility down to -20°C. The NMR and conductivity data for C18O2 : $LiBF_4$ (1 : 0.12) complex may perhaps be reconciled if confined columns of neutral aggregates disproportionate, for example

$$Li_2(BF_4)_2 \cdot Li_2(BF_4)_2 \cdot Li_2(BF_4)_2 \rightarrow Li_2(BF_4)_2 \cdot Li^+ [Li(BF_4)_2]^- \cdot Li_2(BF_4)_2$$
$$\rightarrow Li_3(BF_4)_2^+ \cdot [Li(BF_4)_2]^- \cdot Li_2(BF_4)_2$$

Such confined ion pairs should have neutral response to an electric field but the dynamics of the disproportionation processes taking place between the neighboring aggregates will be observed in the ^{7}Li NMR signal. However, these columns of highly mobile aggregates should provide a substrate for mobile charges if they were to become positively charged by Li^+ doping from nearby CmO5 segments *e.g.*

$$2Li^+ + LiA \cdot LiA \cdot Li_2A_2 \cdot Li_2A_2 \rightarrow . Li_2A^+ \cdot LiA \cdot Li_3A_2^+ \cdot Li_2A_2$$
$$\rightarrow LiA \cdot Li_2A^+ \cdot Li_2A_2 \cdot Li_3A_2^+ \cdot$$

The lifetime of 'free' Li^+ and the state and mobility of anions is as yet unclear. A solid-state ^{19}F and ^{7}Li NMR study is in progress and will be published presently.

3.4. *Conductivities of 3-component systems*

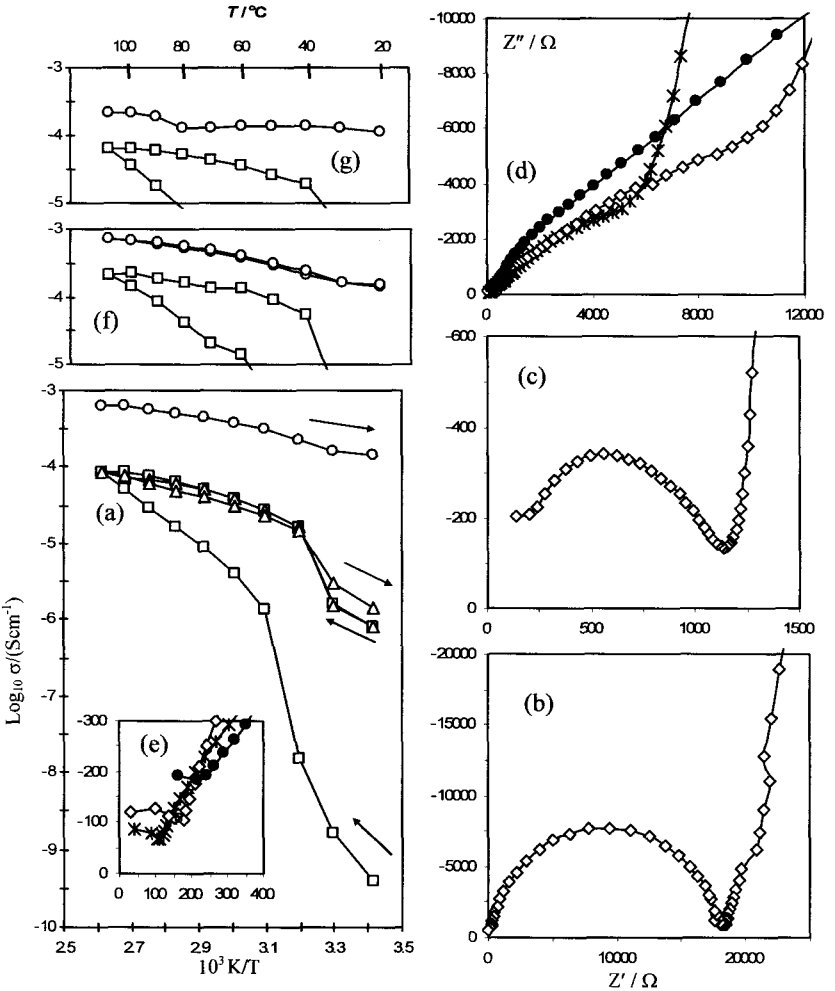

Figure 6. Conductivity data for C18O2O5(p%) : **III** : $LiBF_4$ systems.
(a) p = 24.8. □, △ and ○ are for first, second and third heating cycle, respectively. (b) and (c) are impedance planes at 50 °C for first heating and second cooling cycles of (a). (d) is third cooling cycle of (a) at temperatures •, 20°C; ◇, 40°C; *, 60°C. (e) detail of (d). (f) p = 39.6. (g) p = 13.6.

Figures 6 show log σ *versus* 1/T plots for 3-component systems **I** : **III** : $LiBF_4$. In all cases the conductivities of the initial blended mixtures are very low but after heating to 110°C ($\sim T_{lc \rightarrow iso}$) during cooling and subsequent heating cycles the materials undergo a transformation to a new state having conductivities between 10^{-4} and 10^{-3} S cm^{-1} with low temperature-dependence down to ambient. The impedance planes at 50° C for the system in Figure 6(a) (p = 24.8) are shown in Figs 6(b) and (c) and the impedance planes at 20°C, 40°C and 60°C from the third cooling cycle (upper) conductivity plot in Fig. 6(a) are shown in Fig. 6(d). The high frequency detail of Fig. 6(d) is shown in Fig. 6(e). The dramatic changes in behaviour apparently arise from structural transitions in the materials brought about on cooling through the *isotropic* → *lc* transition followed by slow cooling (0.3°C min^{-1}) through the *lc* phase. The course of the transition is illustrated by comparing the impedance plots for first, second and third heating cycles. The corresponding changes in morphology between the first and third cycles are shown in Figure 7. The development of the more conductive morphology is apparent in the appearance of the finer birefringent texture after heating to 110°C. Supposedly, the lamellae become aligned in the *lc* phase such that the interdigitated side chains lie along the substrates (electrodes) so that the ion-containing channels or 2-dimensional cavities are favourably oriented

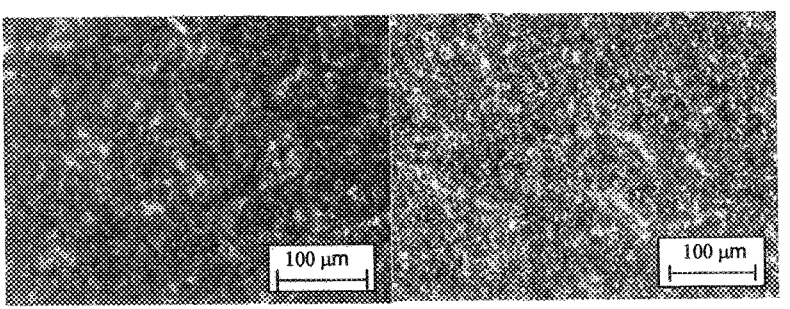

Figure 7. Textures of C18O2O5(25%) : **III** : $LiBF_4$ at room temperature before heating (left) and after cooling from 110°C. Photographed with identical conditions between crossed polars.

normal to them. However, experimental support for this conjecture is yet to be obtained.

Whilst the three 'central 'compositions shown in Figure 6 demonstrate significant transitions to the high conductivity regime, the 'outer' systems given in Table 1, p = 7.5 and 70.5, gave plots which declined progressively to low ambient conductivities ($\sim 10^{-6}$ S cm^{-1}) after 3 thermal cycles.

However, the results reported here, whilst demonstrating the transition to the higher conductivity regime previously observed with CmO1 copolymers, suggest

that the C18O2-based systems have levels of conductivity slightly lower than we have observed in C18O1-based systems and the transformation to the higher level of conductivity is rather slower. This suggests that C18O1 is the more effective mesogenic segment in the self-organisation process and so new copolymers incorporating this segment whilst retaining flexibility are being investigated.

Acknowledgements We are grateful to the EPSRC for support of this work and for grants to Y-P.L., Y.Z and J.L.

References

1. F. M. Gray, *Polymer Electrolytes*, Royal Society of Chemistry, Cambridge, UK, 1997 Chapter 2, p.34.
2. M. Watanabe, T. Endo, A Nishimoto, K Miura amd M. Yanagida, *J . Power Sources* **81-82**, 786 (1999).
3. S. Matsui, T. Muranaga, H. Higobashi, S. Inoue and T. Sakai, *J. Power Sources* **97-98**, 772 (2001).
4. P. M.Blonsky, D.F.Shriver, P.Austin and H.R. Allcock, *J.Am. Chem. Soc.* **106,** 6854 (1984).
5. S. Schantz and L.M. Torrell, *Solid State Ionics*, **60**, 47 (1993); F.M.Gray, J.Shi, C.A. Vincent and P.G. Bruce, *Phil. Mag. A*, **64**, 1091 (1991); F. M. Gray, *Polymer Electrolytes*, Royal Society of Chemistry, Cambridge, UK, 1997 Chapter 3, p.83.
6. Y. Chatani and S. Okamura, *Polymer* **28**, 1815 (1987); Z. Gadjourova, Y.G. Andreev. D. P. Tunstall and P.G. Bruce, *Nature* **412**, 520 (2001).
7. A.Honig, M. Mandel, M.L.Stitch, C.H. Townes, *Phys. Rev.* **96**, 629 (1954).
8. Y. Zheng, F. Chia, G. Ungar and P.V. Wright, *Chem. Commun.* 1459 (2000); Y. Zheng, F. Chia, G. Ungar, P.V. Wright, *Electrochim. Acta* **46**, 1397 (2001); F. Chia, Y. Zheng, J. Liu, G. Ungar, P.V. Wright, *Solid State Ionics* **147**, 275, (2002); F. Chia, Y. Zheng, J. Liu, N. Reeves, G. Ungar, P.V. Wright, *Electrochim. Acta* **48**, 1939 (2003);Y. Zheng, J. Liu, Y-P. Liao, X. Zeng, G. Ungar and P.V. Wright, *J. Chem Soc. Dalton Transactions*, 3053 (2004).
9. J. Liu, Y. Zheng, Y-P. Liao, X. Zeng, G. Ungar and P.V. Wright, *J. Chem Soc. Faraday Transactions.*, **128**, 363 (2005), *ibid.* pp412 (discussions).
10. J. Liu, Y. Zheng, Y-P. Liao, D.C. Apperley, G. Ungar and P.V. Wright, Electrochimica Acta, **50**, 3815 (2005).

Polymer Electrolytes - Simple Low Permittivity Solutions?

I. Albinsson[1] and B.-E. Mellander[2]
[1]*Department of Physics, Göteborg University, S-412 96 Göteborg, Sweden*
[2]*Department of Applied Physics, Chalmers University of Technology, S-412 96 Göteborg, Sweden*

Abstract

Polymer electrolytes may in some aspects be compared to traditional low permittivity liquid electrolytes. The solvation process of a salt involves a competition between interionic and ion-dipole forces. For liquid electrolytes a dissolved ion is surrounded by a primary solvation sheath which is carried along with the moving ion. This means that the interaction between dipoles of the solvation sheath and free dipoles is of great importance for ionic transport. For polymer electrolytes we do not have a primary solvation sheath in the traditional sense since the surrounding dipoles are parts of the polymer chain and thus limited to only a local movement. Ionic transport is in this case involved with a rearrangement of the nearest surrounding dipoles. That is, while an ion is moving the coordinated dipoles are continuously replaced by other dipoles and this thereby provides a possibility for the ion to move. Ion transport is therefore possible in spite of the coordination to dipoles which are restricted to a more limited region. Since this study is limited to low permittivity solvents we know that the salt does not dissociate completely. Ion pairs, triplets and even larger ionic species exist in equilibrium with dissociated ions. For a 1,1-electrolyte ion pairs are the most obvious dipoles with dipole moments probably larger than the (low permittivity) solvent dipoles. This is seen as a rapid increase followed by a saturation of the static permittivity, ε_S, with increasing salt concentration. The static permittivity mirrors the dipolar properties of the material where mainly ion pairs and solvent dipoles contribute. In this paper ionic association and transport is discussed in terms of dielectric properties, conductivity and thermal properties for polymer electrolytes with and without filler materials.

DEPENDENCE OF CONDUCTIVITY ENHANCEMENT ON THE DIELECTRIC CONSTANT OF THE DISPERSOID IN POLYMER-FERROELECTRIC COMPOSITE ELECTROLYTES

AMREESH CHANDRA [a,b], PRAMOD K.SINGH [a] AND SURESH CHANDRA [a]
[a] Physics Department, Banaras Hindu University, Varanasi – 221005, India
[b] Max Planck Institute for Polymer Research, Mainz, Germany
Email : sureshchandra_bhu@yahoo.co.in

H^+, Na^+ and Li^+ ion conducting polymeric composites have been prepared by using two different Sr^{2+}-doped $BaTiO_3$ ferroelectric ceramics as dispersoids viz. (i) $Ba_{0.88}Sr_{0.12}TiO_3$ having T_c~90^{0}C, abbreviated as BST 90 and (ii) $Ba_{0.70}Sr_{0.30}TiO_3$ having T_c~30^{0}C abbreviated as BST 30. The dielectric constants of BST 90 at 20 ^{0}C and its dielectric phase transition temperature T_c (where ε is highest) are respectively ~1100 and ~5500 while for BST 30 the corresponding values are ~2400 and ~7500. The values of σ at 20^{0}C for BST 30 dispersed samples for all compositions have been found to be higher than those having BST 90 as dispersoid because of the higher dielectric constant of the former. Further, studies on the temperature dependence of conductivity show that the enhanced conductivity passes through a peak at the respective T_c's, where the dielectric constant of the dispersed ferroelectric is highest i.e. at 30 ^{0}C and 90 ^{0}C respectively for composites containing BST 30 or BST 90 as dispersoid.

1. Introduction

Attempts to develop polymer electrolytes with high ionic conductivity are extensively being made because of their applications in fuel cells and polymer batteries. Polar polymers (like polyethylene oxide, PEO) complexed with suitable salts have proved themselves as strong contenders for such applications. Most of the polymer-salt complexes showed room temperature conductivity $\leq 10^{-5}$ S cm^{-1}. However, this value falls short of ideal requirements for fuel cell or battery applications. One would like to have conductivities of the order of 10^{-1}-10^{-3} S cm^{-1} for efficient electrochemical devices. Therefore, many efforts have been made to improve the value of ionic conductivity of such polymer electrolytes. Some of the early efforts in this direction are to use: polar polymers of different chain lengths or plasticizers to increase the amorphicity of the polymeric membrane or copolymerisation to modify T_g etc. [1,2]. More recent approach is to form 'composites' by dispersing inert (insulating) fillers. Generally, insulating fillers like Al_2O_3, ZrO_2, SnO_2, etc. have been used. The addition of fillers leads to the formation of additional dissociated charge carriers near the electrolyte-insulating filler interface [3] or modification of the ionic mobility near the interface. Recently, we [4] have suggested that dielectric constant of the dispersoids would also play a role in the creation of additional dissociated charge carriers near the interface resulting in enhanced conductivity. The role of dielectric constant of the dispersoid

has been shown earlier [4] only for one complex of a proton conducting polymer electrolyte. This paper is a more comprehensive report extended over composites of Na^+ conducting polymer electrolyte PEO:NaI, H^+ conducting polymer electrolyte PEO:NH_4I and Li^+ conducting polymer electrolyte PEO:$LiBF_4$. Following experiments have been carried out to show the role of dielectric constant of the dispersoid in modifying the conductivity of the composites:

(i) Ferroelectrics with almost similar structural features but different dielectric constants (due to different amounts of substitutional dopants) have been used as dispersoids. The ferroelectric system chosen is Sr^+ - doped $BaTiO_3$. In particular, we have used $Ba_{0.88}Sr_{0.12}TiO_3$ and $Ba_{0.70}Sr_{0.30}TiO_3$ with dielectric constants of 1100 and 2400 respectively at 20 ^{0}C. Composites with different amounts of dispersoids have been prepared and their room temperature conductivities have been compared.

(ii) Another manner in which we can create a different dielectric constant environment in the ionic matrix of the composite is to vary the temperature. The ferroelectrics are known to pass through a dielectric phase transition at their Curie temperatures, T_c. For example, $Ba_{0.88}Sr_{0.12}TiO_3$ (BST 90) has T_c~90^{0}C and the value of T_c for $Ba_{0.70}Sr_{0.30}TiO_3$ (BST 30) is T_c~30^{0}C. Therefore, we expect an abrupt change in the conductivity of composites with BST 90 at ~90^{0}C and at ~30^{0}C with BST 30. This aspect has been verified by studying the temperature dependence of conductivity of composites with the above ferroelectrics as dispersoids. The results are discussed below.

2. Experimental

PEO (Mol. Weight ~ 5 x 10^5) was dissolved in dehydrated methanol and stirred thoroughly for complete dissolution. The complexing salt solutions of NH_4I or NaI or $LiBF_4$ in 80:20 wt% ratio of PEO:salt was added and stirred on magnetic stirrer for complexation for 4-6 hours. The stirring was further continued at ~40 ^{0}C after adding the dispersoid BST 90 or BST 30 in desired ratio till the solution became highly viscous. This was poured in polypropylene petridishes to obtain composite membranes of (PEO:NH_4I) + x BST or (PEO:NaI) + x BST or (PEO:$LiBF_4$) + x BST.

The method of preparing $Ba_ySr_{1-y}TiO_3$ (y = 0.88 and 0.70) is similar to that described by us earlier [4]. In brief, a mixture of the solutions of $Ba(NO_3)_2$ and $Sr(NO_3)_2$ in desired ratio of Ba:Sr was co-precipitated with $(NH_4)_2CO_3$ to obtain the precursor material $Ba_ySr_{1-y}CO_3$. This was filtered/dried. Then, the stoichiometric amount of TiO_2 was added with the dried filtrate and ball milled. Subsequently, this mixture was calcined at ~1150 ^{0}C for 6 hours which gave powdered $Ba_ySr_{1-y}TiO_3$. Pellets of these (with PVA as binder), on further sintering at 1300 ^{0}C for 6 hours, resulted in dense $Ba_ySr_{1-y}TiO_3$ ceramic. This was powdered and used as dispersoid for obtaing polymer composite membrane as described above.

The ionic conductivity was evaluated by the standard method of complex impedance plot. The impedance was measured in the frequency range 40 Hz to 100 kHz using LCR Hi Tester (HIOKI, Japan, model 3520).

3. Results

It is well known that the conductivity of the composites depends upon the amount of dispersoid. Therefore, to demonstrate the role of dielectric constant of the dispersoid on the conductivity in composites, we prepared composites with different dielectric constant dispersoids for a large number of compositions (PEO:salt) + x BST 30 or BST 90 having values of x as 0, 1, 2, 3, 4, 5, 6, 7, 8, 10, 12, 14, 16, 18 and 20 weight percent. The measured values of conductivity are given in Table 1. It is obvious that for composites of each polymer electrolyte system, the values of conductivity of composites with BST 30 (ε = 2400) are higher than those with BST 90 (with ε = 1100). This clearly shows the role of dielectric constant in enhancing the conductivity of composite polymer electrolytes.

Table 1 : The conductivity at 20 ^{0}C (in S cm^{-1}) of composites of PEO:$LiBF_4$ (80:20), PEO:NH_4I (80:20) and PEO:NaI (80:20) polymer electrolytes dispersed with BST 30 and BST 90 having dielectric constants of 2400 and 1100 respectively

Wt % of BST	PEO:$LiBF_4$ composite dispersed with		PEO:NH_4I composite dispersed with		PEO:NaI composite dispersed with	
	BST 30	BST 90	BST 30	BST 90	BST 30	BST 90
0	1.4×10^{-6}	1.4×10^{-6}	6.4×10^{-7}	6.4×10^{-7}	1.5×10^{-7}	1.5×10^{-7}
1	2.5×10^{-6}	1.6×10^{-6}	1.8×10^{-6}	9×10^{-7}	2.4×10^{-7}	2.0×10^{-7}
2	2.7×10^{-6}	1.8×10^{-6}	1.0×10^{-5}	3×10^{-6}	5.2×10^{-7}	3.2×10^{-7}
3	-	-	1.8×10^{-5}	9×10^{-6}	1.2×10^{-6}	9×10^{-7}
4	1.5×10^{-5}	7.8×10^{-6}	-	-	4.6×10^{-7}	3.9×10^{-7}
5	-	-	1.1×10^{-6}	7.3×10^{-7}	-	-
6	4.3×10^{-6}	2.8×10^{-6}	-	-	3.7×10^{-7}	3.2×10^{-7}
7	-	-	9×10^{-7}	7×10^{-7}	-	-
8	3.0×10^{-6}	2.6×10^{-6}	-	-	4.1×10^{-7}	3.1×10^{-7}
10	2.6×10^{-6}	2.3×10^{-6}	1.7×10^{-6}	8×10^{-7}	6.3×10^{-7}	3.3×10^{-7}
12	3.5×10^{-6}	2.1×10^{-6}	7×10^{-6}	3.4×10^{-6}	1.6×10^{-6}	9.5×10^{-7}
14	7.3×10^{-6}	3.5×10^{-6}	-	-	5.3×10^{-7}	3.8×10^{-7}
16	1.8×10^{-5}	3.2×10^{-6}	-	-	-	-
18	2.8×10^{-6}	2.6×10^{-6}	1.2×10^{-6}	9.2×10^{-7}	-	-
20	1.6×10^{-6}	1.4×10^{-6}	1.1×10^{-6}	8.6×10^{-7}	2.7×10^{-7}	1.8×10^{-7}

According to the electrolyte dissociation theory, the dissociation of salts (responsible for the generation of ionic charge carriers) depends upon the dissociation energy (U) and dielectric constant of the medium (which, in turn, leads to larger effective field). The number of dissociated charge carriers (n) are:

$$n = n_0 \exp\left(-\frac{U}{\varepsilon kT}\right)$$

As consequence of the above relation, the values of n will be more for higher values of ε as observed by us and discussed above.

To reinforce the above conclusion, we carried out measurement of conductivity on a particular composite (with the same dispersoid) at different temperatures. The ferroelectric dispersoids BST 30 or BST 90 have strong temperature dependence of dielectric constant with their respective dielectric constants peaking at T_c's of 30 ^{0}C or 90 ^{0}C, respectively [4]. Therefore the σ vs. temperature plot will be a reflection of σ vs. dispersoid dielectric constant plot. The Figure 1 and Figure 2 show the values of conductivity of (Polymer electrolyte) + 3 wt% BST 30 and (Polymer electrolyte) + 3 wt% BST 90. It is clear that the conductivity peaks at ~ 30 ^{0}C with BST 30 and at ~ 90 ^{0}C with BST 90 which are the respective T_c's at which the dielectric constants of these ferroelectrics have highest values of 7500 (as against the room temperature value of 2400) and 5500 (as against the room temperature value of 1100).

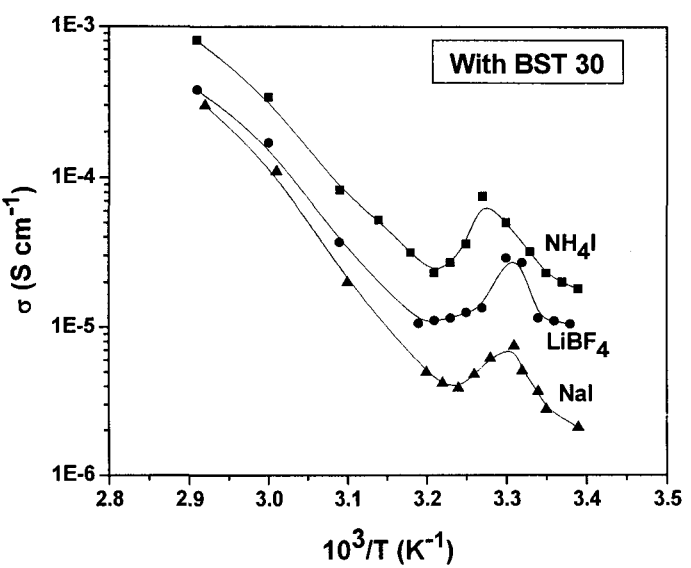

Fig.1: Temperature dependence of conductivity of composites having 3 wt% BST 30 as dispersoid in different polymer electrolyte matrices viz. PEO:NaI (▲), PEO:$LiBF_4$ (●) and PEO:NH_4I (■).

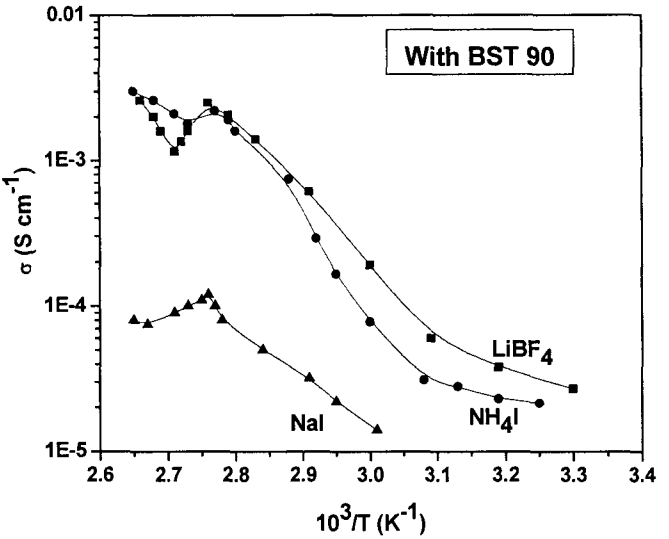

Fig.1: Temperature dependence of conductivity of composites having 3 wt% BST 90 as dispersoid in different polymer electrolyte matrices viz. PEO:NaI (▲), PEO:NH_4I (●) and PEO:$LiBF_4$ (■) in 80:20 ratio.

In conclusion, it can be said that a high dielectric constant dispersoid is to be preferred in developing composite electrolytes having relatively higher conductivities.

Acknowledgements

One of us (SC) thanks UGC for grant of Emeritus Scientist fellowship and the other (PKS) acknowledges CSIR for award of Research Associateship.

References

1. J.R.MacCallum and C.A. Vincent (Eds.), *Polymer Electrolyte Reviews Vol 1&2*, Elsevier, London (1987 and 1989)
2. F.M. Gray, *Solid Polymer Electrolytes – Fundamentals and Technological Applications*, VCH Pub., UK (1991)
3. J. Maier, *Prog. Solid State Chem.* **23**, 171 (1995)
4. P.K. Singh and Amreesh Chandra, *J. Phys.D Appl. Phys.* **36**, L93 (2003).

DESIGN AND APPLICATION OF BORON COMPOUNDS FOR HIGH-PERFORMANCE POLYMER ELECTROLYTES

TATSUO FUJINAMI
Shizuoka University, 3-5-1 Johoku,
Hamamatsu, 432-8561, JAPAN
E-mail: tctfuji@ipc.shizuoka.ac.jp

This paper deals recent studies on molecular design and utilization of boron compounds in polymer electrolytes. Well designed boron compounds have been used as dissociative lithium salts or anion receptors for enhancement of ionic conductivity and lithium ion transference number. Boron-containing polymers have not only anion trapping ability but also improving effects on properties of interface between electrolytes and electrodes. Special ion conduction phenomena in polymer electrolytes have been found using insoluble lithium orthoborates or a boric ester with crown ether substituents. Relationships between structures of boron compounds and properties of polymer electrolytes are discussed, and future directions of investigation on boron compounds for high-performance polymer electrolytes are outlined.

1. Introduction

With the aim of avoiding leakage of electrolyte and severing fire in lithium rechargeable batteries, the solid polymer electrolytes have aroused interests to be used as the safer alternatives to liquid electrolytes. However, the problem is remained in the ionic conductivity of polymer electrolytes at a low temperature. Many attempts have been undertaken by modification of the structures of polymer electrolytes in order to enhance ionic conductivity. However ionic conductivity has not been enough for charge-discharge performance below room temperature and lithium ion transference number is usually low for modified polymer electrolytes.

For application in lithium rechargeable batteries, it is important for poly-electrolytes to possess the good conductivity and the high cationic transference number as well. High lithium ion transference numbers have been obtained by incorporation of borates or boroxine rings as anion receptors into polyethers. Boroxine polymers are also good additives to reduce the interfacial resistance between polymer electrolytes and electrodes. Single ion conducting polymer is an ideal electrolyte because constant currents are maintained during charge-discharge process, but it tend to exhibit low ionic conductivity due to strong

ion pairing between mobile lithium ion and counter anion fixed to the polymer backbone. Some excellent single ion conducting polymer electrolytes containing lithium orthoborate structures have been reported.

Recently, an insoluble lithium orthoborate with weak interaction between lithium ion and counter anion has been designed and synthesized. The mixture of insoluble salt and a polymer exhibited unusual ion conduction. This specific ion conduction gives a new concept for polymer electrolyte. Special phenomena of ion conduction have been also found in polymer electrolytes containing a new additive of a boric ester with crown ether substituents.

Well designed boron compounds will be useful for the development of high-performance polymer electrolytes.

2. Lithium orthoborates

Recently, highly dissociative lithium salts have been reported as shown in Fig. 1. Electron withdrawing groups on boron atom are effective to enhance dissociation of the salts. LiBOB **1a**[1] and tetrakis(trifluoroacetatoxy) borates **1b**[2] have been attracting attentions as lithium salts in liquid and polymer electrolytes[3]. Lewis acidic boron compounds such as BF_3 can react with anion to promote dissociation of lithium salt such as **1c**.[4]

Lithium orthoborates are also obtained by reaction of $LiBH_4$ with protonic compounds. Ate complex lithium salts containing electron withdrawing groups and oligoether chains on anion centers were synthesized as ionic

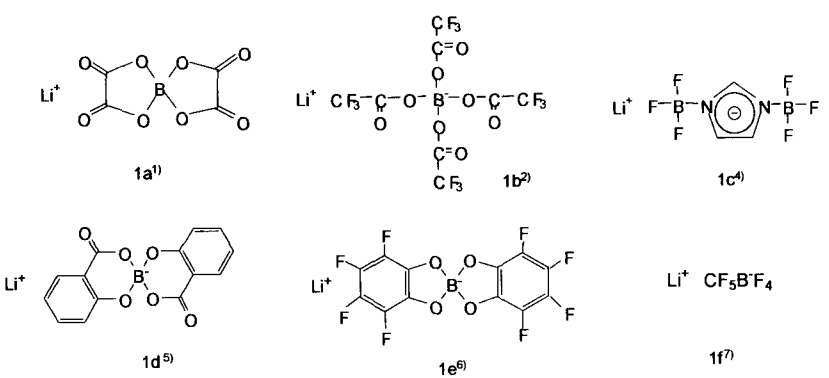

Fig. 1 Boron based lithium salts

liquids which exhibited high ionic conductivity and lithium ion transference number (Fig. 2).[8] These salts were effective to enhance lithium transference number of polyether-salt systems.[9]

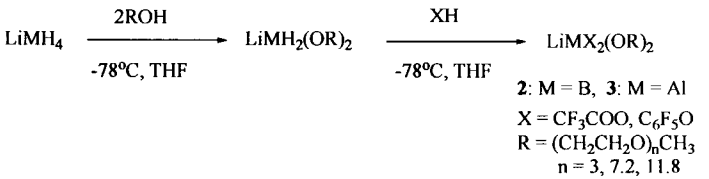

Fig. 2 Synthesis of liquid lithium salts

Although boron atom has formally negative charge in the lithium borates **2**, it is shown that the boron atom has a positive charge from the optimization calculations in MOPAC. Therefore, lithium ion is not attracted to the boron atom but interacts with the oxygen atoms bound to the boron atom because partial negative charges are located on oxygen atoms. Since negative charges on oxygen atoms in borate **2** are smaller than that for aluminate **3** (Fig. 3), borates exhibited higher conductivity than aluminates. From these results, it is important to reduce negative charges on electronegative atoms bound to the ate complex center.

Lithium borates and lithium aluminates were mixed to get hybrid salts. Higher ionic conductivities were observed for hybrid salts than for pure

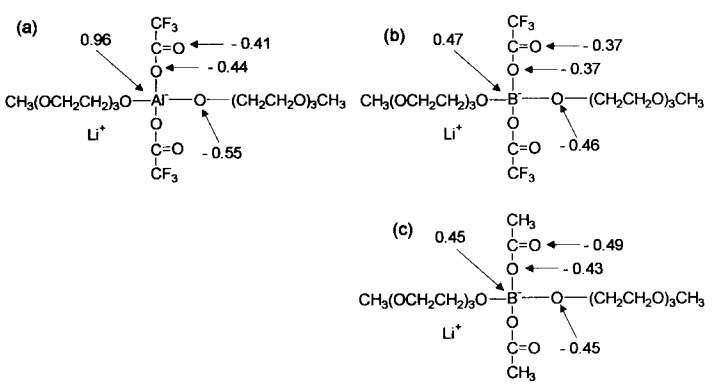

Fig. 3 Partial charge of oxygen atoms and ate complex center atoms from optimization calculations in MOPAC (PM5)

salts.[10] Solid-state polymer electrolytes based on mixed lithium salts with poly-(ethylene oxide) (PEO) as polymer matrix have been produced. Good mechanical properties, improved ionic conductivities, and excellent interfacial performances were observed for the mixed salt systems.[11]

3. Single-ion conducting polymer electrolytes

Single-ion conducting polymer is an ideal electrolyte for rechargeable batteries but the ionic conductivity is usually very low due to strong ion pairing between lithium ion and counter anion which is fixed to polymer chain. As mentioned above, single ion conducting polymer electrolytes with weak interaction between lithium ion and counter anion can be designed using orthoborate structures with electron withdrawing groups. Polyanionic electrolytes **4a** with LiBOB salt structures were designed and synthesized[12] Ionic conductivities of the polyelectrolytes **4a** are found to be high (10^{-5} Scm^{-1} at r.t.) relative to those of most dry single-ion conducting polymer electrolytes.

Borate complex polymers **4b-B** containing fluoroalkane dicarboxylate as an electron withdrawing group and oligoether groups were synthesized.[13] Ionic conductivity of the borate polymer containing long ether chains was high (10^{-5} Scm^{-1} at r.t.). Aluminate polymers **4b-A** showed lower conductivity than borate polymers **4b-B**. PEO (20wt %) was added to the lithium borate polymers in order to improve mechanical properties. Self-standing films were obtained and exhibited high single-ionic conductivity.[14]

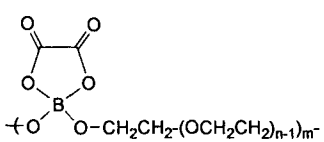

4a

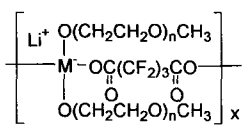

A : M=Al, n=3, 7.2, 11.8

B : M=B, n=3, 7.2, 11.8

4b

Fig.4 Single-ion conducting polymers

4. Anion trapping polymer electrolytes

Lewis acidic boron atom is suitable to form an anion receptor group. [15] Boroxine compounds[16] and borosiloxane polymers[17] acted as effective anion receptors in polymer electrolytes. In order to enhance lithium ion transference number, anion receptor groups have been introduced to polymer chains. Anion trapping polyethers **5a** with boroxine rings as anion receptor groups were synthesized and exhibited high lithium transference numbers.[18] The mixture of boroxine polymer and PEO forms mechanically strong films.[19] Other anion trapping polymers **5b**[20], **5c**[21] and **5d**[22] containing boric ester groups as anion receptors were reported.

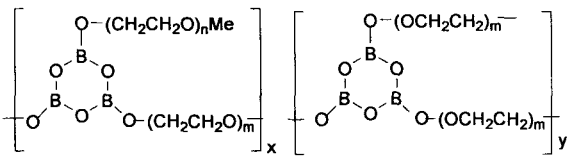

5a

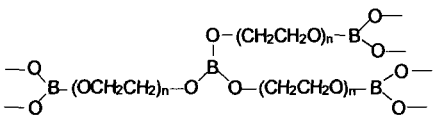

5b

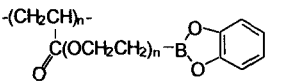

5c

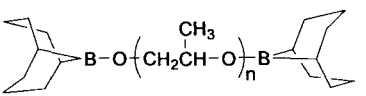

5d

Fig. 5 Anion trapping polymer electrolytes

Large interfacial resistance between PEO polymer electrolyte and electrode such as lithium metal anode or a cathode is usually observed. Boroxine polymer (5a) was an effective additive to depress the interfacial resistance between polymer electrolytes and electrodes.[23] This results in good charge-discharge performance of lithium secondary batteries.[24]

5. Polymer electrolytes composed of insoluble salts and polymers

Usually solubility is required for salts in electrolytes. Recently, we reported that the composites of an insoluble lithium salt with polymers exhibited unusual ionic conductivity. Lithium tetrakis(pentafluorobenzene-thiolato) borate (LiTPSB) was designed to have weak interaction of lithium ion with counter anion as a estimation by optimization calculations in MOPAC (Fig. 6). On the other hand, LiTPOB has negative charges on oxygen atoms which interact with lithium ion. LiTPSB was simply synthesized by reaction of $LiBH_4$ with C_6F_5SH. Although LiTPSB was insoluble in any solvents and polymers, it's composite films with PEO[25] or poly(fluorocarbon)[26] exhibited ionic conductivity (Fig. 7).

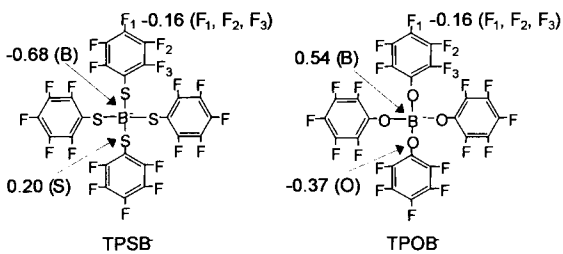

Fig. 6 Partial charges in TPSB anion and TPOB anion

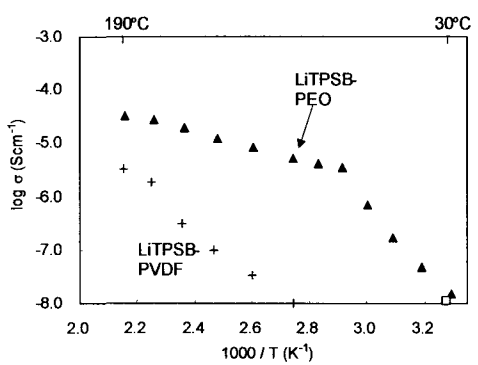

Fig. 7 Temperature dependence of ionic conductivity for LiTPSB / PEO (salt 50 wt%) (▲) and LiTPSB / PVDF (salt 50 wt%) (+).

It is estimated that lithium ion transport is promoted in flexible interfacial PEO phase with low glass transition temperature for polymer electrolytes containing LiTPSB (Fig. 8).

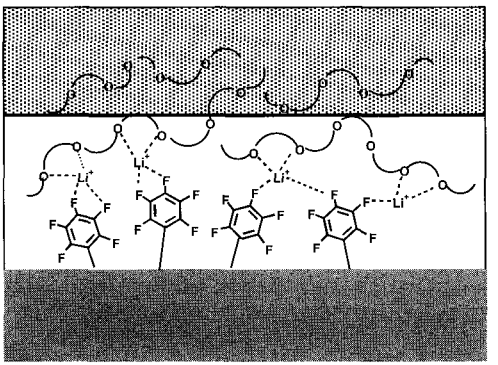

Fig. 8 Ion transport in the interfacial region suggested for polymer electrolytes based on insoluble LiTPSB and PEO.

Higher ionic conductivity was obtained for LiTPSB in polymer gel electrolyte.[27] Ate complexes with four imidazoyl groups (Im) were also insoluble. Lithium tetraimidazoyl aluminate, $LiAlIm_4$ was insoluble salt but it's composite with PEO exhibited ionic conductivity.[28] Boron analogue was not obtained as a pure salt by the similar procedure.

6. Crown ether substituted boric ester

Crown ethers are known to be effective additives to enhance ionic conductivity of PEO electrolytes but the increase of ionic conductivity is usually less than one order. Recently, we found that crown substituted boric ester has a special effect for PEO electrolyte. Time dependence of ionic conductivities for $LiCF_3SO_3$ – PEO electrolytes are shown in Fig. 9. When boric ester TCB containing three14-crown-4 groups was added to $LiCF_3SO_3$ – PEO electrolyte, ionic conductivity at room temperature was increased from 10^{-8} Scm^{-1} order to 10^{-7} Scm^{-1} order. During storage of the electrolyte film under dry conditions at ambient temperature, the ionic conductivity gradually increased and 10^{-5} 10^{-7} order of high ionic conductivity was obtained after 300 hours.[29] On the other hand, 14-crown-4 or linear origoether substituted boric

ester enhanced ionic conductivity of PEO electrolyte, but constant conductivities were observed during storage.

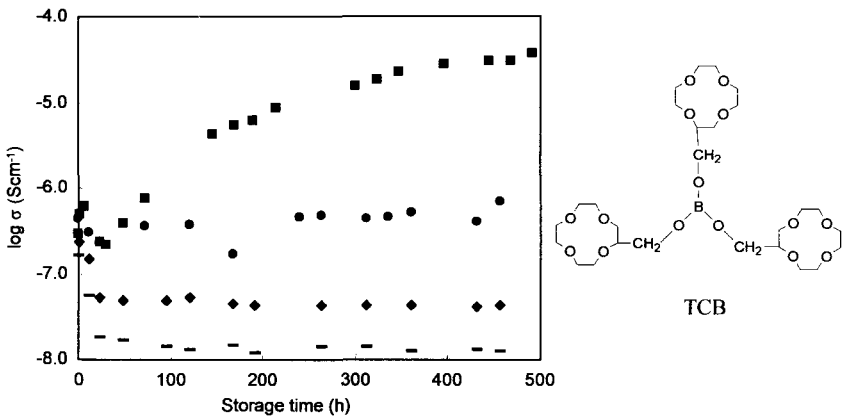

Fig. 8 Storage-time dependence of ionic conductivity for additive-CF_3SO_3Li / PEO electrolytes (EO / Li = 20 / 1) at 30 °C
Additive (7 wt%) : ■ TCB, ● $B[O(CH_2CH_2O)_3CH_3]_3$, ♦ 12-crown-4, — No additive

Lithium ion transference number of $LiCF_3SO_3$-PEO electrolyte was also increased from 0.2 to 05 by addition of TCB. The reason for the large increase in ionic conductivity and lithium ion transference number of PEO electrolyte has not been clear but these novel phenomena are interesting for progress in the field of solid polymer electrolytes.

Conclusion and outlook

As mentioned in this review, boron compounds have made significant progress in solid polymer electrolytes. Molecular design of boron compounds is very important for their application to electrolytes because various organic and inorganic groups can be introduced on three coordinated neutral boron atom or four coordinated anionic boron atom. Further studies will be continued to develop polymer electrolytes using new boron compounds for large improvement of ionic conductivity, ion transference number, electrochemical stability, and interfacial resistance. In addition, detail studies

on ion conduction phenomena and battery performance for boron based polymer electrolytes are also important. At present, we have no polymer electrolyte whose properties are enough for lithium secondary batteries. I hope that research on novel and well designed boron compounds may be of value in achieving the goal of polymer electrolyte.

I would like to thank Dr. Takahiro Aoki and Mr. Akira Hujimori for their collaboration. Our work has been partially supported by Grant-in-aid for Scientific Research (B) (No. 16350099) from the Ministry of Education, Culture, Sports, Science and Technology of Japan

References

1. W. Xu, C. A. Angell, *Solid-State Lett.*, **4**, E1(2001)
2. H. Yamaguchi, H. Takahashi, M. Kato, J. Arai, *J. Electrochem. Soc.*, **150**, A312(2003).
3. G. B. Appetecchi, D. Zane, B. Scrosati, *J. Electrochem. Soc.*, **151**, A1369 (2004).
4. T. J. Barbarich, P. F. Driscoll, *Electrochem. Solid-State Lett.*, **6**, A113 (2003).
5. Y. Sasaki, M. Handa, K. Kuroshima, T. Tonuma, K. Usami, *J. Electrochem. Soc.* **148**, A999(2001).
6. J. Barthel, R. Buestrich, E. Carl, H. J. Gores, *J. Electrochem. Soc.*, **143**, 2572(1996)..
7. Z. B. Zhou, M. Takeda, T. Fujii, M. Ue, *J. Electrochem. Soc.*, **152**, A351 (2005).
8. T. Fujinami, Y. Buzoujima, *J. Powere Sources*, **119-121**, 438(2003); R. Tao, D. Miyamoto, T. Aoki, T. Fujinami, *J. Power Sources*, **135**, 267 (2004); R. Tao, T. Fujinami, *J. Powere Sources*, **135**,267(2004).
9. H. Shobukawa, H. Tokuda, M. A. B. H. Susan, M. Watanabe, *Electrochim. Acta*, **50**, 3872(2005).
10. R. Tao, T. Fujinami, *Electrochim Acta*, **50**, 1993(2005).
11. R. Tao, T. Fujinami, *J. Power Sources*, **146**, 407(2005).
12. W. Xu, M. D. Williams, C. A. Angell, *Chem. Mater.*, **14**, 401(2002).

13. T. Aoki, A. Konno, T. Fujinami, *J. Electrochem. Soc.*, **151**, A887(2004).
14. T. Aoki, A. Konnno, T. Fujinami, *Electrochim. Acta*, **50**, 301(2004).
15. Y. M. Lee, J. E. Seo, N. S. Choi, J. K. Park, *Electrochim. Acta*, **50**, 2843 (2005); H. S. Lee, Z. F. Ma, X. Q. Yang, X. Sun, J. MacBreen, *Electrochim. Acta*, **151**, A1429(2004)16. M.A. Mehta, T. Fujinami, S. Inoue, K. Matsushita, T. Miwa, T.Inoue, *Electrochimica Acta*, **45**, 1175(2000); F. Zhou, D. R. MacFarlane, M. Forsyth, *Electrochim. Acta*, **48**, 1749(2003).
17. R. Kurono, M.A.Mehta, T. Inoue, T. Fujinami, *Electrochimca Acta*, **47**, 483(2001).
18. M. A. Mehta, T. Fujinami, *Chem. Lett.*, 915(1997).
19. Y. Yang, T. Inoue, T. Fujinami, M. A. Mehta, *Solid State Ionics*, **140**, 353 (2001).
20. Y. Kato, K. Hasumi, S. Yokoyama, T. Yabe, H. Ikeda, Y. Uchimoto, M. Wakihara, *Solid State Ionic*s, **150**,355(2002).
21. T. Hashimoto, M. Nihiura, M. Watanabe, *J. Electrochem. Soc.*, **46**, 1609 (2001); S. Tabata, T. Hirakimoto, M. Nihiura, M. Watanabe, *Electrochim. Acta*, **48**, 2105(2003).
22. T. Mizuno, K. Sakamoto, N. Matsumi, H. Ohno, *Electrochim. Acta*, **50**, 2843(2005).
23. R. Tao, T. Fujinami, *Trans. Matr. Res. Soc. Jpn.*, **29**, 1021(2004).
24. R. Tao, T. Fujinami, *J. Applied Electrochem.*, **35**, 163(2005).
25. T. Aoki, T. Fujinami, *J. Electrochem. Soc.*, **152**, A2352(2005).
26. T. Aoki, T. Fujinami, *J. Powere Sources*, **146**, 412(2005).
27. T. Aoki, T. Fujinami, *Electrochim Acta*, in press.
28. A. Fujimori, T. Aoki, T. Fujinami, submitted.
29. A. Fujimori, T. Kan, T. Fujinami, submitted.

STRUCTURAL, VIBRATIONAL AND AC IMPEDANCE ANALYSIS OF NANO COMPOSITE POLYMER ELECTROLYTES BASED ON PVAc

S.SELVASEKARAPANDIAN*, R.MANGALAM, M.HEMA, R.BASKARAN, T.SAVITHA

Solid State and Radiation Physics Lab, Department of Physics, Bharathiar University, Coimbatore-641 046, Tamil Nadu, India

E-Mail: sekarapandian@yahoo.com

MARIE-PIERRE CROSNIER-LOPEZ, CLAUDE BOHNKE , ODILE BOHNKE

Institut de Recherche en Ingénierie Moléculaire et Matériaux Fonctionnels (FR CNRS 2575) Laboratoire des Oxydes et Fluorures (UMR 6010 CNRS), Université du Maine, Avenue O.Messiaen 72085 Le Mans Cedex 9, France

M.VIJAYAKUMAR

Department of Physics, College of William & Mary, Williamsburg- 23187, Virginia, USA

ABSTRACT

In the present study the nano sized TiO_2 has been dispersed into the gel polymer electrolyte 70PVAc:20DMF:10$LiClO_4$ at different concentrations by solution casting technique. XRD results reveal the dispersion of rutile phase nanoTiO_2 filler particles in the gel polymer matrix. The FTIR spectra show the interaction of Li^+ ion with the ester and carbonyl oxygens of PVAc and also with TiO_2. The ac impedance analysis reveals the distribution of relaxation time in all the compositions of composite polymer matrix. The conductivity of 70:20:10 (PVAc:DMF:$LiClO_4$) gel polymer electrolyte has been found to be 2.53 x 10^{-5} Scm^{-1} which increases to the maximum of 3.23x10^{-4} Scm^{-1} with the dispersion of 15 m% TiO_2 filler at ambient temperature.

1. Introduction

Polymer electrolytes resulting from the complexation of low lattice energy salts with solvating polymers have generated a widespread and sustained interest with in the scientific community. Gel polymer electrolytes exhibit high ionic conductivities, however the mechanical properties of these electrolytes are not sufficient enough for practical applications. The recent attention to gel polymer electrolytes is thus focused on high ionic conductivity and mechanical properties. Therefore a new method of introducing inert ceramic grains such as Al_2O_3, TiO_2, SiO_2, CeO_2 etc., into the polymer matrix has been developed. The particle size and the nature of the filler play a fundamental role in improving the polymer electrolyte properties. The reduction of the ceramic particle size from microns to nanometer leads to a further

increment in the conductivity and allow one to synthesize lightweight composites which can be processed easily. These polymer electrolytes are finding variety of applications in all solid state electrochemical devices such as batteries, fuel cells, sensors, electrochromic display devices, pace makers, coulometer and analog potential memories etc.

2. Experiment

The nano composite polymer electrolytes were obtained by the dissolution of PVAc and DMF followed by the addition of salt $LiClO_4$. Finally the inert nano filler TiO_2 was added. The suspension obtained was stirred until visibly homogenous and then cast in petridishes and the solvent was allowed to evaporate in air at room temperature. The films were further vacuum dried to remove any traces of acetone. This procedure provided mechanically stable and flexible films. The particle size of the dispersed nano filler (500-900nm) has been confirmed from Laser granulometry and SEM[1].The FTIR spectra was recorded using SHIMADZU 8000 Spectrophotometer in the frequency range 400-4000 cm^{-1}. Powder X-Ray diffraction (XRD) patterns were recorded at room temperature on a Philips X'Pert PRO diffractometer equipped with an X'celerator detector, using the Cu Kα radiation in the 2θ range from 5 to 90°. The impedance of the film was studied over the frequency range 42 Hz to 5 MHz in the temperature range 303 K to 343 K using computer controlled HIOKI LCR meter 3532.

3. Results and discussion

3.1 F TIR Analysis

In the present study FTIR spectra is used to establish the interactions among polymer, plasticizer, salt and PVAc+DMF+$LiClO_4$ with various concentrations of TiO_2. The spectra of all these complexes has been presented in Fig 1 (a-g). The vibrational bands at 2923, 2865and 1375 cm^{-1} in pure PVAc are ascribed to CH_3 asymmetric stretching, symmetric stretching and symmetric bending vibrations. The vibrational bands at 1245 and 1730 cm^{-1} of pure PVAc are ascribed to C-O-C symmetric stretching and C=O stretching frequency [2]. The band assignments for DMF have already been reported in the literature [3]. As per the reports the bands observed in the polymer electrolyte fig(1.c) at 2857, 1439 cm^{-1} are ascribed to C-H

stretching and CH_3 asymmetric deformation mode of DMF respectively. Also the vibrational bands observed at 1676, 1507, 1388 and 659 cm^{-1} are ascribed to C=O stretching, C-N stretching, C-H bending and O=C-N stretching modes of DMF respectively. The vibrational bands at 1620, 1320, 1070, 940 and 750 cm^{-1} are ascribed to $LiClO_4$ [2]. The vibrational band at 637.91 cm^{-1} of pure TiO_2 is ascribed to Ti=O stretching vibration.

The vibrational band at 940 cm^{-1} of pure $LiClO_4$, [Fig 1 (a)] gets shifted in the polymer complexes and all other bands of $LiClO_4$ were found to be absent in the polymer complex indicating the dissociation of salt into the polymer matrix. The stretching frequency at 1730 cm^{-1} which corresponds to C=O stretching of pure PVAc, [Fig 1 (b)], gets shifted to lower wave number (1720-1710 cm^{-1}) in the complexes. The shift observed in the carbonyl stretching frequency of the complexes indicates interaction of the Li^+ ion with the carbonyl oxygen of the polymer. The addition of $LiClO_4$ causes a small decrease of the C-O-C stretching down to lower wavenumbers due to the coordination of the ester oxygen with the lithium cation, [Fig 1 (c)].

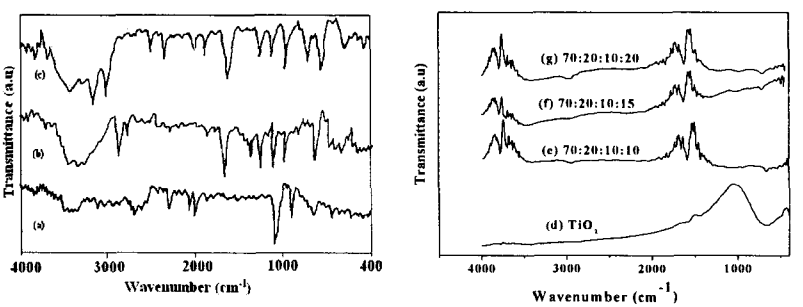

Figure 1 FTIR Spectra of (a) $LiClO_4$, (b)PVAc, (c) PVAc:DMF:$LiClO_4$ (d,TiO_2 and (e-g) composite PVAc:DMF:$LiClO_4$:TiO_2

The stretching frequency at 1676 cm^{-1} which corresponds to C=O stretching of pure DMF gets shifted to lower wave numbers (1670-1660 cm^{-1}) in the composite polymer electrolytes indicating the interaction of the Li^+ with carbonyl oxygen of DMF. The O=C-N stretching mode at 659 cm^{-1} is sensitive to the salt present in the sample. The shifting and the appearance of the new band at 720 cm^{-1} is attributed to

the interaction of Li^+ with O=C-N group of DMF. The splitting of the C-N symmetric stretching vibration of the plasticizer into a doublet at 862 and 884 cm^{-1} is the evidence for the plasticizer-polymer interaction [Fig 1 (c)].The peak observed around 673.91 cm^{-1} is attributed to Ti=O stretching of pure TiO_2, get shifted to lower wave number (673– 670.96 cm^{-1}) in the composites, [Fig. 1 (e, f, g)]. This indicates the interaction of Li^+ with the TiO_2.The broadening and shifting of the vibrational bands correspond to pure PVAc, DMF and TiO_2 in the composite polymer electrolyte systems imply the weak interactions of Li^+ with the polymer, DMF and TiO_2.

3.2 X-Ray Diffraction analysis

In order to investigate the influence of the concentration of nano TiO_2 filler, XRD studies were performed for pure PVAc, PVAc+DMF+$LiClO_4$, TiO_2 and for 5 m% and 20 m% of TiO_2 complexes and they are shown in [Fig. 2 (a-e)]. The diffractogram shown in [Fig. 2 (a)] clearly indicates two broad peaks at 2θ = 14.8°, 21.6 ° which are ascribed to pure PVAc which reveals the amorphous nature of the polymer. From [Fig. 2 (b)] the diffraction peak at 2θ =14.8° found in pure PVAc was found to be absent in the PVAc+DMF+$LiClO_4$ plasticized system. Also the diffraction peak at 2θ = 21.6° has been slightly shifted in the plasticized system, due to the interaction of polymer with the plasticizer which is in good agreement with the FTIR results. The diffraction peaks of pure $LiClO_4$ at 2θ = 18.392°, 21.90°, 23.2°, 31° and 32° (PCPDF-30-0751) [4] were found to be absent in the polymer complex indicating the complete dissociation of the salt in the polymer and also the complexation. [Fig 2 (c)] shows the powder X-ray Diffraction pattern, recorded at room temperature of the synthesized TiO_2 powder [1,5]. From [Fig 2 (d-e)] the diffraction peak at 2θ = 27.5°, 36.5°, 54.5°, 56.8° and 69° are attributed to TiO_2 (PCPDF- 34 – 0180) [6], which indicates the dispersion of the nano filler particles in the composite polymer electrolytes. The intensity of peaks corresponding to 2θ values of the TiO_2 were found to be increased in the [Fig 2 (e)] indicating the higher concentration of the filler (20 mol% - TiO_2).In the composite polymer complex some less intense peaks were observed around 2θ = 9.5° and 44.32° corresponding to

$LiClO_4$. All the remaining peaks for $LiClO_4$ are absent in the complex indicating the complete dissociation of the salt and hence the complexation.

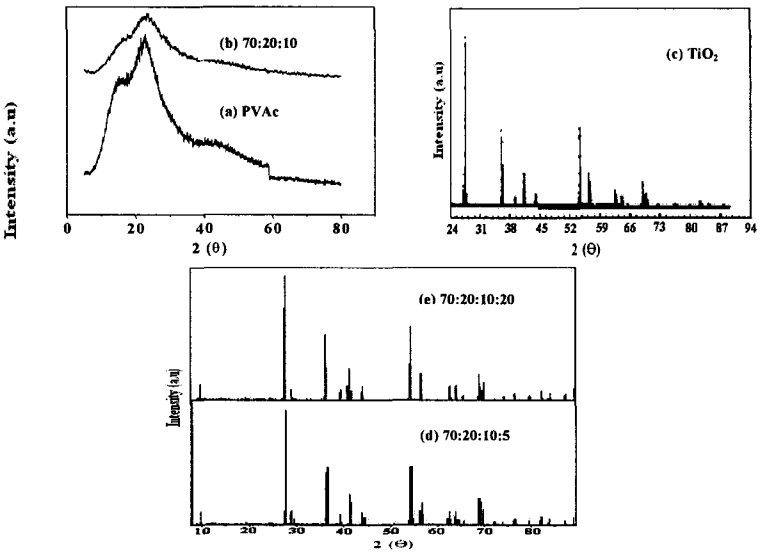

Figure.2 XRD pattern of(a) PVAc, (b)PVAc:DMF:$LiClO_4$, (C)TiO_2 and (d,e) composite PVAc:DMF:$LiClO_4$:TiO_2

3.3 Impedance analysis

The complex impedance plot (Z' vs Z") for all the samples at 303K [fig.3] show two well defined regions : (i) the semicircular portion at high frequency region arising from a parallel combination of the bulk resistance and bulk capacitance of the electrolyte (ii) the linear region in the low frequency side is due to the effect of blocking electrodes. By knowing the value of bulk resistance along with the dimensions of the sample, the ionic conductivity has been calculated and has been given in Table.1. From Fig.3, it was observed that the diameter of the semicircle is high for the plasticized system and it gradually decreases with the addition of TiO_2 filler particles. From the impedance results the highest conductivity of 3.23×10^{-4} Scm^{-1} at room temperature has been observed for the composite with 15m% of TiO_2. The complex impedance plot for this polymer electrolyte at various temperatures (303-343K) is shown in Fig. 4. From the impedance response behaviour the disappearance of high frequency semicircle as the temperature increases led to a

conclusion that the current carriers are ions and this leads one to further conclude that the total conductivity is mainly as the result of ion conduction [7].

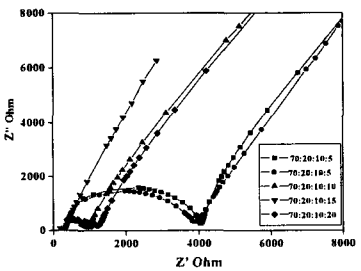

Fig.3 Impedance plot for all the samples at 303K

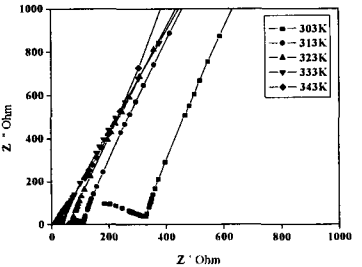

Fig.4 ColeCole plot for composite with 15m% of TiO_2 at various temperatures

3.4 Temperature dependent Ionic conductivity

The temperature dependence of electrical conductivity of the polymer films is shown in Fig.5. The non- linearity in the plot indicates that the ion transport in polymer electrolytes is dependent on polymer segmental motion [8].

Table.1 : Conductivity, Hopping frequency ,Relaxation Time for all the samples

Composition PVAc:DMF: $LiClO_4$: TiO_2	Conductivity (Scm^{-1})			Hopping frequency ω_p Hz	Relaxation Time τ sec
	303K	323K	343K	303K	303K
70:20:10	2.5×10^{-5}	1.2×10^{-4}	9.38×10^{-4}	4.58×10^{6}	1.18×10^{-5}
70:20:10:5	3.2×10^{-5}	1.9×10^{-4}	9.47×10^{-4}	6.22×10^{6}	8.38×10^{-6}
70:20:10:10	1.0×10^{-4}	1.1×10^{-3}	4.9×10^{-3}	2.48×10^{7}	2.36×10^{-6}
70:20:10:15	3.3×10^{-4}	1.5×10^{-3}	7.47×10^{-3}	7.67×10^{7}	1.69×10^{-6}
70:20:10:20	7.1×10^{-5}	1.6×10^{-3}	2.66×10^{-3}	1.74×10^{7}	2.64×10^{-6}

Thus the result may be more effectively represented by the Vogel-Tamman-Fulcher (VTF) equation

$$\sigma = AT^{-1/2} \exp [-E_a/K (T-T_g)] \qquad (2)$$

where A-fitting constant proportional to the number of charge carriers. Ea-pseudo activation energy, K-Boltzmann constant and T_0-equilibrium temperature of the system corresponding to zero configuration entropy. T_g-the thermodynamic glass transition temperature of the system. Fig.6 shows the variation of conductivity with TiO_2 concentration for different temperatures. The enhancement in the ionic

conductivity with the increasing concentration of TiO_2 may be due to TiO_2 which interacts with either of both the anion and cation thereby reducing ion pairing and increases the free charge carriers. The same type of behaviour has been reported in Al_2O_3 dispersed PEO-LiTFSI based polymer composites [9].

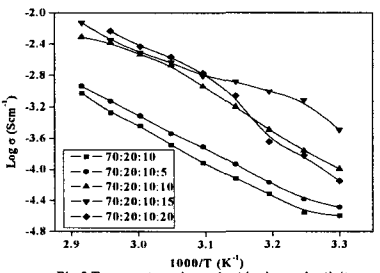

Fig.5 Temperature dependent ionic conductivity for all samples

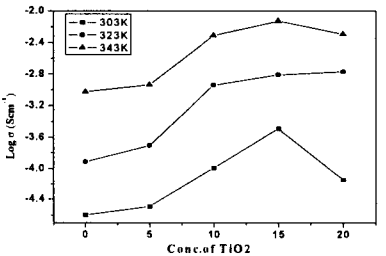

Fig 6 Dependence of ionic conductivity on filler concentraton for PVAc+DMF+LiClO4 polymer complex at different temperatures

A further increment in TiO_2 concentrations results in a decrease in conductivity which may be due to the restricted ionic and polymer segmental mobility in a rigid matrix at room temperature. As the temperature increases the charge carries are thermally activated and the free volume increases and more vacant sites are created for the motion of ions, which in turn enhances the conductivity.

3.5 ac Conductivity analysis

The variation of the ac conductivity with frequency for different TiO_2 concentration with polymer electrolytes at 303K is shown in Fig.7. The frequency dependent ac conductivity of the polymer electrolyte is described by Almond and West formalism [10],

$$\sigma(\omega) = \sigma_{dc} + A\omega^n \qquad (3)$$

where A and n are material parameters, $0<n<1$, σ_{dc} is dc ionic conductivity and ω is the angular frequency. The plot shows three regions: The first one is the low frequency dispersion region observed which can be ascribed to the space charge polarization at the blocking electrodes. The second region corresponds to the frequency independent plateau region. The conductivity is found almost frequency independent in this region and the extrapolation of the plot to zero frequency gives the value of dc conductivity at all temperatures. The high frequency conductivity dispersion is prominent at lower temperatures. As temperature increases, the frequency independent conductivity region decreases and thus the polarization effect

becomes prominent. From the plot it is observed that the conductivity increases from $2.5x10^{-5}Scm^{-1}$ to $3.23x10^{-4}$ Scm^{-1} with increase of TiO_2 concentration up to 15 m% and after which the conductivity ceases which is in good agreement with the impedance analysis.

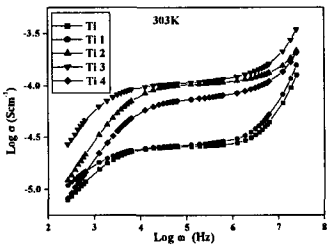

Fig (7) Variation of conductivity with frequency for all the samples at 303K

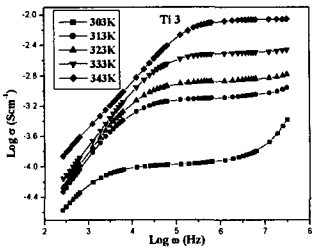

Fig (8) Variation of conductivity as a function of frequency for the sample with 15m% of TiO2 at different temperatures

The possible decrease in the ionic conductivity at 20 m% TiO_2 can be attributed to the restricted motion of ions in the rigid polymer matrix. Fig.8 shows the temperature dependent conductance spectra of 15 m% TiO_2. As temperature increases, more and more charge accumulation occurs at the interface between electrode and electrolyte, which leads to a decrease in the conductivity at low frequencies. According to Almond and West formalism, the hopping frequency of charge carriers (ω_p) is found from,

$$\omega_p = 2\,\sigma_{dc} \qquad (4)$$

The hopping frequency calculated for PVAc:DMF:$LiClO_4$ and PVAc:DMF:$LiClO_4$ doped with different concentrations of TiO_2 have been tabulated in Table-1. The maximum hopping rate 7.67 x 10^7 Hz is observed for the sample with 15 m% TiO_2 and PVAc:DMF:$LiClO_4$ and it is found to have the minimum hopping rate of $4.58x10^6$ Hz at room temperature.

3.6 Dielectric Studies

The frequency dependence of the dielectric permittivity curve for all samples at different temperatures is shown in Fig 9. The dielectric constant decreases with increase of frequency followed by an intermediate plateau and it gets saturated at higher frequencies. The high value of dielectric permittivity at low frequencies can be attributed to the accumulation of charge carriers near the electrodes [11]. The higher values of ε' for 15 m% TiO_2 (higher conductivity) is due to the enhanced

charge carrier density at the space charge accumulation region, resulting in a rise in the equivalent capacitance. As the temperature increases the dielectric constant ε′ of the sample gets increased. The intermediate plateau is observed in all samples, and this step like behaviour in the dielectric constant coincides with the transition frequency region from ac to dc conductivity [12]. At higher frequencies, the dielectric constant decreases due to the high periodic reversal of the applied field.

Fig. 10 shows the variation of dielectric loss (ε") with frequency at different temperatures for 15 m% of TiO_2 system. From the plot the peak observed at high frequencies is due to β-relaxation and this relaxation processes may be caused by movement of the side chains [13]. It is also observed that as the temperature increases there appears a second relaxation peak which may be attributed to motion of the main chain which is pronounced in the low frequency range [13].

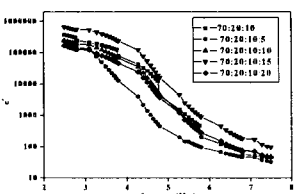

Fig .9 Variation of ε' vs log ω at 303K

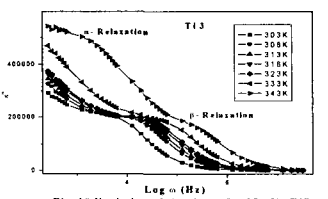

Fig. 10 Variation of ε' vs log ω for 15m% TiO_2

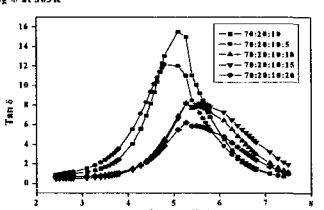

Fig.11 Plot of Tan δ vs Log ω for all the samples at 303K

The variation of dissipation factor, tan δ = ε"/ ε', as a function of frequency is given in Fig 11 for all compositions at room temperature. Well defined peaks observed in the plot corresponds to the dielectric relaxation phenomena. This low temperature relaxation peak may be attributed to the side chain motion (β-relaxation) in the polymer electrolytes and is in good agreement with the peak observed in the imaginary part of the dielectric permittivity. The position of peak shifts to higher frequencies with increasing concentration of TiO_2 which implies the fact that more sites are created for ion hopping as the filler concentration increases and hence a

decrease in the relaxation time. The relaxation times calculated from the plots are show in Table.1.

4.Conclusion

The nano composite polymer electrolytes have been prepared by solution casting technique. From the FTIR analysis it is evident that there exits a weak interaction of Li^+ with polymer, plasticizer and TiO_2. From the XRD results, the well defined peaks for TiO_2 in the composites reveals the dispersion of the nano filler in the polymer matrix. From the impedance analysis it has been found that the high ionic conductivity of $3.23x10^{-4}$ Scm^{-1} at 303K is obtained for the composite with 15m% TiO_2. This enhancement in conductivity is due to the dispersion of nano TiO_2 filler which creates free pathways for the ions to move. The dielectric relaxation studies reveals two peaks in the imaginary part of the relative permittivity.

Acknowledgements

One of the authors R. Baskaran acknowledges the Council of Scientific and Industrial Research (CSIR), Government of India, for the award of Senior Research Fellowship (SRF).

Reference

1. Odile Bohnke, Universite du Maine, France (Personal communications).
2. R. Baskaran, S. Selvasekarapandian, G. Hirankumar, M.S. Bhuvaneswari, *Journal of Power Sources* **134** (2004) 235-240.
3. A.S. Quist, J.B. Bates, G.E. Boyed, *J. Chem. Phys* **54** (1971) 4896.
4. Pustelnik, Soloniewicz, Rocz, *Chem.*, **46**, 1961, (1972).
5. M. Vijayakumar, C. Bohnke, *Chem. Matter.* **16**, 2719-2724. 2004.
6. Smith, Zolensky, Dept. Geol. Sc, Penn State Univ, University Park, PA, USA, ICDD, Grant-in-Aid [1979].
7. M.M.E. Jacob, S. Radhakrishna, *Solid state Ionics* **104** 267 (1997).
8. Y. Okamoto, T.A. Skotheimk, *J.Polym. Sci A: Poly. Chem* **31**,2573,(1993)
9. P.A.R.D. Jayathilaka, *Electrochimica Acta* **47** 3257-3268. (2002)
10. D.P. Almond and A.R. West, *Solid State Ionics*, **23** 27 (1987).
11. R.D. Armstrong, *Electronal Chem & Interfacial Electrochem.* **53** 389, (1974)
12. A. Pimenov, J. Ullrich, P.Lunkenheimer, *Solid State Ion.* **109** 111. (1998)
13. Borisova, T.I., in Relaxation Phenomena in Polymers, ed. G.M. Bartenew and Y.V. Zelenew, Halsted, NewYork, , **P. 25.**,1974.

ABSORPTION INTENSITY VARIATION WITH ION ASSOCIATION IN PEO BASED ELECTROLYTES

J. E. FURNEAUX, ALLISON M. MCCOY, VARUNI SENEVIRATNE*, AND
Homer L. Dodge Department of Physics and Astronomy,
University of Oklahoma,
Norman, OK 73019, USA
E-mail: furneaux@ou.edu

ROGER FRECH
Department of Chemistry and Biochemistry,
University of Oklahoma
Norman, OK 73019, USA

The validity of the extended version of Beer's Law, that the integrated absorption of the $\delta_s(CF_3)$ mode in PEO:$LiCF_3SO_3$ is independent of $CF_3SO_3^-$ ion association, is tested and found to be valid. An infrared absorption marker, AsF6- is found to be effective for the quantitative comparison of absorption intensity in different samples.

1. Introduction

Polymer electrolytes are ion conducting solid phases formed by dissolving salts in ion-coordinating macromolecules. Poly(ethylene oxide), PEO, complexed with lithium salts are the most often studied examples of polymer electrolytes. Here, we extend previous work [1-7] focusing on PEO with $LiCF_3SO_3$, lithium triflate (LiTf).

The molecular-level understanding of the ionic conductivity mechanism in polymer electrolytes is poor, although it is known that ionic association, cation-polymer interactions, and polymer segmental motion play critical roles. Local structures identified by X-ray diffraction and vibration spectroscopy have provided valuable insight about cation-anion association and cation-polymer interactions. Here, we extend vibration spectroscopic studies to give a foundation for quantitative studies of ionic association and polymer configurations.

Quantitative comparisons of vibration spectra of polymer electrolytes have been hampered by the lack of standards. It is difficult to quantitatively compare

* Current address: Department of Physics, University of Peradeniya, Peradeniya, Sri Lanka

different samples because measuring sample thickness to better than 10% when the sample is less than 10 μm thick and not uniform is extremely difficult. Temperature dependent experiments can be further complicated by changes in sample thickness with temperature, especially if the sample is melted. Thus, only relative intensity changes for samples are commonly compared [1-8]. For more complete analyses including more quantitative information, some marker that enables relative thickness to be measured between samples is needed. We have found such a marker, actually a series of markers depending on the particular experiment. These are the XF_6^- ions where X = P, As, Sb. These ions have a strong ν_3 mode between 640 cm^{-1} and 750 cm^{-1} depending on ion, that allows easy measurement of the absorption at molar concentrations of less than 0.002 [8-10].

Our aim, when beginning this study was to examine the validity of Beer's Law in an extended form. It is clearly true that the absorption intensity for a given mode is proportional to the concentration of that species within a sample. As all absorptions are a mixture of molecular motions, there is no guarantee that the mixture will not depend on the local environment, in this case ionic association. There are some modes where the absorption intensity clearly depends on environment, *e.g.* the ν_1 mode for these ions which is completely forbidden as an infrared absorption in high symmetry cases, and becomes allowed if the symmetry is broken by ion association. Burba [8] has shown that the PF_6^- ion sometimes shows a ν_1 absorption when it is a contact-ion pair in solution while showing no absorption without the ion association. Others have commonly uses relative intensity of split lines, *e.g.* the triflate $\delta_s(CF_3)$ mode, to infer relative concentrations of ionically associated species [1-7]. This analysis has depended on an, until now, unverified extended version of Beer's Law that the absorption intensity of the studied mode is independent of ion association for the case under study. This is not always the case.

Here we examine the triflate $\delta_s(CF_3)$ mode as a function of temperature and of triflate concentration in PEO. If the sample is highly crystalline, dramatic changes in triflate ion association are possible when the PEO melts [4]. We exploit this fact, while using an AsF_6^- marker, to test the validity of the extended version of Beer's Law for the triflate $\delta_s(CF_3)$ mode.

2. Experimental Procedure

2.1. *Sample Preparation*

In order to produce samples of PEO:LiTf that could be quantitatively analyzed at different ether oxygen to LiTf concentrations and at different temperatures, a large quantity of PEO:$LiAsF_6$ at 500:1 was first prepared. Low molecular weight, 2,000 Da, PEO was chosen to minimize hysteresis and maximize cation-anion association changes with temperature. This PEO was dried for 48 h at 10^{-2} mBarr and 45-50°C. Then 10 g was dissolved in acetonitrile with sufficient $LiAsF_6$ to give an ether oxygen to AsF_6^- ratio of 500:1 and stirred for at least 24 h. The solvent was then extracted to yield quantitatively marked PEO, portions of which were used for all subsequent sample preparation in this study. We chose $LiAsF_6$ as a marker because the AsF_6^- ion has a very strong, constant intensity, ν_3 absorption at 700 cm^{-1} (see Fig. 1), which is isolated from all PEO and triflate absorption bands.

Weighed amounts of the AsF_6^- marked PEO were dissolved in acetonitrile with appropriate amounts of $LiCF_3SO_3$ to give ether oxygen to triflate ratios of x:1 where x = 10, 15, 20, 30, and 40 and again stirred for at least 24 h. The resulting viscous solution was cast thinly on a single ZnSe window and mounted in a Bruker IFS66V vacuum FTIR spectrometer. In the spectrometer under vacuum at 10 mBarr, the sample was heated to 80°C, held there for 1 h, and cooled back to room temperature. This procedure was used to insure that the samples had no residual morphological effects from the solvent casting, and no residual water. A single window was chosen to minimize Fabry-Pérot artifacts and to enhance water extraction. We found by testing that only small changes in sample thickness occurred upon subsequent heating and cooling, even above the melting point of PEO, 60°C.

All sample preparation outside the spectrometer was performed in a glove box under inert Ar atmosphere.

2.2. *Data Collection*

Infrared absorption spectra were collected at a resolution of 1 cm^{-1} using the IFS66V FTIR spectrometer and a temperature controlled transmission cell. For each concentration including the neat marked PEO, PEO:$LiAsF_6$ at 500:1, 13 spectra were obtained as a function of temperature. These were at room temperature (23-24°C), every 10°C to 80°C going up in temperature. The temperature sequence was then reversed going down in temperature. We were especially interested in recording the spectral changes associated with the

crystalline PEO melting at 60°C. As the absorption of the ZnSe windows is temperature dependent, a separate background spectrum was used for each temperature.

2.3. *Data Analysis*

For our data analysis procedure, we wished methods that are as independent of the baseline and undesirable artifacts as possible. In particular we desired a procedure for scaling the data that depended as much as possible on the data itself rather than somewhat arbitrary choices of curve fitting. The procedure that we devised is described and illustrated here.

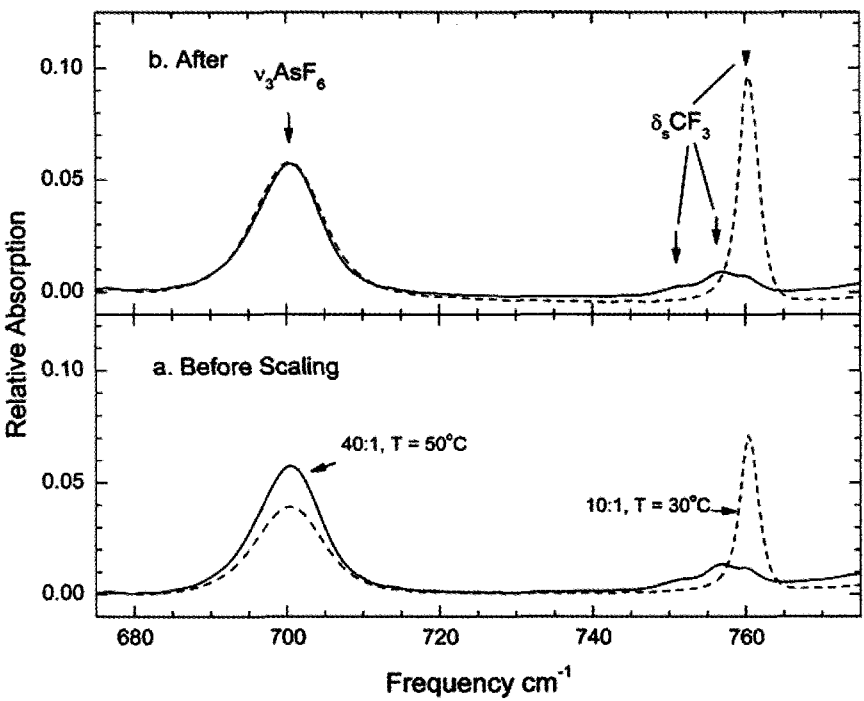

Figure 1. Spectra of (PEO:$LiAsF_6$):LiTf showing the effectiveness of the scaling procedure.

Data from 500 cm^{-1} to 800 cm^{-1} of interest here was extracted from the complete spectra. Example data including the ν_3AsF_6 and the δ_sCF_3 bands is shown in Fig. 1a for different concentrations and temperatures. Here the difference in absorption for the ν_3AsF_6 band for different samples is clearly seen.

To obtain a measure of this absorption intensity that is relatively independent of the baseline, a numerical derivative of the data was taken as

shown in the inset to Fig. 2. The same difference in absorption is evident here. Such derivative data was extracted for each set of absorption data. This data was then all averaged to give the overall average of the derivative data. Each curve was then plotted versus this average data to generate the relevant scale factors as shown in Fig. 2.

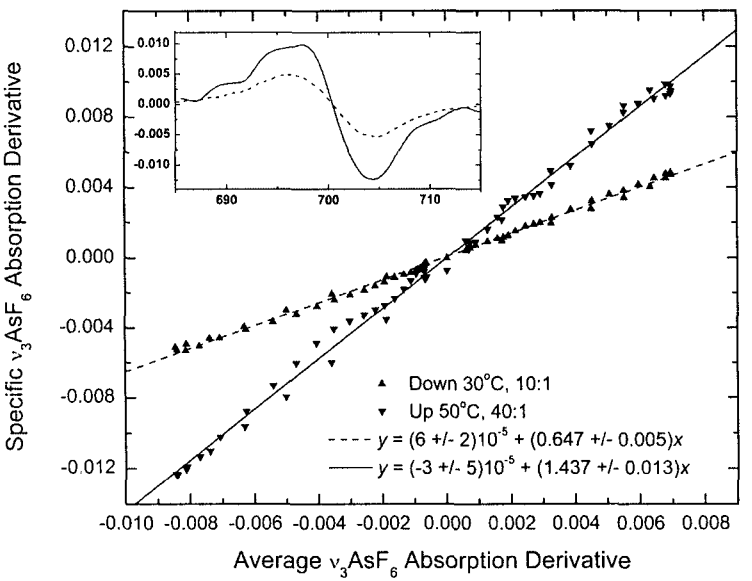

Figure 2. Scaling procedure example showing linear fits to numerical ν_3AsF_6 derivatives of the two data sets from Fig. 1 giving scale values for each data set. Inset: numerical derivatives of the data in Fig. 1.

The best-fit lines are also shown with their appropriate equations including calculated standard deviations for each of the parameters in Fig. 2. The scale factor is the slope of the line and is uncertain by less than 1% in the examples here which is typical of all the data. Maximum statistical uncertainties are somewhat larger than 1% but less than 1.5%. Major sources of systematic uncertainty are the slight shifts in line position for different data sets and residual background effects that are not included here.

These extracted scale factors were then applied to the original data so that each data set had the same intensity for the ν_3AsF_6 line as the averaged data. The results of this scaling are shown in Fig. 1b. It is clear that this scaling procedure has been very successful.

To reduce the effects due to the background PEO and to demonstrate the effectiveness of the scaling, the scaled spectrum of the neat marked PEO at each temperature was subtracted from the PEO:LiTf spectra for that temperature. In the resulting spectra, the region between 685 cm^{-1} and 715 cm^{-1} shows no evidence of the ν_3AsF_6 line; the resulting data are consistent with noise. The resulting $\delta_s(CF_3)$ modes were numerically integrated from 742 cm^{-1} to 772 cm^{-1} to give the total scaled intensity for this mode for all concentrations and temperatures shown in Figs. 3 and 4.

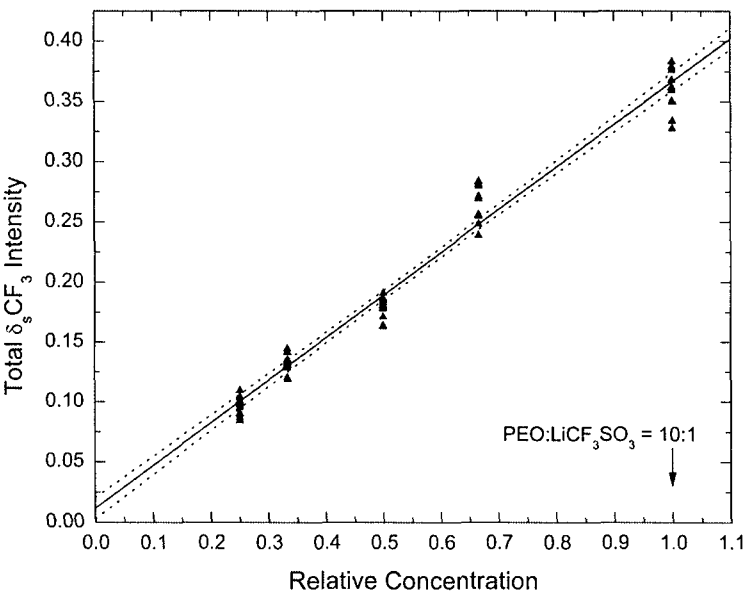

Figure 3.Total integrated δ_sCF_3 absorption intensity versus LiTf concentration relative to PEO:LiTf 10:1 at all temperatures. The solid line is a least squares linear fit to the data, and the dotted lines are 95% confidence levels. The data is consistent with Beer's Law.

3. Results

The total intensities for the $\delta_s(CF_3)$ extracted as described in the previous section are plotted versus the concentration relative to the highest concentration PEO:LiTf studied, 10:1 ether oxygen to Tf, in Fig. 3 along with the linear least-squares fit to the data. Confidence limits at 95% are also shown as dashed lines. The data is consistent with the extended form of Beer's Law; the absorption

intensity is independent of ionic association and proportional to concentration. Differences in the data for the different temperatures seen in Fig. 3 are probably due to the systematic effects discussed in Sec. 2.3.

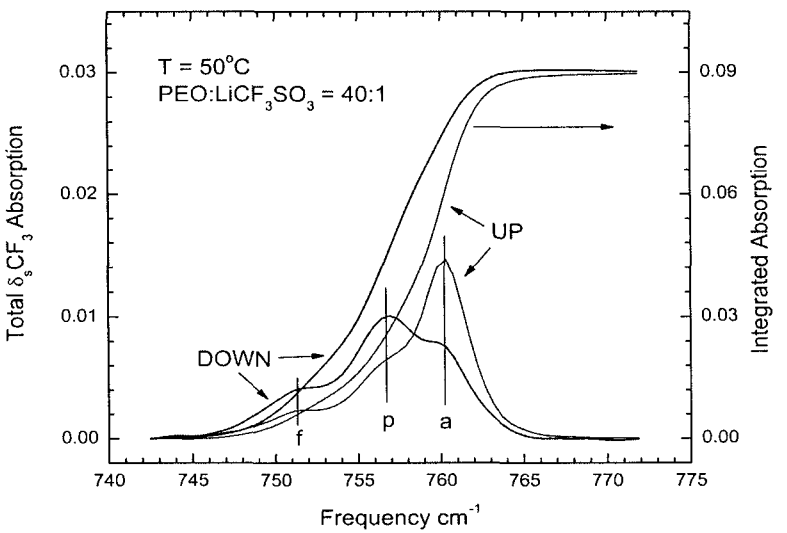

Figure 4. Spectra of $\delta_s CF_3$ absorption and integrated absorption for PEO:LiTf 40:1 at 50°C. The relative concentrations of free (labeled f), contact ion pair (labeled p), and aggregate (labeled a) triflate species are clearly different for the case going up in temperature and the case going down in temperature. The total integrated intensities are essentially identical.

Further evidence for the applicability of Beer's Law for the $\delta_s(CF_3)$ mode independent of ion association is available for specific temperatures near 60°C, the melting point of PEO as there is hysteresis in its melting and recrystallization. In Fig. 4 considerably more aggregate species, the line just above 760 cm^{-1} labeled a, is seen when the temperature is increasing, "up", than when it is decreasing, "down". Consistently, the free, labeled f, and contact-ion pair, labeled p, lines are greater when the temperature is decreasing. Even though the integrated intensity difference between increasing temperature and decreasing temperature is almost 50% near 758.5 cm^{-1}, the total integrated intensity is constant. Similar invariance of integrated intensity with differing ion association is seen for every case where significant hysteresis is seen in the data.

4. Conclusion

The intensity of the $\delta_s(CF_3)$ mode for $CF_3SO_3^-$ is independent of Li^+ association for PEO:$LiCF_3SO_3$ in agreement with an extended version of Beer's Law. As this manuscript goes to press, confirming evidence for this conclusion has been found for LiTf solutions in liquid diglyme[11].

Acknowledgments

We gratefully acknowledge funding from NASA via the power sources section of the NASA Oklahoma EPSCoR grant.

References

1. S. Schantz, J. Sandahl, L. Borjesson, L. M. Torell, J. R. Stevens, *J. Chem. Phys.*, **28-30,** (1988) 1047.
2. R. Frech, W. Huang, *Polymer*, **35,** (1994), 235
3. R. Frech, W. Huang, *Macromolecules*, **28,** (1995), 1246.
4. S. Chintapalli and R. Frech, *Electrochimica Acxta,* **43,** (1998), 1395.
5. C. P. Rhodes, R. Frech, *Macromolecules*, **34,** (2001), 2660.
6. V. Seneviratne, J. E. Furneaux, R. Frech, *Macromolecules*, **35**, (2002), 6392.
7. V. Seneviratne, *Dissertation,* University of Oklahoma 2004.
8. C. M. Burba and R. Frech, *J. Phys. Chem B*, **109,** (2005), 15161.
9. V. Seneviratne, R. Frech, J. E. Furneaux, *Electrochimica Acta*, **48,** (2003), 2221.
10. V. Seneviratne, R. Frech, J. E. Furneaux, M. Khan, *J. Phys. Chem B*, **108,** (2004), 8124.
11. M. Petrowsky, R. Frech, S. N. Suarez, J. R. P. Jayakody, S. Greenbaum, *J. Phys. Chem B*, in press.

STUDY OF ION-POLYMER INTERACTIONS IN CATIONIC AND ANIONIC IONOMERS FROM THE DEPENDENCE OF CONDUCTIVITY ON TEMPERATURE AND PRESSURE.

M. DUCLOT, F. ALLOIN, O. BRYLEV, J-Y. SANCHEZ, J-L. SOUQUET
Laboratoire d'Electrochimie et de Physicochimie des Matériaux et des Interfaces
(UMR CNRS, INPG, Université Joseph Fourier Grenoble, N° 5631),
ENSEEG BP 75 - 38402 Saint Martin d'Hères – France
E-mail: Michel.Duclot@lepmi.inpg.fr

Ionic transport in usual polymer electrolytes involves both cations and anions. In order to separate their respective contributions, cationic (Li^+, Na^+, K^+), or anionic (Cl^-, Br^-, I^-, BF_4^-, $(CF_3SO_2)_2N^-$) single-ion conducting ionomers (t_+ or $t_- = 1$) were synthesized. In both cases, the counter ion is grafted to the macromolecular skeleton in the same synthesis step of cross-linking of the polymer. Experimental results for conductivity variations as a function of pressure (1 - 5000 bar) and temperature (20 - 140° C) show a great similarity for cationic and anionic ionomers. To interpret qualitatively the experimental results, a microscopic model is proposed. Charge carriers formation would result from the dissociation of the grafted salts. Their mobility would proceed by a "free volume" mechanism. This model introduces two local variations in volume, namely the local variation of volume associated with the dissociation process and the critical free volume necessary for the ionic migration. The interpretation of our results according to this model shows that the volume associated to the dissociation process is negative and can be attributed to a local reorganisation of the macromolecular chains around the dissociated charged species. The critical free volume for ionic migration is positive and larger than the "dry" ionic volume, confirming the participation of the polymer chain segments in the ionic transport.

1. Introduction

Salt-polymer complexes are extensively studied for potential applications as electrolytes in lithium batteries. The polymer matrix, generally made of poly(oxyethylene) (POE), acts as a solvent for a lithium salt. The lithium salts can be lithium halogenides, lithium triflate $Li^+CF_3SO_3^-$ or lithium trifluoromethanesulfonylimide $Li^+N(CF_3SO_2)_2^-$, (LiTFSI). In such a polymer electrolyte, both the anion and cation are simultaneously mobile. Transport number measurements show that the anionic conductivity is generally higher than the cationic one [1 - 5].

To separately study anion and cation migrations, we have synthesized purely cationic and anionic ionomers in which the counter ions are grafted and then immobilized on the macromolecular chain. Their conductivities are measured over the glass transition temperature in a pressure range from 1 to 5000 bar and a temperature range from 20 to 140°C.

2. Experimental

Firstly, a pre-polymer is obtained by the polycondensation reaction between α, ω dihydroxyoligopolyoxyethylene (PEG) ($\overline{M_W}$ = 1000) and an unsatured dihalide isobutenyl compound, 3-chloro-2-chloromethyl-1-propene [6]. Linear chains of the pre-polymer are then obtained in which polyoxyethylene segments, each containing about 23 oxygen atoms, alternate with unsaturated isobutenyl group. Afterwards

cross linking of the polymer is performed. The cross-linking may occur directly between unsaturated isobutenyl group (Fig. 1a) but also with the simultaneous grafting of an alkali N,N-diallyl amido-1-tetrafluoroethane sulfonate salt for cationic ionomers (M^+ = Li^+, Na^+, K^+), or of a diallyldimethylammonium salt $R_N{}^+X^-$ (X^- = Cl^-, Br^-, I^-, BF_4^-, $(CF_3SO_2)_2N^-$) for anionic ionomers as represented in Fig. 1b and 1c. The concentration in ionic groups is expressed as the ratio O/M or O/X for cationic or anionic ionomers. Polymer synthesis and grafting processes were detailed in previous papers [7]. The glass transition temperature T_g of the ionomers, determined by DSC, lies between 220 to 240 K with no significant dependence on the nature or the concentration of the grafted salt.

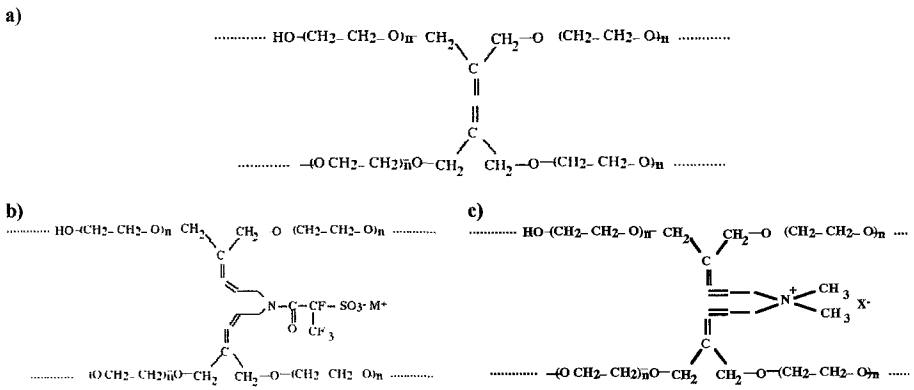

Figure 1. Pre-polymer cross-linking : a) directly between two isobutenyl group ; b) and c) with the grafting of a cationic or an anionic salt.

The conductivity as a function of pressure (1 - 5000 bar) and temperature (20 – 140°C) is determined by impedance spectroscopy in the frequency range 5 Hz-13 MHz. The experimental set up and experimental procedures have been described in previous papers [7 – 9].

3. Experimental results

3.1 Conductivity variations with temperature

At a constant pressure, in the range of 1 – 5000 bars, the conductivity data expressed as the σT product as a function of reciprocal temperature define curves suggesting a VTF behaviour as it is generally the case for amorphous salt-polymer complexes [10] or glass forming melts [11, 12] studied above their glass transition temperature T_g.

The VTF dependence of conductivity with temperature, T, is usually represented by the relationship :

$$\sigma T = A \exp(-\frac{B}{R(T - T_0)}) \qquad (1)$$

where A is the pre-exponential term, R the ideal gas constant and B has the dimensionality of an energy. According to the free volume approach, T_0 is the ideal glass transition temperature, lower than the glass transition temperature T_g determined by DSC.

Determination of the three parameters A, B, T_0 from experimental data is inaccurate when the fitting procedure allows the simultaneous variations of the three parameters. For this reason, a constant T_0 value, T_0 = 195 K, about 35°C below the mean value of T_g, has been chosen allowing the determination of the two parameters, A and B, by the best fit with experimental data with Eqn. 1. Values of A are found between 10 to 10^3 $S.cm^{-1}.K$ and B $\approx$ 0.1 eV as usually observed on salt polymer complexes [13]. No significant differences in these values are observed between cationic and anionic ionomers.

3.2 Conductivity variations with pressure

For all the studied ionomers, the conductivity strongly decreases with pressure. In Fig. 2, conductivity variations for Na^+ and Cl^- ionomers with pressure are represented. The observed linear dependence of logarithmic variation of electrical conductivity versus pressure allows a volume ΔV^* to be calculated by the following relationship :

$$\left(\frac{\partial \ln \sigma}{\partial P}\right)_T = -\frac{\Delta V^*}{RT} \tag{2}$$

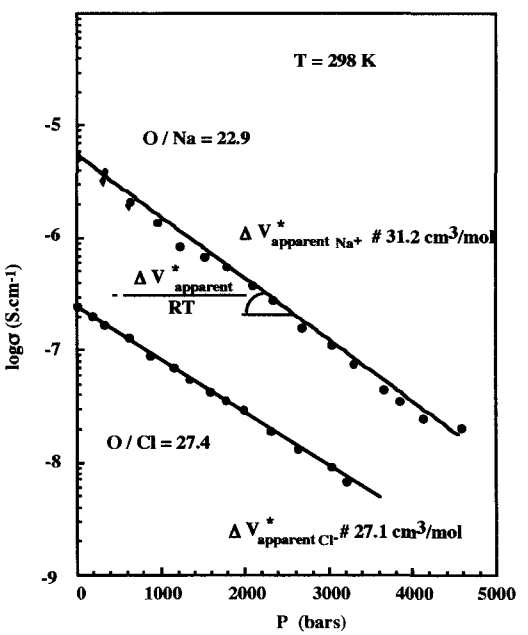

Figure 2. Isothermal conductivity variations with pressure for Na^+ and Cl^- ionomers.

At room temperature, the conductivity decreases by about one order of magnitude when pressure increases from 1 to 4000 bar. Consequently, ΔV^* is positive and is of the order of several tens of $cm^3.mol^{-1}$ as observed for other ionic conductive polymers [14, 15]. Since for the ionomers studied, the conductivity does not follow an Arrhenius type law at constant pressure, we cannot qualify ΔV^* as an activation volume and we will identify it as an "apparent activation volume" ΔV^*_{app}.

The calculated variations of ΔV^*_{app} with temperature are shown in Fig.3a and 3b for different cationic or anionic ionomers. A continuous and important decrease in ΔV^*_{app} with temperature is observed. This behaviour is similar to the variation of the apparent activation volume with temperature observed in glass forming molten salt mixtures [16].

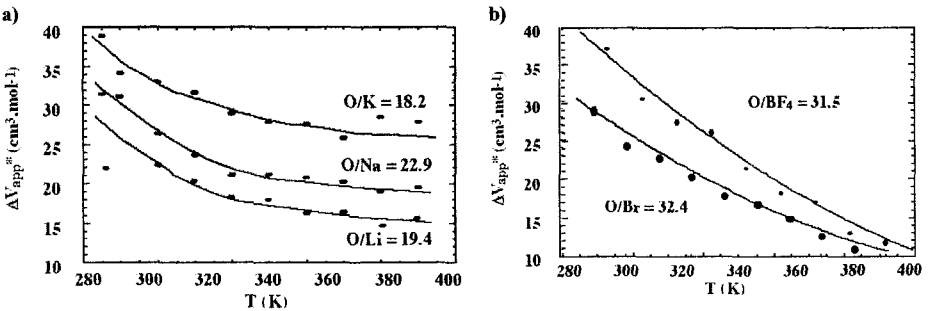

Figure 3. Variations with temperature of the "apparent activation volume" ΔV^*_{app} for some a) cationic ionomers, b) anionic ionomers.

4. A model for ionic transport in salt-polymer complexes

The physical meaning of A and B parameters in Eqn. 1 can be deduced from a microscopic interpretation of ionic transport in polymers above T_g proposed in an earlier work [13]. Due to their low dielectric constant, salt polymer complexes are considered as weak electrolytes in which charge carriers are generated by partial dissociation from the polymer matrix. The mobility of these charge carriers would proceed by a free volume mechanism as it is observed for many ionic melts. The resulting conductivity σ is expressed by the following expression

$$\sigma = Fn_i\mu_i \tag{3}$$

where F is the Faraday constant, n_i is ionic charge carriers concentration and μ_i is their mobility. In the polymer matrix, a charge carrier can be presented as an anion or a cation leaving its normal site near its grafted counter ion to occupy a position in a neighbouring site, forming a charged defect comparable to an interstitial pair for ionic crystals. This charged defect could then migrate by an ionic transfer from one grafted counter ion to another. Charge carriers concentration is a function of the free energy, $\Delta G_i = \Delta H_i + T\Delta S_i$ required for the charged defect formation and the salt concentration n in the ionomer :

$$n_i = n\exp(-\frac{\Delta G_i}{2RT}) \tag{4}$$

The free volume model [17, 18] and Brownian movement equations, lead to the following expression for the mobility:

$$\mu_i = \frac{Fd^2\nu_0}{6RT}\exp(-\frac{V_f^*}{\overline{V}_f}) \quad (5)$$

where ν_0 is the attempt frequency and d the jump distance of a charge carrier. The exponential term expresses the probability for the charge carrier to have access to the critical free volume V_f^* required for an elementary displacement. $\overline{V}_f$ is the mean value of the available free volume in the ionomer. An increase in pressure will decrease this available free volume $\overline{V}_f$ and, according to Eq. 5, will reduce the ionic mobility μ_i and consequently the ionic conductivity.

As suggested earlier [19], the dependence of $\overline{V}_f$ on pressure can be deduced from the simple assumption that the $\overline{V}_f$ dependence on temperature and pressure follows a state equation similar to ideal gas. This state equation, where the usual RT factor is replaced by $R(T-T_0)$, can be justified by the fact that the free volume disappears below the ideal glass transition temperature T_0, then :

$$P\overline{V}_f = R(T-T_0) \text{ or } \overline{V}_f = \frac{R(T-T_0)}{P} \quad (6)$$

Associating (3), (4), (5) and (6), the following equation for the σT product is obtained :

$$\sigma T = \frac{F^2nd^2}{6R}\nu_0\exp(-\frac{\Delta G_i}{2RT})\exp(-\frac{V_f^*P}{R(T-T_0)}) \quad (7)$$

Expression (7) can be reduced to a VTF equation if $\exp(-\frac{\Delta H_i}{2RT})$ does not vary significantly in the investigated temperature range (300 < T < 400 K) compared to the $\exp(-\frac{V_f^*P}{R(T-T_0)})$ term. By identification with Eq. 1,

$$A = \frac{F^2nd^2}{6R}\nu_0\exp(\frac{\Delta S_i}{2R}) \quad (8)$$

The pre-exponential factor $\frac{F^2nd^2}{6R}\nu_0$ can be estimated from reasonable values of n and ν_0. For the attempt frequency ν_0, the usual value 10^{13} Hz for an ionic oscillator, can be chosen. The O/X composition scale for salt-polymer complexes does not allow to estimate the concentration n of salt molecules by unit volume. In order to propose an order of magnitude, the density of a Cl^- conductive membrane for O/Cl = 8.1 has been measured. The obtained experimental value, 1.52 g.cm^{-3}, leeds to a n value equal to 10^{21} cm^{-3} and a mean distance d of 10 Å between two grafted counter cation sites ($d \approx 1/n^{1/3}$). These assumptions allow to estimate the value of $\log_{10}\frac{F^2nd^2}{6R}\nu_0$ which is close to 4.5. Such a value corresponds to those observed for solid electrolytes in which the charge carriers migrate in a rigid matrix. Experimental values of $\log_{10}A$ are lower than the calculated ones and this difference

can be attributed to the $(\frac{\Delta S_i}{2R})$ term. From this difference one can evaluate ΔS_i negative values varying from -40 to -120 $J.K^{-1}.mol^{-1}$, which is of the order of magnitude for an ionic dissociation with a strong interaction of ions with the solvent [13, 20]. Differentiation of Eqn. 7 allows to express $\left(\frac{\partial \ln\sigma}{\partial P}\right)_T$ as a function of V_f^* and the activation volume ΔV_i related to the charge carrier formation by ionization. It is defined by $\Delta V_i = \left(\frac{\partial \Delta G_i}{\partial P}\right)_T$.

$$\left(\frac{\partial \ln\sigma}{\partial P}\right)_T = -\frac{V_f^*}{R(T-T_0)} - \frac{\Delta V_i}{2RT} \tag{9}$$

By identification with Eqn. 2 we obtain

$$-\frac{\Delta V_{app}^*}{RT} = -\frac{V_f^*}{R(T-T_0)} - \frac{\Delta V_i}{2RT} \tag{10}$$

that means

$$\Delta V_{app}^* = \frac{\Delta V_i}{2} + V_f^* \frac{T}{T-T_0} \tag{11}$$

5. Comparison with experimental results and conclusion

For a more quantitative verification of Eqn. 11 one may notice that ΔV^*_{app} dependence versus $T / (T\text{-}T_0)$ is expected to be linear. This linear dependence of ΔV^*_{app} versus $T / (T\text{-}T_0)$ is shown in Fig. 4a and 4b for different cationic or anionic conducting ionomers. The slopes can be identified as V_f^* and ΔV_i can be deduced from the extrapolation to $T / (T\text{-}T_0) \rightarrow 0$. At this point, it should be emphasized that calculated V_f^* and ΔV_i values greatly depend on the chosen value for the ideal glass transition temperature. These calculated volumes tend to increase with a lower value of the parameter T_0.

For T_0 = 195 K, corresponding values for ΔV_i and V_f^* for different charge carriers are reported in Table 1. The same table includes the anionic molar volumes calculated from the Pauling ionic radius for halogens anions and alkali cations or molecular modelling [21] for $TFSI^-$ and BF_4^- anions.

Table 1 : Local variations of activation volume ΔV_i associated with the dissociation process and critical free volume V_f^* for ionic migration. V_{ion} is the volume of the "dry" cation or anion.

	O/Li = 31.2	O/Na = 22.9	O/K = 18.2
ΔV_i cm³/mol	- 6	- 12	- 1
V_f^* cm³/mol	8.1	10	12.9
V_{ion} cm³/mol	0.8	2.3	5.9

	O/Cl = 27.4	O/Br = 32.4	O/I = 33.2	O/BF_4 = 31.5	O/TFSI = 31.4
ΔV_i cm³/mol	- 57	- 71	- 30	- 119	- 44
V_f^*cm³/mol	19	23	14	35	17
V_{ion} cm³/mol	14.9	18.9	26.7	30.7	49.4

For all ionomers, ΔV_i has a negative value, which can be explained by a local volume contraction associated with the solvation of the charged species after dissociation (interstitial pairs and grafted counter ion). This solvation may increase the local order explaining the negative and high values for the dissociation entropy ΔS_i. For all ionomers studied, except TFSI⁻ and I⁻, V_f^* is higher than the proper volume of the isolated ion. This difference can be qualitatively interpreted by assuming that the moving species is not only the charged carriers but also their global solvation shells formed by the interaction with the oxygen ligands of the polyether chains. This difference which is higher for cationic ionomers can signify a stronger interaction of the cation with the macromolecular chain compared with the anion.

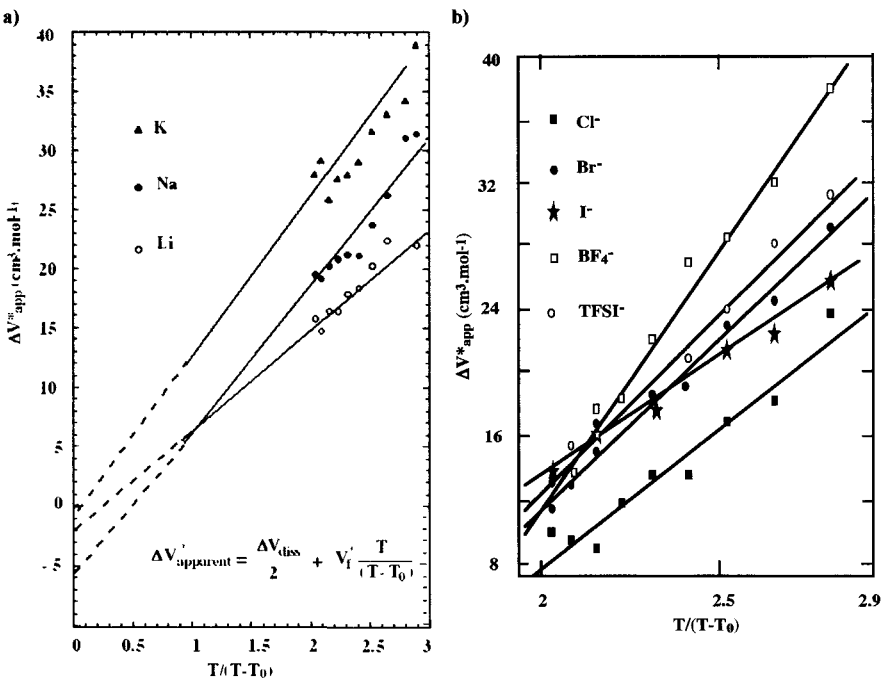

Figure 4 : Dependence of the "apparent activation volume" ΔV^*_{app} as a function of $T/(T-T_0)$ to determine the dissociation activation volume ΔV_i and the critical free volume V_f^* for a) cationic ionomers. and for b) anionic ionomers. (T_0 = 195 K)

These lower interactions between the anions and the macromolecular chains make the anionic migration easier and would explain its higher transference number compared to the associate cation when a lithium salt is dissolved in a polymer solvent without grafting [2, 3, 19, 20]. For the anions I⁻ and TFSI⁻, the activation volume is found lower than the anionic volume, this particularity probably resulting from the deformability of these two anions.

References

[1] J.S. Tonge and D.F. Shriver, *in "Polymers for Electronic Applications" Ed. J.H.Lai, CRC Press* (1989).
[2] J. Evans, C.A.Vincent and P.G. Bruce, *Polymer,* **28**, 2324 (1987).
[3] W. Gorecki, M. Jeannin, E. Belorizky, C. Roux and M. Armand, *J. Phys. Condens. Matter.* **7,** 6823 (1995).
[4] J. Xu and G.C. Farrington, *J. Electrochem. Soc.* **143 (12),** L44, (1996).
[5] F. Alloin, D. Benrabah and J-Y Sanchez, *Journal of Power Sources*, **68**, 372 (1997).
[6] F. Alloin, J-Y. Sanchez and M. Armand, *J. Electrochem. Soc.* **141**, 1915 (1994).
[7] M. Duclot, F. Alloin, O. Brylev, J.Y. Sanchez and J.L. Souquet, *Solid State Ionics*, **136-137**, 1153 (2000).
[8] M. Duclot, F. Alloin, O. Brylev, J.Y. Sanchez and J.L. Souquet, *Electrochimica Acta,* **50,** 5015 (2005).
[9] Y. Grincourt, M. Henault, M. Duclot and J-L. Souquet, *Phys. Chem. Glasses*, **37**, 236 (1996).
[10] S. Seki, A.B.M. Susan, T. Kareko, H. Tokuda, A. Noda and M. Watanabe, *J. Phys. Chem. B* **109**, 3886 (2005).
[11] C.A. Angell, *J. Phys. Chem* **68 (1),** 218 (1964).
[12] R.E. Tickle, *Phys. and Chem. Glasses*, **8 (3),** 101 (1967).
[13] JL. Souquet, M. Duclot and M. Levy, *Solid State Ionics*, **85**, 149 (1996).
[14] C. Bridges, A.V. Chadwick, *Solid State Ionics*, **28-30**, 965 (1988).
[15] J.J. Fontanella, M.C. Wintersgill, J.S. Wainright, R.F. Savinell and M. Litt, *Electrochim. Acta* **43**, 1289 (1998).
[16] C.A. Angell, L.J. Pollard and W. Strauss, *J. Chem. Phys.*, **50**, 2694 (1969).
[17] M.H. Cohen and D. Turnbull, *Journal of Chemical Physics*, **31 (5)**, 1164 (1959).
[18] R. Zallen *in "The Physics of Amorphous Solids", John Wiley & Sons* (1983).
[19] JL. Souquet, F. Alloin, O. Brylev, M. Duclot, and JY. Sanchez, *Ionics,* **4,** 1 (1998).
[20] W.E. Dasent, *in "Inorganic energetics, An introduction." Cambridge University Press* 2^{nd} *ed.* (1982).
[21] Makoto Ue, *J. Electrochem. Soc.* **141 (12)**, 3336 (1994).

TRIOL BASED POLYURETHANE GEL ELECTROLYTES FOR ELECTROCHEMICAL DEVICES

A. R. KULKARNI
Metallurgical Engineering and Materials Science
Indian Institute of Technology-Bombay Powai Mumbai 400076, INDIA

Polyurethane gel electrolytes with various solvents such as propylene carbonate (PC), propylene carbonate – ethylene carbonate (PC-EC) and γ-butyrolactone – ethylene carbonate (GBL-EC) were synthesized and studied by different characterization tools. Impedance spectroscopy and nuclear magnetic resonance spectroscopy (NMR) provides the insight on ionic mobility in the gel electrolyte. The syneresis effect was studied by observing the weight loss as a function of time. Morphology of the gel electrolyte was investigated by ESEM. Among the various compositions, the maximum conductivity was observed for 35%PU-60%EC/GBL-5%$LiClO_4$. The maximum conductivity of gel electrolytes was found to be 3.98 x 10^{-3} S/cm at the room temperature, which is higher than that reported in the domain of published literature for the thermoplastic polyurethane family. Moreover, merely 3.5% weight loss was observed for the period of 30 days. The 3.5% wt solvent loss has negligible effect on the conductivity of the gel electrolyte. Test cell was fabricated using polyurethane gel electrolyte and discharge characteristic was studied.

1. Introduction

Polymer gel electrolytes are receiving considerable attention in electrochemical applications such as rechargeable lithium batteries and electrochromic displays, owing to their high ionic conductivity[1]. These electrolytes are obtained by incorporating a large quantity of liquid plasticizer and/or solvents in a polymer matrix as a host that is capable of forming a stable gel[2-4]. Polymeric materials with a polar group, such as poly(ethylene oxide), poly(acrylonitrile), poly(methyl methacrylate), poly(vinyl chloride) and poly(vinylidene fluoride), have been widely used as host polymers in gel electrolytes[5].

In recent years, significant interest has been shown on gels with thermoplastic and cross-linked polyurethane as hosts because their structures and properties can be varied over a wide range[6-8]. The variety in the reactants, namely polyols and diisocyantes, provides the degree of freedom in designing the polyurethane. In polyurethane matrix, diisocyante acts as a hard segment, which accounts for the good mechanical properties of the material, while the soft segment, polyol, assists in the transportation of lithium ions[9]. Moreover, by fixing the reactants, the properties can be further fine tuned by changing its composition[10,11]. However, the thermoplastic polyurethane gel electrolytes show poor mechanical properties at

higher temperature[12]. Cross-linked polyurethane could solve the problem of mechanical stability, gels with controlled thickness are difficult to obtain[12].

In order to achieve controlled thickness and good mechanical properties at higher temperatures, triol based partly crosslinked polyurethane (PU) gel electrolyte with single and mixed solvents say ethylene carbonate – propylene carbonate (EC-PC) and ethylene carbonate - γ-butyrolactone (EC-GBL) are reported in this work. The conductivity of this gel electrolyte is higher than that of any other thermoplastic polyurethane reported till date[13-15]. The effect of concentration of liquid electrolyte on glass transition temperature (T_g), conductivity, ionic mobility, structure and morphology of the electrolytes are discussed in detail. Fabrication and performance of test cells with gel electrolytes are discussed.

2. Experimental

Polyurethane matrices with different compositions were synthesised from MDI (Huntsman, India) with an average molecular weight of 4500 and polyoxyethylene triol (Huntsman, India) with an average molecular weight of 5500. MDI and polyoxyethylene triol was vacuum dried at 75 °C for 24h, prior to the synthesis of polyurethane gel electrolyte. The liquid electrolyte was prepared from propylene carbonate (PC) (Spectrochem, India) and $LiClO_4$ (Aldrich). The molar ratio of carbonyl group in PC to the cation in $LiClO_4$ was fixed at 1:12. At this molar ratio, maximum conductivity of the liquid electrolyte could be achieved and hence was chosen for our study[16]. The same composition holds true for the mixed solvents, which has equimolar ratio between them.

Polyurethane gel electrolyte was synthesized by adding polyoxyethylene triol followed by MDI to the liquid electrolyte at room temperature. The solution was mixed thoroughly and kept at room temperature for 24h to complete the polymerization leading to the gel formation. The gel electrolytes thus obtained were kept in an oven at 50^0C for 12h to remove the excess solvent. Polyurethane gel electrolytes with different compositions were synthesized. The maximum uptake of PC in a self-standing polyurethane gel electrolyte was found to be ~60-wt%. Among the various compositions of polyurethane gel electrolytes, the polyurethane matrix with 1:4 volume ratio of polyoxyethylene triol and MDI only shows the desired properties such as homogeneity and are self-standing. Hence further studies such as thermal analysis, electrical conductivity measurements were carried out on polyurethane of this composition as a host and varying PC content. For mixed solvents, only polyurethane with higher intake of liquid electrolytes was chosen. The compositions of these electrolytes are given in table 1.

Table 1: Composition of PU based polymer gel electrolytes

Code	Polymer (PU)	Solvent (PC)	Salt ($LiClO_4$)
PU1	64.13	33.00	2.87
PU2	61.96	35.00	3.04
PU4	56.52	40.00	3.48
PU6	51.09	45.00	3.91
PU8	45.66	50.00	4.34
PU10	40.22	55.00	4.78
PU12	34.78	60.00	5.22
PU-PC-EC	34.78	60.00	5.22
PU-EC-GBL	34.78	60.00	5.22

Thermal analysis of the polymer gel electrolytes was carried out with NETZSCH 200PC Differential Scanning Calorimeter (DSC). The samples sealed in aluminum pans were scanned from -125 to 150^{O} C at the heating rate of 10^{O}C min^{-1}. Above 150^{O} C, the gel electrolytes undergo continuous loss of solvent accompanying a baseline drift in the DSC curve.

Frequency dependent conductivities of these gel electrolytes were measured with an Alpha high resolution analyzer coupled to a Novocool temperature control [Novocontrol Gmbh, Germany] system in the frequency range of 10^{-1} Hz to 10^{-7} Hz and the temperature range of -80 to +50^{O}C in steps of 10^{O}C. Gels of uniform thickness were placed between two gold electrodes to ensure the good contact between the gels and electrodes.

Dynamic mechanical analysis was carried out on rectangular samples having dimensions (~ 15x2x1 mm) using Tritec 2000 DMA (Triton Technology, UK) under tension mode using a dynamic frequency of 1 Hz from -100^{O}C to room temperature at a heating rate of 4.0 ^{O}C /min.

Experiments of small angle X-ray scattering on polymer gel electrolytes were performed in pinhole geometry, using SAXS camera (Anton Paar GmbH). The Cu Kα line was used as incident radiation from PANalytical X-ray source at 40 kV (40mA). Image plate reader, (Packard Bioscience, Inc) was used to record the scattering rays. The scattering intensities were presented as a function of the magnitude of the scattering vector $q = (4\pi/\lambda)$ Sin θ, where λ is the wavelength of the radiation and 2θ is the scattering angle.

The Li NMR spectra and the diffusion coefficients were measured by a Bruker Advance 400WB spectrometer. The diffusion coefficients of the cations were measured by the Pulse Field Gradient-Spin-Echo (PFG-SE) method for the Li NMR signal of the sample. The surface morphology of the polymer gel electrolyte was examined by using Philips environmental scanning electron microscope (ESEM) model XL-30. The transmittance of polymer gel electrolytes was measured with

SHIMADZU UV 160A UV-Visible spectrophotometer in the wavelength range of 200 to 1100 nm.

The discharge characteristics of the cells were studied using 6514 Keithley electrometer. The electrolyte was sandwiched between the lithium sheet anode and graphite cathode. The cathode and anode were pressed to improve the contact and compactness of the cell.

3. *Results and Discussion*

3.1 *DSC Studies*

Figure 1 shows the DSC spectra of PU gel electrolytes with different amount of liquid electrolytes. DSC spectra for all the compositions are featureless upto 150^{o}C except for the T_g. Absence of any crystalline or melting peak in the temperature range −125 to +150^{o}C indicates that the gels are highly amorphous in nature. The

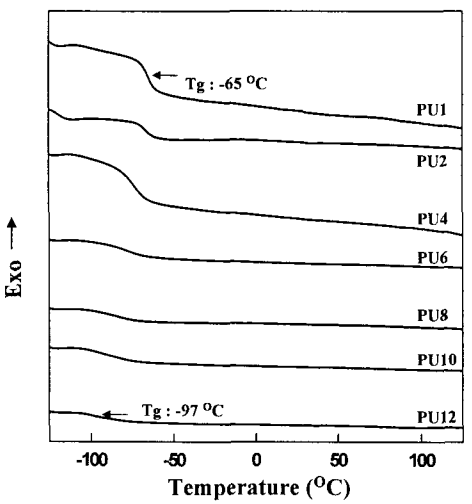

Figure 1: DSC curve of PU based polymer gel electrolytes

T_g value of the polyurethane gel electrolytes decreases with increase in PC content as shown in table 2. Among these compositions, the gel with 60-wt% PC (PU12) showed the lowest T_g – 97 ^{o}C which is closer to that of the corresponding liquid electrolyte i.e., -104^{o}C. The T_g of PU12 is atleast 30 ^{o}C lower than the value reported by Yoshimoto et al.[13] for a thermoplastic PU gel. The glass transition of mixed solvents almost falls near to the gel electrolyte with PC solvent.

3.2 *Ionic Conductivity*

Ionic conductivity of the PU based polymer gel electrolytes was obtained from AC impedance analysis. Figure 2 shows a typical Cole-Cole plot for PU12 gel electrolyte. The inset represents the corresponding equivalent circuit. The components in the equivalent circuit, C1 is attributed to the double-layer capacitance at the lectrode/electrolyte interface, R1 and C2 are attributed to the bulk electrolyte resistance and capacitance, respectively. The equivalent circuit was

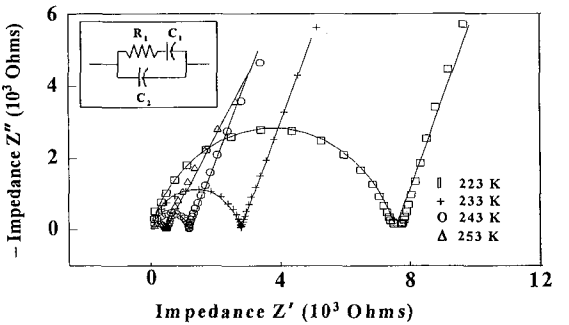

Figure 2: Cole-Cole plot for PU12

found to be applicable to all gel electrolytes and at all temperatures. The DC conductivity of the polymer gel electrolyte is calculated from the bulk resistance R1. Table 2 shows the DC conductivity of the single and mixed solvents based polymer gel electrolytes at room temperature. The maximum conductivity of 3.98x 10^{-3} S/cm was achieved for the composition of PU-EC-GBL at room temperature, which is an order higher than the value reported by Yoshimoto et al., Tian et al. and Wen et al.[13-15].

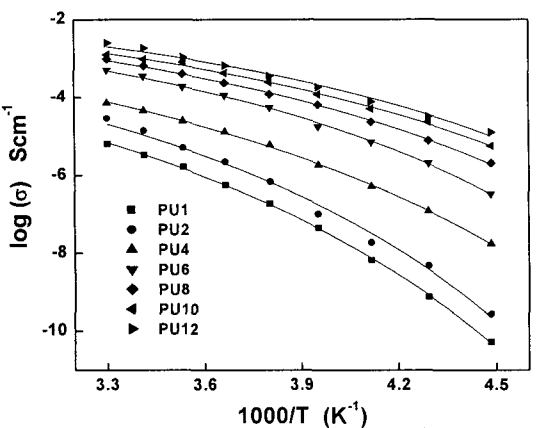

Figure 3: Arrhenius plot of polymer gel electrolytes. Solid lines are VTF fit to the data

Figure 3 shows the variation of the DC conductivity with inverse temperature for different composition of gel electrolytes with single solvent. The variation fits well with VTF relationship[17]. The relationship is given as $\sigma = AT^{-1/2} \exp(-B/T-T_o)$

Here A is a constant which is independent of temperature, B is the pseudo activation energy which is related to polymer segmental motion, T_o is the ideal glass temperature may also be compared with the T_g obtained from DSC. The results of the regression and the DSC data of the gel electrolytes are tabulated in table 2. The VTF equation was found to provide a good fit and describes the transport properties in a viscous matrix[18].

Table 2: VTF fit data and Tg from DSC for PU based gel electrolytes

Code	σ_{DC} at RT (S/cm)	Ea (kJ/mol)	T_o(K)	T_g (K)
PU1	6.578×10^{-6}	5.37	160	208
PU2	2.919×10^{-5}	4.622	155	205
PU4	7.891×10^{-5}	4.206	151	199
PU6	5.134×10^{-4}	3.017	147	193
PU8	9.813×10^{-4}	2.785	139	185
PU10	1.560×10^{-3}	2.726	134	181
PU12	2.530×10^{-3}	2.319	128	176
PU-PC-EC	2.990×10^{-3}	4.040	154	179
PU-EC-GBL	9.260×10^{-3}	7.570	134	177

Figure 4 shows the variation of conductivity and activation energy with PC content in the gel electrolyte. The conductivity of the gel electrolyte increases with increase in PC content. The inflation rate of conductivity decreases gradually and

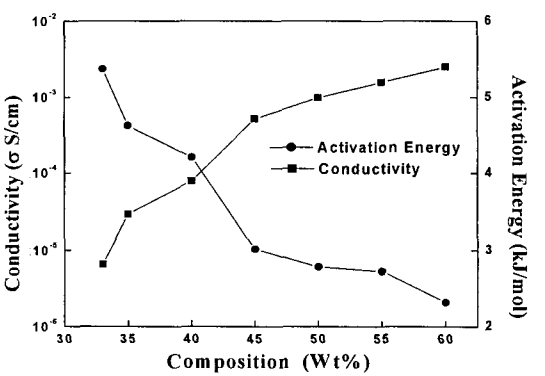

Figure 4: Variation of DC conductivity and Activation Energy with increase in PC composition of the gel electrolytes. Solid lines are guidelines to Eye

attains maximum value. The variation of conductivity with composition shows two distinct paths. The presence of two paths gives the insight of change in structure of gel electrolyte. The insight is well supported by the dynamic mechanical analysis of the polymer gel electrolyte.

3.3 *DMA Studies*

Figure 5 shows the variation of tan(δ) with temperature. It may be noted that the tan(δ) peak broadens at higher concentration of PC and narrows at lower concentration. When these values are plotted in master plot shown in figure 6, the structural change is observed in the polyurethane gel electrolyte upon addition of PC content, when PC content varied from PU4 to PU6. The structural change after certain concentration can be assumed from the conductivity is that the PC may be continuous in the gel electrolyte which provides easy channel for the lithium ion to migrate

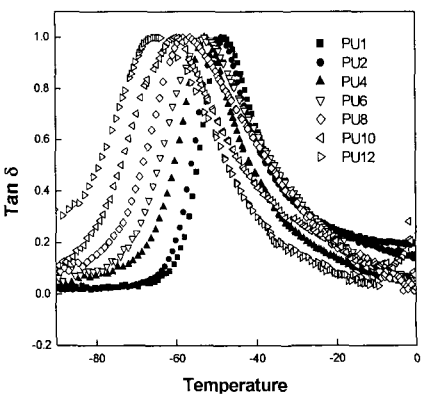

Figure5: Variation of mechanical tan(δ) with temperature measured at 1Hz

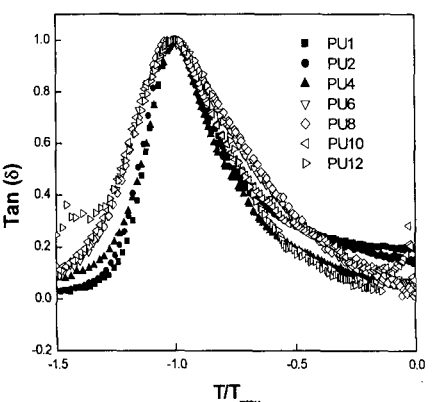

Figure 6: Master plot of mechanical loss tan(δ)

3.4 *NMR Information*

In general, the line width of a NMR spectrum is a measurement of ion mobility in the system. The faster the ion migrates the narrower the line width of the spectrum. Figure 7 shows the ^{7}Li spectra at 303K for the gel electrolytes PU (a), PU-PC (b) and EC-EBL (c). All the samples show three components; a broad one having ~3000Hz, and a narrow peak having two overlapping components at its up-field side.

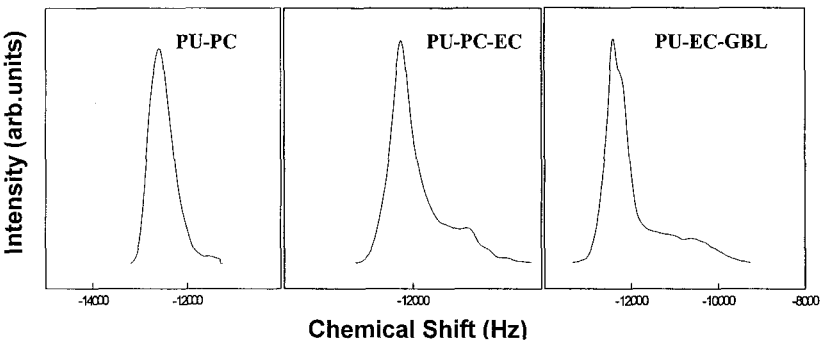

Figure 7: Li NMR spectra for PU based gel electrolytes

The broad one grows much more for the mixed solvents. In these systems, there are three kinds of Li+ ions which correspond to each of the components in the NMR spectrum. The narrow peak is caused by the fast ion transport. The broad peak corresponds to the slow mobile ions. The NMR spectrum of the gel samples has the same profile of liquid electrolyte but with a chemical shift of 5ppm. This behavior shows that all the peak of the gel electrolytes are corresponding to the lithium ion in the solvent phase and not from the polymer matrix. PGSE-NMR method was used to determine the self diffusion coefficient of lithium ion. The conductivity was calculated from diffusion coefficient using Nernst-Einstein relation. The calculated conductivity is in excellent agreement with the conductivity of the gel electrolyte obtained from complex impedance spectroscopy which is shown in table 3. The comparable conductivities show that the movement of most of lithium ion in the gel is not influenced by the polymer matrix.

Table 3: Observed and calculated conductivity of PU based gel

Temperature (K)	PU-PC ($x10^{-3}$ S/cm)		PU-PC-EC ($x10^{-3}$ S/cm)		PU-EC-GBL ($x10^{-3}$ S/cm)	
	Obs.	Cal.	Obs.	Cal.	Obs.	Cal.
303	2.53	2.71	2.94	2.56	3.98	4.21
313	3.81	4.19	3.71	3.20	5.72	6.28
323	4.72	4.98	4.95	4.23	8.31	11.5

3.5 *Morphology Studies*

The cross sectional view of polyurethane based gel electrolytes is shown in figure 8. The fracture was done by freeze fracture technique

i.e., quenching the gel into liquid nitrogen. Figure 8a shows wrinkled cloth like morphology. In order to find whether the wrinkleness is because of vaccum in ESEM (1 Torr) or inherent morphology, the sample is dipped in liquid nitrogen and immediately the morphology is recorded. Figure 8b confirms the wrinkleness is because of vacumm produced by ESEM. The micrograph also confirms that there is no phase separation between the polymer and the solvent, that may lead to pore formation, makes the solvent difficult to exude from the gel.

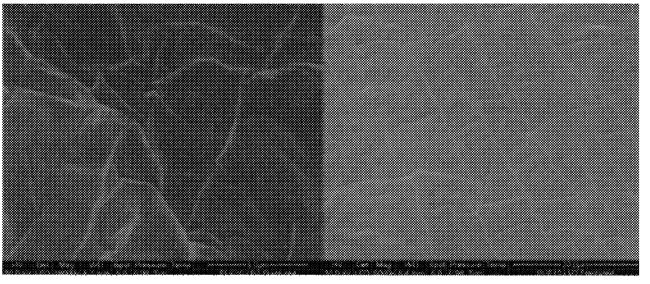

Figure 8: ESEM Micrograph of PU-PC based gel electrolytes

3.6 *Syneresis Effect*

Gel polymer electrolytes may undergo solvent exudation upon long storage. This phenomenon, known as the syneresis effect, has been encountered in many gel

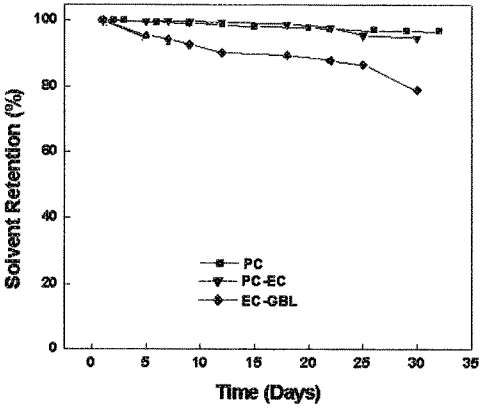

Figure 9: Syneresis studies of PU based gel electrolytes

polymer electrolyte systems[19-20]. In order to investigate the solvent exudation upon long storage in PU gel, the weight loss and conductivity was measured as a function of storage time in open atmosphere. Figure 9 illustrates the decrease in weight with the function of time for all the composition of PU gel. The maximum weight loss was seen merely 3.5% of PC. The absence of pores in the PU based gels suggest a strong interaction between the PU and PC makes the organic solvent difficult to exude from the polymer matrix. Figure 10 depicts the behavior of the conductivity with the function of time for PU12. The ionic conductivity remains nearly constant, which means there is very less effect on conductivity for a 3.5% weight loss. The addition of EC to the PU-PC gel electrolyte makes much stronger interaction while the addition of GBL leads to heavy loss of solvent because of its vapor pressure.

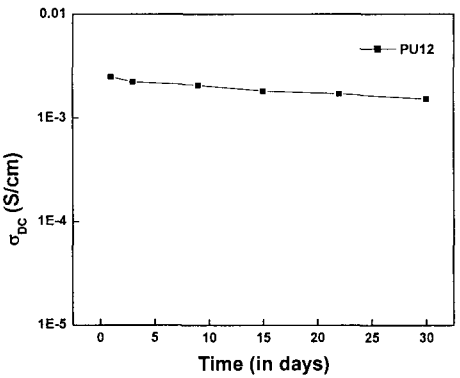

Figure 10: Variation of DC conductivity with the function of time on PU12

3.7 *Transmittance Studies*

The transmittance of polymer gel electrolytes for all the composition shows more than 90% over the visible range. Figure 11 shows the UV-VISIBLE spectra for PU12 of 2mm thickness. Apart from high transmittance, the gel sticks well with the glass and metal surface. Because of these excellent properties it can also be used in electrochromic devices.

3.8 *Discharge Characteristics*

The discharge characteristic of electrochemical cell based on PU-PC is shown in figure 12. The discharge of the cells was studied at room temperature at different

current drains (0.02, 0.075 and 0.2 mA/cm^2). It has been observed that at 0.02 mA/cm^2 current drain, the voltage was constant for more than 3 hrs. The capacity and power density of the batteries will be calculated according to this drain current.

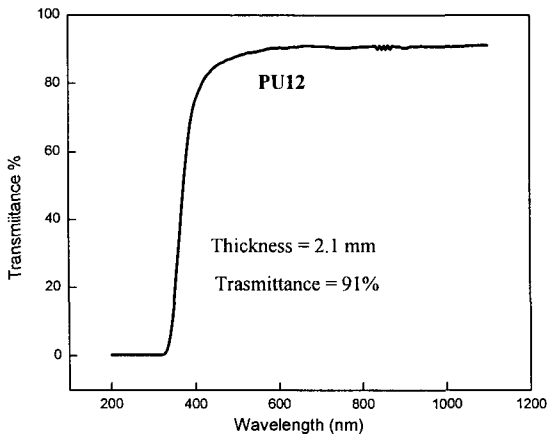

Figure 11. UV-VIS pattern of polyurethane based gel electrolytes

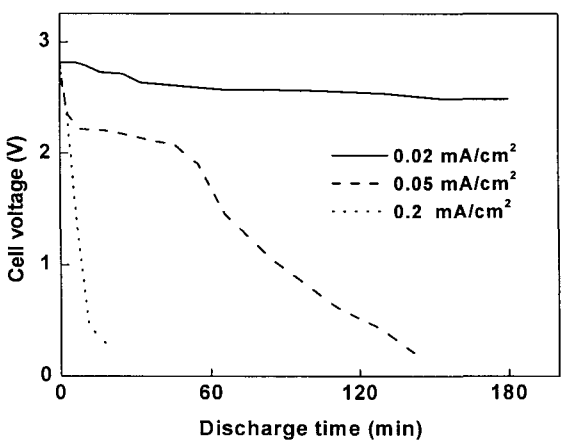

Figure 12: Discharge study of the cell with PU-PC gel electrolyte.

4. *Conclusions*

The ionic conductivity of PU based gel electrolyte is much higher (3.98x10^{-3} S/cm) than the reported for thermoplastic PU gels at room temperature. The characteristic

of mixed solvents based gel electrolytes has similar effect of PC based gel electrolyte except the syneresis effect. Syneresis study shows there is a strong interaction between the PU and PC and it makes the organic solvent difficult to exude from the polymer matrix. Because of transparent nature and high ionic conductivity, PU gel electrolyte also has potential applicability in electrochromic devices.

References

1. B. Scrosati, *Electrochemical Applications of Electroactive Polymer*, Chapman and Hall, London
2. K. Kajiwara, Y. Osado, *Gel Handbooks* Academic press 1997
3. K. te Nijenhuis, *Thermoreversible Networks*, Springer, New York
4. L. H. Sperling, *Introduction to Physical Polymer Science*, Wiely, New York
5. Y. J. Song, Y. Y. Wan, C. C. Wan, J. Power Sources **77**, 183 (1999).
6. Y-L. Du, T-C. Wen, Materials Chemistry and Physics **71**, 62 (2001).
7. J. V. Van Bogart, P. E. Gibson, S. L. Cooper, J. Polymer Science., Polymer Physics **21**, 65 (1983).
8. C. Hepburn, *Polyurethane Elastomers*, Elsvier Applied Science, London
9. G. Oertel, *Polyurethane Handbook,* Hanser Publication, New York
10. S. L. Cooper, A. V. Tobolosky, J. Appl. Polymer Sci. **10**, (1966).
11. X. Wang, B. Fang, L. Wang, X. Tang, F-C. Chang, *J. Appl. Polym. Sci.* **82**, 541 (2001).
12. H. Xiaobin, R. Tianbin, Z. Xian, T.Xiaozhen, Polymer International **54**, 1294 (2003).
13. L-Y Tian, W-H. Zhu, X. Tang, *J. Appl. Polym. Sci.* **90**, 2310 (2003).
14. N. Yoshimoto, H. Nomura, T. Shirai, M. Ishikawa, M. Morita, *Electrochimica Acta* **50**, 275 (2004).
15. T-C. Wen, Y-L. Du, M. Digar, Europen Polymer Journal **38**, 1039 (2002).
16. X. Xuan, J. Wang, J. Tang, G. Qu, J. Lu, Spectrochimica Acta **56**, 2131 (2000).
17. A. D'Aprano, M. Salomon, M. Iammarino, J. Electroanalytical Chemistry 403, 245 (1996).
18. J. L. Souquet, M. Levy, M. Duclot, *Solid State Ionics* 70-71, 337 (1994).
19. J. L. Souquet, M. Duclot, M. Levy, *Solid State Ionics* 83, 149 (1996).
20. F. Croce, F. Gerace, G. Dautzenberg, S. Passerini, G. B. Appetecchi, B. Scrosati, *Electrochim. Acta* 39, 2187 (1994).

Contributed Papers

This page is intentionally left blank

Accurate Conductivity Measurements to Solvation Energies in Nafion®

M. Maréchal*, J.-L. Souquet

École Nationale Supérieure d'Électrochimie et d'Électrométallurgie de Grenoble, Laboratoire d'Électrochimie et de Physico-chimie des Matériaux et des Interfaces, UMR 5631 CNRS-INPG-UJF, Domaine Universitaire, BP 75, 38402 Saint Martin d'Hères, France.

*Corresponding author e-mail: manuel.marechal@inpg.fr

The wide scattering of experimental data shows unambiguously that Nafion®117 conductivity is very sensitive to climatic conditions, temperature and relative humidity. Conductivity measurements have been carried out by impedance spectroscopy between 10°C to 95°C in a broad domain of relative humidity i.e. 10 to 98%RH. These accurate data enable a power relationship to be proposed at constant temperature between conductivity and relative humidity. This suggests that the solvation process of a sulfonic group involves four water molecules. Assuming a protonic mobility weakly dependent on temperature, a solvation enthalpy of a perfluorosulfonic acid group by water of -135 kJ·mol^{-1} is deduced from conductivity variations with the temperature.

Keywords: proton conductivity; Nafion®117; solvation; enthalpy.

1 Introduction

Nafion® membranes and their analogues are extensively used as polymer electrolytes for electrolysis or in PEM fuel cells. These membranes are made of a hydrophobic fluorinated macromolecular skeleton with dangling perfluorosulfonic acid groups. The swelling by water is induced by these acidic side chains. The mobile charge carriers i.e. the protons are provided by the partial ionization of these acid groups.

2 Experimental

2.1 Membrane preparation

Nafion®117 is purchased from Dupont de Nemours (Ref. Aldrich: 274674-1EA). Membrane samples of about 20 cm2 and about 180 μm thickness (0.007 inch dry) are immersed in a 3 mol·L^{-1} solution of nitric acid for two hours to achieve the acidification of sulfonic groups. The acid excess is then extracted by Soxhlet using distilled water for one week. The membranes are balanced with distilled water for one week. Samples of about 1 cm^2 are then taken for conductivity measurements. The low volume of the samples, about 10 mm^3 between the electrodes, has been chosen to allow a relatively fast equilibrium with partial pressure of water at different temperatures.

The water diffusion coefficient D_{H_2O}, depending on water content in Nafion®117, is between 5 x 10-7 to 7.5 x 10-6 cm2·s-1 at 30°C[1, 2]. The time t necessary to reach equilib-

rium in the sample volume can be estimated from the relation $\frac{D_{H_2O} \cdot t}{l^2} \approx 1$ where l is the radius of the electrode tightening surface. For l≈2 mm, t can be estimated between 2 and 22 h.

2.2 Conductivity cell

The conductivity cell provides constant cell parameters with climatic conditions for a small membrane sample. The gold electrodes are circular with a small dissymmetric size (2.1 and 2 mm in diameter) to prevent them moving off-center. For the same reason, the gold cylindrical electrodes are embossed in Macor ceramic cylinders. The electrode distance may be accurately adjusted and measured by the displacement of the ceramic cylinder in a metallic support. For a series of measurements on a sample, the cell parameter (about 0.64 cm^{-1}) is determined from a previous calibration by immersion of the cell in a 0.1 $mol \cdot L^{-1}$ KCl solution at 20°C.

2.3 Climatic chamber

The climatic chamber (Vötsch VC 4018) allows the relative humidity to be stabilized in a temperature range from -40°C to 180°C. The temperature was limited between 10°C and 95°C range in which RH can be adjusted between 10 and 98%.

2.4 Impedance measurements

The conductivity measurements were carried out using a Hewlett Packard 4192A LF frequency response analyzer. Impedance measurements between the different cells are automatically driven by an Agilent 34970A Switch unit equipped with 34901A 20 channel card. The spectra were recorded between 5 Hz and 13 MHz. At low impedances of the sample, the resistive contribution of the set up to the overall resistance (leads and connections) may range from 1 to 10% of this value. For this reason, the impedances measured are corrected from the set up impedance measured in the same frequency range. This impedance can be represented below 4 MHz by an inductance of 5 μH associated to a resistance of 1.3 Ω in serie. The resistance of the membrane is taken at the minimum in the electrochemistry Nyquist plot, which is usually between 10^4 and 10^6 Hz.

3 Results and discussion

For more clarity, the variations of conductivity as a function of T and RH have been separately represented in figure 1 and 2 respectively.

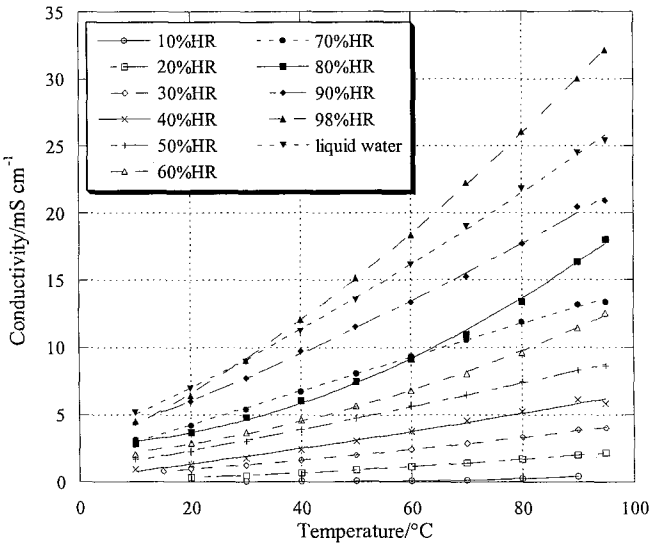

Figure 1. Nafion®117 conductivities as a function of the temperature at constant RH values.

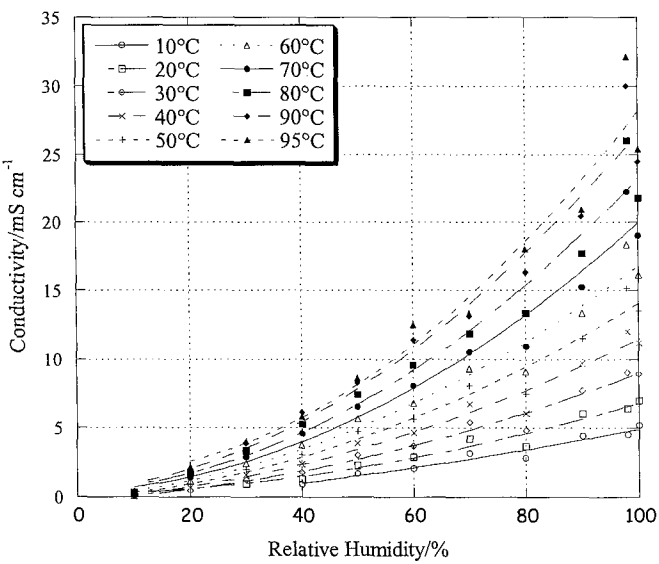

Figure 2. Isothermal values of Nafion®117 conductivities as a function of RH.

These conductivity values are obtained with a total uncertainty of 30% in the broad domain of data. This new database can be used as a data chart to study the impedance of Electrode Membrane Assembly and the water content in working (drying, flooding, cells modelling interest).

3.1 Isothermal conductivity variations with partial pressure of water

The significant influence of partial pressure of water on conductivity σ must be emphasized. This dependence appears more clearly in figure 3 which plots log σ as a function of log RH.

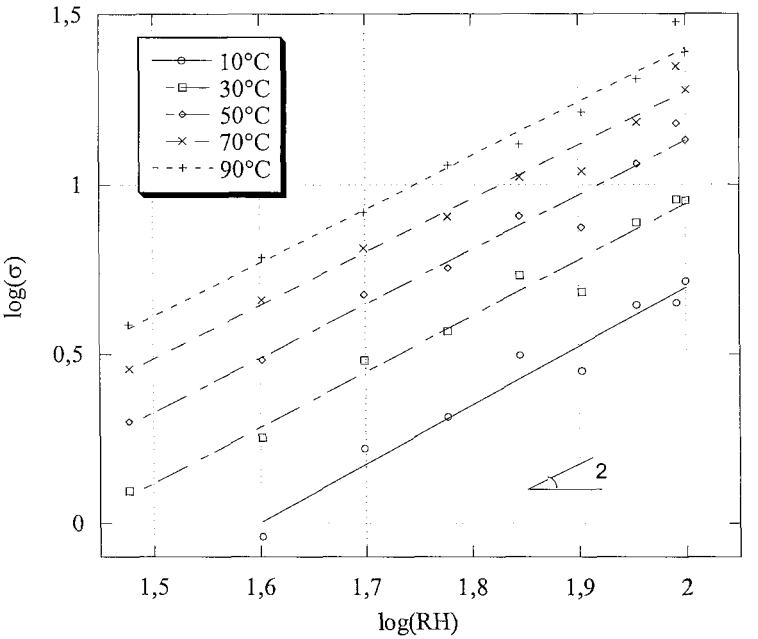

Figure 3. Isothermal values of log σ versus log RH of Nafion®117. For clarity, not all data are represented. Isothermal straight lines obtained from the best linear fit correspond to a temperature difference of 20°C.

In this representation, experimental data define approximately straight lines whose slope $\frac{d(\log\sigma)}{d(\log RH)} \approx 2$. This behaviour can be simply interpreted assuming a low partial ionization of the sulfonic group, with the water adsorbed in the membrane according to the equilibrium:

$$-SO_3^-H^+ + pH_2O \rightleftarrows -SO_3^-nH_2O + H^+mH_2O \qquad (1)$$

In this relationship, n and m are the number of water molecules associated with a sulfonic group and a proton after ionic dissociation. The total number of water molecules implied in this solvation equilibrium is p = m+n. In this process, the electrostatic attraction between an $-SO_3^-$ anion and a proton is compensated by hydrogen bonds and ion dipole interactions formed with water molecules. Assuming a partial dissociation of the sulfonic group, the following relationship links the components of equilibrium (1):

$$K_{(T)}^{solv} = \frac{\left|-SO_3^- nH_2O\right|\left|H^+ mH_2O\right|}{P_{H_2O}^p(T)} \quad (2)$$

In this equation, $K_{(T)}^{solv}$ is the solvation constant of –SO3H group at temperature T and $P_{H_2O}(T)$ the partial pressure of water in equilibrium with the water adsorbed by the membrane. If the concentration of ionized species remains low, their activities may be considered as proportional to their concentration. Since $\left|-SO_3^- nH_2O\right| = \left|H^+ mH_2O\right|$ the concentration of solvated protons $\left|H^+ mH_2O\right|$ is proportional to $P_{H_2O}^{p/2}(T)$. If we assume that the solvated proton mobility remains constant at a constant temperature, the conductivity is proportional to the number of solvated protons. The solvation constant $K_{(T)}^{solv}$ may then be considered as proportional to the proton conductivity σ:

$$K^{solv}(T) = \frac{\left|H^+ mH_2O\right|^2}{P_{H_2O}^p(T)} \quad (3)$$

$$K^{solv}(T) \propto \frac{\sigma^2}{P_{H_2O}^p(T)} = \frac{\sigma^2}{(\%RH \cdot \bar{P}_{H_2O}^{sat})_T^p} \quad (4)$$

where $\bar{P}_{H_2O}^{sat}$ is the partial pressure of water in equilibrium with liquid water.

Finally, isothermal values in log σ are proportional to log RH according to $\log\sigma \propto \frac{p}{2} \cdot \log RH + cons\,tant$ since at a constant temperature P_{H_2O} is proportional to RH. The slopes of the straight lines represented in figure 8 suggest $\frac{p}{2} \approx 2$ then $p \approx 4$.

According to our hypothesis, it means that four water molecules are involved in the solvation process of a sulfonic group. At this point, it is not possible to estimate the number of water molecules, n and m, associated to the anion or cation. Interestingly, a previous work on proton transfer in Nafion®117[3] concluded on a vehicular mechanism for which the proton is strongly linked to about 3 water molecules in highly humidified Nafion®117. Taking into account this result, it would mean that in the solvation equilibrium suggested in (1), n and m would be respectively 1 and 3.

3.2 Conductivity variations with temperature

Considering again equation (3):

$$K^{solv}(T) = \frac{\left|H^+ mH_2O\right|^2}{P_{H_2O}^p(T)} = \frac{\left|H^+ mH_2O\right|^2}{(\%RH \cdot \bar{P}_{H_2O}^{sat})_T^p} \quad (3bis)$$

$$\ln K_T^{solv} = \ln \frac{\left|H^+ mH_2O\right|^2}{(\%RH \cdot \overline{P}_{H_2O}^{sat})_T^p} \qquad (5)$$

Assuming now a proton mobility weakly temperature dependent as usual in aqueous solution[4] variations of conductivity with temperature can be attributed mainly to variation in charge carriers concentration. Consequently:

$$\ln(K_T^{solv}) = \frac{\Delta S_{solv}}{R} - \frac{\Delta H_{solv}}{RT} \propto \ln \frac{\sigma_T^2}{(\%RH \cdot \overline{P}_{H_2O}^{sat})_T^p} \qquad (6)$$

with p = 4 as previously determined.

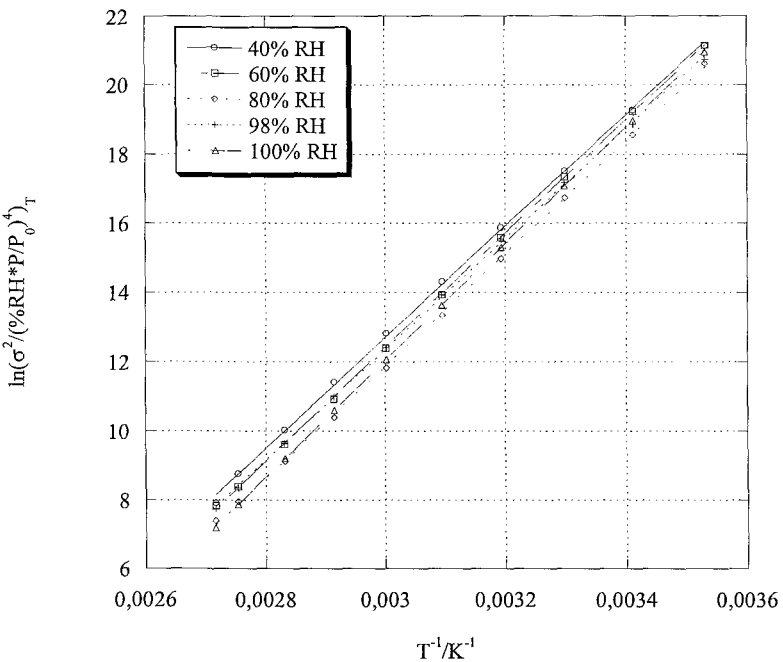

Figure 4: $\ln \frac{\sigma_T^2}{(\%RH \cdot \overline{P}_{H_2O}^{sat})_T^4}$ at constant RH values versus the reciprocal of absolute temperature. For clarity, not all data are represented.

In figure 4 are reported $\ln \frac{\sigma_T^2}{(\%RH \cdot \overline{P}_{H_2O}^{sat})_T^4}$ as a function of the reciprocal of absolute temperature T. Experimental data define straight lines from which we can estimate a solvation enthalpy $\Delta H_{solv} \approx -135$ kJ·mol-1. This value is of the expected order of magnitude

for a solvation process[5-7]. ΔSsolv cannot be determined since the mobility of the proton charge carrier in Nafion® is not known.

4 Conclusions

Accurate conductivity measurements on Nafion®117 allow to establish a quantitative relationship between isothermal protonic conductivity data and the relative humidity ($\sigma \propto (RH)^{p/2}$). This dependence can be interpreted by the variation in the concentration of protonic charge carriers with the amount of water adsorbed by the membrane. These protonic charge carriers would stem from the partial dissociation of the sulfonic groups grafted to the macromolecular skeleton. The parameter p is identified with the number of water molecules necessary for the solvation of a sulfonic group. In the present case, our experimental results suggest $p \approx 4$. From conductivity dependence with temperature, an exothermic solvation enthalpy of -135 kJ·mol-1 is estimated.

Acknowledgements

The authors would like to thank Professors Jean-Yves Sanchez and Jean-Paul Diard for helpful criticism and fruitful discussions. Financial assistance from SAGEM is acknowledged.

References

1. T. A. Zawodzinski, T. E. Springer, J. Davey, R. Jestel, C. Lopez, J. Valerio and S. Gottesfeld, *J. Electrochem. Soc.*, **140**, 1981 (1993).
2. T. A. Zawodzinski, Jr, C. Derouin, S. Radzinski, R. J. Sherman, V. T. Smith, T. E. Springer and S. Gottesfeld, *J. Electrochem. Soc.*, **140**, 1041 (1993).
3. M. J. G. Jak, S. Raz, L. N. V. Rij, J. Schoonman and I. Riess, *Solid State Ion.*, **143**, 205 (2001).
4. A. A. Kornyshev, A. M. Kuznetsov, E. Spohr and J. Ulstrup, *J. Phys. Chem. B*, **107**, 3351 (2003).
5. S. J. Paddison, L. R. Pratt, T. Zawodzinski and D. W. Reagor, *Fluid Phase Equilib.*, **150-151**, 235 (1998).
6. G. J. Tawa, I. A. Topol and S. K. Burt, *J. Chem. Phys.*, **109**, 4852 (1998).
7. N. J. Harris, T. Ohwada and K. Lammertsma, *J. Comput. Chem.*, **19**, 250 (1998).

ION CONDUCTING BEHAVIOUR OF COMPOSITE POLYMER GEL ELECTROLYTE: PEG - PVA - $(NH_4CH_2CO_2)_2$ SYSTEM

S.L.AGRAWAL, A.AWADHIA AND S.K.PATEL
Department of Physics, A.P.S. University, Rewa (M.P) 486003-INDIA
E-mail: sla_ssi@rediffmail.com

Abstract

Efforts have been made here to develop a proton conducting composite polymeric gel electrolyte, namely, PEG-PVA-$(NH_4CH_2CO_2)_2$ system and investigate its ion conducting behavior. The gel samples with varying PVA concentration have been prepared in 1 M solution of $(NH_4CH_2CO_2)_2$ in Dimethyl Sulphoxide used as casting solvent. The XRD of samples exhibit crystalline nature of composite gel electrolytes which increases with increase of PVA concentration in the gel .Shift in endothermic transitions of constituents and corresponding broadness in DSC thermograms of as synthesized samples have been attributed to the formation of composite gel electrolytes. The room temperature ionic conductivity of gel electrolytes ($3.5x10^{-4}$ S. cm^{-1})have been found to be comparable to that of liquid electrolytes($5.52x10^{-4}$ S. cm^{-1}) . Temperature dependence studies of ionic conductivity reflects VTF character of gel electrolytes

Keywords: Polymer electrolytes, ion conductors, composites, gels

1.0 Introduction

Polymer Electrolytes have become attractive electrolyte materials for different electrochemical applications in the past two decades on account of certain distinct properties like ease of fabrication, mouldability into any shape and size etc [1]. It is well known that ionic conductivity in solid polymer electrolytes is essentially confined in the amorphous phase and so conductivity values are quite low as compared to liquid electrolytes. A number of approaches have been tried over the years to augment the ionic conductivity in these polymer electrolytes besides developing new electrolyte systems including dispersal of inorganic/organic fillers in the polymer matrix to form composite polymer electrolytes [2-4]. In the past decade, few systems like polyacrylamide (PAAM) and polyvinyl alcohol (PVA) based composite polymer electrolytes have been reported wherein ionic conductivity and mechanical integrity improves considerably [5-7]. Among the other approaches, gel formation techniques have become popular in recent years, as they offer an approach to attain high conductivity value approaching that of liquid electrolytes alongwith good elastomeric and adhesive properties[3]. These gel polymer electrolytes have enough mechanical strength, but there still remains the exudation problem of liquid electrolyte due to phase separation between polymer matrix and encapsulated liquid electrolyte. Recently, use of modified copolymers with two or more functional monomers have been suggested as a solution to this leakage problem and improvement of mechanical strength [8].Some of the reported gel system belonging to this category are poly(VC-AN), poly (MMA-VC), poly(styrene-AN), poly (styrene-butadiene) [8-11].With in this framework, an attempt has been made in the present work to develop a Polyethylene glycol based polymer composite gel electrolyte, namely, Polyethylene glycol- Polyvinyl alcohol –$(NH_4CH_2CO_2)_2$ system. This system has been studied on account of the fact that both Polyethylene glycol (PEG) and polyvinyl alcohol (PVA) are separately reported to form highly amorphous complexes/ gels with

salts and acids [11-14].Further these polymers possess properties of forming good miscible blends[15].

2.0 Experimental

2.1 *Synthesis*

In the present investigation, PEG (MW - 10,000), Aldrich make; PVA (average MW -85000-146000),Aldrich make; $(NH_4CH_2CO_2)_2$, AR grade, Rolex chem make and aprotic solvent dimethyl sulfoxide (DMSO) AR grade, sd fine chem make were used for synthesis of composite gel electrolyte. PVA was dispersed in different stoichiometric ratios in PEG dissolved in 1M of liquid electrolyte of $(NH_4CH_2CO_2)_2$ in DMSO. Addition of polymers to liquid electrolyte was carried out very slowly for formation of homogeneous gel. After syneresis, gels in form of thick films were taken out and dried at room temperature for few days to obtain stable gel electrolytes. The resulting gel films were stored carefully to avoid further exudation of solvent

2.2 *X-ray diffractogram*

XRD pattern of as synthesized comports gel electrolytes were obtained on Rigaku International Corporation make diffractometer (model RU-3HR) with Cu-Kα (λ=1.544 Å) radiation to assess their complexation behaviour and morphology.

2.3 *DSC studies*

Differential scanning calorimetry of pristine materials as well as few gel electrolyte samples were performed on a Dupont series 2000 thermal analyser, USA,with a scanning rate of $5K.min^{-1}$ in a nitrogen purged cell in the temperature range 298-523K to assess their thermal behaviour and morphology.

2.4 *Electrical measurements*

The gel electrolytes were sandwiched between two platinum electrodes and electrical conductivity measurements were performed on an Hoiki make LCR meter (Model 3520) in the frequency range 40Hz -100kHz at various temperatures ranging between 287 K and 373 K.

3.0 Results & Discussion

3.1 *XRD Analysis*

Fig 1 depicts the XRD patterns of pristine materials PEG, PVA and $(NH_4CH_2CO_2)_2$ together with that of PEG: PVA blend (65:35 wt. ratio). (PEG: $(NH_4CH_2CO_2)_2$: PVA) composite gel electrolytes for two concentrations of PVA. XRD patterns of pristine polymers and 65:35 wt. ratio pure blend (curve a, b, c)

exhibit occurrence of back ground modulation generally observed in the case of polymeric systems. The relatively sharp characteristic peak at 2θ=19.6° and shoulder at 2θ=9° (curve-c) related to DMSO casted PVA and two closely spaced peaks around 2θ=21° and 22° related to pure PEG (curve-b) were noticed [11, 16]. In case of PEG: PVA blend (curve c), a relatively intense peak at 2θ= 11.6° was observed (curve-d) and not assignable to components. The appearance of this peak Can be correated to formation of miscible blend resuting from interaction among component moreover, appearance of peak at lower 2θ value is probably account of better solvation of components as solvent swollen characteristics of PVA and plasticization property of PEG is well known [17,18].When PVA is added to pristine PEG: $(NH_4CH_2CO_2)_2$ gel electrolyte to form composite gel system, a broadening in peak related to pure polymer is noticed together with occurrence of an intense sharp peak superimposed on the broadening together with a shoulder around $2\theta=26^0$. Comparison of XRD patterns of pristine materials with this XRD curve suggests that the

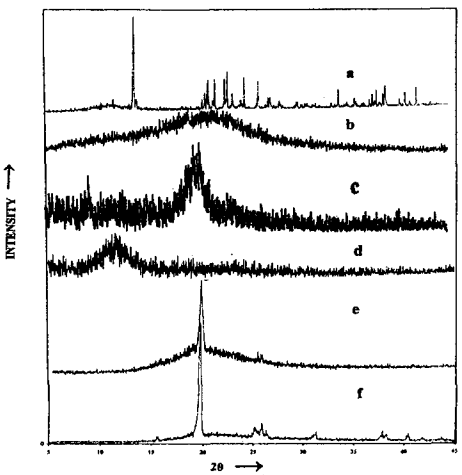

Fig.1. X-ray diffractogram of (a) (NH4CH2CO2)2(b) Pure PEG (c) DMSO casted PVA film along gel film containing (d) PEG:PVA Blend (e) 20wt% (f) 30wt% PVA

observed intense peak is not assignable to any of the peak of pristine materials. However, the kink around 26° can be correlated to the presence of salt in traces as no other peaks of salt (curve-a) could be observed in XRD pattern. These results indicate formation of a microcrystalline composite gel system through strong interaction among components. As evidenced from diffractogram, crystallinity is seen to improve with increase of PVA content Closer

Table 1.Crystallte size and d-spacing of composite gels along with salt

Sample	2θ (degrees)	Crystallite Size L (Å)	d-Spacing (Å)
Pure PEG	22	5.7	4.04
PVA film casted in DMSO	19.6	21.2	4.52
PEG:PVA Composite	11.2	16.06	7.89
Gel electrolyte containing 20 wt% PVA	19.7	10.62	4.52
Gel electrolyte containing 30 wt% PVA	19.6	22.15	4.45

examination of diffractograms also reveal the presence of salt in traces (appearance of weak XRD peak related to salt at $2\theta=26.22^{\circ}$ and 28.36°)at higher PVA content. The crystallite sizes related to pure PEG were evaluated using the well known Scherrer equation [19] to assess the morphology of gel electrolytes and listed in table 1. It is being noticed that as the fraction of PVA in the pristine gel enhances, though there is insignificant change in 2θ value and d spacing, crystallite size decreases significantly. Such a shift in 2θ values could be associated to interaction among components and formation of PVA: $(NH_4CH_2CO_2)_2$ complexes.

3.2 *DSC studies*

One of the pertinent factors for miscibility of polymers to form compatible blends is that one of the components should be highly crystalline while the other be highly amorphous.[15].Within this framework, Polyethylene glycol which is mostly crystalline is expected to show compatibility with amorphous polyvinyl alcohol.Fig2, which depicts DSC profiles of few gel composites prepared by soaking ammonium succinate electrolyte, ascertains this hypothesis. The observed low temperature endothermic transitions around 333K can be correlated to complex crystalline part of PEG which has a melting point of 336K. Further it is noticed from the given DSC profiles that upon increase of PVA content (till 30wt%) in composite gel, this endothermic transitions shifts towards lower temperature before vanishing at 30wt% PVA content. Shifting of the peak can be attributed to increase in intra molecular and inter molecular coordinations between coordinating sites on different polymer chains caused by salt ions acting as transient crosslinks [11]. The disappearance of this melting isotherm corresponding to PEG also suggests complete miscibility of PEG with PVA leading to formation of single phase system. The occurrence of endothermic transition in the temperature range 423-445K exhibits the presence of unsolvated salt for all compositions of composite electrolyte. This argument is in correlation in with the DSC curve for pure salt (curve a) and in accordance with XRD results. All the DSC thermograms show a broad endothermic transition above 448K. This transition can be considered as a consequence of mixing of thermal transitions related to evaporation temperature of the solvent DMSO (466K) and complex crystalline part of PVA owing to interaction between PVA and the salt. PVA has been known to form complexes with ammonium salts and

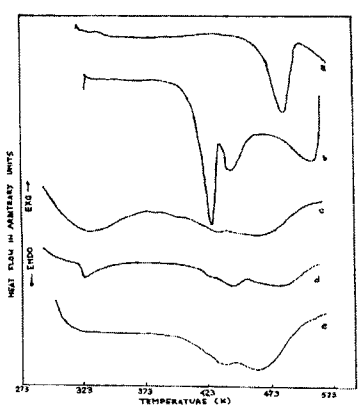

Fig. 3.DSC thermograms of (a)pure PVA (b) (NH4CH2 CO2)2 and gels containing (c)20wt% (d) 25wt% and (e) 30wt% in composite

give rise to protonic conduction [12]. As a result of this complexation, the melting isotherm shifts toward lower values while the isotherm related to DMSO does not change. Consequently, the broadening of peak beyond 448K seems to reduce considerably upon increase in PVA content in the composite thereby making the transitions sharper. Presence of DMSO and complexation of PVA with ammonium succinate is thus concluded from the occurrence of transition above 448k. The increase in enthalpy of melting related to PVA for the composite gel with increase of PVA content shows increasing crystalline nature of gel films.

3.3 *Conductivity Studies*

The first step in the development of highly conductive polymeric gel is to synthesize a non aqueous electrolyte based on a polar solvent having high dielectric constant, low viscosity, high boiling point and low melting point. DMSO is one such solvent possessing these properties [16] and so used in the present work. The optimum σ_{rt} ($=3.7\times10^{-3}$ s.cm^{-1}) was obtained for 1M solution and so used here for preparation of composite gel electrolytes.

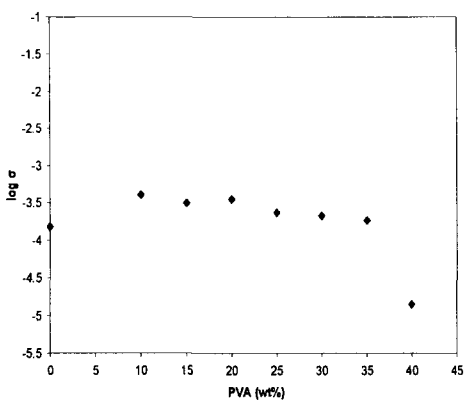

Fig3. Variation of conductivity with increase in PVA content in composite gel

The observed conductivity behavior (fig.3) for as synthesized composite gel electrolytes shows a small drop in ionic conductivity with increase of PVA content up to 35 wt%. This feature is in contrast with the conductivity behaviour of composite solid polymer electrolytes where significant change in conductivity wit filler concentration has been reported. [5,7]. Rather, it resembles to that of pristine polymeric gel electrolytes containing lithium salts [3,5]. Thus it is conjectured from the observed conductivity behavior that PVA is essentially increasing the microviscosity of the gel system. This in turn lowers the ionic mobility of the composite system and so the ionic conductivity in accordance with Walden's rule given by the relation,

$$\sigma = n e^2 / 6 \pi r \eta \qquad (1)$$

where n is charge carrier concentration ,η the viscosity and r the radius of mobile ion .Small variation of ionic conductivity upto 35wt% PVA concentration suggests its limited active role in the composite gel and thought of as PVA is only improving the morphology of the electrolytes besides holding the liquid electrolyte on account of its solvent swollen characteristics [18] .Another plausible reason for small dip in ionic conductivity with increasing PVA concentration can be associated to micro crystalline nature of composite gel in the presence of filler PVA as also evidenced in XRD studies (Table-1). When PVA is admixed in excess of 35wt% a significant

fall in ionic conductivity is noticed which can be attributed to ion association effect observed for PVA based composite polymer electrolytes [19].

3.4 *Temperature dependence of conductivity*

Figure-4 shows the temperature dependence of conductivity of few synthesized composite gel electrolytes. The temperature dependence studies indicate that the change in conductivity is very small within an order of magnitude in the studied temperature range signifying liquid like ion transport. Conductivity variation with temperature for all the composite gels correspond to a VTF type behavior, described by the relation,

$$\sigma = \sigma_o \exp\left(-B/T-T_o\right) \quad (2)$$

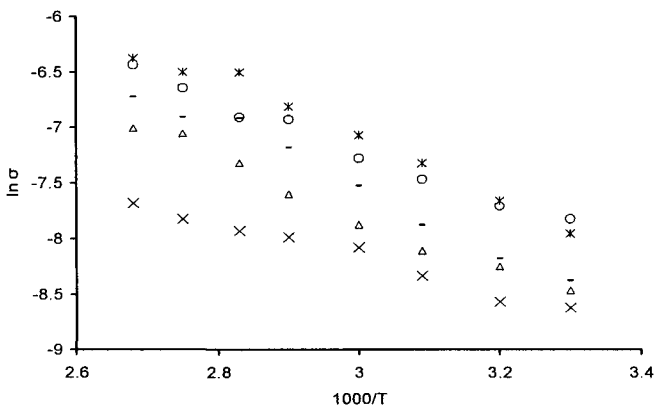

Fig 4. Temperature dependence of conductivity of gels containing (o) 10 wt% (*) 20wt% (−) 25wt% (Δ) 30wt% (x) 35wt% PVA in composite gel

where σ_o is the pre exponential factor, B a constant related to activation energy and T_o (=Tg-60°) is quasi equilibrium glass transition temperature. Such a behaviour can be attributed to the fact that DMSO is present in the gel films and it provides conducting pathway for the mobile carriers beyond the critical temperature. The activation energies alongwith pre-exponential factors for temperature below T_o have been listed in table 2. Extremely low E_a values show liquid like ion transport in these gel films.

Table 2 Values of σ_o and Ea for gel films in the arrhenious region

PVA concentration in composite gel (in wt %)	σ_o (Scm^{-1})	E_a (eV)	T_0(K)
10	0.74	0.20	
20	7.16	0.26	364
25	16.9	0.30	360
30	2.96	0.26	362
35	0.45	0.21	357

Conclusion:

A new type of polymeric gel electrolyte based on polymer composites have been reported in the present work. The studies have been focussed on composite system PEG-PVA-$(NH_4CH_2CO_2)_2$. The XRD and DSC studies reveal complexation of salt and polymer with increasing crystillinity (lowering in the degree of crystillinity related to PVA and extremely small value of crystallite size) upon addition of polymer. Experimental investigations on PEG-PVA-$(NH_4CH_2CO_2)_2$ system reveal formation of a compatible blend based gel electrolyte having an ionic conductivity approaching to that of liquid electrolytes (3.7×10^{-3}S cm^{-1}). The conductivity has been reported to decreases very slowly with PVA concentration (up to 35wt% PVA) suggesting the role of PVA as that of active filler improving the morphology of the system. Temperature dependence of conductivity seems to follow VTF relationship with extremely low activation energy (< 0.3 ev).

Acknowledgements

Authors are grateful to UGC, N. Delhi for the financial support in form of minor research project. Authors are thankful to the University of Hyderabad for providing XRD facility. Authors are thankful to M/s Birla Ericsson Optical Ltd., Rewa for providing DSC facility.

References

[1]. F .M. Gray, Solid Polymer Electrolytes: Fundamentals and Technological Applications, VCH, New York 1991

[2] W. Wieczorek. K. Such. S. H. Chung, and J.R. Stevens, J. Phys. Chem., 98, 9047 (1994).

[3] S.S.Sekhon, Bull. Mater. Sci., 26, 321 (2003)

[4]A. Chandra and S. Chandra, Bull. Electrochem.,11, 88(1995).

[5]W. Wieczoek, K Such, Z Florjanczyk and J R Stevens, Electrochim. Acta, 40, 2417 (1995).

[6] W. Wieczorek. K. Such. S. H. Chung, and J.R. Stevens, J. Phys. Chem., 98, 6840 (1994).

[7] S.L.Agrawal and P.K.Shukla, Ionics 6 312 (2000)

[8] B.Oh, Y.K. Sun, and D.W. Kim, Bull. Korean Chem. Soc. 22, 1136 (2001)
[9] M. Yamazaki, Y. Soji, S.Yoshimura and K. Nishio, T. Saito, Sanyo Electric Co., Japanese Patent Publication No. 07, 320781(1995)
[10]T. Ichino,Y.Takeshima,M.Takeshima and.S.Nishi ,NTT Co.Japanese Patent publication, 07, 335258 (1995)
[11]Th. Joykumar Singh and S. V.Bhat, Bull.Mater. Sci.,26, (2003)
[12]P.K. Shukla & S.L. Agrawal, Ind. Pure & App. Phys, 38, 53 (2000)
[13]P.N. Gupta and K.P. Singh, Proc. 10th International Conference on Solid State Ionics, Singaore p.317 (1995)
[14]S. L. Agrawal and Arvind Awadhia, Bull. Mater. Sci., 27 (2004)
[15]D.R.Paul&Newman,PolymerBlends, Acad. Press New York Vol.1 (1978)
[16] A.awadhia,S.K.Patel,R.B.Patel and S.L.Agrawal, *ICEP*-2004, Dalhousie 2004
[17] C.A.Finch,*Polyvinyl Alcohol, Properties and Applications*, Wiley &Sons New York (1973)
[18] Ke-cheng gong, Huang Shou-cai ,*Mat.Res.Soc.* 135(1989)
[19] B.D. Cullity,*Elements of X-ray Diffraction,* Wesley Publishing Company, Inc. London(1978)
[20]M. Deepa, N. Sharma, Pradeep Varshney, R. Chandra and S. A. Agnihotry, Ion Conducting Materials: Theory and Applications, Eds.A. R. Kulkarni and P. Gopalan, Narosa Publishing House, New Delhi p.74 (2001)
[21]G.Saibaba,D.Srikanth and A.Ramach.Reddy,Bull.Mater.Sci.,27 51 (2004)
[22]P.K. Shukla and S. L. Agrawal, Phy. Stat. Sol. (a) 172 ,329 (1999).
[23] A. Awadhia, *Ph. D. Thesis*, A. P .S. U. Rewa, (2006)

IMPEDANCE SPECTROSCOPY AND DSC STUDIES OF POLY(VINYL ALCOHOL)/SILICOTUNGSTIC ACID CROSSLINKED COMPOSITE MEMBRANES

ARFAT ANIS* AND A. K. BANTHIA
Materials Science Centre,
Indian Institute of Technology, Kharagpur-721302, India
E-mail: ajitbanthia2000@yahoo.co.in

Chemically crosslinked composite membranes consisting of poly(vinyl alcohol) (PVA) and silicotungstic acid (STA) have been prepared by solution casting method and evaluated as proton conducting polymer electrolytes. The proton conductivity of the membranes were investigated as a function of blending composition, crosslinking density and temperature. The conductivity mechanism was investigated by using Impedance spectroscopy in the region between 40 Hz and 10 MHz. Membranes were also characterized by FTIR spectroscopy to confirm the crosslinking reaction and differential scanning calorimetry (DSC) to assess the thermal stability. Membrane swelling decreased with increase in crosslinking density accompanied by improvement in mechanical properties. The proton conductivity of the membranes were of the order of 10^{-3} S/cm and showed similar resistance to methanol permeability than Nafion 112 under the same measurement conditions.

1. Introduction

Polymer electrolytes have received extensive attention, especially for polymer electrolyte membrane fuel cells (PEMFCs) operating at temperatures above 100 °C. As alternatives to the currently available perfluorosulfonic acid (PFSA) membranes, the newly developed polymer membrane electrolytes can be classified according to the way they are prepared. Most of the conventional polymers can be modified by attaching charged units within their structures and in this way obtain the ionic conductivity. The charged unit is commonly an anion, typically sulfonate (–SO_3–) as in the sulfonated hydrocarbon polymers, e.g. polysulfone (PSF) [1], polyetheretherketone (PEEK) [2] and polybenzimidazole (PBI) [3–6].

The second method is to incorporate a polymer matrix with solid inorganic compounds, the so-called inorganic–organic composites or hybrids. Typical polymers in this group include polymers without functional groups such as polyethylene oxides (PEO) [7] and PBI [8–10] and polymers with functional groups such as Nafion [11], sulfonated polysulfone (SPSF) [12], sulfonated polyetheretherketone (SPEEK) [13]. The solid inorganic compounds include oxides such as amorphous silica and inorganic proton conductors such as zirconium phosphate (ZrP), ($Zr(HPO_4)_2 \cdot nH_2O$), phosphotungstic acid (PWA), ($H_3PW_{12}O_{40} \cdot nH_2O$) and silicotungstic acid (SiWA), ($H_4SiW_{12}O_{40} \cdot nH_2O$).

The third method is via chemical interactions between basic polymers and strong acids [14–16] or polymeric acids [17]. Earlier studies employed basic polymers such as PEO, polyvinyl acetate (PVAc), polyacrylamide (PAAM) and polyethyleneimine (PEI). Most of these acid doped polymers exhibit proton

conductivity less than 10^{-3} S cm^{-1} at room temperature. High acid contents result in high conductivity but sacrifice mechanical stability, especially at temperatures above 70–80 °C. In order to improve the conductive, thermostable and mechanical properties of the acid/polymer membranes, cross-linked polymers (e.g. PEI [18]), thermally stable polymers (e.g. polyoxadiazole (POD) [19] and PBI [14–16]) and introduction of inorganic fillers or/and plasticizers [8,20] have recently been investigated.

In this work we have explored the suitability of polyvinylalcohol (PVA) for preparing inorganic-organic composite membranes by incorporating silicotungstic acid in the polymer matrix. PVA is a possible candidate because of its good chemical stability, film forming ability and high hydrophilicity and availability of crosslinking sites to create a stable membrane with good mechanical properties and selective permeability to water. PVA is water-soluble polymer that readily reacts with different cross-linking agents to form gel. PVA is also biocompatible and biodegradable and is widely used in medical, cosmetic, and packaging materials. For PVA, several cross-linking methods have been published for different uses, for example, chemically cross-linked PVA are prepared by glutaraldehyde. PVA shows excellent insulation performance as a polymer material for pure dry materials; its conductivity can reach 10^{-10}–10^{-14} S cm^{-1}. In these materials, the doping impurity ions act as the primary electric carrier. PVA membranes have also been used in alcohol dehydration to break the alcohol–water azeotrope [21,22] and due to its high selectivity for water to alcohol, it can effectively reduce the methanol crossover through the membrane when used in direct methanol fuel cells (DMFCs). In-situ crosslinking of the hydroxyl functional groups available in PVA can effectively control the water uptake and hence the degree of swelling of the membranes. Optimizing the crosslinking density of the membranes can provide membranes with good mechanical property and will also solve the problem of acid leaching from the membranes under hydrated conditions by effectively immobilizing the acid within the polymer matrix due to formation of crosslinked networks. Composite membranes with different wt % of silicotungstic acid and crosslink density were prepared and characterized by ATR-FTIR, Impedance spectroscopy (IS), methanol permeability measurements and differential scanning calorimetry (DSC) to determine their suitability for use as proton conducting polymer electrolytes for fuel cell applications.

2. Experimental

2.1 *Materials and membrane preparation*

PVA (Mw: 1,25,000 & degree of hydrolysis approx. 88%), and Glutaraldehyde (GA) (25% content in water) were obtained from s.d. fine-Chemicals Ltd. (Mumbai, India). Silicotungstic acid (STA) was obtained from Sisco Research Laboratories Pvt. Ltd (Mumbai, India). To prepare 5 % (w/v) solution, PVA was dissolved in water at 80 ^{0}C with continuous stirring. To 20 g of 5 wt % PVA solution, desired amount of STA was added and the resulting mixture was stirred until a

homogeneous solution was obtained. To this solution desired amount of the GA crosslinking agent was added and the solution was further stirred for few minutes. After that the homogeneous solution was poured into petri dish and allowed to dry at room temperature.

2.2 *Infrared spectroscopy*

Attenuated Total Reflection (ATR)-FTIR spectra in the range of 4000-400cm^{-1} of the polymer electrolyte films were measured with FTIR Spectroscope (NEXUS-870, Thermo Nicolet Corporation) running Omnic software, and a uniform resolution of 2 cm^{-1} was maintained in all cases.

2.3 *Impedance Spectroscopy*

Conductivity measurements were made at room temperature after equilibrating the membrane in deionized water for 24 h. The membrane was sandwiched between stainless steel electrodes; ac impedance spectra of the membranes were obtained by using Agilent 4294A Precision Impedance Analyzer under an oscillation potential of 10 mV from 40 Hz to 10 MHz. The conductivity was calculated from the bulk resistance obtained from the high frequency intercept of the imaginary component of impedance with the real axis.

2.4 *Methanol permeability measurement*

Diffusion coefficient measurements were performed using an in house built diffusion cell having two compartments which were separated by the membrane situated horizontally. Prior to measurements, the membranes were equilibrated in aqueous methanol solution 50 % v/v for 24 hours. The methanol concentration of the receptor compartment was estimated using a differential refractometer (Photal OTSUKA Electronics, DRM-1021); the differential refractometer is highly sensitive to methanol. The change in refractive index of the diffusion samples were averaged over 52 scans in the differential refractometer to determine the change in refractive index.

2.5 *Differential Scanning Calorimetry*

A Perkin–Elmer DSC-6 was used for studying the melting and crystallization behavior of the polymeric membranes. The temperature and energy scales were calibrated with the standard procedures. The melting studies were performed in the temperature range of -30 to 200°C at the heating rate of 10°C/min in N_2 atmosphere.

3. Results and discussion

3.1 *Infrared Analysis*

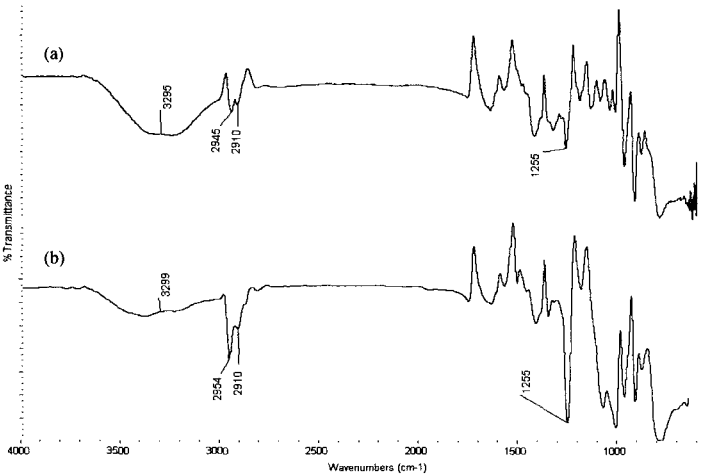

Fig. 1 ATR-FTIR spectra of PVA-STA composite membranes with a crosslinking density of (a) 2. 33 mole % (b) 3. 73mole % respectively

The ATR-FTIR spectra of the composite membranes with different degree of crosslinking are shown in Fig. 1. The bands in the IR spectrum of the membranes correspond well to those of STA, showing the typical features of Keggin anions. The four absorption bands at 779, 880, 920, 978 cm^{-1} are assigned to the ν ($W\text{-}O_a$-W), ν ($W\text{-}O_b$-W), ν ($W\text{-}O_c$-W), ν ($W\text{-}O_d$-W) respectively. The spectra of PVA-STA composite membranes with different compositions (not shown here) shows an increase in intensities for the peaks assigned to STA as the amount of the heteropolyacid is increased. Fig. 1 shows the spectra of PVA-STA composite membranes of different crosslinking density. A decrease in the absorbance of the peak at 3300-3400 cm^{-1} arises due to disappearance of the hydroxyl groups upon reaction with the aldehydes. An increase in the absorbance of the peaks between 970 and 1385 cm^{-1} arises due to formation of an acetal ring and ether linkages as a result of the reaction between the hydroxyl groups and the aldehyde.

3.2 *Ionic conductivity Analysis*

AC impedance was performed to determine the conductivity (σ) of these composite membranes. The result was plotted as a Cole-Cole plot to show the real/imaginary parts of the impedance at various frequencies. A typical Cole-Cole plot of a composite membrane sandwiched between stainless steel electrodes is shown in figure 2. The profile shows that the impedance decreases with increasing frequency.

It indicates that the interfacial impedance decreases with increasing frequency, which is attributed to double layer formation and charge transfer reaction. The bulk resistance is obtained when the impedance approaches pure resistance at higher frequencies and the conductivity of the membrane is determined by $\sigma = (l/R_b)(l/A)$, where R_b , l and A represent bulk resistance, membrane thickness and area of the

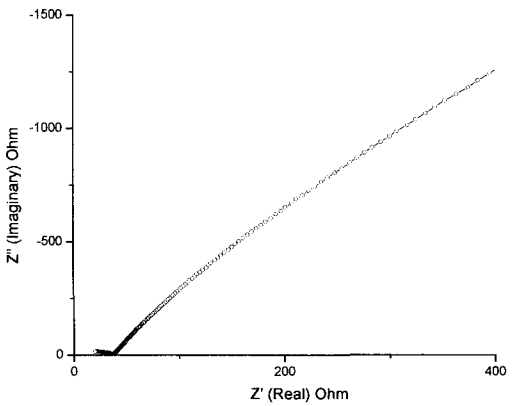

Fig. 2 Cole –Cole plot of the composite membrane, impedance frequency from 40 Hz to 10 MHz

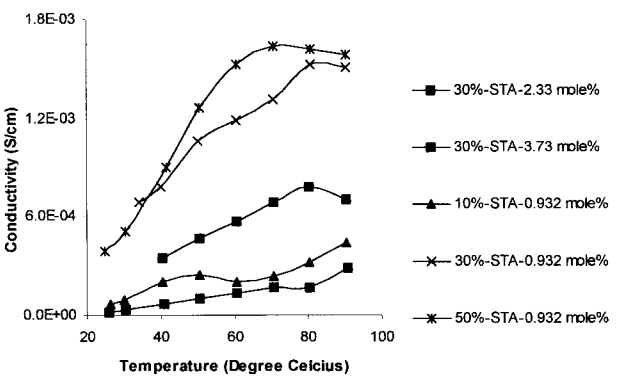

Fig. 3 Variation of conductivity with temperature for the composite membranes

electrode, respectively. The variation of conductivity with temperature for the different composite membranes is shown in figure 3. The Arrhenius plots of the

temperature dependency of the conductivity exhibits convex upward curved profiles; therefore, experimental data have been fitted with the Vogel-Tamman-Fulcher (VTF) equation for conductivity for such electrolytic materials (not shown here). The VTF equation is $\sigma = \sigma_o \exp [-B/(T-T_0)$ where the constants , σ_o (Scm^{-1}), B (K) and T_0 (K) are adjustable parameters. Heteropolyacids exist in a series of hydrated phases, i.e. the structural unit of STA is $H_4SiW_{12}O_{40} \cdot nH_2O$, where the number of water molecules, n, might be in a range of 0–30, depending strongly on the temperature and RH. In the hydrated composite membranes the proton conduction are likely to happen by vehicular mechanism, rather than by Grotthuss mechanism, resulting in a long range conductivity, with protons percolating through the sample.

3.3 *Methanol Permeability*

The methanol permeability through the PVA-STA composite membranes, were measured as a function of both STA content and crosslinking density of the membrane. For comparision, methanol permeability of Nafion 112 was measured under the same experimental conditions. The methanol permeability of Nafion 112 at room temperature was found to be 1.10×10^{-6} cm^2s^{-1}. For the PVA-STA composite membranes, the methanol permeability increased with STA content of the membrane owing to the hydrophilic nature of the doped silicotungstic acid. However a decrease in methanol permeability was observed with increase in cross linking density of the membranes. Therefore it can be concluded that the effect of crosslinking in PVA-STA composite membranes overcomes the swelling effect due to hydrophilic nature of doped STA. The methanol permeability values were found to vary in the range from 1.21×10^{-6} to 2.49×10^{-6} cm^2s^{-1} for these composite membranes. The lowest value of methanol permeability of 1.21×10^{-6} cm^2s^{-1} was observed for the membrane with 30 wt % STA content and a crosslinking density of 1.4 mole %.

3.4 *Differential Scanning Calorimetry*

DSC was used to examine the effect of silicotungstic acid doping and crosslinking density on the glass transition temperature of these composite membranes. Figure 4 shows the DSC thermograms of the composite membranes. The glass transition temperature of the composite membrane with 30 wt % STA content is 63 °C and increases to 74 °C with increase in acid concentration to 50 wt %. This indicates that the complexation of the heteropolyacid in the polymer matrix partially arrests the local motion of the polymer segments resulting in increase in glass transition temperature of the composite membrane. However, the glass transition temperature initially decreases with increase in crosslinking density but increases at higher crosslink densities. This is an interesting behavior that can be explained by considering the factors affecting the glass transition temperature of crosslinked polymers. These factors are main chain rigidity, crosslinking density and the chemical structure of the cross-linker. In case of PVA the hydroxyl groups contribute to the stiffness of the polymer via hydrogen bonding. When the hydrophobic cross-linker is introduced, the number of hydroxyl groups available for hydrogen bonding decreases thereby decreasing the stiffness. An important property derived from the chemical structure of the cross-linker itself is its flexibility. In our

case, the cross-linker consists of a sequence of three methylene groups. This has the effect of increasing the flexibility in the individual polymer chains and leads to a lower glass transition. This means that the expected initial increase in T_g due to the formation of the chemical network is insignificant when compared to the decrease in T_g ought to the weakening of the physical network and to the plasticizing effect of the introduced flexible moieties. The Tg of the composite membranes with cross linking density of 0.0932 mole % is almost same as that of the composite membrane with a crosslinking density of 3.73 mole % and is around 63 °C.

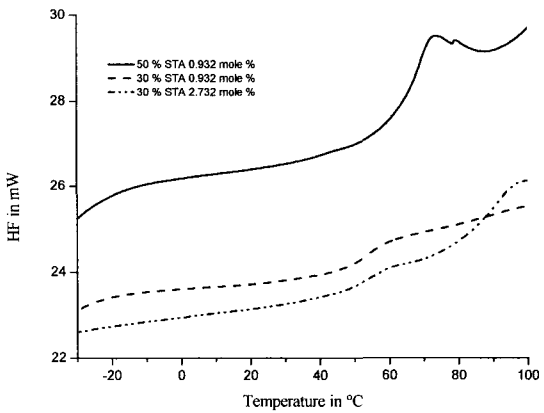

Fig. 4 DSC thermograms of the composite membranes

4. Conclusion

The AC electrical response of the PVA-STA crosslinked proton conducting composite membranes has been investigated by using Impedance Spectroscopy in the frequency range 40 Hz-10 MHz, between 25 and 90 °C. The highest proton conductivity of 1.64 x 10^{-3} Scm^{-1} was obtained for the membrane with 50 wt % STA content with a crosslinking density of 0.932 mole % at 70 °C. FTIR results proved the formation of crosslinked networks. Additionally these composite membranes have good mechanical and thermal stability. Furthermore, the PVA polymer used is biodegradable, non hazardous and environmentally benign. The present investigation suggests that these composite membranes if optimized may serve as a potential alternative proton conducting membrane for polymer electrolyte membrane fuel cell applications.

Reference

1. F. Lufrano, I. Gatto, P. Staiti, B. Antonucci and E. Passallacqua, Solid State Ionics 145, 247 (2001)
2. J. Kerres, A. Ullrich, F. Meier and T. Haïing, Solid State Ionics 125, 243 (1999)
3. R.J. Spry, M.D. Alexander, Jr., S.J. Bai, T.D. Dang, G.E. Price, D.R. Dean, B. Kumar, J.S. Solomon and F.E. Arnold, J. Polym. Sci., Part B: Polym. Phys. 35, 2925 (1997)
4. P. Staiti, F. Lufrano, A.S. Aricò, E. Passalacqua and V. Antonucci, J. Membr. Sci. 188, 71 (2001)
5. J.-M. Bae, I. Honma, M. Murata, T. Yamamoto, M. Rikukawa and N. Ogata, Solid States Ionics 147, 189 (2002)
6. D.J. Jones and J. Rozière, J. Membr. Sci. 185, 41 (2001)
I. Honma, Y. Takeda and J.M. Bae, Solid State Ionics 120, 255 (1999)
7. P. Staiti, M. Minutoli and S. Hocevar, J. Power Sources 90, 231 (2000)
8. P. Staiti and M. Minutoli, J. Power Sources 94, 9 (2001)
9. P. Staiti, Mater. Lett. 47, 241 (2001)
10. P. Costamagna, C. Yang, A.B. Bocarsly and S. Srinivasan, Electrochim. Acta 47, 1023 (2002)
11. C. Poinsignon, I. Amodio, D. Foscallo and J.Y. Sanchez, Mater. Res. Soc. Symp. Proc. 548, 307(1999)
12. B. Bonnet, D.J. Jones, J. Rozière, L. Tchicaya, G. Alberti, M. Casciola, L. Massinelli, B. Bauer, A. Ieraio and E. Ramunni, J. New Mater. Electrochem. Syst. 3, 87 (2000)
13. J.S. Wainright, J.-T. Wang, D. Weng, R.F. Savinell and M. Litt, J. Electrochem. Soc. 142 7, L121 (1995)
14. R. Bouchet and E. Siebert, Solid State Ionics 118, 287 (1999)
15. M. Kawahara, J. Morita, M. Rikukawa, K. Sanui and N. Ogata, Electrochim. Acta 45, 1395 (2000)
16. J.A. Kerres, J. Membr. Sci. 185, 3 (2001)
17. R. Tanaka, H. Yamamoto, A. Shono, K. Kubo and M. Sakurai, Electrochim. Acta 45, 1385 (2000)
18. S.M.J. Zaidi, S.F. Chen, S.D. Mikhaikenko and S. Kaliaguine, J. New Mater. Electrochem. Syst. 3, 27(2000)
19. J.C. Lassègues, J. Grondin, M. Hernandez and B. Marée, Solid State Ionics 145, 37 (2001)
20. Rhim, J W and Kim, Y K, J. Appl. Polym. Sci., 75, 1699 (2000)
21. Chiang, W Y and Chen, C L, Polymer, 39, 2227 (1998)

$(PEO)_n:Na_4P_2O_7$ - A REPORT ON COMPLEX FORMATION

AMRTHA BHIDE * AND K. HARIHARAN

Solid State Ionics Laboratory, Department of Physics,
Indian Institute of Technology Madras, Chennai – 600 036, India.
*Corresponding author. Tel: +91-44-22578667; Fax: +91-44-22578651.
E-mail : amrith@physics.iitm.ac.in

ABSTRACT

A new polymer electrolyte, based on poly (ethylene oxide) complexed with $Na_4P_2O_7$, is investigated. $(PEO)_n:Na_4P_2O_7$ polymer metal salt complexes with different n = [ethylene oxide]/ Na ratio (80,100,120,160 and 200) are prepared by solution casting method. Dissolution of the salt into the polymer host is investigated by X-ray diffraction, differential calorimetry and Scanning electron microscopy techniques. The formation of the complex has been confirmed by (i) the broadening and reduction in the intensity of the Bragg peaks (ii) the reduction in the percentage of crystallinity by DSC and (iii) the increase in the glass transition temperature of the polymer with addition of the salt. Maximum reduction in crystallinity from 76.1 % to 56.2 % is observed for $(PEO)_{120}:Na_4P_2O_7$ system. Qualitative analysis of FTIR spectra in the range 3000-500 cm^{-1}, reveals broadening of the bands corresponding to the C-O-C symmetric stretching modes around 840 cm^{-1} and 1057-1160 cm^{-1}. These conformal changes have inferred the coordination of the ether oxygen of the PEO with the metal salt ion. Compositional dependence of conductivity studies show a maximum value of 7.58×0^{-7} S/cm at 351 K for O:Na = 120.Conductivity of the above electrolytes proceeds via an activated conduction mechanism with two activation energies, 0.62 eV and 0.78 eV above and below the softening of the polymer. The electronic transport number measured by dc polarization technique shows that, the conducting species are ionic in nature.

1. INTRODUCTION

Solvent free metal salt complexes belong to the class of superionic materials called polymer electrolytes. These materials are extensively studied in recent years and potentially used in solid state electrochemical devices such as secondary batteries, electro chromic display devices etc [1]. Polymer electrolytes are particularly attractive because of their flexibility, ease of processing into thin film of large surface area, electrochemical stability and volumetric stability over repeated charge discharge cycles of the device.

In order to achieve a well complexed polymer metal salt complex system, choice of polymer as well as the metal salt plays a key role and only a few very common guidelines are available for choosing the polymer host and the metal salt [2, 3]. The choice of polymer host mainly depends on the factors [4] such as (i) presence of a sequential polar group with large sufficient electron donor power to form coordination with cation (ii) low hindrance for bond rotations, favoring easier segmental motion and (iii) suitable distance between coordinating centers, in order to form multiple intrapolymer ionic bonds. It is found that the anions with larger radius possess least lattice energy and those with low charge density have least tendency to form tight ion pairs. Therefore the most common anions, aiding the complexation include, I^-, SCN^-, ClO_4^-, $CF_3SO_3^-$, BF_4^-, AsF_6^- etc. However the coordination of cation with the functional group of the polymer and stability of the complexation depends on Hard Soft Acid Base (HSAB) principle [1, 2]. In this context, a large number of polymer hosts such as Poly (ethylene oxide), Poly(propylene oxide), Poly(ethylene imine) have been reported complexing with various alkali metal

salts. The polymer, poly (ethylene oxide)(PEO), receives much attention as the host polymer, because of its ability to dissolve high concentration of a wide variety of metal salts, better electrochemical stability and flexibility as compared to the other polymer hosts [5]. The choice of the cation is restricted to a group of small ions, because of the scope of the electrolyte in device application, and hence the size of the anion finds important role in fulfilling the criteria of lattice energy. On the basis of these factors, solubility of the various alkali metal salts in PEO, has been well reviewed in the literature [3,4].

Recently, we have reported complex formation of sodium metaphosphate with PEO, viz.,$(PEO)_n$:$NaPO_3$ [6] . As on date no report seems to be available on PEO complexing with alkali metal salt with multivalent anion. In this context, we have further investigated complex formation of sodium metal salt with a multivalent anion viz., sodium pyrophosphate ($Na_4P_2O_7$) with the polymer host PEO. $(PEO)_n$:$Na_4P_2O_7$ polymer metal salt systems (n = 80,100,120,160,200) have been prepared and the complex formation has been investigated through X-ray diffraction, differential scanning calorimetry and scanning electron microscopy and fourier transform infrared spectroscopy (FTIR) techniques. The conductivity of these systems and transport number measurements were also studied by ac impedance spectroscopy and dc polarization techniques.

2. EXPERIMENTAL

PEO (Mol wt. 4×10^6, Aldrich) was dried under vacuum at 50°C for 10 h prior to use. Anhydrous $Na_4P_2O_7$ was obtained on heating the $Na_4P_2O_7$. $10H_2O$ (Merck) salt at 150 °C for about 24 h. Appropriate quantities of PEO and of anhydrous sodium orthophosphate were estimated, in order to prepare polymer metal salt complexes with ether oxygen to sodium ion concentration (O:Na) ratio of 80,100, 120, 160, 200. Each of these compositions was dissolved in acetonitrile (AR grade) and stirred continuously using a magnetic stirrer for approximately 24 h. The resulting homogeneous viscous solution was poured into a PTFE petri dish and vacuum dried at 50 °C for 48 h in order to remove all the traces of solvent.

X-Ray diffraction patterns of the anhydrous $Na_4P_2O_7$ salt, PEO and polymer electrolytes in the form of film were obtained by PANalytical X-ray generator in the 2θ range 10° to 60 ° using Cu-K_α radiation. All the measurements were taken under identical condition for unambiguous comparison. Thermal behavior of the complexes has been studied using NETZSCZ DSC (200 Phox), over the temperature range of -100 to 100 °C. Polymer samples of about 5-6 mg were sealed in aluminum pans and experiments were carried out under nitrogen gas atmosphere. Surface morphology of gold coated polymer films has been carried out using JEOL Scanning Electron Microscope (JSM 840). FTIR absorption spectra were recorded by a Perkin-Elmer spectrometer in the frequency range 3000 cm^{-1} to 500 cm^{-1} at a resolution of 2 cm^{-1}. The impedance measurements were performed using a Keithley 3330 impedance analyzer in the frequency range 40 Hz to 100 kHz and the impedance data has been collected through a GPIB (IEEE-488) interface bus.

3. RESULTS AND DISCUSSION

3.1 Characterization of the polymer electrolytes - XRD ,DSC and SEM studies

A comparison of XRD pattern of $Na_4P_2O_7$ salt, PEO and polymer metal salt complexes with different O:Na ratio are shown in Fig 1. Pure PEO shows two broad peaks around

20° and 23°, indicating the semi crystalline nature of the polymer. XRD pattern of the complexes showed broadening and reduction in the intensity of the PEO peaks. This can be attributed to enhancement in the amorphous phase, due to the destruction of the ordered arrangement of the polymer side chains. In addition, low intense peaks corresponding to the strong lines of the $Na_4P_2O_7$ are observed.

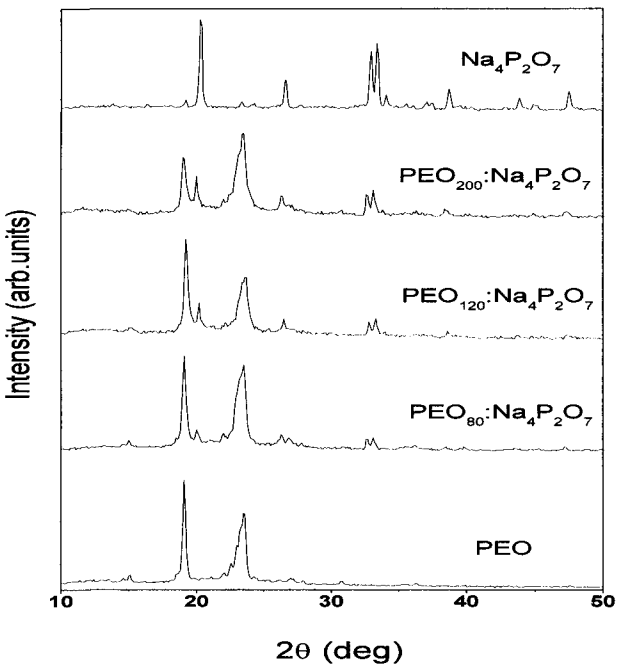

Fig. 1. XRD patterns of PEO, $Na_4P_2O_7$ and $(PEO)_n$:$Na_4P_2O_7$ polymer electrolytes

Table 1 shows the thermal properties of the polymer metal salt complexes. The value of glass transition temperature (T_g) is found to increase with increase in salt concentration. The increase in the value of T_g can be attributed to the reduction in polymer chain flexibility due to the interaction of the ether oxygen of the polymer chain and the Na^+ ion. The melting points of the polymer electrolytes are found to vary over a range of few degrees with respect to that of pure PEO (63.7 °C). This indicates the presence of crystalline regions of various degrees of perfections in the complexed samples [7]. The polymer-salt interaction occurring, due to the addition of salt causes disorder in oriented crystalline rich phase. The crystallinity of polymer metal salt complex is calculated from the equation

$$X_C = \frac{\Delta H_m}{\Delta H^0_{PEO}} \quad (1)$$

where ΔH_m is the enthalpy of melting of the sample and ΔH^0_{PEO} is the enthalpy of melting of 100 % crystalline PEO, 213.7 Jg^{-1} [8].
At the lower concentrations of the salt (high O/Na ratio) the change in crystallinity is least affected. Crystallinity of the composition with O: Na = 120 has reduced to a minimum of 44.9% compared with 63 % for the polymer host. On further increase in the salt concentration crystallinity increases and this can be attributed to the crystalline rich phase with uncomplexed salt.

Table 1 Thermal properties of the PEO and and $(PEO)_n$:$Na_4P_2O_7$ polymer electrolytes

O:Na ratio	T_g (°C)	T_m (°C)	Crystallinity (%)
Pure PEO	-61.1	63.7	63.1
200	-54.2	60.2	56.6
160	-53.6	64.1	54.7
120	-52.5	62.6	44.9
100	-51.0	61.9	50.4
80	-49.3	60.9	53.0

Fig 2a-2d shows scanning electron micrograph of the pure PEO and $(PEO)_n$: $Na_4P_2O_7$ metal salt complexes. The micrograph of the pure PEO shows bright and dark regions in the form of stripes, which corresponds to the crystalline and amorphous phase of the polymer film. On addition of the salt the dark region corresponding to the amorphous phase increases, indicating enhancement in the amorphous phase. At higher salt concentration (O: Na = 80), micrograph shows a region of uncomplexed salt, as well as amorphous rich region. On further decreasing the salt concentration, amorphous rich phase and uniformly arranged spherulitic nuclei like structure was observed.

3.2 Infrared spectroscopy studies:

On addition of salt into the polymer host, the cation of the metal is expected to coordinate with the ether oxygen of the polymer, resulting in complextaion. This type of interaction will influence the local structure of the polymer back bone and certain infrared active modes of vibration will become affected. In this context, infrared spectroscopic studies will give the evidence of the complextaion. FTIR spectra of pure polymer, $Na_4P_2O_7$ and polymer electrolytes with different O:Na ratio are shown in Fig 3. Spectral features of the polymer electrolyte systems are found to be similar to that of pure PEO. Prominent changes were observed in the following spectral region indicating the compelxtaion. (i) In the spectral range 1050 -1160 cm^{-1}, significant changes have been observed in width and intensity of the vibrational bands of PEO, with the addition of $Na_4P_2O_7$ at different concentrations. These conformal changes correspond to C-O-C symmetric vibrational

modes[9,10] . These conformal changes, corresponding to those IR active vibrational bands involving ether oxygen, indicate the complexation of alkali metal ion to the ether oxygen (ii) The width of the strong absorption band of C-H stretching modes seen in the region 2800-2950 cm^{-1}, decreases with increasing salt concentrations. (iii) The rest of the bands in the above range are found to be similar to that of PEO, confirming that the guche CO-CO conformation of pure PEO remains unaffected on complexation. Similarly, the vibrational bands seen in the range 1242-1280 cm^{-1} assigned to the CH_2 wagging modes and those observed in the range 992-1012 cm^{-1} assigned to CH_2 rocking remain unchanged [9]. A detailed analysis has not been carried out because of poor resolution of the spectra.

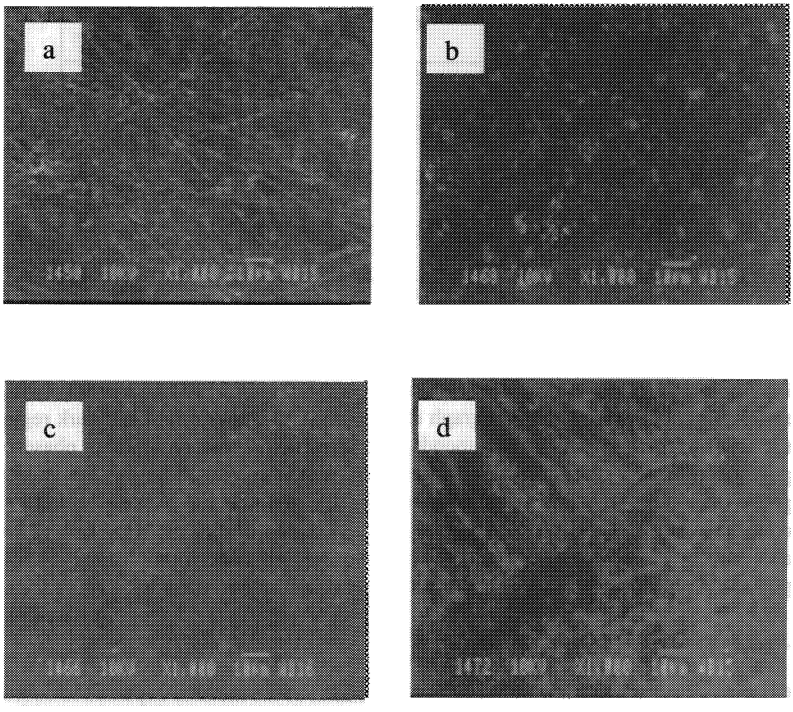

Fig.2 Scanning electron micrographs : (a) pure PEO, (b) O:Na = 80 (c) O:Na= 120 (d) O:Na = 200

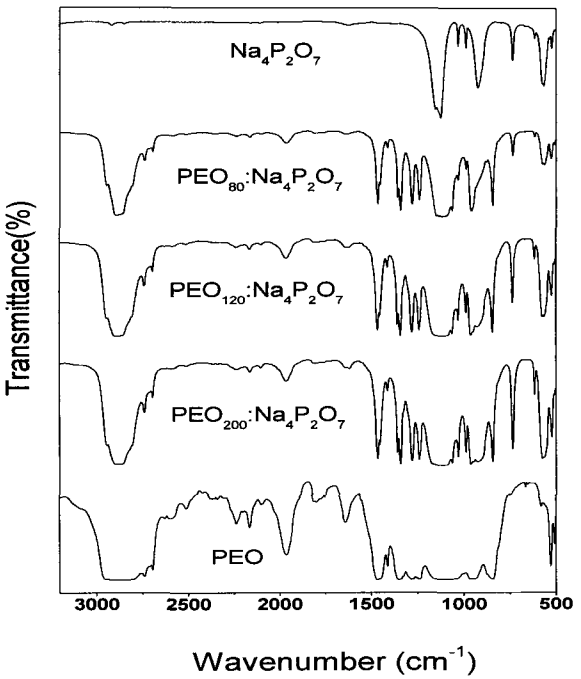

Fig. 3.FTIR spectraof pure PEO, $Na_4P_2O_7$ and $(PEO)_n:Na_4P_2O_7$ polymer electrolytes

3.3 Conductivity studies

Conductivity measurements of the above polymer electrolyte samples have been carried out as a function of temperature. The samples were heated to 350 K and the measurements were carried out while cooling the sample. Conduction characteristics were investigated from the experimental data collected in terms of modulus of complex impedance | Z | and phase angle θ, as a function of frequency. Subsequently the values of real (Z′) and imaginary (Z″) part of the impedance were plotted on a complex plane. The impedance plots were analyzed using 'EQUIVCRT' non linear fitting programme to obtain the bulk resistance. Knowing the dimensions of the sample, conductivity has been calculated.

The temperature dependent conductivity of polymer electrolytes of different O:Na ratio is shown in Fig. 4. The plots show Arrhenius behavior with distinct change in the slope around 340 K, above which the polymer metal salt complex starts softening. This feature indicates that the polymer metal complex has crystalline phase throughout the temperature range. The plots are fitted to the relation

$$\sigma = \sigma_0 \exp\left(\frac{-E_a}{K_B T}\right) \tag{2}$$

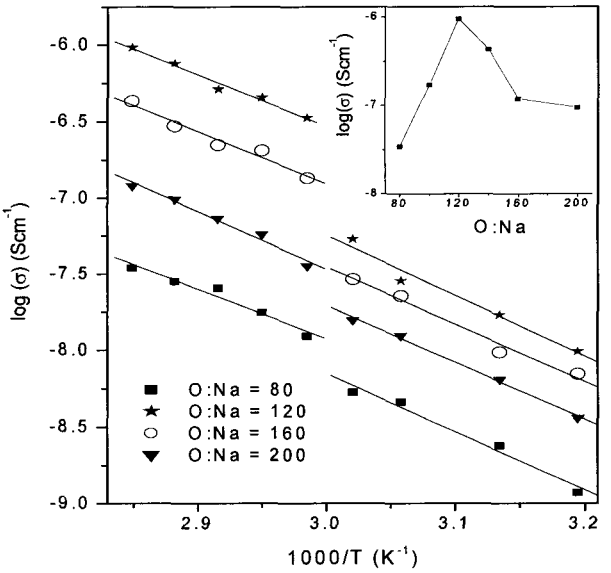

Fig 4. Temperature dependent conductivity of different compositions .Inset: Conductivity as the function of composition at 450 K.

using linear fit program, where σ_0 is the pre exponential factor , E_a is the activation energy, K_B is the Boltzmann constant and T is the absolute temperature. All the samples consistently show higher conductivity above the softening point with low activation energy, indicating that the amorphous phase is responsible for ionic conduction. The polymer electrolyte system $(PEO)_{120}$:$Na_4P_2O_7$ has exhibited a maximum conductivity of 7.58 x 10^{-7} Scm^{-1} at 351 K, which is above the softening point of the polymer electrolyte system. This conductivity value clearly indicates an enhancement in the ionic conductivity compared to the value of polycrystalline $Na_4P_2O_7$, reported to be less than 10^{-9} Scm^{-1} at 473 K [11]. On further increasing or decreasing the salt concentration, the conductivity decreases (Inset of Fig 4). The activation energy for ion migration is found to be 0.80 eV and o.62 eV at below and above the softening point of polymer host respectively. In the case of polymer electrolyte systems, the elastomeric phase favors the migration of carrier ions via the micro-Brownian motion of polymer segments. Also the ions find easier path ways in interchain and intrachain polymer segments, favoring the enhancement in the conductivity [12].

3.4 Transport number measurement

The sample has been placed between a pair of silver blocking electrodes and maintained at 345 K for two hours. On application of a 100 mV dc potential, to the above configuration, instantaneous initial current I_0, was found to be 13 μA. After a long interval of 18 h, the cell got completely polarized, reaching a steady state current of 0.32

nA., the polarization current can be attributed to the migration of ions due to the applied field, which is balanced by diffusion, due to the concentration gradient. Thus the resulting steady state current is only due to electrons or holes and the electronic contribution is found to be 0.02. The ionic contribution evaluated through the equation [13],

$$t_i = 1 - \left(\frac{I_s}{I_0} \right) \quad (3)$$

is found to be nearly equal to unity.

CONCLUSIONS:

Polymer electrolytes of PEO complexed with sodium pyrophosphate have been prepared by solution casting method and the complexation has been confirmed through XRD, FTIR and SEM studies. XRD results indicate dissolution of salt in the polymer host with an enhancement in the amorphous nature. The DSC results indicate a decrease in the crystallinity with increase in the salt concentration along with a increase in glass transition temperature. Scanning electron micrographs have distinctly shown semi-crystallinity of the polymer host and enhancement in the amorphous phase upon complexation. Conformal changes in the IR active bands of the PEO, have indicated the coordination of the alkali metal ion with the ether oxygen of the polymer. Polymer metal salt $(PEO)_{120}$:$Na_4P_2O_7$, exhibiting amorphous rich phase has shown maxium ionic conductivity with an activation energy of 0.60 eV, above softening point of the polymer. Transport number measurement studies reveal ionic nature of the conducting species in the polymer electrolyte.

REFRERENCES:

1. P. G. Bruce, Solid State Electrochemistry, Cambridge University Press: Cambridge,1995.
2. F.M.Gray , Polymer Electrolytes :Fundamentals and Technological Applications, VCH publications, New York, 1991.
3. C. A. Vincent, *Prog. Solid State Chem.*, **17**, 145 (1987).
4. M. A. Ratner and D.F.Shriver, *Chem. Rev.*, **88,** 109 (1988) .
5. J.R. MacCallum and C. A. Vincent, in Polym. Electrolyte Rev., Vol 1, Elsevier,1989.
6. Amrtha Bhide and K.Hariharan, *J. Power Sources*, Article in press (2006) .
7. B.L. Papke, M.A. Ratner and D.F.Shriver , *J.Electrochem. Soc.*, **129**, 1434 (1982)
8. M. D. Glasse, R.J.Latham, R. G .Linford , W.S.Schlindwein and A. Careem, *Solid State Ionics* , **72**, 127 (1994)
9. J.H. Shin, K.W.Kim, H.J.Ahn and J.H.Ahn , *Mat. Sci. Eng.*, **B 95**, 148 (2002).
10. S.J. Wen, T.J.Richrdson, D.I.Ghantous, K.A.Striebel, P.N. Ross and E.J.Cairns, *J. Electroanal. Chem.*, **408**,113 (1996).
11. S.Villain, E.Nigrelli and G.Nihoul, *Solid State Ionics*, **116**,73 (1999).
12. Masayosshi Watanabe and Naoya Ogata, *Brit. Poly.J.*, **20**,181 (1988).
13. N. Srivastava, A.Chandra and S.Chndra, *Phys.Rev.*, **B 52**,225 (1995).

EXPERIMENTAL STUDIES ON (PVC+$LiClO_4$+DMP) POLYMER ELECTROLYTE SYSTEMS FOR LITHIUM BATTERY

CH. V. SUBBA REDDY, Y. Y. QI, Q. Y. ZHU, H. X. LIU, X. J. ZHAO, W. CHEN[†]

Institute of Materials Science and Engineering, Wuhan University of Technology, Wuhan, 430070, P.R.China

Poly (vinyl chloride)(PVC)-based solid polymer electrolyte films with $LiClO_4$+plasticizer (dimethyl phthalate) have been prepared by the solution -cast technique. Various experimental techniques have been used, such as X-ray diffraction (XRD) and infrared spectroscopy (IR), a.c. impedance spectroscopy and transport number measurements, to characterize these polymer electrolyte films. The complexation has been confirmed from XRD and IR studies. A maximum room temperature conductivity (1.1×10^{-4}S/cm) has been observed for (PVC+$LiClO_4$+DMP)(20:5:75) complex. The temperature dependent conductivity plots show Arrhenius behaviour. The activation energy is estimated and the results are discussed. The transference number data indicated that the conducting species in these electrolytes are the anions. Using this electrolyte, electrochemical cells are fabricated and their discharge profiles are studied under constant load.

1. Introduction

Solid polymer electrolytes, i.e. polymer salt complexes, are of technological interest due to their possible application as solid electrolytes in various electrochemical devices such as energy conversion units (batteries/ fuel cells), electrochromic display devices/smart windows, photoelectrochemical solar cells, etc. [1-6]. Among the polymer systems reported, poly (ethylene oxide)(PEO) is the most widely studied in terms of its complexation behaviour with several metal salts [7,8]. PEO/metal –salt complexes exhibit high ionic conductivities at (or) near ambient temperature and thus are attractive candidates for electrochemical applications. The poor mechanical strength of PEO electrolytes in the high conduction region is, however, a severe drawback.

Poly (vinyl chloride) (PVC) is a commercially available, inexpensive polymer and is compatible with many plasticizers such as dibutyl phthalate (DBP) and dioctyl adipate (DOA). The resulting plasticized PVC has good mechanical strength and is widely used in the form of films, sheets and moldings for plastic leather and curtains, lead-wire coating, flooring, wallboard, etc. A reproduction

[†] Corresponding author. Tel.: +86 27 87651107; fax: +86 27 87864580.
E-mail address: chenw@mail.whut.edu.cn (W. CHEN)

in the resistivity of plasticized PVC is sometimes required to obtain anti-electrostatic properties. Elasticized PVC has been widely used as membranes in ion-selective electrodes [9-13]. Further, a PVC-based polymer electrolytes system plastcized by ethylene carbonate and propylene carbonate has been reported [14] as being applicable to lithium and lithium –ion secondary batteries. In this context, it is important to optimize the conductivity and electrochemical properties of plasticized PVC systems.

In the present paper, we report a new polymer electrolyte (PVC+$LiClO_4$) system with DMP in various mole ratios for Li^+ conduction. Investigations with X-ray diffraction (XRD), infrared spectroscopy (IR), and a.c. impedance spectroscopy are undertaken and measurements of electrical conductivity are reported.

2. Experimental

PVC (molecular weight: 1.5×10^5) and $LiClO_4$ were mixed with DMP in various weight ratios. Solution –cast films with thickness of 100 m were obtained by pouring the solutions of PVC and $LiClO_4$ in distilled tetrahydrofuran (THF) on Teflon bushes and then drying at room temperature (303K). The films formed were again dried in a vacuum oven at 323K at a pressure of 10^{-3} Torr for 24 h. The polymer films thus obtained were stored in a desiccator. The composition details of the samples are shown in the Table 1.

Table 1.Composition details of samples

Sample	PVC (wt%)	$LiClO_4$ (wt%)	DMP (wt%)
A	20	5	75
B	25	5	70
C	35	5	60
D	45	5	50

The XRD patterns of the films were made with a HZG4/B-PC X-ray diffractrometer with CoKα radiation and graphite monochrometer. Fourier transform infrared (FT-IR) absorption spectra of the films were recorded using a 60-SXB IR spectrometer with a resolution of 4 cm-1. The measurements were taken over a wave number range of 690-4000cm-1. The ac impedance measurements of the polymer electrolytes were performed using an Agilent 4294A precision impedance analyzer in the range 40Hz to 100kHz and temperature range 298-373K. The transport number was evaluated using the technique described by Linford [15]. In this technique a freshly prepared film of

(PVP+$LiClO_4$+DMP) was polarized in a configuration of C/ (PVP+$LiClO_4$+DMP)/ C under a dc bias potential of 1.5 V. The resulting current was monitored as a function of time using a Keithley electrometer. The cationic transference number is given by:

$$\tau_+ = I_{+\infty}/I_T$$

Here $I_{+\infty}$ is the cationic current at saturation and I_T is the total ionic current at time zero.

Solid-state electrochemical cells were fabricated with a configuration of Li/(PVC+$LiClO_4$+DMP)/ (C+I_2). Details of the fabrication of the electrochemical cell are given elsewhere [16]. The cathode was made in the form of a pellet at a pressure of ~5 ton/cm2 after proper mixing of the iodine + graphite (I_2+C) (1:1 ratio).

3. Results and discussion

The XRD patterns of pure PVC, $LiClO_4$ and complexed PVC are presented in Figure 1. The patterns of pure PVC and complexed PVC indicate low crystallinity. By contrast, $LiClO_4$ is found to be crystalline. No peaks corresponding to $LiClO_4$ are observed in complexed PVC, which indicates the absence of excess salt (uncomplexed) in the materials.

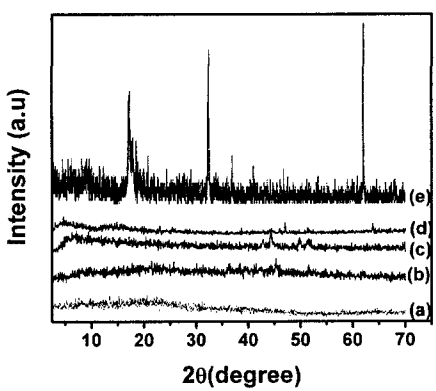

Figure 1. XRD patterns of $LiClO_4$ complexed (PVC+DMP):(a) Sample A; (b) Sample B; (c) Sample C; (d) Sample D and (e) Pure $LiClO_4$.

The IR spectra were recorded in the range 690 to 4000 cm^{-1} in the transmittance mode. The spectra for pure PVC, pure $LiClO_4$, DMP and PVC+$LiClO_4$+DMP complexes are shown in Figure 2. The peak at 1275cm^{-1} is assigned to the CH-rocking vibration in pure PVC, which is shifted to 1290 cm^{-1}

in the complex. This suggests that the Li ion may be located on the vinyl chloride of the polymer chain- $[CH_2\text{-}CHCl\text{-}]_n$.

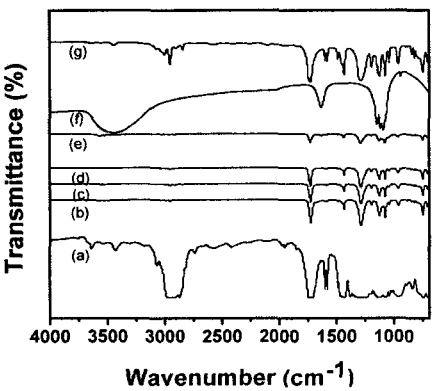

Figure 2. IR spectra of $LiClO_4$ complexed (PVC+DMP):(a) Pure PVC; (b) Sample A (c) Sample B; (d) Sample C (e) Sample D; (f) DMP and (g) Pure $LiClO_4$.

A comparison indicates that some additional peaks appear in complexed PVC at 1724, 1434 and 1193cm^{-1}. These peaks are not associated with pure PVC, $LiClO_4$ or DMP. In addition to this, the disappearance of pure PVC bands at 3640, 3429, 2564, 1355 and 1075cm^{-1} in the complexes suggests the co-ordination or complexation of Li^+ ions to the chlorine of PVC. The disappearance of some of the peaks observed for pure $LiClO_4$ (3444, 2903, 2033 and1956cm^{-1}, etc.) in polymer complexes may be due to the fact that ClO_4^- ion is in different surroundings in the polymer complexes compared with those in the pure $LiClO_4$ salt. In summary, these observations confirm the complexation of $LiClO_4$ with PVC.

The ionic conductivity has been calculated from ac impedance analysis using the cell with blocking electrodes as described in Section 2. The typical impedance plot of (PVC+$LiClO_4$+DMP)(20:5:75) at ambient temperature is shown in Figure 3. The bulk resistance of the system was measured from the high frequency intercept on the real axis. The lower frequency region spur in Figure 3 shows the ion blocking nature of the steel-steel electrode.

The variation of the logarithm of ionic conductivity (log σ) with inverse absolute temperature for various complexes is presented in Figure 4. There is a linear relationship which can be described as 'apparently Arrhenius' and is given by $\sigma = \sigma_0 \exp(-E_a / kT)$ where σ_0 is a constant, k, the Boltzmann constant and

E_a, the activation energy. The conductivity values and activation energies of the four complexes are listed in Table 2.

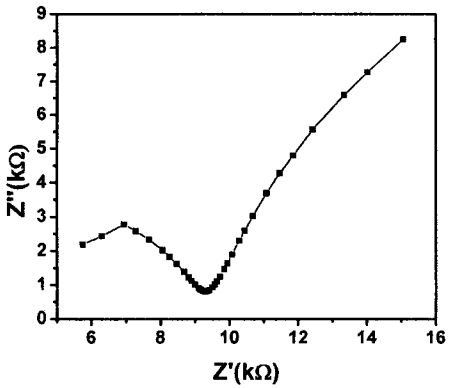

Figure 3. Impedance plot of the Sample A polymer electrolyte at ambient temperature.

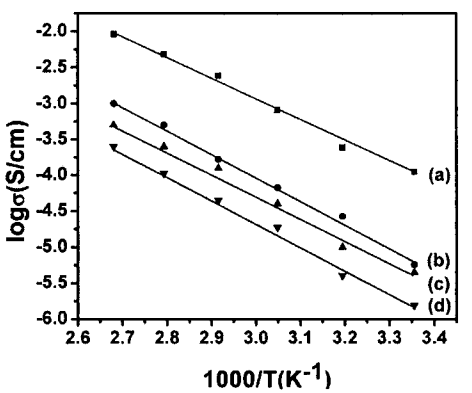

Figure 4. Log plots of conductivity vs.1000/T for (a) Sample A; (b) Sample B; (c) Sample C; (d) Sample D.

The conductivity decreases markedly, from 10^{-4} to 10^{-7}S/cm, as the mole fraction of PVC is increased from 20 to 45 and the logarithm of the conductivity decreases almost proportionally with increase in the PVC mole fraction. The decrease in conductivity is mainly due to the decrease in mobility of the ions. Although it has been found [17] that the addition of PVC facilitates ionic dissociation in a solution of $NaBPh_4$ in a PVC membrane plasticized by dioctyl sebacate, the addition of PVC to the present ionic system seems to reduce the

ionic mobility and the degree of dissociation does not seem to be enhanced by the PVC addition. The ionic conductivity increases with temperature, in agreement with theoretical considerations. It was found that the ionic conductivity increases as the concentration of plasticizer increases. This may be due to the lowering of viscosity with increasing plasticizer concentration.

Table 2. Conductivity values of (PVC+$LiClO_4$+DMP) polymer electrolytes

Sample	Conductivity ($\times 10^{-4}$ S/cm)				Activation energy E_a(eV)
	298K	328K	358K	373K	
A	1.1	8.11	48.10	92	0.15
B	0.057	0.67	5	10	0.27
C	0.044	0.40	2.5	5	0.34
D	0.015	0.36	1.67	2.5	0.38

The plot of C/(PVC+$LiClO_4$+DMP)(20:5:75)/C for transference numbers is given in Figure 5. The transference number of the lithium ions in the polymer electrolytes is around 0.20. This implies that the major conducting species in these electrolytes are anions ClO_4^-. The saturated polarization current is the cationic current, the anionic current has been impeded by concentration polarization. Other reports have obtained lithium ion transference number between 0.40 and 0.50 with $LiCF_3SO_3$ as the salt [18], 0.30 with $LiBF_4$ salt [7] and 0.03-0.08 with LiTFSI salt [18].

The first discharge curve of the (PVC+$LiClO_4$+DMP)(20:5:75) at room temperature is shown in Figure 6. The initial sharp decrease in voltage from 3.92 to 3.68V of the cell due to polarization and /or formation of a thin layer of lithium salt at the electrode/electrolyte interface. The open circuit voltages (OCVs), short circuit currents (SCCs), current density, power density and energy density were respectively found to be 3.92 V and 415 μA, 27.8 μA/cm^2, 56.92 mW/kg and 39845 mWh/kg for the cell.

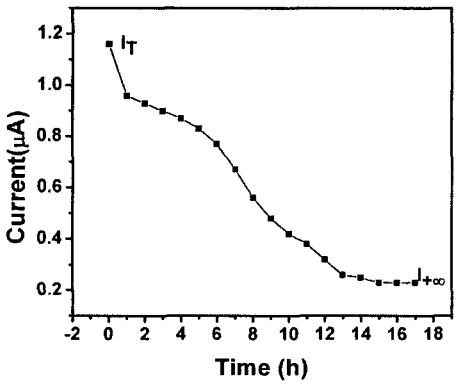

Figure 5. Current vs. time plot of Sample A polymer electrolyte system.

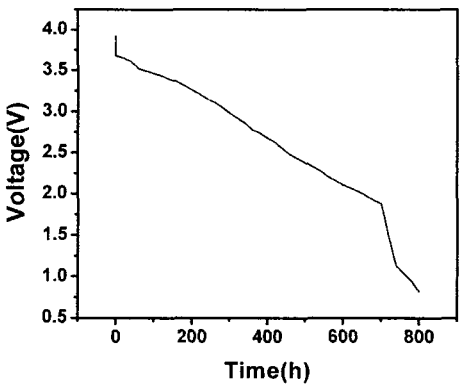

Figure 6. Initial discharge curve of the Sample A polymer electrolyte system.

4. Conclusions

The conductivity decreases markedly, from 10^{-4} to 10^{-7}S/cm, as the mole fraction of PVC is increased from 20 to 45 and the logarithm of the conductivity decreases almost proportionally with increase in the PVC mole fraction. The value of the activation energy decreases with increasing ionic conductivity and vice versa. The transference number data has indicated that the conduction in these electrolytes are due to anions. Using (PVC+$LiClO_4$+DMP) polymer electrolyte systems, electrochemical cells have been fabricated for which the OCVs and SCCs are founded to be 3.92Vand 415 μA for sample A.

Acknowledgments

One of the authors (Ch.V.S.Reddy) wishes to thank the Wuhan University of Technology Management for the financial support in the form of a Post Doctoral Fellowship to carry out the above work. "The project supported by the foundation for Innovative Research Team of Hubei province (No.2005ABC004)".

References

1. M. B. Armand, Annu.*Rev.Mater.Sci.***16**, 245 (1989).
2. J. R. MacCallum, C. A. Vincent (Eds.), Polymer Electrolytes, *Elsevier, Amsterdam*, 1987
3. M. A. Ratner, D. F. Shriver, *Chem.Rev.***88**, 109 (1988).
4. J. R. Owen, in: A. L. Lasker, S. Chandra (Eds.), Superionic Solids and Solid Electrolytes-Recent Trends, *Academic Press, New York*, p.111 (1989).
5. C. A. Vincent, Prog. *Solid State Chem.***17**, 145(1987)
6. M. A. Ratner, *Mater.Forum* **15**,1 (1991).
7. J. R. Mac Callum, C. A. Vincent, Polymer Electrolyte Reviews, **Vol.2**, *Elsevier, London,* 1989.
8. J. Prozyluslci, *J.Solid State Phenom*, **11-12**, 208 (1990).
9. G. J. Moody, R. B. Oke, J. D. R. Thomas, Analyst **95**, 10 (1970).
10. G. J. Craggs, J. D. R. Moody, J. Thomas, *J.Chem.Educ.***51**, 541(1974).
11. W. E. Morf, W. Simon, in: H. Freiser (Ed.), Ion-Selective Electrodes in Analytical Chemistry, *Plenum, New York*, p.211, (1978).
12. S. Rajendran, T. Uma, *J. Power Sources* **87**, 218 (2000).
13. S. Ramesh, A. K. Arof, *Mat.Sci.Eng.B* **85**, 11 (2001).
14. M. Alamgir, K. Abraham, *J.Electrochem.Soc.***140, 96** (1993).
15. R. G. Linford, in: B. V. R. Chowdari, S. Radhakrishna (Eds.), Solid State Ionic Devices, *World Scientific, Singapore*, p.551, (1986).
16. M. Jaipal Reddy, D. Srinivas Reddy, S. Sreepathi Rao, U. V. S. Rao, *Mater.Lett.***23,** 129 (1995).
17. R. D. Armstrong, M. Todd, *J.Electroanal.Chem.***237**, 181 (1987).
18. M. Watanabe, A. Nishimoto, *Solid State Ionics* **79**, 306 (1996).

STABILITY OF THE GEL ELECTROLYTE, PAN : EC : PC : $LICF_3SO_3$ TOWARDS LITHIUM

K.PERERA[a], M.A.K.L. DISSANAYAKE[b*], S. SKAARUP[c], K. WEST[d]

[a]*Department of Electronics, Wayamba University of Sri Lanka, Kuliyapitiya, Sri Lanka,*
[b]*Department of Physics, University of Peradeniya, Peradeniya, Sri Lanka,*
*(*E-mail: director@pgis.lk)*
[c]*Department of Chemistry, Technical University of Denmark, Denmark,*
[d]*Riso National Laboratory, Denmark*

The stability of the gel electrolyte consisting of polyacrylonitrile (PAN), ethylene carbonate (EC), propylene carbonate (PC) and lithium trifluoromethanesulfonate ($LiCF_3SO_3$ – LiTF) towards metallic lithium was investigated using the time evolution of impedance plots. Symmetric cells of the form Li / PAN : EC : PC: LiTF / Li were assembled and impedance data were collected at room temperature for one week. A clear indication of growth of a resistive layer could be seen. The electrolyte resistance remained constant. The growth of the passivation layer became constant after first two days. These observations suggest that this gel electrolyte is suitable for use with metallic lithium.

1. Introduction

Gel electrolytes were first introduced in 1975 by Feuillade and Perche[1] and later Watanabe et al.[2]. A large amount of work has been done on many aspects of the type of material. Preparation is accomplished by encapsulating a liquid electrolyte in a suitable polymer matrix. The observed level of ionic conductivity values of those gel electrolytes have resulted a considerable attention towards exciting novel applications. Among the polymer matrices use for gel electrolytes, polyacrylonitrile has shown a promising candidacy for various applications [3,4]. But, due to the presence of liquid electrolytes, all gel electrolytes have a higher tendency to react with metallic lithium than the pure polymer system. Hence, it is of prime importance to investigate their stability towards metallic lithium mainly because most applications are associated with metallic lithium.

2. Experimental

A mixture of ethylene carbonate (EC) (ALDRICH, 98%) and propylene carbonate (PC) (Bie and Berntsen A-S, 99%) of 1:1 (by weight) was dried over molecular sieves for 24 hrs. The required amount of lithium trifluoromethanesulfonate

($LiCF_3SO_3$ – LiTF) (3M) was mixed in purification was done using activated alumina. The required amount of polyacrylonitrile (PAN) (ALDRICH) was dissolved and the mixture was heated at 140 ^{0}C for 1 hr. The resulting homogeneous and viscous mixture was poured between two well cleaned glass plates and pressed. On cooling, transparent films could be obtained which were free from bubbles. All the preparation steps were carried out in side an Argon filled glove box. Two disc shaped samples of lithium and an electrolyte of the identical diameter were used for AC measurements. A symmetric cell of the form, Li / polymer electrolyte / Li was assembled in a sample holder in side an Argon filled glove box. Impedance data were collected at room temperature using a computer controlled Solatron 1170 frequency response analyzer for a period of one week. The frequency range used was in the range 10 mHz to 1 MHz. The time evolution of the impedance plots was plotted to investigate the growth of resistive layers. Impedance data were analyzed using NLLS (Non – Linear Least Square) fitting routine developed by Boukamp[5] to determine electrolyte resistance and passivation layer resistance.

3. Results and Discussion

Fig. 1 shows the time evolution of the complex impedance plots at room temperature. The gradually increasing nature of the arcs is an indication of a growth of a passivation layer on the electrolyte / electrode interface. In each impedance plot, the usual semi circle at high frequency range is absent. It may be due to the insufficient frequency range selected for the investigation. Whenever lithium is exposed to a non aqueous system, reactions occur forming surface solid compounds of organic and inorganic lithium salts on the surface. These films deposit until they reach a certain thickness and prevent the lithium surface from further attacks. Electrical properties of the lithium- electrolyte interface are thought to appear as a combination of several types of time constants reflecting several processes. Some of them are charge transfer resistance coupled with metal-film interfacial capacitance, film resistance to lithium ion migration coupled with film capacitance and lithium ion diffusion [6].

The electrolyte components in the system studied here (EC, PC) are well known for reacting with lithium. However, they do not both have the same reactivity towards lithium. This means that the selectivity of reaction processes which lead to formation of surface films changes while building up process is going on. Indeed, the formation of an interface composed of several layers of different compositions and structures appears to be the most favoured. Because of this, we tend to assign the two semi circles in the impedance plots to a porous interface and to a dense interface. It should be noted that the semi circle at high frequency section represents a dense layer and the other a porous

layer. Furthermore, it has been reported that a definite role is played by the electrolyte salt in controlling the phenomenon[7]. In this case, it may be possible to assume that F in $LiCF_3SO_3$ reacts with Li_2O, Li_2CO_3 and LiOH which are reported to exist on lithium electrodes [8]. The expected reaction product is LiF. Depending on the porosity of this LiF layer, solvents may permeate to lithium and react with it.

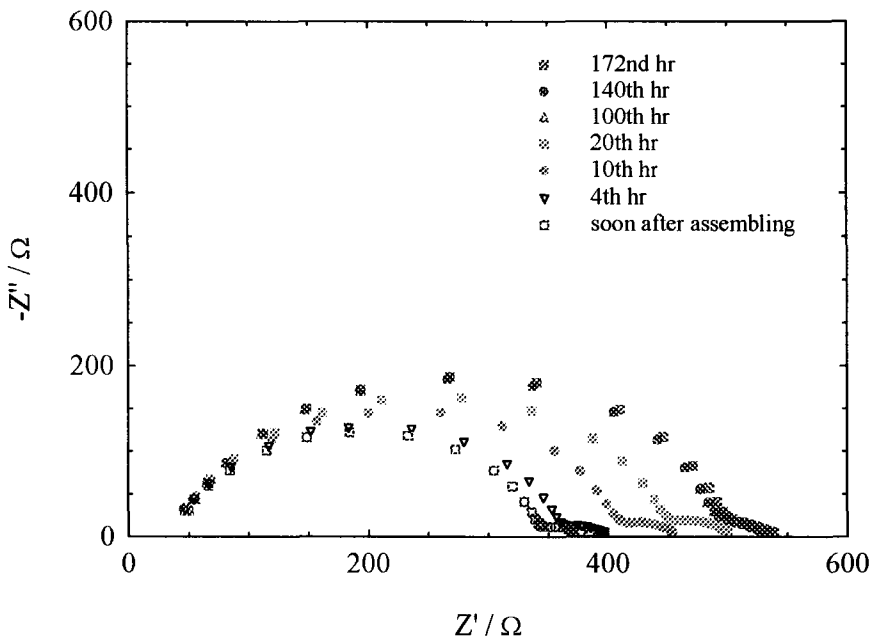

Fig. 1 Time evolution of the impedance arcs measured with the symmetric cell, Li / PAN : EC : PC : $LiCF_3SO_3$ / Li at room temperature

The impedance data analysis was carried out using the NLLS (non linear least square) fitting routine - EQUIVCRT developed by B. A. Boukamp to determine the electrolyte resistance and the passivation layer resistance [5]. Their time evolution is shown in Fig. 2.

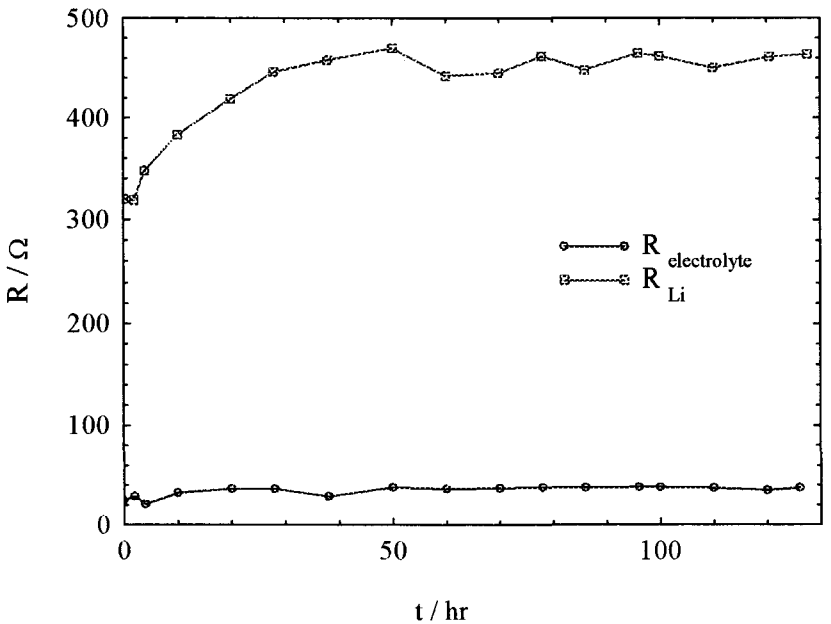

Fig. 2 Time evolution of resistance of the polymer electrolyte and the lithium electrode as extracted from impedance data

The bulk electrolyte resistance has remained almost constant. This indicates that the encapsulated liquid electrolyte in the polymer matrix has not changed its electrochemical properties with time [9,10]. However, it is clearly seen that although there is an increase of the passivation layer resistance, the growth rate has been faster during first two days. This occurs when the initially created passivation layer masks further reaction. A similar observation has been reported by H. Hong et al for the system PAN : EC : PC : $LiClO_4$ [11].

It is a common fact that the nature and mechanism of passivation depend not only on the type of electrolyte but also on the temperature of operation and the residual impurities. D. Ostrovskii et al have suggested that in PAN based electrolytes, polymer matrix groups are the species reacting with lithium electrodes[12]. Inherent reactivity of cyano (C≡N) group versus lithium has been assumed as responsible for formation of the passivation film.

4. Conclusion

The relatively constant electrolyte resistance suggests that the encapsulated liquid electrolyte in the polymer matrix has not changed its electrochemical properties. Since the growth rate is fast only during the first two days, the initially created passivation layer may hinder further growth. Therefore, the effects of a change in the passivation layer decrease with time. The results suggest that the investigated gel electrolyte can be used in combination with lithium electrodes without blocking the electrode reactions.

Acknowledgements

Authors wish to gratefully acknowledge the support provided by the International Programmes in Physical Sciences, Uppsala University, Sweden.

References

1. G. Feuillade, Ph. Perche, J. Appl. Electrochem., 1975, 5,63
2. M. Watanabe, M. Kanba, K. Nagaoka, I. Shinotvara, J. Polymer Science, Poly.Physics Edition 21(983)939.
3. K.M. Abraham, H.S. Choe, D.M. Pasquariello, Electrochim. Acta, 43/16- 17(1998)2399.
4. F.M. Gray, (Ed.) in: Polymer Electrolytes; F.M. Gray (Ed.) The Royal Society of Chemistry, United Kingdom, 1997, Chapter 5.
5. B.A. Boukamp, Equivalent Circuit Users Manual, Second Edition, 1989.
6. A. Zaban, E. Zinigrad, D. Aurbach, J. of Phys. Chem., 100 (1996)3089-3101.
7. F. Croce, F. Gerace, G. Dautzemberg, S. Passerini, G.B. Appetecchi, B. Scrosati, Electrochimica Acta, 39 / 14(1994)2187-2194.
8. K. Kanamura, H. Tamura, S. Shiraishi, X. Takehara, J. of Electrochem Soc., 142/2(1995)340.
9. Dong-Won Kim, Young-Roak Kim, Jung-Ki Park, Seong-In Moon, Solid State Ionics, 106(1998)329-337.
10. K. M. Abraham, Z. Jiang, B. Carroll, Chem. Mater., 9(1997)1978-1988.
11. Hong, H., Liquan, C., Xuejie, H., Rongjian, X., Electrochimica Acta, 37 / 9(1992)1671-1673.
12. D. Ostrovskii, L. M. Torell, G. B. Appetecchi, B. Scrosati, Solid State Ionics, 106(1998)19-24.

MONTMORILLONITE AS A CONDUCTIVITY ENHANCER IN $(PEO)_9LiCF_3SO_3$ POLYMER ELECTROLYTE

C. H. MANORATNE[1], R. M. G. RAJAPAKSE[1*], M. A. K. L. DISSANAYAKE[2], W. M. A. T. BANDARA[1] and D. T. B. TENNAKOON[1]

[1]*Department of Chemistry, University of Peradeniya, Peradeniya*
[2]*Department of Physics, University of Peradeniya, Peradeniya*

The solid polymer electrolyte systems, based on poly(ethylene oxide) (PEO) and lithium ions have attracted much attentions as a potential electrolyte medium in secondary energy sources and electrochromic devises. They show a characteristic property of an enhanced ionic conductivity when a plastizier is added. In this research work, PEO and lithium triflate have been taken as the electrolyte medium and an attempt was paid to improve the ionic conductivity of $(PEO)_9LiCF_3SO_3$ polymer electrolyte system by choosing montmorillonite (MMT) as the plastisizer. The ionic conductivity, thermal transitions, crystallinity, and bonding of the complex system of $(PEO)_9LiCF_3SO_3$ + x wt.% MMT (x = 0, 3, 4, 5, 6, 10, 15, 20) were systematically characterized by ac-impedance spectroscopy, differential scanning calorimetry (DSC), X-ray diffraction (XRD) spectroscopy and fourier transformed infrared (FTIR) spectroscopy, respectively.

The ac-impedance data reveal that the ionic conductivity of $(PEO)_9LiCF_3SO_3$ system is changed with the concentration of MMT, maximum conductivity of 4.14857×10^{-7} S cm^{-1} at room temperature was observed for the system of $(PEO)_9LiCF_3SO_3$ + 5 wt.% MMT . However, the ionic conductivity of the above system was increased with the increase of temperature, and the highest conductivity of 2.63×10^{-4} S cm^{-1} was observed at 80°C. The DSC and XRD data clearly show that the crystalline nature of PEO is reduced when MMT is added. The glass transition temperature (-46.37°C) and melting temperature (53.72°C) of the above system is reduced compared to those of other systems. This supports to the conductivity enhancement in an amorphous environment.

The FTIR spectra obtained for MMT, PEO, $(PEO)_9LiCF_3SO_3$, and $(PEO)_9LiCF_3SO_3$ + 5 wt.% MMT clearly indicative that the interactions take place between these constituents, as the intensities of typical stretching vibrational modes of 916 cm^{-1} ν (Al-O-H), 1040 cm^{-1} ν (Si-O) and 3300-3700 cm^{-1} ν (O-H) in MMT, and the vibrational modes of CH_2 rocking at 948 and 840 cm^{-1} and C-O stretching at 1149 and 1090 cm^{-1} in PEO are shifted. The change of symmetric bending mode of CF_3 [δ_s (CF_3)] at 752 cm^{-1} in lithium triflate has altogether supported the bonding characteristics in the electrolyte system and the corresponding conductivity enhancements.

1.0 Introduction

The ionically conducting polymers, widely called "polymer electrolytes" have been the subject in the early 1970s. Wright and Armand who were the pioneers of the studying of ionically conducting polymers opened an innovative area of

materials research [1,2]. This has been further enhanced with the relentless work of Shirakawa, Heeger and MacDiarmid on electrically conducting polymers, such as poly(acetylene) (PAC), poly(pyrrole) and poly(aniline) and the applicability of electronically conducting polymers in long-lasting and reduced volume lithium batteries manufactured for cellular phones and note books, redox type laminated supercapacitors, multichromic optical windows and high-energy rechargeable batteries for electric vehicles and in organic oxide intercalation cathodes [3]. The composites based on ionically conducting polymers and layered clay are widely being studied in the development of nanotechnology [4]. These hybrid materials show same properties as of their conventional composites in the scale of nanometers. The increased optical properties, Young's Modulus, strength, heat resistance, decreased gas permeability and flammability, and conductivity enhancement are some characteristic properties, associated with these complex composites [5].

It is clear that much attention have been focused on the polymer electrolytes based on high molecular weight poly (ethylene oxide) (PEO) and metal salts (e.g. $LiClO_4$, $LiCF_3SO_3$, $LiBF_3$, LiCl and $NiCl_2$ in the fundamental and application-oriented studies [6-8]. The improved mechanical properties, ease of fabrication as thin films and good contact and compatibility with electrode materials, e.g. Li metal and lithiated metal oxides ($LiMn_2O_4$, $LiCoO_2$ or $LiNiO_2$) have been the intense characteristics in these materials [9]. However, some unfavorable properties associated with them have lead to a considerable delay in their use in commercial applications [1,5,10,11]. One typical drawback is its low conductivity at ambient temperatures [12]. Even though PEO has remarkable solvating properties on alkali metal salts, its high crystalline nature reduces the ambient temperature conductivity or the Li^+ ions transport in these electrolyte materials. It has been observed that the structure of polymer electrolytes (PEs) has clear influence on the conductivity. Therefore, the

straightforward approach to overcome this problem is the modification of the structure of the solvating polymer, whereby decreasing the crystallinity and glass transition temperature, T_g of the polymer electrolyte [13]. Several methods have been tried to address this problem such as the use of co-polymers, the addition of plasticizers and radiation cross-linking [14]. However, compare with other method addition of plasticizers has many advantages viz increase of free volume of the polymer, the usability of variety of plasticizers and lower the glass transition temperature by decrease in polymer-polymer interaction and increase in polymer-plasticizer interactions. In addition to that the film preparation from these materials is a simple process and cost of plasticized material is comparatively low. The purpose of plasticizing a polymer electrolyte matrix is to reduce the local viscosity and thereby facilitating the faster ion mobility (e.g. Li^+) within the electrolyte medium, which in turn enhances the conductivity [15]. In early stages liquid plasticizer have been widely used in the development of polymer electrolyte. The addition of low molecular weight organic nonaqueous solvents, like ethylene carbonate (EC), propylne carbonate (PC), dimethyl sulphoxide (DMSO), dimethyl carbonate (DMC), diethyl carbonate (DEC), and oligomeric poly (ethylene glycols) and their derivatives have been proposed as the effective plasticizers used in previous works [5,15,16]. However, the use of liquid plasticizers have been gradually declined due to some associated problems such as poor mechanical properties, higher reactivity towards lithium anode, confined difficulties in handling, battery cyclability and high reactivity, prone to leakage and an evidence of plasticizers loss during long term storage [1,5,13]. This has led to the use of solid plasticizers in place of solid plasticizers. The addition of high surface area nano-scale ceramic fillers such as Al_2O_3, SiO_2, TiO_2 and γ-$LiAO_2$ in PEO based polymer electrolytes can act as solid plasticizers. These complex systems are known as "nanocomposite polymer electrolytes" [6]. This can improve the

amorphous phase in the electrolyte system at ambient temperatures giving rise to an enhanced ionic conductivity by decreasing the crystallinity of the polymer and also improved mechanical and thermal stability in the range of 30-80°C, electrochemical stability and higher cation transport number [17]. It is also clear in the open literature that the esters of benzene 1, 2 dicarboxylic acids such as dioctyl phthalate (DOP), dibutyl phthalate (DBP) and dimethyl phthalate (DMP) have been used as novel class of plasticizers in PEO-$LiClO_4$ electrolyte system instead of aprotic solvents or inert fillers [15].

Nickel Chloride has also been used as a solid plasticizer in the synthesis of solid polymer electrolytes. A number of Electrochemical Impedance Spectroscopy (EIS) measurements in the frequency range 10^{-2} - 6.5×10^{4} Hz and in the temperature range 20-130°C have been reported for system of Ni/$(PEO)_xNiCl_2$/Ni, and this electrolyte has also been found to be an anionic conductor [18]. The use of smectite clay or montmorrilonite as a plasticizer in polymer electrolytes has been known for several decades, since their potential mechanical, structural and electrical properties in the modern opto-electronic applications [3,6,19]. Though PEO based electrolytes are having lack of dimensional stability and/or mechanical strength, addition of mineral clay can produce huge interfacial area to sustain the mechanical property of electrolyte system and imports salt-solvating power to dissolve the lithium salts. One such approach has been made by Lemmon and his group who have reported the intercalation of PEO within the inter gallery of Na-MMT by the process of exfoliation/adsorption method. It has been reported that the change of polymer/Na-MMT ratios influences the inter-gallery spacings in montmorrilonite. One such example is the increased interlayer spacing at higher polymer ratio [1,20-22].

A recent report focuses on the understanding the nanocomposites of modified montmorrilonite and poly(ethylene oxide). It showed that the addition of specific amount of poly(oxy propylene) diamine (d2000) and montmorrilonite

in the PEO-based electrolyte system could improve the enhanced conductivity at room temperature. In this study the specific interactions among silicate layer, d2000, ether oxygen, and lithium cation and the ionic conductivities have been investigated using differential scanning calorimetry (DSC), fourier transformed infrared (FT-IR), and alternating current impedance (AC Impedance). The effect of clay composition in the systems of $(PEO)_8LiClO_4$ and $(PEO)_8LiClO_4$/d2000 has been reported where the maximum conductivity was observed at 17 wt% in former system and at 9 wt% in latter. The overall outcome of this study is that, addition of a plasticizer such as montmorrilonite; d2000 can overcome the kinetic (lower T_g) and thermodynamic (dissolve the lithium ions) hindrances and produce a good environment for the lithium transference [1]. Since the understanding of some apparently inert and electrically insulating materials, which can promote the ionic conductivity of solid electrolyte, many scientists in all over the world have been involving to find out a suitable compound that will enhance the conductivity of solid electrolytes. Some relevant examples are alumina doped metal halides, such as LiI: Al_2O_3, AgBr: Al_2O_3 and AgCl: Al_2O_3 [23,24]. The defects concentration in the space charges at the interface between the alumina and AgBr enhanced the conductivity of the above composites. Accordingly the attention has been paid to the use of montmorrilonite, as a heterogeneous dopant due to its structure of charged platelets which might function as attractive centers for silver cation, should be a promising compound for the conductivity enhancement. The ionic conductivity of AgBr-montmorrilonite has been found to be increasing as a function of montmorrilonite in the range from 20 to 410°C. In this case the maximum conductivity has been observed at low montmorrilonite composition, and with increasing montmorrilonite composition the conductivity decreases. However, the composite shows higher conductivity than that of pure AgBr at low temperature range and at higher temperature it decreases than pure AgBr [25].

2.0 Experimental

2.1 *Materials*

The clay, sodium montmorillonite (Bentonite) was purchased from (Aldrich Chemicals, Milwaukee, WI). The crystalline poly (ethylene oxide) (PEO) (Aldrich Chemicals) with a weight-average molecular weight of 400,000, and the lithium trifluoromethanesulfonate (lithium triflate) ($LiCF_3SO_3$-LiTf) (Aldrich Chemicals, Milwaukee, WI), were used as received. Generally, the PEO, and salts are highly hygroscopic, therefore it is required to ensure the dryness of these materials prior to sample preparation. Normally, the salt is dried at 80-150°C for 24 h and then at room temperature for 24 h under dynamic partial vacuum (10^{-5} Pa). The PEO is dried at 40°C for 24 h under high vacuum.

2.2 *Preparative methods*

2.2.1 *Purification of montmorillonite*

The clay sample (montmorillonite) may consist of organic and inorganic impurities. Therefore, it is desirable to eliminate them as much as possible. The centrifuging and washing method were employed, which will have a least effect to the structure and chemical composition. The montmorillonite (50 g) was suspended in excess de-ionized water and stirred magnetically for about 48 h at room temperature. The suspension was centrifuged at 5000 rpm for two minutes, and the clear supernatant was decanted. The resultant slurry was re-dispersed in excess of de-ionized water and the above procedure continued. This procedure was repeated several times until the supernatant was free of any impurity. The clear supernatant observed, confirmed the absence of organic impurities in the montmorillonite. This slurry thus obtained kept in the normal environment to air-drying and used in other applications.

2.2.2 *Preparation of the solid polymer electrolyte (SPE) system of $(PEO)_9LiCF_3SO_3$ + x wt.% MMT*

The amounts of each of PEO, $LiCF_3SO_3$, and MMT were measured precisely as to the configuration of $(PEO)_9LiCF_3SO_3$ + x wt.% MMT, where x = 0, 4, 5, 6, 10, 15, and 20. Doubly distilled water was used as a solvent. In the first step the précised amounts of PEO and LiTf were completely dissolved in 5.00 cm^3 doubly distilled water by stirring for few minutes. Then a required amount of montmorillonite was mixed and further added 5.00 cm^3 of doubly distilled. The mixture was then magnetically stirred for 48 h until a homogenous suspension was observed. Thin films with 0.04–0.09 mm thickness were prepared by casting the gelatinous polymer suspension onto a Teflon sheet, allowing it to gradually drying in the normal environment. The samples were air dried at room temperature for two days and then kept in a decicator. However, all the samples were vacuum dried at 50°C for 48 h prior to measurements.

2.3 *Instrumentation and Characterization*

2.3.1 *AC impedance characterization*

The ac impedance measurements were carried out using a computer-interfaced SI 1260 IMPEDANCE/GAIN-PHASE ANALYSER over the frequency range of 8-10 MHz at the voltage of 20 mV. The composite film was sandwiched between stainless steel blocking electrodes (1.27 cm diameter.) and the temperature changed from 25°C to 80°C. The films thickness varied from .04 mm to 2.5 mm.

2.3.2 *XRD characterization*

In this work the X-ray diffraction patterns were conducted by SIEMENCE X-ray diffractometer (SIEMENCE, German). The effect of montmorillonite on crystallinity of PEO has been systematically studied.

2.3.3 *FTIR characterization*

FTIR spectra were collected on a JASCO FT/IR-410 spectrometer from 400 to 4000 cm^{-1}. The effect of addition of montmorrilonite to the polymer electrolyte of $(PEO)_9LiCF_3SO_3$ was systematically investigated.

2.3.4 *Differential Scanning Calorimetry (DSC) characterization*

The thermal characteristics of nanocomposite electrolytes were typically evaluated by Perkin Elmer Pyris 1 DSC differential scanning calorimeter with a liquid-nitrogen-cooled heating element. The samples, 10-20 mg were contained in aluminum DSC pans and sealed with a lid. An empty aluminum pan was used as reference. The samples were slowly cooled and then heated at a heating rate of 10°C min^{-1} from –120°C to + 120°C. A flow of N_2 gas was maintained over the perforated pan to keep away atmospheric moisture and to remove any decomposition products.

3.0 Results and Discussion

3.1 *XRD characterization*

3.1.1 *The effect of montmorillonite on crystallinity of PEO*

As reported elsewhere that the crystalline nature of PEO comparatively reduces the conductivity and low crystalline nature or amorphous nature support the conductivity in PEO based solid electrolyte systems [1]. We have systematically studied the effect of MMT on PEO crystallinity. The XRD spectra obtained for the pure PEO and MMTPEO system show that the crystalline nature of pure PEO is disturbed with the presence of MMT, see Fig. 1. As shown in the figure 1 the intensity of the peaks in PEO appearing at the 2θ of 19 and 23 is reduced and instead of sharp narrow peaks there appear broaden peaks. Some peaks appearing at 2θ of 26 and 27 completely disappear with the presence of MMT. In addition to that it was observed that the reducing capacity of crystallinity does

not depend on the concentration of MMT in the system. This was assumed to be due to the interactions that occur between clay layers and PEO molecules, thus breaking the helical structure of PEO molecules.

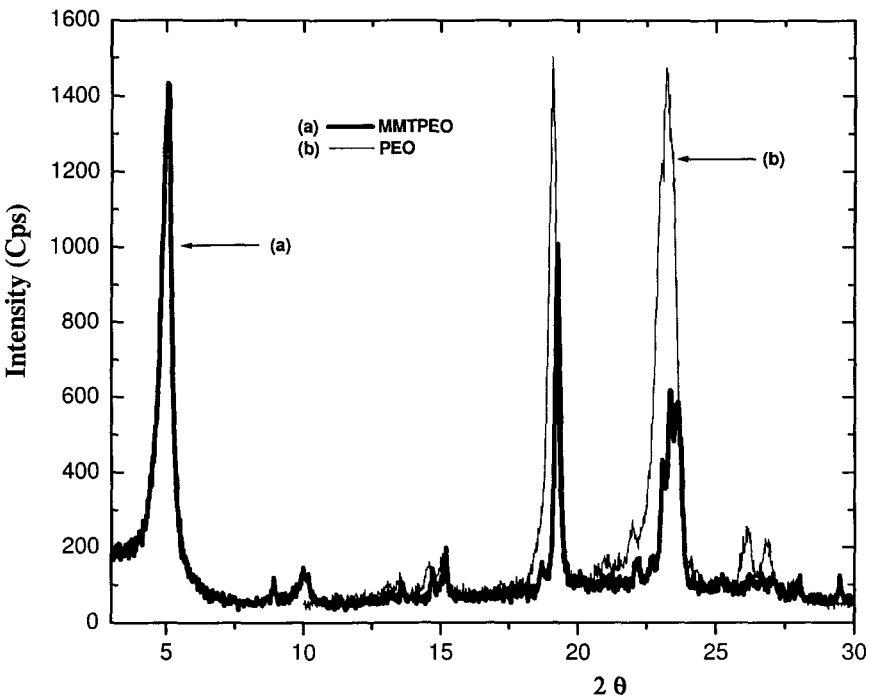

Fig. 1. The crystalline nature of (a) MMTPEO and (b) PEO.

3.2 *Conductivity characterization*

3.2.1 *The system of polymer electrolyte of* $(PEO)_9LiCF_3SO_3$ + *x wt.% MMT*

Figure 2 presents the temperature dependent Arrhenius plots of the ionic conductivity for the $(PEO)_9LiCF_3SO_3$ + x wt.% MMT electrolyte nanocomposites containing various MMT compositions. The ionic conductivity

curves obtained for the $(PEO)_9LiCF_3SO_3$ electrolyte system without MMT and pure MMT were included for comparison. The ionic conductivity spectra of these polymer electrolyte nanocomposite systems showed an enhanced ionic conductivity upon variation of MMT content. It was observed that when the MMT composition increases the ionic conductivity increases and attains a maximum value when the MMT composition is 5%. Figure 3 clearly shows the ionic conductivity dependency of the $(PEO)_9LiCF_3SO_3$ + x wt.% MMT observed at 298 K .

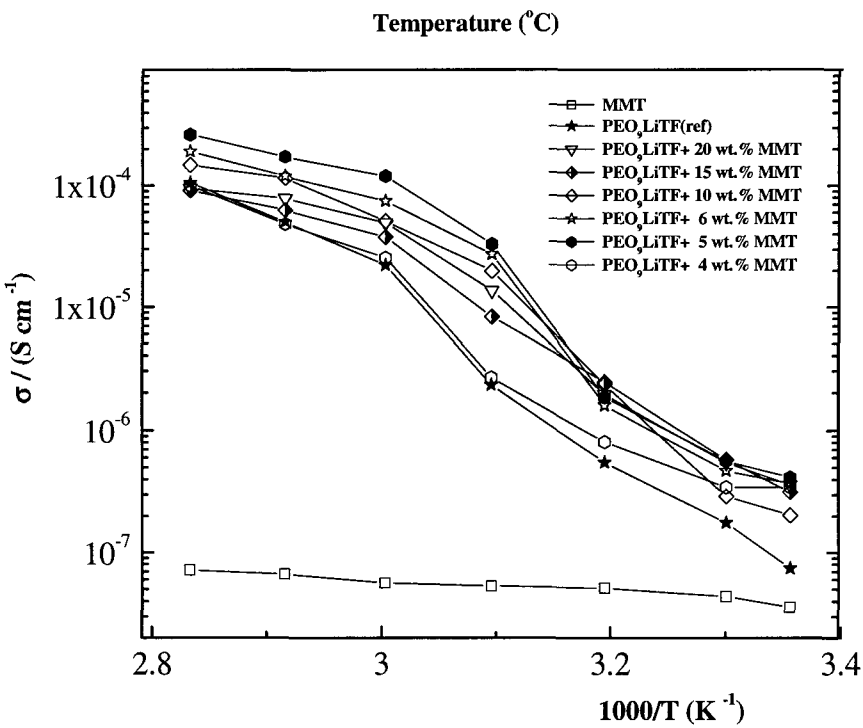

Fig. 2. Variation of the ionic conductivity with reciprocal temperature for the montmorrilonite and the system of $(PEO_9)LiCF_3SO_3$+ x wt.% MMT, x = 0, 3, 4, 5, 6, 10, 15, and 20.

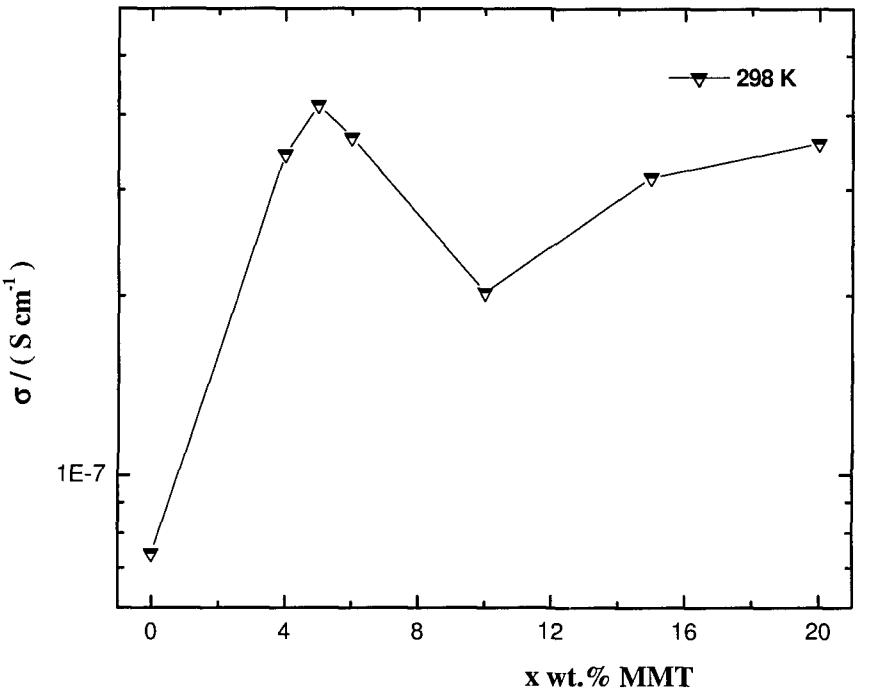

Fig. 3. Ionic conductivity dependency of $(PEO)_9LiCF_3SO_3$ composite electrolyte containing various MMT contents at 298 K.

It was observed that the ionic conductivity measured at room temperature for $(PEO)_9LiCF_3SO_3$ electrolyte system with varying MMT composition showed a conductivity enhancement in comparison to the electrolyte without MMT. With the increase of temperature the ionic conductivity increases. As observed in the conductivity curves the polymer electrolyte follows the arrhenius-type relationship over two linear ranges separated by a knee which, attributes to the melting point of PEO as confirmed by DSC characterization. This transition temperature (T_t) varies between 40°C and 60°C. It was observed that the conductivity enhancement is greatly influenced at 4-6 % composition of MMT and a maximum conductivity was observed at 5 wt.% MMT content. With a further increase in MMT content, the ionic conductivity decreases. When the

MMT is reduced to 4% the conductivity decreases considerably. However a slight difference can be observed at 15 wt.% MMT and 20 wt.% MMT content. In the $(PEO)_9LiCF_3SO_3$ + 15 wt.% MMT system it can be seen that the at low temperature region (25-40°C) the ionic conductivity is higher than in the system of $(PEO)_9LiCF_3SO_3$ + 10 wt.% MMT, and at higher temperature region it shows a lower enhancement. In the case of $(PEO)_9LiCF_3SO_3$ + 20 wt.% MMT, it shows a lower enhancement at low temperature region (25-40°C) than in the system of $(PEO)_9LiCF_3SO_3$ + 15 wt.% MMT, and at high temperature region it shows the opposite way. In the $(PEO)_9LiCF_3SO_3$ system without MMT exists transient cross-links between ether oxygen in PEO and Li^+. In addition to that polymer-polymer interaction may also remain which enable the crystalline nature of PEO [26]. As PEO has lower dielectric constant the solvation of the $LiCF_3SO_3$ is less. In addition to that the viscous nature of the medium restricts the mobility of Li^+ cations. Mnotmorrilonite in general has a high dielectric constant; as such it accelerates solvation of compound $LiCF_3SO_3$. On the other hand the negative clay layers tend to interact the Li^+ cations. Therefore, the addition of MMT decreases the attraction between PEO molecules, while reducing the crystalline nature of PEO. Due to these various interactions between PEO and MMT and Li^+ altogether influence the glass transition temperature (T_g) of the system. The DSC study showed that the presence of MMT tends to decrease the glass transition temperature in the $(PEO)_9LiCF_3SO_3$ system. The glass transition temperature observed for $(PEO)_9LiCF_3SO_3$ in this study is about -42.40°C, and it was observed that with the addition of MMT to the system reduces the T_g of the polymer electrolyte system. The T_g observed for the $(PEO)_9LiCF_3SO_3$ + 5 wt.% MMT system is -46.37°C. The bulky anion of $CF_3SO_3^-$ is large and its movement is comparatively less. It has been reported that the lithium salts with bulky anions such as lithium(bis)trifluoromethanesulfonate imide (LiTFSI or $Li(CF_3SO_2)_2N$) reduces the re-crystallization kinetics of the polymer electrolyte systems, thus enabling the conductivity at ambient temperatures [27]. It can also

be assumed that the $CF_3SO_3^-$ anion associates with H atoms of the free water molecules attached to surface of the clay layers. Therefore, the dominant mobile ion in this system is Li^+ cations. However, the overall conductivity data implies that the addition of an optimized MMT content able to drastically enhance the ionic conductivity in comparison to the polymer electrolyte without MMT. Moreover as observed, the presence of MMT in these polymer electrolytes increases the mechanical and thermal properties of the system, such as thin films preparation, strength of the films, flexibility, and durability etc. The large surface area of the MMT layers (200 m^2/gm, in the presence of water) also helps in creating more conducting pathways for Li^+ cations in addition to amorphous PEO network [18]. The crystalline nature of MMT also an important factor in considering the conductivity of polymer electrolyte system. Further the addition of MMT to the system increases the retention of average crystalline phase within the system. This can be seen as the T_g of the system shows a high value except in the system of $(PEO)_9LiCF_3SO_3$ + 10 wt.% MMT. However in this system the melting temperature (T_m) shows relatively high value than other systems. From all these available data it is understood that the balanced interactions in each constituent, in this case $(PEO)_9LiCF_3SO_3$ + 5 wt.% MMT supports the enhanced conductivity in the electrolyte system. It was already understood that the ionic conductivity in polymer electrolytes depends on the number of charge carriers and ionic mobility [28]. With the increase of temperature the mobility of Li^+ cations in each system accelerated, by which an enhanced ionic conductivity observed. The increasing temperature also contributes to the dissociation of ion pair, thus enhancing conductivity.

It is understood that beyond the melting temperature the polymer electrolyte is amorphous by its own nature, thus with high conductivity [29]. This can be attributed due to the specific interactions between the MMT layers and both PEO molecules and Li^+ cations. It implies that a reasonable conductivity

enhancement can be achieved by adding a correct amount of MMT content into the polymer electrolyte system.

3.3 *DSC characterization*

3.3.1 *Thermal behavior of polymer electrolyte system of $(PEO)_9LiCF_3SO_3$ + x wt.% MMT, x = 0, 5, 10,15, and 20*

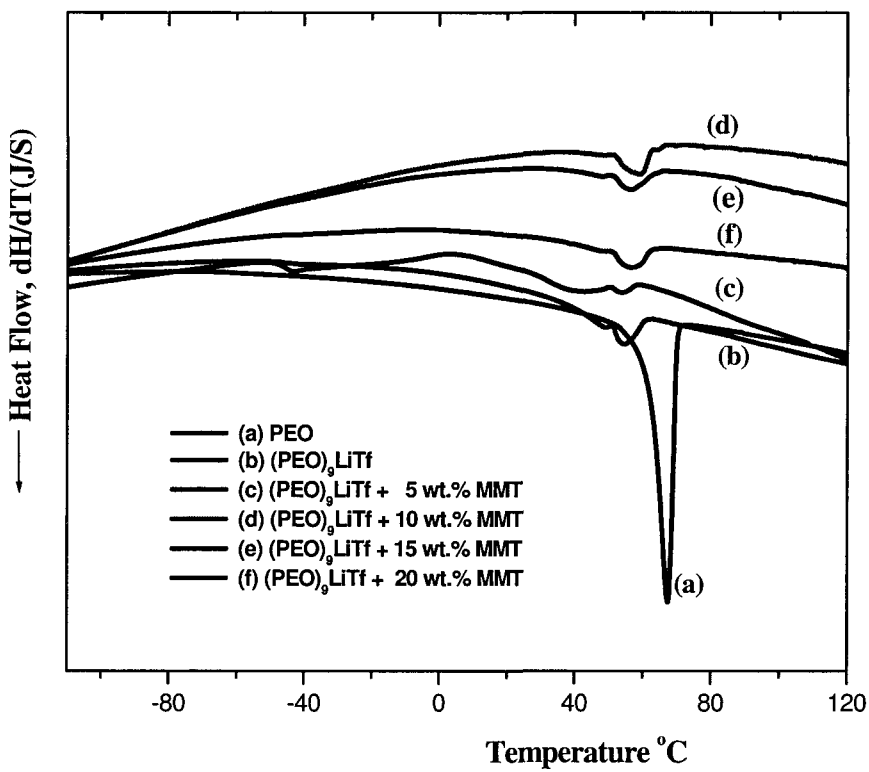

Fig. 4. DSC thermograms obtained for (PEO)9LiCF3SO3 + x wt.% MMT nanocomposite polymer electrolyte with the addition of various clay concentration (wt.%); (a) PEO, (b) (PEO)9LiCF3SO3, (c) 5 wt.% MMT, (d) 10 wt.% MMT, (e) 15 wt.% MMT, and (e) 20 wt.% MMT.

Table 1. The values of the melting temperature and glass transition temperature determined for PEO, $(PEO)_9LiCF_3SO_3$, $(PEO)_9LiCF_3SO_3$ + 5 wt.% MMT, $(PEO)_9$ $LiCF_3SO_3$ + 10 wt.% MMT, $(PEO)_9$ $LiCF_3SO_3$ + 15 wt.% MMT, and $(PEO)_9$ $LiCF_3SO_3$ + 20 wt.% MMT.

Sample Name	**Melting Temperature (T_m/°C)**	**Glass Transition Temperature (T_g/ °C)**
PEO	67.49	-55.97
$(PEO)_9LiTf$	64.80	-42.40
$(PEO)_9LiTf$ + 5 wt.% MMT	53.72	-46.37
$(PEO)_9LiTf$ + 10 wt.% MMT	58.69	-44.10
$(PEO)_9LiTf$ + 15 wt.% MMT	56.49	-44.86
$(PEO)_9LiTf$ + 20 wt.% MMT	56.55	-44.38

The thermal characterization of the system of pure, undoped PEO, the $(PEO)_9LiCF_3SO_3$ electrolyte, and $(PEO)_9LiCF_3SO_3$ + x wt.% MMT solid polymer electrolyte with varying MMT concentration has been systematically studied. Figure 4 shows the DSC thermograms obtained for pure PEO (Fig. 4(a)), $(PEO)_9LiCF_3SO_3$ (Fig. 4(b)), and $(PEO)_9LiCF_3SO_3$ + x wt.% MMT polymer electrolyte system containing 5, 10, 15, and 20 wt.% MMT. The values of T_m and T_g determined for each system are summarized in Table 1. The pure PEO shows an endothermic first order transition at ~ 67.49°C, which corresponds to the melting temperature of crystalline PEO phase. The DSC curves indicate that the addition of montmorrilonite can disturb the PEO crystalline nature, thus developing the softer and amorphous structure. In each MMT added polymer electrolyte system, the melting peak of crystalline PEO phase varies and is shifted to lower temperature than that of pure PEO and $(PEO)_9LiCF_3SO_3$. As shown in the thermograms a significant difference is observed in the system of $(PEO)_9LiCF_3SO_3$ + 5 wt.% MMT. In this system two endothermic first order transitions can be observed, which attribute to the glass transition temperature at ~ -46.37°C and melting temperature at ~ 53.72°C respectively. In addition to that the melting peak area of that system was

comparatively reduced, thus lowering the heat of melting temperature of crystalline phase. The ionic conductivity of polymer electrolytes is favored when the glass transition temperature and melting temperature are lowered [1,5]. According to the results of ionic conductivity enhancement of the systems of $(PEO)_9LiCF_3SO_3$ + x wt.% MMT, the maximum conductivity is reported in the system of $(PEO)_9LiCF_3SO_3$ + 5 wt.% MMT, in which both the glass transition temperature and melting temperature have been rationally lowered. This significant change of thermal behavior is due to the specific interactions between MMT layers, PEO and Li^+ cations in the polymer electrolyte system. This result is consistent with conductivity enhancement and FTIR analysis. Even though the change of glass transition temperature in the $(PEO)_9LiCF_3SO_3$ + x wt.% MMT systems, except $(PEO)_9LiCF_3SO_3$ + 5 wt.% MMT could not be traced the relative values were systematically determined using the available data. The above observations are consistent with other polymer electrolyte systems [30]. It was assumed that the polymer electrolytes based on alkali salt and PEO are in the crystalline state [31]. The addition of particular amount of MMT to the $(PEO)_9LiCF_3SO_3$ system interrupt the attraction between PEO and Li^+ cations. As such it reduces the crystalline nature of polymer matrix, thus forming a softer amorphous structure that will enable ionic transport in the polymer electrolyte. However, with further increase of MMT concentration the T_m increases and reaches a maximum value at 10% MMT and decreases as the MMT content is further increased. The FTIR analysis has shown that the specific interactions take place between MMT layers and Li^+ cations. Therefore, with the addition of MMT it breaks the interactions between PEO and Li^+ cations and makes bonds with clay layers. According to this phenomenon the PEO segments tend to recrystalize due to greater PEO chain flexibility. It is understood that the PEO used in this study may contain both crystalline nature and amorphous nature. With the addition of MMT above 5 wt.% the tendency to

convert the amorphous portion to crystalline also takes place. This is due to the interactions between MMT layers and PEO segments. As such the amorphous PEO gains an ordered arrangements improving crystallinity. Therefore now the T_m and T_g increase. Further addition of MMT shows that the PEO crystallinity is reduced. It can be seen that the T_m and T_g values obtained for the $(PEO)_9LiCF_3SO_3$ + 15 wt.% MMT and $(PEO)_9LiCF_3SO_3$ + 20 wt.% MMT remain almost same. It confirms that MMT layers rapidly interact with Li^+ cations. In addition to that the ether oxygen in PEO tends to associate with free –OH groups of octahedral layers in MMT. The bulky like medium due to the interactions of MMT and triflate anion also behave as crystalline retarders, thus inhibiting or disturbing crystalline nature. As such the T_m decrease. However, the small increment of T_g was observed at each successive addition. This can be assumed that, the crystalline nature of MMT itself presence in theses system more.

3.4 *FT-IR Characterization*

3.4.1 *Comparison of FTIR spectra of systems of $(PEO)_9LiCF_3SO_3$ + x wt.% MMT for x = 0, 4, 5, 10, 15, 20*

An attempt was made to understand the bonding conformations upon the varying of MMT composition in $(PEO)_9LiCF_3SO_3$ polymer electrolyte system. Figure 5 presents the FTIR spectra of $(PEO)_9LiCF_3SO_3$ + x wt.% MMT, x = 0, 4, 5, 10, 15, and 20 in the region 4000- 400 cm^{-1}. In addition, the spectra of analogous $(PEO)_9LiCF_3SO_3$ complex, and pure MMT are included for comparison.

It can be seen that with the increase of MMT composition in the $(PEO)_9LiCF_3SO_3$ polymer electrolyte system conspicuous changes occur in the regions of 3700-3100 cm^{-1} and 3000-2600 cm^{-1} . It is seen that the band at 3624 cm^{-1} which, corresponds to isolated –OH groups and a small shoulder appeared

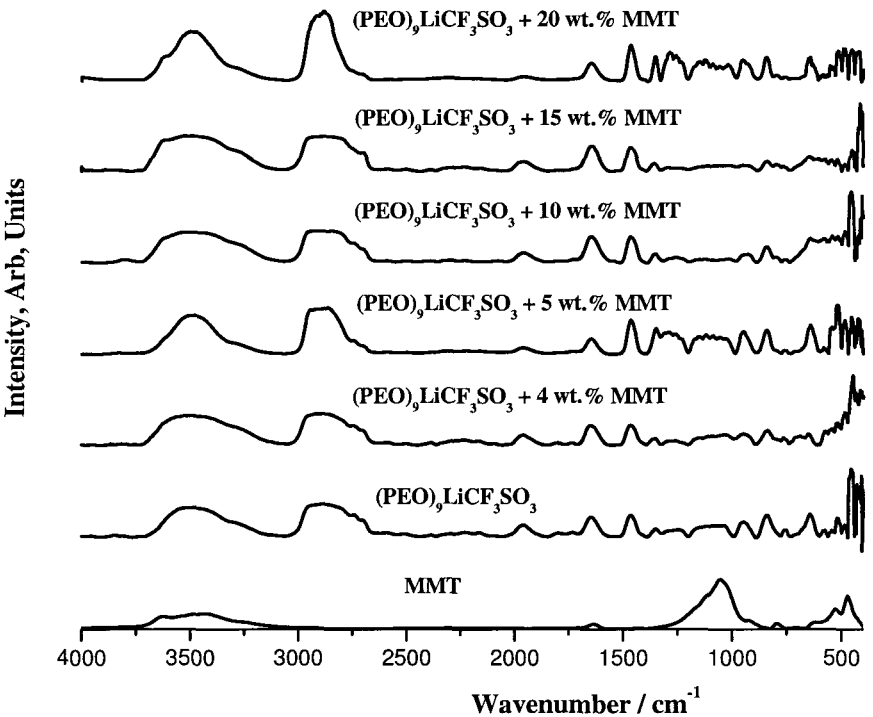

Fig. 5. FTIR spectra of the system of $(PEO)_9LiCF_3SO_3$ + x wt.% MMT for x = 0, 4, 5, 10, 15, 20.

at 3245 cm^{-1} in MMT were not observed in the system of $(PEO)_9LiCF_3SO_3$ + 4 wt.% MMT and $(PEO)_9LiCF_3SO_3$ + 5 w t.% MMT. However, with the increase of MMT composition they appear gradually. As seen in the $(PEO)_9LiCF_3SO_3$ + 10 wt.% MMT system these bands are slightly observable, in $(PEO)_9LiCF_3SO_3$ + 15 wt.% MMT system and $(PEO)_9LiCF_3SO_3$ + 20 wt.% MMT system they are clearly observed. Similar type of bonding mechanism can be seen in the region of 3000-2600 cm^{-1}, which corresponds to the $\nu(CH_2)_a$. The interactions between MMT and Li^+ cations increase as the MMT composition increases. This reduces the attractions between PEO and Li^+ cations. This happens up to a certain point, in this study at the $(PEO)_9LiCF_3SO_3$ + 5 wt.% MMT system. At higher MMT

concentration the medium becomes more viscous and bulky thus inhibiting characteristics bonding between MMT and Li^+ cations. Due to the PEO chain flexibility, the interactions between intermolecular forces in PEO molecules increase, which tends to arrange in an ordered manner. Accordingly the intensity of the band in 3000-2600 cm^{-1} region increases. The changes of the bands observed in the region of 2000-1700 cm^{-1} are also strategic. In the complex $(PEO)_9LiCF_3SO_3$ polymer electrolyte clear new two bands were observed at 1963 and 1735 cm^{-1}, which are not present either in pure PEO or $LiCF_3SO_3$. The bands can be assigned to the vibrational modes of CC and CO of the PEO. Here also the bands intensity increases as the MMT composition increases, except in the system of $(PEO)_9LiCF_3SO_3$ + 5 wt.% MMT, which shows an enhanced intensity. This also shows that the interactions occur between MMT layers and ether-oxygen of PEO segments. Similar type, but noticeable features were seen at 1646 cm^{-1} and 1465 cm^{-1}. A band in pure PEO at 1641 cm^{-1}, corresponding to the asymmetric CO stretching, $\nu(C\text{-}O)_a$ has been shifted to higher frequency in $(PEO)_9LiCF_3SO_3$ and centered at 1646 cm^{-1}. The band intensity increases upon the addition of MMT. This can be assumed that the Li^+ cations interact with ether-oxygen in PEO. It is known that the band at 1632 cm^{-1} which, corresponds to the bending vibrational mode, δ(O-H) of water molecules in pure MMT is also shifted to higher frequency when added to the polymer electrolyte system. It is also conspicuous that, the addition of MMT to the $(PEO)_9LiCF_3SO_3$ system, the intensity of the main band at 1646 cm^{-1} increases. This can be interpreted as the interactions of free –OH in MMT to the ether-oxygen.

This same bonding mechanism can be observed in the region of 1400-900 cm^{-1}, where asymmetric CH_2 bending mode in PEO is observed.

However, in the system of $(PEO)_9LiCF_3SO_3$ + 5 wt.% MMT a moderately increased band is observed. This further confirms the typical interactions between each constituent. The similar type of behavior was also observed at

1352 cm^{-1} and 1347 cm^{-1} absorption band which, corresponds to the wagging mode of CH_2 ($w(CH_2)_a$) and crystalline phase in PEO. Even though the band changes according to the increase of MMT composition, a drastic changes observed in $(PEO)_9LiCF_3SO_3$ + 5 wt.% MMT system. It confirms that at this addition the crystalline phase in PEO is significantly decreases. As discussed in earlier chapters it was shown that the vibrational modes of $t(CH_2)_a$, C-F, $\nu(COC)_a$, ν(Si-O), and $\nu(SO_3)$ are observed in the region of 1300 and 1000 cm^{-1}. Noticeably, the change of each mode in each polymer electrolyte system increases, except in $(PEO)_9LiCF_3SO_3$ + 5 wt.% MMT system. It can be interpreted that the MMT layers interact with PEO in addition to Li^+ cations, thus changing whole charge environment in the system. However, the balance interactions can only be observed in $(PEO)_9LiCF_3SO_3$ + 5 wt.% MMT which shows the typical properties in conductivity enhancement. The typical changes occur in the region of 1000-700 cm^{-1} are supporting in characterizing the effect of MMT and the conformation of PEO in the polymer electrolyte system. A significant change was observed at 958 cm^{-1} and 840 cm^{-1}, where $r(CH_2)_a$ and $r(CH_2)_s$ are critical. Although the intensity changes according to the MMT addition, they are intensed in $(PEO)_9LiCF_3SO_3$ + 10 wt.% MMT system than in $(PEO)_9LiCF_3SO_3$ + 15 wt.% MMT. These bands are sensitive to the interactions of cation with PEO backbone. Therefore, this confirms that the MMT layers rapidly interact with Li^+ cations, forming more crystalline phase. This phenomenon is consistent with the DSC studies discussed in other chapter. The symmetric bending mode of CF_3 ($\delta(CF_3)_s$) in $LiCF_3SO_3$ is particularly sensitive to the local anionic environment. In this $(PEO)_9LiCF_3SO_3$ + x wt.%. MMT system it is apparent that these three states of free anions, ion pairs, and $Li_2CF_3SO_3^+$ are present. However with the addition of MMT the intensity of above band increases, except in $(PEO)_9LiCF_3SO_3$ + 5 wt.%. MMT. As shown in figure, the band is conspicuous in the later system than rest. It is further confirmed the specific interactions by which typical properties are observed.

These results are consistent with the conductivity enhancement and corresponding DSC analysis. The overall data indicate that it is required to add a particular amount of plasticizer to a polymer electrolyte. According to the previous discussions it was assumed that the specific, balanced interactions between each constituent are behind the corresponding properties. Therefore, in the system of $(PEO)_9LiCF_3SO_3$ + 5 wt.% MMT typical interactions take place in supporting characteristics properties observed.

4.0 Conclusions

The application of gel-type $(PEO)_9LiCF_3SO_3$ polymer electrolyte, plasticized with MMT in the fabrication of electronic devices such as high power redox supercapacitors, secondary batteries and laminated electrochromic windows is a very promising new class of emerging future technology. The polymer electrolyte system of $(PEO)_9LiCF_3SO_3$ + x wt.% MMT showed considerable ionic conductivity enhancement than that of MMT free $(PEO)_9LiCF_3SO_3$. It was understood that the addition of an optimum amount of MMT to the system of $(PEO)_9LiCF_3SO_3$ increases the ionic conductivity at room temperature by one order of magnitude over that of $(PEO)_9LiCF_3SO_3$. In conforming that the system of $(PEO)_9LiCF_3SO_3$ + 5 wt.% MMT showed the maximum conductivity of 4.15×10^{-7} S cm^{-1} at room temperature out of different MMT added systems. The XRD and DSC studies confirmed that the crystallinity of PEO in this electrolyte system is disturbed, thus creating an amorphous environment, suitable for enhanced ionic conductivity. The FTIR spectra obtained for the polymer electrolyte system of $(PEO)_9LiCF_3SO_3$ + x wt.% MMT have provided further evidence to show that the helical structure of PEO that is responsible for PEO crystallinity has been distorted. This shows that the balanced attractive forces among silicate layers, lithium cations and ether oxygen give rise to an optimum ionic conductivity.

References

1. Chen, H. W., Chiu, C. Y., Wu, H. D., Shen, I. W., Chang, F. C., *Polymer.* **43**, 5011-5016 (2002).
2. Lobitz, P., Fullbier, H., Reich, A., Ambrahsat, K., *Solid State Ionics.* **58**, 49-54 (1992).
3. Scrosati, B., *Polymer International.* **47**, 50-55 (1998).
4. Alexandre M., Dubois, P., *Materials Science and Engineering.* **28**, 1-63 (2000).
5. Croce, F., Appetecchi, G. B., Persi, L., Scrosati, B., *Nature.* **394**, 456-458 (1998).
6. Bonino, F., Selvaggi, A., Scrosati, B., *Solid State Ionics.* **28-30**, 853-856 (1988).
7. Croce, F. Panero, S., Prosperi, P., Scrosati, B., *Solid State Ionics.* **28-30**, 895-899 (1988).
8. Daniel, M. F., Desbat, B., Lassegues, J. C., *Solid State Ionics.* **28-30**, 632-636 (1988).
9. Liu, J., Pan, J., Chen, J., *Solid State Ionics.* **82**, 225-227 (1995).
10. Wenhai, Y., Dazhi, W., Bin, Z., Shenjun, W., Lixin, X., *Solid State Commun.* **61**, 271 (1987).
11. Goswamee, R. L., Ayral, A., Bhattacharyya, K. G., Dutta, D. K., *Mater. Let.* **46** (2-3) (2000) 105-108; *Chem. Abstr.* **134** (7), 91602 (2001).
12. Hamdi, B., Kessaissia, Z., Donnet, J. B., Wang, T. K., *Ann. Chim. (paris).* **25** (6), 481-494 (2000); *Chem. Abstr.* **134** (7), 91510 (2001).
13. Robledo, A., Garcia, N. J., Bazan, J. C., *Solid State Ionics.* **139**, 303-308 (2001).
14. Deer, W. A., Howie, R. A., Zussman, J. (Ed.) An introduction to the Rock-Forming Minerals. Essex: ELBS Press, (1992).
15. Sekhon, S. S., Gurjinder, S., Agnihotry, S. A., Chandrac, S., *Solid State Ionics.* **80** (1-2), 37-44 (1995).

16. Rossi, S., Luckham, P. F., Tadros, T. F., *Colloids and Surfaces A: Physicochem. Eng. Aspects 00.* 1-10 (2002).
17. Barbara, G. O., *Applied Clay Science.* **22** (5), 251-259 (2003).
18. Eduardo, R. H., Galvan, J. C., Merino, J., Casal, B., Aranda, P., Antonia, J. M., *Solid State Ionics.* **85** (1-4), 313-317 (1996).
19. Montarges, E., Michot, L. J., Ildefonse, P., *Microporous and Mesoporous Materials.* **28** (1), 83-101 (**1999**).
20. Ralph, E. G., *Clay Mineralogy.* Australia: McGraw-Hill International Series, (1968).
21. Duane, M. M., Robert, C. R., X-Ray Diffraction and the Identification and Analysis of Clay Minerals. Oxford: Oxford University Press, (1989).
22. Whittingham, M. S., *Solid State Ionics.* **25**, 295 (1987).
23. Whittingham, M. S., *Solid State Ionics.* **32-33**, 344 (1989).
24. Zecchina, A., Bordiga, S., Spoto, G., Marchese, L., Petrini, G., Leofanti, G., Padovan, M., *J. Phys. Chem.* **96**, 4991-4997 (1992).
25. Helen, J. B., Simon, A. T. R., Simon, M. C., *Mineralogical Magazine.* **6**, 647 (1998).
26. Bandara, L. R. A. K., Dissanayake, M. A. K. L., Mellander, B. E., *Electrochimica Acta.* **43**, 1447-1451 (1998).
27. Chen, H. W., Chang, F. C., *J. Polymer Science: Part B: polymer Physics.* **39,** 2407-2419 (2001).
28. Jayathilaka, P. A. R. D., Dissanayake, M. A. K. L., Albinsson, I., Mellander, B. E. *Electrochimica Acta.* **47**, 3257-3268 (2002).
29. Fan, Y., Wu, H., *Solid State Ionics.* **93**, 347-354 (1997).
30. Wang, C., Liu, Q., Cao, Q., Meng, Q., Yang, L., *Solid State Ionics.* **53-56**, 1106 (1992).
31. Bartolotta, A., Di Marco, G., *Solid State Ionics.* **58**, 55-60 (1992).

POLYMERIC GEL ELECTROLYTES FOR ELECTROCHEMICAL CAPACITORS

Masayuki MORITA, Jin-Li QIAO, Naoki OHSUMI, Nobuko YOSHIMOTO and Minato EGASHIRA
Department of Applied Chemistry, Graduate School of Science and Engineering, Yamaguchi University
2-16-1 Tokiwada, Ube 755-8611, Japan
E-mail: morita@yamaguchi-u.ac.jp

Three kinds of the polymer matrix, poly(ethylene oxide)-grafted polymethacrylate (PEO-PMA), poly(vinyldene fluoride) (PVdF) and poly(vinyldene-co-hexafluoropripylene) (PVdF-HFP), were used for gel preparation. A proper amount of organic salts or acids were dissolved in the polymer matrix together with organic plasticizers, dimethylformamide (DMF) and/or poly-(ethylene glycol)-dimethylether (PEGDE), without water. Thin films of the polymeric gel were obtained by either direct polymerization of the mixed monomer solution or a thermal casting method. The composition of the polymer-electrolyte complex system is optimized to obtain good capacitor performances of the electrochemical capacitor (ECC) system.

1. General Introduction

The electrochemical capacitor (ECC) devices are based on charge storage processes either at the electric double-layer on the high surface-area carbon or fast surface-reactions of redox active materials. The use of solid ion-conductor as the electrolyte enables the device being safe and highly reliable. We have developed different types of polymeric gel electrolytes for all-solid ECC devices. The gel electrolytes generally consist of polymer matrices swollen with non-aqueous solutions of organic or inorganic electrolytes. In this paper, the basic properties of the gel electrolytes and their applicability to the ECC devices are reported in detail.

2. Polymethacrylate-based Gel Electrolyte for EDLC[1, 2]

2. 1. Introduction

Proton-conducting polymeric materials have aroused much interest in fundamental research for understanding ionic conduction properties as well as the field of practical applications because of their possible use as thin film solid electrolytes in various electrochemical devices.[3,4] In such ployelectrolyte-based systems as Nafion® and analogues, the proton conduction consists of the migration of hydronium ions (H_3O^+) through the hydrophilic clusters of sulfonate aggregates,[5] or hopping between the "gap" of the polymer matrix or the hydrophilic functional

groups,[6,7] which require water supply for retaining their proton conductivity.

On the other hand, it has been demonstrated that dissolution of H_3PO_4 in poly(methylmethacrylate) plasticized by dimethylformamide (PMMA/DMF) or poly(glycidylmethacrylate) with DMF or propylene carbonate (PGMA/DMF, PGMA/PC)[8-10] produces so-called polymeric gel electrolytes with high proton conductivities at ambient temperatures. The absence of water simplifies in principle the study of the conduction behavior of the system, and is likely to provide better electrochemical and thermal stability of not only the material but also the devices using them.

We report here a novel non-aqueous polymeric gel electrolyte that consists of poly(ethylene oxide)-modified poly(methacrylate) (PEO-PMA) containing poly(ethylene glycol dimethyl ether) (PEGDE) as an organic plasticizer, in which anhydrous H_3PO_4 was chosen as a proton donor. A variety of experiments have been made for optimizing the gel composition to achieve high ionic conductivity as well as chemical stability. We have also examined the applicability of the PEO-PMA-based polymeric gels as the solid electrolyte of an all-solid electric double layer capacitor (EDLC) system.

2. 2. Experimental

Non-aqueous polymeric gel membranes were prepared by photo-induced radical polymerization of poly(ethylene oxide) monomethacrylate (PEM; $CH_2=C(CH_3)CO_2(CH_2CH_2O)_9CH_3$) and poly(ethylene oxide) dimethacrylate (PED; $CH_2=C(CH_3)CO_2(CH_2CH_2O)_9COC(CH_3)=CH_2$).[11, 12] Anhydrous H_3PO_4 was dissolved in PEGDE (M_W = *ca.* 400), or a mixture of PEGDE and DMF. Then, PEM/PED (3:1 by molar ratio) and a radical initiator were added to the H_3PO_4/PEGDE (or H_3PO_4/PEGDE+DMF) solution, followed by continuous stirring to yield a homogeneous solution. The resulting mixture was then developed onto an Al pan and exposed to UV light for polymerization at room temperature, which yielded H_3PO_4-doped poly(ethylene oxide)-modified poly(methacrylate) polymeric gel: (PEO-PMA)/PEGDE(or PEGDE+DMF)/H_3PO_4 (see Figure 1). All steps of the preparation procedure were carried out under a dry Ar atmosphere.

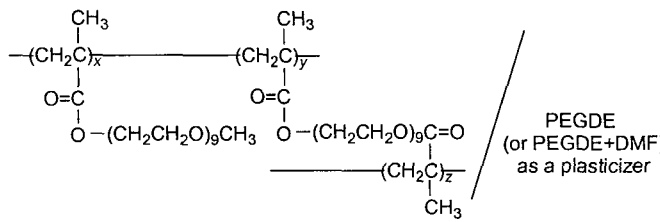

Figure 1. Structure of cross-linked PEO-PMA containing PEGDE as a plasticizer.

The ionic conductivity of the gel membrane was measured by an AC impedance method using an electrochemical impedance analyzer (S-5720C, NF Electronics), where the AC frequency was scanned from 100 kHz to 1 Hz. The sample

membrane (13 mm in diameter, 0.6 - 1.1 mm in thickness) was sandwiched between two stainless steel blocking electrodes in a sealed Teflon cell case. The AC impedance was measured in the temperature range from 20 to 90 °C.

An activated carbon fiber (ACF) cloth of 1300 m^2 g^{-1} BET surface area was used as the test electrode of the EDLC performance. The cell has a stacked structure with two ACF electrodes between which the polymeric gel film is sandwiched as the solid electrolyte. For comparison, aqueous H_3PO_4 solution (2.0 mol dm^{-3}) was used as the liquid electrolyte of the EDLC. The EDLC performances were evaluated by charge and discharge cycling under constant current conditions in the temperature range between 30 and 90°C, where the capacitor was first charged to 1.0 V and then discharged to 0 V at constant current from 0.13 to 2.6 mA.

2. 3. Results and Discussion

Optically transparent and uniform polymeric gel membranes were obtained in a wide range of the components, 13 - 52 mass% for H_3PO_4, and 0 - 77 mass% for PEGDE. The membranes have sufficient mechanical strength to measure their electrochemical properties. Figure 2 shows variations in the conductivity of the (PEO-PMA)/PEGDE/H_3PO_4 polymeric gel membranes as a function of H_3PO_4 content. The conductivity measured in this work was essentially ionic. The conductivity for the sample containing 13 mass% of H_3PO_4 was about 3.3×10^{-6} S cm^{-1}. The conductivity increased sharply to 1.3×10^{-4} S cm^{-1} when the gel contained 52 mass% of H_3PO_4 ([PEO-PMA]/PEGDE/H_3PO_4 = 18/30/52 in mass). The increase in the conductivity with the acid content is mainly due to the increased numbers of the charge carriers in the gel. The presence of H_3PO_4 also decreased the viscosity of the polymeric gel complex, which makes the polymeric chain flexible and consequently the carrier ions are easy to transport in the gel complex.

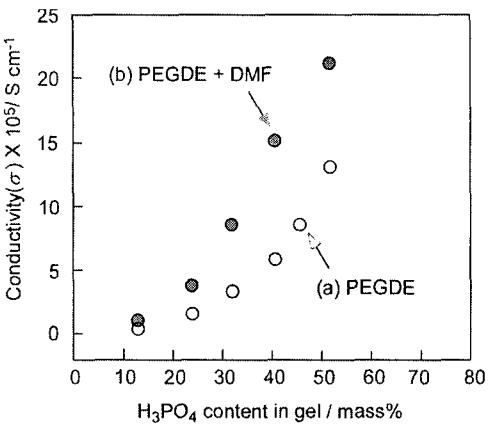

Figure 2. Conductivity changes as a function of H_3PO_4 content for PEO-PMA-based polymeric gels.
a: PEGDE as the plasticizer, and (PEO-PMA)/PEGDE (in mass) = 38/62,
b: PEGDE+DMF as the plasticizer, and (PEO-PMA)/PEGDE/DMF (in mass) = 38/47/15.

The conductivity was enhanced by the addition of the second plasticizing component DMF. The conductivity was increased by addition of 7 mass% of DMF from 3.3×10^{-6} to 7.2×10^{-6} S cm^{-1} for the system containing 13 mass% of H_3PO_4, and from 1.1×10^{-4} to 2.1×10^{-4} S cm^{-1} for the sample containing 52 mass% of H_3PO_4 at 22 ± 2 °C. The addition of DMF reduces the viscosity of the gel and increases the dissociation of H_3PO_4. As the conductivity of pure DMF and PEGDE is extremely low (< 10^{-10} S cm^{-1} at room temperature), the increased conductivity by the DMF addition is due to the indirect contribution of DMF to the ionic property of the complex.

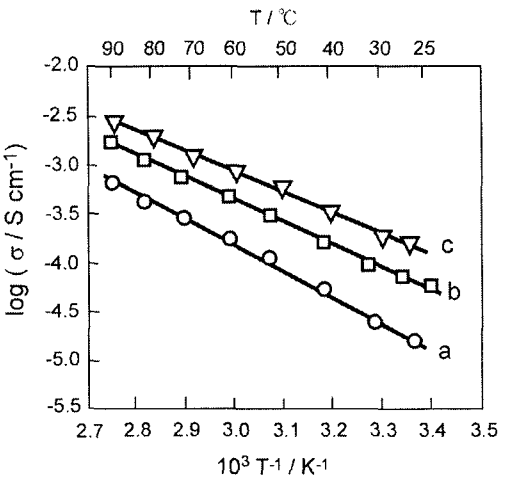

Figure 3. Temperature dependence of the ionic conductivity for PEO-PMA-based polymeric gels with different polymer compositions, H_3PO_4 content: 52 mass %, (PEO-PMA)/PEGDE (in mass): 100/0 (a), 50/50 (b), and 23/77 (c).

Figure 3 shows the temperature dependence of the ionic conductivity obtained for gel membranes with different compositions. A linear relation was observed on every $\log\sigma$ *vs.* $1/T$ plot. The slope of the linear plot gives apparent activation energy (E_a) for the ionic conduction. Figure 4 shows the variations in the activation energy with the composition of the polymeric gel. The E_a value increased with an increase in the H_3PO_4 content in the gels, but weakly depended on the polymer matrix composition, (PEO-PMA)/PEGDE ratio. The addition of DMF tended to decrease the activation energy, but the difference became small when the polymeric gel complexes contained high acid contents. This suggests that the activation process of the conduction becomes similar in the gels with high H_3PO_4 contents. Note that the E_a values in the present non-aqueous gels were generally higher than those observed for the hydro-gels containing H_3PO_4[11] or acetic acid,[12] where around 10 kJ mol^{-1} was obtained. This is probably due to the fact that the present polymeric gel system does not contain free water that would act as the active site of the proton transport via hydrogen bonding.[12] In the non-aqueous gel, however, the proton conduction would proceed mainly through the molecular

coordination of proton with ethylene oxide (EO) units in the polymer matrix and/or the amide group of the plasticizing molecule. The proton conduction mechanism appears to change with the increase in the H_3PO_4 content. That is, for the samples with high H_3PO_4 contents, a vehicle-type mechanism dominates the ionic conduction, whereas for the samples with low acid contents and/or high solvent contents, a Grotthus-type mechanism appears to be the primary route of the ion-conduction.[13]

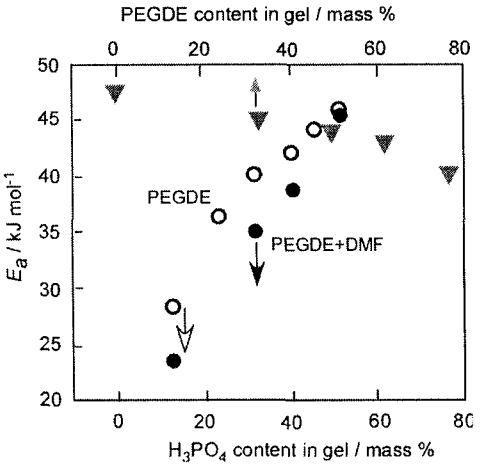

Figure 4. Variations in the apparent activation energy as functions of H_3PO_4 and PEGDE contents for PEO-PMA-based polymeric gels.
(○) (PEO-PMA)/PEGDE=38/62. (●) (PEO-PMA)/PEGDE/DMF=38/46/15.
(▼) H_3PO_4 content: 46 mass%.

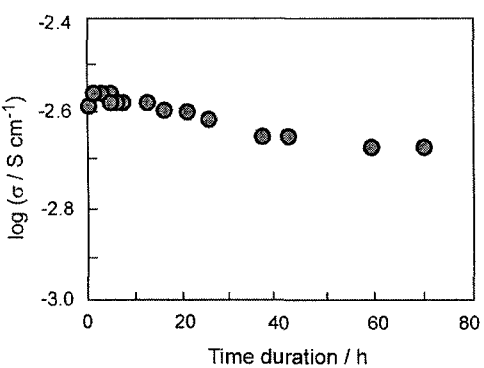

Figure 5. Time course of the ionic conductivity of PEO-PMA-based polymeric gel at 100°C.
Polymeric gel composition: (PEO-PMA)/PEGDE/H_3PO_4 = 21/33/46.

Figure 5 shows the variation in the ionic conductivity with time measured at 100 °C for the sample of (PEO-PMA)/PEGDE/H_3PO_4 (21/33/46 in mass). The initial conductivity of the polymeric gel complex was 2.6×10^{-3} S cm^{-1} at 100 °C. The conductivity increased once to 2.7×10^{-3} S cm^{-1} within 2 h, then gradually decreased to 2.1×10^{-3} S cm^{-1} after 70 h.

Charge and discharge cycling tests were conducted for the EDLC cells using ACF electrodes and the polymeric gel electrolyte. In Figure 6, the specific capacitance obtained at 90 °C is plotted against the cycling current density. Here, the iR-free values of the capacitance are shown to discuss the rate performances. When the cell was cycled at relatively low rate (0.5 mA cm^{-2}) , about 120 F g^{-1} of the discharge capacity was obtained for the cell with the plasticizer-free electrolyte. This value was about half of the capacitance obtained for a cell using aqueous liquid electrolyte. For the cells with plasticized non-aqueous electrolyte, we have achieved almost the same level of the capacity as that observed in the liquid electrolyte. The rate dependence was not significant up to 2.0 mA cm^{-2}, which corresponds to several "*C* rate" for conventional battery systems. In addition, from Fig. 6, it can also be seen that gel polymer electrolyte plasticized by PEGDE gave the highest capacitance, although its ionic conductivity was lower than in the gel containing DMF as the plasticizer, even at high temperature (90 °C). The rate capability shown in Fig. 6 corresponds to the capacitor performance (power density) of *ca.* 200 W kg^{-1} at the energy density of *ca.* 10 Wh kg^{-1}, when the calculation is based on the mass of the ACF electrodes.

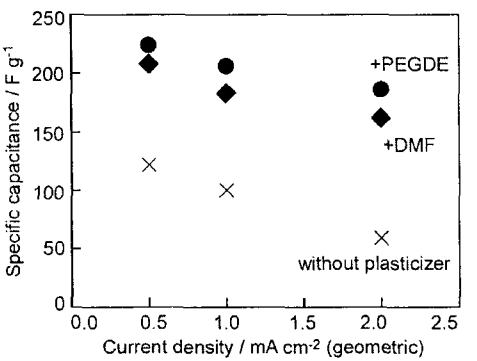

Figure 6. Variations in the specific capacitance of ACF with current density for the test cells with polymeric gel electrolytes (at 90 °C), ×: without plasticizer, ●: PEGDE, ◆: DMF.

3. Poly(vinylidenefluoride)-based Gel Electrolytes for Redox Capacitors[14]

3. 1. Introduction

The electrochemical capacitors (ECCs) are classified two types: one is electric double layer type (EDLC), which is based on the non-Faradaic process of polarizable electrodes, and the other type is pseudo-capacitor, also called redox

capacitor, in which Faradaic reactions, or redox reactions of electro-active materials. A typical electrolyte system of EDLC is non-aqueous one consisting of organic solvent solutions. This non-aqueous system has wide potential windows that lead to high energy density of the capacitor device. The other category is an aqueous system, *eg.*, aqueous solutions of sulfuric acid or potassium hydroxide. The latter has generally higher ionic conductivity that enables the capacitors high rate-capability

In recent years, the technologies in the advanced capacitors have been directed to two ways, smaller sizes for electronics and larger sizes for power sources of FCEV. In both cases, application of solid electrolyte will be key technology, because solid electrolytes have such merits as safety and reliability of the device. However, the solid system has such demerits as low rate capability, because of relatively low ionic conductivity and difficulty of the structuring the electrode/electrolyte interface. Up to the present, many kinds of polymeric gel electrolytes have been proposed. We have reported in the first part of this paper that the applicability of proton conducting gel electrolyte to an EDLC. In this part, we have aimed to confirm the applicability of non-aqueous gel system to the ECC, especially the redox capacitor electrode. We adopted PEO-PMA-based polymer and poly(vinylidenefluoride) (PVdF)-based polymer as the matrix for the polymeric gel, and examined the compatibility of the resulting gel electrolyte with the redox active metal oxide. Here, we used ruthenium oxide hydrate ($RuO_2 \cdot xH_2O$) and investigated its voltammetric response and the charge/discharge cycling in the gel.

3. 2. Experimental

The polymeric gel was composed of PVdF or PVdF-hexafluoropropylene co-polymer swollen with DMF solution of trifluoromethanesulfonic acid (CF_3SO_3H) as the proton source. The matrix polymer and the acid were first mixed with DMF solvent, and then casted on an Al pan under dry argon atmosphere, followed by curing at 110 °C under reduced pressure. This procedure yielded a flexible thin film of the gel electrolyte. The ionic conductivity of the gel electrolyte was measured by the same AC method as described in the previous part over the temperature range from 30 to 90°C.

The ruthenium oxide hydrate ($RuO_2 \cdot xH_2O$) was prepared by a so-gel method, which was first proposed by Zhen, et. al.[14] The oxide powder was mixed with a binder under a dry condition, then mounted on a current collector with a conductive resin. This type of the electrode will be called Type I. The other one is called Type II made by a "wet process", where the oxide powder and the binder were suspended in an organic solvent, and then the resulting slurry was coated on a current collector made of stainless steel. The organic solvent in the coating was thoroughly evaporated by heating under a reduced pressure. Cyclic voltammetry and constant current polarization using a three-electrode cell were conducted for characterizing the metal oxides as the capacitor electrodes in the gel electrolytes.

3.3 Results and Discussion

The conductance characteristics of the PVdF-based polymeric gel electrolytes are

shown in Figures 7 and 8. The temperature dependence of the ionic conductivity generally reveals Arrhenius-type behavior. The use of trifluoromethanesulfonic acid (CF_3SO_3H) gave much higher conductivity than phosphoric acid (H_3PO_4). About 6 mS cm^{-1} of the conductivity was obtained for the PVdF-based gel containing CF_3SO_3H at 60 °C.

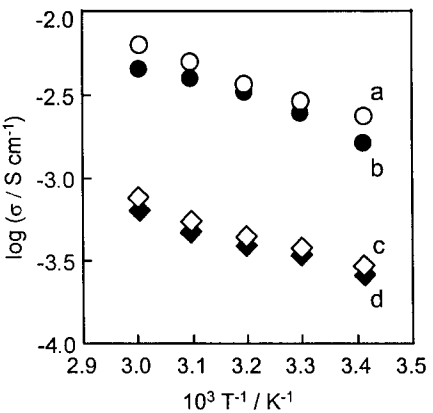

Figure 7. Temperature dependence of the ionic conductivity for PVdF- and PVdF-HFP-based gel electrolytes.
a: PVdF / 0.5M CF_3SO_3H (DMF), b: PVdF-HFP / 0.5M CF_3SO_3H (DMF)
c: PVdF / 15% H_3PO_4 (DMF), d: PVdF / 10% H_3PO_4 (DMF).

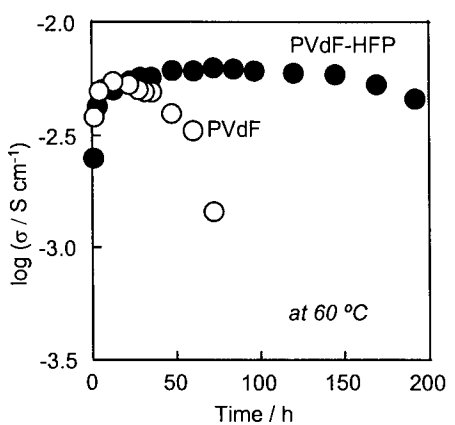

Figure 8. Variations in the ionic conductivity with time for PVdF- and PVdF-HFP-based gel electrolytes at 60 °C. Content of the polymer in the gel: 15 % in mass.

Figure 8 shows the comparison of the variations in the ionic conductivity for PVdF- and PVdF-HFP-based gels (15 mass% of the polymer content) at 60 °C.

The initial conductivity of the gel using PVdF-HFP co-polymer host was lower than that of the gel using PVdF homo-polymer. However, the durability of the conductivity was much better for PVdF-HFP co-polymer than PVdF homo-polymer. The IR spectra of the gels after 50 h storage at 60 °C proved that the most of the DMF component was lost in the gel using PVdF homo-polymer. his peak almost disappeared after 50 h storage at 60 °C for PVdF homo-polymer gel. That is, the PVdF-HFP copolymer was much superior to PVdF homo-polymer in the plasticizer stability.

The PVdF-HFP-based gel consists of polymeri-rich crystal phase and the liquid-rich amorphous phase. The proton conduction mainly occurs in the liquid phase percolation, where the donor site of the plasticizer, DMF, assists the proton transport. Thus, a mechanism of Grottus-type conduction[13] is also proposed for the present gel system.

Next we have examined the applicability of the PVdF-based gel electrolyte to redox capacitor electrode. Cyclic voltammetry for the $RuO_2 \cdot xH_2O$ electrode made by a "dry" process (Type-I electrode) showed a rather small current response in the PVdF-HFP-based gel electrolyte. The discharge capacitance measured under a constant current condition (2 mA cm^{-2}) was initially about 100 F $g(RuO_2)^{-1}$, but it decreased with the cycling. This was probably due to insufficient utilization of the electrode/electrolyte interface. Thus, we changed the electrode preparation process to make better interface between a solid electrode and a gel electrolyte.

Figure 9 shows the voltammetric response of the $RuO_2 \cdot xH_2O$ electrode made by a "wet" process (Type-II electrode). The voltammetric current was much higher than that of Type I ("dry process) electrode. It was demonstrated that the optimization of the electrode/electrolyte interface can improve the redox process of the oxide electrode in the solid gel electrolyte.

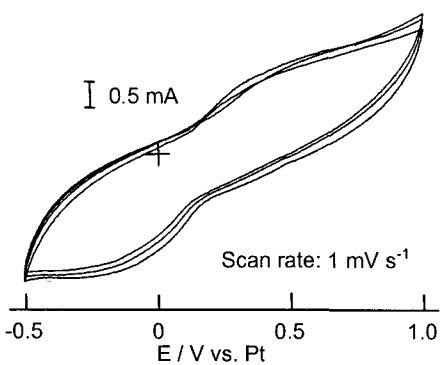

Figure 9. Cyclic voltammogram for $RuO_2 \cdot xH_2O$ electrode (Type-II) in gel electrolyte, PVdF-HFP/ 0.5 M CF_3SO_3H (DMF) (15 mass% of the polymer content).

In Figure 10, the discharge capacitances of the Type-II electrode are plotted against the cycle number under constant-current charge-discharge cycling. The discharge capacitance at constant current was also higher than that of Type I

electrode. When we used lower current density, 1 mA cm^{-1}, the initial capacity exceeded 300 F g^{-1} at 60 °C, and the cycleability was better than Type I electrode. Optimization of the electrode composition is now under investigation to improve the rate capability of the oxide electrode in the polymeric gel electrolyte.

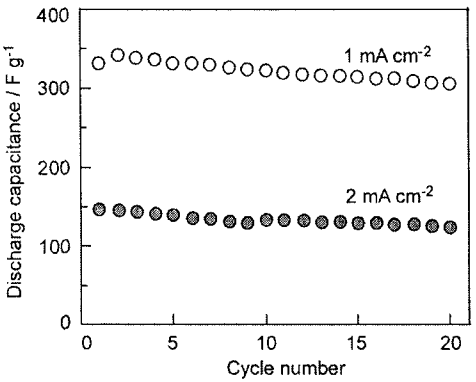

Figure 10. Variations in the discharge capacitance with the cycle number for $RuO_2 \cdot xH_2O$ electrode (Type-II) in gel electrolyte, PVdF-HFP/ 0.5 M CF_3SO_3H (DMF) (15 mass% of the polymer content).

4. Summary

We have successfully developed proton conducting non-aqueous polymeric gel systems for ECC use. These have high ionic conductivity as well as compatibility with a high surface area carbon material as well as the metal oxide for the hybrid capacitor device.

References

1. J. L. Qiao, N. Yoshimoto, M. Ishikawa and M. Morita, *Chem. Mater.*, **15**, 2005 (2003).
2. M. Morita, J. L. Qiao, N. Yoshimoto and M. Ishikawa, *Electrochim. Acta*, **50**, 832 (2004).
3. M. Rikukawa and K. Sanui, *Prog. Polym. Sci.*, **25**, 1463 (2000).
4. K. D. Kreuer, *Solid State Ionics*, **97**, 1 **(1997)**,
5. K. Miyatake, K. Fukushima, S. Takeoke and E. Tsuchida, *Chem. Mater.*, **11**, 1171 (1999).
6. S. R. Samms, S. Wasmus and R. F. Savinell, *J. Electrochem. Soc.*, **143**, 1225 (1996).
7. M. A. Vargas R. A. Vargas and B.-E. Mellander, *Electrochim. Acta*, **44**, 4227 (1999).
8. J. R. Stevens, W. Wieczorek, D. Raducha and K. R. Jeffrey, *Solid State Ionics*, **97**, 347 (1997).

9. D. Raducha, W. Wieczorek, Z. Florjanczyk and J. R. Stevens, *J. Phys. Chem.*, **100**, 20126 (1996).
10. W. Wieczorek, G. Zukowska, R. Borkowska, S. H. Chung and S. Greenbaum, S. *Electrochim. Acta*, **46**, 1427 (2001).
11. J. L. Qiao, N. Yoshimoto and M. Morita, *J. Power Sources*, **105**, 45 (2002).
12. J. L. Qiao, N. Yoshimoto, M. Ishikawa and M. Morita, *Electrochim. Acta*, **47** 3442 (2002).
13. G. Zukowska, N. Chojnacka and W. Wieczorek, *Chem. Mater.*, **12**, 3578 (2000).
14. M. Morita, N. Ohsumi, N. Yoshimoto and M. Egashira, *2nd International Conference on Polymer Batteries and Fuel Cells*, Paper No. 191, June 14, 2005, Las Vegas, USA.
15. J. P. Zheng, P. J. Cygan, T. R. Jow,, *J. Electrochem. Soc.* **142**, 2699 (1995).

ELECTRICAL CONDUCTIVITY STUDIES ON PROTON CONDUCTING POLYMER ELECTROLYTES BASED ON POLY (VINYL ACETATE)

D. ARUN KUMAR, T. SAVITHA, S. SELVASEKARAPANDIAN, R. BASKARAN

Solid State and Radiation Physics Lab, Department of Physics,
Bharathiar University, Coimbatore-641 046, Tamil Nadu, India
E-mail: sekarapandian@yahoo.com

Abstract

Proton conducting polymer electrolytes based on Poly (vinyl acetate) (PVAc) and perchloric acid ($HClO_4$) has been prepared by solution casting technique with various compositions. FTIR spectra analysis reveals the interaction between proton and ester oxygen of Poly (vinyl acetate) (PVAc). Ac impedance spectroscopy reveals that 75m%PVAc:25m%$HClO_4$ exhibits maximum conductivity, $6.2X10^{-2}$ Scm^{-1} at room temperature (303K). The increase in conductivity with increase in dopant concentration and temperature may be attributed to the enhanced mobility of the polymer chains, number of charge carriers and rotations of side chains. The temperature dependence of conductivity shows non-arrhenius behaviour at higher temperatures. Dielectric loss spectra show two relaxations α (high temperature) and β (low temperature) relaxations in low and high frequency range respectively

Keywords: Proton conductors, PVAc, FTIR, Impedance analysis

1. Introduction:

In the recent years, proton conducting polymer electrolytes attracted considerable attention due to the possibility of their application in a variety of electrochemical devices, such as fuel cells, humidity and gas sensors, electrochromic displays and windows [1]. In general proton-conducting polymers are usually based on polymer electrolytes, which have negatively charged groups attached to the polymer backbone. Complexes of basic polymers such as Poly (ethylene oxide) (PEO), poly (ethylene imine) (PEI), poly (acryl amide) (PAAM) and poly (vinyl alcohol) (PVA) with strong acids have been shown to possess high proton conduction in the range of 10^{-4} – 10^{-3} Scm^{-1} [2]. PVAc happens to be one of the polymers which possess large dipole moments and high relaxation time which are due to its side chains connected to ester oxygen [3]. PVA complexed with inorganic acid has been already reported by R.A. Vargas et.al, and he reported the plastification effect of acids and water in PVA [4]. In this investigation, proton conducting polymer electrolytes based on Poly (vinyl acetate) (PVAc) and perchloric acid ($HClO_4$) has been prepared by solution casting technique with various compositions. Plasticization effect of acid on Poly (vinyl acetate) (PVAc)

has been discussed using FTIR. Impedance spectroscopy has been performed to analyze effect of acid on the conductivity of pure polymer.

2. Experimental analysis:

The polymer complexes have been prepared by solution casting technique. Poly (vinyl Acetate) (PVAc) Himedia and Perchloric Acid ($HClO_4$) Qualigens are used as received. First PVAc is dissolved using acetone and then the dopant $HClO_4$ was added to this solution and stirred well to get a homogenous solution, and the solution was poured in to small Petri dishes to form thin film, and kept in room temperature for one day and then in vacuum oven at a temperature of 60^0c to remove the traces of acetone. The ion interaction studies of the complex PVAc-$HClO_4$ has been studied using FT-IR analysis using shimadzu 8000- Spectrophotometer instrument in the range 4000-400 Cm^{-1}. To study the ionic conductivity of the samples Ac impedance spectroscopy was performed using HIOKI 3532 LCR Hitester, in the frequency range 42Hz -5MHz for the temperature range 303 K- 343 K using aluminium as blocking electrodes.

3. Results and Discussion

3.1. FT-IR Spectroscopic Analysis

The FT-IR spectrum of pure PVAc, and PVAc-$HClO_4$ complexes of various compositions are shown in Fig.1. The vibrational bands observed at 2923, 2865 and 1375 cm^{-1}, are ascribed to CH_3 asymmetric stretching, symmetric stretching and symmetric bending vibrations of pure PVAc respectively. The peaks at 1245, 1100 and 1090 cm^{-1}, are ascribed to C-O-C symmetrical stretching, C-O and C-C stretching vibrations of pure PVAc respectively. The peak observed at 625 cm^{-1}. (Fig.1b) in the proton exchange membrane is ascribed to the ClO_4^- ion which is slightly shifted to lower wave numbers 610 cm^{-1} at higher concentrations of $HClO_4$. This result indicates the coordination of ClO_4^- ion with the polar group present in the polymer of the polymer complexes. In Fig. 1(b-c), the peak observed at 3728 cm^{-1} is ascribed to the weak inter ionic bonding between H^+ and ClO_4^- as (H^+ ClO_4^- --- H^+ ClO_4^-).

Fig.1 (b) and (c) well reflect the different degree of coordination of cation to both the C-O-C and C=O moieties. The appearance of strong band in the spectrum at 1730 cm^{-1} which corresponds to C=O stretching frequency of pure PVAc is slightly shifted to lower wave number (1719-1705 cm^{-1}) in the polymer- acid complexes. This effect is due to the coordination of the cation with the oxygen, which results in the weakening of the C=O bond and hence the wave number of absorption decreases. The similar results have been reported by Weihua Zhu et.al and S.SelvasekaraPandian et. al for the PEG-PU/$NaClO_4$ and PVAc-NH_4SCN complexes, respectively [5,6]. Moreover the addition of $HClO_4$ causes a small decrease (1238-1232 cm^{-1}) of the C-O-C stretch down to lower wave numbers due to the coordination of the ester oxygen with the cation. The similar effect was reported by Wieczorek et.al. [7] for the polyether- poly (methyl methacrylate) blend based system. The polymer- acid complex formation and the proton interaction has been confirmed from the above analysis.

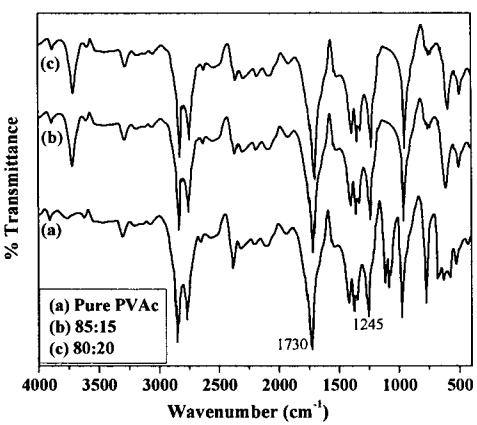

Fig.1 FT-IR spectrum of a) pure PVAc b)15m%$HClO_4$ c)20m% $HClO_4$ doped PVAc

3.2 Impedance Spectra:

Figure (2a) shows the Nyquist plot or cole-cole plot for all the samples PVAc-$HClO_4$. The complex impedance diagram shows two well defined regions, a chord in the high frequency region which is related to the conduction process in the bulk of the electrolytes and a linear region in the low frequency range that can be attributed to the effect of blocking electrodes. At low frequency the complex

impedance plot shows a straight line parallel to the imaginary axis, but the double layer at the blocking electrodes causes the curvature. The disappearance of the high frequency chord portion in the complex impedance plot illustrates that the total conductivity is mainly due to the result of ionic conduction. [8]. The appearance of semi-circle can be represented by a parallel combination of a resistor and a capacitor. The resistor may be attributed to the migration of ions through the free volume of the polymer matrix, and the capacitor to the polarized polymer chains due to the alternating field applied. In the low frequency range the observed inclined spike represents a finite or infinite diffusion of mobile charge carrier which occurs into the electrode materials [9].

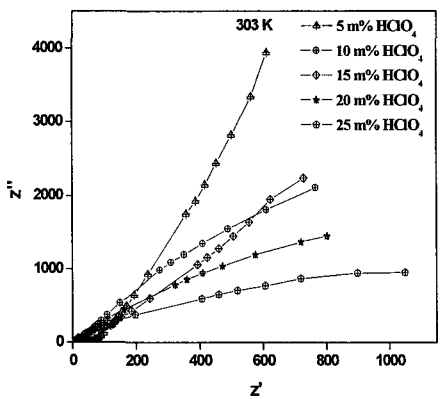

Figure (2a) Nyquist plot for $PVAc\text{-}HClO_4$ complexes at 303K

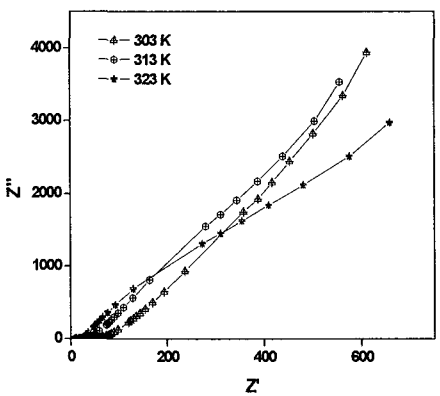

Figure (2b) Nyquist plot 95m% PVAc-5m%$HClO_4$ at various temperatures

From Fig (2b) it is observed that the impedance value decreases with increase in temperature for the sample 95mol% PVAc- 5mol%HClO4. And this has been observed in all the samples. As the temperature increases the segmental motion of the polymer chain and dissociation of the acid increases resulting in the decrease of impedance, hence high conductivity. The bulk resistance has been calculated by extrapolating the spike into the x-axis and the conductivity has been calculated using the relation,

$$\sigma = 1/R_B \; A/d \;\; Scm^{-1} \qquad (1)$$

Where A- area of the electrode electrolyte contacts and, d - thickness of the sample. The maximum conductivity 6.2 x 10^{-2} Scm^{-1}has been observed for the sample 75mol%PVAc: 25mol%$HClO_4$ at room temperature.

3.3 Conductance Spectra:

Fig (3a) shows the plot between log ω and log σ for all the samples at room temperature. The curve consists of three different regions; the low frequency spike which is followed by a medium frequency plateau and a spike at high frequencies. The low frequency spike may be attributed to the space-charge polarization at the electrode- electrolyte interface. The medium frequency plateau represents the DC conductivity due to the hopping of ions in the polymer chains and the high frequency spike is due to the bulk of the relaxation phenomenon.

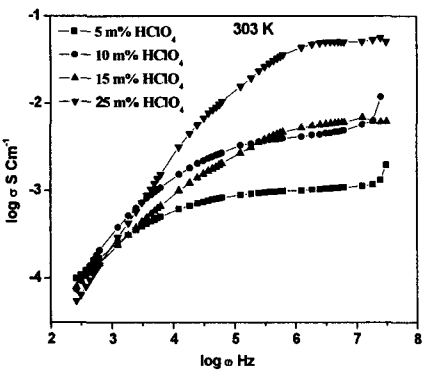

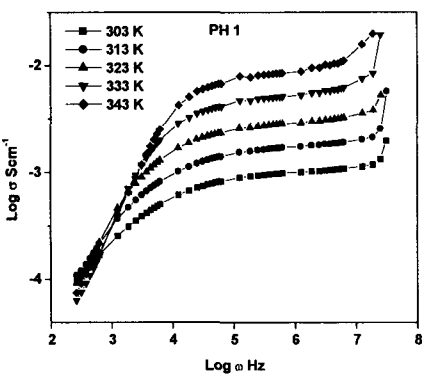

Fig(3a) Conductance spectra for PVAc-$HClO_4$ complexes Fig(3b) Conductance spectra for 5m% $HClO_4$ doped polymer electrolyte

According to Jonscher's Power law [10], the frequency dependent of Ac conductivity of polymer electrolytes is described by the following equation,

$$\sigma = \sigma_0 + A\omega^n . \qquad (3)$$

σ_0 - D. C conductivity and A, n – material parameters.

The value of σ_0 has been found by extrapolating the plateau in the y-axis, and they are in good agreement with the values obtained from impedance plot. Fig (3b) shows the conductance plot for the sample [95mol%PVAc : 5mol%HClO4] for various temperatures. From the plot it is clear that as the temperature is increased the spike get increased due to the increase in mobile charge carrier and the DC plateau region

shifts towards high frequency region. The high frequency spike disappears as the temperature increases within the frequency region measured.

3.4 Temperature dependent conductivity:

Fig. 4 shows the plot between temperature and conductivity. For low concentration of acid doped samples, conductivity value increases linearly with increase in temperature up to 345 K and for higher temperature it shows Non-Arrhenius behaviour.

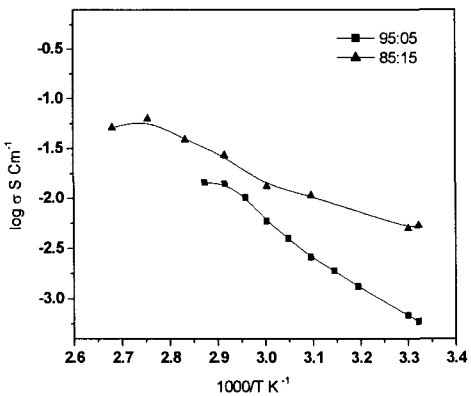

Fig4: Temperature dependent conductivity for 5m% and 10m% $HClO_4$ doped PVAc complexes

As the acid concentration is increased polymer electrolytes shows Non-Arrhenius behaviour in the temperature range studied. This Non-Arrhenius behaviour may be attributed to the reduction of T_g due to the plasticization effect of acid [4]. The same phenomenon has been observed by Vargas et.al in the system PVA complexed with $KHSO_4$. The nonlinearity in figure 4 shows that ion transport in polymer electrolytes is dependent on polymer segmental motion. Thus the result may be described by VTF relation which describes the transport properties in a viscous matrix.

3.5 Dielectric spectra Analysis:

The complex permittivity (ε) or dielectric constant of a system is defined by

$$\varepsilon^* = \varepsilon' + i\varepsilon'' = \varepsilon' - j(\sigma/\omega\varepsilon_o) \qquad (4)$$

where ε' – real part of the dielectric constant, ε'' – imaginary part of the dielectric constant of the material, σ - conductivity of the material, ω - angular frequency, εo – permittivity of free space. The plot ε' Vs log ω is shown in figure(5a) for all the

samples at room temperature. The dielectric permittivity rises sharply towards low frequencies due to electrode polarization effects. At high frequencies the periodic reversal of the electric field occurs so fast that there is no excess ion diffusion in the direction of the field. The polarization due to the charge accumulation decreases, leading to the decrease in the value of ε' [11]. Figure (5b) shows the plot between ε'' Vs logω for all the samples at room temperatures. The dielectric loss is very large at low frequencies due to the free charge motion within the material.

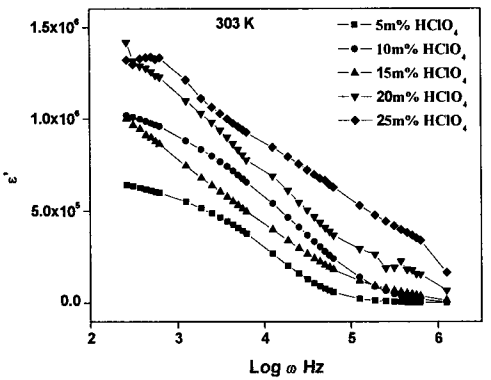

Fig. 5a Variation of dielectric constant with frequency for $HClO_4$ doped PVAc complexes

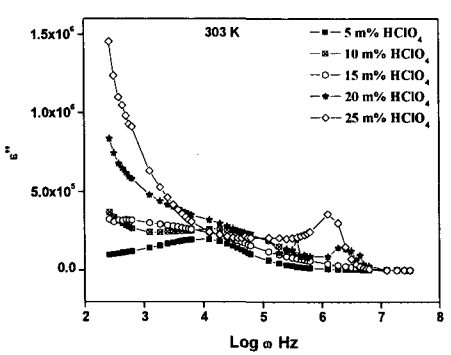

Fig(5b) Dielectric loss spectra for PVAc : $HClO_4$

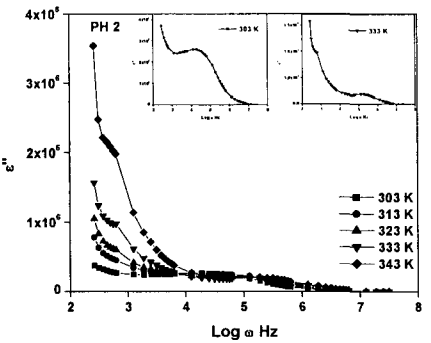

Fig(5c) Dielectric loss spectra for 90m% PVAc : 10m% $HClO_4$

These values do not correspond to the bulk dielectric processes but are due to the free charges build up at the interface between the material and the electrodes. From the plot, high dielectric loss has been observed for the sample 75mol%PVAc:

25mol%$HClO_4$ which has high conductivity than other samples. In the figure (5c) the appearance of dominant dielectric relaxation peak, whose maximum shifts gradually towards high frequencies with rise in temperature for 90mol%PVAc: 10mol%$HClO_4$. At higher temperatures a new peak has been observed at lower frequencies along with a peak in the high frequency. This new peak at lower frequencies observed only at high temperature is due to the main chain relaxation (α - relaxation process). So the peak at high frequency may be attributed to the side chain relaxation (β - relaxation process) [11].

4.Conclusion:

Proton conducting polymer electrolytes based on Poly (vinyl acetate) (PVAc) and perchloric acid ($HClO_4$) has been prepared. FTIR spectra analysis reveals the interaction between proton and ester oxygen of Poly (vinyl acetate) (PVAc). 75m%PVAc: 25m%$HClO_4$ has been found to exhibit maximum conductivity, $6.2X10^{-2}$ Scm^{-1} at 303K. The temperature dependence of conductivity shows non-arrhenius behaviour at higher temperatures. Dielectric loss spectra show two relaxations α (high temperature) and β (low temperature) relaxations in low and high frequency range respectively.

Reference:

1. W.Wieczorek, Z. Florjanczyk, *Solid State Ionics* **154-155**, 45-49 (2002)
2. M. Rikukawa, K. Sanui, *Progress in Polymer Science* **25**, 1463-1502 (2000)
3. Ajeet Kumar Srivastva, Harder Singh Virk *Radiation Physics and Chemistry* **59** 31-37,(2000)
4. R. A. Vargas, A. Garcia, *Electrochimica Acta*, **43,** 1271-1274 (10-11) (1998).
5. Weihua Zhu, Xinling Wang, Bing Yang, Xiaozhen Tang, *Journal of Polymer Science: Part B: Polymer Physics*, **Vol.39 (11)**, 1246-1254 (2001)
6. S. Selvasekarapandian, R. Baskaran, M. Hema, *Physica B: Condensed Matter*, **357,** 412- 419 (2005)
7. W. Wieczoreck, J.R. Stevens, *J. Phys. Chem. B*, **101,** 1529- 1534 (1997)
8. L. Fan, Zhimin Dang, Ce-Wen Nan *Electrochimica Acta* **48,** 205-509 (2002)
9. V. Hornebecq, J.M. Reau, J. Ravez *Solid State Ionics* **127,** 231 -240 (2000)
10. M. Siekierski, W. Wieczorek, *Electrochimica Acta* **43 (10-11)**, 1339-1342 (1998).
11. K.P. Singh, P.N. Gupta European *Polymer Journal* **34(7),** 1023 - 1029 (1998).

CONDUCTIVITY AND THERMAL STUDIES ON PLASTICIZED NANO-COMPOSITE SOLID POLYMER ELECTROLYTE, PEO: EC: LiTf: Al_2O_3

H.M.J.C. PITAWALA [a, b], M.A.K.L. DISSANAYAKE [a, b] AND V.A. SENEVIRATNE [b]

[a] *Postgraduate Institute of Science and* [b] *Department of Physics, University of Peradeniya, Peradeniya, Sri Lanka*

Email: director@pgis.lk

Poly (ethylene oxide)-(PEO)-based composite polymer electrolytes are of great interest for solid-state-electrochemical devices. This paper presents the results of a preliminary study on electrical conductivity and thermal behavior (DSC) of composite polymer electrolytes (CPEs) containing PEO: $LiCF_3SO_3$ complexed with plasticizer (EC) and incorporating nano-sized particles of the ceramic filler Al_2O_3. Ionic conductivity enhancement in these electrolytes has been obtained by optimizing the combined effect of the plasticizer and the ceramic filler. Nano-composite, plasticized polymer electrolyte films (400-600μm) were prepared by common solvent casting method. It was revealed that the presence of the Al_2O_3 filler in PEO: LiTf polymer electrolyte significantly enhanced the ionic conductivity in the temperature range of interest, giving the maximum conductivity for $(PEO)_9LiTf$+15 wt.% Al_2O_3 CPE [σ_{RT} (max)=$2x10^{-5}$ S cm^{-1}]. It was also observed that the addition of plasticizer (EC) to this electrolyte up to a concentration of 50 wt. % EC, showed a further conductivity enhancement [σ_{RT} (max) =$1.5x10^{-4}$ S cm^{-1}]. It is suggested that the conductivity is enhanced mainly by two mechanisms. The plasticizer (EC) would directly contribute by reducing the crystallinity and increasing the amorphous phase content of the polymer electrolytes. The ceramic filler (Al_2O_3) would contribute to conductivity enhancement by creating additional sites to migrating ionic species through transient bonding with O/OH groups in the filler surface. The decrease of T_g values of plasticized CPE systems seen in the DSC thermograms points towards the improved segmental flexibility of polymer chains, increasing the mobility of conducting ions.

1. Introduction

The development of solid polymer electrolytes is of practical importance for various applications in electrochemical devices such as separators electrolyte membranes in high energy density lithium ion rechargeable batteries, fuel cells, electrochromic displays and smart windows. The high molecular weight poly (ethylene oxide) (PEO) – based composite polymer electrolytes are emerging as the best candidates to be used as polymer matrix because of their solvation power, complexion ability and ion transport mechanism directly connected with the alkaline salt (Li^+). However, the ionic conductivity of PEO–lithium salts (LiX) electrolytes at ambient temperature (10^{-7}- 10^{-6} S cm^{-1}) is not high enough for most practical applications. In order to overcome this problem, consistent research efforts have been devoted to improve the ionic conductivity in PEO–LiX (X = ClO_4^- , $CF_3SO_3^-$, BF_4^- , PF_6^- etc.) composite polymer electrolytes (CPEs).

Ionic conductivity enhancement in these polymer electrolytes have been achieved mainly by using two techniques [3, 6]. One of these techniques is the

dispersion of nano-sized inorganic ceramic filler particles (Al_2O_3 , SiO_2 , TiO_2) in the host polymer matrix in order to utilize their role of creating additional conducting pathways for migrating ionic species through transient bonding with O/OH groups in the filler surface [3, 4, 5, 9] . The other technique is the addition of low molecular weight plasticizers such as ethylene carbonate (EC), propylene carbonate (PC) and polyethylene glycol (PEG) into the conventional PEO-LiX systems [7, 11]. The plasticization is the conventional way to reduce the crystallinity and increase the amorphous phase content of the composite polymer electrolytes. Therefore, the conductivity and thermal studies on plasticized composite polymer electrolytes incorporating nano-sized ceramic particles are of great interest. However, a very few publications are available in the literature which discuss the combined effect of the plasticizer and the ceramic filler on PEO-LiX based polymer electrolytes [7, 8].

This paper reports, the result of a preliminary study on electrical conductivity and thermal behavior of composite polymer electrolyte: $(PEO)_9LiCF_3SO_3$, plasticized with ethylene carbonate (EC) and incorporating nano-sized Al_2O_3 as the ceramic filler.

2. Experimental

Poly (ethylene oxide) (PEO, MW $4x10^6$), Lithium triflate ($LiCF_3SO_3$), Al_2O_3 powder (pore size 5.8 nm, 150 mesh, neutral) and Ethylene Carbonate (EC) (purity of 98%), purchased from Aldrich, were used as starting materials. Prior to use, PEO was vacuum dried at 50 °C for 24 hrs whereas LiTf and Al_2O_3 were vacuum dried for 24 hrs at 120 °C and 200 °C respectively. Appropriate quantities of PEO and LiTf required for either oxygen to Li^+ ratio 9:1 were dissolved in acetonitrile and stirred well for 24 hrs at room temperature and the slurry was cast on a Teflon support. The polymer electrolyte film was dried in a vacuum oven for 24 hrs. The composite polymer electrolytes $(PEO)_9LiTf$ + x wt.% Al_2O_3 (x = 5,10,15,20,25) were prepared by adding x wt% of Al_2O_3 of the total PEO + LiTf weight using the same procedure as mention above. Subsequently, $(PEO)_9LiTf$ + 50 wt.% EC CPE was prepared by adding 50 wt.% of EC to the filler free polymer electrolyte. Finally the composite polymer electrolytes: $(PEO)_9LiTf$ + 50 wt.% EC + x wt.% Al_2O_3 (x = 10, 15 wt.% of the total PEO + LiTf + EC weight) were prepared by using the standard solvent casting technique. All the CPE films were finally dried in a vacuum oven for 24 hrs.

The complex impedance measurements were carried out on disc shaped samples sandwiched between two stainless steel electrodes of 13 mm diameter, using a computer controlled Schlumberger SI 1260 impedance analyzer in the 1 Hz to 10 MHz frequency range over a temperature range of 25 °C to 100 °C in 10 °C intervals on heating. The DSC thermograms were recorded using a PERKIN ELMER Pyris 1 Differential Scanning Calorimeter at a heating rate of 10 °C min^{-1} from -120 °C to 120 °C in the heating cycle. The ionic conductivity was derived

from the complex impedance data and the glass transition temperature, T_g, and the melting temperature, T_m, of different samples were extracted from DSC thermograms.

3. Results and Discussion

The temperature dependence of ionic conductivity for the composite polymer electrolytes $(PEO)_9LiCF_3SO_3$ + x wt.% Al_2O_3 (x = 10, 15, 20, 25) is shown in Figure 1. According to these observations, the addition of nano-sized alumina fillers has increased the ionic conductivity of the polymer salt complex giving the maximum conductivity enhancement for samples with 15 wt. % Al_2O_3. Also a closer inspection of all the curves reveals that the semi-crystalline to amorphous phase transition occurs around 60 °C and that a much greater conductivity enhancement occurs in the crystalline phase compared to that in the amorphous phase. The discontinuity observed in the conductivity plot of filler free electrolyte around 60 °C has essentially disappeared for the sample with 15 wt. % Al_2O_3, which appears to obey the VTF behavior, indicating its amorphous nature.

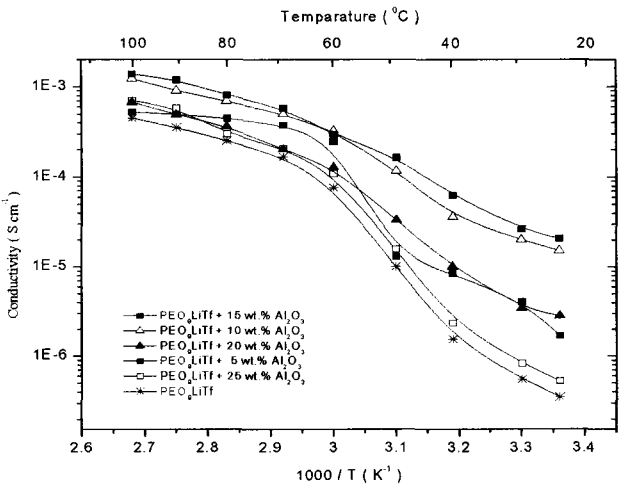

Figure 1. Variation of ionic conductivity with inverse temperature for the composite polymer electrolyte samples, $(PEO)_9LiCF_3SO_3$ + Al_2O_3 incorporating different wt.% of nano-sized alumina filler particles.

The plots of the variation of conductivity versus wt. % Al_2O_3 at various temperatures (conductivity isotherms) for the $(PEO)_9LiCF_3SO_3$ + Al_2O_3 nano composite polymer electrolyte is shown in Figure 2. The composition $(PEO)_9LiCF_3SO_3$ + 15 wt. % Al_2O_3 CPE exhibits the maximum conductivity from 25 °C to 100 °C, with a room temperature value of 2.1×10^{-5} S cm^{-1} (at 25 °C).

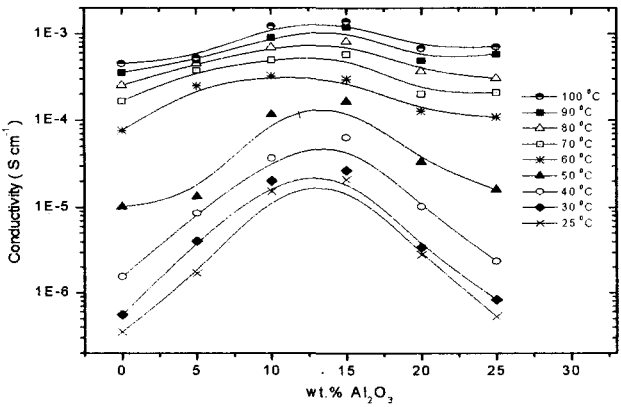

Figure 2. Variation of ionic conductivity vs. wt. % Al_2O_3 for the polymer electrolyte $(PEO)_9LiTf$ + Al_2O_3.

The plots depicting the conductivity versus 1/T variation for the electrolyte samples : (a) $(PEO)_9LiTf$, (b) $(PEO)_9LiTf$ + 50 wt.% EC , (c) $(PEO)_9LiTf$ + 10 wt.% Al_2O_3 , (d) $(PEO)_9LiTf$ + 15 wt.% Al_2O_3 , (e) $(PEO)_9$ LiTf + 50 wt.% EC + 10 wt% Al_2O_3 and (f) $(PEO)_9$ LiTf + 50 wt.% EC + 15 wt.% Al_2O_3 are shown in Figure 3.

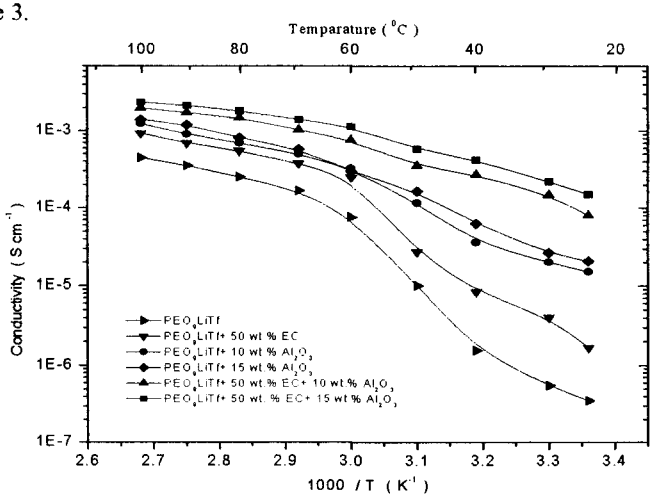

Figure 3. Variation of the ionic conductivity with inverse temperature for the composite polymer electrolyte systems : $(PEO)_9LiTf$, $(PEO)_9LiTf$ + 50 wt.% EC , $(PEO)_9LiTf$ + 10 wt.% Al_2O_3 , $(PEO)_9LiTf$ + 15 wt.% Al_2O_3 , $(PEO)_9$ LiTf + 50 wt.% EC + 10 wt.% Al_2O_3 , $(PEO)_9$ LiTf + 50 wt.% EC + 15 wt.% Al_2O_3.

According to Figure 3, there is a significant conductivity enhancement due to the addition of the plasticizer, EC to the $(PEO)_9LiTf$ electrolyte. Also, the presence of the filler (Al_2O_3) has shown a conductivity enhancement of the plasticizer-free polymer electrolyte. However, the conductivity enhancement in the polymer electrolyte with filler was higher than that of the plasticized CPE. Also, the conductivity enhancement in the plasticized CPE with filler was superior to all other samples studied. The highest room temperature conductivity enhancement of more than three orders of magnitude was obtained for the electrolyte, plasticized CPE with 15 wt. % Al_2O_3 filler concentration (Table 1). The conductivity (log σ) versus 1/T plot for the plasticized, nano-composite polymer electrolytes exhibits the amorphous behavior described by the Vogel-Tammon-Fulcher (VTF) equation.

Table 1. Conductivity values of different composite polymer electrolyte samples at room temperature (25 ° C).

Composite polymer electrolyte	Conductivity (S cm^{-1})
$(PEO)_9LiTf$	3.5×10^{-7}
$(PEO)_9LiTf$ + 50 wt.% EC	1.6×10^{-6}
$(PEO)_9LiTf$ + 10 wt.% Al_2O_3	1.5×10^{-5}
$(PEO)_9LiTf$ + 15 wt.% Al_2O_3	**2.1×10^{-5}**
$(PEO)_9$ LiTf + 50 wt.% EC + 10 wt.% Al_2O_3	8.2×10^{-5}
$(PEO)_9$ LiTf + 50 wt.% EC + 15 wt.% Al_2O_3	**1.5×10^{-4}**

Figure 4 and Table 2 show the DSC results of the different composite polymer electrolyte samples incorporating alumina filler and plasticizer (EC). These results clearly show that both the glass transition temperature (T_g) and the crystallite melting temperature (T_m) have decreased due to the addition of the filler and the plasticizer. The T_g and T_m values obtained in this work for $(PEO)_9LiTf$ electrolyte closely agree with the values reported in literature for the $(PEO)_9LiTf$ polymer electrolyte systems [3,4,6,7]. The T_g and T_m values of the $(PEO)_9LiTf$ were -44 ^{0}C and 58 ^{0}C respectively. For the plasticized $(PEO)_9LiTf$ + 15 wt.% Al_2O_3, T_g has decreased to -56 ^{0}C and T_m to 39 ^{0}C. These observations clearly suggests that a major contribution to the conductivity enhancement comes from the structural modifications associated with the polymer host caused by the plasticizer and the filler.

Table 2. Crystallite melting temperatures, T_m and glass transition temperatures, T_g of different composite polymer electrolyte samples extracted from DSC thermograms.

Composite polymer electrolyte	T_m (°C)	T_g (°C)
$(PEO)_9LiTf$	**58**	**- 44**
$(PEO)_9LiTf$ + 50 wt.% EC	57	- 48
$(PEO)_9LiTf$ + 10 wt.% Al_2O_3	54	- 49
$(PEO)_9LiTf$ + 15 wt.% Al_2O_3	51	- 50
$(PEO)_9LiTf$ + 50 wt.% EC + 10 wt.% Al_2O_3	42	- 53
$(PEO)_9LiTf$ + 50 wt.% EC + 15 wt.% Al_2O_3	**39**	**- 56**

From Figure 4, it can be seen that the T_g values of the plasticized polymer electrolyte as well as the polymer electrolyte with filler are lower than the T_g of $(PEO)_9LiTf$ electrolyte. The T_g value of the plasticized CPE with 15 wt% of the filler is the lowest. These observations correlates very well with the highest conductivity enhancement observed for the $(PEO)_9LiTf$ + 50 wt.% EC+ 15 wt.% Al_2O_3 polymer electrolyte sample.

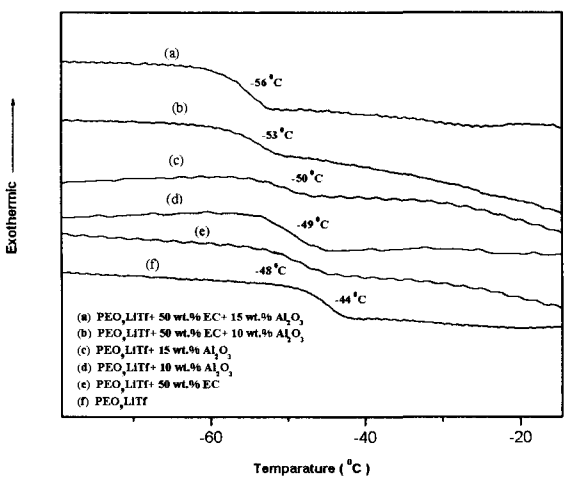

Figure 4. DSC thermograms of the different CPE films showing glass transition temperatures.

In general, for any polymer electrolyte, T_g represents the temperature at which the glassy phase becomes a rubbery, amouphous phase on heating while T_m is attributed to the melting of PEO-rich crystalline phase. Data reported in the literature for several polymer electrolyte systems reveal that there is a correlation between T_g and T_m, suggesting that the same factors related to main-chain stiffness of the polymer controls both these temperatures[10]. Therefore, a significant contribution to the observed conductivity enhancement in the plasticized, filler-added electrolyte, $(PEO)_9LiTf$ + 50 wt.% EC+ 15 wt.% Al_2O_3, having the lowest T_g and T_m values, evidently comes from the increased segmental flexibility and the increased amouphos nature of the host polymer caused by the plasticizer and the filler.

The role played by the filler needs a special consideration. As mentioned earlier, the addition of the filler to the PEO-salt complex can contribute to the lowering of T_g by increasing the volume fraction of the amorphous phase caused by the modification of the host polymer structure. The contribution to the conductivity enhancement due to the filler at temperatures below T_m should possibly be due to this effect. According to our results the conductivity has increased also in the amorphous phase above T_m due to the presence of the Al_2O_3 filler giving maximum conductivity enhancement for 15 wt .% Al_2O_3. Even in the low temperature phase below T_m, a closer comparison of the conductivity and DSC results of the plasticizer-added and filler-added samples clearly points towards the existence of a second conductivity enhancement mechanism, other than that involving the polymer host directly. Despite the comparable values of T_g in the $(PEO)_9LiTf$ + 50 wt.% EC system (T_g = - 48 °C) and the $(PEO)_9LiTf$ + 15 wt.% Al_2O_3 system (T_g =-50 °C), reflecting essentially similar effects by the plasticizer and the filler on the host polymer chain, the conductivity in the filler-added system ($2.1x10^{-5}$ S cm^{-1}) is about ten times higher than that in the plasticized system ($1.6x10^{-6}$ S cm^{-1}). This conductivity enhancement at temperatures above as well as below T_m, should therefore be caused by a different mechanism directly associated with filler grains. As described earlier by Wieczorek et al [13], it possibly results from Lewis acid- based type interactions of migrating ionic species with O/OH surface groups on alumina grains. This mechanism can provide transient sites for the hopping ions, thereby providing additional conductivity path ways for ionic motion. The combined effect of the different mechanisms as explained above, appears to contribute to the overall conductivity enhancement in the plasticized, filler-added, solid polymer electrolyte samples.

4. Conclusion

The ionic conductivity enhancement shown in the $(PEO)_9LiTf$: EC polymer electrolyte incorporating nano-sized Al_2O_3 possibly result from the combined effect of the increased amorphous content caused by the plasticizer and the filler as well as by the creation of favorable conducting pathways through Lewis acid-base type interactions of ionic species with O/OH surface groups on alumina filler grains.

Acknowledgements

Support from the National Science Foundation (NSF) (Grant number: RG/2001/P01) and the IPPS, Uppsala, Sweden are gratefully acknowledged.

References

1. S. Roy Morrison, The chemical Physics of surfaces, Second edition, Simon Fraser University, Canada, 1990.
2. D. J. Bannister, G. R. Davies, I. M. Ward and J. E. McIntyre, POLYMER, Vol. 25, 1984.
3. M. K. A. L. Dissanayake, P. A. R. D. Jayathilake, R. S. P. Bokalawela, I. Albinson and B. -E. Mellander, *Journal of power sources* **1-6**, 5330 (2003).
4. P. A. R. D. Jayathilake, M. K. A. L. Dissanayake, I. Albinson and B.-E. Mellander, *Electrochemica Acta* **47**, 3257 (2002).
5. F. Croce, L. Persi, B. Scrosati, F. Serraino-Fiory, E. Plichta and M. A. Hendrickson, Electrochemica Acta **46**, 2457 (2001).
6. L. R. A. K. Bandara, M. A. K. L. Dissanayake and B. E. Mellander, Electrochemica Acta **43**, 1447 (1998).
7. C. J. Leo, G. V. Subba Rao and B. V. R. Chowdari, Solid State Ionics **148**, 159 (2002).
8. C.W. Lin, C.L. Hung, M. Venkateswarlu and B.J. Hwang, Journal of power sources **146**, 397 (2005).
9. Jingyu Xi, Xinping Qiu, Xiaomei Ma, Mengzhong Cui, Jun Yang, Xiaozhen Tang, Wentao Zhu, Liquan Chen, Solid State Ionics **1249**,176 (2005).
10. Y. W. Kim, W. Lee, B. K. Choi, Electrochemica Acta **45**, 1473 (2000).
11. J. -H. Ahn, G. X. Wang, H. K. Liu and S. X. Dou, Journal of Power Sources **119-121**, 422 (2003).
12. G. B. Appetecchi, F. Croce, L. Persi, F. Ronci and B. Scrosati, Electrochemica Acta **45**, 1481 (2000).
13. W. Wieczorek, P. Lipka, G. Zukowska and H. Wycislik, J. Phys. Chem. **B 102** 6968 (1998).

INVESTIGATION OF TRANSPORT PROPERTIES OF A NEW BIOMATERIALS – GUM MANGOSTEEN

SOURAV S. PRADHAN and A. SARKAR

Dept. of Physics, B. K. Girls' College, 5/3 M. G. Road, Howrah 711101, India, E-mail: alokesarkar@vsnl.net.

Biomaterial has occupied leading position in material science for various scientific and technological applications. This present work is carried out over a natural gum extracted from raw fruit of Mangosteen, an east Indian tree (*Gercinia Mangostana*) following extraction and purification process. Solid specimen of the said gum is developed following sol-gel like process.

AC and DC electrical analysis on the dried solid specimen of the gum were carried out and showed high electrical conduction with $\sigma \sim 1$ E-03 S/cm, of which ionic and electronic contributions are 70% and 30% respectively. Analysis shows that origin of high electrical conductivity is due to presence of substantial amount of organic acid unit in its polysaccharide background. In fact the observed σ is about 1000 times of that observed in gum Arabica. Optical absorption of this new bio- materials are also studied using UV-VIS analysis. The results show its high absorption co-efficient in UV and blue part of analysed range. A complete electrical characterization of the material have been made. It has also been observed that the electronic conduction can be enhanced to 70% of the total electrical conductivity by forming complex with Iodine and organic (Citric) acid from *Lemon* fruit. This high potential material is being studied for development of electronic device application.

1. Introduction

In the recent period soft matter [1] occupies leading position in material science research. The most of the soft matters are derived from living things. Biomaterials especially the Biopolymers are playing most crucial role in the soft matter studies. The Bioloymers/Biomaterials systems are mostly dominated by weak, non-covalent interactions, and fluctuation like Browinan motion are also present in them. The high interdisciplinary research has gained tremendous importance from the view point of material science and modern biology.

In earlier studies [2-4] it has been found that the plant gum Acacia Arabica exhibits many interesting features from material science view point. Plant gum consists of polysaccharides, formed by the polymerization of sugar with charged groups. These polymers glue together the cellulose microfibril tomake the composite structure – most plant gum are belong to this class.

This present work is carried out over a natural gum extracted from raw fruits of *Mangosteen*, a tree (*Gercinia Mangostana*) of east Indian origin. Following appropriate extraction and purification process solid specimen of the said gum is developed by sol-gel like process. In this work an experimental study on the gum specimen has been carried out to investigate its charge transport in it and also for its potential application. The experimental probes have been employed in this study are DC and AC electrical analysis and optical absorption in the UV-VIS region.

2. Experimental

2.1 *Material Preparation*

The raw fruits from Mangosteen plant are cleaned and its chopped pieces are allowed to stand in distilled water at around 60 C for 5-6 hours. The filtrate is allowed to evaporate to obtain a thick viscous gel like matter. Hence the solid specimens are prepared in the pallet form by proper drying. The transparent near tea coloured pallet is sandwiched between two high polished Cu electrodes to obtain specimen for electrical experiments.

2.2 *Electrical Analysis*

The developed specimen of the gum is subjected to electrical analysis to investigate the nature of electrical transport in it. DC electrical experiments are carried out (1) to determine its ion – transference number following Wagner Polarisation technique [5] and it was carried out using a high sensitive micro-processor based set up that was capable to record the transient polarization current with time. (2) DC volt ampere characteristics of the specimen are recorded using Keithley (USA) 2400 Electrometer.

AC electrical experiments were carried out to investigate greater aspect charge transport through the specimen and was carried out using HIOKI (Japan) 3522 LCZ Meter.

2.3 *Optical Experiment*

The physicsl appearance of the specimen exhibit colour hence its optical absorption characteristics in the UV-VIS region were studied to investigate the photo- charge separation in the specimen. It is studied using Systronics (India) 2020 UV-VIS, spectrophotometer.

3. Results

The ion transference number (τ) for the specimen was estimated from polarization current data following relation,

$$\tau = \frac{I_t - I_e}{I_t}$$

where It is the initial transient current and Ie is the final steady electronic current. The τ for the pure specimen was eliminated to be 70% hence electronic contribution to the total current is 30%. However the value of τ obtained for complex present gum is found to be of lower value. Results of Iodine complex and citrate complex of the gum show an enhanced electronic contribution upto 70% of the total contribution. The enhancement was found to vary with concentration of the guest over host pure gum.

The results of DC V-I characteristics is shown in Fig. 1. Figure 2 shows the V-I characteristics for Iodine complex of the gum.

There exists a marked difference in the characteristics due to formation of the complex. In this regard it is to be noted that Iodine Solid at RT do not exhibit any such V-I characteristics. The DC electrical behaviors also shows that the marked electronic contribution reduces space charge effect which is very predominant in a superionic solid.

Figure 3 shows the variation of AC conductivity of the pure specimen with frequency of the impressed ac signal between frequency range 1Hz-100KHz.

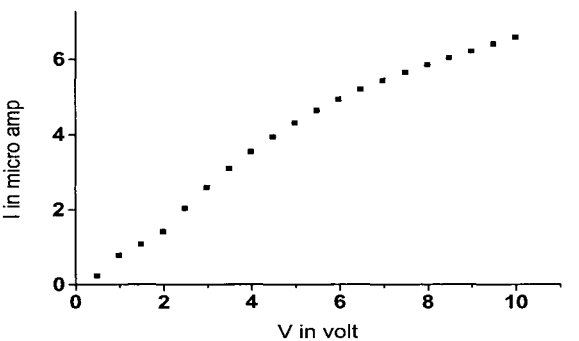

Fig. 1. V-I characteristics of pure Gub material at RT. (Sample thickness-0.5 mm, Sample area-1.0 sq cm)

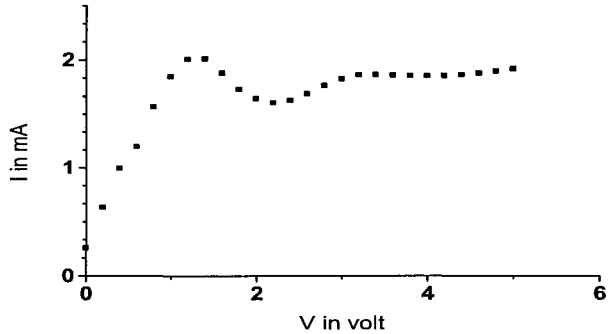

Fig. 2. V-I characteristics of Iodine Complex of Gum material at RT. (Sample thickness-0.5 mm, Sample area- 1.0 sq cm)

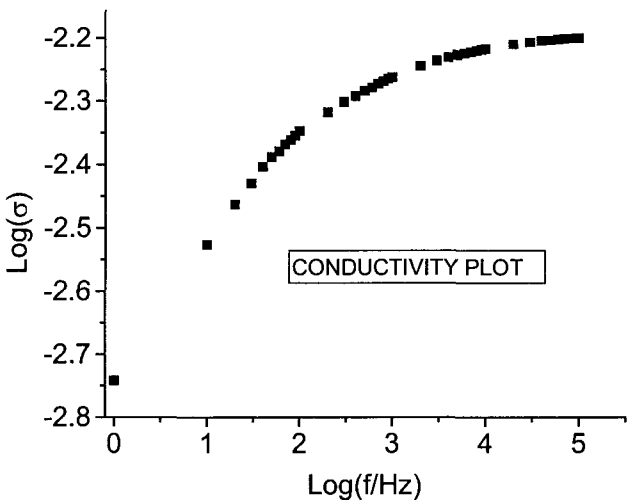

Fig. 3. Variation of σ with frequency (f) for pure specimen at RT. (Sample thickness-0.5 mm, Sample area- 1.0 sq cm)

Figure 4 shows the optical absorption of the pure gum in the wavelength range 200 nm to 900 nm.

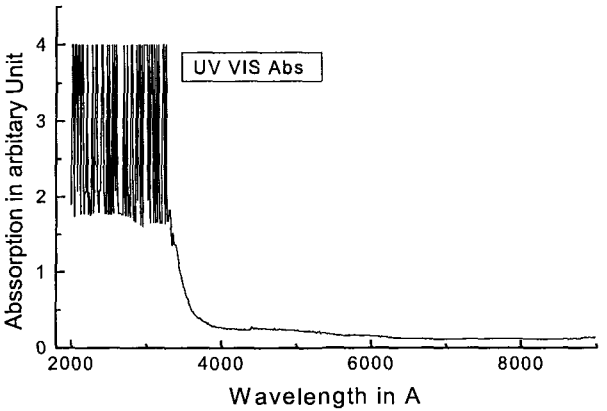

Fig. 4. UV-VIS absorption of Pure gum Mangosteen at RT.

Figure 5 shows the same for the Iodine complex of the gum specimen which has a marked distinction over that pure gum and Iodine.

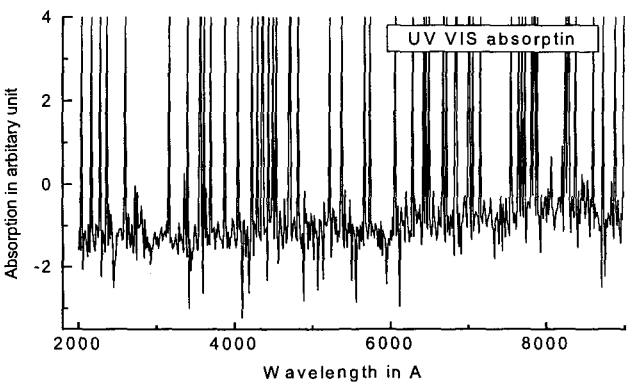

Fig. 5. UVVIS absorption for Iodine complex of gum Mangosteen.

4. Discussions

The result of ion transference number measurement shows that the gum has a mixed conduction nature. The electronic conduction in the gum is strongly

modified under addition of weak organic acid unit in its structure. The inclusion of iodine in the gum perhaps form a complex and behaving as n-type dopant in the pure gum.

The result of dc V-I characteristics (Fig. 1) on the pure gum specimen shows its electron conducting nature like n-doped conducting polymers. The effect of electrode reaction is not very predominant but substantial contact resistance. The electronic conductivity for the pure specimen is estimated to be 3E-07 S/cm. The nature of V-I characteristics (Fig. 2) for iodine complex of the gum definitely showing the enhancement of electronic contribution in the total conductivity. The non-linear nature of the V-I characteristics in Fig. 2 shows its material potential for electronic device application. The dc conductivity estimated from the initial part of Fig. 2 is found to be 3E-04 S/Cm.

The total electrical conductivity of the material estimated from bulk resistance of the specimen following Fig. 3 was found to be ~ 6E-03 S/Cm at 1 Hz. This value is substantially high for solid biomaterials/biopolymers. The nature of Fig. 3 is also an indicator for enriched electronic contribution in the pure gum specimen.

The results of optical absorption of the pure gum (Fig. 4) exhibit high absorbance in the UV to mid visible region. In fact this is a most important characteristics of many biomaterials. The said absorption has been greatly modified by its complex formation with Iodine. The nature of absorption form the Fig. 5 shows its marked characteristics. The optical absorption confirm that because of strong photo-absorption the molecular charge separation occurs leading to high electrical conduction over its normal ionic conduction.

The over all material characteristics those investigated so far are very interesting. The presence of organic acid unit in the molecular structure may provide high electrical conduction. The presence photo-absorbing group induce charge separation to provide high carrier concentration. The photo induced charge separation [6] is observed in many bio-materials and the property has also been realized in development of bio-material complex. The inclusion of Iodine is found to be more effective than that of organic natural acid. Since the former enhance photo-absorption and provide substantial charge carrier however the later require adequate activation to generate carrier.

Using the very fascinating character of the gum and its complex few device applications are in the process of development.

5. Conclusions

The gum Mangosteen is a high conducting biomaterials with substantial electronic contribution due presence of organic acid unit in it.

Acknowledgement

Author acknowledge U.G.C., New Delhi, India for support this research (No. 30-2/2004 SR)

References

1. *Soft Condensed Matter*, R.A.L Jones, Pub. Oxford Univ. Press Inc, New York, 2002, Ch-8.
2. H. Mallick and A. Sarkar, Bull. Mat. Sc. **23**, pp. 319–325, 2000.
3. H. Mallick, N. Gupta and A. Sarkar, Mater. Sci. Engg. C (Elsevier) **C20**, pp. 215–218, 2002.
4. H. Mallick and A. Sarkar, *Ion Conducting Materials, Theory and Application*, eds. A.R. Kulkarni and P. Gopalan, Narosa Pub. House, New Delhi, 2001, p. 38–42.
5. *Superionic Solids – Principle and Application*, S. Chandra, NHPC, Amsterdam, 1981.
6. *Supramolecular Chemistry*, J. W. Steed and J. L. Atwood, Pub. John Wiley and Sons Ltd., England, 2000, Ch. 5–8.
7. H. Mallick, P. Mukhopadhaya and A. Sarkar, Solid State Ionics, **175**, pp. 769–772, 2004.

INVESTIGATION OF IONIC CONDUCTIVITY OF PEO- $MgCl_2$ BASED SOLID POLYMER ELECTROLYTE

M.SUNDAR, P.N.POOVIZHI, J.ARUNKARTHIKEYAN and S.SELLADURAI*

Ionics Lab, Department of Physics, AnnaUniversity, Chennai-25, India

Abstract

Novel solid polymeric electrolyte (SPE) consisting of Poly (ethylene oxide) PEO with magnesium chloride as the electrolyte salt has been prepared by solution casting technique. Measurements with differential scanning calorimetry (DSC) indicates the modification of PEO crystalline structure with increasing content of magnesium salt up to 20 wt% and increase in crystallinity at higher concentration. FTIR studies indicates the interaction of Mg cations with ether oxygen of PEO, Ionic conductivity increases with increase in salt content, and it is optimized at 20 wt% Mg salt. The decrease in ionic conductivity at higher salt content above 20 wt% is due to ion-ion interaction, which leads to ion pair formation and increase in relative crystallanity fraction due to recrystallization above 15wt%.

Keywords: Polymer electrolyte, conductivity, ion-ion interaction.

Introduction

Polymers found application in various fields and in recent past much focus is being given for the development of Polymer electrolyte membranes for high energy density batteries, The interest for these materials parallels that for polymers in general, whose appearance in new scientific domains or applications have been steadily increasing. Properties which includes suppression of dendrite growth, endurance to varying electrode volume during cycling, less reactive than their liquid counterpart, improved safety, good conductivity led to lot of interest on research and development of polymer electrolyte for various solid state batteries [1-4], In all these structural modification of the polymer plays an effective role in enhancing its utility in the above mentioned device.

Polyethylene oxide (PEO)- based polymeric electrolyte is the earliest and are still among the most extensively studied polymeric ionic conductors because of beneficial structure in supporting fast ion transport and its exceptional solvating

nature for variety of ionic salts to form an electrolyte [5-16]. In PEO cations are coordinated with the oxygen atoms of the polyether chain due to Lewis acid-base interaction. The ionic transport in this polymer may be interpreted on the basis of hopping mechanism of coordinated cations between the polymer chains [17-19]. In the present study we report ionic conductivity studies of solid polymer electrolyte based on PEO – $MgCl_2$ at ambient temperature and citing critical evidence of ion-polymer and ion-ion interaction from FTIR spectroscopic, Differential scanning calorimetry and demonstrate their impact on Ionic conductivity.

Experimental

The polymer electrolyte films of pure PEO (M.W. 7,00,000) purchased from Aldrich) and various compositions of complexed films of PEO with magnesium chloride salt were prepared in weight percent ratios (70:15), (80:20), (75:25) and (70:30) have been prepared by solvent casting method at 30°C, polymer and salt were dissolved in suitable solvent (methanol) the solution of the salt and polymer are stirred for 10 hours for making perfect complexation .The above solution is casted on to polypropylene dishes, the solvent is removed by slow evaporation and the final product is treated under vacuum to remove residual solvent, traces of residual solvent which is capable of acting as nucleation sites are the limitation of this method, the film obtained is self standing with thickness 80 to 100 microns. Infra red spectra were recorded on Shimadzu instrument with a wave number resolution of 4 cm^{-1} in the frequency of 400-4000 hertz, for that measurement the mixed slurry were cast on the KBr wafer and dried via the same steps used in the preparation of polymer electrolyte films. Differential scanning calorimeter measurements were carried out on Netzsch thermal analyzer, all the measurements were carried out at a heating rate of 5°/min from 30° to100°, the sample weights are maintained at 5-10 mg and all experiments are carried out under nitrogen flow to avoid any contact with atmospheric moisture, and empty aluminum pan was used as a reference. CHEN-HWA (model 1061) LCZ bridge is used for measuring conductivity values in A.C impedance method by applying frequency ranges from 40 Hz to 200 kHz.

Conductivity values are calculated by the formula

Conductivity = $t / (A \times R_b)$ S/cm

t-thickness of the sample, A-Area of the sample

R_b-bulk resistance

Results and discussion

IR spectroscopic studies

Polymer complexes with ionic salts have been characterized by IR spectroscopy [7,9,10,12,20,21,28]. This technique provides a powerful means to characterize the organic and inorganic components and their composite formation. The IR spectra of pure PEO and its blending with $MgCl_2$ are compared and the following results are obtained. In Figure 1marked changes were found when PEO is blended with $MgCl_2$ salt. The aliphatic C-H stretching vibration band (2800 –2900) cm^{-1} found in PEO decreases in intensity and wave number with increasing in magnesium salt concentration, it is because of the acid –base coordination between Mg cations & oxygen of ether of PEO which involves the dipole-dipole interaction. The interaction is clearly indicated by influence directly on C-O-C stretching ranging between 1000-1200 cm^{-1} .the C-O-C stretching band decreases around 1100 cm^{-1} and decrease is pronounced with increase in salt concentration. This suggests the complexation of the salt with the polymer. Vibrational spectroscopy results clearly indicate there is an association of Mg salt with PEO.IR spectra of PEO blended with Mg salt indicated in the range of 600 – 650 cm^{-1}, at salt content of 20wt % and above clear frequency band is developed which indicates different conformations possible for the complex between Mg and the polymer

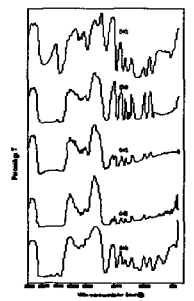

Figure 1 : FTIR patters of the PEO: $MgCl_2$ polymer electrolyte system
(a)0 wt%,(b) 15wt%,(c)20wt%,(d)25wt%,(e)30wt%

PEO, at 20wt% salt concentration C-O-C stretching band values are at 1114 cm^{-1} and the peak broadening takes place in the case of C-H stretching band. These results clearly indicates the presence of large number of free Mg cations and complexation is minimum at this particular composition. The intensity of the band suggests that reassociation of chlorine ions with magnesium cations above 20wt% of salt content.

DSC studies

DSC studies have been employed to determine the thermal behavior of PEO: Mg polymer complexed system. The DSC curves shown in figure 2 suggests the heat of fusion and melting temperature decreases with increase in salt content to the PEO till 15wt%, in addition the melting endotherm becomes narrower, both reducing melting temperature and narrowing of endotherm are consistent with the notion of PEO interaction with Mg, which leads to smaller PEO crystallites up to 15wt%.

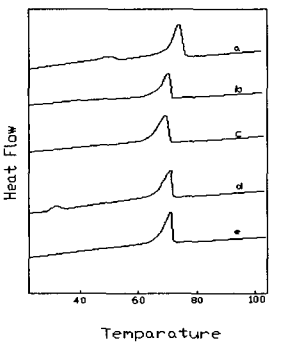

Figure 2 DSC curves of PEO: $MgCl_2$system
(a)0 wt%,(b) 15wt%,(c)20wt%,(d)25wt%,(e)30wt%

The relative crystalline percentage has been calculated by means of the equation [$\Delta H_f / \Delta H^0_f$] ΔH^0_f is the heat of fusion of pure PEO, ΔH_f related to complexed PEO .It is interesting to note that crystallinty is suppressed more effectively due to disruption of PEO crystallinity up to 15%. At high salt concentration (i.e. 25% & 30%) $MgCl_2$ acts as a nucleating agent and recrystallization occurs which is indicated by increase in relative crystallinity and increase in melt temperature.

Table 1 The IR spectra of pure PEO and its blending with $MgCl_2$

$MgCl_2$ (wt%)	C-H (stretching vibration) cm^{-1}	C-O-C (stretching vibration) cm^{-1}
0	2900	1100
15	2885	1066
20	Broad band (2900)	1114
25	2810	1083
30	2828	1055

Ionic conductivity

The variation in conductivity as a function of salt concentration of Mg salt added to PEO is displayed at ambient temperature in table 2. The results indicate that the room temperature conductivity of PEO is about 10^{-9} [22] and increase sharply with increase in magnesium salt content. The charge transport in PEO solid polymer electrolyte complex involves dissociation of cations from its coordinating oxygen to an adjacent site [28]. The high ionic conductivity in an electrolyte is attributed to increased ionic mobility and increased ionic charge carrier concentration .The enhancement of ionic conductivity increases with increases salt concentration and maximum value at 20wt%. Clearly the decrease in conductivity at high salt concentration is due to decrease in free ions due to formation of ion-ion paring. This trend is similar to the results reported by various researchers in studies on lithium salt in PEO –based polymer electrolyte systems using the concept of ion association and formation of charge multiplets [23,24,25,28]. The IR studies indicate clearly the ion –ion pairing occurs with increase in salt concentration above 20wt%. Mg cations give a stronger acid –base interaction with the polymer substrate in comparison to lithium salts. Therefore the tendency to form an ion pair is stronger, but at the same time the interaction with ether oxygen is also stronger compared to lithium. These above factors lead to a decrease in the free Mg ion fraction in the PEO at high salt uptake, where the conductivity deteriorates [26-28]. In this present study we site another reason for decrease in conductivity with respect to DSC studies the results shows that increasing the salt content from 15 % to20%, 25%& 30% wt recrystallization takes place in the polymer electrolytes as indicated by increase of melting temperature, relative crystallinty, this result also suggests that both Mg-PEO association, and ion pairing complexes disrupts PEO crystallinty upto 15 wt%, and above 15 wt%

recrystallization also may cause the decrease in conductivity values in addition to ion -pairing.

Table 2 Melting temperature (Tm), crystalline percentage, w (%) and ionic conductivity of PEO: $MgCl_2$system

$MgCl_2$ (wt%)	Tm (degrees)	Relative crystallinity (%)	Conductivity(s/cm)
0	72.7	100	3.569×10^{-9}
15	59.28	30.13	4.546×10^{-7}
20	60.1	30.98	2.985×10^{-6}
25	63.5	31.67	2.743×10^{-6}
30	68	32.42	1.987×10^{-6}

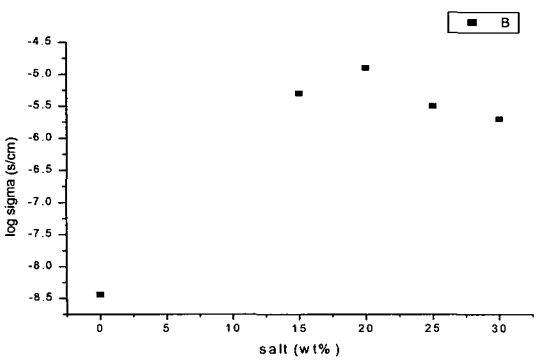

Fig .3 Compositional conductivity of PEO: $Mgcl_2$ system.

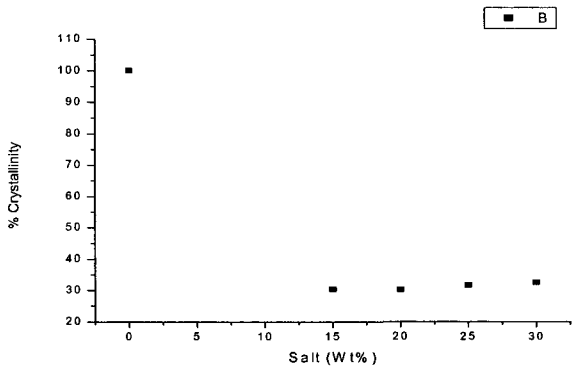

Fig 4 Compositional crystallinity of PEO: $Mgcl_2$ system.

Conclusion:

Interaction of cations of Magnesium salt and ether oxygen of PEO shows a compositional dependency of ionic conductivity. The optimum value of ionic conductivity is found to be at 20 wt %. The subsequent decrease in ionic conductivity is due to the consumption of free Mg ions through the ion pair association of Mg cations and chlorine ions and increase in relative crystallinty due to recrystallization above 15 wt%, which retards the ion mobility. Thus in PEO- $MgCl_2$ based solid polymer electrolyte the optimum ionic conductivity value of 2.985×10^{-6} is at 20wt % and recrystallization takes place above 15wt% and these films shall be considered as polymer electrolyte film in secondary solid state magnesium batteries.

References

[1] M.B. Armand, Ann. Rev. Mater. Sci. 16 (1986) 245.

[2] M.A. Ratner, D.F. Shriver, Chem. Rev. 88 (1988) 109.

[3] J.R. Mac Callum, C.A.Vincent (Eds.), Polymer Electrolyte Reviews,Elsevier, Amsterdam, 1987.

[4] J.Y. Song, Y.Y. Wang, C.C. Wan . Journal of Power Sources 77 1999 183–197

[5] K. Murata, Electrochim. Acta 40 (1995) 2177.

[6] S.A. Hashmi, A. Chandra, S. Chandra, in: B.V.R. Chowdari, et al.

Eds.), Solid State Ionics: Materials and Applications, World Scientific, Singapore, 1992, p. 567.

[7] S. Sreepathi Rao, M. Jaipal Reddy, E. Laxmi Narsaiah, U.V. Subba Rao, Mater. Sci. Eng. B 33 (1995) 173.

[8] W. Gorecki, M. Jeannin, E. Belorizky, C. Roux, M. Armand, J. Phys.Condens. Matter 7 (1995) 6823.

[9] S.Selladurai, Trends in solid state Ionics,raj publishing house ,chennai.

[10] T. Sreekanth, M. Jaipal Reddy, S. Subramanyam, U.V. Subba Rao,Mater. Sci. Eng. B 64 (1999) 107.

[11] A.L. Oleksiak, H.D. Inerowicz, J. Power Sources 81/82 (1999) 813.

[12] T. Sreekanth, M. Jaipal Reddy, S. Ramalingaiah, U.V. Subba Rao, J.Power Sources 79 (1999) 105.

[13] J.M. Philas, B. Marsan, Electrochim. Acta 44 (1999) 2351.

[14] F. Lemaitre-Anger, J. Prudhomme, Electrochim. Acta 46 (2001) 1359.

[15] M.B. Armand, in: J.R Mac Callum, C.A. Vincent (Eds.), Polymer Electrolyte Reviews, Elsevier, Amsterdam, 1987, p. 1.

[16] S. Lascaud, M. Perrier, A. Vallee, S. Besner, J. Prudhomme, M.Armand, Macromolecules 27 (1994) 7469.

[17] H. Cheradame, P. Niddam-Mercier, Faraday Disc. Chem. Soc. 88 (1989) 77.

[18] S. Ramalingaiah, D. Srinivas Reddy, M. Jaipal Reddy, E. Laxmi Narsaiah, U.V. Subba Rao, Mater. Lett. 29 (1996) 285.

[19] C. Liebenow, A. Reiche, P. Lobitz, Electrochim. Acta 40 (1995) 2375.

[20] S.A. Hashmi, A. Kumar, K.K. Maurya, S. Chandra, J. Phys. D. 23 (1990) 784.

[21] K.K. Maurya, S.A. Hashmi, S. Chandra, J. Phys. Spc. Jpn. 61 (1992) 1709.

[22] M. Jaipal Reddy, P.P. Chu, Electrochim. Acta 47 (2002) 1189.

[23] K.K. Maurya, B. Battacharya, S. Chandra, Phys. Stat. Sol. (a) 148 (1995) 347.

[24] M.A. Ratner, A. Nitzman, Faraday Disc. Chem. Soc. 88 (1989) 19.

[25] M. Jaipal Reddy, U.V. Subba Rao, J. Mater. Sci. Lett. 17 (1998) 1613.

[26] M. Doeff, P. Georen, J. Qiao, J. Kerr, L.C. De Jonghe, J. Electrochim. Soc. 146 (1999) 2024.

^{1}H NMR AND RAMAN ANALYSIS OF PROTON CONDUCTING POLYMER ELECTROLYTES BASED ON PARTIALLY HYDROLYZED POLY (VINYL ALCOHOL)

G. HIRANKUMAR , S. SELVASEKARAPANDIAN*
Solid State and Radiation Physics Laboratory, Department of Physics, Bharathiar University, Coimbatore 641 046, India
E-mail: sekarapandian@yahoo.com

J. KAWAMURA , N. KUWATA, O. KAMISHIMA
Institute of Multidisciplinary Research for Advanced Materials, Tohuku University, Sendai, Japan

T. HATTORI
Department of Applied Physics, Tokyo University of Science, Tokyo, Japan

The proton conducting solid polymer electrolytes comprising of partially hydrolyzed Poly (vinyl alcohol) and Ammonium thiocyanate have been prepared at different composition by solution cast method. The solid polymer electrolytes have been subjected to ^{1}H NMR, Raman and AC impedance spectroscopy analysis. Raman analysis confirms the amorphous nature and complexation of solid polymer electrolytes. Raman studies also provide the details about aggregation of ions in the polymer electrolyte system. ^{1}H NMR analysis indicates that the observed chemical shift at 6.3 ppm is due to NH_4^+ ion. It is also observed that the intensity of the peak at 6.3 ppm is maximum for 15 mol% NH_4SCN doped polymer electrolyte which indicates the free NH_4^+ ions is maximum for this concentration. This result is consistent with conductivity data which indicates the maximum conductivity at 15 mol% NH_4SCN doped polymer electrolyte and ionic conductivity has been found to be 3×10^{-3} S cm^{-1}. The temperature dependent ^{1}H NMR studies indicate that the acetate ion which is the residual part of partially hydrolyzed PVA also involved in the conduction process. The ^{1}H NMR also confirms that the mobile species in the polymer electrolytes are NH_4^+ ion.

1. Introduction

In recent years, intensive research efforts have been rendered to develop a new proton conducting solid polymer electrolytes for fuel cell applications [1]. The protonic transport in polymer electrolytes generally involves motion of the groups like H^+, NH_4^+, H_3O^+, OH^- etc. Ammonium salts have been reported as good proton donors to the polymer matrix such as poly (vinyl alcohol) [2], poly (ethylene oxide) [3], poly (ethylene succinate) [4], poly (vinyl acetate) [5]. Among them, poly (vinyl alcohol) (PVA) is a water soluble poly hydroxyl polymer which is employed in many practical applications because of its easy preparation, excellent chemical & physical properties and completely biodegradable nature [6]. MacFarlane et al. [7] have studied the lithium ion mobility in poly (vinyl alcohol) based polymer electrolytes and they have also observed that the lithium ion mobility is greater for partially hydrolyzed (88 %) poly (vinyl alcohol) compared to the fully hydrolyzed PVA. Hence, the present work focuses the development of new polymer electrolytes comprising of partially hydrolyzed (88 %) poly (vinyl alcohol) and NH_4SCN at different salt concentration.

^{1}H Solid State NMR and Raman measurements, together with conductivity of PVA-NH_4SCN systems are presented in this work in order to investigate the conduction mechanism of partially hydrolyzed poly (vinyl alcohol) based polymer electrolyte.

2. Experimental

Thin films of Polymer electrolyte (200 μm) of pure poly (vinyl alcohol) (Mw = 1,25,000) (Degree of hydrolysis = 88%) and poly (vinyl alcohol) doped with ammonium thiocyanate with different compositions have been prepared in the mole ratios (95:5), (90:10), (85:15) and (80:20) by solution cast technique. Aqueous solutions of poly (vinyl alcohol) and NH_4SCN mixtures were thoroughly stirred to obtain homogeneous mixture. The mixture was then poured on to a glass plate and evaporated slowly at room temperature. The smooth, uniform thin films which are transparent to visible light with good mechanical properties have been obtained. The final product was then vacuum dried. Raman measurements have been carried out on the polymer electrolyte samples in the wavenumber range of 100-3800 cm^{-1}. The 40 mW 514.5 nm laser beam from Ar^+ laser is focused to the sample to a spot size of about 0.1 mm diameter. ^{1}H solid state NMR spectra have been performed using a Bruker Spectrometer with the Larmor frequency 200.13 MHz and chemical shift have externally referenced to TMS. The ^{1}H NMR measurements have been taken as a function of temperature and salt concentration in order to establish the relationship between the dynamic properties of proton ion and the polymer chain. The resonance peak has been fitted by using the commercial software PEAKFIT. The electrical conductivity study of the polymer electrolytes has been carried out in the temperature range of 303 – 373 K over a frequency range of 42 Hz – 1 M Hz using a computer controlled HIOKI 3532 LCR meter with a cell having Stainless steel electrodes.

3. Results and Discussion

3.1. Raman studies

Figure 1 displays Raman spectra of PVA-NH_4SCN systems at different salt concentrations (systems b, c, d, e) along with the spectrum of the host polymer (PVA) (system a) in the range 600 – 2100 cm^{-1}. Frequencies and their assignments for the system pure PVA, PVA-NH_4SCN at room temperature are presented in Table 1. The Raman bands of pure PVA agree well with the reported values [8].

Table 1 Raman band assignments of PVA-NH_4SCN polymer electrolyte.

Pure PVA	PVA–NH_4SCN				Assignment
cm^{-1}	(95:5) cm^{-1}	(90:10) cm^{-1}	(85:15) cm^{-1}	(80:20) cm^{-1}	
	755	752	756	754	C-S (s)
850	847	837	835	834	C-C (s)
908	914	904	913	917	C-C (s)
1012	1022	1013	1015	1018	C-O (s), O-H (b)
1073	1075	1074	1073	1071	C-O (s), O-H (b)
1130	1126	1124	1126	1121	C-C (s), C-O (s)
1355	1364	1364	1372	1365	C-H (b), O-H (b)
1437	1438	1431	1439	1430	C-H (b), O-H (b)
2887	2890	2886	2898	2887	C-H (s)
2914	2912	2914	2925	2916	C-H (s)

Iwamoto et.al [9] used laser Raman spectroscopy to demonstrate peaks at 1147 cm^{-1} and 1094 cm^{-1} in PVA are crystallinity - dependent. In the present study, the broad bands at 1130 and 1073 cm^{-1} have been observed along with a shoulder at 1012 cm^{-1}. The 1130 cm^{-1} band is due to C-C stretching and C-O stretching while the bands at 1073 and 1012 cm^{-1} may be attributed to a mixture of C-O stretching and O-H bending. These peaks get affected (observed as broad) by the presence of water molecule which has been used as solvent. According to Iwamoto et.al [9], the Raman mode at 1121 cm^{-1} for PVA can be due to the presence of amorphous nature of polymer. Thomas et.al [8] have also observed that crystallinity dependent region of PVA are affected by the presence of water molecule. In the present study, the broad nature of the crystallinity dependent region (1000 – 1200 cm^{-1}) and the presence of broad peak at 1121 cm^{-1} confirm the amorphous nature of PVA.

It has been observed that the addition of NH_4SCN (b, c, d, e) introduce a broad band centered at 1580 cm^{-1} which can be attributed to NH_4^+ ion [10].

It is well known that the introduction of larger anion from the salt to the polymer matrix helps to improve amorphous nature of host polymer because of its role as plasticizer. This change in crystalline nature to amorphous nature of the electrolyte due to the addition of NH_4SCN has been confirmed by broadening of the mode at 1130 cm^{-1}. The Raman modes at 1437 cm^{-1} and 1355 cm^{-1} in the region (600 – 2100 cm^{-1}) can be attributed to mixture of C-H bending and O-H bending vibrations. These modes give rise to broad peak with the addition of NH_4SCN (b, c, d, e). The band broadening in Raman spectra is usually an indication of amorphous nature of the polymer electrolyte. It is also observed that the intensity of the mode at 1437 cm^{-1} and 1355 cm^{-1} decreases with increase of NH_4SCN concentrations. This

intensity drop is related to the formation of ionic bond with less polarization. The increase in ionic bond is the result of charge localization in the polymer. The charge localization is a clear evidence of strong interaction between the dissociated salt and PVA.

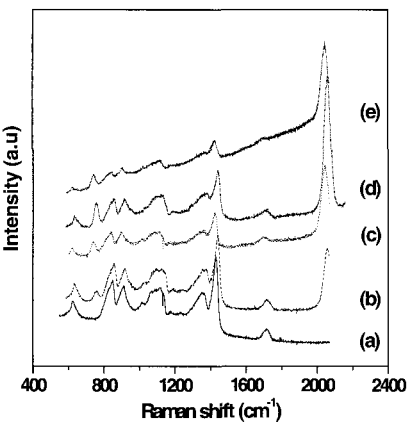

Figure 1 Raman spectra of the PVA-NH_4SCN systems at different salt concentrations a) 0 mol% (pure PVA) b) 5 mol% c) 10 mol% d) 15 mol% e) 20 mol%

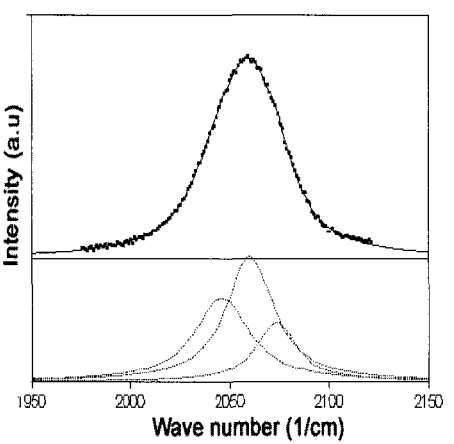

Figure 2 The Raman band associated to the C≡N stretching mode for 85 mol% PVA-15 mol% NH_4SCN system fitted by Lorentzian

The addition of NH_4SCN to the pure PVA gives rise to new characteristic peaks at 756 cm^{-1} and 2060 cm^{-1} which are attributed to C-S stretching [11] and

C≡N stretching [12] respectively. To study the ion-ion interaction, it is usual to investigate the C≡N stretching vibrational mode of anion because its spectral mode is clearly dominant from the other vibrational modes. Figure. 2 shows the Raman band associated with the C≡N stretching mode for 15 mol% NH_4SCN doped polymer electrolyte system. The band is fitted by a Lorentzian line shapes at 2046 cm^{-1}, 2060 cm^{-1} and 2073 cm^{-1} which are ascribed to free SCN^- ion, contact ion pair (NH_4^+...SCN^-) and triple ion formation. It has also been observed that the intensity of the band at 2046 cm^{-1} corresponding to free ions, increases with increase of salt content up to 15 mol%. The intensity of the band at 2046 cm^{-1} decreases while the intensity of the band at 2073 cm^{-1} increases with further addition of salt to the polymer matrix. This may be due to the large number of triple ion formation at higher salt concentration (20 mol%). The intensity of the Raman band at 756 cm^{-1} is progressively increased with increase of NH_4SCN concentration.

3.2. NMR analysis

The solid state ^1H NMR spectra of pure PVA and PVA doped with different amounts of NH_4SCN (b, c, d, e) at room temperature are shown in Figure 3. In the ^1H NMR spectrum of pure PVA(a), a relatively broad peak has been observed. The broad nature of the signal is primarily due to strong ^1H – ^1H dipolar interactions [13] in PVA, which causes decrease in mobility of the polymer chain. From the Figure 3, a new peak at 6.3 ppm for 5 mol% NH_4SCN (b) doped polymer electrolyte has been observed. This peak can be attributed to the NH_4^+ ion as predicted by Ratcliffe et al. [14].

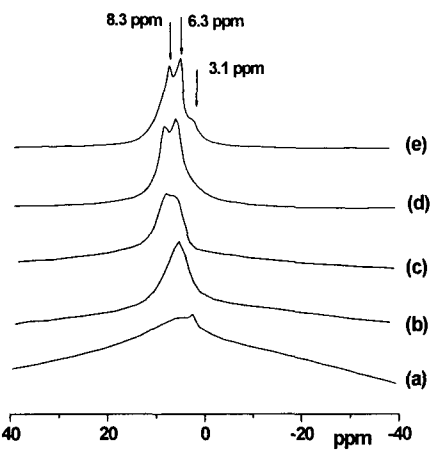

Figure 3. ^1H NMR spectra of PVA doped with a) 0 mol% (pure PVA) b) 5 mol% c) 10 mol% d) 15 mol% e) 20 mol% of NH_4SCN

As evidenced from the Figure 3, for PVA doped with 10 mol%, 15 mol%, 20 mol% of NH_4SCN, the chemical shift of 8.3 ppm, which corresponds to N-H has been noticed. This peak is more prominent as the NH_4SCN concentration increases. The small NMR peak at 3.1 ppm for 20 mol% NH_4SCN doped sample has also been observed and this chemical shift can be ascribed to methyl proton in the acetate group [15] of partially hydrolyzed PVA. At higher salt concentration of NH_4SCN, SCN^- may replace the acetate group from the polymer matrix. This may be due to strong electronegative nature of SCN^- than CH_3COO^- ion. The replacement of CH_3COO^- ion by SCN^- ion causes the free CH_3COO^- ion in the polymer matrix and this acetate ion gives the NMR peak at 3.1 ppm.

The normalized intensity of NH_4^+ ion for the PVA-NH_4SCN system has been tabulated in table 2. It has been observed that the intensity of the resonance peak at 6.3 ppm for 15 mol% NH_4SCN (d) doped electrolyte is greater than that of the 20 mol% NH_4SCN doped electrolyte, which reveals the formation of ion aggregates in the 20 mol% NH_4SCN (e) doped electrolyte. As a consequence, the number of free ammonium ions decreases at higher salt concentration for the system.

The interaction between the NH_4^+ ion and the polymer chain is further supported by the change in its chemical shift with salt concentration (b, c, d, e). The chemical shift of NH_4^+ ion at 6.3 ppm for PVA-NH_4SCN shifts to downfield with increasing salt concentrations. This chemical shift change is also due to the interactions of the NH_4^+ cation with the polymer chains. The marked difference in NMR spectra between the undoped and doped samples indicates that the mobility of the polymer chain has been affected by addition of salts. Thus, the change in intensity and chemical shift of the proton signals in the complexes support the formation of polymer complexes between PVA and NH_4SCN.

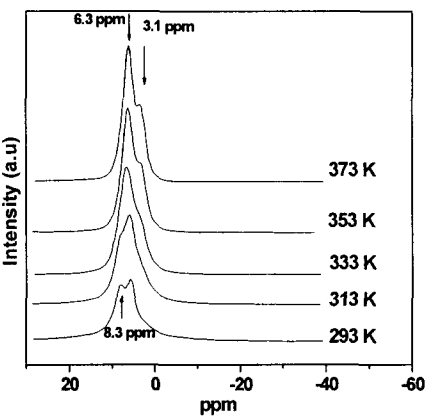

Figure 4. Temperature dependence of the ^1H NMR spectra for 85 mol% PVA - 15 mol% NH_4SCN

The ^1H NMR spectra of 15 mol% NH_4SCN (d) doped poly (vinyl alcohol) at different temperatures are shown in Figure 4. The resonance peaks have been best

fitted by Lorentzian at all temperatures. From the Figure 4 (293 K), two peaks have been observed at 6.3 ppm and 8.3 ppm, which can be ascribed to the proton in NH_4^+ and N-H respectively. The intensity of the peak at 8.3 ppm reduces as the temperature increases and this peak disappears at higher temperatures. It has also been observed that the intensity of the resonance peak at 6.3 ppm increases with increase of temperature. As the temperature increases, the full width half maximum of this resonance peak decreases as a result of increased ammonium ion mobility. A new peak at 3.1 ppm, which is due to methyl proton in acetate group, is visible at 313 K and the intensity of this peak increases with further increase of temperature. This may be due to the formation of free acetate ions from the PVA at higher temperature. It is observed that the full width half maximum of this peak decreases with increase of temperature, which indicates that the acetate ions has also involved in the conduction process in polymer electrolyte.

From the NMR analysis, the intensity of NH_4^+ ion peak is maximum for 85 mol% PVA – 15 mol% NH_4SCN which indicates that the free NH_4^+ ion is maximum for this concentration. The NMR results indicate that the NH_4^+ is responsible for conduction in these systems.

Table 2 Normalized intensity of the NH_4^+ proton peak and conductivity value for PVA - NH_4SCN complex at room temperature

	Normalized intensity of the NH_4^+ proton peak	Conductivity (Scm^{-1})
95mol% PVA - 5mol% NH_4SCN	0.11	1.86×10^{-6}
90mol% PVA - 10mol% NH_4SCN	0.38	1.44×10^{-4}
85mol% PVA - 15mol% NH_4SCN	0.77	2.95×10^{-3}
80mol% PVA - 20mol% NH_4SCN	0.31	4.46×10^{-4}

3.3. Conductivity analysis

Figure 5 shows the variation of normalized intensity of the NH_4^+ ion and log (σ) as a function of salt concentration. The conductivity of the partially hydrolyzed PVA is 9.7×10^{-10} S cm^{-1}. The conductivity of the PVA increases as the salt concentration increases upto 15 mol % of NH_4SCN concentration. The maximum conductivity has been found to be 2.95×10^{-3} S cm^{-1} and is consistent with the ^1H NMR analysis which shows the intensity of NH_4^+ proton is high (table 2). Then the further increase of salt concentration decreases the conductivity. This result is also consistent with Raman analysis which shows formation of ion aggregation at high salt concentration. These results match well with the results of NMR analysis, which show the drop in intensity (number of free ions) of the peak of NH_4^+ ion

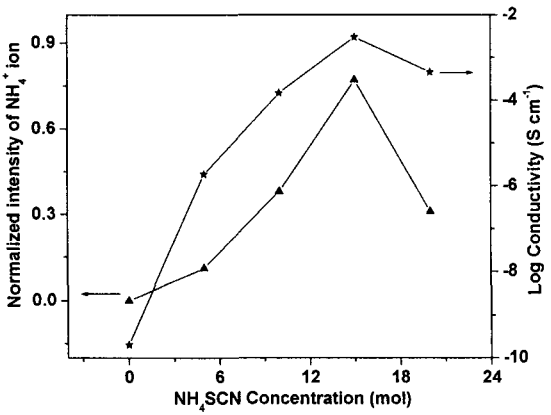

Figure 5. Variation of normalized intensity of NH_4^+ ion and logarithmic conductivity as a function of NH_4SCN concentration

4. Conclusion

The conductivity of the electrolyte strongly depends on the salt concentration and maximum conductivity has been found to be 2.95 x 10^{-3} S cm^{-1} for 15 mol % of salt concentration. This result is consistent with the Raman and ^1H NMR analysis. ^1H NMR study shows that the protonic transport in PVA-NH_4SCN system is mainly contributed by NH_4^+ion. It is noticed that the conductivity is also due to the motion of acetate ion, which is the residual part of PVA.

Acknowledgement

One of the authors G. Hirankumar would like to acknowledge the Council of Scientific and Industrial Research for their funding in the form of Senior Research Fellow.

References

1. O.Savadogo, *J. power Sources* **127** 135 (2004).
2. G. Hirankumar, S. Selvasekarapandian, N. Kuwata, J. Kawamura, T. Hattori, *J. Power Sources* **144** 212 (2005).
3. K. K. Maurya, S. A. Hashmi, S. Chandra, *J. Mat. Sci.* **27** 6357 (1992).
4. N. Srivastava, S. Chandra, *Phys. Stat. Sol. a* **163** 313 (1997).
5. S. Selvasekarapandian, R .Baskaran, M. Hema, *Physica B* **357** 412 (2005).
6. F L Martein, *Encyclopedia of polymer science and engineering*, vol. **17**, Willey, New York, 1986, p. 167.
7. H A Every, F Zhou, M Forsyth, D R MacFarlane, *Electrochemica Acta*, **vol 43, No 10-11**, 1465 (1998).
8. P. S. Thomas, B. H. Stuart, *Spectrochim. Acta Part A* **53** 2275 (1997).
9. R. Iwamoto, M. Miya, S. Miya, *J. Polym. Sci. B. Polym. Phys.* **17** 1507 (1979).
10. I. A. Degen, G. A. Newman, *Raman Spectrochim. Acta A*, **49A** 859 (1992).
11. B. H. Stuart, *Spectrochim. Acta Part A* **53** 107 (1997).
12. I. A. Degen, G. A. Newman, *Raman Spectrochim. Acta A*, **49A** 859 (1992).
13. D. E .Bugay *Pharmaceutical Research*, **10-3** 317 (1993).
14. C. J. Ratcliffe, J. A. Ripmeester, J. S. Tse, *Chem. Phys. Lett.*, **120** 427 (1985)
15. Y. R. Sharma, O. P. Vig, in *'Elementary Organic Spectroscopy'*, S. Chand and Company Ltd. New Delhi, p.178.(1992).

INFLUENCE OF AL_2O_3 NANOPARTICLES ON THE PHASE MATRIX OF POLYETHYLENE OXIDE - SILVER TRIFLATE POLYMER ELECTROLYTES

S. AUSTIN SUTHANTHIRARAJ* AND D.JOICE SHEEBA
Department of Energy, University of Madras, Guindy Campus, Chennai-600025, India.
*Email: suthan98@yahoo.com

Solid polymer electrolytes comprising polyethylene oxide (PEO), silver triflate ($AgCF_3SO_3$) and varying weight percentage of Al_2O_3 (0, 2, 5, 10, 15) nanoparticles, were prepared by solution casting technique using acetonitrile as the common solvent. These polymer electrolytes were formed as very thin films of large surface area and the thickness of these films was measured using Air-Wedge technique. Typical values for the thickness of these films ranged from 30 to 100 μm. The effect of the dispersion of various amounts of Al_2O_3 nanoparticles in polyethylene oxide - silver triflate polymer electrolytes was characterized by X-ray diffraction (XRD), Differential scanning calorimetry (DSC) and Wagner's polarization techniques. The X-ray diffraction pattern, indicated the amorphous nature of the polymer electrolyte. The DSC traces showed slight change in the glass transition temperature (T_g), whereas the degree of crystallization (X_c) decreased from 99.2%(pure PEO) to 27.3% for the nano - Al_2O_3 blended polymer electrolytes. The total ionic transference number (t_{ion}) calculated by wagner's polarization technique was found to be approximately unity, reveling that the significant contribution to electrical conduction was due to ions.

1. Introduction

Over the past few decades solid state batteries are known to play a major role in the realm of power sources and many electronic devices. New solid electrolytes are developed by doping an ionic conductor with an inert filler for realization of enhanced conduction. The incorporation of fillers in general improves the transport properties, mechanical stability and amorphous nature of a polymer matrix. Though several polymers have since been studied polyethylene oxide is still one of the most promising solid polymer electrolyte (SPE) to date because of its good mechanical stability and ease of making thin solid films. Eventhough PEO-based polymer electrolytes has high degree of crystallinity it exhibits the property of dissolving high concentrations of wide variety of salts to form solid polymeric electrolytes giving rise to high ionic conductivity. [1-3]

This work presents the experimental results for PEO_{50}-$AgCF_3SO_3$ complexed polymer electrolytes modified by the incorporation of Al_2O_3 nanoparticles (particle size = 40 – 47 nm). Analytical measurements using XRD, DSC and transport number studies have been carried out for the determination of various factors such as glass transition temperature T_g, melting enthalpy ΔH_m, degree of crystallinity X_c%, and ionic transport number t_{ion} values.

2. Experimental

2.1 *Materials and prepearation of SPE films*

Polyethylene oxide (PEO) of molecular weight, $M_w = 5\times10^6$, silver triflate, $AgCF_3SO_3$ and Al_2O_3 nanoparticles of particle size 40 – 47 nm were obtained from Aldrich and used as such. $AgCF_3SO_3$ was dried for an hour in a vacuum oven at 393 K before use. Required quantities of PEO and $AgCF_3SO_3$ were mixed in acetonitrile medium.

Aldrich grade PEO and $AgCF_3SO_3$ were initially mixed together using acetonitrile as the common solvent by maintaining the oxygen/metal (O/M) ratio as 50:1. The mixture was stirred magnetically for about 4 hours. Subsequently, Al_2O_3 nanoparticles were first dispersed in acetonitrile and then both the suspensions were thoroughly mixed until it became homogeneous. Thin films ($\approx$ 100 μm) were formed when the suspension was poured into clean dry flat bottomed petri dishes and kept in a vacuum oven at 333 K for the solvent to evaporate completely. Aluminium oxide concentrations of 0, 2,5 10 and 15 wt.% were used in the present investigation for the synthesis of thin film specimens of PEO_{50}-$AgCF_3SO_3$-x wt.% Al_2O_3 nanocomposite polymer electrolytes followed by subsequent drying. After removal of moisture and acetonitrile, dry thin solid composite polymer electrolyte films were obtained and stored in a vacuum desiccator for further studies.

2.2 *Measurements*

2.2.1. *X-ray diffraction studies*

The complexation of the films has been investigated through X-ray diffraction

studies using a Siefert model SF60 X-ray diffraction system with Cu-$K_{\alpha 1}$ radiation at room temperature.

2.2.2. *Thermal studies*

The differential thermograms were recorded in the temperature domain 173 – 373K using a NETZSCH DSC 204 instrument at a heating rate of 5 $Kmin^{-1}$ in nitrogen atmosphere. All the patterns were recorded by loading the sample in an aluminium crucible.

2.2.3. *Transference number measurement*

The ionic transference number, t_{ion} was measured using Wagner's polarization technique on a cell configuration of the type Ag|polymer electrolyte|C. A constant DC voltage of 300 mV was applied across the blocking electrodes of the cell and the current passing through the cell was monitored as a function of time for about 4 hours to let the samples get polarized. A KEITHLEY model 614 electrometer has been employed for the accurate measurement of current as a function of time.

3. Results and Discussion

3.1. *X-ray diffraction studies*

X-ray diffraction patterns for the solid polymer electrolyte films of PEO and the complexed polymer with various concentrations of Al_2O_3 nanoparticles (x = 0, 2, 5, 10, and 15) are shown in Figure 1. The appearance of peaks between 2Θ = 18 and 30 for pure PEO and the complexed polymer system corresponds to characteristic peaks of the polymer. An increase in the concentration of Al_2O_3 nanoparticles from 0 wt% to5 wt% revealed a corresponding decrease in the intensities of the observed peaks pointing towards the fact that complexed between PEO and the salt takes place. Further increase in the concentration of Al_2O_3 nanoparticles led to a significant increase in the intensities of these peaks. This behaviour reveals that the aggregation of excess Al_2O_3 eventually would lead to the phase separation of alumina from solid

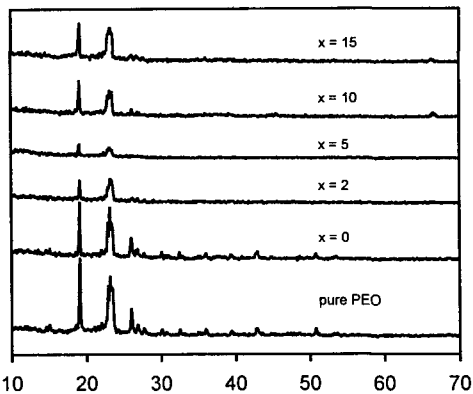

Figure 1. XRD pattern for pure PEO and PEO_{50} - Ag CF_3 SO_3 – x wt.% Al_2 O_3

polymer electrolytes. It can also be seen from the above figure that the pattern obtained for the complexed polymer has not revealed new peaks suggesting the absence of any new crystalline complex. [4,5] Further proof of lowering of crystallinity has clearly been observed from the DSC analysis.

3.2. *Thermal properties of SPE*

Thermal properties of PEO, PEO_{50}-$AgCF_3SO_3$ and Al_2O_3 blended polymer electrolytes at various weight percentages were studied using differential scanning calorimetry in order to observe the changes in the glass transition temperature and degree of crystallinity. The glass transition temperature T_g, melting enthalpy ΔH_m and the degree of crystallinity for all the samples are listed in Table. 1.

Table. 1. Thermal parameters and Transference number obtained for various compositions of the polymer electrolyte system.

Polymer electrolyte	T_g (K)	ΔH_m (J/g)	X_c %	t_{ion}
PEO	211.1	204.4	99.2	-
PEO_{50} $AgCF_3SO_3$	219.5	140.1	68	0.98
PEO_{50}-$AgCF_3SO_3$-2 wt.%Al_2O_3	210.7	137.9	66.9	0.98
PEO_{50}-$AgCF_3SO_3$-5 wt.%Al_2O_3	210.5	108	52.4	0.99
PEO_{50}-$AgCF_3SO_3$-10 wt.%Al_2O_3	211.7	85.94	41.7	0.99
PEO_{50}-$AgCF_3SO_3$-15 wt.%Al_2O_3	210.5	56.36	27.3	0.98

Figure 2 shows the DSC thermograms for pure PEO and PEO_{50}-$AgCF_3SO_3$-x wt.% Al_2O_3 (x = 0 and 5) in the temperature domain, 173 to 373 K. Pure PEO exhibits the melting peak (T_m) at 340.1 K which agrees well with the standard value. On complexation of pure PEO with $AgCF_3SO_3$, two exothermic peaks were observed. The peak at 339.6 K corresponds to the melting point of PEO and the other peak at 330.9 K, may be assigned to the melting point of complexed polymer electrolyte. It is evident that the glass transition temperature T_g increases markedly from 211.1K (pure PEO) to 219.5K by the addition of silver triflate confirming the fact that ion-dipole interaction reduces the segmental motion of PEO. On the other hand, the incorporation of Al_2O_3 nanoparticles to the polymer complexed electrolyte

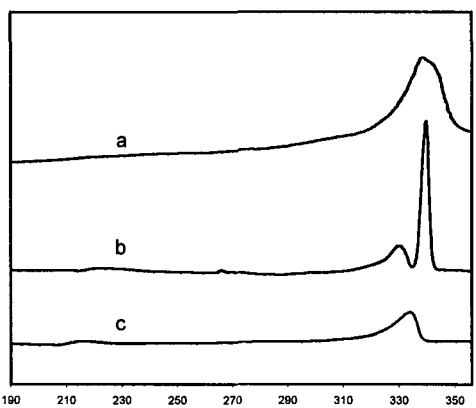

Figure 2. DSC curves for (a) pure PEO, (b) PEO_{50} - Ag CF_3 SO_3 and (c) PEO_{50} - Ag CF_3 SO_3 – 5 wt.% Al_2 O_3.

influences slightly on the glass transition temperature. [5,6] Though T_g was not affected much by the addition of Al_2O_3 nanoparticles the degree of crystallinity (X_c%) decreases from 99.2% for pure PEO was observed to fall to 27.3% for the Al_2O_3 blended complexed polymer electrolyte. Considering the area of the melting peak as the melting enthalpy ΔH_m of the polymer electrolytes, the degree of crystallinity can be calculated from the following equation.

$$X_c = (\Delta H_m / \Delta H_m^{\Phi}) \times 100\% \quad (1)$$

where ΔH_m (J/g) is the melting enthalpy of a polymer sample measured by DSC and ΔH_m^{Φ} (J/g), the melting enthalpy of 100% crystalline PEO material. [7] The

decrease in the degree of crystallinity and a slight change in the T_g increases the flexibility of the polymer chain and plays a vital role in the enhancement of ionic conductivity. [8]

3.3. *Transport number measurements*

The total ionic transference number values for thin solid polymer electrolyte films of cell configuration Ag|polymer electrolyte|C, were evaluated using Wagner's

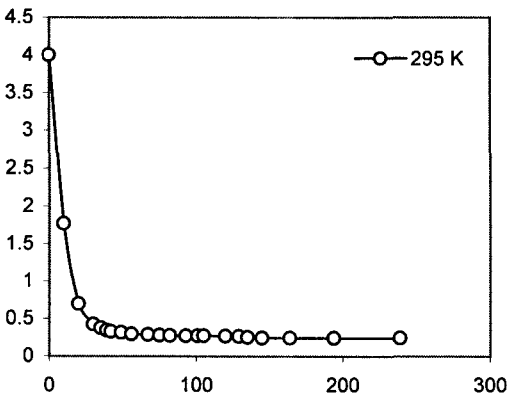

Figure 3. Polarization current versus time graph for PEO_{50}- $AgCF_3$ SO_3 film

polarization technique. Figure 3. shows the current versus time plot for the cell Ag|PEO_{50}- $AgCF_3$ SO_3|C, after the complete polarization of cell at 295 K. Transference number t_{ion} has been obtained from the equation

$$t_{ion} = (I_i - I_f)/I_i \qquad (2)$$

where the initial current I_i is the sum of ionic and electronic currents and the final current I_f is just the electronic current alone. [9-11] Evaluated transference number, t_{ion} values are listed in Table 1. The t_{ion} values obtained from the transport number measurements are approximately unity and hence the charge transport in these thin polymer electrolyte films are highly ionic and electronic contribution to the total current is negligible.

4. Conclusion

The PEO_{50}-$AgCF_3SO_3$ films blended with various amounts of Al_2O_3 nanoparticles have been prepared by solution casting technique. From the XRD and thermal (DSC) analysis it is observed that the crystallinity of the polymer matrix decreased with the increasing weight percentage of Al_2O_3 nanoparticles which confirms the amorphous phase as well as the complexation of the polymer matrix. The ionic transference number is almost unity and hence the charge transference is mainly due to ions.

Acknowledgement

The financial assistance received from the University Grants Commission, New Delhi under the programme "University with Potential for Excellence", in the form of a research project (# HDP8) is gratefully acknowledged by the authors.

References

1. G S Mac Glashan, Y G Andreev, P G Bruce, Nature **398** 792 (1999).
2. Y G Andreev, P G Bruce, Electrochim. Acta **45** 1417 (2000).
3. D Fenton, J M Parker, P V Wright, J. Polym. **14** 589 (1973).
4. S A Hashmi, A Kumar, K K Maurya, S Chandra, J.Phys. D: Appl. Phys. **23** 1307 (1990).
5. P S Anantha, K Hariharan, Solid State Ionics **176** 155 (2005).
6. C Capiglia, J Yang, N Imanishi, A Hirano, Y Takeda, O Yamamoto, Solid State Ionics **154 - 155** 7 (2002).
7. Z Li, G Su, X Wang, D Gao, Solid State Ionics **176** 1903 (2005).
8. S A Suthanthiraraj, D J Sheeba, Indian J. Phys. **79** 807 (2005).
9. J B Wagner, C Wagner, J. Chem. Phys. **26** 1597 (1957).
10. D Saikia, A Kumar, Indian J. P. App. Phys. **41** 961 (2003).
11. M J Reddy, D S Reddy, S S Rao, U V S Rao, Mat. Letters **23** 129 (1995).

EFFECT OF DIFFERENT TYPES OF CERAMIC NANO - FILLERS ON THERMAL AND TRANSPORT PROPERTIES OF PEO_9 LiTf SOLID POLYMER ELECTROLYTE

K. VIGNAROOBAN [1], B.-E. MELLANDER [2], I. ALBINSON [2] AND M.A.K.L. DISSANAYAKE [1]

[1] *Postgraduate Institute of Science (PGIS) and Department of Physics, University of Peradeniya, Peradeniya, Sri Lanka*

[2] *Department of Applied Physics, Chalmers University of Technology, Gothenburg, Sweden*

(e- mail : f5xrk@fy.chalmers.se ; director@pgis.lk)

One of the most promising ways to improve the potential for applications of plasticizer-free, PEO – based solid polymer electrolytes is through the incorporation of ceramic fillers. However, to our knowledge, literature on PEO_9 LiTf reporting the dependence of ionic conductivity on the nature of different types of ceramic fillers is lacking. In this work, we have studied thermal and transport properties of the polymer electrolyte PEO_9 LiTf + 15 wt% filler, incorporating four different types of ceramic fillers TiO_2, Al_2O_3, ZrO_2 and $BaTiO_3$. Presence of the first three ceramic fillers with dielectric constants 435, 20 and 12.5 enhanced the ionic conductivity substantially. However $BaTiO_3$ filler having a relatively very high dielectric constant (3000) compared to other three ceramic fillers, gave a negative effect on conductivity. Presence of 15 wt% TiO_2 exhibited the maximum enhancement in conductivity ($\sigma_{RT} = 4.2 \times 10^{-4}$ S cm^{-1}) The observed conductivity enhancement has been attributed to Lewis acid-base type surface interactions of ionic species with O/ OH groups on the filler surface.

Keywords : PEO, Ionic conductivity, Nano - composite polymer electrolyte, Ceramic fillers, TiO_2 , Al_2O_3, ZrO_2, $BaTiO_3$

1. Introduction

A variety of materials such as polymers, ceramics, glasses and their combinations are being investigated and developed as solid electrolytes for lithium re-chargeable batteries. Among the polymer electrolytes of practical interest, the Poly (ethylene oxide) – Lithium salt (PEO- LiX) system has emerged as one of the most promising electrolyte for applications in rechargeable lithium batteries. PEO excels as a polymer host because of its commercial availability, high solvating power for the lithium ions and its compatibility with the lithium electrode[1]. However, the ionic conductivity of PEO based electrolytes at room temperature ($\sigma \sim 10^{-7}$ S cm^{-1} at 25 ^{0} C) is still too low to be used in practical applications [2,3]. The ionic conductivity has been enhanced by various means, but one of the most promising method is to incorporate fine ceramic fillers such as TiO_2 , Al_2O_3 , ZrO_2, SiO_2 etc. to the polymer electrolyte, where different degrees of conductivity enhancement have been reported [1,2,4,5].

The dielectric properties of the fillers are important as they affect the PEO dipole orientation by their ability to align dipole moments, while the thermal history determines the flexibility of the polymer chains for Li ion migration[6].

In this work, we have studied thermal and transport properties of the polymer electrolyte $PEO_9LiTf + 15$ wt% filler incorporating four different types of ceramic fillers TiO_2 , Al_2O_3 , ZrO_2 and $BaTiO_3$ having dielectric constants 435, 20, 12.5 and 3000 respectively, maintaining the same thermal treatment for all the samples. In a review article Quartarone et. al.[7] have reported that, the addition of fillers improve both the transport and mechanical properties of the electrolyte films and the maximum conductivities were generally found in the 10 - 20 wt% range of the ceramic additive. Previous work reported by our group has also shown that 15 wt% alumina gives the maximum conductivity enhancement in the PEO_9 LiTf system [8].

2. Experimental

Poly (ethylene oxide) (PEO) (molecular weight $4x10^6$) and $LiCF_3SO_3$ (Lithium triflate, LiTf) both from Aldrich were used as starting materials. Four types of ceramic powders Al_2O_3 ($\varepsilon_r = 20$) , ZrO_2 ($\varepsilon_r = 12.5$) , $BaTiO_3$ ($\varepsilon_r = 3000$) all from Aldrich and TiO_2 ($\varepsilon_r = 435$) from Huntsman were used as fillers. Prior to use, PEO and $LiCF_3SO_3$ were vacuum dried for 24 hrs at 50 ° C and 120 ° C respectively and all the ceramic powders were vacuum dried at 200 ° C for 24 hrs.

Appropriately weighed quantities of PEO and LiTf required for ether oxygen to Li^+ ratio of 9:1 were dissolved in anhydrous acetonitrile after adding the required amount of the ceramic powder, and the solution was magnetically stirred at room temperature at least for 24 hrs, until a homogeneous solution was obtained. The amount of the filler added was fixed at 15 wt% of the total (PEO + LiTf) weight. All the weighings were done inside the glove box. The resulting slurry after stirring was cast onto a Teflon plate and kept inside the fume box for 24 hrs in order to let the solvent slowly evaporate. This procedure yielded visually homogeneous composite polymer electrolyte films of average thickness 100 – 200 μm, which were stored inside the glove box.

Complex impedance measurements were made on disc shaped samples sandwiched between two stainless steel electrodes of 5 mm diameter, using an HP 4291 A RF impedance analyzer in the 1 MHz – 1.8 GHz frequency range. A flow of nitrogen gas was maintained over the sample holder to avoid any contact with atmospheric moisture. The temperature of the sample was varied from -20 ° C to 80 ° C and the measurements were taken at approximately 10 ° C intervals on heating. Thermal measurements were carried out using a Mettler Toledo DSC 30 differential scanning calorimeter at a heating rate of 10 ° C min^{-1} from – 120 ° C to 120 ° C in the heating cycle and from 120 ° C to -120 ° C in the cooling cycle.

3. Results and Discussion

3.1 Ionic Conductivity

Fig.1 shows the variation of conductivity with inverse temperature for the composite polymer electrolyte system (PEO_9 LiTf + 15 wt% filler) for the four different types of ceramic fillers TiO_2 , Al_2O_3 , ZrO_2 and $BaTiO_3$, taken on the heating run starting from -20 °C. According to these observations, the addition of nano-sized ceramic fillers TiO_2, Al_2O_3 and ZrO_2 have obviously increased the ionic conductivity of the polymer-salt complex considerably and the maximum enhancement is observed for15 wt% TiO_2. However, $BaTiO_3$ filler having a relatively very high dielectric constant (3000) compared to other three ceramic fillers, exhibited a drop in conductivity. Table 1 shows the comparison of ionic conductivity values at two different temperatures.

In the case of PEO based, filler-free polymer electrolytes such as PEO-$LiClO_4$, PEO- $LiCF_3SO_3$ and PEO- $LiBF_4$, the conductivity drops to low values at temperatures below the crystalline melting temperature of about 60 ° C due to re-crystallisation. In many of the reported systems, this can clearly be seen as a discontinuity in the log σ versus 1/ T graphs around 60 ° C, where the amorphous phase with high conductivity changes to the crystalline phase with low conductivity.

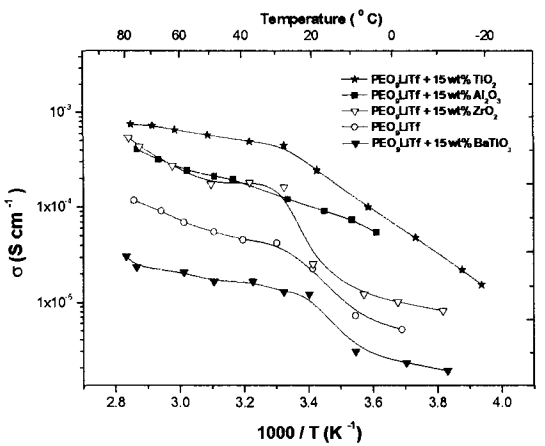

Fig.1 : Variation of the ionic conductivity with inverse temperature for the system PEO_9 LiTf + 15 wt% filler, taken on heating (filler = TiO_2 , Al_2O_3 , ZrO_2 and $BaTiO_3$)

In the systems shown in Fig.1 however, the melting temperature of the PEO crystalline phase (T_m) has shifted to low values, around 30 °C resulting higher conductivity values even at room temperature. This is possibly due to the thermal history of the samples used. When impedance measurements were taken, starting from -20 °C, the sample was left for about 40 minutes at each temperature allowing

the samples to reach thermal equilibrium. In many of the reported data, impedance measurements have been taken starting from the room temperature. The dependence of ionic conductivity of the PEO: $LiBF_4$: TiO_2 system on thermal history has been studied in detail by Scanlon et al [20] where they have observed a similar drop in T_m by about 30 °C due to heat treatment.

The following two effects may account for the observed enhancement in conductivity of the nano-composite PEO- based polymer electrolyte.

(1) ceramic filler grains may lower the PEO reorganization tendency and thereby promoting structural modifications of the polymer chains, increasing the fraction of the amorphous phase present at lower temperatures. This, in turn, would favour Li^+ ion migration.

(2) Lewis acid-base interactions as proposed by Wieczorek et.al.[9] between the polar surface groups of the inorganic filler and the electrolyte ionic species, which would provide additional " transient" hopping sites for migrating ionic species. This appears to be the dominant mechanism in the amorphous phase above 60 ° C.

Table 1 : Ionic conductivity of the samples incorporating the fillers at 25 ° C and 80 ° C

Ceramic powder	Dielectric constant	Specific surface area (m^2 / g)	Particle size	Conductivity of PEO, LiTf + 15 wt% ceramic filler at 25 ° C (S cm^{-1})	Conductivity of PEO, LiTf + 15 wt% ceramic filler at 80 ° C (S cm^{-1})
TiO_2	435 [10]	Not specified	200 nm	3.39 x 10^{-4}	7.57 x 10^{-4}
Al_2O_3	20 [10]	155	150 mesh (pore size = 5.8 nm)	1.12 x 10^{-4}	4.35 x 10^{-4}
ZrO_2	12.5 [11]	35 – 45	20 - 30 nm	7.60 x 10^{-5}	5.46 x 10^{-4}
$BaTiO_3$	3000	Not specified	30 - 50 nm	1.23 x 10^{-5}	3.12 x 10^{-5}
Filler free	------	--------	----------	3.08 x 10^{-5}	1.31 x 10^{-4}

Note : Dielectric constants, specific surface areas and particle sizes of the respective ceramic powders are from the manufacturers specifications unless otherwise referenced.

Incorporation of TiO_2 gave the maximum enhancement in σ eventhough it has a relatively larger particle size (200 nm) compared to other three ceramic fillers. In a paper on PEO + 10 wt % $LiClO_4$ + 5 wt % TiO_2, Lin et.al[12]. reported that, the effect of TiO_2 particle size on the transport properties of the nano-composite polymer electrolyte is negligible, if its size is larger than 22 nm. Therefore, the maximum enhancement of ionic conductivity by the incorporation of TiO_2, eventhough it has a particle size of 200nm, may be due to its high dielectric constant and high Lewis acid character. Our results for TiO_2 is consistent with the work reported by Chung

et.al.[13] on PEO$LiClO_4$ + 10 wt% TiO_2 nano-composite electrolyte which exhibited the maximum conductivity enhancement compared to Al_2O_3 and SiO_2. According to these authors, the highest Lewis- acid character of TiO_2 would have also contributed to the conductivity enhancement. The Lewis acid character varied as TiO_2 > Al_2O_3 > SiO_2.

In a paper on PEO$LiClO_4$ + 10 wt% SiO_2 by Kwang - Sun Ji et.al.[6] , it has been reported that, the enhancement of ionic conductivity due to a ceramic filler having a higher dielectric constant compared to PEO, (for PEO, $\varepsilon_r = 2.8 - 3.3$) like TiO_2 might be due to the active dissociation of the Li salt resulting an increased concentration of mobile carriers. However, when adding a ceramic filler with dielectric constant lower or comparable to that of PEO, the increase in conductivity is very likely due to the increased mobility of the ions.

Out of the fillers used in our work, Al_2O_3 ($\varepsilon_r = 20$) and ZrO_2 ($\varepsilon_r = 12.5$) have dielectric constants comparable to that of PEO. Therefore, the conductivity enhancement due to the incorporation of these two ceramic fillers is very likely due to the increased mobility of the ions. Similar results substantiated also with high frequency dielectric relaxation measurements have been reported for the PEO_9 LiTFSI : Al_2O_3 system [14]. The comparable ionic conductivity values of Al_2O_3 added sample and ZrO_2 added sample at high temperatures strongly support this assumption.

From Fig.1, it is clearly shown that the conductivity of the PEO_9 LiTf electrolyte has dropped due to the presence of 15 wt% $BaTiO_3$ ceramic filler of dielectric constant 3000. Although, in general, many nano-sized ceramic fillers enhance the ionic conductivity of PEO based polymer electrolytes, there were several exceptions in the literature similar to our results for $BaTiO_3$ added samples [5, 7, 10, 15]. The ferroelectric nature and the blocking effect of the $BaTiO_3$ appears to be responsible for the observed conductivity drop in the $BaTiO_3$ added material.

3.2 Thermal properties

Fig. 2 shows the DSC traces taken during heating. Table 2 shows the melting temperature(T_m) and heat of melting (H_m) taken on heating .

Table 2 : Melting Temperature (T_m) and Heat of Melting (H_m) from DSC measurements taken on heating

Polymer Electrolyte	Melting Temperature on Heating (T_m) (°C)	Heat of melting (H_m) ($J g^{-1}$)
PEO_9LiTf	69.82	86.23
PEO_9LiTf + 15 wt% TiO_2	68.60	78.88
PEO_9LiTf + 15 wt% Al_2O_3	67.83	68.14
PEO_9LiTf + 15 wt% ZrO_2	68.47	61.75
PEO_9LiTf + 15 wt% $BaTiO_3$	66.15	38.66

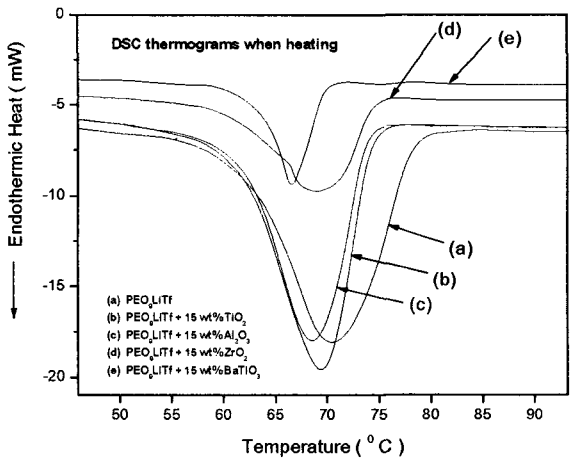

Fig. 2 : DSC traces taken on heating run

As shown in Table.2, heat of melting (H_m) decreases from 86.23 J g^{-1} to 78.88 J g^{-1} (for TiO_2) and below this (for other fillers) when the nano-sized fillers were added to the polymer electrolyte. This indicates that the fraction of the crystalline phase in the filler-added material has become smaller. The increased fraction of the amorphous phase also contributes to the enhancement of conductivity. However, the value of H_m for $BaTiO_3$ added electrolyte is the minimum although the conductivity has decreased for this electrolyte. Other properties of $BaTiO_3$ filler such as its ferroelectric nature which may have an effect on the conductivity evidently play a dominant role and further studies are necessary in order to understand the mechanism involved. The value of H_m for pure PEO is 203 J g^{-1}, indicating the 100 % crystalline nature[16]. The crystalline melting temperature (T_m) has also decreased slightly when ceramic fillers are added indicating the more amorphous nature of the filler- added electrolytes. Some recent studies using several PEO – LiX complexes with nano-scale SiO_2 have shown that the addition of fillers does not change significantly the thermal properties of the material but it gives to the electrolyte better resistance to crystallization[15]. For the composite polymer electrolyte studied in this work also, the fillers have not changed the thermal properties of the material significantly.

4. Conclusion

The results of the thermal and ionic conductivity measurements on the PEO_9 LiTf + 15 wt% filler, with nano-sized ceramic fillers TiO_2 , Al_2O_3 , ZrO_2 and $BaTiO_3$ reported in this paper demonstrates the following. The presence of the fillers enhanced the ionic conductivity substantially except the $BaTiO_3$ filler. $BaTiO_3$ incorporation decreased the conductivity of the electrolyte possibly due to the ferro-electric nature and the blocking effect. TiO_2 filler gave the maximum enhancement in conductivity. The amount of enhancement appears to depend on the Lewis acid character of the respective filler. According to the DSC results, there is a significant reduction in heat of melting (H_m) due to the incorporation of fillers, suggesting that fillers make the material more amorphous. While this is expected to enhance the conductivity, a more dominant contribution to conductivity enhancement, observed above and below the PEO crystallite melting temperature, appears to come from the Lewis acid-base type interactions of mobile ionic species with O/OH surface groups on filler surface. These interactions could provide transient hopping sites for migrating ionic species thus facilitating ionic migration. In addition, for the TiO_2 added material, increased ionic dissociation giving rise to an increased carrier concentration could also contribute to conductivity enhancement.

Acknowledgements

Authors wish to thank the International Program in the Physical Sciences(IPPS), Uppsala University, Sweden , VR / SIDA Research Links, Sweden and the National Science Foundation(NSF), Sri Lanka(Grant number : RG / 2001 / P01) for research support.

References

1. S. Zhang , Jim Y. Lee , L. Hong , J. Power Sources **126** (2004) 125 – 133.
2. F.M. Gray , Solid Polymer Electrolytes, VCH , Weinheim , 1991.
3. M. Gauthier , A. Belanger , B. Kapfer , G. Vassort , M. Armand, in : J.R. MacCallum, C. Vincent (Eds.), Polymer Electrolyte Reviews, vols. 1 and 2, Elsevier, London, 1987/ 1989.
4. Binod Kumar , Lawrence G. Scanlon , Robert J. Spry, J. Power Sources **96** (2001)337 – 342.
5. Z. Florjanczyk , M. Marcinek , W. Wieczorek , N. Langwald, Polish J. Chem. **78** (2004) 1279 – 1304.
6. Kwang – Sun Ji, Hee- Soo Moon , Jong – Wook Kim , Jong – Wan Park , J. Power Sources **117** (2003) 124 – 130.

7. Eliana Quartarone , Piercarlo Mustarelli , Aldo Magistris , Solid State Ionics **110** (1998) 1 -14.
8. M.A.K.L. Dissanayake, P.A.R.D. Jayathilaka, R.S.P. Bokalawela, I. Albinson, B.- E. Mellander, J.Power Sources **119- 121** (2003) 409- 414.
9. W.Wieczorek, P. Lipka, G. Zukowska, H. Wycislik, J.Phys. Chem. **B 102** (1998) 6968.
10. A.S. Best, J. Adebahr, P. Jacobsson , D.R. MacFarlane, M. Forsyth , Macromolecules **34** (2001) 4549 – 4555.
11. http://www.clippercontrols.com/info/dielectric_constants.html (Clipper controls Inc.).
12. C.W. Lin , C.L. Hung, M. Venkateswarlu , B.J. Hwang, J. Power Sources **146** (2005) 397 – 401.
13. S.H. Chung , Y.Wang, L. Persi , F. Croce , S.G. Greenbaum , B. Scrosati , E.Plichta, J. Power Sources **97 – 98** (2001) 644 – 648.
14. P.A.R.D. Jayathilaka , M.A.K.L. Dissanayake , I. Albinsson , B.- E. Mellander , Electrochimica Acta **47** (2002) 3257 – 3268.
15. H.Y. Sun , H.- J. Sohn , O. Yamamoto , Y. Takeda , N. Imanishi , J. Electrochem. Soc. **146** (1999) 1672.
16. Y.W. Kim , W. Lee , B.K. Choi , Electrochimica Acta **45** (2000) 1473 – 1477.
17. I. Albinsson , B.- E. Mellander, J.R. Stevens, Solid State Ionics **72** (1994) 177.
18. Binod Kumar, Lawrence G. Scanlon , J. Power Sources **52** (1994) 261 – 268.
19. J.E. Weston, B.C. Steele, Solid State Ionics **7**, 75 (1982).
20. Binod Kumar, Lawrence G. Scanlon, Solid State Ionics **124** (1999)239-254.

CHARACTERIZATION OF PVP BASED SOLID POLYMER ELECTROLYTES USING SPECTROSCOPIC TECHNIQUES

C.S. RAMYA, S. SELVASEKARAPANDIAN*, M. S.BHUVANESWARI, T. SAVITHA

Solid State and Radiation Physics Laboratory, Department of Physics, Bharathiar University, Coimbatore-641 046. India.

E-Mail: sekarapandian@yahoo.com

Abstract

Polymer electrolytes based on poly (vinyl pyrrolidone) - ammonium thiocyanate have been prepared by solution cast technique. The interaction of salt with the polymer has been examined using Raman spectroscopy. Results revealed that the interaction of the salt has been found to be through the carbonyl group of the polymer matrix. Conductivity measurements showed that these systems conduct ionically. The possible correlation between the conductivity and the structure of these electrolytic systems was also investigated which shows that the conductivity values are directly related to the total "free anion" concentration. Conductivity analysis showed that the addition of ammonium thiocyanate as a dopant in the polymeric electrolyte system enhanced the ionic conductivity. 20 mol% ammonium thiocyanate doped polymer electrolyte exhibits high ionic conductivity and has been found to be 1.7 X 10^{-4} S cm^{-1}, at room temperature.

1. Introduction

Recent trends in energy technology have driven considerable interest in proton conducting electrolytes with high ionic conductivity [1]. To improve the ionic conductivity, polymer - salt electrolytes have been investigated for their possible application in various electrochemical applications [2]. To date, several types of polymer electrolytes have been developed and characterized, those based on vinyl polymers such as poly(vinyledene fluoride)[3], poly vinyl alcohol (PVA) [4] poly (vinyl pyrrolidone) PVP [3] etc., for various electrochemical applications. However, there are only little information is available for polymers like poly (vinyl pyrrolidone) PVP. The electrical and optical properties of polymers can be suitably modified by the addition of dopants depending on their reactivity with the host matrix [5]. Raman spectroscopy has been proved sensitive to the change of microstructure in a polymer electrolyte and can help to identify it [6]. Raman spectroscopy has also been useful for determining the state of ions in the polymer electrolytes. It is also useful to confirm and better understand the interaction of salt with the polymer matrix [7].

In the present study, a novel polymer electrolytes using poly (vinyl pyrrolidone) - ammonium thiocyanate have been studied using various spectroscopic techniques such as Raman, Impedance and absorption spectroscopic techniques.

2. Experimental

Polymer electrolytes PVP (SISCO, M_w = 40,000) with NH_4SCN were prepared using solution cast technique. Films of pure PVP, and PVP - NH_4SCN with molar ratios 95:5, 90:10, 85:15, 80:20, 75:25 mol% have been prepared using distilled water as a solvent and the films are allowed to evaporate at room temperature. The Raman spectra has been performed using a Renishaw 1000 spectrometer, with a 1200 lines/mm grating using the 784 nm line from a Infrared laser in the range of 400 – 4000 cm^{-1}, at room temperature. Curve-fitting analysis of the spectral data has been done using a commercial program, PEAK FIT to fit the Raman bands. The ionic conductivity of the polymeric electrolyte sandwiched between two aluminium block electrodes has been measured using an LCR meter Hioki 3532 in the frequency range 42 Hz – 5 MHz. UV-Visible spectrophotomety has been carried out on Shimadzu spectrophotometers using a CARY 500 Scan UV-VIS-NIR Spectrophotometer in the range 175 – 600 nm.

3. Results and discussion

3.1 UV – Visible Analysis

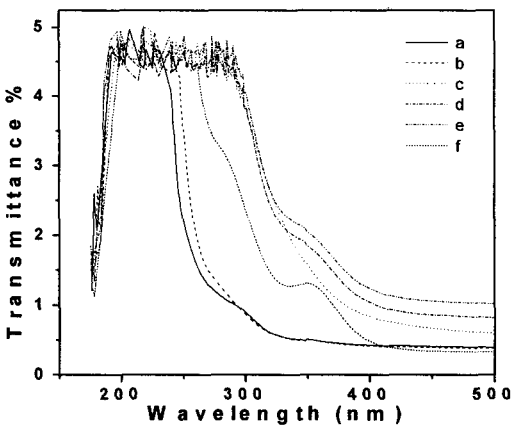

Fig 1. UV visible spectra of PVP-NH_4SCN systems for a) 0 mol % b) 5 mol % c) 10 mol% d) 15 mol % e) 20 mol % f) 25 mol % of NH_4SCN concentration

Figure 1 shows the UV visible spectra of PVP as well as that of the PVP–NH_4SCN polymer complexes. New bands were observed at ca.294 nm ammonium thiocyanate doped polymer electrolyte and may be attributed to the formation of a complex between PVP and NH_4SCN through charge transfer. The absorption bands at 294 nm for the 5 mol% ammonium thiocyanate doped polymer electrolyte may be assigned to $\pi \rightarrow \pi^*$ [8] transition which comes from unsaturated bond, mainly C=O. As the salt concentration increases the band shifts towards the higher wavelength region.

3.2 Raman Analysis

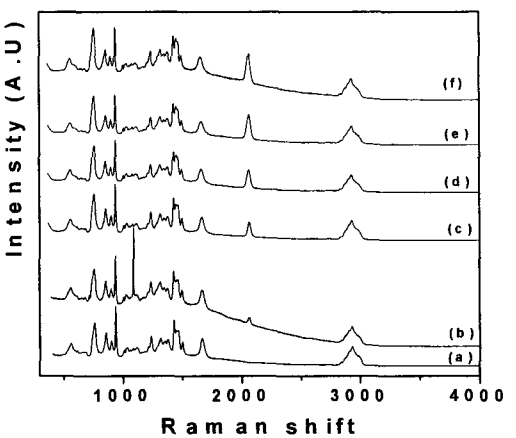

Fig.2 Raman spectra of polymer electrolyte systems for a) 0 mol % b) 5 mol % c) 10 mol% d) 15 mol % e) 20 mol % f) 25 mol % of NH_4SCN concentration

Figure 2 shows the Raman spectra of PVP-NH_4SCN system at different salt concentrations along with the spectra of the host polymer, PVP in the range 400 – 4000 cm^{-1}. The changes in the Raman spectra of ammonium thiocyanate doped PVP polymer electrolytes that occur with increasing salt concentration have been presented in Table 1.

Table 1: Raman band Frequencies and their Assignments

Wave number cm^{-1}						Assignment
Pure PVP	PVP: NH_4SCN (mol %)					
	95: 05	90:10	85: 15	80:20	75:25	
738	740	738	738	736	737	C-N
-	748	746	744	744	747	C-S stretching
758	758	757	756	757	759	C-N
899	899	897	901	898	899	CH_2 rocking
935	935	936	936	936	936	C – C stretching
1028	1029	1031	1029	1029	1029	CH_2 symmetric stretching
1232	1233	1233	1233	1234	1235	C – N stretching
1426	1425	1425	1425	1425	1425	C – H bending
1663	1661	1661	1657	1661	1659	C=O
-	1674	1676	1677	1674	1673	C-O---H
-	2042	2050	2047	2044	-	SCN^{-1} free ion
-	2061	2062	2061	2061	2058	SCN^{-1} contact ion pair
-	-	2074	2074	2074	2071	SCN^{-1} aggregates
2928	2926	2926	2929	2930	2930	C-H stretching

From Figure 2, it has been observed that the intensity of the Raman band corresponding to C-C stretching vibration at 936 cm^{-1} in the pure polymer electrolyte decreases with increase of NH_4SCN concentration. The significant changes in the C-C vibrational band can be associated with the interaction of the salt with the polymer. The bands at 1232 cm^{-1} and 1426 cm^{-1} can be attributed to C–N stretching and C-H bending vibrations of Pure PVP respectively. It has been observed that the bands related to ν(C–N) stretch modes and ν(C-H) bending vibrations of salt doped system gets broaden as the salt concentration increases. The band broadening in Raman spectra is usually an indication of amorphous nature of the polymer electrolyte [9]. The Raman bands for the undoped polymer electrolyte at 736 cm^{-1}

and 757 cm^{-1} can be attributed to C-N vibrations. For the ammonium thiocyanate doped polymer electrolytes an additional band at ~748 cm^{-1} corresponding to C-S stretching vibrations [10] of thiocyanate ion has been observed. The ~748 cm^{-1} band slightly shifts towards the lower frequencies with the increase of salt concentration at the expense of the 736 cm^{-1} and 757 cm^{-1} bands. This may be due to the interaction of the salt with the polymer.

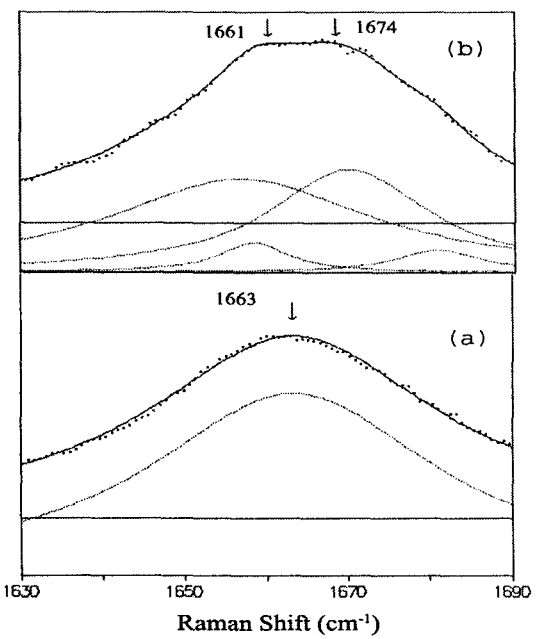

Fig.3. Raman band associated to the C=O stretching mode for (a) undoped (b) 5 mol% NH_4SCN doped polymer electrolyte.

The changes in the C=O spectral region are very important for the elucidation of the interaction of the polymer with that of the dopant ammonium thiocyanate. Figure 3 compares the deconvoluted spectrum of the virgin PVP film with the spectrum of PVP doped with 05 mol % ammonium thiocyanate in the C=O spectral region. The C=O of pure polyvinyl pyrrolidone polymer electrolytes at 1663 cm^{-1} has been appeared as double bands at 1661 cm^{-1} and 1674 cm^{-1} in the salt doped PVP which

indicates the hydrogen bond interaction of the salt with the carbonyl group of the polymer.

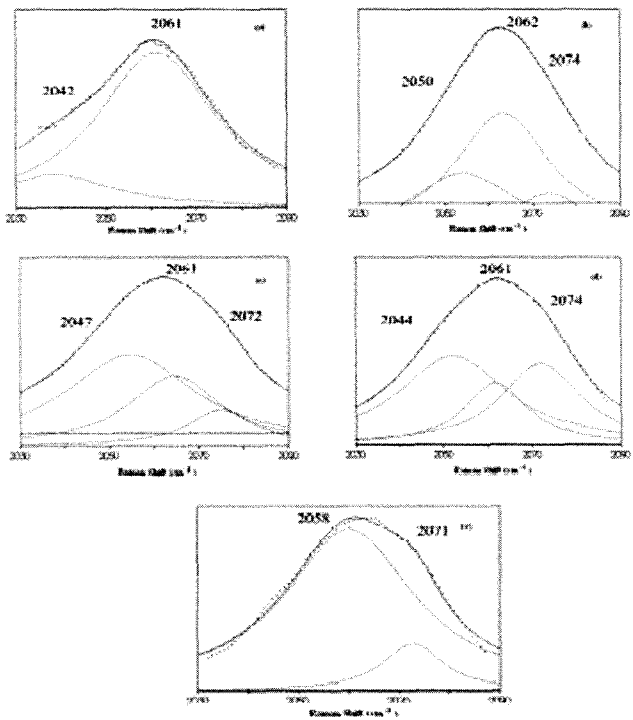

Fig.4. The deconvoluted Raman band associated to the $\nu(SCN^-)$ stretching mode for (a) 5 mol% (b) 10 mol% (c) 15 mol% (d) 20 mol% and (e) 25 mol% NH_4SCN doped systems.

The change in the relative intensity and the location of the SCN^- anion within the complex depend on the concentration of the NH_4SCN salt. Consequently, these changes can be attributed to the interactions involving the SCN^-. Figure 4 shows the $\nu(SCN^-)$ mode for all salt doped polymer complexes. The main spectral component centered at ~2042 cm^{-1} has been assigned to spectral mode of free SCN^- ions. The spectral band at ~ 2061 cm^{-1} whose area increase as the salt concentration increases has been assigned to SCN^{-1} contact ion pairs. The band at ~ 2074 cm^{-1} appearing at higher salt concentrations has been assigned to the formation of ion aggregates. The

area under the peak ~2042 cm^{-1} as a function of salt concentration has been shown in Figure 5. The area under the peak is proportional to the relative concentration of the free ions. The concentration of the free ions increases gradually from 5 mol% to 20 mol % of salt concentration. For 25 mol % salt doped system the band at 2042 cm^{-1} disappears in the expense of 2061 cm^{-1} and 2074 cm^{-1} indicating that less free ions exist in this system which accounts for the decrease in conductivity.

3.3 Conductivity Analysis

The ionic conductivity as a function of salt concentration has been shown in Figure 5.

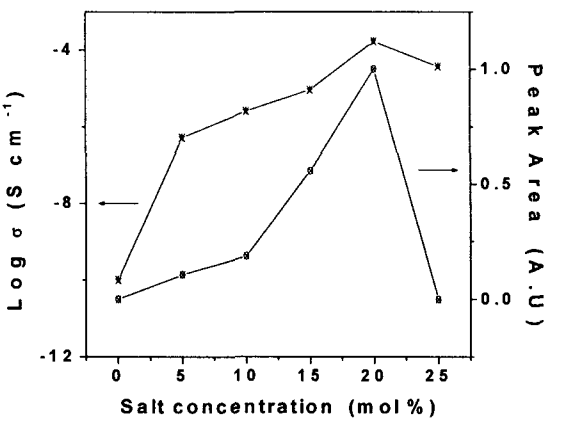

Fig 5. Conductivity and free-ion concentration as a function of concentration of ammonium thiocyanate at room temperature.

The increase in the ionic conductivity with increasing salt concentration can be related to the increase in the number of mobile charge carriers in the polymer electrolyte. When the concentration of ammonium thiocyanate increases, the relative amount of free ions also increases. The increase of ionic conductivity is in good agreement with the increase of the free ions in the PVP/NH_4SCN complex. The maximum conductivity has been found to be 1.7 X 10^{-4} S cm^{-1} for 20 mol % salt doped system. Further addition of salt decreases the ionic conductivity, which can be explained by formation of ion aggregates as explained from Raman analysis.

4. Conclusion

The proton conducting polymer electrolytes based on Poly (vinyl pyrrolidone), PVP and ammonium thiocyanate, NH_4SCN have been prepared by solution cast method. The interaction of the salt with the polymer has been explained using UV visible and Raman spectroscopic studies. The introduction of a new peak in the UV spectra for the salt doped system indicates the formation of charge transfer complexes. The room temperature conductivity has been found to be 1×10^{-7} Scm^{-1} for 80 mol% PVP: 20 mol% NH_4SCN polymer system. The decrease in conductivity at higher salt concentration (25 mol %) in these polymer electrolytes has been found to be due to the formation of ion aggregates. This fact has been confirmed using Raman spectroscopic analysis.

References

1. Vito Di Noto, Michele Vittadello, Sandra Lavina, Simone Biscazzo, Maurizio Fauri, *Electrochimica Acta* **48,** 2047-2058 (2003).
2. AC Impedance Studies on Proton Conducting Polymer Electrolyte Complexes (PVA-CH_3COONH_4), *Ionics* **10,** 135-138 (2004).
3. Ningping Chen, Liang Hong, *Solid State Ionics* **146,** 377–385 (2002).
4. M.A. Vargas MA, R.A. Vargas, B-E. Mellander, *Electrochimica Acta* **44,** 4227-4232 (1999).
5. Hirankumar, S. Selvasekarapandian, N. Kuwata, J. Kawamura, T. Hattori *Journal of Power Sources* **144,** 262–267 (2005).
6. Zhaoxiang Wang, Weidong Gao, Liquan Chen, Yujun Mo, Xuejie Huang, *Solid State Ionics* **154–155,** 51– 56 (2002).
7. SF. Johnston, I.M. Ward, J. Cruickshank, G.R. Davies, *Solid State Ionics* **90,** 39-48 (1996).
8. M. Abd El-Kader, A. S. Orabi, *Polym. Test.* **21,** 591-595 (2002).
9. A. D. M. Vosshage, B. V. R. Chowdari, *Solid State Ionics* **62,** 205-216 (1993).
10. B.H. Stuart, *Spectrochimica Acta Part A* **53,** 107-110 (1997).

ELECTROCHEMICAL AND STRUCTURAL PROPERTIES OF POLYVINYLIDENE FLUORIDE – SILVER TRIFLATE SOLID POLYMER ELECTROLYTE SYSTEM

S. AUSTIN SUTHANTHIRARAJ* AND B. JOSEPH PAUL
Department of Energy, University of Madras, Guindy Campus, Chennai-600025, India.
*Email: suthan98@yahoo.com

A new polymer gel electrolyte system consisting of polyvinylidene fluoride (PVDF) and silver triflate ($AgCF_3SO_3$) has been investigated and reported in the present work. Thin film specimens of PVDF + x wt.% $AgCF_3SO_3$ (where x = 10, 20, 30, 40, 45, 50, 55 and 60 respectively) were prepared by solution casting technique using dimethyl formamide (DMF) as the common solvent. Complex impedance measurements were carried out on all the specimens in the frequency range 20 Hz – 1 M Hz within the temperature domain 298 to 333 K. The room temperature ionic conductivity of the polymer electrolyte was found to increase from 10^{-5} to 10^{-3} Scm^{-1} i.e. by two orders of magnitude with increasing concentration of silver triflate from 10 to 60 wt.%, whereas the activation energy decreased with an increase in concentration of the dopant salt. The ionic transference number values determined by Wagner's polarization technique showed an increase from 0.33 to 0.99 with an increase in the concentration of silver triflate salt. These results have clearly indicated that the ionic conduction is significant in the case of higher salt concentrations viz., > 20 wt.%. Furthermore, the X-ray diffraction (XRD) patterns have revealed a decrease in the crystallinity of the polymer electrolyte due to complex formation. Fourier transform infrared (FTIR) spectral studies have also confirmed the complex formation between polyvinylidene fluoride and silver triflate owing to the appearance of new absorption bands and gradual shifts observed in certain peaks.

1. Introduction

Discovery of polymers having high electrical conductivity values has opened an important area in research and development of electro chemical devices [1] such as rechargeable solid-state batteries, electrochromic display devices etc. The intense interest in this field has risen because of their inherent properties such as ease of fabrication into thin films, good contact with electrode material and ease of combination with salt. However, most of the polymers have low ionic conductivity at room temperature. Investigations have been focused primarily to enhance conductivity through various approaches like blending of two polymers, [2] adding

plasticizers to polymer electrolytes, complexation of metal salts and addition of inert fillers. Among these methods, complexation of polymer with metal salts has been employed in the present work. Polyvinylide Fluoride (PVDF) acts as the host polymer due to its high dielectric constant and strong electron with drawing group -(C-F)- [3] and silver triflate ($AgCF_3SO_3$) is used as the dopant salt for understanding the transport features of silver ion in the chosen polymer matrices. Ionic conductivity of the polymer electrolyte has been measured using complex impedance spectroscopy. Wagner's polarization method has been employed to measure the ionic transport number. The complexation and molecular interactions between various constituents have been studied using Fourier transform infrared spectroscopy (FTIR) where as the crystallinity of the samples has been examined using X ray diffraction analysis at room temperature.

2. Experimental

2.1. *Materials*

Commercially available chemicals of polyvinylidene fluoride, PVDF (Aldrich, M_w = 275000), Silver triflate, $AgCF_3SO_3$ (Purity - 99.9%, Aldrich) and analytical reagent grade dimethyl formamide, DMF were used as starting materials. Silver triflate was initially dried in vacuum at 393 K for an hour before use. PVDF and DMF were used without any pre-treatment.

2.2. *Preparation of Thin Films*

A series of thin film specimens of the polymer electrolyte system PVDF + x wt.% of $AgCF_3SO_3$ have been prepared using solution casting technique. [4] The polymer host material namely PVDF was initially dissolved in dimethyl formamide (DMF) as the solvent by stirring at 333 K for an hour. Subsequently, an appropriate amount of $AgCF_3SO_3$ was also added into the homogenous solution and stirred well until the slurry mixture became homogenous. The resulting homogenous solution was cast onto a clean and dry petri dish to allow the evaporation of the solvent by drying in vacuum at 333 K. Finally all the synthesized thin film specimens were stored in a vacuum desiccator for the purpose of further characterization studies.

2.3. *Complex impedance measurement*

Electrical conductivities of the synthesized polymer electrolytes were evaluated from the complex impedance data obtained in the frequency range of 20 Hz to 1 MHz using HP 4284 Precision LCR Meter. The thin film specimens were sandwiched between two silver electrodes, which acted as the non-blocking electrodes for ions, and measurements were performed in the temperature range 298 – 333 K.

2.4. *Transport number measurement*

Total ionic transport number t_{ion} was measured using Wagner's polarization technique [5]. Silver and graphite were used as non-blocking and blocking electrode respectively. A fixed DC voltage of 300mV was applied across the electrode and current monitored as a function of time.

2.5. *FTIR Spectral Studies*

The Fourier transform infrared (FTIR) spectra for all the thin film specimens of the PVDF – $AgCF_3SO_3$ polymer electrolyte system were studied using a Perkin Elmer RX1 Spectrometer over the wavelength domain 4000 – 500 cm^{-1} at room temperature with a resolution of 4 cm^{-1}.

2.6. *X-ray diffraction studies*

X-ray diffraction analysis was performed using a PANalytical diffractometer with Cu-$K\alpha_1$ radiation. The intensities of the scattered radiation were measured in the 2θ range 10^0 to 60^0.

3. Results and Discussion

3.1. *Complex impedance analysis*

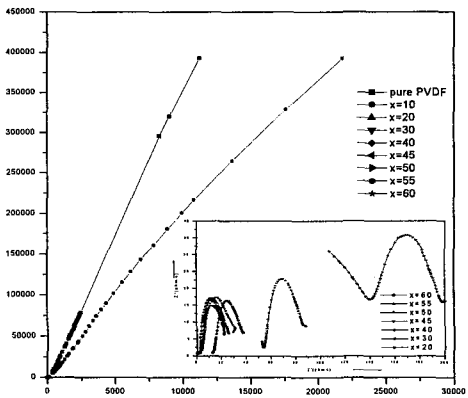

Figure 1. Complex impedance plots for PVDF and PVDF + x wt.% of $AgCF_3SO_3$.

The impedance spectra (Z' Vs Z") obtained for PVDF + x wt.% of $AgCF_3SO_3$ where x = 10, 20, 30, 40, 45, 50, 55 and 60 is shown in Fig. 1. The total electrical conductivities (σ) of these polymer electrolytes were calculated using the formula.

$$\sigma = t / (R_b A) \quad (1)$$

Where t is the thickness of the thin film, A the common area covered by the silver electrodes in contact with the sample and R_b is the bulk resistance of the material obtained from the intercept on the real axis at the high frequency end of the Nyquist plot of complex impedance. [6,7] According to the theoretical analysis given by Watanabe and Ogata, [8] two semicircles should appear in an impedance spectrum for a symmetric cell i.e., one at higher frequency corresponding to bulk electrolyte impedance and the other at lower frequencies related to the interfacial impedance. The disappearance of semicircle portions at higher frequency side led to a conclusion that current carriers in the present system are ions. These leads one to further infer that the total electrical conductivity is mainly due to ions. [9]

The room temperature electrical conductivities of different compositions having 0 to 60 wt. % $AgCF_3SO_3$ are summarized in Table 1. From Table1, it is evident that the conductivity gradually increases with increase in concentration of silver triflate. The conductivity values increased by two orders from 10^{-5} to 10^{-3} compared with that

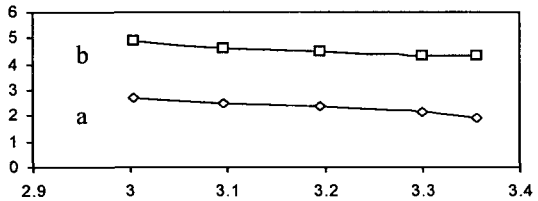

Fig.2. Arrhenius plot for pure PVDF (a) and PVDF + 55 wt.% of $AgCF_3SO_3$(b).

of the pure polymer PVDF thus concluding that dissociation of silver triflate takes place on the polymer matrix. The temperature-dependent ionic conductivities of all these compositions were studied in the temperature range 298 – 333 K. It is also observed that the ionic conductivity increases with increasing temperature as in the case of ionic solids. The activation energies were calculated in the usual manner following the Arrhenius equation and the values are shown in Table 1. It may be inferred from Table 1 that the activation energy value decreases from 0.53 to 0.25 eV with increasing concentrations of the dopant salt. The Arrhenious plots for pure PVDF and 55wt.% $AgCF_3SO_3$ are shown in Fig. 2. These results appear to suggest that silver ions may migrate through the conduction path formed by the modified network structure of PVDF chains.

Table 1. Ionic conductivity, activation energy, transport number data.

Wt. % of $AgCF_3SO_3$	σ Scm^{-1}	Ea (eV)	t_{ion}
0	2.8×10^{-5}	0.54	-
10	5.6×10^{-5}	0.48	0.30
20	5.8×10^{-5}	0.40	0.79
30	2.3×10^{-4}	0.36	0.96
40	0.9×10^{-3}	0.32	0.97
45	3.9×10^{-3}	0.30	0.98
50	4.7×10^{-3}	0.29	0.99
55	6.9×10^{-3}	0.26	0.99
60	2.6×10^{-2}	0.25	0.99

3.2. *Transport number data*

Wagner's polarization technique was used to measure the total ionic transference number of all the composite polymer electrolyte materials under study. [5] In this

technique, a constant DC voltage of 300 mV was applied across the cell (Ag/ polymer electrolyte/C). The DC current passing through the cell was measured as a function of time until the cell completely polarized. The transport number was calculated using the formula.

$$t_{ion} = 1 - (I_s / I_t) \quad (2)$$

Where I_t is the initial current due to both ionic and electric and I_e is final current due to electrons alone. Calculated t_{ion} values are shown in Table 1. The observed transport number value increases from 0.39 to 0.99 with increase in concentration of silver triflate. Thus the electrical conduction in the composite polymer electrolyte is found to be mainly due to the migration of ions.

3.3. Fourier Transform Infrared Studies

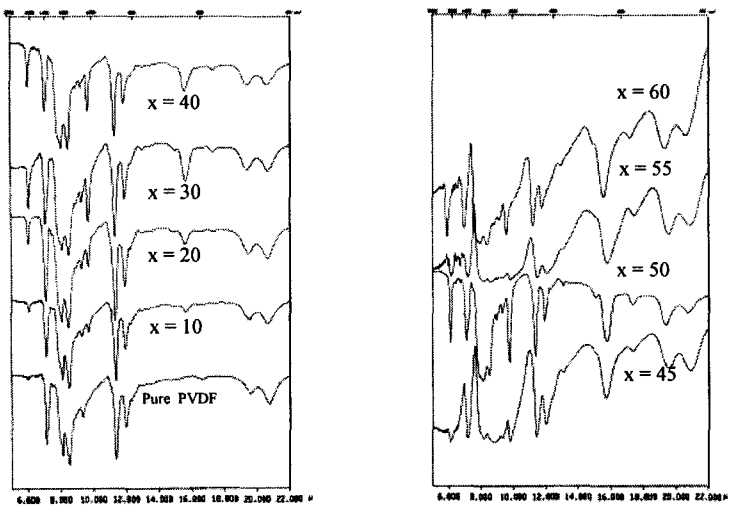

Figures 3(a,b). FTIR Spectra for pure PVDF and PVDF + x wt.% of $AgCF_3SO_3$.

Fourier transform infrared spectroscopic technique has been used to characterize the chain structure of the host polymer and reaction of multifunctional monomers including rearrangements and isomerization. [10,11] The FTIR spectra obtained for the polymer electrolyte system PVDF – x wt.% $AgCF_3SO_3$ (where x = 10, 20, 30, 40 and 50 respectively) in comparison with that of pure PVDF are shown in Figs 3 (a,b). A careful analysis of the present spectra suggests that the observed vibrational band at 1404 cm^{-1} belongs to the deformed vibration of the CH_2 group.

[12] The peak noticed at 881 cm^{-1} belongs to the vinylidene group of the polymer. [13] The vibrational frequencies appearing at 1072 and 834 cm^{-1} appear to indicate the crystalline and amorphous phases of PVDF as reported earlier. Absorption bands seen at 512 and 481 cm^{-1} may be assigned to the wagging and bending vibrations of CF_2 respectively. [14] The appearance of new bands at 1647, 1028, and 639 cm^{-1} has clearly confirmed the complexation between PVDF and $AgCF_3SO_3$. The band at 1404 cm^{-1} of pure PVDF was found to gradually shift towards the higher frequency of 1409 cm^{-1} at higher concentrations of $AgCF_3SO_3$. This may be due to the weakening of interaction between H atom of the CH_2 groups and F atom of the CF_2 groups. [12] On addition of silver triflate, the set of absorption bands from 1660, 1034, and 651 cm^{-1} got shifted to 1638, 1028 and 634 cm^{-1} respectively. Thus, the above feature of shifting and occurrence of new peaks tends to confirm the molecular interaction of the polyvinylidene fluoride with the silver triflate.

3.4. X-Ray Diffraction Characteristics

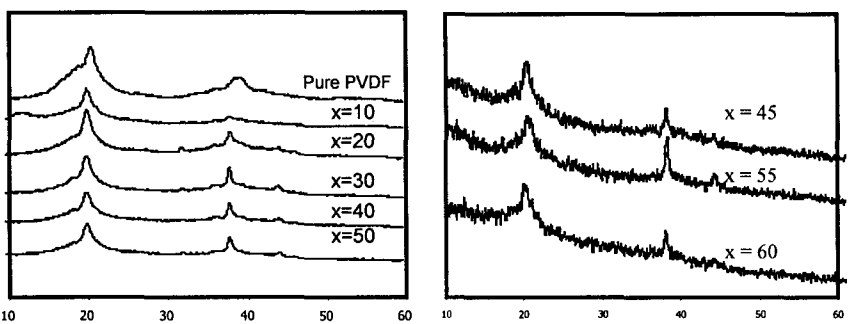

Figure 5 (a,b). XRD Spectra for pure PVDF and PVDF + x wt.% of $AgCF_3SO_3$.

Figures 5 (a,b) show the X-ray diffraction patterns obtained for pure PVDF and eight different compositions in the system PVDF + x wt. % $AgCF_3SO_3$ ($10 \leq x \leq 60$). The characteristic peaks at $2\theta = 20^0$, 38^0 and 44^0 correspond well with the reflection planes (110) and (112) of crystalline PVDF. The intensity of the PVDF diffraction peaks was significantly lower in the complexed polymer electrolyte system than that of the peaks in the pure PVDF indicating a decrease in the crystallinity as a result of complexation. The fact that no new diffraction peaks corresponding to $AgCF_3SO_3$ can be seen in any of the complexed polymer, which implies the complete disassociation of silver salt in the polymer matrices.

4. Conclusion

Thin films of the polymer electrolyte system PVDF + x wt. % of $AgCF_3SO_3$ ($10 \leq x \leq 60$) were prepared using solution casting technique whose ionic conductivity could be enhanced by two orders of magnitude from 10^{-5} to 10^{-3} Scm^{-1} with increasing concentration of silver triflate. The observed increasing trend in transport number value from 0.33 to 0.99 shows that total conductivity in mainly due to ions alone. XRD and FTIR studies have further confirmed the decrease in crystallinity and complexation of silver triflate with the PVDF matrix.

References

1. M. R. Armand, J. M. Chabagno, M. J. Duclot, in: Fast ion transport in solids, ed. P. Vashishta, J. N. Mundy, G. K. Shennay, (North-Holland, Amsterdam, 1971) p.131.
2. D. W. Kim, J. K. Park, H. W Rhee, *Solid State Ionics* **83**, 49 (1996).
3. Zhaohui Li, Guangyao Su, Xiayu Wang, Deshu Gao, *Solid State Ionics* **176,** 1903 (2005).
4. S. A. Suthanthiraraj, D.J. Sheeba, *Indian J. Phys.* **79**, 807 (2001).
5. J. B. Wagner, C. J. Wagner, *Chem Rev.* **26,** 1597 (1957).
6. K. M. Abraham, Z. Jiang, B. Caroll, *Chem. Mater.* **9 (9),** 1978 (1997)
7. M. Watanabe, K. sanui, N. Ogata, T. Kobayashi, Zohtaki. *J. Appl. Phys.* **57 (1),** 123 (1985).
8. M. Watanabe, N. Ogata in *Polymer Electrolyte Review-1*, J. R. MacCallum , C.A. Vincent (Eds), Elsevier, NewYork) 1987.
9. MME. Jacob, SRS. Prabaharan, S. Radhakrishna , *Solid State Ionics* **104**, 267 (1997).
10. D. L. Pavia, G. M. Lampman, G. S. Kriz, in: Introduction to Spectroscopy, Harcourt College Publ. (USA, 2001) p.13.
11. C. S. Kim, S. M. Oh, *Electrochim. Acta* **45**, 2101 (2000).
12. Zhaohui Li, Guangyao Su, Deshu Gao , Xiayu Wang , Xiaoping Li, *Electrochim. Acta* **49**, 4633 (2004).
13. D. Saikia, A. Kumar, *Electrochim. Acta* **49**, 25 (2004).
14. S. Rajendran, O. Mahendran, T. Mahalingam, *Eur. Polym. J.* **38**, 49 (2002).

MICRO RAMAN, ^{7}Li NMR AND ac IMPEDANCE ANALYSIS OF PVAC:$LiClO_4$ SOLID POLYMER ELECTROLYTES

R.BASKARAN, S.SELVASEKARAPANDIAN

Solid State and Radiation Physics Lab, Bharathiar University, Coimbatore-641 046, India

E-mail: sekarapandian@yahoo.com

N.KUWATA, O.KAMISHIMA, J.KAWAMURA

Institute of Multi Disciplinary Research for Advanced Materials, Tohoku University, Japan

T.HATTORI

Department of Applied Physics, Tokyo University of Science, 162-8601 Tokyo, Japan

Abstract

The polymer electrolytes composed of Poly (vinyl acetate) (PVAc) with various stoichiometric ratios of lithium perchlorate ($LiClO_4$) salt have been prepared by solution casting method. The techniques Fourier Transform Infra-red (FTIR) and micro Raman spectroscopy have been used to study polymer- salt complex formation, ion-ion and ion-polymer interactions as a function of salt concentration. The ac impedance results show the depressed semicircles which indicate the non-Debye nature of the polymer electrolytes. The maximum ionic conductivity has been found to be $1.3x10^{-3}$ Scm^{-1} at 373K for the 80PVAc:20$LiClO_4$ polymer complex. The ^{7}Li NMR linewidth decreases with increasing temperature which indicates the enhancement of lithium ion mobility in the polymer electrolytes. The two different environments of Li^+ ion in the polymer electrolytes observed in ^{7}Li NMR have been confirmed by FTIR analysis.

Keywords: Polymer electrolytes; ^{7}Li NMR; ac impedance; micro Raman; FTIR

1. Introduction

Solid Polymer Electrolytes have found wide applications in various electrochemical devices, such as batteries, fuel cells, electrochromic display devices [1-2]. Lithium-ion conducting polymer electrolytes are of great research interest due to their possible application to lithium- polymer batteries with high energy density [3]. To date different polymers, such as PAN [4], PMMA [5] and PVdF [6] have been studied. Among the different choices, poly (vinyl acetate) (PVAc) offers good mechanical stability and easy film formation. Raman spectroscopy was used to study the ion- pair dissociation effect by probing the stretching mode of free and paired anion groups. Among the several techniques employed, the nuclear magnetic resonance (NMR) has contributed significantly to the understanding of the physical properties of the polymer electrolytes mainly because it offers the possibility to selectively study the ionic and polymer chain dynamics. In the present study PVAc:

$LiClO_4$ solid polymer electrolytes of various compositions have been prepared by solution casting technique. The complex ac impedance analysis and Lithium (^7Li) NMR lineshapes were measured as a function of temperature in the PVAc- $LiClO_4$ Solid Polymer Electrolytes. The ion-polymer interactions of PVAc:$LiClO_4$ polymer electrolytes are investigated via micro Raman and FTIR analysis.

2. Experimental analysis

PVAc (Himedia) and $LiClO_4$ (Himedia) are dried by heating at 100^0 and 110^0C under vacuum for 10h and 15h, respectively. All the electrolytes have been prepared by the solvent casting technique. Appropriate quantities of PVAc, $LiClO_4$ (table.1) are dissolved by adding in sequence to tetrahydrofuran (THF) (s.d.fine) and stirred for 24h. The resulting solution is poured on to a glass petry dishes and the THF is allowed to evaporate in air at room temperature for 48h. The films are further dried at 60^0C for 24h in vacuum to remove any trace of THF. The polymer electrolytes of various weight ratios such as 90:10; 85:15 and 80:20 (PVAc: $LiClO_4$) have been prepared. FT-IR spectroscopy measurements are carried out using SHIMADZU-8000 spectro- photometer in the range of 400- 4000 cm^{-1}. Raman spectra have been performed in a microscopic Raman spectrometer using the Ar ion laser line of 514.5 nm with power 0.28W. The ^7Li NMR measurements are performed in the temperature range 303-373K, using a Bruker NMR spectrometer operating at a ^7Li resonance frequency of 155.4 MHz.

3. Results and discussion

3.1. FTIR analysis

The FT-IR spectrum of pure $LiClO_4$, PVAc, and PVAc-$LiClO_4$ complexes of various compositions are shown in Fig.1(a-e). In Fig.1(b), the vibrational bands observed at 2923, 2865 and 1375 cm^{-1}, are ascribed to CH_3 asymmetric stretching, symmetric stretching and symmetric bending vibrations of pure PVAc respectively. The peaks at 1245, 1100 and 1090 cm^{-1}, are ascribed to C-O-C symmetrical stretching, C-O and C-C stretching vibrations of pure PVAc respectively. The carbonyl stretching band at 1730 cm^{-1} is sensitive to the complexation of Li^+ cations to the carbonyl oxygen and is used to probe this complexation. The appearance of strong band in the spectrum at 1730 cm^{-1} which corresponds to C=O stretching

frequency of pure PVAc is broadened and shifted to lower wave number (1730-1706 cm^{-1}) in the polymer- salt complexes upon the increase in concentration of $LiClO_4$. The perturbation to the carbonyl band in the presence of Li salt arises from complexation of Li^+ cation to the carbonyl oxygens, the more extensive the complexation, the larger the spectral perturbation. Similarly in the FT-IR spectra of the ester oxygen region the C(O)-O-C symmetric stretch frequency decreases from 1246 to 1235 cm^{-1} and broadens which reveals the weakening of the C-O-C bond due to the interaction of Li^+.

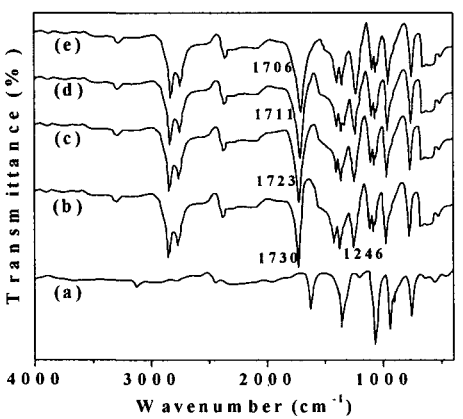

Fig.1. FTIR spectra of (a) $LiClO_4$; (b) pure PVAc; (c) 90:10; (d) 85:15; (e) 80:20 PVAc:$LiClO_4$ polymer complexes

The Li^+ interaction with ester oxygens disturbs the delocalization of electrons in the ester oxygens, and hence an inductive withdrawal of electron density from the ester linkage occurs through the C=O. Similar reports of Li^+ and Na^+ cation interactions with the carbonyl oxygen of polymers have already been reported by W.Wieczorek et.al. and Weihua Zhu et.al for the polyether-PMMA-$LiCF_3SO_3$ and PEG-PU/$NaClO_4$ complexes, respectively [7-8]. The coordination of cation with the ester oxygen and C=O in PVAc-$LiClO_4$ polymer complex has been figurated as shown in scheme.1.

3.2. Laser Raman Spectroscopy Analysis

Fig.2 shows the Laser Raman spectra of PVAc-$LiClO_4$ polymer electrolyte complexes in wide frequency window. The appearance of the strong band at

934 cm^{-1} is ascribed to the symmetric (ν_1) vibration of the perchlorate anion [9]. As seen in Fig.2 (a-b) the splitting of band indicates the different ionic environments for the perchlorate anions. In Fig.3(a&b), the band is fitted by using PEAKFIT software with Lorentzian fitting. For the 85PVAc:15$LiClO_4$ polymer salt complex, two Lorentzian curves are needed to fit the Raman band. Curve fitting analysis of the $\nu_s(ClO_4)$ mode in the 85PVAc:15$LiClO_4$ system indicates a strong band at 934 cm^{-1} (FWHM=5.3 cm^{-1}) corresponding to free perchlorate anions and a weak high frequency shoulder at 939 cm^{-1} (FWHM=2.19 cm^{-1}) ascribed to contact ion pairs (Fig.3a). For higher salt concentration samples (80PVAc:20$LiClO_4$), the ν_1 band is fitted by three Lorentzian curves as shown in Fig.3 (b). At higher salt concentration the intensity and line width (FWHM=5.5, 7.04 cm^{-1}) of the first low frequency band at 933 cm^{-1} and the component at 939 cm^{-1} increase which indicate the concentration of the free anions and contact ion ($Li^+...ClO_4^-$) pairs increase. The possible species responsible for the third very weak Lorentzian peak at 945 cm^{-1} are trimers ($Li^+...ClO_4^-...Li^+$), tetramers or higher order ionic clusters of sub micron scale. The narrow line width (FWHM=1.6 cm^{-1}) of the third peak, in comparison with the width of the other peaks, suggests that it is not associated with a broad distribution of clusters of different sizes.

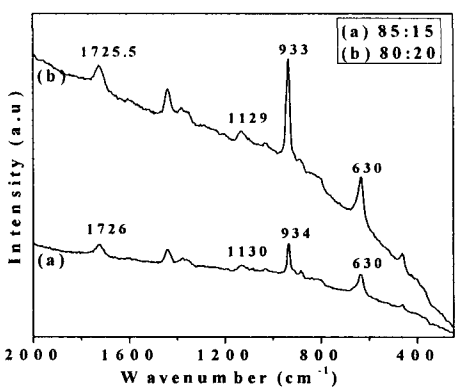

Fig.2. Micro- Raman spectra for (a) 85:15 and (b) 80:20 (PVAc: $LiClO_4$) polymer complexes

The intensity of the band due to ester oxygen C(O)-O-C region 1130 cm^{-1} is found to increase with increasing salt concentration which may be due to the

interaction of ClO_4^- with ester carbon and interaction of Li^+ cation with the ester oxygen C(O)-O-C present in the host polymer PVAc.

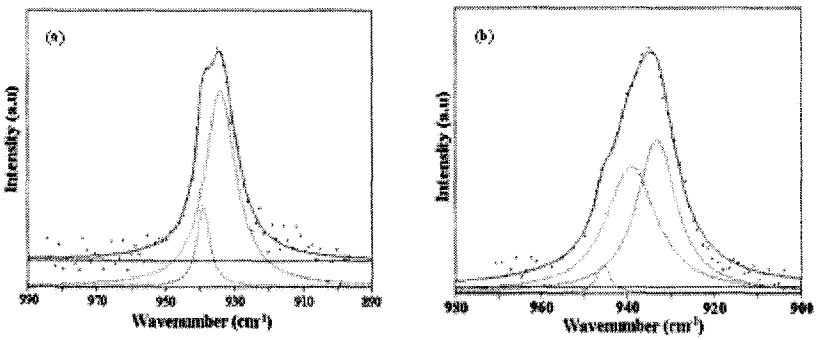

Fig.3. Peakfit analysis of $\nu_s(ClO_4)$ mode of (a) 85:15 and (b) 80:20 PVAc:$LiClO_4$ complexes

W.Wieczorek et.al. reported the coordination of C-O-C ether oxygen with the Li^+ cation [7]. The band corresponding to the free carbonyl stretch at 1726 cm^{-1} is resolved and it is seen that the intensity of this band increases with increasing salt concentration suggests the coordination between carbonyl carbon and ClO_4^- anion as shown in scheme.1. S.Selvasekarapandian et.al reported the interaction of both Li^+ and SCN^- with the polar groups present in PVAc [10].

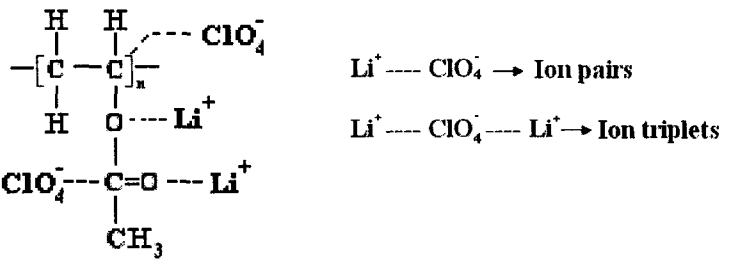

Scheme:1 Schematic representation of the coordination of Li^+ and ClO_4^- in PVAc-$LiClO_4$ complex

3.3. Impedance spectroscopy analysis

The Nyquist plots for PVAc-$LiClO_4$ polymer electrolyte samples of different compositions at 303K are presented in Fig.4. The plots consist of a high frequency depressed semicircle and a low- frequency spike. The high frequency part of impedance plots can be related to bulk relaxation processes according to

Armstrong's model of a solid electrolyte [11]. The low frequency spur results from electrode/ electrolyte interface properties. It is noted that the semicircle observed at high frequency region gradually fades away and the semicircle depression decreases as the content of $LiClO_4$ increases (Fig.4).

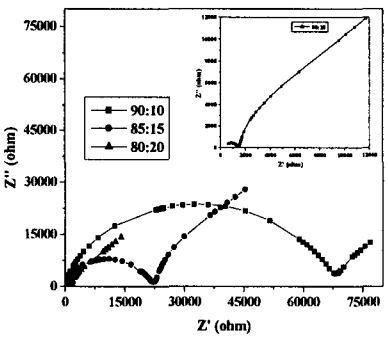

Fig.4. Impedance spectra of various concentrations of PVAc:$LiClO_4$ polymer complexes at 303K; Inner plot: Enlarged Impedance spectra of 80:20 (PVAc:$LiClO_4$) polymer complex

The ionic conductivity is calculated using the equation: $\sigma = (L/R_b)A$, where 'L' is the thickness of the polymer electrolyte film and 'A' the surface area of the film. The amount of $LiClO_4$ deeply affects the ionic conductivity of these hybrid films. The highest room temperature conductivity value is found to be $6.2x10^{-5}$ Scm^{-1} (table. 1) for the system 80wt%PVAc- 20wt%$LiClO_4$. The improved ionic conductivity is due to the enhancement of the ionic mobility and number of carrier ions, as the many previous workers have already reported [12].

Table:1 Conductivity parameters of PVAc-$LiClO_4$ polymer electrolyte complexes

PVAc-$LiClO_4$ compositions (wt%)	**Conductivity (σ_b) (Scm^{-1})**		
	303K	**333K**	**373K**
90:10	$7.6x10^{-7}$	$8.1x10^{-6}$	$1.3x10^{-4}$
85:15	$2.9x10^{-6}$	$1.9x10^{-5}$	$2.1x10^{-4}$
80:20	$6.2x10^{-5}$	$2.8x10^{-4}$	$1.3x10^{-3}$

3.4. ^7Li NMR analysis

The ^7Li NMR spectra of 90PVAc: 10$LiClO_4$ polymer electrolytes at various temperatures is shown in Fig.5(a). In the temperature range 303-333K, the spectra are characterized by a narrow main absorption (full width at half maximum $7.8x10^2$

Hz) corresponding to the central +1/2↔ -1/2 transition (i.e. homonuclear ^{7}Li-^{7}Li dipole-dipole), superimposed on a broader baseline whose width decreases with increasing temperature, which is due to the quadrupolar distribution of the satellite transitions ± 3/2↔ ±1/2 [13]. This distribution of nuclear quadrupole transition is attributed to a distribution of electric field gradients at the lithium sites, due to the heterogeneous Li nearest-neighbor configuration in the PVAc:$LiClO_4$ polymer electrolyte complexes. The line width of the ^{7}Li NMR absorption peak is found to be narrower with increase of the temperature in all compositions of PVAc-$LiClO_4$ polymer electrolytes, which indicates that the mobility of the lithium ions is increased with increase in temperature. Motional narrowing is attributed to modulation of the ^{7}Li-^{1}H (the protons are, of course, in the polyester chain) magnetic dipole-dipole interaction resulting from polymer segmental motion above T_g. Similar results for Li salt-polymer complexes have been reported elsewhere [14]. In Fig.5(b), the ^{7}Li NMR spectra at 373K are deconvoluted into three Lorentzian line shapes by using PEAKFIT software. Two shoulder peaks (2.06 and 2.80 ppm) near the central part of the spectrum, indicates that there exist at least two inequivalent ^{7}Li quadrupole interactions accompanied two distinct local environments existing in the polymer complexes.

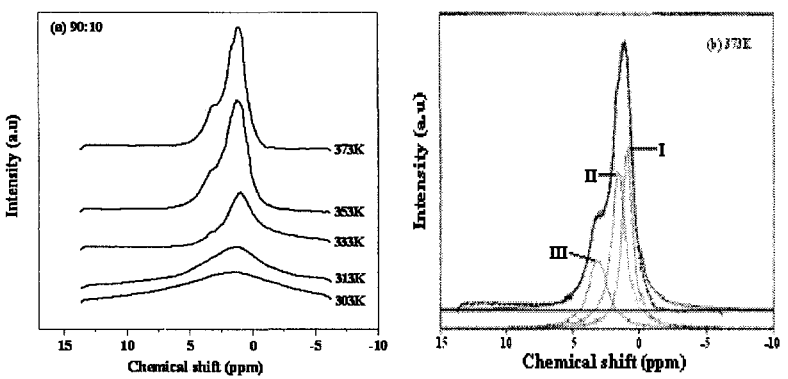

Fig.5 (a) ^{7}Li NMR spectra of 90:10 PVAc:$LiClO_4$ polymer electrolyte at different temperatures; (b) Peakfit analysis of ^{7}Li NMR spectra for PVAc:10$LiClO_4$ at 373K

4. Conclusion

The Solid Polymer Electrolytes PVAc:$LiClO_4$ at various compositions have been prepared by solution casting technique. FTIR and Micro Raman spectra analysis indicates the interaction of Li^+ cations with the ester oxygens of PVAc polymer matrix. The maximum conductivity values are found to be $1.3x10^{-3}$ Scm^{-1} at 373K for the system 80wt%PVAc- 20wt%$LiClO_4$. In ^7Li NMR spectra reveals the existence of at least two inequivalent ^7Li quadrupole interactions existing in the polymer-salt complexes.

Acknowledgements

One of the authors R.Baskaran acknowledges the Council of Scientific and Industrial Research (CSIR), Government of India, for the award of Senior Research Fellowship (SRF).

References

1. Kazuo Murata, *Electrochimica Acta* **Vol. 40, No. 13-14,** 2177 (1995)
2. D.R. MacFarlane, J. Sun, M. Forsyth, , *Solid State Ionics* **86-88**, 959 (1996)
3. J.R. MacCallum, C.A. Vincent (Eds.), *Polymer Electrolyte Reviews*, Vol.1, Elsevier, Applied Science, London, 1987
4. H. Akashi, K. Tanaka, K. Sekai, *J. Electrochem. Soc.*, **145,** 881 (1998)
5. K.M. Abraham, M. Abraham, *J. Electrochem. Soc.*, **136,** 1657 (1990)
6. Z. Jiang, B.Carrol, K.M. Abraham, *Electrochim. Acta*, **42,** 2667 (1997)
7. W. Wieczoreck, J.R. Stevens, *J. Phys. Chem. B*, **101,** 1529- 1534 (1997)
8. W. Zhu, X. Wang, *Journal of Polymer Science:Part* B:**39(11)** 1246-1254 (2001)
9. S. Schantz, L. M. Torell, *J.Chem. Phys.* **94 (10)** 6862-6867 (1991)
10. S. Selvasekarapandian, R. Baskaran, *Physica B* **357,** 412- 419 (2005)
11. R.D. Armstrong, *J. Electroanal. Chem.*, **52,** 413 (1974)
12. Seong Hun Kim, Jun Young Kim, *Solid State Ionics*, **116,** 63-71 (1999)
13. S.D. Brown, S.G. Greenbaum, *Solid State Ionics* **67,** 257 (1994)
14. S.G. Greenbaum, S. Panero and B. Scrosati, *Electrochim. Acta* **37,** 1533 (1992)

STUDY OF Na^+ ION CONDUCTION IN PVA-NaSCN SOLID POLYMER ELECTROLYTES

G.M.BRAHMANANDHAN, J.MALATHI, M.HEMA, G.HIRANKUMAR, D.KHANNA, D.ARUN KUMAR, S.SELVASEKARAPANDIAN*

Solid state and radiation physics lab, Department of physics, Bharathiar University, Coimbatore-641 046, India.

E-mail: sekarapandian@yahoo.com

Abstract:

In the present study, PVA based solid polymer electrolyte films complexed with NaSCN at different salt concentration have been prepared by the solution cast technique. This PVA-NaSCN polymer electrolyte has been characterized by FTIR and ac impedance spectroscopy techniques. The FTIR study confirms the polymer-salt complex formation. The temperature dependant conductivity of the polymer electrolyte follows the Arrhenius relationship. It has been observed that the conductivity increases with increasing salt concentration for all temperatures. The maximum conductivity has been found to be 3.28×10^{-3} Scm^{-1} at 303K for 20 mol% of NaSCN doped electrolyte. The dielectric spectra, modulus spectra and dielectric loss tangent have also been analyzed.

1. Introduction:

The development of polymeric systems with high ionic conductivity is one of the main objectives in polymer research. This is due to their potential application as an electrolyte in solid state batteries. Polymer battery has advantage of having high energy density, solvent-free condition, leak proof, easy processability and light weight. Poly (vinyl alcohol) (PVA) is one of the most important polymeric materials as it has many applications in industry and is of relatively low cast [1]. PVA is a potential material having a very high dielectric strength, good charge storage capacity and dopant – dependent electrical and optical properties. The electrical conductivity of the PVA blend with inorganic acids and water has been already reported by R.A.Vargas and co workers. It is reported that the water content in PVA based electrolyte enhanced the conductivity while preserving the dimensional stability of the electrolyte [2]. Literature studies reveal that many sodium ion conducting polymers have been reported based on Poly ethylene oxide (PEO), Polypropylene oxide (PPO), poly bis-methoxy ethoxy ethoxy phosphazene (MEEP) complexed with NaI, $NaClO_4$, NaSCN, $NaCF_3SO_3$. Many rechargeable batteries have also been reported based on the Na^+ ion conducting polymers. A new polymer

electrolyte PVA+NaSCN has been prepared and characterized by FTIR and AC impedance spectroscopy techniques to find out suitable composition for polymer batteries and the results have been presented in this paper.

2. Experimental:

Thick film of polymer electrolyte (200μm) of pure poly (vinyl alcohol) (Merck, Mw=1,25,000) (degree of hydrolysis = 88%) and poly (vinyl alcohol) doped with sodium thiocyanate have been prepared for different ratios by a solution cast technique. Aqueous solutions of poly (vinyl alcohol) and NaSCN mixtures have been thoroughly stirred to obtain a homogenous mixture. The mixtures are then poured onto a glass plate and evaporated slowly at room temperature. The smooth, uniform thick films, which are transparent to visible light and good mechanical properties, have been obtained. FT-IR measurements have been made with a Shimadzu-8000 spectrophotometer instrument in the wave number range of 4000 – 400 cm^{-1}.The electrical conductivity study of the polymer electrolytes has been carried out in the temperature range of 303K to 333K over a frequency range of 42 Hz – 1 MHz using computer controlled HIOKI 3532 LCR meter with a cell having stainless steel electrodes.

3. Results and discussion:

3.1 FTIR analysis

The FTIR spectra of pure PVA and PVA doped with 20 mol% NaSCN are shown in Figure 1 and 2 respectively. The absorption peaks of pure PVA at 3376 cm^{-1}, 1430 cm^{-1} and 1336 cm^{-1} are assigned to O-H stretching, CH_2 wagging and C-OH plane bending respectively. The vibrational frequencies at 1254 cm^{-1} and 1736 cm^{-1} of pure PVA are assigned to C-O-C stretching and C=O stretching of acetate group which is the residual part of PVA. It is to be noted that PVA used in the present study is 88% hydrolyzed. The peaks at 2912 cm^{-1}, 2944 cm^{-1} and 850 cm^{-1} are assigned to C-H symmetric stretching, C-H asymmetric stretching and C-H rocking of pure PVA respectively. The characteristic predominant O-H stretching vibration band of pure PVA at 3376 cm^{-1} found to be less intense in salt doped system which indicates the strong interaction of the salt with the polymer matrix. The new peaks at 2030 cm^{-1} and 2049 cm^{-1} have been observed for NaSCN doped

electrolyte, which can be attributed to free ion and contact ion pair of C≡N stretching of SCN^- ion respectively [3].

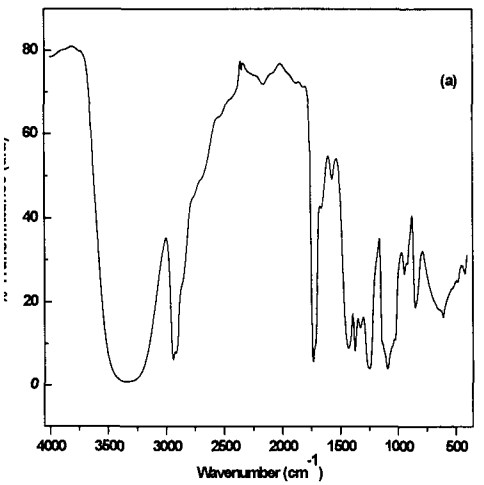

Figure 1: FTIR spectrum of pure PVA - NaSCN

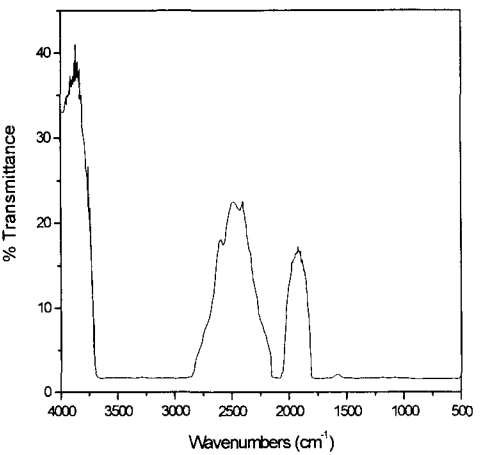

Figure 2: FTIR Spectrum of 80 mol% PVA+ 20 mol% NaSCN

Analysis of the changes in the vibrational frequency of SCN^- anion helps to study the effect of ion – ion interaction in the polymer electrolytes. When SCN^- ions were added to PVA, the crystalline phase of PVA has been progressively transformed into amorphous phase since large-size anions from the salt can play a role of plasticizer.

3.2 Conductivity analysis

The typical log σ_{ac} versus log ω relation for the polymeric electrolyte system with different NaSCN concentrations at room temperature is shown in figure: 3. The plot consists of three regions; the low frequency spike which is followed by the medium frequency plateau and a spike at high frequencies. The high frequency part of the plot corresponds to bulk relaxation phenomenon, whereas the plateau region is connected with the σ_{dc} of the polymer electrolytes. The low frequency spike describes electrode-electrolyte interfacial phenomena [4].

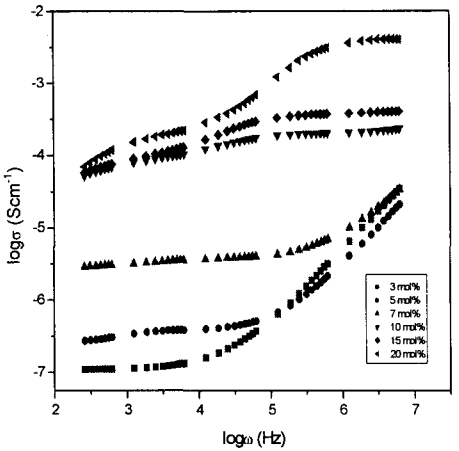

Figure: 3 Conductance spectra of PVA – NaSCN at different salt concentrations

3.3 Temperature dependent conductivity

The variation of the logarithmic ionic conductivity with inverse absolute temperature of the polymer electrolyte is shown in figure:4. The temperature dependence of dc conductivity, studied from conductivity spectra has been found to obey Arrhenius relation

$$\sigma_{dc} = \sigma_0 \exp(-E_a/kT) \qquad \text{---------- (1)}$$

The experimental data indicate that the ionic conductivity of all the samples is enhanced with increase of temperature. When the temperature is increased, the mobility of polymer chain is enhanced, and the fraction of free volume in the polymer electrolyte system increases accordingly, which facilities the translational motion of ions. The segmental motion either allows the ions to hop from one site to another site or provides a pathway for ions to move. Hence, the ionic motion in the polymer electrolyte is due to hopping of ions from one site to another site and the dynamic segmental motion of the polymer, which leads to an increase in the ionic conductivity of the polymer electrolyte.

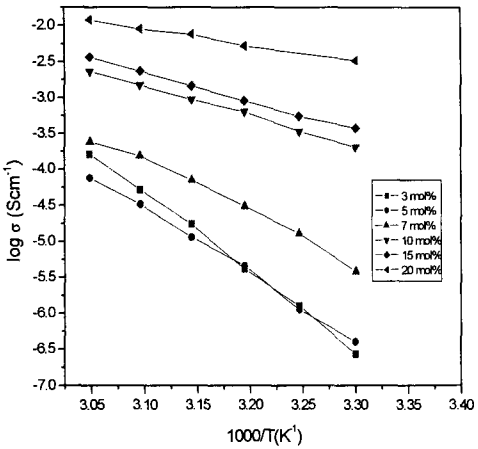

Figure: 4 Temperature dependent conductivity of PVA – NaSCN at different salt concentrations

3.4 Composition dependence analysis

The effect of addition of salt concentration in the polymer matrices on the logarithmic conductivity is shown in figure:5. The conductivity has been observed to increase with the addition of salt concentration. The initial increase in the conductivity is presumably due to an increase in the number of charge carriers in the matrix.

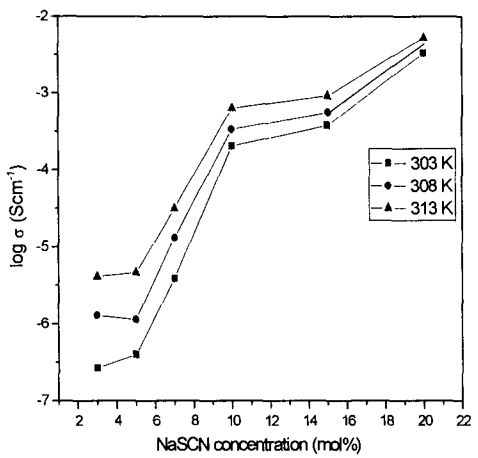

Figure: 5 Variation of logarithmic conductivity of PVA as a function of NaSCN salt concentration

The highest conductivity at room temperature has been found to be 3.28 x 10^{-3} S cm^{-1} for 20 mol% NaSCN doped electrolyte. The activation energy (E_a) has been found to be 0.19 eV for 20mol% NaSCN doped electrolyte.

3.5 Dielectric analysis

The measured impedance and phase angle data have been used to calculate the real (ε') and imaginary (ε") parts of the complex dielectric permittivity as

$$\varepsilon^* = 1/j\omega C_0 Z^* \quad \text{---------- (2)}$$

where Z* is the complex impedance, $C_0 = \varepsilon_0$ A/d, A is the area of the sample, d is the thickness of the sample and ε_0 is the permittivity of the free space. The frequency dependence of the dielectric constant for NaSCN doped polymer electrolyte at 303 K are shown in figure 6. The dielectric constant decreases with increase of frequency and saturates at high frequencies. High value of dielectric constant at low frequencies has been observed and it may be explained by the presence of space charge effects, which is contributed by the accumulation of charge carriers near the electrodes [5]. The low frequency aspects of the dielectric behavior have also been explained by space charge polarization arising due to the hopping of ions in unequal barrier heights. The observed variation in ε' with frequency has been represented as $\omega^{(n-1)}$ variation or the non Debye type of behaviour, where the space charge regions with respect to the frequency is explained in terms of ion diffusion.

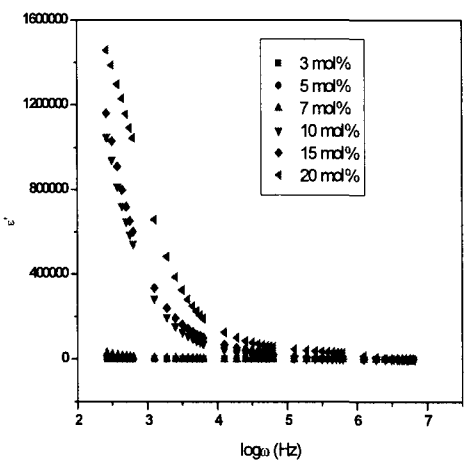

Figure: 6 Variation of ε' with log ω for PVA – NaSCN system at different salt concentrations

At higher frequencies, the periodic reversal of the electric field occurs so fast that there is no excess ion diffusion in the direction of the field. The polarization due to charge accumulation decreases, leading to the decrease in the value of ε'.

3.6 Dielectric loss tangent

The variation of loss tangent (tanδ) as a function of frequency at different temperatures for the polymer electrolyte system 95 mol% PVA – 5 mol% NaSCN is shown in figure 7.

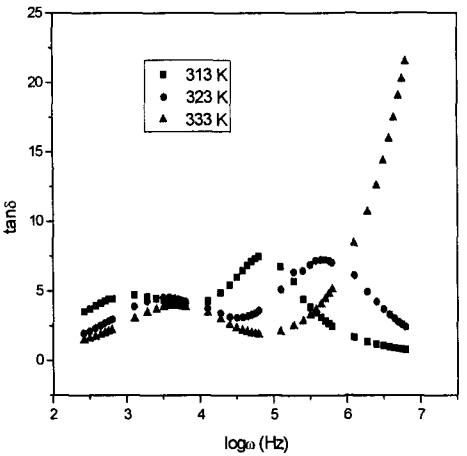

Figure: 7 Plot of tan δ versus log ω for 95 mol% PVA – 5 mol% NaSCN at different temperatures.

Tan δ has been found to increase with frequency for all temperatures, pass through a maximum value $(\tan\delta)_{max}$ and thereafter decreases. As the temperature is increased $(\tan\delta)_{max}$ gets shifted to higher frequencies. It is clear from the figure that there exist two types of relaxation peaks. One type occurring at higher frequency (so called β-relaxation) may caused by side group dipoles and other set at lower frequency (α-relaxation) may be caused by the movement of main chain dipole segment. The appearance of two types of relaxation peaks indicate that PVA shows two different types of relaxation process having different relaxation time.

3.7 Modulus analysis

Many researchers opted to study the dielectric response caused by ion relaxation using the reciprocal quantity M*, known as the electric modulus in which the

electrode polarization artifacts are suppressed. Electric modulus can be represented by the following equation,

$$M^* = 1 / \varepsilon^* = M' + M'' = j\omega C_o Z^* (\omega) \quad \text{---------- (3)}$$

Typical features of modulus spectrum include a broad asymmetric peak in the imaginary part and a sigmoidal step in the real part. This feature is due to the storage of mechanical stress associated with relaxation process of the conducting species.

The possible presence of peaks in the modulus spectra at higher frequencies due to bulk effect for the polymer electrolyte indicates that the electrolytes are ionic conductors. The peak height decrease with increase of temperature suggesting the presence of different type of relaxation mechanisms [6]. At low frequencies, M'' approach to zero indicating that the electrode polarization phenomena make a negligible contribution. The observed long tail at low frequencies is due to the large capacitance associated with the electrodes [4].

Conclusion:

The polymer electrolyte thick films of PVA complexed with NaSCN with different composition have been prepared by solution cast technique. It has been observed that the system PVA doped with 20mol% NaSCN has the highest conductivity, 3.28×10^{-3} Scm^{-1}.

References:

1. M. Krumova, D. Lopaz, R. Benavente, C. Mijangos, J.M. Perena, *Polymer* **41,** 9265 (2000)
2. M.A. Vargas, R.A.Vargas, B.E. Mellander, *Electrochim. Acta* **45**, 1399-1403 (2000)
3. D. Saar, P. Petrucci, *J.Phys. Chem.* **88,** 3326 (1986)
4. S. Ramesh, A. K. Arof, *Mat. Sci. Eng. B* **85,** 11-15 (2001)
5. R. D. Armstrong, W. P. Race, *J. Electroanal. Chem.*, **74,** 125 (1976).
6. R. Mishra, N. Baskaran, P.A. Ramakrishnan, K.J. Rao, *Solid State Ionics* **112,** 261-273 (1998)

EFFECT OF FILLER ADDITION ON PLASTICIZED POLYMER ELECTROLYTE SYSTEMS

M.SUNDAR AND.SELLADURAI*

Ionics Lab, Department of Physics, Anna University, Chennai-25, India.

Abstract

Poly (ethylene oxide) PEO based polymer electrolyte films were prepared by solution casting method by incorporating PEG -2000 as plasticizers. To find out the effect of fillers in the plasticized system TiO_2 is added. The interactions between filler, plasticizers and PEO chains are studied by Differential Scanning Calorimeter (DSC) and FT-IR techniques. Effects of filler and plasticizers on the properties of the PEO-based electrolyte, such as ionic conductivity and thermal behavior are studied. The ionic conductivity of the plasticized system does not found to change much with the addition of filler.

Keywords: Plasticizer, polymer electrolyte, ionic conductivity, filler, FTIR, DSC.

Introduction

Research on Polymer electrolytes has attracted ever-increasing interest, both in academia and industry, for the past two decades due to the potentially promising applications of such electrolytes, not only in all solid-state rechargeable batteries, but also in other electrochemical devices such as supercapacitors, electrochromic windows, and sensors. Much of the efforts till date has focused on poly (ethylene oxide) (PEO) as the host material for solid polymer electrolyte because of its beneficial structure in supporting fast ion transport and its exceptional solvating nature for variety of ionic salts to form an electrolyte [1-6], but it exhibits poor ambient temperature conductivity and mechanical stability. To improve the conductivity, modifications of the PEO system and evaluation of various plasticizers to PEO, have been much studied. Inorganic fillers, such as glasses, alumina, silica or other ceramics on being added to the polymer–salt systems generally improves the transport properties and resistance to crystallization [7-9]. In this paper we report the effect of filler addition on plasticized polymer electrolyte systems. The interactions between filler, plasticizers and PEO chains are studied by Differential Scanning

Calorimeter (DSC) and FT-IR techniques. Effects of filler on the properties of the PEO-based plasticized electrolyte, such as ionic conductivity and thermal behavior are studied.

Experimental

The Polymer electrolyte films of pure PEO (M.W. 7,00,000) purchased from Aldrich and various compositions of complexed films of PEO with magnesium chloride salt, PEG and TiO_2 were prepared in weight percent ratios by solvent casting method at 30°C. Polymer, filler and salt were dissolved in suitable solvent (methanol) and the solution of the salt, filler and polymer are stirred continuously to achieve the homogenous dispersion of the filler in the solution. When complete homogenisation of mixture has

occurred, the slurry was cast onto a polypropylene dish and left to evaporate solvent slowly at room temperature for 24 hours. The film were finally dried at vacuum. Traces of residual solvent which is capable of acting as nucleation sites are the limitation of this method, the film obtained is self standing with thickness 80 to 100 microns. Infra red spectra were recorded on Perkin Elmer instrument with a wave number resolution of 4 cm^{-1} in the frequency of 400-4000 cm^{-1}, for that measurement the mixed slurry were cast on the KBr wafer and dried via the same steps used in the preparation of polymer electrolyte films. Differential scanning calorimeter measurements were carried out on Netzsch thermal analyzer, all the measurements were carried out at a heating rate of 5°C/min from -100°C to150°C, the sample weights are maintained at 5-10 mg and all experiments were are carried out under nitrogen flow to avoid any contact with atmospheric moisture, and empty aluminum pan was used as a reference. CHEN-HWA (model 1061) LCZ bridge is used for measuring

Conductivity values in A.C impedance method by applying frequency ranges from 40 Hz to 200 kHz.

Conductivity values are calculated by the formula

Conductivity = $t / (A \times R_b)$ S/cm

t-thickness of the sample, A-Area of the sample

R_b-bulk resistance

Results and discussion

IR spectroscopic studies

Polymer complexes with ionic salts, fillers and plasticizer are characterized by IR spectroscopy [10-14,18,19]. This technique provides a powerful means to characterize the complex formation.

Formation of PEO-TiO_2-$MgCl_2$ complex

Marked changes were found when PEO is blended with PEG, TiO_2, and $MgCl_2$ salt, The absorption band at 2865 cm^{-1} in PEO is attributed to the stretching vibration of C-H group, with addition of PEG the band shifts to 2896.1 cm^{-1}, but the band shifts to 2864 $cm^{-1}$with the addition of TiO_2, The band at 679.6 cm^{-1} corresponding to stretching band of Ti-O had been shifted to 653 Cm^{-1} with the addition of PEO and $MgCl_2$ thus indicating the complexation and bond formation between PEO-TiO_2. The resulting bond breaks when PEG is being added to the complex, all these indicate the formation of PEO-PEG-$MgCl_2$-TiO_2 complex.

Reaction of Lewis Acid TiO_2 with PEO

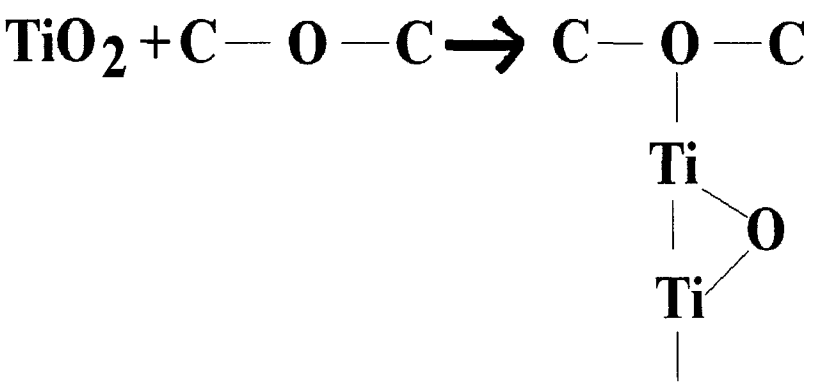

Table 1: The IR spectra of pure PEO-$MgCl_2$ and its blending with TiO_2 filler.

PEO cm^{-1}	PEO + $MgCl_2$ cm^{-1}	PEO + $MgCl_2$ +20 %PEG cm^{-1}	TiO_2 cm^{-1}	PEO-TiO_2 cm^{-1}	PEO+ $MgCl_2$+10% TiO_2 cm^{-1}	PEO + $MgCl_2$ +20 %PEG+10% TiO_2 cm^{-1}
3399			3379	3506.4	3350.5	
					3133.5	3172.6
			2917			
2865.3		2896		2816	2871.5	2864
	2742.6					
	2700					
2236.3		2240.5		2240.7	2240.4	2244.2
2165.6		2088.6				2088.9
1965.7	1967	1968.7		1986.4	1971.4	1972.4
1798.0				1807.5		
1644.7	1622	1665.9	1603	1644.8	1662	1662.1
1460.8	1460	1461.4	1465.8	1462.6	1462.9	1463.3
1348.2	1348.1	1350.0	1383.1	1349.5	1350.3	1350.6
1272.8	1242.1	1276.1		1276.1	1278.4	1277.4
1104.8	1114.8	1146.8	1106.1	1137.8	1120.0	1091.8
950.2	960.5	950.1		951.4	949.8	950
841.5		839.7		841.4	799	837.5
						762.5
			679.6	676.7	653	
					487.4	

DSC studies have been employed to determine the thermal behavior of the polymer electrolyte system. The DSC curves of PEO-$MgCl_2$ based polymer electrolyte are shown in figure 2. The data presented in Table 2, suggests that thermograms obtained in the heating cycle for these films showed a clear glass transition at Tg, at which a glassy phase becomes a rubbery amorphous phase on heating. The DSC curves suggest the Tg, heat of fusion and melting temperature does not found to vary with the addition of TiO_2 in the plasticized system.

Ionic conductivity

The charge transport in PEO solid polymer electrolyte complex involves dissociation of cations from its coordinating oxygen to an adjacent site. The high ionic conductivity in an electrolyte is attributed to increased ionic mobility and increased ionic charge carrier concentration. The IR studies clearly indicate the complexation occurring between polymer, salt and filler.

Table 2: Tm, Tg, melting heat and conductivity data of polymer electrolyte systems

Composition (wt %)	Tm °C	Tg °C	ΔHm (J/g)	Conductivity(s/cm)
PEG 5%	64.3	-8.2	101.5	3.7642
PEO + $MgCl_2$+20 %PEG	62.2	-15	67.3	5.3055
PEO+$MgCl_2$+20%PEG +10% TiO_2	62.3	-13.7	68.3	4.5477

Fig 1. FTIR spectra of (a) pure PEO; (b) TiO_2; (c) PEO+ TiO_2; (d) PEO+ $MgCl_2$+10% TiO_2; (e) PEO + $MgCl_2$ +20 %PEG; (f) PEO+ $MgCl_2$+10% TiO_2+20 % PEG

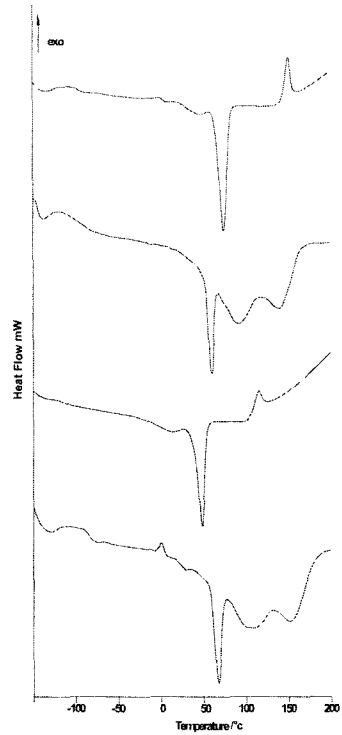

Fig 2.DSC thermograms of (a) pure PEO; (b) PEO+$MgCl_2$+20% PEG; (c) PEO+ $MgCl_2$+10% TiO_2+20% PEG;
(d) PEO+ $MgCl_2$+10% TiO_2

Generally Mg cations give a stronger acid – base interaction with the polymer substrate in comparison to lithium salts. Therefore the interaction with ether oxygen is stronger compared to lithium .The C-O-C stretching vibration band found in PEO is being affected greatly due to the above coordination reaction. In the system with no plasticizers, the host polymer can interact with ions significantly and hence conductivity is being reduced, but on adding the plasticizer the band at 1114.8 cm^{-1} corresponds to C-O-C stretching mode of unplasitcized system is being shifted to 1146.8 cm^{-1} that is the increase in wave number causes the bond length to decrease

and C-O-C band is being least affected, hence the cross linking effect of the salt in distinct PEO chains is decreased, that is in the case of plasticized systems the Mg ions are coordinated partially by the polymer matrix and partially by the plasticiser molecules, leading to the decoupling of Mg ions from the polymer segments. But on adding TiO_2 in the plasticized system the wave number shifts to 1091.8 cm^{-1} the decrease in wave number causes the bond length to increases, complexation/coordination takes place, that is the Lewis acid sites on the surface of the added filler interact with some of the oxygen atoms of PEG and hence decreases the effective interaction of the plasticizer with the ether oxygen of PEO.

Conclusion

The IR results clearly indicate the interaction of PEG with polymer and filler i.e. (Ti – O (oxygen of PEO)).

In plasticized systems:

Mg cations are coordinated partially by the polymer matrix and partially by the plasticizer molecule, leading to a decoupling of cations from the polymer segment hence conductivity improvement.

Filler added plasticized system:

Lewis acid sites on the surface of the added filler interact with some of the oxygen atoms of PEG and hence decreases the effective interaction of the plasticizer with the ether oxygen of PEO hence conductivity decreases.

References:

[1] K. Murata, Electrochimica. Acta 40 (1995) 2177.

[2] S.A. Hashmi, A. Chandra, S. Chandra, in: B.V.R. Chowdari, et al. Solid State Ionics: Materials and Applications, World Scientific, Singapore, 1992, p. 567.

[3] S. Sreepathi Rao, M. Jaipal Reddy, E. Laxmi Narsaiah, U.V. Subba Rao, Mater. Sci. Eng. B 33 (1995) 173.

[4] W. Gorecki, M. Jeannin, E. Belorizky, C. Roux, M. Armand, J. Phys.Condens. Matter

7 (1995) 6823.

[5] S.Selladurai, Trends in solid state Ionics, raj publishing house, chennai.

[6] T. Sreekanth, M. Jaipal Reddy, S. Subramanyam, U.V. Subba Rao, Mater. Sci. Eng.

B 64 (1999) 107.

[7] H.J. Walls, J. Zhou, J.A. Yerian, J. Power Sources 89 (2000) 156.

[8] K. Narin, M. Forsyhn, Solid State Ionics 86–88 (1996) 589.

[9] M.S. Michael, M.M.E. Jacob, S.S.R. Prabaharan, Solid State Ionics

98 (1997) 167.

[11] S.A. Hashmi, A. Kumar, K.K. Maurya, S. Chandra, J. Phys. D. 23 (1990) 784.

[12] K.K. Maurya, S.A. Hashmi, S. Chandra, J. Phys. Spc. Jpn. 61 (1992) 1709.

[13] F. Croce, G.B. Appetecchi, L. Persi, B. Scrosati, Nature 394 (1998) 456.

[14] F. Croce, R. Curini, A. Martinelli, L. Persi, F. Ronci, B. Scrosati, J.Phys. Chem.

B 103 (1999) 10632.

[15]X.Kornmann,R.Thomann,R.Mulhaupt,J.FinterandL.A.Berglund,Polymer Engineering and Science sep 2002 vol.42 No.9

[16] M. Doeff, P. Georen, J. Qiao, J. Kerr, L.C. De Jonghe, J. Electrochim.Soc. 146 (1999) 2024.

[17] R. Dupon, B.L. Papke, M.A. Ratner, D.H. Whitmore, D.F. Shriver, J.Am. Chem. Soc. 104 (1982) 6247.

[18] M. Jaipal Reddy, P.P. Chu / Journal of Power Sources 109 (2002) 340–346

[19] BinodKumar, Stanley j.rodrigues, Robert.j.spry.Electrochimica Acta 47(2002) 1275- 1281

IONIC MOTION IN *PEDOT* AND *PPY* CONDUCTING POLYMER BILAYERS

U.L. ZAINUDEEN [a] AND M.A. CAREEM [b]
Department of Physics, University of Peradeniya, Sri Lanka
[a]ulzdeen@yahoo.com , [b]mac@pdn.ac.lk

S. SKAARUP
Department of Chemistry, Technical University of Denmark,
DK-2800 Lyngby, Denmark
skaarup@kemi.dtu.dk

Conducting polymer bilayers with poly(3,4-ethylenedioxythiophene) (PEDOT) and polypyrrole (PPy), each containing dodecyl benzenesulfonate (DBS) as immobile dopant species, were synthesized galvanostatically. The electrochemical behaviour of the bilayers was investigated using cyclic voltammetry, optical absorption spectroscopy and electrochemical quartz crystal microbalance (EQCM) techniques. Two important conclusions of relevance for actuator performance were reached: It is possible to make a bilayer film that does not delaminate – the two polymers are compatible; and both polymers are active in the redox process as ions are able to move through the PEDOT layer and penetrate into PPy.

1. Introduction

Studies on ion exchange during redox processes of conducting polymers (CPs) such as polyanilene (PAn), polypyrrole (PPy), polythiophene (PT) and their derivatives have been carried out extensively. CPs can exchange both anions and cations, depending on the polymerization conditions,[1,2] the type and size of the counter ions incorporated during synthesis,[1-5] and ions present in the cycling electrolyte.[5,6] Ionic movement accompanied by varying number of solvent molecules results a change in volume in the CPs, which can be exploited in a soft polymer actuator.[7] PPy is being extensively investigated and developed as the active component in *electro-chemo-mechanical actuators*, or "artificial muscles". PPy is an electronically conducting polymer whose properties can be changed in a controlled way by the application of a redox potential. Mechanical properties such as length and stiffness vary as ions from a cycling electrolyte moves in and out of the polymer during cycling. An exact knowledge of the nature and amount of ionic motion is therefore crucial to understanding and controlling the actuation process.

PPy is a prime candidate for a conducting polymer actuator, but has the disadvantage that the electronic conductivity decreases by two or three orders of magnitude as the polymer is reduced. This causes a decrease in performance; since only a small part of the polymer film will then be actively contributing to the actuation.[8] A standard solution to this problem involves the addition of an extra

electron conductor, e.g. Au or Pt as thin patterns or as helices. The use of a corrugated gold layer on PPy improved the performance of the actuator.[9]

The present work is an attempt to solve the conductivity problem by using a second, more highly conducting polymer, to enhance the electronic conductivity. The candidate material chosen for this purpose was poly(3,4-ethylene-dioxythiophene), PEDOT, which has a very high conductivity. The cyclic voltammograms as well as the UV-visible spectra of PEDOT and PPy are very different, pointing towards the possibility of being able to separate the two films experimentally – even when combined in a single film.

In this paper, we report the preliminary characterization of the bilayer system (PEDOT/PPy) having two conducting polymers of PEDOT and PPy by using UV-visible spectroscopy and electrochemical quartz crystal microbalance (EQCM) techniques. Both polymers are doped electrochemically with dodecyl benzenesulfonate (DBS) anions to have homogeneous dopants in the film. Different thickness combinations were tested, and were compared with those of pure PEDOT and PPy films.

2. Experimental

Pyrrole (Aldrich 98%) monomer was distilled under nitrogen and stored in cold and dark capped vials prior to use. EDOT monomer (Aldrich 98%) was used without any further purification. Other chemicals, sodium dodecyl benzenesulfonate (NaDBS) (Aldrich) and NaCl (Merck) were used as received. Both PEDOT(DBS) and PPy(DBS) layers were formed by galvanostatic electropolymerization with a current density of 0.5 mA cm^{-2}. 0.05M SDBS aqueous electrolyte containing 0.05 M pyrrole or 0.02 M EDOT was used for the synthesis of PPy(DBS) and PEDOT(DBS) layers respectively.

For the EQCM experiments, the PEDOT(DBS) layers were prepared first on 0.2 cm^2 gold electrodes on AT-cut 10 MHz quartz crystals, to have a thickness corresponding to a charge of 32 mC cm^{-2}. They were rinsed in water before the deposition of the other layer. The synthesis cell was then filled with the corresponding electrolyte to deposit the PPy(DBS) layer on the first layer, and a charge of 64 mC cm^{-2} was used to give a calculated thickness 0.4 μm. The final bilayer PEDOT/PPy was rinsed in water before characterization. A Hewlett-Packard E4916A crystal analyzer in combination with a potentiostat (Autolab PGSTAT 30) was used for combined mass and redox cycling experiments. The cycling electrolyte (1 M NaCl) was purged with nitrogen gas to remove dissolved oxygen. A Pt sheet was used as counter electrode and Ag/AgCl (3 M KCl) as a reference electrode.

UV-visible optical absorption study was performed on bilayer films prepared, as described above, on ITO coated glass (Current density = 0.1 mA cm^{-2}) using an

Agilent 8453 UV-visible spectrometer. The thicknesses of the PEDOT(DBS) and PPy(DBS) layers corresponded to charges of 40 and 80 mC cm^{-2} respectively.

3. Results and discussion

3.1. *Formation of PEDOT/PPy bilayer*

Fig. 1 shows the potential and mass response during the galvanostatic synthesis of (a) PPy(DBS) and (b) PEDOT(DBS) on the EQCM Au electrode. During the polymerization of PPy(DBS) an overshoot of potential in the first few seconds (indicates the initially difficult formation of dimers and oligomers) followed by a constant potential of *ca.* 0.7 V (suggesting the same reaction during the whole film formation) was observed, and the corresponding mass change is 68.5 g/mol of electrons. It takes a longer time to reach a constant potential (*ca.* 1.0 V) during the synthesis of PEDOT(DBS). The mass change stabilizes at 90.7 g/mol of electrons.

Fig. 1(c) and (d) show the growth of PPy(DBS) on top of the PEDOT(DBS) layer and of PEDOT(DBS) on top of the PPy(DBS) layer respectively. During the formation of PPy on PEDOT, the growth stabilizes after ca. 40s, and the potential and growth rates are then nearly the same values observed for pure PPy(DBS) film.

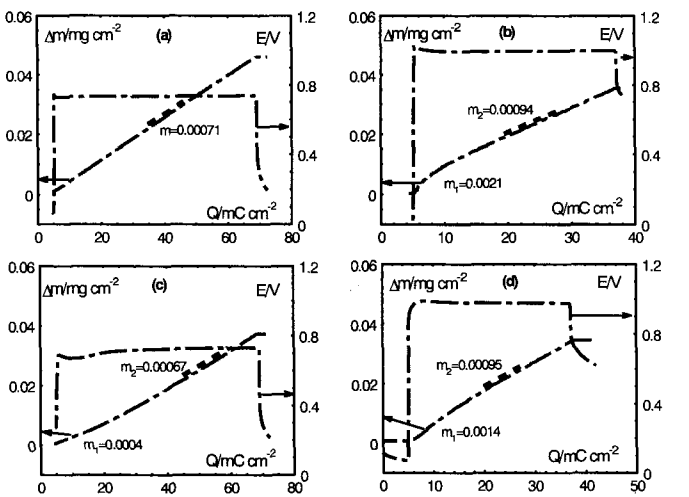

Figure 1. Potential and mass response during galvanostatic synthesis of (a) PPy(DBS), (b) PEDOT(DBS) on pure EQCM Au electrode, and (c) PPy(DBS) on top of the PEDOT(DBS) layer, and (d) PEDOT(DBS) on top of the PPy(DBS) layer.

Initially, the current is consumed not only for the polymerization of PPy but also for the oxidation of the PEDOT layer underneath, causing a potential drop and a lower rate of growth. During the growth of PEDOT on PPy, the mass and potential

responses are almost similar to those of the pure PEDOT layer. The results indicate that it is possible to form the two layers electrochemically on top of each other.

3.2. *Optical characterization*

In-situ UV-visible spectra were recorded while films were kept at different potentials between -1.0 and 0.5 V vs Ag/AgCl electrode in a 1 M NaCl electrolyte. The absorption spectra of pure PEDOT and PPy layers are shown in Fig.2. The two polymers have different absorption spectra. In the reduced state, the PEDOT has a π-π^* peak at a lower energy, indicating a smaller band gap for PEDOT than for PPy.

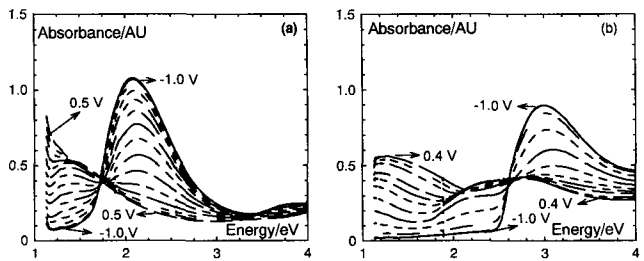

Figure 2. In-situ UV-visible absorption spectra of (a) PEDOT(DBS) and (b) PPy(DBS) films at different potentials in 1 M NaCl aqueous electrolyte.

To study the optical absorption behaviour of bilayers, a bilayer was prepared with the PPy(DBS) layer on top of the PEDOT(DBS) layer so that PPy(DBS) is exposed directly to the cycling electrolyte. The changes of the spectra for this bilayer as a function of potential are shown in fig. 3(a). Fig. 3(b) shows the spectra of the bilayer prepared with opposite combination of layers so that the PEDOT(DBS) layer is exposed to the electrolyte.

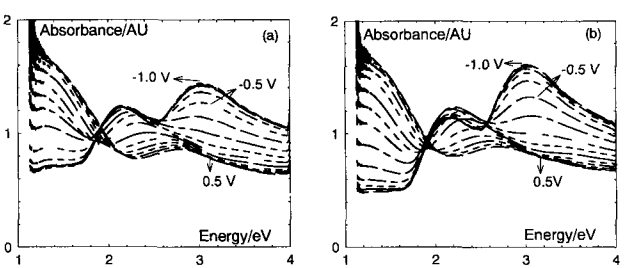

Figure 3. In-situ UV-visible absorption spectra of a PEDOT/PPy bilayer at different potentials in 1 M NaCl aqueous electrolyte; (a) outer layer is PPy, (b) outer layer is PEDOT

The spectral response at three different potentials for the bilayer are compared to that of pure PEDOT(DBS) and PPy(DBS) films in fig. 4. The bilayer spectra

show the characteristic features of both pure constituents. Furthermore, the sum of the absorption intensities of the respective single layers is almost equal to that of the bilayer.

The spectra obtained in the oxidized state (> 0.1 V) show a strong absorption band centered at 1.4 eV and a broader peak at 2.8 eV (Fig. 4a). The first band shows typical bipolaron features from both layers while the latter peak is only seen in PPy (Fig. 4a). Upon reduction (with decreasing potential by 0.1 V) the intensity of the peak at 1.4 eV decreases, the peak at 2.8 eV grows and another peak develops in between. Eventually, in the reduced state, the spectra exhibit two clearly separated

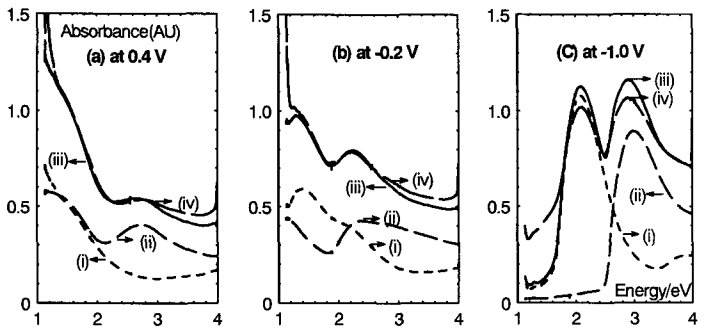

Figure 4. Comparison of spectra of a PEDOT/PPy bilayer (iv) with pure PEDOT(DBS) (i) and PPy(DBS) (ii) at three selected potentials; (iii) indicates the sum of the spectra of the pure layers. Layer thicknesses correspond to a charge of 40 mC cm^{-2} for both layers.

peaks, one at 2.1 eV and the other at 3.0 eV, and these positions are exactly the same peak positions of respective pure films (refer Fig. 4c). These peaks at 2.1 eV and 3.0 eV can be assigned to π-π^* electronic transitions in PEDOT(DBS) and PPy(DBS) layers respectively.[10-12] Similar spectral behaviour with increasing potential (upon oxidation) was observed (not shown). Accordingly, ions in the cycling electrolyte are able to diffuse through the outer layer (PEDOT or PPy) to the inner layer during the redox process. Furthermore, these results indicate that the neutral bilayer has an effective lower band gap than that of the pure PPy layer. However, this is true only for thin bilayer films, as for thicker layers one polymer may dominate, depending on the thickness. The spectra allow us to conclude that both polymers take part in the redox processes. The bilayers are related, but not identical to, the interpenetrating networks formed from the vapour phase.[13]

After a number of cycles, the main features of the spectra remain same but the absorption intensity corresponding to PPy(DBS) layer in both configurations decreases considerably while that of the PEDOT(DBS) layer remains unchanged. This indicates that the PEDOT(DBS) layer is more stable than the PPy(DBS) layer.

3.3 *Electrochemical characterization*

For the study of charge compensation process accompanied with uptake/release of ions in/out of the bilayer films, an EQCM technique in combination with cyclic voltammetry was used. The freshly synthesized films on EQCM electrode were immersed in monomer free 1 M NaCl aqueous solutions and their frequency changes due to insertion or expulsion of electrolyte ions and current responses were simultaneously recorded in the potential range from 0.5 to -1.0 V. It is worth to note that cyclic voltammograms (CVs) of PEDOT(DBS) and PPy(DBS) are different in shape and size as shown in fig. 5(a) and (b) (scales are different). The CV of the pure PPy(DBS) film exhibits strong and well defined reduction and oxidation peaks. On the other hand, the PEDOT(DBS) has a capacitive-like current and two pairs of barely distinguishable redox peaks.

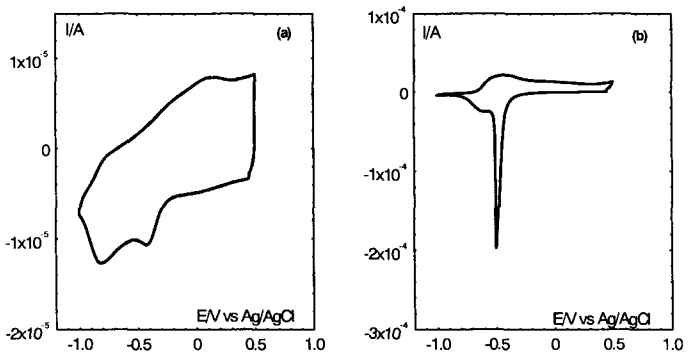

Figure 5. Cyclic voltammograms of (a) PEDOT(DBS) and (b) PPy(DBS) films in 1 M NaCl aqueous electrolyte, scan rate 10 mV s^{-1}. Note the different current scales.

Typical CV and EQCM results obtained for the PEDOT/PPy bilayer (outer layer is PPy) are shown in fig. 6. For comparison, the results obtained for pure PEDOT(DBS) and PPy(DBS) films are plotted in the same figure. The CV of the PEDOT/PPy bilayer films displays the same features as pure PPy(DBS). This indicates that the PPy layer plays the dominant role in the redox process of the PEDOT/PPy bilayer. However, PEDOT also influences the CV, especially at lower potentials (< 0.7 V). This is more clearly observed with bilayers having a thinner layer of PPy. This shows that both PEDOT and PPy take part in the redox process. This assumption was confirmed by adding CVs of pure PEDOT and PPy films, which is almost same as that of the bilayer film. Y. Syritski *et al* suggest this phenomenon as formation of three dimensional structures where the redox process occurred both at the surface and in the bulk of the structure involving the participation of the inner layer.[14] As PEDOT and PPy were doped with the large

anion DBS^-, the charge compensation during the redox cycling occurs mainly through cation motion. This is because the larger dopant anion is more strongly bound to the polymer and it has low tendency to be replaced by smaller mobile Cl^- ions present in the electrolyte. On the other hand, the frequency curve of the bilayer

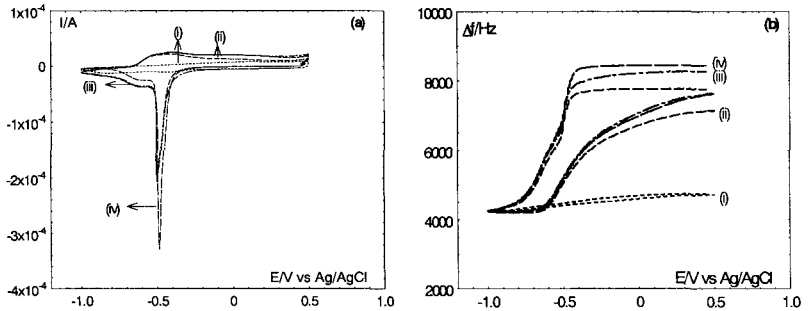

Figure 6. (a) Cyclic voltammograms and (b) mass change plots of (i) a PEDOT(DBS) film, (ii) a PPy(DBS) film and (iv) a PEDOT/PPy bilayer (outer layer is PPy) in 1 M NaCl aqueous solution. Scan rate 10 mV s^{-1}. Sum of the (i) and (ii) are indicated by (iii).

has a steep decline centered at the potential where the reduction peak occurred for the pure PPy(DBS) film, showing an increasing electrode mass in these ranges. This represents the insertion of cations (Na^+) with some amount of water molecules into the polymer. Upon oxidation, the electrode mass decreases over a broad potential range, ascribed to the expulsion of Na^+ ions accompanied with water from the film. In the pure PEDOT(DBS) film, the electro de mass change is small compared to that of the PPy(DBS) during both the cathodic and anodic parts of the cycle, corresponding to the smaller peak current observed in fig. 5. A possible explanation

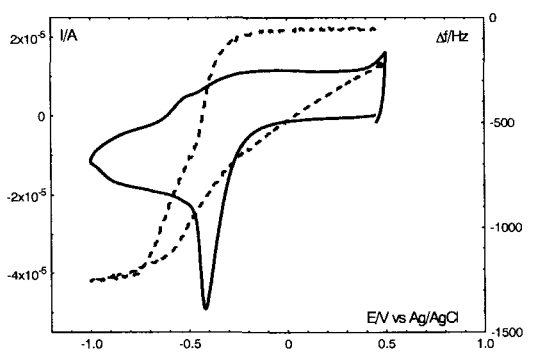

Figure 7. Cyclic voltammogram and mass change response of a PEDOT/PPy bilayer with a thinner PPy layer (16 mC cm^{-2}) in 1 M NaCl aqueous solution. Scan rate 10 mV s^{-1}.

is that PEDOT(DBS) may have less tendency to accommodate both ions and solvent. However the sum of the frequency changes of the pure films is almost equal to the frequency change observed for the bilayer film during reductive/oxidative cycling. This may indicate some participation of the PEDOT inner layer in the redox process of the bilayer film.

Fig. 7, obtained for a bilayer PEDOT/PPy with a smaller relative amount of PPy (thinner layer), shows a clear effect of PEDOT on the CV and frequency curve. This reconfirms our assumption that ion transport does take place in both polymers in the bilayer films. With increasing amount of PPy, the influence of PEDOT is seen to be masked by the domination of the influence of PPy for the electrochemical response of the system PEDOT/PPy.

4. Conclusion

Two important conclusions of relevance for actuator performance were reached:
It is possible to make a bilayer film that does not delaminate – the two polymers are compatible. (Delamination is a major problem when using metal coating). Both polymers are redox active and ions are able to move through the PEDOT layer and penetrate into PPy. The results show the feasibility of using bilayers (or multilayers) of different conducting polymers in actuators.

Acknowledgements

Financial assistance from the International Programme in the Physical Sciences, Uppsala University, Sweden, is gratefully acknowledged.

References

1. M.A. Vorotyntsev, E. Vieil and J. Heinze, *Electrochim. Acta.* **41**, 1913 (1996).
2. K. Naoi, M. Lien and W.H. Smyrl, *J. Electroanal. Chem.* 272, 273 (1989).
3. K. Naoi, M. Lien and W.H. Smyrl, *J. Electroanal. Soc.* **138**, 440 (1991).
4. T. Shimidzu, A. Otan and K. Honda, *J. Electronal. Chem.* **251**, 323 (1988).
5. C. Zhong, K. Dobhofer and G. Weinberg, *Faraday Discuss. Chem. Soc.* **88**, 307 (1989).
6. G. Inzelt, V. Kerteze and A-S. Nyback, *J. Solid State Electrochem.* **3**, 251 (1999).
7. R.H. Baughman, *Synth. Met.* **78**, 339 (1987).
8. L. Bay, K. West, N. Viachopoulos and S. Skaarup, *Proceedings of SPIE, The International Society for Optical Engineering* **54-58**, 4329 (2001).
9. L. Bay, K. West, P.S. Larson, S. Skaarup and M. Benslimane, *Adv. Mater.* **15**, 310 (2003).
10. Chun Li and Toyoko Imae, *Macromol,* **37**, 2411 (2004).
11. C. Karnstrom, H. Neugebauer, S. Blomquist, H.J. Ahonen, J. Kankare and A. Ivaska, *Electrochim. Acta.* **44**, 2739 (1999).
12. S. Skaarup, K. West, B. Zachau-Christiansen and T. Jacobsen, *Synth. Met.* **51**, 267 (1992).
13. B. Winther-Jensen and K. West, *Synth. Met.* **148**, 105 (2005).
14. V. Syritski, K. Idla and A. Opik, *Synth. Met.* **144**, 235 (2004).

FILM FORMATION MECHANISM AND ELECTROCHEMICAL CHARACTERIZATION OF V_2O_5 XEROGEL INTERCALATED BY POLYANILINE

Q. Y. ZHU, A. P. JIN, W. CHEN†, CH. V. S. REDDY, H. X. LIU, X. J. ZHAO

Institute of Materials Science and Engineering, Wuhan University of Technology, Wuhan 430070, P. R. China

The nanocomposite films are prepared from a V_2O_5 sol and aniline by sol-gel method, followed by anode electrophoresis deposition (EDP), and characterized by IR and NMR, cyclic voltammetry and ac-impedance spectroscopy, etc. IR spectroscopy and NMR results demonstrate the presence of PANI in its emeraldine salt form, as the xerogel is formed by negatively charged ribbons, V_2O_5 act as a counterion to compensate the positive charge present on the nitrogen atoms. Electrochemical impedance data at -0.7 V show that the Li^+ diffusion coefficient in the $(PANI)_{0.51}\cdot V_2O_5\cdot 1.30H_2O$ film is 2.92×10^{-11} $cm^2\cdot s^{-1}$, in contrast to the value of 5.10×10^{-12} $cm^2\cdot s^{-1}$ obtained for V_2O_5 and the electronic conductivity of the nanocomposite increases compared to V_2O_5.

1. Introduction

The synergic effect which results from the combined properties of organic-inorganic components in a unique material can produce interesting new properties, especially in electrochemistry, electrochromism and conductivity. V_2O_5 as the host material is known to be an attractive material as Li secondary battery cathodes and electrochromic devices [1-2]. A particularly attractive feature of V_2O_5 is that it can be prepared easily by a V_2O_5 power melt quenched. However, there are some disadvantages including a low electronic conductivity, a relatively low Li^+ diffusion coefficient within the host matrix. An approach to solving the problem of low conductivity is to prepare composites comprising V_2O_5 and electronically conducting polymers. Several groups have examined ways of producing composites of V_2O_5 with such polymer, including polypyrrole (PPY), polyaniline (PANI), poly (N-propane sulfonic acid aniline) (PASPAN) and poly(2,5-dimercapto-1,3,4-thiadiazole)(PDMcT) + polyaniline [3-7]. The aim of this paper is to synthesize and characterize nanocomposite films produced from combination V_2O_5 and PANI. The synthetic route involves in situ oxidative

† Corresponding author. Tel.: +86 27 87651107; fax: +86 27 87864580.
E-mail address: chenw@mail.whut.edu.cn (W. CHEN).

polymerization of aniline monomer in solutions of V_2O_5 sol, prior to gelation [8]. Moreover, the film preparation is difficult. An electrophoresis deposition method is used in order to achieve better film uniformity and homogeneity.

2. Experimental

2.1. *Sample preparation*

V_2O_5 sol was synthesized by the way of V_2O_5 melt quenched. Briefly, The V_2O_5 powders (99.5 %) were heated to 800 ℃ and kept this temperature for 10 min, then were quickly poured into distilled water. A brownish V_2O_5 sol was formed. The molar concentration was 0.1 M. The V_2O_5 film was prepared on ITO substrate with cathode electrophoresis deposition through V_2O_5 sol. The nanocomposites of PANI/V_2O_5 were obtained by mixing 0.2 M aqueous solution of aniline with V_2O_5 sol in the molar ratio of 0.6:1, the reaction mixture was kept under constant stirring at room temperature for 24 h in air, resulting in a dark green suspension. It was then cast on ITO substrate with anode electrophoresis deposition. During electrophoresis deposition process, a dc voltage of 20 V was applied between the two electrodes (thin graphite slice and ITO substrate) for 10 min. At last, the films were heated for 2 h at 80 ℃ in vacuum. The nanocomposite material has the following formula, evaluated by thermogravimetric analysis [8]: $(PANI)_{0.51}\cdot V_2O_5\cdot 1.30H_2O$.

2.2. *Characterization*

X-ray diffraction (XRD) experiments were performed on a D/MAX-III X-ray diffractrometer with Cu$K\alpha$ radiation and graphite monochrometer, 40 kV, 30 mA, scanning rate 0.1 °/s. Fourier transform infrared (FTIR) absorption spectra were recorded on a Nicolet SXB-60 IR spectrometer as KBr pellets, the measuring wavenumber range is 400~4000 cm^{-1}.Thermogravimetric analysis (TG) were performed on a NETZSCH STA449C thermal analysis system in a flowing atmosphere of air using a heating rate of 10 ℃/min. All NMR experiments were performed using a Varian infinity plus-300 spectrometer, pulse delay 5 s, pw90=4 um, ct=3 ms, 4 mm probe-head, magic angle spinning-speed 5 kHz.

The electrochemical experiments were carried out with an Autolab model PGSTAT30 (GPES/FRA) potentiostat/galvanostat interfaced to a computer. The conventional three-electrode arrangement was used. The counter electrode was a platinum sheet with an area of 1 cm^2. The quasireference electrode was saturated calomel electrode. An electrolytic solution of 1M $LiClO_4$ (Aldrich) in propylene carbonate (PC) (Aldrich) was used in all experiments. The working electrode

was the thin film on ITO substrate prepared by EDP. Electrochemical impedance spectroscopy (EIS) experiments were carried out in the frequency range 1 mHz to 10 KHz by using FRA electrochemical system. The excitation signal on the system at the equilibrium potential was 10 mV peak to peak.

3. Results and discussion

In Figure 1, X-ray diffraction patterns are shown for V_2O_5 and $(PANI)_{0.51}{\cdot}V_2O_5{\cdot}1.30H_2O$ in film form. The result indicates that the lamellar structure of the V_2O_5 xerogel is preserved (001 basal reflection indices are largest), but the inter-planar space increased from 1.129 nm to 1.355 nm in agreement with many previous reports for intercalation of organic polymers into V_2O_5 [6, 8], suggesting that some of the PANI fraction intercalated into V_2O_5 to produce an inorganic-organic nanocomposite with expanded inter-planar spacing.

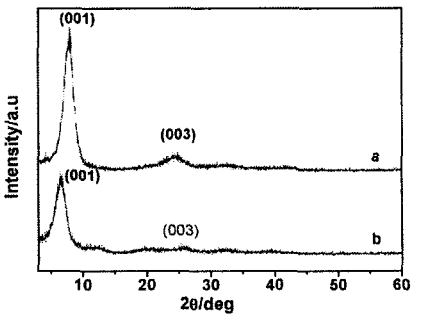

Figure 1. X-ray diffraction patterns of the (a)V_2O_5 xerogel film and (b) $(PANI)_{0.51}{\cdot}V_2O_5{\cdot}1.30H_2O$ nanocomposite film.

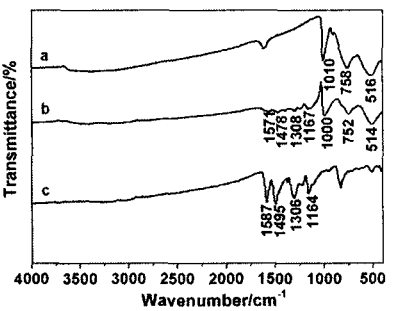

Figure 2. FT-IR spectra of (a) V_2O_5 xerogel, (b) $(PANI)_{0.51}{\cdot}V_2O_5{\cdot}1.30H_2O$ Nanocomposite and (c) bulk polyaniline (emeraldine salt).

Figure 2 shows the FTIR spectra of bulk polyaniline (emeraldine salt) synthesized using previously reported methods [9], V_2O_5 film and the $(PANI)_{0.51}{\cdot}V_2O_5{\cdot}1.30H_2O$ nanocomposite film. The V_2O_5 xerogel exhibits three main vibration modes in the 400-1100 cm^{-1} due to the V=O vibration at 1010 cm^{-1}, the V-O-V symmetric stretch at 516 cm^{-1} and the V-O-V asymmetric stretch at 758 cm^{-1}. The absorption at 914 cm^{-1} is associated to the presence of H_2O-V bonds [10]. The FTIR spectrum of the $(PANI)_{0.51}{\cdot}V_2O_5{\cdot}1.30H_2O$ nanocomposite film (curve b) shows that the characteristic intense peaks corresponding to the skeletal ring breathing modes, quinoid and benzoid C=C stretching at 1571 cm^{-1} and 1478 cm^{-1}, and C-N vibration band at 1308 cm^{-1} (1587 cm^{-1}, 1495 cm^{-1} and 1306 cm^{-1} for bulk polyaniline, respectively), confirm the presence of PANI in its emeraldine salt form, which can be described as a

repeat unit consisting of three benzenoid rings and a quinine diimine, as the xerogel is formed by negatively charged ribbons, V_2O_5 act as a counterion to compensate the positive charge present on the nitrogen atom [10]. These are the reasons that films can be cast with anode electrophoresis deposition. When intercalating PANI into the V_2O_5 xerogel, the position of the V-O-V vibration bands are 514 cm^{-1} and 752 cm^{-1}, which are similar to those found for the V_2O_5 xerogel. The V=O vibration shifts from 1010 to 1000 cm^{-1} , which can be explained by a banding interaction between PANI and the V_2O_5 framework, most likely via NH—O=V bonds [4]. Other important point associated to the intimate contact between PANI and the V_2O_5 xerogel is the disappearance of the band at 914 cm^{-1}. This fact can be attributed to the expulsion of water molecules coordinated to the vanadium ions by the inserted PANI, which is consistent with the results of XRD analyses.

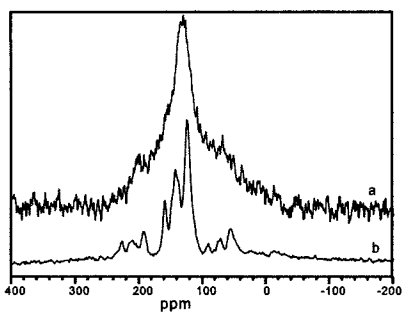

Figure 3. ^{13}C MAS NMR spectra for (a) nanocomposite $(PANI)_{0.51}{\cdot}V_2O_5{\cdot}1.30H_2O$ and (b) bulk polyaniline (emeraldine salt).

Figure 3 shows the ^{13}C MAS-NMR spectra of bulk polyaniline (emeraldine salt) and $(PANI)_{0.51}{\cdot}V_2O_5{\cdot}1.30H_2O$ nanocomposite at a spinning frequency of 5kHz. As can be seen, the NMR spectrum for bulk polyaniline shows three narrower peaks at 120 ppm, 140 ppm and 160 ppm, corresponding to different sp^2 carbon sites, which is expected to lie in the range 110-170 ppm (all shifts are referring to TMS) [11]. For nanocomposite, there is only a different broader peak at 130 ppm with increasing the relative peak intensity and line width and the other peaks are probably hindered in their free rotation due to a dynamic effect. The large difference in the chemical shift between bulk polyaniline and $(PANI)_{0.51}{\cdot}V_2O_5{\cdot}1.30H_2O$ nanocomposite could indicate a different type of chemical condition around polyaniline. These results show that aniline is polymerized between the layers of V_2O_5, which is consistent with the FTIR ones that there is a banding interaction between PANI and the V_2O_5 framework.

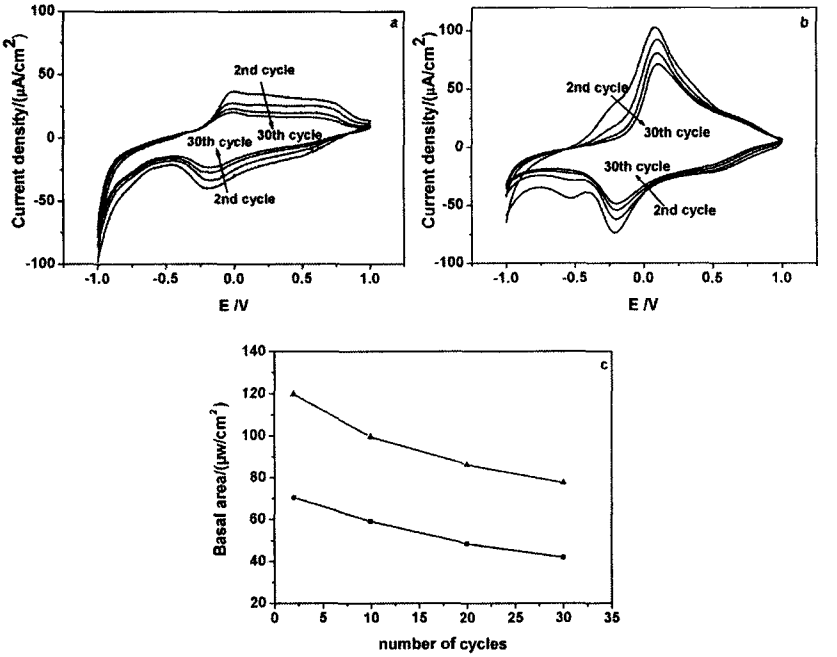

Figure 4. Cyclic voltammograms of (a) V_2O_5 and (b) $(PANI)_{0.51}{\cdot}V_2O_5{\cdot}1.30H_2O$ film for cycles 2 through 30,v=50mVs^{-1},and (c)variation of the basal area as a function of the cycle number for V_2O_5 (●) and $(PANI)_{0.51}{\cdot}V_2O_5{\cdot}1.30H_2O$ (▲).

The electrochemical stability and reversibility of the films was tested by redox cycling. The area A_i (i is the number of cycles) that is surrounded by each cycle curve represents the amount of the insertion of Li^+ ions. The cycle efficiency is calculated by the following equation,

$$Q_i = A_i / A_1 \tag{1}$$

where Q_i is cycle efficiency, A_1 is the area of the first cycle curve and A_i is the area of the *ith* cycle curve. Figure 4a and 4b show cyclic voltammmograms of the V_2O_5 and $(PANI)_{0.51}{\cdot}V_2O_5{\cdot}1.30H_2O$ xerogel films respectively, in which the second, tenth, twentieth and thirtieth cycle curves are plotted. The peak potentials shift considerably with cycling, and the amount of the insertion of Li^+ ions decreases. Figure 4c shows plots of the basal area *vs.* number of cycles for V_2O_5 and the nanocomposite. The voltammetry for the two materials is almost similar, with both showing peaks near -0.2 V that are characteristic of the V (V/IV) redox couple, but the oxidation peak is different. The composite also

shows a broader cyclic voltammetric envelope and somewhat higher charging currents at potentials positive of this peak, characteristic of the redox response expected for PANI. These results demonstrate a very substantial improvement in the amount of the insertion of Li^+ ions for the nanocomposite compared to the parent oxide. This is evidenced by the fact that the basal area at the second cycle, A_2 and A_{30} for the nanocomposite are 119.727 μW/cm^2 and 77.452 μW/cm^2, respectively. This is in contrast to the V_2O_5 film, which is only 73.402 μW/cm^2 at the second cycle.

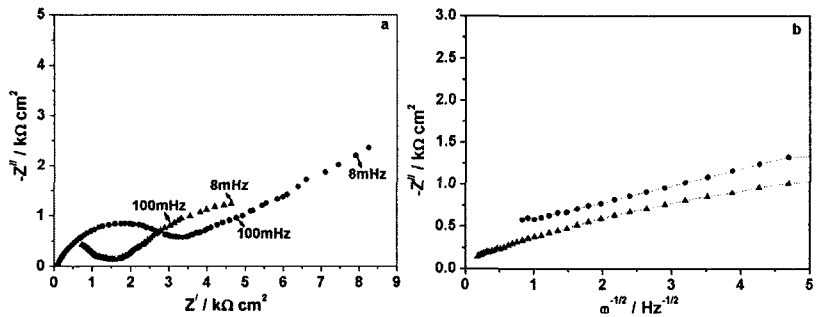

Figure 5. (a)Nyquist diagrams and (b) impedance modulus as a function of the square root of angular frequency for (•) V_2O_5 and (▲) $(PAN)_{0.51}\cdot V_2O_5\cdot 1.30H_2O$. E=-0.7V. Electrolytic solution: 1 M $LiClO_4$/PC. Sample mass: 100μg.

Electrochemical injection of Li^+ into the $(PANI)_{0.51}\cdot V_2O_5\cdot 1.30H_2O$ film use the standard three electrodes method, the reaction may be written [4],

$$xLi^+ + xe^- + [PAN^+]_y[V_2O_5]^{y-} \rightarrow Li_x[PAN^+]_y[V_2O_5]^{(x+y)-} \rightarrow Li_{(x+y)}[PAN]_y[V_2O_5]^{(x+y)-} \quad (2)$$

The electronic conductivity and mobility of Li^+ ions injected into host matrixes can be analyzed with impedance spectroscopy. Figure 5 shows the Nyquist diagrams for V_2O_5 and $(PANI)_{0.51}\cdot V_2O_5\cdot 1.30H_2O$. The data were obtained at an applied potential of -0.7 V, under conditions where the films are nearly completely reduced. These Nyquist plots (Figure 5a) exhibit a semicircle at high frequency from which the film bulk resistance (R_b) can be obtained, and a semi-infinite behavior at low frequency. Figure 5b shows impedance modulus as a function of the square root of angular frequency. Analysis of these data using standard methods [11], we can approximately calculate Li^+ diffusion coefficient in film. The chemical diffusion coefficient D can be obtained by the formula below [12]:

$$A = \left| \frac{V_M (dE/dx)}{\sqrt{2} Z F D^{1/2} a} \right| \tag{3}$$

where A is Warburg impedance which can be obtained from the slope of the plots $-Z''$ *vs.* $\omega^{-1/2}$, and ω is the angular frequency. a is the electrode area (0.65 cm^2 and 0.35 cm^2 for V_2O_5 and $(PANI)_{0.51} \cdot V_2O_5 \cdot 1.30H_2O$ at the same weight, respectively), V_M is the effective molar volume of Li^+ in the material (=54 $cm^3 \cdot mol^{-1}$) [13], Z is the charge of Li^+ (Z=1), F is Faraday constant, dE/dx is the slope of potential as a function of the stoichiometric number of lithium ions within the host matrix. Test temperature is 300 K. According to the coulometer titration curve [13], dE/dx=0.75 ($0.8/0.9 < x < 1$). At a result, the Li^+ diffusion coefficients at -0.7 V are 5.10×10^{-12} and 2.92×10^{-11} $cm \cdot s^{-1}$ for V_2O_5 and $(PANI)_{0.51} \cdot V_2O_5 \cdot 1.30H_2O$ films, respectively, which indicated that the intercalation of PANI enhance the mobility of Li^+ in V_2O_5. From the Nyquist diagrams, we can obviously see that the semicircle diameter (the film resistance) at high frequency of the $(PANI)_{0.51} \cdot V_2O_5 \cdot 1.30H_2O$ film is reduced compare to V_2O_5 film. Namely, the intercalation of PANI increases the electronic conductivity of V_2O_5 xerogel.

4. Conclusions

The nanocomposite films are prepared by PANI intercalation in V_2O_5 xerogel in sol-gel and EDP method. The inter-planar spacing of V_2O_5 xerogel increases when PANI is intercalated in V_2O_5 xerogel interlayer. The FTIR spectra and NMR show a banding interaction between PANI and V_2O_5, most likely via NH—O=V bonds, which effectively shields the electrostatic interaction between V_2O_5 interlayer and Li^+ ions. $(PANI)_{0.51} \cdot V_2O_5 \cdot 1.30H_2O$ nanocomposite films have much higher charge capacity and better electrochemical stability relative to V_2O_5 films. The Li^+ diffusion coefficients are greater for the $(PANI)_{0.51} \cdot V_2O_5 \cdot 1.30H_2O$ nanocomposite film than the V_2O_5 xerogel by one order of magnitude and simultaneously the electronic conductivity is greatly enhanced by PANI intercalated in V_2O_5 xerogel.

Acknowledgments

This work was financially supported by the National Natural Science Foundation of China (50172046), the Foundation for Innovative Research Team of Hubei Province (2005ABC004) and International Cooperation Technology Project of Wuhan City, P. R. China (050418).

References

1. A. L. Tipton, S. Passerini, B. B. Owens, and W. H. Smyrl, *J. Electrochem. Soc.* **143**, 3473 (1996).
2. S. Papaefthimiou, G. Leftheriotis, P. Yianoulis, *Thin Solid Films* **343-344**, 183 (1999).
3. J. Harreld, H. P. Wong, B. C. Dave, B. Dunn, and L. F. Nazar, *J. Non-Cryst. Solids.* **225**, 319(1998).
4. F. Leroux, G. Goward, W. P. Power, and L. F. Nazar, *J. Electrochem. Soc.* **144**, 3886(1997).
5. H. Fritz, M. T. Roberto, and A. B. Daniel, *J. Electrochem. Soc.* **149**, A546 (2002).
6. H. Fritz, T. P. G. Maria, M.T. Roberto, et al, *J. Electrochem. Soc.* **147**, 2437(2000).
7. S. Eiichi, A. B. Daniel, *Langmuir* **15**, 669 (1999).
8. K. Seong-Gu, M. K. Kwang, P. Nam-Gyu, S. R. Kwang, C. Soon-Ho, *Journal of Power Source* **133**, 263 (2004).
9. L. H. C. Mattoso, A. G. MacDiarmind, A. J. Epstein. *Sythetic Metals* **68**, 1 (1994).
10. H. Fritz, A. T. Edson, M. T. Roberto, *Electrochimica Acta* **47**, 3179 (2002).
11. A. Raghunathan, G. Rangarajan, D. C. Trivedi, *Sythetic Metals* **81**, 39 (1996).
12. C. Ho, I. D. Raistrick, R. A. Huggins, *J. Electrochem. Soc.***127**, 343 (1980).
13. J. Farcy, R. Messina, J. Perichon, *J. Electrochem. Soc.* **137**, 1337 (1990).

EFFECT OF NH_4NO_3 CONCENTRATION ON THE CONDUCTIVITY OF PVA BASED SOLID POLYMER ELECTROLYTE

M.HEMA, S. SELVASEKERAPANDIAN,G.HIRANKUMAR,J.MALATHI, G.M.BRAHMANANDHAN

Solid State and Radiation Physics Laboratory, Department of Physics, Bharathiar University, Coimbatore – 641 046. INDIA.

E-Mail: sekarapandian@yahoo.com

ABSTRACT

Due to lack of good proton conductive polymer electrolyte working at ambient temperatures, search for the new systems have been hotly pursued in the past few years. Hence an attempt has been made to synthesis PVA based polymer electrolyte with various compositions of ammonium nitrate using solution casting technique. The formation of the complex has been confirmed by FT-IR spectral studies and XRD analysis. In the impedance response curve, the absence of the high frequency semicircular portion leads to the conclusion that the current carriers are ions & therefore the total conductivity is mainly the result of ion conduction. The high ionic conductivity at ambient temperature is found to be $7.5X10^{-3}$ Scm^{-1} for 20mol% ammonium nitrate doped PVA. Dielectric behaviour is analyzed using dielectric constant(ε') and dielectric loss (ε") of the samples .The low frequency dispersion of the dielectric constant implies the space charge effects arising from the electrodes. The dielectric loss spectra show the very large ($\sim 10^6$) dielectric loss at lower frequencies due to free charge motion within the material.

Key words: proton conduction, XRD, FTIR, ac conductivity.

1. INTRODUCTION

Solid polymer electrolytes are attractive topics for both electrochemical and materials scientists due to its unique mechanical and electrical properties ,ease of fabrication into film of desirable sizes & interactions to strengthen electrode/electrolyte contact [1],which bears many important application in high energy storage & generation devices. Within the realm of solid polymer electrolytes, proton conducting polymer electrolytes have become materials of growing interest .This is because of their wide ranging applications in electrochemical devices, fuel cells and other devices. Various polymer electrolytes in this category are complexes of strong inorganic acids or ammonium salts with commercially available electro-donor Poly vinyl alcohol (PVA), Polyethylene oxide(PEO);Polyethylene imide (PEI), Polyacrylic acid(PAA) & Polyvinyl pyrrolidone(PVP). The protonic transport in these polymer electrolytes generally involves motion of groups like H^+, NH_4^+,H_3^+,OH^- .It has also been found that proton

polymeric electrolytes many a times exhibit conductivities higher than alkali metal analogues .Proton conducting polymer complexes with inorganic acids have been shown to suffer from chemical degradation and mechanical integrity making them unsuitable for practical applications .Considering this fact and due to lack of good proton conductive polymer electrolyte working at ambient temperatures, search for the new systems have been hotly perused in the past few years. The present work aims at developing a new type of proton conducting polymer electrolyte with PVA as the host. Polyvinyl alcohol (PVA) which is considered as a good insulating material with low conductivity & charge storage capability can be markedly influenced by doping the suitable impurities. Also , very few reports are available on ammonium salts as dopant, hence an attempt has been made to synthesis PVA based polymer electrolyte with ammonium nitrate as salt .The prepared polymer electrolytes have been characterized by using XRD, FTIR, and electrical conductivity studies .

2. EXPERIMENTAL

The polymer PVA (S.d.Fine); Mol. wt.= 1,25,000 and the salt Ammonium nitrate (LOBA Chemie) were used as the raw material in this study. Dimethyl Sulphoxide (DMSO) was used as the solvent. Separate solutions of PVA & NH_4NO_3 in DMSO were prepared &subsequently mixed in incremental proportions resulting in a series of transparent solutions ranging in PVA:NH_4NO_3 ratios of 97:3 to 70:30 by mol% .The solution was then casted in glass Petri dishes and the samples were subjected to an extended drying period in a vacuum chamber prior to analysis until complete solvent removal takesplace.Thick films of thickness in micrometer range was obtained.

The FTIR spectrum exhibited by the polymer electrolyte was recorded using SHIMADZU 8000 SPECTROPHOTOMETER in the frequency range 400 cm^{-1} to 4000 cm^{-1}. Electrical measurements were performed on a HIOKI make LCZ meter (model 3532) in the frequency ranging from 42 Hz – 1MHz at various temperature ranging from 303K to 323K using stainless steel as blocking electrode.

3. RESULTS AND DISCUSSION

3.1 FTIR spectroscopic analysis

FTIR spectra of PVA and it's complexes with NH_4NO_3 in different ratios were shown in the fig .1 .It is observed that the peak at 1706 cm^{-1} assigned to C=O stretching in the acetate group of PVA is absent in the complexes suggesting the formation of intermolecular hydrogen bonding between NH_4NO_3 & PVA.The peak at 1104 cm^{-1} assigned to C-O stretching of secondary alcohol of PVA are absent in the complexes .This may be attributed to the decreased number of C-O groups in the complexes & the specific interactions in the polymer matrices.The peaks at 1295 cm^{-1} , 856 cm^{-1} are assigned C-C stretching and CH rocking of PVA [2].These peaks are less intense in the complexes which gives a strong indication of specific interactions between NH_4NO_3 and PVA.The relative intensities of the peaks at 2198 cm^{-1}, 2385 cm^{-1} corresponding to pure PVA are found to be decreased in the complexes .This confirms that complexation has been occurred in the polymer –salt complexes.

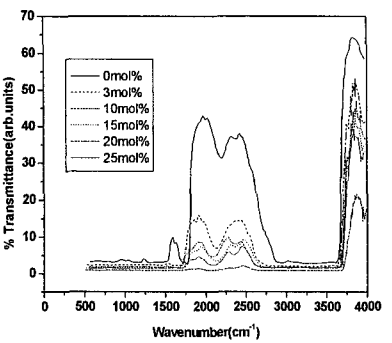

Fig. 1 FTIR spectra of PVA and its complexes with NH_4NO_3 in different ratios

3.2 X-Ray diffraction analysis

The XRD patterns of the pure PVA and it's complexes with NH_4NO_3 in different ratios are shown in fig.2. According to these observations, a broad peak appears at 19.7° [2] which is ascribed to the amorphous nature of pure PVA films. This peak has been found to be shifted in the doped system indicating the complex formation. Also, the broadness of the peak increases with increase of NH_4NO_3 concentration revealing the increase in amorphous nature of the complexed system.A less intense peak between 36° and 46° appears in the complexed system.

This may be due to NH_4NO_3 concentration. All other peaks corresponding to pure NH_4NO_3 is absent in the complex indicating a complete dissociation of salt in the polymer matrix.

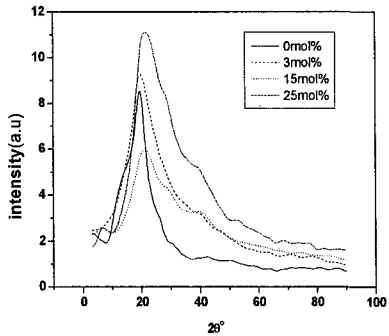

Fig.2 X-ray Diffraction pattern of PVA and it's complexes with NH_4NO_3 in different ratios

3.3 Impedance spectroscopy

The ionic conductivity of a polymer electrolyte depends on the concentration of the conducting species and on their mobility .The ionic conductivity values of the electrolytes are calculated by using the equation: $\sigma = l/R_bA$,where l, A are the thickness and known area of the electrolyte film & R_b is the bulk resistance of the electrolyte film which is obtained from the intercept of real part of complex impedance plot. The plot for the PVA (70mol%) :NH_4NO_3 (20 mol%) complex in the temperature range 303-323 K is shown in fig-3. In the impedence response curve, the absence of the high frequency semicircular portion leads to the conclusion that the current carriers are ions & therefore the total conductivity is mainly the result of ion conduction [3].

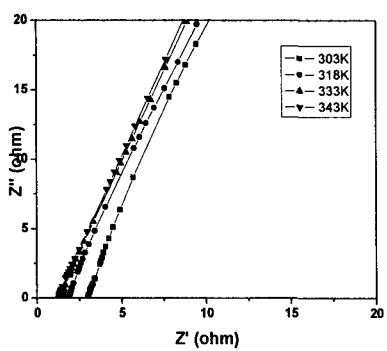

Fig.3 Nyquist plot of 20mol% NH_4NO_3 doped PVA at various temperatures

3.4 Conductance spectra

According to Almond and west the frequency dependence of ac conductivity (σ_{ac}) of polymeric electrolytes is described by the following equation

$$\sigma_{ac}(\omega) = \sigma_{dc} + A\omega^{n} \quad (1)$$

where A and n areparameters $0< n< 1$. σ_{dc} is a dc ionic conductivity and ω is an angular frequency.

The typical $\log\sigma_{ac}$ versus $\log\omega$ relation for the ammonium nitrate doped PVA system is as shown in the fig-4. The curve consists of two distinct regions with in the measured frequency range. The low frequency spike describing electrode – electrolyte interfacial phenomena which is ascribed to the space charge polarisation at the blocking elctrodes[4], followed by the frequency independent plateau region connected with the σ_{dc} of the complexed polymer electrolyte. As the temperature increases, the low frequency dispersion region becomes prominent and shifts to higher frequency region and the frequency independent plateau region decreases .Hence, the polarisation effect becomes dominant as the temperature increases.The variation of conductivity value is in accordance with those obtained from the complex impedence plot.

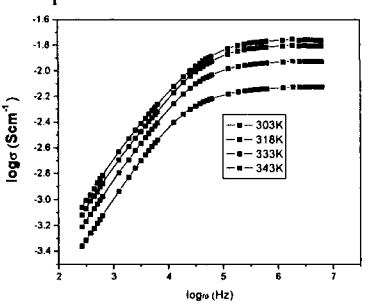

Fig.4 Conductance spectra of 20mol% NH_4NO_3 doped PVA for various isotherms

3.5 Effect of salt Concentration on the ionic conductivity

Conductivity is related to the number of charge carriers (n_i) and their mobility (μ_i) according to the following equation:

$$\sigma = \sum n_i q_i \mu_1 \quad (2)$$

where q_i is the charge on each charge carrier.

The variation of logarithm conductivity of PVA with the salt concentration is as shown in the fig-5. Three characteristic regions can be easily distinguished.

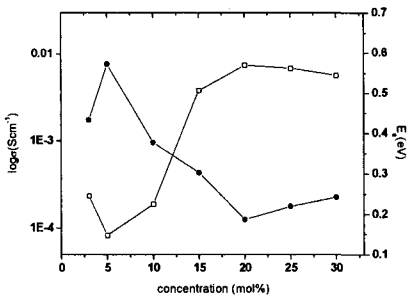

Fig.5 Variation of ionic conductivity as a function of NH_4NO_3 concentration at 303K.

The initial low concentration region in which a decrease in conductivity is observed has been ascribed to ion pair formation ,as is known to occur for solvents of low dielectric consant.The subsequent linear region showing an increase in conductivity beyond the minimum(at about 5mol%) , could be a result of triple ion formation or a redissociation effect [5] .The final high salt concentration region in which a decrease in conductivity is observed may be due to a rapid increase in viscosity [6]. The high ionic conductivity at ambient temperature is found to be $7.5X10^{-3}$ Scm^{-1} for 20mol% ammonium nitrate doped PVA.

3.6 Effect of temperature on the ionic conductivity

Fig. 6 represents the temperature dependence of proton conductivity of ammonium nitrate doped PVA. It is found that the proton conductivity of the membranes increases with increasing temperature for all the compositions. The conductivity verses temperature plots follow Arrhenius equation,

$$\sigma = \sigma_0 \exp (Ea/RT) \qquad (3)$$

where σ_0 is the pre-exponential factor; E_a is the activation energy; R is the Boltzmann constant . E_a values for different composition are shown in the table-1.It is clear from the table that the lowest activation energy (0.19 eV) is observed for 20

mol% ammonium nitrate doped PVA system which is a characteristic for the electrolyte film of the highest conductivity.

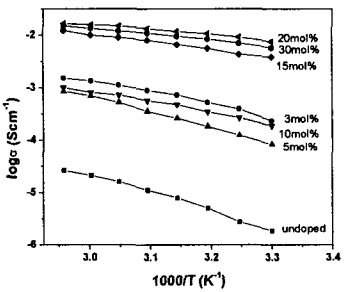

Fig.6 Arrhenius plot of PVA- NH_4NO_3 complexes for different NH_4NO_3 compositions

Table-1: Ionic conductivity values of the polymer film with different NH_4NO_3 Concentration

Conc of NH_4NO_3 (mol%)	Ionic conductivity (x 10^{-3}Scm^{-1})				Activation Energy (eV)
	303K	323K	333K	338K	
0	0.002	0.011	0.021	0.026	0.66
3	0.2	0.9	1.4	1.5	0.43
5	0.08	0.4	0.7	0.9	0.57
10	0.2	0.6	0.8	1.0	0.38
15	3.8	8.0	10.0	12.2	0.30
20	7.5	13.3	15.8	16.6	0.19
25	7.0	10.9	14.8	15.9	0.22
30	5.7	10.9	13.5	14.9	0.24

3.7 Dielectric analysis

The frequency dependence of real (ε') & imaginary (ε") part of dielectric constant is as shown in the fig -7. It has been seen that the dielectric constant decreases with increase of frequency and saturates at higher frequencies. The

reason for sharp rise in dielectric permittivity towards low frequencies is due to the electrode polarization effects. At high frequencies, the periodic reversal of the electric field occurs so fast that there is no excess ion diffusion in the direction of the field. The polarization due to the space charge accumulation decreases, leading to the decrease in the value of ε'. The variation of ε" with logω clearly indicates the existence of β -relaxation due to some local movement of side group diploes [7].

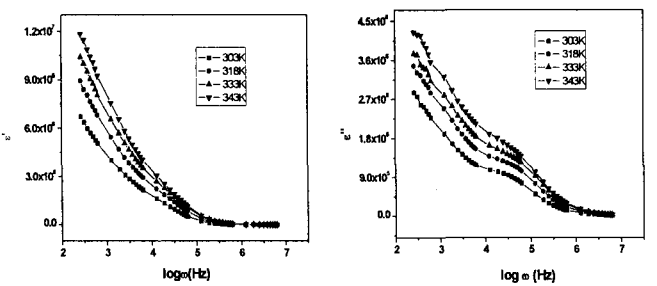

Fig.7 Variation of ε' & ε" with logω for 20mol% NH_4NO_3 doped PVA at various temperatures

4.Conclusion

PVA based polymer electrolyte with various compositions of ammonium nitrate has been prepared using solution casting technique. The structural and complexation behaviour has been studied by XRD and FTIR analysis. The ionic conductivities of the electrolytes have been measured by AC –Impedance technique at various temperatures. The influence of salt concentration in the polymer complexes is discussed. The maximum conductivity value ($7.5X10^{-3}$ Scm^{-1}) is obtained for the polymer complex with 20mol% NH_4NO_3.

Reference:

1. M.B.Armond,Annu, *Rev.Mater.Sci.***16**, 245 (1986).
2. S. Rajendran et.al , *Journal of Power sources* **124** (2003) 225-230.
3. M.M.E.Jacob, S.R.S.Prabaharan, S.Radhakrishnan, *Solid State Ionics* **104**, 267 (1997).
4. J.R. Macdonald, *Impedance Spectroscopy Emphasizing Solid materials and system*, John Wiley & Sons, New York (1987).

5. S.F. Johnson et.al., *Solid state Ionics* **90** 39-48 (1996).
6. I. Aibinssion, B.E. Mellander and J.R. Stevens, *J.Chem.Phys* **.96,** 681 (1992).
7. K.P.Singh, P.N.Gupta, *Eur.Polym.J.***Vol.34, No.7**, 1023-1029, 1998.

DIELECTRIC AND CONDUCTIVITY STUDIES OF PVA-KSCN BASED SOLID POLYMER ELECTROLYTES

J.MALATHI, G.M.BRAHMANANDHAN, M.HEMA, G.HIRANKUMAR, D.KHANNA, D.ARUN KUMAR S.SELVASEKARAPANDIAN*

Solid State and Radiation Physics Lab, Department of Physics, Bharathiar University, Coimbatore-641 046, INDIA

E-mail: sekarapandian@yahoo.com

Abstract:

A systematic investigation has been carried out in PVA complexed with potassium thiocyanate prepared by solution cast technique. This PVA-KSCN polymer electrolyte has been characterized by FTIR and ac impedance spectroscopy techniques. The temperature dependant conductivity of the polymer electrolyte follows the Arrhenius relationship. The maximum conductivity has been found to be 1.63×10^{-3} Scm^{-1} for 15 mol% KSCN doped electrolyte at 303K. It has been observed in the loss tangent spectra as the frequency increases, relaxation peak shift towards higher temperature region showing that the relaxation frequency increases with temperature. The appearance of two sets of relaxation peaks indicates that the system shows two different types of relaxation process having different relaxation times.

1. Introduction:

Polymer salt complexes with significant ionic conductivity have been extensively investigated over the past few decades due to their potential applications as electrolyte material in high energy density solid state batteries [1]. These materials consist of alkali metal salt complexes of solid polar polymer, such as poly (ethylene oxide) (PEO) [2], poly (ethylene glycol) (PEG)[3] , Poly (propylene oxide) (PPO) [4] etc. Among these polymer electrolytes based on PVA has attracted many researchers due to their good electrical and mechanical properties. Most of the commercial poly (vinyl alcohol) samples have been prepared by hydrolyzing the poly (vinyl acetate). Due to the presence of hydroxyl group, the hydrogen bond between the interchains of the PVA has been developed. This causes the high melting point and good mechanical stability of PVA. Arof and co - workers developed nickel – zinc cell using PVA - KOH solid polymer electrolyte. But the literature survey reveals that the PVA complexes with alkali salts are rare.

The study of dielectric relaxation in solid polymer electrolytes is a powerful approach for obtaining information about the characteristic ionic and molecular

interactions. The dielectric parameters associated with relaxation processes are of particular significance in ion conducting polymers such as dielectric constant which shows the ability of a polymer material to dissolve salts. In this paper, an effort has been made to study the effects of alkali ion concentration on dielectric behavior of solid polymer complex electrolytes of PVA - KSCN in different stoichiometric ratios by measuring the dielectric parameters of the samples. The relaxation characteristics are discussed in terms of conductivity and dielectric parameters. FTIR study has been carried out to confirm the polymer-salt complex.

2. Experimental:

Poly (vinyl alcohol) (Merck, Mw=1,25,000) (degree of hydrolysis = 88%)and the inorganic salt sodium thiocyanate (KSCN) (Sisco) are used in the present study. The appropriate weight of PVA and KSCN are dissolved in water. The solution is then stirred continuously until the mixture shows a homogenous viscous liquid appearance. The resulting solution is poured into a glass Petri dish and the water is allowed to evaporate in air at room temperature. The smooth, uniform thick films (200 μm), which are transparent to visible light and having good mechanical properties, have been obtained FT-IR measurements have been made with a Shimadzu-8000 spectrophotometer instrument in the wave number range of 4000 – 400 cm^{-1}.The electrical conductivity study of the polymer electrolytes has been carried out in the temperature range of 303K to 333K over a frequency range of 42 Hz – 1 MHz using computer controlled HIOKI 3532 LCR meter with a cell having stainless steel electrodes.

3. Results and discussion:

3.1 Fourier Transform Infrared analysis

The polymer electrolytes have been subjected to FTIR analysis to confirm the complexation between the salt and the polymer host. The FTIR spectra of pure PVA and PVA doped with 15 mol% KSCN are shown in figure: 1 and 2 respectively. The absorption peaks of pure PVA at 3376 cm^{-1} and 1336 cm^{-1} are assigned to O-H stretching, and C-OH plane bending respectively. The vibrational frequencies at

1254 cm^{-1} and 1736 cm^{-1} of pure PVA are assigned to C-O-C stretching and C=O stretching of acetate group which is the residual part of PVA. It is to be noted that PVA used in the present study is 88% hydrolyzed. The peaks at 2912 cm^{-1}, 2944 cm^{-1} and 850 cm^{-1} are assigned to C-H symmetric stretching, C-H asymmetric stretching and C-H rocking of pure PVA respectively. The characteristic predominant O-H stretching vibration band of pure PVA at 3376 cm^{-1} found to be less intense in salt doped system indicating weak interaction of the salt with the hydroxyl group of the polymer matrix. It has been observed that the peak at 1736 cm^{-1} is shifted to the higher wave number at 1746 cm^{-1}. This shift towards the higher wave number may be due to the interaction of K^+ ion with carbonyl group (C=O) of the PVA.

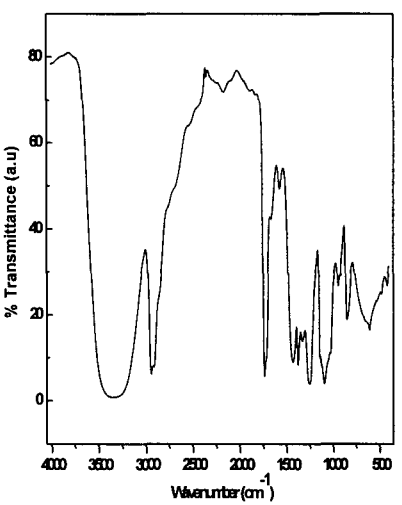

Figure 1: FTIR spectrum of pure PVA

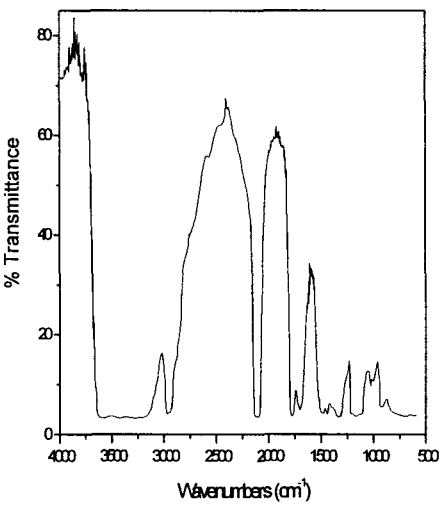

Figure 2: FTIR Spectrum of 85 mol% PVA+ 15 mol% KSCN

3.2 Impedance analysis

The typical impedance plots (Z' vs Z'') for the polymeric electrolytes are shown in figure: 3. The complex impedance diagram (93 mol% PVA: 7 mol% KSCN) (a) shows two well defined regions: a chord in the higher frequency range which is related to conduction process in the bulk of the electrolytes and the linear region in the lower frequency range that is attributed to the effect of blocking of electrodes.

The angle which the semicircle is depressed below the real axis and the amount of inclination in the straight line are related to the width of the relaxation time distribution [5]. These results suggest the presence of a constant phase element (CPE) at the electrode and electrolyte interface. The disappearance of the high frequency chord portion and appearance of the spike confirms the current carriers are ions and this leads to a result that the total conductivity is mainly due to ionic conduction. Inset (a) and (b) shows the impedance plots of 93 mol% PVA: 7 mol% KSCN and 80 mol% PVA: 20 mol% KSCN respectively. The maximum conductivity has been found to be 1.63 x 10^{-3} S cm^{-1} for 15 mol% KSCN doped electrolyte at 303 K respectively.

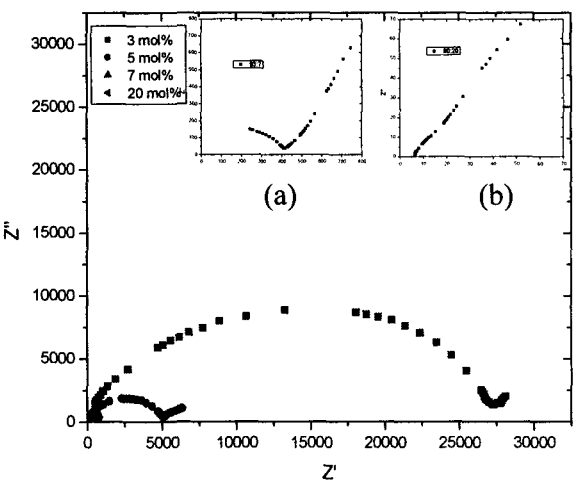

Figure: 3 Impedance plots of all the compositions of polymer electrolytes at 303K : (a) 93 mol% PVA : 7 mol% KSCN; (b) 80 mol% PVA : 20 mol% KSCN .

3.3 Conductance Spectra

The frequency dependent conductivity for various compositions at room temperature is shown in figure: 4. The spectra consists of three different regions. The low frequency spike, medium frequency plateau and a high frequency spike. The high frequency spike is attributed to the bulk relaxation phenomena, where as

the plateau region corresponds to dc conductivity. The low frequency spike describes space charge polarization.

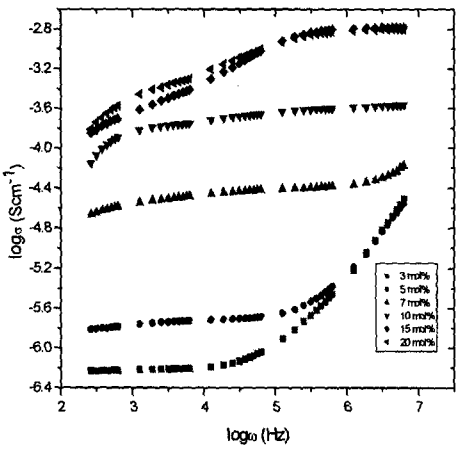

Figure: 4 Conductance spectra of PVA – KSCN at different salt concentrations at room temperature

3.4 Temperature dependence of the conductivity

The temperature dependent ionic conductivity measurements are carried out to analyse the mechanism of ionic conduction in polymer electrolytes. Figure: 5 shows the Arrhenius plots of various compositions of PVA – KSCN based polymer electrolytes in the range of 303 – 333 K. Linear relations are observed in all polymer electrolytes and this meant that there is no phase transition in polymer matrix by the salt addition in the temperature range studied. These results suggested that there is no dynamic conformational change in polymer matrix. The temperature dependence of dc conductivity, extracted from conductivity spectra has been found to obey Arrhenius relation

$$\sigma_{dc} = \sigma_0 \exp(-E_a/kT) \quad \text{---------- (1)}$$

where σ_0 is the pre-exponential factor and E_a is the activation energy. In polymer electrolytes, the change in conductivity with temperature has been explained in terms of segmental motion that results in an increase in the free volume of the

system which, in turn, would also facilitate the motion of ionic charge. The activation energy (Ea) has been found to be 0.26eV for 15 mol% KSCN doped electrolyte system.

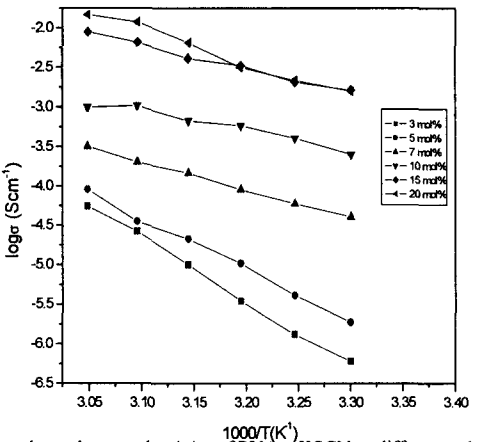

Figure: 5 Temperature dependent conductivity of PVA – KSCN at different salt concentrations in mol%

3.5 Dielectric studies

Dielectric studies have been used to study the ion dynamics in polymer materials as well as the transport mechanism for charge carriers. The dielectric response can be completely characterized by

$$\varepsilon^*(\omega) = \varepsilon'(\omega) + i\,\varepsilon''(\omega) \qquad \text{---------- (2)}$$

where the real (ε') and imaginary (ε'') components represent the storage and loss of energy during each cycle of electric field respectively. The log ω vs log ε' and log ω vs ε''plots for all compositions of PVA – KSCN electrolytes at room temperature are shown in figures 6 and 7 respectively. In figure.6 the low frequency dispersion region is attributed to the contribution of charge accumulation at the electrode – electrolyte interface. A step like feature in dielectric constant reveals the transition frequency region from ac to dc conductivity and indicates the existence of an additional relaxation.

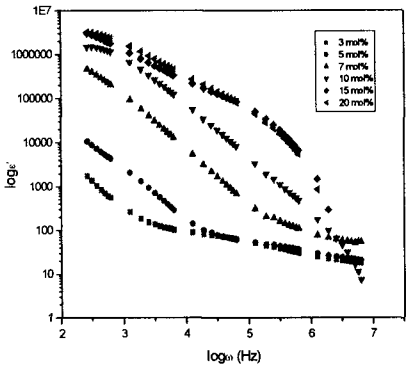

Figure: 6 Variation of log ε' with log ω PVA:KSCN complexes at room temperature

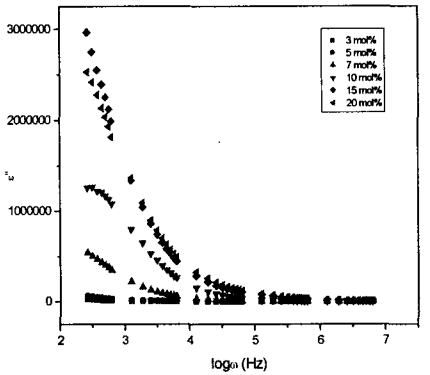

Figure: 7 Variation dielectric loss with log ω PVA:KSCN complexes at room temperature

At high frequencies, due to high periodic reversal of the field, the contribution of charge carriers (ions) towards the dielectric constant decreases with increasing frequency. The higher dielectric constant for 15 mol% KSCN doped PVA compared to other salt doped electrolytes implies smaller electrostatic attraction between the mobile ions and greater probability of their existence in the free states and hence, higher the conductivity [6].

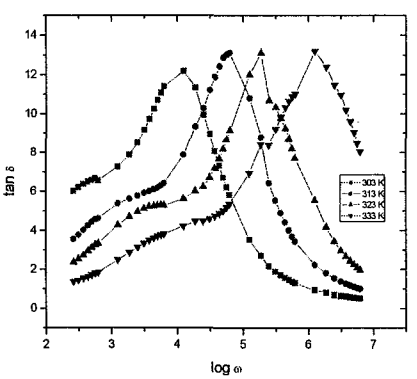

Figure:8 variation of tan δ with log ω at different temperatures

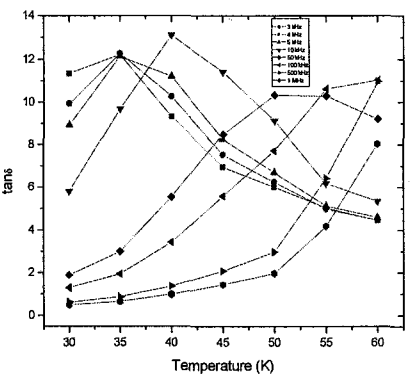

Figure:9 Loss tangent as a function of temperature at different frequencies

The variation of loss tangent (tanδ) for the polymer electrolyte system 95 mol% PVA – 5 mol% KSCN with respect to frequency and temperature are shown in

figures 8 and 9 respectively. Tan δ has been found to increase with frequency for all temperatures, pass through a maximum value $(\tan\delta)_{max}$ and thereafter decreases.

As the temperature is increased $(\tan\delta)_{max}$ gets shifted to higher frequencies. It is clear from the figure.8 that there exist two different types of relaxation peaks. One type occurring at higher frequency (so called β-relaxation) may be caused by side group dipoles and other set at lower frequency (α-relaxation) may be caused by the movement of main chain dipole segment. The appearance of two different types of relaxation peaks indicate that PVA shows two different types of relaxation process having different relaxation time. The peak has been observed in loss tangent as the function of temperature for various frequencies. As the frequency increases the peak of the relaxation shifts towards a higher temperature region showing that the relaxation frequency increase with temperature.

4.Conclusion:

The polymer electrolyte thick films of PVA complexed with KSN with different composition have been prepared by solution cast technique. It has been observed that the system PVA doped with 15m% KSCN has the highest conductivity, $1.63x10^{-3}$ Scm^{-1}. The appearance of two different types of relaxation peaks indicate that PVA shows two different types of relaxation process having different relaxation time.

References:

1. M.B.Armand, *Solid State Ionics.* **9/10**, 745 (1983)
2. D.E.Fenton, J.M.Parker, and P.V.Wright. *Polymer* **14,** 589 (1973)
3. A.Zalewska, J.Stygar, E.Ciszewska, M.Wiktorko, and W.Wieczorek, *J. Phys. Chem. B* **105**, 5847-5851 (2001)
4. P.V.Wright, Br. *Polymer. J.*, **7**, 319 (1976)
5. J.R.Macdonald, (Ed), Impedance Spectroscopy, Wiley, New York, 1987.
6. N. G. MaCrum, B. E. Read, G. Williams, 'An elastic and Dielectric Effects in Polymeric Solids', Dover Publications, New York, 1991

This page is intentionally left blank

Part IV
Emerging Applications

This page is intentionally left blank

Invited Papers

This page is intentionally left blank

THE USE OF SOLID STATES IONIC MATERIALS AND DEVICES IN MEDICAL APPLICATIONS

R. G. LINFORD

North East Wales Institute for Higher Education,
Mold Road, Wrexham, LL11 2AW, Wales, U.K.

Electrolyte materials used in solid state polymer batteries can also be utilised in a special type of drug delivery system called an iontophoretic device. This review will describe the history, applications and limitations of iontophoretic and related systems and also the use of batteries and biofuel cells in medicine.

1. Introduction

Life is controlled by electrochemistry. Without redox reactions taking place within the body, and without control of the passage of ions in living tissues, life as we know it would cease. Electrochemistry also enables the production and storage of electrical energy from chemical reactions in power sources such as batteries and fuel cells. Solid state power sources have become increasingly important as they are inherently robust, compact and spill-proof, thus being particularly well suited to medical requirements, especially for implanted devices.

Advances in solid state ionics applications have required painstaking and careful materials development over the past forty years. Medical applications of power sources and of their component materials impose their own strict requirements and constraints on device and material selection and often involve highly miniaturised systems. In this paper, three particular areas at different stages of maturity - iontophoretic devices, biomedical power sources and biofuel cells - have been chosen to illustrate present and future applications of solid state ionic devices and their component materials in medicine. Applications up to the early part of this decade have been reviewed elsewhere.[1-8]

2. Iontophoretic and Related Devices

There are many routes, each with its own advantages and limitations, that can be chosen to convey a drug from outside the patient to the physiological site of

action within the body.[8] For example, many drugs can be taken by mouth (perhaps encapsulated in an appropriate excipient) but the oral route is unsuitable for strong tasting substances. More importantly, some drugs cannot survive in the required active form when they enter the body through the relatively destructive digestive tract, and others have adverse effects on the digestive processes. In such cases, one of a number of alternative pathways needs to be chosen[8] such as

- Insertion of a suppository or a catheter into an orifice other than the mouth
- Injection from a syringe that penetrates through the skin into a muscle or a vein
- Inhalation, either nasally or orally, of a drug carried either in wet droplets or as dry powder in a carrier gas, into the lung (which has a very large internal surface area)
- Topically, i.e. by external application of ointments containing volatile active drug which diffuses into the eye, tooth, nail or skin to relieve chafes, scratches, cuts and bites
- Transdermally, by dry powder syringe which itself does not penetrate the skin but which projects the drug material into the subcutaneous layers below
- Transdermally by "passive device" patches, e.g. nicotine worn by smokers trying to give up, which act as a local reservoir of an appropriate drug which permeates through the skin to the site of action unaided by additional fields or forces other than diffusion
- Transdermally, assisted electrically (i.e. iontophoretically) and/or in other ways

Non-invasive routes minimise the chances of cross infection especially by the AIDS virus.

Skin is one of the largest of the bodily organs, covering 2 m^2, weighing 5 kg and being 2-3 mm thick. There are two key parts – the outer layer (epidermis)

and the inner layer (dermis), between which there is a basement membrane. The most important layer within the epidermis is the stratum corneum, a 10-15 μm thick lipophilic barrier that minimizes transepidermal water loss, acts as a high-integrity barrier against egress of foreign material and has a high electrical resistance. The equivalent circuit is essentially the same as that for a polymer electrolyte as the stratum corneum has a high electrical resistance, in series with the dermis, which comprises a leaky capacitor (constant phase element) and a resistor in parallel. The stratum corneum is dry (20% moisture compared with 70% for most of the rest of the body). Penetrating through the epidermis and providing a path from the outside world to deep within the dermis are hair follicles and pores which, in human skin, take up only about 0.1% of the surface area. The pH of the stratum corneum is 4–6, being lowest just below the surface, whereas the hydrated tissue just under the basement membrane has a pH of about 7.3.

The history of iontophoresis has been described elsewhere.[7-9] The term "iontophoresis was introduced in the 19th century[10] but electric shocks from torpedo fish were used much earlier in ancient Greece to treat gout and the first example of the use of an electric current to increase penetration of ionic drugs into and through surface tissue was in 1747.[8] Iontophoretic devices are in 3 parts – a power source providing up to 4mA at constant current (corresponding to a 8 cm^2 patch delivering the maximum desirable current density of 0.5 mA/cm^2) which, in the future, could well be a polymer electrolyte battery – a drug electrode which provides the reservoir of active ingredient – and an "indifferent" (or ground or dispersive) electrode.[11,12] The reservoir can be made from materials analogous to the polymer electrolytes originally developed by Michel Armand and Peter Wright.[13-16] Sensor control of drug flux is very desirable and an impedance-based implantable microelectromechanical system (MEMS) device has recently been reported.[17] Drug penetration can be enhanced by chemical penetration enhancers such as PPG[18] or by sonophoresis using ultrasound.[19]

There is a range of techniques related to iontophoresis.[7,20] Electroporation can be used to deliver DNA into cells and also to allow transdermal delivery of non-ionic drugs.[21] Reverse iontophoresis is used for non-invasive sampling of glucose and other blood constituents.[22] A recent study on the effect of charge and molecular weight on iontophoretic delivery of zwitterionic dipeptides showed that the flux is linearly correlated with the charge to molecular weight

ratio.[23] Iontophoresis can be used to treat hyperhidrosis or excess sweating, although "botox" has been found to be more successful[24] and it has also been successfully used to treat diseases of the eye.[25]

A range of drugs can usefully be delivered by iontophoresis[7,20] including lidocaine for local anaesthesia, cisplatin for basal cell carcinoma, vasopressin as an anti-diuretic, salmon calcitonin to control post-menopausal osteoporosis, heparin as an anticlotting agent[26] and fentanyl for pain relief.[27] Analogues of polymer electrolyte materials prepared for conventional solid state ionic devices have been shown to be suitable as iontophoretic reservoirs for lithium for the treatment of manic depression[28] and for lidocaine hydrochloride.[29]

3. Medical Applications of Solid State Power Sources

External or implanted power sources such as batteries and fuel cells are used in a variety of ways in medicine,[2] including motorised wheelchairs; surgical tools; cardiac pacemakers and defibrillators; dynamic prostheses; sensors and monitors for physiological parameters; neurostimulators; devices for pain relief; and iontophoretic, electroporative and related devices for drug administration. It is helpful to separate applications by location of the power source

- external, i.e. connected to the patient by wire. In some cases the power source can be attached or transdermal, i.e. external to the body but located on the skin.

- implanted, i.e. within the body.

In some cases such as that of the heart pacemaker battery, the implanted power source is situated remotely, i.e. at a different location from that of the device which it powers.[30] In others, such as planned autonomous sensor-transmitters powered by ultra-miniature fuel cells, the power source will be attached to the device.[5]

3.1 *External Applications*

Some applications such as motorized wheelchairs and some battery powered surgical implements have power requirements which are too large to be met by solid state devices.[2] There are other cases, e.g. left ventricular assist devices

used for patients awaiting heart transplants, where a substantial power requirement is met by a combination of external and implanted batteries.[30]

Prototype devices are being developed to take over the functions of the semicircular canals in the ear, which act as physiological rotation sensors to preserve balance. They use piezoelectric vibrating gyroscopes to measure the angular velocity of the head. Pt electrodes are powered by Li batteries which, together with the sensors and computerised frequency converters are mounted externally.[31] A variety of sensors and monitors such as glucose sensors for diabetics and "halter" monitors storing electrocardiogram signals are powered by external batteries at present.[30] In the future, many of these may be developed to utilise miniaturised and implanted fuel cells.[5] to provide "real time, true location" signal detection.

A variety of power sources has been used for iontophoresis[7–9,20] and for related processes such as electroporation.[32] External power sources have also been used to control drug delivery from implantable reservoirs[2] in order to improve patient compliance with a given therapy, the relative ease of self-dosing eliminating the need for multiple intravenous injections.[33]

Power sources for transdermal devices for iontophoresis and related processes can themselves be located on the skin and integrated with the drug reservoir and electrodes.[7-9]

3.2 *Implanted Power Sources*

Monitoring the responses of individuals to drugs and other stimuli is very important as, in the West, drugs are presently administered at frequencies and doses based on averages which have been optimised for large, often heterogeneous, populations. Individual behaviour differs, either permanently or temporarily, from the average, as is well recognised in Chinese medicine. It is therefore desirable to have individualised, integrated medical systems comprising implanted sensors, batteries, amplifier, processor and actuator for such applications as heart pacemakers and defibrillators.[34]

Most implanted power sources are located remotely from the device they power. Neurostimulators for pain relief, tremour reduction in Parkinson's disease,[2] incontinence[35] and epilepsy[36] also have a power demand within the

range of implanted batteries. Recent studies have investigated the possible interaction between such devices and the high magnetic fields used in MRI scanning.[37]

The largest application of remote, implanted batteries, however, is the heart pacemaker in which the Li battery is located below the skin between the shoulder and the neck and is connected to electrodes in the heart muscle.[38] The heart pacemaker was initially developed in 1959[39] and the first that was powered with a Li battery was implanted in 1972.[40] It is designed to assist in bradycardia, an illness where the heart beats too slowly. A similar device, the implantable cardiac defibrillator, addresses tachycardia, a medical condition where the heart beats too quickly[41] and which, if untreated, can degenerate into ventricular fibrillation and death.

An example of a power source directly attached to an implanted device, which is currently undergoing clinical trials is a fully implanted hearing aid using pacemaker-type batteries integrated with the rest of the device and located just behind the ear.[42] Perhaps the most exciting future development, hopefully to be realised soon, is implantable sensor-transmitter systems, smaller than 1 mm^3 powered by integral glucose – oxygen biofuel cells.[5]

3.3 *Types of Solid State Power Sources used in medicine*

Li / Silver vanadium oxide (SVO) batteries are used, in conjunction with stacked plate aluminium electrolytic capacitors, to power implantable cardioverter-defibrillators. The electrode balance needs to be carefully optimised.[43] Alternative systems include Li / CF_x and Li / MnO_2 (MDX).[44] The Li / I_2-PVP primary battery is the system of choice for low rate applications such as pacemakers.[45,46] Implantable Li Ion batteries have been used in test systems for undulation pump total artificial hearts.[47] Potential nanobiotechnological devices including molecular motors and artificial organs and their power sources have recently been reviewed.[48] Optimisation studies are being performed to facilitate future implantable fuel cells.[49] Systems involving chitosan (extracted from shellfish shells, one of the world's largest sources of discarded materials) are also being proposed for implanted batteries.[3050] Dangers accompanying the use of batteries in medicine have recently been reviewed elsewhere.[2]

4. Enzymatic Biofuel Cells

Batteries and fuel cells are both electrochemical devices in which electrons move through an external circuit where they can do electrochemical work and the charge compensating ions move from one electrode to another through an electrolyte membrane. In the former, the electrode material cannot be replenished (although in rechargeable or secondary batteries, the ions can be sent back to the electrodes from which they came) whereas in the latter, the electrode fuel, usually gaseous or liquid, can be continuously supplied and is catalytically converted to active electrode material, usually by a precious metal catalyst.

A biological fuel cell or biofuel cell is a hybrid of fuel cell technology and biotechnology and the catalysts are enzymatic, either contained in microorganisms or as isolated proteins. There was a particular interest in the USA in the 1960s in developing biofuel cells as energy-saving, waste disposal systems for extended space flights.[51] Biofuel cells cannot approach the performance of conventional systems. Platinum based hydrogen – air and methanol fuel cells can achieve 1 A/cm^2 and 0.65V and 0.5 A/cm^2 and 0.5V respectively whereas the best methanol-air biofuel cells produce less than 10 m A/cm^2.[52]

The focus in this paper is on biofuel cells for medical use (often in miniaturized form), powered by physiologically available reactants and used for diagnostic and related applications. Biofuel cells are similar to biosensors and other devices which use enzymatic biocatalysis although biocatalysed sensors are often inexpensive enough to be disposable, so stability for sensors is not a major issue. Bioelectrocatalysts form molecular transducers which convert chemical into electrical signals.[3]

Biofuel cells are described as microbial if living cells are involved and as enzymatic if they are not. A further distinction is between direct and indirect biofuel cells. In the former, fuel is oxidised at the surface of the electrode in an enzymatically catalysed reaction whereas in the latter, the fuel reacts in solution or in a separate compartment and a redox active mediator shuttles electrons between the reaction site and the electrode. Often, enzymes are used in direct fuel cells and microorganisms in indirect configurations.[51]

Maximising Vcell and Icell so that power and energy output are as large as possible represent key challenges to biofuel cell development. For a direct fuel cell, Vcell is the difference between the potentials of the fuels, corrected for overpotentials (which are non-trivial and reflect the effects of slow kinetics of heterogeneous electron transfer, ohmic resistances and concentration gradients). For an indirect cell, Vcell is the difference between the mediator potentials, again corrected for overpotentials.[6] Icell is influenced by such factors as electrode size, rate of electrode processes and rate of ion transport across the electrolyte membrane. Power lost to irreversible processes usually appears as heat, the management of which is vital in biofuel cells as enzymes are very temperature sensitive.[51]

The most common cathodic fuel for biofuel cells is O_2, being readily available with a harmless reaction product (water). It is thermodynamically a good oxidant although kinetically it is poor. ABTS (2,2'-azinobis(3-ethylbenzothiazoline-6-sulphonate) has been used as a cathodic mediator to facilitate diffusion processes.[3]

For conventional fuel cells, typical anodic fuels are H_2, methane, natural gas, gasoline, diesel fuel or methanol but for biofuel cells reactions involving fuels such as glucose, which are present in the bloodstream, are of particular interest. The common cofactor or anode mediator of choice is nicotinamide adenine dinucleotide (NAD^+) which is reduced by the fuel to NADH and subsequently reoxidised to continue the enzymatic reaction. Over 60% of the oxidoreductases listed in *Enzyme Nomenclature* have NAD^+ or its phosphorylated equivalent $NADP^+$ as reactant or product.[3] The standard electrode potential is -0.32V at pH 7.0 with respect to the normal hydrogen electrode (-0.62V vs. SCE at pH 7.5) but in practice, because activities are not unity, there is a 1V overpotential which requires to be minimised if practical biofuel cells are to be achieved.

It can be desirable to contain the enzymes and electron transfer mediators within a small volume to maximise concentration and activity. Membranes cause an unacceptable restriction in diffusional flux and so immobilisation of the active species on a surface, or within a tethered polymer brush or network is preferred.[3] Similar issues are encountered in the design of polymer electrolyte materials for flexible battery applications.[7]

Enzymes are not only efficient catalysts; they are also very selective. An upper rate limit for enzyme catalysis is around 100 Coulombs per minute from 1 mg of enzyme, i.e. about 1.6A. In practice, however, allowing for practical specific activities, 1mA is more realistic.[51]

The issues involved in using entire microorganisms in fuel cells have been well reviewed elsewhere.[6] In these microbial fuel cells bacteria such as clostridium butyricum can lead to the production of hydrogen from the fermentation of glucose by a more complicated pathway than is needed for enzymatic fuel cells. In bacteria, glucose is converted to pyruvate and NADH by the Embden-Meyerhof pathway. The pyruvate is then oxidised with ferredoxin$_{ox}$ oxidoreductase to produce acetyl – CoA together with CO_2 and ferredoxin$_{red}$. At the same time, the NADH also reacts with ferredoxin$_{ox}$ to produce NAD^+ and ferredoxin$_{red}$. The ferredoxin$_{red}$ produced by both routes reacts with protons in the presence of hydrogenase to form H_2. Ideally 4 mol of H_2 would be produced from 1 mol of glucose but in practice the yield is only a quarter of this.[6]

In enzymatic fuel cells, the demanding operating conditions required to ensure the continuous fermentation of whole living cells are replaced by different, but no less stringent, requirements to ensure the stabilisation and efficient utilisation of sensitive and expensive enzymes. Just as batteries can be used in medicine either as implanted or external devices, enzymatic fuel cells can be developed as external power sources or as miniaturised, implantable devices. For external applications for potential medium power applications, a mediated approach has to be used because redox enzymes cannot directly transfer electrons to the electrodes; their redox centres are insulated by the protein matrices that surround them. A variety of possible approaches have been developed by Willner and co-workers.[6]

The most promising area for medical applications of biofuel cells is as implantable power sources for macro-scale (e.g. heart pacemaker) or micro-scale (e.g. in-situ, diagnostic, integrated, miniaturised, self-powered sensor) applications.

4.1 *Macro Device applications*

Natural biocatalysts are physiological species which have adapted to optimise their functioning in complex physiological environments at physiological temperature (~ 37°C) and near neutral pH (~7). They utilise naturally occurring fuels and oxidants and produce reaction products that the host can tolerate. All these features are promising for potential implantable applications as biocatalytic coated electrodes need not be sealed off from physiological fluids. This is just as well because the price of achieving stability by using protective barrier membranes would be to reduce reactant mass transfer. Typical reactants are already present in rather low concentrations (glucose, 5mMol/L; oxygen 0.1 mMol/L; lactate 1 mMol/L) and maximum current density is therefore limited by the ability of such reactants to diffuse into the bioelectrodes. In the case of electrodes situated in blood vessel walls, transport can be enhanced by blood flow (typically 1 to 10 cm/s). The flux of glucose has been calculated[3] to be only about 1 mA/cm^2 and rates would be even lower in tissue.

Heart pacemakers and a variety of other implanted devices were described in section 3.2. At present the lifetime of a 1 Wh/mL battery with a typical operating regime of 1 μW exceeds 10 years which suffices for pacemaker applications. The best biofuel cell operating today can just achieve one-hundredth of this energy density, giving a lifetime measured in days. Potentially, however, if glucose from the body is used as fuel and oxygen dissolved in body fluids provides the oxidant, the implantable biofuel cell could achieve high power density and infinite energy density.[3]

Damage is caused by the implantation process, especially into blood vessels where clotting is a hazard. Here the surgical procedures are worthwhile only if the cell itself is stable and benign enough to survive more than a year, whereas in tissues shorter lifetimes may still confer benefit. Another risk issue for tissues is the toxicity of the implanted cell components. Many of the relevant enzymes have received GRAS (generally recognised as safe) recognition from the US Food and Drug Administration.[52] Mediators sometimes involve osmium compounds, certain of which are considered as toxic although others have been used for treatment of arthritis[53] and haemophilia.[54] It is suspected that, whereas concentrations involved in manufacture may be hazardous, toxicity at in vivo concentrations may be low.[55]

The range of difficulties outlined above means that, even at the present day, the majority of enzyme fuel cells actually involve only one bioelectrode, coupled with a noble metal counter electrode.[3] True biofuel cells involving two enzyme electrodes are still either limited to levels of performance below those which would be useful (e.g. 5 $\mu W/cm^2$) for implantable applications, or which are microbial rather than enzymatic.[3] A key problem is to achieve two electrodes both working at the physiological pH value of 7. This has been achieved in a methyl viologen mediated bacterial cell in which both electrodes had carbon felt sheets immersed in pH 7 phosphate buffer with freely diffusing catalysts and mediators, the two compartments being separated by an anion exchange membrane. The voltage was adequate at 1.17V and the current density was 0.45 mA/cm2 but the lifetime was unacceptably low at 2 hours[56]; the same team are also working on a compartmentless glucose – oxygen cell.[57]

4.2 *Microscale devices*

Heller[5] has recently reviewed the work of his team in developing miniature, low cost glucose – oxygen fuel cells to power autonomous sensor-transmitters designed for implantation in the tissue under study. Their goal is to produce fuel cells smaller than 1 mm^3, lighter than 100 μg and costing less than 1$ to power autonomous sensor – transmitter packages broadcasting such information as

- local tissue temperature so that inflammation can be monitored
- local pressure in particular blood vessels or other fluid channels so that fluid blockage and the success of steps taken for its release can be monitored
- deviation from the normal concentration of a chosen chemical whose presence can be used to monitor the progress of a disease.

The sensor is likely continuously to consume only about 1μW. The remaining few μW produced by the miniature fuel cell are needed to charge a small ultracapacitor, capable of storing about 1 μJ which can produce 1 GHz bursts of 10mW, for 1 ms every 10s to power the transmitter.[5]

A number of prototype fuel cells have been built which are more than 100 times smaller than the smallest present day battery or fuel cell. This size

reduction has been achieved by eliminating seven of the nine components needed in conventional fuel cells. The redundant items are

- plumbing to anode and cathode compartments as the cell is surrounded by its fuel dissolved within the ambient body fluids
- an external case and case seal, designed to encapsulate the cell components and prevent leakage into the environment
- a membrane and seal providing a sealed matrix for the ion conducting electrolyte

A conventional fuel cell using a platinum group metal as catalyst has to incorporate a membrane because the catalyst is capable of promoting not only the desired oxidation of the fuel but also the highly undesirable reduction of O_2 and a compartment-separating membrane is needed to prevent this. Incidentally, many early glucose – electrooxidising cells also required a membrane because the platinum metal catalysts at their O_2 electrodes were fouled by the glucose electrooxidation products. The selectivity of enzyme based catalysts means that undesirable side reactions are not promoted and compartment isolation becomes unnecessary.[5] The classic development that led to biofuel cells without membranes was when Willner and co-workers used immobilised bioelectrocatalysts, their enzymes being "wired" to electrodes through electronically conducting hydrogels, to catalyse either glucose oxidation at the anode or O_2 reduction at the cathode but not vice versa.[58]

An early design involved enzymatic electrodes immobilised within, and mediated by, osmium-based redox hydrogels deposited on 7 μm diameter carbon fibres. At present, the cell operates at pH 5 in a citrate buffer saturated with air and containing 15 mMol/L of glucose and produces 340 $\mu A/cm^2$ and 0.4V at 37°C. Current density decreases by 8% a day because of limitations in anode performance.[3] The pH is too far from the physiological level, the redox potential of the anode mediator is too high and the deposited hydrogel film is too thick to permit rapid electron transport. A variant on this design uses an anode mediator with a lower redox potential and a cathode catalyst that functions at pH 7.[59] The voltage is 0.52 V and the current density is 340 $\mu A/cm^2$, thus more than doubling the power density achieved. The stability, however, is only marginally better at 6% current density loss per day. Recent developments are summarised

by Heller.[5] Barton and colleagues have discussed[3] the key issues that need to be addressed for implanted biofuel cells to be widely adopted – biocompatibility; better activity and stability (achieved by engineering both the protein molecule and also its environment, perhaps by biomimetics[60]); increased current density; improved mediators and / or better immobilisation using controlled nanoporous substrates; extended device lifetimes; greater power (mW to W scale in blood vessels and μW in tissue); and better integration with electrical devices, including multi power source stacks.

Solving these problems requires the same type of multi-disciplinary approach (from chemists, chemical engineers, materials scientists and, of course, biologists) as was needed to launch the field of solid state ionics.

References

1. R.G.Linford and W.S.Schlindwein, *Solid State Ionics*, (2006) in press
2. R.J.Latham, R.G.Linford and W.S.Schlindwein, *Solid State Ionics*, **172**, 7 (2004)
3. S.C. Barton, J. Galloway and P. Atanassov, *Chem. Rev.*, **104**, 4867 (2004)
4. E.Katz, O.Lioubashevski and I.Willner, *J. Amer. Chem. Soc.*, **127**, 3979 (2005)
5. A.Heller, *Phys.Chem.Chem.Phys.*, **6**, 209 (2004)
6. E.Katz, A.N.Shipway and I.Willner in: W.Vielstich, H.A.Gasteiger, A.Lamm (Eds.), *Handbook of Fuel Cells – Fundamentals, Technology and Applications*, John Wiley and Sons, London, (2003), **vol.1**, ch 21, p.355
7. R.J.Latham, R.G.Linford and W.S.Schlindwein, *Ionics*, **9**, 41 (2003)
8. R.J.Latham, R.G.Linford and W.S.Schlindwein in: B.V.R.Chowdari, S.R.S. Prabharan, M.Yahaya, I .A.Talib (Eds.), *Solid State Ionics – Trends in the New Millenium*, World Scientific, Singapore (2002), p.283
9. [F.O.V.da Cunha, M. M.C.Forte, A.Barnes, R.J.Latham, R.G.Linford and W.S. Schlindwein in: K.Getlecker (Ed.), Functional Nanomaterials, American Scientific Publishers, Stevenson Ranch, California, (2006) in press
10. A. Helmstadter, *Pharmazie*, **56**, 583 (2001)
11. A. Sharma. in 205th Meeting of The Electrochem. Soc., San Antonio, (2004), p.720.
12. J B Phipps in 205th Meeting of The Electrochem. Soc., San Antonio, (2004), p.714
13. M. B. Armand, J. M. Chabagno and M. J. Duclot. in *Second International Conference on Solid Electrolytes* St. Andrews, Scotland, (1978).
14. M. B. Armand, J. M. Chabagno and M. J. Duclot. in: P. Vashishta, J.N.Mundy, G.K.Shenoy (Eds.), *Fast Ion Transport in Solids,* Elsevier North-Holland Inc., (1979), p. 131
15. C.Berthier, W.Gorecki, M.Minier, M.B.Armand and P.Rigaud, *Solid State Ionics*, **9**, 1125, (1983)
16. D.E.Fenton, J.M.Parker and P.V.Wright, *Polymer*, **14**, 589, (1973)
17. A M Johnson, D R Sadoway, M J Cima and R Langer, *J.Electrochem. Soc.*, **152**, H6 (2005)
18. A K Banga, Electrically Assisted Transdermal and Topical Drug Delivery, Taylor and Francis, London, (1998)
19. S Mitragotri and J Kost, *Adv. Drug Delivery Rev.*, **56**, 589 (2004)
20. Y.N.Kalia, A.Naik, J.Garrison and R.H.Guy, *Adv.Drug Del. Rev.*, **56** , 619, (2004)
21. A-R Denet, R Vanbever, V Préat, *Adv. Drug Delivery Rev.*, **56**, 659, (2004)
22. B Leboulanger, R H Guy, M B Delgado-Charro, *Physiol. Measurement*, **25,** R35, (2004)
23. N.Abla, A. Naik, R.H.Guy and Y.N. Kalia, *Pharmaceutical Research,* **22(12)**, 2069 (2005)

24. E Fitzgerald, T M Feeley, S Tierney, *Surgeon-Journal Royal Coll. Surgeons Edinburgh & Ireland*, **2**, 311 (2004)
25. M.E.Myles, D.M.Neumann and J.M.Hill, *Adv. Drug Delivery Rev*, **57 (14)**, 2063, (2005)
26. S.Pancini, T.Punzi and M.Gulisano, *Pharm. Res.*, **23**, 114, (2006).
27. E.R.Viscusi, L.Reynolds and S.Tait, **102**, 188, (2006)
28. T Sahota, R Latham, R Linford, P Taylor, *Drug Dev. Ind. Pharm.*, **25**, 307, (1999)
29. T Sahota, R Latham, R Linford, P Taylor, *Drug Dev. Ind. Pharm.*, **26** , 1039, (2000)
30. C.F.Holmes, *Interface*, **12,** 19 (2003)
31. W.S.Gong and D.M.Merfeld, *Ann.Biomed.Eng.*, **28**, 572 (2000)
32. A-R Denet, R.Vanbever and V.Preat, *Adv.Drug Del.Rev,,*. **56** , 659 (2004)
33. S Sershen and J West, *Adv Drug Deliver Rev.*, **54** , 1225 (2002)
34. A.Heller, *AICHE Journal*, **51** , 1054 (2005)
35. J. Groen, and C.Amiel , *JLHR Bosch, Neurourology and Urodynamics*, **24** , 226 (2005)
36. EH Kossoff, EK Ritzl, JM Politsky, AM Murro, JR Smith, RB Duckrow, DD Spencer and GK Bergey *Epilepsia*, **45** , 1560 (2004)
37. KB Baker, JA Nyenhuis, G,Hrdlicka AR Rezai, JA Tkach and FG Shellock *J. Mag.Res.Imag*, . **21** , 72 (2005)
38. M.H.Schoenfisch, M.Ovadia and J.E.Pemberton, *J.Biomed. Mater. Res.*, **51** , 209 (1999)
39. W. Greatbatch, and W. Chardack, *Proc. New England Res. & Eng. Meeting*, **1**, 8 (1959)
40. G. Antonioli, F. Baggioni, F. Consiglio, G. Grassi, R. LeBrun and F. Zanardi, *Minerva Med.*, **64** , 2298 (1973)
41. A. Agarwal, M.York, B.K.Kantharia and M.Ezekowitz, *Ann. Rev. Med.*, **56** , 475 (2005)
42. http://www.stcroixmedical.com/Envoy_device.htm (2005)
43. PM Skarstad, *J. Power Sources*, **136** , 263 (2004)
44. W. Greatbatch, V.C.F. Holmes, E.S. Takeuchi and S.J. Ebel, *Pacing & Clinical Electrophysiology*, **19** , 1836 (1996)
45. C.L. Schmidt and P.M. Skarstad, *J. Power Sources*, **97-98** , 742 (2001)
46. E.S. Takeuchi and R.A. Leising, *MRS Bull.*, **27**, 624 (2002)
47. E Okamoto, T Inoue, K Watanabe, T Hashimoto, E Iwazawa, Y Abe, T Chinzei, T Isoyama, S Kobayashi, I Saito, F Sato, H Matsuki, K Imachi and Y Mitamura, *Artificial Organs*, **27** , 184 (2003)
48. H Klefenz, *Eng in Life Sci*, **4**, 211 (2004)
49. S.C. Barton, *Electrochim. Acta*, **50**, 2145 (2005)
50. M Yamada and I. Honma, *Electrochim. Acta*, **50** , 2837 (2005)
51. G Tayhas, R Palmore and G M Whitesides, *ACS Symp. Ser.*, **566**, 271 (1994)
52. www.cfsan.fda.gov/~rdb/opa-g106.html; www.cfsan.fda.gov/~rdb/opa-g122.html
53. R Bessant, A Steuer, S Rigby and M Gumpel, *Rheumatology*, **42** , 1036 (2003)
54. X Ayral, *Haemophilia*, **7**, 20 (2001)
55. I Schott, *Chem. Eng. News*, **81** , 146 (2003)
56. S.Tsujimura, M.Fujita, H.Tasumi, K.Kano and T.Ikeda, *Phys. Chem.Chem.Phys.*, **3** , 1331 (2001)
57. S.Tsujimura, K.Kano and T.Ikeda, *Electrochemistry*, **70** , 940 (2002)
58. E Katz, I Willner and A B Kotlyar, *J. Electroanal. Chem.*, **479** , 64 (1999)
59. N Mano, F Mao and A Heller, *J. Amer.Chem.Soc.*, **124** , 1962 (2002)
60. R Boulatov, *Pure Appl. Chem.*, **76**, 303 (2004)

DEVELOPMENT OF ALL-SOLID-STATE LITHIUM BATTERIES

V. THANGADURAI[a], J. SCHWENZEL[b] AND W. WEPPNER

Chair for Sensors and Solid State Ionics
Faculty of Engineering, Chr.-Albrechts University Kiel
Kaiserstr. 2, 24143 Kiel, Germany
ww@tf.uni-kiel.de

The present lithium ion battery technology is based on liquid organic electrolytes, which have several disadvantages and severe problems. These are related to safety concerns because of potential electronic short circuits of the electrodes, formation of reaction product layers at the interfaces ("solid electrolyte interfaces, SEIs"), leakage of the liquid, low electrochemical decomposition voltages and flammability of the electrolyte, and accordingly restrictions with regard to higher energy densities. Solid electrolytes may provide solutions to the problems. However, so far all discovered compounds had either high ionic conductivity or high electrochemical stability, but not both. In addition, some of the compounds became predominantly electronic conductors, e.g., (Li,La)TiO_3, within the lithium activity range given by the cathode and anode. Furthermore, since polycrystalline materials are being used for practical applications, large grain boundary resistances are commonly observed in addition to the bulk resistance and therefore control the total cell resistance.

Here, we report predominant ionic conduction in garnet-type structures of the general composition $Li_6ALa_2M_2O_{12}$ (M = Ta, Nb; A = Sr, Ba) and we show that these materials overcome the existing problems. The tantalum compounds are stable against reaction with molten elemental lithium, have high decomposition voltages, which allow application of the highest energy density cathodes, and exhibit fast 3-dimensional lithium ion conductivity similar to that of the best (but unstable) known solid electrolytes. Furthermore, the grain boundary resistance is negligible compared to that of the bulk.

Thin film all-solid-state lithium batteries have been made on the basis of chemically and electrochemically stable solid electrolytes with high voltage intercalation type cathodes and aluminium as anode in the discharged state.

1. Introduction

Development of solid-state lithium ion conductors (SSLICs) for all-solid-state secondary (rechargeable) lithium batteries and other galvanic cell applications has become an important task since a few decades [1-5]. Lithium batteries are attractive as energy sources for several types of portable electronic equipment, including notebooks, cameras, toys, mobile phones, and increasingly electrical transportation.

Useful solid-state lithium-ion conductors for high energy density lithium secondary batteries should have the following electrical, chemical and physical properties [6-8]:

(i) High lithium ion conductivity at the operating temperature (preferably room temperature);

---

[a]Present address: University of Calgary, Canada, Email: vthangad@ucalgary.ca

[b] Present address: Applied Films, Alzenau, Germany, Email: schwenzel.julian@vdi.de

(ii) Negligible electronic conductivity over the entire employed range of lithium activities (i.e., from the activity of elemental lithium (a_{Li} = 1) to at least that of $LiCoO_2$ ($a_{Li} = 10^{-70}$) and range of temperature;
(iii) Small or no grain-boundary, electrode-electrolyte interface and charge transfer resistance;
(iv) Stability against chemical reaction with anodes, especially with elemental Li or Al, LiAl;
(v) High electrochemical decomposition voltage (~ 6 V vs. elemental Li);
(vi) Stability against chemical reactions with the cathode material;
(vii) Matching thermal expansion coefficients (TEC) with both the anode and cathode material;
(viii) Environmental benignity, non-hygroscopicity, low cost and easiness of preparation.

Up to now, lithium ion conduction was reported for a wide range of crystalline and non-crystalline metal oxides, sulfides and halides with different types of structure [6,7,9-10], e.g., $Li_{14}ZnGe_4O_{16}$ (LISICON), Li_3N, Li-β-alumina, NASICON-type $LiTi_2(PO_4)_4$ phosphate, Li_4SiO_4, Li_3PO_4 and perovskite type (Li,La,□)TiO_3 and glasses. Among them, silicate (SiO_4^{4-}) and phosphate (PO_4^{3-}) frame-work structure based electrolytes exhibit high electrochemical stability and chemical compatibility with both electrodes (cathode and anode) [11,12].

Current all-solid-state thin film Li-battery developments make use of LiC_6, elemental lithium or inorganic compounds such as silicon-tin oxynitrides, Sn_3N_4, Zn_3N_2 or metal films that include Cu and In as anodes, $LiCoO_2$ and $LiMn_2O_4$ as cathodes and LiPON as electrolyte [12].

In our attempt to develop advanced solid-state lithium ion conductors for application in secondary batteries, we have investigated compounds with similar constituents as in the case of the known best lithium ion conductor (Li,La,□)TiO_3 but without Ti as well as other metal ions such as W, Mo or V which may be readily reduced by lithium. The investigated compounds with the nominal chemical compositions $Li_5La_3M_2O_{12}$ and $Li_6ALa_2M_2O_{12}$ (A = Ca, Sr, Ba; M = Nb, Ta) show a garnet-like structure, which is a new crystal structure for fast lithium ion conduction.

We have also successfully replaced elemental Li by Al metal as anode and conventional $LiCoO_2$ by other alternative high-voltage cathode materials, e.g., 3D spinel structured $Li_2MMn_3O_8$ (M = Fe, Co) [13], to increase the operating voltage compared to present all-solid state batteries that utilize LiPON as electrolyte [11,12].

2. Structure and Conductivity of Garnet-Like $Li_5La_3M_2O_{12}$ (M = Nb, Ta)

Garnets are orthosilicate minerals with the general chemical formula $A_3^{II}B_2^{III}(SiO_4)_3$,

where A and B refer to 8- and 6-coordinated cation sites, respectively. The structure is a 3D framework built of BO_6 octahedra and SiO_4 tetrahedra, in which each octahedron is connected to six tetrahedra by sharing corners. Each tetrahedron

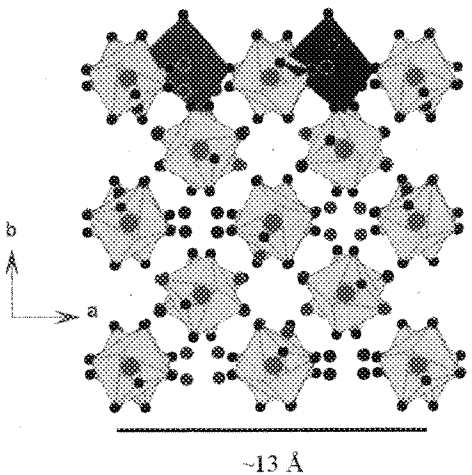

Fig. 1. Crystal structure of $Li_5La_3M_2O_{12}$ showing a garnet-like structure (a = 12.797 Å for Nb and a = 12.804 Å for Ta; space group $I2_13$, No.: 199) with an excess of 16 lithium atoms. M and Li occupy the 6- fold oxygen coordination sites [16].

shares its corners with four octahedra. The composition of the framework is equal to "$B_2Si_3O_{12}$" [14,15]. A has a larger ionic size and occupies the 8-fold coordination (dodecahedral) site 24c in the framework (space group: *Ia3d*) [14,15].

A variety of complex metal oxides was found to crystallize in garnet-like structures with other elements replacing silicon and having the general composition $A_3B_5O_{12}$ (A = alkali, alkaline earth ions, Mg, Y or Ln = La or rare earth; B = transition metal ions such as Al, Fe, Ga, Ge, Mn, Ni, V) [14,15].

Metal oxides with the nominal chemical formula $Li_5Ln_3M_2O_{12}$ (Ln = La or rare earths; M = Nb, Ta) were found to crystallize in a cubic symmetry, for example, with the lattice constant a = 12.797 Å for Nb and a = 12.804 Å for Ta and the space group $I2_13$ (space group no. 199, Z = 8) with an excess of 16 lithium atoms compared to the ideal garnet composition. La^{3+} and Nb^{5+} ions occupy the 8- and 6-coordination sites, respectively, and the Li^+-ions occupy 6-fold coordination sites (Fig. 1) [16-18].

The similarity between the structures of the ideal garnet and $Li_5La_3M_2O_{12}$ is that the rare earth ions occupy the dodecahedral (8-fold) coordination site, and B and M

atoms occupy the 6-fold coordination site. The main difference is that Si (or other metal ions) in the former case occupy the 4-fold coordination and Li in the latter case occupies the highly distorted octahedral sites. Among the two types of lithium, $Li(I)O_6$ is more distorted than $Li(II)O_6$. MO_6 octahedra are surrounded by six LiO_6 octahedra and two vacant lithium sites. For the same composition, a different garnet space group *Ia3d* has been proposed based on powder XRD data, in which all the sites are completely occupied. In this model, Li ions are distributed over both 4- and 6-fold coordination sites [17].

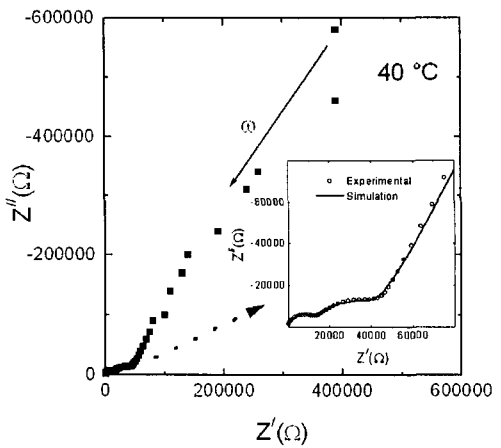

Fig. 2. Ac impedance data of $Li_5La_3Ta_2O_{12}$ at 40 °C em-ploying lithium ion blocking Au electrodes. A very small bulk resistance is observed in the high frequency regime. Grain boundary contributions and a tail are observed at the low frequency side. The inset shows an enlargement of the high frequency part of the impedance spectrum.

Compounds with the garnet-like chemical formula $Li_5La_3M_2O_{12}$ (M = Nb, Ta) can be prepared by solid-state reaction using required amounts of $La(NO_3)_3{\cdot}6H_2O$ or La_2O_3 (heated at 900 °C for at least 24 h), $LiOH{\cdot}H_2O$, and M_2O_5 (M = Nb, Ta) at elevated temperatures [19]. 10 wt.% excess of $LiOH{\cdot}H_2O$ was added to compensate the loss of lithium oxide due to evaporation at elevated temperatures [19].

Figure 2 shows typical impedance plots (HP 4192 A Impedance and Gain-Phase Analyzer, 5 Hz-13 MHz; Au electrodes) of Li_5La_3-Ta_2O_{12} measured in air at 40 °C using sintered pellets (~ 0.2 cm in thickness and ~ 0.95 cm in diameter), indicating clearly the bulk (grain interior, R_b) resistance at the high-frequency side, grain boundary (R_{gb}) resistance and a tail in the low frequency regime. Accordingly, the low temperature impedance plots could be well resolved into bulk, grain boundary and elec-trode effects. The appearance of a low-frequency tail is a first indication that the con-duc-tivity of the investigated garnet type material is ionic in nature [20-

22]. The impedance diagram is similar to that of the perov-skite-type lithium ion conductor (Li,La,□)TiO_3.

Figure 3 shows the equilibrium conductivity data of the total (bulk + grain boundary) ionic conductivity of $Li_5La_3M_2O_{12}$ (M = Nb, Ta). Both $Li_5La_3M_2O_{12}$ compounds exhibit the same order of magnitude of lithium ion conductivity of about $\sim 10^{-6}$ S/cm at 25 °C. The activation energies for the electrical conductivity (< 300 °C) are 0.43 and 0.56 eV for $Li_5La_3Nb_2O_{12}$ and $Li_5La_3Ta_2$-O_{12}, respectively [19].

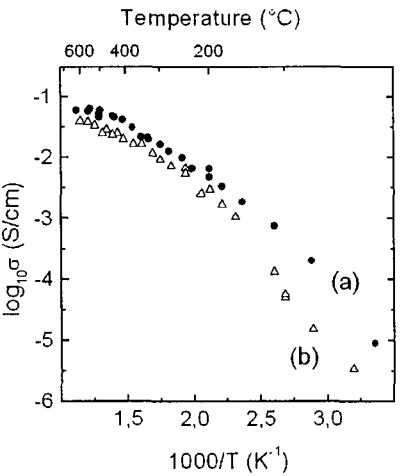

Fig. 3. Arrhenius plot of the total (bulk + grain boundary) conductivity of (a) $Li_5La_3Nb_2O_{12}$ (•) and (b) $Li_5La_3Ta_2O_{12}$ (Δ) [19].

3. Alkaline Earth Ions Doped $Li_5La_3M_2O_{12}$ (M = Nb, Ta)

Since the garnet-like compounds $Li_5La_3M_2O_{12}$ (M = Nb, Ta) show low lithium ion conductivity, we have optimized the electrical conductivity by further doping of the La-positions. Compounds of the nominal chemical compositions $Li_6ALa_2M_2O_{12}$ (A = Ca, Sr, Ba) have been prepared by solid state reactions at 700-900 °C using appropriate amounts of high purity (> 99 %) La_2O_3 (pre-dried at 900 °C for 24 h), $LiOH{\cdot}H_2O$, $Ca(NO_3)_2{\cdot}4H_2O$, $Sr(NO_3)_2$, $Ba(NO_3)_2$ and M_2O_5 (M = Nb, Ta) [8, 23, 24]. Powder XRD patterns of $Li_6ALa_2Nb_2O_{12}$ show that all members of the investigated compounds crystallize in the parent garnet-like $Li_5La_3Nb_2O_{12}$ structure. The cubic lattice constant increases with increasing ionic radius of the alkaline earth ion. The 8-coordinated ionic radius in-creases in the order Ca^{2+} (1.12 Å) < Sr^{2+} (1.25 Å) < Ba^{2+} (1.42 Å). The corresponding value for La^{3+} is 1.18 Å [25].

$Li_6CaLa_2Nb_2O_{12}$ shows both bulk and grain-boundary contributions, especially at lower temperature. The magnitudes of the capacitances of the bulk, grain boundary and electrode-electrolyte interface region are of the order of 10^{-11}, 10^{-8} and 10^{-6} F/cm^2, respectively. These are characteristic values for the bulk, grain boundary and electrode-electrolyte interface contributions of ionically conducting ceramic materials [20-22].

The Sr- and Ba-substituted compounds (Fig. 4) show nearly a single arc for the bulk conductivity contribution at high frequencies and a tail in the low frequency regime, which results from the lithium ion blocking Au electrodes. It is surprising that the grain boundary contribution is only about 10 % of the bulk contribution at room temperature (~ 20 °C) and decreases further with increasing temperature [23,24]. As a general feature, the alkaline earth ion substitution in the parent compound $Li_5La_3Nb_2O_{12}$ decreases drastically the grain boundary resistance. This

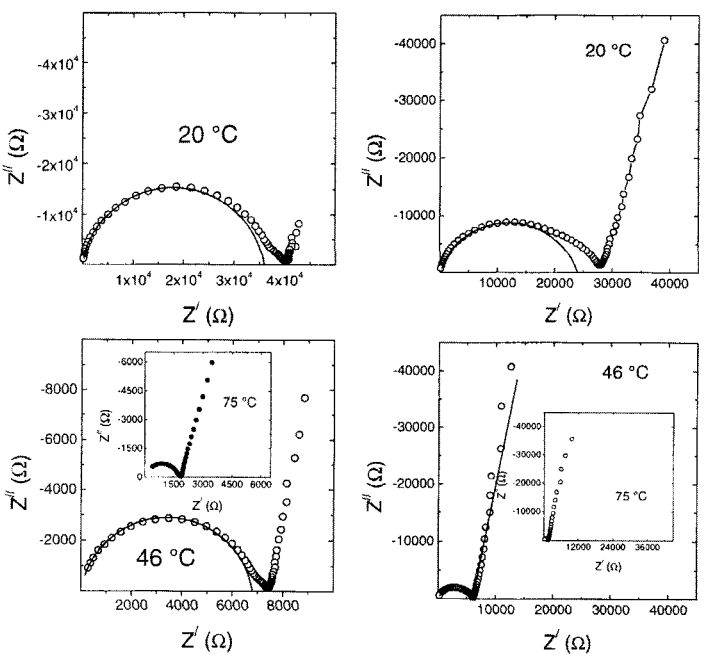

Fig. 4. Ac impedance (5 Hz-13 MHz) data of (left) $Li_6SrLa_2Nb_2O_{12}$ and (right) $Li_6BaLa_2Nb_2O_{12}$ at a few temperatures employing lithium ion blocking Au electrodes. The applied voltage was 100 mV. A bulk resistance at high frequencies, a grain boundary contribution and a tail at low frequencies are observed. The appearance of the tail at the low frequency side indicates blocking nature for the mobile lithium ions and provides evidence that the garnet-type materials are ionic conductors. The open circle shows measured data and the solid line represents simulated data using the EQUIVALENT (B.A. Boukamp, Equivalent Circuit, Report No. CT88/265/128/CT89/214/128, University of Twente, Enschede, 1997) program with an equivalent circuit consisting of a parallel resistance-capacitance and capacitance contributions $(R_bQ_b)(Q_{el.})$ [23].

finding is a most attractive feature of the investigated garnet-type material compared with other ceramic lithium ion conductors. For comparison, the best lithium ion conductor based on perovskite $(Li,La,\square)TiO_3$ exhibits a very high grain-boundary resistance ($R_{gb} \approx 50\ R_b$) under similar solid state synthesis conditions.

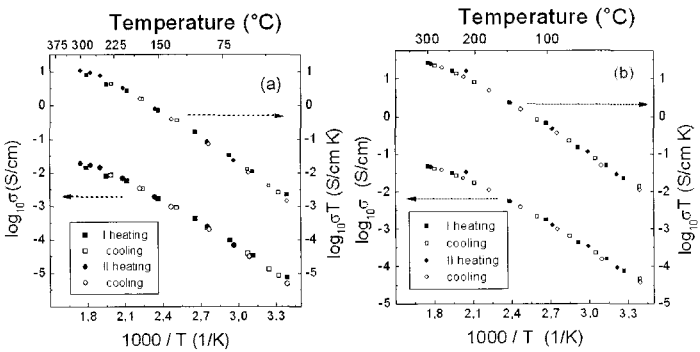

Fig. 5. Arrhenius plots of the bulk and grain boundary conductivity of (a) $Li_6SrLa_2Ta_2O_{12}$ and (b) $Li_6BaLa_2Ta_2O_{12}$. The conductivity data obtained during the first heating and cooling and subsequent cycle follow the same line, indicating equilibrium conductivity being observed [24].

The Arrhenius plots of the total (bulk + grain boundary) conductivities of $Li_6ALa_2Ta_2O_{12}$ (A = Sr, Ba) are shown in Fig. 5.

Table 1 lists the electrical conductivity data and activation energies of lithium ion conductivity of $Li_6ALa_2M_2O_{12}$ together with that of the parent compound. Among the compounds investigated, $Li_6BaLa_2Ta_2O_{12}$ exhibits the highest ionic conductivity of 4.0×10^{-5} S/cm at room temperature with an activation energy of 0.40 eV. The conductivity is higher than in the case of Li- β-alumina, thin film $Li_{2.9}PO_{3.3}N_{0.46}$ (LiPON) [11,12], Li_9SiAlO_8 [26], LiI + 40 mol Al_2O_3 [27] and $Li_{3.5}Si_{0.5}P_{0.5}O_4$ (LiSiPO) [28] and is comparable to that of the rather unstable Li_3N (decomposition voltage 0.445 V vs. Li). The high ionic conductivity in the present class of materials is believed to be due
to the migration of lithium ions through interstitial sites (Fig. 6). In contrast to Li-β-alumina and Li_3N, the garnet is an isotropic compound and hence the conductivity occurs in three dimensions [18].

Using reversible elemental lithium as electrode, $Li_6ALa_2Ta_2O_{12}$ (A = Sr, Ba) shows a single semicircle with a total resistance of 22.5 kΩ for the Sr- and 7.5 kΩ for the Ba-compound at 23 °C [24]. The appearance of the low-frequency intercept in this case is a second and more definite indication of lithium ion conduction in the investigated garnet-type materials, while using lithium ion blocking electrodes has shown a tail in the low frequency regime due to blocking of the mobile lithium ions.

The resistance values obtained using AC and DC methods using reversible lithium electrodes are nearly the same, indicating the absence of electrolyte-electrode interface resistances due to possible formation of interface reaction products [24].

Table 1. Comparison of Cell Constant and Lithium Ion Conductivity Data of $Li_5La_3M_2O_{12}$ (M = Nb, Ta) and $Li_6ALa_2M_2O_{12}$ (A = Ca, Sr, Ba; M = Nb, Ta)

Compound	Lattice constant (Å)	σ_{RT} (S/cm)	E_a (eV)
$Li_5La_3Nb_2O_{12}$	12.826	8.0×10^{-6}	0.43 (< 300 °C)
$Li_5La_3Ta_2O_{12}$	12.829	1.3×10^{-6}	0.56 (< 300 °C)
$Li_6CaLa_2Nb_2O_{12}$	12.697(2)	1.6×10^{-6}	0.55 (25-300 °C)
$Li_6SrLa_2Nb_2O_{12}$	12.811(1)	4.2×10^{-6}	0.50 (20-200 °C)
$Li_6BaLa_2Nb_2O_{12}$	12.868(1)	6.0×10^{-6}	0.44 (20-200 °C)
$Li_6SrLa_2Ta_2O_{12}$	12.808(2)	7.0×10^{-6}	0.50 (20-300 °C)
$Li_6BaLa_2Ta_2O_{12}$	12.946(3)	4.0×10^{-5}	0.40 (20-300 °C)

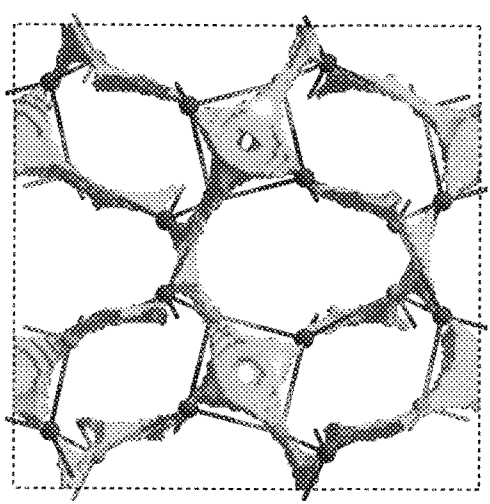

Fig. 6. Bond valence models for Li^+ transport pathways in $Li_5La_3Nb_2O_{12}$ in the "global instability index (GII)"-optimized model for $\Delta V(Li) = 0.1$ v. u. [18].

4. Chemical Reactivity Investigations Employing Lithium Battery Electrodes

Stability of $Li_6BaLa_2Ta_2O_{12}$ against chemical reaction with several potential lithium battery cathode materials were investigated by reacting mixed powders of the electrolyte and cathode material in approximate 1:1 wt.% ratio at 400, 600, 800 and 900 °C for 24 h in air. Commercially available (Merck, Darmstadt) $LiCoO_2$, $LiNiO_2$, and $LiMn_2O_4$ cathode powders were mixed with $Li_6BaLa_2Ta_2O_{12}$ powders and ballmilled overnight in 2-propanol. The powders of $Li_2MMn_3O_8$ (M = Fe, Co) were prepared by the glycine-nitrate combustion method. Appropriate amounts of $LiNO_3$, $Co(NO_3)_3{\cdot}6H_2O$, $Fe(NO_3)_3{\cdot}9H_2O$, $Mn(NO_3)_2{\cdot}4H_2O$ and $H_2NCH_2CO_2H$ were dissolved in a minimum volume of de-ionized water to obtain aqueous solutions. We observed that $Li_6BaLa_2Ta_2O_{12}$ is found to be chemically stable against chemical reaction with layered structured $LiCoO_2$ up to 900 °C, while Ni, Mn and Co,Mn containing electrodes react with the electrolyte at relatively low temperature. Figure 16 shows the powder XRD data of reaction mixtures of $Li_6BaLa_2Ta_2O_{12}$ and $LiCoO_2$ [8].

Stability of $Li_6ALa_2Ta_2O_{12}$ (A = Sr, Ba) against chemical reaction with molten lithium was investigated inside an Ar filled glove box by reacting the sample powders, pellets or crucibles with large excess of molten lithium for 3-7 days in Mo crucibles. The results show that the colour and XRD patterns of the materials remain the same before and after the reaction, suggesting that the electrolyte is chemically stable against reaction with elemental lithium [24].

5. All-Solid-State Lithium Ion Cells

The galvanic cells

$$(-)\ Al \mid LiPON \mid Li_2MMn_3O_8\ (M = Co, Fe)\ (+) \qquad (II)$$

were deposited onto alumina substrates with a typical LiPON thickness of 1 μm. Sputtered Pt10wt.%Rh films were used as current collectors. The various layers were prepared according to the sequence: (i) sputtering of the Pt/Rh current collector layer, (ii) e-beam evaporation of one of the cathode materials ($Li_2MMn_3O_8$ (M = Co, Fe)) (~500 nm), (iii) annealing at 700 °C in air, (iv) rf sputtering of the LiPON layer (~1 μm) and (v) rf sputtering of the aluminium layer (100 nm) [25,26].

An ionic conductivity of the LIPON thin films of about 10^{-6} S/cm is obtained at room temperature with an activation energy of about 0.5 eV. These values are comparable with those reported in the literature [11,12].

Galvanostatic charge and discharge measurements were made using constant currents. The results are shown in Fig. 7 a) and b) for the Co- and Fe-member, respectively. The first cycle consisted of a charging process until a voltage of 4.8 V was reached, whereas a maximum voltage of 5 V was allowed during the following cycles. There exist two plateaus which are expected from the valence changes of Mn at 3.7 V vs. Al,LiAl and of Co / Fe at around 4.8 V vs. Al,LiAl [32].

The chemical diffusion coefficient ($\tilde{D}$) was found to be of the order of 10^{-13} to 10^{-12} cm^2/sec for any com-position x of $Li_{2-x}MMn_3O_8$ (M = Fe, Co) in the range from 0.1 to 1.6 by employing the galvanostatic inter-mittent titration technique (GITT). AC impedance studies revealed a charge transfer resistance of 260-290 Ω

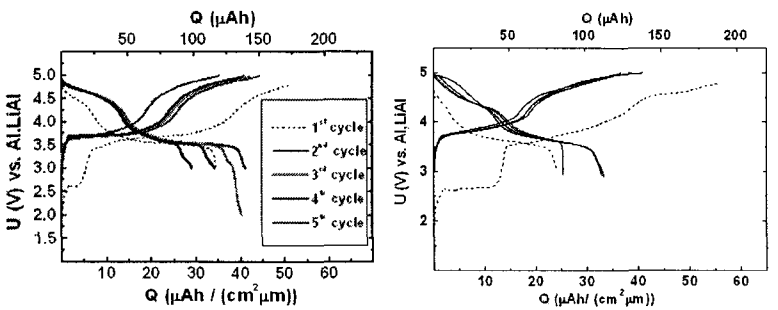

Fig. 7. Galvanostatic charge and discharge measurements of the complete solid state cell set-up, i.e., (–) Al | LiPON | $Li_2MMn_3O_8$ | Pt10wt.%Rh (+), (a: M = Co and b: M = Fe) using a constant current of 5 μA and an electrode area of 6.7 cm^2. The thicknesses of $Li_2CoMn_3O_8$, LiPON and Al layers are 500 nm, 1 μm and 100 nm, respectively. During the first cycle, the cell was charged until a voltage of 4.8 V was reached, whereas a maximum voltage of 5 V was allowed during the following cycles [32,33].

and a double layer capacity of ~ 45-70 μF for an electrode area of 6.7 cm^2 [25].

6. Conclusions

In the present study we have shown that the garnet–type $Li_5La_3M_2O_{12}$ and $Li_6ALa_2Ta_2O_{12}$ (A = Ca, Sr, Ba; M = Nb, Ta) materials form an attractive new class of fast solid lithium ion conductors with the highest con-ductivities (besides that of bulk Li_3N and (Li,La,)TiO_3, which are practically not applicable). The Ca-substituted $Li_5La_3M_2O_{12}$ exhibits both bulk and grain boundary contributions to the total resistance, while the Sr-and Ba-substituted compounds show mainly bulk resistances with a rather small grain boundary contributions (~10 % of the total resistance at 20 °C) which further decrease with increasing temperature.

Among the investigated compounds, the Ba-compound $Li_6BaLa_2Ta_2O_{12}$ shows the highest ionic conductivity of 4.0×10^{-5} S/cm at 22 °C. The activation energy of 0.40 eV is comparable with those of other lithium ion conductors, especially with the presently employed solid electrolyte lithium phosphorus oxynitride (LiPON) for all-solid-state lithium ion batteries. More importantly, unlike other fast lithium ion conducting compounds, such as $Li_{14}ZnGe_4O_{16}$, $(Li,La,\square)TiO_3$ and $Li_{1.3}Ti_{1.3}Al_{0.3}(PO_4)_4$, the members of the garnets investigated here, especially the Ta-members, are less reducible by lithium metal than the Nb analogue, and the conductivity occurs in three dimensions.

All-solid-state thin film batteries are feasible by employing an Al anode and LiPON electrolyte fabricated by subsequent deposition of these materials by sputtering and $Li_2MMn_3O_8$ (M = Fe, Co) as cathode by e-beam evaporation. These thin film cells could be operated between 3 and 5 V vs. Al,LiAl.

The chemical diffusion coefficients for these materials, as determined by the galvanostatic intermittent titration technique (GITT), resulted in values for both cases in the range of 10^{-13} to 10^{-12} cm^2/s. This indicates that diffusion of lithium in the cathode material is the rate determining step.

7. Acknowledgments

Dr. V. Thangadurai also wishes to thank the AvH-Foundation for a Research Fellowship and the DAAD for a Guest Professorship for a financial support.

8. References

1. Solid Electrolytes General Principles, Characterization, Materials, Applications (P. Hagenmuller and W. Van Gool, Eds), Academic Press, New York, 1978.
2. C. Julien and G.A. Nazri, Solid State Batteries: Materials Design and Optimization, Kluwer Academic Publishers, Boston, 1994.
3. Solid State Electrochemistry (P.G. Bruce, Ed), Cambridge University Press, Cambridge, 1995.
4. Lithium Ion Batteries Fundamentals and Performace (M. Wakihara and O. Yamamoto, Eds.), Wiley-VCH, Berlin, 1998.
5. Handbook of Battery Materials (J.O. Besenhard, Ed.), Wiley-VCH, Berlin, 1999.
6. A.D. Robertson, A.R. West and A.G. Ritchie, Solid State Ionics, **104**, 1 (1997).
7. V. Thangadurai and W. Weppner, Ionics, **8**, 281 (2002).
8. V. Thangadurai and W. Weppner, J. Power Sources, in press.
9. G. Adachi, N. Imanaka and H. Aono, Adv. Mater. **8**, 127 (1996).

10. H. Aono, N. Imanaka and G. Adachi, Acc. Chem. Res. **27**, 265 (1991).
11. X. Yu, J.B. Bates, G.E. Jellison and F.X. Hart, J. Electrochem. Soc. **144**, 524 (1997).
12. J.B. Bates, N.J. Dudney, B. Neudecker, A. Ueda and C.D. Evans, Solid State Ionics **135**, 33 (2000).
13. H. Kawai, M. Nagata, H. Tukamoto and A.R. West, J. Power Sources **81-82**, 67 (1999).
14. A.F. Wells, Structural Inorganic Chemistry, 5th Edition, Clarendon Press, Oxford, 1984.
15. R.W.G. Wyckoff, Crystal Structures: Inorganic Compounds $R_x(MX_4)_y$, $R_x(M_nX_p)_y$, Hydrates and Ammoniates, vol. 3, 2nd Edition, Interscience Publishers, New York, 1960.
16. H. Hyooma and K. Hayashi, Mater. Res. Bull. **23**, 1399 (1988).
17. D. Mazza, Mater. Lett. **7**, 205 (1988).
18. V. Thangadurai, S. Adams and W. Weppner, Chem. Mater. **16**, 2998 (2004).
19. V. Thangadurai, H. Kaack and W. Weppner, J. Am. Ceram. Soc. **86**, 437 (2003).
20. V. Thangadurai, R.A. Huggins and W. Weppner, J. Power Sources **108**, 64 (2002).
21. J.T.S. Irvine, D.C. Sinclair and A.R. West, Adv. Mater. **2**, 132 (1990).
22. R.D. Armstrong and M. Todd in ref. 2. pp 264-291.
23. V. Thangadurai and W. Weppner, J. Am. Ceram. Soc. **88**, 411 (2005).
24. V. Thangadurai and W. Weppner, Adv. Funt. Mater. **15**, 107 (2005); V. Thangadurai and W. Weppner, German Patent, filed under DE 102004010 892.7.
25. J. Schwenzel, V. Thangadurai and W. Weppner, J. Powder Sources, submitted.
26. J. Schwenzel, V. Thangadurai and W. Weppner, in: New Trends in Intercalation Compounds for Energy Storage and Conversion (K. Zaghib, C.M. Julien and J. Prakash, Eds.), ECS proceedings, PV2003-20, 2003, pp. 573-583.

Reversible Intermediate Temperature Solid Oxide Fuel Cells

B.-E. Mellander[1] and I. Albinsson[2]
[1]*Department of Applied Physics, Chalmers University of Technology, S-412 96 Göteborg, Sweden*
[2]*Department of Physics, Göteborg University, S-412 96 Göteborg, Sweden*

Abstract

Intermediate temperature solid oxide fuel cells have attracted considerable attention due to their good performance at relatively low operating temperatures, 450 – 650°C. This temperature range is favourable for many reasons, the temperature is high enough for efficient catalysis, still low enough to avoid problems associated with high temperature operation. Reversible fuel cells may operate as regular fuel cells as well as electrolysers and are therefore an interesting option in applications where the demand and surplus of energy is alternating, as for example, in solar energy plants. The possibilities to use reversible intermediate temperature solid oxide fuel cells using ceria-based electrolytes are reported in this paper.

NANO-SIZE EFFECTS IN LITHIUM BATTERIES

P. BALAYA, Y. HU AND J. MAIER

Max Planck Institute for Solid State Research, D-70569 Stuttgart, GERMANY
E-mail: p.balaya@fkf.mpg.de

Apart from the reduced scale of transport lengths, enhanced surface-to-volume ratio in nanocrystals lead to a variety of exciting phenomena in the field of nano-ionics. We consider here some of those with special emphasis in the context of lithium batteries, addressing anomalies in thermodynamic, transport and storage properties: (a) Nanocrystallinity does not only lead to modifications in the cell voltage typically ≤ 100 mV due to Gibbs-Kelvin term in the chemical potential, it also affects the shape (no longer necessarily plateau) of the discharge curves in a lithium battery. (b) Nanocrystallinity also allows for a storage anomaly. RuO_2 and IrO_2 electrode materials, exhibit a high storage capacity (600 - 1130 mA h g^{-1}) with nearly 100% Columbic efficiency at the first discharge/charge cycles. (c) Nano-sized rutile exhibits remarkable electrochemical performance in up-taking 0.8 Li^+ per TiO_2 as compared to bulk rutile (which incorporates only about 0.1 - 0.25 Li^+) and showing excellent capacity retention and rate performance. (d) Apart from the enhanced storage capacity and efficiency, another important feature of nanocrystallinity is "Heterogeneous interfacial storage" explaining extra Li storage at low potential. Here, we briefly present both the experimental and theoretical results supporting this interfacial storage mechanism.

1. Introduction

Nanocrystalline materials have triggered great excitement due to both technological as well as of fundamental interest.[1-3] An often cited example is the change of thermodynamic stability, for example, the suppression of the melting point in the case of nano-sized Au particles by several hundreds of degrees which is due to the excess surface free energy of the small particles[4] according to:

$$\mu_{MX}(\text{nano}) = \mu^{\infty}_{MX} + (2\bar{\gamma}/\bar{r})v \qquad (1)$$

where, $\bar{\gamma}$ is the average surface tension, $\bar{r}$ is the average radius and v is the molar volume. While electronic materials are widely investigated at nano-size[1, 2], this is not so much the case for ionically as well as mixed conducting materials, although they play a significant role in a variety of applications such as batteries, fuel cells and sensors. Though classical in nature, nano-ionic effects are by no means less striking[3, 5-7]. In the present article, we emphasize these nano-size effects in ionic/mixed conducting materials and present few phenomena that we observed recently with special emphasis to the lithium batteries, addressing few selected anomalies in storage, thermodynamics and transport properties.

2. Thermodynamics of Nanoparticles

Energetics of nanoparticles have been well studied using calorimetric techniques, among which the excess surface enthalpy measured by molten calorimetry experi-

ments on nanoparticles of alumina and titania by the group of Navrotsky are worth mentioning.[8,9] Electrochemical e.m.f. measurements are also known to provide thermodynamic data of both excess surface enthalpy as well as entropy if measured as a function of temperature.[10,11] Our recent e.m.f. measurements on nanosized rutile particles (25 and 100 nm) in the temperature range 300 – 400°C using an electrochemical e.m.f. cell comprising of a composite of $Na_2Ti_6O_{13}$, rutile and gold powder separated by Na-ß" alumina as electrolyte - provided valuable thermodynamic information in particular of the excess surface contributions. While the reference electrode consists of 2 μm sized rutile, the working electrode contains nano-sized rutile particles of either 25 nm or 100 nm. To a first approximation the e.m.f. is related to the Gibbs free energy of coarsening through the Nernst equation by:

$$(2\bar{\gamma} / \bar{r})v = - n F E \qquad (2)$$

It has however to be pointed out that in e.m.f. method the experimentally accessible interfacial contributions stem from the electrode particles at the electrode/electrolyte interface.[10,12] A stable excess e.m.f. of about 62 mV was obtained at 350°C for the nano-sized rutile of 25 nm versus 2 μm bulk rutile which corresponds to an effective $\bar{\gamma}$ of 0.75 J m^{-2}.[13]

3. Transport Anomalies in Nanostructured Materials

In the nanocrystalline materials, owing to a largely enhanced surface-to-volume ratio, the overall electrical response may be dominated by the boundary contributions. The space charges at boundaries might refer to accumulation or depletion situations.

Epitaxial heterolayers of CaF_2/BaF_2 prepared by molecular beam epitaxy by Sata et al.,[14] have shown anomalous transport behavior with mesoscopic situation in which all the electro-neutral bulk has disappeared and the boundary layers overlap resulting in an artificial ion conductor.

Acceptor doped, ZrO_2, CeO_2 and $SrTiO_3$ ceramics are well investigated materials for the depletion situation, where the grain boundaries have been found to be positively charged and accompanied by space charge zones in which electron holes and oxygen vacancies are depleted.[15,16] Detailed impedance analysis of dense nanocrystalline $SrTiO_3$ ceramics (80 nm) in comparison to microcrystalline samples (2500 nm) gives direct and unambiguous evidence of a space charge overlap as characteristic size effect.[17] While, two relaxation times are clearly identified for the microcrystalline $SrTiO_3$ (2500 nm), in nanocrystalline $SrTiO_3$ only a single relaxation time referring to the low frequency signal remains. Thus unlike microcrystalline $SrTiO_3$ exhibiting both bulk and semi-infinite interfacial contributions to conduction, in nanocrystalline $SrTiO_3$ the bulk contribution disappears and space charge effects are observed throughout. The Debye length is deduced to be larger than the grain size, thus confirming the appearance of a mesoscopic phenomenon that the depleted space charges overlap within the grains.[17] This phenomenon is the counterpart to the accumulation layer overlap discussed above[14] but occurs at much larger spacing owing to a lack of screening (depletion of carriers) and the larger dielectric constant.

4. Lithium Batteries

Nanostructured materials are advantages for device applications that operate at temperatures that are low or moderate. In this context, nanosized materials are highly beneficial for lithium batteries that work at room temperature. Let us now discuss a few phenomena related to nanocrystallinity that are relevant to lithium batteries.

4.1 Anomalous Energy storage

Rechargeable Li ion batteries are key components of modern portable electronic devices. Commercial rechargeable Li ion battery which uses rocking chair cell[18,19] with $LiCoO_2$ and C as the positive and negative electrodes respectively has the advantages of both excellent cyclic performance and coulombic efficiency (exceeding 95%). However, such a homogeneous storage process suffers from low storage capacity resulting in a low energy density (~ 150 W h kg^{-1}). Most of today's high-performance portable microelectronic devices demand a high energy density. In this context, high lithium storage has been achieved in several transition metal oxide compounds (CoO, NiO, FeO, Cr_2O_3 etc.,) using a reversible heterogeneous reaction[20] that involves conversion of oxides to a composite of metal and Li_2O at nano-size on incorporation of Li. Apart from oxides, this heterogeneous conversion reaction has also been reported in fluorides, such as TiF_3, VF_3, FeF_2, *etc.* [21-23] Although an enhanced Li storage capacity (in the range 800-1200 mA h g^{-1}) has been achieved through conversion reaction in the above cited materials, the reversible capacity (coulombic efficiency) during first cycle is only about 70 – 80 %, while remaining 20-30% of lithium is lost permanently within the Li_2O host matrix.

We have shown that RuO_2 as an exceptional material exhibits not only high lithium storage capability but nearly 100% coulombic efficiency.[24] Fig. 1 shows the reversible Li storage in a RuO_2/Li electrochemical cell using nano-sized (100 nm) as well as micro-sized (10 μm) RuO_2. During first discharge, three distinct regions (a, b and c) are observed for 100 nm sized RuO_2. The first short plateau (a) appears at 2.1 V due to insertion of Li into RuO_2, the second plateau (b) occurs at 0.9 V due to the conversion reaction forming Ru/Li_2O nanocomposite in the size range 2- 5 nm while the third sloped region (c) is an extra storage of Li due to the formation of a Li-containing solid electrolyte interface (SEI) and the interfacial storage discussed later. Thus high Li storage of ~ 1130 mA h g^{-1} has been achieved due to the incorporation of 5.6 Li^+ at a rate of C/20. Furthermore, virtually all Li^+ ions can be extracted out in the case of 100 nm RuO_2 corresponding to a nearly 100 % coulombic efficiency at the first cycle. It may be noted that RuO_2 exhibits very high electronic conductivity (σ_{eon})[25] and reasonably high Li diffusivity.[26] Moreover, the preliminary thermogravimetric measurements on RuO_2 suggest that it is relatively easy to introduce non-stoichiometry within RuO_2 providing an indirect indication of high oxygen diffusion. Thus, achieving a complete reversibility through complex heterogeneous solid-state electrochemical reactions is believed to be due to the formation of nanoscale Ru/Li_2O (2-5 nm) composites during Li incorporation and nano-RuO_2 (2-5 nm) during Li excorporation, in addition to the favorable transport properties of RuO_2 itself.

Micro-sized RuO_2 exhibits similar electrochemical behavior as seen from Fig. 1; however, the first plateau occurs at 1.1 V, that is the insertion reaction at a rate of C/20 seems to be too sluggish for 10 μm RuO_2 and occurs at 1.1 V due to polarization. On discharge at a rate of C/200, the first plateau occurs at 1.5 V, revealing the kinetic problem of the incorporation of Li into 10 μm RuO_2. Owing to high σ_{eon} insertion is limited by the Li^+ conductivity. It is worth mentioning that the conversion reaction occurs at the same potential in both samples and a complete extraction of Li has been achieved in both nano- and micron- sized RuO_2

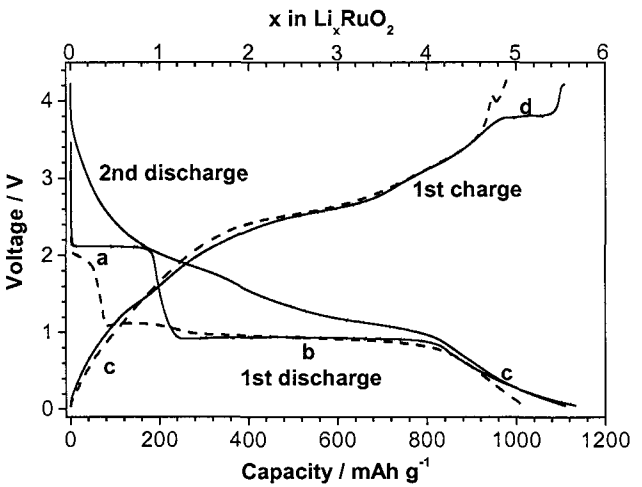

Figure 1. Electrochemical discharge/charge curves for the RuO_2/Li cell. Solid lines refer to 100 nm grain size, while the dashed line refers to 10 μm RuO_2. Note that the grain size of RuO_2 during second discharge (solid line) is around 5 nm.[24]

Electrochemical performance of IrO_2 having similar rutile structure as that of RuO_2 is investigated in the same voltage window (0 – 4.3V). Both RuO_2 as well as IrO_2 exhibit nearly the same order of electronic conductivity,[25] and the insertion reaction is reported to occur nearly at the same potential (2.1 V).[27] Fig. 2 shows the discharge/charge curve for IrO_2 of 10 μm particles with a porous structure resulting in rod shaped grains of 100x400 nm. Such a mesoporous IrO_2 exhibits a high Li storage of ~ 650 mA h g^{-1} upon incorporation of 5.4 Li. Analogous to RuO_2, the incorporation of Li^+ into IrO_2 involves three regions: first, plateau (a) due to insertion of Li into IrO_2, second, plateau (b) due to conversion reaction forming Ir/Li_2O nanocomposites and third, the slope region (c) due to extra Li storage. No alloy reaction between Li and Ir has been observed. As seen from Fig. 2 and, unlike RuO_2, during charging only about 74 % of Li could be extracted from the Ir/Li_2O nanocomposite. The first plateau due to the incorporation of Li into IrO_2 indeed occurs at 1.3 V much below the expected potential of 2.1 V. However, upon incorporation at a slow rate, the insertion occurs at a slightly higher potential of 1.6 V (not shown in Fig. 2).

Comparison of the insertion of Li^+ into RuO_2 and IrO_2 indicates that the incorporation reaction requires sufficient ion conductivity (σ_{con}). The fact that only 74 % of Li could be extracted from IrO_2 indicates a sluggish mass transport within IrO_2. By introducing oxygen non-stoichiometry into IrO_2 intentionally through appropriate heat treatment under reduced atmosphere, extraction of Li^+ was achieved to nearly 100% from Ir/Li_2O nanocomposite, indicating the importance of oxygen transport during the reversible reaction.

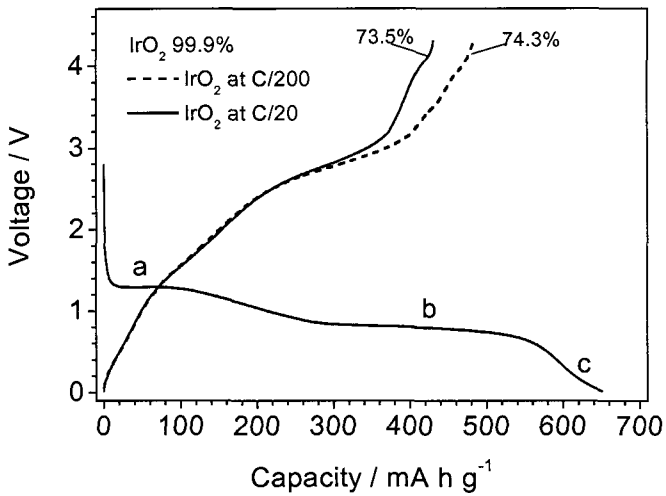

Figure 2. Discharge and charge curves for IrO_2/Li cell. Note that the Coulombic efficiency increases on charging with slow rate.

4.1 *Cell Voltage and Shape of the Curve*

Nano-size results in an excess cell voltage that can be estimated by Eqn. 1. For a grain size of 1 nm, $\bar{\gamma}$ being ~ 0.1 J m^{-2} and v, the molar volume assumed to be 25 cm^3 $mole^{-1}$, the cell voltage may be modified by about 100 mV.[28]

In general, different storage mechanisms will result in different charging/discharging curves during conversion reaction. Since these curves usually are affected by overpotentials due to kinetic reasons, we assume here that the charging rates are very small, such that the curves can be considered on a thermodynamic basis. We may expect three storage mechanisms: (i) homogeneous insertion of Li into bulk. The corresponding charge/discharge curve will be slightly sloped due to the entropy part and the interaction terms of the Li chemical potential (anomalies are possible due to structural transitions). (ii) As the saturation limit is reached, the conversion reaction takes place, where the charge/discharge curve is flat. A non-vanishing slope (see the second discharge of RuO_2 in Fig. 1) occurs due to nano-size effects according to Eqn. 1. (iii) After the completion of the conversion reaction, a further storage is possible due to the presence of interfaces. This storage mechanism, which will be explained in the next section, yields a capacitor like charging/discharging behavior.

Note again the consequences of the Gibbs-Kelvin Term for the Li chemical potential (v_{Li} is the partial volume of Li in LiX):

$$\mu_{Li}(\bar{r}) = \mu_{Li}^{\infty} + 2(\frac{\bar{\gamma}(\bar{r})}{\bar{r}})v_{Li} \qquad (3)$$

Not only does a variation of $\bar{\gamma}$ and $\bar{r}$ with Li content explain variation in the slope of the discharge/charge curve in macroscopically non-variant situations, Eqn. (3) also predicts, according to a constancy of $\mu_{Li}(\bar{r})$ within the nanocrystalline electrode, a composition distribution in the grain ensemble as a consequence of the grain size distribution. [28]

4.3 Interfacial Storage

A recent striking observation in M/Li_2O nanocomposites (where M means transition metals such as Co, Cu, Fe, Ni, Mo, *etc.*, that do not alloy with Li) investigated for rechargeable Li batteries, is the occurrence of an extra Li storage at low potential.[20,29] To make this point clear let us recall the storage behavior of the RuO_2 electrode material. As mentioned earlier, incorporation of 4Li per RuO_2 formula unit leads to the formation of a Ru/Li_2O nanocomposite with crystallite sizes of 2-5 nm.[24] Further incorporation (up to 5.6Li per RuO_2) results in a sloped behavior. On charging, if the voltage is limited between 0.02-1.2 V (as the slope ends at 1.2 V), a reversible Li-storage capacity of 120 mA h g^{-1} is observed at a slow rate (i.e. discharge in 45 min.) with a capacitive behavior.[30] A storage capacity of 70 mA h g^{-1} was achieved at a fast rate (*i.e.* discharge in 1.3 min.) within this voltage window. A similar behavior observed in the Co/Li_2O nanocomposite at low potential has been tentatively explained by a reaction of Li with the conducting-type polymer film formed *in situ*.[29] However, at least in the case of Ru/Li_2O nanocomposite, it is clear from the high resolution transmission electron microscope images[24] that the passivation layer mainly decomposes on charging beyond the sloped region (1.2 V). This observation and the fact that the storage can occur even at a fast rate suggest that the extra Li-storage is due to a process that is different from the homogeneous insertion and heterogeneous conversion reactions. Another explanation given in the literature[31] is the segregation of metal at the grain boundaries/interface and subsequent alloy reaction of metal with the incorporated Li. This possibility is, however, unlikely in the case of the Ru/Li_2O nanocomposite, as no alloy reaction has been known between Ru and Li metals.

In Ref. [28], a Heterogeneous interfacial charge storage mechanism was proposed to explain the origin for this anomaly. As shown in Fig. 3 according to this model, Li^+ ions are stored on the oxide's side of the interface while electrons (e^-) are localized on the metallic side resulting in a double layer storage. If the spacing of the interface is of the order of the screening length the difference between a capacitor and a battery is blurred.

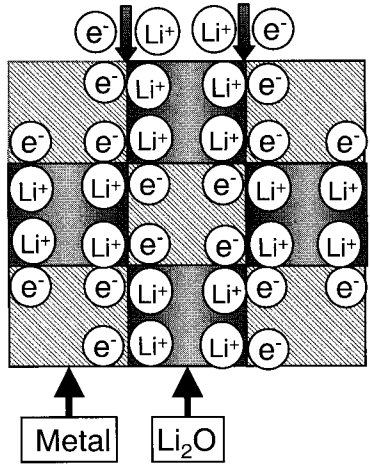

Figure 3. Schematic representation of the interfacial lithium storage.

In order to check these ideas, in Ref. [30] *ab initio* hybrid DFT-HF B3PW calculations were performed for the Li_2O/Ti interface. Although it is known that TiO_2 cannot be electrochemically reduced to metal, the Li_2O/Ti interface has been chosen here as a *model* interface mainly due to a proper lattice matching and absence of irregular structures and steps at the interface. The Li_2O/Ti interface is modeled by a slab infinite in two dimensions and containing six (111) planes of Li_2O, in contact with one or two Ti (0001) planes.

Different positions of inserted Li atoms have been considered: positions at the slab surface opposite to the Ti/Li_2O interface, positions at octahedral interstitial sites inside the slab, and finally at the interface between Ti and Li_2O slab. Self-consistent calculations in this special case show a considerable electron transfer from excess Li atoms towards Ti atoms if it is close to the interface, providing evidence for the interfacial lithium storage.[30]

4.4 Lithium storage in nano-sized rutile TiO_2

Amongst the transition metal oxides, nanostructured TiO_2 has been widely investigated for Li insertion because it is not only a low-voltage insertion host for Li, but also a fast Li insertion/extraction host, which renders it a potential anode material for high-power Li-ion batteries.[32-35] Fig. 4 presents, the electrochemical behavior (lithium insertion/extraction) of rutile with different particle sizes and shapes. The difference in Li insertion between the micro- and nano-sized rutile is evident. For all the micrometer-sized particles, only a small degree of Li insertion (0.1-0.25 mol) into rutile was observed, as it is typical for micro-sized rutile.[35] In contrast, in the case of nano-sized rutile, a substantially higher amount of 0.8 mol Li can be inserted in the first discharge process, and about 0.5 mol Li can be reversibly inserted/extracted in the subsequent discharge/charge processes. This major difference in the electrochemical behavior of nano- and micro-sized rutile is explained by the small diffusion length and the anisotropy of mass transport.

Fig. 5 in which cycling was carried out at a rate of C/20 between voltage limits of 1 and 3 V, shows an irreversible capacity in the first discharge and charge process, which was also observed for anatase,[32] or TiO_2-B nanowire,[36] and is not fully understood so far. However, after the first cycle, the coulombic efficiency is above 98% and thereafter the retention of capacity on cycling is excellent, which can be ascribed to the stability of the morphology and the better accommodation of the structural changes at nano size. Another excellent property of this nano-sized rutile is the high rate capability. Results are shown in Fig. 5 in which rates of up to 30C have been employed. The cell was first cycled at C/20 and, after 50 cycles, the rate was increased in stages to 30C. A specific charge capacity of around 160 mA h g^{-1} was obtained at a rate of C/20 after 50 cycles; this value is lowered to 150 mA h g^{-1} at C/5, 132 mA h g^{-1} at 1C, 110 mA h g^{-1} at 5C, 100 mA h g^{-1} at 10C, 81 mA h g^{-1} at 20C, and finally, 70 mA h g^{-1} at 30C. As far as titania is concerned, this seems to be the best rate performance especially at higher rate.[37] This high rate capability results from the transport advantages of this special nanostructure, such as shorter transport lengths for both electronic and Li^+ transport as well as a higher electrode/electrolyte contact area.

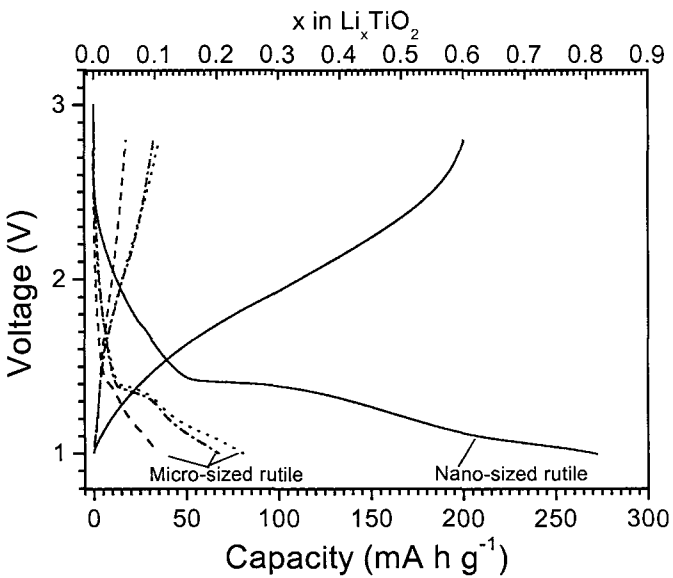

Figure 4. Voltage profiles of rutile electrodes with different particle sizes and shapes cycled between 1 and 2.8 V (Ref. 37).

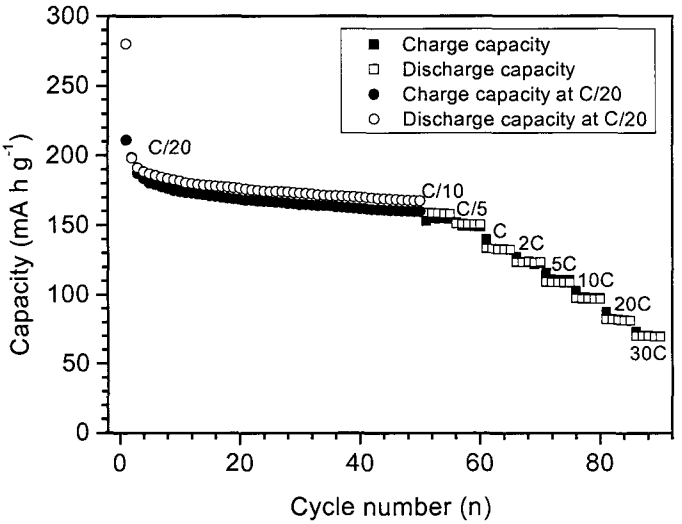

Figure 5. Variation in discharge/charge capacity versus cycle number for nano-sized rutile electrode cycled at C/20, C/10, C/5, 1C, 2C, 5C, 10C, 20C, and 30C between voltage limits of 1 and 3 V. (Ref. 37)

5. Conclusions

In this article, we have discussed different anomalous phenomena due to nano-size effects. The emerging field of nano-ionics is relevant not only for fundamental science, but also important for technological applications. It is shown that the nanocrystalline electrodes exhibit both high storage capacity as well as high coulombic efficiency and in some cases high rate performances. An interfacial lithium storage mechanism which is a consequence of nanocrystallinity has been discussed to explain the extra storage at low potential in metal/Li_2O nanocompoites.

Acknowledgements

Authors thank E.A. Kotomin, Yu. F. Zhukovskii, J. Jamnik, H. Li and Yu. Guo Guo for useful discussions.

References

1. F. Rosei, *J. Phys. Condens. Matter.* **16**, S1373 (2004).
2. E. L. Brus, *J. Chem. Phys.* **80,** 4403 (1984).
3. J. Maier, *Nature Mater.* **4,** 805 (2005).
4. Ph. Buffat, J.-P. Borel, *Phys. Rev. A* **13**, 2287 (1976).
5. J. Maier, *Prog. Solid St. Chem.* **23**, 171 (1995).
6. H. L. Tuller, *Solid State Ionics* **131**, 143 (2000).
7. J. Schoonman, *Solid State Ionics* **135**, 5 (2000).
8. M. R. Ranade et al., *PNAS* **99,** 6476 (2002).

9. J. M. McHale, A. Auroux, A. J. Perrota and A. Novrotsky, *Science* **277,** 788 (1997).
10. P. Knauth, G. Schwitzgebel, A. Tschöpe and S. Villain, *J. Solid State Chem.* **140,** 295 (1998).
11. K. T. Jacob, K. P. Jayadevan, R. M. Mallya and Y. Waseda, *Adv. Mater.* **12**, 440 (2000)
12. A. Schroeder, J. Fleig, D. Gryaznov, J. Maier and W. Sitte, *J. Phys. Chem.B (2006, submitted)*
13. P. Balaya and J. Maier, *in preparation*
14. N. Sata, K. Eberman, K. Eberl and J. Maier, *Nature* **408**, 946 (2000).
15. I. Denk, J. Claus and J. Maier, J. *Electrochem. Soc.* **144**, 3526 (1997).
16. R. A. De Souza, J. Fleig, J. Maier, O. Kienle, Z. Zhang, W. Sigle and M. Rühle, *J. Am. Ceram. Soc.* **86**, 922 (2003).
17. P. Balaya, J. Jamnik, J. Fleig and J. Maier, *Appl. Phys. Lett.* **88,** 062109 (2006).
18. M. B. Armand, in *Materials for Advanced Batteries* (Proc. NATO Symp. Materials Adv. Batteries). Eds. D.W. Murphy, J. Broadhead, and B.C.H. Steele, Plenum, New York, 145-161 (1980).
19. K. Mizushima, P.C. Jones, P. J. Wiseman, and J. B. Goodenough, *Mater. Res. Bull.* **15**, 783 (1980).
20. P. Poizot, S. Laruelle, S. Grugeon, L. Dupont, and J. -M. Tarascon, *Nature* **407**, 496 (2000).
21. H. Li, G. Richter and J. Maier, *Adv. Mater.* **15**, 736 (2003).
22. H. Li, P. Balaya and J. Maier, *J. Electrochem. Soc.* **151**, A1878 (2004).
23. F. Badaway, N. Pereira, F. Cosandey and G. G. Amatucci, *J. Electrochem. Soc.* **150**, A1209 (2003).
24. P. Balaya, H. Li, L. Kienle and J. Maier *Adv. Func. Mater.* **13**, 621 (2003).
25. N. Tsuda, K. Nasu, A. Fujimori and K. Siratori, Electronic conduction in oxides, Springer, Second edition, 2000.
26. M. Armand, F. Dalard, D. Deroo and C. Mouliom, *Solid State Ionics* **15**, 205 (1985).
27. D. W. Murphy, F.J. Di Salvo, J.N. Carides and J. V. Waszczak, *Mat. Res. Bull.* **13**, 1395 (1978).
28. J. Jamnik and J. Maier, *Phys. Chem. Chem. Phys.* **5,** 5215 (2003).
29. S. Laruelle, S. Grugeon, P. Poizot, M. Dolle, L. Dupont and J. -M. Tarascon, *J. Electrochem. Soc.* **149**, A627 (2002).
30. Yu. Zhukovskii, P. Balaya, E. Kotomin and J. Maier, *Phys. Rev. Lett.* **96**, 058302 (2006).
31. L. Y. Beaulieu, D. Larcher, R.A. Dunlap and J.R. Dahn, *J. Electrochem. Soc.* **147**, 3206 (2000).
32. G. Sudant, E. Baudrin, D. Larcher and J. -M. Tarascon, *J. Mater. Chem.* **15**, 1263 (2005).
33. M. Wagemaker, A. P. M. Kentgens and F. M. Mulder, *Nature*, **418**, 397 (2002).
34. L. Kavan, M. Grätzel, S. E. Gilbert, C. Klemenz and H. J. Scheel, *J. Am. Chem. Soc.*, **118**, 6716 (1996).
35. L. Kavan, D. Fattakhova and P. Krtil, *J. Electrochem. Soc.* **146**, 1375 (1999).

36. R. Armstrong, G. Armstrong, J. Canales, R. Garcia and P. G. Bruce, *Adv. Mater.*, **17**, 862 (2005).
37. Y. -S. Hu, L. Kienle, Y. -G. Guo and J. Maier, *Adv. Mater.* in press (2006)

ELECTROCHROMICS: FUNDAMENTALS AND APPLICATIONS

C. G. GRANQVIST

Department of Engineering Sciences, The Ångström Laboratory, Uppsala University, P. O. Box 534, SE-75121 Uppsala, Sweden
E-mail: claes-goran.granqvist@angstrom.uu.se

A. AZENS

ChromoGenics Sweden AB, Märstagatan 4, SE-75323 Uppsala, Sweden
E-mail: andris.azens@chromogenics.se

Electrochromic (EC) materials are able to change their optical properties, persistently and reversibly, under insertion/extraction of ions and electrons. When integrated in solid state devices, they can be used for a variety of applications such as energy efficient "smart windows" in buildings and vehicles, visors and goggles, displays, *etc.* This paper summarizes some recent work with special emphasis on nano features of EC materials and devices.

1. Introduction

Modern Man normally spends some 90 % of his time inside buildings and vehicles. The quality of the indoor environment hence is of the greatest importance, and more and more energy is used to maintain it at a level that is both comfortable and healthy. Looking at the EU, some 40 % of the energy supply is used for heating, cooling, ventilation, and lighting of buildings, as well as for appliances; in financial terms this corresponds to some 4 % of the Gross National Product.[1,2]

The purpose of this article is to emphasize that new solid state ionic nanomaterials offer a number of attractive alternatives to employ solar energy for maintaining a benign indoor environment. More specifically, we consider heating, cooling, lighting, and visual contact between indoors and outdoors, which calls for "smart windows" capable of changing their throughput of visual light and solar irradiation by utilizing electrochromic (EC) materials characterized by specific nanostructures, thereby avoiding excessive solar heating while taking advantage of this heating when there is a need for such.[3,4] Other nanomaterials, which lie outside the scope of this article, include cheap nanomaterials-based sensors for air quality used to accomplish

energy efficient "ventilation on demand", and nano-structured photo-catalysts that can be used for solar-energy-related air cleaning[5] and consequently reduced ventilation. Most of the results summarized below are from recent work by the authors and their collaborators, as apparent from the citations to the various publications.

2. Electrochromics for Energy Efficient "Smart Windows": Device Design and Materials

Figure 1 shows a prototype of a "smart window" with four 30 x 30 cm^2 EC foils[4,6,7] mounted between glass panes. The upper two panels are fully colored while the lower two are fully bleached. Each of the panels can shift gradually and reversibly between the dark and transparent states in about a minute, *i.e.*, during the time it takes for the human eye to adapt to different lighting conditions. It is important to note that the window maintains its primary function—that of providing unmitigated visual indoors/outdoors contact—irrespective of the state of coloration. The windows cannot give privacy, though.

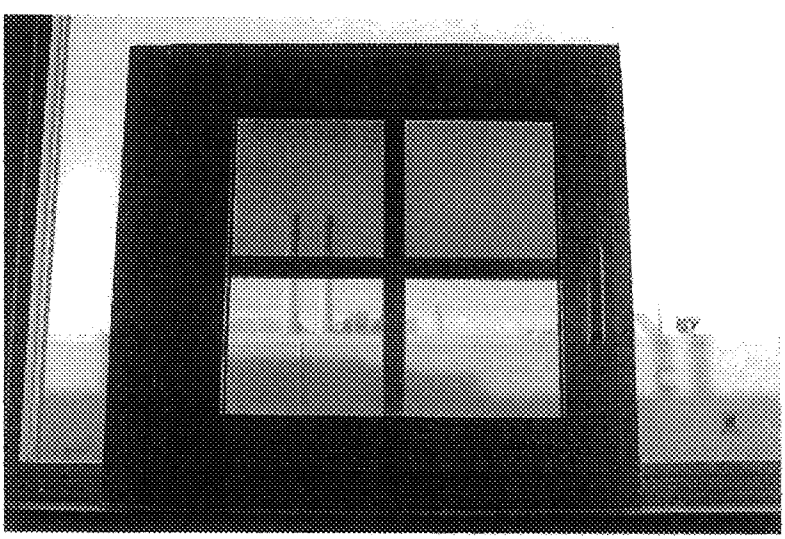

Fig. 1. Smart window prototype with four 30 x 30 cm^2 panels.

The EC "smart window" exhibits some resemblance to a thin-film electrical battery, as evident from Fig. 2. The device has five superimposed layers on a transparent substrate, typically of glass or flexible polyester foil, or positioned between two such substrates in a laminate configuration.[3] The outer-

most layers are transparent electrical conductors, typically of In_2O_3:Sn (*i.e.*, Indium Tin Oxide, ITO).[8] One of these layers is coated with an EC film, whereas the other is coated with an ion storage film, with or without EC properties. Both of these films must comprise nanomaterials characterized by well specified nano-porosities. A transparent ion conductor (electrolyte) is at the middle of device and joins the EC and ion storage films. A voltage pulse applied between the transparent electrodes leads to charge being shuttled between the EC and ion storage films, and the overall transparency is thereby changed. A voltage pulse with opposite polarity—or, with suitable material combinations, short circuiting—makes the device regain its original properties. The optical modulation requires a DC voltage of as little as 1 to 2 V. The charge insertion into the EC film(s) is balanced by electron inflow from the transparent electrode(s); these electrons can make intervalency transitions (*i.e.*, yield polaron absorption), which constitutes the basic reason for the optical absorption.

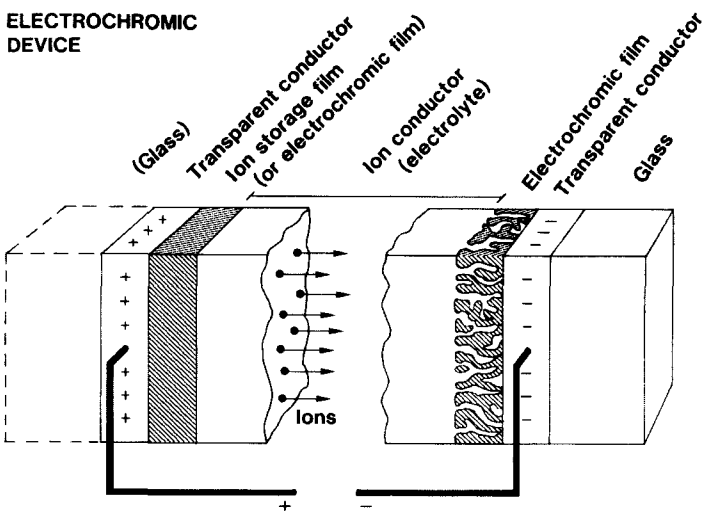

Fig. 2. Prototype EC device, showing transport of positive ions under the action of an electric field. From Ref. 3.

Regarding materials in EC devices, the ITO can be replaced by ZnO:Al, SnO_2:F, or similar oxides.[9,10] The global availability of In is larger than is sometimes anticipated,[11] and ITO may well be the option even for large-scale production of EC-based "smart windows". The EC film is WO_3-based in

almost all devices for window applications, whereas there are many possibilities for the counter electrode.[3,12,13] Among the latter, films based on IrO_2 and NiO have enjoyed much interest recently. IrO_2-based alternatives are inherently expensive, but good EC properties are maintained after dilution with cheaper Ta_2O_5.[14] Figure 3 shows a high-resolution transmission electron micrograph of an IrO_2 film from which a well defined nanostructure with nanometer-sized crystallites is apparent;[15] films containing Ta displayed a more fine-grained structure. NiO-based films combine moderate cost with excellent optical properties, especially when the NiO is mixed with another oxide characterized by a wide band gap such as MgO or Al_2O_3.[16] EC devices can use many different electrolytes, either being hydrous oxides exhibiting proton conduction or polymers with ion conduction due to added salts.

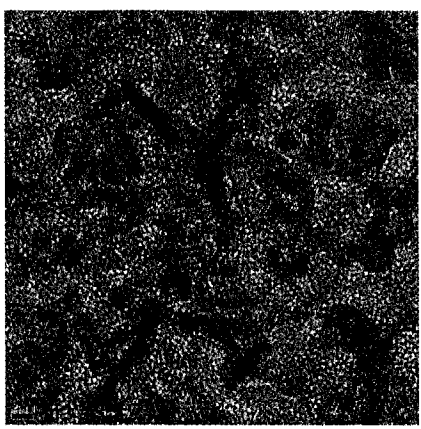

Fig. 3. High-resolution transmission electron micrograph of an IrO_2 film made by reactive magnetron sputtering. From Ref. 15.

EC devices have been discussed a long time, ever since the display-type devices presented shortly after the discovery of electrochromism in WO_3 films.[17] Generally speaking, the progress of technologies based on electrochromism has been slow, which may be associated with the necessity of simultaneously mastering a range of non-conventional technologies as follows: (*i*) the ITO must combine excellent electrical conductivity with very low optical absorption, which is challenging in particular for films on temperature sensitive substrates such as polyester; (*ii*) the EC and counter electrode films must exhibit well specified nano-porosities over large areas, which require non-standard coating technologies; (*iii*) viewing the EC device as a

type of "thin film battery", it is evident that charge insertion/extraction and charge balancing must be accomplished by properly controllable and industrially viable techniques, such as gas treatments;[18] (*iv*) the electrolyte must combine good ion conductivity with adhesiveness and high transparency for ultraviolet irradiation; and (*v*) long-term cycling durability demands adequate strategies for voltage and current control during coloration/bleaching—just as it does for charging/discharging of batteries. All of these challenges can be successfully met, however, and EC technology finally may emerge as a technology for large-area, large-scale applications.[19]

Film porosity on the nano scale is necessary, as stressed above. Virtually any thin film technology may be capable of achieving the desired properties, though with more or less difficulty. Regarding sputtering, the deposition parameters should be confined to those giving "zone 1" films in the well known "Thornton diagram".[20] The specific nano-topography then accomplished has been referred to as "parallel penniform" at least in the case of some TiO_2 films.[21] Figure 4 shows a cross-sectional image of such a film. The combination of large internal surface and contiguity makes this structure ideally suited for applications in electrochromics as well as in other types of solid state ionic devices.

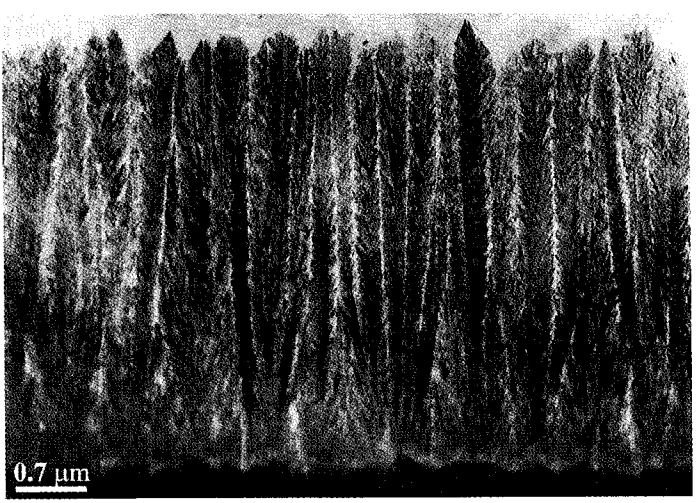

Fig. 4. High-resolution transmission electron micrograph of a cross section through a TiO_2 film made by reactive DC magnetron sputtering. From Ref. 21.

3. Device Data and Energy Efficiency

Figure 5 shows characteristic data for a 5 x 5 cm^2 flexible EC foil incorporating WO_3, NiO modified by addition of a wide band gap oxide such as MgO or Al_2O_3, PMMA-based electrolyte, and ITO films.[6,7] The mid-luminous transmittance (T_{550}, where the subscript denotes the wavelength in nanometers) rapidly attains ~68 % upon bleaching and drops to ~36 % during a coloration period of 50 s. Still lower values can be reached with extended coloration times. The modulation is smaller, but still significant, for blue light (T_{400}) whereas it is larger for red light (T_{775}). The substantial transmittance at the ultraviolet end of the spectrum is associated with the oxide added to the NiO. Durability was manifest for several tens of thousands of coloration/bleaching cycles. The open circuit memory is excellent, and the optical properties are maintained virtually unchanged for many hours.

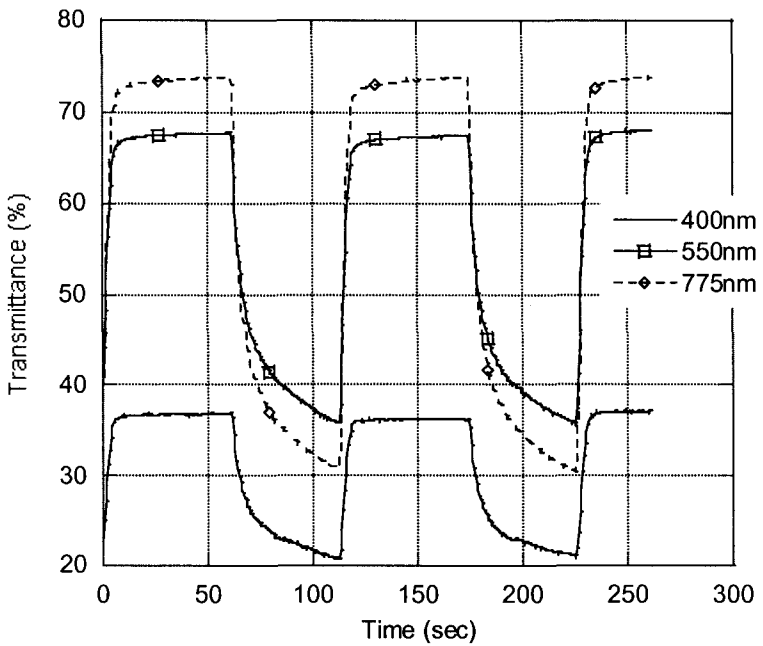

Fig. 5. Time-dependent transmittance during coloration/bleaching of an EC device, recorded at three wavelengths.

The energy efficiency inherent in the "smart windows" technology has been difficult to come to grips with, partly since the most fundamental function of a window or glass façade—that of providing unmitigated visual contact between indoors and outdoors—has not always been fully appreciated. From a strict energy perspective, it may be beneficial to eliminate the windows entirely, but this is highly detrimental to the wellbeing and working efficiency of the persons using the building, who normally would rather prefer a panoramic view of their ambience. Energy efficiency of the windows hence must be reached with a full understanding of their need to provide transparency.

A "back-of-an-envelope-analysis" of the energy efficiency[22] can be made by first setting the solar energy falling onto a vertical surface per year to 1000 kWh/m^2. This represents a nominal value, and more correct numbers for South-facing/North-facing/horizontal surfaces are 850/350/920,1400/450/1700, and 1100/560/1800 kWh/m^2 for Stockholm (Sweden), Denver (U.S.A.), and Miami (U.S.A.), respectively. Half of this, *i.e.*, 500 kWh/m^2, is visible light. This latter number is used in the analysis since infrared radiation can be eliminated—at least in principle—by use of known technology for "solar control" that does not require variable transmittance.[9,10] If the transparency can be altered between 7 and 75 %[22]—which is by no means unlikely given further EC technology development—the difference between having the window constantly colored and constantly bleached is 340 kWh/m^2. Actually, the stated range of optical modulation can be accomplished already today,[22] but at the expense of slow coloration dynamics and some degradation under extended cycling.

The next issue is then to contemplate when the "smart window" should be colored and when it should be bleached. With physical presence of persons as the basis of the control strategy, the question is when a room is in use—or, more precisely, the fraction of the solar energy that enters when nobody is present. Considering that a normal (office) room is empty during vacations, holidays and weekends, early mornings and late afternoons (when the sun stands near the horizon), *etc.*, it may be a conservative estimate that 50 % of the energy enters when no one is present to look through the window. This estimate then yields that 170 kWh/m^2 is the amount of energy *saved* annually by adopting the given control strategy. In order to answer the question whether this savings is significant or not, one can note that 17 % is a typical value for today's best thin-film solar cells and sub-modules.[23] Thus these solar cells would be able to *generate* 170 kWh/m^2 if they were to replace the "smart window" in the example. Clearly the analogy between energy savings in "smart windows" and energy generation in solar cells is not

tied to the choice of the incident solar energy being 1000 kWh/m^2 but applies generally irrespectively of the orientation of the surface under examination. The "smart window" saves thermal energy, but if a cooling machine for providing comfort cooling—operating with an efficiency of 300 %, say—runs on electricity generated with an efficiency of 33 % then the analogy becomes perfect. This latter consideration implies that one employs a "national scenario" for the energy, with a "Coefficient-of-Performance" ("COP-factor") equal to unity.

A complementary view on the energy efficiency of "smart windows" can be reached from building simulations, which have been completed recently.[24,25] Specifically, calculations for a standard office module with well defined size, window area, lighting demand, occupancy, equipment, *etc.*, showed that the energy savings potential was considerable for the cooling load. The studied office block was oriented with one façade facing South and one facing North, and the simulations were performed with climate data applicable to Rome (Italy), Brussels (Belgium), and Stockholm (Sweden). When using "smart windows" instead of conventional static solar control windows, the energy for space cooling, on an annual basis, could be reduced by as much as 40 to 50 %. The amount of saved energy is obviously climate dependent. In moderately warm climates, such as those of Brussels and Stockholm, the number of days with very high outdoor temperatures is relatively small but the energy required for balancing excessive solar energy inflow nevertheless is substantial, and an interesting result of the simulations was that the cooling power could be reduced so that air conditioning may be completely avoided when "smart windows" are used, thus indicating that the additional cost for "smart windows" can be more than balanced by the elimination of an air conditioning system. Similar analyses can be made with regard to vehicles.[26]

Irrespectively of the analysis being intuitively based or rooted in elaborate energy simulations, the energy efficiency is very significant and the "smart windows" technology stands out as a very important one for alleviating our current dependence on non-renewable energy resources. But there are other assets of relevance as well. Thus the ability to change the transparency at will makes it possible to create an ambience with enhanced indoor comfort, characterized by less glare and thermal stress, when the room is in use. Lowered electrical lighting is another interesting possibility.[27]

References

1. M. Santamouris, in: *Solar Energy: The State of the Art*, J. Gordon (Ed.), James & James Sci. Publ., London, UK, 2001, pp. 1-28.

2. C. F. Reinhart, in: *The Future for Renewable Energy 2*, James & James Sci. Publ., London, UK, 2002, pp. 79-114.
3. C. G. Granqvist, *Handbook of Inorganic Electrochromic Materials*, Elsevier, Amsterdam, The Netherlands, 1995 (reprinted 2002).
4. G. A. Niklasson and C. G. Granqvist, *J. Appl. Phys.*, submitted.
5. A. Fujishima, K. Hashimoto and T. Watanabe, *TiO_2 Photocatalysis*, Bkc, Tokyo, Japan, 1999.
6. A. Azens, G. Gustavsson, R. Karmhag and C.G. Granqvist, *Solid State Ionics* **165**, 1 (2003).
7. A. Azens, A. Avendaño, J. Backholm, L. Berggren, G. Gustavsson, R. Karmhag, G. A. Niklasson, A. Roos and C. G. Granqvist, *Mater. Sci. Engr.* **B 119**, 214 (2005).
8. C. G. Granqvist and A. Hultåker, *Thin Solid Films* **411**, 1 (2002).
9. C. G. Granqvist, in: *Materials Science for Solar Energy Conversion Systems*, C. G. Granqvist (Ed.), Pergamon, Oxford, UK, 1991, pp. 106-167.
10. K. G. T. Hollands, J. L. Wright and C. G. Granqvist, in: *Solar Energy: The State of the Art*, J. Gordon (Ed.), James & James Sci. Publ., London, UK, 2001, pp. 29-107.
11. U. Schwartz-Schampera and P. M. Herzig, *Indium: Geology, Mineralogy, and Economics*, Springer, Berlin, Germany, 2002.
12. C. G. Granqvist, *Solar Energy Mater. Solar Cells* **60**, 201 (2000).
13. C. G. Granqvist, E. Avendaño and A. Azens, *Thin Solid Films* **442**, 201 (2003).
14. J. Backholm, A. Azens and G. A. Niklasson, *Solar Energy Mater. Solar Cells* **90**, 414 (2006).
15. J. Backholm and E. Coronel, unpublished.
16. E. Avendaño, A. Azens, G. A. Niklasson and C. G. Granqvist, *Solar Energy Mater. Solar Cells* **84**, 337 (2004).
17. S. K. Deb, *Solar Energy Mater. Solar Cells* **39**, 191 (1995).
18. A. Azens, L. Kullman and C. G. Granqvist, *Solar Energy Mater. Solar Cells* **76**, 147 (2003).
19. C. G. Granqvist, *Nature Mater.* **5**, 89 (2006).
20. J. A. Thornton, *Ann. Rev. Mater. Sci.* **7**, 239 (1977).
21. J. Rodríguez, M. Gómez, J. Lu, E. Olsson and C. G. Granqvist, *Adv. Mater.* **12**, 341 (2000).
22. A. Azens and C. G. Granqvist, *J. Solid State Electrochem.* **7**, 64 (2003).
23. M. A. Green, K. Emery, D. L. King, S. Igari and W. Warta, *Progr. Photovoltaics: Res. Devel.* **13**, 49 (2005).
24. A. Roos, M.-L. Persson, W. Platzer and M. Köhl, in: *Proc. Glass Processing Days*, Tampere, Finland, 2005, pp. 566-569.
25. M.-L. Persson and A. Roos, to be published.
26. N. I. Jaksic and C. Salahifar, *Solar Energy Mater. Solar Cells* **79**, 409 (2003).
27. E. S. Lee and D. L. DiBartolomeo, *Solar Energy Mater. Solar Cells* **71**, 465 (2002).

ELECTROCHEMICAL CO_2 GAS SENSORS

K. SINGH

Department of Physics, RTM Nagpur University, Nagpur-440033, INDIA
e-mail: msrl1@hotmail.com

Gas sensors has been currently in great demand due to serious concern over environmental pollution and public health considerations resulting from tremendous growth of industrialization. Concurrently, there have been continuous efforts to obtain sensors with improved performance. This article presents the factors contributing towards a gradual development of electrochemical solid-state gas sensors in terms of a continuous tailoring of its two basic components i. e., solid electrolyte and reference electrode. Particularly, the conductivity data of optimized carbonate based solid electrolytes indicated about three orders of magnitude enhancement in conductivity due to glass dispersion. The sensor performance of glass as well as ferroelectric dispersed composite electrolytes is better than mono-phase.

1. Introduction

Today the whole world is in the grip of global warming, ozone layer depletion, acid-rain and toxicity resulting from various gaseous pollutants released by tremendously grown industries, automobiles and homes.

Most industrial processes and their safety as well as operability in turn the economic performance depend substantially on how perfectly they have been controlled. Therefore, significant incentives exist to either employ controls to processes that be short of in them or make better the control of those already being regulated. Sensors, in general, and gas sensors, in particular have been the root of a number of intelligent control systems used for improved process operation and environmental protection. Consequently, there has been ever increasing demand for compact, economical sensor for making a device, which detects gases in real-time.

Both legislation and marketing factors have greatly influenced devices based on gas sensor in recent years and the state of art achieved technology [1, 2]. However, the current dominant influence with regard to gas detectors/analyser development, without doubt, been pressure from environmental protection and vehicle pollution control. Present paper deals with technical subject on CO_2 electrochemical gas sensors. It was thought imperative to discuss the present state of art followed by our own experimental details, results and discussion on each technical part.

As a matter of fact, CO_2 gas is very difficult to detect by conventional gas sensors for the reason of its high stability at ordinary temperatures. Many kinds of

compact CO_2 sensors using various materials, such as solid electrolytes [3-6], mixed oxides [7], zeolites [8], polymers with carbonate solutions [9] and so on, have been investigated so far. None of them seems to have achieved sufficient performance characteristics for practical use. Among these, solid electrolyte based sensors have been of particular interest again from the viewpoint of low-cost, simple structure, high sensitivity and simplicity of detection mechanism.

The CO_2 sensors developed, in initial stages, have been utilised carbonate based solid electrolyte and gaseous (CO_2+O_2+Ar) reference electrode. The use of gaseous reference electrode, however, has been found very cumbersome and involved complexity in many practical applications. Nevertheless, the use of alkali carbonates makes the best choice for its high selectivity. These electrolyte materials suffers from the following major drawbacks:

- Hygroscopic nature of pure carbonates (e.g. K_2CO_3[10,11]) drifts the cell *emf* under humid condition. Other alkali carbonates employed, including Li_2CO_3 [12,13], Na_2CO_3 [14-18], and Cs_2CO_3 [19], slightly lowers the water cross-sensitivity.
- Required to operate at high temperatures to get sufficiently high ionic conductivity (~10^{-4} S cm^{-1} or greater) [20-22].
- Porosity and poor mechanical strength of pure alkali carbonates has also restricted their use.

In order to overcome the last two difficulties, mentioned above, altogether a different configuration (type III cell) has been proposed. In this configuration any good ionic conductor is used as an electrolyte over which a thin layer of carbonate is spread for gas sensing purpose.

The first type-III CO_2 gas sensor has been proposed with use of NASICON ($Na_3Zr_2Si_2PO_{12}$) and Na-β-alumina as electrolyte [23]. A porous layer of Na_2CO_3 has been attached on one of its surface as gas sensitive auxiliary phase. Various ratios of Na_2O/Al_2O_3 in the solid electrolyte have been tried. The following equation gives the theoretical emf of sensor

$$E = -\frac{\Delta G^{o}_{Na_2O} + \Delta G^{o}_{CO_2} - \Delta G^{o}_{Na_2CO_3}}{2F} - \frac{RT}{2F}\ln\frac{a_{Na_2O}P_{CO_2}}{P^{*}} \qquad (1)$$

where ΔG_i^o is the standard free energy of formation for species i, a_{Na2O} the activity of Na_2O in NASICON, P_{CO2} and P^* *are* CO_2 partial pressure and atmospheric pressure of 1.01×10^5 Pa, respectively. The activity of reference has e been fixed by the electrolyte itself. A comparison of performance of different sensors having either gaseous or sealed reference electrode is given in table 1. The major drawback associated with gaseous or sealed reference electrodes is its hermetic sealing from test gas. Moreover, for the sensors where reference activity is fixed by the

Table 1: A comparison of potentiometric CO_2 sensors with gas reference and sealed reference electrodes (concentration is in ppm unless specified)

Sr.#	Reference	Electrolyte/ Test electrode	T (°C)	t_{90} (sec)	Range (ppm)	Cross sensitivity	Ref
1.	Gas	$0.99Na_2CO_3$+ $01BaCO_3$	560	-	0.8-1.4 V%	H_20, SO_2&Cl_2	[29]
2.	Gas	Na_2CO_3+$BaCO_3$+Y_2O_3	500	1-2	1.5-103Pa	Humidity	30]
3.	Gas	Li1.3Al0.7Ti0.7 $(PO_4)_3$ Li_2CO_3 AP	-	4-5	80-13000	N_2 for PCO_2<80	[31]
4.	Gas	$LiTi_2(PO_4)_2$+$0.2Li_3PO_4$ Li_2CO_3+Li_2O AP	650	<30	-	-	[32]
5.	Gas	$LiTi_2(PO_4)_2$+$0.2Li_3PO_4$ Na_2CO_3+Li_2CO_3+K_2CO_3 AP	350	30	80-13000	NO_2, SO_2 < 20; H_2O	[33]
6.	Gas	Na_2CO_3+$BaCO_3$;Na_2CO_3+Ba CO_3 + Y_2O_3 AP	500	1-2	1.5-10^3Pa	H_2O	[34]
7.	Pt, Na_2O	NASICON /Na_2CO_3 AP	523	-	1.11x105Pa	-	[35]
8.	Pt, Na_2O	NASICON/Na_2CO_3 AP	417	<2	-	H_2O&HCl	[36]
9.	Pt	NASICON/Na_2CO_3+46at%B aCO_3 AP	550	8	4ppm-4%		[37]
10.	Pt	NASICON/Na_2CO_3+60at%Sr CO_3 AP	550	-	-	H_2O at high P_{CO2}	[38]
11.	Pt sealed	K_2O-Sm_2O_3-$6SiO_2$/K_2CO_3 AP	270-600	~4	10ppm-1%		[39]
12.	Pt sealed	Li_2O-Sm_2O_3-$2SiO_2$/Li_2CO_3 AP	450-550		0-3x10^4 Pa in air		[40]
13.	Pt sealed	$MAlSi_2O_6$ (M: Li, Na, K, Rb & Cs) AP	400	~1			[41]

AP – Auxiliary phase

electrolyte itself, e.g. NASICON, Na-β-alumina, ionic glass, etc. formation of Na_2CO_3 or corresponding carbonate at reference electrode becomes unavoidable at higher CO_2 partial pressures.

Hygroscopic nature of pure carbonates has been the chief impediment in realizing a practical CO_2 sensor. Strikingly, high concentrations of alkali earth carbonates *viz.*, $CaCO_3$, $SrCO_3$, $BaCO_3$, etc., as a second component in alkali carbonates, has suppressed completely the humidity cross-sensitivity at 497-554°C [24-27]. The response time for the sensor with cell configuration O_2, CO_2, N_2, Na_2CO_3-$BaCO_3$, Pt/ NASICON /Pt was found much reduced, as short as < 8 sec [28]. This has been attributed to modification in surface energy and grain topography of test electrode responsible for reaction kinetics. Other binary and ternary compounds of alkali carbonates have also been tested as an auxiliary phase with alkali ion conducting phosphates as electrolyte and gaseous reference [42]. The sensors with Li_2CO_3:Li_2O has been found quite sensitive to SO_2 (P_{SO2}>20ppm) and water vapour, forming Li_2SO_4 or LiOH at 650°C. With the use of eutectic mixture of Li_2CO_3-K_2CO_3-Na_2CO_3, operating temperature of the device has been brought down to 350°C.

The inert particle dispersed heterogeneous composites reported to enhance the rate of electrode kinetics due to increased defect concentration near grain boundary [43]. Dubbe et al have used Na_2CO_3+$BaCO_3$+Y_2O_3 as electrolyte and Na_2CO_3+$BaCO_3$ as an auxiliary phase with gaseous reference [44]. Jacob and his coworkers have achieved much reduced response time t_{90} >1 sec following an Arrhenius type law [45]

$$t_{90} = A \exp(E_a/kT). \quad (2)$$

Both the response time t_{90} and the activation energy E_a have been found dependent on metal electrode and electrolyte materials. Noteworthy, yttria addition gave increase in the response time on the other hand, exactly opposite results seen upon $BaCO_3$ addition. However, above equation has not been found valid for t_{90} well below one second [46]. In recent past, a sensor with Li_2CO_3-Li_3PO_4-Al_2O_3 composite electrolyte and reversible cathode $LiMn_2O_4$, as reference electrode, has been successfully tested for dry and wet (50%RH) air [47]. Room temperature potentiometric sensor based on NASICON with In_2O_3 initially shown cross sensitivity to humidity has been improved by addition of Na_3PO_4 or Na_2CO_3 or $NaHCO_3$ [48].

NASICON and Na-β alumina have been used extensively for the fabrication of type-III sensor (table-II.2). These electrolytes not only possess good ionic conductivity at elevated temperatures but also they are thermodynamically stable. In addition to these, they provide good mechanical compatibility with large number of electrolytes (auxiliary) and electrode materials. However, they require relatively higher operating temperatures, and develop micro-cracks after large thermal cycling. NASICON, particularly, has been found quite sensitive to SO_2 concentration (>20ppm) in the test gas, which ultimately hampers the performance [49]. In order to overcome these drawbacks, the different types of glass ceramic and vitreous solid electrolytes have been developed.

The rare earth silicates, M_2O: Re_2O_3: $nSiO_2$ (M = Li, Na, K, Rb and Cs; RE = La, Nd, Sm, Gd, Dy, Y, Ho, Er, Yb; n =1-14), investigated for sensor applications, have been composite of glass-ceramics i.e., $LiRESiO_4$ comprises $Li_xRe_{10-x}Si_6O_{24}O_{3-x}$ ($1 \leq x \leq 3$) and amorphous phase including some kinds of lithium silicate glasses [50]. Sensors using Li^+ conductors *viz.* $LiLaSiO_4$, $LiNdSiO_4$, $LiSmSiO_4$, $Li_2Zr(PO_4)_2$ and $LiAlSi_2O_6$ have been tested with Li_2CO_3 auxiliary phase [51]. In one of the attempts the sensor with K_2O-Sm_2O_3-$6SiO_2$ has been used in sensor [52]. Similarly, different aluminum silicate solid electrolytes ($MAlSi_2O_6$; M = Li, Na, K, Rb & Cs) have been exploited for miniaturization low cell impedance [53]. The $KAlSi_2O_6$ based sensors offered reduced operating temperature

along with increased temperature range of operation. Sealed reference electrode, all these sensors, has been one of the major technical difficulties.

Sensors with binary or ternary alkali carbonate auxiliary electrode and corresponding alkali metal phosphate electrolytes such as $LiTi_2(PO_4)_2$ $+0.2Li_3PO_4$ 54], MZP: $MZr_4(PO_2)_6$ (M: Mg and Zn)[55] have been tried either with or without gas reference electrode. Problems associated with reference electrode could be solved if some electrolyte insensitive to test gas but sensitive to oxygen would be used with porous carbonate layer for CO_2 sensing.

Use of established O_2 gas sensor with O^{2-} ion conductor as an electrolyte and carbonate auxiliary electrode has been found to make an intelligent choice. This electrolyte being immune to presence of CO_2 at the reference electrode; and O_2 pressure being equal at both the sides its effect will be cancelled. Miura has proposed use of MgO-stabilized zirconia (MSZ) with coating of Li_2CO_3 fixed to it by melting [56]. The response time and recovery time of the order of tens of seconds about 8 min, respectively have been seen. To achieve an electrochemical junction between Li_2CO_3 and MSZ, the presence of a solid phase containing both the Li^+ and the O^{2-} at the interface has been assumed, to act as a so-called *ionic bridge*, as Li_2ZrO_3. In the same study, sensor with LaF_3 as solid electrolyte and Li_2CO_3 auxiliary phase has been successfully tested. Similar type of sensors has also been reproduced and tested with cells Pt /Au, O_2, CO_2, Me_2CO_3 / YSZ /O_2, (CO_2), Pt with Me = Li, Na, K but with no stable response [57]. Owing to failures in reproducibility of these sensors and high operating temperatures, a very few sensors of this kind have been realized. However, a more practical variant of this configuration has been developed using two electrolytes as a separator between the test and reference electrode as discussed below.

Introducing a layer of alkali ion conductor as a second electrolyte has modified the sensor with O^{2-} conducting electrolyte, and largely studied. The first bi-electrolyte galvanic cell consisted of NASICON or Na-β-alumina and an oxygen ion conductor [58]. In these sensors, the equilibrium between the carbonate and the electrolyte with the surrounding gas atmosphere comprises not only CO_2 but also necessarily O_2. The thermodynamic condition at the Na-β-alumina and stabilized zirconia interface has been proved to give more stable performance than above one [59]. The use gold wires for internal electronic short circuiting, through the alkali ion conductors, guarantees instantaneously balance of sodium potential gradient through out this layer is out by an ambipolar sodium diffusion. Recently, few high-performing sensors have been reported with bi-electrolyte configuration as compiled in table 2. From the performance of various types of cell configurations discussed, it could be seen that for the development of fast sensors, which fulfills

the other characterization parameters, rate of electrode interactions is to be enhanced.

Table 2: A comparison of CO_2 sensors with anion conducting electrolytes and pt reference.

Sr.#	Electrolyte/ Test electrode	T (°C)	t_{90} (min)	Range	Cross-sensitivity	Ref.
	Reference / Electrolyte (anion) / Auxiliary electrode, Test gas					
1.	MSZ/ Li_2CO_3 AP	440-600	10	60-1000ppm	-	[60]
2.	LaF_3 /Li_2CO_3 AP	400-650	10-20	40-2000ppm,	50ppmNO, 50ppm NO_2	[61]
3.	MSZ/Li_2CO_3 AP	-do-	1	-do-	wet air	[62]
	Reference / Electrolyte I (anion) / Electrolyte II (cation) /Test gas					
1.	YSZ / NASICON /Na_2CO_3 AP	723	-	30Pa	-	[63]
2.	YSZ /Na_2O-Al_2O_3-4SiO_2 /Na_2CO_3 AP	450	<2	10-10^4ppm	H_2O	[64]
3.	YSZ /Li_2O:Sm_2O_3:2SiO_2/Li_2CO_3 AP	400-600	<4	0-3x10^4 Pa in air.	No influence of humidity.	[65]

The potentiometric CO_2 gas sensors prepared with open reference electrodes are one of the best-reported sensors so far with very short response time (1s), large sensitivity and good thermodynamic stability [66]. Moreover, the demand of sensor operation under low oxygen pressure directed the researchers in utilizing the oxide materials as a reference electrode, to give stable potential on wide range of partial pressures. Maier et al have constructed a simple electrochemical cell using open solid reference, which responded to P_{CO2} in a thermodynamic way [67,68]. Moreover, such sensor can, as a whole, be exposed to a uniform atmosphere without the necessity of sealing. Later, he elaborated this idea and developed a sensor using various new solid-state open reference electrodes [69]. A comparison of sensor with metal and open reference electrodes in table 3.

Table 3 : Comparison of CO_2 sensors with metal and open reference electrodes:

S#	Reference electrode	Electrolyte/ Test electrode	T (°C)	t_{90} (sec)	Range	Ref
Metal reference / Electrolyte / (auxiliary phase)Test gas						
1.	Ag	K_2CO_3-Ag_2SO_4	726	-	-	[70]
2.	Na	β"-Al_2O_3/ Na_2CO_3 AP	450	few	-	[71]
Open reference / Electrolyte / (auxiliary phase)Test gas						
3.	$Na_2O_xMO_2$+ MO_2	Na-β"-Al_2O_3/ Na_2CO_3 AP	300-600	2	0.12-9.2%	[72]
4.	Na_2ZrO_3+ ZrO_2	Na-β"- Al_2O_3/Na_2CO_3 AP	-	-	-	[73]
5.	Na_2CoO_2	Na-β"- Al_2O_3/Na_2CO_3 AP	400-500	-	-	[74]
6.	$LiMn_2O_4$	Li_2CO_3+Li_3PO_4+Al_2O_3	330-420	90-110	100-10000	[75]

The use of open reference electrode in CO_2 sensor is not only convenient and easy method to prepare but also convenent to employ for a number of practical purpose.

2 Experimental

The details of procedures followed for preparation of electrolyte, sensor fabrication and evaluation were similar to discussed elsewhere [76]. The open reference electrode materials (Li_2TiO_3, Na_2ZrO_3 and Na_xCoO_{2-y}) were prepared by employing solid state sintering technique. The initial ingredients (Li_2O, TiO_2, ZrO_2, CoO_2) were of 99.99% pure (Aldrich, USA).

3. Results and Discussion

The conductivity data of optimised compositions is summarised in table 4. Evidently, the glass dispersion in $MeCO_3$ enhances the conductivity by about two orders of

Table 4: The pre-exponential factor $\log(\sigma T)_0$], conductivity (σ) and activation energy (E_a) of optimised carbonate based solid electrolytes.

Sl.#	Optimised composition	$\text{Log}(\sigma T)_0$ (S/cm K)	σ(200 °C) (S/cm)	σ(400 °C) (S/cm)	E_a (eV)
1.	Li_2CO_3:Li-glass	7.671	2.50×10^{-6}	2.48×10^{-3}	0.996
2.	Na_2CO_3:Na-glass	5.620	2.05×10^{-7}	8.33×10^{-3}	
(b).	ABO_3 type compound dispersion:				
(i)	$BaTiO_3$ dispersion:				
3.	$50Li_2CO_3$:$50BaTiO_3$	5.424	1.34×10^{-6}	3.44×10^{-4}	0.809
4.	$80Na_2CO_3$:$20BaTiO_3$	5.983	9.01×10^{-7}	3.81×10^{-4}	0.879
(ii)	$LiNbO_3$ dispersion:				
5.	$50Li_2CO_3$:$50LiNbO_3$	7.733	1.12×10^{-6}	1.47×10^{-3}	1.034
6.	$60Na_2CO_3$:$40LiNbO_3$	6.129	5.37×10^{-7}	2.93×10^{-4}	0.914
(iii)	$KNbO_3$ dispersion:				
7.	$70Li_2CO_3$:$30KNbO_3$	5.349	7.27×10^{-7}	2.10×10^{-4}	0.828
8.	$60Na_2CO_3$:$40KNbO_3$	4.845	5.63×10^{-7}	2.93×10^{-4}	0.914
(c)	Inert particle dispersion:				
9.	$70Li_2CO_3$:$30Al_2O_3$	7.001	9.56×10^{-8}	7.99×10^{-6}	1.066
10.	$90Na_2CO_3$:$10Al_2O_3$	5.685	6.69×10^{-7}	2.52×10^{-7}	0.863
(d)	Binaries of some carbonates:				
11.	$90Li_2CO_3$:$10Na_2CO_3$	8.925	-	7.27×10^{-3}	1.133
	$20Li_2CO_3$:$80Na_2CO_3$	8.887	-	4.12×10^{-3}	1.139
12.	$90Li_2CO_3$:$10K_2CO_3$	8.925	-	5.57×10^{-3}	1.119
	$10Li_2CO_3$:$90K_2CO_3$	8.887	-	2.05×10^{-4}	0.976
13	$70Li_2CO_3$:$30CaCO_3$				0.859
14	$70Li_2CO_3$:$30BaCO_3$	4.963	5.09×10^{-4}	8.93×10^{-3}	0.743

magnitude at 400°C. Further more, $50Li_2CO_3$:$50LiNbO_3$ composite is seen to be the highest conductivity giving composition amongst the ferroelectric ($BaTiO_3$/$LiNbO_3$/$KNbO_3$) dispersed composites. A marked conductivity enhancement (about two orders of magnitude) in both glass and ferroelectric dispersed composites is due to formation of space charge layer across heterogeneous interface giving rise to high ion conducting percolating paths.

A typical response curve for Au/Li_2CO_3+$BaCO_3$/LT+TiO_2+Elect./Au sensor is depicted in figure 1a. The emf of sensor increases exponentially from 500 mV and attains 650 mV (saturation in emf) on switching the gas concentration from 250 to 1000 ppm and vice versa. The response time is found to be ≈ 45 seconds. The identical behavior of sensor (nature of change and saturated emf value) on each cycle (Fig. 1a) suggests good reversibility. The variation of sensor emf with time, at

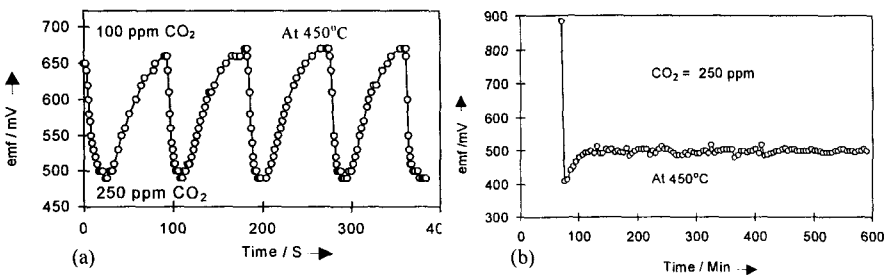

Figure 1: Sensor emf versus time (a) after change in P_{CO_2} and (b) at a fixed P_{CO_2} and temperature.

a fixed CO_2 partial pressure (at 400 °C), shown in figure 1b indicates its good operational stability. Invariance in sensor emf over a long period of time also suggests negligible electronic transport number of solid electrolyte. Figures 2a and

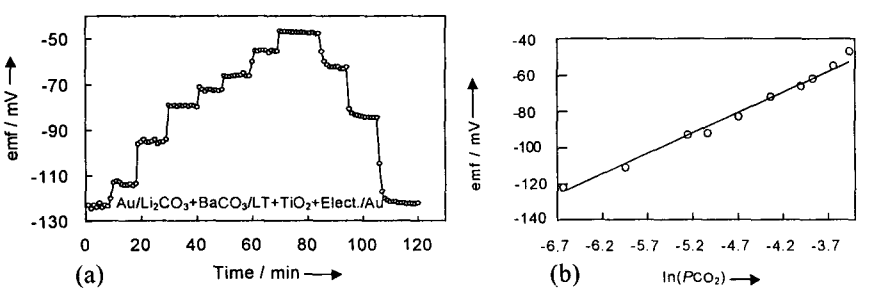

Figure 5: Variation of emf (a) with time after change in P_{CO_2} and (b) as a function of P_{CO_2}.

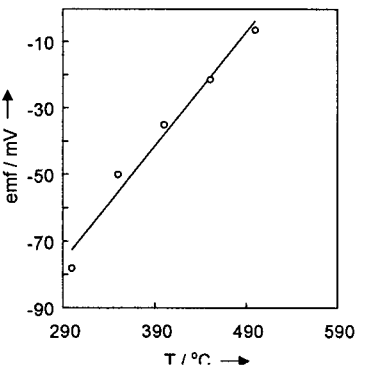

Figure 3: Variation of CO_2 sensor emf with operating temperature.

2b depict variation of sensor emf with time (for various gas concentrations) and $\ln(P_{CO2})$, respectively. Evidently, sensor seen to obeys the Nernst law within the concentration range of investigation. It is worth mentioning here that the electrolyte content in the reference electrode was optimized so as to achieve good electrode-electrolyte interface thereby good reversibility, stable cell emf and fast response time.

The variation of sensor emf with operating temperature depicted in figure 3 suggests its operability over a temperature range 300-490 °C. It is to mention here that the response time was found faster at higher temperature vis-

Table 5: Comparison of CO_2 sensor parameters with earlier reporting.

Sl. #	Reference Electrode	Solid Electrolyte	Sensing electrode	T_o(°C)	t_r	R	Ref
1.	Na or Na_xCoO_2	Na^+-β"-Al_2O_3	Na_2CO_3/Pt	350-550	5m	1-6.3%	[71]
2.	Na_2ZrO_3/ZrO_2	Na-β-Alumina	Na_2CO_3/Au	350-750	Sec	1-3.0%	[73]
3.	Na_2SnO_3/ SnO_2 $Na_2Ti_6O_{13}/TiO_2$	Na-β-Alumina Na-β-Alumina	Na_2CO_3/Au Na_2CO_3/Au	675-775 350-775	Sec Sec	0.14-8% 0.12-9%	[28]
4.	$Li_{1.3}Al_{0.3}Ti_{0.7}$	$CaCO_3$/CaO	Li_2CO_3/Pt	650	Min	0.008-1%	[71]
5.	Na_xCoO_{2-y}	Na^+-β"-Al_2O_3 or NASICON	Na_2CO_3/Pt	400	Min	0.001-1%	[73]
8	$Li_2TiO_3 + TiO_2$	$80Li_2CO_3$:$20Al_2O_3$	Na_2CO_3/Pt	400	30S	-do-	*
12	Na_2ZrO_3/ZrO_2	$70Na_2CO_3$:$30BaCO_3$	Li_2CO_3/Au	-do-	Sec	-do-	*
13	Na_2ZrO_3/ZrO_2	$70Na_2CO_3$:$30CaCO_3$	Li_2CO_3/Au	-do-	Sec	-do-	*
16	Na_2ZrO_3/ZrO_2	$80Na_2CO_3$:$20BaTiO_3$	Li_2CO_3/Au	-do-	Sec	-do-	*
17	Na_2ZrO_3/ZrO_2	$Na_2CO_3 + LiNbO_3$	Li_2CO_3/Au	-do-	Sec	-do-	*
18	Na_2ZrO_3/ZrO_2	$50Na^+$glass+$50Na_2CO_3$	Li_2CO_3/Au	-do-	Sec	-do-	*

$T_o \rightarrow$ Operating temperature; $t_r \rightarrow$ Response time; $R \rightarrow$ Sensing range; *→ Present study.

à-vis lower one. It is also observed during the investigation that for detection of higher CO_2 concentration, the sensor should be operated at relatively lower temperature. On the other hand, it should be operated at high temperature for the measurement of very low concentrations; i. e. by changing the sensor operating temperature one can modify its detection/sensitivity range. The cross sensitivity for NO_2, H_2 and Cl_2 is found negligible. The performance of a few CO_2 sensors investigated is compared with earlier reported one in table 5.

Acknowledgements

The author is thankful to DST, New Delhi for providing the financial support to carry out this work.

References

1. N. Yamazoe and N. Miura, Sensors and Actuators B, **20** 95 (1994).
2. T. Kobayashi, Sensors and Actuators, **9** 235 (1986).
3. M. Gauthier and A. Chamberland, J. Electrochem. Soc. **124** 1579 (1977).
4. T. Maruyama, S. Sasaki and Y. Saito, Solid State Ionics, **23** 107 (1987).
5. R. Cote, C. W. Bale M. Gauthier, J. Electrochem. Soc. **131** 63 (1984).
6. N. Imanaka, T. Kawasato and G. Adachi, Chem. Lett., 497 (1990).
7. T. Ishihara, K. Kometani, M. Hashida Y. Takita, J. Electrochem. Soc. **138** 173 (1991).
8. Y. Ishiguro, Y. Nagawa H. Futata, Proc. 2nd Int. Meet, Chemical Sensors, Bordeaux, France (1986) 719.
9. Y. Shimizu, K. Komori and M. Egashira, J. Electrochem. Soc. **136** 2256 (1989).
10. M. Gauthier et al, Anal. Chem. Symp. Ser. 17(1983)353.
11. R. Cothe, C. W. Bale and M. Gauthier, J. Electrochem. Soc. **13**163 (1984).
12. T. Ogata, J. Mater. Sci. Lett. 5(1986)285.
13. N. Imanaka, T. Kawasato and G. Adachi, Chem. Lett. (1991)1743.
14. T. Ogata, J. Mater. Sci. Lett. 5(1986)285.
15. J. Liu and W. Weppner, Eur. J. Solid State Inorg. Chem.**28** 1151 (1991).
16. T. Maruyama, Solid State Ionics 24(1987)281.
17. Y. Sadaoka, Y. Sakai, M. Matsuguchi and T. Manabe, J. Mater. Sci. **28** 5783 (1993).
18. A. Dubbe, H. D. Wiemhofer, Y. Sadaoka and W. Gopel, Sens. Actuat. **B25** 600 (1995).
19. R.Cothe, C.W. Bale and M. Gauthier, J. Electrochem. Soc., **13**163 (1984).
20. G. Hotzel, and W. Weppner, Sensors and Actuators, **12** 449 (1987).
21. Y. Saito and T. Maruyama, Solid State Ionics, **28-30** 1644 (1988).
22. K. Singh and J. S. Ratnam, Solid State Ionics **31**221-226 (1988).
23. Y Saito and T Maruyama, Solid State Ionics **28-30** 1644-1647 (1988).
24. S. Yao, Y. Shimizu, N. Miura and N. Yamazoe, Chem. Lett. 2033 (1990).
25. S. Yao, S. Hosohara, Y, Shimizu, N. Miura, H. Futata and N. Yamazoe, Chem. Lett. 2069-2072 (1991).
26. N. Miura, S. Yao, Y. Shimizu and N. Yamazoe, J. Electrochem. Soc. **139** 1384 (1992).
27. A. Dubbe, Y. Sadaoka and Y. Sakai, Chemical Sensors 10 A, Proc. 18th Chemical Sensors Symp., Sendai, Japan (1994)81.
28. N.Miura , S.Yao, Y.Simizu and N.Yamazoe, Sensors and Actuators **B,**9165-170 (1992)

29. H. D. Wiemhofer, H. Keller, S. Brosda, V. Guth and W. Gopel, Proc. SPIE. Int. Soc. Opt. Eng, 1716(1993)482-489.
30. A. Dubbe, M.Wake and Y. Sadaoka, Solid State Ionics, **96** (1997)201-208.
31. N. Imanaka, T. Kawasato and Gin-ya Adachi, Chemistry Letts. (1990)497-500.
32. N. Imanaka, T. Murata, T. Kawasato and Gin-ya Adachi, Sensors & Actuators B**13-14** 476-479 (1993).
33. N. Imanaka, T. Murata, T. Kawasato and Gin-ya Adachi, Sensors & Actuators B **13-14** 476-479 (1993).
34. A. Dubbe, M.Wake and Y. Sadaoka, Solid State Ionics,**96** 201-208 (1997).
35. Y Saito and T Maruyama, Solid State Ionics **28-30** 1644-1647 (1988).
36. Y. Sadaoka, M. Mitsuguchi, Y. Sakai and D. Manabe, J. Materials Science **28** 2035-2039 (1993).
37. N.Miura, S.Yao,Y.Simizu and N.Yamazoe, Sensors and Actuators **B9** 165-170 (1992).
38. N. Miura , S. Yao, Y. Simizu and N. Yamazoe, Sensors and Actuators **B9** 165-170 (1992).
39. S Nakayama, S Kuwata, M. Sato, M Sakamoto and Y Sadaoka J Ceramic Soc. Japan **103 (3)** 255-257 (1997).
40. S. Nakayama, Y. Shiozaki, S. Kuwata, E. Sugimoto, T. Ichimori, T. Hino, H. Shikama and M. Okazaki, J. Ceram. Soc. Japan **106(1)** 112-115 (19987).
41. S. Nakayama, T Asahi, S. Kuwata, S. Imai and M Sakamoto, J. Ceramic. Soc. Japan **107 (6)** 587-590 (1999).
42. N. Imanaka, T. Murata, G. Adhachi and T. Kawasato, Sensor & Actuators B **13-14** 476-479 (1993).
43. J. Maier, Prog. Solid St. Chem. **23** 171-263 (1995).
44. A. Dubbe, M.Wake and Y. Sadaoka, Solid State Ionics, **96** 201-208 (1997).
45. R. Akila and K. T. Jacob, Sens. Actuat. **16** 311 (1989).
46. A. Dubbe, H. D. Wiemhofer, Y. Sadaoka and W. Gopel, Sens. Actuat. B **25** 600 (1995).
47. D. H. Kim, J. Y. Yoon, H. C. Park and K. H. Kim, Sensors and Actuators B **76** 594-599 (2001).
48. K. Obata, S. Kumazawa, K. Shimanoe, N. Miura and N. Yamazoe, Sensors and Actuators B **76** 639-643 (2001).
49. N. Imanaka, T. Kawasato and G. Adachi, Chemistry Letters, (1991)13-16.
50. M.Sato,Y.Kono, H.Ueda, K.Uematsu and K.Toda, Solid State Ionics, **83** 249-56 (1996).
51. S. Nakayama, T Asahi, S kuwata, S Imai and M Sakamoto, J Ceram. Soc. Japan **107(6)** 587-590 (1999).
52. S Nagayama, S Kuwata, M Sato, M Sakamoto and Y Sadaoka, J. Ceram. Soc. Japan **105(3)** 255-257 (1997).
53. S Nakayama, S Kuwata, T Ichimori, M Okazaki, M Okamasa, S Imai, M Sakamoto and Y Sadaoka J Ceramic Soc. Japan **106 (7)** 715-718 (1998).
54. N. Imanaka, T. Murata, T. Kawasato and Gin-ya Adachi, Sensors & Actuators B, **13-14** 476-479 (1993).
55. S. Ikeda, S. Kato, K. Nomura, K. Ito and H. Einaga, Solid State Ionics, **70/71** 569-571 (1994).
56. N Miura, Y Yan, M Sato, S Yao, Y Shimizu and N Yamazoe, Chemistry Letters,(1994)393-396.
57. H. Nafe, J. Electrochem. Soc.,**144(3)** 915 (1997).
58. T. Maruyama, S. Sasaki, Y. Saito, Solid State Ionics, **23** 107 (1987).
59. H. Nafe, Solid State Ionics **93** 117-123 (1997).
60. N. Yamazoe and N. Miura, J. Electroceramics **2:4** 243-255 (1998).

61. N. Miura , Y. Yan, M. Sato, S. Yao, S. Nonaka, Y. Simizu and N. Yamazoe, Sensors and Actuators B, **24-25** 260-265 (1995).
62. N. Miura , Y. Yan, M. Sato, S. Yao, S. Nonaka, Y. Simizu and N. Yamazoe, Sensors and Actuators B, **24-25** 260-265 (1995).
63. Y Saito and T Maruyama, Solid State Ionics **28-30** 1644-1647 (1988).
64. H. Aono, H. Supriyano and Y. Sadaoka, J. Electrochem. Soc.,**145(9)** 2981-2984 (1998).
65. S. Nakayama, Y. Shiozaki, S. Kuwata, E. Sugimoto, T. Ichimori, T. Hino, H. Shikama and M. Okazaki, J. Ceram. Soc. Japan **106(1)** 112-115 (19987).
66. M. Holzinger, J. Fleig, J. Maier and W. Sitte, Proc. 17th Riso Internaional Symposium on Materials, (eds.) F. W. Poulsen, N. Bonanos, S. Linderoth, M. Mogensen and Zachau-Christiansen, Denmark.
67. J. Maier and U. Warhus, J. Chem. Thermodyn, **18** 309 (1986).
68. J. Maier: Science and technology of fast ion conductors, eds. H. L. Tuller, M. Balkanski Plenum Press, New York (1989) 299.
69. J. Maier, M. Holzinger and W. Sitte, Solid State Ionics, **74** 5-9 (1994).
70. M Gauthier, A Chamberland and A Belanger (1975)NATO Advanced Study Inst., Electrode Processes in Solid State Ionics, Ajaccio, Crsica.
71. J. Liu and W. Weppner, Solid State Ionics, (eds) M. Balkanski, T. Takahashi and H. L. Tuller, (1992) 61-68.
72. J. Maier, M. Holzinger and W. Sitte, Proc. MRS Meeting, Boston, 1994.
73. J. Maier, Solid State Ionics, **62** 105-111 (1993).
74. H. Schettler, J. Liu, W. Weppner, R.A. Huggins, Appl. Phys. A, **57** 31-35 (1993).
75. D. H. Kim, J. Y. Yoon, H. C. Park and K. H. Kim, Sensors and Actuators B **76** (2001) 594-599.
76. S. S. Bhoga and K. Singh, Solid State Electrochemistry, **3(5)** 258 (1999).

POLYPYRROLE FOR ARTIFICIAL MUSCLES: IONIC MECHANISMS

STEEN SKAARUP
Department of Chemistry, Technical University of Denmark
DK-2800 Lyngby, Denmark

Some conjugated polymers can convert electrical energy to mechanical energy (via chemical energy), thereby acting as *electro-chemo-mechanical actuators* or "artificial muscles". The advantage of this type of actuator is that the process can be driven by the application of a small potential (1-5 V), opening the possibility of making control and measurement both safe and accurate. The actuation process is identical to charging and discharging an electrochemical cell during redox cycling of a rechargeable battery. It involves ions moving between the electrolyte and being inserted in, or expelled from the matrix of a polymer electrode – thereby causing volume expansion which can be converted into work. Solvent molecules are able to penetrate the polymer too. A precise description of the nature of these ionic and solvent movements is therefore important for understanding and improving the performance. This work examines the influence of solvent, ionic species and electrolyte concentration on the fundamental question about the ionic mechanism involved: Is the actuation process driven by anion motion, cation motion, or a mixture of the two? In addition: What is the extent of solvent motion? The discussion is centered on polypyrrole (PPy), which is the material most used and studied. The tetraethyl ammonium cation (TEA) is shown to be able to move in and out of PPy(DBS) polymer films, in contrast to expectations. There is a switching between ionic mechanisms during cycling in TEACl electrolyte.

1. Introduction

The discovery of electronically conducting polymers in the 1970's (three pioneering researchers were awarded the Nobel Prize in chemistry for 2000), opened a new class of materials and the possibility for new types of phenomena[1]. A novel property of these polymer materials was their ability to switch between different states by the application of a small (1-5 V) voltage. Within certain limits, many properties can be controlled reversibly[2], including conductivity, optical absorbance, capacitance, hydrophobicity and also mechanical properties such as stiffness and volume. Increasing and decreasing the voltage is identical to charging and discharging an electrochemical cell, and is accompanied by the reversible motion of ions from an electrolyte in and out of the polymer matrix which functions as an electrode.

In most of the applications, the volume change is either an irrelevant side effect or a nuisance, since it may cause lack of electronic contact after repeated redox cycling, but during the 1990's it was recognized that the effect might be turned into an advantage. The expansion/contraction made possible the controlled transformation of electrical energy to mechanical energy (via chemical energy)[3]. These types of "artificial muscles" were soon demonstrated in practice, both as simple bending actuators[4], and in the form of ingenious microdevices[5].

The field of conducting polymer actuators received a strong impetus by a seminal article published in 1996 by Baughman[6]. This work compared the polymer muscles with different types of natural muscle, and estimated the maximum achievable energy and power densities. The analysis yielded favorable predictions for the strengths and speed of conducting polymer artificial muscles, and although especially the estimate of the power density was probably overly optimistic, there was still scope for the production of highly promising actuator systems. A large number of different designs and applications have been proposed and developed in the past 10 years[7], including the very important field of biomedical applications[8].

Since the actuation depends on the insertion or expulsion of ions into the polymer matrix, a precise description of the mechanisms of ion motion is necessary for understanding the process. This work examines the influence of the choice of electrolyte and ions in the cycling electrolyte, as well as the synthesis conditions on the ionic mechanisms responsible for the performance of PPy artificial muscles.

Of prime importance is the question of whether the actuation is driven by the insertion of cations during the cathodic sweep (reduction), by the insertion of anions during the anodic sweep (oxidation), and which role the solvent molecules play. It is also of importance to determine if the mechanism is stable during cycling (the ideal case), or whether it gradually changes making control of the actuator more complicated, since there is no longer a one-to-one correspondence between applied potential and force/position values. One way to distinguish between the two mechanisms is to observe the direction of the expansion process, which is differs for the two mechanisms because of the necessity of charge neutrality:

- Anion mechanism: Expansion on oxidation, contraction on reduction.
- Cation mechanism: Expansion on reduction, contraction on oxidation.

Since polypyrrole can only accept a positive charge on the backbone, PPy is formed by oxidative polymerization, and is therefore necessarily formed with charge compensating *anions* incorporated as counterions in the polymer matrix:

Synthesis: $$nPy + nxA^- \rightarrow poly(Py^{x+} \cdot xA^-)_n + nxe^- \quad (1)$$

Where x is the maximum possible oxidation level per pyrrole monomer (x ~ 0.30-0.35) and A^- is a monovalent counterion. In the remainder of the article, the term $poly(Py^{x+} \cdot xA^-)_n$ will be abbreviated to $PPy^{x+} \cdot xA^-$ for convenience. It is advantageous to keep in mind that two distinct situations can be defined[9]:

- A^- is a small, and therefore mobile anion, e.g. Cl^-, BF_4^-, ClO_4^- etc.
- A^- is a large and/or entangled, and therefore immobile anion, e.g. dodecyl benzene sulphonate (DBS^-).

It is also important to be aware that the first reduction *may be significantly different from the succeeding cycles*. Both because conformation changes take place, perhaps accompanied by the irreversible insertion of solvent molecules, and because more ionic options are available to the system after the first reduction.

2. Results and Discussion

2.1 *The simplest picture: Small, mobile synthesis anions, small cycling ions, anion mechanism*

If any contribution from solvent insertion is at first ignored, the simplest model involves performing the synthesis in the presence of small anions, with subsequent cycling in an electrolyte also containing small anions (not necessarily the same anion). The *first* reduction will then involve the expulsion of anions:

Reduction: $PPy^{x+} \cdot xA^- + xe^- \rightarrow PPy^0 + xA^-$ (2)

Oxidation: $PPy^0 + xA^- \rightarrow PPy^{x+} \cdot xA^- + xe^-$ (3)

In this case, the oxidation is just the reverse of the reduction, and the subsequent cycles *repeat the same mechanism*: Expansion on oxidation (figure 1).

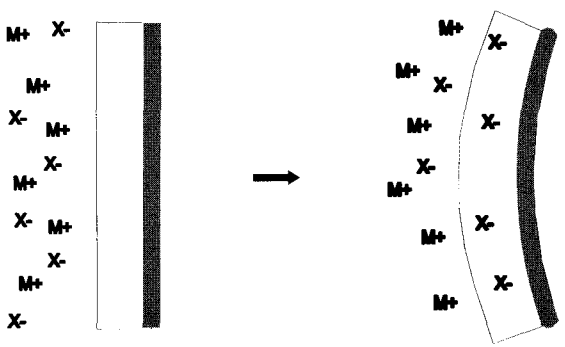

Figure 1. Anion mechanism: Expansion on oxidation by the insertion of X^- ions. A PPy film on a non-expanding backing (gray) forms a bilayer bending actuator (seen from the side).

In this model, the size, shape and charge of the cations do not interfere with the actuation process. By analysis of the dependence of the potentials of the peaks in PPy cyclic voltammograms on the electrolyte concentration, it was shown that this mechanism is the dominant one when using Li^+ and ClO_4^- in propylene carbonate[10].

2.2 *Small, mobile synthesis anions, small cycling ions, cation mechanism*

When cycling the same type of PPy films using Li^+ and ClO_4^- in acetonitrile instead, the result was unexpected: The data corresponded to a *cation* mechanism[10]. The *first* reduction can now be written:

Reduction: $PPy^{x+} \cdot xClO_4^- + xe^- + xLi^+ \rightarrow PPy^0 \cdot x(Li^+ \cdot ClO_4^-)$ (4)

Oxidation: $PPy^0 \cdot x(Li^+ \cdot ClO_4^-) \rightarrow PPy^{x+} \cdot xClO_4^- + xe^- + xLi^+$ (5)

The oxidation is again just the reverse of the reduction, and subsequent cycles are identical to the first. The result showed an unexpected influence of the solvent, which does not formally enter into the reaction equation. This was an indication that the solvent may play a decisive role in determining the nature of the redox process[11].

A significant difference between equations (2) and (4), is that the reduced form in the latter case, $PPy^0 \cdot x(Li^+ \cdot ClO_4^-)$, formally contains the neutral salt $LiClO_4$. The ions are not necessarily directly combined with each other in pairs, but it still leaves open a new option: *Salt draining,* since both ions are small and mobile:

Salt draining: $PPy^0 \cdot x(Li^+ \cdot ClO_4^-) \rightarrow PPy^0 + xLi^+(aq) + xClO_4^-(aq)$ (6)

This phenomenon has been identified as a slow (~1000 s) process in PPy synthesized in the presence of the tosylate anion (TsO^-), which was originally believed (erroneously) to be bulky enough to remain permanently in the polymer[12]. The gradual draining of LiTsO means that the mechanism changes with time when cycled in $LiClO_4$: The synthesis follows equation (1) with $A^- = TsO^-$. The first reduction and first few cycles correspond to a Li^+ cation mechanism as in equations (4) and (5) with TsO^- instead of ClO_4^-, since the tosylate ion is bulky enough to move only slowly. After sufficient time to for the salt draining to be completed, the mechanism then shifts to an anion mechanism, as in equations (2) and (3) with $A^- = ClO_4^-$. The extent of salt draining can be influenced by keeping the polymer at a fixed potential for longer periods of time: At a reducing potential to enhance, and at an oxidizing potential to minimize the process.

The gradual switch in mechanism in the $PPy^{x+} \cdot xTsO^-$ polymer cycled in aqueous $LiClO_4$ electrolyte underscores two points:

- The initial mechanism may not be identical to that of the ultimate, steady state situation – slow conformation relaxation, draining processes etc. may occur. Only cycling perhaps hundreds of times enables unambiguous conclusions about the mechanism.
- Determining whether an ion can be regarded as "small", i.e. mobile or "large", i.e. immobile in the polymer matrix is no simple matter. TsO^- is immobile for the first few cycles, but mobile under long term cycling, or after being kept at reducing potentials for an extended period.

2.3 *Large, immobile synthesis anions, small cycling ions, cation mechanism*

Since the object is to be able control positions and forces in a precise way, the ideal actuation mechanism involves only one type of ions moving. A stable mixture of anion and cation mobility is also a feasible solution, but the opposing motions would tend to produce a smaller volume change. Models of bender actuators have been based on this stability assumption[13-15]. An attempt to solve this is to

incorporate a large immobile anion during synthesis, thereby forcing the mechanism to be dominated by cations. This was achieved by using the surfactant molecule dodecyl benzene sulphonate (DBS)[16]. Figure 2 shows five monomer units of a PPy polymer chain together with two different isomers of DBS^- anions.

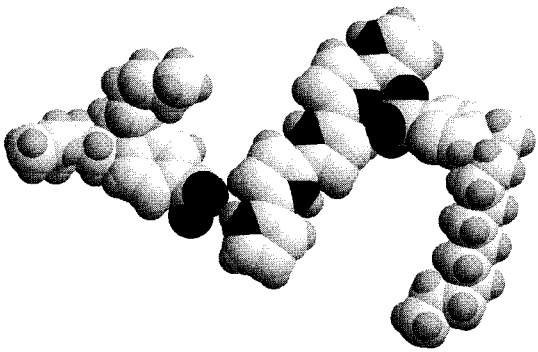

Figure 2. Model of a 5 monomer unit segment of a polypyrrole chain with two different isomers of dodecyl benzene sulphonate ions associated (one strongly branched, the other almost linear). The two sulphonate groups are assumed to be attracted to N-H groups of pyrrole.

Two anions per five pyrrole monomers would correspond to a degree of doping, x = 0.40, not far from the maximum values obtained (0.35-0.37). The figure indicates two points:

- The DBS^- ion is not likely to be easily able to move, both because of its size, and because of the possibility of entanglement.
- The detergent anions occupy a very large percentage of the polymer volume (~50%). Despite this, the film has the properties of "normal" PPy in most respects.

The expected mechanism for this system cycled in aqueous NaCl is then:

Synthesis: $$nPy + nxDBS^- \rightarrow poly(Py^{x+} \cdot xDBS^-)_n + nxe^- \quad (6)$$

Reduction: $$PPy^{x+} \cdot xDBS^- + xe^- + xNa^+ \rightarrow PPy^0 \cdot x(Na^+ \cdot DBS^-) \quad (7)$$

Oxidation: $$PPy^0 \cdot x(Na^+ \cdot DBS^-) \rightarrow PPy^{x+} \cdot xDBS^- + xe^- + xNa^+ \quad (8)$$

The experimental results verified the cation mechanism, at least for the initial cycles, as determined by the direction of bending[17], and also by peak potential dependence, Electrochemical Quartz Crystal Microbalance (EQCM) and force measurements[18].

Salt draining was a priori not expected in this system, but was found to occur to some degree if the polymer film is held in the neutral (reduced) state for a long time[17]. In this state, there is no charge on the PPy backbone to attract the DBS^- anion; in addition, the polymer is swollen because of the presence of inserted

cations, making diffusion out of the matrix easier. Furthermore, the polymer can also incorporate a significant number of water molecules at this potential, as discussed in the next section. This makes movement of all species more feasible.

2.4 *Solvent influence: Solvated H_2O and osmotic effect: Complications of the simple mechanisms*

Combining cyclic voltammetry with *in situ* mass measurements via EQCM is a powerful way of elucidating the nature of mobile species: The voltammogram is sensitive to charged particles moving or reacting at the film surface, whereas the microbalance will show the direction and magnitude of *all* changes of mass, thereby revealing also the influence of uncharged solvent molecules entering or leaving the film. The results were of great importance to the understanding of the actuation process: A large number (10-20) of H_2O molecules was observed to move in and out of the PPy(DBS) film during redox cycling[18]. This means that the main volume expansion/contraction cycle is actually dominated by solvent motion rather than by ionic insertion/expulsion.

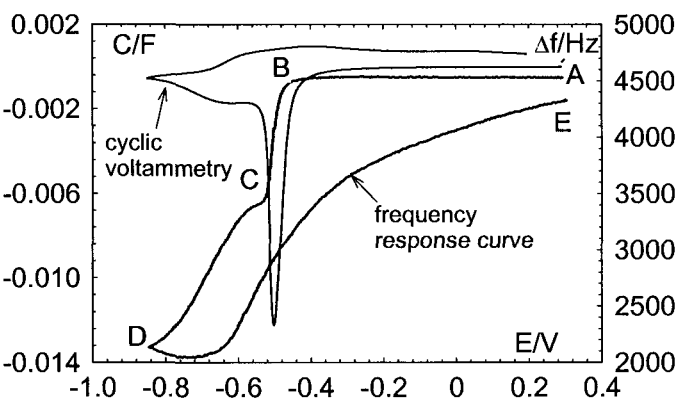

Figure 3. First reduction/oxidation cycle of PPy(DBS) in aqueous 1 M NaCl. Simultaneous cyclic voltammetry and EQCM. The cycle starts at A and ends at E. A 1 Hz frequency decrease (relative to 10 MHz) corresponds to a mass *increase* of 0.904 nanogram. Potentials vs Ag/AgCl.

Figure 3 shows the simultaneous measurement of capacity and frequency (i.e. mass) change. From A to B there is no current and also no mass change: Neither charged nor uncharged species interact with the film. From B to C, the frequency falls steeply – this correlates exactly with the very sharp cathodic reduction peak

centered at -0.5 V. Since this is the first reduction the peak can only be interpreted as representing Na^+ ions entering the film (equation (7)). This is borne out by the fact that BC represents a mass *increase*. However, an unexpected phenomenon occurs form C to D: There is a large increase of mass over the whole potential interval, but there is no reduction reaction associated with it (the broad capacity peak around -0.7 V is known to stem from the reduction of dissolved O_2 on the film surface – it can be removed totally without changing the mass increase). The mass increase even continues for a while after the current is reversed at D – another indication that it signifies something different from ions reacting with the film.

This unexpected observation was explained by the development of an osmotic model for H_2O and Donnan equilibria between the polymer and the aqueous electrolyte solution[19]. The mass increase at B to C is caused by the insertion of Na^+ ions, but turns out to be much larger than corresponding to the charge calculated from integration of the sharp cathodic peak: About 4 H_2O molecules follow the cation – this is interpreted as being the *inner solvation shell* of Na^+ in water. The insertion of these ~4 strongly bound molecules is as fast as the Na^+ insertion. The C to D segment corresponds to the insertion of about 6.2 H_2O molecules – this osmotic mechanism is much slower, and since it is dependent on the value of the potential alone, it is not reversed immediately on reversing the current.

The osmotic model predicts that the number of solvent molecules inserted in the C to D segment should depend on the concentration of the cycling electrolyte: Being largest at very low concentrations, and decreasing at high concentrations. These predictions have been verified by experiments on NaCl electrolytes[20]: The number of molecules inserted via the osmotic effect is ~10 at 0.1 M and only about 1 molecule at 5 M.

The difference in time constants of the BC and CD mass (and volume) changes has important connotations for actuator use: If fast actuation is desired, it may be necessary (and unavoidable) to bypass the slow, osmotic insertion – thereby exploiting solely the faster insertion of Na^+ ions with strongly bound H_2O attached[21]. The idea that faster scan rates will decrease the importance of the slow osmotic insertion has been verified experimentally[22].

As a further complication, the osmotic model also predicts that the balance between cation and anion mechanisms should depend on the electrolyte concentration[19]: At low concentration, the cations will dominate – at higher concentrations (up to ~5 M in NaCl), the anions become more important, and the mechanism approaches an almost 50/50 mixture[19]. This conclusion has also been verified by experiment[20], and is important for understanding and designing actuator performance. The analysis based on figure 3 is not affected by this complication since it refers to the *first* reduction, which has cation insertion only.

2.5 *Forcing a simple mechanism I? Charge of cycling ions*

The gradual realization of the complexity of cycling mechanisms even when using a large, immobile synthesis anion (e.g. DBS^-), provided the momentum for attempting to find ways of simplification. One path explored was to choose the cycling ions in the electrolyte so as to avoid both ions moving. Since the inserted cations are attracted to the DBS^- ions by Coulomb forces, an obvious idea is to use a divalent or trivalent cation in combination with a monovalent anion. During the initial, *first* reduction, cations will have to be inserted, since there are no small anions in the film to expel. Perhaps the cations will then stay fixed in the film and subsequent cycles will be via a pure anion mechanism.

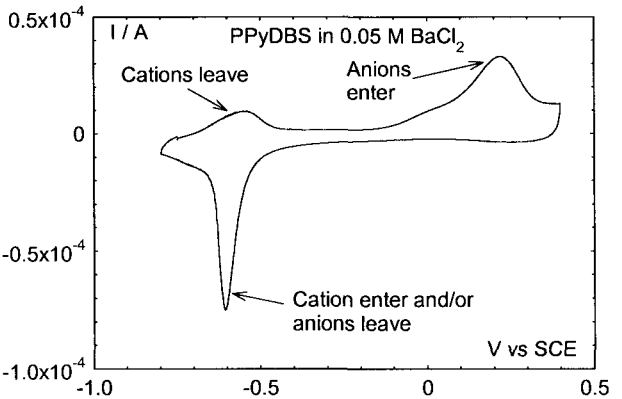

Figure 4. First full cyclic voltammogram cycle (starting with reduction from +0.3 V) of a PPy(DBS) polymer in $BaCl_2$ electrolyte. Cl^- anions dominate the oxidation because the divalent Ba^{++} ions inserted during the first reduction are bound more strongly in the film.

Figure 4 shows the results of such an attempt, using $BaCl_2$ as cycling electrolyte[23]. As is typical for PPy(DBS) in aqueous electrolytes, there are only three distinct current peaks: a sharp reduction peak at -0.6 V, a broad oxidation peak at ca. -0.55 V, and a second broad oxidation peak at ca. +0.3 V. The latter peak is known only to occur when mobile *anions* enter as part of the process. The other broad anodic peak is known to signify *cations* being expelled. Even with a mixed cation/anion mechanism, there is usually only a single, sharp cathodic peak; it therefore represents cations entering *simultaneously* with anions leaving the film[22]. The reason for the ions operating in tandem is probably associated with the strong decrease in electronic conductivity as the polymer is reduced past the cathodic peak. The *first* reduction, however, can involve only cations entering.

Figure 4 indicates that the idea is partially confirmed: The charge (area) of the -0.6 V cathodic peak is considerable larger than that of the -0.55 V anodic peak, and there is a very large charge associated with the anion insertion at +0.3 V. The mechanism is then dominated (but not exclusively) by anions, as predicted. The following reactions can be written:

Synthesis: $nPy + nxDBS^- \rightarrow poly(Py^{x+} \cdot xDBS^-)_n + nxe^-$ (9)

1st Reduction: $PPy^{x+} \cdot xDBS^- + xe^- + x/2Ba^{++} \rightarrow PPy^0 \cdot x/2Ba^{++} \cdot xDBS^-$ (10)

1st Oxidation: $PPy^0 \cdot x/2Ba^{++} \cdot xDBS^- + (1\text{-}r)xCl^- \rightarrow$

$PPy^{x+} \cdot (1\text{-}r)x/2Ba^{++} \cdot xDBS^- \cdot (1\text{-}r)xCl^- + xe^- + rx/2Ba^{++}$ (11)

2nd Reduction: $PPy^{x+} \cdot (1\text{-}r)x/2Ba^{++} \cdot xDBS^- \cdot (1\text{-}r)xCl^- + xe^- + rx/2Ba^{++} \rightarrow$

$PPy^0 \cdot x/2Ba^{++} \cdot xDBS^- + (1\text{-}r)xCl^-$ (12)

In the reaction set, r is the fraction of Ba^{++} ions that move. Equations (11) and (12) are her depicted as just the reverse of each other, but actually, r changes during cycling, so that the simple model is not valid until after 10-20 cycles, where a steady state, mixed mechanism is reached. A pure anion mechanism does not occur, and the results underscore the prospect of yet another complicating factor: The possibility of gradually building up a concentration of neutral salt inside the polymer – at all potentials, not just in the reduced state as in equation (6).

2.6 *Forcing a simple mechanism II? Size and shape of cycling ions*

A second way of attempting to impose a single ion mechanism on the actuator is to use a large and perhaps three-dimensional ion as part of the cycling electrolyte. We have performed experiments using tetraethyl ammonium chloride (TEAC) for cycling PPy(DBS) polymers. The TEA^+ cation is shown in figure 5. It is both bulky and three-dimensional and therefore may be expected to compel the system to work via a pure anion mechanism in the steady state. Since the *first* reduction can involve cations only, it is expected to be very different from the subsequent cycles.

Figure 6 shows the first two cycles. The first reduction confirms to expectation: It seems to be difficult to insert TEA^+ into the film. On oxidation, a sharp peak in the potential region usually associated with anion insertion occurs, whereas there is no sign of cation expulsion.

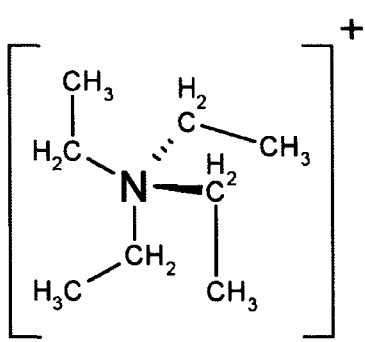

Figure 5. Structure of the tetraethyl ammonium ion (TEA).

The second cycle is very different, as expected, but does not seem to correspond to an obvious anion mechanism. The anodic peak seems to indicate cation mobility, or perhaps a mixed mechanism (subsequent cycles are identical to the second). The EQCM results are difficult to interpret, and may be strongly influenced by H_2O motion.

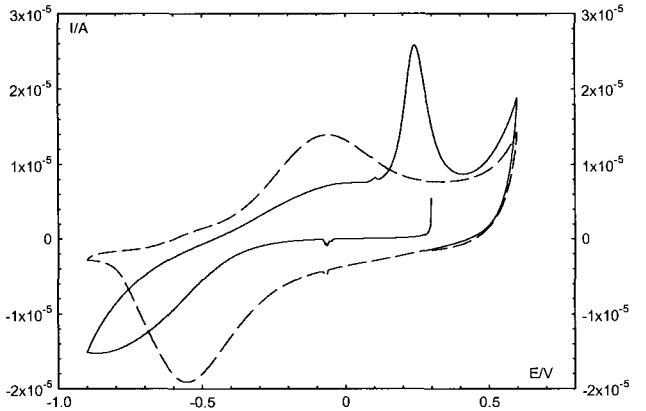

Figure 6. First (full line) and second (dashed) cycles (10 mV/s) of a PPy(DBS) film in 0.1 M TEAC aqueous electrolyte. Starting with reduction from +0.3 V vs Ag/AgCl.

This was an unexpected result, and expansion measurements were performed to further investigate the mechanism. The results (not shown, but analogous to those of figure 7 *after* 6000 s: One maximum and one minimum per cycle) confirmed the cycling data: The film expanded during reduction and contracted during oxidation as expected from a *cation* mechanism. (More negative ΔL = expansion).

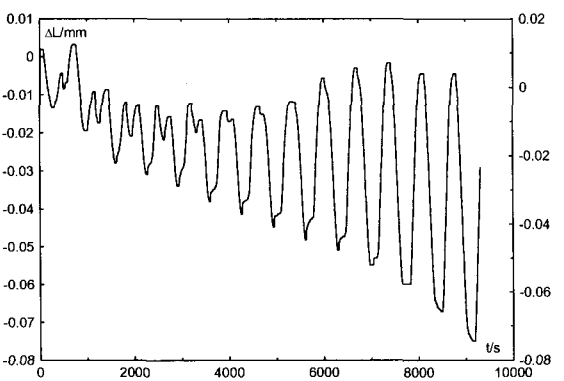

Figure 7. Length change of a 5 mm PPy(DBS) film cycled in TEAC electrolyte. 14 cycles.

The film was then held at -0.9 V for 16 hours to see if any change in mechanism occurred. The results are shown in figure 8, which depicts the first 4000 seconds of figure 7, and is very different from the normal and steady state situations:

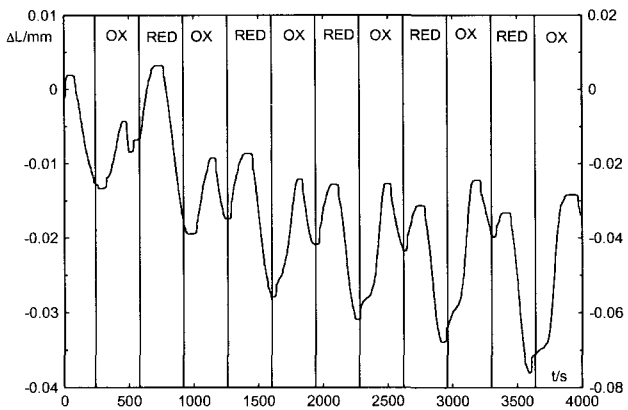

Figure 8. The first 5 cycles of a 5 mm PPy(DBS) film in TEAC electrolyte after 16 h at -0.9 . Reduction and oxidation part of the cycles are indicated. More negative ΔL = expansion.

The length/time curve is now more complex, with two maxima per cycle, and even more surprising, there is an initial *contraction* upon reduction, corresponding to an *anion* mechanism. The mechanism unexpectedly seems to switch to mainly anion for about 5 cycles after long term reduction. The two competing processes means that the strain obtained is rather low initially (0.021 mm, ~0.4%). The mechanism gradually switches back to cation domination (figure 7, last cycles), and the relative expansion then reaches 0.079 mm, or 1.6%. This very interesting phenomenon is difficult to explain at the present and deserves further investigation.

3. Conclusions

The many complex interactions in the solvent/electrolyte cation/electrolyte anion/synthesis anion/polymer system means that these systems do not have a well-defined state or mechanism. It is necessary to reach a steady state before concluding, and the system may still switch between mechanisms.

Avoiding this dependence on solvent and redox history may be the reason for the success of system using ionic liquids, which do not contain any solvent. 1 million cycles has been reached, and they may represent the most promising type of conjugated polymer actuator at the present[24].

Acknowledgements

Financial assistance from the International Programme in the Physical Sciences, Uppsala University, Sweden, has made many years of fruitful collaboration with Sri Lankan scientists possible, and is gratefully acknowledged. The enthusiastic work by my project students, Kasper, Mads, Nadia and Peter, in the fall of 2005, forms the basis for some of the conclusions.

References

1. A.G. MacDiarmid, *Rev. Mod. Phys.* **73**, 701 (2001).
2. M.J. Aldissi, *J. Mater. Educ.* **9**, 333 (1987).
3. Q. Pei and O. Inganäs, *J. Phys. Chem.* **96**, 10507 (1992).
4. Q. Pei and O. Inganäs, *Adv. Mater.* **4**, 277 (1992).
5. E. Smela, O. Inganäs and I. Lundström, *Science* **268**, 1735 (1995).
6. R.H. Baughman, *Synth. Met.* **78**, 339 (1996).
7. Y. Bar-Cohen (ed.), *Electroactive Polymer [EAP] Actuators as Artificial Muscles, Reality, Potential and Challenges,* SPIE Press (2001).
8. E. Smela, *Adv. Mat.* **15**, 481 (2003).
9. M.R. Gandhi, P. Murray, G.M. Spinks and G.G. Wallace, *Synth. Met.* **73**, 247 (1995).
10. S. Skaarup, K. West, L.M.W.K. Gunaratne and K.P. Vidanapathirana, *in B.V.R. Chowdari, K. Lal, S.A. Agnihotry, N. Khare, S.S. Sekhon, P.C. Srivastava and S. Chandra (eds.) "Solid State Ionics, Science and Technology", (World Scientific, Singapore)* p. 163 (1998).
11. S. Skaarup, K. West, B. Zachau-Christiansen, M.A. Careem and G.K.R. Senadeera, *Solid State Ionics* **72**, 108 (1994).
12. Q. Pei and O. Inganäs, *Synth. Met.* **55-57**, 3718 (1993).
13. M. Benslimane, P. Gravesen, K. West, S. Skaarup and P. Sommer-Larsen, *in Y. Bar-Cohen (ed.) "Electroactive Polymer Actuators and Devices"*, Proc. SPIE **3669**, 87 (1999).
14. P.G.A. Madden, J.D.W. Madden, P.A. Anquetil, N.A. Vandesteeg and I.W. Hunter, *IEEE J. Ocean. Eng.* **29**, 696 (2004).
15. G. Alici, P. Metz and G. Spinks, *Smart Mater. Struct,* **15**, 243 (2006).
16. M.-A. DePaoli, R.C.D. Peres, S. Panero and B. Scrosati, *Electrochim. Acta* **37**, 1173 (1992).
17. Q. Pei and O. Inganäs, *J. Phys. Chem.* **97**, 6034 (1993).
18. S. Skaarup, K. West, L.M.W.K. Gunaratne, K.P. Vidanapathirana and M.A. Careem, *Solid State Ionics*, **136-137**, 577 (2000).
19. L. Bay, T. Jacobsen, S. Skaarup and K. West, *J. Phys. Chem. B* **105**, 8492 (2001).
20. Y. Velmurugu and S. Skaarup, *Ionics* **11**, 370 (2005).
21. S. Skaarup, N. Mogensen, L. Bay and K. West, *in Y. Bar-Cohen (ed.) Electroactive Polymer Actuators and Devices (EAPAD)"*, Proc. SPIE **5051**, 423 (2003).
22. Y. Velmurugu, M.A.Careem, S. Skaarup and K. West, *in B.V.R. Chowdari, H.-L. Yoo, G.M. Choi and J.H. Lee (eds.) "Solid State Ionics: The Science and Technology of Ions in Motion", (World Scientific, Singapore)* p. 1073 (2004).
23. S. Skaarup, L. Bay, K. Vidanapathirana, S. Thybo, P. Tofte and K. West, *Solid State Ionics*, **159**, 143 (2003).
24. W. Lu, A.G. Fadeev, B. Qi, E. Smela, B.R. Mattes, J. Ding, G.M. Spinks, J. Mazurkiewicz, D. Zhou, G.G. Wallace, D.R. MacFarlane, S.A. Forsyth and M. Forsyth, *Science* **297**, 983 (2002).

DEVELOPMENT AND CHARACTERISATION OF POLYFLUORENE BASED LIGHT EMITTING DIODES AND THEIR COLOUR TUNING USING FORESTER RESONANCE ENERGY TRANSFER

BY

P. C. MATHUR*, AMIT KUMAR, P. K. BHATNAGAR,

DEPARTMENT OF ELECTRONIC SCIENCE, UNIVERSITY OF DELHI SOUTH CAMPUS, NEW DELHI- 110 021,INDIA.

K.TADA AND M.ONODA,

DEPT. OF ELECTRICAL ENGG., AND COMPUTER SCIENCE,UNIVERSITY OF HYOGO, HIMEJI, JAPAN.

Abstract

Conducting polymers have high potential for FRET. The development of Light Emitting Diodes (LED) has taken place at quite a fast pace due to their nontoxic, easy processing and low cost development techniques. The LEDs based on conducting polymers are mechanically flexible and strong. However, the commercialization of these devices has not yet been made. During the work on the development of conducting polymer based (MEH-PPV) LED, we have identified four problems which have to be taken care of before the device fabrication:

a) To maintain a balance between electron and hole concentrations one has to use a composite structure of two polymers one a hole transporting layer (HTL) and other a electron transporting layer (ETL). To use a single layer of emissive polymers is not desirable.

b) The thickness of ETL must be optimized so that the recombination of injected electrons and holes takes place near the cathode; the exciton will break due to high electron affinity of ETL resulting in the loss of electro luminescence (EL). On the other hand if the recombination takes place near anode, the exciton will again break due to high ionization potential of HTL.

c) The work function of the cathode should be as low as possible so that the potential barrier for electron injection at the cathode is low. To use buffer layers of material such as LiF, K or Ba with optimized thickness between the ETL and Al cathode contacts is a possible solution.

d) The mobility of the injected carriers should be as high as possible. For this the morphology of the films should be improved by optimizing the concentration of the solute before spin coating the film on the ITO coated glass substrates. The speed and duration of spin coating should also be optimized.

After studying all the above-mentioned problems, using MEH-PPV/Alq_3 composite LED structures we entered into the area of development of blue LED using PFO and its copolymers such as F8BT, PF3t, $PFTSO_2$ and TPP. The blue LEDs are in great demand for full colour display. They are more stable as compared to the MEH-PPV based LEDs.

These commercially available polymers are dissolved in solvents xylene and toluene. The films of PFO, PFO/F8BT, PFO/PF3T, PFO/$PFTSO_2$ and PFO/TTP are spin coated on ITO coated glass substrates. The concentrations of the copolymers of PFO and TPP are optimized so that Forster Resonance Energy Transfer (FRET) occurs between the two composite materials. In that case the PL from PFO (donor) is quenched and PL from the copolymers is significantly enhanced. Colour tuning right from blue to red wavelength region with highly stable and intense EL can be obtained in this way. The cathode contacts are Al with Ba buffer layer while the anode contacts are ITO with a buffer layer of PDOT-PSS. The thickness of the buffer layer is optimized to achieve maximum possible intensity of EL. Attempt is also made to reduce the turn on voltage of the devices and keep it below 10 Volts.

Conjugated polymer based opto-electronic devices such as Light Emitting Diodes (LED) and Solar Cells have high potential due to their non-toxic environmentally friendly techniques, high mechanical strength and flexibility and low cost as compared to inorganic semiconductor based devices. Though a large number of papers have been published in this area, the commercialization of these devices has not taken place as yet. We have been working for the past four years or so on the development and characterization of MEH-PPV based LED and have successfully produced devices giving electroluminescence (EL) at a peak of 580 nm (yellow-orange region) and shelf life ~ 1400 hrs. [1-3]. The half life of these diodes ~100 hrs, luminance 500 cd/m^2 and power efficiency `0.2 lm/watt at an operating voltage of 15 volt. The EL characteristics of these devices at three

different bias voltages are shown in Fig.1.The I-V characteristics of one of the devices is shown in Fig.2.

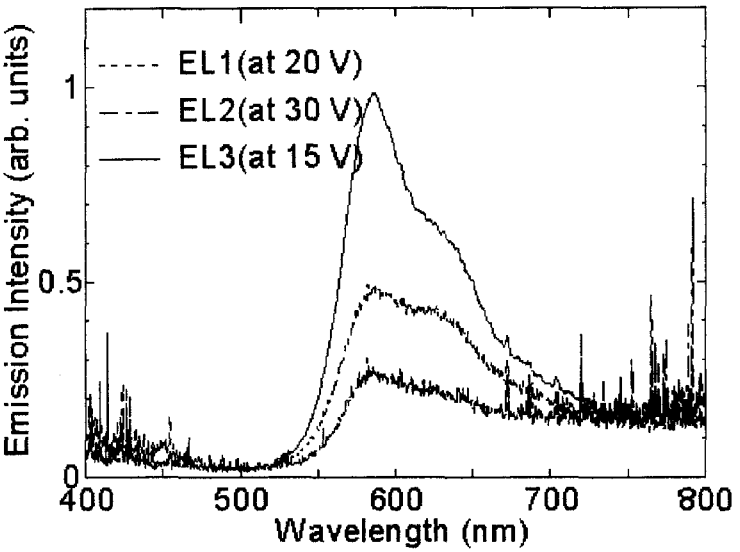

Fig.1 A typical MEH-PPV LED at three different bias voltages

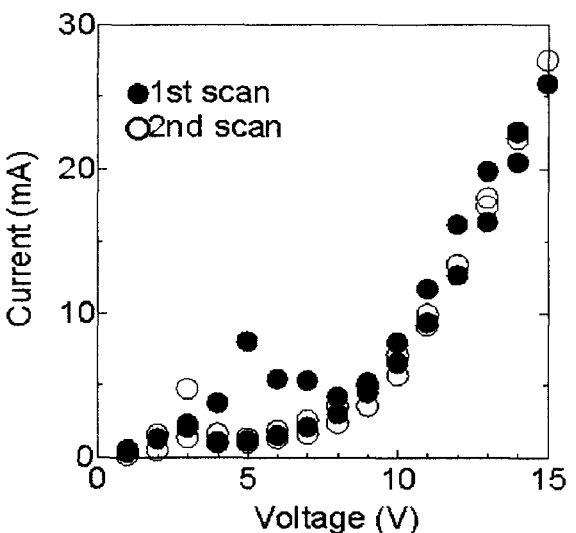

Fig. 2 Current voltage characterstic of a typical MEH-PPV LED

While the MEH_PPV based working LED have been successfully been produced by us, long way has to go if they are to be commercialized. During the course of our work we realized that there are few outstanding problems, which have to be taken care of first before we can try to produce a workable efficient and stable LED. These are the following:

(i) Rather than using a single layer of the emissive polymer one must use a composite structure of two polymers, one a hole transporting layer (HTL) and the other an electron transporting layer (ETL).This because in most of the polymers the mobility of holes is much higher than that of electrons, resulting in imbalance of hole injected from anode and holes from cathode. Working of a typical LED is shown in Fig.3 and Fig.4.The ETL must have its LUMO level below that of the emissive polymer so that the injected electrons encounter a work function, which enables them to pass through ETL. Similarly the HOMO level of ETL must be well below that of the emissive material so the holes injected from the anode are blocked to go to ETL and recombination of electrons and holes occurs in the emissive region. Due to these reasons we selected a composite of MEH-PPV/Alq_3 for our LED.

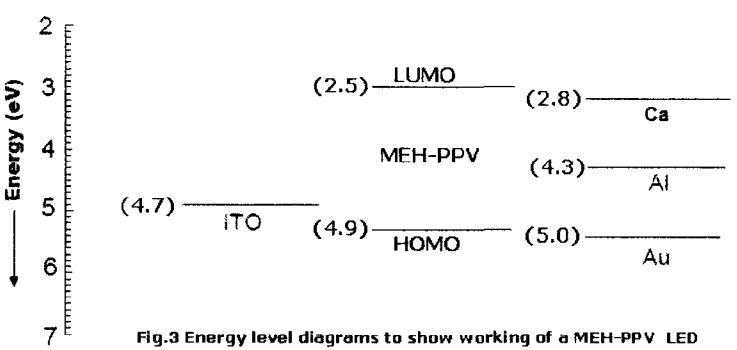

Fig.3 Energy level diagrams to show working of a MEH-PPV LED

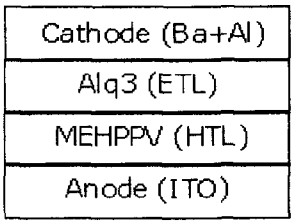

Fig. 4 Structure of the MEH-PPV LED

(ii) The next important point is optimization of the concentration of the emissive polymer in the solvent. For MEH-PPV we selected p-xylene as a solvent and used the spin coating technique for depositing the films on ITO coated glass substrates. We found that if the concentration of the solute is too high, the morphology of the films is not good and they suffer from kinks, disorder and overlapping of the chains. It is also found that the mobility of charge carriers in the films is very low and these films are not suitable for device fabrication. On the other hand if the concentration of the solute is too low, the EL emission from the material will be very poor. For MEH-PPV we found the optimum concentration of the polymer to be ~ 10mg/ml.

(iii) The recombination of injected electrons and holes must take place near the polymer ETL interface, but in the emissive material. If recombination takes place near the cathode its high electron affinity will break the exciton before it can decay from the excited state to the ground state. Similarly if the exciton is formed very close to the anode, it will not be allowed to decay radiatively because the high ionization potential of the anode will dissociate the exciton. Knowing the mobility of the holes and electrons one can calculate the desired thickness of the films. It was found that the optimum thickness of the MEH-PPV films is ~180nm and that of $Alq_{3\ films}$ is~ 100nm.

(iv) One of the most prominent problems encountered in the development of the polymer based LED is a growth of suitable cathode contact. The cathode must have low work function and ideally the LUMO level of the conducting polymers lower than the work function of the cathode. This will allow the electrons injected from the cathode to enter the ETL without encountering any potential barrier. We tried to develop Ca contacts on our MEH-PPV films. The work function of this material is 2.8 ev and therefore the potential barrier for the electron injection in MEH-PPV is very low. However Ca has tendency to form clusters and gets oxidized easily. Besides this it also forms Ca^{++} ions. The Ca cathode contacts are therefore deteriorated very fast.

The material that is very stable and suitable for the Cathode contacts is Al. However, the work function of Al is very high (~ 4.3ev) and therefore the injected electrons encounter a very high potential barrier. While we did use Al as a cathode contact material for our MEH-PPV LED, we put a thin buffer layer of 30-50nm thick Ba between Al and the polymer. The optimum evaporation rate of Ba was found to be 0.3 nm /sec and that of Al was 0.6 nm/sec. We measured the J-V characteristics of the device with and without buffer layer. These are shown in Fig. 5. It is found that there is a significant increase (more than by an order of magnitude) in the current densities as a result of inserting the buffer layer. This shows that the buffer layer significantly lower the potential barrier for electron injection.

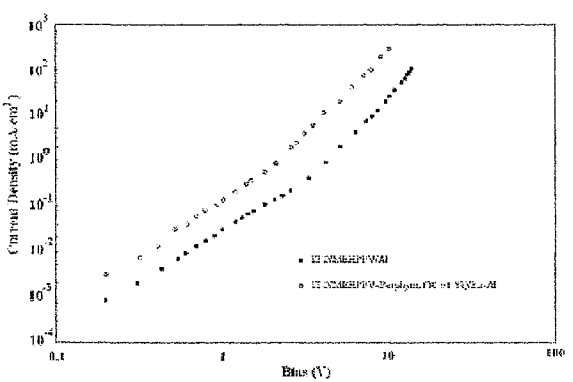

Fig.5 J-V characteristics of a typical MEH-PPV LED with and without Ba buffer layer

We are applying all these experiences acquired from our work on MEH-PPV diodes for the development of a blue PLED based on PFO. This material has a energy gap of 3.68 ev [4] and the primary emission peak is at 436 nm [5]. For ETL we have selected PBD, which has got LUMO and HOMO levels at 2.5ev, and 6.0 ev respectively [6]. The LUMO level of PFO is at 2.1 ev and the HOMO level at 5.8ev [7]. The conditions for PBD to act as an ETL are therefore satisfied. ETL will also block the diffusion of Al and Ba atoms into the polymer thereby preventing the generation of quenching centers. For PFO we are using xylene and toluene as the solvent .The purpose of using two solvent is to examine the effect of the solvent on the morphology of the film and hence on the onset voltage of the device. We are also using a thin PEDOT layer (~100-200nm thick) in between ITO and the PFO. This layer acts as a HTL and also lowers the potential barrier for hole injection from the anode. Our objective is to obtain a luminance of 3500 cd/m^2 and power efficiency of 0.8 lumens/watt at 6 volts.

For colors tuning several workers [8,9] have used copolymers of PFO such as F8BT, PF3T, $PFTSO_2$ and TPP with alternate arrangement of PFO and copolymer molecules eg. ABABAB where A is PFO and B is copolymer. However we shall use FRET [10] to obtain colour tuning. We shall grow a composite film of the PFO and the copolymer and shall optimize the concentration of the copolymer to obtain efficient FRET between the two. This means that the blue PL from the PFO will be quenched and the characteristic Pl from the copolymer will be significantly be enhanced and the efficient FRET between the two occurs. We shall be able to colour tune the LED from blue to red wavelength region in this way.

References :

1. Amit Kumar, P.K.Bhatnagar, P.C.Mathur, Sandip Sengupta, Jayant Kumar *J.Applied Physics*, **98**, 024502, (2005).
2. Amit Kumar, P.K.Bhatnagar, P.C.Mathur, K.Tada, M.Onoda, *J.Material Science Letters*, **40**, issue 14,3849-51 (2005).
3. Amit Kumar, P.K.bhatnagar, P.C.Mathur, K.Tada, M.Onoda, *J.Applied Surface Science* (2006) In Press.
4. A.Grice, Bradley, M.Bernius, M.Inbasekaran, W.Wu, E.Woo, *Appl.Phys Lett*, **73**, 629, (1998).
5. M.Inbasekaran, W.Wu ,E.P.Woo, US Patent 5 777 070, (1998).
6. Shun-Chichang, Gufeng He, Feng Chung Chen, Tzung-Fang Guo and Yang Yang, *Appl.Phys.Lett.*, **79**, 2088, (2001).
7. WanaliMa, Parameshwar K. Iyer, Xiong Gong, Bin Liu, Daniel Moses, Guillermo.C.Bazan, Allen J Heeger, *Adv.Mat*, **17**, 274, (2005).
8. J. P. Choi, K. T. Wang,Y. M. Chen, J. K.Yu, P. T. Chouand, A. J. Bard, *J. Phys. ChemB*, **107**, 14407, (2003).
9. A.Kanibolostsky, R.Berridge, P.J.Skabora, I.F.Perepichka, D.D.C Bradley and M.Koeberg, *J.Am.Chem.Soc.*, **126**, 13696, (2004).
10. D.L.Dexter, *J.Chem.Phys*, **21**, 836, (1953).

MESOPOROUS AND NANOPARTICULATE METAL OXIDES: APPLICATIONS IN NEW PHOTOCATALYSIS

COLIN BOXALL
Centre for Materials Science, University of Central Lancashire, Preston PR1 2HE, UK
E: cboxall@uclan.ac.uk; T: +44 1772 893530; F: +44 1772 892996

Semiconductor metal oxides find application in dye-sensitised solar cells and as photocatalysts for a range of environmentally and industrially useful reactions. In both technologies, the systems are driven by the initial absorption of photons to form charge carriers. These charge carriers may subsequently recombine or diffuse to the oxide surface where they may undergo interfacial electron transfer. In the case of modern solar cells, this involves transfer of the photogenerated charge from the sensitising dye to the semiconductor matrix; in the case of photocatalysis, this involves transfer of the photogenerated charge from the semiconductor to solution. In solar cells, the semiconductor is most often employed in the form of a mesoporous layer; in photocatalysis, it may be in form of either a mesoporous layer or as nanoparticles.

Since 1972, the main foci of photocatalysis have been the photodestruction of organic pollutants and the splitting of water for hydrogen generation. Our studies have focussed on new applications of photocatalysis beyond these areas, in particular the applications of photocatalysis in nuclear fuel reprocessing; the development of novel, magnetic nanocomposite photocatalysts; and the production and characterisation, for sensor applications, of conducting mesoporous metal oxide films that exhibit high degrees of photo-induced superhydrophilicity.

This lecture will present an overview of these studies, concentrating on our work on superhydrophilic materials – the onset of superhydrophilicity in metal oxides being thought to be due to the photogeneration of oxygen vacancies within the semiconductor lattice. We are currently using Quartz Crystal Microbalance-based photo-induced condensation experiments (Fig. 1, the first time such a phenomena has been reported) to study these systems and shall report on our attempts to correlate the degree of condensation within the metal oxide mesopores with photo-induced surface energy changes on the metal oxide by use of the Kelvin Equation for capillary condensation.

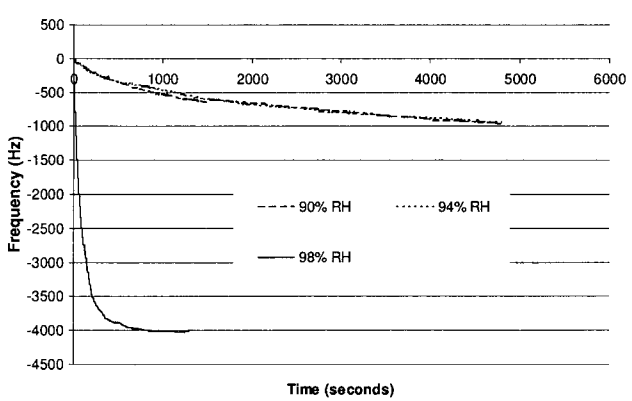

Fig. 1. $MTiO_2$ on QCM: Frequency (mass increase) v time measurements conducted using 315 nm light with varying relative humidity.

PROTON CONDUCTING (PC) PEROVSKITE MEMBRANES FOR HYDROGEN SEPARATION AND PC-SOFC ELECTRODES AND ELECTROLYTES

HRUDANANDA JENA, B. RAMBABU

Solid State Ionics Laboratory, Department of Physics
Southern University and A&M College Baton Rouge, Louisiana-70813, USA

FANNIE POSEY EDDY

National Renewable Energy Laboratory (NREL),
1617 Cole Blvd. Golden CO 80401, USA.

Abstract

$SrCeO_3$, $SrCe_{1-x}M_xO_3$ compositions were synthesized by sonochemical treatment followed hydrothermal method and sintering is done by microwave heating. CeO_2 hydrated gel was obtained from Ce(IV) ammonium nitrate and mixed with $Sr(OH)_2$ and sonicated for 30 min., then the reactants were subjected to hydrothermal treatment at 150^0C for 4 h. $SrCeO_3$ was found to form orthorhombic perovskite above 1200^0C of heat-treatment. The powders were characterized by XRD, TEM, and EIS techniques. The effect of ball milling was also studied on sintering of the pellets. The 10% substitution of dysprosium at Ce site does not form single phase. Instead Sr_2CeO_4 is formed along with $SrCeO_3$. Similarly, Eu, Er (10 % and 90 %Ce) were also attempted to substitute at Ce site; however, $SrCe_{1-x}M_xO_3$ (x=0.10) does not take up 10 % substitution. The electrical conductivity measurements were carried out on the single phase pellets by ac impedance techniques. The results of the experimental results obtained in this study are discussed in this paper.

1. Introduction

Proton conducting perovskite solids have been investigated by many research groups across the globe to arrive at optimized compositions to achieve enhanced proton conductivity at relatively lower temperatures. The property of selective hydrogen permeation through the solid in a wide a range of temperatures makes it attractive to be considered as hydrogen separation membrane [1-6]. Proton conducting solids can be used as electrolyte in solid oxide fuel cells in place of traditionally known oxide ion conducting ytteria stabilized zirconia (YSZ) electrolyte (Fig.1). YSZ or Sr- and Mg-doped $LaGaO_3$ (LSGM) are good oxide ion conducting solid electrolytes, however, these materials need to be operated at 700-1000^0C temperatures to work as an effective electrolyte. The higher operating temperature of the electrolyte affects the material life, problems in operating the cell at higher temperature, selecting the compatible electrode and interconnects components. The higher operating temperature of solid oxide fuel cell can be avoided by replacing intermediate temperature proton conducting perovskite solid electrolytes in place of oxide ion conducting electrolytes. Perovskites can be suitably tailored to exhibit proton

conduction at relatively lower temperatures which will enable fabrication of low or intermediate temperature fuel cells (Fig.1) and hydrogen separation membranes (Fig.2).

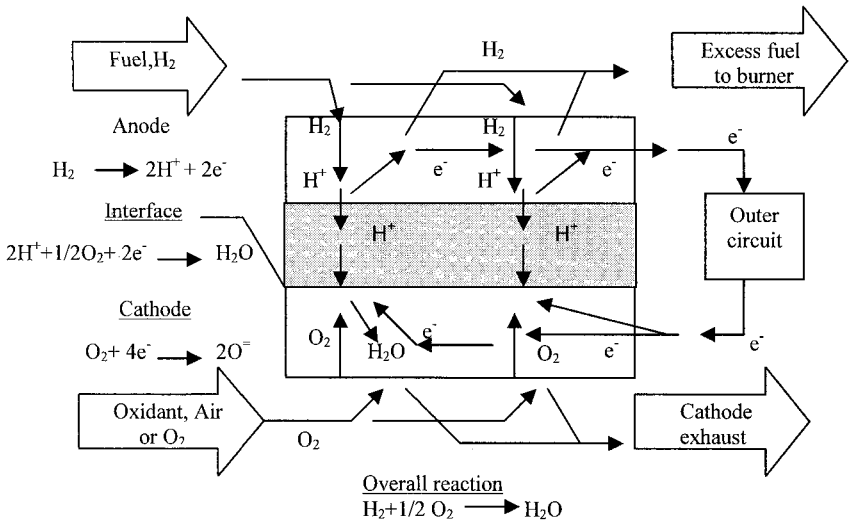

Figure 1. Schematic of SOFC with proton conducting perovskite solid electrolyte.

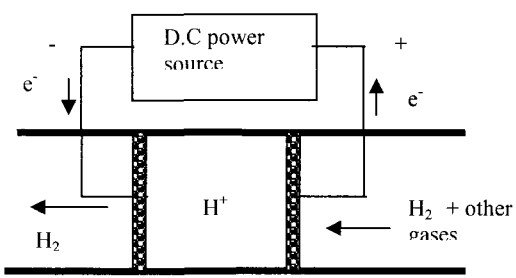

Hydrogen separation membrane/
hydrogen pump

Figure 2. Schematic of hydrogen separation membrane

This could be done by doping a single phase oxide or by forming a two-phase composite material. We are investigating the structure and transport properties of a number of doped and undoped perovskites. Dense perovskite membranes made of mixed electronic and protonic conductors

provide a simple, efficient and cost-effective means to separate hydrogen from gas streams. High proton conductivity has been reported for various perovskite-type oxides such as cerates and zirconates in hydrogen/humid atmosphere. However, only a few, if any, satisfy both high protonic conductivity and thermodynamic stability that are prerequisites for the application of such membranes as successful separators. This paper deals with the study and development of dense, thin ceramic membranes of : 1) proton conducting perosvskites ($A^{2+}B^{4+}O_3$) as hydrogen separation membranes, and 2) mixed [electron & H^+] aliovalent ion substituted perovskites ($A^{2+}_{1-x}M_xB^{4+}_{1-y}N_yO_{3\pm\delta}$) as electrode (porous) and electrolyte for proton conducting (PC)-SOFCs.

The limitations of the perovskites used as electrolytes in PC-SOFCs are: 1) high grain boundary resistance observed in case of ytteria doped $BaZrO_3$ (BYZ) which leads to reduced ionic conductivity, and 2) stability of the B-cation in the 4^+ oxidation state in cerates which influence the ionic conductivity and structural distortion of the crystal lattice. To overcome these limitations, we have adopted novel wet chemical methods of synthesis including: 1) sonochemical, 2) hydrothermal, 3) gel to crystallite conversion, and 4) regenerative sol gel methods to achieve nano particles for improving sintered density while stabilizing high symmetry single phase structures (alkali and rare-earth substituted strontium cerates, composite $Ba(Zr,Ti)O_3$) with enhanced proton conductivity at low temperatures. The mechanism of proton conduction and the influence of preparation conditions on the microstructure and proton conductivity of the $A^{2+}B^{4+}O_3$ perovskites and its doped compositions are reported.

$BaCeO_3$, $SrCe_{1-x}M_xO_3$ compositions were synthesized by sonochemical treatment followed hydrothermal method and sintering is done by microwave heating. CeO_2 hydrated gel was obtained from Ce(IV) ammonium nitrate and mixed with $Sr(OH)_2$ and sonicated for 30 min., then the reactants were subjected to hydrothermal treatment at 150^0C for 4 h. $SrCeO_3$ was found to form orthorhombic perovskite above 1200^0C of heat-treatment. The 10% substitution of dysprosium at Ce site does not form single phase. Instead Sr_2CeO_4 is formed along with $SrCeO_3$. The electrochemical and surface chemistry, cell testing measurements were performed using advanced spectro-electrochemical characterization techniques such as XRD, TEM, and EIS techniques. The effect of ball milling was also studied on sintering of the pellets.

2. Experimental

2.1 Hydrothermal method

Stoichiometric concentrations of $Sr(OH)_28H_2O$ and $Ce^{4+}(NH_4)_2(NO_3)_6$ were taken. Ce^{4+} $(NH_4)_2(NO_3)_6$ was dissolved in deionized water and NH_4OH was added to precipitate CeO_2. x H_2O . $Sr(OH)_2$ was added to a teflon bowl and CeO_2. x H_2O was transfered in to the bowl. The bowl was kept in stainless steel autoclave and heated at 150^0C for 4 h. The content was transferred and heated to dryness and

calcined at 1150^{0}C for 6 h. The powders were characterized by XRD and other techniques.

2.2 Ball milling

Stoichiometric concentrations of $Sr(OH)_2$ $8H_2O$ and $Ce^{4+}(NH_4)_2(NO_3)_6$ were taken and ball milled for 1 hour in a SPEX CertiPrep 8000-series MIXER/MILL. The powder obtained after ball milled was palletized and heated in a furnace at 900^{0}C and 1200^{0}C. The powder and pellets were characterized by XRD.

2.3 Glycine nitrate combustion

Stoichiometric concentrations of $Sr(OH)_2$ $8H_2O$ and $Ce^{4+}(NH_4)_2(NO_3)_6$ were taken and dissolved to clear solution and adding 1:1 HNO_3 and ultrasonication using a ultrasonic processor (M/s. Sigma Aldrich), 750 watt power. To the clear solution glycine was added and the entire reactant beaker was heated on a hot plate (at ~100^{0}C). The solution froth and yielded a fluffy mass. Substitution of Dy, Eu, Er were substituted at Ce site as 10 % and 5 % by taking corresponding concentrations and same procedure was followed to prepare the substituted compositions. The precursor powder was further calcined at 750^{0}C and 1200^{0}C for 6 h each. The powders were characterized by XRD and other techniques.

2.4 Characterization

The powders were characterized by X-ray diffractometry using Siemens D 500 or D5000 machine with a scan rate of 0.02 deg./sec and a counting time of 1 sec per step. Elecrical conductivity of the pellets were measured at 25-1000^{0}C using a HP impedance spectrometer.

3. Results and discussions

The hydrothermal technique is a very suitable method of preparation for perovskites with higher concentration of hydroxyls. The hydrothermal method used here did not yield single phase perovskites of $SrCeO_3$ or its doped compositions after hydrothermal treatment at 150^{0}C/4h. The precursor formed contains nano-crystalline CeO_2 hydrated gel along with other amorphous constituents. This was observed from the XRD (Fig. 3) peaks which correspond to CeO_2. The nanocrystalline nature of CeO_2 was also confirmed from the selected area electron diffraction (SAED) pattern as shown in the Fig. 4(a) and TEM micrograph (Fig.4 (b)). The ring pattern (Fig. 4(a)) is indicative of nano-crystalline nature of the particles. Then hydrothermal method did not yield single phase $SrCeO_3$ or its doped compositions at 150^{0}C/4h condition. The preparation of $SrCeO_3$ and its doped compositions by hydrothermal method needs optimization to yield the final product at elevated temperatures or by changing the solvents. The substitution of Dy, Er, Eu at 10% level at Ce-site did not form single phase, instead two or three phase mixture of compounds were obtained. The phases like $SrCeO_3$, Sr_2CeO_4 and CeO_2 were obtained as shown in

Fig. 2. The CeO_2 lattice constants calculated by indexing the corresponding XRD patters are a= 5.411 Å, space group=Fm3m. The Sr_2CeO_4 lattice constants are a=6.119 Å, b= 10.349 Å, c=3.597 Å .The stability of phase pure compositions with 5 % substitution is under progress. In case of ball milling methods of preparation, $Sr(NO_3)_2$ was observed at initial stage of reaction at room temperature. On calcinations to higher temperature (1250^0C/6h) single phase $SrCeO_3$ was formed. The crystal structure of $SrCeO_3$ on indexing the XRD pattern was found to be orthorhombic with a lattice constant of a=6.153Å, b=6.012 Å and c=8.589 Å, Space group=Pbnm.. I

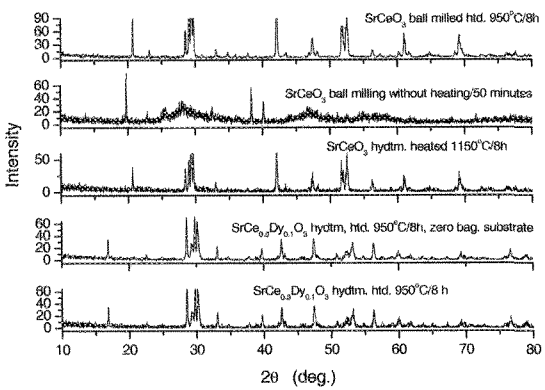

Figure 3 XRD patterns of $SrCe_{1-x}M_xO_3$ (M=Dy,) shows the evolution of phase on calcining at various temperatures

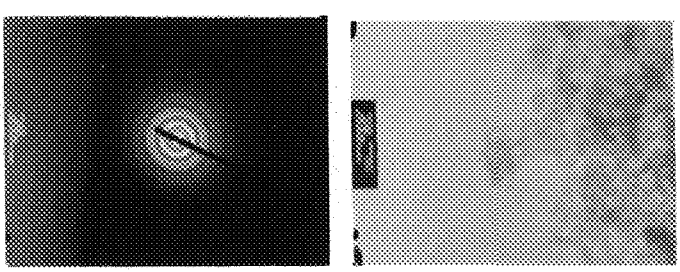

(a) (b)

Figure 4 (a) SAED of $SrCeO_3$ hydrothermal precursor heated at 400^0C, showing nano-crystalline nature of CeO_2 gel (b) TEM micrograph of the hydrothermal precursor gel.

The glycine nitrate method also did not form phase pure perovskites immediately after charring the precursor on a hot plate. This may be attributed to the insufficient provision of insitu heating to form the product. On adding excess glycine the powders were observed with burning flame. The precursor powders needed further calcinations to yield the phase pure $SrCeO_3$.

The electrical conductivity of the compositions was measured by ac impedance method. The electrical conductivity plot on $SrCeO_3$ is shown in Fig. 5. The electrical conductivity of the sample increases with increasing applied frequency and temperature. The electrical conductivity observed at 25^0C or room temperature is attributed to adsorbed water and the hydroxyls present in the lattice. On increasing the temperature above 100^0C the electrical conduction seen is attributed to the prevalence of hydroxyl protons in the $SrCeO_3$. Similar experiments on alkaline zirconates and titanates [7] showed the presence of hydroxyl protons in the perovskite lattice. The electrical conduction in these perovskites is enhanced by oxygen vacancies at and above 500^0C. The electrical conductivity observed to increase above 350^0C as shown in Fig.5.

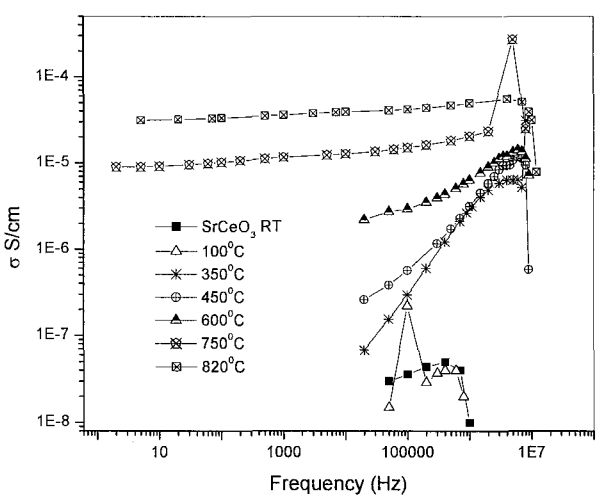

Figure 5 Electrical conductivity measurements on $SrCeO_3$ prepared by ball-milling and sintered at 1250^0C/6 h

The electrical conduction observed below 500^0C is attributed to the migration of hydroxyl protons (Grotthus mechanism) along the oxygen octahedra in the perovskite lattice. Above 500^0C to 820^0C it is observed to

be higher and the charge carriers are observed to be mobile at low applied frequency of 20-50 Hz. The details on the mechanism of electrical conductivity, phase and structural satability of these compositions are beyond the scope of this paper. The preparation of thin membranes from the substituted perovskites and electrical conductivity measurements on the the membranes will be communicated separately.

4. Conclusions

The preparation methods like hydrothermal needs to be carried out at higher temperatures to avoid carbonate formation. The ball milling method produces the product on calcining the precursor at 1250^0C/6h, but it contains nitrate of Sr- as intermediate phases during the course of ball milling. The glycine nitrate method yields the product but needs to be optimized to obtain the single phase product at lower temperature of heat-treatment to retain the high symmetry phase and nanocrystalline nature of the particles so that it can be used to achieve pore free membranes. The suitable aliovalent substitution in the perovskites can led to introduction of mixed conduction (electron, oxide ion and proton or two of them) in perovskites. Mixed conducting perovskites can be used for SOFC electrode purposes in combination with proton conducting electrolyte.

Acknowledgement

BRB acknowledge the support of U.S-DOE-NREL and U.S-DOE-NETL through grants # ACQ-4-33623-01, #DE-FG26-03NT4195. H. Jena thanks the IGCAR for granting extraordinary leave for availing exchange visitor assignment in Southern University, USA.

References:

[1]. H. Matsumoto, T. Shimura, H. Iwahara, T. Higuchi, K. Yashiro, A. Kaimai, T. Kawada and J. Mizusaki, "Hydrogen separation using proton-conducting perovskites" , J. Alloys and Compounds, **408-412**, (2006) 456-462 ,

[2]. N. Sata, H. Matsuta, Y. Akiyama, Y. Chiba, S. Shin and M. Ishigame,"Fabrication of proton conducting thin films of $SrZrO_3$ and $SrCeO_3$ and their fundamental characterization" Solid State Ionics, **97**, (1997)437-441.

[3]. H. Yugami, H. Naito and H. Arashi," Fabrication of $SrMO_3$ (M = Ce and Zr) thin films and $SrCeO_3/SrZrO_3$ superlattices by laser ablation", Applied Surface Science, **113-114** (1997)222-226.

[4]. R. V. Kumar,"Application of rare earth containing solid state ionic conductors in electrolytes" J. of Alloys and Compounds, **250**, (1997) 501-509 .

[5]. H. Iwahara," Proton conducting ceramics and their applications", Solid State Ionics, **86-88**, (1996) 9-15.

[6]. H.Yugami, F. Iguchi and H. Naito," Structural properties of $SrCeO_3/SrZrO_3$ proton conducting superlattices" Solid State Ionics, 136-**137**(2000) 203-207,.

[7]. H. Jena, K.V.G. Kutty and T.R.N.Kutty,"Proton transport and structural relations in hydroxyl-bearing $BaTiO_3$ and its doped compositions synthesised by wet-chemical methods" Mater. Res.Bull., **39** (2004) 489-511.

Contributed Papers

This page is intentionally left blank

ELECTROCERAMIC MATERIALS FOR THE DEVELOPMENT OF NATURAL GAS FUELLED SOFC/GT PLANT IN DEVELOPING COUNTRY (TRINIDAD &TOBAGO (T&T))

RAMSEY SAUNDERS[1], HRUDANANDA JENA[2] and B. RAMBABU[2]

Faculty of Agriculture and Natural Sciences
[1]Department of Physics,The University of the West Indies
St.Augustine, Trinidad and Tobago, West Indies

[2] Solid State Ionics laboratory, Department of Physics
Southern University and A&M College
Baton Rouge, Louisiana-70813, USA

Abstract

Various compositions of ceria, Gd-doped ceria and perovskite such as Sr-, Mg- doped $LaGaO_3$, Sr-doped $LaMnO_3$, Sr-doped lanthanum ferrate, cobaltate, $LaCrO_3$ and doped compositions were prepared by adopting several preparation methods. The materials were tailored to be used as anode, cathode, and electrolyte and interconnect in solid oxide fuel cells (SOFCs). The materials were characterized by XRD, TEM and other spectrochemical methods. Electrical conductivity of the compositions was measured by electrochemical impedance spectroscopy (EIS). These experiments were carried out to optimize the composition and various properties of the materials to be used in natural gas fuelled SOFCs. The study is aimed at developing materials to fabricate natural gas fueled SOFC hybridized to a gas turbine (SOFC-GT) to enhance power production and maximum utilization of resources in Trinidad.

1. Introduction

It has been said over and over again by many experts that the T&T in the Caribbean region is ideally located to promote the advanced power source technologies based on natural gas (NG). At present the NG reserves are estimated at approximately 27 trillion cubic feet with a current production rate of about one billion cubic feet per day. Crude oil and condensate reserves are about 550 million barrels with production levels for 122,627 barrels per day. Almost 75 % of the country's energy consumption come from NG and use it for electricity, petrochemical, and other industries. In the last four years, the natural gas industry has been growing at an average annual rate of 10%. The World Bank has ranked T&T as "an upper middle-income oil producing country" which has lead to an intensive industrialization thrust, and believed to be most prosperous among the Caribbean countries. The vision of T&T is moving towards shifting from oil-based economies to knowledge-based economies in which innovation and implementation in energy sector is key to long-term competitiveness. Power generation by fuel cells and gas conversion in Fischer-Tropsch synthesis are creating possibilities for making T&T a strong industrialized nation.

To utilize the NG assertively for sustainable development and growth of the region, there is an urgent need to explore distributed energy

sources fuelled by NG that can provide customers with reliable, local energy supplies while lowering the emissions of air pollutants. In this scenario, the renewable energy technology for power generation that is in the verge of commercialization is the fuel cell technology for both stationary, and transportation applications. Very recently, Dr. Ramsey Saunders of University of west Indies, Trinidad, and Dr. Bobba of Southern University, Baton Rouge, USA proposed to establish a national center for research excellence for promoting hydrogen economy entitled "Center for Hydrogen Energy and Advanced Power [CHEAP]" for conducting study, research, consultancy, organizing seminars and conferences in areas of fuel cells and hydrogen, and establishing a model decentralized 10-50 KW NG fuelled solid oxide fuel cell (SOFC) power plant in T&T jointly with the T&T NG Company. All activities of the centre will move from materials research for component and cell development, production, and formulating strategies for developing decentralized power generation source that can be highly efficient, clean, quiet, scalable, reliable, and potentially cheap. Such power packs will become popular for energizing the medium, and business complexes (malls), hospitals, centralized office complexes, airports, educational institutions, residential complexes, and remote villages in T&T. Global market analysts expect that the overall market for fuel cell technology could reach $95 billion by the year 2010. The vision of this industrial/academic R &D CHEAP is to prepare T&T for grabbing the market share that belong to decentralized power based on NG.

Solid oxide fuel cell (SOFC) is a high temperature device that permits the electrochemical conversion of chemical energy to electricity. The tubular SOFC of Siemens-Westinghouse (SW) Power Corporation operates at around 900-1000°C, while Delphi planar SOFC operates at around 750-800°C. It has ceramic-based membrane and electrodes. The standard materials for the tubular cell components are: Yttria-stabilized zirconia (YSZ) for the dense electrolyte, a porous mixture of Sr-doped $LaMnO_3$(LSM) + YSZ for the cathode, a porous mixture of Ni + YSZ for the anode and doped $LaCrO_3$ and high temperature alloys for the interconnect. The tubular SOFC system has been developed by Siemens-Westinghouse and other European and Japanese companies; units as large as 200 kW have been success-fully demonstrated. The uniqueness and attractiveness of the tubular design is that it is a seal-less design, because sealing is an extremely challenging problem at high operating temperatures. However, the tubular SOFC has quite low volumetric and area power density. For example, the maximum power density of the tubular SW cells is only 2.5 kW/m^2(0.25 W/cm^2) at 1000°C. The high temperatures have resulted in very high cost of the components of the balance of power plant. Hence recently, the interest has shifted to the planar SOFC concepts, operating at 700-800°C, with research focusing on even lower temperatures, 650°C or lower. The planar SOFC system being developed by Delphi Corporation has 5 kW capacity and 106 cm^2cell area. The SOFC based on the concept of planar, anode-supported design has led to power densities approaching 20 kW/m^2

at 800°C in small cells, and as high as 10 kW/m^{2}in short stacks (up to 10 × 10 cm 10 cell stacks) . At 700°C operating temperature, the cost of the metallic interconnect, manifolds and end plates reduce significantly. Lower temperature operation makes available numerous materials for the seals, and reduces the insulation size and the associated cost. However, with the lower temperatures, the internal resistance of the cell rises sharply leading to a significant drop in the power density.

NG fueled SOFC system, in general consists of three converter units shown in Figure 1: They are: 1) a high temperature chemical conversion in a fuel processor, where methane based fuel is transformed to syn gas, 2) the electrochemical combustion of syn gas within the SOFC stack to generate heat and d.c electricity, and 3) electrical unit that converts and maintains the SOFC module to a useful application.

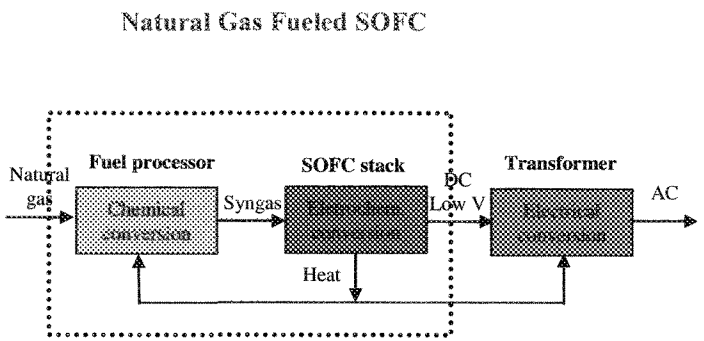

Figure.1 Schematic of natural gas fueled SOFC.

In the first (chemical converter shown in Fig. 1) mixed ionic-electronic conducting ceramics (MIEC), can be employed to process the feed fuel into syngas by means of partial oxidation. In the second (electrochemical convertor), the ceramic cells determine the system electrical efficiency by means of their internal resistance. Due to the high operating temperature, an important factor in the design of a solid oxide fuel cell stack is the matching of thermal expansion coefficient of the cell components and interconnects, to prevent cracking of the intrinsically brittle ceramic cells, gas leakage and loss of electrical contact.

A SOFC is mainly composed of two electrodes (the anode and the cathode), and a solid electrolyte. The fuel is also important as the principal parameter but independent of the other as it is most of the time converted into hydrogen. The SOFC, which relies on O_2 oxygen ion transport, also works with high purity hydrogen, but it does not rely upon this fuel, which is expensive to produce and difficult to handle. The main function of the electrode is to bring about reaction between the reactant (fuel or oxygen) and the electrolyte, without itself being consumed or corroded. It must also bring into contact the three phases, i.e., the gaseous fuel, the solid electrolyte and the electrode itself. The anode, used as the negative post of

the fuel cell, disperses the hydrogen gas equally over its whole surface and conducts the electrons, which are freed from hydrogen molecule, to be used as a useful power in the external circuit. The cathode, the positive post of the fuel cell, distributes the oxygen fed to it onto its surface and conducts the electrons back from the external circuit where they can recombine with oxygen ions, passed across the electrolyte, and hydrogen to form water. The electrolyte determines the operating temperature of the fuel cell and is used to prevent the two electrodes to come into electronic contact by blocking the electrons. It also allows the flow of charged ions from one electrode to the other to maintain the overall electrical charge balance. It can either be an oxygen ion conductor or a hydrogen ion (proton) conductor. Each component of the SOFC serves several functions and must therefore meet certain requirements such as: 1) proper stability (chemical, phase, morphological, and dimensional), proper conductivity, chemical compatibility with other components, similar thermal expansion to avoid cracking during the cell operation, dense electrolyte to prevent gas mixing, porous anode and cathode to allow gas transport to the reaction sites, High strength and toughness properties, fabricability, amenable to particular fabrication conditions, compatibility at higher temperatures at which the ceramic structures are fabricated, and low cost.

Figure 2 shows the schematic of all perovskite anode supported planar SOFC system, under progress at the Solid State Ionics Laboratory in the Southern University lead by Dr. Bobba.

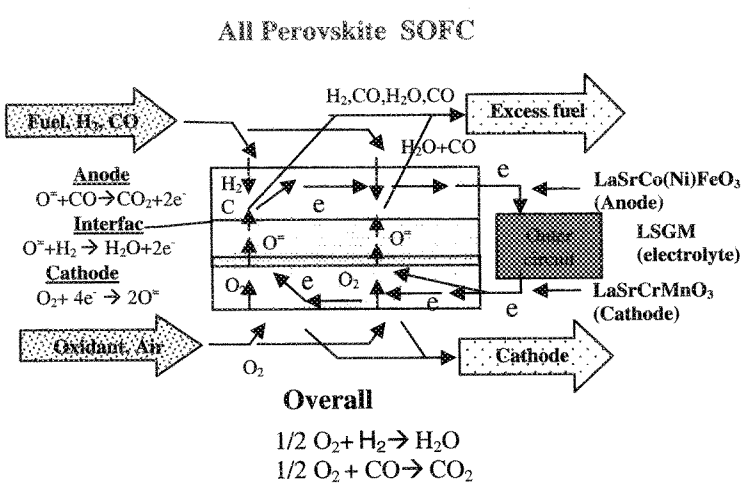

Figure 2 Schematic of all perovskite SOFC

In this paper, we report the progress of the proposed hybrid SOFC/GT system shown in Figure 3 with an emphasis on utilizing the nanocrystalline electroceramic materials synthesized at low temperatures. To date, the following electrocerceramic materials: 1) nanocrystalline

(La,Sr)(Ga,Mg)O_3 (LSGM) electrolyte, 2) $La_{0.9}Sr_{0.1}Co_{0.9}M_{0.1}O_3$ (M=Fe,Ni,Mn) cathode, 3) Ni-based perovskite cermet or (La,Sr)(Ga,Mn)O_3 (LSGMn) anode, 4) $LaCrO_3$ interconnect, and 5) ceria based anodic catalysts materials, were prepared in the form of bulk and thin films using innovative wet chemical processing methods, and pulsed laser deposition (PLD) techniques [1-3]. The interfacial reactions between electrolytes and anodes or cathodes were studied. The exceptional structural and chemical compatibility of LSGM with $La_{0.9}Sr_{0.1}Co_{0.9}M_{0.1}O_3$ (M=Fe,Ni,Mn) as perovskite based cathode, as anode, makes it a unique electrolyte for all perovskite based IT-SOFC.

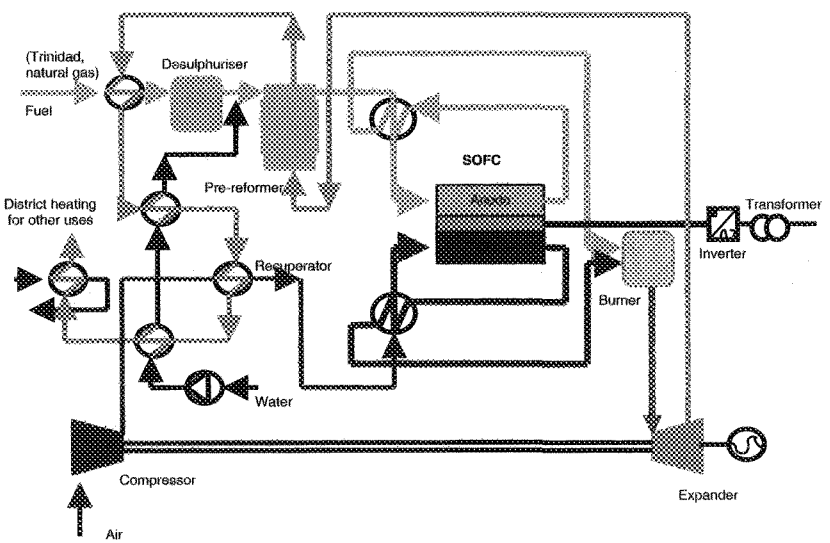

Figure 3 Schematic of natural gas fuelled SOFC-GT hybrid.

1.1 Conversion of natural gas (NG) to Syngas

Hydrogen would be preferred fuel cell feed. As it is not yet distributed the next best choice falls on methane. There are three reactions which produce hydrogen from methane: partial oxidation ($CH_4 + ½ O_2 \rightarrow 2H_2 + CO$), steam reforming ($CH_4 + H_2O \rightarrow 3H_2 + CO$), and cracking. Cracking should of course be avoided as it produces a carbon deposit in the anode and gradually poisons it. At temperatures of 800 to 1000°C, the partial oxidation of methane is difficult to control, especially since complete oxidation must be avoided as it does not produce any hydrogen. Steam reforming is therefore the most commonly used reaction in industry, either in external reformers or in internal reforming within high temperature cells. In general two types of SOFCs will be used for the catalytic and

electrocatalytic experiments: (i) The conventional type where CH_4 is fed to the anode compartment of the SOFC and (ii) the simplified SOFC type where the mixture of CH_4 + H_2O and O_2 is supplied to the reactor so that both anode and cathode are exposed to CH_4+ H_2O and O_2 mixture respectively. In the case of the conventional type the anode should exhibit high resistance to carbon deposition, resulting mainly from the methane decomposition reaction producing C and H_2. Therefore the catalytic properties of these electrocatalysts should adsorb C originating from methane dissociation with high thermodynamic activity, thus preventing C-nucleation to graphite at low C coverages on the catalytic surface.

In decreasing order of efficiency the steam reforming catalysts used are: Ru > W > Rh > Ir > Ni > Co > Os > Pt > Fe > Mo > Pd > Ag. Nickel (Ni) is the most widely used today because of its excellent cost/efficiency ratio. Moreover, it is contained in today's most commonly used SOFC anode material: a zirconia-nickel compound belonging to the cermet family. We are developing alternate materials such as ceria (doped and undoped) and transition metal containing perovskites and fluorite-related structures [2]. The target for electronic conductivity for anode materials is often set to be 100 S cm^{-1}, but the actual requirement depends on the cell design and particularly the length of the current path to the current collection locations. A suitable benchmark material is the perovskite $La_{1-x}Sr_xCrO_3$, which has been thoroughly investigated as an interconnect material for SOFCs and is also a potential anode material for SOFCs due to the relatively good stability in both reducing and oxidizing atmospheres at high temperatures. The acceptor doping gives high p-type conductivity in air but, as with all p-type materials, this decreases under reducing conditions The introduction of other transition elements into the B-site of $La_{1-x}Sr_xCr_{1-y}MyO_3$ (M = Mn, Fe, Co, Ni) has been shown to improve the catalytic properties for methane reforming.

2 Experimental

Various wet chemical preparation methods have been used to prepare the (1) anode (2) cathode (3) electrolyte (4) interconnect materials. The techniques used were (i) combustion synthesis (ii) co-precipitation methods (iii) sonochemical methods. Stoichiometric concentrations of reactants were taken for preparing specific compositions and dissolved to made solutions then ligating agents were added to form complexes and the complex was heated on hot plate to decompose and finally on calcinations yielded the product. The details are available in our earlier publications [1-3].

3. Results and Discussions

3.1 Anode

The materials selection for an SOFC anode is determined by a number of factors. First, the function required of it as the site for the electrochemical oxidation of the fuel associated with charge transfer to a conducting contact. Second, the environment in which it operates, at high temperature

in contact not only with the fuel, including possible impurities and increasing concentrations of oxidation products, but also with the other materials, the electrolyte and contact components of the cell, and all this with stability over an adequate commercial lifetime at high efficiency. With regards to stability, whilst in normal operation the ambient oxygen partial pressure is low, it can vary over several orders of magnitude, and to accommodate fault conditions or even just to provide flexibility of operating parameters, the ability to recover even after brief exposure to air at high temperature would be advantageous. A further aspect of this stability is the maintenance of structural integrity over the whole temperature range to which the component is exposed, from the sintering temperature during fabrication through normal operating conditions and then, repeatedly, cycling down to ambient temperature. Compatibility with other cell component materials implies an absence of solid state contact reactions, with interdiffusion of constituent elements of those materials or formation of reaction product layers which would interfere with anode functionality. It also requires a match of properties, such as shrinkage during sintering and thermal expansivity to minimise stresses during temperature variations due to operating procedures, start-up and shut-down. By definition of its role, it is a requirement that the anode material should be an adequate electronic conductor, and also be electrocatalytically sufficiently active to sustain a high current density with low overpotential loss. Ceramic anodes, made of perovskite-type rare-earth and strontium cobaltites substituted in both sublattices, exhibit a high electrocatalytic activity for the oxygen evolution reaction in alkaline media. We have analyzed the relationship between cation composition, defect structure, electronic conductivity and electrochemical performance for a wide group of perovskite-like cobaltites, including $Ln_{1-y}A_yCoO_{3-\delta}$ (Ln = Pr, Nd, Sm; A = Sr, Ca; y= 0-0.4), $La_{1-x-y}Sr_xBi_yCoO_{3-\delta}$ (x = 0-0.6, y = 0-0.1), $La_{0.7}Sr_{0.3}CoO_{3-\delta}$, $Sr_{1-x}Ba_xCoO_{3-\delta}$(x = 0.1-0.2) and $SrCo_{1-y}M_yO_{3-\delta}$ (M = Fe, Ni, Ti, Cu; y = 0.10.6). SOFC anodes are fabricated from composite powder mixtures of electrolyte material (YSZ, GDC, or SDC) and nickel oxide NiO (the nickel oxide subsequently being reduced to nickel metal prior to operation, which serves to inhibit sintering of the metal particles and to provide a thermal expansion coefficient comparable to those of the other cell materials.

3.2 Cathode

Perovskite-type lanthanum strontium manganite, $LaSrMnO_3$ (LSM) and lanthanum calcium manganite, $LaCaMnO_3$ (LCM) offer excellent thermal expansion match with zirconia electrolytes and provide good performance at operating temperatures above 800^{0}C. For applications requiring lower temperature operation (600–800^{0}C), a range of alternative perovskite-structured ceramic electrode materials are available. These include: Lanthanum strontium ferrite (LSF), $(LaSr)(Fe)O_3$, Lanthanum strontium cobaltite (LSC), $(LaSr)CoO_3$, Lanthanum strontium cobaltite ferrite (LSCF), $(LaSr)(CoFe)O_3$,Lanthanum strontium manganite ferrite (LSMF),

(LaSr)(MnFe)O_3, Samarium strontium cobaltite (SSC), (SmSr)CoO_3, Lanthanum calcium cobaltite ferrite (LCCF), (LaCa)(CoFe)O_3, Praseodymium strontium manganite (PSM), (PrSr)MnO_3, and Praseodymium strontium manganite ferrite (PSMF), (PrSr)(MnFe)O_3. For even better electrode performance, some companies offer a line of composite electrode powders, with electrolyte materials (YSZ, SDC or GDC) admixed with the perovskite electrode materials (LSM, LSF, or PSMF). As in the other fuel cell types, the oxygen reduction largely determines the efficiency of the SOFC. Cathodes using $LaSrMnO_3$, $La_{0.6}Sr_{0.4}Co_{0.2}Fe_{0.8}O_3$ (LSCF) have the advantages of lower losses at lower temperatures (600–700 °C) and are reported to be less sensitive to Cr-poisoning. LSM thin film was prepared by pulsed laser deposition by our team, the TEM micrograph of the film with columnar microstructure are shown in Fig. 4

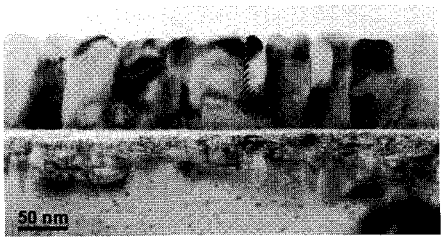

Figure 4. Columnar growth in PLD of LaSrMnO3 (LSM).

In our laboratory various compositions have been attempted to optimize conductivity of the electrode for ions and electrons and the accessibility for oxidant, improvement in microstructure and phase composition at load conditions.

3.3 Electrolyte

The properties of electrolytes used in SOFC are mainly, but not only, dictated by the high operating temperature, high ionic conductivity ($\geq$0.1 S cm^{-1}); low electronic transference number ($<10^{-3}$); large electrolytic domain; chemical stability with respect to electrode materials, oxygen, and fuel gas; thermodynamic phase stability; a good match of thermal expansion coefficient (TEC) with other cell components; gas tightness; fracture toughness. Current technology employs several ceramic materials for the active SOFC components. Although a variety of oxide combinations has been used for solid non-porous electrolytes, the most common to date has been the stabilised zirconia with conductivity based on oxygen ions (O_2), especially yttria-stabilized zirconia (Y_2O_3—stabilized ZrO_2 or YSZ, $(ZrO_2)_{0.92}(Y_2O_3)_{0.08}$ for example) in which a tiny amounts of the element yttrium, a silvery-grey metal, is added to the zirconia during manufacture. This choice is mainly due to availability and cost. YSZ exhibits purely oxygen ionic conduction (with no electronic conduction). The crystalline

array of ZrO_2 has two oxide ions to every zirconium ion. But in Y_2O_3 there are only 1.5 oxide ions to every yttrium ion. The result is vacancies in the crystal structure where oxide ions are missing. So, oxide ions from the cathode leap from hole to hole until they reach the anode.

The most commonly used stabilizing dopants are CaO, MgO, Y_2O_3, Sc_2O_3 and certain rare earth oxides such as Nd_2O_3, Sm_2O_3, Yb_2O_3. Other oxide based ceramic electrolyte that can be used in SOFCs include:Cerium oxide doped with samarium (SDC), $(Ce_{0.85}Sm_{0.15})O_{1.925}$ Cerium oxide doped with gadolinium (GDC),$(Ce_{0.90}Gd_{0.10})O_{1.95}$. Recently, the sunthesis and electrical property measurements on nano-crystalline ceria and Gd-doped ceria has been done in our lab. The XRD and TEM results are given in Fig.5 and Fig.6 (a-b) respectively.

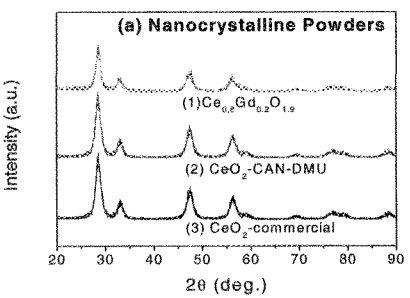

Figure 5. XRD pattern of nano-crystalline ceria powders

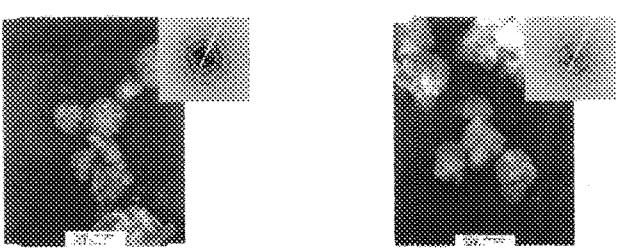

Figure 6 TEM and SAED of a) CeO2 cerium nitrate and DMU (b) Ce0.8Gd0.2O1.9

For operation at 600 °C or even lower, $La_{0.9}Sr_{0.1}Ga_{0.8}Mg_{0.2}O_{2.85}$ electrolytes offer superior conductivity, but exhibit stability problems caused by evaporation of Ga, and low mechanical stability and high gallium costs. Scandium doped ZrO_2 offers improved oxygen ion conductivity and relatively high mechanical strength, at the expense of using high cost scandium. Lanthanum gallate ceramic that include lanthanum strontium gallium magnesium (LSGM), $(La_{0.80}Sr_{0.20})$ $(Ga_{0.90}Mg_{0.10})O_{2.85}$ or $(La_{0.80}Sr_{0.20})(Ga_{0.80}Mg_{0.20})O_{2.80}$, Bismuth yttrium oxide (BYO), $(Bi_{0.75}Y_{0.25})_2O_3$, Barium Cerate (BCN), $(Bi_{0.75}Y_{0.25})_2O_3$, and Strontium Cerate (SYC), $Sr(Ce_{0.95}Yb_{0.05})O_3$

To produce submicron LSGM powders for high-quality membrane fabrication, the combustion technique via aqueous solutions is usually

preferred to the conventional solid-state mixed-oxide method. The solution route provides many advantages, for example, molecular homogeneous precursors, reduced sintering temperature for obtaining dense ceramics, and controllability of uniform superfine grain size. One major disadvantage of LSGM is the high cost of the gallium containing precursors. Once LSGM materials are used as electrolyte in commercial stage, regeneration of LSGM will be a cost-effective effort. Based on this concern, we have explored the possibility of regenerating the LSGM ceramics to be aqueous solution precursor. Although the solid Ga_2O_3 remains insoluble, our experiments have shown the LSGM ceramics are completely soluble in the acidic solution. In addition, the regenerative route is also cost-effective and time-saving for in-lab researches which usually prepare large amount of LSGM samples, for example, to tailor effects of composition or synthesis condition on the properties of LSGM.

The sintering behaviour of the materials prepared from the various routes was examined by Scanning electron microscopy (SEM) shown in Figure 7 The pellets prepared by regenerative sol-gel technique produce nano-crystalline powders which has better sintering properties as indicated in Fig. 7 a-b and Fig. 7c-d.

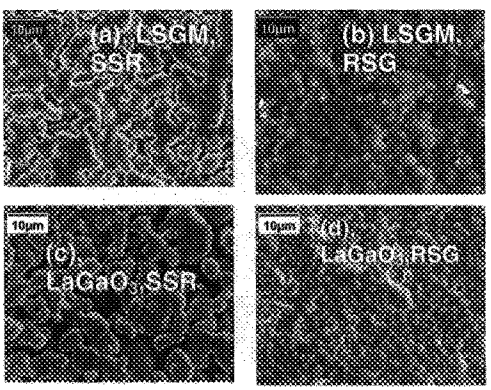

Fig.7.SEM micrographs of La0.8Sr0.2Ga0.85Mg0.15O2.825 (LSGM-2015) and LaGaO3: heated at 14000C/8h
(a) solid-state route(SSR) pellet of LSGM-2015;
(b) RSG pellet of LSGM-2015;
(c) solid-state route pellet of LaGaO3; and
(d) RSG pellet of LaGaO3

The Fig. 8 illustrates the impedance spectroscopy measurement of the LSGM-2015 pellets synthesized through both the regenerative sol-gel route and solid-state route. The resistances in all bulk and in all grain-boundary (R_b and R_{gb}) of the pellets were estimated from the real axis intercepts of the depressed semicircles based upon the equivalent series circuit of two R-C parallel circuits. The first depressed semicircle near the origin corresponds to the bulk resistance and the second corresponds to the grain-boundary resistance. The first real axis intercept offers the R_b and the second offers the sum of R_b and R_{gb}. The resistances were unified by multiplying the ratio of area to thickness of the measured pellets. Although we got the resistances, because volume fractions of the bulk and grain-boundary are unknown, it is impossible to calculate the bulk and grain-boundary conductivities. The Arrhenius relations of the bulk and the grain-

boundary resistances in [3] indicate the grain boundary resistance is almost equal to the bulk resistance. Based on the Arrhenius relation of T/R $\propto$ Exp(-E/kBT), we estimated the activation energies for the oxide-ion conduction across the whole pellet (E_t=1.01 eV), the bulk part (E_b= 0.97 eV), and the grain-boundary part (E_{gb}= 1.03 eV). The Arrhenius relation of the total conductivities [3] indicates the regenerative sol-gel LSGM-2015 has a higher temperature-dependent conductivity than that of the solid-state route LSGM-2015. At 800°C and 700°C, the solid-state route LSGM-2015 has a conductivity $\sigma_t \approx 0.056$ and 0.025 S/cm respectively, and the regenerative sol-gel LSGM-2015 has a conductivity $\sigma_t \approx 0.066$ and 0.029 S/cm respectively, which is 16-18 % more than the solid-state LSGM-2015 conductivity and is comparable to the conductivity of conventional sol-gel route LSGM starting from liquid-mixing of salt solutions (refer to [3], $La_{0.9}Sr_{0.1}Ga_{0.8}Mg_{0.2}O_{2.85}$, $\sigma_t \approx 0.065$ S/cm and 0.034 S/cm at 800°C and 700°C respectively.

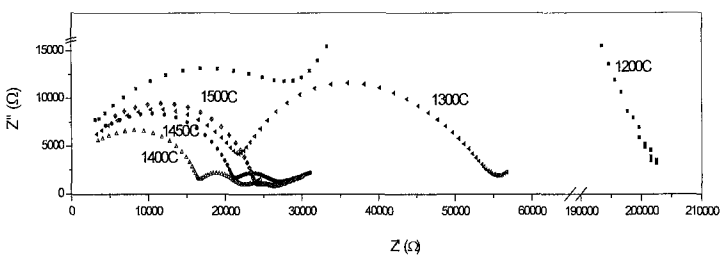

Figure 8. Cole-Cole plots recorded on LSGM pellets.

3.4 Interconnects

Separator plates are in SOFC mostly called interconnects. At high temperatures, one option is to use ceramic interconnects. The ceramic plates are based on $LaCrO_3$. Doping with Ca, Sr or Mg leads to higher electrical conductivity. Pure ceramic plates have the tendency to be partially reduced at the anode side, leading to warping and breakage of the sealing besides, more cost effective materials and fabrication methods are needed for bringing this technology to the commercial stage. Metallic interconnects would lead to lower fabrication costs, are less brittle and have a higher electrical and thermal conductivity.

3.5 SOFC-GT hybrid system

The Hybrid system comprises of a natural gas fueled SOFC with a gas turbine as shown in the Fig. 3. Natural gas with necessary purification is sent to the anode chamber and excess gas is recycled. Similarly, air is sent (pumped) to the cathode compartment and recycled. Since the fuel cell operates at high temperatures ~8000C and produces DC current, the used

hot gases can be sent to the gas turbine (GT) to produce AC current by the gas turbine turbine and generator.Thereby, increasing the efficiency of the process. By doing so maximum utilization of gas and heat can be achieved. A prototype set up will be fabricated and the fuel cells will be tested in our site.

4. Conclusion

Exploitation of fossil fuels to produce energy is reaching its limits. Future alternatives must therefore be developed for long-term and environmental-friendly energy supply needed by a constantly growing world population. SOFCs provide highly efficient, pollution free power generation. Their performance has been confirmed by successful operation of power generation systems throughout the world. Electrical-generation efficiencies of 70% are possible nowadays, along with a heat recovery possibility.SOFCs appear to be an important technology for the future as they operate at high efficiencies and can run on a NG produced in Trinidad.

References

1. X-ray Absorption Near Edge Spectroscopy (XANES) measurements of ceria based solid electrolytes, J. Hormes, B Balazas and B. Rambabu, Solid State Ionics 2 (2000) 390-399

2. .Novel wet-chemical synthesis and characterization of nanocrystalline CeO_2 and $Ce_{0.8}Gd_{0.2}O_{1.9}$ as solid electrolyte for intermediate temperature solid oxide fuel cell (IT-SOFC) applications, B.Rambabu, Samrat Ghosh and Hrudananda Jena, J. Mater. Sci. (in press, 2006) .

3. An exploratory study on solution assisted synthetic routes to prepare nano-crystalline $La_{1-x}MxGa_{1-y}NyO_3$ (M=Sr, N=Mn,Mg) for IT-SOFC applications. Hrudananda Jena and B. Rambabu, Mater. Chem. Phys. (in Press, 2006).

4.Innovative processing of dense LSGM electrolytes for IT-SOFC's, B. Rambabu, Samrat Ghosh, Weichang Zhao and Hrudananda Jena, J. Power Sources (Accepted)

5) Nanostructured Bulk and Thin Films of $LaSrMnO_3$, K.I. Gnanasekar, Xin Xiang, Josef Hormes, Ronald Tilts Worth, Mher and B. Rambabu, Solid State Ionics 148 (2002) 575-581

6) Effect of sonochemical, regenerative sol gel, and microwave assisted synthesis techniques on the formation of dense electrolytes and porous electrodes for all perovskite IT-SOFCs, Hrudananda Jena, and B. Rambabu, Journal of Fuel Cell Science and Technology, 2006.

Acknowledgement: BRB acknowledge the support of U.S-DOE-NREL and U.S-DOE-NETL through grants # ACQ-4-33623-01, #DE-FG26-03NT4195. Ramsey Sanders acknowledge the support of UWI-St-Augustine Campus and the NGC-T&T for supporting this collaborative project.

THIN FILM SOFC SUPPORTED ON NANO-POROUS SUBSTRATE

J. H. JOO and G. M. CHOI*

Fuel Cell Research Center and Department of Materials Science and Engineering, Pohang University of Science and Technology, Pohang, Gyeongbuk 790-784, Korea

** Corresponding author, E-mail: gmchoi@postech.ac.kr*

A typical solid oxide fuel cell (SOFC) consists of an oxygen-ion conducting solid-electrolyte, usually yttria-stabilized zirconia (YSZ), and electrodes deposited on two sides of electrolyte. The SOFC usually operates between 800-1000□. The high operating temperature is due to the low oxygen-ion conductivity of the electrolyte at low temperature and also due to slow electrode kinetics. In this study, we made a SOFC using GDC (Gd_2O_3-doped CeO_2) thin film on nano-porous substrate. Anodic nano-porous alumina membrane has been employed as a substrate. The substrate has nanometer-size columnar pores (200nm) which penetrate the substrate vertically. Porous Pt thin-film as an anode was deposited onto the substrate by DC sputtering. On top of Pt anode, dense GDC thin film (~2㎛) was deposited by pulsed laser deposition. To measure the resistance of GDC and the open-circuit voltage (OCV) of cell, another Pt electrode as a cathode was painted on the surface of GDC thin film. Substantial OCV was developed when humidified H_2 gas was flown over anode below ~500□. However, the measured OCV was lower than the theoretical OCV due to low activity of Pt electrode. The enhanced OCV will be expected when highly active electrodes were used

Keywords: SOFC, doped-ceria thin film electrolyte, nano-porous substrate, OCV

1. Introduction

Solid Oxide Fuel Cell (SOFC) has been rapidly developing for clean and efficient power generation using a variety of fuels. Current SOFCs employ YSZ as an electrolyte and require operating temperature 800~1000□ to minimize ohmic loss [1]. Recent focus has been on the advances of SOFCs through the lowering of the operating temperature for the use of fuel cells in portable devices. However, as the temperature is reduced, the ionic conductivity significantly decreases. This can be overcome by decreasing the thickness of electrolyte. The most promising approach in decreasing the thickness is to make the electrolyte by thin film deposition process [2]. With the advent of thin film technology, efforts have been made to make miniaturized SOFC [3-4]. Miniaturized SOFC is potential high efficiency, high energy density replacements for batteries in the mW-W power generation for portable consumer and military electronic devices. Miniaturized SOFC offers great advantages over their macroscopic counterparts such as lower operating temperature, easy integration with the required electrical components, small size and reduced weight.[5]

Recently, considerable efforts have been directed to intermediate temperature SOFC based on thin film electrolytes of doped ceria. Rare earth oxide doped ceria is one of the candidates for the electrolytes of intermediate temperature SOFC.[6] In this study, we made a SOFC using GDC (Gd_2O_3-doped Ceria) thin film on nano-porous substrate by pulsed laser deposition method. Pulsed laser deposition method

has become an increasingly important technique for depositing thin films of a variety of materials. Its main advantage is the ability to deposit many materials while preserving the stoichiometry of multi-component. The microstructure and impedance analysis of GDC film are characterized and the OCV values of cell are discussed.

2. Experimental procedure

Anodic nano-porous alumina membrane has been purchased and employed as a substrate. As nano-porous substrates, commercial inorganic filters (Anodisc®, Whatman, UK) were used. The substrate is made by anodic oxidation of aluminium, and has nanometer-ordered columnar pore (200nm) structure Fig. 1a. Since this membrane is an electrical insulator, porous Pt thin-film as an anode was deposited onto the substrate by DC sputtering. Pt electrode was deposited at 3 mTorr and showed pores of 100-200nm size as shown in Fig. 1b. On top of Pt anode, dense GDC thin film (thcikness~2㎛) was deposited by pulsed laser deposition at oxygen partial pressure of ~50 mTorr. A stainless steel chamber was evacuated to a base pressure of $5*10^{-6}$ Torr using a turbo molecular pump. Pulsed laser ablation was carried out with a KrF excimer laser (248 nm with 30 ns pulse width) at a pulse energy of ~1.5 J/cm^2 and repetition rate of 10 Hz. The laser beam was focused on GDC (1mol%Ga_2O_3-doped $Ce_{0.8}Gd_{0.2}O_{2-\delta}$) target which rotated at ~10 rpm. To enhance the densification of GDC film, 1mol%Ga_2O_3-doped GDC target was used. Substrates were positioned parallel to and 5㎝ away from the target. This distance allows sufficient interaction between the plasma plume and the background oxygen gas. The substrate temperature was maintained at 500℃.

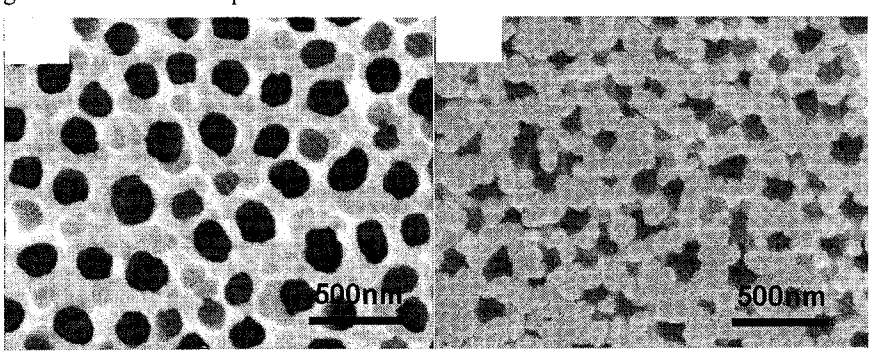

Fig. 1.(a) SEM image of the anodic alumina substrates having average pore diameter of 200nm. (b) SEM image of sputter deposited Pt with pore size of 100-200nm.

To measure the electrical resistance of GDC and the open-circuit voltage (OCV) of cell, another Pt electrode as a cathode was painted on the surface of GDC thin film. The schematic configuration of measurement cell was shown in Fig.2. The

impedance spectra were obtained in the frequency range 0.1Hz-5MHz using impedance analyzer (model SI1260 Impedance analyzer, Solartron, UK). Cell was tested in the 400-500□ temperature range using H_2+3%H_2O as fuel and air as the oxidant. The OCV was measured with digital electrometer (Keithley, K196). The phase of thin film was characterized by x-ray diffraction (XRD) using Cu-K_α radiation (MAC Science, M18XCE, Japan). Microstructure observation was performed by a field-emission scanning-electron-microscope (JEOL, model 3330F, Japan).

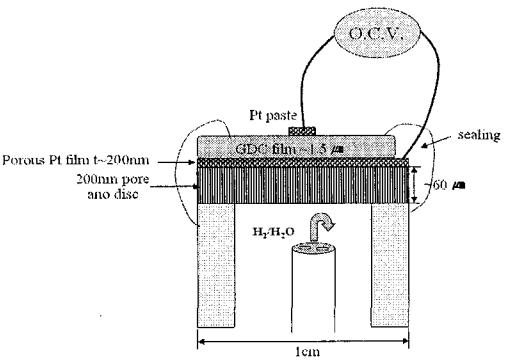

Fig. 2. Schematic of the seting up employng nano-porous substrate-supported SOFC for measuring OCV.

3. Results and discussion

3.1. Microstructure of GDC thin film on anodic alumina substrate

The crystalline phase of GDC film was determined by using XRD. Fig.3. shows XRD patterns of anodic alumina substrate and GDC thin film deposited on substrate. The XRD patterns obtained from the films were consistent with the reference data for single phase GDC with cubic fluorite structure (JCPDS 46-0507). The polycrystalline cubic nature of the films is apparent in XRD patterns. No secondary phases due to film/substrate interaction were detected. A strongly preferential orientation of (111) planes in the film was obtained.

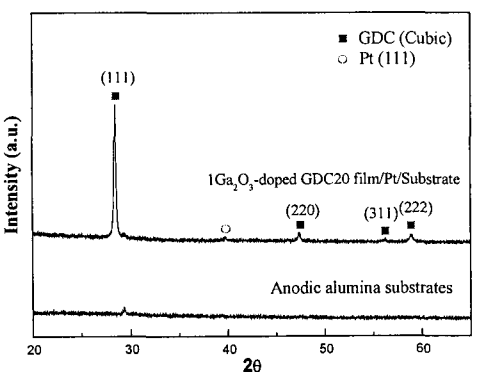

Fig. 3. XRD patterns of anodic alumina substrate and GDC thin film deposited on substrate.

SEM pictures of the thin films were examined to study the morphology. Fig.4. shows the surface (left) and cross-sectional (right) SEM micrographs of thin film GDC (thcikness~2㎛) deposited on porous Pt anode/anodic alumina substrate. The columnar growth of the grain is apparent for films. The thin film shows negligible porosity as shown in Fig.4.(a). Nanocrystalline morphology was observed with an average column diameter of ~150nm.

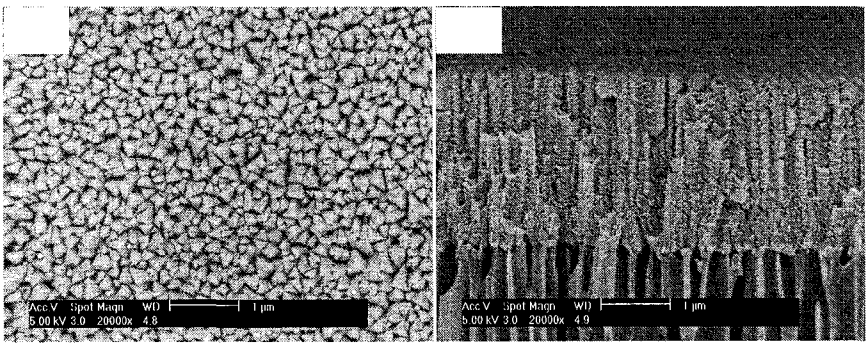

Fig. 4. Surface and cross-sectional SEM micrographs of GDC thin film grown on porous anode Pt/ anodic alumina substrate.

3.2. Impedance analysis and OCV measurement

The resistance of thin film GDC was measured by impedance spectroscopy. Due to the possible incomplete contact of porous Pt cathode, the calculation of the conductivity from the measured resistance has not been possible. The incomplete contact at the porous Pt/GDC film interface can cause the conductivity drop of GDC film. Thus, only resistance values are discussed. Complex imedance spectra were obtained in the temperature range 200-300℃ in air as shown Fig.5. The impedance spectrum of thin film consists of a high-frequency semicircle caused by grain process and a low-frequency curve attributed to the interface between GDC film and Pt electrodes. No grain boundary contribution was shown for films. This may partly be due to the columnar structure of thin film, in which the grain boundary is parallel to the current direction [7,8]. In other words, the highly oriented growth of the thin film GDC shows that the current flow is not limited by grain boundaries in the parallel plate geometry.

Fig. 6 shows the arrhenius plots of the GDC film resistance as a funtion of temperature. The apparent activation energy corresponding to this resistance was calculated from the solid fitting line. From the Arrhenius plot, the activation energy for ion conductivity was estimated to be 0.86±0.018 eV, similar to the reported value (~0.82eV) for GDC($Ce_{0.8}Gd_{0.2}O_{2-\delta}$) grain bulk [9].

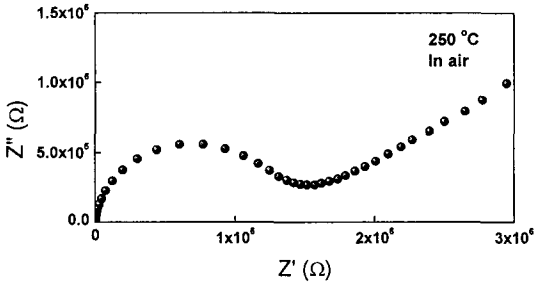

Fig. 5. Impedance spectra of GDC thin films deposited on porous Pt film.

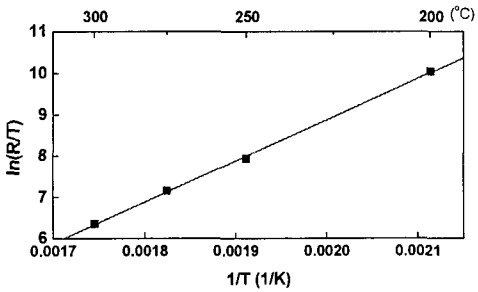

Fig.6. Arrhenius plots of the GDC film resistance as a funtion of temperature.

The OCV was measured between 400□ and 500□ in 50□ intervals using H_2+3%H_2O as fuel and air as the oxidant. In Fig.7. the OCV was plotted against the temperature for a cell which had a GDC electlolyte thin film. However, the measured OCV was lower than the theoretical OCV (~1V) under the experimental condition[10]. This is most likely due to poor electrode reaction of Pt electrode. OCV depends on the kind of electrode materials, which indicates the data are not free from kinetic aspect of the interfacial reactions. Matsui et al. reported that Pt/$Ce_{0.8}Sm_{0.2}O_{0.19}$/Pt cell showed OCV of ~0.5V at 450□ and ~0.65V at 500□ due to the low electrode reaction of Pt[11]. The low activity of the Pt electrode below 500□ may be correlated with Pt-O formation[12]. The enhanced OCV will be expected when highly active electrodes were used

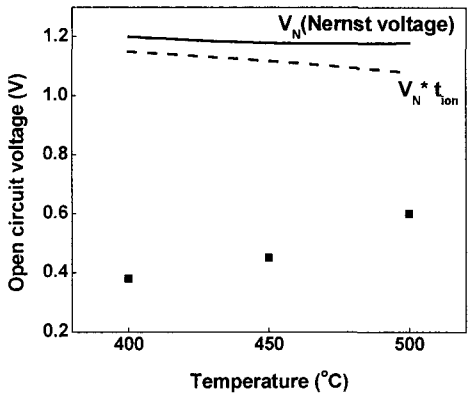

Fig.7. Open circuit voltage of cell as a function of temperature. Solid line: OCV curve calculated using the Nernst equation. Dotted line: Theoretical OCV curve of $Ce_{0.8}Sm_{0.2}O_{0.19}$ calculated using mixed conduction (H_2+3%H_2O as fuel and air as the oxidant).[11]

4. Conclusions

SOFC using GDC thin film on nano-porous anodic-alumina substrate was fabricated. Dense and well crystallized GDC film was successfully grown. The impedance spectrum of thin film consists of a high-frequency semicircle caused by grain process and a low-frequency curve attributed to the interface between GDC film and Pt electrodes. No grain boundary contribution was shown for films due partly to the columnar structure of thin film, in which the grain boundary is parallel to the current direction. Substantial OCV was developed when humidified H_2 gas was flown over anode below ~500□. However, the measured OCV was lower than the theoretical OCV due to low activity of Pt electrode. The enhanced OCV will be expected when highly active electrodes were used

Acknowledgements:
Supported by Core Technology of Fuel Cell Program, MOCIE, Korea

5. References

[1] Minh, N ,Q, and Takahashi, T., *Science and Technology of Ceramic Fuel Cells*, Elsevier Science, New York (1995).

[2] J. Will, A. Mitterdorfer, C. Kleinlogel, D, Peredins, L.J. Gaucker, *Solid State Ionics*, **131**, 79 (2000).

[3] J.L. Hertz and H.L. Tuller, *J. Electroceram.* **13**, 663 (2004).

[4] G.J. Lao, J.L. Hertz, H.L. Tuller, Y. S. HORN, *J. Electroceram.* **13**, 691 (2004).

[5] C.D. Baertsch, K.F. Jensen, J.L. Hertz, H.L. Tuller, S.T. Vengallatore, S.M. Spearing, M.A. Schmidt. *J. Mater. Res.* **19(9)**, 2604 (2004)

[6] B.C.H. Steele, *Solid State Ionics*, **129**, 95-110 (2000).

[7] R. Radhakrishnan, A. V. Virkar, S. C. Singhal, G. C. Dunham and O. A. Marina, *Sensor Actuat. B- Chem.* **105**, 312 (2005).

[8] D. Kek, P. Panjan , E. Wanzenberg, and J. Jamnik, *J. Eur. Ceram. Soc.* **21,** 1861 (2001).

[9] Z. Tianshu, Will, P. Hing, H. Huang, J. Kilner, *Solid State Ionics*, **148**, 567 (2002).

[10] S. Zha, C. Xia, G. Meng, *J. Power Sources*, **115**, 44 (2003).

[11] T. Matsui, T. Kosaka, M. Inaba, A. Mineshige, Z. Ogumi, *Solid State Ionics*, **176**, 663 (2005).

[12] T. Arakawa, A.Saito, J. Shiokawa, *Bull.Chem.Soc.Jpn.* **55**, 2273 (1982).

CHARACTERIZATION AND FABRICATION OF SILVER SOLID STATE BATTERY $Ag/AgI\text{-}AgPO_3/I_2,C$

E. KARTINI, MARDIYANTO, GUNAWAN, A..HINDASYAH AND M. IHSAN
Technology Center for Industrial Nuclear Materials,
National Nuclear Energy Agency (BATAN),
Kawasan Puspiptek Serpong, Tangerang INDONESIA

M.F.COLLINS
Department of Physics & Astronomy,
McMaster University,
1280 Mainstreet West, Hamilton,Ontario, CANADA

The demand for compact and high energy density batteries is constantly increasing with miniaturization of micro batteries for portable devices. All solid state batteries that consist of solid electrolyte and two electrodes have attracted much attention, because of their potential for flexibility, safety and further miniaturization. Superionic glass $AgI\text{-}AgPO_3$ is well known superionic conductor that has been investigated by many different techniques. Its high conductivity up to~ 10^{-2} S/cm at ambient temperature has attracted many researchers to understand the mechanism of ionic conductivity. The neutron scattering studies revealed the existence of prepeak at low Q in the structure factor S(Q) and the boson peak at low energy in the dynamic structure factor S(Q,E). Those results showed that many interesting phenomena were found out in this material. However, its application as solid electrolyte in a solid state rechargeable battery is only little known. In order to complete the feature of this material, we fabricated cell batteries $Ag/\ AgI\text{-}AgPO_3\ /I_2,C$. The silver and iodine-carbon were used as the anode and cathode, respectively. This paper will describe the recent results of solid electrolyte $AgI\text{-}AgPO_3$ and the performance of the new solid state battery.

1.Introduction

A battery is a device that converts the chemical energy contained in its active materials directly into electric energy by means of an electrochemical oxidation-reduction (redox). The type of reaction involves the transfer of electron from one material to another through an electric circuit. One cell battery consists of three major components, an anode or negative electrode, where oxidation takes place during discharge, a cathode or positive electrode, where reduction takes place, and the electrolyte-the ionic conductor-which provides the medium for transfer of electrons, as ions, inside the cell between the anode and cathode. For the most

electrolyte in the market is typically a liquid, such water or other solvents. The disadvantages of liquid electrolyte are leakage, need special handling and packaging, short life time and also will contaminate the equipments after being used. It is not also fulfill the requirement for mounting the energy source on the electronic circuit board [2]. Therefore, the concept of solid state battery with the solid electrolyte attracted renewed interest every time a new solid electrolyte and new electrodes were invented. The solid state batteries are expected to have high energy density, wide range temperature of operation and long shelf life.

The solid electrolyte is a relatively new component in the all solid state battery compared to liquid electrolyte batteries. Some of the criteria for the solid electrolyte are (i) high ionic conductivity (ii) the transference number close to unity (iii) thermodynamically stable (iv) chemically and physically stable with the anode and cathode (v) can be process as thin film for the miniaturization of the device. Some of those criteria were shown in superionic solid materials. Superionic solid is a solid electrolyte that characterized by high ionic conductivity ~ 10^{-2} S/cm, compared with the well known ionic solid(e.g. NaCl, KCl~10^{-16} S/cm) [1]. However, many superionic solids for example crystalline AgI, Ag_2S exhibit such high ionic conductivity at high temperature [3]. In order to obtain a superionic solid at room temperature, so that the electrolyte can be used in a solid state battery the researches have been started by modifying the already existing structure AgI with another second component like polymer, ceramic, crystal or glass. In this work, we concentrate on developing superionic glass based on silver phosphate glasses AgI-$AgPO_3$. The glass contains non-toxic and no-hazardous materials, free from leakage, easy to be produced and formed as a thin film. Another important aspect, that this glassy material is safe and environmentally friendly. The glassy electrolyte must have good ionic conductivity but not be electrically conductive, as this would caused internal short-circuiting

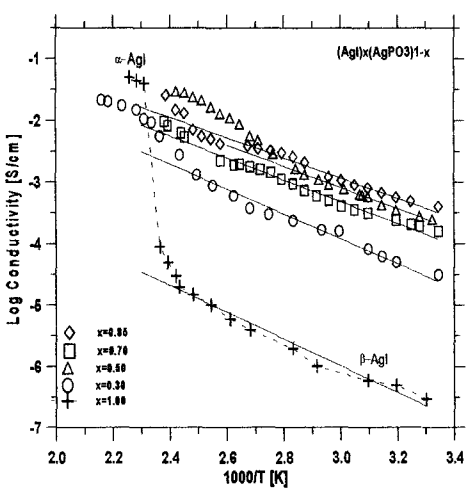

Figure 1. The ionic conductivity of the $(AgI)_x(AgPO_3)_{1-x}$ as a function of temperature and composition (x) [4].

Superionic glass $(AgI)_x(AgPO_3)_{1-x}$ is well known electrolyte which has its potential applications in many electrochemical devices such as batteries , sensors, and memory. As glass based electrolytes in general, the glass based silver phosphate not only has high ionic conductivity but also has many other advantages over its crystalline counterparts, such as, ease in preparation, wide selection of composition & glass forming region, absence of grain boundaries, isotropic properties, negligibly small electronic conductivity, inert to atmosphere, high stability, etc., [1-3]. At ambient temperature $AgPO_3$ shows low ionic conductivity (~ 10^{-7} S/cm), but the mixture of $(AgI)_x(AgPO_3)_{1-x}$ shows the conductivity increase by few orders of magnitudes with increasing AgI and temperature as shown in figure 1 [4-6]. The optimum conduction composition is achieved for $(AgI)_{0.5}(AgPO_3)_{0.5}$ in a glassy state and $(AgI)_{0.7}(AgPO_3)_{0.3}$ in a composite-glassy state.

The observed variation of conductivity with the AgI content in the superionic glass is explained by correlating the IR, DSC and conductivity results [7,8]. From this study, ionic conductivity increases due to (a) Ag^+ ion concentration, which is also in accordance with the conductivity (σ) expression

$$\sigma = ne\mu \qquad (1)$$

where n is the number of charge carriers, e is the charge and μ is the mobility and (b) the increase of mobility of the Ag^+ ion. Based on equation (1) above the ionic conductivity increases with the increase of the Ag^+ ion concentration. However, the solubility of the AgI in glass matrix is limited, i.e the maximum solubility limit (x) of AgI is about 0.57 [5]. Further increasing the AgI will reduce the mobility of Ag+ ions to move due to some cluster or precipitate of AgI. This is shown in the x-ray data, where some crystalline Bragg peaks correspond to AgI appear at the composition $(AgI)_{0.7}$ $(AgPO_3)_{0.3}$. The later is called a superionic composite-glass. Recently, our group has also investigated its structural and dynamic behavior via neutron diffraction and inelastic neutron scattering methods [9-12]. The results reveal an interesting relation among the first sharp diffraction peak, boson peak and the ionic conductivity in this superionic glass

Though the superionic glass AgI-$AgPO_3$ has been well studied by many different methods, the application of the superionic glass AgI-$AgPO_3$ as a solid electrolyte in a solid state battery is not well studied. Therefore, main objective of this study is to develop new solid state battery based on the AgI-$AgPO_3$ glassy electrolyte. In the previous section, the optimum conduction composition was obtained for $(AgI)_{0.5}$ $(AgPO_3)_{0.5}$ and $(AgI)_{0.7}(AgPO_3)_{0.3}$. Therefore these composition were chosen as the electrolyte separator of a battery cell. The objective of the rechargeable silver battery program is to develop batteries that have high energy density, high power density, good cycle life and charge retention, and to provide high performance reliably and safely. The selection of cell components and designs is necessarily a compromise to achieve the optimum balance. The process of rechargeable batteries must be reversible and the reaction that occur during recharge affect all of the characteristics and the performance of subsequent cycling. In this paper two cells batteries $Ag/(AgI)_{0.7}(AgPO_3)_{0.3}/I_2$ and

$Ag/(AgI)_{0.5}(AgPO_3)_{05}/I_2,C$, have been developed and their performance will be discussed.

2.Experimental Method

2.1.Preparation of Solid Electrolyte

Superionic glasses $(AgI)_{0.5}$ $(AgPO_3)_{0.5}$ and $(AgI)_{0.7}(AgPO_3)_{0.3}$ were prepared at the Nuclear Industrial Material Division, Technology Center for Nuclear Industrial Material Technology, BATAN and the method of preparing this material has been described elsewhere [6]. The glasses were prepared by melting the mixtures of ground AgI (purity 99.9%, Aldrich. Co), $AgNO_3$ and $NH_4H_2PO_4$ were heated gradually up to 600° C for about 6 hours. The molten mixture then was quenched into liquid nitrogen. A yellow transparent glass was obtained for $(AgI)_{0.5}$ $(AgPO_3)_{0.5}$ and an opaque glass for $(AgI)_{0.7}(AgPO_3)_{0.3}$. The quality of the sample was measured by x-ray diffraction.

2.2.Selection of Electrode Materials

An important aspect on designing a battery is the combination of anode and cathode materials, which will determine the cell voltage and capacity. In our experiment, the anode/cathode couple Ag/I_2 will be chosen for this solid state battery, because of several reasons. Silver metal was the obvious choice as an anode material because it is necessary to use a material of the same nature as the mobile ion in the electrolyte ($AgI-AgPO_3$) to assure uniform and continuous electrical charge transport through the three components of the battery. It shows also properties: efficient as a reducing agent, high coulombic output (Ah/g), good conductivity, stable, easy of fabrication. The choice of cathode in most cases happened to meet essential requirement that, efficient oxidizing agent, be stable when contact with the electrolyte, and have a useful working voltage. Simultaneously, the solid electrolyte has to withstand this potential without decomposing the constituents. Thus the anode/cathode couple Ag/I_2 was chosen for the first silver solid state battery. It is known that the I_2 electrode is very reactive and it sublimes easily in the air. To prevent iodine reaction it is suggested to use the graphite (C) so that the second anode/cathode couple becomes $Ag/I_2,C$. For protecting the electrode from sublimation and reacting with the other materials we tried to mould the battery cell with resin.

2.3.Fabrication of new solid state Battery

By using this electrolyte and electrode couple, first cell battery was built with the configuration $Ag/(AgI)_{0.7}(AgPO_3)_{0.3}$ $/I_2$ as shown in the figure 2. The dimension of the first battery is 15 mm diameter and 5.0 mm thickness. The second cell was arranged with the configuration $Ag/(AgI)_{0.5}(AgPO_3)_{0.5}$ $/I_2,C$ with the dimension of 11.5 mm diameter and 3.0 mm thickness. The electrolyte, anode, and cathode

powder were sandwiched as illustrated in the figure 2. For current collectors, two Cu disks were attached at the both sides of the sandwich. For protecting the I_2 electrode from sublimation and reacting with the other materials, the cell was molded by resin.

2.4. Test Characteristic of the Battery

For having the characteristics of the battery, a charge-discharge measurement was performed by loading with fixed external resistance (20kΩ, 50kΩ). All the output voltage data was measured using a pico DAQ during the charge-discharge process and recorded automatically in a computer.

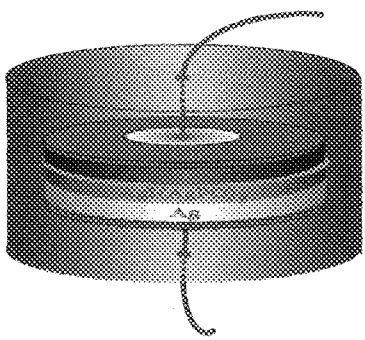

Figure 2. Preliminary design of coin type battery

Table1. Configuration of two solid state batteries

Battery	Electrolyte	ELectrodes	Dimension (dia/mm x thick./mm)	OCV (volt)
Type I	$(AgI)_{0.7}(AgPO_3)_{0.3}$ or AIX07	Ag / I_2	15.0 x 5.0	0.67
Type II	$(AgI)_{0.5}(AgPO_3)_{0.5}$ or AIX05	Ag / I_2,C	11.5 x 3.0	0.66

3.Results and discussion

The configuration of two batteries are shown in table 1. The open circuit voltage (OCV) are 0.67 volt and 0.66 volt for batteries with configuration Ag/AIX07/I_2 and Ag/AIX05/I_2,C , respectively. A simple construction to test performance of the both battery has been made. The battery was simply discharged by using external resistance 20 KΩ. The first test result of the one cell battery system is illustrated in Figure 3. The potential decreases from OCV and it works at around 0.42 volt for

many hours. This is shown that the working voltage of the first battery is around 0.42 volt , when discharged under the load of 20 KΩ.

In a typical cell reaction, the $(AgI)_{0.7}(AgPO_3)_{0.3}$ electrolyte retains iodine during charge and release during discharge. The cell reaction is $Ag + 1/2I_2 \rightarrow AgI$, with OCV is 0.66 volt, which is similar to the cell reaction of $Ag/AgI/I_2$ that has an open circuit voltage (OCV) of 0.7 volts [13]. This kind of battery has low capacity and low current density has low current density of about 5-10 μ/cm^2 of the anode. One of the problems of this ionic cell is the used of I_2 as a cathode. This material sublimates at room temperature, and reduces the capacity for the cell to keep its reaction. Iodine is a hygroscopic material. In the humid environment it will absorb water and soon ion I^- is created. The ion I^- will make further reaction with I_2 to form I_3, which is very reactive material. To reduce this reaction, an absorbent material should be added and in this case we chose powder carbon (C) or graphite, so that the anode/cathode couple becomes $Ag/I_2,C$ [14]. The combination of this anode/cathode couple has been used in the second battery with the configuration of $Ag/(AgI)_{0.5}(AgPO_3)_{0.5}/I_2,C$. The open circuit voltage (OCV) for this configuration is ~ 0.66 volt, which similar to other silver solid battery system. Here, it is shown that the carbon does not change significantly the potential between the two electrodes Ag/I_2.

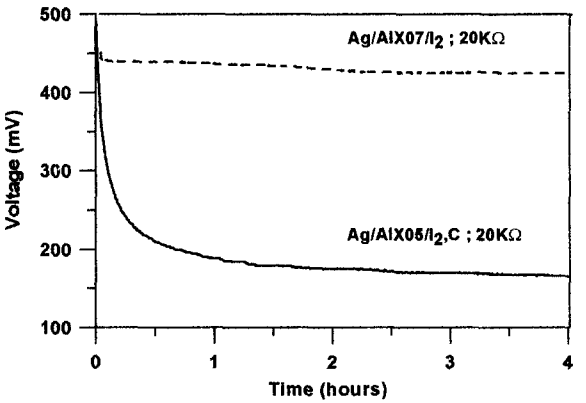

Figure 4. Discharge curve of $Ag/AIX07/I_2$ and $Ag/AIX05/I_2,C$ under the load 20KΩ.

Another similar test has been performed to the second battery by loading the cell under the 20 KΩ external resistance. The result in Figure 4 shows that the potential of $Ag/AIX05/I_2,C$ decreases gradually from 0.66 volt to 0.25 volt for the first one hour, then it stabilized at around the working voltage 0.25 volt for 6 hours before we stopped the program. The different between the two batteries on loading the same resistance, is due to the different in dimension and size of the cell battery, as listed in table 1. The larger is the contact area of the electrode-electrolyte, the higher is the current density. However, the used of C influences on the potential stability, not the capacity. Figure 5 shows the second battery was discharged under different load, 50KΩ and 20KΩ. It is clear that the working voltage will be lower when the load given to the battery is larger. However, the capacity of the battery

must be the same. In this experiment, unfortunately, we were unable to record the discharge curve until it becomes zero potential, since it last for more than 120 hours. The capacity of the cell can be calculated approximately ~3 mAh.

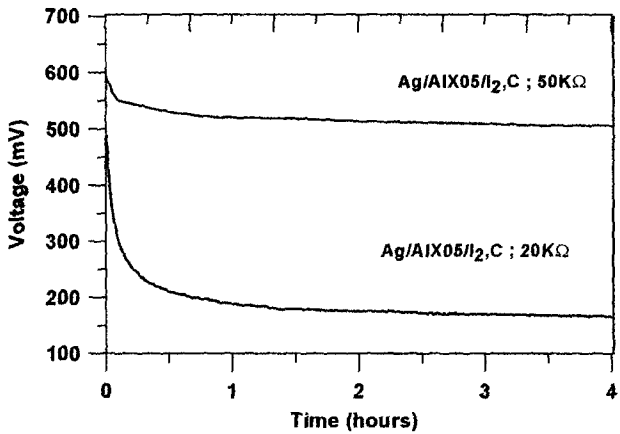

Figure 5. Discharge curve of Ag/ AIX05 /I_2,C under load 50 kΩ and 20 kΩ

4.Conclusion

In this experiment, two cell batteries of Ag/$(AgI)_{0.7}(AgPO_3)_{0.3}$ /I_2 and Ag/$(AgI)_{0.5}$ $(AgPO_3)_{0.5}$ /I_2,C were constructed. The results have illustrated the discharged characteristics of the silver battery when it was discharged with fixed load or fixed current values at room temperature. The typical discharge curves are relatively flat when it is operated below its limiting current. At the higher discharge current the operating voltage was lower. It is similar with the characteristics of all battery systems.

The Ag was chosen as the anode material due to some reasons such as for making the reduction and oxidation reaction take place uniformly and continuously during charge-discharge process, ease to be fabricated and can be used as an anode in the form of powder pellet, plate or grid. In the battery system, the electrodes are usually made from composite materials fabricated in more porous form in order to have electrodes with large area. With a large area electrode, the energy loss due to both active and concentration polarizations at the electrode surface can be minimized and the electrode efficiency can be improved [6]. The choice of I_2 cathode is to meet the essential requirement that the potential different must be high and the ionic transportation among the three components of the battery can flow naturally and continuously. Hence, the anode-cathode of Ag/I_2 couple was preferred. Iodine is a hygroscopic material. In the humid environment it will absorb water and soon ion I^- is created. The ion I^- will make further reaction with I_2 to form I_3^-, which is very reactive material. To reduce this reaction, an absorbent material should be added and in this case we chose powder carbon (C). By using this

material at least two advantages may be obtained i.e. the reduction of the I_3 ion and the larger area of the electrode. For isolating the battery from the further reaction with the water that comes from the surrounding, resin was used. It has been shown that the use of C can improve performance of the battery. Further improvement of the silver battery is now being progressed.

Acknowledgement

Technology Center for Nuclear Industrial Materials, National Nuclear Energy Agency (BATAN), Indonesia.is greatly acknowledged for the use of the facilities. This work has been funded by the Ministry Research and Technology, Indonesia through the Indonesian International Joint Research Program (RUTI-IV) under the contract no.6D/Perj/Dep.III/RUTI/PPKI/II/2005.

References

1. David Linden, *Handbook of Batteries*, McGraw-Hill. Inc., New-York, USA 1995
2. M.Z.A. Munshi Ph.D, *Handbook of Solid State Batteries & Capacitors*, World Scientific, Singapore 1995
3. L.W. Strock, *Z. Phys. Chem* **B25** (1934) 411
4. E. Kartini, RUT VI Final Report, National Research Council, Indonesia (2000)
5. M.F. Collins and E. Kartini, Chapter 7 *in* Recent Research Development of *Solid State Ionics* **Vol.I** (2003) 167-174; and reference therein.
6. E. Kartini, M.F. Collins, S. Yusuf, T. Priyanto, N. Indayaningsih, E.C. Svensson, S.J. Kennedy, *Phys.Rev.* **B 61** (2000) 1036.
7. M.Tatsumisago, K.Okuda, N.Itakura, T. Minami, *Solid State Ionics* **121**(1999) 193
8. D.A. Keen, *J. Phys. Condens. Matter* **14 9** (2002) R819.
9. E. Kartini, S. J. Kennedy, K. Itoh, T. Fukunaga, S. Suminta and T. Kamiyama, *Applied Physics* **A74** [Suppl.] (2002) s1236-1240
10. E. Kartini, S.J. Kennedy, K.Itoh, M.F. Collins and S. Suminta, *Solid State Ionics* **167** (2004) 65-74
11. E.Kartini, F.Mezei, M.Arai, M. Nakamura and M. Russina, in *Proc. International Conference on Neutron Scattering 2005*, Sydney, Australia; to be published in *Physica* **B** (2006)
12. M.Nakamura, M. Arai, E.Kartini, M. Russina, in *Proc. International Conference on Neutron Scattering 2005*, Sydney, Australia; to be published in *Physica* **B** (2006)
13. J.E. Oxley, in , *Proc. Annual Power Sources Symposium*, **vol.22** (1968) 20
14. T.Takahashi, I. Ikeda and O. Yamamoto, *J. Elctrochem. Soc.*, **119** (1972) 477

PERFORMANCE OF LITHIUM POLYMER CELLS WITH POLYACRYLONITRILE BASED ELECTROLYTE

KUMUDU PERERA[a], M.A.K.L. DISSANAYAKE[b*], STEEN SKAARUP[c] AND KELD WEST[d]

[a]*Department of Electronics, Wayamba University of Sri Lanka, Sri Lanka,*
[b*]*Department of Physics and Postgraduate Institute of Science (PGIS), University of Peradeniya, Sri Lanka,* [c]*Technical University of Denmark, Denmark,*
[d]*Riso National Laboratory, Denmark*

**E-mail: director@pgis.lk*

The performance of lithium polymer cells fabricated with Polyacrylonitrile (PAN) based electrolytes was studied using cycling voltammetry and continuous charge discharge cycling. The electrolytes consisted of PAN, ethylene carbonate (EC), propylene carbonate (PC) and lithium trifluoromethanesulfonate ($LiCF_3SO_3$ – LiTF). The polymer electrode material was polypyrrole (PPy) doped with dodecyl benzene sulfonate (DBS). The cells were of the form, Li / PAN : EC : PC : $LiCF_3SO_3$ / PPy : DBS. Polymer electrodes of three different thicknesses were studied using cycling at different scan rates. All cells had open circuit voltages in the range, 3.0 – 3.5 V vs Li. With increasing scan rates as well as thickness of the polymer electrode, diminishing of peaks and increase of peak separation in cyclic voltammograms was seen. Charge values obtained with constant charge discharge cycling and with cyclic voltammetry at slow scan rates were similar. The charge factor remained close to unity. These results show the fact that satisfactory cell performance can be achieved with thin electrode films and cycling at slow scan rates.

1. Introduction

Due to the unending progress of modern technology, there has been ample development in the field of battery technology towards high energy density, light weight and environmental friendliness. One aspect of improvement is connected with the electrolytes used in the batteries. At present, intensified research efforts are focused on gel electrolytes due to their considerable ionic conductivities and ability to act as free standing films[1,2]. Great attention has been put forward on polyacrylonitrile based electrolytes. The goal of fabricating batteries with high energy density, light weight and safety has resulted in lithium polymer batteries which are of the form Li / polymer electrolyte / conducting polymer cathode. The performance of those types of cells can be investigated using cycling voltammetry and charge-discharge cycling.

2. Experimental

A mixture of ethylene carbonate (EC, ALDRICH, 98%) and propylene carbonate (PC, Bie and Berntsen A-S, 99%) of 1:1 (by weight) was dried over molecular sieves for 24 hrs. Then, the required amount of lithium trifluoromethanesulfonate ($LiCF_3SO_3$, 3M)) was added and purification was done by percolating through activated alumina. In a certain amount of so-prepared electrolyte, the corresponding quantity of PAN (ALDRICH) was dissolved with the aid of magnetic stirring. The mixture composing of PAN : EC : PC: $LiCF_3SO_3$ was heated at 140 ^{0}C for 1 hr in a Buchi model (T0-50) furnace. The resulting homogeneous, viscous hot mixture was poured between two well-cleaned glass plates and pressed. On cooling, transparent film membranes could be obtained which were free from bubbles and pinholes. All the preparation steps were carried out inside a glove box (Vacuum Atmospheres Corporation) purged with Argon. Polymer electrodes were deposited on stainless steel electrodes. Cell preparation was done inside the glove box. A circular pellet was cut from the electrolyte membrane. A lithium electrode of the same diameter as the electrolyte was used as the anode. A brass sample holder was used to house the cell assembly.

For each cell fabricated, cyclic voltammetry tests were done in the potential range of 2.2 – 3.5 V vs metallic lithium using a computer controlled potentiostat / galvanostat. The PPy electrode served as the working electrode, lithium was used as both counter and reference electrodes. Cyclic voltammetry studies were performed at low as well as at high scan rates (0.1, 0.2, 0.3, 0.4, 0.5, 1.0, 2.0, 5.0, 10.0, 20.0, 50.0, 80.0 and 100.0 mV / s). Thereafter, those cells were tested for their ability to endure continuous charge and discharge cycling. For this purpose, they were galvanostatically discharged to 2.0 V immediately followed by a potentiostatic charge at 3.5 V by using a computer controlled charge-discharge set-up. Possible reactions leading to electrolyte decomposition are limited as the potentiostatic charge guarantees that electrode does not exceed the given potential. Besides, the steady decrease of charge current indicates the absence of any parasitic processes, which would result in self discharge. Numerical values of maximum charge and discharge currents were equal (25 μA). In this experiment, the charge was set to terminate when the current falls to a predetermined fraction (10%) of its maximum value.

3. Results and Discussion

All cells had open circuit voltages in the range 3.0 – 3.5 V. Cyclic voltammograms obtained for the cells with PPy : DBS films of thicknesses 1, 2, 4 μm are shown in Fig.1.

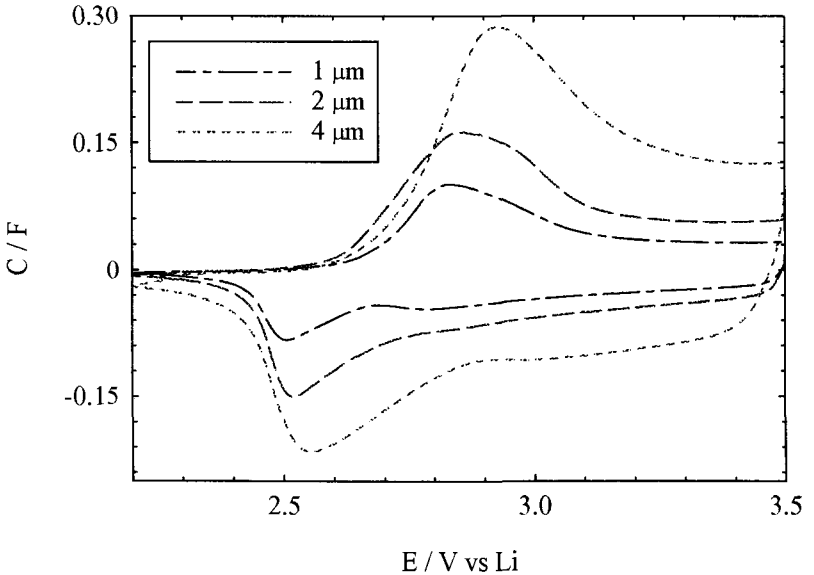

Fig. 1 Cyclic voltammograms obtained for cells of the configuration, Li / PAN : EC : PC : $LiCF_3SO_3$ / PPy : DBS with PPy : DBS films of thicknesses 1, 2, 4 μm (Scan rate = 0.4 mVs^{-1}).

It is seen from the cyclic volatammograms in Fig.1 that with increasing thickness of PPy electrode, a shift in the anodic peak position occurred at 0.4 mV/s, whereas the cathodic peak does not change much Synthesis charge and expected charge according to the film thickness is shown in Table 1. The synthesis charge was calculated according to the assumption that a charge of 240 mC cm^{-2} produces a film of thickness 1 μm^3. To calculate the expected charge, it was assumed that 0.33 anions per monomer participate in cycling. Increasing peak separation with thickness in Fig. 1 is most likely due to the fact that iffusion in thicker films is slower as proposed by some workers[4]. With slow diffusion, complete reduction and oxidation takes place at too far away potentials. As a result, the separation of the peaks increases. This is especially the case during the anodic sweep, showing that the time constant for oxidation is somewhat larger than for reduction. Kinetic limitations may be expected to arise with increasing thickness either due to inability of ions to follow the increased diffusion paths or may be due to the enhanced cross links of the PPy which hinders ion diffusion. The variation of charge

Table 1. Synthesis charge and expected cycling charge according to the film thickness

Thickness / μm	Synthesis charge / C	Expected cycling charge / C
1	0.36	0.05
2	0.72	0.10
4	1.44	0.20

variation of charge values from the expected values mainly in the cells with thicker electrodes might be due to the difference in the doping levels. For calculating the expected charge, a doping level of 33% was used. But, if the actual doping value was less that 33%, the resulting charge will be smaller. Cyclic voltammograms obtained for varying scan rates are shown in Fig.2 for the cells having PPy : DBS film of 1 μm thickness.

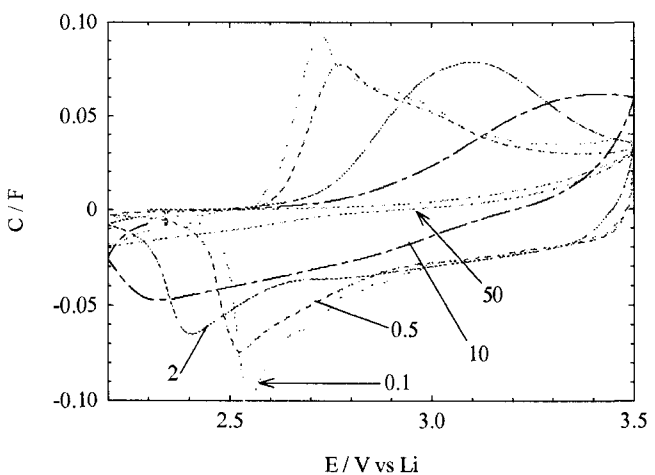

Fig. 2 Cyclic voltammograms obtained for scan rates, 0.1, 0.5, 2.0, 10.0, 50.0 mVs^{-1} for PPy : DBS film of 1 μm thickness.

One of the clear features is that the peaks have shifted with increasing scan rate in a way such that oxidation peaks to anodic side and reduction peaks to cathodic side. This gives rise to a higher peak separation at high scan rates. Furthermore peaks tend to diminish at higher scan rates. With increasing scan rates, the peak separation increases because ions cannot follow the scanning rate to complete reduction and oxidation. This pushes the peaks apart. This is also the reason for the diminishing of the peaks at high scan rates. At slow scan rates, the charge obtained is almost constant. That is, the capacity does not depend on kinetics. Instead, better conjugation in the films may govern the amount of available charge It has been reported that polymerization of PPy in detergents such as DBS results in better conjugated films[5]. With increasing scan rate the charge decreases faster. A considerable amount of charge was available around 2.6 – 2.7 V vs Li at slow scan rates. It may be due to the fact that PPy switches from non-conducting state to conducting state around 2.8 V vs Li.[6]. Charge values obtained for different scan rates and for thicknesses of 1, 2 and 4 μm are shown in Table 2.

Table 2. Charge values obtained from the cells with PPy : DBS films of thicknesses 1, 2 and 4 μm at different scan rates

	Scan Rate / mVs^{-1}	**Charge / C (1 / μm)**	**Charge / C (2 / μm)**	**Charge / C (4 / μm)**
PPy : DBS	0.1	0.042	0.083	0.165
	0.5	0.040	0.065	0.133
	2.0	0.041	0.062	0.111
	10.0	0.025	0.026	0.038
	50.0	0.004	0.001	0.001

Compared to the expected charge (Table 1), the observed values are successively smaller at high scan rates. The capacity variation as a function of cyclic number for different PPy : DBS film thicknesses are shown in Fig.3. Sudden apparent capacity increases could be seen as spikes. An example is the cell having 4 μm thick PPy : DBS electrode. The sudden capacity increase in Fig. 3 occurs probably due to a short-circuit of the electrolyte. Proper cell behaviour is obtained as the discharge capacity of the subsequent cycles becomes constant at a reasonable value. This is equivalent to the formation of soft dendrites often described for polymer electrolytes based cells, and showing the tendency for self healing. The systems under study here had this property of self healing. The same capacity values obtained from the CV

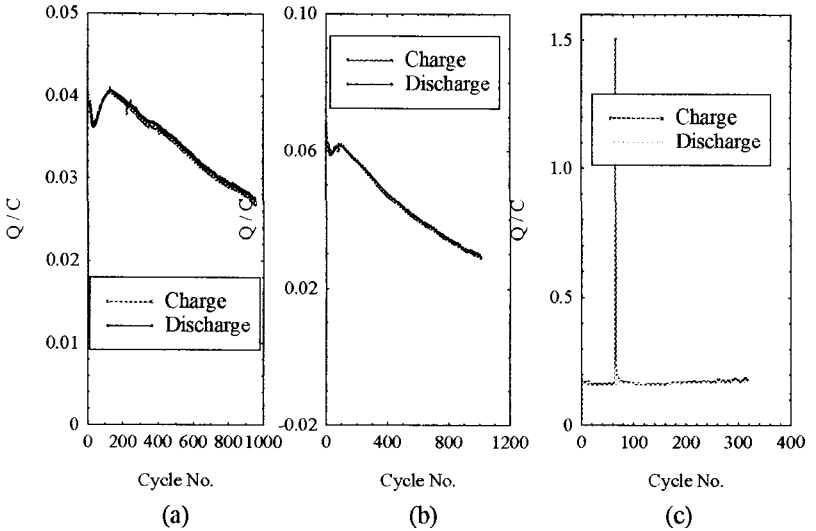

Fig. 3. Capacity variation with cycle number for different Ppy : DBS film thicknesses (a) : 1 μm, (b) : 2 μm, (c) : 4 μm.

studies at low scan rates with cells of thin electrodes are available even with continuous cycling. With increasing thickness of the electrodes, the capacity increases, but not in proportion to the thickness. However, the number of cycles has gone down. Thin film electrode films sometimes show capacity increase during cycling. It may be due to introduction of imperfections and or improved contacts. Upon cycling, some cells show an initial capacity decrease following by a capacity increase and then a capacity decrease again. This can be attributed to changes at electrode contact and decomposition of components. The charge factor (the ratio between the charge and the discharge capacity) remained close to unity. This indicates the absence of parasitic reactions.

4. Conclusion

The calculated theoretical charge could be achieved from cells with thin film electrodes when cycled at slow scan rates, but not for thicker cells and/or higher scan rates. This

delimits the maximum performance attainable with this battery system. The retention of a charge factor close to unity is an indication of the absence of parasitic reactions.

Acknowledgements

Authors wish to gratefully acknowledge the support from International Programmes in Physical Sciences (IPPS), Uppsala University, Sweden.

References

1. K. Shani, J. B. Wagner, B. B. Owens; in Lithium Batteries, Edit. J. P. Gabano, Academic Press, London, 1983, Ch.15.
2. J. Vondrak, M. Sedlarikova, J. Reiter, T. Hodal, Electrochimica Acta, 44 (1999) 3067- 3073.
3. Diaz A.F., Castillo J.I., J. Chem. Soc., Chem. Communi., (1980)397.
4. Osaka,T., Naoi,K., Ogano, S., J. of Electrochem. Soc., 135 / 5(1988)1071
5. Waren L.F., Anderson D.P., J. of Electrochem Soc., 134(1987)105.
6. S. Skaarup, K. West, B.Z. Christiansen, M.A. Careem, G.K.R. Senadeera, Solid State Ionics, 72(1994)108.

HYDROTHERMAL SYNTHESIS AND ELECTROCHEMICAL BEHAVIOR OF MOO_3 NANOBELTS FOR LITHIUM BATTERIES

W. CHEN†, Y. Y. QI, L. Q. MAI, Q. XU, H. X. LIU, X. J. ZHAO

Institute of Materials Science and Engineering, Wuhan University of Technology, Wuhan 430070, P.R. China

Molybdenum trioxide nanobelts have been synthesized via the simple hydrothermal reaction by using MoO_3 sols as precursor. The morphology and structure of the samples were characterized by XRD, SEM and TEM. The results indicate that the samples are α-MoO_3 nanobelts with the thickness of 20~70 nm and with length up to 10 μm, and the nanobelts are single crystals elongated preferentially in the [001] direction. The effect of different reaction time on the structure and morphology of the samples and the growth mechanism for MoO_3 nanobelts have been studied. The electrochemical properties of the MoO_3 nanobelts have been investigated finding that Li^+ ions showed better reversibly insertion/extraction cycles in as-synthesized MoO_3 nanobelts than in bulk MoO_3 samples.

1. Introduction

In 1984, nanoparticles were firstly synthesized by German scientist—Gleiter, which has triggered a variety of research interests spanning a spectrum of scientific fields [1-4]. At the same time, nanostructured materials, especially one-dimensional (1-D) nanomaterials including nanotubes, nanorods, nanobelts and nanofibers, have been actively studied due to both scientific interests and potential applications [5,6].

The outstanding structural versatility of the transition metal oxides and their derivatives have been receiving significant attention with respect to applications in catalysis, sensors and as electrochemical devices [7]. Orthorhombic molybdenum trioxides have been linked to interesting physical and chemical properties because of their desirable characteristics and typical two-dimensional layered structure. Due to the size effect and quantum confinement effect, 1-D MoO_3 nanomaterials are becoming more and more important and necessary. Zach and co-workers prepared molybdenum oxide nanowires on a stepped graphite surface by an electrodeposition method [8]. Li et al synthesized single-

† Corresponding author. Tel.: +86 27 87651107; fax: +86 27 87864580.
E-mail address: chenw@mail.whut.edu.cn (W. CHEN)

crystal α-MoO_3 nanobelts and nanotubes by infrared irradiation heating a Mo foil [9,10]. Zhou et al prepared MoO_2 nanowire arrays by thermal evaporation in a vacuum chamber, and obtained MoO_3 nanowire arrays by further treatment in the growth chamber [11]. However, no attempts have been made so far to study the electrochemical lithium insertion/extraction property of MoO_3 nanostructures.

Herein, orthorhombic MoO_3 (α-MoO_3) nanobelts were successfully fabricated via a hydrothermal route using MoO_3 sols as precursor at low temperature (180 ℃) and autogenous pressure. XRD, SEM, TEM and electrochemical analysis were performed to study the structure, growth process and electrochemical properties of MoO_3 nanobelts.

2. Experimental

2.1. *Synthesis*

The synthesis of MoO_3 nanobelts from sols was carried out as follows. MoO_3•nH_2O sols were prepared by the ion exchange of $(NH_4)_6Mo_7O_{24}\cdot 4H_2O$ (≥ 99.0 %) through a proton exchange resin. After ion exchange, the clear light-blue MoO_3•nH_2O sols (the final pH is about 2.0) was obtained. Then, the solution was directly added into a Teflon-lined autoclave and kept at 180 ℃ for 1~4 h. After the hydrothermal reaction, the light blue sample was washed with distilled water and ethanol and dried at 80 ℃ for 8 h.

2.2. *Characterization*

The X-ray powder diffraction (XRD) measurement was performed on a D/MAX-III X-ray diffractrometer with CuKα radiation and graphite monochromator. Fourier-transformed infrared (FTIR) absorption spectrum was recorded using the 60-SXB IR spectrometer with a resolution of $4cm^{-1}$. The SEM images were collected with JSM-5610LV scanning electron microscope. The TEM images were taken with a JEOL-2010 microscope operated at 200 kV. The electrochemical properties were studied with a multichannel galvanostat/potentiostat system (MacPile). Electrochemical cells were prepared using a lithium pellet as negative electrode, 1 M solution of $LiPF_6$ in ethylene carbon (EC)/dimethyl carbonate (DMC) as electrolyte and a pellet made of the nanobelts, acetylene black and PTFE in a 10:7:1 ratio as the positive electrode.

3. Results and Discussion

To confirm the structure of the samples, the X-ray diffraction (XRD) investigation was performed. Figure 1 shows the XRD patterns of the

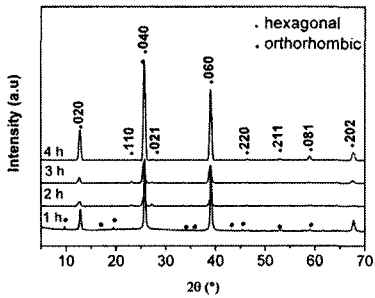

Figure 1. X-ray diffraction patterns of the hydrothermal samples at different reaction time.

molybdenum oxide obtained from the MoO_3 sols for various reaction time at 180 ℃. The light blue particles formed for 1~2 h are a mixture of orthorhombic and hexagonal phases. As the reaction time rises only the peaks of orthorhombic MoO_3 (α-MoO_3) are observed suggesting that hexagonal MoO_3 phase are entirely transformed into orthorhombic MoO_3 phase. With respect to the α-MoO_3, the strong intensity of reflection peaks of (020), (040) and (060) indicate the anisotropic growth. The orthorhombic structure is also identified by IR spectrum as shown in Figure 2. The absorption bands at 997 and 868 cm^{-1} are assigned to

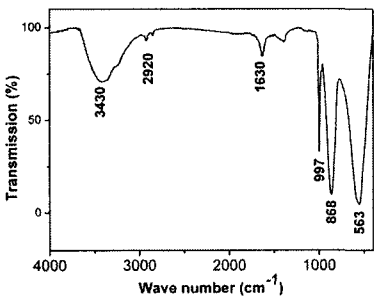

Figure 2. IR spectrum of the MoO_3 nanorods synthesized for 4 h.

Mo-terminal oxygen band, and the bending mode of Mo-O-Mo is located at 563 cm^{-1} [12-14]. The weak signals between 1600 and 3600 cm^{-1} in the sample are attributed to the presence of remaining H_2O and CH_3CH_2OH.

Figure 3 displays the scanning electron microscopy (SEM) images of the samples. It can be seen that the typical hexagonal rods with the length of 15~30 μm are formed and a few one-dimensional nanostructures are also observed at 1 h (Figure 3a). The hexagonal structures begin to dissolve at the tip which results in the formation of spindle-like structure and the quantity of nanostructures obviously increases at 2 h (Figure 3b). The belt-like MoO_3 nanomaterials are

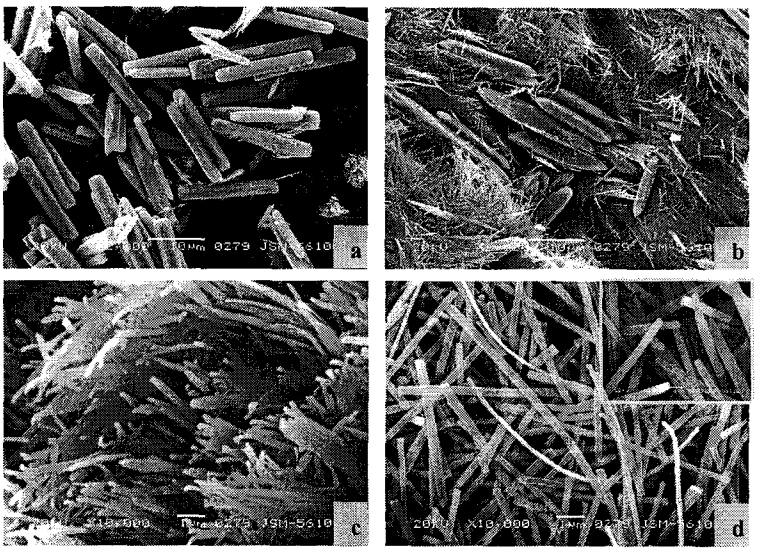

Figure 3. SEM images of the hydrothermal samples at different reaction time (a) 1 h, (b) 2 h, (c) 3 h and (d) 4 h.

completely obtained at 3 h (Figure 3c) and when the reaction was extended to 4 h, the well-defined belt-shaped nanocrystals are synthesized successfully (Figure 3d). With respect to the well nanobelts synthesized for 4 h at 180℃, the rectangular-like cross section of the materials is clearly visible in the SEM image. The width of the nanobelts are between 80 nm and 400 nm and their length lies between 1 and 10 μm. The average thickness of the belts is about 50 nm, as estimated from the SEM image (Figure 3d). The above results are further confirmed by TEM investigation. Figure 4b shows a HRTEM image and ED pattern recorded from a single nanobelt in Figure 4a. It reveals that the MoO_3 nanobelt is structurally uniform single crystal without dislocation and the surface of the nanobelts are clean. The spacing of 2 nm ± 0.005 nm between adjacent lattice planes corresponds to the distance between (200) crystal plans, which proves [l00] is the width direction perpendicular to the growth direction ([00l]). By recording selected area electron diffraction (SAED) pattern, it is also possible to determine that the nanobelt is single crystal with the [001] direction parallel to the rod axis (inset of Figure 4b). All nanobelts, we observed, exhibit the [001] direction for the rod axis. The result is the same as that in previous report [15].

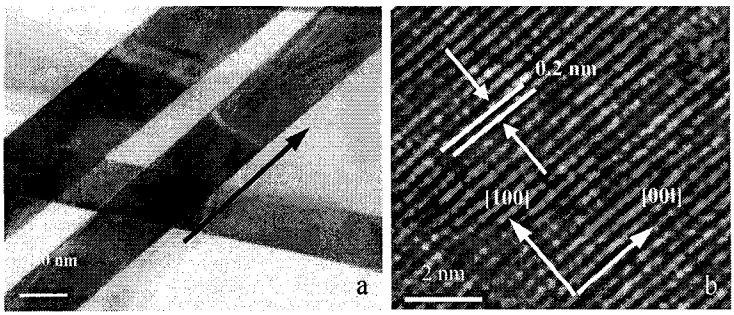

Figure 4. TEM images of MoO_3 nanobelts synthesized for 4 h and selected area electron diffraction pattern of a single MoO_3 nanobelt. (a) low magnification TEM images; (b) HRTEM image and the inset is the corresponding SAED pattern.

As exhibited in above results, hexagonal MoO_3 microrods are firstly formed and subsequently transformed into the α-MoO_3 nanobelts in the hydrothermal reaction process. Hexagonal molybdenum trioxide is a metastable phase of molybdenum oxides and the structure consists of a three-dimensional array of corner-sharing MoO_6 octahedra and there are some vacancies in Mo sites [16]. With longer reaction time, the metastable microrods begin to dissolve and the basic units (MoO_6 octahedra) are free. The orthorhombic structured MoO_3 is a typical two-dimensioned layered structure consisting of double layers of edge- and vertex-sharing MoO_6 octahedra being weakly held together by Van Der Waals bonds (Figure 5). Two Mo-O bonds will form if the units add along the

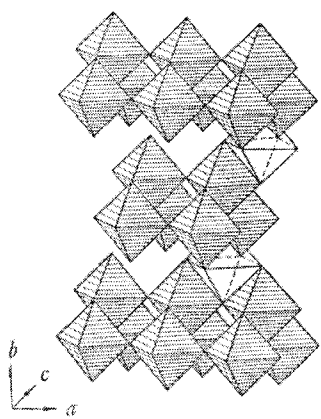

Figure 5. Crystalline structure of α-MoO_3.

[001] direction, while only one Mo-O bond form in the case of the growth along the [100] direction and the corresponding energy release along the [001] direction is greater. So the MoO_6 octahedra are preferentially stacked in the [001] direction, then belt structure are formed.

Figure 6 is the first discharge curve of the cell with the as-synthesized

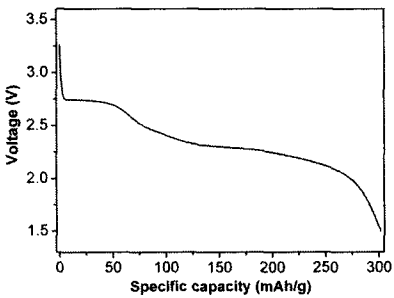

Figure 6. Initial discharge curve of MoO_3 nanobelts synthesized for 4 h.

nanobelts. It is known that the charge-discharge reaction of an α-MoO_3 electrode at potential range of 1.5~3.25 V can be expressed by the equation

$$xLi^+ + MoO_3 + xe^- \underset{\text{charge}}{\overset{\text{discharge}}{\rightleftharpoons}} Li_xMoO_3 \qquad (1)$$

In the first cycle the highest discharge capacity is 301 mAh/g, corresponding to an intercalation of around 1.6 Li per formula unit (~$Li_{1.6}MoO_3$). And there are two obvious sloping potential ranges (2.7~2.8 V and 2.2~2.4 V vs Li^+/Li) for the lithium intercalation reaction. Figure 7 shows 14 complete charge-discharge

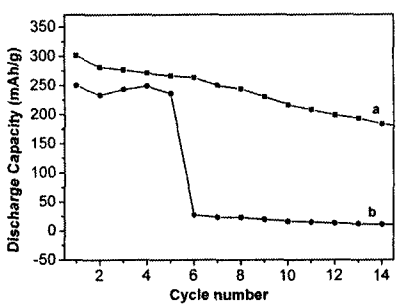

Figure 7. Cycling property of MoO_3 nanobelts synthesized for 4 h (a) and bulk MoO_3 (b).

cycles of the batteries and the first specific discharge capacity of the MoO_3 nanomaterials (301 mAh/g) is higher than that of bulk MoO_3 (249 mAh/g). Moreover, the specific discharge capacity of the nanostructures decreases smoothly (Figure 7a) and the cell exhibits a capacity loss of only 10% after 5 cycles. But the specific discharge capacity of bulk materials is only 27 mAh/g after 5 cycles (Figure 7b). The above results indicate that the MoO_3 nanobelts have good electrochemical performance because of the highly ordered beltlike structural arrangement. Although the discharge plateau of the α-MoO_3 nanobelt electrode is lower than that of the commercially used cathode materials, α-MoO_3 nanobelts exhibit a high discharge capacity of 301 mAh/g and better cycling reversibility. Consequencely, the α-MoO_3 nanobelts can be a promising cathode material in the field of rechargeable lithium batteries.

4. Conclusions

This paper describes a rational hydrothermal treatment to prepare single-crystal molybdenum trioxide nanobelts starting from the relatively cheap $(NH_4)_6Mo_7O_{24}\cdot 4H_2O$. Reaction time is the decisive factor in determining phase content. With the increase in reaction time, the hexahedral microrods dissolve and are transformed to the stable structure of orthorhombic phase (α-MoO_3 nanobelts). The activated MoO_3 nanomaterials exhibit 301 mAh/g capacity in the initial discharge process and have good cycling property.

Acknowledgments

This work was supported by the National Natural Science Foundation of China (Grant No. 50372046, 50372048), the Key Project of Chinese Ministry of Education (Grant No. 104207), the Teaching and Research Award Program for Outstanding Young Professors in Higher Education Institute, MOE, P. R. China and the Foundation for innovation Research Team of Hubei Province (No. 2005ABC004).

References

1. H. Gleiter, *Europhysics News* **20,** 223 (1989).
2. X. C. Jiang, T. Herricks and Y. N. Xia, *Nano Lett.* **2**, 1333 (2002).
3. M. H. Huang, S. Mao, H. Feick, H. Q. Yan, Y. Y. Wu, H. Kind, E. Weber, R. Russo and P. D. Yang, *Science* **292**, 1897 (2001).
4. Y. H. Lee, C. H Choi, Y. T. Yang, E. K. Kim, B. K. Ju, N. K. Min and J. H. Ahn, *Appl. Phys. Lett.* **81**, 745 (2002).
5. R. E. Cavicchi and R. H. Silsbe, *Phys. Rev. Lett.* **52**, 1435 (1984).

6. P. Ball and G. Li, *Nature* **355**, 761 (1992).
7. W. Chen, Q. Xu, Y. S. Hu, L. Q. Mai and Q. Y. Zhu, *J. Mater. Chem.* **12**, 1926 (2002).
8. M. P. Zach, K. H. Ng and R. M. Penner, *Science* **290**, 2120 (2000).
9. Y. B. Li, Y. Bando, D. Golberg and K. Kurashima, *Appl.Phys.Lett.* **81**, 5048 (2002).
10. Y. B. Li and Y. Bando, *Chem. Phys. Lett.* **364**, 484 (2002).
11. J. Zhou, N. Sh. Xu, Sh. Zh. Deng, J. Chen, J. C. She and Zh. L. Wang, *Adv. Mater.* **15**, 1835 (2003).
12. G. Guzman, B. Yebka, J. livage and C. Julien, *Solid State Ionics* **407**, 86 (1996).
13. W. Dong, and B.Dunn, *J. Non-Cryst Solids* **225**, 13 (1998).
14. G. A. Nazri and C. Julien, *Solid State Ionics* **80**, 271 (1995).
15. X. L. Li, J. F. Liu and Y. D. Li, *Appl. Phys. Lett.* **81**, 4832 (2002).
16. Y. Muraoka, J.C. Grenier, S. Petit and M.Pouchard, *Solid State Sciences* **2**, 133 (1999).

ELECTROCHEMICAL BEHAVIOUR OF A PPY(DBS)/POLYACRYLONITRILE :LITF:EC:PC/ LI CELL

K.VIDANAPATHIRANA
Department of Electronics, Wayamba University of Sri Lanka, Kuliyapitiya, Sri Lanka
kamalpv@sltnet.lk

M. A. CAREEM
Department of Physics, University of Peradeniya, Peradeniya, Sri Lanka
mac@pdn.ac.lk

S. SKAARUP
Department of Chemistry, Technical University of Denmark, Denmark
skaarup@kemi.dtu.dk

K. WEST
Riso National Laboratory, Denmark.
Keld.west@riso.dk

The electrochemical behaviour of Li rechargeable cells with Polypyrrole (PPy) as the cathode material was investigated using cyclic voltammetry. The PPy used was doped with the large surfactant anion dodecyl benzenesulphonate (DBS^-). The cells were constructed with PAN:LiTF:EC:PC gel electrolyte with Li as anode. The results indicate that during the first reduction, cations are inserted into the PPy film forming LiDBS neutral salt. During the next oxidation/reduction cycles, the mechanism then switches to anion movement. Cyclic voltammetry studies also verified that complete electrochemical reversibility could be obtained at very low sweep rates.

1. INTRODUCTION

The conducting polymer Polypyrrole (PPy) has been extensively studied as a prominent candidate for cathode material in Li rechargeable cells[1-3]. However in most of the studies, cells fabricated with small anions were used. It has been reported that the cycling capacity of those cathodes is very low and that their stability is poor[4]. The use of large surfactant anion salts has been found to provide a solution for the above drawbacks[4]. In this study a large surfactant anion salt, sodium dodecyl benzene sulphonate (SDBS), was used and the electrochemical behaviour of the cell in the configuration PPy : DBS / PAN : EC : PC : $LiCF_3SO_3$ / Li is reported.

2. EXPERIMENTAL

Film preparation

PPy / DBS films were prepared galvanostatically with a current density of 1 mA cm^{-2} on a polished stainless steel disk in a three electrode cell containing an

aqueous solution of 0.05 M SDBS and 0.2 M pyrrole monomer. A Saturated Calomel Electrode (SCE) and a Pt wire were used as the reference and counter electrodes. Films were prepared to have a calculated thickness of 1 μm. After polymerization, the films were thoroughly rinsed with distilled water.

For the study of variation of peak potential with the concentration of cycling electrolyte, PPy/DBS films were prepared on Pt-wire electrode using a current density 62.5 μA cm^2. The polymerization electrolyte and monomer concentration were same as above.

Polymer Electrolyte preparation

A polymer electrolyte based on polyacrylonitrile (PAN, ALDRICH) prepared by the method described by K. M. Abraham et al.[5] was used.

Cell fabrication

An airtight special brass sample holder was used for assembling the cell inside an Ar filled glove box. A circular shaped membrane was cut from the electrolyte to the same size as the PPy / DBS film and used as a separator. A piece of Li metal of the same diameter was used as the anode. The cell was assembled in the configuration of PPy :DBS / PAN : EC : PC : $LiCF_3SO_3$ / Li .

Cyclic Voltammetry

The cell was reduced to 2.2 V vs Li starting from its open circuit voltage which was measured prior to starting the experiment Thereafter the cell was cycled several times in the potential range 2.2 to 3.5 V with respect to Li at different sweep rates. PPy served as the working electrode while Li acted as both counter and reference electrodes.

For the study of variation of peak potential with the concentration of cycling electrolyte, PPy/DBS films were cycled in $LiCF_3SO_3$ /PC liquid electrolytes having concentrations ranging from 0.05 M to 1.0 M at the scan rate of 5 mV s^{-1}. Metallic lithium was used as the reference electrode.

3. RESULTS AND DISCUSSION

Fig. 1 shows the cyclic voltammograms obtained for a polymer electrolyte cell with a 1 μm PPy / DBS film..

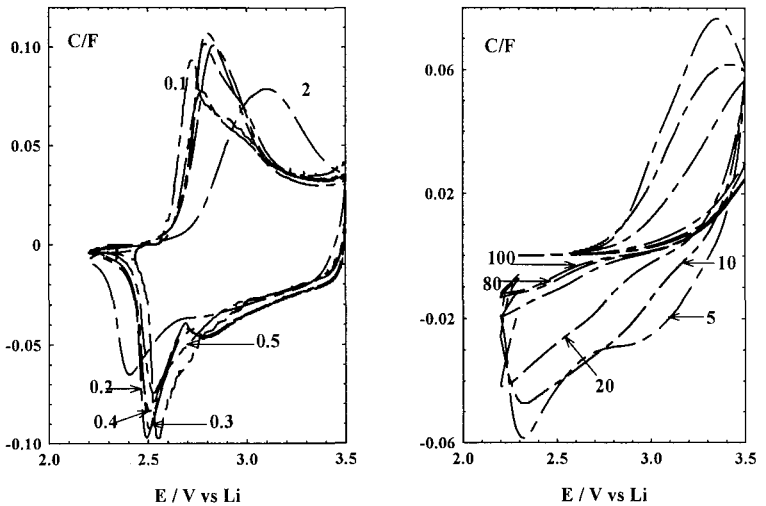

Figure 1.Cyclic voltammograms of a cell in the configuration of a Li/PAN:EC:PC: $LiCF_3SO_3$/PPy:DBS cell at different scan rates. PPy film thickness 1 μm. (a) cyclic voltammograms with scan rates 0.1 to 2 mV s^{-1}, (b) cyclic voltammograms with scan rates 5 to 100 mV s^{-1}

The cyclic voltammograms corresponding to lower sweep rates (0.1 to 2 mV s^{-1}) are shown in Fig. 1(a). When the cycling speed is increased, the peak positions seem to be shifting apart resulting in much broader peaks with less capacity. This is because the oxidation and reduction process may not be able to follow the high scan rate. In other words the total reaction that should occur at a particular potential will not occur and will be shifted to higher potentials with broader peaks. These features are also visible in Fig. 1(b), in which the cycling capacity has also drastically decreased as the scan rate is increased from 5 mV s^{-1} to 100 mV s^{-1}. But when the scan rate is very low (e.g. 0.1 mV s^{-1}), the peak separation becomes smaller, indicating an approximate electrochemical reversibility[6].

The electrochemical reactions of cells based on conducting polymer cathodes are related to the oxidation and reduction of conducting polymer electrode. During charging and discharging of the cell, ion incorporation or ejection occurs in the PPy film according to oxidation and reduction of the polymer.

The ion incorporation and ejection during oxidation and reduction depends on the type of the doping ion used during the polymerization of PPy. It is known that when PPy is doped with small anions, they can be responsible for the electrochemical reactions[7-8]. In contrast, when PPy is doped with considerably larger anions, it is reported that instead of anions, cations take the dominant role in electrochemical reactions[9]. However, this is experimentally proven only for aqueous electrolytes. Very

few investigations have been carried out to find out which kind of ions take part in the redox process in PPy films in non-aqueous electrolytes, when they are prepared with large anions.

The cyclic voltammograms of a PPy/DBS film cycled in different concentrations of $LiCF_3SO_3$ / PC electrolytes and the peak potential variation with the cycling electrolyte concentration (in logarithmic scale) are given in Fig.2.

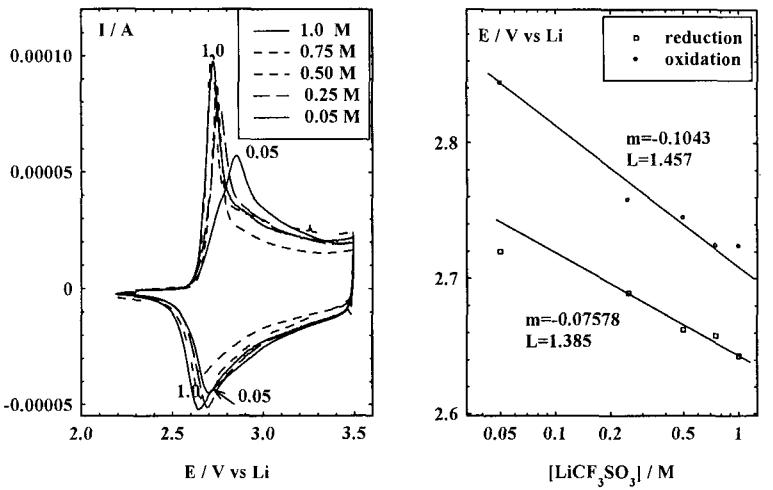

Figure 2. (a) Cyclic voltammograms of PPy/DBS obtained after the first reduction, cycled in different concentrations of $LiCF_3SO_3$ /PC electrolyte. Scan rate 5 mV s^{-1}.
(b) Peak potential variation with the cycling electrolyte concentration for the curves in (a)

As the cycling electrolyte concentration increases, both the oxidation and reduction potentials have shifted towards lower potentials. This is quite opposite to what was observed for the PPy / DBS films in aqueous electrolytes[10]. In non aqueous electrolytes also the peak potentials should vary in accordance with the Nernst relationship given by Eq. (1).

$$Ox + n.e^- \rightarrow red \qquad \Rightarrow \qquad E \approx E_o \cdot \frac{RT}{nF} \ln \frac{a_{red}}{a_{Ox}} \qquad (1)$$

For the Li reference electrode, Eq. (1) yields

$$Li^+ + e^- \rightarrow Li \quad \Rightarrow \quad E = E_o^{Li} - 0.059 \log \frac{1}{C_{Li^+}} \qquad (2)$$

where the activity of Li^+ has been approximated by the concentration. As in the aqueous electrolytes, the oxidation and reduction processes of PPy / DBS system is determined by either insertion / ejection of cations or by ejection / insertion of anions.

If cations are moving

$$PPy^+/DBS^- + Li^+ + e^- \rightarrow PPy/DBS^-/Li^+$$

$$E_{PPy} = E_o^{PPy} - 0.059 \log \frac{a_{PPy.DBS^-.Li^+}}{a_{PPy^+.DBS^-}.C_{Li^+}} \qquad (3)$$

Here the activity ratios are assumed to be constant and the concentration of Li^+ and $CF_3SO_3^-$ are identical.

If anions are moving

$$PPy^+/DBS^-/Li^+/TF^- + e^- \rightarrow PPy/DBS^-/Li^+ + TF^-$$

$$E_{PPy} = E_o^{PPy} - 0.059 \log \frac{a_{PPy.DBS^-.Li^+}.C_{TF^-}}{a_{PPy^+.DBS^-.Li^+.TF^-}} \qquad (4)$$

For the cation movement the total reaction of PPy is found by subtracting equation (2) from (3).

$$PPy^+/DBS^- + Li \rightarrow PPy.DBS^-.Li^+$$

$$E_{PPy} - E_{Li^+} = E_o^{/} + 0.059 \log C_{Li^+} - 0.059 \log C_{Li^+} = E_o^{/} \qquad (5)$$

The activity ratio between polymer/ion complex has been assumed to be constant at the peak maximum[11] and absorbed in $E_o^{/}$.

Similarly for anion movement, the total reaction of PPy electrode can be obtained by subtracting equation (2) from (4).

The activity ratio between PPy / DBS- / Li^+ and PPy^+ / DBS^- / Li^+ / $CF_3SO_3^-$ complexes has again been assumed as constant and absorbed in $E^{//}_o$.

If pure anion mobility exists then the peak potential should decrease by 118 mV as the concentration is increased by a factor of 10. On the other hand pure cation mobility should give peak potentials which are independent of the salt concentration.

According to Fig. 2, both oxidation and reduction peak potential variations approximately correspond to the straight lines predicted by the Nernst equation. The slopes of the lines are -104 and -75 mV / decade for oxidation and reduction respectively. These values are close to the -118 mV/decade predicted for the anion movement by equation (6) and far from the slope of zero predicted for cation movement by equation (5).

When the first reduction curves indicated in Fig. 3 are considered, reduction at 0.05 M concentration has a broad peak. This is because the redox process could not follow the 5 mV s^{-1} scan rate.

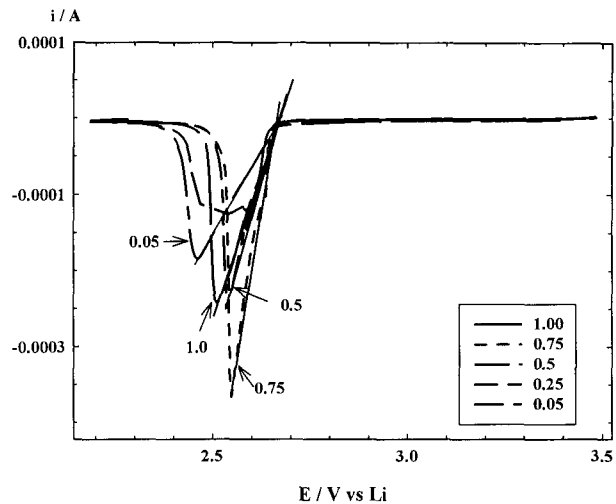

Figure 3. First reduction scans of a PPy/DBS film cycled in different concentrations of $LiCF_3SO_3$ /PC liquid electrolytes. Scan rate 5 mV s^{-1}.

However, when the straight lines are drawn to the peaks as in Fig. 3, they meet at the same point where the potential has started to change. This means that the peak potential variation is independent of the cycling electrolyte concentration. According to equation (3), cations are moving into the film during the first reduction.

The slope for the reduction of the later cycles (Fig. 2b) is around 35% less than that for the pure anion movement. This can be attributed to a number of causes such

as kinetic effects caused by the change in conductivities of the electrolyte and the polymer, different activity coefficients at 0.05 and 1.00 molar concentrations, peak during reduction may contain several contributions and some amount of cation insertion may also occur during reduction. Considering all the above factors it can be summarized that, when PPy / DBS film is cycled in non-aqueous electrolytes, cations (in this case Li^+) are inserted into the film during the 1st reduction. This will form a neutral salt (LiDBS) inside polymer chain. Thereafter, during oxidation and reduction, anions ($CF_3SO_3^-$) are moving in and out of the film to maintain charge neutrality.

From the above results, the following electrochemical reactions can be proposed during charge/ discharge procedures of the cell:

During the first reduction, anions cannot move out, since there are only large immobile anions (DBS) present. Instead Li^+ ions must be incorporated into the polymer electrode as indicated by Eq. (7).

At the anode; $$Li \Rightarrow Li^+ + e^-$$

At the cathode; $$PPy^+DBS^- + Li^+ + e^- PPy^0 \Rightarrow DBS^-Li^+ \quad (7)$$

These incorporated Li^+ may form LiDBS salt inside the polymer matrix and it will be quite stable there. With this situation, in the following cycles, $CF_3SO_3^-$ may move in and out during oxidation and reduction respectively. Therefore, in the following charging cycle of the cell (oxidation of the PPy film), $CF_3SO_3^-$ should enter the polymer structure to maintaining charge neutrality as in Eq.(8).

$$PPy^0DBS^-Li^+ + CF_3SO_3^- \Rightarrow PPy^+DBS^-Li^+CF_3SO_3^- + e^- \quad (8)$$

Reduction of the cell will then cause the expulsion of anions ($CF_3SO_3^-$). This process is expected to continue during charging and discharging of the cell. The cell therefore switches from cation to anion mechanism after the incorporation of cations during the first reduction

4. CONCLUSION

When PPy films prepared with large surfactant anion (DBS^-) are cycled in non aqueous electrolytes, cations are inserted into the film during the first reduction forming a neutral salt. Similar mechanism occurs during the first reduction in polymer electrolyte cells with PPy/DBS as cathodes. However, the subsequent cycles show anion movement as in cells with small inorganic anions where anions in the electrolyte move in and out during oxidation and reduction of the cell. There is therefore a change in mechanism during first cycle and subsequent cycles taking place in cells. It can also be concluded that the polymer electrolyte cell with the configuration PPy : DBS / PAN : EC : PC : $LiCF_3SO_3$ / Li can achieve approximate electrochemical reversibility at low scan rates.

5. ACKNOWLEDGEMENTS

We acknowledge the assistance from IPPS, Uppsala, Sweden, Technical University of Denmark, Denmark and University of Peradeniya, Sri Lanka.

6. REFERENCES

1. S. Kakuda, T. Momma, T Osaka, G. B. Appetecchi and Bruno Scrosati, J. Electrochem. Soc. **142/1**, L1(1995).
2. M. Mermilliod, J. Tanguy and F. Petiot, J. Electrochem. Soc. **133**, 1073(1986).
3. Mohammadi, M., Inganas, O., Lundstrom, I., J. Electrochem. Soc. **133**, 947(1986).
4. B. Scrosati, *Electrode and electrolyte materials for polymer-based Lithium Batteries*, J. Electrochem. Soc. **136**, 2774 (1989).
5. K. M. Abraham, A. M. Alamgir, *Li+ -Conductive solid polymer electrolytes with liquid like conductivity*, J. of Electrochem. Soc., **137/5**, 1657(1990).
6. T. A. Skotheim, S. W. Feldberg and M. B. Armend, J. De. Physque, **44**, C_3-615(1983).
7. T. A. Skotheim (editor), Handbook of conductive polymers Vol I and II, Maecel Decker, New York (1986).
8. B. Scrosati, Prog. Solid. St. Chem., **19**, 1(1989).
9. S. Panero, P. Prosperi and B. Scrosati, Electrochem. Acta, **37 / 3,** 419(1992).
10. Steen Skaarup, Keld West, L.M.W.K. Gunaratne and K.P. Vidanapathirana:
In B.V.R. Chowdari, K. Lal, S.A. Agnihotry, N. Khare, S.S. Sekhon, P.C. Srivastava and S. Chandra (eds.) "Solid State Ionics, Science and Technology", (World Scientific, Singapore) page 163-172 (1998).
11. K. West, Z. Christiansen, T. Jacobson and S. Skaarup, Mater. Sci. Eng., **13**, 229(1993).

CHARACTERISTICS OF THICK FILM CO_2 SENSORS BASED ON NASICON USING Li_2CO_3-$CaCO_3$ AUXILIARY PHASES

HAN JI KIM, HAN BYEL SHIM, JUNG WOON CHOI AND KWANG SOO YOO[a]
Department of Materials Science and Engineering, University of Seoul, Seoul 130-743, Korea

SHIN DO KIM
Department of Environmental Engineering, University of Seoul, Seoul 130-743, Korea

Potentiometric devices were fabricated using a NASICON ($Na_{1+x}Zr_2Si_xP_{3-x}O_{12}$) thick film and auxiliary layers. The powder of a precursor of NASICON with high purity was synthesized using the sol-gel method. Using the NASICON paste, an electrolyte was prepared on the alumina substrate through screen printing and then sintered at 1,000°C for 4 hours. In the present study, a series of Li_2CO_3-$CaCO_3$ system was deposited on the Pt sensing electrode. Within a wide range of CO_2 volume ratio concentration from 1,000 ppm to 10,000 ppm, the output of the sensor showed good electromotive force (EMF) response that was very close to the theoretical value. The device to which Li_2CO_3-$CaCO_3$ (1:2) was attached showed good sensing properties at low temperatures.

1. Introduction

The carbon dioxide (CO_2) sensor has been greatly demanded for monitoring or controlling CO_2 in various fields. So far, many kinds of CO_2 sensors using various materials, such as solid electrolyte, mixed oxide capacitors, polymers with carbonate solution and so on, have been investigated [1,2]. Among them, solid electrolyte-type CO_2 sensors are of particular interest from the viewpoint of low-cost, high-sensitivity, high-selectivity and simple-element structure [3].

Most researches concerning the use of NASICON as active element for gas sensors have been focused on the $Na_{1+x}Zr_2Si_xP_{3-x}O_{12}$ formula, in the composition range of $1.8 < x < 2.4$, because in this range, which conductivity shows the largest value [4-6]. A commercial NASICON with a nominal-composition $Na_3Zr_2Si_2PO_{12}$ has been investigated as a CO_2 electrochemical sensor [7,8].

CO_2 sensing properties can be upgraded with auxiliary phases in sensing electrodes, which are binary carbonate systems such as Na_2CO_3-$BaCO_3$ and Li_2CO_3-$BaCO_3$. The binary systems bring about several advantages such as better long-term stability, quick response time, and resistance to water vapor interruption [9-11].

In this paper, the material of NASICON was synthesized using the sol-gel method so that a dense and homogeneous electrolyte could be prepared. After that, attempts to improve the sensor properties by modifying the sensing electrode material were

[a]Corresponding author: ksyoo@uos.ac.kr

performed and devices that were based on a series of Li_2CO_3-$CaCO_3$ system were systematically investigated for CO_2 sensing characteristics.

2. Experimental

2.1. Fabrication of the Sensors

The NASICON powder was prepared using the sol-gel method, starting from the solutions of $ZrO(NO_3)_2 \cdot 8H_2O$, $NH_4H_2PO_4$, and $Na_2SiO_3 \cdot 9H_2O$ [12]. The solutions were mixed together to form a sol, which was further dehydrated at 80°C to form a gel. The gel was then dried at 120°C for 8 hours to form a fine dry powder, which was then ground and calcined at 750°C for 1 hour to eliminate the organic remains. Afterwards, the calcined material was reground.

The planar sensor design requires the electrolyte to be screen-printed onto the substrate. Commercially available alumina tiles with 50x50 mm^2 and 0.5 mm in thickness were chosen as the substrate materials. Each tile was laser-scribed to allow several individual sensors to be printed on one substrate. The NASICON layer was screen-printed from a paste. The Pt electrodes were also screen-printed on the designated regions before and after the deposition of the NASICON layer. The assembly was sintered at 1,000°C for 4 hours in air. After this, a series of auxiliary phases (Li_2CO_3-$CaCO_3$) was screen-printed on the Pt sensing electrode. The schematic diagram of the sensors is shown in Fig. 1.

To control the operating temperatures, a Pt heater was formed on the rear side of the alumina substrate by printing the Pt paste. Pt wires were used as lead wires and were attached using a silver paste.

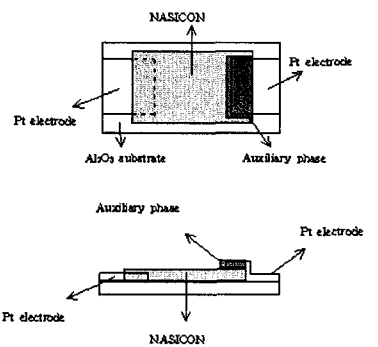

Fig. 1. Schematic view of the devices.

2.2. Characterization of the Sensors

The CO_2 gas-sensing measurements were carried out by the sensor testing equipment especially prepared in our laboratory. The operating temperature was controlled by monitoring the applied voltage and current using the power supply.

The gas mixtures of CO_2/air with the CO_2 concentration varied from 1,000 to 10,000 ppm. The solid electrolyte thick films were characterized through an FESEM (Hitachi 4300, Hitachi) and using an x-ray diffractometer (XRD, 3000 PTS, Rich. Seifert & Co.). The electromotive force of the sensors was measured by a digital electrometer.

3. Results and Discussion

3.1. XRD Analysis and FESEM Observation

It is important to know the optimum sintering temperature to crystallize the NASICON without a secondary phase. Avoiding traces of the tetragonal ZrO_2, which was the most important second phase that easily appeared in the synthesized NASICON, is a key factor in synthesizing the NASICON phase because the additional phase decreases the ion conductivity of NASICON at a low operating temperature [13].

From the XRD analysis shown in Fig. 2, the resulting materials that were sintered at 1,000°C for 4 hours were already converted into NASICON without ZrO_2.

Figure 3 shows FESEM image of the NASICON thick film on the alumina substrate.

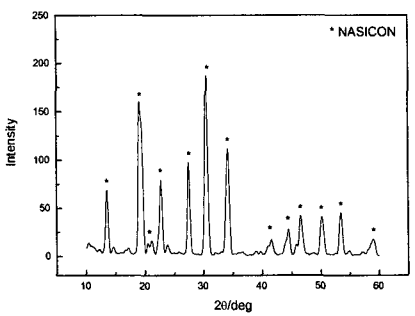

Fig. 2. XRD pattern of NASICON thick film sintered at 1000°C for 4 hours.

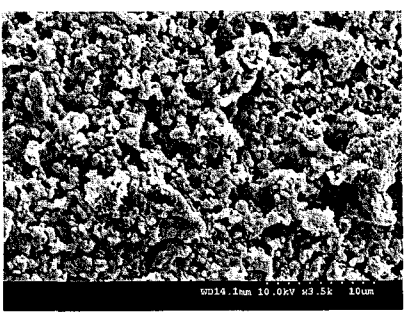

Fig. 3. SEM image of NASICON thick film sintered at 1000°C for 4 hours.

3.2. CO_2 Gas-sensing Properties

Five types of sensors were fabricated from NASICON as a solid electrolyte. A series of Li_2CO_3-$CaCO_3$ mixtures at the molar ratio range of 1:0-1:2 was attached to the sensing electrode. Figure 4 shows the EMF response to CO_2 as a function of the CO_2 concentration at various temperatures.

The EMF variation for each sensor at 470°C agreed well with the theoretical value of 74.0 mV/decade, based on a two-electron electrochemical reaction. As the temperature decreased, however, the slope tended to deviate from the ideal. Quite noticeably, the deviation could be suppressed very effectively with Li_2CO_3-$CaCO_3$ (1:2), which allowed 53.8 mV/decade to be kept at temperatures as low as approximately 400°C. An increase in the amount of $CaCO_3$ at the auxiliary phase is fairly effective for keeping the theoretical value at lower temperatures, whereas an adverse effect occurred when the $CaCO_3$ content was insufficient.

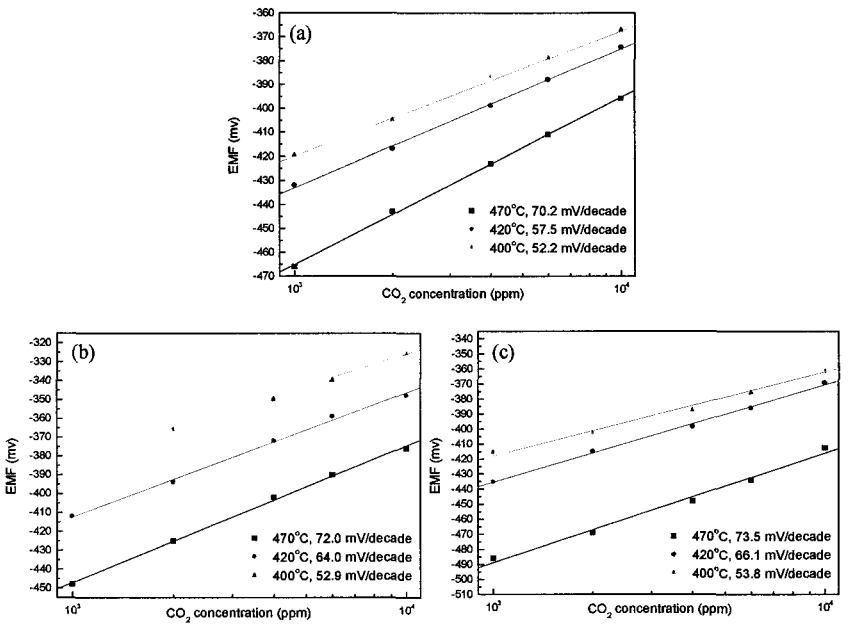

Fig. 4. CO_2 concentration vs. EMF for the NASICON devices attached with (a) Li_2CO_3-$CaCO_3$ = 1:0.5, (b) Li_2CO_3-$CaCO_3$ = 1:1.5 and (c) Li_2CO_3-$CaCO_3$ = 1:2.

Figure 5 shows the response time of the sensor to which Li_2CO_3-$CaCO_3$ (1:2) was attached to determine the CO_2 concentration. The response times for 90% saturation were as short as 16 seconds at 420°C.

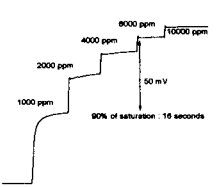

Fig. 5. Response time measured at 420°C to CO_2 gas.

4. Summary

A CO_2 sensor with an internal heater was fabricated using a NASICON thick film prepared using the sol-gel method. The device to which Li_2CO_3-$CaCO_3$ (1:2) was attached showed fairly good sensing properties at low temperatures. The response time was less than 16 seconds at 420°C.

Acknoledgement

This work was supported by the Seoul Research and Business Development Program 2005.

References

1. Y. Miyachi, G. Sakai, K. Shimanoe and N. Yamazoe, *Sensors and Actuators B*, **93**, 250 (2003).
2. T. Kida, Y. Miyachi, K. Shimanoe and N. Yamazoe, *Sensors and Actuators B*, **80**, 28 (2001).
3. F. Qiu, L. Sun, X. Li, M. Hirata, H. Suo and B. Xu, *Sensors and Actuators B*, **45**, 233 (1997).
4. J. P. Boilot, P. Salanié, G. Desplanches and D. Le Potier, *Mater. Res. Bull.*, **14**, 1469 (1979).
5. D. H. H. Quon, T. A. Wheat and W. Nesbitt, *Mater. Res. Bull.*, **15**, 1533 (1980).
6. G. Desplanches, M. Rigal and A. Wicker, *Am. Ceram. Soc. Bull.*, **59**, 546 (1980).
7. N. Miura, S. Yao, Y. Shimizu and N. Yamazoe, *Sensors and Actuators B*, **9**, 165 (1992).
8. Y. Sadaoka, Y. Sakai, M. Matsumoto and T. Manabe, *J. Mater. Sci.*, **28**, 5783 (1993).
9. S. Yao, Y. Shimizu, N. Miura and N. Yamazoe, *Chem. Lett.*, **1990**, 2033 (1990).
10. N. Miura, S. Yao, Y. Shimizu and N. Yamazoe, *J. Electrochem. Soc.*, **139**, 1384 (1992).
11. S. Yao, Y. Shimizu, N. Miura and N. Yamazoe, *Jpn. J. Appl. Phys.*, **31**, L197 (1992).
12. Y. Shimizu, Y. Azuma and S. Michishita, *J. Mater. Chem.*, 7(8), 1487 (1997).
13. F. Qiu, Q. Zhu, X. Yang, Y. Quan and L. Sun, *Sensors and Actuators B*, **93**, 237 (2003).

SOLID STATE BATTERY DISCHARGE CHARACTERISTIC STUDY ON FAST SILVER ION CONDUCTING COMPOSITE SYSTEM: $0.9[0.75AgI:0.25AgCl]: 0.1TiO_2$

R.K. NAGARCH, R. KUMAR* AND PURNIMA RAWAT

Solid State Ionics Research Laboratory, Department of Physics & Electronics,

Dr. H.S. Gour University Sagar (M.P.) - 470003 India

Email: ranveerssi@yahoo.com

ABSTRACT

Solid-state batteries have been fabricated with the cell configuration: Anode // 0.9[0.75AgI: 0.25AgCl]: $0.1TiO_2$ (OCC) // Cathode. Ag-metal was used as anode while different cathodes material such as mixture of elemental iodine & carbon powder (i.e. $C+I_2$) in 1:1 wt% ratio and mixture of elemental iodine, carbon powder & electrolyte (i.e. $C+I_2$+ electrolyte) in 5:5:1 wt% ratio were used. The solid-state batteries discharge characteristic studies have been carried out under different load conditions. Cell parameters viz. current density, power density, discharge capacity and energy density were evaluated and reported. The transference number (t_{ion}~1) has also been measured for the composite electrolyte systems using electrochemical cell potential technique which is identical to the value reported earlier by TIC technique for the composite system. The battery was fabricated using ($C+I_2$+electrolytes) as a cathode materials, it shows higher stability for long time (~300 hours) at high load resistance as compare to cell fabricated using ($C+I_2$) as a cathode material.

Key words: Solid electrolyte, Solid State batteries, composite electrolyte, transference number and TIC technique etc.

1. INTRODUCTION:

After the energy crisis in early seventies (1970) and possible threat of exhaust of the available conventional energy sources viz., petroleum, coal etc. Tremendous efforts have been made to look for new, economical and pollution-free non-conventional energy sources of power to cope with the energy requirements. Many of the major limitations of liquid/aqueous electrolyte batteries i.e. limited temperature range of operation, device failure due to electrode corrosion by electrolyte solution, bulk in size and less rugged etc. [1] could be easily overcome by the solid electrolyte for the solid state devices. In fact, several miniaturized solid state devices such as heart pace-makers; mini/micro-batteries etc. are already commercially available. In addition to this, a large numbers of batteries have been fabricated for vehicular traction as well as for electrical transport. [2-4]. The efficiency and reliability of these solid-state battery systems depends on the appropriate choice of the battery constituent's (viz. electrolyte, cathode and anode materials). Several attempts were made to fabricate solid state battery using normal ionic solids such as alkali/silver halides as electrolytes but with very little success, as these batteries delivered very low output due to very high internal resistance. However after the discovery of fast Ag^+ ion conductors at ambient temperature, the first solid state battery using Ag^+ ion conductor reported by Takahashi and Yamamoto in 1966 [5]. Several solid-state batteries have been

investigated and reported in which Ag^+ ion conducting materials were used as an electrolyte [6-11].

In this paper we report here, the fabrication of solid-state batteries and their discharge characteristic studies carried out under different load conditions. The present fast silver ion conducting composite electrolyte system: 0.9[0.75AgI:0.25AgCl]: $0.1TiO_2$ have been used as an electrolyte for fabrication of solid state batteries. The details of sample preparation, transport properties and structural characterization investigations have been reported earlier [12]. New silver ions conducting solid-state batteries were fabricated in the following cell configurations as:

Cell-I- Anode (Ag-metal)//electrolyte/cathode ($C+I_2$)

Cell-II- Anode (Ag-metal)//electrolyte/cathode ($C+I_2$+ electrolyte)

The various cell parameters such as: current density, power density, discharge capacity and energy density etc. were evaluated under different load conditions for both the cells. Ionic transference (t_{ion}) number was measured using electrochemical cell potential technique for the present composite electrolyte systems.

2. EXPERIMENTAL DETAILS:

2.1 Material preparation:

The TiO_2 dispersed composite electrolyte system: 0.9[0.75AgI:0.25AgCl]: $0.1TiO_2$ was mixed homogenously and heated at about 700^0C in electric furnace for 20min. (soaking time), then quenched rapidly in liquid nitrogen (LN_2). The extra pure chemicals AgI, AgCl (purity> 98%), TiO_2 (purity> 99%) have been used for the material preparation. The finished product of composite electrolyte system has been ground to fine powder then pressed at about 3 ton/cm^2 to form of pellets of dimensions 2-3 mm in thickness and 1.3 cm in diameters.

2.2 Solid state battery fabrication:

To prepared different cathode materials, elemental iodine (I_2) & carbon powder (C) in 1:1 wt. ratio were mixed uniformly and elemental iodine (I_2), carbon powder (C) & solid electrolyte in 5:5:1 wt. ratio were also separately mixed. Finally these cathode materials were ground to fine powder then pressed at about 2 ton/cm^2 to form of pellets of dimensions 1-3 mm in thickness and 0.9 cm in diameters. Solid-state batteries were fabricated using composite electrolyte systems as an electrolyte in two different cell configurations as mentioned in section 1. The above mentioned two different cathode materials i.e. $C+I_2$ & $C+I_2$+ electrolyte in 1:1 & 5:5:1 wt. ratio respectively have been used, while Ag - metal was used as an anode for fabrication of the above cells. These cells were sealed with epoxy resin to inhibit the surface diffusion of iodine. The Cell-I were discharged at different load conditions and for cell-II discharged at 500kΩ. Various cell parameters viz. current density, power density, discharge capacity and energy density were carried out for both the cells. A digital multimeter was employed for the cell potential measurements performed in a desiccator to avoid the effect of moisture.

3. RESULTS AND DISCUSSION:

Fig. 1 represents the cell potentials vs. time plots for the cell -I at different loads: such as: 500KΩ and 100KΩ. The same plot for the cell-II at 500KΩ is also drawn

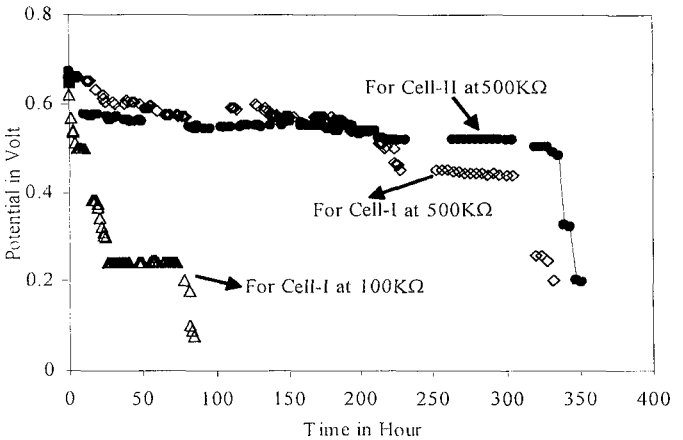

Fig 1. Potential discharge profiles at different load resistances for Cell-I & cell-II

for comparison in this figure. The value of the open circuit voltage (OCV) ~ 0.684 V was obtained for both the cells (I & II). The cell potential i.e. working voltage (~ 0.661V) remained practically constant except for a small initial drop, for about 210 hours respectively, during low current drain or high load resistance 500KΩ at which cell was discharged. However the cell potential for this cell dropped quickly and gets stabilized at lower values for 50 hours when discharged at high (100 KΩ) load resistance. The cell potential i.e. working voltage for the cell-II remained practically constant at about 0.555V for ~ 310 hours after an initial drop for cell-II. It is observed from comparison of the discharge behavior of both the cells that a better stabilized cell potential has been observed for the cell-II for a long discharge time (~ 310 hour). Hence cell-II shows better cell performance and exhibit more stability for longer time then that of cell-I, discharge at same load condition. The initial drop was observed in the cell voltage with time is due to the build up polarization as well as formation of low conducting AgI at cathode/ electrolyte interface [1].

Table1. Lists the some important cell parameters obtained from plateau region of the potential profiles of the cells.

Cells	Load resistance (KΩ)	Working voltage (mV)	Current drawn from Cell (μ A)	Current density (μ A cm^{-2})	Discharge capacity (μ A h)	Power density (mWK g^{-1})	Energy density (mWhKg^{-1})
Cell-I	500 100	610 242	1.2 2.42	1.84 3.72	252 121	0.4 0.205	84 10.2
Cell-II	500	555	1.11	1.7	349	0.201	63.3

Both the cells exhibit the high stabilized voltage at high load resistance or (i.e. 500KΩ). Some important cell parameters such as: current density, power density, discharge capacity and energy density etc. have also been calculated from plateau region of potential vs. time plot for both the cells and are listed in table1.

The ionic transference number can be evaluated by electrochemical potential method using following equation:

$$t_{ion} = E' / E \quad (1)$$

where E & E' are theoretical and measured value of OCV respectively. The transference number (t_{ion}) ~ 0.99 was obtained for the present composite electrolyte systems used as an electrolyte in the cells. This value of t_{ion} is same for the composite electrolyte system investigated through TIC technique [13]. It is concluded from this investigation that the present system is pure ionic system.

4. CONCLUSION:

Solid state battery studies on a recently investigated composite electrolyte system: 0.9[0.75AgI:0. 25AgCl]: 0.1TiO_2 were carried out at different load conditions and cathode materials. The cells were discharge at different load conditions and various cell parameters were evaluated at room temperature. The solid state battery exhibited better performance at high load resistance or low current drain as compared to low load resistance or high current drain. The cell parameters such as: current density, power density, discharge capacity and energy density etc. were also calculated for both the cells at room temperature and in is concluded that cell-II shows better performance at high load resistance. The transference number (t_{ion} ~ 1) was obtained using electrochemical cell potential technique, for the present composite electrolyte system, which is of the same value as reported earlier by TIC technique.

ACKNOWLEDGEMENT:

The financial support by Third World Academy of Science (ICTP); Italy by Project No. 00-0046, RG/ PHYS/AS is gratefully acknowledged.

REFERENCES:

[1] S. Chandra and R. C. Agrawal, Solid State Battery- Prospects and Limitations (Nat. Academy of Science, India, Golden Jubilee Communication Volume) - (1980).

[2] S. Chandra, "Superionic Solids, – Principles and Application" (North Holland, Amsterdam) (1981).

[3] P. Hogenmuller and W. Van Gool, (eds.) Solid Electrolytes, Materials Science Series (Academic Press. New York) (1978).

[4] M. Z. A. Munshi and B. B. Owens, in: Superionic Solids and Solid Electrolytes - Recent Trends (eds.) A.L. Lasker and S. Chandra (Academic Press, New York) (1989)

[5] T. Takahashi and O. Yamamoto, J. Electrochim. Acta **11**, 779 (1966)

[6] S.C. Levy and M. E. Foorino, J. Electrochem. Soc. 'Interface' winter **25,** (1995).

[7] S. Magahed and B. Scrosati, J. Electrochem. Soc. 'Interface' winter **35** (1995).

[8] R.C. Agrawal, R. Kumar, R.K. Gupta, M. Saleem, J. Non-Cryst. Solids, **181**, 110 (1995).

[9] R.C. Agrawal, M. L. Verma, R.K. Gupta and R. Kumar; Ion Conducting Materials: Theory and Materials (eds.) A. R. Kulkarni and P. Gopalan (New Delhi India) 176, (2001)

[10] R.C. Agrawal, R.K. Gupta, C. K. Sinha, R. Kumar, and G. P. Pandey, Ionics **10,** 113 (2004).

[11] A. K. Arof, E. B. Saniman and M.Z. Mastor, J. Phys III France **4,** 849 (1994)

[12] R. K, Nagarch R, Kumar and R. C. Agrawal, J. Non – Cryst. Solids (In Press 2006).

[13] S. Chandra, S. K. Tolpadi and S. A. Hashmi Solid State Ionics **651,** 28 (1988).

INTERCALATING PROTONIC SOLID-STATE BATTERIES WITH SERIES AND PARALLEL COMBINATION

K. SINGH, S.S. BHOGA AND S. M. BANSOD

MSRL, Department of Physics, R.T.M. Nagpur University, Nagpur –440033, India

e-mail: msrl1@hotmail.com

The protonic solid-state batteries with different intercalating cathodes such as MnO_2, PbO_2 and V_2O_5 were fabricated using composite zinc as an anode and montmorillonite ($Al_2O_3.4SiO_2.H_2O.xH_2O$) as solid electrolyte. The discharge profile of these electrochemical cells, in series and parallel combinations, was recorded at constant current drain. Proton transference number, which determines efficiency of electrochemical cells, evaluated by EMF method was found to be ~ 0.90 with very negligible electronic contribution. The battery with MnO_2 as cathode exhibits maximum energy density and low internal impedance amongst all.

1. Introduction

Solid-state proton conductors have been the very attractive materials for high energy density primary and secondary batteries because of low weight of hydrogen and high Gibbs energy of formation of hydrogen compounds. In a practical solid-state battery, involving protonic reaction, the solid electrolyte must not be only proton conductor but should also possess ion transport number very close to unity. Such solid proton conductors (SPC) facilitate possible use of solid electrode materials, which were unstable in the presence of a liquid electrolyte[1-5]. For example, the positive MnO_2 electrode can be associated with a solid protonic conductor containing H^+ at high concentration to exhibit benefit of its high acidic potential. The negative electrode delivers protons to the electrolyte when anodically polarized, then ceasing cathodic reaction facilitates the insertion of protons into MnO_2, thereby, formation of Mn^{2+}. The oxides such as MnO_2 dissolve as Mn^{2+} in an acidic aqueous electrolyte during cathodic discharge consequently electrode material disappears.

Another interesting case has been that of PbO_2, a good insertion cathode for other cations, wherein protons cannot be cathodically inserted in presence of sulphuric acid due to lead sulphate interfacial precipitation i.e. PbO_2 is chemically unstable. The intercation has been possible with the use of proton conducting solid

electrolyte. During the discharge, negative electrode must supply protons to solid electrolyte, which have been carried to another electrode by a translocation / vehicular mechanism, i.e. they must penetrate into the positive electrode material. In such batteries both electrodes must have mixed conductivity i.e. electronic as well as protonic. The proton conduction paths must be same in the three materials for rapid proton transfer reaction at both interfaces, and over potential at both the electrodes should be negligible. Lamberterie et al[8] fabricated the all-solid state protonic batteries with following configuration

$$HUP,Ti_{1.1}\ NiH_2 / HUP / \gamma\text{-}MnO_2\ ,\text{acetylene-black, } HUP \qquad (1)$$

The practical energy density of 88Wh/kg has been obtained under discharge current drain of 100μA/cm^2. Mohri et al[9] have reported a charge discharge characteristics of protonic cell having following configuration:
$TiNiMmH_x / Sb_2O_5 . 4H_2O / \gamma\text{-}MnO_2$,acetylene-black, Sb_2O_5

All above factors have prompted us to undertake a study of all solid-state protonic rechargeable battery, using different cathode materials. Also, the efforts were directed to investigate the implications of series and parallel combination of cells on overall battery performance.

2. Experimental

The initial ingredient, industrial montmorillonite ($Al_2O_3.4SiO_2.H_2O.xH_2O$) was used as solid electrolyte. On the basis of thermodynamic stability and better conductivity optimized composition of the electrolyte + zinc + zinc sulphate[7] as anode and MnO_2, PbO_2 and V_2O_5 mixed with graphite treated as cathode materials. The electrochemical cells with the following configurations were fabricated by pressing above mentioned the cathode, the anode and the electrolyte in the form of circular discs of dimensions 10 and 2mm diameter and thickness, respectively.

$Zn/Zn+ZnSO_4$+Electrolyte/Montmorillonite/MnO_2+Gr	Cell-I
$Zn/Zn+ZnSO_4$+Electrolyte/Montmorillonite/PbO_2+Gr	Cell-II
$Zn/Zn+ZnSO_4$+Electrolyte/Montmorillonite/V_2O_5+Gr	Cell-III

The open circuit voltage (OCV) and short–circuit current (SCC) and other parameters of cells I-III were determined using Keithley 617 programmable electrometer. The discharge characteristics of cells were recorded under constant

current drain conditions, at the interval of one hour till the load voltage reached to 60 % of its initial value using in house experimental setup.
The complex impedance data of the electrochemical cells before, during and after the discharge was measured over the frequency range 10Hz – 13MHz with the help of computer controlled HP- 4192A LF impedance analyzer[10].

3. Results and Discussion

Figures 1, and 2 show the discharge characteristics at constant current drain 15, 12 and 15 μA for series and 50μA for parallel are set of cell I, II and III, respectively.

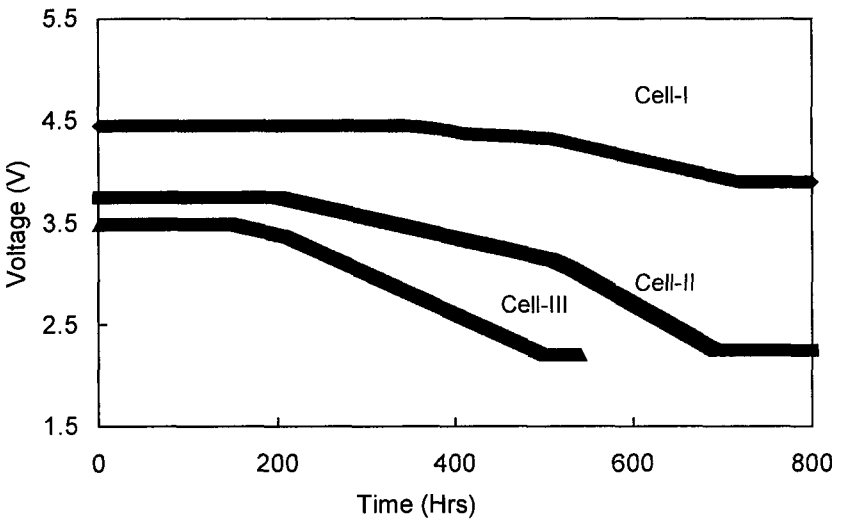

Figure 1: The discharge characteristics under constant drain condition for three electrochemical cells (cell-I, cell-II and cell-III): three cell of each configuration connected in series to obtain battery.

As expected, the cell voltage initially remains fairly constant and decreases in steps with increase in discharge time and attains another constant value of cell voltage within few hours. After two to three discharge steps finally battery discharges to its last limit i.e., 60% of its OCV. A clear plateau is seen in all batteries during the current drains indicate structural modification of cathode during discharge.

The battery performance parameters of the cells in series and parallel modes, obtained from the discharge characteristics, are presented in tables 1 and 2, respectively. A close look at the tables and figures reveals that the cell with MnO_2,

as one of the constituents in the cathode and zinc composite anode exhibits maximum discharge time 500 - 600 hrs at constant current drain of 15μA in series

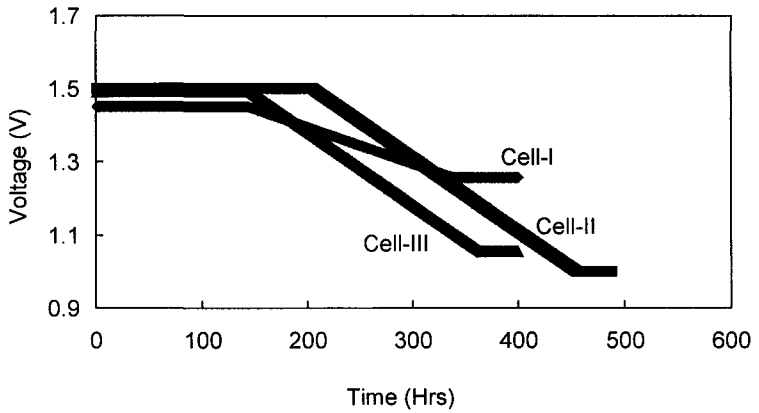

Figure 2: The discharge characteristics under constant drain condition for three electrochemical cells (cell-I, cell-II and cell-III): three cell of each configuration connected in parallel to obtain battery.

combination and 50μA in parallel combination. Furthermore, same battery provides maximum energy density and cell capacity amongst all other batteries under study. Nevertheless, the cell with PbO_2 cathode and composite zinc anode, at constant current of 12μA in series and 50μA in parallel combination, exhibits discharge time of the order of 200 - 250 hrs with slightly lower energy density as compare to MnO_2. On the other hand, V_2O_5 cathode exhibits quite a feeble performance in comparison with other two. Evidently, MnO_2 cathode gives maximum discharge current, although PbO_2 provides highest voltage amongst all cathodes under study.

The complex impedance plots after various charge-discharge cycles of battery,

Table 1: Battery discharge parameters for series combination.

Cell No.	OCV (V)	SSC (μA)	I_d (μA)	V_o (V)	T_o (Hrs)	Cell weight (kg)	Cell capacity (mAhr)	Energy density (whr/kg)
I	4.51	60	15	4.45	605	0.0036	9.075	11.21
II	3.65	50	12	3.35	185	0.0035	2.22	2.12
III	4.00	65	15	3.75	508	0.0037	7.62	7.72

I_d-Current drain; SSC-short circuit current; Vo- cell operating voltage; To – discharge time

MnO_2 based cathode, are depicted in figure 3. A tail at low frequency followed by two small loops at higher frequencies is discernible[11]. The long tail at lower frequency regime is a part of the huge semicircle due to electrodes. The lower limit

Table- 2: A Comparison of the electrochemical cell parameters in parallel mode

Cell No.	OCV (V)	SSC (μA)	I_d (μA)	V_o (V)	T_o (Hrs)	Cell weight (kg)	Cell capacity (mAhr)	Energy density (whr/kg)
I	1.65	500	50	1.45	302	0.0036	15.1	6.08
II	2.00	325	50	1.51	255	0.0036	12.75	5.35
III	2.10	550	50	1.52	426	0.0037	21.3	8.75

of HP- 4192A LF impedance analyzer, 5Hz, restricted the study of this phenomenon in detail.

The semicircular arc in high frequency domain corresponds to the ionic transport through electrolyte. As the discharge cycles proceeds, a semicircular arc becomes bigger in size compare to previous one. Thus, it can be inferred that as the number of discharge cycle increases the total cell impedance increases. The first semicircle observed in the figure-3 is attributed to electrode-electrolyte interface and that at the low frequency straight line to cathode itself[12]. The absence of interaction between interface and cathode is clearly demonstrated from the overall

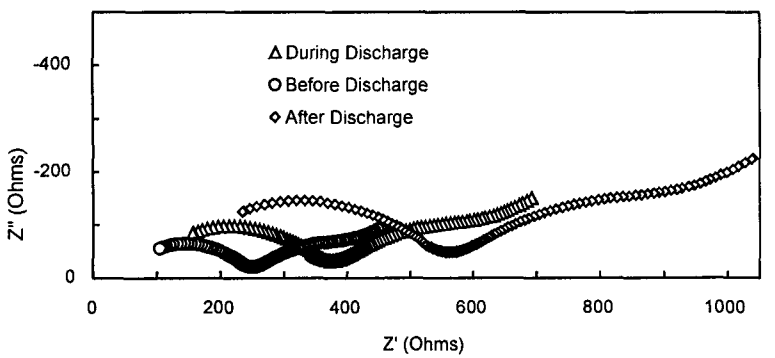

Figure 3: Complex impedance plots for before, during and after the discharge of the battery with cathode MnO_2.

impedance behavior and also from the fact that they can easily be separated. Thus, the semicircle part of the impedance is not a charge-transfer resistance and parallel double layer capacitance due to the MnO_2 or PbO_2 electrode. Consequently, the

semicircle must be due to a resistance and capacitance associated with electrode-electrolyte interfaces, together with any contact resistance-capacitance contribution within the cathode matrix[12]. It is clear from the above discussion that the higher frequency semicircle is generated by the electrolyte, while the lower frequency semicircle is due to the cathode-electrolyte interface. The cell reactions during the discharge are as follow:

$$H_2O \rightarrow H^+ + OH^-$$

$$Zn + 2OH^- \rightarrow Zn(OH)_2 + 2e^- \quad (2)$$

$$Zn(OH)_2 + 2OH^- \rightarrow [Zn(OH)_4]^{2-} \quad (3)$$

$$2e^- + 2MnO_2 + H_2O \rightarrow Mn_2O_3 + 2OH^- \quad (4)$$

$$Zn + 2MnO_2 \rightarrow ZnO + Mn_2O_3 \quad (5)$$

Figure 4 exhibits the functional dependence of the internal resistance of the cells on discharge time. Interestingly, the cell impedance before the discharge is higher than

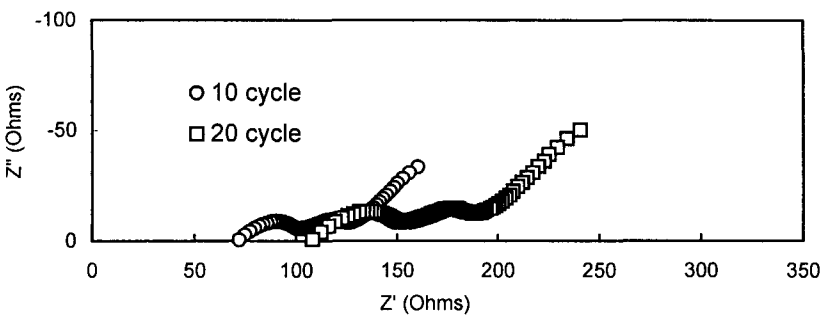

Figure 4: Complex impedance plots after discharging of 10th cycle and 20th cycle of battery with cathode MnO_2.

that at the onset of discharge. Moreover, as discharge proceeds, initially cell impedance decreases due to increase in the cell activity and later it attains a minimum during discharge, and increases thereafter indicating complete discharge. The increase followed by a minimum impedance reveal the formation of low conducting reaction products at the electrode[13].

4. Conclusion

The MnO_2, PbO_2 and V_2O_5 can be utilized as cathode in all solid-state proton conducting secondary battery operating at room temperature. These electrodes allow anodic as well as cathodic reactions to occur without any complication;

otherwise normally not observed due to polarization in aqueous electrolytes. The chief advantage of these electrodes is that they do not require any hermetic sealing. These batteries are cost effective in comparison with other solid-state rechargeable one. The materials used in the cells are environment friendly and no special atmospheric conditions are required for cell fabrication as in case of lithium cells.

Acknowledgments

The authors are thankful to UGC, New Delhi, India for providing financial assistance to carry this work under DRS (SAP) programme.

References

1. P. E. Childs, A. T. Howe and M. G. Shilton, J. Power Sources, **3** 105 (1978).
2. M. G. Shilton and A. T. Howe, Mater. Res. Bull., **12** 701 (1977).
3. P. E. Childs, T. K. Halstead, A. T. Howe and M. G. Shilton, Mater. Res. Bull., **13** 609 (1978).
4. S. Chandra and A. Kumar, Solid State Ionics, **40/41** 255 (1989).
5. T. Takahashi, S. Tanase, O. Yamamoto, and S. Yamauchi, J. Solid State Chem., **17** 355 (1976).
6. T. Takahashi, S. Tanase and O. Yamamoto, J. Appl. Electrochem., **10** 415 (1980).
7. K. Singh, R. U. Tiwari and V. K. Deshpande, J. Power Sources, **40** 65 (1993).
8. P. de Lamberterie, M. forestier, J Guitton, A. Rouault R. Fuchart, and D. Fuchart, C.R. Acad. Sc. Paris t. 30 serie II, n^0 (1985) 14.
9. M. Mohri, H. Tanaka, T. Yoneda, Y. Tajima and M. Kasahara, The 26^{th} battery symposium, Koyato in Japan, (1985) 261.
10. K. Singh, Solid State Ionics, **28-30** 1371 (1988).
11. K. Singh, S. S. Bhoga and V. K. Deshpande, in B. V. R. Chowdary and S. Radhkrishna (eds.), Solid State Ionic Devices, World Scientific, Singapore, (1980) 415.
12. S. P. S. Badwal, J. Electroanal. Chem., **161** 75 (1984).
13. K. Singh, R. U. Tiwari and V. K. Deshpande, J. Power Sources, **46** 65 (1993).
14. K. Singh, R. U. Tiwari, P. Ambekar and S. S. Bhoga, Proceedings of ISAEST – VII, 27 Nov.-2002.

Synthesis and Characterization of ZnO Fiber by Microwave Processing

Lin Wang[1], Jian Zhou[2*], Guizhen Liu[2], Hanxing Liu[3], Shixi Ouyang[2], Wen Chen[3]

1 School of Information Engineering, Wuhan University of Technology,

2 State Key Laboratory of Advanced Technology for Materials Synthesis and Processing, Wuhan University of Technology,

3 School of Materials Science and Technology, Wuhan University of Technology, Luoshi Road 122, Wuhan 430070, P R China

Abstract We report on a novel synthetic method of microwave processing with a domestic 2450MHz microwave synthesis system to prepare ZnO fiber using pure ZnO powder. We also studied and report on structure and morphology of the resultant products by XRD and SEM. XRD revealed that a single phase ZnO fiber can be synthesized quickly and easily by microwave processing. The results indicate that microwave processing is a promising method of processing ZnO fiber.

Key words ZnO fiber, microwave processing, ZnO powder

1. Introduction

Wide bandgap materials, such as silicon carbide (SiC, E_g=~3.0 eV for the 6H polytype), gallium nitride (GaN, E_g=3.39eV), aluminum nitride (AlN, E_g=6.2eV), and zinc oxide (ZnO, E_g= 3.37eV) have become the focal point of research in semiconductors and optoelectronics during the past decade because of an increasing need for short wavelength ultraviolet lasers, photonic devices and high-power, high-frequency electronic devices [1], data-storage [2], biochemical and chemical sensors[3]. ZnO is a promising material for UV/blue light-emitting and UV light detection devices. In fact it has several fundamental advantages over its chief competitor GaN [4]: (1) its free exciton binding energy is 60meV, much higher than that of GaN (21-25meV), that may be useful for efficient UV laser applications based on stimulated emission due to the recombination of excitons at room temperature (KT=25meV); (2) low power thresholds for optical pumping at room temperature; and (3) tunable band gap by alloying with other ions. Meanwhile, ZnO is more resistant to radiation damage compared to other common semiconductor materials. Traditionally, zinc oxide (ZnO), although having wide bandgap and wurtzite structure analogous to GaN, has been primarily used in its polycrystalline form in piezoelectric transducers, varistors, phosphors, and transparent conducting films. Recently, most ZnO single crystals have been fabricated in forms of films[5] and nano-structure, such as nanowires, nanorods [6], nanoneedle array [7], nanobelts[8] and some with tubular hollow texture were synthesized as well [9-11].

Microwave-heating process is a relatively new technology for materials processing whose heating mechanism is fundamentally different from conventional heating methods. In a conventional heating process, the heat generated by external heating source is transferred to the material samples via radiation, conduction, or convection. While in the microwave process, the heat originated from the microwave energy is absorbed by the materials positioned in microwave field. Conventional heating based on the thermal transfer results in higher surface temperatures, but microwave heating based on the energy conversion can produce an inverse temperature profile, the surface temperatures are lower than the interior due to thermal losses on the surfaces[12-13],

In this paper, it was reported that the ZnO fibers have been fabricated using microwave-heating growth method which is selectivity and rapid heating and also friendly to the environment without pollution. Recent progress in several areas has brought the great potential of ZnO to light, rivaling GaN as ultra-violet (UV) and deep UV coherent light sources and detectors.

2 Experiments

The preparation of ZnO fibers involved a microwave-heating process of the ZnO in 200 nm and 20nm powder

* Corresponding Author. Tel: 86-27-87646984, Fax:86-27-87879468
E-mail Address: zhoujian@mail.whut.edu.cn

mixed with acetone for 1h in agate mortar and then been pressed into pills. The parameter of the equipment used as follows: 2.45 GHz/5kW, TE_{103} microwave cavity. The ZnO pill was on the quartz plate and placed in the microwave cavity. The heating-temperature was controlled in 1296□for 15min or 1200□for 30min respectively. Finally, there are a lot of transparent crystals growing in the center of and around the pill along some direction. Morphologies were observed by scanning electron microscope (SEM, JSM - 5610LV by Japanese electronic company). The X-ray diffraction (XRD, D/max-rB by Japanese RIGAKU company,) was used to determine the phase composition and crystal structure.

3 Results and Discussion

XRD patterns of ZnO rod synthesized in 1296□×15min using pure ZnO powder with 200 nm as raw materials by microwave process are shown in Figure 1.

The morphology and microstructure of the product were analyzed in SEM, which revealed that the product contains ZnO regular rod. As shown in Fig.2 the ZnO rod with a well faceted end and side surfaces, the average diameter and the length are respectively 10μm and 40μm. It is a pure ZnO structure with a=0.324nm, c=0.519nm. There is no decompound in the microwave heating process, but the product is not a fiber, and just like rod.

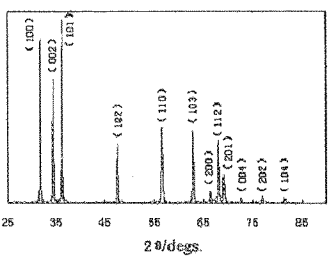

Figure 1. XRD patterns of ZnO product synthesized microwave process in 1296□×15min .(pure ZnO. 200 nm as raw materials)

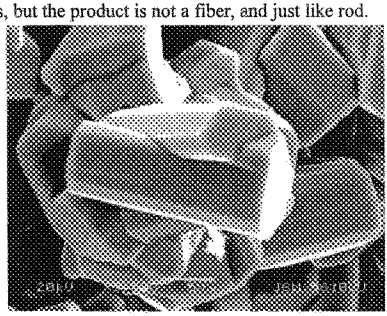

Figure 2. SEM images of ZnO product synthesized by microwave by process in 1296□×15min.(pure ZnO powder with 200 nm powder with as raw materials)

If mixed 20nm ZnO powder with 20% into 200 nm ZnO powder as raw material, then synthesized in 1200□×30min by microwave process, the SEM of product is shown in Figure 3.

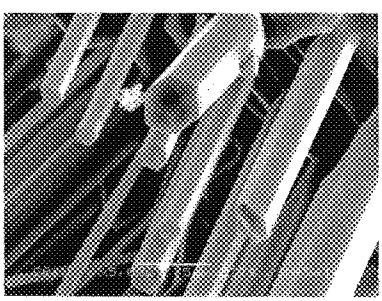

Fig.3. SEM images of ZnO fiber via microwave-heating method in 1200□×30min.(mixed 20nm ZnO powder with 20% into 200 nm ZnO powder as raw material)

As shown in Fig.3 the ZnO fiber is in good crystal structure and smooth face with about 5—20μm in length. Until now, it is still not clear how ZnO fiber structures formed. A suggesting growth mechanism based on the vapor-liquid-solid model well explained most catalyzed growth of one-dimensional nanostructures. Recently Wang *et al.* reported a nonvapor-liquid-solid method to synthesize nanotubes via pyrolysis of ZnO powder[14]. As the microwave heating method without any metal catalyst synthesized the ZnO fiber, the growing process of ZnO fiber by microwave heating is proposed as follows. Firstly, the ZnO activation energy was lower than normal because of the microwave highly enhanced reaction/synthesis kinetics[15] The ZnO powder vaporized at 1100℃ in the region of high temperature which was filled with ZnO(g), Zn(g), O_2(g) especially for 20nm powder. In the top of the sample, is a region of low temperature, the Zn (g) and O_2 generated chemical reaction and decomposed at the vapor-solid interface, the process are expressed as:

$$Zn\,(g)+\frac{1}{2}O_2\,(g) \Rightarrow ZnO\,(g) \tag{1}$$

$$ZnO\,(g) \Rightarrow ZnO\,(s) \tag{2}$$

According to the Gibbs-Thomson equation:

$$\Delta G = 4\pi r^2\sigma - \frac{4}{3}\pi r^3 \frac{RT}{V_0}\ln\frac{P}{P_0} \tag{3}$$

Where ΔG is the Gibbs energy, $\frac{P}{P_0}$ is the vapor pressure of the saturation, r is the radial of the new phrase, V_0 is the volume of ZnO molecule, σ is the interface energy of new phrase and vapor phrase, R is universal gas constant and has the value R=8.31 J/mol·K. The heating temperature is higher, the P_0 is bigger. The critical of the radial is: $r^* = \frac{2\sigma V}{kT\ln(P/P_0)}$, k is Boltzmann constant and has the value k=1.38×10^{-23} J/K. V is mole volume of ZnO.

So the temperature influences the radial of the ZnO crystal nucleus, which grew at the interface gradually when the temperature of the sediment and evaporation is proper, P/P_0 is more close to 1, the r^* is bigger. So the temperature is important to control the radial of the nucleus.

On the other side, the screw dislocations engendered in the process of crystal growth, which became the new source of growth. Especially, the screw dislocations cause the growth along radial orientation and the landscape orientation, so the length of the rods was longer and longer, the diameter was wider and wider, and form ZnO fiber.

4 Conclusion:

Due to the microwave strengthening the oxygenic and zinc ions diffusing, we successfully synthesized the ZnO fiber at 1200℃ for 30min. The ZnO fiber with the average diameter and the length respectively 2μm and 20μm grew in the air condition. It is proposed to explain that the growth mechanism of ZnO fiber is vapor-solid mechanism. A single phase ZnO fiber can be synthesized quickly and easily by microwave processing which is a promising method of processing ZnO fiber.

Acknowledgements

This work was supported by Hubei Natural Science Foundation (No 2003ABB011,No 2004ABA099) and Open

Fund from State Key Laboratory of Advanced Technology for Materials Synthesis and Processing (No SKLZDJJ04-02), Wuhan University of Technology, P R China.

References:

1 X. F. Duan, Y. Huang, R. Agarwal and C. M. Lieber, Nature. 421 (2003), 241

2 Y. C. Kong, D. P. Yu, B. Zhang, W. Fang, and S. Q. Feng, Appl. Phys. Lett. 78(2001), 4.

3 Y. Cui, Q. Wei, H. Park, and C. M. Lieber, Science (Washington, D.C., U.S.) 293 (2001), 1289.

4 D. C. Look, Materials Sci. and Eng. **B80**(2001), 383.

5 Y X Liu, Y C Liu, C L Shao and R Mu, Appl. Phys. (2004) 3025

6 M. H. Huang, S. Mao, H. Feick, H. Yan, Y. Wu, H. Kind, E. Weber, R. Russo, and P. Yang, Science 292(2001), 1897.

7 Y. W. Zhu, H. Z. Zhang, X. C. Sun, S. Q. Feng, J. Xu, Q. Zhao, B. Xiang, R. M. Wang, and D. P. Yu, Appl. Phys. Lett.83(2003), 144

8 Z. W. Pan, Z. R. Dai, and Z. L. Wang, Science 291 (2001), 1947.

9 J. Q. Hu and Y. Bando, Appl. Phys. Lett.82(2003), 1401.

10 Y. J. Xing, Z. H. Xi, Z. Q. Xue, X. D. Zhang, and J. H. Song, R. M. Wang, J. Xu, Y. Song, S. L. Zhang, and D. P. Yu, Appl. Phys. Lett.83(2003), 1689

11 J. Cheng, R. Guo, and Q. Wang, Appl. Phys. Lett. **85**(22) (2004), 5140

12 J. Cheng, R. Guo, and Q-M. Wang, Appl. Phys. Lett. **85** (22) (2004), 5140

13 J. Cheng, D. Agrawal, Y. Zhang, B. Drawl, and R. Roy, American Ceramic Society Bulletin, **79** (9) (2000),71

14 Z.L. Wang, J. Phys.: Condens. Matter 16(2004), 829

15 J. Cheng, D. Agrawal, Y. Zhang, and R. Roy, J. Mater. Sci. Lett., **20**(2001), 77

PREPARATION OF SnGe ALLOY COATED Ge NANOPARTICLES AND SnSi ALLOY COATED Si NANOPARTICLES BY BALL-MILLING

J.K.D.S. JAYANETTI
Department of Physics, University of Colombo, Colombo 3, Sri Lanka
E-mail:sumedha@phys.cmb.ac.lk

S.M.HEALD
Pacific Northwest National Lab, Richland, WA, USA
E-mail: Steve.Heald@pnl.gov

Sn is a material that is essentially insoluble in Ge and Si in the bulk form. In this study, Sn/Ge and Sn/Si powders were ball milled for long durations (~36 hrs.) while varying the ratio of Sn to Ge and Si respectively. Milling was carried out in an Ar gas atmosphere. Analysis made using XRD showed that the particle sizes of Ge and Si go down with the decreasing atomic composition of Sn. Particle size estimated using x-ray diffraction line broadening showed that the sizes of Ge and Si particles in Sn/Ge and Sn/Si samples with 20% vol. Sn in Ge and 10% vol. Sn in Si reach nano-scale dimensions. Analysis made using X-ray Absorption Fine Structure Spectroscopy (XAFS) showed that there were surface layers of SnGe and SnSi alloys around Ge and Si particles. Thus ball milling of Sn/Ge and Sn/Si powders produces SnGe alloy coated Ge nanoparticles and SnSi alloy coated Si nano particles.

1. Introduction

Ball milling is a widely established technique that is applied to achieve nanocrystalline solids, mechanical alloying of solid compounds and solid state amorphization of inorganic materials. Ball milled Sn/Ge powders of varying ratios of Sn to Ge show a decreasing melting enthalpy of Sn with decreasing ratio of Sn to Ge[1]. This behavior was investigated in detail in a previous analysis that was made using X-ray Absorption Spectroscopy (XAFS), X-ray Diffraction (XRD), and Differential Scanning Calorimetry (DSC)[2]. Results showed the formation of several monolayers thick stable surface layer of 50% at. SnGe alloy around Germanium particles causing the reduction of the melting enthalpy of Sn. Alloying is in contrast to the solubility of Sn in Ge in the bulk form which is less than 1.0 at.% at room temperature. Simultaneously, it was seen that the particle sizes of Ge reach nanoscale dimensions below the exciton Bohr radius of Ge when the Sn content was reduced below a certain value. Similar results were observed for Si particles in ball milled Sn/Si powders, another binary system in which the solubility of Sn in Si at room temperature is 0.12 at.%. This report provides the reader with some quantitative information about the

synthesis of SnGe alloy coated Ge nanoparticles and SnSi alloy coated Si nanoparticles by ball milling.

2. Experimental

All the experimental measurements required for this analysis were made at the Division of Materials Sciences, Brookhaven National Laboratory, Upton, New York, USA. A detailed account of the experimental procedure in analyzing the ball milled Sn/Ge powders has been given elsewhere[2,3]. A similar experimental procedure was followed for preparing and analyzing the ball milled Sn/Si powders[3,4]. For sample preparation, Sn, Ge and Si powders (-100 mesh, 99.999% pure) were used as starting materials. Sn/Ge and Sn/Si powder samples were milled using a Brinkmann, Model MM2, Standard Mixer Mill operated in an Ar ambient. Powder couples were enclosed and milled in a sealed hardened tool steel vial, using a steel ball. Loading and unloading of powders to the vial and preparation of samples for XAFS, XRD and DSC measurements were done inside a dry box with moisture and oxygen content of < 5 ppm. Powders with varying Sn/Ge volume ratios (20, 30, and 40 vol.% Sn) and Sn/Si volume ratios (10,25, and 40 vol.% Sn) were milled for nearly a constant time of about 35 hours.

Sn K-edge XAFS, of the powder samples, diluted to achieve an absorption step of approximately 1.5 at the Sn K-edge using Boron Nitride powder, were made at beamline X-11A at the National Synchrotron Light Source at Brookhaven National Laboratory, USA. The incident and the transmitted x-ray beams were monitored using Ar and Kr gas filled ionization chambers respectively by maintaining the monochromator entrance slit at 0.25mm. The energy resolution at the Sn K-edge (29200 eV) was estimated to be 6.5 eV. Sn K-edge XAFS measurements of Sn/Ge and Sn/Si samples were made at temperatures of 10 K, 100 K and 200 K, in a rough vacuum. For comparison, Sn K-edge XAFS spectrum of metallic Sn (99.999% pure) powder was also obtained.

XRD measurements of the samples were made at room temperature at energy of 8.5 keV. Measurements were made at beamline X-11B using a modified Phillips goniometer with an INEL 120° curved position sensitive detector. In order to confirm results obtained by Jang *et al.*[1]. Sn/Ge samples were subject to Differential Scanning Calorimetric (DSC) analysis. For DSC analysis, samples were sealed in Aluminum pans and analysis was achieved using a DuPont 910 DSC system.

3. Data Analysis and Results

The XAFS data analysis procedure discussed below was carried out using the University of Washington XAFS data analysis software package. The oscillations in an XAFS spectrum above an edge are due to scattering of the outgoing photo electron from different near neighbor shells. These oscillations are of different frequencies determined by the near neighbor distances R_j. The oscillations isolated from the background spectrum, known as $\chi(k)$ data, were Fourier transformed in order identify the contributions to XAFS from different coordination shells.

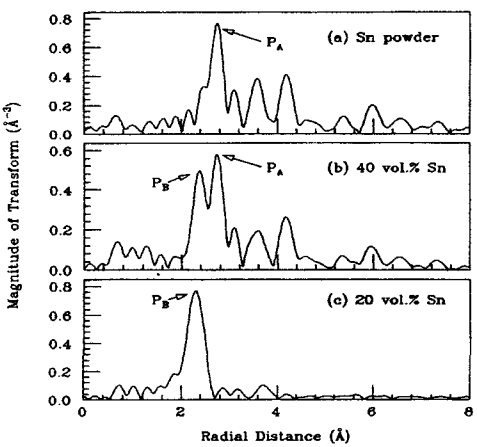

Figure 1. Fourier transforms of XAFS $k^2\chi(k)$ obtained at 10 K for Sn K-edge for (a) Sn powder (b) 40 vol. % Sn in Ge and (c) 20 vol. % Sn in Ge.

Figure 1 shows the Fourier transforms of spectra taken at 10 K corresponding to the samples (a) Sn powder (b) ball milled Sn/Ge powder with 40 vol.% Sn and (c) ball milled Sn/Ge powder with 20 vol.% Sn. The evolution of a new phase is evident by the peak P_B, in the ball milled Sn/Ge samples. Analysis of data of the Sn/Ge sample with 20 vol.% Sn shows that this peak is due to change of coordination of environment of Sn from Sn to Ge neighbors.

Our approach to fitting the spectra was to use a 50 at.% SnGe alloy with a Sn atom surrounded by 4 Ge atoms in a chemically ordered zinc blend structure. This model is justified by the existence of 50 at. % α-SnGe epitaxial thin films grown on Ge substrates as has been reported by Hochst *et al.*[5] XAFS corresponding to the model was calculated using the FEFF theoretical code (Version 4.08). Figure 2 shows the corresponding fits made by inverse Fourier transforming the peak P_B at all three temperatures. A two shell model that included Sn-Sn near neighbors in the metallic Sn arrangement was also attempted to account for the presence of metallic

Sn as shown by very small peaks in the XRD spectrum at 20 vol. % Sn and observed during DSC analysis. Even though a satisfactory fit was made for data at 10 K, at 100 K and 200 K, the best fits were obtained for models that included only Sn-Ge near neighbors.

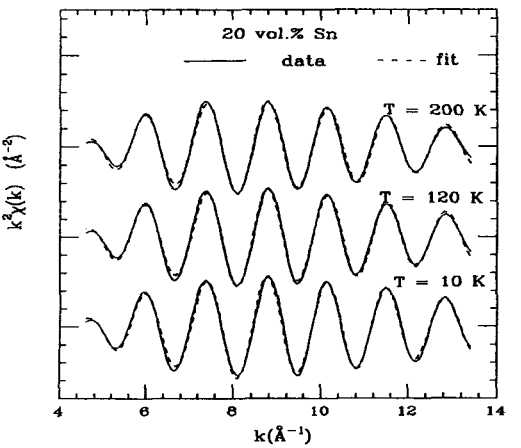

Figure 2. Fits (dashed lines) obtained for 20 vol. % Sn in Ge sample compared to data (solid line) at 10 K, 120 K and 200 K.

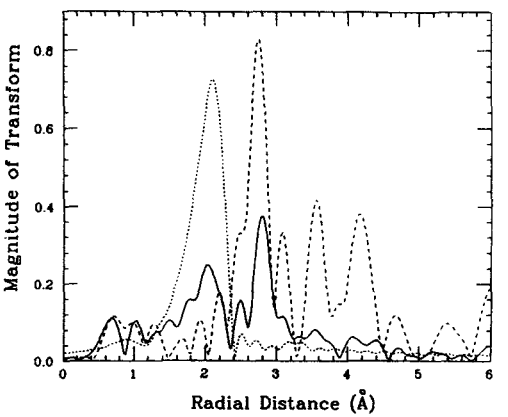

Figure 3. Fourier transforms of XAFS $k^2\chi(k)$ at 10 K for Sn K-edge for 10 vol. % Sn in Si (solid line), Sn powder (dashed line) and ,50 at. % SnSi alloy (dotted line).

A similar, but a less dramatic change was observed in the ball milled Sn/Si sample with 10 vol. % Sn. Figure 3 shows Fourier transforms of XAFS $k^2\chi(k)$ at 10

K corresponding to the sample with 10 vol.% Sn in comparison with the Fourier transforms of XAFS $k^2\chi(k)$ data of spectra corresponding to Sn powder (dashed line) and theoretical calculation for a 50 at. % SnSi alloy with the Sn atoms surrounded by 4 Si atoms in a chemically ordered zinc blend structure (dotted line). Figure 3 shows that Sn/Si powder sample contains a significant amount of metallic Sn even at a concentration of 10 vol. % Sn. The amounts of metallic Sn and 50 at. % SnSi alloy present in the sample were determined by fitting for data filtered in the range of 1.2 - 3.35 Å to include both peaks in the filtering range. Figure 4 shows fits obtained at all three temperatures, 10 K, 120 K and 200 K. Table 1 shows the results obtained from fitting.

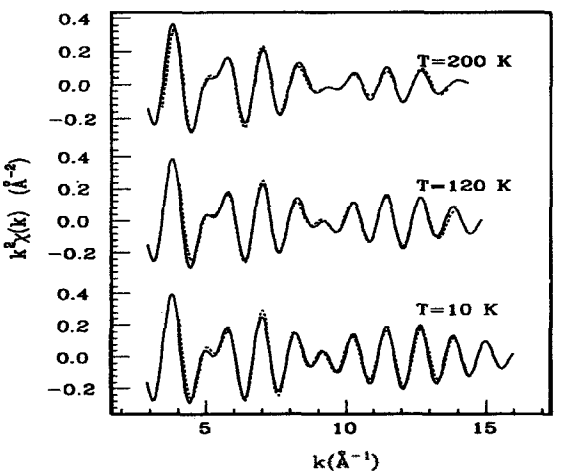

Figure 4. Fits (dashed lines) obtained for 10 vol. % Sn in Si sample, compared to data (solid line) at 10 K, 120 K and 200 K.

The variation of mean-square displacement (Debye-Waller factor), σ^2, of atoms in a coordination shell as a function of temperature was used to determine the nature of bonding between Sn-Ge and Sn-Si neighbors using the Einstein model of lattice vibrations[6,7]. By comparison with the experimentally obtained σ^2 values corresponding Einstein temperature was determined. The Einstein temperatures obtained for SnGe and SnSi alloys were 325±29 K and 351±37 K respectively. These values are in the range of Einstein temperatures found for the covalent bonding in tetrahedral semiconductors such as Ge (352 K), GaAs (318) and ZnSe (269 K) and are much higher than metallic Sn (150 K)[1].

Table 1. XAFS fitting results obtained for (a) 20 vol. % Sn/Ge sample and (b) 10 vol.% Sn/Si sample at three different temperatures.

(a) 20 vol.% Sn/Ge sample			
T(K)	$N_{Sn\text{-}Ge}$	$R_{Sn\text{-}Ge}$ (Å)	$\sigma^2_{Sn\text{-}Ge}$ (Å^2)
10	2.48 ± 0.40	2.64 ± 0.03	0.0031 ± 0.0009
120	2.52 ± 0.40	2.64 ± 0.03	0.0038± 0.0010
200	2.48 ± 0.40	2.64 ± 0.03	0.0043± 0.0012

(b) 10 vol.% Sn/Si sample					
T(K)	$N_{Sn\text{-}Si}$	$R_{Sn\text{-}Si}$ (Å)	$\sigma^2_{Sn\text{-}Si}$ (Å^2)	$N_{Sn\text{-}Sn}$	$\sigma^2_{Sn\text{-}Sn}$ (Å^2)
10	1.16 ± .12	2.59 ± .02	.0039 ± .0010	2.84 ± .12	.0012 ± .0010
120	1.08 ± .12	2.59 ± .02	.0040 ± .0015	2.89 ± .12	.0017 ± .0010
200	1.08 ± .12	2.59 ± .02	.0054 ± .0020	2.92 ± .12	.0017 ± .0010

The Sn-Ge and Sn-Si nearest neighbor distances, 2.64 Å and 2.59 Å, obtained from fitting, lead to lattice constants of 6.10 Å and 5.98 Å respectively for SnGe and SnSi alloys in the zinc blende structure. Interestingly, the crystallographic data show that the average of the lattice constants of Sn & Ge and Sn & Si are 6.10 Å and 5.96 Å respectively justifying the models that were used to fit the experimental data. Our analysis, however does not confirm whether the atomic arrangements of alloys are of ordered or disordered nature.

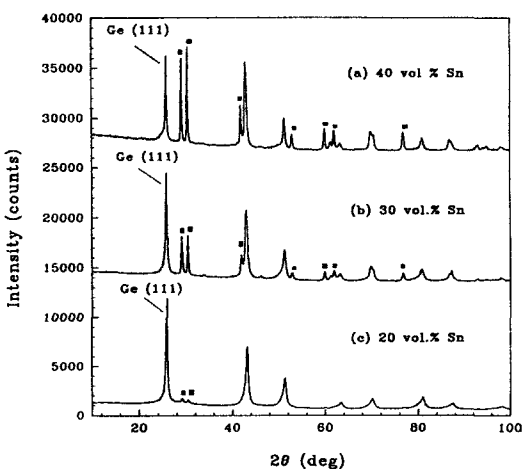

Figure 5. The x-ray diffraction data of Sn/Ge powders. Metallic Sn peaks are identified by ■.

The x-ray diffraction data (Figure 5) of Sn/Ge powders also shows a systematic decrease in the intensity of metallic Sn peaks with decreasing Sn

concentration. At 20 vol.% Sn, the Sn peaks have almost disappeared indicating that Sn is in a different state. Another clear feature is the systematic increase in broadening of the Ge peaks as the Sn concentration is decreased. Since the powders are ball milled, broadening can be caused by both the particle size and a non-uniform strain. Therefore in order to determine the particle size, the method described by DeKeijser *et al.*[8] was applied. The results are given in Table 2.

The DSC analysis showed a reduction of melting enthalpy of Sn in Sn/Ge samples showing that the enthalpy decreases significantly at 20 vol. % Sn (3.6 J/g) compared to pure Sn powder (61.5 J/g). These results were consistent with previously made observations[1]. A similar decrease was observed in Sn/Si powders.

Table 2. Average particle sizes of Ge and Si particles in Sn/Ge samples and Sn/Si samples at three different Sn concentrations.

Sn/Ge powders		Sn/Si powders	
Sample (vol.% of Sn)	Average Ge particle size D (Å)	Sample (vol.% of Sn)	Average Si particle size D (Å)
40	405 ± 155	40	795 ± 225
30	300 ± 95	25	640 ± 180
20	250 ± 70	10	170 ± 55

4. Discussion

Our analysis identified a new phase that evolved at the Sn-Ge and Sn-Si interfaces as suggested by Turnbull *et al.*[9]. Sn/Ge samples of higher Sn concentrations contained a mixture of bulk and interfacial Sn phases. At 20 vol.% Sn, the sample essentially contained only the interfacial phase. In Sn/Si powder samples, the interfacial phase could not be isolated even at 10 vol. % of Sn. This is attributed to the higher lattice mismatch between Sn and Si which is 20% compared to that between Sn and Ge (14.3%). XAFS analysis showed that the interfacial phase is due to the formation of SnGe and SnSi alloys in the two systems. Decreasing enthalpy of melting in the two systems confirmed that the alloys were stable above the melting point of metallic Sn. This is further supported by the theoretical work of Brudevoll *et al.*[10]. An estimate was made to find out the extent of alloying around core Ge and Si particles of the powders at 20 vol. % of Sn in Ge and 10 vol. % of Sn in Si respectively. It was assumed that the particles have a cubic geometry with their body diagonal being equal to the average particle size determined using XRD line broadening. The extent of SnGe layer around Ge core particles was found to be approximately 9 Å which is equivalent to roughly four monolayers. The extent of the SnSi alloy around Si particles was found to be approximately 2 Å showing the

interfacial alloying between Sn and Si was less extensive. The XRD spectra did not show evidence for the presence of alloy in the powder samples due to the relatively smaller extent of interfacial alloying or their disordered nature or both. It will be interesting to characterize these particles from nano-science point of view.

5. Conclusions

Ball milling was used to mill the Sn/Ge and Sn/Si powders with varying Sn concentrations. Particle size estimated by XRD line broadening showed that both Ge and Si particles reach nano-scale dimensions below the exciton Bohr radii of them. Around Ge and Si particles, stable SnGe and SnSi alloy phases of small thickness are formed. The extent of alloying of SnGe around Ge particles was higher compared to that of SnSi around Si core particles.

Acknowledgements

This work was supported by the U.S. Department of Energy, Division of Materials under Contract No. DE-AC02-76CH00016. The X-11 beamlines are also supported by the DOE Division of Materials under Contract No. DE-AS05-80ER10742. J.K.D.S.J thanks the University of Colombo, Sri Lanka for granting him leave during this period.

References

1. J. S. C. Jang and C. C. Koch, *J. Mater . Res.* **5**, 325 (1990)
2. J. K. D. S. Jayanetti, S. M. Heald and Z. Tan, *Phys. Rev. B* **47**, 2465 (1993)
3. J. K. D. S. Jayanetti, *Ph.D. Thesis, City University of New York, USA* (1993)
4. S. M. Heald, S. Jayanetti and K. I. Pandya, *Jpn. J. Appl. Phys.* **32**, 499 (1992)
5. H. Hochst, M. A. Engelhardt, and I. Hernandez-Calderon, *Phys. Rev. B* **40**, 9703 (1989)
6. B. A. Bunker, *Ph.D. Thesis, University of Washington, USA* (1980)
7. E. Sevillano, H. Meuth and J. J. Rehr, *Phys. Rev. B* **20**, 4908 (1979)
8. C. Balasingh, A. Abuhasan and P.K. Predeki, *Powder Diffraction* **6**, 16 (1991)
9. D. Turnbull, J. S. C. Jang, and C. C. Koch, *J. Mater. Res.* **5**, 1731 (1990)
10. T. Brudevoll, D. S. Citrin, N. E. Christensen and M. Cardona, *Phys. Rev. B* **48**, 17128 (1993)

SYNTHESIS OF ULTRAFINE AND CRYSTALLIZED TiO_2 BY ALKOXIDE FREE POLYMERIZABLE PRECURSOR METHOD

M. VIJAYAKUMAR*, M-P. CROSNIER-LOPEZ,

Claude BOHNKE , Odile BOHNKE

[1] *Laboratoire des Oxydes et Fluorures, UMR 6010 CNRS*

Institut de Recherche en Ingénierie Moléculaire et Matériaux Fonctionnels, FR CNRS 2575

Université du Maine, Av. O. Messiaen, 72085 LE MANS Cedex 9, France

The fine powder of TiO_2 has been synthesized by totally alkoxide free sol gel method. The ammonium citratoperoxotitanate (IV) has been synthesized and used as molecular precursor which is highly stable in air. This starting precursor allows us to avoid the use of titanium alkoxide or titanium tetrachloride, which are extensively reported in literature. The synthesis has been carried out in ambient atmospheric conditions. The modified polymerizable precursor method has been adopted for the sol gel chemistry of TiO_2. The final powder precursor has been analysed by thermal analysis (TG and DTA) to explore the thermal kinetics. The X-ray diffraction analysis through Rietveld method confirms that the final product is highly pure rutile TiO_2 powder. The laser granulometry and SEM analysis show the agglomeration of fine particles with size in the order of 200 nm.

1. Introduction

The titanium oxide (TiO_2) is one of the most promising materials due to its potential applications in various fields such as, photocatalysis, solar energy, emulsion and gas sensors [1]. Apart from these applications, the recent developments of polymer electrolytes with dispersed TiO_2 powder also spurred the research interest in this material [2]. Hence there is strong urge to develop fine powder of TiO_2 material for these applications and various authors reported the formation of fine powders by various methods (wet chemical method, sol gel method etc.,) [3,4]. Especially the sol gel method, which is well known for the synthesis of metal oxides, is studied extensively for the preparation of TiO_2 powder. The conventional sol gel methods are based on the hydrolysis and condensation of the molecular precursors. So far the researchers developed the titanium oxide by sol gel methods using the titanium alkoxides (such as titanium isopropoxide etc.,) or titanium tetrachloride ($TiCl_4$) as molecular precursors which are highly reactive and sensitive to moisture. Further it is very difficult to control hydrolysis reaction rates of these molecular precursors

*Present Address: Department of Physics, College of William and Mary, Williamsburg, VA-23187, USA. *E-mail: mxvija@wm.edu*

due their high reactivity, which results in the loss of microstructural control over the final oxide. Hence the whole experiments should be carried out in an inert atmosphere, which makes the synthesis process more difficult in nature. P.Arnal et al, [5] suggested the use of non-hydrolytic method to control the reactivity of these molecular precursors and to synthesize titanium oxides. Even this non hydrolytic method needs complicated reactions such as etherolysis and alcoholysis of $TiCl_4$ to reduce the reactivity of the molecular precursor $TiCl_4$. Hence there is a strong need to find a simple and atmospheric friendly way to obtain a titanium oxide using the sol gel synthesis. Recently Kakihana et al [6], reported the formation of highly water soluble titanium citrate complex, by using titanium metal powder and citric acid. This titanium citrate complex has been used as molecular precursor for the synthesis of TiO_2 by polymerizable method and the detailed procedure of synthesis has been described in this paper.

2. Experimental

For the synthesis of fine powder of TiO_2, Ti powder (98.5 %) from Fluka ,hydrogen peroxide (30 %) from Carlo Erba and ammonia (35 %) from Fischer Scientific, citric acid (99.5 %) and ethylene glycol (99 %) from Aldrich are used as starting materials. The detailed procedure of the synthesis is given in the next part of the paper. Thermal analysis (TGA and DTA) were performed with a Setaram TGDTA92 equipment at a heating rate of 5 °C min^{-1} in air using Pt crucibles. Powder X-ray diffraction patterns (CuK_α radiation) have been recorded at room temperature with a Philips X'Pert PRO diffractometer, equipped with a X'celerator detector, in the 2θ range from 5 to 123° with an interpolated step of 0.008°. The Rietveld method [7] using the Fullprof program [8] is used for the structural refinement with a peak shape described by a pseudo-Voigt function. In addition to the lattice and atomic parameters, the zero shift, the scale factors and the background parameters are also refined.

Microstructure observations were performed using a Hitachi 2300 Scanning Electron Microscope (SEM). Granulometry has been carried out with a Beckman Coulter equipment in water at room temperature. In-situ ultrasonic vibration has been used before measurement of the particles size.

3. Results and Discussion

3.1 Synthesis and calcination of the polymer precursor

The crucial step in this modified Pechini-type method was to prepare a highly water soluble precursor to avoid the use of alkoxides, which are not stable in open air. This has been carried out by dissolution of Ti metal in hydrogen peroxide and ammonia solution, as previously reported [9]. Initially 0.25 g of Ti metal powder is dissolved in cold aqueous solution containing 20 ml of H_2O_2 (30 %) and 5 ml ammonia solution (35%) at room temperature. This yields a yellowish transparent solution which is a peroxo complex of titanium, such as peroxy titanate

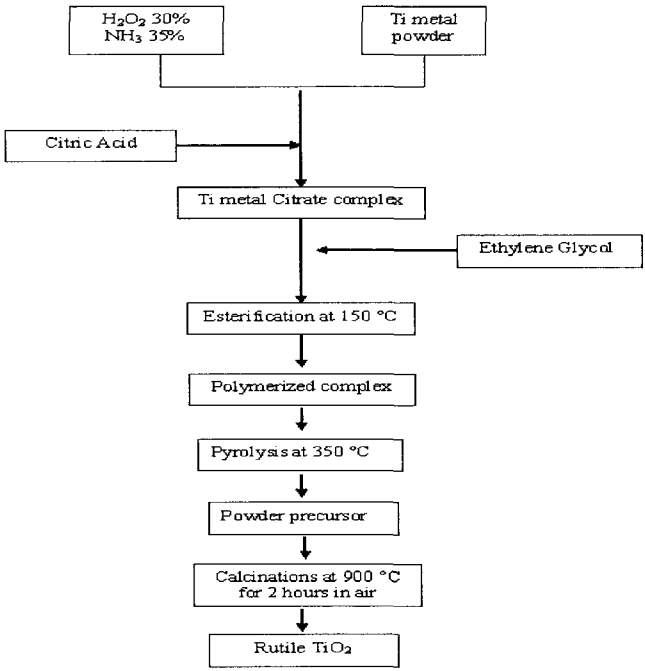

Fig.1. Flow chart for preparing TiO_2 by a modified Pechini-type polymerizable precursor technique.

$[Ti(OH)_3O_2]^-$ ion [10]. In order to form titanium metal citrate complex, 0.1 mol% of Citric acid (19.2 g) is added in excess to the above titanium peroxo solution. This reaction yield citratoperoxotitanate $[Ti(C_6H_4O_7)O_2]^{2-}$ which is highly soluble in water [11]. This titanium metal citrate complex has been added with 0.4 mol% of Ethylene glycol (25 g), which results in redish color viscous solution. The citric acid / ethylene glycol molar ratio was taken as 1:4. This ratio ensures a large excess of hydroxyl groups to promote the formation of low molecular weight oligomers [12]. The temperature is then increased to 150 °C to promote esterification between the hydroxyl groups of ethylene glycol and the carboxylic acid groups of citric acid and polymerization. A black polymer precursor, which is stable in air, is then formed. Therefore pyrolysis of the polymer is performed at 350 °C that yields a black powder precursor, called hereafter "powder precursor". The black color indicates that the powder contains carbon. The final powder precursor is subjected to calcination in open air for 2 hours at 900 °C. The calcination at 900 °C yields highly pure and rutile phase TiO_2 powder. Fig.1 shows the typical flow chart of the synthesis procedure used to prepare TiO_2.

3.2 TGA-DTA analysis

Fig.2 shows the TGA and DTA curves obtained from the powder precursor in air using a heating rate of 5 °C min^{-1} in the temperature range from 30 to 1200 °C. The TGA curve indicates a small weight loss of 3 % up to 100 °C, an abrupt weight loss of 81 % in the temperature range from 300 to 500 °C and no further weight loss up to 1200 °C. The first weight loss is mostly due to water desorption. The second abrupt weight loss is due to the degradation of the polymer, converting the organic component into CO_2 and H_2O.

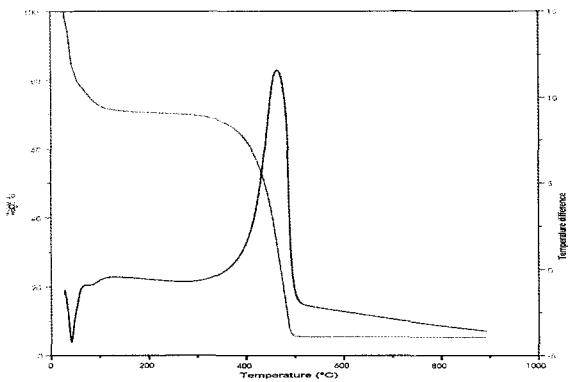

Fig.2 TG and DTA spectrum of the TiO_2 precursor measured in open air atmosphere

The DTA curve shows three exothermic peaks in the temperature range from 300 to 600 °C. They can be associated to the weight loss shown in the TGA curve and are indicative of organic combustion steps. The main exothermic peak around 500 °C is due to the degradation of organic material from the powder precursor that is accompanied to CO_2 and H_2O gases evolution and then to a considerable weight loss. After this, there is no change in weight, which confirms the complete burnout of residual carbon from the precursors.

3.3 XRD analysis

Fig. 3 shows the powder X-ray diffraction pattern of the rutile TiO_2, synthesized by sol gel method. The X-ray diffraction pattern has been analysed by pattern matching through the Fullproof software. The theoretical and experimental peak matches well and no impurity phases have been identified by this pattern matching analysis. The structure of the rutile TiO_2 has been identified as tetragonal

(space group P 42/M N M) and the cell parameters are found to be a = b = 4.5938 Å and c = 2.9598 Å, which agrees with previous reported values [13].

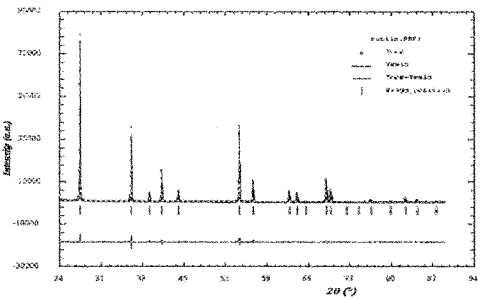

Fig.3 Calculated and observed powder X-ray diffraction pattern of TiO_2 sample prepared by a modified Pechini-type polymerizable precursor technique

3.4 Morphology of the TiO_2 powder

Fig. 4 shows SEM micrographs of TiO_2 after calcination at 900 °C. It reveals the microstructure of the ceramic. It can be observed that after heating at 900 °C for 2 hours, the ceramic is made of small grains of diameter around 200 nm (Fig. 4). However these grains agglomerate as shown in Fig. 4b. These agglomerates, as big as 100 μm can be observed. This is clearly revealed by laser granulometry, (not shown here), which shows the average agglomerated particle size as ~50 μm. The particle size histogram has been obtained from the same TiO_2 powder as used for SEM experiments. The powder has been ultrasonically treated in-situ in water for 1 min with a power of 20 W. This indicates that the grains are strongly bounded with each others.

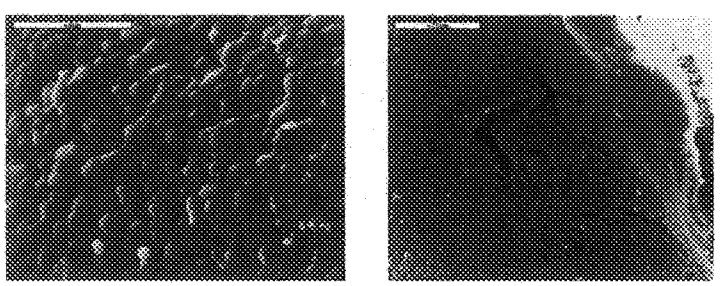

Fig. 4 SEM image of the rutile TiO_2 prepared by polymerizable precursor method.

4. CONCLUSION

The rutile phase, TiO_2, has been synthesized by a Pechini-type polymerizable precursor method using highly water soluble Titanium metal citrate molecular precursor. This highly water soluble precursor helps us to avoid the use of alkoxides, which are not stable in open air. The final powder, obtained by heating the powder precursor at 900 °C for 2 hours in air, is a pure and well crystallized rutile phase of TiO_2 as revealed by powder X-ray diffraction. Both SEM and granulometry showed that the final powder is made of small particles of around 200 nm in size.

ACKNOWLEDGMENTS

The author M.Vijayakumar thanks the "Région des Pays de la Loire" for postdoctoral fellowship. We also thank Prof. Yoshioki Inaguma, Gakushuin University, Japan for his fruitful discussions and M. J-J. Péchon-Rossel from the Institute of Technology of the "Université du Maine" for the possibility of granulometry measurements.

REFERENCES

1. (a)A. Fujishima, T. N. Rao, Donald A. Tryk, Journal of Photochemistry and Photobiology C: Photochemistry Reviews 1 (2000) 1-21 [and references therein] (b) B.O. Regan and M. Grätzel, *Nature* 353 (1991), pp. 737–740.
2. J. -H. Ahn, G. X. Wang, H. K. Liu and S. X. Dou, *Journal of Power Sources, 119-121, (2003),422-42.*
3. N. Uekawa, J. Kajiwara, K. Kakegawa and Y. Sasaki, Journal of Colloid and Interface Science,250, (2002) 285 – 290.
4. S.R.Dhage, Renu Pasricha, V.Ravi, Materials Research Bulletin 38 (2003) 1623-1628.
5. L. Miao , S. Tanemura , S. Toh , K. Kaneko and M. Tanemura, *Journal of Crystal Growth, 264, 1-3,(2004), 246-252*
6. P. Arnal, R.J.P. Corriu, D. Leclercq, P.H. Mutin and A.Vioux, Journal of Materials Chemistry, 6, *12,(1996) 1925 – 1932.*
7. M.Kakihana, J. Szanics and M. Tada, Bull.Korean Chem.Soc. 20 (1999) 893-896.
8. Rietveld, H.M; J. Appl. Crystallogr. 2, 1969, 65
9. J.R. Carjaval, FULLPROF program, Rietveld Pattern Matching Analysis of Powder Patterns, ILL, Grenoble, 1990.
10. M. Tada, K. Tomita, V. Petrykin and M. Kakihana, *Solid State Ionics, 151, (2002), 293-297*
11. M. Kakihana, M. Tada, M. Shiro, V. Petrykinm Minoru Osada and Y. Nakamura, Inorganic Chemistry 40, (2001) 891-894.
12. Liu, W; Farrington, G.C; Chaput, F; Dunnm, B; J.Electrochem.Soc, 143 (1996) 879.
13. V. Swamy, J. D. Gale and L. S. Dubrovinsky, Journal of Phys. and Chem. of Solids 62 (2001) 887-895.

DEVELOPMENT AND CHARACTERIZATION OF POLYTHIOPHENE/FULLERENE COMPOSITE SOLAR CELLS AND THEIR DEGRADATION STUDIES.

BY

P. K. BHATNAGAR*, SUKHBINDER SINGH, P. C. MATHUR

DEPARTMENT OF ELECTRONIC SCIENCE, UNIVERSITY OF DELHI SOUTH CAMPUS, BENITO JUAREZ ROAD, NEW DELHI-110 021,INDIA.

SANDIP K. SENGUPTA AND JAYANT KUMAR

CENTER FOR ADVANCED MATERIALS, UNIVERSITY OF MASSACHUSETTS AT LOWELL, MA 01854.

Abstract

The development of polymer-fullerene plastic solar cells has made significant progress in recent years. The quality of the device depends on the efficiency of the photoinduced charge generation and on how fast these charges are separated so that the excitons are not able to decay radiatively to ground state emitting photoluminescence. For the excitons to be broken into free charge carriers and for their fast collection it is necessary to use a composite structure of the device such as P3HT/C_{60}. The former being a donor and the later being an acceptor for the photoinduced electrons. An interpenetrating phase segregated structure of the donor and the acceptor helps fast collection (within few femtoseconds) of the photoinduced carriers. Besides these there are other factors also which affect the efficiency and shelf life of plastic solar cells. We have studied these factors using the solar cell structure ITO/PEDOT:PSS/P3HT:C_{60}/LiF/Al.We have found that the selection of the solvent, morphology of the film and the ratio of the donor P3HT and acceptor C_{60} (Buck minster fullerene) are some of the important factors on which the stability and shelf life of the PV cell depend. Selection of a proper solvent on the basis of parameters such as index of refraction, dielectric constant, molecular size and Hildebrand solubility parameter is extremely important in order to achieve high efficiency, stability and long shelf life of the device. It has also been found that increasing the C_{60} content in the polymer leads to a decrease in degradation of the device but excess amounts of C_{60} speeds up the degradation process.

Introduction

Solar Cells developed from conjugated polymers have distinct advantages over conventional solar cells fabricated from inorganic semiconductors. Some of these are:

1. The absorption coefficient of conducting polymers is much higher (~10^6 Cm^{-1}) as compared to that for inorganic semiconductors (10^2 - 10^3 Cm^{-1} for Si). A thin layer of conducting polymer ~ 100 nm is therefore enough to absorb the solar spectrum. Large area, uniform and mechanically flexible polymer thin films can be grown from solution at low cost using environmentally friendly non toxic processing techniques.
2. The electronic properties of the conducting polymers can be easily adjusted through changes in their molecular structure [1].
3. The optical properties of the conjugated polymer systems can be easily controlled. For example doping a conducting polymer only with a few weight percent of fullerene can enhance the photoconductivity by more than two orders of magnitude [2,3].

A very distinct feature of conducting polymer-based solar cells is that the photo absorption leads to the production of excitons and not free electro-hole pairs as the case with inorganic semiconductors. These excitons have a typical lifetime of few picoseconds [4] and they decay to the ground state emitting photoluminescence (PL) or they can decay even non-radiatively. For the solar cell to function, it is essential that these photoinduced excitons dissociate into free charges which are collected by the electrodes before the excitons get chance to decay. This can be achieved by mixing a suitable material such as fullerene, which has a high electron affinity and thus can break the exciton. The electron can be collected at the LUMO level of the fullerene. Similarly if the ionization potential of the polymer is higher as compared to the fullerene, the excitons will be dissociated and the holes will be collected at the HOMO level of the polymer. This charge transfer must occur within a few femtoseconds in order that the solar cell works efficiently.

In order to achieve such a fast charge transfer, the polymer (donor)–fullerene (acceptor) composite should form a phase segregated interpenetrating structure on a nanometric scale [5-7]. While such structures have a very high potential for developing stable and efficient solar cells, the morphology of the donor acceptor blend plays a very important role.

In the present work we have investigated the effect of the solvent and composition on the donor-acceptor P3HT/C_{60} structures and have examined some of the factors, which significantly affect the stability, and shelf life of a heterojunction polymer photovoltaic (PV) cell and the results have been presented for a typical ITO/PEDOT:PSS/P3HT:C_{60}/LiF/Al solar cell structure.

We have found that the selection of the solvent, morphology of the film and the ratio of the donor P3HT and acceptor C_{60} (Buck minster fullerene) are some of the important factors on which the stability and shelf life of the PV cell depend. It has also been found that the absorption coefficient decreases with ageing leading to degradation of the solar cell shelf life. The decrease in absorption coefficient may be due to changes in film morphology with time. Yet another factor, which may affect the performance of the solar cell is the blue shift observed in the absorption spectrum and the decrease in the absorption coefficient with the increase in concentration of C_{60} in the active polymer P3HT. It has been concluded that the solubility of the solvent should not be the sole criteria for its selection but the other solvent properties such as index of refraction, dielectric constant, molecular size and Hildebrand solubility parameter must match with those of the solute. Since C_{60} has lower solubility as compared to the polymer, in the present work the solvent selection has been made on the basis of properties of C_{60}. As shown by Ruoff et. all [8], C_{60} with an index of refraction n =1.96, static dielectric constant ε=3.61 and molar volume V = 429cm^3mol^{-1} has high solubility (mg/ml) in Xylene, 1,2-dichlorobenzene, and 1,2,4-trichlorobenzene. Investigations were made using these

three solvents. It was found that although the solubility of C_{60} is higher in 1,2-dichlorobenzene, yet this solvent is not satisfactory for the solar cell stability since the above-mentioned parameters for this solvent and C_{60} widely differ. It was found the decrease of absorption coefficient due to ageing with 1,2,4-tricholorobenzene, as a solvent is much lower therefore it is a better solvent in spite of its slightly lower solubility for C_{60}.

Experimental Details

The devices were prepared from P3HT and C_{60} dissolved in a common solvent 1,2,4-trichlorobenzene in the ratios of P3HT:C_{60} varying from 1:0.25 to 1:2 by weight. The prepared solutions were ultrasonically mixed and were filtered using 0.45-micron syringe filters. The devices were fabricated on ITO coated glass substrates (resistivity~15 ohmcm). The ITO was patterned using PVC tape and HCl as the etchant for a duration of 15 min. The ITO was patterned into 0.3 cm wide strips with a separation of 0.5 cm between successive strips. The etched glass (substrate) was washed with sodium bicarbonate solution to neutralize any residual acid. The PVC tape was removed and the substrates were cleaned in an ultrasonic cleaner using acetone and subsequently isopropyl alcohol. The substrates were then dried in a nitrogen atmosphere and were spin coated with a 100nm thick PEDOT:PSS layer (1.3wt% Sigma Aldrich). The polymer fullerene blend was spin cast on the dried PEDOT:PSS layer and the thickness of the film was kept between 80 to 100nm. After drying the polymer:C_{60} composite layer a thin film of LiF (thickness ~1nm) was deposited under vacuum (10^{-6} torr) onto the polymer composite layer. Subsequently a layer of Al (thickness ~100nm) was evaporated onto the LiF layer. The structure so obtained was ITO/PEDOT:PSS/P3HT:C_{60}/LiF/Al with the ITO being the positive electrode and Al the negative electrode for the illuminated solar cell. A single substrate contained four devices of 0.09cm^2 area each. To improve the morphology [9] the device was annealed at 140°C for 4 minutes in inert atmosphere. For absorption studies the samples were spin cast using the polymer fullerene blends onto ultrasonically

cleaned glass slides. The absorption measurements were made using a Shimadzu UV-2450 UV-VIS spectrometer.

Results

The absorption spectrum for P3HT:C_{60} composites corresponding to various concentrations of C_{60} in 1,2,4-trichlorobenzene is shown in Fig.1. It is found that addition of C_{60} leads to broadening of the absorption spectrum, which is very desirable for a photovoltaic device. However the disadvantage of adding C_{60} is that there is a decrease in the peak intensity of the absorption spectrum with the increase of C_{60} concentration. It is also observed that there is a significant shift in the absorption peak towards lower wavelength for concentration of C_{60} beyond 0.5 ratios by weight. This is a great disadvantage because the useful wavelength is in the wavelength range 500-600nm. Therefore it is concluded that while the presence of C_{60} is highly essential, to achieve a fast transfer of photoinduced charges. Its concentration must be chosen very carefully.

The variation of open circuit voltage Voc for the solar cell for different composite ratios of C_{60} is shown in Fig.2. The variation of short circuit current density Jsc with concentration of C60 is also shown in fig. 2 (inset) and it follows the same pattern as Voc. It is found that the value of Voc increases initially with the increase of concentration of C_{60}, reaches a maximum for C_{60} = 0.5 ratio by weight and subsequently decreases rapidly with increase in C_{60} concentration. The initial increase in Voc with the concentration of C_{60} is due to increase in rate of photo induced charge transfer. However for concentrations of C_{60} beyond 0.5 the decrease in the absorption coefficient becomes significant, resulting in a lower value of Voc. Similar studies were also made using 1,2-dichlorobenzene as the solvent. It was found that for this solvent the value of Voc is lower as compared to that obtained for 1,2,4-trichlorobenzene (e.g. for C_{60} = 0.5 by weight

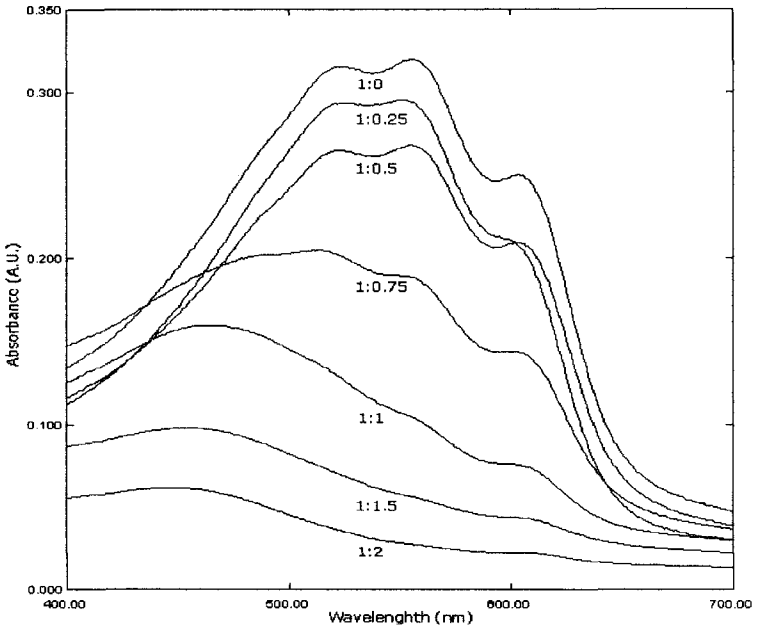

Fig. 1 Absorption for different P3HT:C_{60} composite ratios

Voc = 0.58V for 1,2,4-trichlorobenzene and Voc = 0.40V for 1,2-dichlorobenzene). The results with Xylene as the solvent are even worse and hence this solvent was not used for further studies.

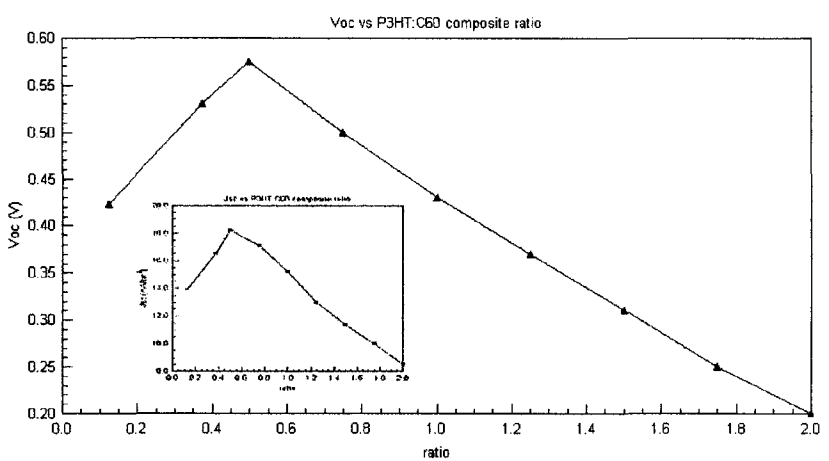

Fig. 2 Variation of V_{oc} with concentration of C_{60}; variation of J_{sc} with concentration of C_{60} (inset)

The absorption coefficient was measured immediately after the devices were fabricated and after also after 1 and 2 week durations of storage at room temperature under dark conditions in ambient atmosphere. The absorption coefficients for various concentrations of C_{60} for 1 and 2-week storage durations are shown in Fig.3 and Fig.4 respectively. A decrease in the absorption coefficient with the passage of time is observed. A significant result of this study is that the degradation of absorption coefficient is minimum for 1:1 ratio of P3HT:C_{60}. Similar measurements of absorption coefficient were also made using 1,2-dichlorobenzene. It was found that the decrease of absorption coefficient with increase in storage time in this case is much faster (e.g. for the 1:0.75 ratio the decrease in absorption coefficient in one week for this case is 9.9% while for the case of 1,2,4-trichlorobenzene, the absorption coefficient decreases only by 8.5% in one week.

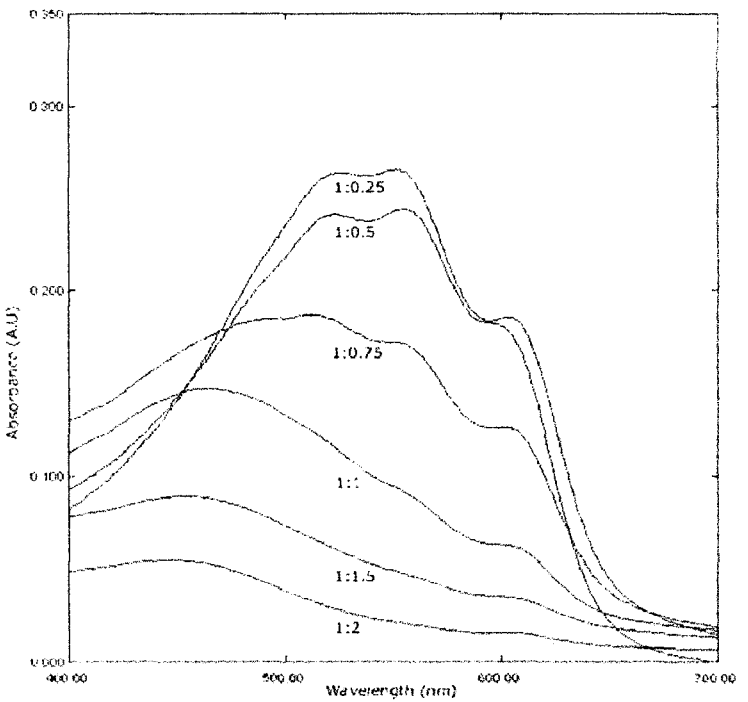

Fig.3 Absorption for different P3HT:C_{60} concentrations after 1 week duration

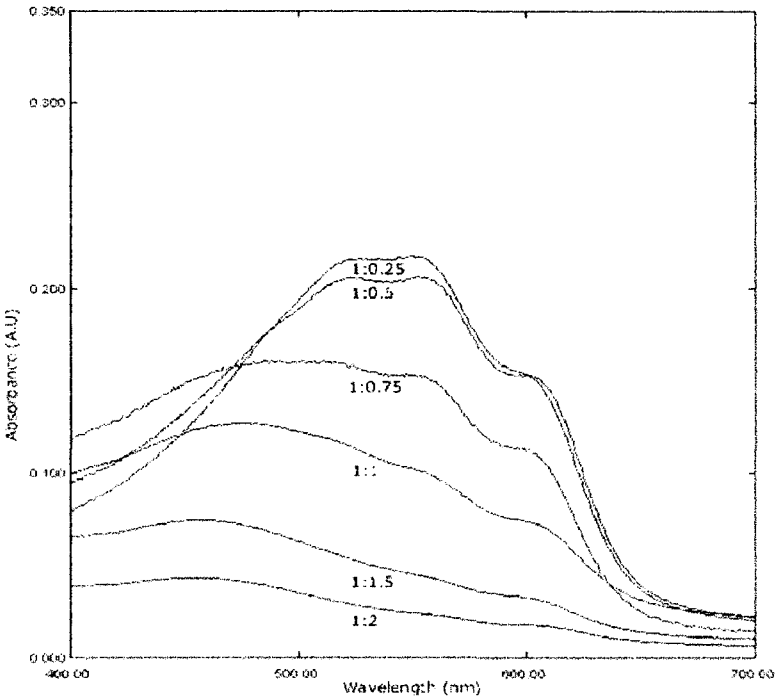

Fig.4 Absorption for different P3HT:C_{60} concentrations after 2 week duration

The observed decrease in the absorption coefficient with time may be due to the oxidation of the polymer. However a significant feature of the result is that as the concentration of C_{60} increases from 1:0 to 1:1 weight ratio, the degradation of absorption coefficient diminishes, the degradation of absorption coefficient with the passage of time becomes slower. The degradation of absorption coefficient becomes faster when the weight ratio of C_{60} becomes higher than 1. In the initial stages, the C_{60} retards the oxidation of the polymer by allowing the formation of positive charged polarons on the chains, which decreases strongly the reactivity of the polymer against oxygen [10]. The increase in degradation with C_{60} concentration above 1:1 is due to phase segregation [11].

Suitable electrical contacts were developed for the I-V measurements. ITO was taken as the lower contact and vacuum deposited aluminum served as upper contact. P3HT/C_{60} composites showed an increase in the photocurrent with the increasing C_{60} content. Addition of C_{60} allows ultra fast photo-induced electron transfer from the P3HT to C_{60} and enhances the charge carrier generation in the P3HT by preventing recombination. However, the I-V measurements also confirmed that the rate of increase of current decreases with increasing concentration of C_{60} above 1:1. Therefore optimization of the composite ratio is necessary for best performance of the device. The 1:0.75 composite ratio was found to be the best choice in terms of absorption and I-V measurements. PEDOT: PSS is known as a p type semiconductor, a good hole transport material, and assures a better hole collection from the polymer/fullerene composite layer on to the ITO electrode. The PEDOT: PSS spin coated on to the ITO smoothens its surface and therefore any possible short-circuiting due to the spiky roughness of the surface is prevented. A thin LiF (<15 Å) layer between the polymer/fullerene blend and the aluminum layer increases both the open circuit voltage and the fill factor of the device, yielding increased power conversion efficiency [12].

Conclusions

It can be concluded from the present work that the solubility should not be the main criterion for selecting a solvent for a conjugated polymer, care should be taken to match the parameters such as index of refraction, dielectric constant, molecular size and Hildebrand solubility parameter for the solute and the solvent in order to achieve high stability and long shelf life of the PV cell. It also follows from the present work that the concentration of C_{60} should be optimized in view of the fact that it reduces the absorption and shifts the absorption spectrum to lower wavelengths.

References

[1] Allen J. Heeger, *Solid State Communication*, **107**, 673, (1998).

[2] C. S. Kuo, F. G. Wakin, S. K. Sengupta and S. K. Tripathy, *Solid State Communication*, **87**, 115, (1993).

[3] N. S. Sarisiftci, L. Smilowitz, A. J. Heeger and F. Wudl, *Science*, **258**, 1474, (1992).

[4] C. J. Brabec, G. Cerullio, S. De-Silvestric, S. Luzatti, J. C. Hummelen and N. S. Sarisiftci, *Chem Phys. Lett.*, **340**, 232, (2001).

[5] H. Antoniadis, B. R. Hsieh, Abkowitz, S. A. Jenekhe, M. Stolka, *Synth. Met.*, **62**, 265, (1994).

[6] W. R. Seleneck, *Philos Trans.Roy Soc.London Ser.A.* , **355**, 789, (1997).

[7] J. M. Halls, R.H.Friend, *Synth.Met.*, **85**, 1307, (1997).

[8] R.S.Ruoff, Doris S. Tse, Ripudaman Malhotra, Donald C. Lorents, *J. Phy. Chem.* **97**, 3379, (1993).

[9] Y. Kim, S. Cook, S. A. Choulis, J. Nelson, J. R. Durrant, D. D. C. Bradley, *Synth. Met.*, **152**, 105, (2005).

[10] H.Neugebauer, C. J. Brabec, J.C.Hummelen, N.S.Sariciftci, *Solar Energy Materials & Solar Cells*, **61**, 35 (2000).

[11] Z.Zhu, S.HadjiKyriacon, D.Waller, R.Gandiana, *Journal of Macromolecular Science Part-A-Pure And Applied Chemistry* **41**, 1467, (2004).

[12] C. J Brabec, S. E. Shaheen, C. Winder and N. S. Sariciftci, *Appl. Phys. Lett.*, **80**, 1288, (2002).

This page is intentionally left blank

Author Index

6170 hc
ISBN 981-256-877-8

www.worldscientific.com